UNCLASSIFIED

AD NUMBER

AD512542

CLASSIFICATION CHANGES

TO: **unclassified**

FROM: **confidential**

LIMITATION CHANGES

TO:

Approved for public release, distribution unlimited

FROM:

Distribution authorized to U.S. Gov't. agencies and their contractors; Administrative/Operational Use; JAN 1970. Other requests shall be referred to Air Force Flight Dynamics Lab., Wright-Patterson AFB, OH 45433.

AUTHORITY

WL/DOOS ltr, 7 Feb 1991; WL/DOOS ltr, 7 Feb 1991

THIS PAGE IS UNCLASSIFIED

AD- 512542

SECURITY REMARKING REQUIREMENTS

DOD 5200.1-R, DEC 78

REVIEW ON 28 JAN 90

SECURITY

MARKING

The classified or limited status of this report applies to each page, unless otherwise marked.
Separate page printouts MUST be marked accordingly.

THIS DOCUMENT CONTAINS INFORMATION AFFECTING THE NATIONAL DEFENSE OF THE UNITED STATES WITHIN THE MEANING OF THE ESPIONAGE LAWS, TITLE 18, U.S.C., SECTIONS 793 AND 794. THE TRANSMISSION OR THE REVELATION OF ITS CONTENTS IN ANY MANNER TO AN UNAUTHORIZED PERSON IS PROHIBITED BY LAW.

NOTICE: When government or other drawings, specifications or other data are used for any purpose other than in connection with a definitely related government procurement operation, the U. S. Government thereby incurs no responsibility, nor any obligation whatsoever; and the fact that the Government may have formulated, furnished, or in any way supplied the said drawings, specifications, or other data is not to be regarded by implication or otherwise as in any manner licensing the holder or any other person or corporation, or conveying any rights or permission to manufacture, use or sell any patented invention that may in any way be related thereto.

CONFIDENTIAL

AFFDL-TR-70-66

AD512542

AD512542

(TITLE UNCLASSIFIED)

INVESTIGATION OF AIRFRAME-INLET INTERACTION FOR SUPERSONIC TACTICAL FIGHTER AIRCRAFT

Constant Prokop
Robert J. Sanator
Fairchild Hiller - Republic Aviation Division

TECHNICAL REPORT AFFDL-TR- 70-66
January 1970

DDC
RECEIVED
DEC 9 [illegible]
A

STATEMENT #2 CLASSIFIED

In addition to security [illegible] must be met, this
document is subje[illegible] each
transmittal to [illegible] is may
be made only with [illegible]

Group 3 - Optional - Not Automatically Declassified

THIS MATERIAL CONTAINS INFORMATION AFFECTING THE NATIONAL DEFENSE OF THE UNITED STATES WITHIN THE MEANING OF THE ESPIONAGE LAWS, TITLE 18 U.S.C., SECTIONS 793 AND 794, THE TRANSMISSION OR REVELATION OF WHICH IN ANY MANNER TO AN UNAUTHORIZED PERSON IS PROHIBITED BY LAW.

Air Force Flight Dynamics Laboratory /FDMM
Air Force Systems Command
Wright-Patterson Air Force Base, Ohio 45433

CONFIDENTIAL

DOWNGRADED AT 12 YEAR
INTERVALS; NOT AUTOMATICALLY
DECLASSIFIED. DOD DIR 5200.10

(TITLE UNCLASSIFIED)

INVESTIGATION OF AIRFRAME-INLET INTERACTION FOR SUPERSONIC TACTICAL FIGHTER AIRCRAFT

Constant Prokop
Robert J. Sanator

Group 3 - Optional - Not Automatically Declassified

THIS MATERIAL CONTAINS INFORMATION AFFECTING THE NATIONAL DEFENSE OF THE UNITED STATES WITHIN THE MEANING OF THE ESPIONAGE LAWS, TITLE 18 U.S.C., SECTIONS 793 AND 794, THE TRANSMISSION OR REVELATION OF WHICH IN ANY MANNER TO AN UNAUTHORIZED PERSON IS PROHIBITED BY LAW.

FOREWORD

This report was prepared by the Republic Aviation Division of the Fairchild Hiller Corporation, Farmingdale, New York, for the Flight Dynamics Laboratory, Air Force Systems Command, United States Air Force, on Contract Number F33615-68-C-1658.

The program was a cooperative Air Force NASA effort with funding provided by the Air Force and test facilities by NASA.

All the work reported herein was conducted under the technical cognizance of Mr. L. E. Surber of the Flight Dynamics Laboratory, Internal Aerodynamics Group. The program was conducted as part of Project 1476, "Airframe Propulsion Compatibility," Task 147603. The program began in June 1968. This report was submitted by the author in January 1970.

The contract effort was conducted at Republic Aviation Division of Fairchild Hiller under the direction of Dr. Robert J. Sanator and the technical management of Mr. Constant Prokop with significant contribution of M. Walter, and M. Romano. Grateful acknowledgement is given to the staff of the NASA-Ames test facility and ARO, Inc. for their cooperation throughout the experimental phase of the program.

Further acknowledgement is extended to Messrs. H. Liu, P. Goutas, C. Long, E. Mueller, and S. Nedelton for their assistance during the various phases of the program.

This report contains no classified information extracted from other classified documents.

This technical report has been reviewed and is approved.

Philip P Antonatos

PHILIP P. ANTONATOS
Chief, Flight Mechanics Division
Air Force Flight Dynamics Laboratory

INDEX TO CLASSIFIED PAGES

The following pages are classified:

Page	Classification
566	Confidential
567	Confidential
568	Confidential
569	Confidential

All other pages in this document are unclassified. Removal of the classified pages serves to declassify this document.

PRECEDING PAGE BLANK-NOT FILMED

UNCLASSIFIED ABSTRACT

The tactical class of weapon system is required to perform effectively over a wide range of flight Mach number and altitude, providing large thrust margin and high maneuvering capability throughout the normal operating envelope. To achieve this combination of performance and maneuverability requires a sophisticated propulsion system closely integrated with the airframe. Recent operational experience indicates that the vehicle induced flow environment can influence the performance of these closely integrated propulsion systems, ranging from minor performance degradation to engine flame out. The objective of this program was to improve the basic understanding of the effects of airframe-inlet interaction. This was accomplished by a parametric experimental program conducted to establish the relationship between representative vehicle geometries, the attendant flow field characteristics, and the installed inlet performance. Additionally, these data were compared with analytically derived flow fields to evaluate the capability of simplified analytical methods to predict the vehicle flow fields. The program accomplished its major goals in that a large bank of relevant experimental data was generated, a basic understanding of the flow phenomena was obtained, and promising analytical techniques were evolved.

PRECEDING PAGE BLANK-NOT FILMED

CONTENTS

Section			Page
I	INTRODUCTION		1
II	SUMMARY		2
III	SYSTEMS REVIEW AND DESIGN SELECTION		4
	3.0 Introduction		4
	3.1 Definition of Geometric Parameters		5
	3.2 Aircraft Nose Characteristics		11
	3.3 Aircraft Canopy Characteristics		15
	3.4 Aircraft Fuselage Characteristics		19
	3.5 Aircraft Wing Characteristics		26
	3.6 Inlet Characteristics		27
	3.7 Configuration Synthesis		32
	3.8 Detail Inlet Design		36
		3.8.1 General	36
		3.8.2 Two-Dimensional Inlet	37
		3.8.3 Axisymmetric Inlet	47
	3.9 Summary		52
IV	THEORETICAL ANALYSES		60
	4.0 General		60
	4.1 Approach		61
	4.2 Example Calculation		65
	4.3 Substantiation of Theoretical Approach		70
V	WIND TUNNEL MODEL		73
	5.0 General		73
	5.1 Design		74
		5.1.1 Flow Field Survey System	77
		5.1.2 Inlet Duct Total Head Rake	83
		5.1.3 Mass Flow Meter	83
		5.1.4 Inlet Throat Bleed System	84
		5.1.5 Instrumentation	86

CONTENTS (Concluded)

Section			Page
VI	EXPERIMENTAL PROGRAM		90
	6.0	General	90
VII	DATA ANALYSIS		97
	7.0	General	97
	7.1	Fuselage Alone (Data Format I)	97
		7.1.1 General	97
		7.1.2 Nose and Canopy Effects	97
		7.1.3 Fuselage Effects	127
		7.1.4 Correlation of Experimental Data with Theory	205
		7.1.5 Refinement of the Reference Plane Technique	217
	7.2	Fuselage Alone (Data Format IV)	283
		7.2.1 General	283
		7.2.2 Fuselage Effects	285
		7.2.3 Wing Effects	320
	7.3	Inlet Alone (Data Format V)	349
		7.3.1 General	349
		7.3.2 Two-Dimensional Inlet	351
		7.3.3 Axisymmetric Inlet	363
	7.4	Inlet/Fuselage Combined (Data Format II)	378
		7.4.1 General	378
		7.4.2 Nose and Canopy Effects	379
		7.4.3 Fuselage Effects	388
	7.5	Inlet/Fuselage Combined (Data Format III)	435
		7.5.1 General	435
		7.5.2 Fuselage Effects	436
		7.5.3 Wing Effects	501
	7.6	Probe Interference Effects	535
VIII	CONCLUSIONS		553
	REFERENCES		556
	APPENDIX A		557

LIST OF ILLUSTRATIONS

Figure	Description	Page
3-1	Schematic - Definition of Nose, Canopy and Fuselage Geometric Parameters	8
3-2	Schematic - Definition of Wing Geometric Parameters	9
3-3	Nose Cone Geometric Characteristics	13
3-4	Nose Droop Characteristics	14
3-5	Canopy Geometric Characteristics	16
3-6	Definition - Fuselage Geometric Parameters	21
3-7	Selected Fuselage Lower Quadrant Geometric Characteristics for Experimental Study	23
3-8	Comparison of Six Selected Fuselage Lower Quadrant Geometric Shapes	24
3-9	Inlet Location - Radial and Circumferential Position	29
3-10	Typical Mass Flow Schedule - Augmented Turbofan Engine	38
3-11	Total Pressure Recovery - Double Ramp External Compression Inlet Designed for $M_\infty = 2.20$	39
3-12	Total Pressure Recovery - Double Ramp External Compression Inlet, Designed for $M_\infty = 2.70$	40
3-13	Two-Dimensional Inlet - 1/12th Scale Model	42
3-14	Estimated Critical Mass Flow Ratio - Two-Dimensional Inlet	44
3-15	Estimated Critical Pressure Recovery - Two-Dimensional Inlet	45
3-16	Capture Area Ratio vs Angle of Attack	46
3-17	Total Pressure Recovery - Double Cone External Compression Inlet, Designed for $M_\infty = 2.20$	49

LIST OF ILLUSTRATIONS (Continued)

Figure	Description	Page
3-18	Total Pressure Recovery - Double Cone External Compression Inlet, Designed for $M_\infty = 2.70$	50
3-19	Flow Inclination Approaching Inlet Cowl - Double Cone External Compression Inlet	51
3-20	Axisymmetric Inlet - 1/12th Scale Model	53
3-21	Estimated Critical Mass Flow Ratio - Axisymmetric Inlet	55
3-22	Estimated Critical Pressure Recovery - Axisymmetric Inlet	56
4-1	Fuselage-Plane Schematic	62
4-2	Fuselage Contour Example	66
4-3	Flow Field Calculation Example	69
4-4	Alpha Contour, Alpha = 7.66°, M = 2.0	71
5-1	Model Composite	75
5-2	Fuselage Geometry	76
5-3	Two-Dimensional Inlet	78
5-4	Axisymmetric Inlet	79
5-5	Flow Field Survey Mechanism	80
5-6	Photograph of Flow Field Survey Mechanism	81
5-7	Cone Probe Details	82
5-8	Schlieren Monitoring Technique	85
5-9	Instrumentation Schematic, Fuselage Survey at 30% ACL	87
5-10	Instrumentation Schematic, Fuselage Survey at 50% ACL	88
5-11	Instrumentation Schematic, Inlet Alone	89
6-1	Installed Model, Format IV	92
6-2	Installed Model, Format III	93

LIST OF ILLUSTRATIONS (Continued)

Figure Description Page

7-1 Profiles of Nose and Canopy Shapes 99

7-2 Local Flow Angularity, Fuselage 3, Mach 2.5, $\alpha = -3°$, PCPN, Format I 101

7-3 Local Flow Angularity, Fuselage 3, Mach 2.5, $\alpha = -3°$, PCSN, Format I 102

7-4 Local Flow Angularity, Fuselage 3, Mach 2.5, $\alpha = -3°$, SCPN, Format I 103

7-5 Local Flow Angularity, Fuselage 3, Mach 2.5, $\alpha = -3°$, SCSN, Format I 105

7-6 Local Flow Angularity, Fuselage 3, Mach 2.5, $\alpha = 0°$, SCSN, Format I 106

7-7 Local Flow Angularity, Fuselage 3, Mach 2.5, $\alpha = 5°$, PCSN, Format I 108

7-8 Local Flow Angularity, Fuselage 3, Mach 2.5, $\alpha = 5°$, SCSN, Format I 109

7-9 Local Flow Angularity, Fuselage 3, Mach 2.5, $\alpha = 10°$, PCPN, Format I 111

7-10 Local Flow Angularity, Fuselage 3, Mach 2.5, $\alpha = 10°$, PCSN, Format I 112

7-11 Local Flow Angularity, Fuselage 3, Mach 2.5, $\alpha = 10°$, SCPN, Format I 113

7-12 Local Flow Angularity, Fuselage 3, Mach 2.5, $\alpha = 10°$, SCSN, Format I 114

7-13 Local Flow Angularity, Fuselage 3, Mach 2.5, $\alpha = 15°$, PCPN, Format I 115

7-14 Local Flow Angularity, Fuselage 3, Mach 2.5, $\alpha = 15°$, PCSN, Format I 116

7-15 Local Flow Angularity, Fuselage 3, Mach 2.5, $\alpha = 15°$, SCPN, Format I 117

7-16 Local Flow Angularity, Fuselage 3, Mach 2.5, $\alpha = 15°$, SCSN, Format I 118

7-17 Local Flow Angularity, Fuselage 3, Mach 2.5, $\alpha = 20°$, PCPN, Format I 119

7-18 Local Flow Angularity, Fuselage 3, Mach 2.5, $\alpha = 20°$, PCSN, Format I 120

7-19 Local Flow Angularity, Fuselage 3, Mach 2.5, $\alpha = 20°$, SCPN, Format I 121

7-20 Local Flow Angularity, Fuselage 3, Mach 2.5, $\alpha = 20°$, SCSN, Format I 122

LIST OF ILLUSTRATIONS (Continued)

Figure	Description	Page
7-21	Local Flow Angularity, Fuselage 3, Mach 2.5, $\alpha = 25°$, PCPN, Format I	123
7-22	Local Flow Angularity, Fuselage 3, Mach 2.5, $\alpha = 25°$, PCSN, Format I	124
7-23	Local Flow Angularity, Fuselage 3, Mach 2.5, $\alpha = 25°$, SCPN, Format I	125
7-24	Local Flow Angularity, Fuselage 3, Mach 2.5, $\alpha = 25°$, SCSN, Format I	126
7-25	Local Flow Angularity, Fuselage 3, Mach 2.2, $\alpha = 0°$, PCPN, Format I	128
7-26	Local Flow Angularity, Fuselage 3, Mach 2.2, $\alpha = 0°$, PCSN, Format I	129
7-27	Local Flow Angularity, Fuselage 3, Mach 2.2, $\alpha = 0°$, SCPN, Format I	130
7-28	Local Flow Angularity, Fuselage 3, Mach 2.2, $\alpha = 0°$, SCSN, Format I	131
7-29	Local Flow Angularity, Fuselage 3, Mach 2.2, $\alpha = 15°$, PCPN, Format I	132
7-30	Local Flow Angularity, Fuselage 3, Mach 2.2, $\alpha = 15°$, PCSN, Format I	133
7-31	Local Flow Angularity, Fuselage 3, Mach 2.2, $\alpha = 15°$, SCPN, Format I	134
7-32	Local Flow Angularity, Fuselage 3, Mach 2.2, $\alpha = 15°$, SCSN, Format I	135
7-33	Local Flow Angularity, Fuselage 3, Mach 1.8, $\alpha = 0°$, PCPN, Format I	136
7-34	Local Flow Angularity, Fuselage 3, Mach 1.8, $\alpha = 0°$, PCSN, Format I	137
7-35	Local Flow Angularity, Fuselage 3, Mach 1.8, $\alpha = 0°$, SCPN, Format I	138
7-36	Local Flow Angularity, Fuselage 3, Mach 1.8, $\alpha = 0°$, SCSN, Format I	139
7-37	Local Flow Angularity, Fuselage 3, Mach 1.8, $\alpha = 15°$, PCPN, Format I	140
7-38	Local Flow Angularity, Fuselage 3, Mach 1.8, $\alpha = 15°$, PCSN, Format I	141
7-39	Local Flow Angularity, Fuselage 3, Mach 1.8, $\alpha = 15°$, SCPN, Format I	142

LIST OF ILLUSTRATIONS (Continued)

Figure	Description	Page
7-40	Local Flow Angularity, Fuselage 3, Mach 1.8, $\alpha = 15°$, SCSN, Format I	143
7-41	Local Flow Angularity, Fuselage 3, Mach 0.8, $\alpha = 0°$, SCSN, Format I	144
7-42	Local Flow Angularity, Fuselage 3, Mach 0.8, $\alpha = 10°$, SCSN, Format I	145
7-43	Local Flow Angularity, Fuselage 3, Mach 0.8, $\alpha = 20°$, SCSN, Format I	146
7-44	Local Flow Angularity, Fuselage 2, Mach 0.8, $\alpha = -3°$, PCPN, Format I	147
7-45	Local Flow Angularity, Fuselage 6, Mach 0.8, $\alpha = -3°$, PCPN, Format I	148
7-46	Local Sidewash Angularity, Fuselage 6, Mach 0.8, $\alpha = -3°$, Format I	150
7-47	Local Sidewash Angularity, Fuselage 2, Mach 0.8, $\alpha = -3°$, Format I	151
7-48	Local Flow Angularity, Fuselage 1, Mach 0.8, $\alpha = 0°$, Format I	152
7-49	Local Flow Angularity, Fuselage 4, Mach 0.8, $\alpha = 0°$, Format I	153
7-50	Local Flow Angularity, Fuselage 2, Mach 0.8, $\alpha = 5°$, Format I	154
7-51	Local Flow Angularity, Fuselage 2, Mach 0.8, $\alpha = 10°$, Format I	156
7-52	Local Flow Angularity, Fuselage 2, Mach 0.8, $\alpha = 15°$, Format I	157
7-53	Local Flow Angularity, Fuselage 2, Mach 0.8, $\alpha = 20°$, Format I	158
7-54	Local Flow Angularity, Fuselage 1, Mach 0.8, $\alpha = 10°$, Format I	159
7-55	Local Flow Angularity, Fuselage 4, Mach 1.2, $\alpha = -3°$, Format I	160
7-56	Local Flow Angularity, Fuselage 5, Mach 1.2, $\alpha = -3°$, Format I	161
7-57	Local Flow Angularity, Fuselage 1, Mach 1.2, $\alpha = 0°$, Format I	163
7-58	Local Flow Angularity, Fuselage 4, Mach 1.2, $\alpha = 0°$, Format I	164

LIST OF ILLUSTRATIONS (Continued)

Figure	Description	Page
7-59	Local Flow Angularity, Fuselage 4 Mach 1.2, $\alpha = 5°$, Format I	165
7-60	Local Flow Angularity, Fuselage 3, Mach 1.2, $\alpha = 5°$, Format I	166
7-61	Local Flow Angularity, Fuselage 3, Mach 1.2, $\alpha = 10°$, Format I	168
7-62	Local Flow Angularity, Fuselage 3, Mach 1.2, $\alpha = 20°$, Format I	169
7-63	Local Flow Angularity, Fuselage 4, Mach 1.2, $\alpha = 10°$, Format I	170
7-64	Local Flow Angularity, Fuselage 4, Mach 1.2, $\alpha = 20°$, Format I	171
7-65	Local Flow Angularity, Fuselage 1, Mach 1.8, $\alpha = -3°$, Format I	172
7-66	Local Flow Angularity, Fuselage 2, Mach 1.8, $\alpha = -3°$, Format I	173
7-67	Local Flow Angularity, Fuselage 1, Mach 1.8, $\alpha = 0°$, Format I	174
7-68	Local Flow Angularity, Fuselage 4, Mach 1.8, $\alpha = 10°$, Format I	176
7-69	Local Flow Angularity, Fuselage 5, Mach 1.8, $\alpha = 10°$, Format I	177
7-70	Local Flow Angularity, Fuselage 1, Mach 1.8, $\alpha = 20°$, Format I	178
7-71	Local Flow Angularity, Fuselage 2, Mach 1.8, $\alpha = 20°$, Format I	179
7-72	Local Flow Angularity, Fuselage 3, Mach 1.8, $\alpha = 20°$, Format I	180
7-73	Local Flow Angularity, Fuselage 4, Mach 1.8, $\alpha = 20°$, Format I	181
7-74	Local Flow Angularity, Fuselage 5, Mach 1.8, $\alpha = 20°$, Format I	182
7-75	Local Flow Angularity, Fuselage 6, Mach 1.8, $\alpha = 20°$, Format I	183
7-76	Local Flow Angularity, Fuselage 8, Mach 1.8, $\alpha = 20°$, Format I	184
7-77	Local Flow Angularity, Fuselage 1, Mach 2.2, $\alpha = 0°$, Format I	185

LIST OF ILLUSTRATIONS (Continued)

Figure	Description	Page
7-78	Local Flow Angularity, Fuselage 2, Mach 2.2, $\alpha = 0°$, Format I	186
7-79	Local Flow Angularity, Fuselage 4, Mach 2.2, $\alpha = 0°$, Format I	187
7-80	Local Flow Angularity, Fuselage 5, Mach 2.2, $\alpha = 0°$, Format I	188
7-81	Local Flow Angularity, Fuselage 6, Mach 2.2, $\alpha = 0°$, Format I	189
7-82	Local Flow Angularity, Fuselage 8, Mach 2.2, $\alpha = 0°$, Format I	190
7-83	Local Flow Angularity, Fuselage 1, Mach 2.2, $\alpha = 10°$, Format I	191
7-84	Local Flow Angularity, Fuselage 2, Mach 2.2, $\alpha = 10°$, Format I	192
7-85	Local Flow Angularity, Fuselage 3, Mach 2.2, $\alpha = 10°$, Format I	193
7-86	Local Flow Angularity, Fuselage 4, Mach 2.2, $\alpha = 0°$, Format I	194
7-87	Local Flow Angularity, Fuselage 5, Mach 2.2, $\alpha = 10°$, Format I	195
7-88	Local Flow Angularity, Fuselage 6, Mach 2.2, $\alpha = 10°$, Format I	196
7-89	Local Flow Angularity, Fuselage 8, Mach 2.2, $\alpha = 10°$, Format I	197
7-90	Local Flow Angularity, Fuselage 1, Mach 2.5, $\alpha = 5°$, Format I	198
7-91	Local Flow Angularity, Fuselage 2, Mach 2.5, $\alpha = 5°$, Format I	199
7-92	Local Flow Angularity, Fuselage 3, Mach 2.5, $\alpha = 5°$, Format I	200
7-93	Local Flow Angularity, Fuselage 4, Mach 2.5, $\alpha = 5°$, Format I	201
7-94	Local Flow Angularity, Fuselage 5, Mach 2.5, $\alpha = 5°$, Format I	202
7-95	Local Flow Angularity, Fuselage 6, Mach 2.5, $\alpha = 5°$, Format I	203
7-96	Local Flow Angularity, Fuselage 8, Mach 2.5, $\alpha = 5°$, Format I	204

LIST OF ILLUSTRATIONS (Continued)

Figure	Description	Page
7-97	Static Pressure Distribution, Fuselage 3, Mach 2.2, $\alpha = 5°$, Format I	207
7-98	Local Mach Distribution, Fuselage 3, Mach 2.2, $\alpha = 5°$, Format I	208
7-99	Flow Angularity, Fuselage 3, Mach 2.2, $\alpha = 5°$, Format I	209
7-100	Local Mach Number Profile, Fuselage 3, Mach 2.2, $\alpha = 5°$, Format I	211
7-101	Flow Angularity, Fuselage 3, Mach 2.2, $\alpha = 15°$, Format I	212
7-102	Local Mach Number Profile, Fuselage 3, Mach 2.2, $\alpha = 15°$, Format I	213
7-103	Static Pressure Distribution, Fuselage 3, Mach 2.2, $\alpha = 15°$, Format I	214
7-104	Local Mach Distribution, Fuselage 3, Mach 2.2, $\alpha = 15°$, Format I	215
7-105	Static Pressure Distribution, Fuselage 2, Mach 2.2, $\alpha = 15°$, Format I	216
7-106	Experimental Flow Angularity, Fuselage 2, Mach 2.2, $\alpha = 15°$, Format I	218
7-107	Static Pressure Distribution, Mach 2.2, $\alpha = 15°$, Format I	219
7-108	Schematic of "Deviatory" Angular Relations, Format I	225
7-109	Comparison of Experimental and Theoretical Pressure Ratios, Fuselage 2, Mach 2.2, $\alpha = 15.75°$, Format I	227
7-110	Comparison of Experimental and Theoretical Pressure Ratios, Fuselage 3, Mach 2.2, $\alpha = 15.75°$, Format I	228
7-111	Thermodynamic Properties on Surface of Body at Sta 19.5, Format I	229
7-112	Comparison of Experimental and Theoretical Mach Numbers at Fuselage Surface, Station 19.5, Fuselage 2, Mach 2.2, $\alpha = 15°$, Format I	230
7-113	Comparison of Theoretical and Experimental Mach Numbers at Fuselage Surface, Sta 19.5, Fuselage 3, Mach 2.2, $\alpha = 15°$, Format I	231
7-114	Schematic of Coordinate Systems	233
7-115	Basic Reference Plane Pressure Ratio, Fuselage 2, Mach 2.2, $\alpha = 15°$, Format I	237

LIST OF ILLUSTRATIONS (Continued)

Figure	Description	Page
7-116	Basic Reference Plane Local Mach Numbers, Fuselage 2, Mach 2.2, α = 15°, Format I	238
7-117	Basic Reference Plane Local Temperature, Fuselage 2, Mach 2.2, α = 15°, Format I	239
7-118	Basic Reference Plane Local Velocity, Fuselage 2, Mach 2.2, α = 15°, Format I	240
7-119	Experimental Static Pressure at Sta. 19.5, Mach 2.2, α = 15.75°, β = 0°, Format I	246
7-120	Isobars, Fuselage 2, Mach 2.2, α = 15.75°, Format I	247
7-121	Local Mach Number, Fuselage 2, Mach 2.2, α = 15.75°, Format I	248
7-122	Alpha Local, Degrees, Fuselage 2, Mach 2.2, α = 15.75°, Format I	249
7-123	Sidewash Angle, Degrees, Fuselage 2, Mach 2.2, α = 15.75°, Format I	250
7-124	Isobars, Fuselage 3, Mach 2.2, α = 15.75°, Format I	251
7-125	Local Mach Number, Fuselage 3, Mach 2.2, α = 15.75°, Format I	252
7-126	Alpha Local, Degrees, Fuselage 3, Mach 2.2, α = 15.75°, Format I	253
7-127	Sidewash Angle, Degrees, Fuselage 3, Mach 2.2, α = 15.75°, Format I	254
7-128	Local Mach Number, Fuselage 2, Mach 2.2, α = 15°, Format I	255
7-129	Local Mach Number, Fuselage 3, Mach 2.2, α = 15°, Format I	256
7-130	Local Alpha, Fuselage 2, Mach 2.2, α = 15°, Format I	257
7-131	Alpha Local, Degrees, Fuselage 3, Mach 2.2, α = 15°, Format I	258
7-132	Sidewash Angle, Degrees, Fuselage 2, Mach 2.2, α = 15°, Format I	259
7-133	Sidewash Angle, Degrees, Fuselage 3, Mach 2.2, α = 15°, Format I	260
7-134	A Skewed Plane Intersecting a Fuselage	262
7-135	Fuselage Control Lines and a Typical Cross Section, Format I	264
7-136	Intersection of a Plane at a Transverse Station. Format I	265

LIST OF ILLUSTRATIONS (Continued)

Figure	Description	Page
7-137	Transverse Cross Section at X = XS, Format I	271
7-138	Rotation Angles for Axis Transformation, Format I	273
7-139	Flow Field Plane, Fuselage Intersections, Format I	276a
7-140	Example of Cut Planes, Format I	278
7-141	Static Pressure Distribution, Fuselage 3, Mach 2.2, $\alpha = 15^\circ$, Format I	280
7-142	Local Flow Angularity, Fuselage 1, Mach 0.8, $\alpha = 0^\circ$, Format IV, PCPN	287
7-143	Local Flow Angularity, Fuselage 1, Mach 0.8, $\alpha = 10^\circ$, Format IV, PCPN	288
7-144	Local Flow Angularity, Fuselage 1, Mach 0.8, $\alpha = 19^\circ$, Format IV, PCPN	289
7-145	Sidewash Angle, Fuselage 1, Mach 0.8, $\alpha = 0^\circ$, Format IV, PCPN	290
7-146	Sidewash Angle, Fuselage 1, Mach 0.8, $\alpha = 10^\circ$, Format IV, PCPN	291
7-147	Sidewash Angle, Fuselage 1, Mach 0.8, $\alpha = 19^\circ$, Format IV, PCPN	292
7-148	Local Flow Angularity, Fuselage 4, Mach 0.8, $\alpha = 0^\circ$, Format IV, PCPN	293
7-149	Local Flow Angularity, Fuselage 4, Mach 0.8, $\alpha = 10^\circ$, Format IV, PCPN	294
7-150	Local Flow Angularity, Fuselage 4, Mach 0.8, $\alpha = 20^\circ$, Format IV, PCPN	295
7-151	Sidewash Angle, Fuselage 4, Mach 0.8, $\alpha = 0^\circ$, Format IV, PCPN	296
7-152	Sidewash Angle, Fuselage 4, Mach 0.8, $\alpha = 10^\circ$, Format IV, PCPN	297
7-153	Sidewash Angle, Fuselage 4, Mach 0.8, $\alpha = 20^\circ$, Format IV, PCPN	298
7-154	Local Flow Angularity, Fuselage 4, Mach 1.3, $\alpha = 0^\circ$, Format IV, PCPN	299
7-155	Local Flow Angularity, Fuselage 4, Mach 1.3, $\alpha = 10^\circ$, Format IV, PCPN	300
7-156	Local Flow Angularity, Fuselage 4, Mach 1.3, $\alpha = 20^\circ$, Format IV, PCPN	301
7-157	Sidewash Angle, Fuselage 4, Mach 1.3, $\alpha = 0^\circ$, Format IV, PCPN	302
7-158	Sidewash Angle, Fuselage 4, Mach 1.3, $\alpha = 10^\circ$, Format IV, PCPN	303
7-159	Sidewash Angle, Fuselage 4, Mach 1.3, $\alpha = 20^\circ$, Format IV, PCPN	304
7-160	Local Flow Angularity, Fuselage 3, Mach 1.3, $\alpha = 0^\circ$, Format IV, PCPN	305

LIST OF ILLUSTRATIONS (Continued)

Figure	Description	Page
7-161	Local Flow Angularity, Fuselage 3, Mach 1.3, $\alpha = 10°$, Format IV, PCPN	306
7-162	Local Flow Angularity, Fuselage 3, Mach 1.3, $\alpha = 20°$, Format IV, PCPN	307
7-163	Local Flow Angularity, Fuselage 1, Mach 1.8, $\alpha = 0°$, Format IV	308
7-164	Local Flow Angularity, Fuselage 1, Mach 1.8, $\alpha = 10°$, Format IV	309
7-165	Local Flow Angularity, Fuselage 1, Mach 1.8, $\alpha = 20°$, Format IV	310
7-166	Sidewash Angle, Fuselage 1, Mach 1.8, $\alpha = 0°$, Format IV	311
7-167	Sidewash Angle, Fuselage 1, Mach 1.8, $\alpha = 10°$, Format IV	312
7-168	Sidewash Angle, Fuselage 1, Mach 1.8, $\alpha = 20°$, Format IV	313
7-169	Local Flow Angularity, Fuselage 4, Mach 1.8, $\alpha = 0°$, Format IV	314
7-170	Local Flow Angularity, Fuselage 4, Mach 1.8, $\alpha = 10°$, Format IV	315
7-171	Local Flow Angularity, Fuselage 4, Mach 1.8, $\alpha = 20°$, Format IV	316
7-172	Sidewash Angle, Fuselage 4, Mach 1.8, $\alpha = 0°$, Format IV	317
7-173	Sidewash Angle, Fuselage 4, Mach 1.8, $\alpha = 10°$, Format IV	318
7-174	Sidewash Angle, Fuselage 4, Mach 1.8, $\alpha = 20°$, Format IV	319
7-175	Sidewash Angle, Fuselage 3, Mach 1.8, $\alpha = 10°$ Format IV, PCPN	321
7-176	Sidewash Angle, Fuselage 3, Mach 1.8, $\alpha = 20°$, Format IV, PCPN	322
7-177	Sidewash Angle, Fuselage 1, Mach 2.2, $\alpha = 0°$, Format IV	323
7-178	Sidewash Angle, Fuselage 2, Mach 2.2, $\alpha = 0°$, Format IV	324
7-179	Sidewash Angle, Fuselage 3, Mach 2.2, $\alpha = 0°$, Format IV, PCPN	325
7-180	Sidewash Angle, Fuselage 4, Mach 2.2, $\alpha = 0°$, Format IV	326
7-181	Sidewash Angle, Fuselage 5, Mach 2.2, $\alpha = 0°$, Format IV	327
7-182	Sidewash Angle, Fuselage 6, Mach 2.2, $\alpha = 0°$, Format IV	328
7-183	Sidewash Angle, Fuselage 8, Mach 2.2, $\alpha = 0°$, Format IV	329
7-184	Sidewash Angle, Fuselage 1, Mach 2.2, $\alpha = 10°$, Format IV	330
7-185	Sidewash Angle, Fuselage 2, Mach 2.2, $\alpha = 10°$, Format IV	331

LIST OF ILLUSTRATIONS (Continued)

Figure	Description	Page
7-186	Sidewash Angle, Fuselage 3, Mach 2.2, $\alpha = 10°$, Format IV, PCPN	332
7-187	Sidewash Angle, Fuselage 4, Mach 2.2, $\alpha = 10°$, Format IV	333
7-188	Sidewash Angle, Fuselage 5, Mach 2.2, $\alpha = 10°$, Format IV	334
7-189	Sidewash Angle, Fuselage 6, Mach 2.2, $\alpha = 10°$, Format IV	335
7-190	Sidewash Angle, Fuselage 8, Mach 2.2, $\alpha = 10°$, Format IV	336
7-191	Local Flow Angularity, Fuselage 1, Mach 2.5, $\alpha = 0°$, Format IV	337
7-192	Local Flow Angularity, Fuselage 1, Mach 2.5, $\alpha = 10°$, Format IV	338
7-193	Local Flow Angularity, Fuselage 1, Mach 2.5, $\alpha = 20°$, Format IV	339
7-194	Sidewash Angle, Fuselage 1, Mach 2.5, $\alpha = 0°$, Format IV	340
7-195	Sidewash Angle, Fuselage 1, Mach 2.5, $\alpha = 10°$, Format IV	341
7-196	Sidewash Angle, Fuselage 1, Mach 2.5, $\alpha = 20°$, Format IV	342
7-197	Local Flow Angularity, Fuselage 4, Mach 2.5, $\alpha = 0°$, Format IV	343
7-198	Local Flow Angularity, Fuselage 4, Mach 2.5, $\alpha = 10°$, Format IV	344
7-199	Local Flow Angularity, Fuselage 4, Mach 2.5, $\alpha = 20°$, Format IV	345
7-200	Sidewash Angle, Fuselage 4, Mach 2.5, $\alpha = 0°$, Format IV	346
7-201	Sidewash Angle, Fuselage 4, Mach 2.5, $\alpha = 10°$, Format IV	347
7-202	Sidewash Angle, Fuselage 4, Mach 2.5, $\alpha = 20°$, Format IV	348
7-203	Comparison of Theory and Experiment - Schematic	350
7-204	Inlet Mass Flow Ratio, Comparison of Theory and Experiment, Format V, 2-Dimensional Inlet, Mach 0.8	352
7-205	Inlet Mass Flow Ratio, Comparison of Theory and Experiment, Format V, 2-Dimensional Inlet, Mach 1.2	353
7-206	Inlet Mass Flow Ratio, Comparison of Theory and Experiment, Format V, 2-Dimensional Inlet Mach 1.8	354
7-207	Inlet Mass Flow Ratio, Comparison of Theory and Experiment, Format V, 2-Dimensional Inlet, Mach 2.2	355
7-208	Inlet Mass Flow Ratio, Comparison of Theory and Experiment, Format V, 2-Dimensional Inlet, Mach 2.5	356
7-209	Inlet Total Pressure Recovery, Comparison of Theory and Experiment, Format V, 2-Dimensional Inlet, Mach 0.8	358

LIST OF ILLUSTRATIONS (Continued)

Figure	Description	Page
7-210	Inlet Total Pressure Recovery, Comparison of Theory and Experiment, Format V, 2-Dimensional Inlet, Mach 1.2	359
7-211	Inlet Total Pressure Recovery, Comparison of Theory and Experiment, Format V, 2-Dimensional Inlet, Mach 1.8	360
7-212	Inlet Total Pressure Recovery, Comparison of Theory and Experiment, Format V, 2-Dimensional Inlet, Mach 2.2	361
7-213	Inlet Total Pressure Recovery, Comparison of Theory and Experiment, Format V, 2-Dimensional Inlet, Mach 2.5	362
7-214	Inlet Mass Flow Ratio, Comparison of Theory and Experiment, Format V, Axisymmetric Inlet, Mach 0.8	364
7-215	Inlet Mass Flow Ratio, Comparison of Theory and Experiment, Format V, Axisymmetric Inlet, Mach 1.2	365
7-216	Inlet Mass Flow Ratio, Comparison of Theory and Experiment, Format V, Axisymmetric Inlet, Mach 1.8	366
7-217	Inlet Mass Flow Ratio, Comparison of Theory and Experiment, Format V, Axisymmetric Inlet, Mach 2.2	367
7-218	Inlet Mass Flow Ratio, Comparison of Theory and Experiment, Format V, Axisymmetric Inlet, Mach 2.5	368
7-219	Inlet Total Pressure Recovery, Comparison of Theory and Experiment, Format V, Axisymmetric Inlet, Mach 0.8	372
7-220	Inlet Total Pressure Recovery, Comparison of Theory and Experiment, Format V, Axisymmetric Inlet, Mach 1.2	373
7-221	Inlet Total Pressure Recovery, Comparison of Theory and Experiment, Format V, Axisymmetric Inlet, Mach 1.8	374
7-222	Inlet Total Pressure Recovery, Comparison of Theory and Experiment, Format V, Axisymmetric Inlet, Mach 2.2	375
7-223	Inlet Total Pressure Recovery, Comparison of Theory and Experiment, Format V, Axisymmetric Inlet, Mach 2.5	376
7-224	Comparison of Inlet Performance, Mach 2.5 $\alpha = 0°$, 2-D	380
7-225	Comparison of Inlet Performance, Mach 2.5, $\alpha = 10°$, 2-D	381
7-226	Comparison of Inlet Performance, Mach 2.2, $\alpha = 0°$, 2-D	382
7-227	Comparison of Inlet Performance, Mach 2.2, $\alpha = 10°$, 2-D	383
7-228	Comparison of Inlet Performance, Mach 2.2, $\alpha = 20°$, 2-D	384
7-229	Comparison of Inlet Performance, Mach 1.8, $\alpha = 0°$, 2-D	385
7-230	Comparison of Inlet Performance, Mach 1.8, $\alpha = 20°$, 2-D	386
7-231	Comparison of Inlet Performance, Mach 0.8, $\alpha = -3°$, 2-D	389

LIST OF ILLUSTRATIONS (Continued)

Figure	Description	Page
7-232	Comparison of Inlet Performance, Mach 0.8, $\alpha = 0^\circ$, 2-D	390
7-233	Comparison of Inlet Performance, Mach 0.8, $\alpha = 5^\circ$, 2-D	391
7-234	Comparison of Inlet Performance, Mach 0.8, $\alpha = 10^\circ$, 2-D	392
7-235	Comparison of Inlet Performance, Mach 0.8, $\alpha = 15^\circ$, 2-D	393
7-236	Comparison of Inlet Performance, Mach 0.8, $\alpha = 20^\circ$, 2-D	394
7-237	Comparison of Inlet Performance, Mach 0.8, $\alpha = 25^\circ$, 2-D	395
7-238	Engine Face Profile, Fuselage 2, Mach 0.8, $\alpha = 10^\circ$, 2-D	396
7-239	Engine Face Profile, Fuselage 2, Mach 0.8, $\alpha = 15^\circ$, 2-D	397
7-240	Engine Face Profile, Fuselage 2, Mach 0.8, $\alpha = 20^\circ$, 2-D	398
7-241	Engine Face Profile, Fuselage 1, Mach 0.8, $\alpha = 10^\circ$, 2-D	400
7-242	Engine Face Profile, Fuselage 1, Mach 0.8, $\alpha = 15^\circ$, 2-D	401
7-243	Engine Face Profile, Fuselage 1, Mach 0.8, $\alpha = 20^\circ$, 2-D	402
7-244	Comparison of Inlet Performance, Mach 1.2, $\alpha = -3$, 2-D	403
7-245	Comparison of Inlet Performance, Mach 1.2, $\alpha = 0^\circ$, 2-D	404
7-246	Comparison of Inlet Performance, Mach 1.2, $\alpha = 5^\circ$, 2-D	405
7-247	Comparison of Inlet Performance, Mach 1.2, $\alpha = 10^\circ$, 2-D	406
7-248	Comparison of Inlet Performance, Mach 1.2, $\alpha = 15^\circ$, 2-D	407
7-249	Comparison of Inlet Performance, Mach 1.2, $\alpha = 20^\circ$, 2-D	408
7-250	Comparison of Inlet Performance, Mach 1.2, $\alpha = 25^\circ$, 2-D	409
7-251	Comparison of Inlet Performance, Mach 1.8, $\alpha = -3^\circ$, 2-D	410
7-252	Comparison of Inlet Performance, Mach 1.8, $\alpha = 0^\circ$, 2-D	412
7-253	Comparison of Inlet Performance, Mach 1.8, $\alpha = 5^\circ$, 2-D	413
7-254	Comparison of Inlet Performance, Mach 1.8, $\alpha = 10^\circ$, 2-D	414
7-255	Comparison of Inlet Performance, Mach 1.8, $\alpha = 15^\circ$, 2-D	415
7-256	Comparison of Inlet Performance, Mach 1.8, $\alpha = 20^\circ$, 2-D	416
7-257	Comparison of Inlet Performance, Mach 1.8, $\alpha = 25^\circ$, 2-D	417
7-258	Comparison of Inlet Performance, Mach 2.2, $\alpha = -3^\circ$, 2-D	420
7-259	Comparison of Inlet Performance, Mach 2.2, $\alpha = 0^\circ$, 2-D	421
7-260	Comparison of Inlet Performance, Mach 2.2, $\alpha = 5^\circ$, 2-D	423
7-261	Comparison of Inlet Performance, Mach = 2.2, $\alpha = 10^\circ$, 2-D	424
7-262	Comparison of Inlet Performance, Mach 2.2, $\alpha = 15^\circ$, 2-D	426
7-263	Comparison of Inlet Performance, Mach 2.2, $\alpha = 20^\circ$, 2-D	427

LIST OF ILLUSTRATIONS (Continued)

Figure	Description	Page
7-264	Comparison of Inlet Performance, Mach 2.2, $\alpha = 25°$, 2-D	428
7-265	Comparison of Inlet Performance, Mach 2.5, $\alpha = -3°$, 2-D	429
7-266	Comparison of Inlet Performance, Mach 2.5, $\alpha = 0°$, 2-D	430
7-267	Comparison of Inlet Performance, Mach 2.5, $\alpha = 5°$, 2-D	431
7-268	Comparison of Inlet Performance, Mach 2.5, $\alpha = 10°$, 2-D	432
7-269	Comparison of Inlet Performance, Mach 2.5, $\alpha = 15°$, 2-D	433
7-270	Comparison of Inlet Performance, Mach 2.5, $\alpha = 18°$, 2-D	434
7-271	Inlet Capture Area Schematic	437
7-272	Inlet Capture Area, Format III	438
7-273	Comparison of Inlet Performance, Axisymmetric Inlet, Mach 0.8, $\alpha = -3°$	440
7-274	Comparison of Inlet Performance, Axisymmetric Inlet, Mach 0.8, $\alpha = 0°$	441
7-275	Comparison of Inlet Performance, Axisymmetric Inlet, Mach 0.8, $\alpha = 5°$	442
7-276	Comparison of Inlet Performance, Axisymmetric Inlet, Mach 0.8, $\alpha = 10°$	443
7-277	Comparison of Inlet Performance, Axisymmetric Inlet, Mach 0.8, $\alpha = 15°$	444
7-278	Comparison of Inlet Performance, Axisymmetric Inlet, Mach 0.8, $\alpha = 20°$	445
7-279	Comparison of Inlet Performance, Axisymmetric Inlet, Mach 0.8, $\alpha = 25°$	446
7-280	Comparison of Theory and Experiment, Axisymmetric Inlet, Mach 0.8	447
7-281	Comparison of Inlet Performance, Two-Dimensional Inlet, Mach 0.8, $\alpha = -3°$	448
7-282	Comparison of Inlet Performance, Two-Dimensional Inlet, Mach 0.8, $\alpha = 0°$	449
7-283	Comparison of Inlet Performance, Two-Dimensional Inlet, Mach 0.8, $\alpha = 5°$	450
7-284	Comparison of Inlet Performance, Two-Dimensional Inlet, Mach 0.8, $\alpha = 10°$	451
7-285	Comparison of Inlet Performance, Two-Dimensional Inlet, Mach 0.8, $\alpha = 15°$	452
7-286	Comparison of Inlet Performance, Two-Dimensional Inlet, Mach 0.8, $\alpha = 20°$	453

LIST OF ILLUSTRATIONS (Continued)

Figure	Description	Page
7-287	Comparison of Inlet Performance, Two-Dimensional Inlet, Mach 0.8, $\alpha = 25^\circ$	454
7-288	Fuselage / Two-Dimensional Inlet Sections	455
7-289	Comparison of Theory and Experiment, Two-Dimensional Inlet, Mach 0.8	457
7-290	Fuselage/Axisymmetric Inlet Sections	458
7-291	Comparison of Inlet Performance, Axisymmetric Inlet, Mach 1.2, $\alpha = -3^\circ$	459
7-292	Comparison of Inlet Performance, Axisymmetric Inlet, Mach 1.2, $\alpha = 0^\circ$	460
7-293	Comparison of Inlet Performance, Axisymmetric Inlet, Mach 1.2, $\alpha = 5^\circ$	461
7-294	Comparison of Inlet Performance, Axisymmetric Inlet, Mach 1.2, $\alpha = 10^\circ$	462
7-295	Comparison of Inlet Performance, Two-Dimensional Inlet, Mach 1.2, $\alpha = -3^\circ$	464
7-296	Comparison of Inlet Performance, Two-Dimensional Inlet, Mach 1.2, $\alpha = 0^\circ$	465
7-297	Comparison of Inlet Performance, Two-Dimensional Inlet, Mach 1.2, $\alpha = 5^\circ$	466
7-298	Comparison of Inlet Performance, Two-Dimensional Inlet, Mach 1.2, $\alpha = 10^\circ$	467
7-299	Comparison of Inlet Performance, Two-Dimensional Inlet, Mach 1.2, $\alpha = 15^\circ$	468
7-300	Comparison of Inlet Performance, Two-Dimensional Inlet, Mach 1.2, $\alpha = 20^\circ$	469
7-301	Comparison of Inlet Performance, Two-Dimensional Inlet, Mach 1.2, $\alpha = 25^\circ$	470
7-302	Comparison of Inlet Performance, Axisymmetric Inlet, Mach 1.8, $\alpha = -3^\circ$	471
7-303	Comparison of Inlet Performance, Axisymmetric Inlet, Mach 1.8, $\alpha = 0^\circ$	472
7-304	Comparison of Inlet Performance, Axisymmetric Inlet, Mach 1.8, $\alpha = 5^\circ$	474
7-305	Comparison of Inlet Performance, Axisymmetric Inlet, Mach 1.8, $\alpha = 10^\circ$	475
7-306	Comparison of Inlet Performance, Axisymmetric Inlet, Mach 1.8, $\alpha = 15^\circ$	476

LIST OF ILLUSTRATIONS (Continued)

Figure	Description	Page
7-307	Comparison of Inlet Performance, Axisymmetric Inlet, Mach 1.8, $\alpha = 20°$	477
7-308	Comparison of Inlet Performance, Axisymmetric Inlet, Mach 1.8, $\alpha = 25°$	478
7-309	Comparison of Inlet Performance, Two-Dimensional Inlet, Mach 1.8, $\alpha = -3°$	479
7-310	Comparison of Inlet Performance, Two-Dimensional Inlet, Mach 1.8, $\alpha = 0°$	480
7-311	Comparison of Inlet Performance, Two-Dimensional Inlet, Mach 1.8, $\alpha = 5°$	481
7-312	Comparison of Inlet Performance, Two-Dimensional Inlet, Mach 1.8, $\alpha = 10°$	482
7-313	Comparison of Inlet Performance, Two-Dimensional Inlet, Mach 1.8, $\alpha = 15°$	483
7-314	Comparison of Inlet Performance, Two-Dimensional Inlet, Mach 1.8, $\alpha = 20°$	484
7-315	Comparison of Inlet Performance, Two-Dimensional Inlet, Mach 1.8, $\alpha = 25°$	485
7-316	Comparison of Inlet Performance, Axisymmetric Inlet, Mach 2.2, $\alpha = -3°$	487
7-317	Comparison of Inlet Performance, Axisymmetric Inlet, Mach 2.2, $\alpha = 0°$	488
7-318	Comparison of Inlet Performance, Axisymmetric Inlet, Mach 2.2, $\alpha = 5°$	489
7-319	Comparison of Inlet Performance, Axisymmetric Inlet, Mach 2.2, $\alpha = 10°$	490
7-320	Comparison of Inlet Performance, Axisymmetric Inlet, Mach 2.2, $\alpha = 15°$	491
7-321	Comparison of Inlet Performance, Axisymmetric Inlet, Mach 2.2, $\alpha = 20°$	492
7-322	Comparison of Inlet Performance, Axisymmetric Inlet, Mach 2.2, $\alpha = 25°$	493
7-323	Comparison of Inlet Performance, Two-Dimensional Inlet, Mach 2.2, $\alpha = -3°$	494
7-324	Comparison of Inlet Performance, Two-Dimensional Inlet, Mach 2.2, $\alpha = 0°$	495
7-325	Comparison of Inlet Performance, Two-Dimensional Inlet, Mach 2.2, $\alpha = 5°$	496

LIST OF ILLUSTRATIONS (Continued)

Figure	Description	Page
7-326	Comparison of Inlet Performance, Two-Dimensional Inlet, Mach 2.2, $\alpha = 10°$	497
7-327	Comparison of Inlet Performance, Two-Dimensional Inlet, Mach 2.2, $\alpha = 15°$	498
7-328	Comparison of Inlet Performance, Two-Dimensional Inlet, Mach 2.2, $\alpha = 20°$	499
7-329	Comparison of Inlet Performance, Two-Dimensional Inlet, Mach 2.2, $\alpha = 25°$	500
7-330	Comparison of Inlet Performance, Axisymmetric Inlet, Mach 2.5, $\alpha = -3°$	502
7-331	Comparison of Inlet Performance, Axisymmetric Inlet, Mach 2.5, $\alpha = 0°$	503
7-332	Comparison of Inlet Performance, Axisymmetric Inlet, Mach 2.5, $\alpha = 5°$	504
7-333	Comparison of Inlet Performance, Axisymmetric Inlet, Mach 2.5, $\alpha = 10°$	505
7-334	Comparison of Inlet Performance, Axisymmetric Inlet, Mach 2.5, $\alpha = 15°$	506
7-335	Comparison of Inlet Performance, Axisymmetric Inlet, Mach 2.5, $\alpha = 17.5°$	507
7-336	Comparison of Inlet Performance, Two-Dimensional Inlet, Mach 2.5, $\alpha = -3°$	508
7-337	Comparison of Inlet Performance, Two-Dimensional Inlet, Mach 2.5, $\alpha = 0°$	509
7-338	Comparison of Inlet Performance, Two-Dimensional Inlet, Mach 2.5, $\alpha = 5°$	510
7-339	Comparison of Inlet Performance, Two-Dimensional Inlet, Mach 2.5, $\alpha = 10°$	511
7-340	Comparison of Inlet Performance, Two-Dimensional Inlet, Mach 2.5, $\alpha = 15°$	512
7-341	Comparison of Inlet Performance, Two-Dimensional Inlet, Mach 2.5, $\alpha = 20°$	513
7-342	Comparison of Inlet Performance, Two-Dimensional Inlet, Mach 2.5, $\alpha = 25°$	514
7-343	Comparison of Inlet Performance, Wing Effects, Mach 0.8, $\alpha = -3°$, 2-D	516
7-344	Comparison of Inlet Performance, Wing Effects, Mach 0.80, $\alpha = 0°$, 2-D	517

LIST OF ILLUSTRATIONS (Continued)

Figure	Description	Page
7-345	Comparison of Inlet Performance, Wing Effects, Mach 0.8, $\alpha = 5°$, 2-D	518
7-346	Comparison of Inlet Performance, Wing Effects, Mach 0.8, $\alpha = 10°$, 2-D	519
7-347	Comparison of Inlet Performance, Wing Effects, Mach 0.8, $\alpha = 15°$, 2-D	520
7-348	Comparison of Inlet Performance, Wing Effects, Mach 0.8, $\alpha = 20°$, 2-D	521
7-349	Comparison of Inlet Performance, Wing Effects, Mach 0.8, $\alpha = 25°$, 2-D	522
7-350	Comparison of Inlet Performance, Wing Effects, Mach 1.2, $\alpha = -3°$, 2-D	523
7-351	Comparison of Inlet Performance, Wing Effects, Mach 1.2, $\alpha = 0°$, 2-D	524
7-352	Comparison of Inlet Performance, Wing Effects, Mach 1.2, $\alpha = 5°$, 2-D	525
7-353	Comparison of Inlet Performance, Wing Effects, Mach 1.2, $\alpha = 10°$, 2-D	526
7-354	Comparison of Inlet Performance, Wing Effects, Mach 1.8, $\alpha = -3°$, 2-D	527
7-355	Comparison of Inlet Performance, Wing Effects, Mach 1.8, $\alpha = 0°$, 2-D	528
7-356	Comparison of Inlet Performance, Wing Effects, Mach 1.8, $\alpha = 5°$, 2-D	529
7-357	Comparison of Inlet Performance, Wing Effects, Mach 1.8, $\alpha = 10°$, 2-D	530
7-358	Comparison of Inlet Performance, Wing Effects, Mach 1.8, $\alpha = 15°$, 2-D	531
7-359	Comparison of Inlet Performance, Wing Effects, Mach 1.8, $\alpha = 20°$, 2-D	532
7-360	Comparison of Inlet Performance, Wing Effects, Mach 2.2, $\alpha = -3°$, 2-D	533
7-361	Comparison of Inlet Performance, Wing Effects, Mach 2.2, $\alpha = 0°$, 2-D	534
7-362	Comparison of Inlet Performance, Wing Effects, Mach 2.2, $\alpha = 5°$, 2-D	536
7-363	Comparison of Inlet Performance, Wing Effects, Mach 2.2, $\alpha = 10°$, 2-D	537

LIST OF ILLUSTRATIONS (Continued)

Figure	Description	Page
7-364	Comparison of Inlet Performance, Wing Effects, Mach 2.2, $\alpha = 15°$, 2-D	538
7-365	Comparison of Inlet Performance, Wing Effects, Mach 2.2, $\alpha = 20°$, 2-D	539
7-366	Comparison of Inlet Performance, Wing Effects, Mach 2.5, $\alpha = -3°$, 2-D	540
7-367	Comparison of Inlet Performance, Wing Effects, Mach 2.5, $\alpha = 0°$, 2-D	541
7-368	Comparison of Inlet Performance, Wing Effects, Mach 2.5, $\alpha = 5°$, 2-D	542
7-369	Comparison of Inlet Performance, Wing Effects, Mach 2.5, $\alpha = 10°$, 2-D	543
7-370	Comparison of Inlet Performance, Wing Effects, Mach 2.5, $\alpha = 15°$, 2-D	544
7-371	Comparison of Inlet Performance, Wing Effects, Mach 2.5, $\alpha = 20°$, 2-D	545
7-372	Wing Surface Pressure Ratio Probe Effect	548
7-373	Fuselage Surface Static Distribution in the Presence of the Probe Fuselage Instrumentation Ray = 0°, Fuselage 2	549
7-374	Fuselage Surface Static Pressure Distribution in the Presence of the Probe Fuselage Instrumentation Ray = 0°, Fuselage 1	550
7-375	Fuselage Surface Static Pressure Distribution in the Presence of the Probe Fuselage Instrumentation Ray = 0°, Fuselage 1	551
7-376	Fuselage Surface Static Pressure Distribution in the Presence of the Probe Fuselage Instrumentation Ray = 0°, Fuselage 2	552
A-1	Surveyed Aircraft Configurations	558
A-2	Surveyed Aircraft Configurations (CONFIDENTIAL)	566
A-3	Recent Tactical Aircraft Review Summary, Nose Geometric Characteristics	570
A-4	Foreign Tactical Aircraft Review Summary, Nose Geometric Characteristics	571
A-5	Advanced Tactical Aircraft Review Summary, Nose Geometric Characteristics	572
A-6	Recent Tactical Aircraft Review Summary Canopy, Geometric Characteristics	573

LIST OF ILLUSTRATIONS (Concluded)

Figure	Description	Page
A-7	Foreign Tactical Aircraft Review Summary Canopy, Geometric Characteristics	574
A-8	Advanced Tactical Aircraft Review Summary Canopy, Geometric Characteristics	575
A-9	Recent Tactical Aircraft Review Summary, Fuselage Geometric Characteristics at the Inlet Station	576
A-10	Foreign Tactical Aircraft Review Summary, Fuselage Geometric Characteristics at the Inlet Station	577
A-11	Advanced Tactical Aircraft Review Summary, Fuselage Geometric Characteristics at the Inlet Station	578
A-12	Recent Tactical Aircraft Review Summary, Wing Geometric Characteristics	579
A-13	Foreign Tactical Aircraft Review Summary, Wing Geometric Characteristics	580
A-14	Advanced Tactical Aircraft Review Summary, Wing Geometric Characteristics	581
A-15	Recent Tactical Aircraft Review Summary, Inlet Geometric Characteristics	582
A-16	Foreign Tactical Aircraft Review Summary, Inlet Geometric Characteristics	583
A-17	Advanced Tactical Aircraft Review Summary, Inlet Geometric Characteristics	584

LIST OF TABLES

Table No.	Description	Page
I	Wind Tunnel Test Schedule	94
II	Comparison Between Probe Data and Analytical Equation at 1/2" Distance from Body, $M_\infty = 2.2$, Fuselage 3	236
III	Analytically Derived Flow Properties, Fuselage 2	242
IV	Analytically Derived Flow Properties, Fuselage 3	244
V	Control Line Functions	266

LIST OF ABBREVIATIONS AND SYMBOLS

Symbol	Description
A	Cross-sectional Area
a	Semi-major axis of an ellipse
A_c	Inlet geometric cowl area
A_o	Inlet geometric capture area
ACL	Aircraft length
AR	Aspect ratio
b	Semi- minor axis of an ellipse
BCL	Basic contour line
c	Speed of sound
D	Diameter
°F	Degrees Farenheit
e	Elliptical eccentricity
f	Coefficient of friction
H	Enthalpy
H_I	Inlet height
h/H	Fuselage height factor
HRL	Horizontal reference line
$\Delta H/q$	Inviscid flow loss coefficient
$\hat{i}$	Unit vector
I.D.	Inside diameter
LAMBDA	Inlet total pressure recovery
L/D	Ratio of length of duct section to duct diameter

LIST OF ABBREVIATIONS AND SYMBOLS (Continued)

Symbol	Description
R	Gas constant for air
r	Radius
°R	Degrees Rankine
SC	Secondary canopy
SCPN	Secondary canopy primary nose
SCSN	Secondary canopy secondary nose
SN	Secondary nose
T	Temperature
TLu	Table look up
2D	Two dimensional
V	Velocity
V_L	Local velocity
W_I	Inlet width
X	Longitudinal distance
Y	Lateral distance from vertical centerline of fusleage
y	Horizontal distance in coordinate system of flow field
Z	Vertical distance from reference horizontal plane
z	Vertical distance in coordinate system of flow field
α	Angle of attack
α_{LV}	Angle of attack of the local flow relative to the vehicle centerline

LIST OF ABBREVIATIONS AND SYMBOLS (Continued)

Symbol	Description
M	Mach number
m	Inlet mass flow
m_{bl}	Inlet throat bleed mass flow
M_L	Local Mach number
m_∞	Ideal inlet mass flow
M.C.	Method of Characteristics
m/m_∞	Inlet mass flow ratio
m/m*	Inlet mass flow divided by inlet mass flow at Mach number = 1.0
m_{bl}/m_∞	Bleed mass flow ratio
N	Number of shocks in inlet system design
N_{D_i}	Steady state engine face distortion
N/A	Not available
P	Static pressure
PC	Primary canopy
PCPN	Primary canopy primary nose
PCSN	Primary canopy secondary
PN	Primary nose
psi	Pounds per square inch
ΔP	Pressure differential
P/P_∞	Static Pressure ratio
P_t/P_{t_∞}	Total pressure recovery
q	Dynamic pressure

LIST OF ABBREVIATIONS AND SYMBOLS (Continued)

Symbol	Description
β	Angle of yaw
γ	Ratio of specific heats
γ_a	Average ratio of specific heats
Δ	Angle defined by the oblique line between the fuselage tangency points and the base of the fuselage
δ	Deflection angle
δ_1	Initial deflection angle
δ_2	Second deflection angle
δ_{c1}	Initial cone half angle
δ_{c2}	Second cone half angle
δ^*	Boundary layer displacement thickness
ϵ	Downwash angle
η	Nose angle of incidence
η_{av}	Average total pressure recovery
η_D	Total pressure recovery
θ	Oblique shock wave angle
μ	Radial plane, or cutting plane angle
ρ	Density, or angle encompassing the tangency points of the body whose apex is the vehicle nose in Section VII
σ	Sidewash angle
ϕ	Flow deflection angle
ϕ_o	Flow deflection in zero radial plane
ϕ_u	Flow deflection in μ radial plane

LIST OF ABBREVIATIONS AND SYMBOLS (Continued)

Symbol	Description
ψ	Total deviation factor

Subscripts

o	Stagnation conditions
1	Station in front of pitot shock in Section IV; station behind oblique shock in Section V
2	Station behind pitot shock in Section IV; station at diffuser exit in Section V
3	Inlet station behind terminal shock in N = 3 shock system
1, 2, 3, 4 . . . 19	Orifice position in engine face rake
a	Average
bl	Bleed
c	Cowl lip station
CAV	Cavity
de	Diffuser entrance
M	Flow meter
s	Static
t	Total
α	At angle of attack
μ	In radial plane (24°, 0°, -30°, -60°, -90°)
∞	Free stream

PRECEDING PAGE BLANK-NOT FILMED

SECTION I
INTRODUCTION

The program reported on in this document was directed toward improving current understanding of the interaction between the air induction systems and the airframes of supersonic tactical fighters. Efforts such as these are essential, not only to the improvement of overall aircraft system performance, but also to give meaning to system tradeoff studies and confidence in their results. As in the chain and weak link argument, the value of a system trade-off study is limited by the accuracy with which any single important element has been described. In the present context, a fighter aircraft system trade study would be of dubious value if, for example, a significant airframe flow field characteristic in the region of proposed inlet placement were to be grossly miscalculated, or, in the extreme case, completely ignored! Of the numerous factors that enter into the selection of inlet type and location on integrated configurations, the proposed study focused mainly on the flow environment (and its effect on inlet performance), produced by representative supersonic tactical fighter aircraft at points within their maneuvering envelopes. The models and tests were designed to produce an extremely wide range of parametric airframe flow field and inlet performance data within a reasonable tunnel occupancy time. In this connection, emphasis on versatility and economy yielded a building block model design concept of low cost capable of representing many realistic aircraft configurations. Therefore, the experimental results provide a large bank of parametric, systems oriented data.

SECTION II
SUMMARY

The objective of the contracted program was to conduct a systematic investigation designed to yield a basic understanding of the effects of airframe-inlet interaction on the performance potential of inlet designs associated with supersonic air-breathing tactical fighter aircraft. To accomplish this objective, a program comprised of four major tasks was formulated.

First, pertinent design characteristics of tactical fighter aircraft configurations, as they relate to the problems of airframe-inlet interaction, were studied in a comprehensive systems review of the century-series tactical fighter aircraft. This survey led to the definition of realistic aircraft component geometry. Based upon this statistically derived information. several vehicle configurations were designed. These configurations were then refined to satisfy aerodynamic and subsystem requirements. From among the competitive designs, seven were selected for wind tunnel model design and test. The criteria employed in this selection process insured that a large amount of generalized data would be gathered.

Second, simple analyses of aircraft flow fields and performance estimates for two inlet designs were made for anticipated wind-tunnel freestream flow conditions. Estimates of flow field properties were made using readily available analytical techniques. Simple performance analyses of the inlet designs were accomplished using standard techniques to account for major losses in the system.

Third. an experimental program was conducted to investigate inlet flow fields and the gross effects of upstream flow field nonuniformities and viscous interaction on inlet performance and flow distortion. The experimental program was comprised of three phases designed to provide thorough testing of the forebody variations alone so that better understanding of inlet flow fields was gained. tests of the inlets alone so that a basic performance level for each inlet could be established. and tests of a large number of combined flight vehicle, (forebody-inlet). configurations so that the sensitivity of inlet performance to flow field nonuniformities generated by the airframe could be determined together with the degree of "protection" afforded by the airframe.

Fourth, all data obtained was analyzed and correlated so that some of the basic effects of airframe design on inlet flow field environment as influenced by its location can be determined. Conclusions were drawn regarding inlet-airframe designs and the types of inlet flow field nonuniformities associated with typical airframe design features. Forward of the wing the flow field composition was influenced primarily by fuselage corner geometry. Aft of the wing leading edge, the wing dictated flow field composition.

The techniques employed for analyzing the flow field characteristics and for predicting the resultant impact upon performance were reviewed and empirically refined to a level of accuracy consistent with preliminary design work.

SECTION III

SYSTEMS REVIEW AND DESIGN SELECTION

3.0 Introduction

The primary objective of the systems review task was to provide a broad statistical base of airframe geometry variations based on flying hardware and future systems designs, to incorporate this statistical information into the synthesis of several realistic airframe designs and to select those configurations best suited to a generalized flow field study.

The statistical information was generated, in part, by a review of the conceptual approaches that have been employed in the design of aircraft in the tactical class. Thirty nine present day and near term future aircraft were surveyed during this study, including both domestic and foreign configurations. A majority of the aircraft sampled are or have been operational aircraft. Ten configurations are considered representative of advanced aircraft such as the F-15. Line drawings of all thirty nine aircraft employed for the survey task are shown in appendix A. The geometric characteristics of the aircraft fuselage, inlet, nose, canopy, and wing were cataloged, as were the arrangement of these components with relation to each other. This geometric information was then used to analyze the operational characteristics of each system. For example, good angle-of-attack performance can be predicted for a two-dimensional-horizontal-wedge, side-mounted inlet system. Based upon the information gathered during this review, the advantages and disadvantages of each general design type were delineated.

Chronologically, the review studied recent aircraft first, and advanced designs second. The introduction of time as a classification parameter was critical to the success of the systems review. This was due to the change in vehicle requirements (materials, structures, armament, electronics, etc.) and inlet requirements (sophistication, distortion, engine concepts, etc.) that have evolved as a result of technological advances and increased-Mach-number capability. As a result of these requirement shifts, the relative importance of the inlet design to the overall design has increased markedly. The prevalent design practice of the 1950's, where an inlet was designed after the vehicle was conceptually fixed, is no longer acceptable. This trend in inlet influence upon the overall design is clearly a function of time. The reason for using two categories (recent and advanced) in the study lies in the fact that recent experience has highlighted problems in the design process associated with engine-inlet compatibility. The result has been an increase in the influence of the inlet design upon overall vehicle design. Some design practices have been altered making direct comparison with older designs difficult.

To this point the recommended selections were derived primarily from a knowledge of existing and projected technology plus an examination of the geometric characteristics of the systems review aircraft designs. Next, the aircraft configurations resulting from the integration of the selected components into a complete system were examined. The independently derived components were refined to reflect their installation in a system and the practicality of the resultant aircraft was assessed. Although a strong systems orientation was employed. with respect to the configuration designs, it was necessary to temper this approach sufficiently to produce configuration geometries of interest from a general point of view. By this it is meant that the geometries and data had to be general enough to permit their use in a preliminary design study, either directly, by interpolation between similar configurations, or by a small extrapolation beyond one similar configuration.

Another objective of the program was to obtain experimental data that could be used to gain some insight into the effect of model scale upon ground test results, and the variation between ground test and flight test results. Several U.S. Air Force programs with similar objectives and model geometries were found to exist and an attempt to achieve commonality with these programs was made.

3.1 Definition of Geometric Parameters

In order to provide systematic documentation of the geometric characteristics of each major aircraft component, i.e., nose, canopy, fuselage, wing. and inlet for each of the aircraft studied. a series of descriptive parameters were selected. These data served to establish the degree of geometric similarity from aircraft to aircraft. The parameters also helped identify particularly large geometric differences among the surveyed aircraft. Technical and operational characteristics were employed to assess the significance of these differences.

These geometric parameters are defined in the following subparagraphs and are graphically illustrated in Figures 3-1 and 3-2.

Aircraft Nose

- Fineness Ratio = the length of the nose cone to the radome, divided by the diameter of the nose cone at the radome station = L_{nose}/D_{radome}
- Initial Included Angle = the included angle of the aircraft nose cone = $\sphericalangle_I$
- Equivalent Included Angle = the included angle measured from the nose cone tip to a rounded radome periphery = $\sphericalangle_E$
- Nose Droop = the angle of nose droop measured with respect to the horizontal reference line = $\sphericalangle_D$

Aircraft Canopy

- Fineness Ratio = the ratio of canopy length to canopy height measured along and perpendicular to a canopy reference shoulder line = L_{canopy}/H_{canopy}
- Canopy/Fuselage Size Factor = maximum canopy frontal area divided by maximum forebody frontal area = Area B/Area C
- Canopy/Inlet Size Factor = maximum canopy frontal area divided by the total inlet capture area = Area B/2X (Area D)

- Longitudinal Location = the ratio of canopy leading edge station to the inlet cowl station = Canopy Station/Inlet Station
- Circumferential Location Angle = the included angle containing the canopy as measured radially from the fuselage centerline = $\measuredangle_C$

Fuselage Geometric Parameters at Inlet Station

- Fineness Ratio = the ratio of aircraft length to maximum equivalent diameter = Total Aircraft Length/Max. Equivalent Dia.
- Aspect Ratio = fuselage height to the canopy reference shoulder line divided by fuselage width, measured along the vertical and horizontal centerlines = $H_F/2X\ W_S$
- Size Factor = the fuselage cross-sectional area below the canopy reference shoulder line divided by the radome cross-sectional area = 2X (Area E)/Area A
- Local Aspect Ratio = the ratio of fuselage height to fuselage width measured along the vertical centerline and the horizontal reference line of the fuselage lower quadrant = H/W
- Shape Factor = the fuselage cross-sectional area of a lower quadrant bounded by a fuselage vertical centerline and the horizontal reference line divided by the cross-sectional area possible if the corner radius were eliminated = Area F/H x W

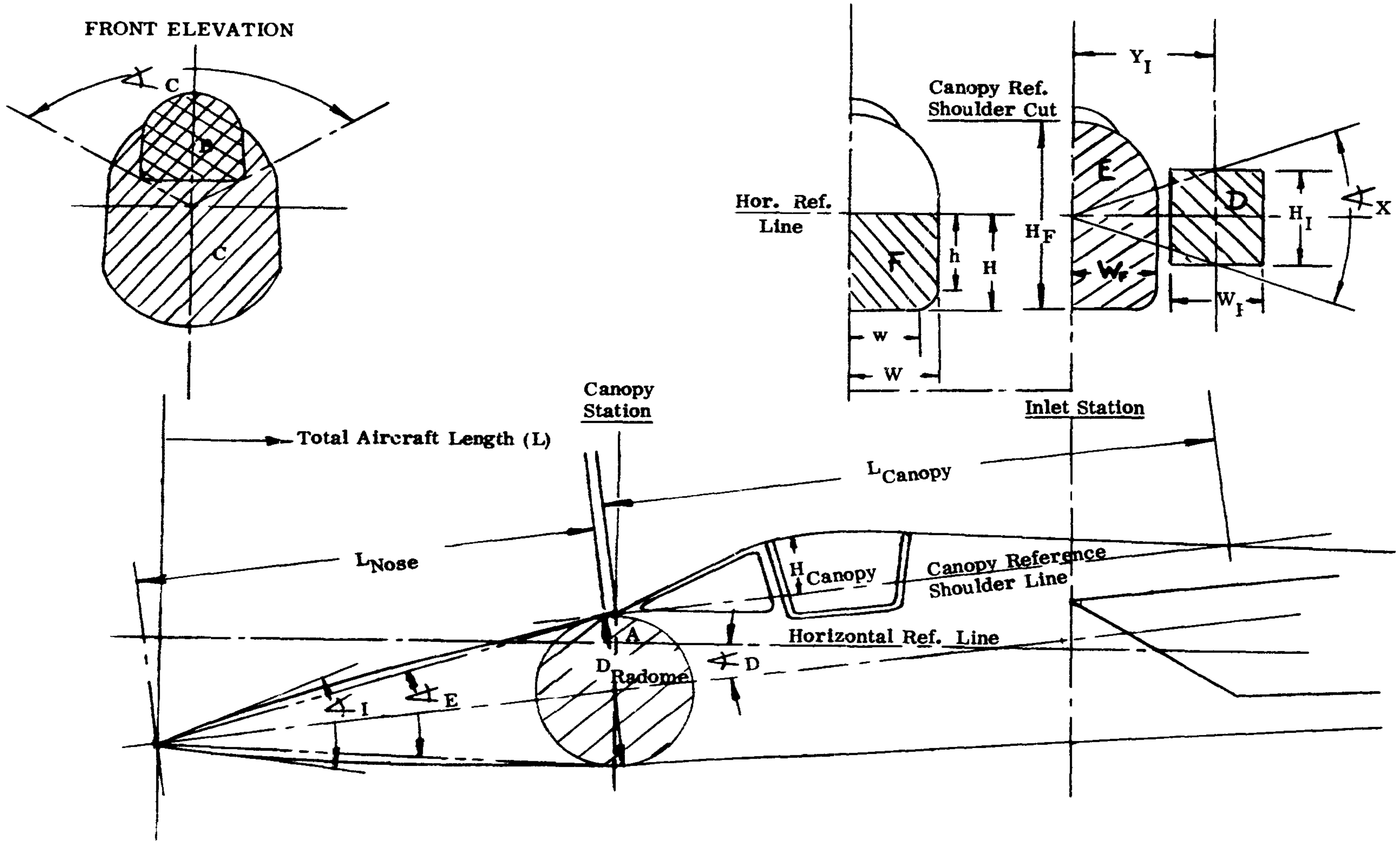
FRONT ELEVATION
∡C
D
C
Canopy Ref.
Shouldor Cut
Hor. Ref.
Line
F
h
H
H_F
E
W_F
D
Y_I
H_I
∡X
W_I
w
W
Canopy
Station
Inlet Station
Total Aircraft Length (L)
L_{Canopy}
L_{Nose}
H_{Canopy}
Canopy Reference
Shoulder Line
Horizontal Ref. Line
A
D_{Radome}
∡D
∡E
∡I

Figure 3-1. Schematic-Definition of Nose, Canopy and Fuselage Geometric Parameters

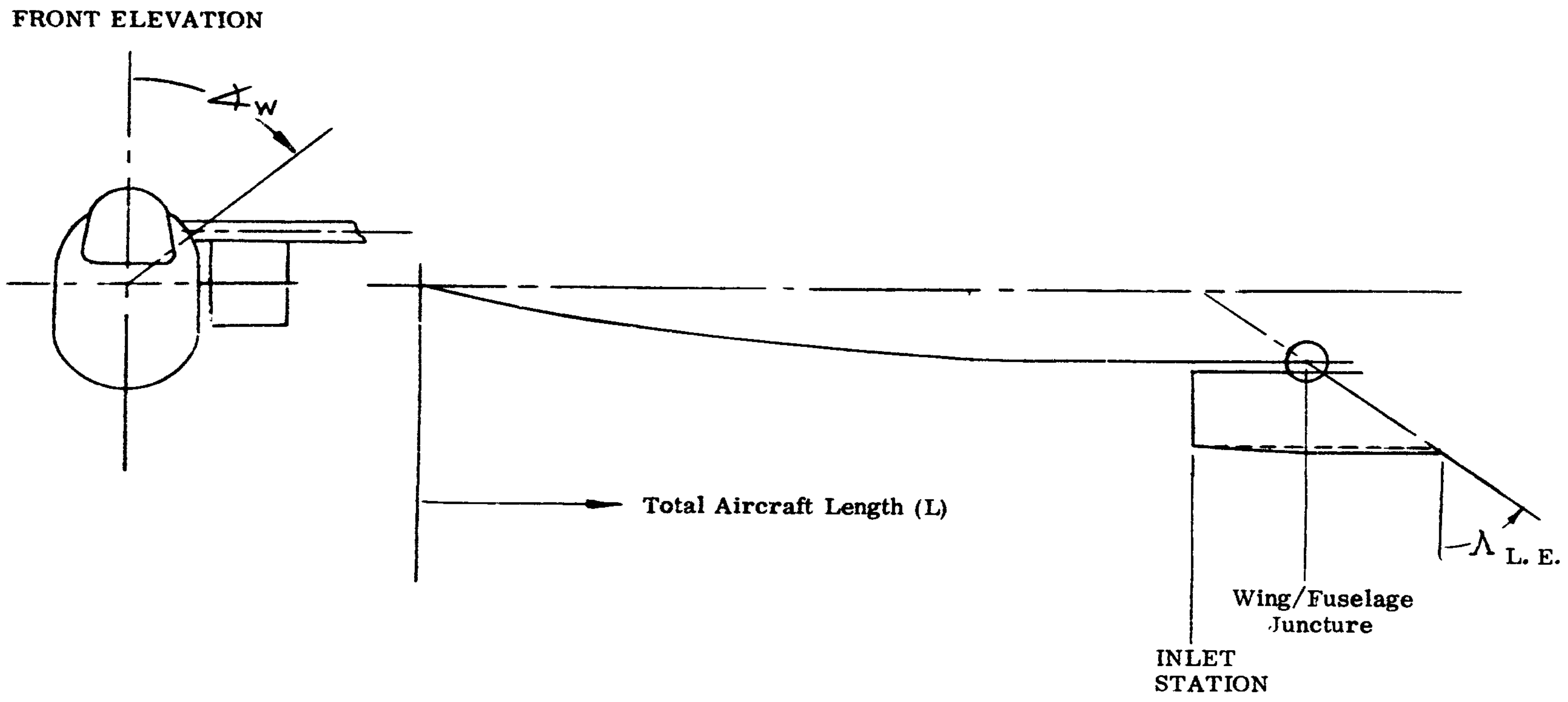
FRONT ELEVATION
$\measuredangle_W$
Total Aircraft Length (L)
$-\Lambda_{L.E.}$
Wing/Fuselage Juncture
INLET STATION

Figure 3-2. Schematic-Definition of Wing Geometric Parameters

- Width Factor = the half-width of the fuselage lower surface, measured from the fuselage vertical centerline to the tangent point of the corner radius, divided by the width possible if the corner radius were eliminated = w/W
- Height Factor = the height of the fuselage side from fuselage horizontal reference line to the tangent point of the corner radius, divided by the height possible if the corner radius were eliminated = h/H

Wing Geometric Parameters

- Longitudinal Location = the station at the wing/fuselage juncture divided by the aircraft length = Station at Wing/Fuselage Juncture/Total Aircraft Length
- Circumferential Location Angle = the circumferential angle of the wing/fuselage juncture, as measured from the fuselage centerline, with respect to the vertical = $\sphericalangle_W$

Inlet Geometric Parameters

- Fineness Ratio = the ratio of subsonic diffuser length to engine face diameter = L/D
- Size Factor = the ratio of the total inlet capture area to the fuselage forebody maximum frontal area = 2X (Area D)/Area C
- Aspect Ratio = the ratio of inlet height to inlet width = H_I/W_I
- Longitudinal Location = the ratio of the inlet cowl station to the aircraft length = Inlet Station/Aircraft Length
- Radial Location = the offset of the inlet centerline from the fuselage vertical centerline divided by the fuselage half-width = Y_I/W_F

- Circumferential Location Angle = the included angle containing the inlet as measured circumferentially from the fuselage centerline $= \measuredangle_X$
- Clearance = the height above the ground line of the inlet lower lip

3.2 Aircraft Nose Characteristics

The geometry of the aircraft nose evolves primarily as a function of the aircraft mission requirements as they relate to flight envelope, inlet-powerplant integration, and pilot visibility. In addition, the type and level of avionics employed has a strong influence upon the nose geometric characteristics selected.

The survey produced three general conclusions; the inclusion of some nose droop is desirable, nose diameter will not vary from present day configurations even though increased avionics miniaturization is anticipated, and ogival nose sections are preferable to conical nose sections. Further, the nose geometric characteristics do not exhibit a trend of nose shape or fineness ratio with Mach number or time period. The nose geometric characteristics for all aircraft surveyed are summarized in appendix A.

In an attempt to be independent of the numerous factors that influence the shape of the nose, the parameter of equivalent included angle, defined as the included angle measured from the nose cone tip to the radome periphery, was used. The equivalent included angle with the nose cone fineness ratio of all the aircraft in the Systems Review is shown in Figure 3-3. The line superimposed is the theoretical relationship between equivalent included angle and nose cone fineness ratio. The data point deviations from this line indicate the degree of accuracy in the measurement taken from the extremely small three view drawings available. However, this accuracy is deemed adequate to provide the basis required to support design selection.

From an aerodynamic viewpoint, increasing Mach number requires the utilization of increasingly larger nose cone fineness ratio and smaller equivalent included angles. In addition, experience has shown that an increase in design Mach number usually requires a higher level of avionics performance. However, advances in avionics miniaturization during this period of increasing flight speed has permitted the attainment of both requirements. For example, among the numerous modifications made between the F-4C and the F-4E aircraft, the equivalent nose cone included angle was reduced from approximately 35° to 26° with an attendant 37% increase in fineness ratio. Another illustration is a comparison of three European aircraft (Draken, Viggen, and Jaguar) with similar mission requirements but differing in the time period of development, therefore, implying a difference in avionics level. Among these three aircraft, the newest weapon system is the joint British/French Jaguar with a nose cone fineness ratio 34% higher than the Viggen and 17.5% higher than the Draken.

For the Advanced Aircraft, such as the ten FX configurations, the nose cone fineness ratio varied between a high of 3.045 to a low of 1.910. One possible explanation for this is a variation in avionics level and the subsequent variation in size of the radar installations. Statistically, a majority of the configurations showed a nose cone fineness ratio exceeding 2.400.

Fuselage nose droop is shown in Figure 3-4 as a function of canopy fineness ratio. The figure shows a variation between 0 and 10.5° droop. Among the aircraft surveyed, excluding aircraft with nose inlet, 79% used some degree of nose droop, but a particular trend is not evident. However from available data, the average droop angle is approximately 3.5° for the recent and foreign aircraft, and 6.0° for the advanced aircraft.

Based upon the Systems Review, two nose configurations were selected so that the effect of geometry variation could be evaluated. Where a clear trend existed, as in Figure 3-3, the parameters were selected to encompass the variation postulated for aircraft of the advanced class. The absence of a clear trend, as in Figure 3-4, necessitated that the centroid of advanced aircraft data points be employed as the basis of selection. The selected configurations are summarized below.

Selection No. 1 - Primary

Nose Cone Equivalent Included Angle = 22°
Nose Cone Initial Included Angle = 30°
Nose Cone Fineness Ratio = 2.56

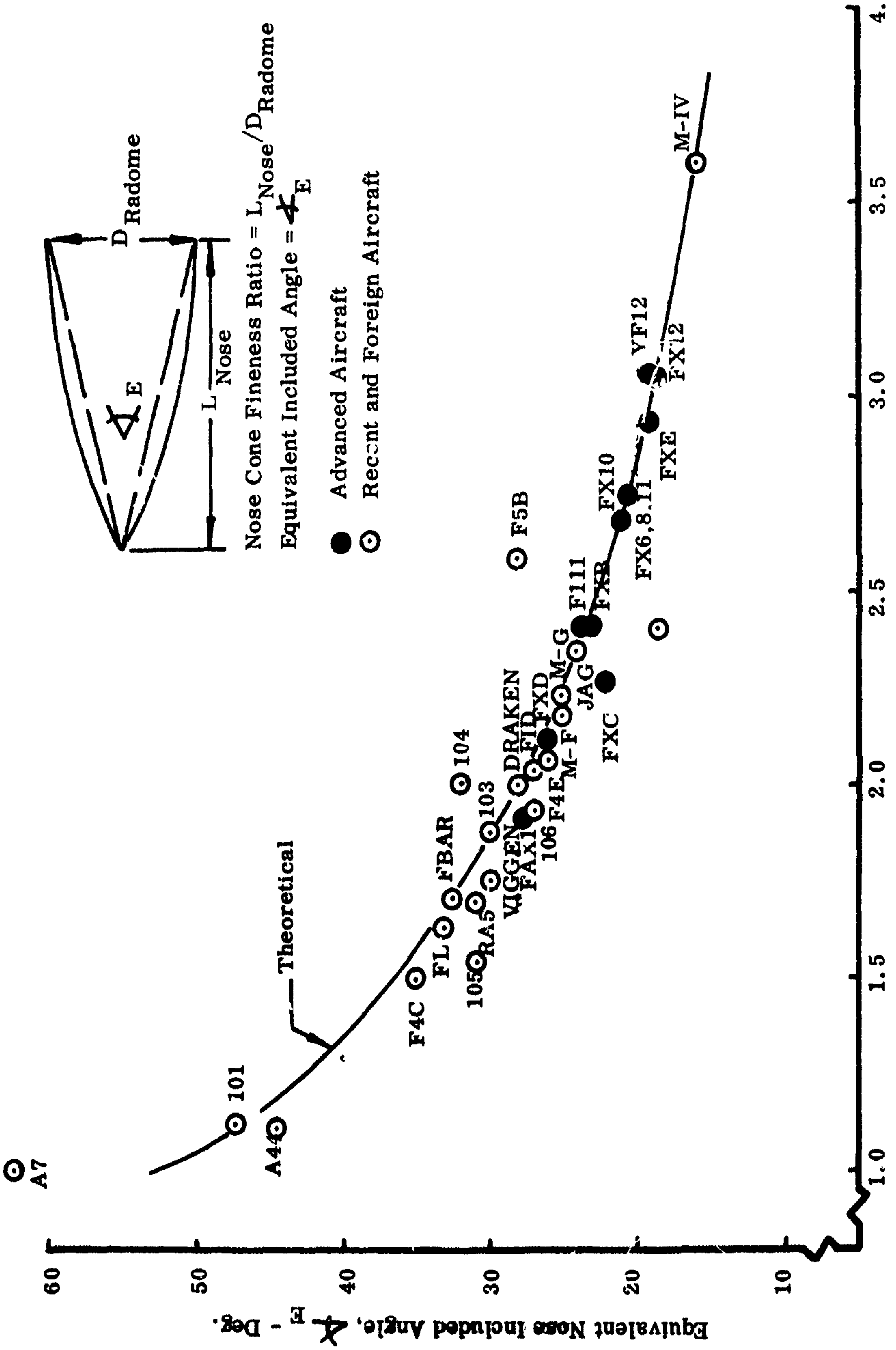

Figure 3-3. Nose Cone Geometric Characteristics

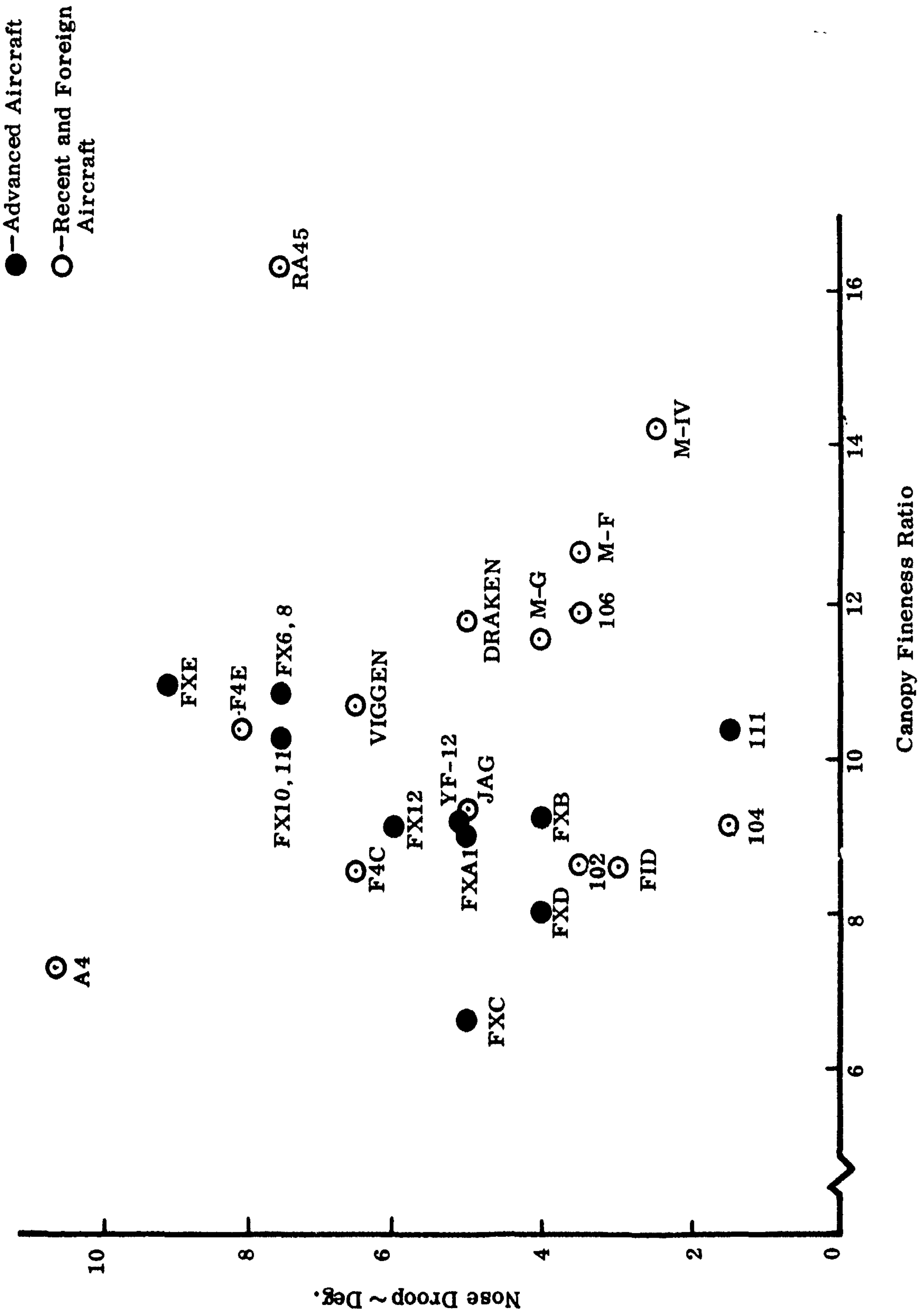

Figure 3-4. Nose Droop Characteristics

Nose Droop Angle = 5.0
Radome Maximum Diameter = 40.0"
Nose Cone Shape - Ogival

Selection No. 2 - Alternate

Nose Cone Equivalent Included Angle = 18°
Nose Cone Initial Included Angle = 24°
Nose Cone Fineness Ratio = 3.14
Nose Droop Angle = 7.5°
Radome Maximum Diameter = 35.0"
Nose Cone Shape - Ogival

Selection No. 1 is judged to be representative of near term aircraft, and Selection No. 2 represents the expected future requirement of higher speed projecting the state-of-the-art in avionics miniaturization. The nose droop angles of 5.0° and 7.5°, though higher than the numerical averages, are more representative of actual and proposed aircraft. The nose cone initial included angle of supersonic aircraft have been found to vary between approximately 1.0 and 1.35 times the equivalent included angle. Therefore, to remain consistent with design practices, this rule-of-thumb for the initial included angle was used. The radome maximum diameter of Selection No. 1 corresponds to the FX Avionics Level 3 enclosing a 34" swing-dish radar of a 36" fixed array radar. For Selection 2, the maximum radome diameter of 35" is projected for future advanced systems.

3.3 Aircraft Canopy Characteristics

The canopy configuration evolves as a function of the equipment to be installed in the cockpit, the number of seats and their arrangement (whether tandem or side-by-side), the height of seats dictated by a glass piercing provision, the mission requirements, such as low altitude high speed, or a zero speed-zero altitude ejection capsule which may require a weightier, more sophisticated mechanism.

Present HIAD cockpit design limits specify an 8-inch minimum head-clearance centered at the pilot's eye, which is the height of the normal horizontal vision line. A 20-inch clearance must be maintained in front of this focal point which is required for the 30-inch minimum cockpit opening for the ejection seat, and which in turn

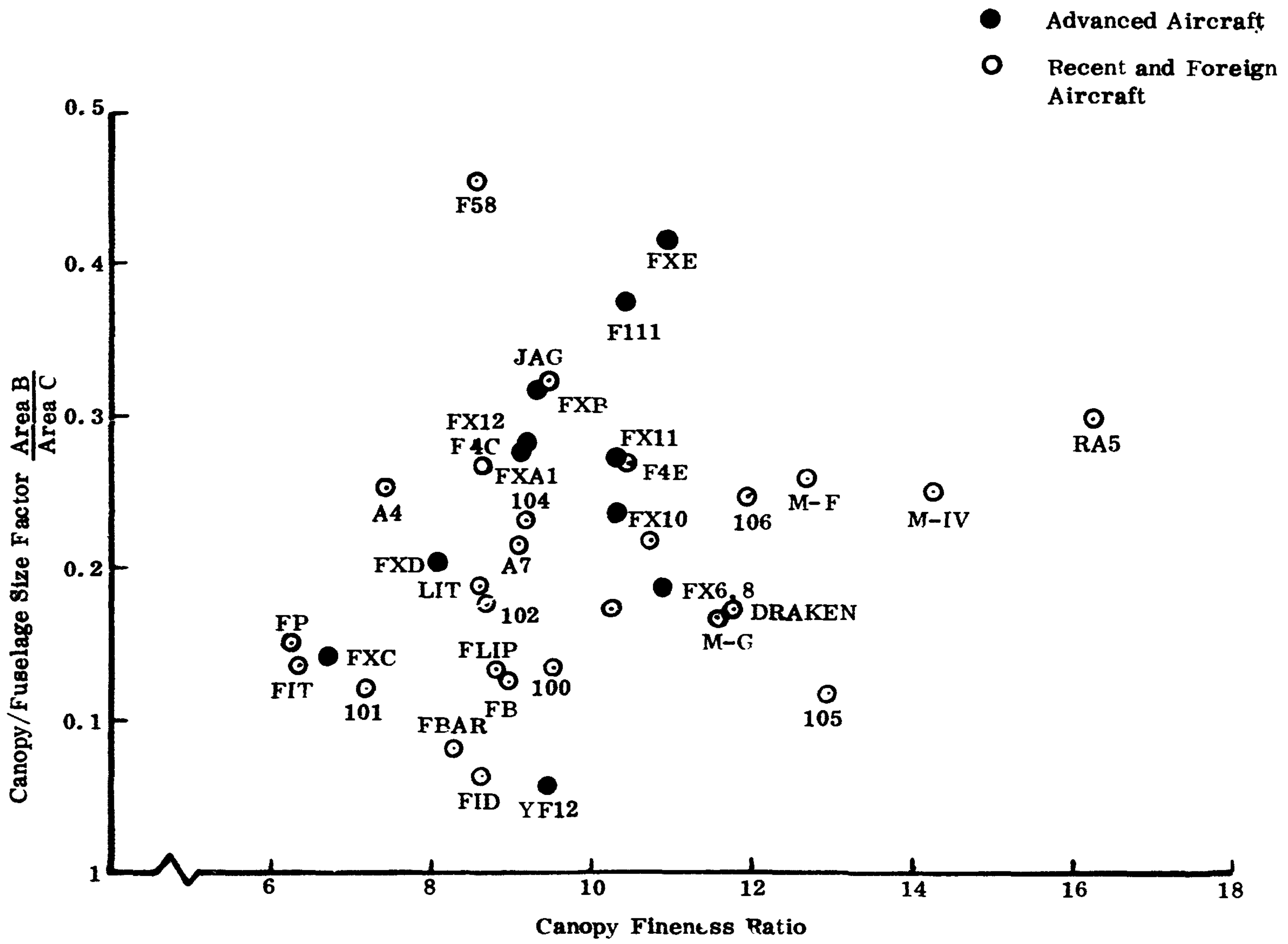

Figure 3-5.. Canopy Geometric Characteristics

predicts the edge of the windshield. For supersonic vehicles the windshield should be inclined less than 20 degrees from the normal horizontal reference line in order to minimize vision distortion. Higher angles of inclination can be employed but are usually accompanied by an increase in frontal area and drag. Acceptance of this increased drag would result from the necessity to satisfy some other essential mission requirement. Canopies are usually designed with circular sections to minimize the structural weight penalties due to pressure loading.

The canopy geometric characteristics of the aircraft in the Systems Review showed a wide divergence in fineness ratio and the fuselage size factor. The size factor is defined as the maximum canopy frontal area divided by fuselage forebody frontal area. The canopy geometric characteristics for the Recent, Foreign, and Advanced aircraft are summarized in appendix A.

As shown in Figure 3-5 the canopy/fuselage size factors of the aircraft in the Systems Review were generally found to vary between 0.150 to 0.300. Notable exceptions are the F-111 with side-by-side seating, the F-5B with an exceptionally large canopy, and the Jaguar with STOL performance. The Russian aircraft in the review employed canopies much smaller than the average, generally with fuselage size factors below 0.150.

Usefulness of the inlet size factor, defined as the maximum canopy frontal area divided by the inlet capture area, at best, is limited. The large scatter is primarily due to the difference in power plants and sizing conditions, and therefore results in the various levels of aircraft thrust loadings. However scatter is compressed considerably for the ten FX configurations where the mission is common and the sizing conditions are most probably coincident. In this case, the average inlet size factor is 0.526 with a majority of the configurations close to the mean. This factor will provide a gross weighting effect of the canopy size potentially influencing the flow field environment for the inlet, particularly at aircraft transient conditions. The commonality of the inlet sizes for the FX configurations is discussed further in paragraph 3.6.

Close examination of the canopy fineness ratio parameter when applied to aircraft categorized in terms of design Mach number, indicated within the accuracy of available data, a trend toward increased canopy fineness ratio with higher design speed. This is perhaps best illustrated by comparing the F-102 and F-106 aircraft with canopy fineness ratios of 8.73 and 11.93, respectively. Among the Advanced aircraft group, excluding the contoured wing/body configurations (YF-12 and FX-C), the average canopy fineness ratio is 10.00 with a high of 11.00 and a low of 8.15.

The design and selection of the windshield must satisfy numerous constraints, such as (1) minimum visibility distortion, (2) adequate thermal loading capability for the design Mach number. (3) low drag, and (4) provision of forward view for the weapons control system (gunsight. depressible reticle, etc.). The Review showed that 70% of the aircraft selected a flat center panel for the windshield. The XF-103 and FX-C were eliminated from this analysis due to the absence of a canopy and insufficient data respectively. The triangular type windshield appeared to have limited application restricted to interceptors such as the F-102, F-106, YF-12, the French Mirage IVA, and the Russian Fiddler. The limited forward visibility of this type of windshield limits its usage. The F-111, due to its side-by-side seating, utilized a rounded two-piece windshield. In this particular case, the wide cockpit probably eliminated the flat center windshield design on the basis of drag and high thermal loading.

The longitudinal location of the cockpit is generally midway between the fuselage nose and the inlet station. The only exception of all the aircraft in the Systems Review is the F-102 with a long subsonic diffuser, (fineness ratio = 10.10). A comparison made of the average canopy location between the Recent and Advanced aircraft group showed only a slight difference. i.e., 45% to 42% of the inlet location. However, if the contoured wing/body configurations were eliminated from the Advanced group, the canopy is then located closer to the inlet at 50%.

Based on the Systems Review, the following canopy geometric characteristics were selected.

Selection No. 1 - Primary

Canopy Fineness Ratio = 9.0
Canopy/Fuselage Size Factor = 0.275
Longitudinal Location = 0.500
Flat Center Panel Windshield

Selection No. 2 - Alternate

Canopy Fineness Ratio = 10.5
Canopy/Fuselage Size Factor = 0.218
Longitudinal Location = 0.450
Flat Center Panel Windshield

The design of the canopy for both selections conform to the HIAD and good design practice in terms of visibility and pilot clearance requirements.

Selection No. 1 is judged to be representative of near term aircraft, and Selection No. 2 represents the expected future requirement of higher speed therefore requiring a higher overall fineness ratio. A reduction in canopy/fuselage size factor, as the fineness ratio is increased, is anticipated as the expected trend. This is due to an increase in overall aircraft fineness ratio and the reduction of radome maximum diameter projected to meet the expected future performance requirements. The canopy longitudinal location of Selection No. 1 is representative of the advanced configurations, whereas Selection No. 2 location is the expected requirement for the small fuselage nose cone equivalent included angle selected in paragraph 3.2.

3.4 Aircraft Fuselage Characteristics

The fuselage configuration evolves mainly from the mission dictated volume requirements for fuel, stores and equipment, powerplant, and structural frame depth.

The degree of airframe-powerplant integration has an important effect upon fuselage design, as does the number of engines employed. Present thinking appears to favor the highly integrated approach with the engines buried within the fuselage to reduce frontal area and wave drag. However, this approach involves more extensive inlet development because of the influence of fuselage flow field upon inlet performance. In addition, a performance penalty is usually expected due to the contoured internal ducting required in this approach. As the degree of integration is reduced the internal ducting can be shortened and straightened. This approach usually entails a trade-off involving drag and weight to optimize the configuration. The other extreme in integration is to hang the engines under the wing in nacelles. This approach increases frontal area; however, the hoped for trade is a better lift to drag ratio and a favorable interference pattern, resulting in a better aerodynamic configuration. The improved aerodynamics coupled with short, straight ducting to the engines, may yield a better overall design.

As the demand for higher performance increases, interaction effects between wing, powerplant, and payload begin to dominate the design. As the airframe and powerplant are more closely merged, conclusions from parametric studies must be derived on the basis of integrated performance, for the conclusions based on individual components may become erroneous when other elements are introduced.

The fuselage geometric characteristics in the vicinity of the inlet station are of particular concern due to the attendant flow field environment generated, and the resultant influence on inlet performance. Operational statistics have illustrated some favorable effects of fuselage shielding for side mounted inlets during certain maneuvering conditions. On the other hand, the nonuniform flow field environment generated by the fuselage, particularly at angles of attack, has produced serious inlet/engine compatibility problems. This adverse flow field has directly affected inlet performance, varying from slight thrust losses, or restrictions on engine transients, to a complete compressor stall. Therefore, the Systems Review on fuselage shapes was concentrated at the inlet station, and was divided into two categories: (1) aspect ratio and size of the fuselage cross-section up to the canopy reference shoulder line, and (2) shape of the fuselage lower corner. A summary of the fuselage geometric characteristics for the thirty nine (39) aircraft in the Systems Review is presented in appendix A.

The fuselage aspect ratio at the inlet station was found to vary considerably, from a low of 0.244 to a high of 1.730. This large variation is reasonable when we consider the many aircraft types, single or dual engines buried or semi-submerged in the fuselage, volumetric allowances for fuel-stores-avionics, performance, and etc. By eliminating aircraft with an aspect ratio $<$ 1.0, which usually signifies that it is a wing/body configuration, a general trend is indicated by comparing the Recent and Foreign Aircraft Group with the Advanced Aircraft Group. Of the seventeen aircraft in the Recent and Foreign Group, the average aspect ratio is 1.30 as compared to the ten aircraft in the Advanced Group with an average aspect ratio of 1.14. The major reason for the difference is due to the higher design Mach number of the aircraft in the Advanced Group, thereby requiring a higher overall fuselage fineness ratio. Consequently, a reduction of fuselage aspect ratio with increasing design Mach number appeared to be the design practice required to satisfy performance considerations.

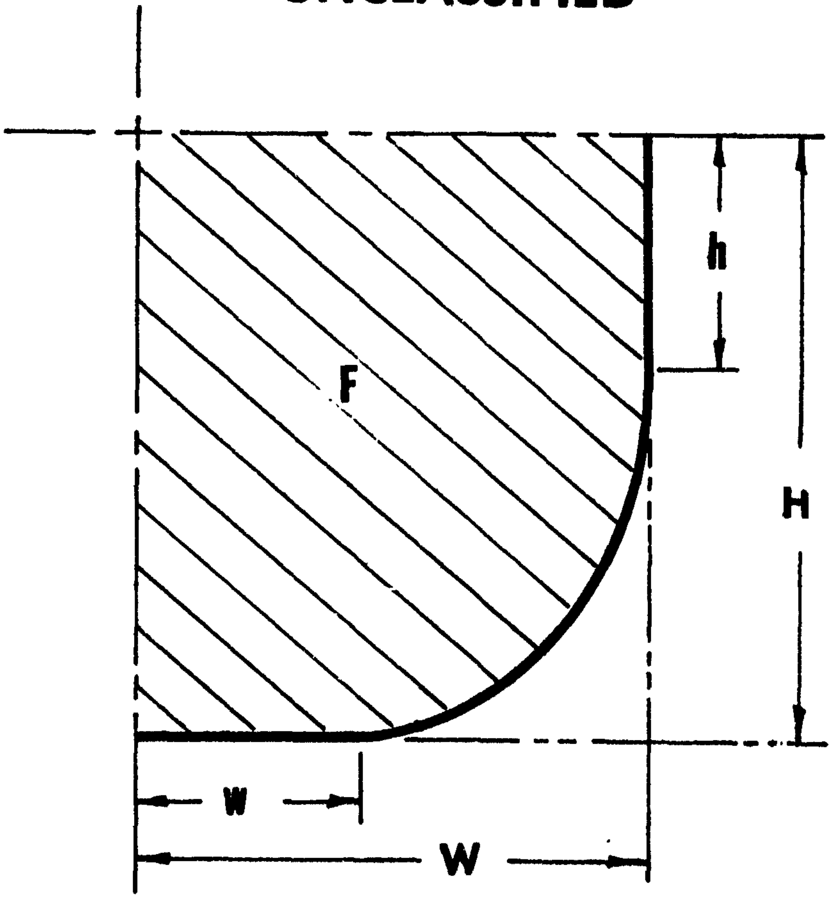

FUSELAGE SECTION - LOWER QUADRANT AT INLET STATION

$$\text{ASPECT RATIO} = \frac{H}{W}$$

$$\text{SHAPE FACTOR} = \frac{F}{H \times W}$$

$$\text{WIDTH FACTOR} = \frac{w}{W}$$

$$\text{HEIGHT FACTOR} = \frac{h}{H}$$

Figure 3-6. Definition - Fuselage Geometric Parameters

The fuselage size factor at the inlet station, defined as the fuselage cross-sectional area up to the canopy reference shoulder line divided by the radome cross-sectional area, did not provide any significant trend probably because requirements, such as forward looking radars, have a first order influence on this parameter.

A cursory examination of all the aircraft used in the Systems Review provides an appreciation for the great variety of fuselage shapes in existence. It is an area in which the aircraft designer has great liberty, provided the volumetric, structural and aerodynamic requirements are satisfied. Since the fuselage lower corner is of primary concern to the fuselage cross section, it was necessary to establish a meaningful identification parameter. Using the fuselage aspect ratio, shape, width and height. a mathematical formula was derived and found accurate in duplicating the actual shape of the fuselage corner. (See figure 3-6.)

Detailed examination of the aircraft in this Review has shown a strong tendency toward utilization of a "flat-bottom" fuselage for the dual engine aircraft - particularly as design Mach number is increased. A dual engine installation inherently projects a rectangular frontal area, thereby maintaining a high fineness ratio. To remain consistent with a high design Mach number and also conform to efficient fuselage contour development, the forebody aspect ratio must be relatively low. Therefore the basic rectangular shape when projected forward will transition gradually. An inherent advantage of the "flat bottom" fuselage is its suitability for carrying internal and external stores.

Consistent with the requirements of the program, eight fuselage shapes were selected for preliminary design. These are illustrated in figure 3-7. The eight fuselages are divided into four major groups with the fuselage lower quadrant aspect ratios varying from < 1.0 to 1.45.

In the first group, aspect ratio = 1.20, Configuration No. 1 has a shape factor of 0.950 and is approximately comparable to the lower fuselage corner of the F-111, F-101, and F-5B. Configuration No. 2 has a shape factor of 0.730 and is similar to the FX-B, F-104, the Swedish Draken ,and the Russian Firebar.

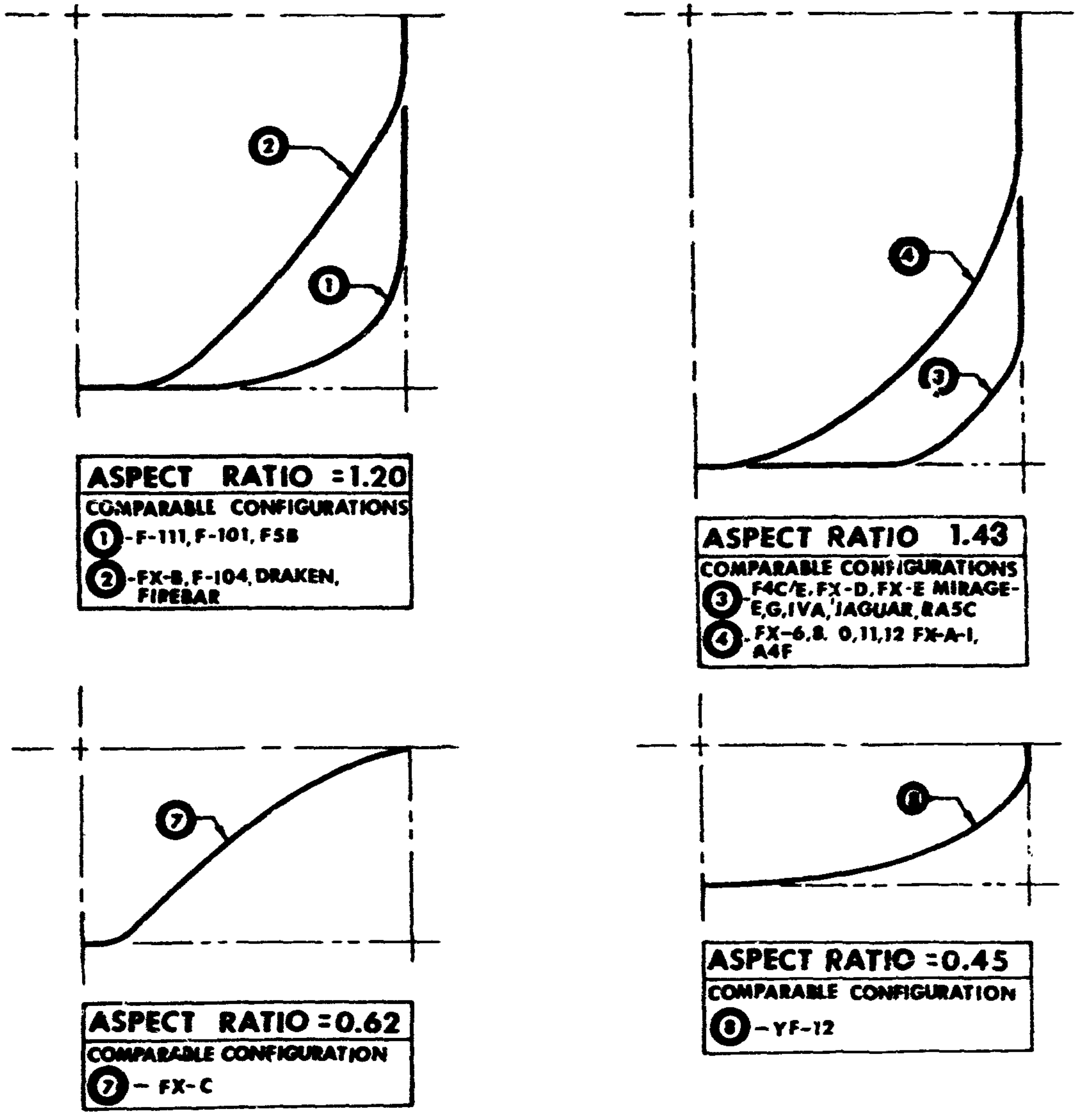
②
①
ASPECT RATIO =1.20
COMPARABLE CONFIGURATIONS
①-F-111, F-101, FSB
②-FX-B, F-104, DRAKEN, FIREBAR
④
③
ASPECT RATIO 1.43
COMPARABLE CONFIGURATIONS
③-F4C/E, FX-D, FX-E MIRAGE-E,G,IVA, JAGUAR, RA5C
④-FX-6,8. 0,11,12 FX-A-I, A4F
⑦
ASPECT RATIO =0.62
COMPARABLE CONFIGURATION
⑦- FX-C
⑧
ASPECT RATIO =0.45
COMPARABLE CONFIGURATION
⑧-YF-12

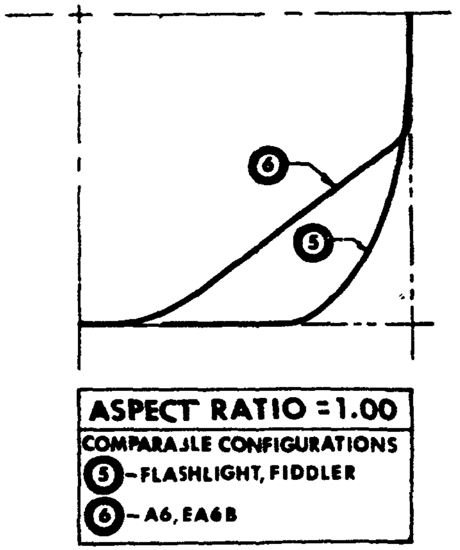
⑥
⑤
ASPECT RATIO =1.00
COMPARABLE CONFIGURATIONS
⑤-FLASHLIGHT, FIDDLER
⑥-A6, EA6B

CONFIG. NO.	SHAPE FACTOR	WIDTH FACTOR	HEIGHT FACTOR
1	0.950	0.410	0.610
2	0.730	0.140	0.160
3	0.965	0.640	0.750
4	0.820	0.100	0.350
5	0.926	0.640	0
6	0.750	0.100	0.340
7	0.470	0.150	0
8	0.819	0	0.200

Figure 3-7. Selected Fuselage Lower Quadrant Geometric Characteristics for Experimental Study

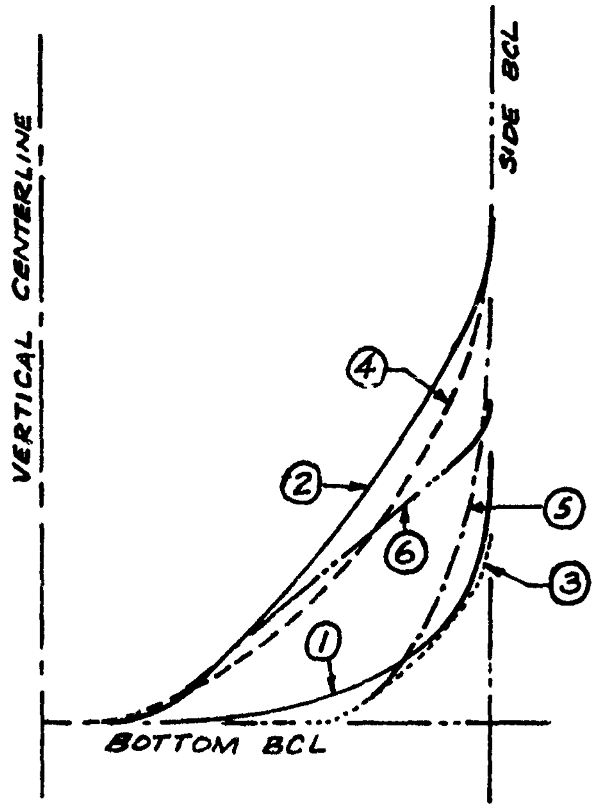
VERTICAL CENTERLINE
SIDE BCL
④
②
⑥
⑤
③
①
BOTTOM BCL

		ASPECT RATIO	SHAPE FACTOR
GROUP 1	CONFIGURATION NO. 2	1.20	0.730
	" NO. 4	1.45	0.820
	" NO. 6	1.00	0.750
GROUP 2	CONFIGURATION NO. 1	1.20	0.950
	" O. 3	1.45	0.965
	" NO. 5	1.00	0.926

Figure 3-8 . Comparison of Six Selected Fuselage Lower Quadrant Geometric Shapes

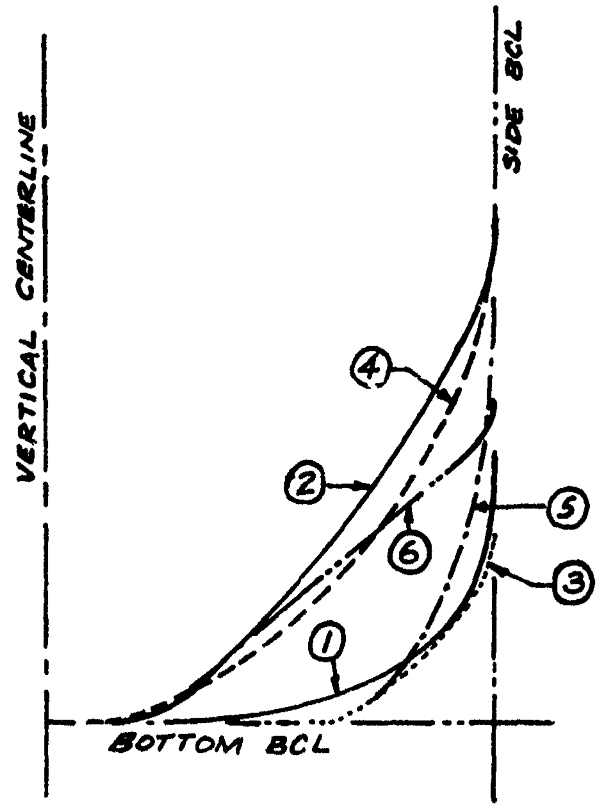
VERTICAL CENTERLINE
SIDE BCL
④
②
⑥
⑤
③
①
BOTTOM BCL

		ASPECT RATIO	SHAPE FACTOR
GROUP 1	CONFIGURATION NO. 2	1.20	0.730
	" NO. 4	1.45	0.820
	" NO. 6	1.00	0.750
GROUP 2	CONFIGURATION NO. 1	1.20	0.950
	" O. 3	1.45	0.965
	" NO. 5	1.00	0.926

Figure 3-8. Comparison of Six Selected Fuselage Lower Quadrant Geometric Shapes

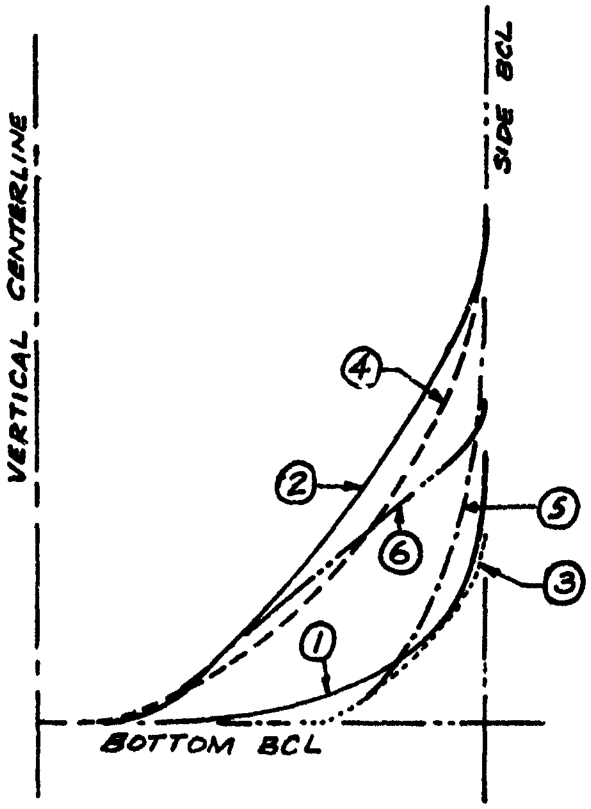
VERTICAL CENTERLINE
SIDE BCL
BOTTOM BCL
④
②
⑥
⑤
③
①

		ASPECT RATIO	SHAPE FACTOR
GROUP 1	CONFIGURATION NO. 2	1.20	0.730
	" NO. 4	1.45	0.820
	" NO. 6	1.00	0.750
GROUP 2	CONFIGURATION NO. 1	1.20	0.950
	" O. 3	1.45	0.965
	" NO. 5	1.00	0.926

Figure 3-8. Comparison of Six Selected Fuselage Lower Quadrant Geometric Shapes

In the second group , aspect ratio = 1.45, Configuration No. 3 has a smaller corner than Configuration No. 1 with a shape factor of 0.965. This selection approximates nine aircraft configurations, F4C/E, FX-D, FX-E, Mirage E, Mirage G, Mirage IV-A, the Jaguar, and the RA5C. Configuration No. 4 is the classic elliptic corner with a shape factor of 0.820 and the width and heightfactors chosen to simulate six advanced configurations. These are FX's-6, 8, 10, 11, 12, and A-1.

In the third group, aspect ratio = 1.0, Configurations Nos. 5 and 6 were chosen as extensions of Configurations Nos. 3 and 4. The initial curvature of No. 5 is identical to No. 3, but falls off more rapidly to obtain a lowered shape factor of 0.926. The shape is considered representative of the flat bottom fuselage modified for a more generous corner. In turn, the initial curvature of No. 6 is identical to No. 4, but then it is extended straight to the BCL. This shape is similar to the A-6 and EA6B aircraft. It is also representative of triangular shape body, inverted to accommodate a high wing installation. It might be mentioned here that a right triangular shape body (F-102, F-106, etc.) was not chosen due to its impracticality with a high wing installation. It is, however, well suited to a low wing configuration. Since the Systems Review indicated a pronounced preference for the high wing approach the right triangular shape body was eliminated.

Configurations Nos. 1, 3, and 5 were selected to investigate three variations of a sharp corner. Configurations Nos. 2, 4, and 6, in turn, were selected to investigate three variations of a more generous corner. A composite picture illustrating all six selections is shown on Figure 3-8.

In the fourth group, aspect ratio < 1.0, indicative of sculptured wing/body shapes, the FX-C and the YF-12 aircraft were selected. Configuration No. 7 with an aspect ratio of 0.62 is comparable to the FX-C proposal. Configuration No. 8 with an aspect ratio of 0.45 is comparable to the YF-12 aircraft.

The overall fuselage aspect ratio at the inlet station of 1.14 was selected as representative of advanced configurations. The fuselage size factor at the inlet station falls out when recommendations of (1) fuselage nose, (2) canopy, (3) fuselage aspect ratio of the inlet station, and (4) the fuselage geometric shapes are satisfied.

3.5 Aircraft Wing Characteristics

The design process to determine the optimum wing geometry is similar to that employed in the selection of powerplant performance characteristics. In both cases it is necessary to provide sufficient thrust (lift in the case of the wing). It is the mission profile, and its required lift-to-drag ratio, that dictate the aircraft wing planform.

Wing position, with respect to the fuselage, is usually categorized as low, mid, or high. Inherent in each of these wing locations are systems oriented advantages and disadvantages, which together with the mission requirements dictate selection of wing position.

With regard to the wing, primary interest during the Systems Review was to identify the location relative to the fuselage, both longitudinally and circumferentially. In addition, where possible, the leading edge sweep was determined.

Location of the inlet relative to the wing and the wing sweep will determine the effect of the wing upon the inlet flow field environment. Selection of wing planform is based primarily on those aerodynamic considerations required to satisfy specified performance requirements. The circumferential location of the wing, i.e., low, mid, or high position, is derived from a trade-off between structural, aerodynamic, and overall vehicle integration considerations.

The wing geometric characteristics, for the surveyed aircraft, are summarized in Appendix A. The wing sweep of the Recent and Foreign Tactical Aircraft varied considerably, due primarily to a large spread in design Mach number. However, similarities do exist when this group of aircraft are viewed in terms of general class. For example, the F-4C/E, F-100D, A4F, and F-105D all have the same wing sweep. This same similarity exists among the RA5C, A-7A, and F-101C. The foreign aircraft studied generally employ a higher sweep angle. This is particularly true for the Russian aircraft where a wing leading edge sweep of 58° is common for the older models. The trend to further increase wing sweep for the new Russian aircraft is evident even from the limited information available (SU-11 and MIG-23). Two of the variable sweep airplanes (F-111A and Mirage G) are identical with a leading edge sweep of 16° extended and 73° retracted. Among the fixed wing advanced aircraft the average sweep angle is approximately 56.5°.

Longitudinal location of the wing/fuselage juncture at 37% of the aircraft length was found to be the mean for the 39 aircraft used in the Systems Review. The Foreign Aircraft Group, in particular the Russian aircraft in the survey. utilized a design such that the wing/fuselage juncture is generally located further forward than the U.S. aircraft. For the advanced aircraft. the mean longitudinal location was found to be 33% of the aircraft length.

The circumferential location of the wing. in terms of low. mid, or high position, showed a definite trend toward utilization of the high wing position as the design Mach number is increased. For the Recent Aircraft Group, the low wing position dominates with 61.5% of the aircraft. only 23.0% utilized the high wing position. For the Foreign Aircraft Group, it is almost equally split between the three wing positions. However, for the Advanced Aircraft Group. only one configuration utilized the mid wing position with all others incorporating a high wing. In view of this latter result, the decision in the present program to investigate only the high wing position appears justified.

Based on the Systems Review a high wing located at 40% of the aircraft length with a wing leading edge sweep of 55° and a thickness ratio of 6% was selected. The selection of longitudinal location, though slightly further aft than most of the advanced configurations, was made because of an inability to clearly delineate variable sweep. Therefore, identifying the wing stub/fuselage juncture, versus fixed wing, was clouded. However, this wing/fuselage juncture is judged to be realistic and can find practical application.

3.6 Inlet Characteristics

The design and selection of the air induction system for any particular aircraft configuration is the product of parametric studies. The more important of these parameters are, (1) net propulsive effort. (2) weight, (3) complexity. (4) mission performance, (5) compatibility. (6) system effectiveness. and (7) cost effectiveness. However, the operational effectiveness provides the final determination of technical excellence used in the design of the air induction system. From the inlet viewpoint, choices exist in inlet concept, location. boundary layer control system, inlet control system, inlet contour, and aspect ratio. Consequently, to support the Design Selection Task of this study properly the Systems Review for the Induction Systems concentrated on parameters related to size and location. The statistical results of the Review for the Recent, Foreign, and Advanced Group are summarized in Appendix A. Other features of the induction system, such as inlet compression system, boundary layer control, and inlet/airframe integration features are qualitatively assessed and are also shown in Appendix A.

Among the aircraft in the review, inlets were primarily located at the aircraft nose and fuselage side positions with the top and bottom fuselage positions not widely utilized. Figure 3-9 shows the radial and circumferential location of the inlet centroid for all aircraft in the review. The fuselage side position, near the 90° axis, is the location chosen for 80% of the aircraft. Radial location averages 1.6 times the fuselage half-width measured from the aircraft axis. Exceptions are the YF-12, FX-C, FX-6, FX-8, Flipper and Firebar. where propulsion nacelles installed outboard of the fuselage aré utilized. The Russians, prior to the recent family of aircraft. have made extensive use of the nose inlet for both subsonic and supersonic aircraft. as opposed to the U.S. with only the F-100 and A7. The disadvantages of an inherently long subsonic diffuser and poor performance at high maneuvering attitudes for the nose inlet were apparently traded in favor of minimum aircraft wetted area and uniform flow field approaching the inlet during cruise.

The longitudinal location of the inlet is strongly dependent on aircraft configuration, type, and design Mach number. However, when aircraft with nose inlets and propulsion nacelles were excluded from consideration, the inlets of the remaining aircraft were located between 30-40% of the aircraft length. The mean longitudinal location of these twenty-four aircraft is 0.330. Among the Advanced Aircraft Group a notable exception is the F-111 employing a short subsonic diffuser and utilizing wing shielding. As a result the inlet is located further aft. (.434)

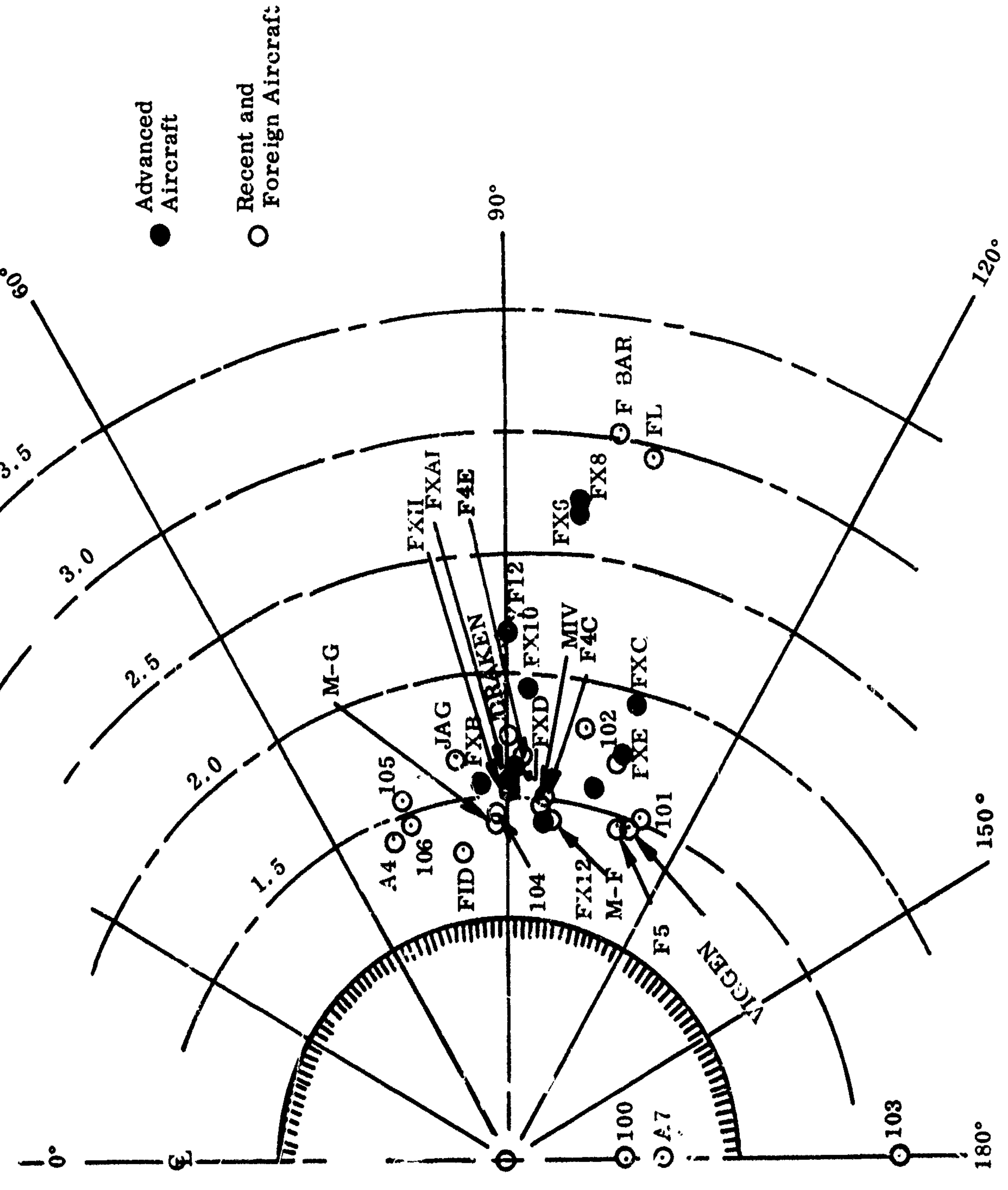

Figure 3-9 . Inlet Location - Radial and Circumferential Position

The inlet size factor, defined as the ratio of the inlet capture area to the fuselage maximum frontal area showed a large variation among aircraft in the Review. The primary reason for this scatter is due to the wide range of aircraft performance requirements among the various aircraft studied. The inlet capture area is a function of aircraft mission, design Mach number, engine characteristics, induction system design, aircraft sizing conditions, etc. From an overall systems point of view the inlet capture area can be related directly to aircraft thrust loading.

A good correlation was obtained for the inlet size factor with the ten FX configurations. The significant reason is the common design ground rules, i.e., fixed mission, gross weight, and maneuverability requirements, combined with the same family of advanced-technology-engines. Among the ten configurations, FX-6, 8, 10, 11, A-1, B, and E, all have an inlet size factor of approximately 0.550. FX-12, with a size factor of 0.398, can be eliminated from this comparison because certain exceptions to the basic ground rules were exercised. The purpose of the FX-12 design was to demonstrate the feasibility of a smaller aircraft to meet the same mission requirement by relaxing some of the design criteria. The FX-C configuration utilized a contoured wing/body planform with the propulsion nacelle located to make advantageous use of wing/body pre-compression, the FX-C inlet size factor is 0.372. However, if the projected area of that portion of the body utilized for pre-compression is charged to the inlet, the size factor is 0.540. Therefore, the FX-C when corrected for wing/body pre-compression is directly comparable to the other configurations.

A synopsis of the general types of inlets used by the aircraft in the Systems Review showed 41% utilized the two-dimensional ramp-type compression system, 38% utilized the three-dimensional conical or semi-conical system, and 21% utilized the pitot inlet. Nine of the ten FX configurations employed an identical inlet concept consisting of a two-dimensional external compression system with double ramps. Seven FX configurations selected horizontally mounted compression ramps, and two configurations mounted the compression ramps vertically. In addition examination of the new family of Russian tactical aircraft showed similar, if not identical, inlet concepts. The main advantage of this type of inlet, with the compression ramps mounted horizontally, is the inherent ability of the compression surfaces to partially compensate for angle of attack. The average inlet aspect ratio of 1.50 was selected from the seven advanced configurations utilizing horizontally mounted compression ramps.

Based on the Systems Review, two inlet types were selected. The characteristics of these inlets are presented below.

Selection No. 1

Two-dimensional, external compression, double ramp, horizontally mounted, sharp lip inlet.

Size Factor = 0.550

Aspect Ratio = 1.50

Location:

Longitudinal = 0.350 (Forward) 0.500 (Aft)

Radial = 1.60

Circumferential = 90°

Selection No. 2

Axisymmetric, external compression, sharp lip inlet

Size Factor = 0.550

Aspect Ratio = 1.000

Location:

Longitudinal = 0 500 (Aft)

Radial = 1.60

Circumferential = 90°

3.7 Configuration Synthesis

With the geometric characteristics of the individual aircraft components selected. it was necessary to integrate them into a complete aircraft system and, having done this, to refine the resultant configuration to reflect good overall design practice. This procedure was followed for each of the 8 selected configurations and the finalized component geometric characteristics were compared with those characteristics statistically derived during the survey task. This comparative study permitted a refinement of the configurations as developed to that point. The configurations, refined as a result of this analysis, were then examined to determine the geometric similarity of the models with those models employed in other related wind tunnel programs. A final refinement of the geometric characteristics was then made to achieve compatibility with three of these related programs.

The development of configurations 1 through 6, which are the wing-body class, resulted in designs that were acceptable after one iteration. The approach selected to improve these configurations was to move the forward inlet location from 35% to 30% of the overall aircraft length. This change improved the area progression while remaining consistent with the findings of the systems survey which indicated the inlet location to be between 30 and 40% of the overall aircraft length. One further refinement was to increase canopy fineness ratio slightly, to further improve the area progression.

Investigation of the aft inlet location indicated that aircraft balance and the maintenance of an acceptable area progression required the use of a highly swept wing glove forward of the inlet station and that this section would be part of a wing design employing variable geometry. Based upon these findings it was decided that the primary and alternate wing configurations would be designed to be representative of the inboard section of wing strake employed with a variable geometry wing. Wing sweep was judged to be the factor of primary interest and, therefore, sweep angles of 55° and 65° were employed. The wing-fuselage juncture was selected by satisfying the constraints of aircraft balance, area rule, and submergence of the inlet within the wing generated shock layer.

Integration of the geometric components of configuration 7 did not initially yield an acceptable aircraft system. The reason appears to be that the design is a blended body and as a result can be developed in an infinite number of ways. Additionally it was based upon only one design employed in the survey task. Therefore several iterations were required to generate an aircraft potentially representative of the tactical class. The conclusion drawn concerning this configuration was that evolution of the body contour lines represented a large development type program. a fact that precluded its use in this investigation. Additionally, the standard inlet. canopy, and nose, to be used in the program, did not integrate well with the fuselage. As a result of these findings it was decided that the configuration was not applicable to the program.

Configuration 8, is in the wing-body class and, as initially developed employed a low aspect ratio fuselage (0.45). Evolution of the configuration indicated that an efficient high wing tactical aircraft could not be developed from the geometric characteristics specified. However, as fuselage aspect ratio was increased, the configuration improved. A final fuselage aspect ratio of 0.70 was selected as producing a potential tactical aircraft configuration while also providing a fuselage aspect ratio lower than 1.0, which is of interest from the general viewpoint.

The findings of the configuration analysis task were employed to refine the geometric characteristics statistically derived during the Systems Review. A final refinement was based upon the "compatability analysis," discussed in the following text.

At the conclusion of the "Configuration Analysis Task" the recommended selections were primarily system oriented without extensive regard for other research programs dealing with airframe/inlet interaction problems. In order to obtain maximum engineering effectiveness, and particularly to support advancement in this state-of-the-art, the efforts under this contract were altered slightly to parallel two other USAF research programs. The other programs involved were: the (1) North American wind tunnel/flight test program utilizing the RA5C aircraft and a 1/8th scale RA5C wind tunnel model to investigate scale effects and inlet/ airframe interaction problems. and (2) General Electric utilization of a .228 scale RA5C wind tunnel model to generate inlet/engine compatibility data in support of the FX/VFAX engine prototype development program. Therefore, data generated from this study utilizing a 1/12th scale model would provide a valuable opportunity for data correlation and scaling comparison with those generated from the full scale, .228 scale, and 1/8th scale model.

Since one of the recommended configurations, (3), already had considerable commonality with the RA5C, i.e., fuselage shape, two-dimensional external compression inlet, and wing location, the feasibility of duplicating the RA5C as an alternate configuration, yet without departure from the main objective of this program, was easily realized. Therefore, the selection of the alternate aircraft nose, canopy, and the two-dimensional inlet aspect ratio was based on the RA5C. The RA5C nose fineness ratio and equivalent included angle is 1.688 and 31° respectively, and the canopy for tandem seating has a high fineness ratio due to the design of the fairing from the canopy high point to the upper fuselage basic contour line (BCL). In view of the RA5C nose geometry, the primary nose cone selection was reduced in equivalent included angle so that the fineness ratio could be increased to provide a better range between the two selections. Consequently, the nose, canopy, and the two-dimensional inlet selections were changed as follows.

I Aircraft Nose

Geometric Parameters	Primary	Alternate
Nose Cone Equivalent Included Angle	20°	31°
Nose Cone Initial Included Angle	27°	46.5°
Nose Cone Fineness Ratio	2.83	1.69
Nose Droop Angle	7.5°	7.5°
Radome Maximum Diameter	40"	40"
Nose Cone Shape	Ogival	Ogival

II Canopy

Geometric Parameters	Primary	Alternate
Canopy Fineness Ratio	9.0	16.3
Canopy/Fuselage Size Factor	0.275	0.298
Longitudinal Location	0.500	0.350
Windshield Shape	Flat Center Panel	Rounded

III Inlet

Geometric Parameters	Two-Dimensional	Axisymmetric
Inlet Size Factor	0.550	0.550
Aspect Ratio	1.10	1.00
Longitudinal Location - Fwd Position	0.30	0.30
Longitudinal Location - Aft Position	0.500	0.500
Radial Location	1.63	1.63
Circumferential Location	90°	90°
Assume Aircraft Length	65'	65'

3.8 Detail Inlet Design

3.8.1 General

The Systems Review and Design Selection Task resulted in the selection of the geometric characteristics of the fuselage components. Additionally, the basic inlet concepts were also determined. In this regard two external compression inlets were selected for the experimental program. These were (1) a two-dimensional, three shock, horizontally mounted ramp inlet and (2) an axisymmetric three shock inlet. It remained, however, to determine the detailed aero/thermodynamic characteristics of these inlet concepts. Achieving this objective involved maximizing inlet performance for a postulated advanced tactical aircraft flight envelope while remaining consistent with several constraints dictated by a) the Systems Review results b) the experimental program budget, and c) good design practice. Based upon these constraints the following inlet design ground rules were established.

- Inlets would be fuselage side-mounted, and when installed in the aft position(50% ACL) would be integrated with the fuselage and shielded by the wing.
- The inlet design would be simple and as such would not include variable geometry requiring remote control.
- Inlets should operate satisfactorily, without major shock/cowl lip interaction problems, for an angle of attack range up to $\alpha = 25°$ and speed range up to $M_\infty = 2.70$.
- The inlets would be faired to a common subsonic diffuser and simulated engine face.
- The inlet instrumentation system would be common to both inlets.
- Both inlets should incorporate a throat boundary layer bleed system.

3.8.2 Two-Dimensional Inlet

3.8.2.1 Design Considerations

The concept of a two-dimensional, external compression inlet was selected based on the Systems Review. The parallel USAF programs mentioned in section 3.7 concern the investigation of airframe/inlet interactions, on the RA5C inlet in wind tunnel models and full scale flight test. Therefore, data generated from this study utilizing a 1/12th scale model provides a valuable opportunity for data correlation and scaling comparison with those generated from the full scale, .228 scale, and 1/8th scale models. Consequently, the decision was made to duplicate the RA5C inlet configuration, in particular the .228 scale model being tested by General Electric in support of the FX/VFAX engine prototype development program.

Examination of the airflow characteristic for a typical advanced technology turbofan engine indicated a rather stringent requirement of m/m_∞ = 0.725 transonically. Shown on Figure 3-10 is the bare engine requirement without any allowance for engine cooling, leakage, boundary layer bleed, and secondary airflows. To meet this mass flow variation a variable geometry inlet would most certainly be required. However, a remotely controlled variable geometry inlet was beyond the scope of this experimental program. Consequently, optimum performance objectives for the complete speed range of interest were relaxed in favor of simple fixed geometry designs.

It was also necessary to modify the geometry of the RA5C inlet, a $M_\infty = 2.0$ design, in order to operate satisfactorily up to $M_\infty = 2.70$. With the experimental program conducted in two facilities; i.e., NASA-Ames 6' x 6' up to $M_\infty = 2.20$, and NASA-Ames 8' x 6' at $M_\infty = 2.50$, it was logical to choose two inlet design conditions.

A parametric study was made to determine the optimum combination of compression angles for a three shock system designed at $M_\infty = 2.20$ and $M_\infty = 2.70$. The results of this study are shown on Figures 3-11 and 3-12 respectively. The optimum combination at $M_\infty = 2.20$ consisted of an initial deflection angle $\delta_1 \approx 12°$ with the second deflection angle $\delta_2 \approx 13°$. At $M_\infty = 2.70$, the optimum combination consisted of $\delta_1 \approx 14°$ with $\delta_2 \approx 18°$.

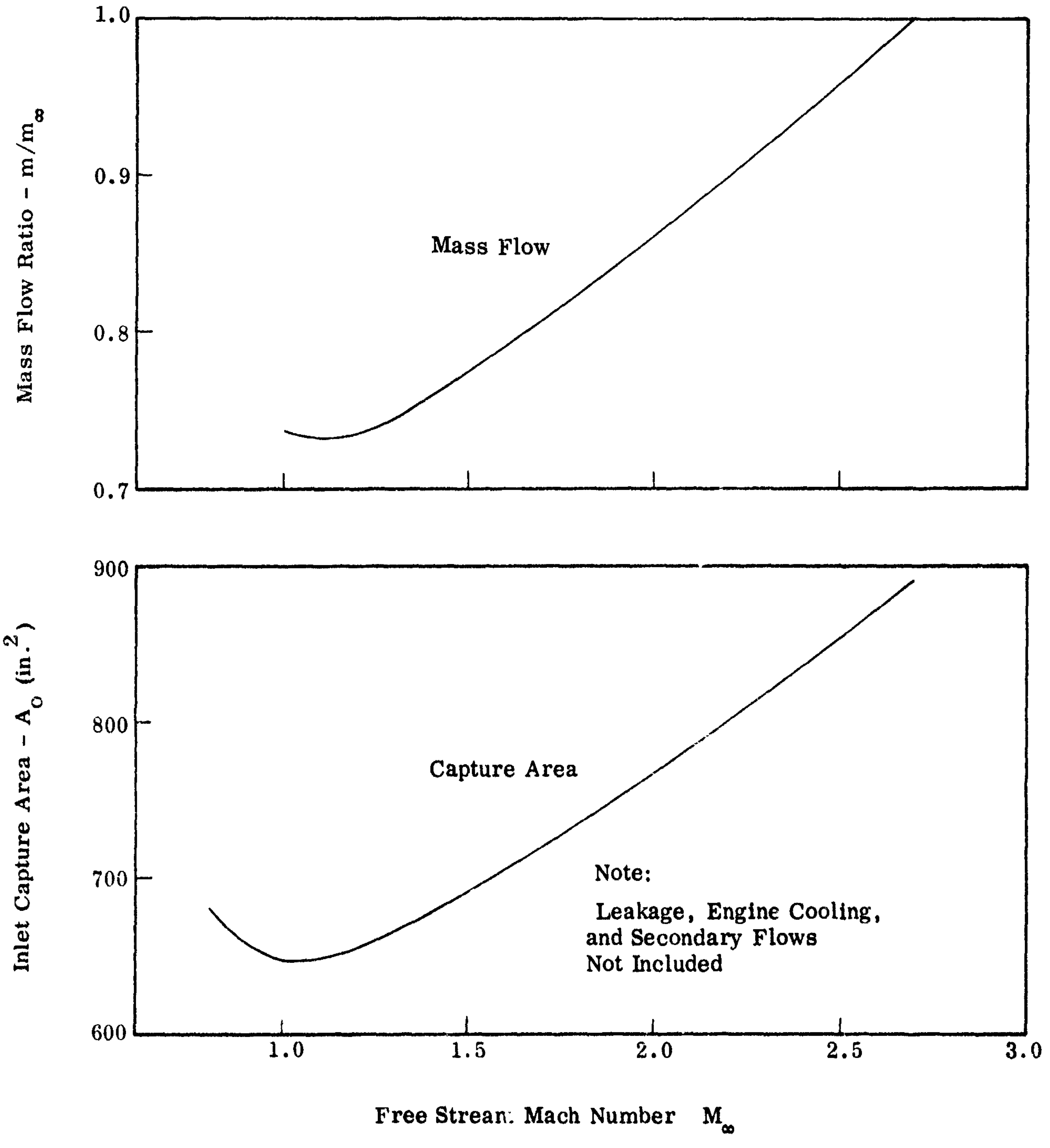

Figure 3-10. Typical Mass Flow Schedule - Augmented Turbofan Engine

$M_\infty = 2.20$

Subsonic Diffuser Losses

Not Included

○ Initial Deflection Angle - $\delta_1 = 6°$

□ Initial Deflection Angle - $\delta_1 = 8°$

◇ Initial Deflection Angle - $\delta_1 = 10°$

△ Initial Deflection Angle - $\delta_1 = 12°$

⬡ Initial Deflection Angle - $\delta_1 = 14°$

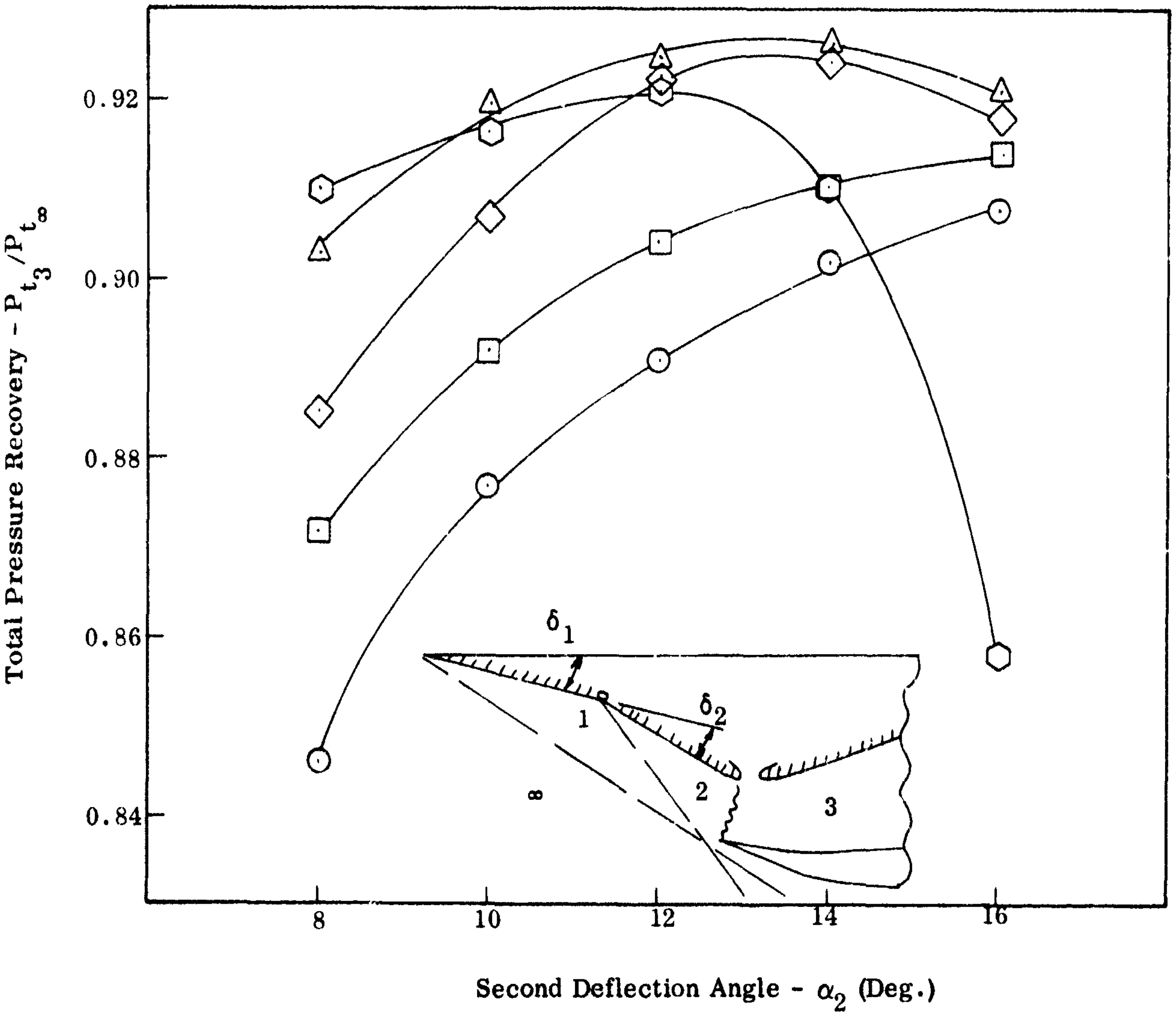

Figure 3-11. Total Pressure Recovery - Double Ramp External Compression Inlet, Designed for $M_\infty = 2.20$

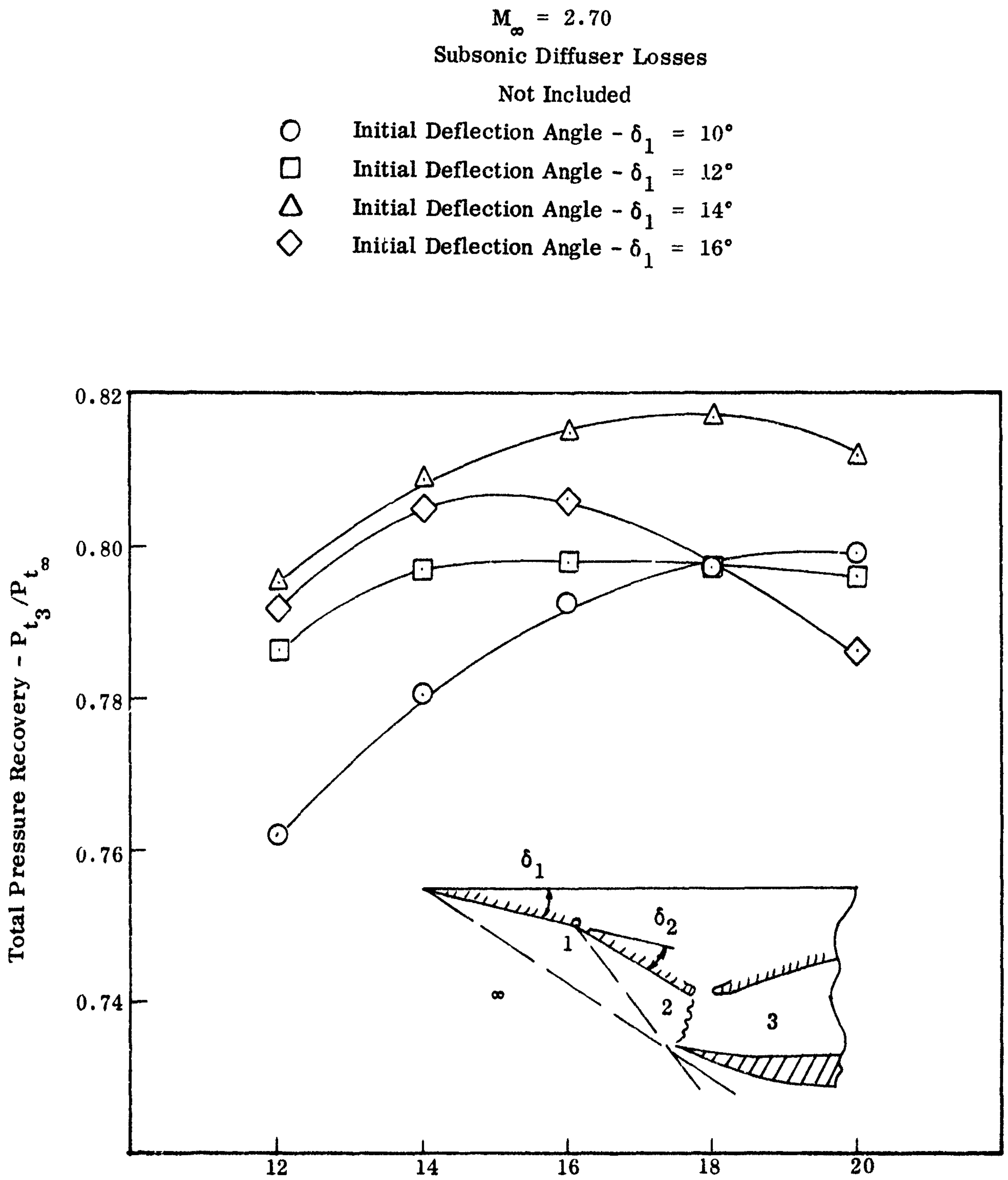

Figure 3-12. Total Pressure Recovery - Double Ramp External Compression Inlet, Designed for $M_\infty = 2.70$

The RA5C inlet utilized an initial wedge angle $\delta_1 = 9^\circ$ with the second wedge angle $\delta_2 = 10^\circ$ at design Mach number ($M_\infty = 2.0$). In order to establish a common base from which to compare data between the .228 and 1/12th scale models, the optimum performance at $M_\infty = 2.20$ was relaxed resulting in the selection of the RA5C inlet geometry with $\delta_1 = 9^\circ$ and $\delta_2 = 10^\circ$. An additional compromise was made by reducing the cowl position parameter to $\theta_c = 34.8^\circ$ in order to eliminate oblique shock wave/cowl lip intersection at $M_\infty = 2.20$. Consequently, when data correlation is made at $M_\infty < 2.20$, the inlet mass flow ratio must be adjusted accordingly. The subsonic diffuser and the simulated engine face characteristics of the GE .228 scale RA5C inlet were adopted and scaled for this program.

At $M_\infty = 2.70$, the selection of the compression angles was constrained by the previously established geometric relationship between cowl and ramp leading edges. Therefore, the initial deflection angle was selected to provide shock on lip operation, and a $\delta_1 = 15^\circ$ and $\delta_2 = 17^\circ$ was chosen. Details of the two-dimensional inlet showing the $M_\infty = 2.20$ and $M_\infty = 2.70$ compression blocks are shown on Figure 3-13.

3.8.2.2 Estimated Performance

Performance of the two-dimensional inlet for a range of angle of attack from -4° to +25°, has been estimated for $M_\infty = 1.30$, 1.80, 2.20, 2.50, and 2.70. Presented in Figure 3-14 is the estimated critical mass flow ratio as a function of angle of attack. The critical total pressure recovery including a subsonic diffuser loss based upon a $\Delta H/q = 0.135$, is presented in Figure 3-15. Inlet mass flow ratio and pressure recovery, for $M_\infty = 1.80$ and 1.30 are based on the geometric characteristics with the $M_\infty = 2.20$ compression block installed.

The mass flow ratio at angle of attack is based on the ratio of the ingested mass flow to the actual captured mass flow. Variation of the capture area at angle of attack with the capture area at $\alpha = 0^\circ$ (geometric capture area) is shown on Figure 3-16.

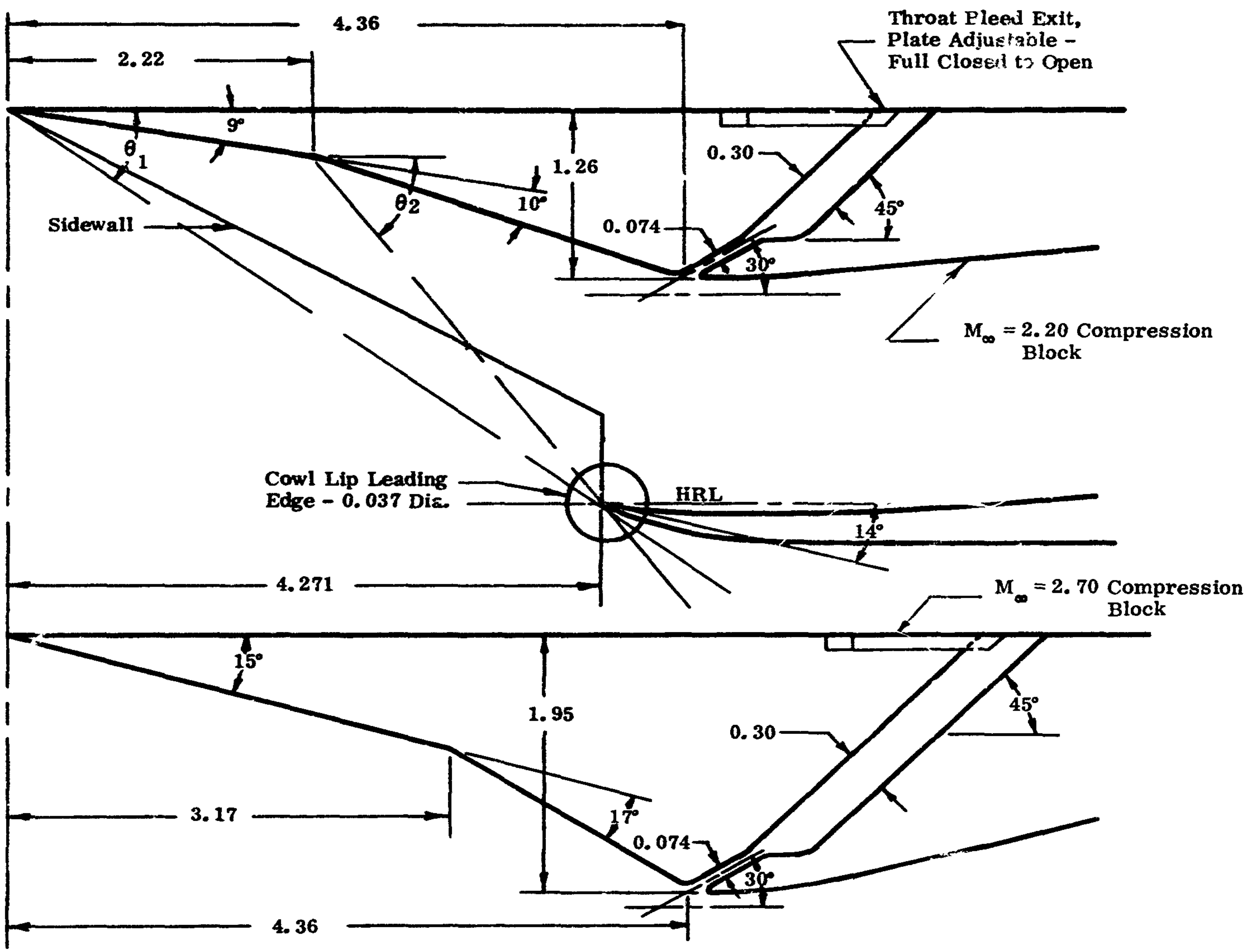
4.36
2.22
Throat Pleed Exit, Plate Adjustable - Full Closed to Open
9°
θ_1
1.26
0.30
θ_2
10°
45°
Sidewall
0.074
30°
M_∞ = 2.20 Compression Block
Cowl Lip Leading Edge - 0.037 Dia.
HRL
14°
4.271
M_∞ = 2.70 Compression Block
15°
1.95
45°
0.30
3.17
17°
0.074
30°
4.36

Figure 3-13. Two-Dimensional Inlet 1/12th Scale Model

FRONT ELEVATION

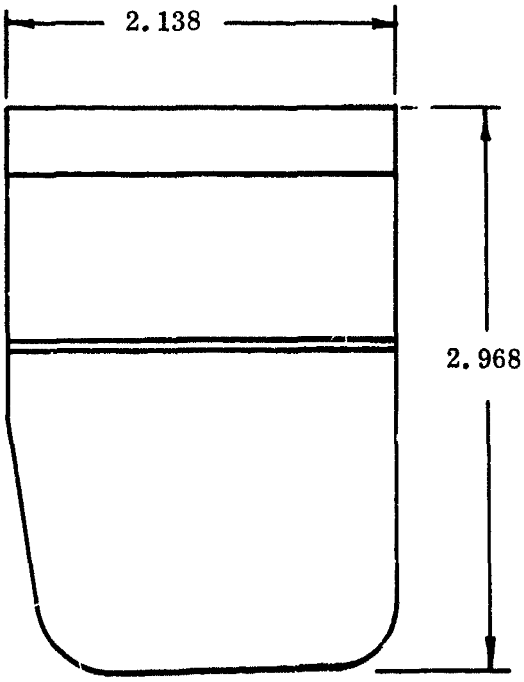

INLET DESIGN CONDITIONS

A. Capture Area - $A_o = 6.15 \text{ in}^2$

B. Double Ramp, External Compression

C. $M_\infty = 2.70$ & 2.20 Focused Waves Shock on Lip

M_∞	=	2.70	M_∞	=	2.20
θ_1	=	34.8°	θ_1	=	34.8°
θ_2	=	62.5°	θ_2	=	51.7°

Figure 3-13.Concluded. Two-Dimensional Inlet 1/12th Scale Model

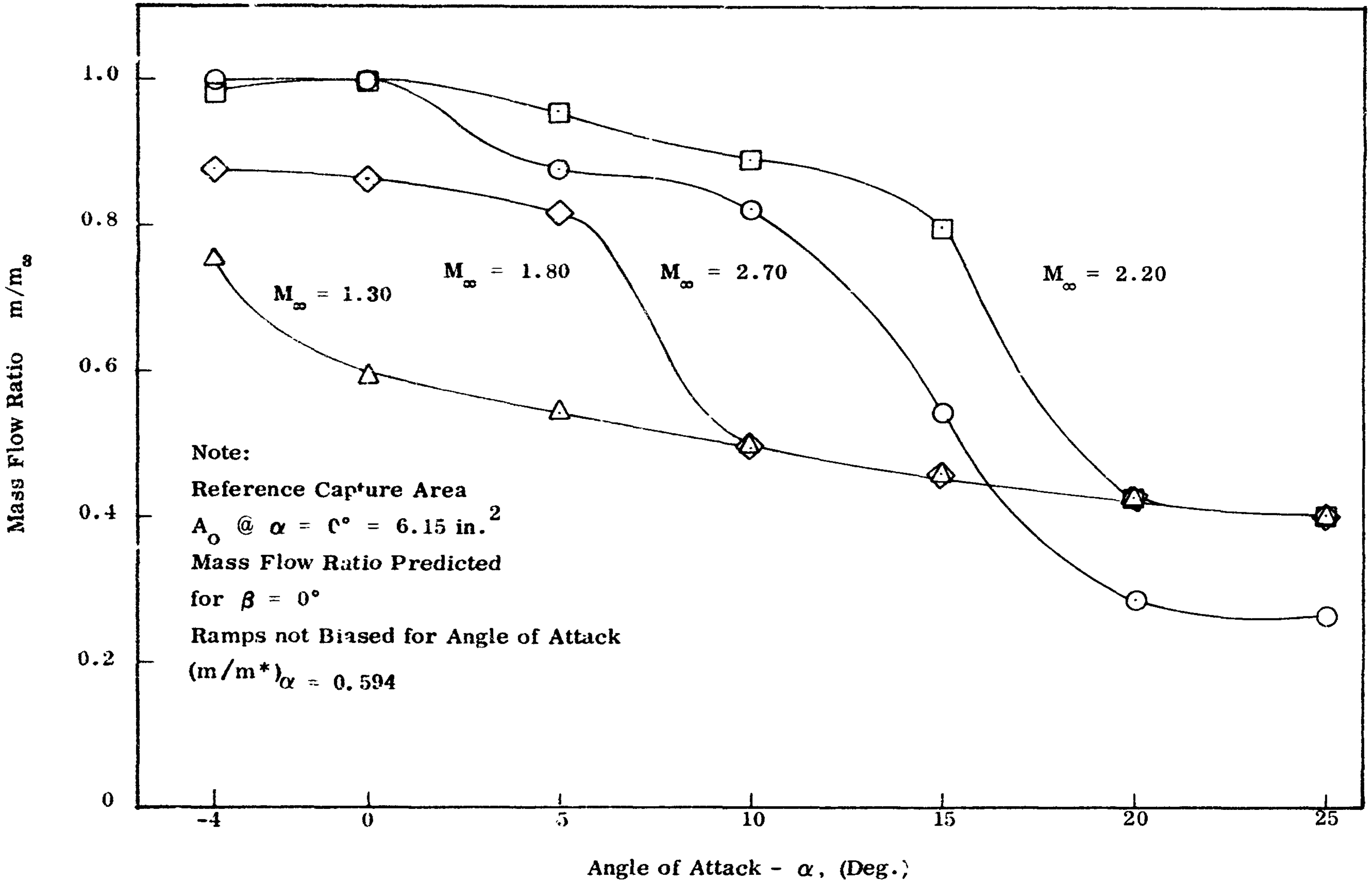

Figure 3-14. Estimated Critical Mass Flow Ratio - Two Dimensional Inlet

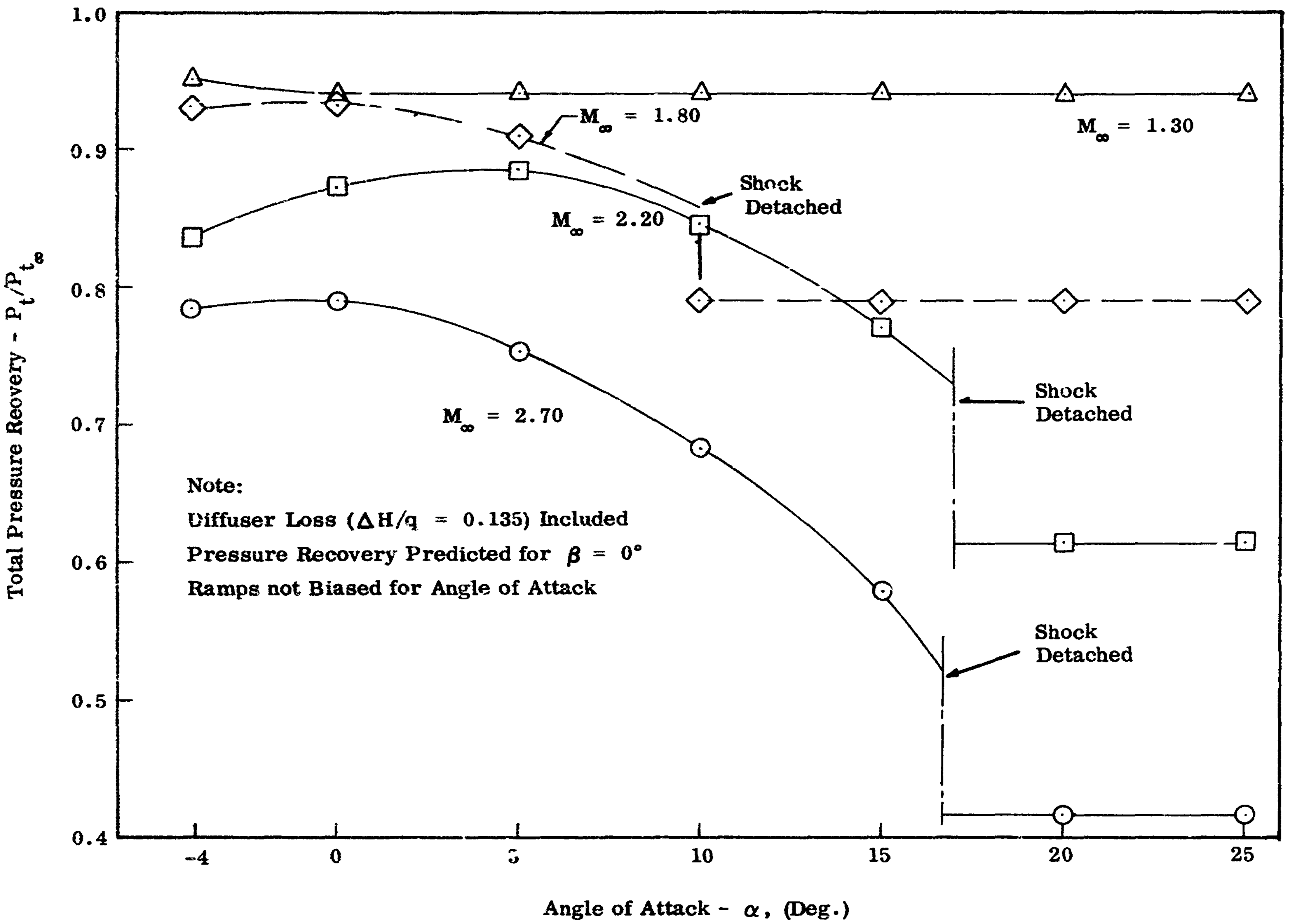

Note:
Diffuser Loss ($\Delta H/q = 0.135$) Included
Pressure Recovery Predicted for $\beta = 0°$
Ramps not Biased for Angle of Attack

Figure 3-15. Estimated Critical Pressure Recovery, Two Dimensional Inlet

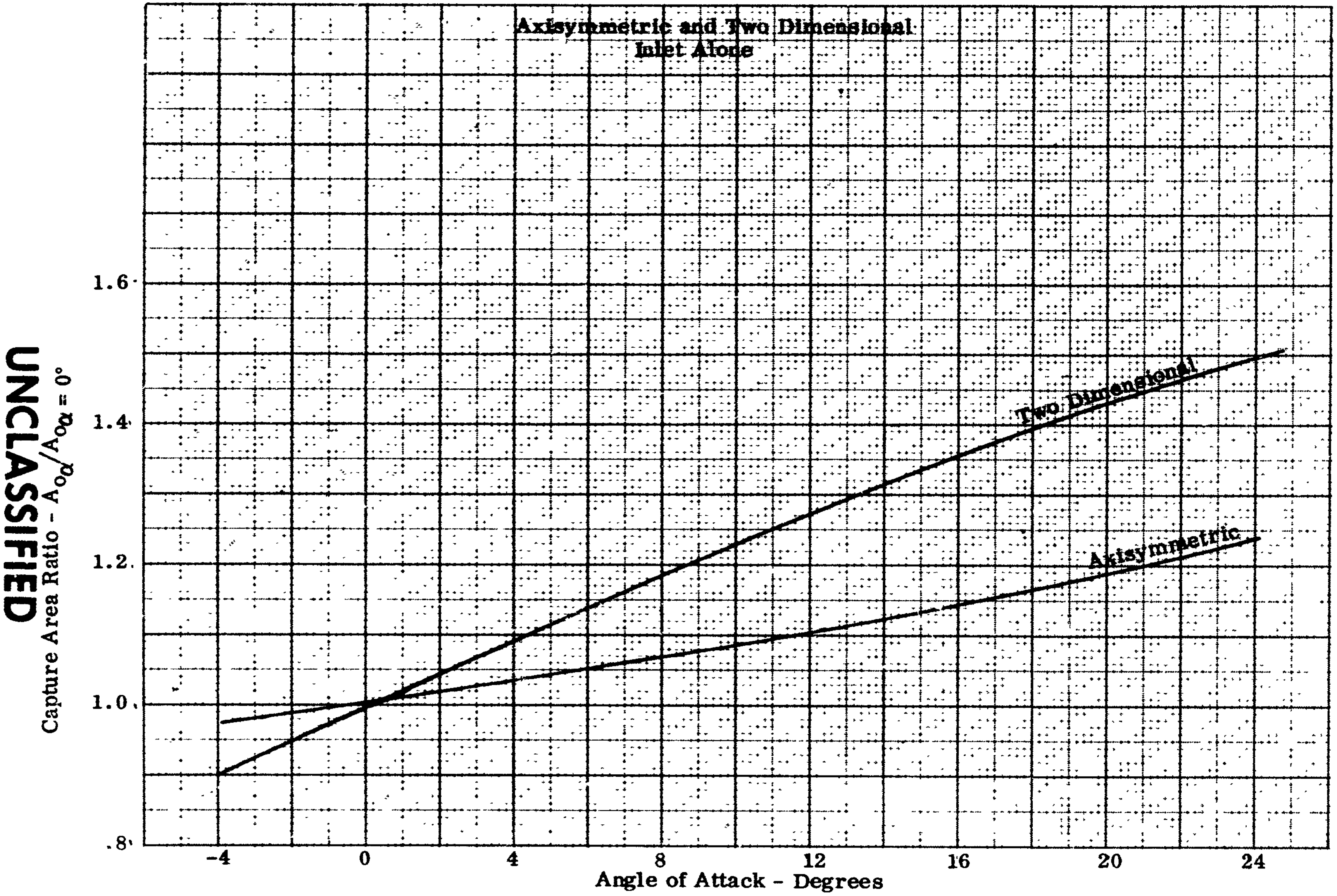

Figure 3-16. Caputre Area Ratio vs Angle of Attack

3.8.3 Axisymmetric Inlet

3.8.3.1 Design Considerations

Any axisymmetric inlet, with its inherent performance sensitivity to angle of attack, will generally require some protection in order to find application with the highly maneuverable aircraft projected for the future. In view of this, an axisymmetric inlet design can be reasonably postulated installed within the wing flow field either in a podded installation or as a segment of a conical inlet integrated with the wing and fuselage. Therefore, the side fuselage mounted axisymmetric type inlet forward of the wing is not expected to be a competitive concept for aircraft designed to meet stringent maneuverability requirements. Consequently, in the interest of maintaining overall program effectiveness and maximizing utilization of available wind tunnel test time, the logical decision was made to investigate the axisymmetric inlet only in the aft position (i.e., under the wing).

The requirement that the inlet be integrated with the wing and fuselage restricted consideration to segments of an axisymmetric inlet. Preliminary studies made to ensure conformity with efficient aerodynamic design practices resulted in the selection of a quarter segment axisymmetric inlet as that having the highest potential for practical application. The selected shape bears a strong resemblance to the F-111 Induction System, however, inlet placement with relation to the wing and body, subsonic diffuser, and simulated engine face characteristics are peculiar to this experimental program. Longitudinal location of the inlet at 50% ACL was determined by the Systems Review and Design Selection Task. Subsonic diffuser contours were developed to conform with efficient one-dimensional diffusion requirement and be compatible with the simulated engine face of the two-dimensional diffuser. The fuselage and wing boundary layer diverters were selected primarily to ensure complete removal of the viscous flow and rapid model configuration changes, without serious attention given to the attendant diverter drag. However, the diverter included angles of 18.5° and 23° are not unreasonable from a drag standpoint.

A parametric study was conducted to examine inlet performance systematically, i.e., total pressure recovery as a function of double cone external compression inlet geometry. The objective being to select the compression system yielding the best overall pressure recovery for the speed range of $M_\infty = 0.8 \rightarrow 2.7$.

However, for an axisymmetric inlet where variable geometry is limited to a sliding or collapsing spike, and a combined translating/collapsing spike is overly complex for practical application, there is available only a limited variation in inlet contraction ratio. Therefore, the attainment of high total pressure recovery and matched mass flow capacity throughout this Mach range was not possible without adopting complex variable geometry. This is illustrated in References 1 through 5 for a $M_\infty = 3.0$ design conical inlet utilizing a translating double cone compression system. The mass flow capacity at transonic speed is low ($m/m_\infty < 0.45$), to achieve an engine/inlet match in the supercritical operating regime. An additional factor exerting a major influence on external compression inlet performance is the high turning of the flow required to obtain high pressure recovery. This is illustrated in Figures 3-17 and 3-18 for $M_\infty = 2.20$ and $M_\infty = 2.70$ respectively. For the range of initial half cone angles employed in the parametric study, peak performance is obtained with the second half cone angle at approximately 40° for a $M_\infty = 2.20$ design. For the $M_\infty = 2.70$ design, a strong dependency on the initial half cone angle was evidenced with peak performance occurring at a higher second half cone angle - generally above 40°. The local flow inclination approaching the inlet cowl is shown on Figure 3-19. With the inlet design at $M_\infty = 2.70$, i.e., with the second half cone angle $\delta_{c_2} = 40 - 50°$, the initial internal inlet cowl angle must be within the range of 20° - 30°. At off-design conditions, however, this cowl inclination will produce a local expansion prior to the terminal shock, resulting in lower pressure recovery and a higher level of airflow distortion. This added disturbance at off-design was undesirable, particularly when the program objective is to identify inlet performance degradation due to inlet/airframe interaction.

To meet the mass flow variation of a typical advanced technology turbofan engine as shown on Figure 3-10, an axisymmetric external compression inlet would most probably utilize sophisticated variable geometry, or deliberately pay a performance penalty by oversizing at the design condition. Such a variable geometry inlet was beyond the scope of this program. Therefore, the design requirement for high pressure recovery, i.e., optimum turning of the flow, was relaxed in favor of a geometry providing acceptable pressure recovery and a mass flow capacity, at transonic speed, well matched to a potential engine.

$M_\infty = 2.20$

Subsonic Diffuser Losses
Not Included

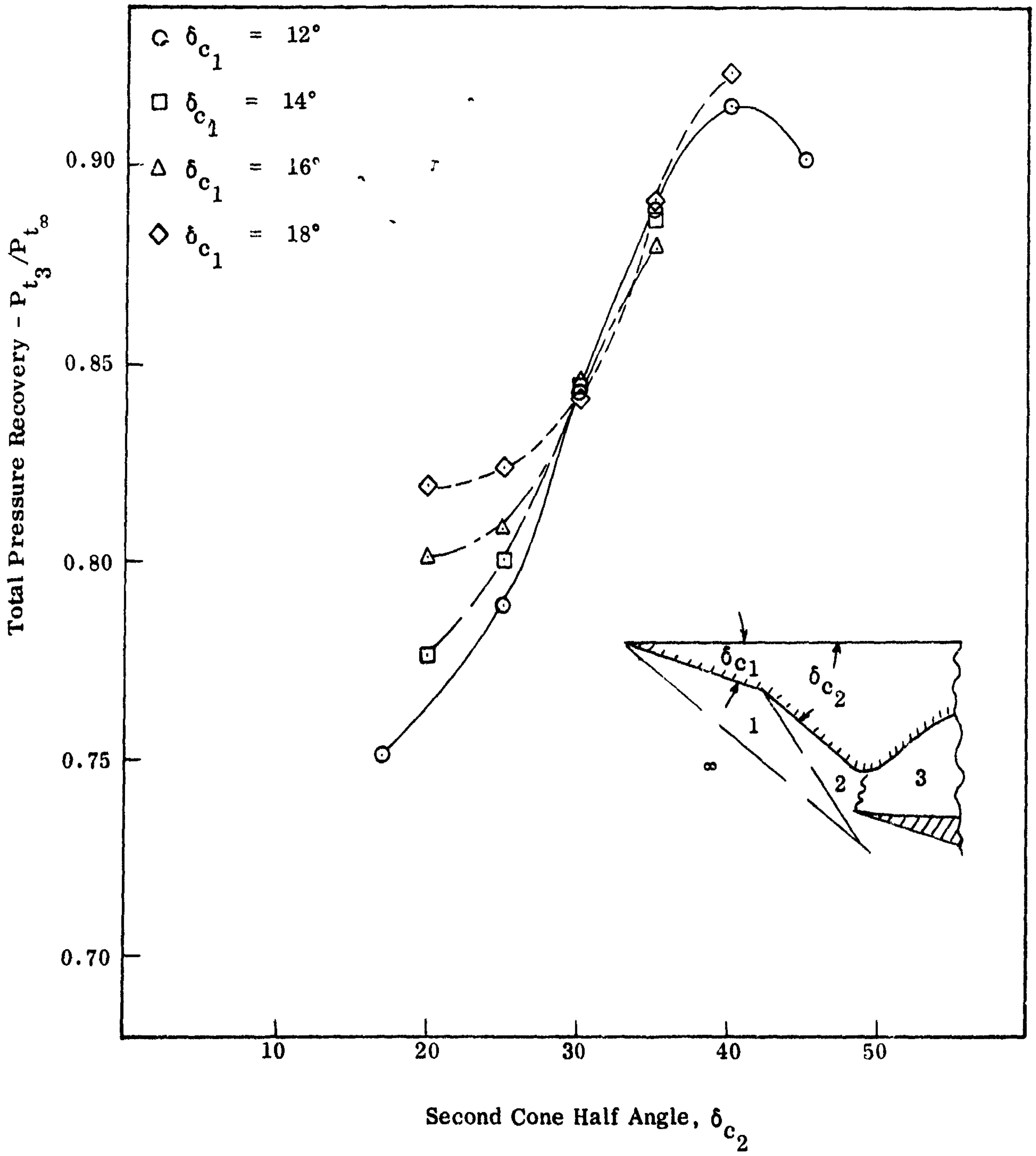

Figure 3-17. Total Pressure Recovery - Double Cone External Compression Inlet, Designed for $M_\infty = 2.20$

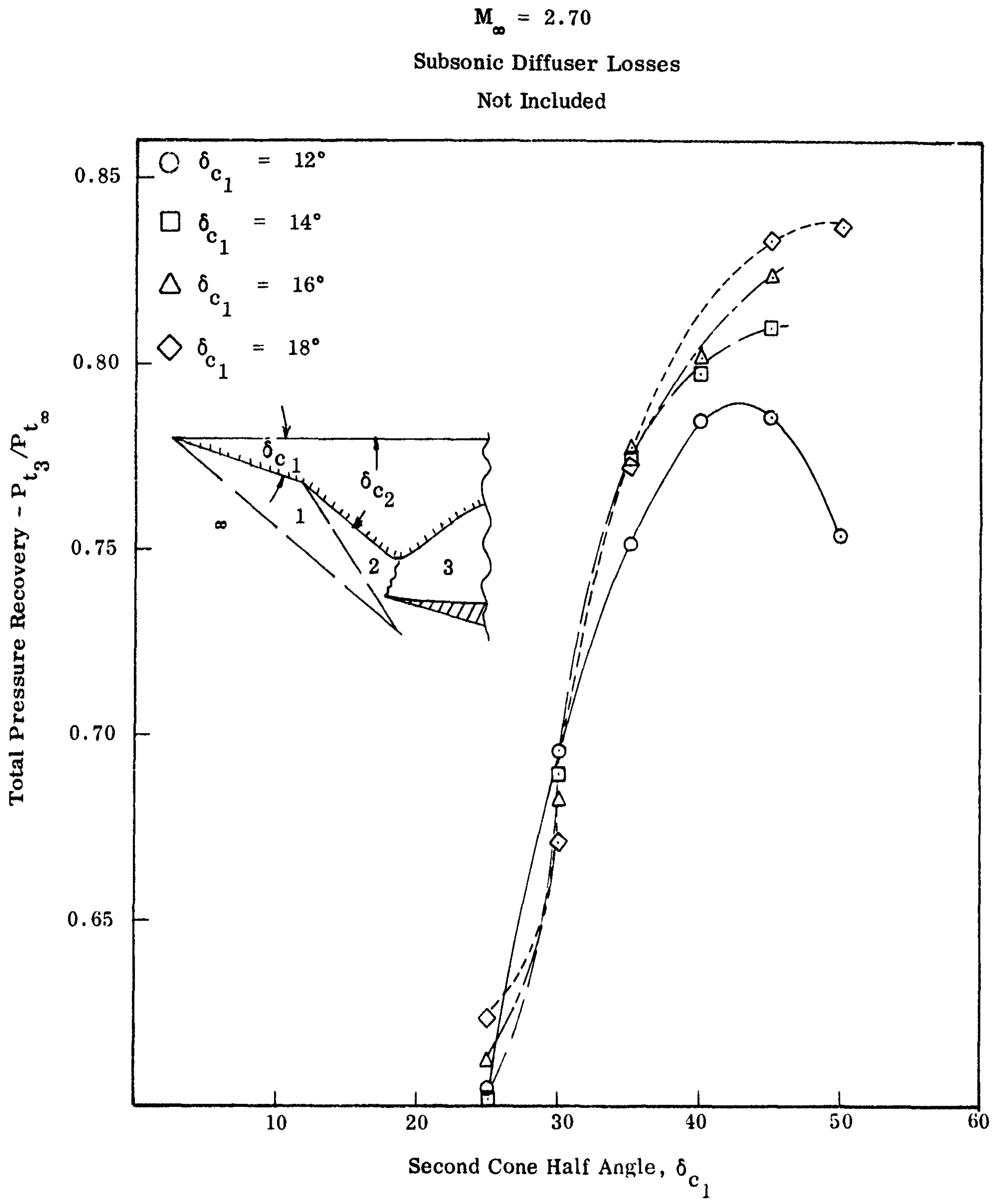

Figure 3-18. Total Pressure Recovery - Double Cone External Compression Inlet, Designed for M_∞ = 2.70

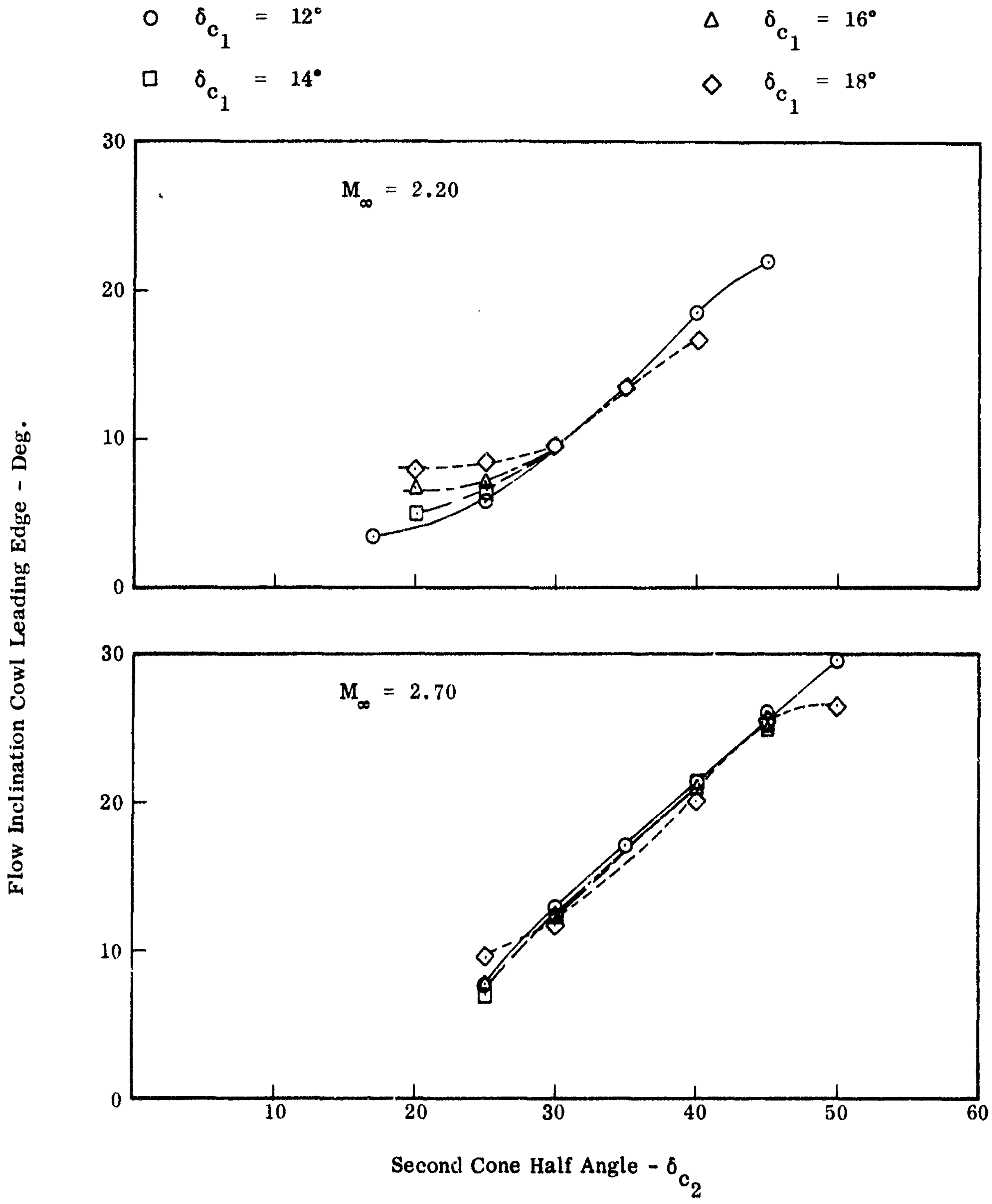

Figure 3-19. Flow Inclination Approaching Inlet Cowl, Double Cone External Compression Inlet

Consequently, a quarter segment, double cone (δ_{c1} = 12.5° and δ_{c2} = 24°) with throat perforations for boundary layer removal was selected. The spike had two positions - retracted position for $M_\infty \leq 2.20$, and the forward position for $M_\infty = 2.70$. Details of the inlet are shown on Figure 3-20.

Capture area of the axisymmetric inlet vs angle of attack is shown in Figure 3-16.

3.8.3.2 Estimated Performance

Performance of the axisymmetric inlet, for a range of angle of attack from -4° to +25°, has been estimated for M_∞ = 1.30, 1.80, 2.20, 2.5 and 2.70. The estimates presented represent average performance for the inlet.

The mass flow ratio at angle of attack Figure 3-21, is based on the ratio of the ingested mass flow to the actual captured mass flow. Variation of the capture area at angle of attack with the capture area at α = 0° is shown in Figure 3-16.

The critical total pressure recovery, Figure 3-22, includes an estimated subsonic diffuser loss based upon a $\Delta H/q = 0.135$. The estimated critical total pressure recovery is shown generally to increase with angle of attack. This characteristic is due to the selection of a δ_{c1}, and δ_{c2} lower than optimum. The increased effective cone angle presented to the approaching flow at angle of attack more closely approaches an optimized geometry and as a result the theoretical pressure recovery improves.

3.9 Summary

The Systems Review and Design Selection Task was based upon a comprehensive evaluation of thirty-nine configurations. These were comprised of representative aircraft in the U.S. and foreign inventory including ten advanced proposals designed to meet FX mission requirements. The geometry of each configuration was divided into five major components of interest, i.e., aircraft nose, canopy, fuselage, wing, and inlet. The geometric parameters defined in paragraph 3.1 were applied to these major components thereby allowing a synthesis of their characteristics into a

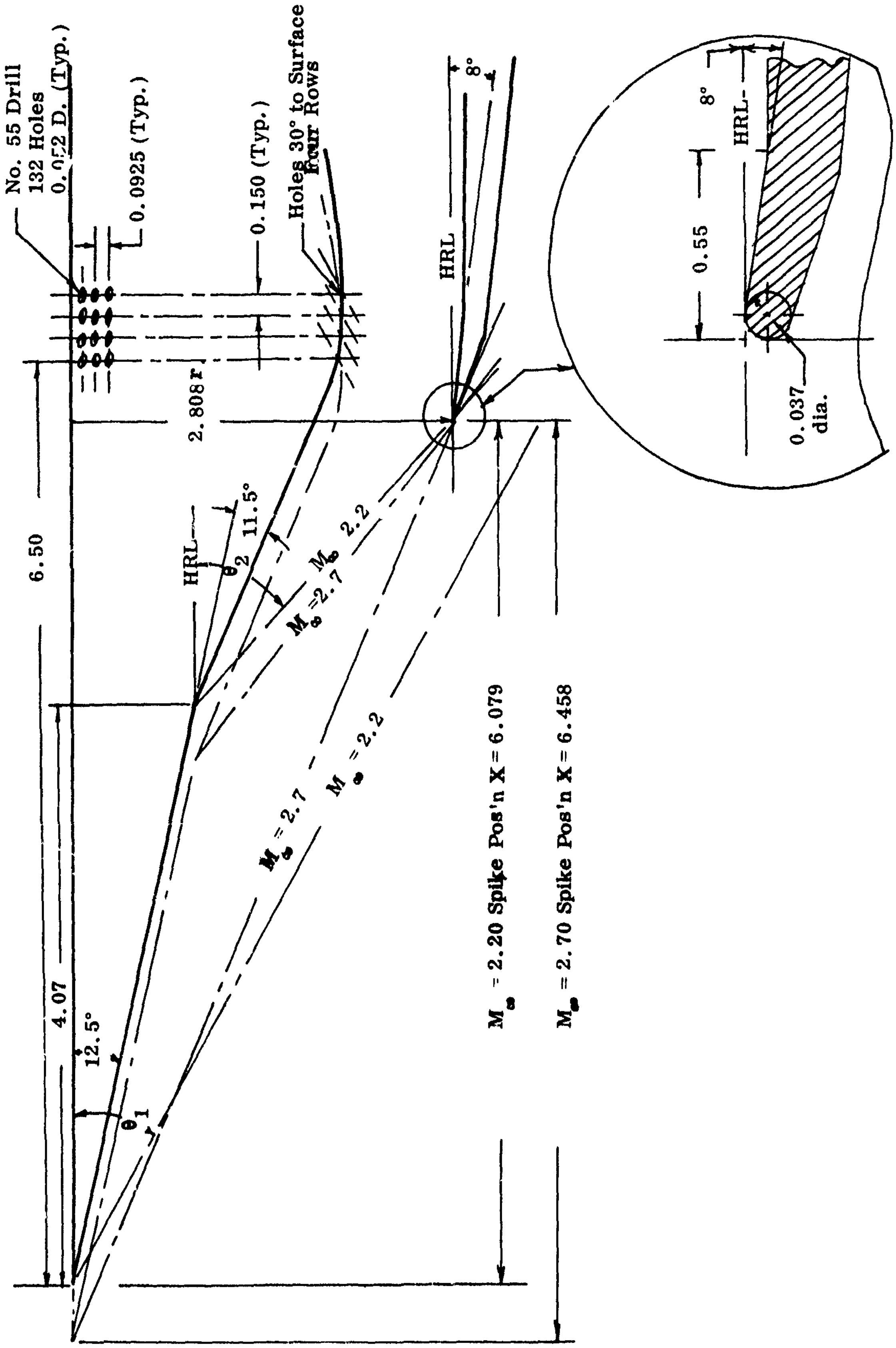
No. 55 Drill
132 Holes
0.052 D. (Typ.)
0.0925 (Typ.)
0.150 (Typ.)
Holes 30° to Surface
Four Rows
HRL
8°
2.808 r
6.50
4.07
12.5°
θ_1
HRL
θ_2
11.5°
M_∞ 2.2
M_∞ =2.7
M_∞ =2.7
M_∞ =2.2
M_∞ = 2.20 Spike Pos'n X = 6.079
M_∞ = 2.70 Spike Pos'n X = 6.458
8°
HRL
0.55
0.037 dia.

Figure 3-20. Axisymmetric Inlet - 1/12 Scale Model

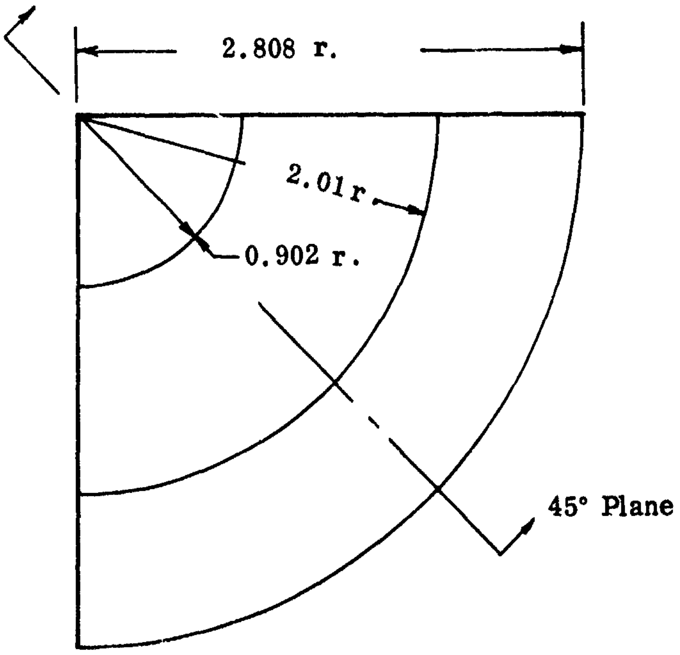

INLET DESIGN CONDITIONS

A. Capture Area - $A_o = 6.15 \text{ in.}^2$

B. Double Cone, External Compression

C. Fixed Compression System - Two Spike Positions Only

D. $M_\infty = 2.70$ No Oblique Shock/Cowl Lip Interaction

E. $M_\infty = 2.20$ Spike Translated, Second Oblique Shock on Lip

F. Thermodynamic Properties Presented for 45° Plane

$M_\infty = 2.70$	$M_\infty = 2.20$
$\theta_1 = 23.5°$	$\theta = 29.7°$
$\theta_2 = 38.6°$	$\theta_2 = 43.5°$

Figure 3-20.(Concluded). Axisymmetric Inlet - 1/12 Scale Model

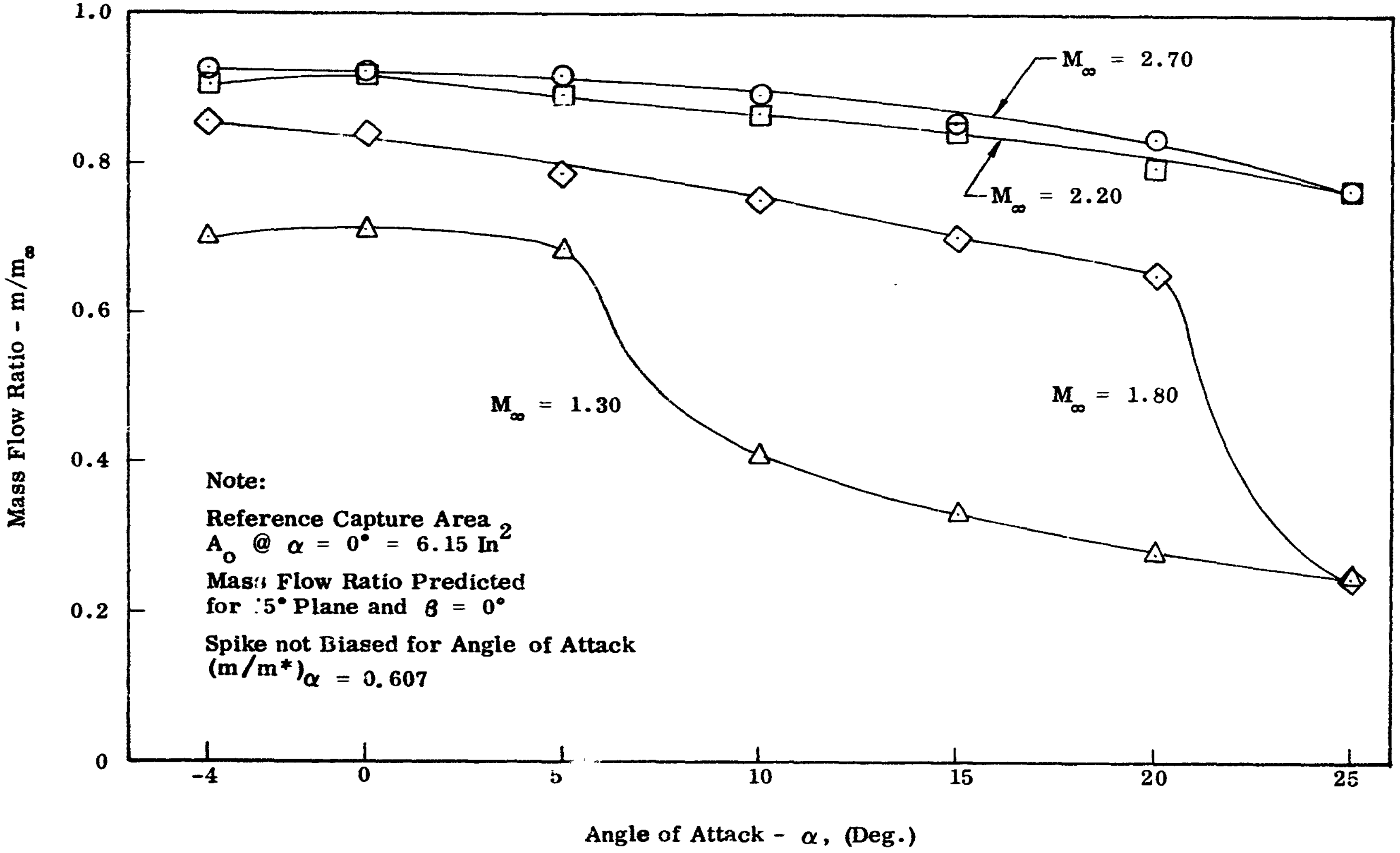

Note:

Reference Capture Area
A_o @ $\alpha = 0° = 6.15$ In^2

Mass Flow Ratio Predicted
for 45° Plane and $\beta = 0°$

Spike not Biased for Angle of Attack
$(m/m^*)_\alpha = 0.607$

Figure 3-21. Estimated Critical Mass Flow Ratio - Axisymmetric Inlet

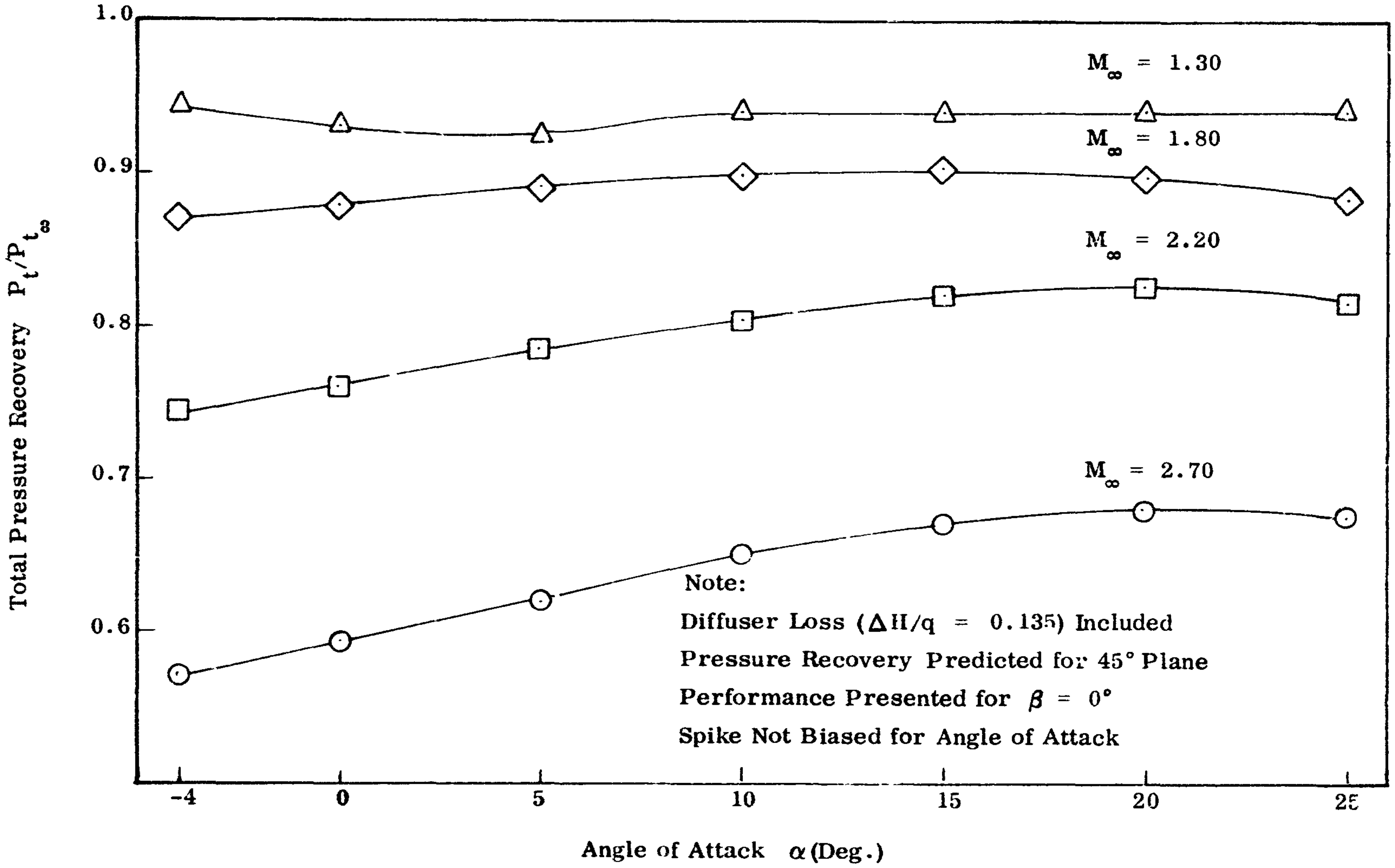

Figure 3-22. Estimated Critical Pressure Recovery, Axisymmetric Inlet

common base for design selection. Cataloging the geometric characteristics of the aircraft components in this manner, as a function of aircraft concept, provides a compilation of design practice, for it is the finalized geometry that has resulted from the trade-off between vehicle induced constraints a. the desire to maximize net propulsive effort. Therefore, by knowing the geometric characteristics, a picture of reasonable design practice emerged and a general feel for the restrictions placed upon this practice by vehicle influence was also obtained. Consideration of operational and technical constraints imposed on each configuration during the period of development, e.g. state-of-the-art in avionics, propulsion, materials, weapon load requirements, weight, etc., ensured the use of consistent evaluation criteria. Inlet types, general characteristics, and inlet/airframe integration features were qualitatively assessed to provide the basis to select the configurations meeting the overall program objectives. Therefore, the Systems Review Study, fortified by systems orientation, ensured the use of realistic configurations. The use of analytically derived geometry provided information that was applicable to the tactical fighter aircraft class, parametric in nature, and of general interest in the investigation of subsonic and supersonic aircraft flow fields.

The Systems Review and Design Selection Task emphasized the utilization of design trends envisioned for high performance supersonic aircraft of the near term future. Consequently, the selected geometric characteristics are judged to be representative of a spectrum of geometry that may find practical application. These selections are summarized below.

I Aircraft Nose

Geometric Parameters	Primary	Alternate
Nose Cone Equivalent Included Angle	20°	27°
Nose Cone Initial Included Angle	25°	32°
Nose Cone Fineness Ratio	2.83	1.69
Nose Droop Angle	7.5°	7.5°
Radome Maximum Diameter	40"	40"
Nose Cone Shape	Ogival	Ogival

II Canopy

Geometric Parameters	Primary	Alternate
Canopy Fineness Ratio	9.0	16.3
Canopy/Fuselage Size Factor	0.275	0.298
Longitudinal Location	0.500	0.450
Windshield Shape	Flat Center Panel	Rounded

III Fuselage

Seven fuselage cross-sectional shapes were selected. The dual basis of selection was that the shapes encompass a wide range of general geometric shapes and in addition they are representative of 29 of the configurations studied. These shapes, together with their geometric characteristics, are shown on Figure 3-7 and discussed in paragraph 3.4.

IV Wing

A decision was made to investigate only the high wing position. This selection appears justified by the trend evidenced from the Systems Review in which the high wing concept predominated. In addition, a wing sweep of 55° and a wing/fuselage juncture located at 40% of the aircraft length were selected to be compatible with the requirements of high performance supersonic aircraft in the 45,000 lb gross wt class.

V Inlet

To provide added flexibility to the objectives of the overall study program, two basic inlet types were selected for investigation, (1) the two-dimensional, external compression, horizontally mounted ramp inlet and (2) an external compression, axisymmetric inlet. Furthermore, the size and the initial location of these inlets are consistent with supersonic aircraft designed to meet stringent maneuverability requirements in the 45,000 lb gross wt class.

The size factor selected for both inlets (0.550) is considered to be representative of FX configurations, and as such reflects the postulated future requirement needed for maneuverability.

The radial and circumferential location of the selected inlets is consistent with the design of the majority of the aircraft in the Review. The forward longitudinal location of the inlet at 30% of the aircraft length was selected to be upstream of the wing/fuselage juncture. The aft position, at 50% of the aircraft length, assures that the inlets are located behind the wing shock pattern.

The selected inlet characteristics are summarized below.

Geometric Parameters	Two-Dimensional	Axisymmetric
Inlet Size Factor	0.550	0.550
Aspect Ratio	1.4	1.00
Longitudinal Location - Fwd Position	0.3	
Longitudinal Location - Aft Position	0.500	0.500
Radial Location	1.60	1.60
Circumferential Location	90°	90°
Assume Aircraft Length	65'	5'

Following selection of the inlet geometric characteristics, a detail inlet design study was made to define the inlet compression surfaces and to estimate the resultant total pressure recovery and mass flow characteristics. This study produced 2 fixed geometry designs with acceptable total pressure recovery levels and mass flow ratios matched to a postulated advanced technology engine.

SECTION IV
THEORETICAL ANALYSES

4.0 General

A major program objective was an evaluation of the ability of a simplified analytical technique to estimate the complex flow fields engendered by the vehicle fuselage. The procedure was to select a simple straightforward, yet potentially accurate, calculation methodology and employ it to estimate the flow field for each of the selected fuselage configurations. These estimates were compared to the experimentally derived flow field characteristics during the "Data Analysis and Correlation" task, thereby establishing its value as a preliminary design tool. In addition, it was hoped that the comparison of analytical and experimental results would lead to a set of empirical rules useful in the refinement of the basic technique.

Following selection of the vehicle geometries, a set of analytical computations describing the aircraft flow fields was generated. These computations were made for free-stream conditions of Mach number, angle of attack, angle of side slip, and flow properties corresponding to those expected in the wind tunnel. The actual flow fields encountered were generally three-dimensional in character, particularly for the cases of high inclination and/or nonelementary forebody geometry. General flow field solutions for these cases are not available, although some inroads have been made into certain sets of restricted problem areas. These would include, for example, inviscid solutions for the supersonic case by means of the numerical three-dimensional method-of-characteristics and also numerical solutions to the boundary layer equation in three dimensions for a very restricted set of cases. Because of the limited utility of the approaches typified by those above (in addition to the time required to obtain useful solutions), these "more general" methods have not easily found their way into preliminary design and analysis, but rather have found application either as a last resort when all else fails or in research studies. The estimating methods used in the current program are typical of those generally used in the aircraft industry and consist largely of simple application of well-known analytical techniques as described below.

For the supersonic speed regime, present state-of-the-art theories are well suited to a preliminary flow field investigation where the object is to establish basic aero/thermodynamic characteristics. These analytical tools can be used alone for the analysis of flow fields generated by elementary fuselage shapes, (conical, etc.), or they can be used in combination to analyze the flow fields generated by complex fuselage shapes.

For the subsonic speed regime, even with a substantial degree of compressibility present, the dominant airframe/inlet interaction for practical configurations stems from the influence of the viscous part of the external flow field. In a sense, this is fortunate because of the difficulty of analyzing complex subsonic inviscid flow fields. Moreover, the subsonic inviscid flows are so intimately related to the effects of viscosity that, even for simple flows, straightforward application of the existing analytical tools will not in general approximate the physical phenomena when flow separation or vortex generation is present. For these cases reliance can be placed on the experimental data to estimate the streamline patterns in hand. A streamtube analysis, which is essentially one-dimensional in nature, can be applied within each streamtube and resulting kinematic and thermodynamic properties computed to develop an empirical solution.

The following subsections describe the effort for this part of the program. The techniques employed for the analyses are also discussed.

4.1 Approach

For the supersonic speed regime, the vehicle flow field was estimated by the following procedures:

- A series of planes is established around the periphery of the fuselage, each emanating from the centerline. An example is shown schematically in Figure 4-1.

- The flow properties are calculated for each plane along the contour developed at the intersection of the plane and the basic contour line of the fuselage. The technique used is a simple two-dimensional or axisymmetric method, whichever is more appropriate, initially disregarding adjacent flows.

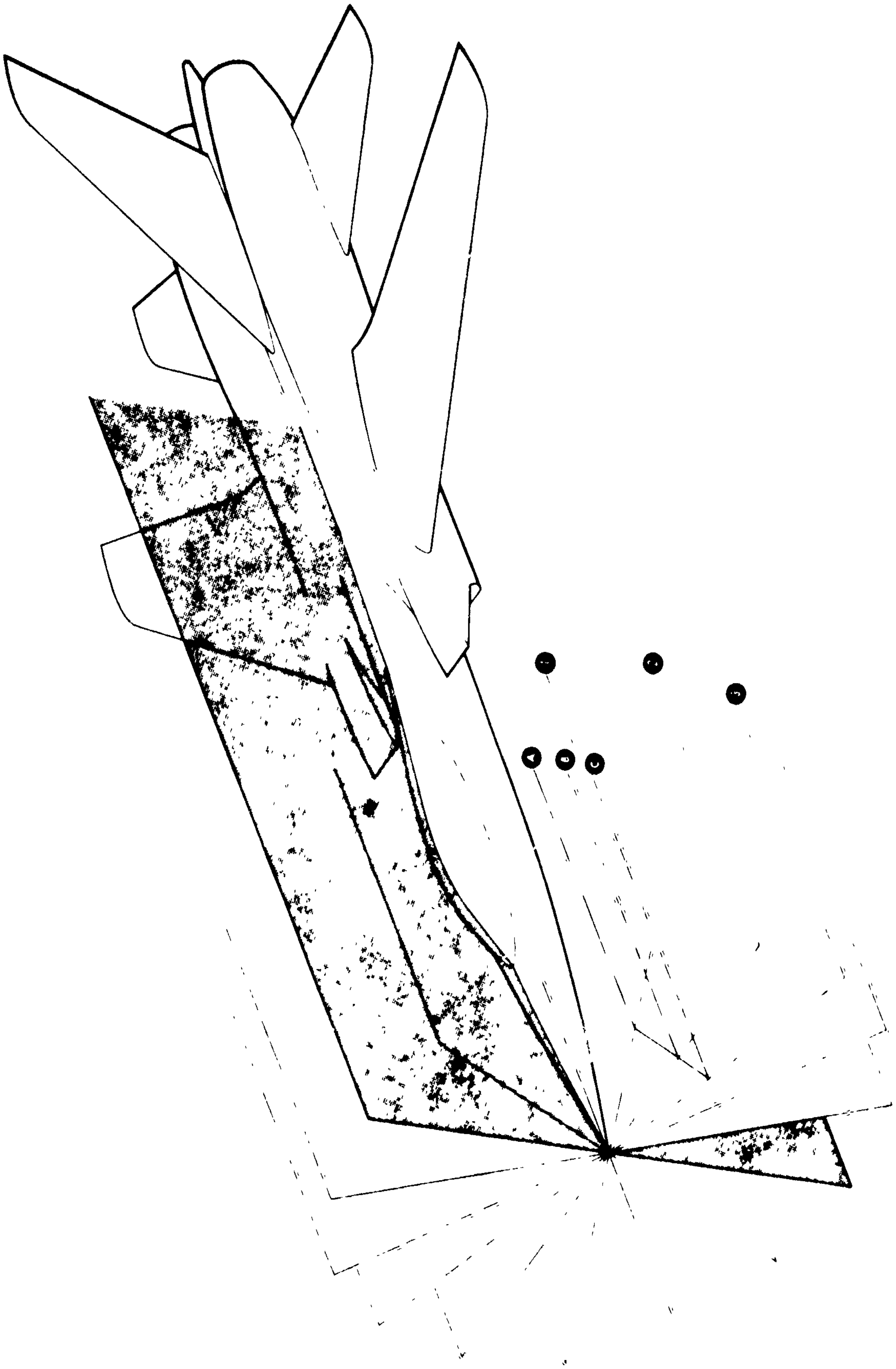

Figure 4-1. Fuselage-Plane Schematic

- The estimated characteristics are adjusted to account for transverse flow potential by bringing locally adjacent points in the flow field into equilibrium by modifying both static pressure and streamline direction.

As a result of this procedure, crude steady-state profiles of the flow field can be developed.

To develop the inviscid portion of the flow field, two-dimensional, conical, and axisymmetric inviscid analyses were applied.

For the analysis of inviscid two-dimensional flow fields in the supersonic regime, the shock-expansion method, which utilizes the Rankine-Hugoniot oblique-shock-wave relations and the conventional Prandtl-Meyer relations, (Reference 5), was applied. A digital computer program is used to calculate the complex inviscid-flow fields involved in a study of this type. The main program treats flow fields in which two family compression/expansion wave interactions are involved and has the capability of simultaneously analyzing the interaction of up to 60 waves. The main program is serviced by 12 subroutines, two of which can also be used independently to analyze flow fields made up of simple compressions or expansions. The program performs a two-dimensional calculation employing the "field technique" for a thermally perfect, calorically imperfect gas. A simple compression is treated by using the conventional oblique-shock-wave equations. The upstream flow conditions and the surface contour are known, and the flow field is determined by successively calculating the change in properties across each compression wave. The appropriate value of "gamma", the adiabatic exponent, is selected by an iterative solution for the average temperature across each wave. This adiabatic process is also used to solve the isentropic compression case by considering the surface to be made up of a large number of small discontinuities in slope rather than one of continuous curvature. This yields a solution extremely close to the isentropic case. A flow expansion is treated as an isentropic process determined by the surface contour and the approaching flow conditions. Prandtl-Meyer relationships are used in the calculation. An iterative solution is again employed to select the appropriate average gamma. Analysis of the more complex portion of the flow field, with wave interaction involved, requires an extension of the straightforward procedures described above. This wave interference case is handled by the basic techniques described above, used in conjunction with a test procedure, to identify the interaction and a trial and error solution. The program identifies the type of interaction occurring as compression/compression or compression/expansion for either the wave/wave or wave/wall case. The proper calculation procedure across each wave is then selected and a solution for the condition downstream of each wave is made by iterating until the values of static pressure and streamline direction downstream of each interacting wave are equal.

The technique developed for treatment of an axisymmetric flow field is the solution for the inviscid flow field about an unyawed circular cone. The technique yields an exact solution for the real gas case and is derived primarily from a method illustrated in Reference 7. The solution is iterative in nature whereby the approaching flow conditions and cone angle are given. The shock angle is approximated and the conditions downstream are calculated, including the tangential velocity. For the shock wave approximation, the conditions at the body are calculated. This procedure is repeated until the shock wave selected results in satisfaction of the boundary condition at the body. The shock layer is then divided into a finite number of divisions, each enclosed between rays emanating from the apex. The flow properties, constant along each of these rays, are then calculated and the complete conical flow field from shock to body is known. The conventional oblique shock wave equations are employed to calculate the change in flow field characteritics downstream of the conical section due to forebody flare and turning.

In addition to the solutions provided by the preceding cases, an accurate method of characteristics solution for supersonic flow about general two-dimensional and axisymmetric bodies has been developed. The program computes the steady-state inviscid flow properties in the supersonic region of the shock layer for bodies with arbitrary nose shapes. The program is applicable to both ideal and real gases in chemical and thermal equilibrium. The calculation can be initiated either by specifying initial data along a noncharacteristic or first-family characteristic direction or by prescribing data along the supersonic portion of an assumed shock shape consistent with the nose geometry of the body. If the latter option is chosen, the program generates its own characteristic net to the body surface consistent with the assumed shock wave shape. With the initial characteristic line determined, the program then continues to calculate the downstream flow field properties and shock wave shape for the prescribed body contour. This option can be used, therefore, to determine the nose shock shape and detachment distance by an indirect iterative process. An intrinsic advantage is available in the method in that local real gas properties are used in constructing the characteristic net used to obtain the correct shock shapes.

The calculation of downstream flow properties includes use of a mass-entropy technique to determine local entropy values and a mass balancing technique to ensure proper accounting of the total mass, thereby vastly decreasing cumulative errors in local flow properties.

4.2 Example Calculation

An example flow field calculation is presented below to illustrate application of the analytical technique. A vehicle fuselage, representative of the tactical aircraft class, was selected for this calculation. It is shown in Figure 4.2. Also shown is a series of cross-sections depicting the development of five basic contour lines at the intersection of five centerline planes with the airframe. These contour lines were developed at 20-degree intervals around the fuselage periphery. The sector chosen for analysis is applicable to the investigation of a side-mounted inlet configuration. Although five planes have been used to make up the sector, the detailed calculation of one of the flow fields will suffice to illustrate the technique.

The contour used for the calculation is at 45 degrees from the vertical. It develops initially as a cone followed by an ogival expanding turn. Approximately 255 inches downstream of the leading edge, the continuous surface curvature is interrupted by the presence of the canopy. The flight conditions used in the calculation are $M_\infty = 2.0$ at an altitude of 36,089 feet with the fuselage at an angle of attack of 7.66 degrees and zero angle of yaw. The solution includes consideration of the angle of attack and yaw. For example, the angle of attack is applied directly in the calculation of a vertical plane while the angle of yaw is used directly for a horizontal plane. As we deviate from these planes, an effective angle is computed. For example, the effective angle of attack for a horizontal plane is zero, regardless of the actual angle of attack.

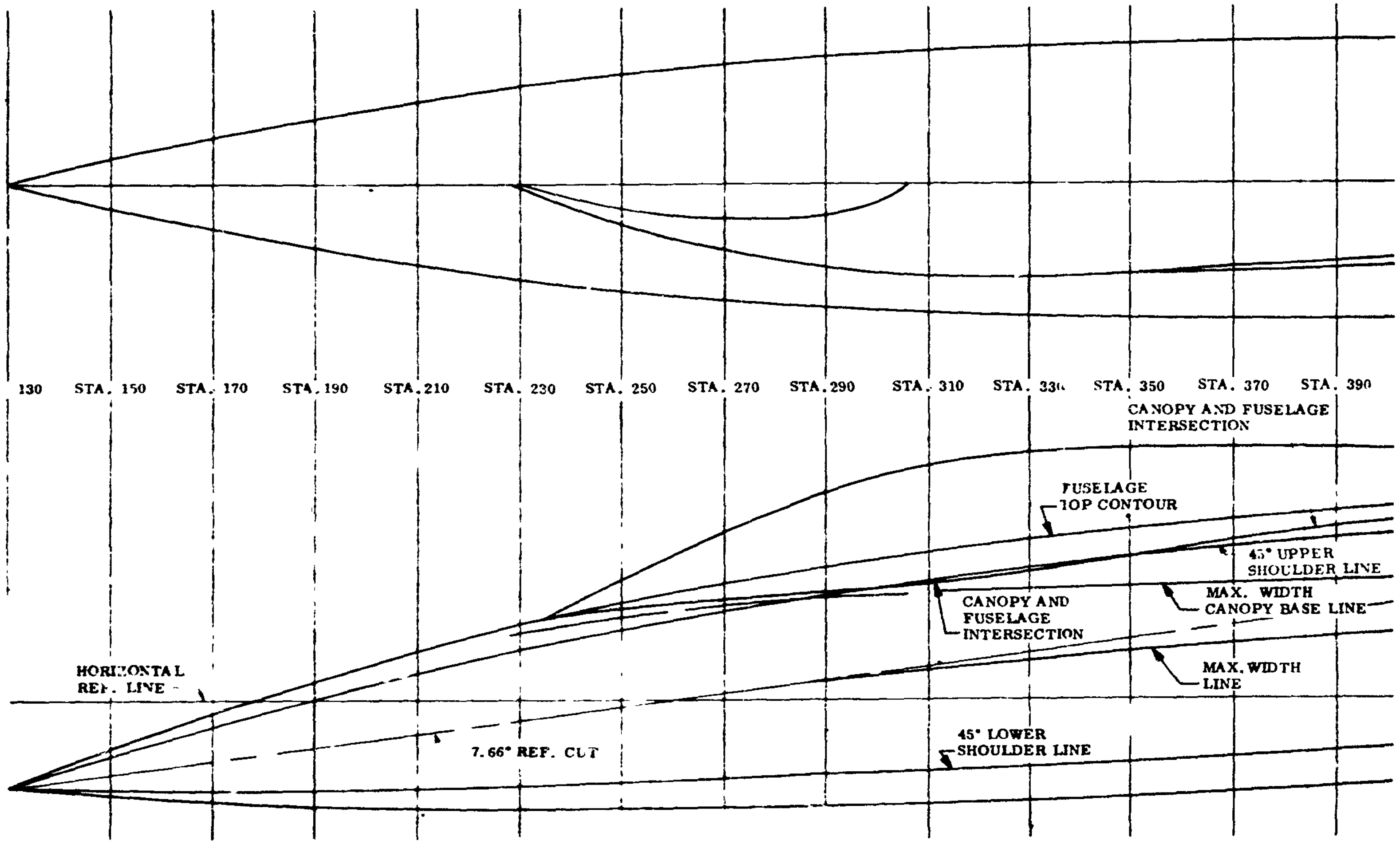
130
STA. 150
STA. 170
STA. 190
STA. 210
STA. 230
STA. 250
STA. 270
STA. 290
STA. 310
STA. 330
STA. 350
STA. 370
STA. 390
CANOPY AND FUSELAGE INTERSECTION
FUSELAGE TOP CONTOUR
45° UPPER SHOULDER LINE
MAX. WIDTH CANOPY BASE LINE
CANOPY AND FUSELAGE INTERSECTION
MAX. WIDTH LINE
HORIZONTAL REF. LINE
7.66° REF. CUT
45° LOWER SHOULDER LINE

(a) Side and Plan View

Figure 4-2. Fuselage Contour Example

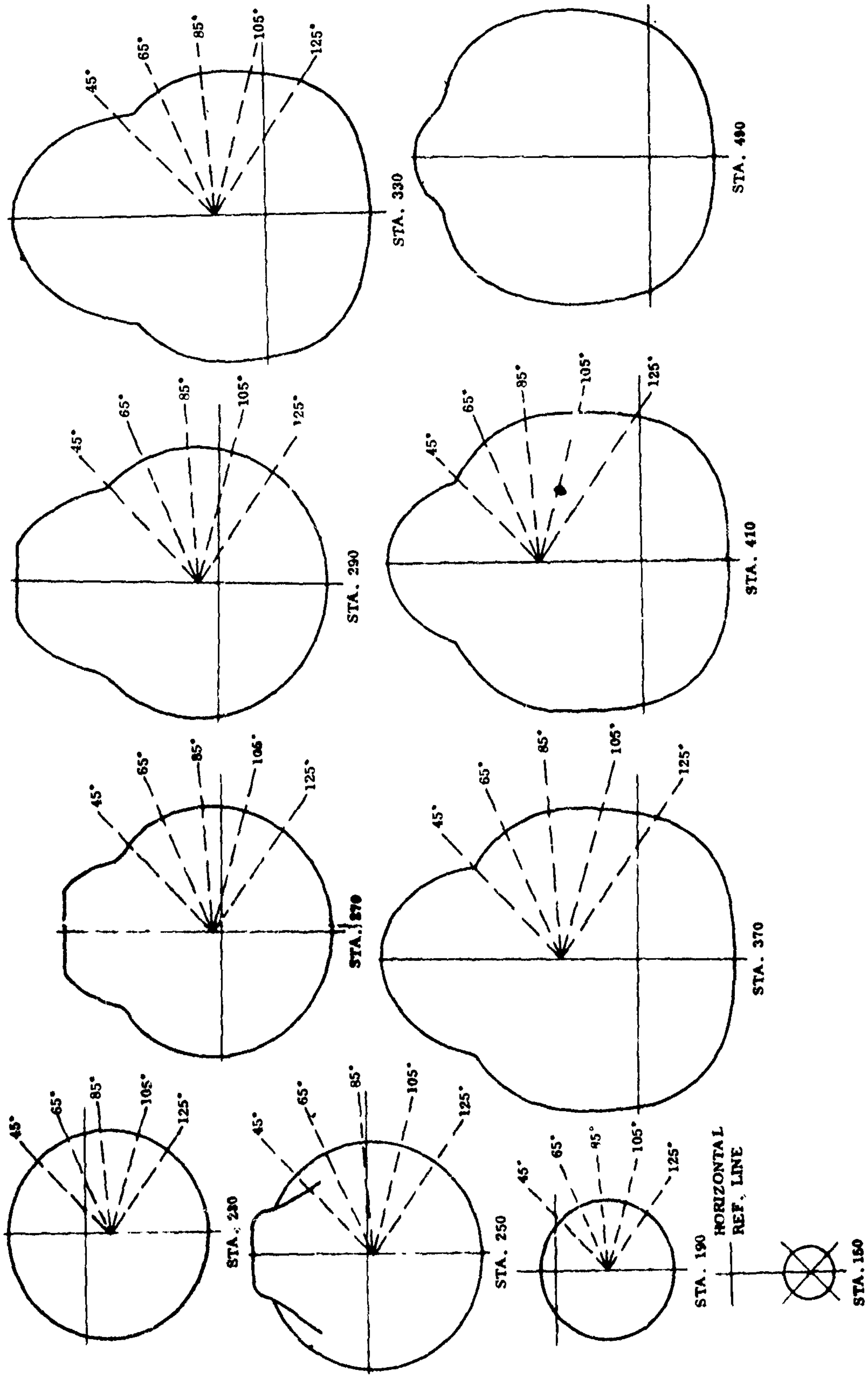
45°
65°
85°
105°
125°
STA. 330
STA. 490
STA. 290
STA. 410
STA. 270
STA. 370
STA. 230
STA. 250
STA. 190
HORIZONTAL REF. LINE
STA. 150

(b) Cross Sections

Figure 4-2. Concluded

The inviscid portion of the flow field from the forebody nose to the canopy leading edge shock wave was estimated by applying the axisymmetric method of characteristics to the effective forebody contour line, while the shock-expansion technique was utilized to estimate the flow field starting from the canopy leading edge shock wave. The thermodynamic properties calculated from the shock to the body immediately upstream of the canopy leading edge shock wave by the method of characteristics solution were used as input for the shock expansion calculation. Development of this flow field is shown in Figure 4-3. The selection of the region between Stations 232 and 252 to display this mesh size is simply for illustrative clarity. Once the two-dimensional canopy shock wave is immersed in the flow field, the mesh size is increased to avoid the necessity for calculating a multitude of very weak shock interactions. To accomplish this, the variation in properties across the upstream flow field is plotted and the values at discrete intervals are used to initiate the shock expansion calculation. In this manner, the tiresome chore of computing the essentially negligible wave interactions is avoided and the analysis remains relatively simple.

To complete the entire flow field calculation, for the sector of interest, the same procedure is followed for each of the remaining planes. Upon completing the individual flow-field calculations, a vector analysis is used to estimate transverse flow effects between adjacent planes. This is done by taking the point of interest in the flow field plus one locally adjacent point on each of the surrounding planes and performing a wave interference calculation in the transverse plane approximated by the three points and their local flow inclination. For example, shown schematically in Figure 4-1 is a transverse plane that has been cut through primary planes 1, 2, and 3. To estimate the transverse flow potential in the region of point B on plane 2, the thermodynamic properties are needed there plus those of points A and C on planes 1 and 3 respectively, which are locally adjacent to point B. With this information, a simple wave-interference calculation is introduced to solve for the downstream streamline angle of point B, in the transverse plane, as well as the thermodynamic properties. The wave-interference calculation is established by assuming that the variation in flow properties between points B and A and points B and C occurs discontinuously, and then representing this discontinuous change in the form of a simple compression or expansion wave. As this wave passes through the boundary between each stream, second-family reflected waves are

X	r	M	T	P	V
Inch	Inch		*R	ATM	FPS
160	31.0	1.62	458	.378	1703
@	36.9	1.55	472	.416	1653
STA. 290	42.2	1.55	473	.418	1651
	47.2	1.41	501	.521	1546
	51.8	1.40	503	.524	1538
	57.8]	1.23	537	.500	1397
	68.2	1.91	406	.202	1882
	82.0	1.91	408	.203	1874

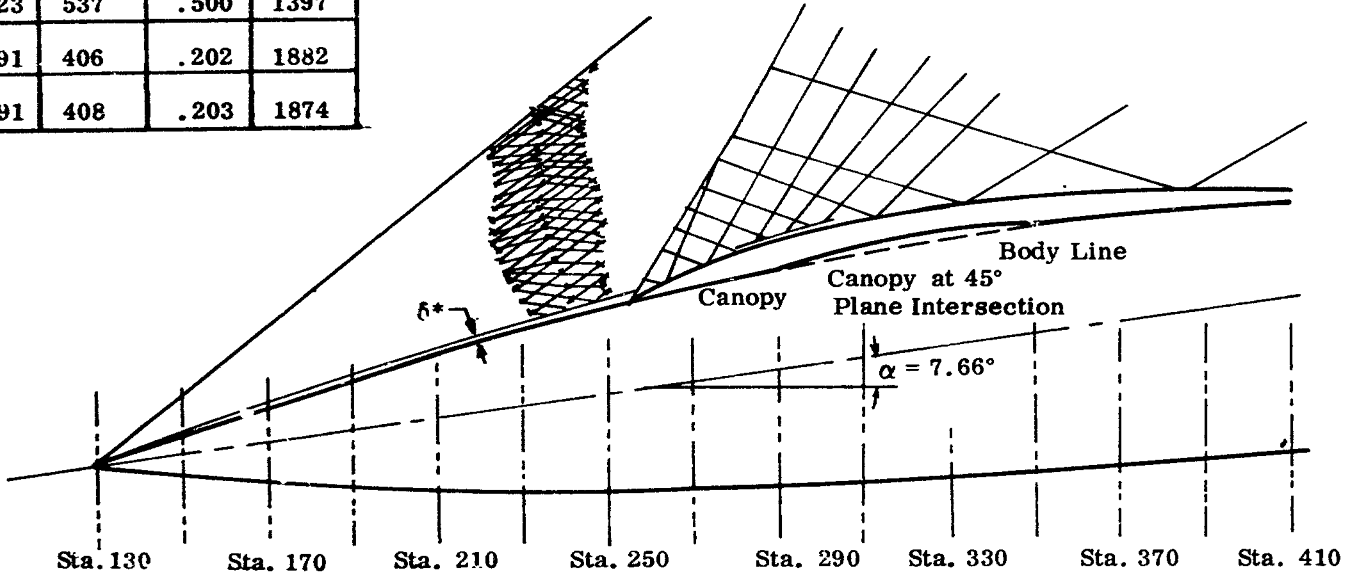
δ*
Canopy
Canopy at 45°
Plane Intersection
Body Line
α = 7.66°
Sta. 130
Sta. 170
Sta. 210
Sta. 250
Sta. 290
Sta. 330
Sta. 370
Sta. 410

Figure 4-3. Flow Field Calculation Example

generated from the intersection of the stream boundary and the primary wave. The strength and character of the reflected wave is determined by the requirement that the downstream static pressures and streamtube flow inclinations on both sides of the boundary must match, and, as a result, the flow direction at point B as well as the thermodynamic properties in the transverse plane are roughly determined.

The corrected values are input into a digital program designed to plot constant value contours for any specified parameter. This program employs a linear interpolation between parameter input points, to select the characteristics of the constant value contour lines. An example output displaying local angle of attack, is shown in Figure 4-4. Inspection of the figure reveals a trend that might be expected from the fuselage configuration test condition combination.

4.3 Substantiation of Theoretical Approach

The theoretical determination of flow properties about the fuselage, as described in the previous section, can only be considered a first order approximation to the actual flow pattern. In general, the flow about an airplane fuselage is highly three-dimensional and would require a three-dimensional flow calculation scheme in order to accurately determine the flow properties away from the body surface. An exact solution of this type would involve a lengthy and complicated three-dimensional characteristics solution of which some existing approaches are in themselves subject to serious criticism.

The absence of a convenient exact theoretical method has prompted the development of more convenient approximate procedures which are of greater utility to the design engineer. As a result, several approximate methods similar to the method proposed in this study have been developed for application to both supersonic and hypersonic three-dimensional flow fields.

In Reference 8 a generalized shock expansion procedure was utilized in meridian planes to calculate the flow field about a body of revolution at small angles of attack. A comparison of the numerical results of that method with experimental data showed good agreement for surface pressures and Mach numbers at angles of attack up to 15 degrees. A refinement of this procedure was presented in Reference

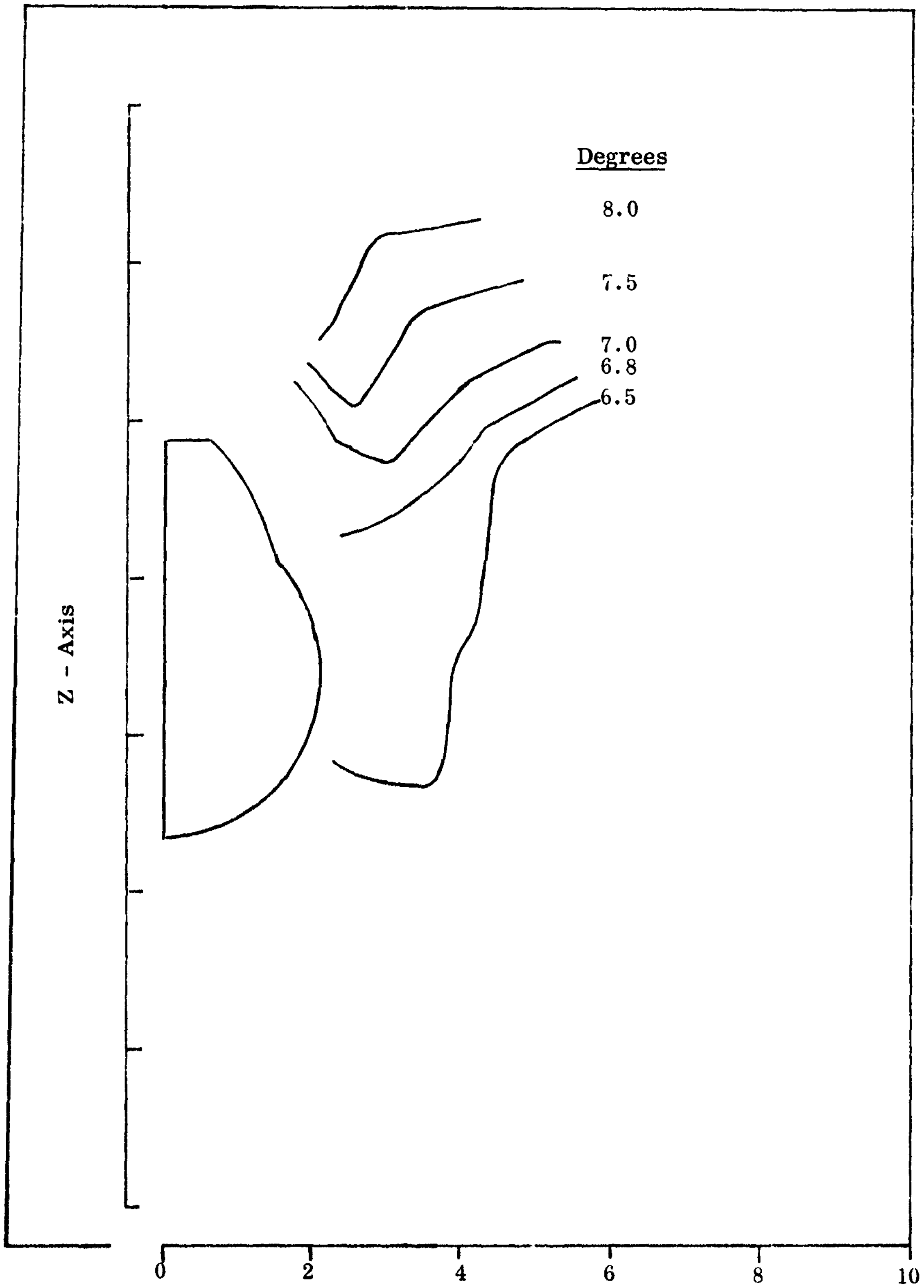

Figure 4-4. Alpha Contour
Alpha = 7.66° M = 2.0

9 for arbitrarily shaped conical bodies at zero incident as well as at angle of attack. The method presented in Reference 9 is based on the equivalent cone theory with corrections to account for pressure exchange between meridian planes. The results of this theoretical approach are shown to agree remarkably well with experimental results for elliptic cone and circular cones at angle of attack.

A modification of this method was applied in Reference 10 to pointed elliptical cones followed by compression surfaces. Although there existed some question as to the validity of the experimental pressures along the major axis of the elliptic forebody, good agreement between theory and experiment was achieved for the pressures along the minor axis of the body.

Based on the favorable results presented in References 8, 9, and 10, it was believed that the theoretical approach utilized during this program to determine the flow field properties about the forward portion of the fuselage possessed the potential to yield adequate engineering estimates required in the design stage of the study. A final assessment of the method, determined from a comparison with the experimental data, is discussed in the data analysis section of the report.

SECTION V

WIND TUNNEL MODEL

5.0 General

With the vehicle component characteristics chosen, it remained to design a wind tunnel model capable of efficiently providing the many geometry variations to be explored while also providing that data required to document both the vehicle flow field and inlet performance.

Based upon a representative tactical aircraft length of sixty five feet, test facility sizing criteria led to the selection of a 0.083 model scale.

The program objectives dictated the testing of five basic model arrangements; namely

- Format I -- Tests of the fuselage alone during which the induced flow field is surveyed at that station representing thirty (30) percent of the overall aircraft length (ACL). In addition to the flow field properties, the fuselage static pressure distribution is recorded along several longitudinal rays. During these tests the nose, canopy, and fuselage geometry are varied.
- Format II -- Tests of the two-dimensional inlet installed at the thirty (30) percent ACL station. During these tests the inlet performance characteristic of total pressure recovery versus mass flow ratio is documented for combinations of nose, canopy, and fuselage geometry.
- Format III -- Tests of both the axisymmetric and two-dimensional inlets, installed at the fifty (50) percent ACL station. This location places the inlet under the aircraft wing. During these tests the inlet total pressure recovery and mass flow ratio are recorded for combinations of wing and fuselage geometry.
- Format IV -- Tests of the fuselage/wing combination during which the induced flow field under the wing is surveyed at the fifty (50) percent ACL station. In addition to the flow field properties, the fuselage static pressure distribution is recorded along several longitudinal rays.

During these tests the wing and fuselage geometry are varied.

- Format V -- Tests of the isolated two-dimensional and axisymmetric inlets. During these tests the inlet total pressure recovery and mass flow ratio are recorded.

The pressure measurements required for the test program consisted of fuselage static pressure, fuselage flow field static and stagnation pressure, inlet duct static pressure, and inlet duct stagnation pressure at the hypothesized engine face location. Those measurements required for each of the test formats is presented in the table below.

Instrumentation	Test Format				
	I	II	III	IV	V
1) fuselage static pressure	X	X	X	X	
2) fuselage flow field static and stagnation pressure	X			X	
3) inlet duct static pressure		X	X		X
4) inlet duct stagnation pressure		X	X		X

To minimize both data recording and model change times, scanivalves were incorporated into the instrumentation system.

5.1 Design

A building block concept was chosen as best suited to the program requirements. The model was comprised of a common fuselage section, attached to the support sting. The nose, canopy, fuselage corner, wing, inlet, and flow field survey components were added to build up the configuration. This approach made possible any combination of components. The model components are presented in the composite photograph in Figure 5-1. A detail drawing of the fuselage geometry is presented in Figure 5-2. The fuselage was also divided longitudinally with the forward section employed to obtain flow field surveys and installed inlet performance at the forward station (30% ACL). The aft fuselage section and the wing were then added for testing at the aft station (50% ACL). Suspension of the two inlet configurations and the flow field survey mechanism from the model support sting permitted

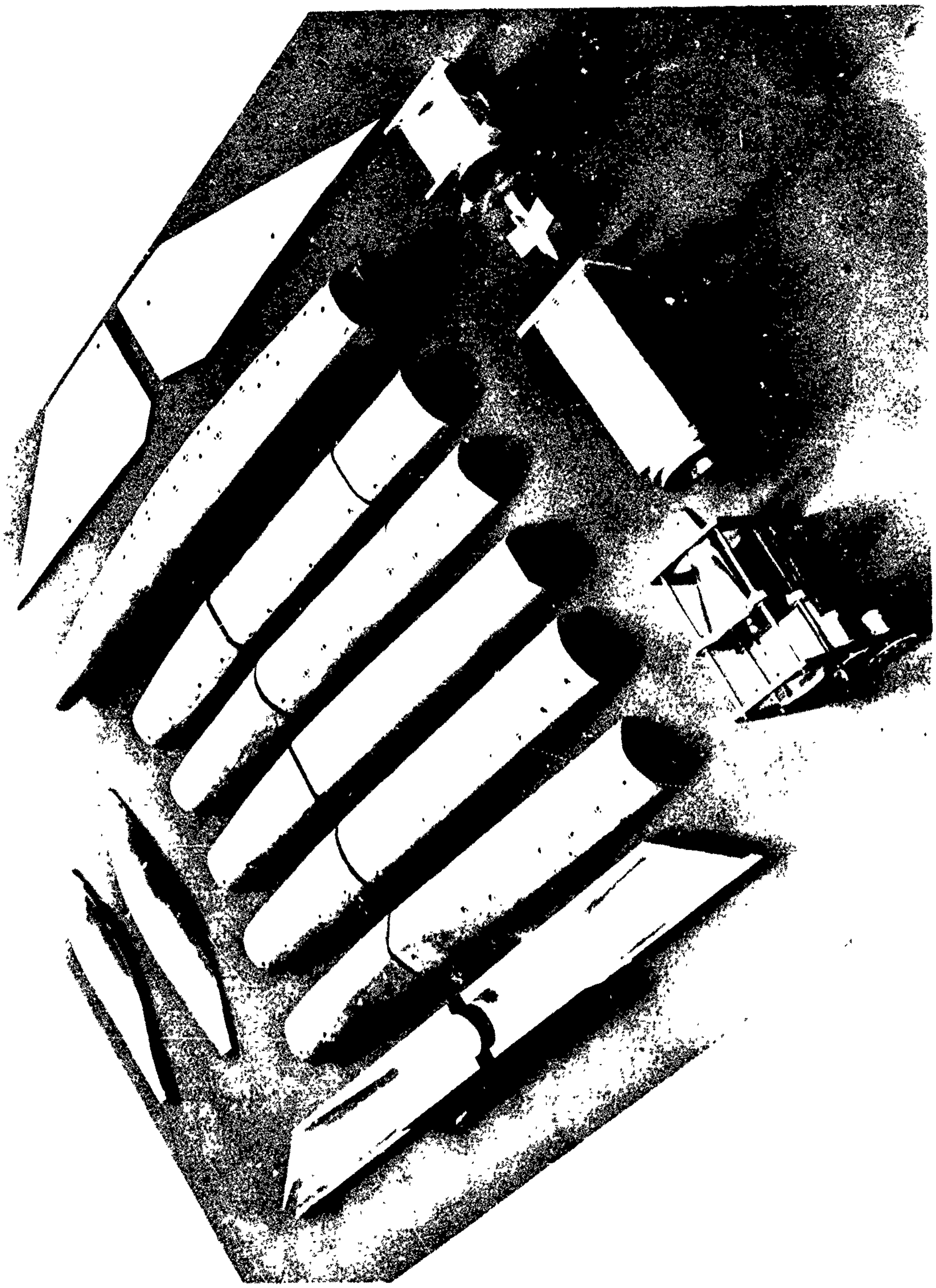

Figure 5-1. Model Composite

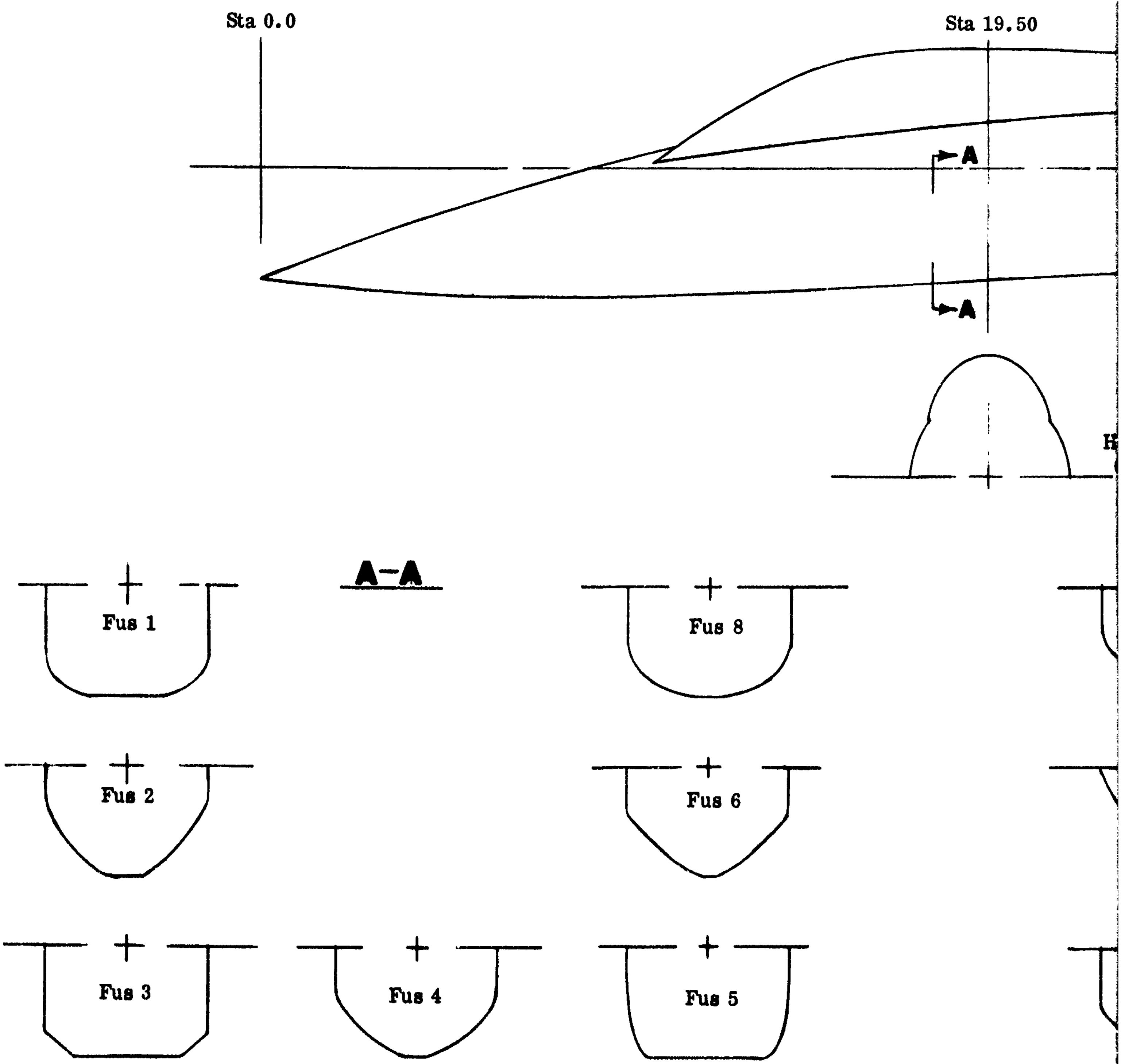
Sta 0.0
Sta 19.50
A
A
H
A-A
Fus 1
Fus 8
Fus 2
Fus 6
Fus 3
Fus 4
Fus 5

Figure 5-2. Fuselage Geometry

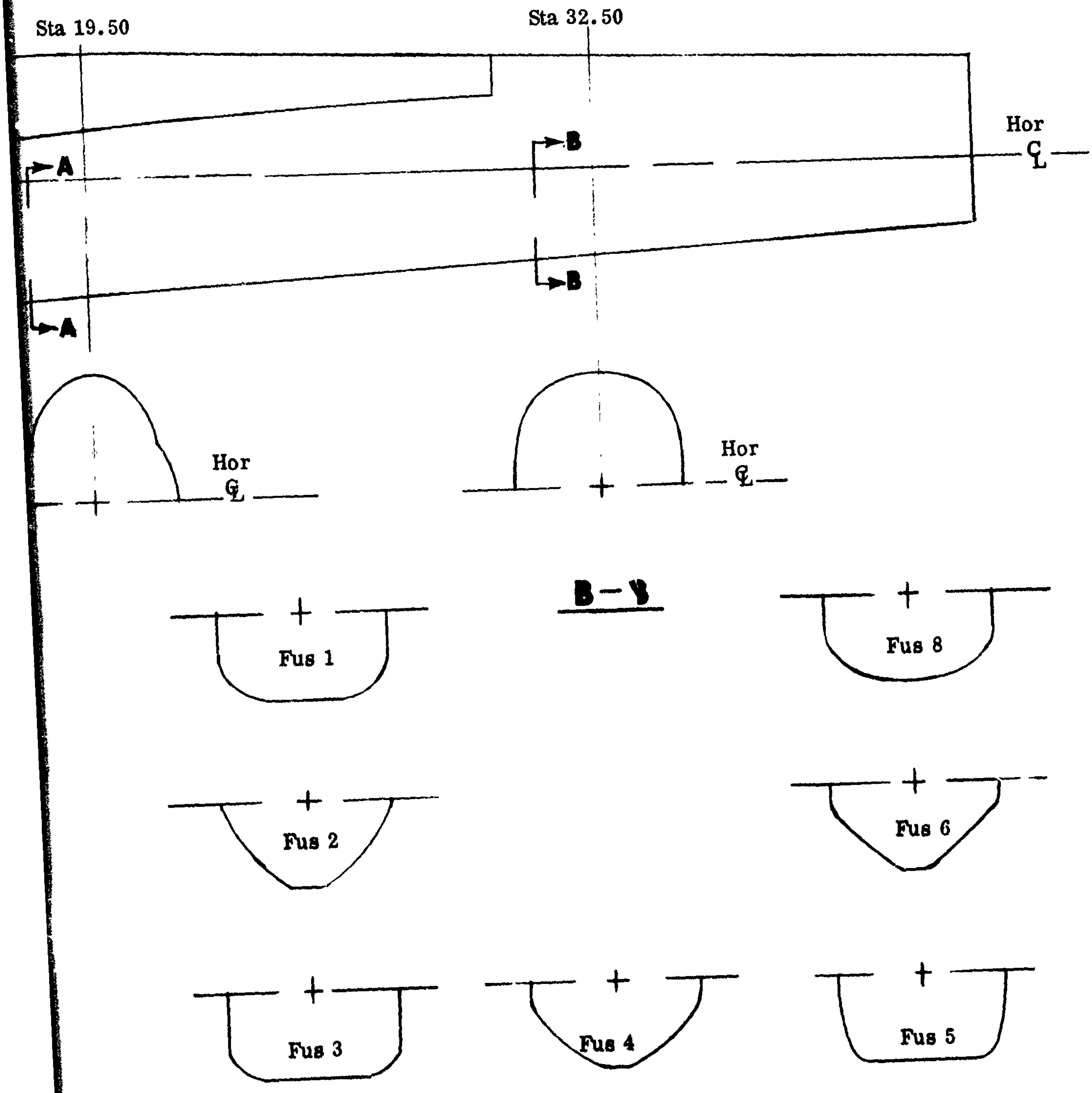
Sta 19.50
Sta 32.50
Hor ℄
A
A
B
B
Hor ℄
Hor ℄
B - B
Fus 1
Fus 8
Fus 2
Fus 6
Fus 3
Fus 4
Fus 5

2

the independent installation and removal of these components thereby providing an efficient means of performing the isolated inlet tests and the calibration tests of the survey mechanism. Detail drawings of the installed two-dimensional and axisymmetric inlets are shown in Figures 5-3 and 5-4 respectively.

5.1.1 Flow Field Survey System

Three (3) conical pitot-static probes, mounted on a remotely actuated drive system, were employed to document the fuselage flow field properties. The probes were 0.125 inch in diameter with an included cone angle of 40 degrees. Each probe incorporated a pitot in the nose and four (4) static pressure taps spaced equidistantly around the periphery of the cone surface. The static taps were located along the cone surface at a point slightly aft of midway between the probe leading edge and the cone shoulder. The probes were fixed to a horizontal strake, with a spacing of 1.4 inches. The strake, in turn, was attached to the drive mechanism capable of imparting a horizontal, vertical, and angular motion. The first two (2) motions served to position the probes in the flow field; the third was used to roughly align the probes with the locally approaching flow such that calibration limits were not exceeded. The horizontal and vertical position of the probes plus their angularity were recorded by potentiometers geared directly to the drive motors. The potentiometer readings were automatically relayed to the data reduction system and converted into inches of travel and relative angle. For each test condition the probes were positioned at a series of predetermined horizontal and vertical locations to obtain a documentation of the flow field. The angular drive was designed to rotate the probes about their tips. Consequently, the horizontal and vertical location was set, for each data point, and then the probes were pitched toward alignment with the local flow field. Approximate alignment was determined from the visual read out of a pressure differential transducer installed between the two vertical static taps of the probe closest to the fuselage. Experimentally derived calibration criteria plus the five pressure values for each probe were used to determine the local Mach number, static pressure, stagnation pressure, angle of pitch, and roll angle. A detail drawing of the system is presented in Figure 5-5. Photographs of the unit are presented in Figure 5-6. Details of one pitot-static conical probe are presented in Figure 5-7.

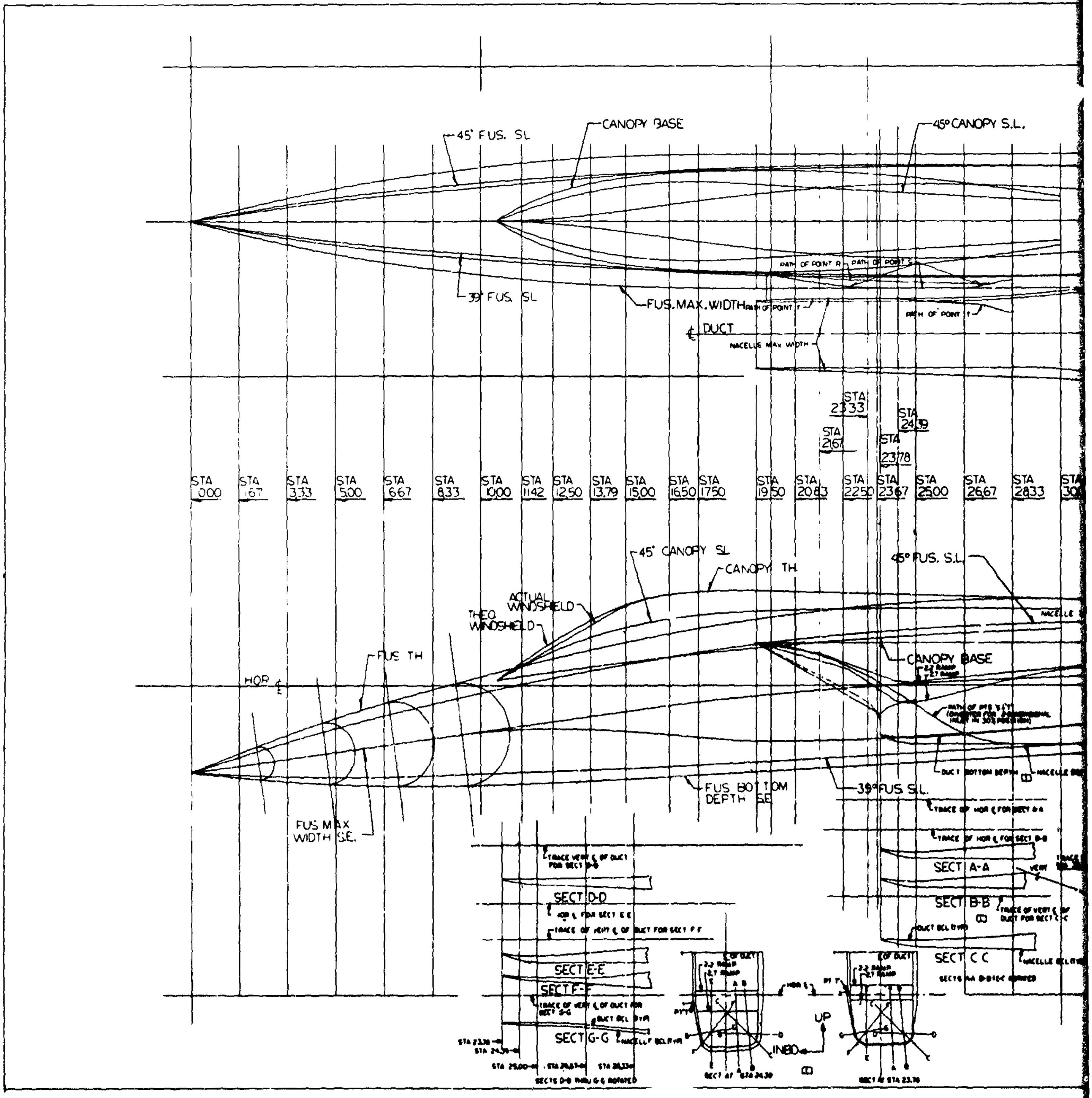
45° FUS. SL
CANOPY BASE
45° CANOPY S.L.
39° FUS. SL
FUS. MAX. WIDTH
PATH OF POINT R
PATH OF POINT S
PATH OF POINT T
PATH OF POINT T
℄ DUCT
NACELLE MAX WIDTH
STA 23.33
STA 24.39
STA 21.67
STA 23.78
STA .000
STA 1.67
STA 3.33
STA 5.00
STA 6.67
STA 8.33
STA 10.00
STA 11.42
STA 12.50
STA 13.79
STA 15.00
STA 16.50
STA 17.50
STA 19.50
STA 20.83
STA 22.50
STA 23.67
STA 25.00
STA 26.67
STA 28.33
STA 30
45° CANOPY SL
CANOPY TH
45° FUS. S.L.
ACTUAL WINDSHIELD
THEO. WINDSHIELD
NACELLE
CANOPY BASE
2.2 RAMP
2.7 RAMP
FUS TH
HOR ℄
PATH OF PTS V & T
FUS MAX WIDTH S.E.
FUS BOTTOM DEPTH SE
39° FUS S.L.
DUCT BOTTOM DEPTH
NACELLE
TRACE OF HOR ℄ FOR SECT A-A
TRACE OF HOR ℄ FOR SECT B-B
SECT A-A
VIEW
SECT B-B
TRACE OF VERT ℄ OF DUCT FOR SECT C-C
DUCT BCL
SECT C C
NACELLE BCL
SECTS AA B-B & C-C ROTATED
TRACE VERT ℄ OF DUCT FOR SECT D-D
SECT D-D
HOR ℄ FOR SECT E E
TRACE OF VERT ℄ OF DUCT FOR SECT F F
SECT E-E
SECT F-F
TRACE OF VERT ℄ OF DUCT FOR SECT G-G
DUCT BCL SYM
SECT G-G
NACELLE BCL SYM
STA 23.30
STA 24.39
STA 25.00
STA 26.67
STA 28.33
SECTS D-D THRU G-G ROTATED
℄ OF DUCT
2.2 RAMP
2.7 RAMP
A
B
C
D
E
F
G
PT T
HOR ℄
UP
INBD
SECT AT STA 24.39
SECT AT STA 23.78

Figure 5-3. Two-Dimensional Inlet

1

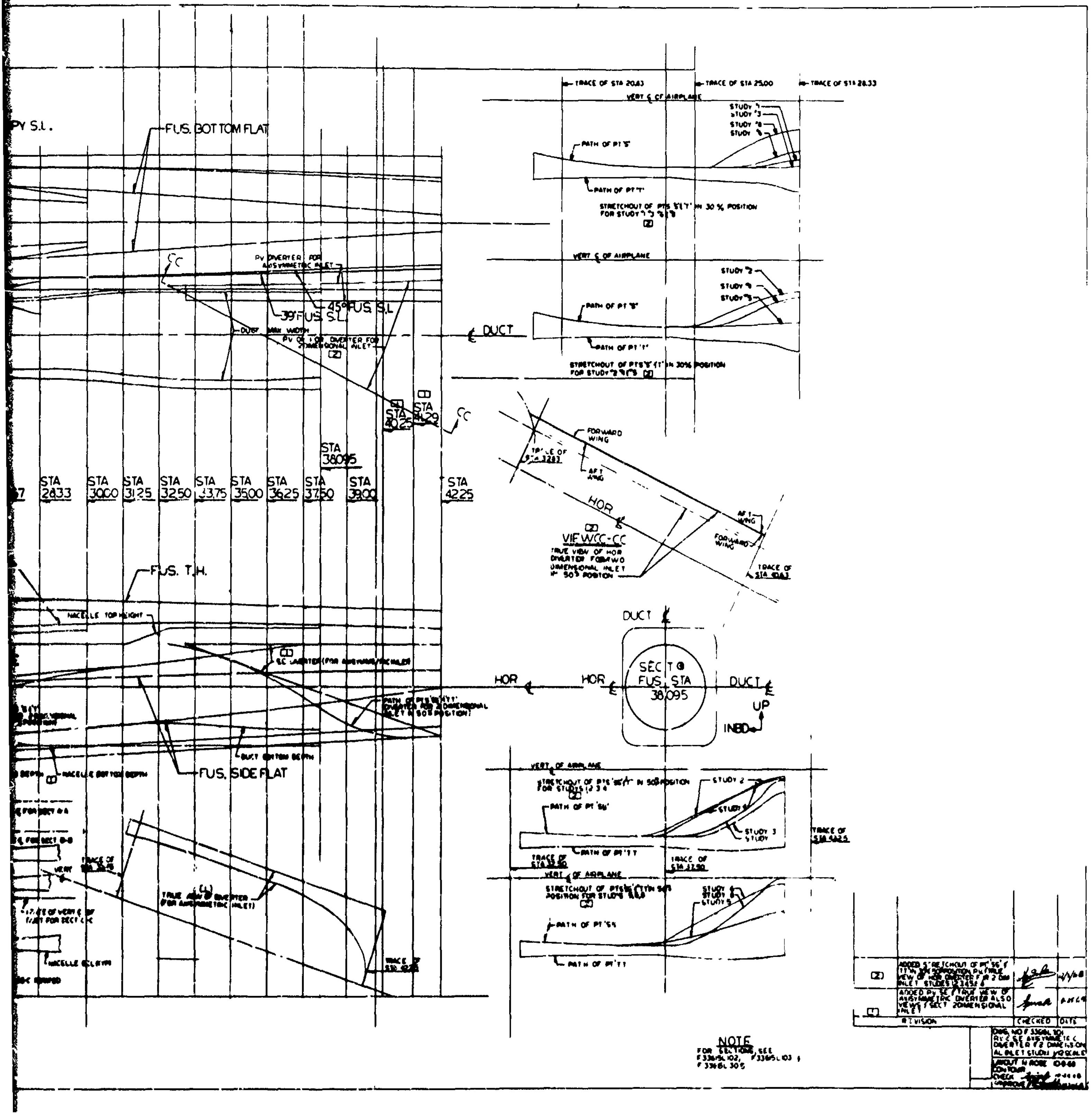
PY S.L.
FUS. BOTTOM FLAT
CC
PV DIVERTER FOR ASYMMETRIC INLET
45° FUS. S.L.
39° FUS. S.L.
DUCT MAX WIDTH
PV OF FOR DIVERTER FOR 2 DIMENSIONAL INLET
2
STA 40.25
STA 41.29
STA 38.095
STA 28.33
STA 30.00
STA 31.25
STA 32.50
STA 33.75
STA 35.00
STA 36.25
STA 37.50
STA 39.00
STA 42.25
FUS. T.H.
NACELLE TOP HEIGHT
SC DIVERTER (FOR ASYMMETRIC INLET)
PATH OF PTS 'SS'&'TT' DIVERTER FOR 2 DIMENSIONAL INLET IN 50% POSITION
DUCT BOTTOM DEPTH
NACELLE BOTTOM DEPTH
FUS. SIDE FLAT
FOR SECT A-A
FOR SECT B-B
TRACE OF STA 33.75
VERT
TRUE VIEW OF DIVERTER (FOR ASYMMETRIC INLET)
NACELLE ℄ L
TRACE OF STA 42.25
TRACE OF STA 20.83
TRACE OF STA 25.00
TRACE OF STA 28.33
VERT ℄ OF AIRPLANE
STUDY 1
STUDY 3
STUDY 8
STUDY 6
PATH OF PT 'S'
PATH OF PT 'T'
STRETCHOUT OF PTS 'S'&'T' IN 30 % POSITION FOR STUDY 1, 3, 6 & 8
2
VERT ℄ OF AIRPLANE
STUDY 2
STUDY 4
STUDY 5
PATH OF PT 'S'
PATH OF PT 'T'
℄ DUCT
STRETCHOUT OF PTS 'S' & 'T' IN 30% POSITION FOR STUDY 2, 4 & 5
2
FORWARD WING
AFT WING
TRACE OF STA 32.83
HOR ℄
2
VIEW CC-CC
TRUE VIEW OF HOR DIVERTER FOR TWO DIMENSIONAL INLET IN 50% POSITION
AFT WING
FORWARD WING
TRACE OF STA 40.83
DUCT ℄
HOR ℄
HOR ℄
SECT @ FUS. STA 38.095
DUCT ℄
UP
INBD
VERT ℄ OF AIRPLANE
STRETCHOUT OF PTS 'SS'&'TT' IN 50% POSITION FOR STUDYS 1, 2, 3, 4
2
STUDY 2
STUDY 1
STUDY 3
STUDY 4
PATH OF PT 'SS'
PATH OF PT 'TT'
TRACE OF STA 32.50
TRACE OF STA 37.50
TRACE OF STA 42.25
VERT ℄ OF AIRPLANE
STRETCHOUT OF PTS 'SS'&'TT' IN 50% POSITION FOR STUDYS 5 & 6
2
STUDY 6
STUDY 5
PATH OF PT 'SS'
PATH OF PT 'TT'
2
ADDED STRETCHOUT OF PT 'SS' & 'TT' IN 30% & 50% POSITION PV & TRUE VIEW OF HOR DIVERTER F/R 2 DIM INLET STUDIES 1, 2, 3, 4, 5 & 6
1
ADDED PV SECT & TRUE VIEW OF ASYMMETRIC DIVERTER ALSO VIEWS & SECT 2 DIMENSIONAL INLET
REVISION
CHECKED
DATE
DWG. NO F 3368L 101
PV & SE ASYMMETRIC DIVERTER & 2 DIMENSIONAL INLET STUDY 1/2 SCALE
LAYOUT
CONTOUR
CHECK
APPROVE
NOTE
FOR SECTIONS, SEE F 3368L 102, F 3368L 103 & F 3368L 305

2

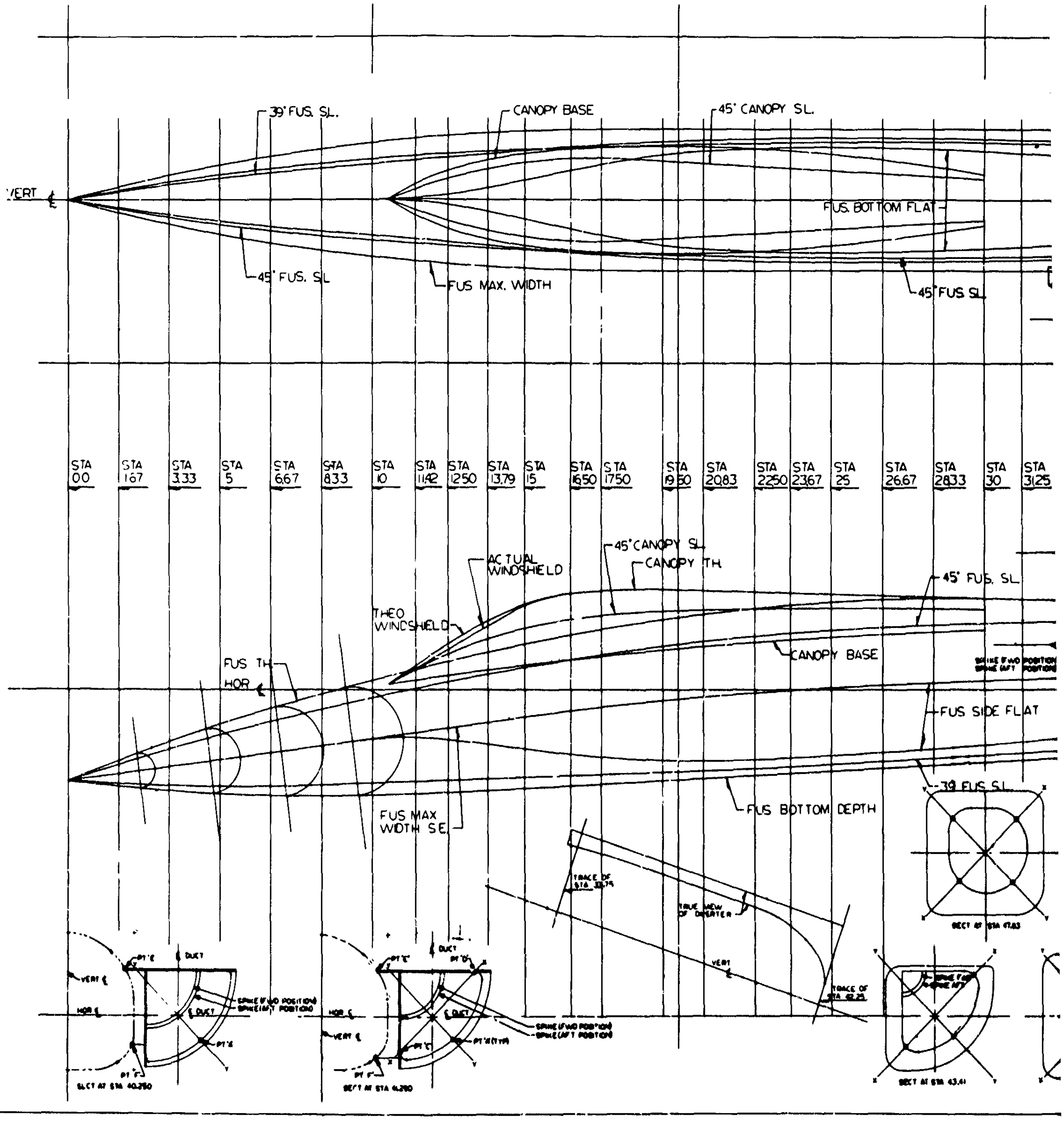
39° FUS. SL.
CANOPY BASE
45° CANOPY SL.
VERT ℄
FUS. BOTTOM FLAT
45° FUS. SL
FUS MAX. WIDTH
45° FUS SL
STA 00
STA 1.67
STA 3.33
STA 5
STA 6.67
STA 8.33
STA 10
STA 11.42
STA 12.50
STA 13.79
STA 15
STA 16.50
STA 17.50
STA 19.50
STA 20.83
STA 22.50
STA 23.67
STA 25
STA 26.67
STA 28.33
STA 30
STA 31.25
ACTUAL WINDSHIELD
45° CANOPY SL.
CANOPY TH.
45° FUS. SL.
THEO WINDSHIELD
FUS TH
HOR ℄
CANOPY BASE
SPIKE (FWD POSITION)
SPIKE (AFT POSITION)
FUS SIDE FLAT
39 FUS SL.
FUS BOTTOM DEPTH
FUS MAX WIDTH S.E.
TRACE OF STA 33.75
TRUE VIEW OF DIVERTER
VERT ℄
TRACE OF STA 42.25
SECT AT STA 47.63
℄ DUCT
PT 'E'
VERT ℄
HOR ℄
SPIKE (FWD POSITION)
SPIKE (AFT POSITION)
℄ DUCT
PT 'E'
PT 'F'
SECT AT STA 40.250
℄ DUCT
PT 'E'
PT 'D'
HOR ℄
VERT ℄
℄ DUCT
SPIKE (FWD POSITION)
SPIKE (AFT POSITION)
PT 'C'
PT 'A' (TYP)
PT 'F'
SECT AT STA 41.250
SPIKE FWD
SPIKE AFT
SECT AT STA 43.41

1

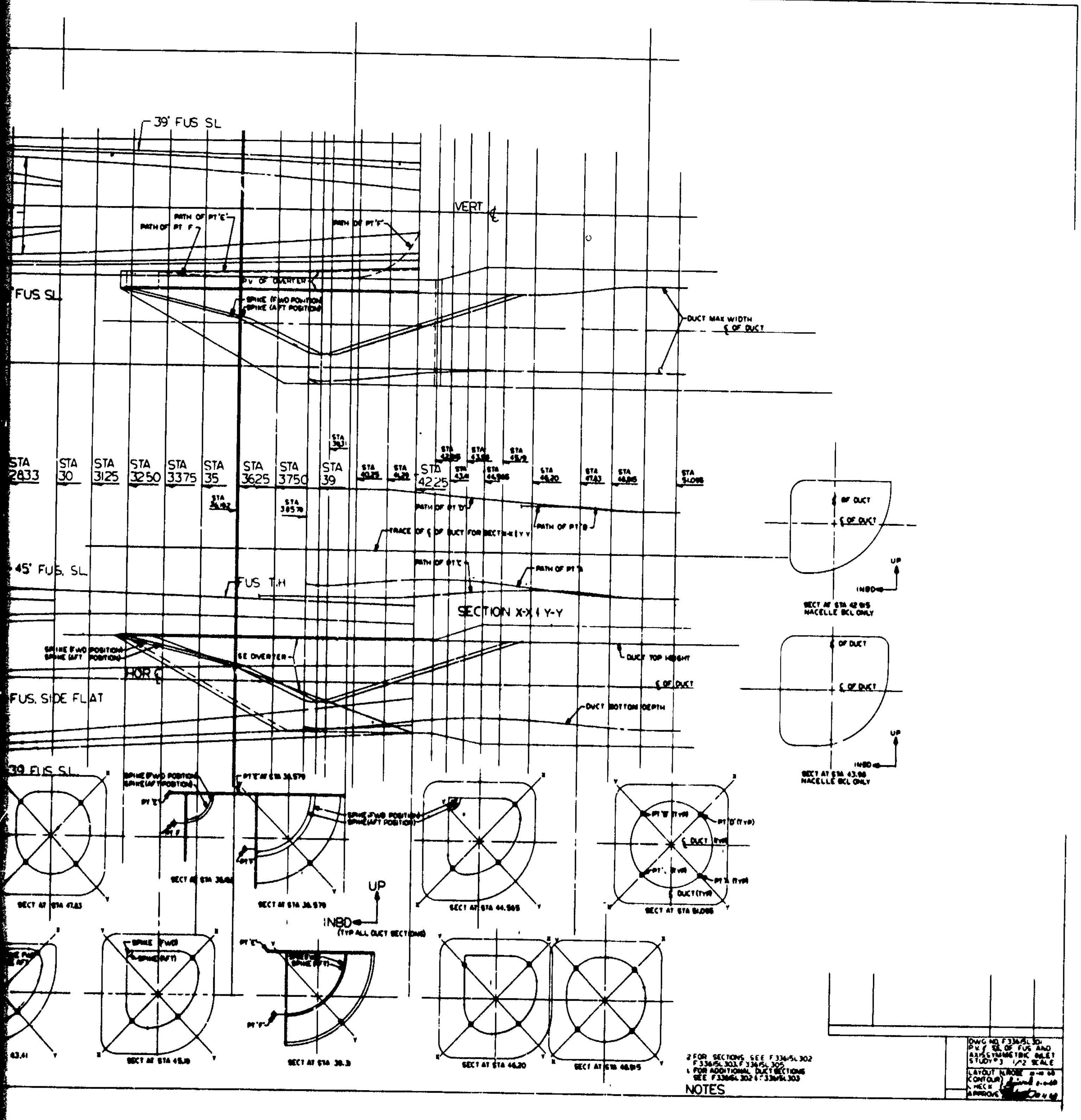
39' FUS SL
PATH OF PT 'E'
PATH OF PT 'F'
PATH OF PT 'F'
VERT ℄
FUS SL
P V OF DIVERTER
SPIKE (FWD POSITION)
SPIKE (AFT POSITION)
DUCT MAX WIDTH
℄ OF DUCT
STA 2833
STA 30
STA 3125
STA 3250
STA 3375
STA 35
STA 3625
STA 3750
STA 39
STA 4225
STA 36.92
STA 38.570
STA 39.31
STA 40.25
STA 41.29
STA 42.95
STA 43.4
STA 43.96
STA 44.565
STA 45.19
STA 46.20
STA 47.43
STA 48.815
STA 51.055
PATH OF PT 'D'
PATH OF PT 'B'
TRACE OF ℄ OF DUCT FOR SECT X-X & Y-Y
PATH OF PT 'C'
PATH OF PT 'A'
45' FUS. SL
FUS T.H
SECTION X-X & Y-Y
SPIKE (FWD POSITION)
SPIKE (AFT POSITION)
HOR ℄
SIDE DIVERTER
DUCT TOP HEIGHT
℄ OF DUCT
DUCT BOTTOM DEPTH
FUS. SIDE FLAT
39 FUS SL
℄ OF DUCT
℄ OF DUCT
UP
INBD
SECT AT STA 42.95 NACELLE BCL ONLY
℄ OF DUCT
℄ OF DUCT
UP
INBD
SECT AT STA 43.96 NACELLE BCL ONLY
PT 'E' AT STA 36.570
PT 'E'
PT 'F'
SECT AT STA 36.92
SECT AT STA 47.43
SECT AT STA 36.570
UP
INBD
(TYP ALL DUCT SECTIONS)
SECT AT STA 44.565
PT 'E' (TYP)
PT 'D' (TYP)
℄ DUCT (TYP)
PT 'C' (TYP)
PT 'B' (TYP)
DUCT (TYP)
SECT AT STA 51.055
SPIKE (FWD)
SPIKE (AFT)
PT 'E'
PT 'F'
43.41
SECT AT STA 45.19
SECT AT STA 39.31
SECT AT STA 46.20
SECT AT STA 48.815
2 FOR SECTIONS SEE F336/SL302 F336/SL303 & F336/SL305
1 FOR ADDITIONAL DUCT SECTIONS SEE F336/SL302 & F336/SL303
NOTES
DWG NO F336/SL301
P V ℄ SL OF FUS AND AXISYMMETRIC INLET STUDY #3 1/2 SCALE
LAYOUT
CONTOUR
CHECK
APPROVE

Figure 5-4. Axisymmetric Inlet

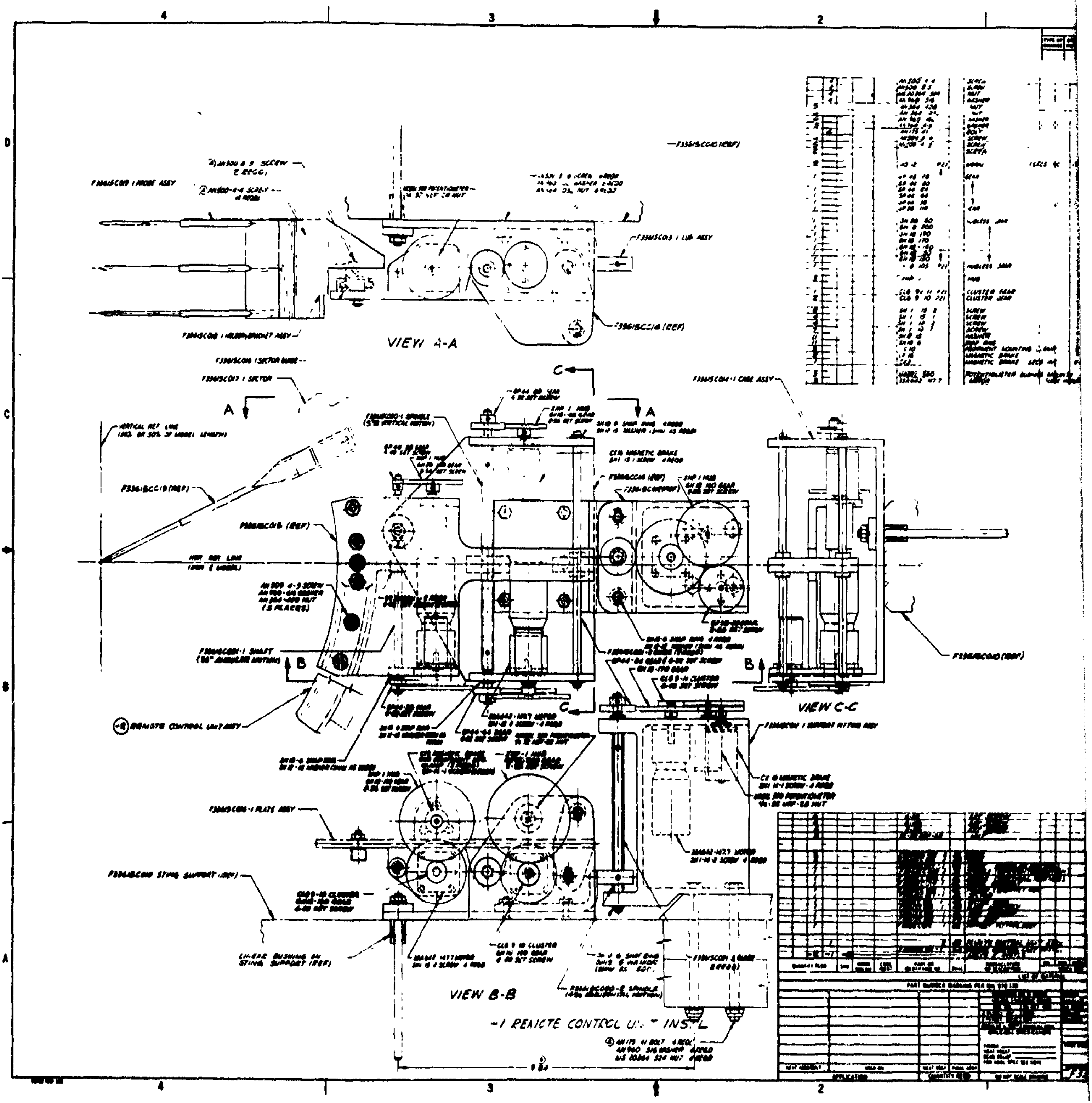
4
3
2
D
C
B
A
VIEW A-A
VIEW B-B
VIEW C-C
A
B
C
-1 REMOTE CONTROL UNIT INSTL

Figure 5-5. Flow Field Survey Mechanism

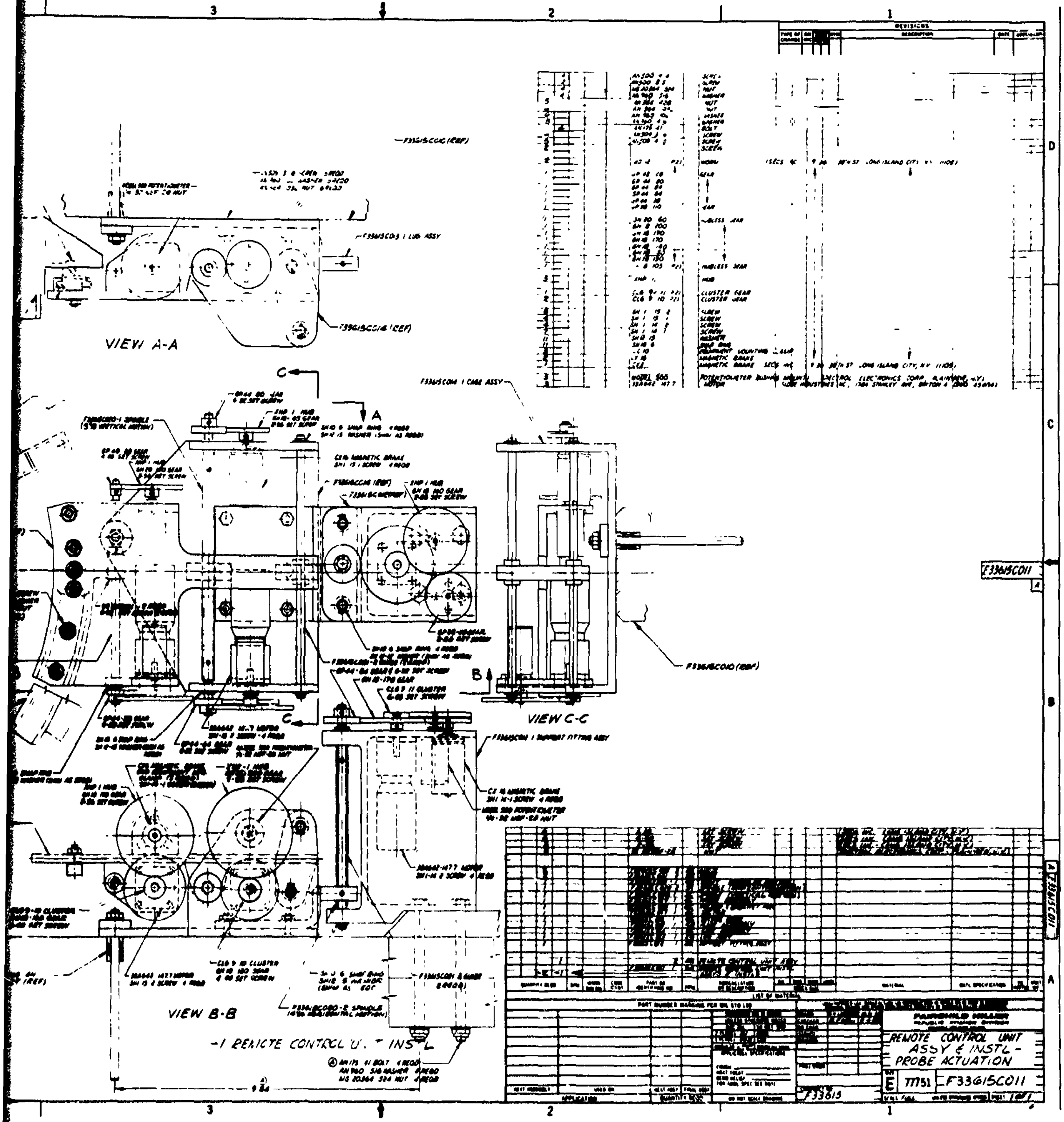
3
2
1
D
C
B
A
REVISIONS
VIEW A-A
VIEW B-B
VIEW C-C
C
A
B
F33615C010 (REF)
F33615C011
-1 REMOTE CONTROL UNIT INSTL
REMOTE CONTROL UNIT
ASSY & INSTL -
PROBE ACTUATION
E
77751
F33615C011
F33615

Figure 5-5. Flow Field Survey Mechanism

2

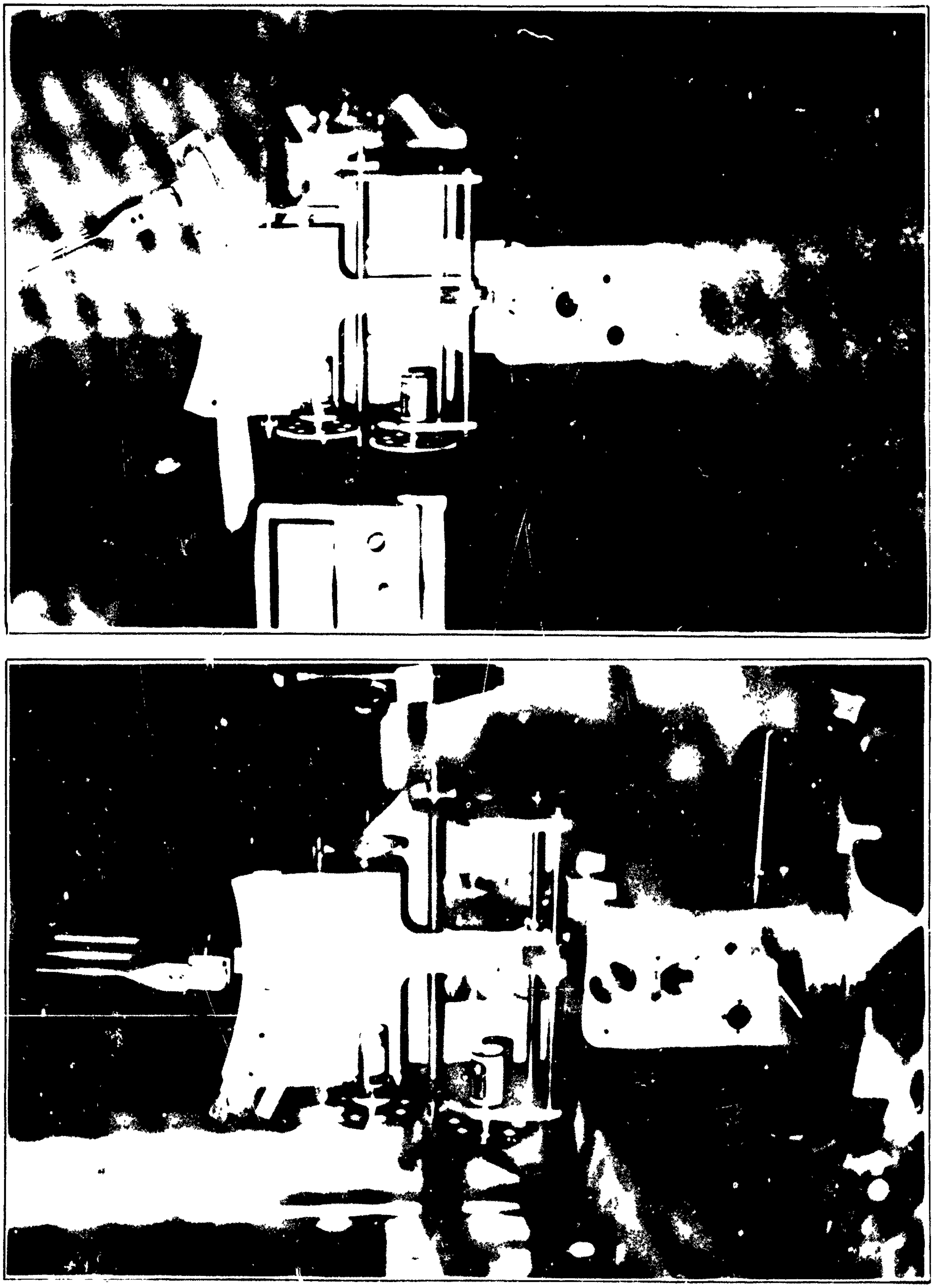

Figure 5-6. Flow Field Survey Mechanism

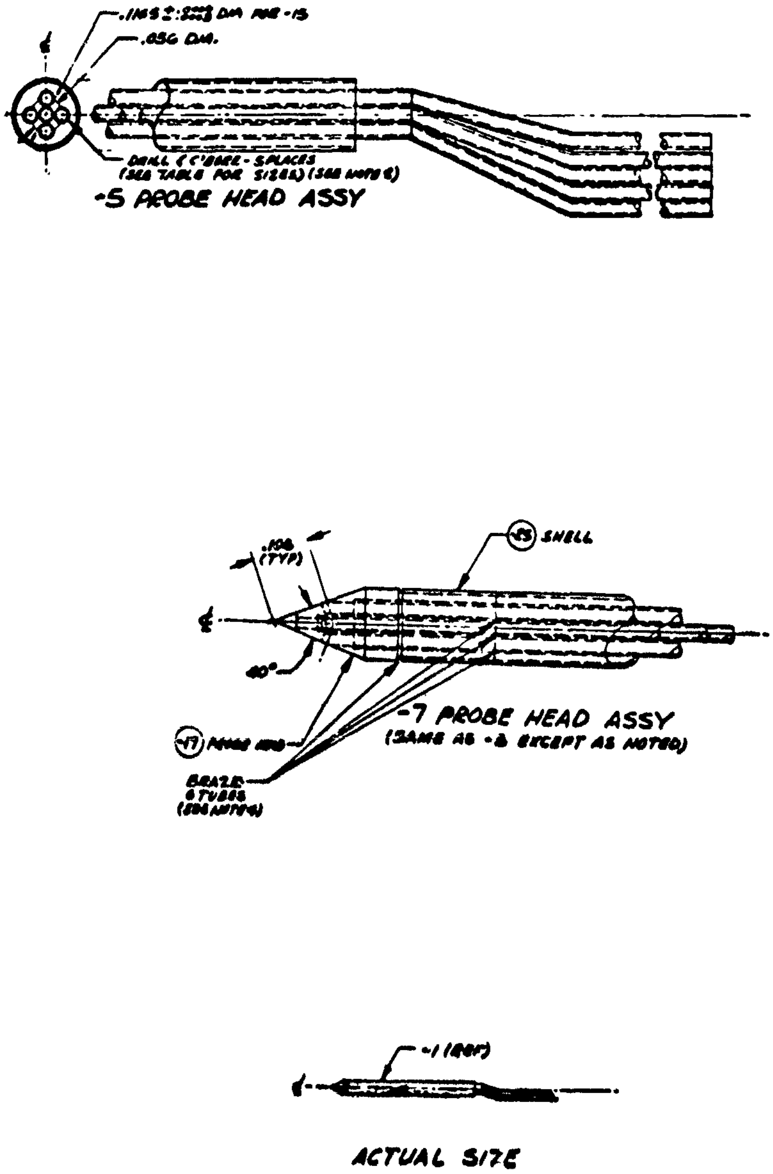
.165 DIA FOR -15
.056 DIA.
DRILL & C'BORE - 5 PLACES
(SEE TABLE FOR SIZES) (SEE NOTE 8)
-5 PROBE HEAD ASSY
.108
(TYP)
SHELL
40°
-7 PROBE HEAD ASSY
(SAME AS -5 EXCEPT AS NOTED)
-17
BRAZE
6 TUBES
-1 (REF)
ACTUAL SIZE

Figure 5-7. Cone Probe Details

5.1.2 Inlet Duct Total Head Rake

During the inlet testing, (Formats II, III, and IV), a total head rake was installed in the inlet duct at the hypothesized engine face station. The rake contained 20 total head probes mounted on 5 radial struts. The probes were located to insure an area weighted recording of the duct stagnation pressure. One of the stagnation probes was connected to a high response transducer with the remaining 19 probes used to record the steady state stagnation pressures. Five static pressure taps were installed in the duct wall, at the rake station, to record the duct local static pressure.

The pressures obtained from the probe designated for high frequency recording (tube #183) was connected through a high frequency transducer (CEC-312) to a tape recorder where the values were printed out in a continuous trace for each run. Unfortunately, trouble was experienced with the transducer during the test program and the data obtained was of no value.

5.1.3 Mass Flow Meter

Throttling of the inlet mass flow ratio was accomplished with a translating conical plug installed immediately downstream of the subsonic diffuser exit. Translation of the plug varied the exit area of the duct. Two static pressure taps were installed at the diffuser exit to monitor plug operation.

The primary function of the mass flow plug was to vary inlet mass flow from supercritical down through subcritical operation.

In the 8' x 7' tunnel sufficient on line data was available to permit the monitoring of the inlet pressure recovery characteristics being generated. In addition, a pressure differential transducer was installed between 2 of the static pressure taps located in the subsonic diffuser and the variation of static pressure was monitored visually. The variation in pressure differential, as a function of mass flow plug position, provided an indication of terminal shock location.

On line data was not available in the 6' x 6' tunnel and as a result only visual monitoring was possible. The differential pressure transducer was employed to estimate the terminal shock location. In addition, the inlet shock structure was observed on the Schlieren screen as a function of mass flow plug position, and appropriate plug settings were selected. To illustrate this technique Figure 5-8 presents a series of Schlieren photographs taken during a run at Mach 2.2, at an angle of attack of 0°, with the 2-dimensional inlet located at 30% ACL. The inlet is hidden in the shadow of the fuselage. However, the inlet cowl shock is visible beneath the fuselage bottom BCL. This typical run was monitored in the following manner.

a) The mass flow plug is retracted, the cowl shock wave appears clean indicating supercritical operation.

b) The plug has been moved toward closure until the visually observed duct static pressure differential indicates that the terminal shock is approaching the inlet throat. The inlet cowl shock is still very clean indicating supercritical operation.

c) The plug has been moved until the observed shock suddenly thickens, indicating that the terminal shock moved from inside the duct to a position immediately forward of the cowl leading edge. For an external compression system this represents operation close to the critical point.

d) The plug has been throttled until the observed shock structure becomes wide spread, indicating increased spillage in the region of the cowl leading edge and subcritical operation.

e) The plug has been throttled further to obtain a lower mass flow operating point. The shock structure has remained steady throughout the entire run.

5.1.4 Inlet Throat Bleed System

During inlet testing a small percentage of the ingested inlet mass flow was bled from the inlet in the region of the throat. This bleed flow was discharged overboard through a cavity in the inlet wall. Two static taps (#191 and #192) were installed in the wall at the exit plane. The average static pressure plus the cavity area was used to estimate the bleed flow rate. The bleed systems for both the two-dimensional and axisymmetric inlets were designed to bleed 8% of the theoretical inlet mass flow at the Mach 2.2 test condition. The two-dimensional inlet was

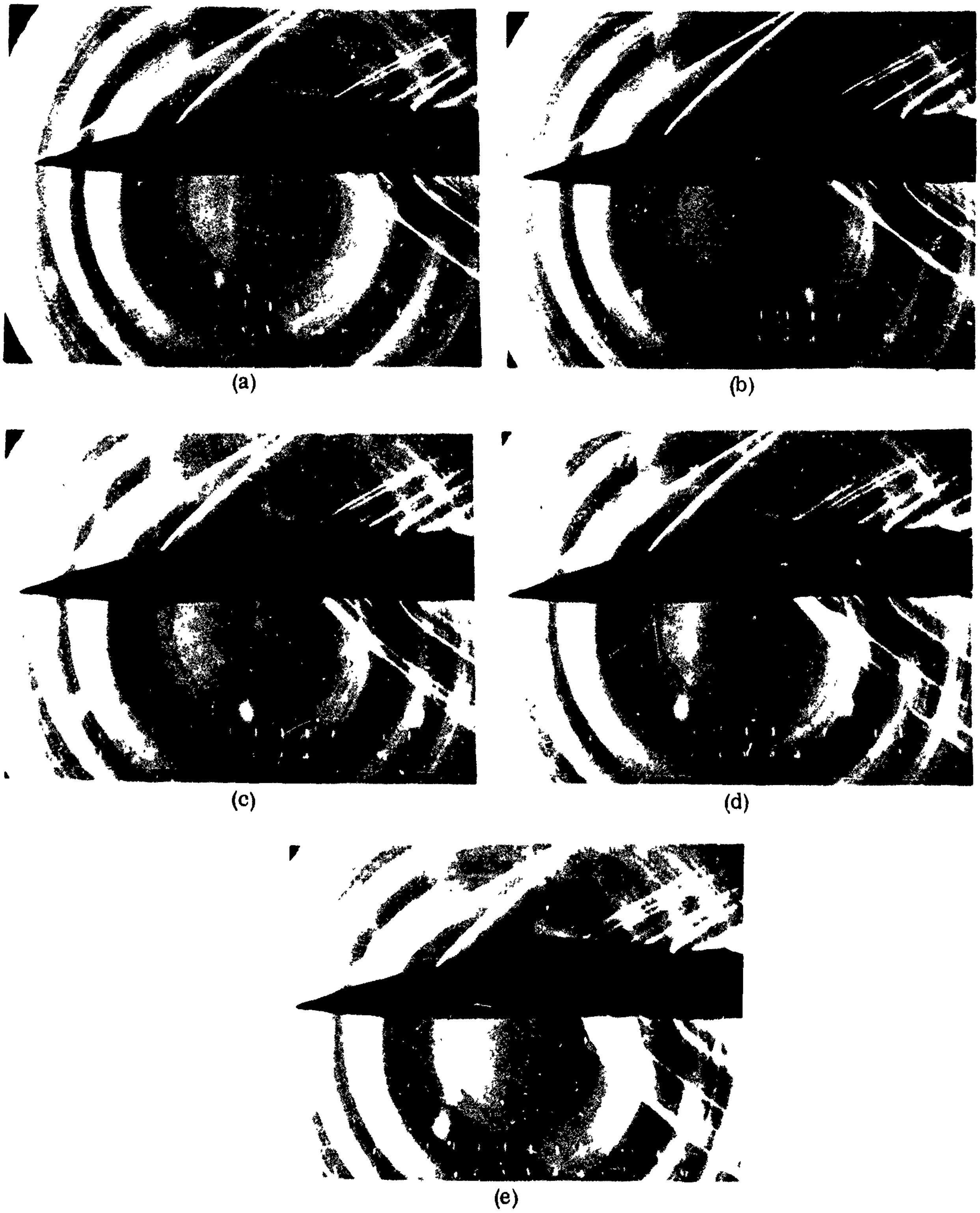

(a) (b) (c) (d) (e)

Figure 5-8. Schlieren Monitoring Technique

designed to bleed the flow through a flush slot located at the throat. The axisymmetric inlet bled the flow through a series of small diameter holes located immediately upstream of the throat.

5.1.5 Instrumentation

The model pressure instrumentation arrangement was designed to satisfy three constraints, namely, sufficient density for adequate documentation, compatibility with the recording capability of the test facility, and locations permitting direct comparison with theoretical estimates.

The fuselage static pressure taps were located along 5 longitudinal rays. The stations selected for the location of individual taps permitted both longitudinal and transverse pressure distributions to be recorded. Several static taps were also installed in the undersurface of both wings in the region of the inlet. The inlets were also fitted with static pressure instrumentation along the subsonic diffuser wall, at the total head rake station, at the mass flow plug, and at the throat bleed system exit.

The total pressure probes were installed in the inlet duct total head rake and in each of the conical probes in the flow field survey rake.

The pressure instrumentation arrangement is shown schematically in Figures 5-9 through 5-11.

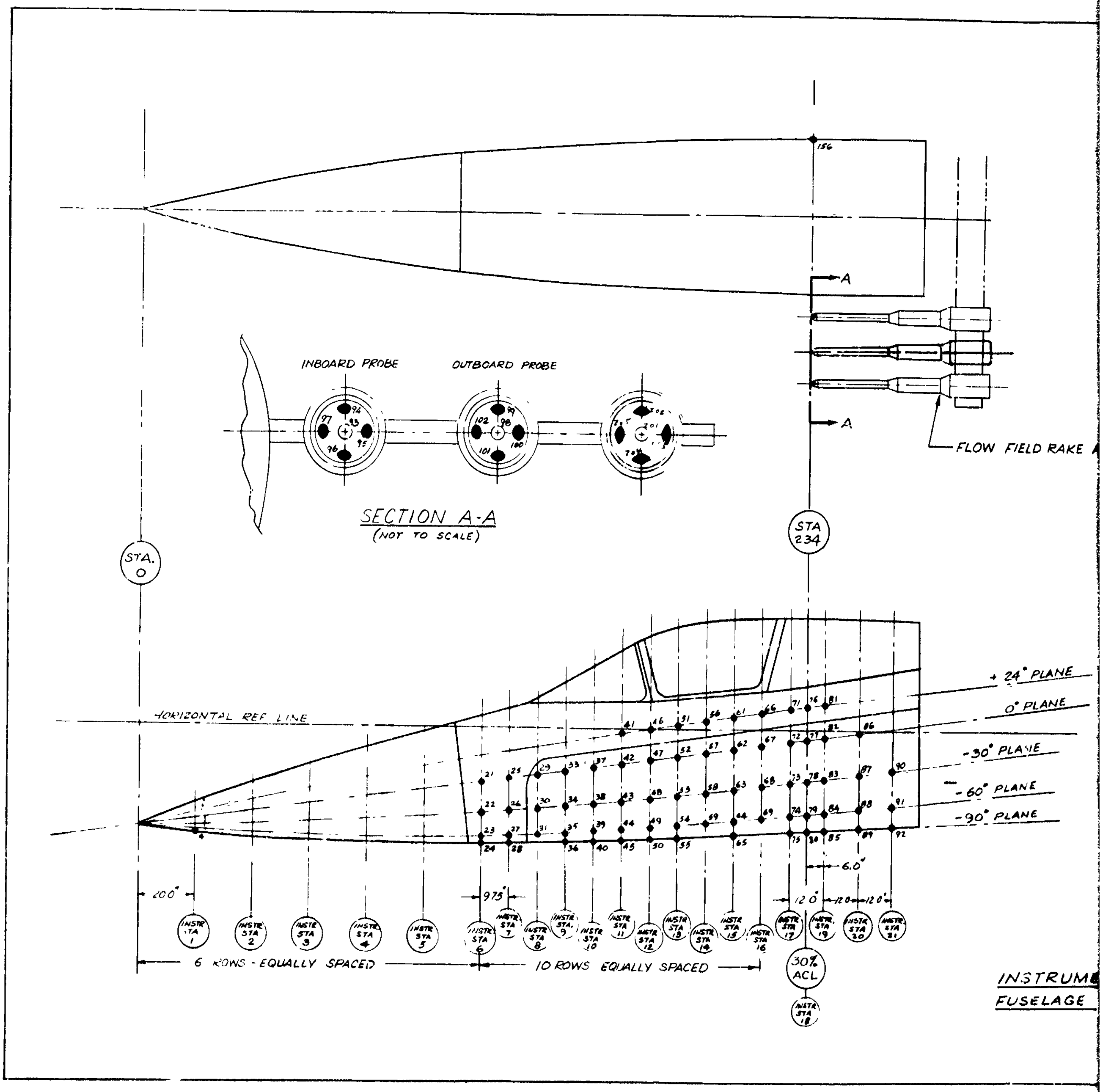
156
A
A
FLOW FIELD RAKE
INBOARD PROBE
OUTBOARD PROBE
SECTION A-A
(NOT TO SCALE)
STA. 0
STA 234
HORIZONTAL REF LINE
+ 24° PLANE
0° PLANE
-30° PLANE
-60° PLANE
-90° PLANE
2.00"
.975"
6.0"
12.0"
12.0
12.0"
INSTR STA 1
INSTR STA 2
INSTR STA 3
INSTR STA 4
INSTR STA 5
INSTR STA 6
INSTR STA 7
INSTR STA 8
INSTR STA 9
INSTR STA 10
INSTR STA 11
INSTR STA 12
INSTR STA 13
INSTR STA 14
INSTR STA 15
INSTR STA 16
INSTR STA 17
INSTR STA 18
INSTR STA 19
INSTR STA 20
INSTR STA 21
30% ACL
6 ROWS - EQUALLY SPACED
10 ROWS EQUALLY SPACED
INSTRUM
FUSELAGE

F
Fu

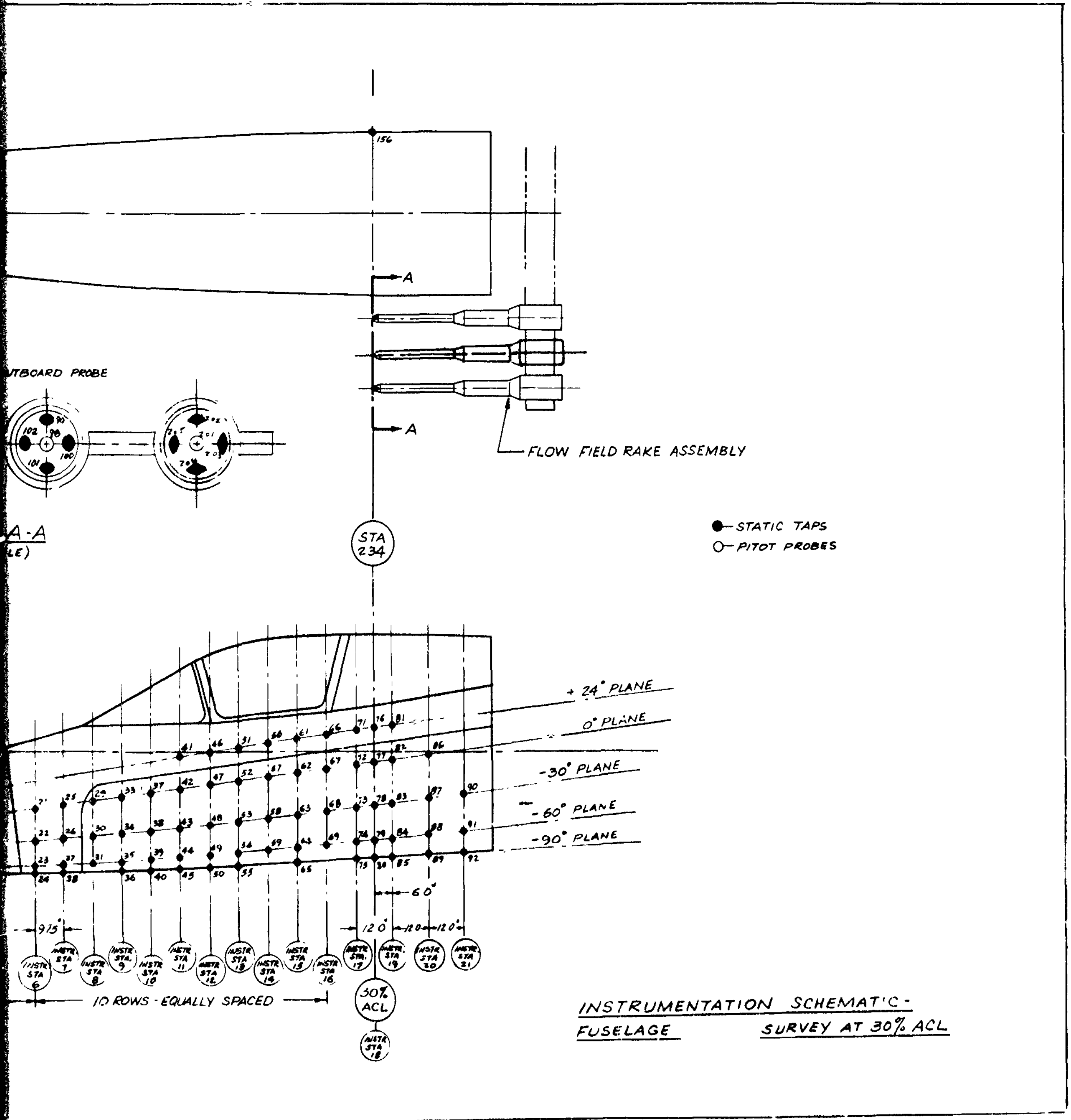
156
A
A
FLOW FIELD RAKE ASSEMBLY
TBOARD PROBE
A-A
LE)
STA 234
● STATIC TAPS
○ PITOT PROBES
+24° PLANE
0° PLANE
-30° PLANE
-60° PLANE
-90° PLANE
60°
12.0°
12.0°
12.0°
9.75°
10 ROWS - EQUALLY SPACED
30% ACL
INSTR STA 6
INSTR STA 7
INSTR STA 8
INSTR STA 9
INSTR STA 10
INSTR STA 11
INSTR STA 12
INSTR STA 13
INSTR STA 14
INSTR STA 15
INSTR STA 16
INSTR STA 17
INSTR STA 18
INSTR STA 19
INSTR STA 20
INSTR STA 21
INSTRUMENTATION SCHEMATIC - FUSELAGE SURVEY AT 30% ACL

Figure 5-9. Instrumentation Schematic - Fuselage Survey at 30% ACL

2

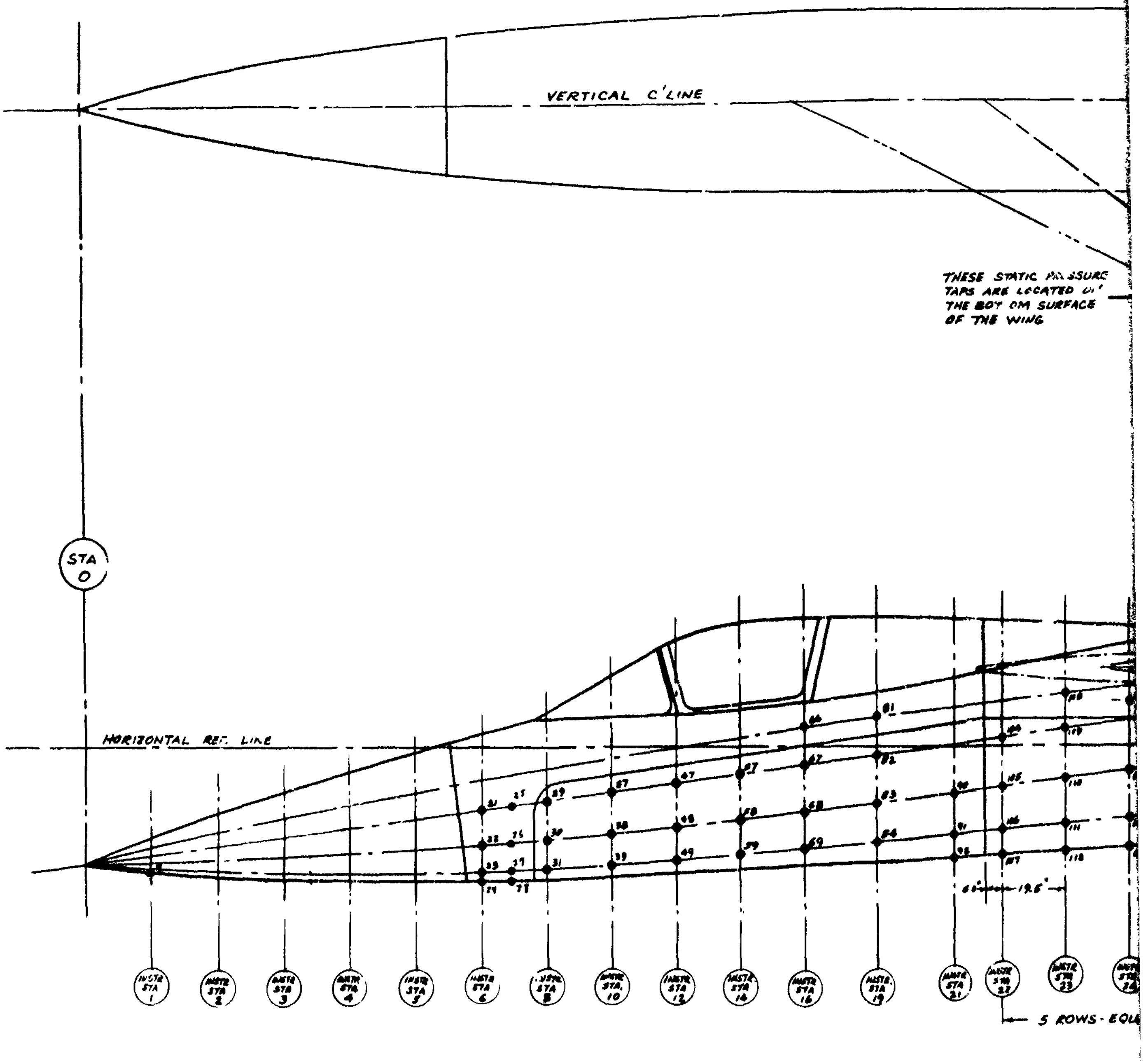
VERTICAL C'LINE
THESE STATIC PRESSURE TAPS ARE LOCATED ON THE BOTTOM SURFACE OF THE WING
STA 0
HORIZONTAL REF. LINE
INSTR STA 1
INSTR STA 2
INSTR STA 3
INSTR STA 4
INSTR STA 5
INSTR STA 6
INSTR STA 8
INSTR STA 10
INSTR STA 12
INSTR STA 14
INSTR STA 16
INSTR STA 19
INSTR STA 21
INSTR STA 22
INSTR STA 23
60°
19.5°
5 ROWS · EQU

1

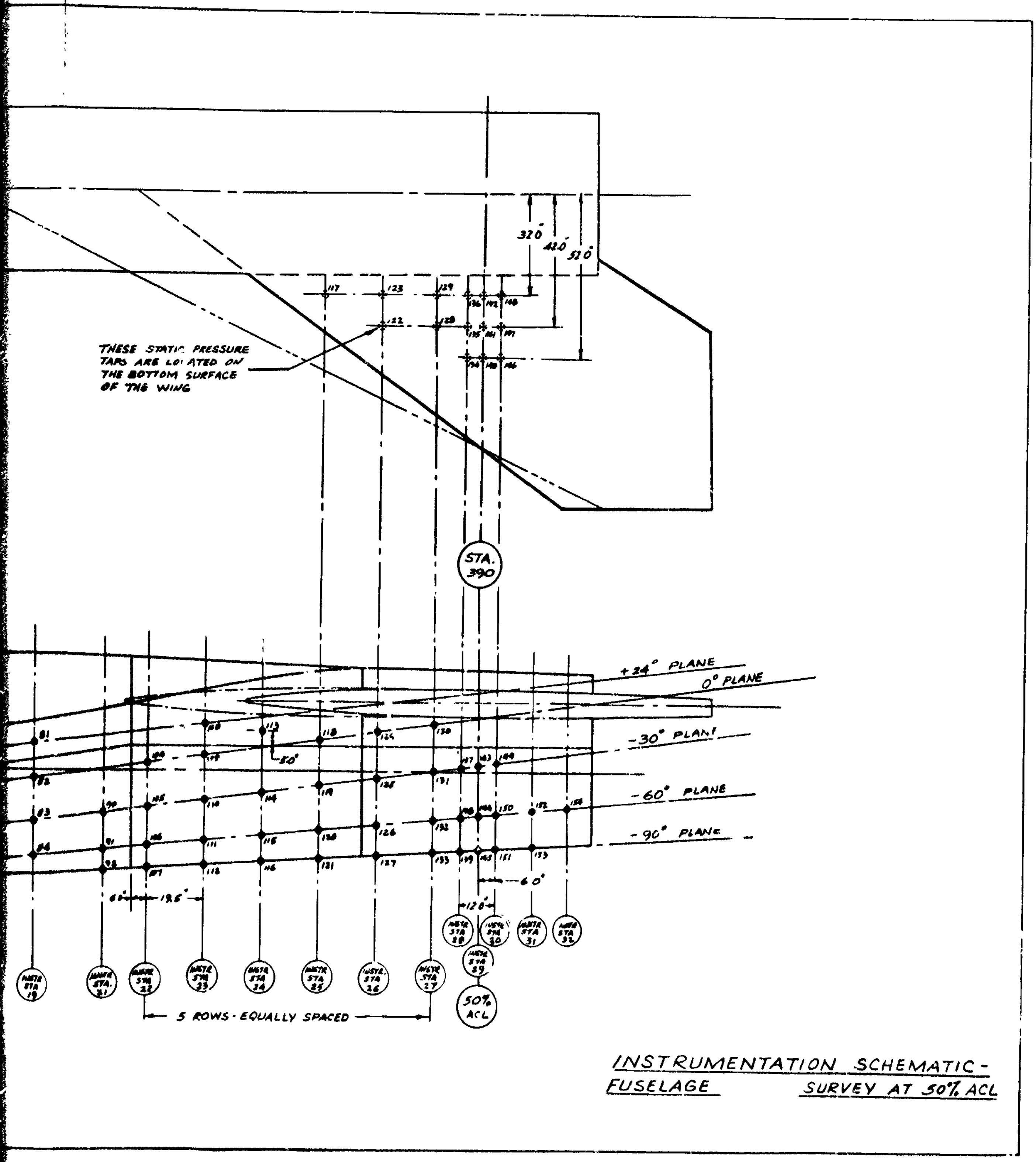
320"
420"
520"
117
123
129
136
142
148
122
128
135
141
147
134
140
146
THESE STATIC PRESSURE TAPS ARE LOCATED ON THE BOTTOM SURFACE OF THE WING
STA. 390
+24° PLANE
0° PLANE
-30° PLANE
-60° PLANE
-90° PLANE
81
82
83
84
89
90
91
92
85
86
87
108
109
110
111
112
113
114
115
116
118
119
120
121
124
125
126
127
130
131
132
133
137
143
149
138
144
150
139
145
151
152
153
154
50°
6.0"
19.6"
12.0"
6.0"
INSTR STA 19
INSTR STA. 21
INSTR STA 22
INSTR STA 23
INSTR STA 24
INSTR STA 25
INSTR. STA 26
INSTR STA 27
INSTR STA 28
INSTR STA 29
INSTR STA 30
INSTR STA 31
INSTR STA 32
50% ACL
5 ROWS - EQUALLY SPACED
INSTRUMENTATION SCHEMATIC - FUSELAGE SURVEY AT 50% ACL

Figure 5-10. Instrumentation Schematic Fuselage Survey at 50% ACL

2

ENGINE FACE RAKE

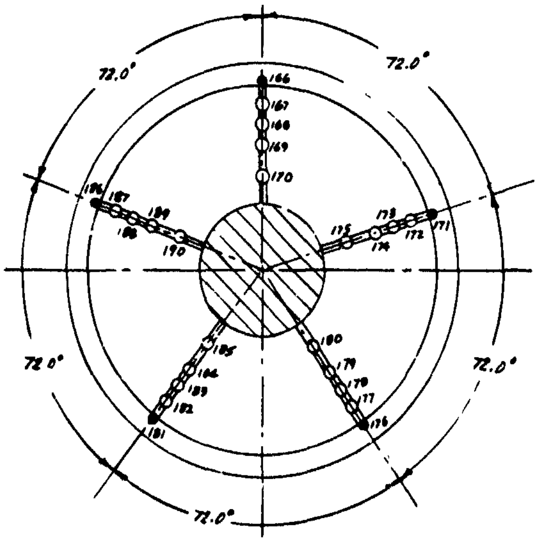
72.0°
72.0°
72.0°
72.0°
72.0°
166
167
168
169
170
186
187
188
189
190
175
173
174
172
171
185
184
183
182
181
180
179
178
177
176

SECTION A-A
(NOT TO SCALE)

- NOTE -
PITOT PROBE NO. 183
IS CONNECTED TO HIGH
RESPONSE TRANSDUCER

● STATIC TAPS
○ PITOT PROBES

MASS FLOW METERING
STATION

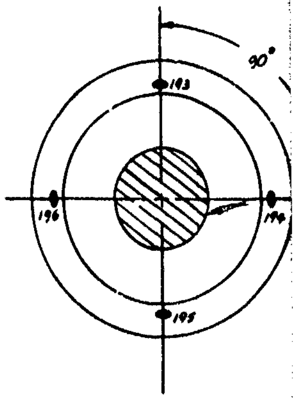
90°
193
196
194
195

SECTION B-B
(NOT TO SCALE)

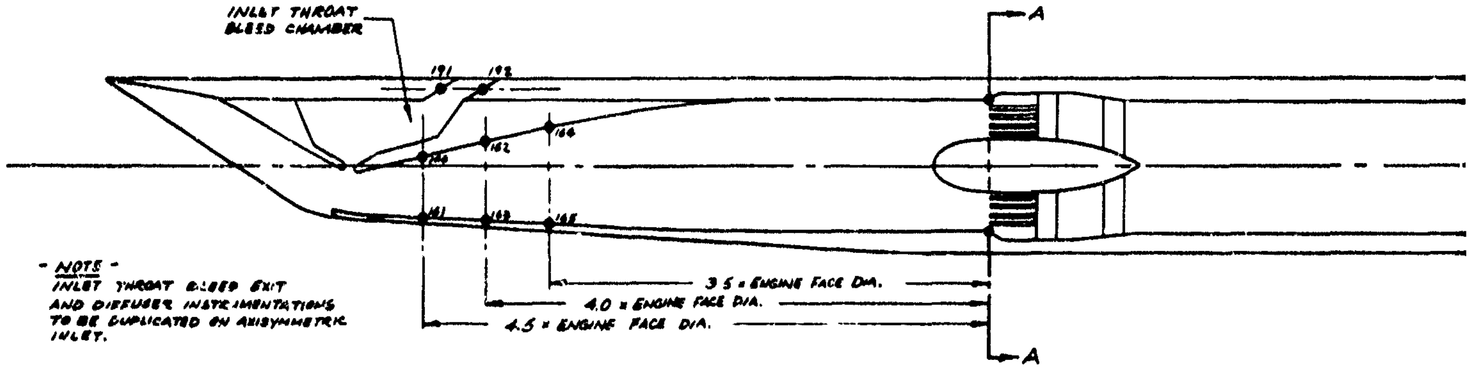
INLET THROAT
BLEED CHAMBER
191
192
160
162
164
161
163
165
3.5 × ENGINE FACE DIA.
4.0 × ENGINE FACE DIA.
4.5 × ENGINE FACE DIA.
A
A

- NOTE -
INLET THROAT BLEED EXIT
AND DIFFUSER INSTRUMENTATIONS
TO BE DUPLICATED ON AXISYMMETRIC
INLET.

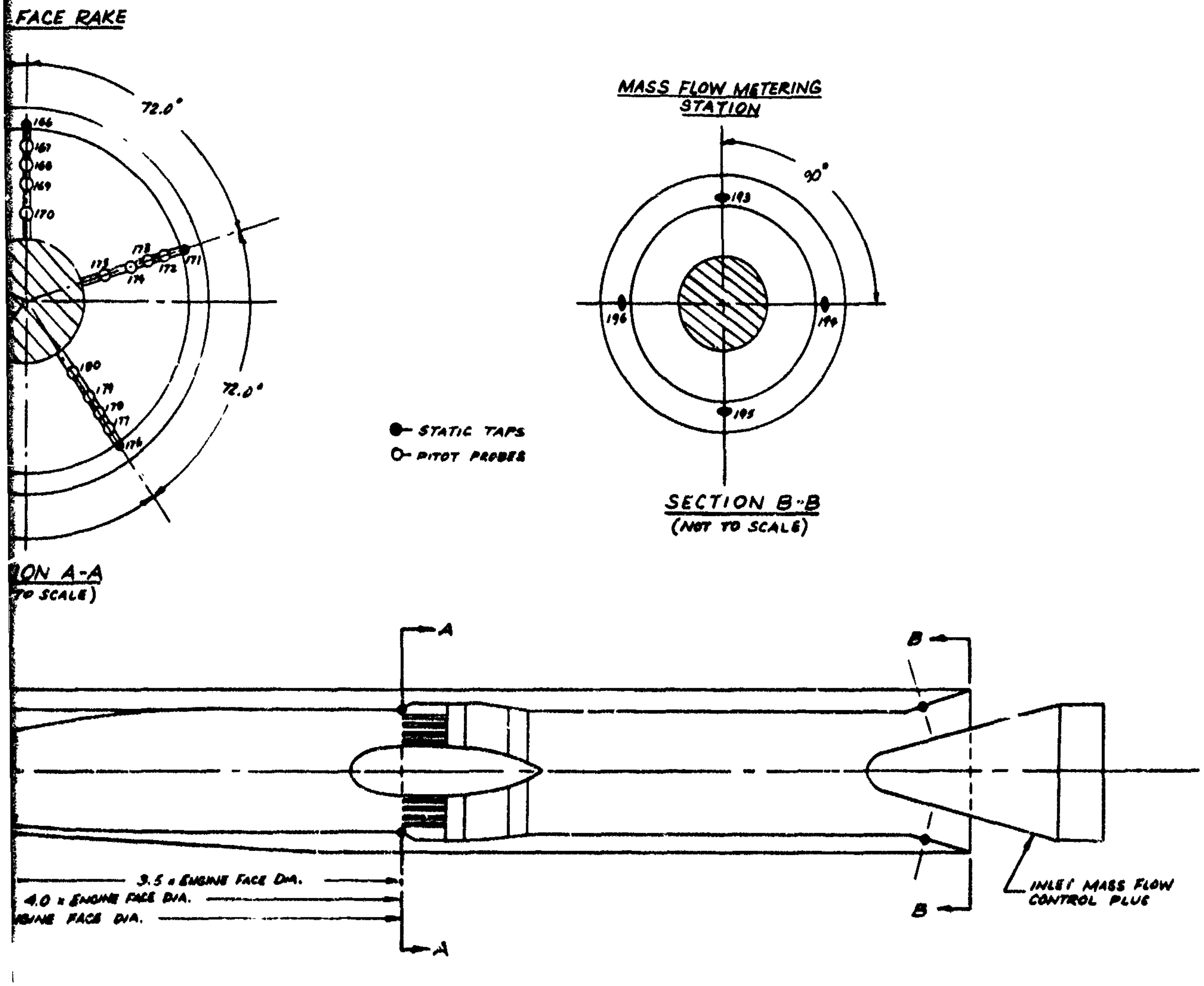
FACE RAKE
72.0°
166
167
168
169
170
175
173
174
172
171
180
179
178
177
176
72.0°
ON A-A
TO SCALE)
● STATIC TAPS
○ PITOT PROBES
MASS FLOW METERING STATION
90°
193
196
194
195
SECTION B-B
(NOT TO SCALE)
A
A
B
B
3.5 × ENGINE FACE DIA.
4.0 × ENGINE FACE DIA.
NGINE FACE DIA.
INLET MASS FLOW CONTROL PLUG

Figure 5-11. Instrumentation Schematic - Inlet Alone

2

SECTION VI

EXPERIMENTAL PROGRAM

6.0 General

The experimental program was conducted between February 10 and April 29, 1969 in the NASA Ames 6' x 6' and 8' x 7' wind tunnels. The test Mach numbers were 0.8, 1.2, 1.6, and 2.2 in the 6' x 6' tunnel, and 2.5 in the 8' x 7' tunnel. At each Mach number an angle of attack range between -3.0° and +25.0° was investigated. The testing of all component geometry combinations was not possible. A geometry matrix was selected that would parametrically display the effect of geometry variation while remaining consistent with the specified tunnel occupancy time. The model configurations selected for testing at each Mach number are defined in Table I.

Test results were continuously monitored by inspection of on-line data print out while testing in the 8' x 7' tunnel, inspection of uncorrected data during tests in both the 6' x 6' and 8' x 7' tunnels, and by visual observation using the Schlieren system.

The test data were recorded on magnetic tape. These tapes were processed to permit automatic plotting of the pressure data and test parameters. The major presentation of the reduced data was in the form of plots showing the variation of flow properties for the different test conditions and configurations. Presented below is a summary of those plots made. Plots one to five are for the fuselage with no inlet, plots six and seven are for the fuselage and inlet combined and plots eight and nine are for the inlet alone.

Fixed Parameters	Quantities Plotted	Variation Parameter
1) M_∞, Configuration, Ray	P vs X	α, β
2) M_∞, Ray, α, β	P vs X	Configuration
3) M_∞, Configuration, α, β	Mach Number Map	
4) M_∞, Configuration, α, β	Local angle of attack map	
5) M_∞, Configuration, α, β	Sidewash angle map	
6) Inlet, M_∞	N_{Di} vs m/m_∞	α, β

Fixed Parameters	Quantities Plotted	Variation Parameter
7) Inlet, M_∞	(P_t/P_{t_∞}) vs m/m_∞	α, β
8) Inlet, M_∞	P_t/P_{t_∞} vs m/m_∞	α, β
9) Inlet, M_∞	N_{Di} vs m/m_∞	α, β

Several photographs were taken to illustrate the model installed in the tunnel. Figure 6-1 shows the model configured for Format IV, with the flow field probes located at 50% ACL. Figure 6-2 presents the model configured for Format III, with both inlets shown at 50% ACL.

INSTALLED MODEL (FORMAT IV)

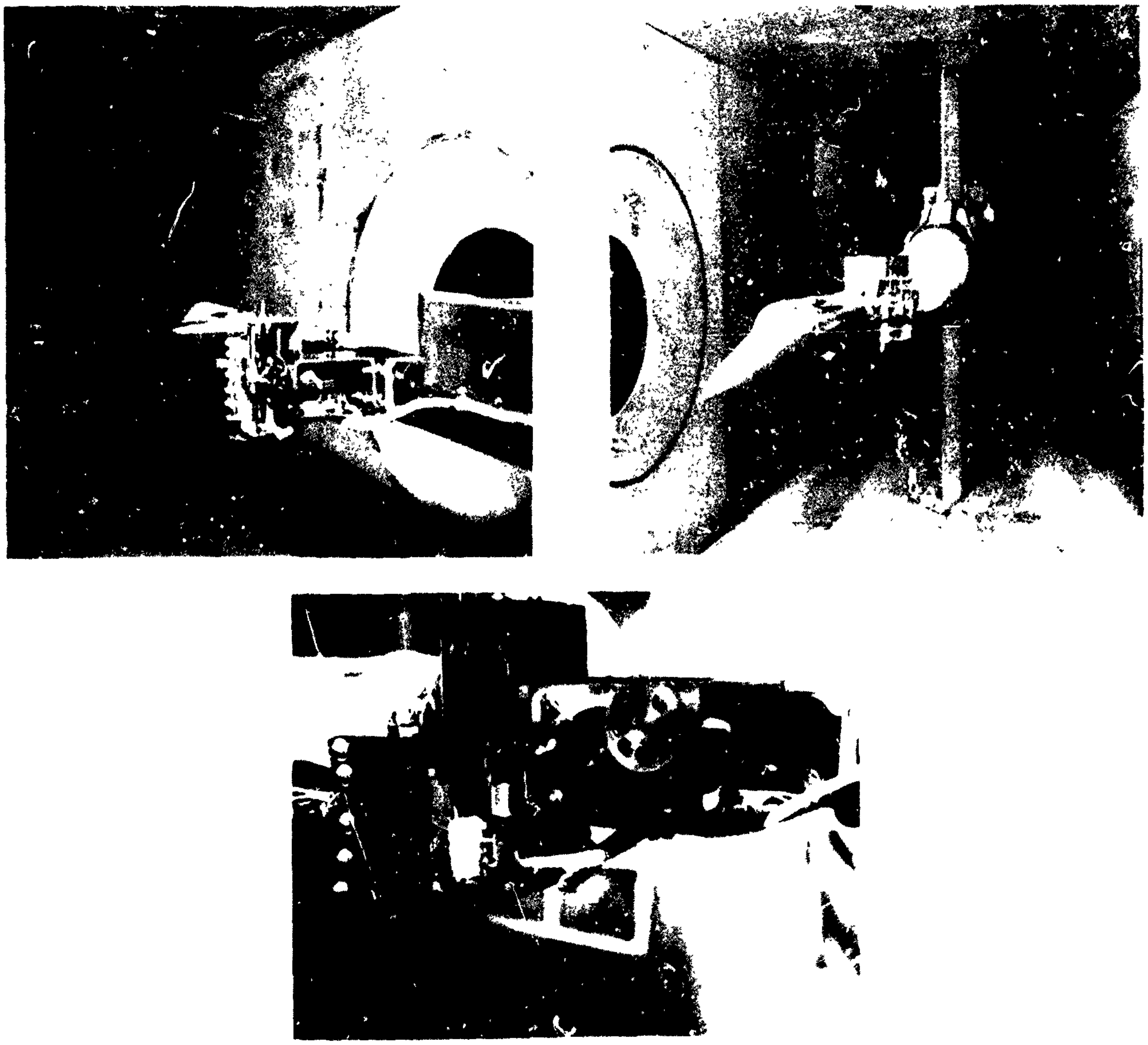

Figure 6-1

INSTALLED MODEL (FORMAT III)

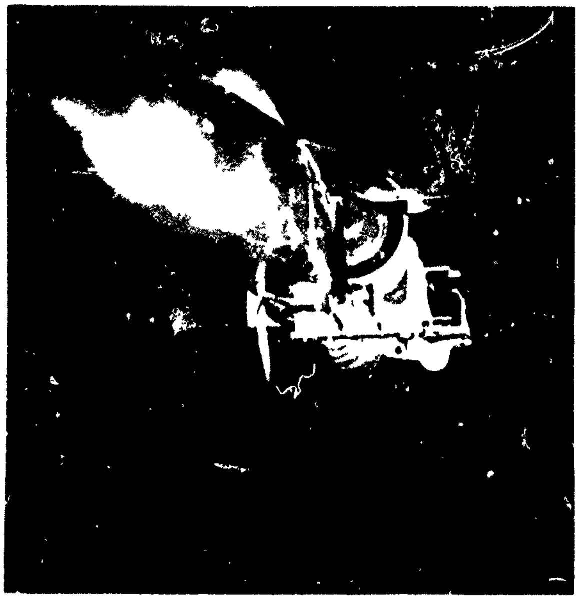

Figure 6-2

TABLE I.

WIND TUNNEL TEST SCHEDULE

Test Block	Fuse.	Inlet	Loca.	Alter	Instr.	Data Format
1	8	None	F	None	IVP	I
2	6	↓	↓	↓	↓	↓
3	5	↓	↓	↓	↓	↓
4	4	↓	↓	↓	↓	↓
5	3	↓	↓	None	↓	↓
6	3	↓	↓	N	↓	↓
7	3	↓	↓	NC	↓	↓
8	3	↓	↓	C	↓	↓
9	2	↓	↓	None	↓	↓
10	1	↓	↓	↓	↓	↓
11	1	2D	F	↓	PFSM	II
12	2	↓	↓	↓	↓	↓
13	3	↓	↓	None	↓	↓
14	3	↓	↓	N	↓	↓
15	3	↓	↓	NC	↓	↓
16	3	↓	↓	C	↓	↓
17	4	↓	↓	None	↓	↓
18	4	2D	W	↓	PESM	III
19	3	↓	↓	None	↓	↓
20	3	↓	↓	L	↓	↓
21	2	↓	↓	None	↓	↓
22	1	↓	↓	↓	↓	↓
23	1	A	↓	↓	↓	↓
24	2	↓	↓	↓	↓	↓
25	3	↓	↓	↓	↓	↓
26	4	↓	↓	↓	↓	↓
27	4	None	W	None	IVP	IV
28	8	↓	↓	↓	↓	↓
29	6	↓	↓	↓	↓	↓

NOTE: See page 95 for symbol definition, TABLE I (Continued)

WIND TUNNEL TEST SCHEDULE

Test Block	Fuse.	Inlet	Loca.	Alter	Instr.	Data Format
30	5	None	W	None	ivp	IV
31	3	↓	↓	None	↓	↓
32	3	↓	↓	L	↓	↓
33	2	↓	↓	None	↓	↓
34	1	↓	↓	↓	↓	↓
35	None	2D	↓	↓	ESM	V
36	↓	A	↓	↓	↓	↓

DEFINITION OF SYMBOLS FOR TABLE I

2D	Two-dimensional inlet
A	Axisymmetric inlet
F	Forward of wing
W	Aft of wing
N	Alternate nose
C	Alternate canopy
L	Alternate wing
IVP	Inviscid flow rake, viscous flow field rake, and fuselage static pressure taps
PESM	Fuselage static pressure taps, engine face rake, duct static pressure taps and mass flow plug
ESM	Engine face rake, duct static pressure taps and mass flow plug
α	Angle of attack
β	Angle of yaw
Data Format I	Flow field survey @ 30% ACL
Data Format II	Inlet installed @ 30% ACL
Data Format III	Inlet installed @ 50% ACL
Data Format IV	Flow field survey @ 50% ACL
Data Format V	Inlet alone

SECTION VII
DATA ANALYSIS

7.0 General

This section presents an analysis of the flow field and inlet performance data. In addition, these data are compared with the analytical predictions and the accuracy of the analyses are evaluated. Finally, methods for improving the accuracy of the analyses are discussed.

Chronologically, the influence of vehicle geometry upon the fuselage flow field characteristics is discussed first. This is followed by an analysis of the isolated inlet performance and the integrated inlet performance.

7.1 Fuselage Alone (Data Format I)

7.1.1 General

This section is concerned with an analysis of the data obtained at the forward fuselage station (30% ACL). Format I examined the impact of vehicle geometry upon the attendant flow field. These tests included the investigation of each of the seven (7) fuselage configurations. In addition, the effects induced by canopy and nose geometry were examined. For these tests a complete matrix of the four (4) possible combinations of primary and secondary nose and canopy was investigated in conjunction with fuselage configuration 3.

7.1.2 Nose and Canopy Effects

7.1.2.1 General Considerations

As an aid in understanding the causal relationships underlying the variations of the measured flow field properties with the geometric parameters, and with angle of attack, certain important differences in the nose and canopy geometries are worth noting.

First, the characteristics of the noses are summarized in the following table.

	Primary Nose (PN)	Secondary Nose (SN)
Fineness Ratio	2.83	1.69
Nose Droop	7.5°	7.5°
Shape	Ogival	Ogival
Semi-Vertex Angle	12.5°	16°
Initial Slope - Top Contour	19.5°	23°
Initial Slope - Bottom Contour	5.5°	9.0°

For both these noses the fuselage shape factor and aspect ratio are 2.13 and 1.12 respectively, where both these parameters are defined in Section III.

The characteristics of the canopies which were tested in combination with these noses are summarized below.

	Primary Canopy (PC)	Secondary Canopy (SC)
Fineness Ratio	9.0	16.3
Canopy/Fuselage Size Factor	.275	.298
Windshield Shape	Flat	Rounded
Station	10.5	6.67

Before examining the flow field properties which were measured at the 30% inlet station (in the absence of the inlet) for the different nose and canopy combinations described above, certain effects of these geometries on the flow can be expected. Thus, the effect of nose droop at low angles of attack should induce a local downwash along the side of the body. This is a consequence of the pressure differential between the top and bottom contours which results from the uneven flow deflections at the vertex of the nose. However, as may be seen in Figure 7-1, the 30% inlet station is situated in a region which is also influenced by the canopy. The windshield induces a high local pressure and an abrupt change in flow angularity and Mach number. This is followed by a rapid expansion around the side of the canopy, that again introduces large changes in pressure, flow angularity, and Mach number. Consequently, the flow undergoes two significant changes in a short span and the resultant influence upon the attendant flow field can be important.

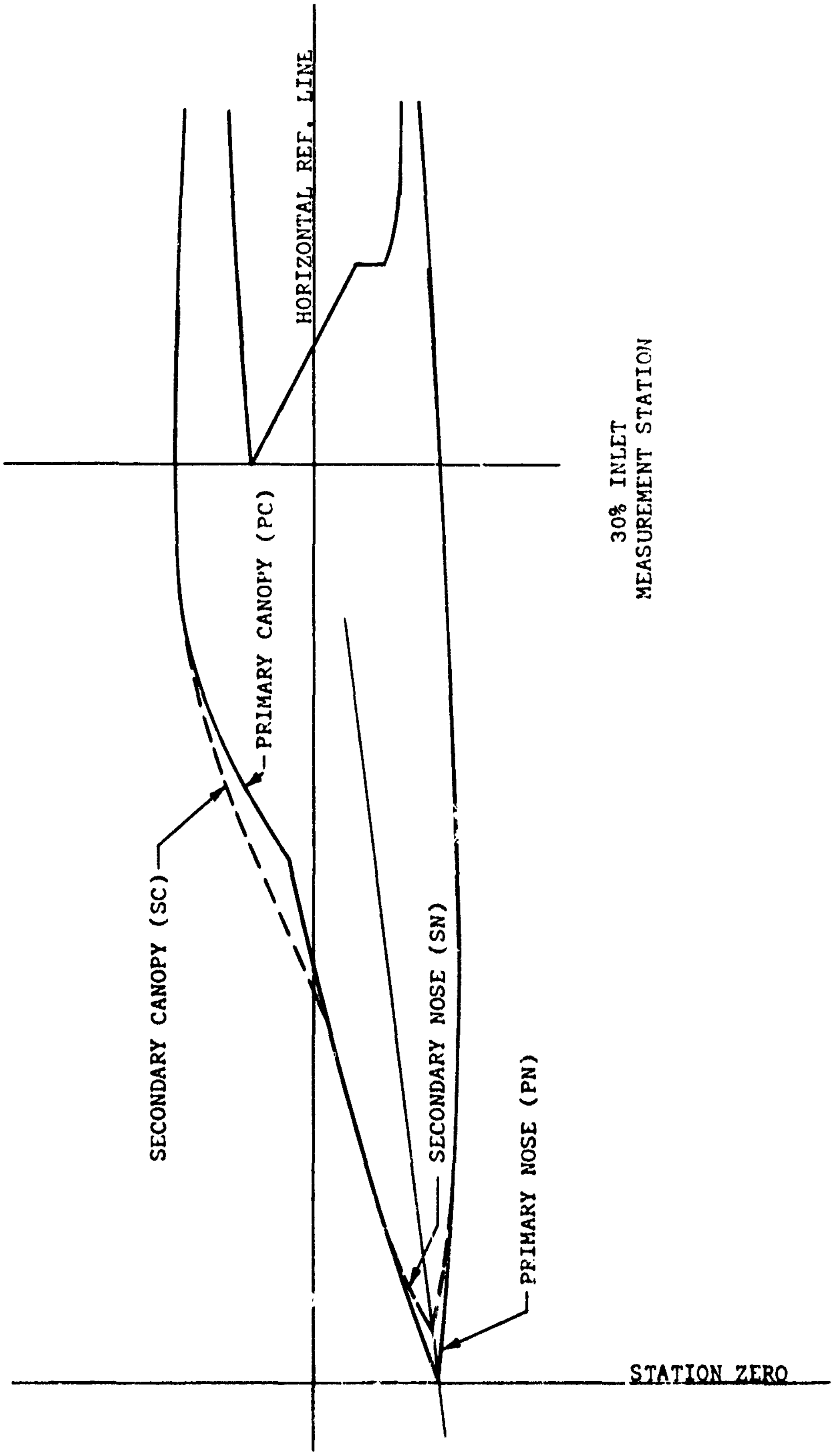
HORIZONTAL REF. LINE
30% INLET MEASUREMENT STATION
PRIMARY CANOPY (PC)
SECONDARY CANOPY (SC)
SECONDARY NOSE (SN)
PRIMARY NOSE (PN)
STATION ZERO

Figure 7-1. Profiles of Nose and Canopy Shapes

It can be anticipated that angle of attack and body geometry will produce effects that are qualitatively similar for all the Mach numbers tested. Therefore, many of the conclusions drawn will be applicable to the data for all Mach numbers.

7.1.2.2 Flow Field Effects

The following discussion presents an interpretation of the flow field data obtained during the test program. It offers a generalized description of the flow field composition and attempts to establish the presence of geometry dependent causal relationships.

Two definitions are appropriate to an understanding of the following discussion, dealing with the identification of local flow angularity. The term upwash denotes a local pitch angle (angle of attack) which exceeds the free-stream angle of attack, whereas downwash denotes the opposite. Sidewash is taken to be positive for the flow directed in towards the fuselage, and negative away from the fuselage.

For a free stream Mach number of 2.5, flow field data was obtained for the four (4) nose/canopy configuration combinations. At negative angle of attack a general downwash condition exists, prompted by the negative attitude of the vehicle and the drooped nose. This condition is reinforced by a canopy induced positive pressure field. The flow field composition remains basically unchanged for all combinations of nose and canopy geometry. This effect can be seen in Figures 7-2 through 7-5 displaying local flow angularity for an angle of attack of -3°. This general condition also exists at zero angle of attack except that the canopy effect has increased while the influence of the vehicle attitude and nose droop has diminished. The basic composition of the flow field remains unchanged at both of these angles of attack as component geometry is varied; however, the interaction between individual components is quite evident from the extent of the various flow regions. For example, the result of employing the fuselage #3 corner radius is basically the same at both angles of attack, and for all component combinations. The effect is seen as a local flow region roughly occupying the lower inboard portion of the survey plane within which the prevailing downwash condition is most negative. This high negative angularity is induced by 1) the favorable and abrupt pressure gradient set up by the small fuselage corner radius and 2) the general flow inclination. While always present, the extent of this region is seen to vary as a function of nose and canopy geometry. Using the primary nose/canopy configuration as a base

Fuselage 3
PCPN
Mach Number = 2.5
$\alpha = -3°$
Format I

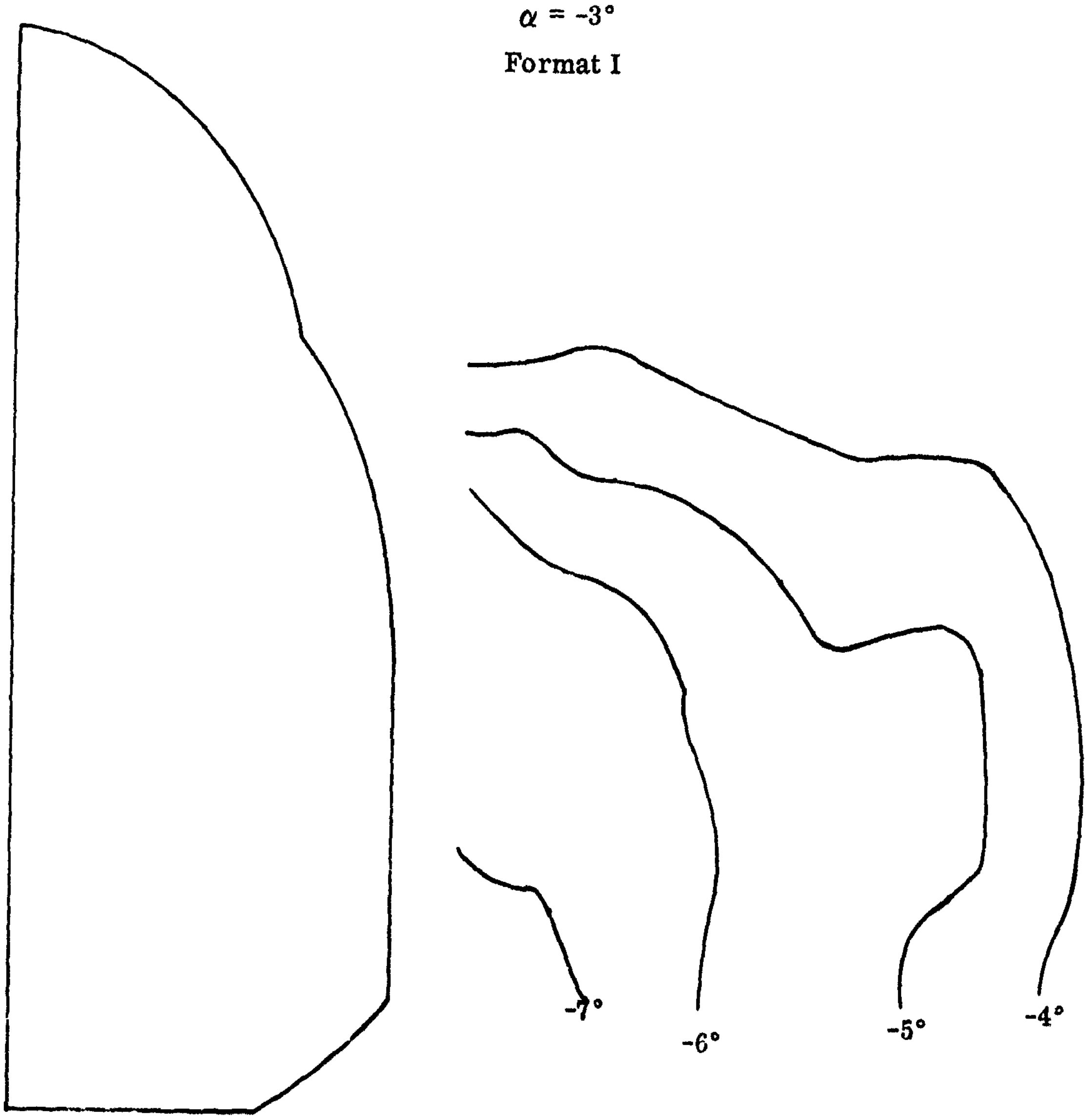

Figure 7-2. Local Flow Angularity

Fuselage 3
PCSN
Mach Number = 2.5
$\alpha = -3°$
Format I

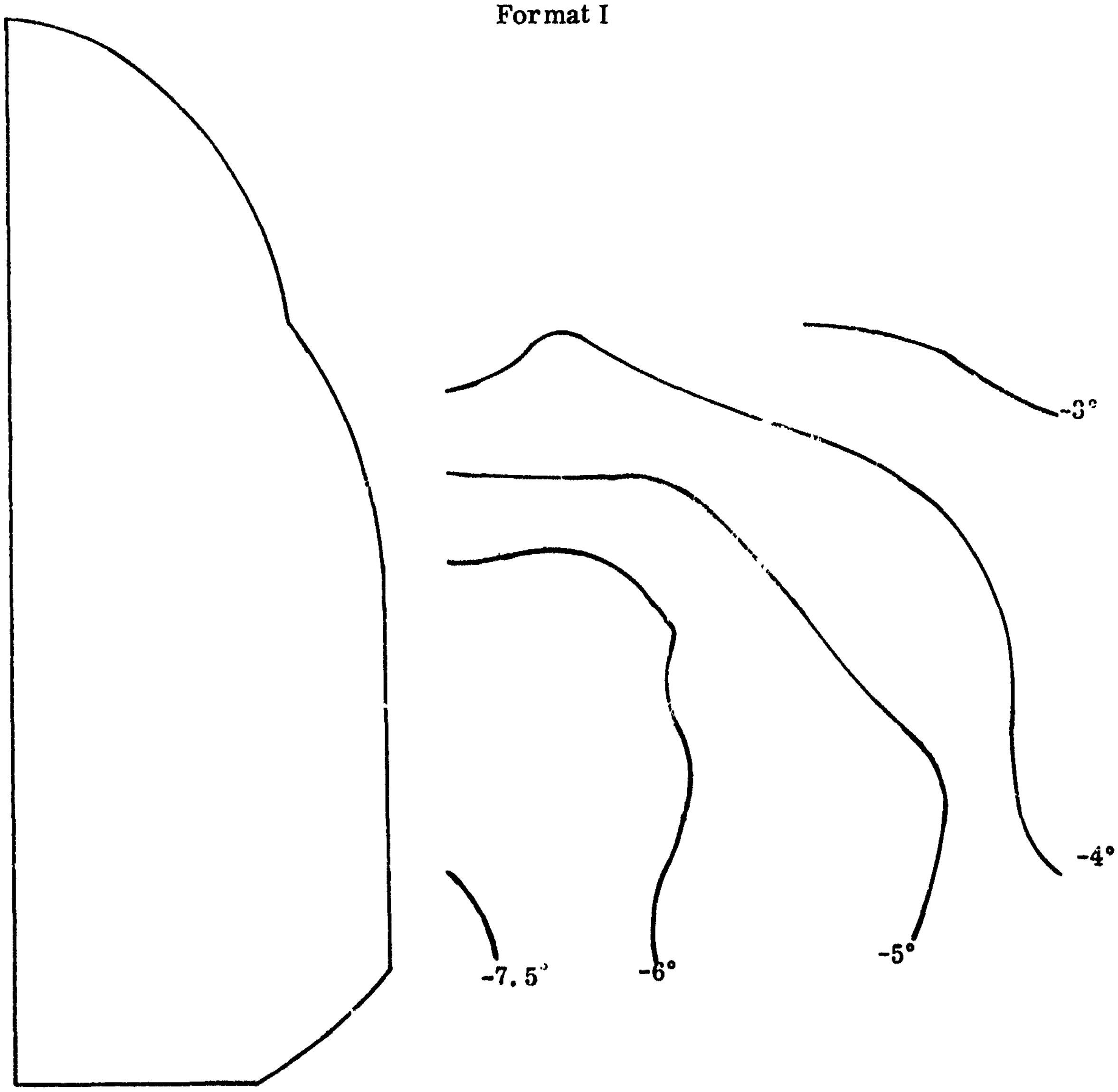

Figure 7-3. Local Flow Angularity

Fuselage 3
SCPN
Mach Number = 2.5
$\alpha = -3°$
Format I

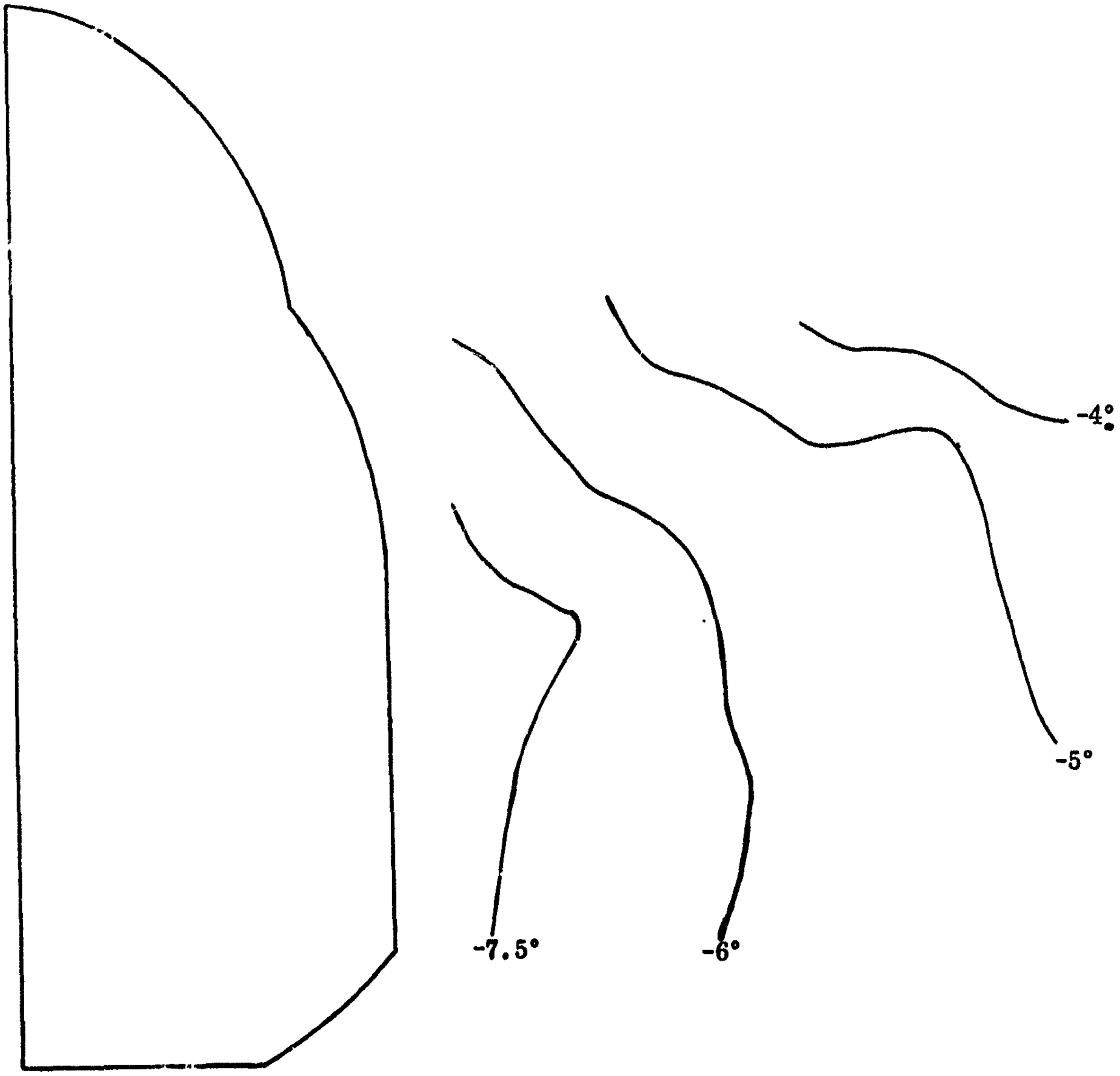

Figure 7-4. Local Flow Angularity

Fuselage 3
SCSN
Mach Number = 2.5
α =-3°
Format I

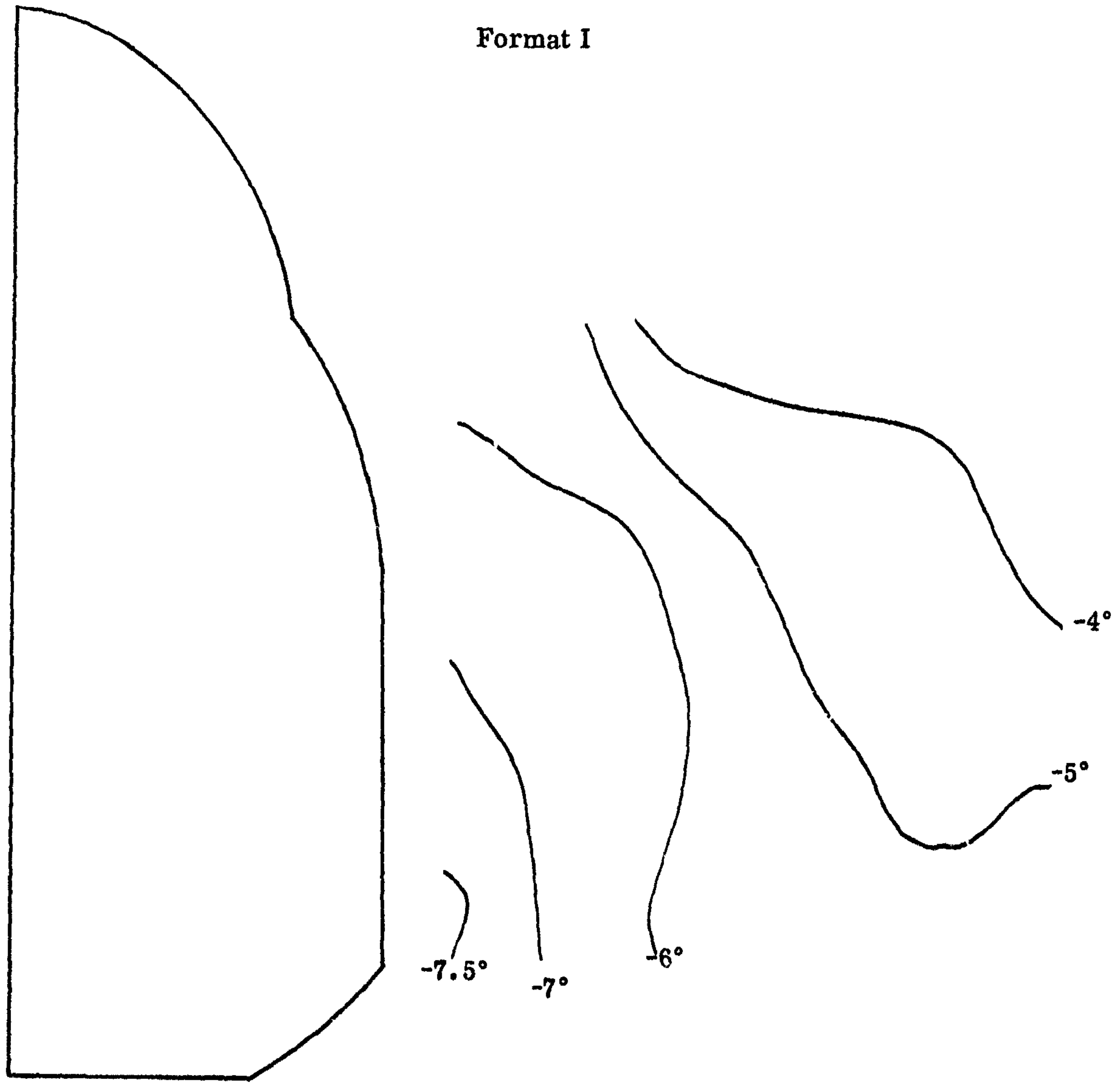

Figure 7-5. Local Flow Angularity

point, the negative angle of attack case (approximately, -3.0 degrees) shows that substituting the secondary nose increases the extent of this high downwash region because the blunter secondary nose has a higher top to bottom surface pressure gradient than the primary nose. The extent of the region increases further as the secondary canopy replaces the primary canopy. This is due to the larger canopy frontal area and stronger shock wave that increases the overpressure, particularly for the inboard portion of the flow field. For the primary nose/secondary canopy combination the high inclination region decreases again due to the weaker peripheral gradient of the more slender primary nose. This region of high flow angularity is also present for zero angle of attack with the extent and shape being determined by the nose and canopy geometry. This similarity in flow field composition can be seen by comparing Figures 7-5 and 7-6, presenting the local flow angularity for the secondary nose/secondary canopy configuration at -3.0°and 0.0° angle of attack respectively. This comparison indicates that average level of flow angularity at 0.0° has increased directly with angle of attack but the most negative flow region still occupies the lower inboard region and the shape of the constant value lines is the same. This effect is also true for the other nose/canopy configurations.

Also present for all geometry combinations and test conditions is a "nominal" flow region, within which the local flow angularity approximates the numerical average of the entire flow field. The portion of the survey plane occupied by this average flow is primarily determined by the prevalent flow direction. For example, when a downwash condition exists, the region originates at the upper inboard section of the survey plane and moves downward toward the lower outboard corner. This zone is seen in Figures 7-1 through 7-5, for the negative angle of attack case, where the -5.0° contour line approximates the numerical average of the flow field. On the other hand, with upwash the average flow originates at the lower inboard section and moves upward toward the outboard section of the survey plane. This effect will be seen in the subsequent inspection of higher angle of attack flow fields.

Finally, a local zone of downwash is generally present, established by the pressure discontinuity across the canopy shock wave as it passes through or near the survey plane. This region is generally situated in the outboard portion of the surveyed flow field. The location of this zone is primarily a function of angle of attack while the extent of the zone appears to be more geometry dependent. For example, at negative and

Fuselage 3
SCSN
Mach Number = 2.5
α = 0°
Format I

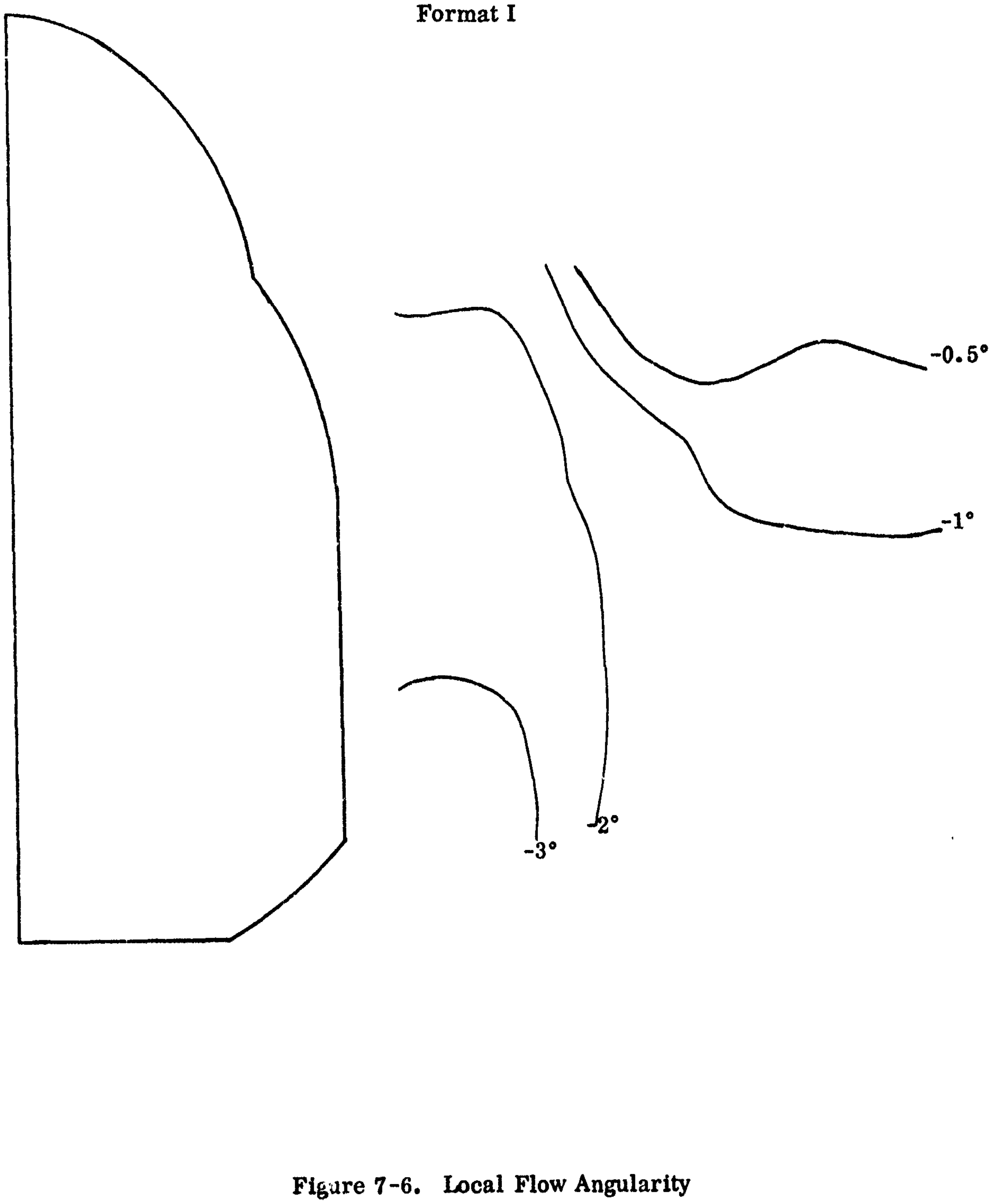

Figure 7-6. Local Flow Angularity

zero angle of attack the fuselage nose is presented to the approaching free stream flow such that the compression along the top surface is maximized producing a low local Mach number approaching the canopy. This results in a relatively weak, rapidly decaying detached canopy shock wave. As a result the downwash region appears in the upper outboard sector of the flow field. The extent is rather small, due to the weak shock, but differences are evident particularly as the nose is changed. The more slender primary nose diffuses the flow less than the secondary nose, a stronger canopy shock results producing a larger downwash zone. The effect of a canopy change, at these conditions, is seen in the distribution of this local region, due to both windshield shape and frontal area. The primary canopy has a flat windshield that delays the onset of canopy shock decay, therefore, as it passes through the survey region the relatively high pressure produces a deep penetration. The large radial gradient toward the body, caused by the rapid expansion around the windshield corner however, keeps the zone confined to the outboard portion of the flow field. On the other hand the secondary canopy shock wave, induced by a rounded windshield, has an early but gentle onset of decay. The result is a weakened shock at the survey plane and a reduced vertical penetration. However, the radial pressure gradient, toward the body, is also more gentle due to the shock curvature and the larger secondary canopy frontal area. Consequently, the zone has a greater lateral extent near the top of the survey region where this lower but more uniform overpressure exists.

With vehicle angle of attack increased to +5 degrees the flow field becomes quite uniform because the nose generates an almost symmetrical flow field, which in turn dampens any effect induced by the fuselage corner. Although small, the canopy influence is most dominant at this condition, as evidenced by the presence of a downwash region both inboard and, in the case of the larger secondary canopy, outboard in the lower region of the flow field. The relative uniformity of the flow field is illustrated in Figure 7-7, showing the primary canopy/secondary nose configuration. Also displayed in this figure is the inboard downwash region established by the canopy induced overpressure. A reorientation of the "nominal" flow region can also be seen, with this zone now occupying a corridor between the lower inboard and upper outboard regions of the flow field. The increased overpressure induced by a substitution of the larger secondary canopy is pictured in Figure 7-8 where the previously mentioned outboard downwash zone can be seen.

Fuselage 3

PCSN

Mach Number = 2.5

α = 5°

Format I

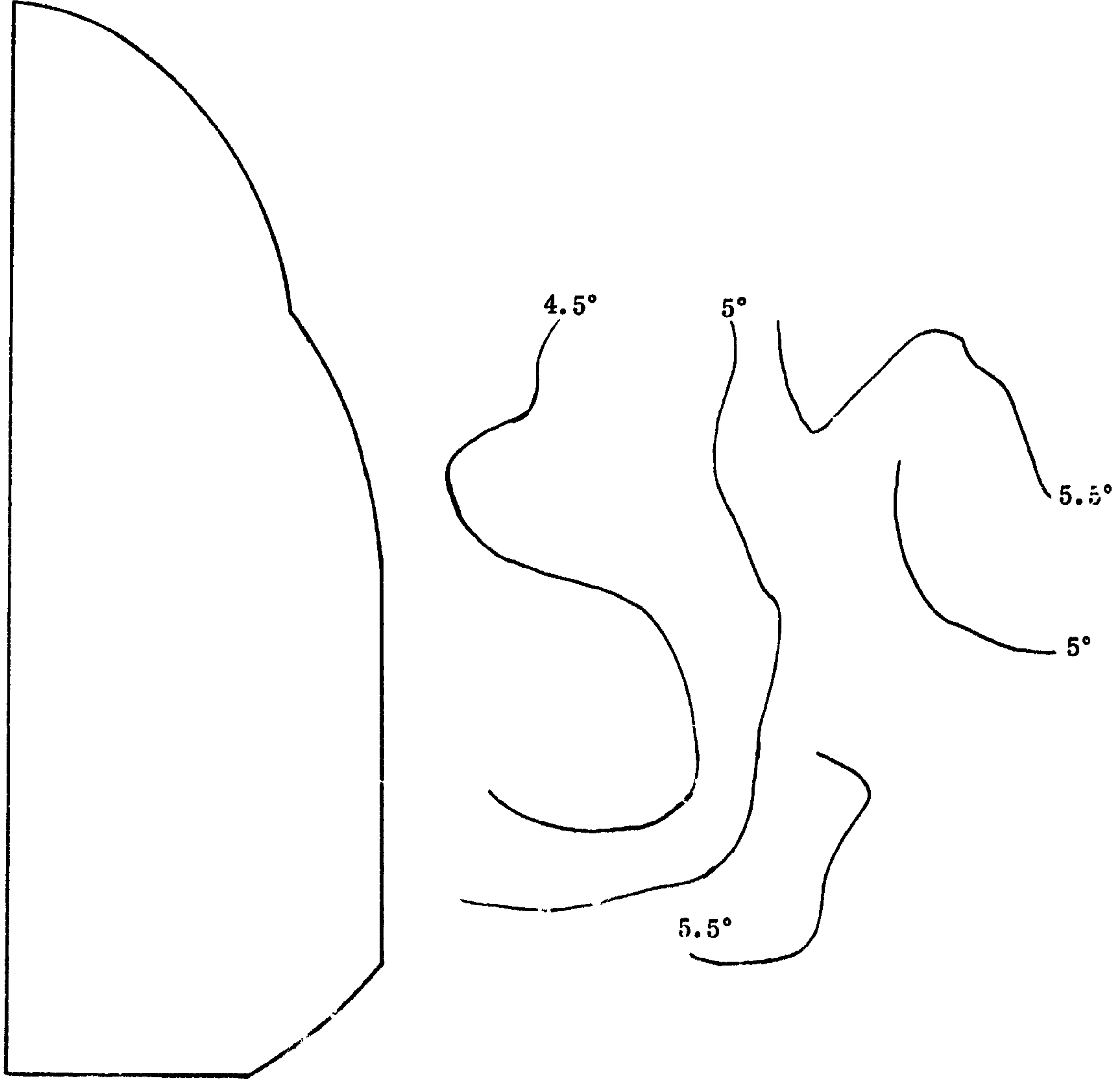

Figure 7-7. Local Flow Angularity

Fuselage 3
SCSN
Mach Number = 2.5
$\alpha = 5°$
Format I

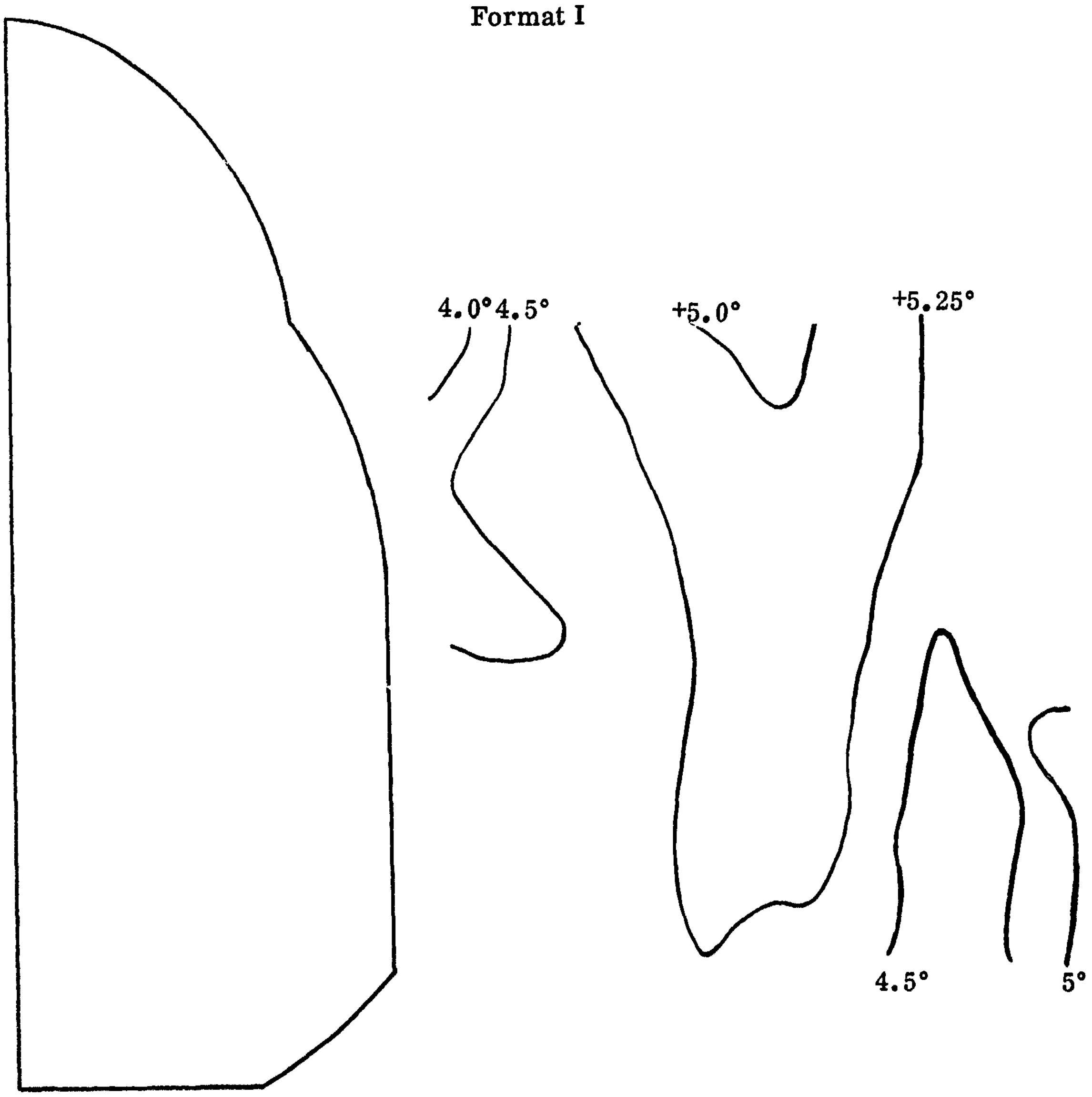

Figure 7-8. Local Flow Angularity

At +10 degrees angle of attack the canopy is clearly the most dominant geometric parameter. With the primary (PCPN) combination, a weak upwash flow field exists with the fuselage corner influence evident. Substitution of the secondary nose (PCSN) produces essentially no change in the flow field. However, the secondary canopy (SCSN) produces two mild downwash regions, one inboard near the body and one outboard near the shock wave. Using the primary nose with the secondary canopy (SCPN) results in a stronger canopy wave, due to the more slender nose, as seen by the increased outboard downwash angularity and the larger extent of the mild downwash region. The local flow angularity is presented in Figures 7-9 through 7-12.

For +15 degrees and +20 degrees angle of attack the canopy shock strength is relatively insensitive to increasing approach Mach number. A three zone upwash flow field exists at these conditions with the distribution dependent, almost entirely. upon the fuselage corner radius; consequently all eight patterns appear similar, as shown in Figures 7-13 through 7-20. The influence of the fuselage corner radius is more pronounced at +20°.

At +25 degrees angle of attack the same general flow field composition exists. The extent of the region influenced by the fuselage corner radius has increased as expected. An interesting effect occurring at this angle of attack is the presence of a downwash zone in the lower outboard region of the surveyed flow field. At this condition the upwash field is wrapped closely around the fuselage. On the other hand the canopy wave has become more detached and, at the survey plane, has moved outboard of the strong upwash gradient. Being unopposed the shock wave induces a local downwash zone with the inner boundary determined by the fuselage corner. The flow field composition, including this downwash region is shown in Figures 7-21 through 7-24. Back tracking to +20 degrees angle of attack we can see the onset of this condition with the primary nose configurations. In both cases the thinner shock layer generated by this more slender nose resulted in the intrusion of a small downwash region in the lower outboard portion of the survey plane.

The influence of the nose and canopy geometry decreases with decreasing Mach number. For the lower supersonic test Mach numbers (M_∞ = 2.2 and 1.8) the basic flow field composition remains essentially the same as that seen at Mach 2.5. Although similarly structured, the flow fields tend to become more uniform at these lower Mach numbers as the local shock induced effects weaken in intensity. To

Fuselage 3
PCPN
Mach Number = 2.5
α = 10°
Format I

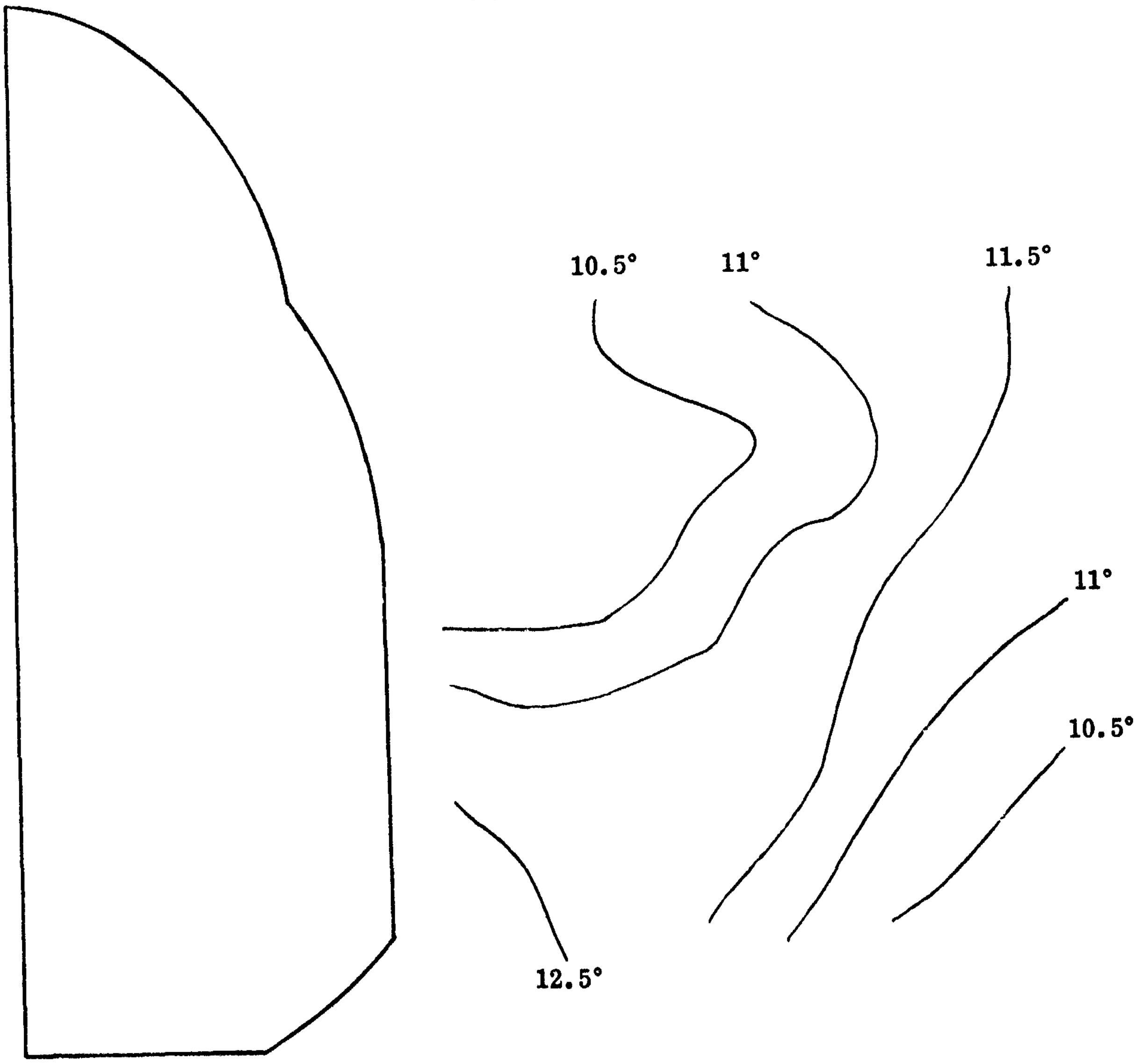

Figure 7-9. Local Flow Angularity

Fuselage 3
PC3N
Mach Number = 2.5
α = 10°
Format I

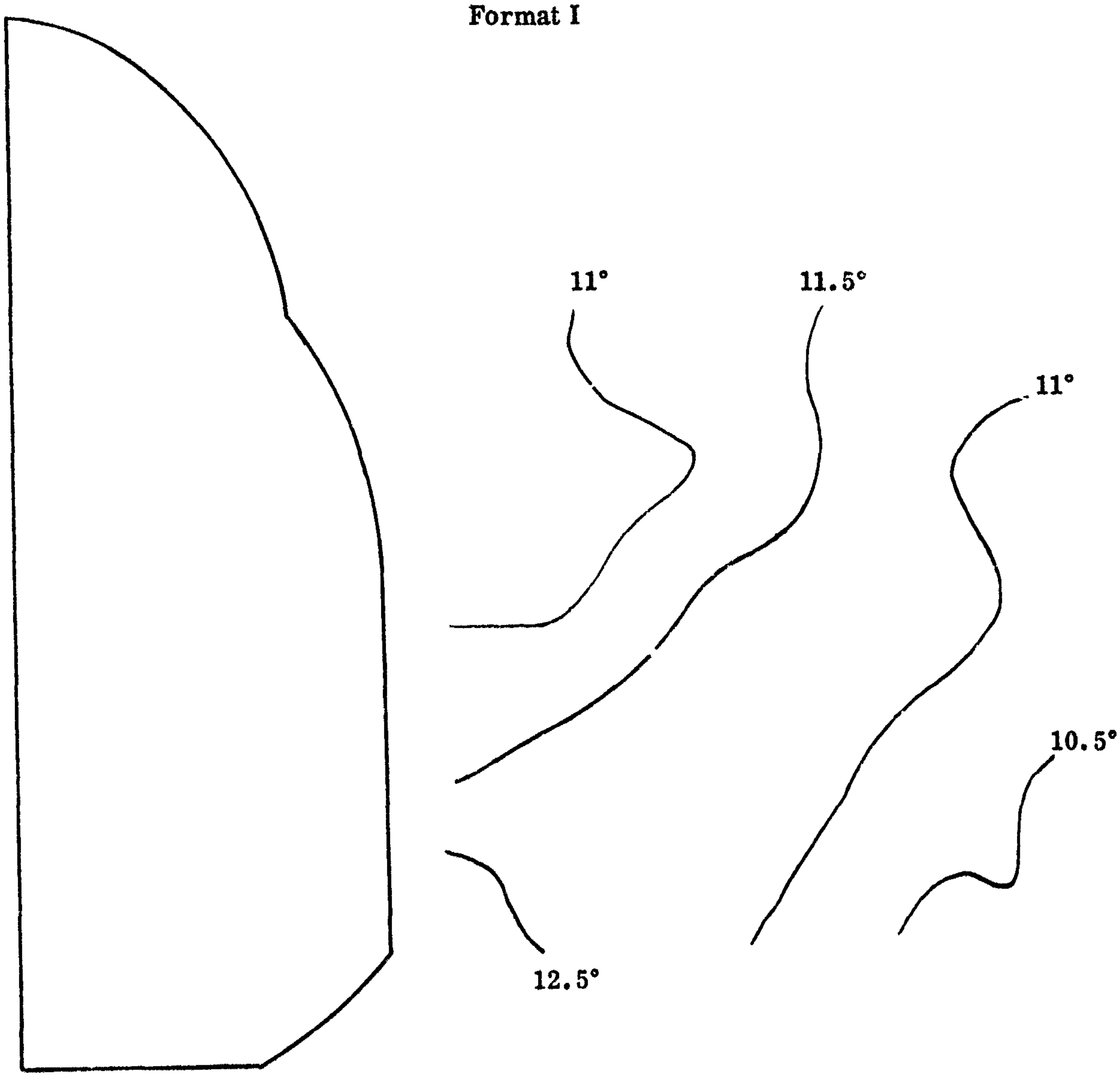

Figure 7-10. Local Flow Angularity

Fuselage 3
SCPN
Mach Number = 2.5
α = 10°
Format I

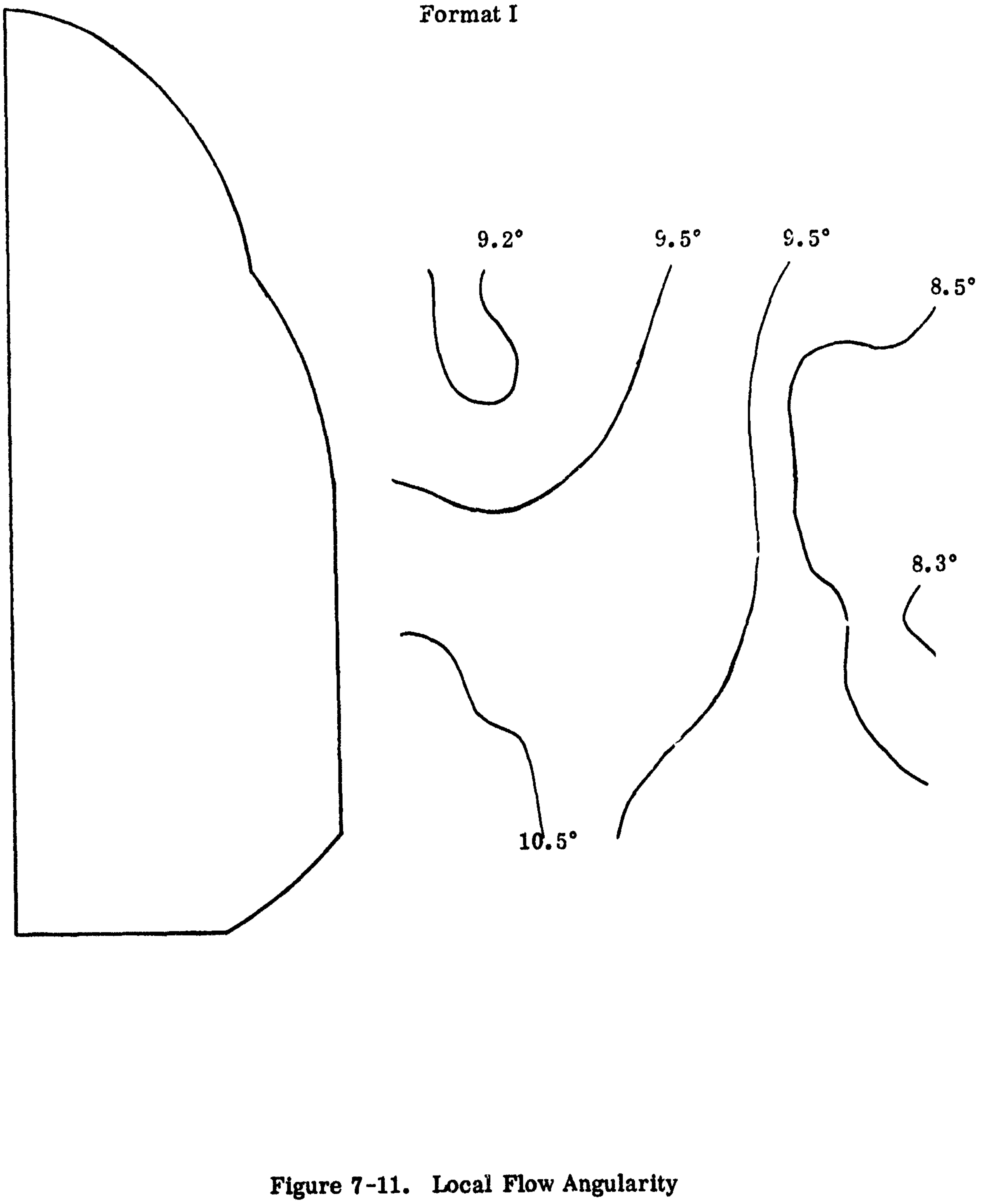

Figure 7-11. Local Flow Angularity

Fuselage 3
SCSN
Mach Number = 2.5
$\alpha = 10°$
Format I

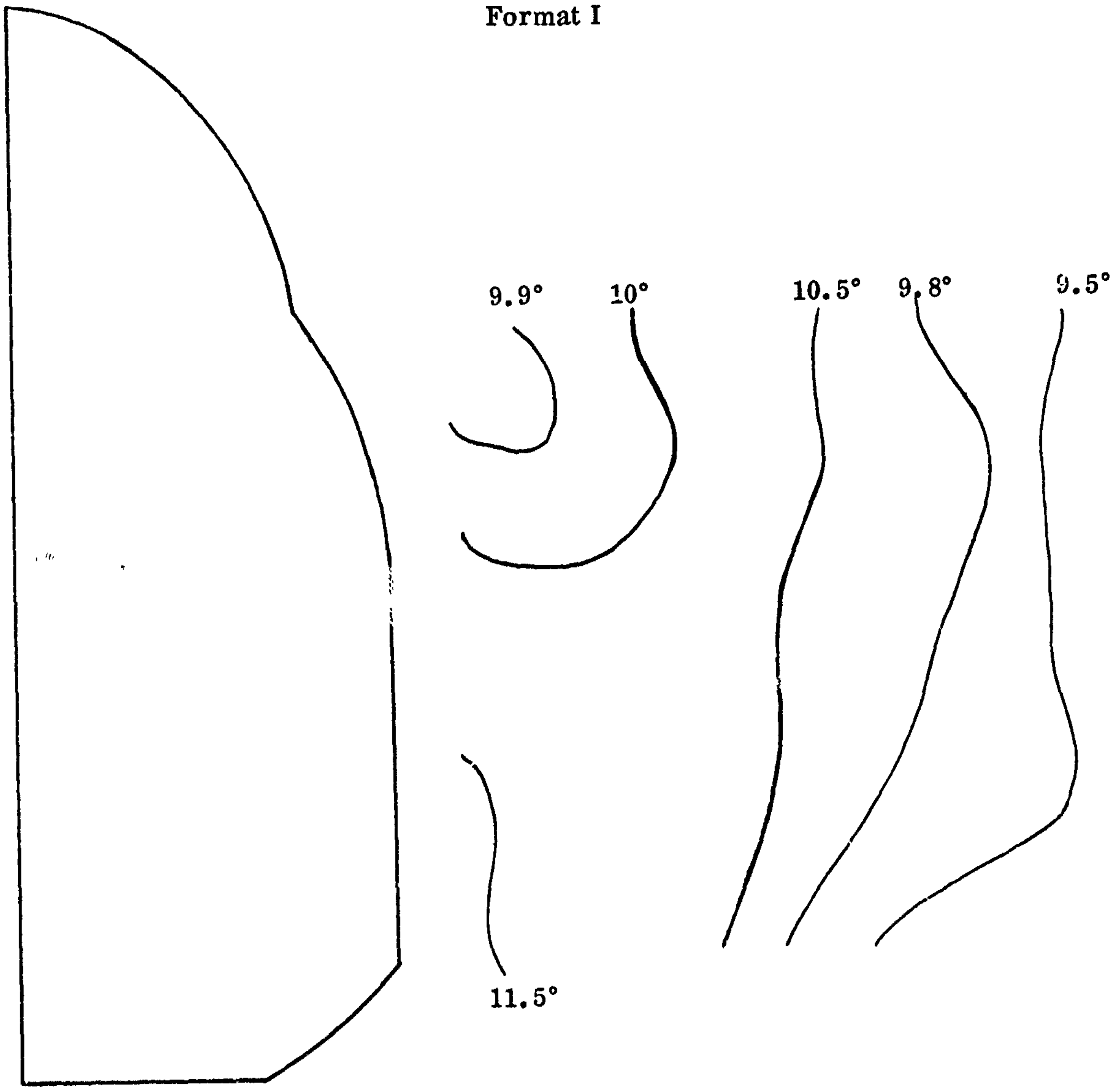
9.9°
10°
10.5°
9.8°
9.5°
11.5°

Figure 7-12. Local Flow Angularity

Fuselage 3
PCPN
Mach Number = 2.5
$\alpha = 15°$
Format I

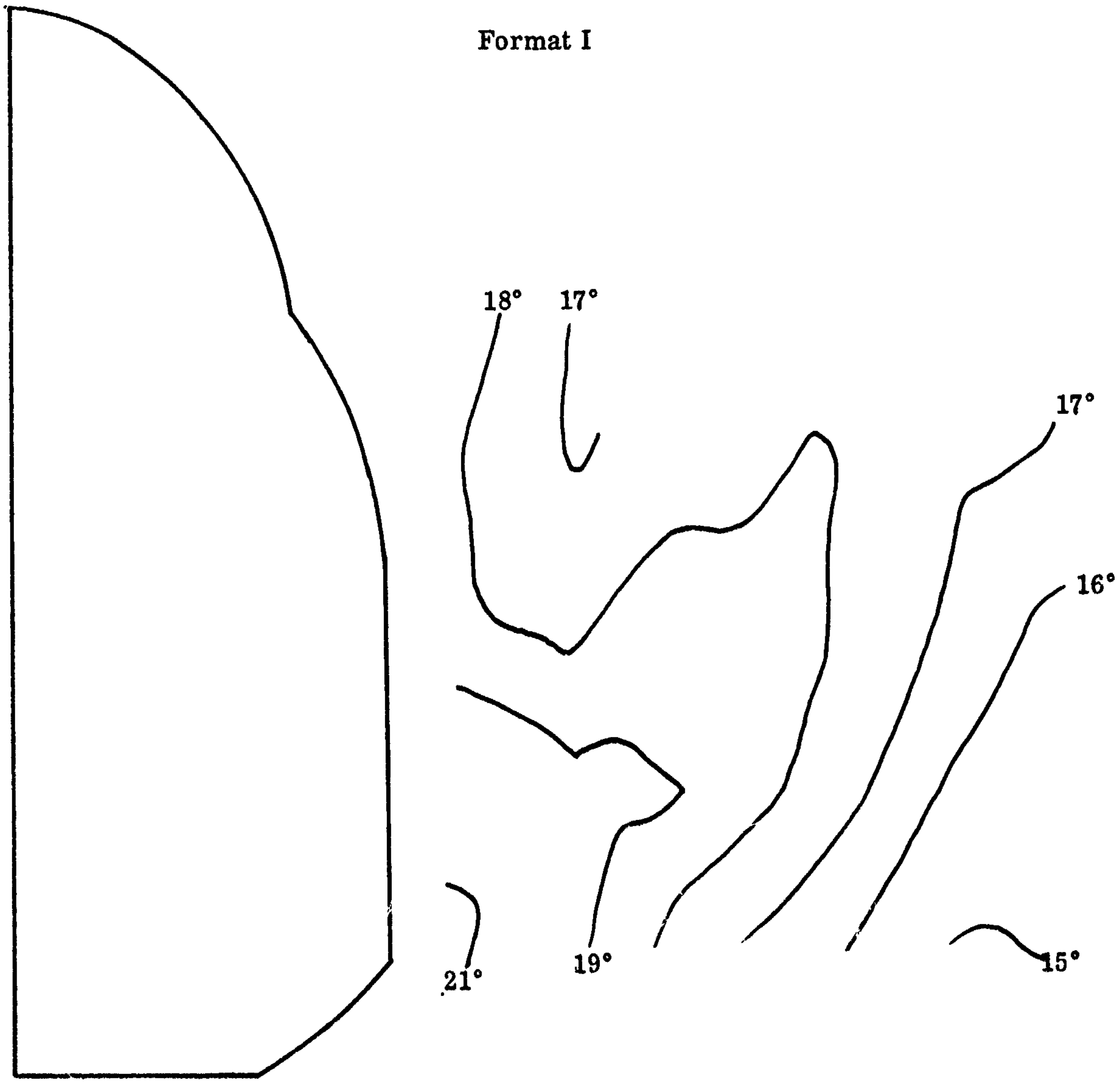

Figure 7-13. Local Flow Angularity

Fuselage 3
PCSN
Mach Number = 2.5
α = 15°
Format I

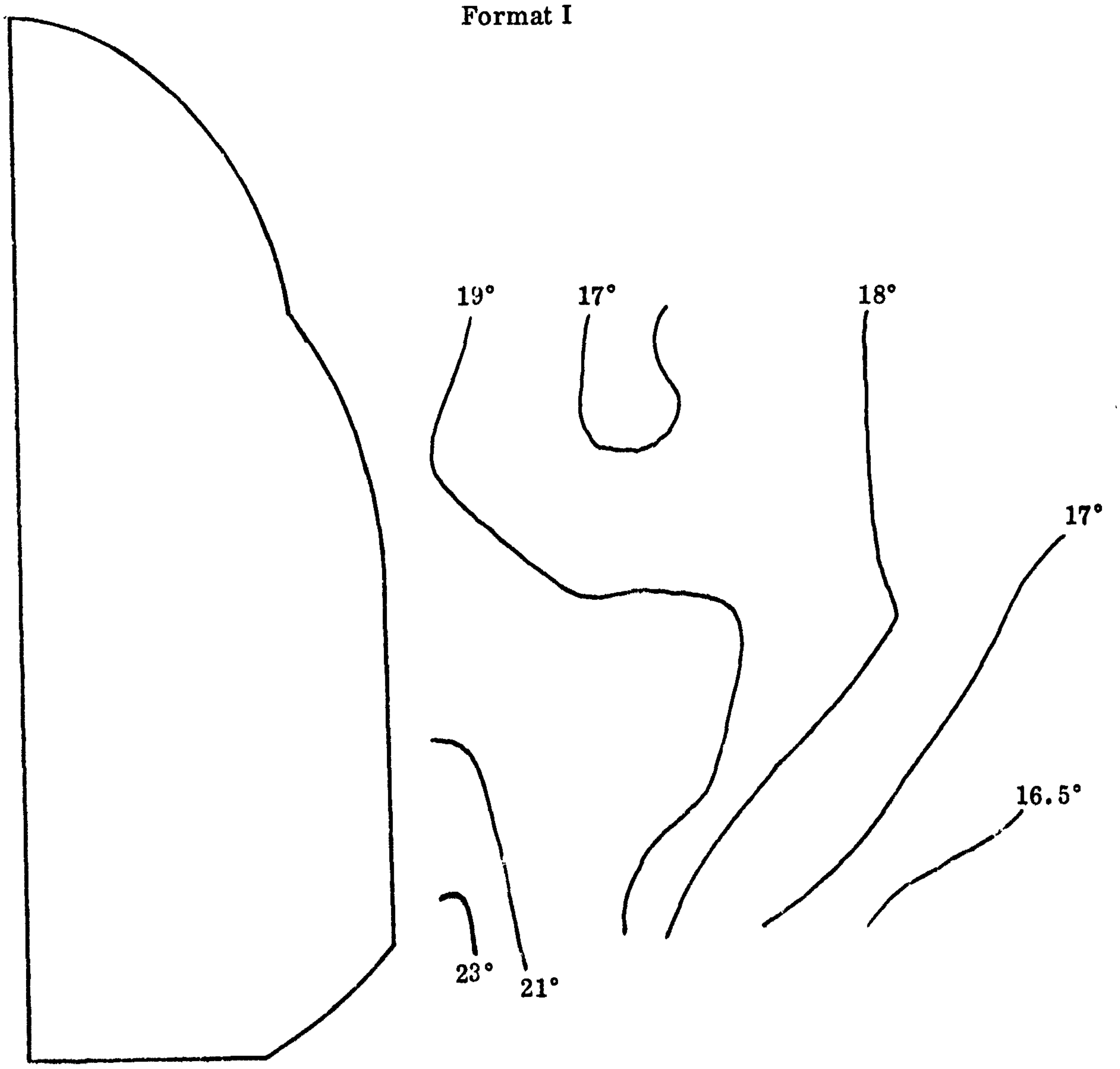

Figure 7-14. Local Flow Angularity

Fuselage 3
SCPN
Mach Number = 2.5
α = 15°
Format I

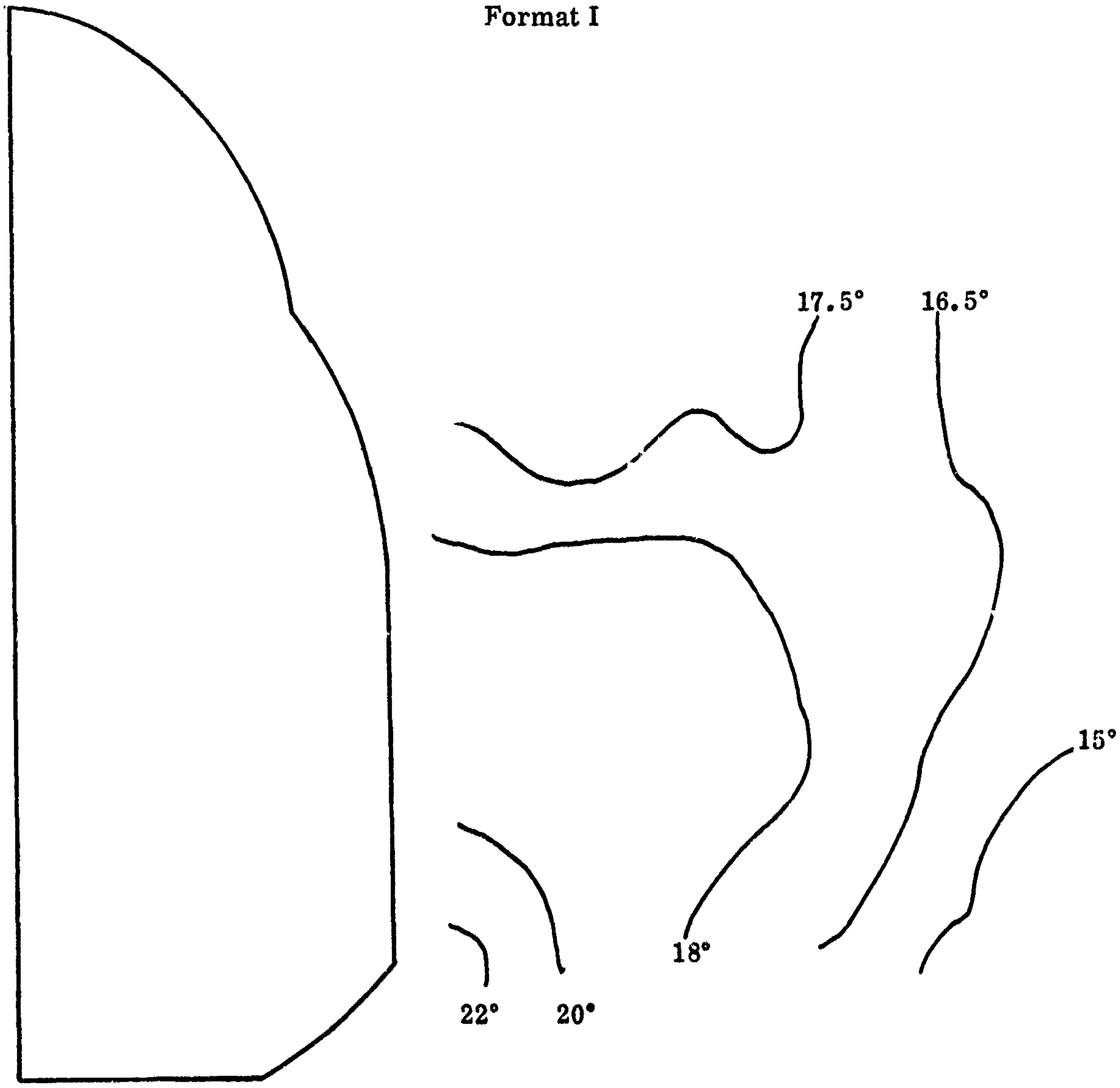

Figure 7-15. Local Flow Angularity

Fuselage 3
SCSN
Mach Number = 2.5
$\alpha = 15°$

Format I

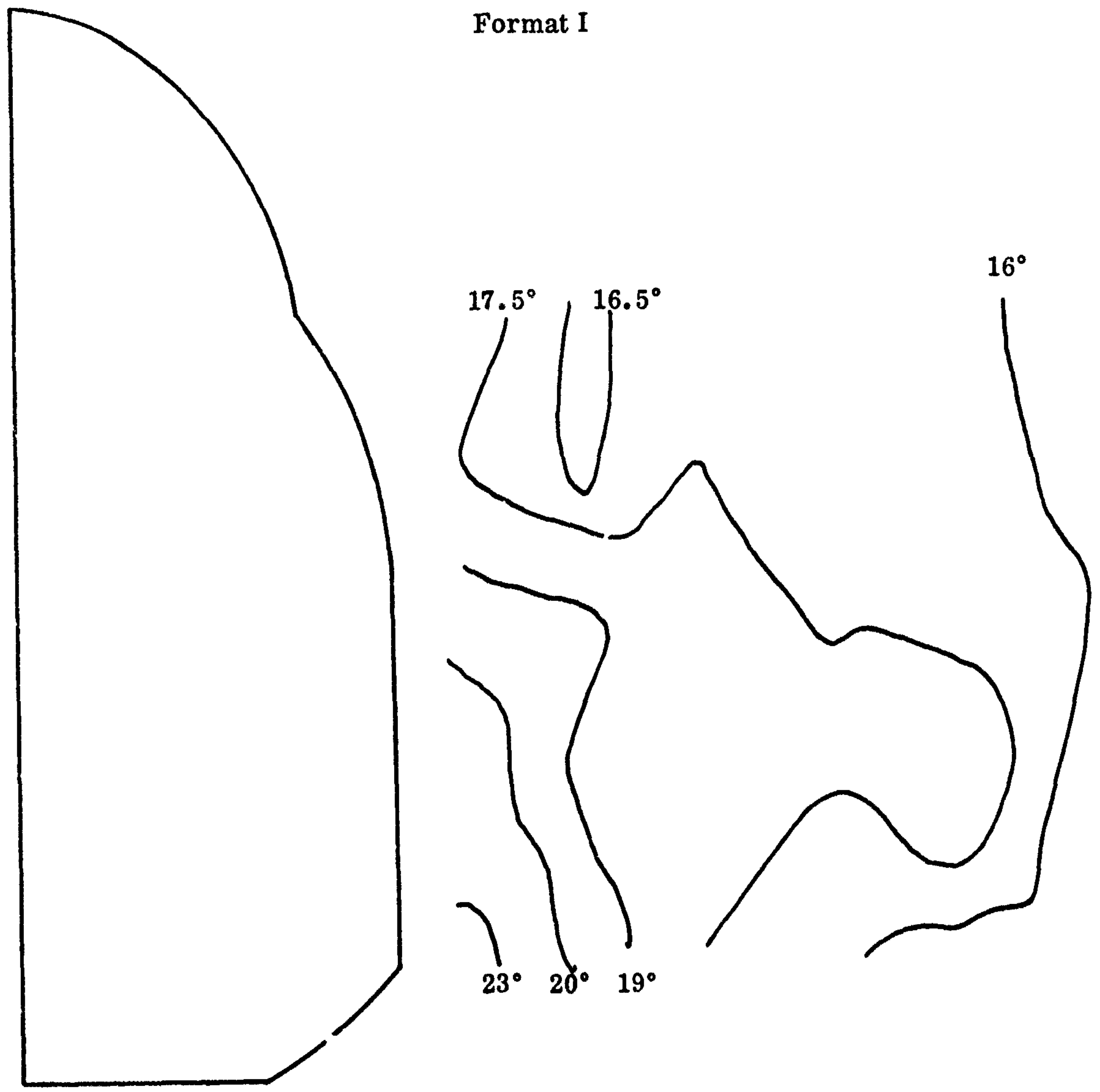

Figure 7-16. Local Flow Angularity

Fuselage 3

PCPN

Mach Number = 2.5

α = 20°

Format I

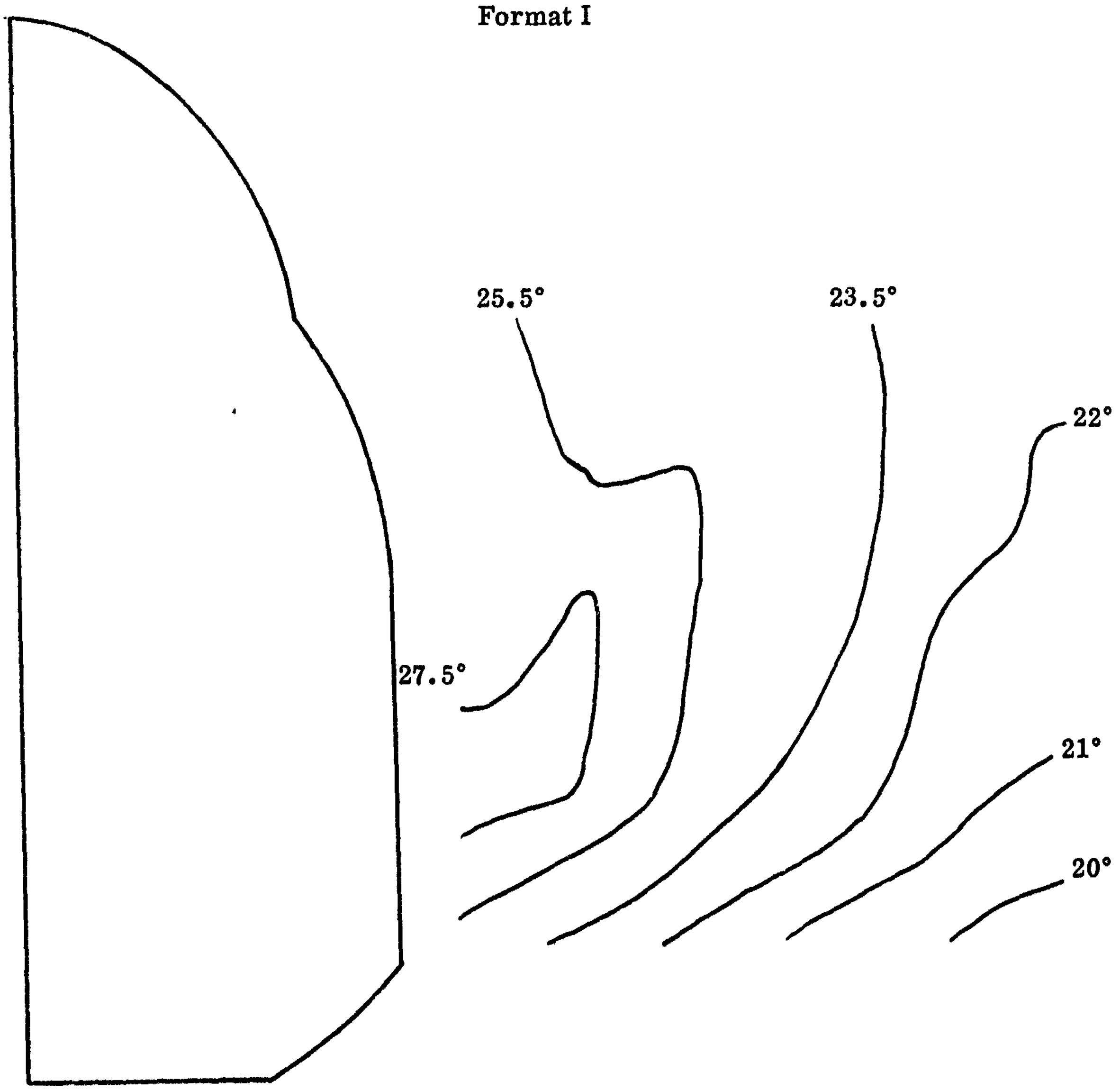

Figure 7-17. Local Flow Angularity

Fuselage 3
PCSN
Mach Number = 2.5
$\alpha = 20^\circ$
Format I

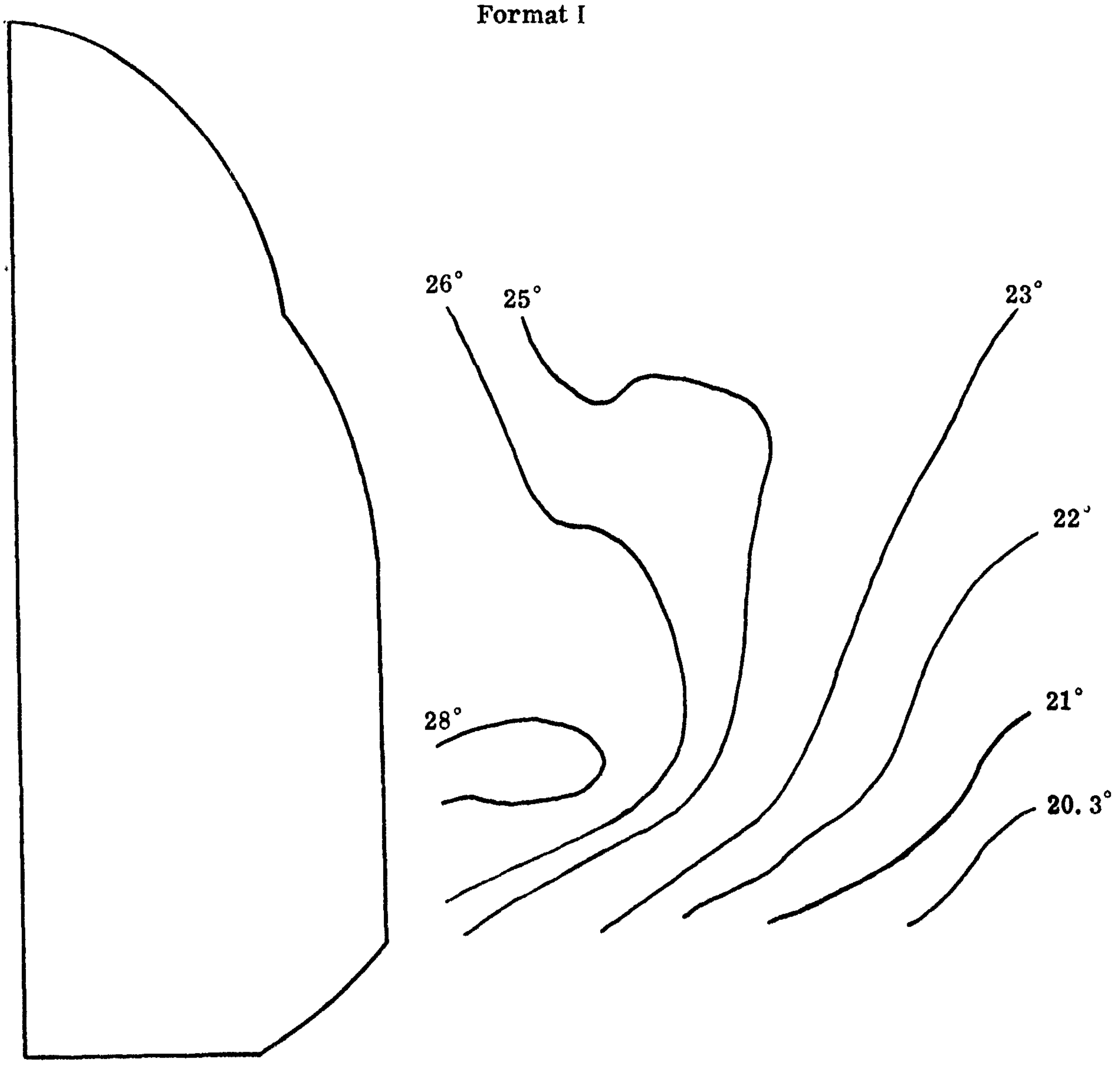

Figure 7-18. Local Flow Angularity

Fuselage 3

SCPN

Mach Number = 2.5

$\alpha = 20°$

Format I

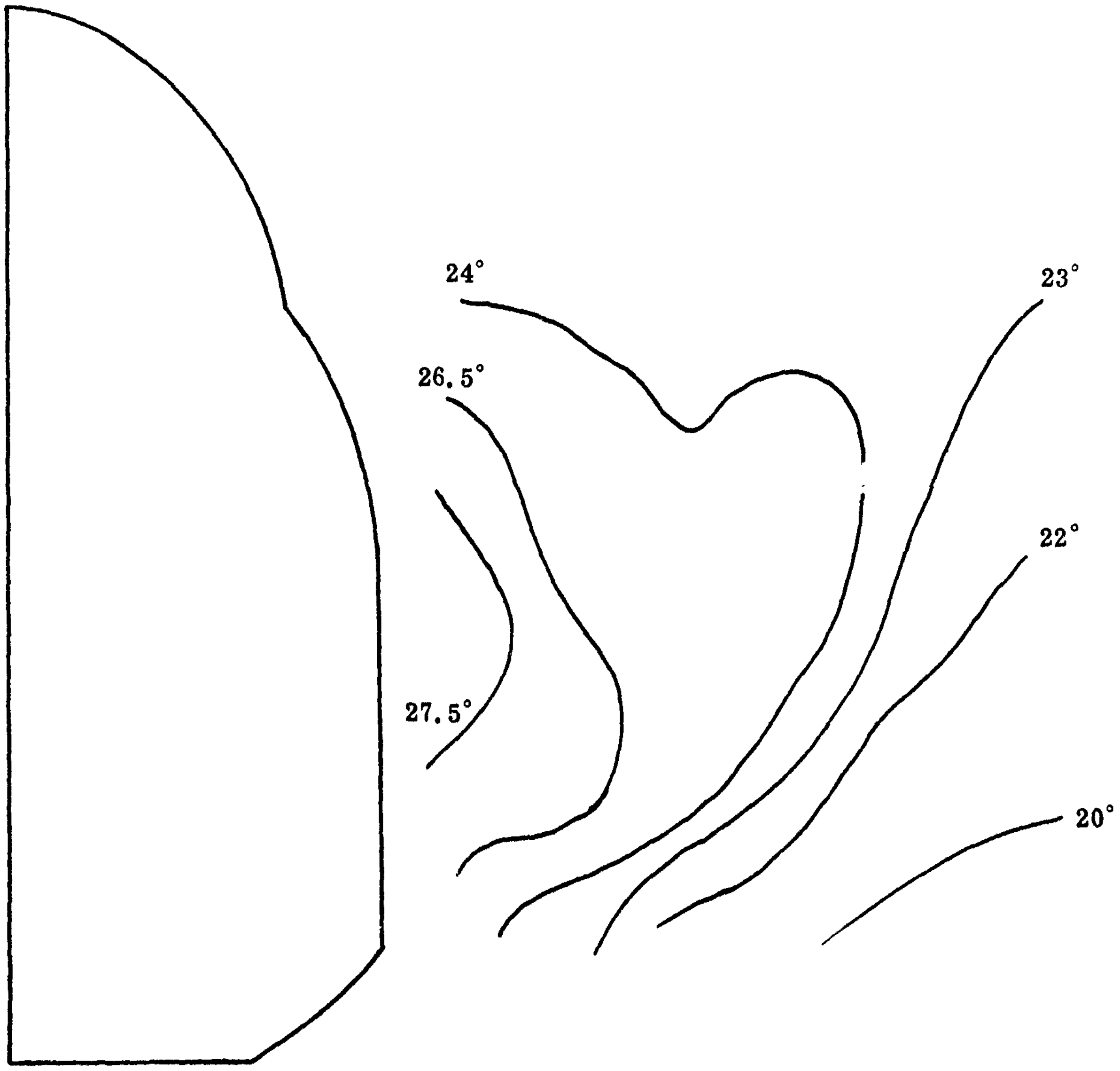

Figure 7-19. Local Flow Angularity

Fuselage 3
SCSN
Mach Number = 2.5
α = 20°
Format I

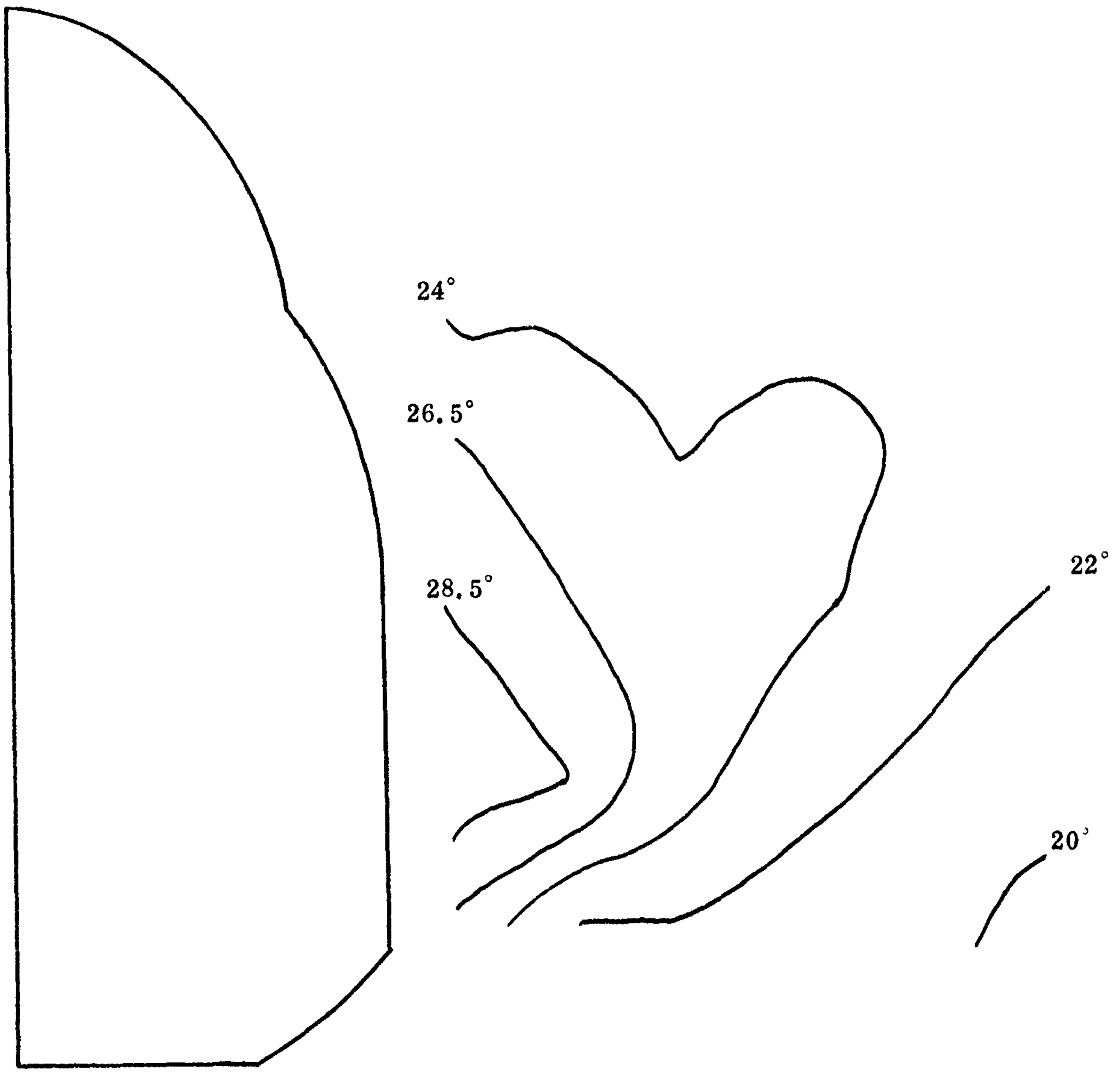

Figure 7-20. Local Flow Angularity

Fuselage 3
PCPN
Mach Number = 2.5
$\alpha = 25°$
Format I

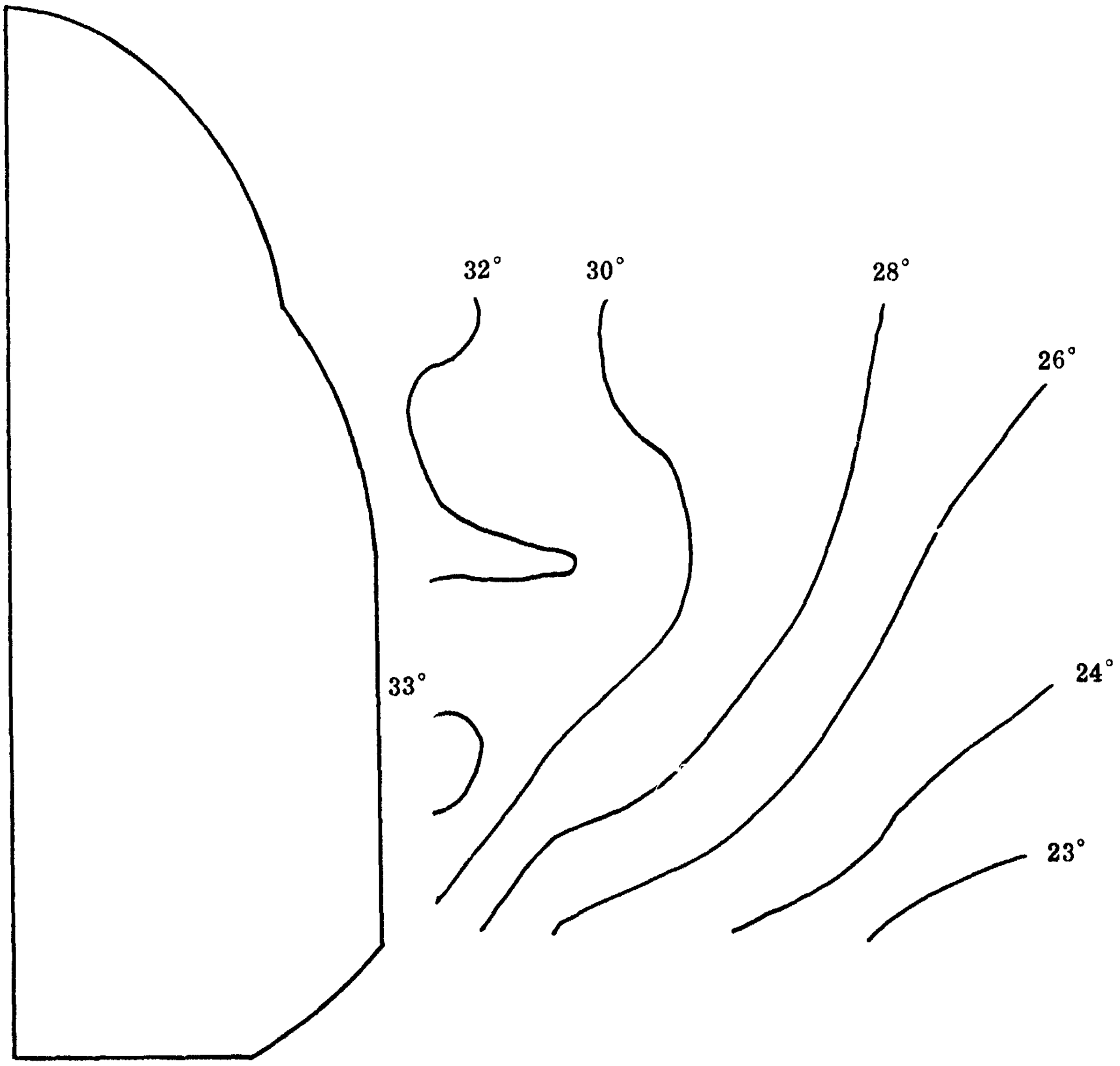
32°
30°
28°
26°
33°
24°
23°

Figure 7-21. Local Flow Angularity

Fuselage 3
PCSN
Mach Number = 2.5
$\alpha = 25°$

Format I

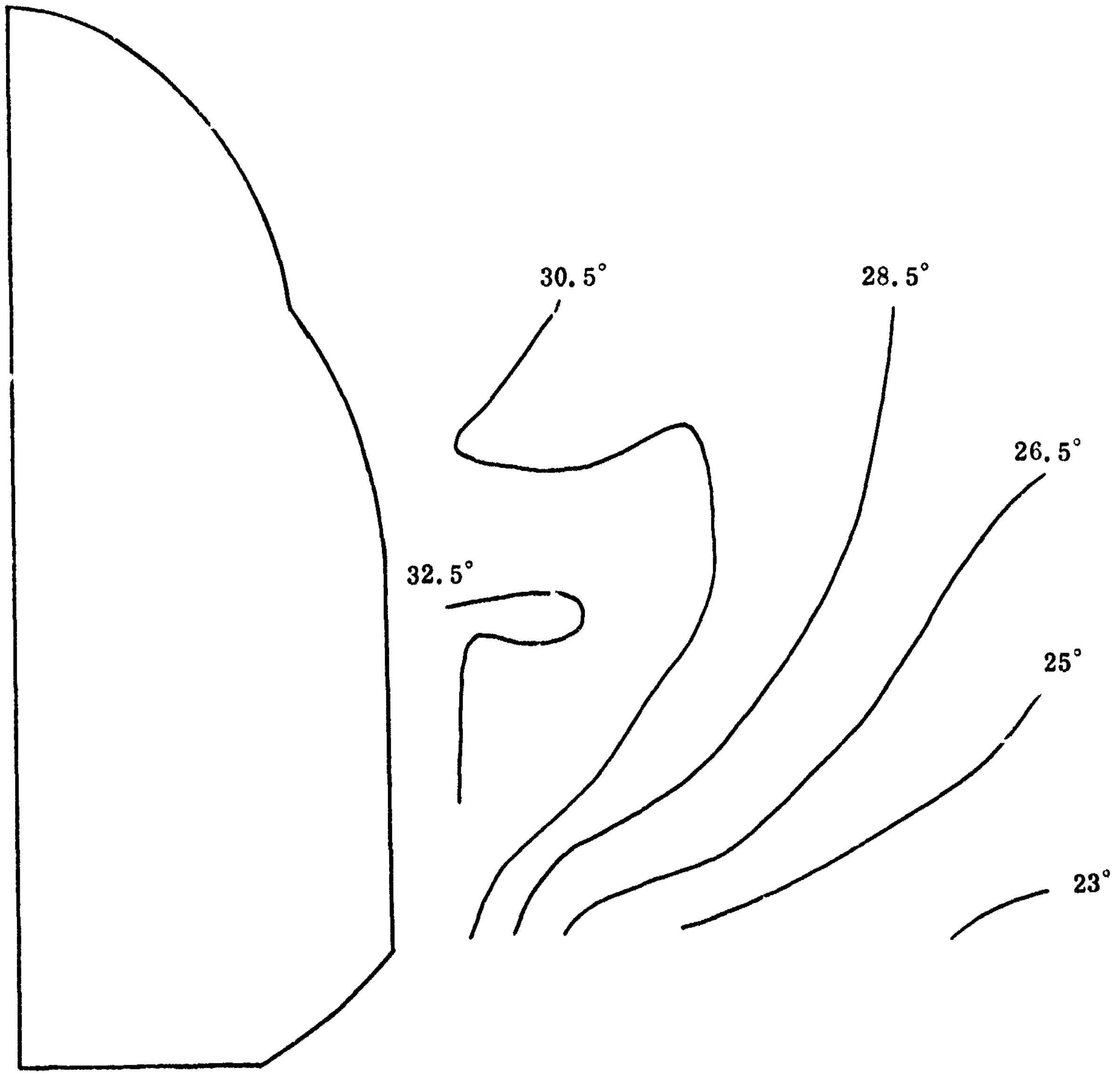

Figure 7-22. Local Flow Angularity

Fuselage 3
SCPN
Mach Number = 2.5
$\alpha = 25^\circ$
Format I

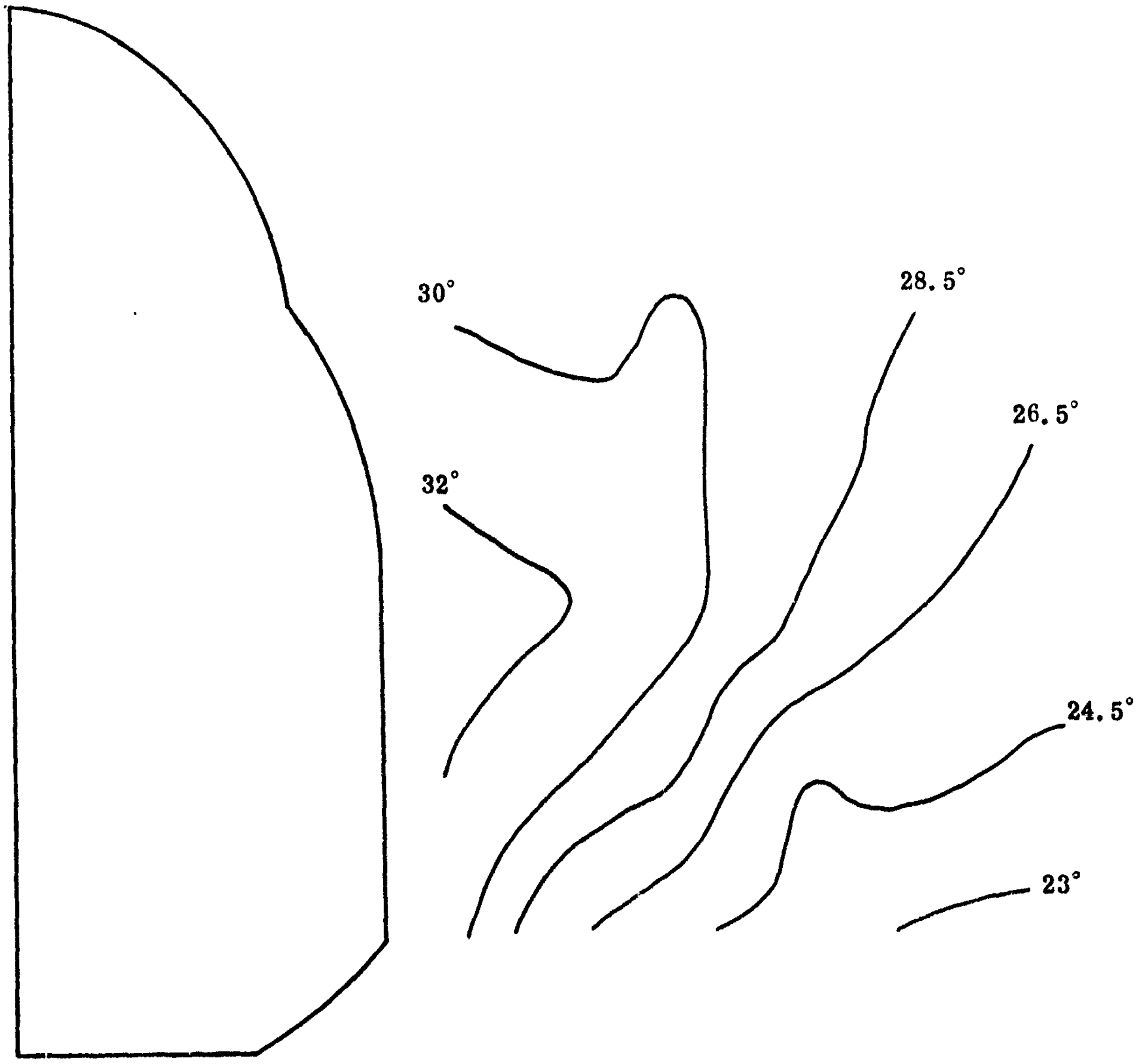

Figure 7-23. Local Flow Angularity

Fuselage 3
SCSN
Mach Number = 2.5
α = 25°
Format I

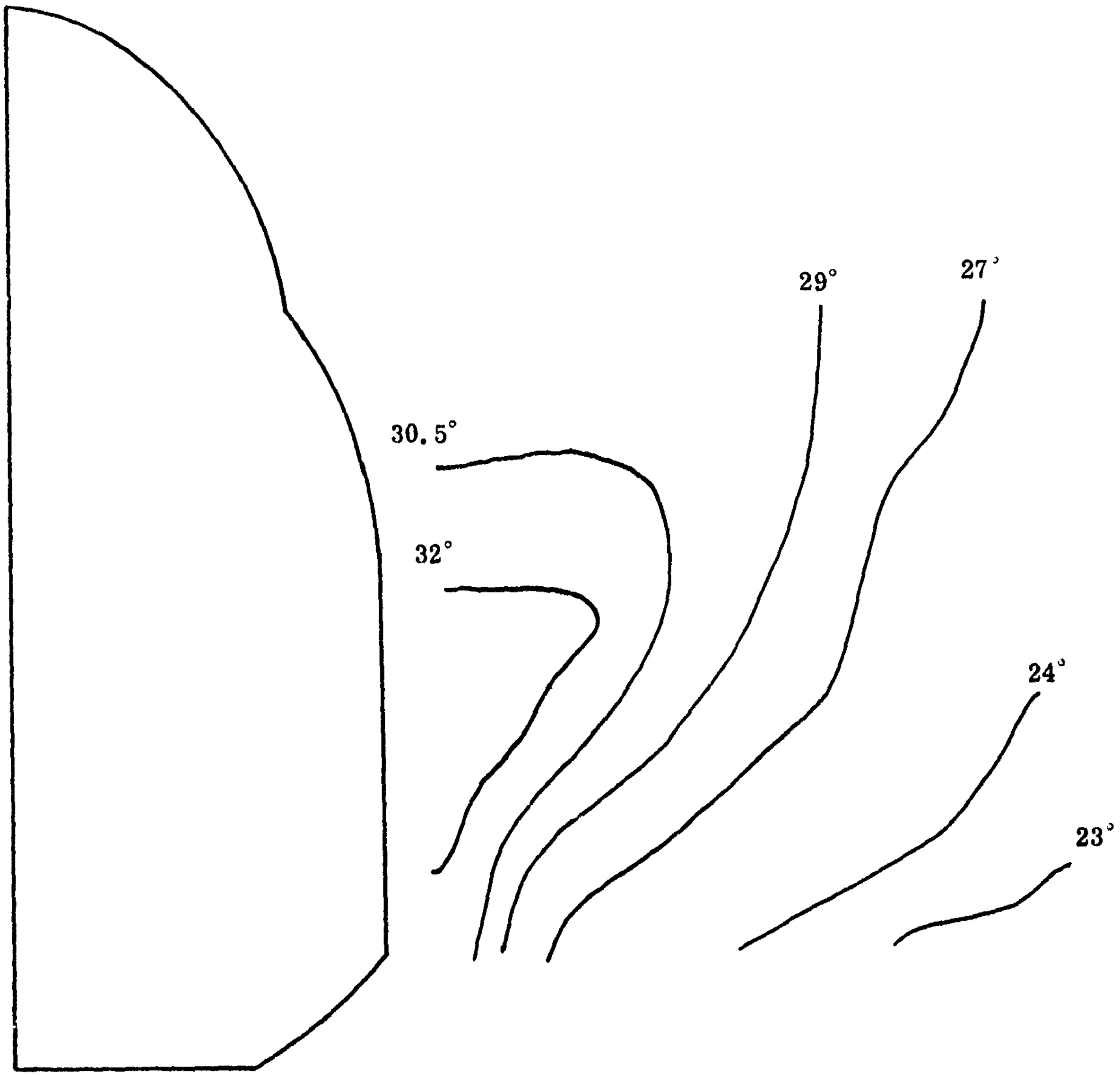

Figure 7-24. Local Flow Angularity

illustrate this effect the local flow field angularity is presented for a low angle of attack ($\alpha = 0^\circ$) and a high angle of attack ($\alpha = 15^\circ$) for both Mach numbers in Figures 7-25 through 7-40. The flow fields at the transonic ($M_\infty = 1.2$) and the subsonic ($M_\infty = 0.8$) test Mach numbers appear different due to the absence of shock induced local pressure gradients. At these two Mach numbers the flow field is essentially independent of geometry, becoming primarily a function of angle of attack. This is shown for angles of attack of 0°, 10°, and 20° in Figures 7-41 through 7-43 for one nose/canopy configuration at Mach 0.8. The relatively uniform flow fields seen in these figures, are also present for the remaining fuselage/canopy combinations at both Mach 1.2 and 0.8.

7.1.3 Fuselage Effects

For this series of tests the model was configured to obtain fuselage flow field data at the postulated forward inlet location - (30% ACL). These data were obtained for all seven fuselages employed in the program. The primary nose and canopy configurations were utilized during these tests.

7.1.3.1 Mach 0.8

For the negative angle of attack condition ($\alpha \approx -3^\circ$) an overall downwash condition prevails within the flow field for all seven fuselage geometries. Although the different fuselage geometries induce variations in the location and extent of the zones of flow angularity the average level of downwash is fairly constant. A typical flow angularity map is presented in Figure 7-44, for fuselage 2. The other fuselages induce similar flow fields with one exception, that being fuselage 6 which has a relatively high level of average downwash. In part, this effect stems from the fact that fuselage 6 has a low height factor (h/H) which introduces the fuselage corner to the prevalent downwash flow field at a relatively high waterline. The corner radius provides a favorable pressure gradient for the downwash flow thereby increasing the negative angularity. This fuselage effect is shown in Figure 7-45. A comparison of these two figures reveals that the height factor is not the only factor inducing a more negative downwash. For example, fuselage 2 has a height factor that is smaller than that of fuselage 6. The prime determinant appears to be the development of the corner, which occurs rapidly on 6 and gently on 2. A more abrupt peripheral pressure decay, encouraging the downwash flow to accelerate rapidly is therefore

Fuselage 3
PCPN
Mach Number = 2.2
α = 0°
Format I

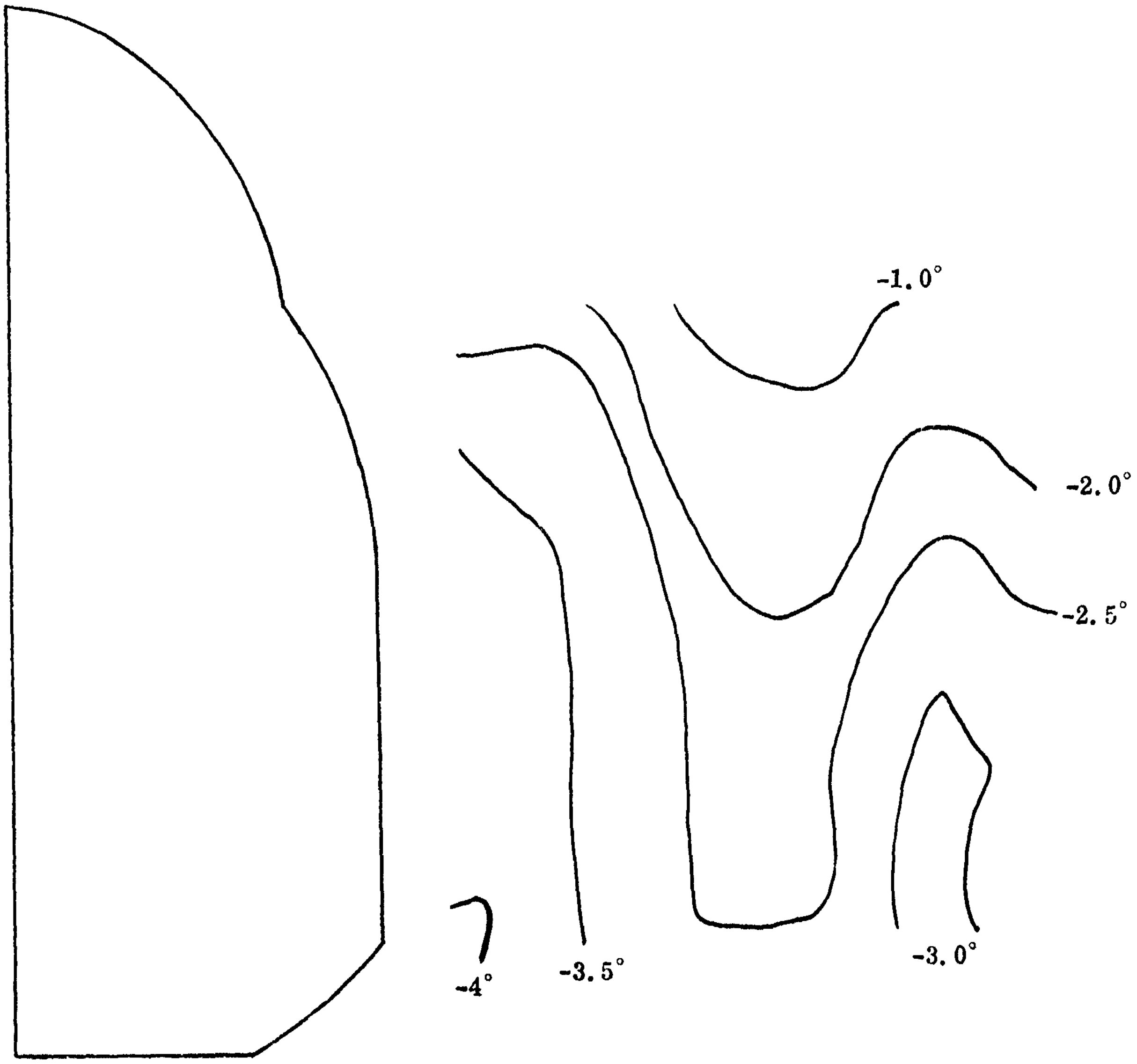

Figure 7-25. Local Flow Angularity

Fuselage 3
PCSN
Mach Number = 2.2
α = 0°
Format I

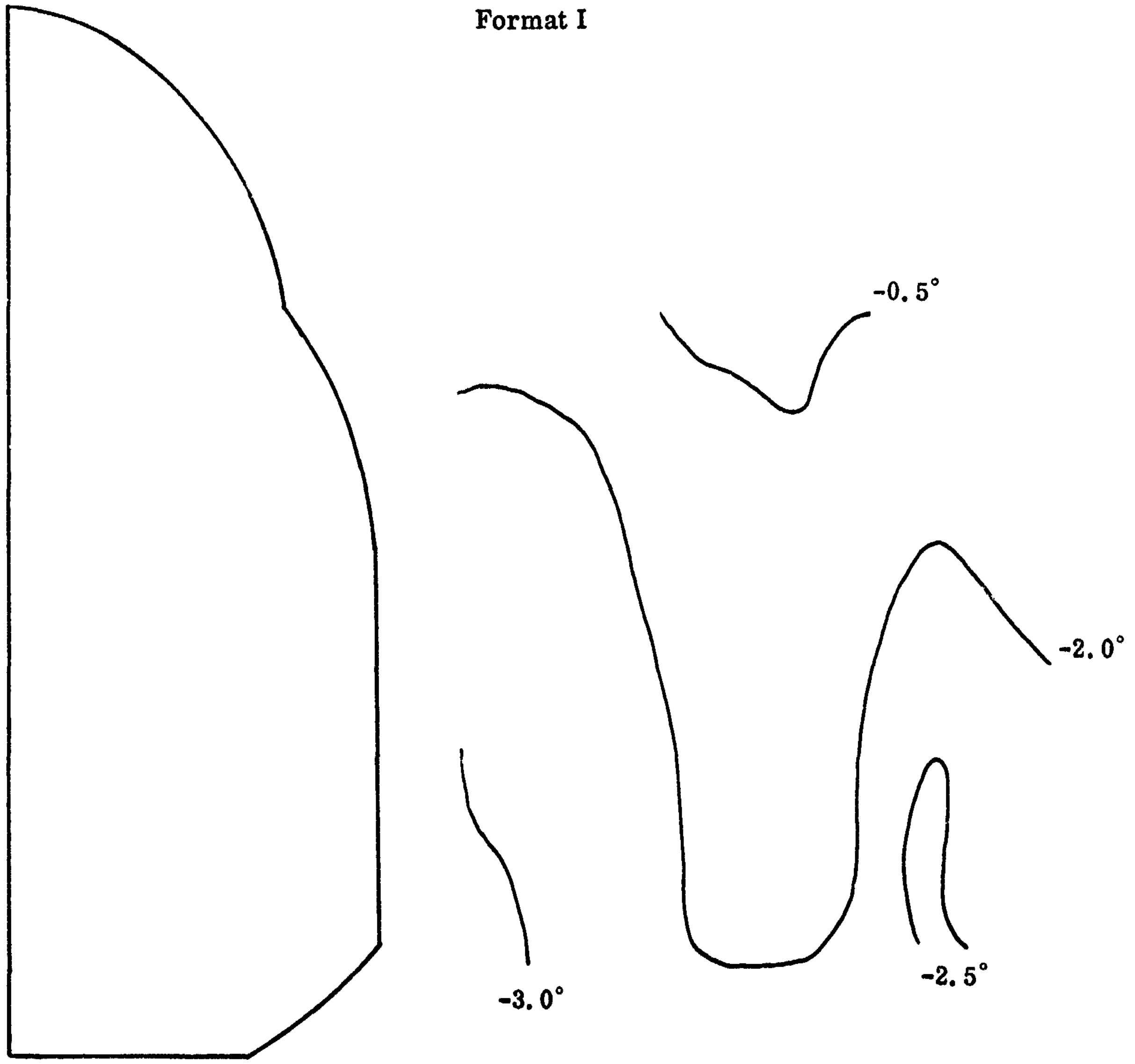

Figure 7-26. Local Flow Angularity

Fuselage 3
SCPN
Mach Number = 2.2
$\alpha = 0°$
Format I

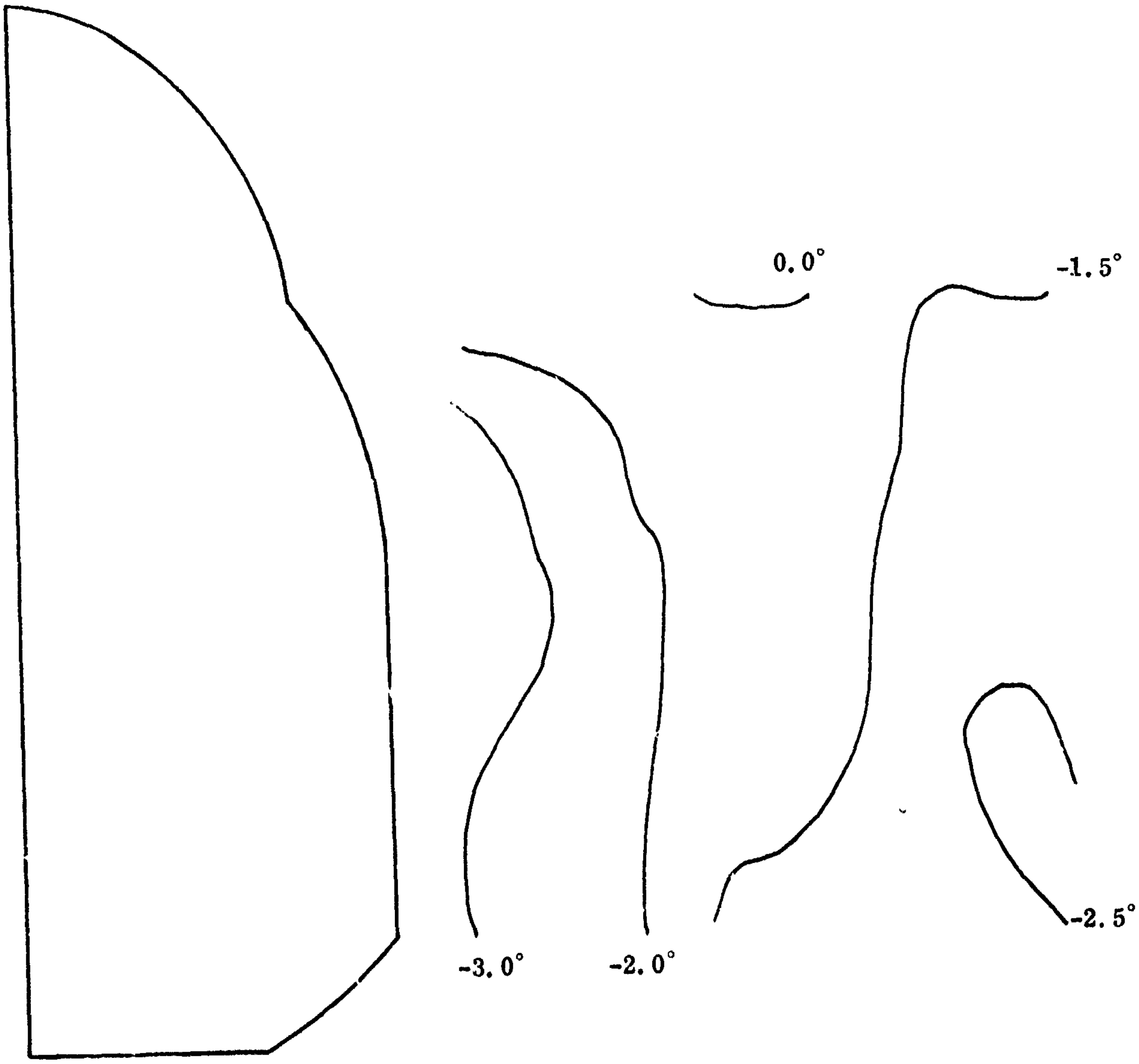

Figure 7-27. Local Flow Angularity

Fuselage 3
SCSN
Mach Number = 2.2
$\alpha = 0°$
Format I

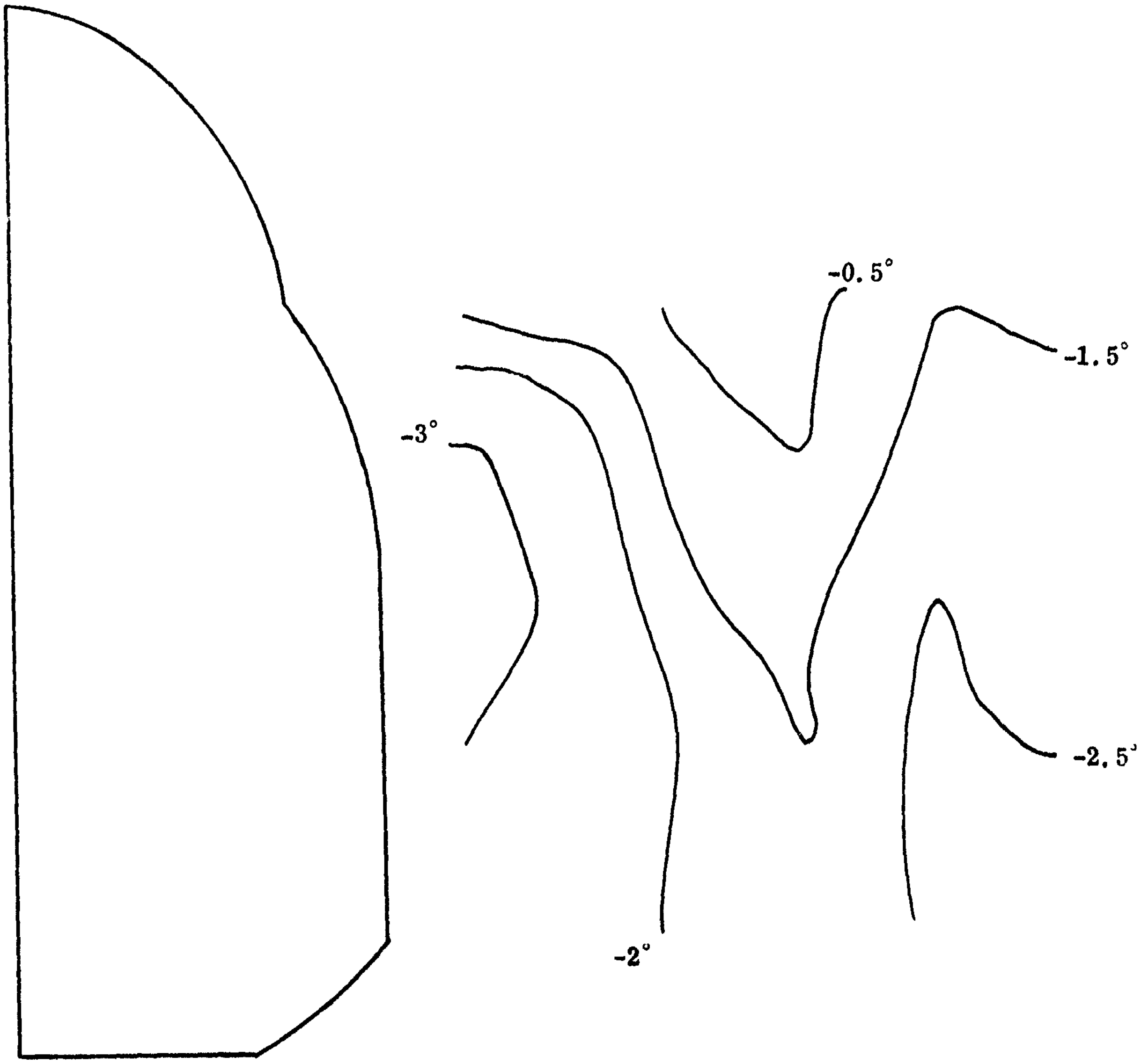

Figure 7-28. Local Flow Angularity

Fuselage 3
PCPN
Mach Number = 2.2
$\alpha = 15^\circ$
Format I

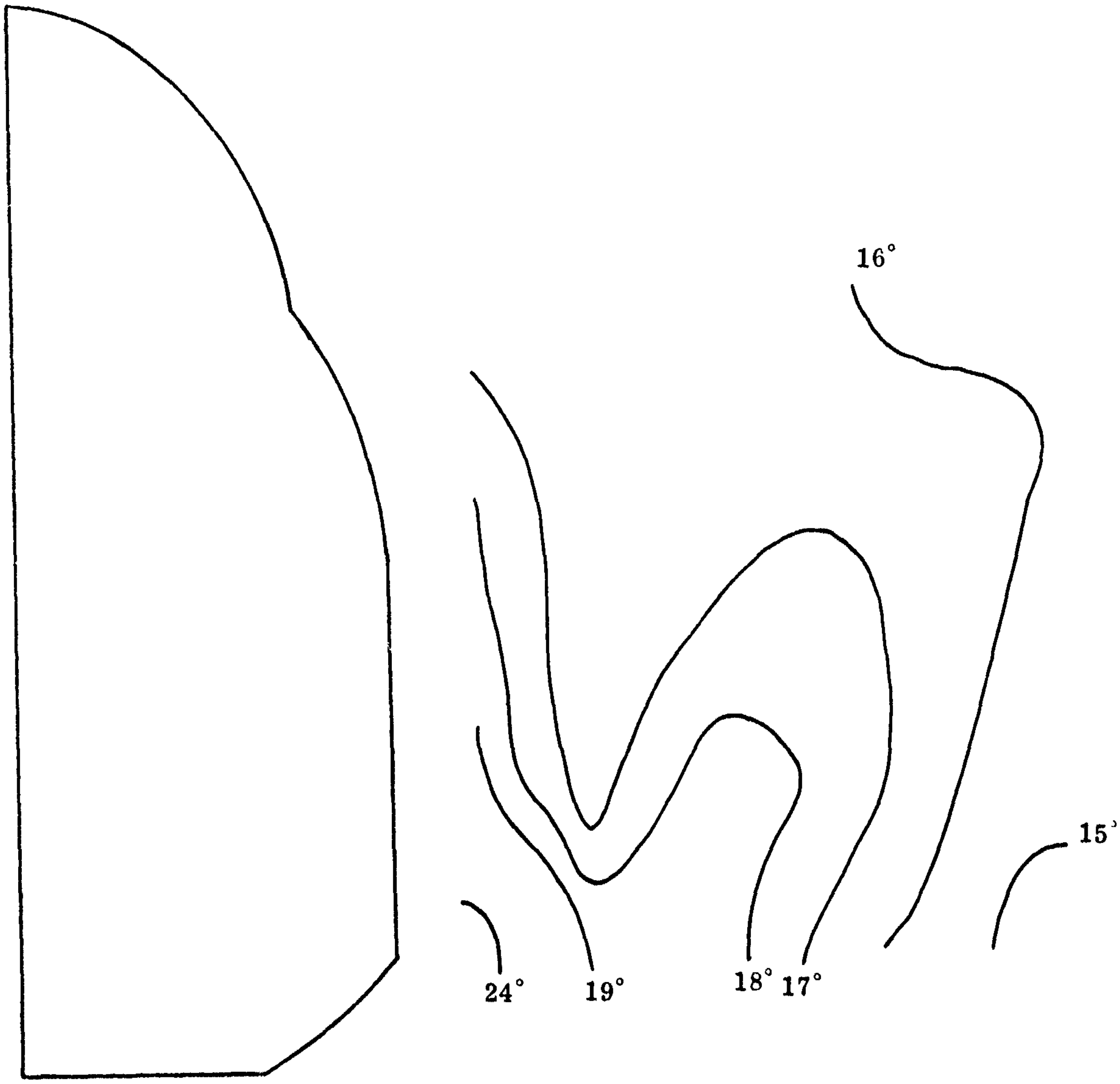

Figure 7-29. Local Flow Angularity

Fuselage 3
PCSN
Mach Number = 2.2
α = 15°
Format I

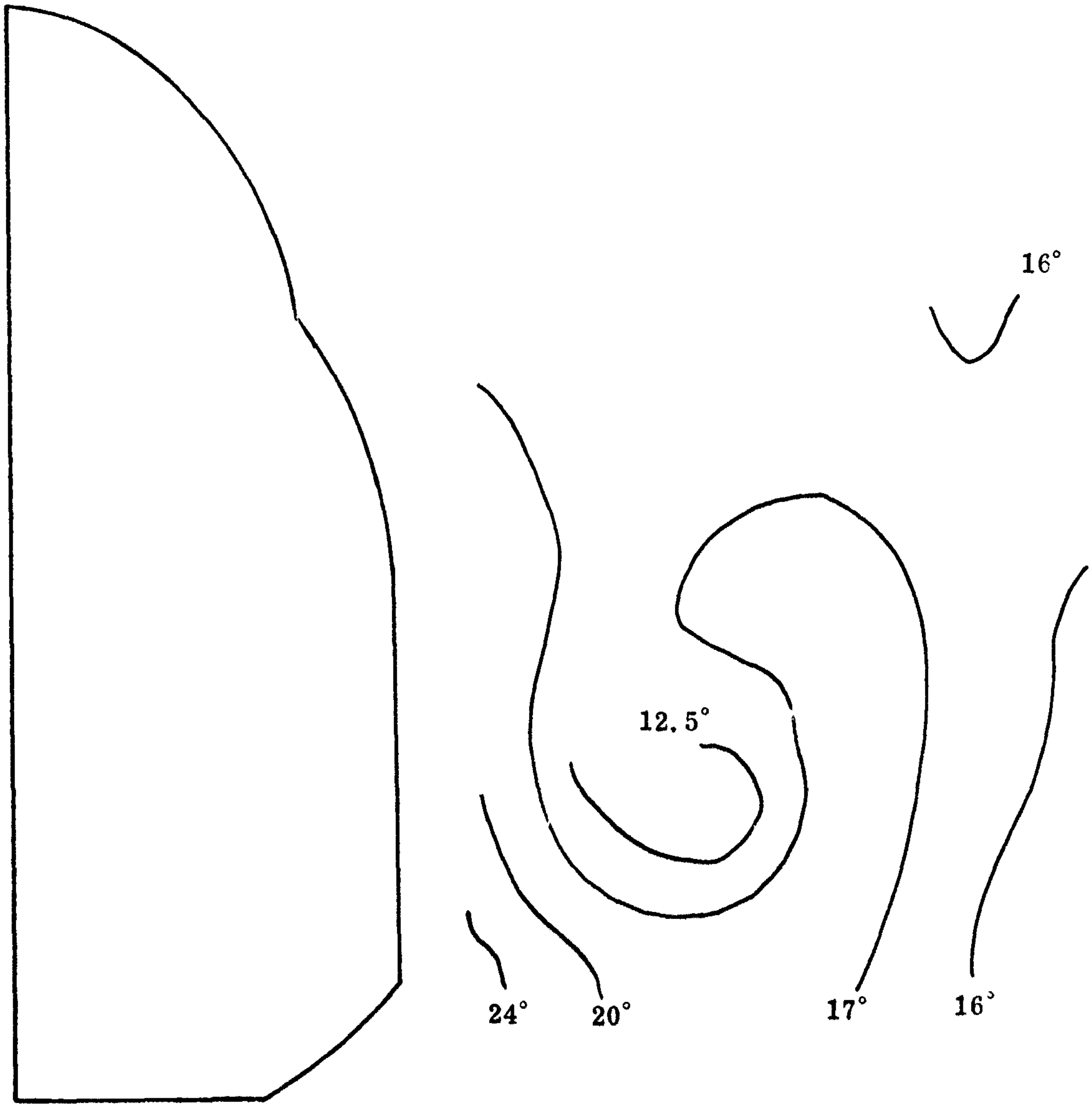

Figure 7-30. Local Flow Angularity

Fuselage 3
SCPN
Mach Number = 2.2
$\alpha = 15^\circ$
Format I

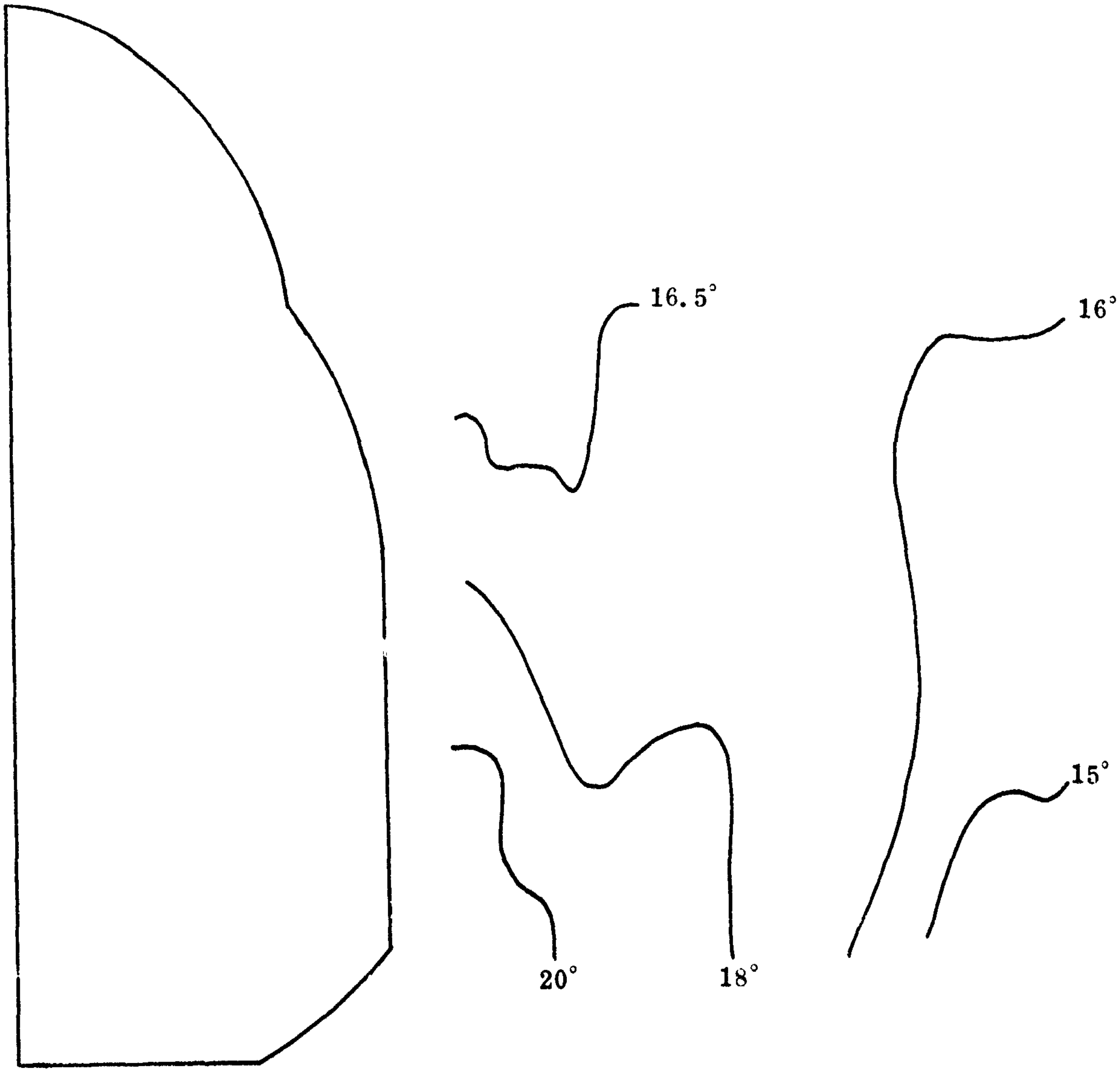
16.5°
16°
15°
20°
18°

Figure 7-31. Local Flow Angularity

Fuselage 3
SCSN
Mach Number = 2.2
$\alpha = 15^\circ$

Format I

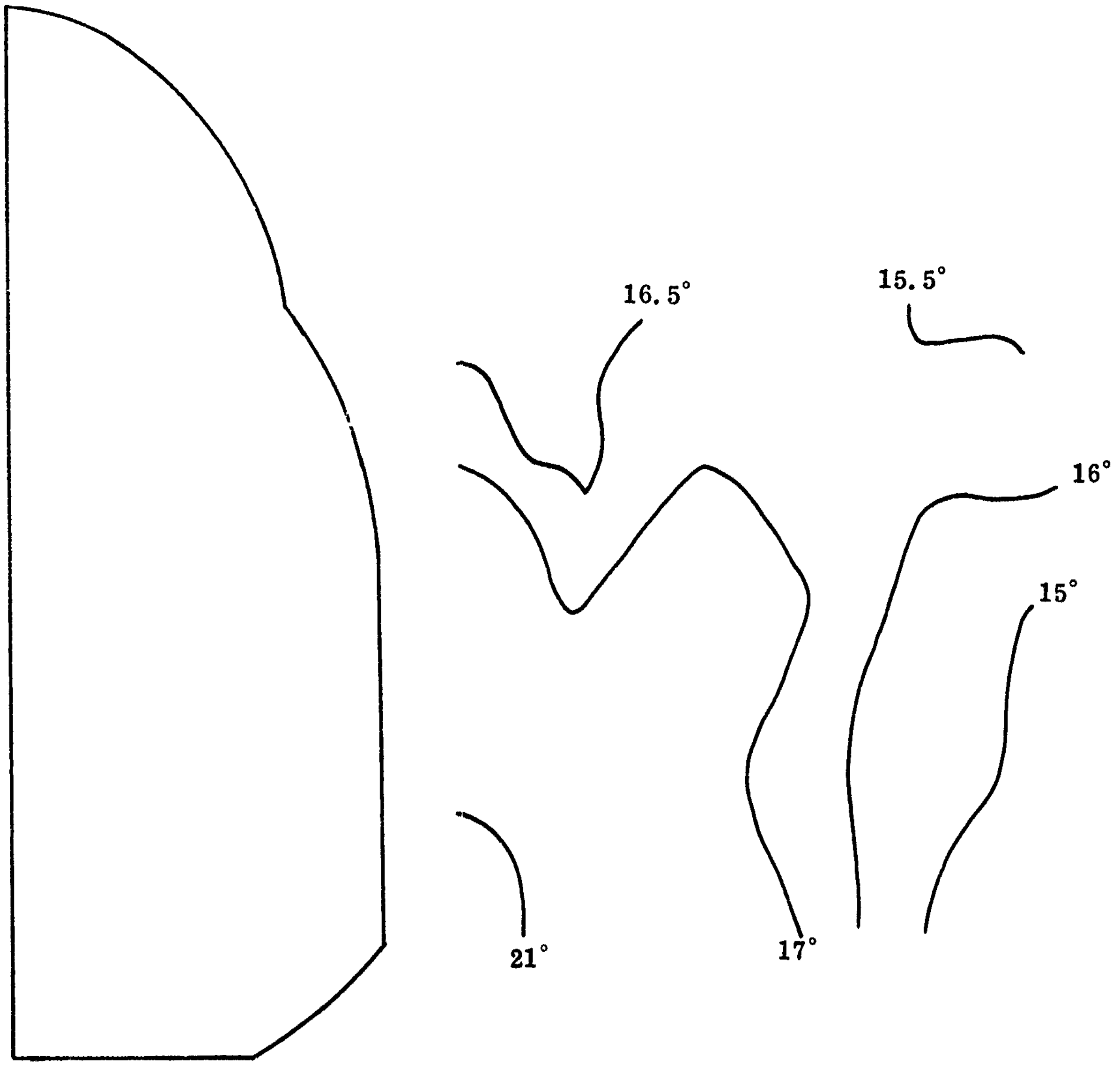
16.5°
15.5°
16°
15°
21°
17°

Figure 7-32. Local Flow Angularity

Fuselage 3
PCPN
Mach Number = 1.8
$\alpha = 0°$
Format I

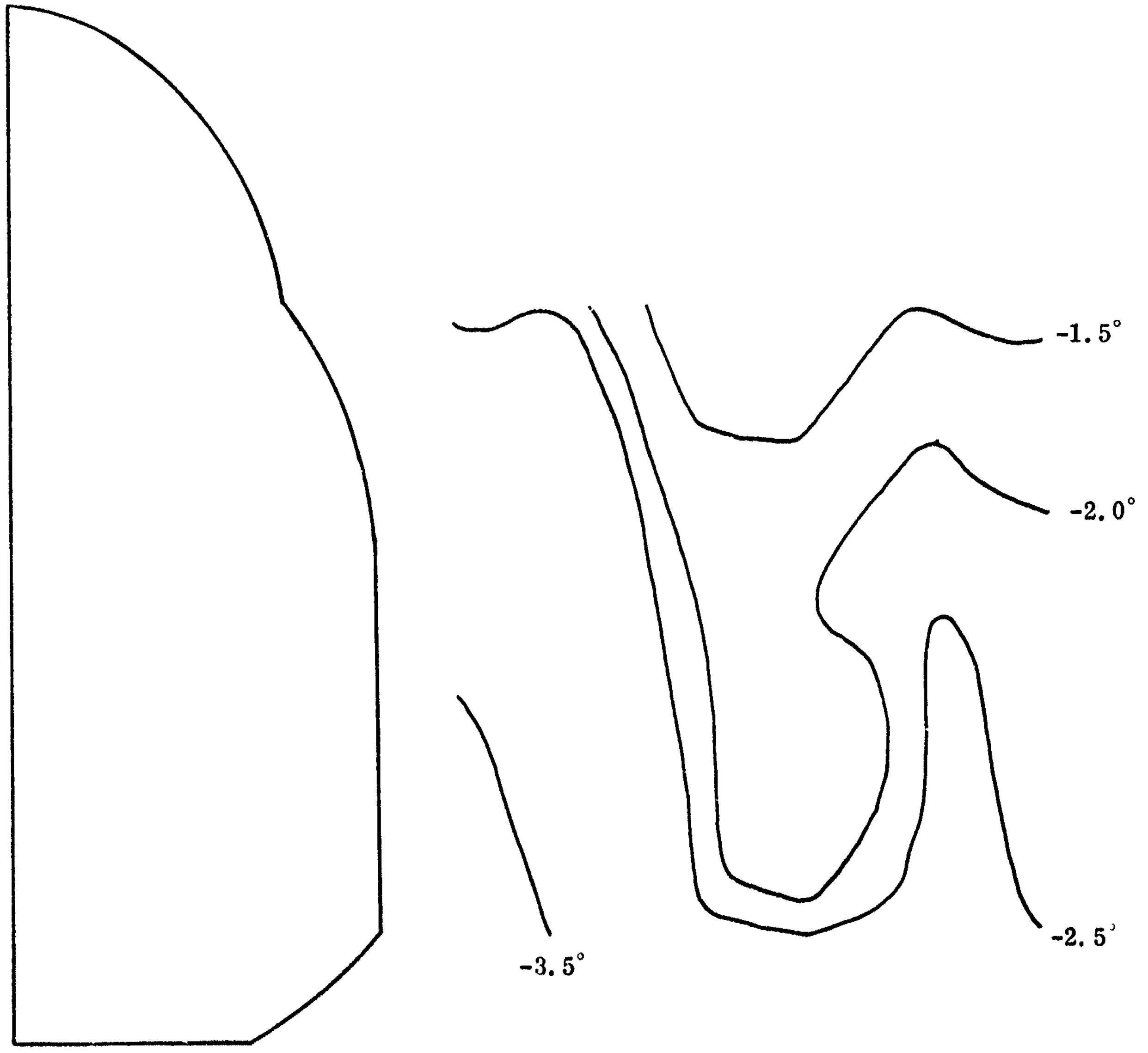

Figure 7-33. Local Flow Angularity

Fuselage 3
PCSN
Mach Number = 1.8
$\alpha = 0°$
Format I

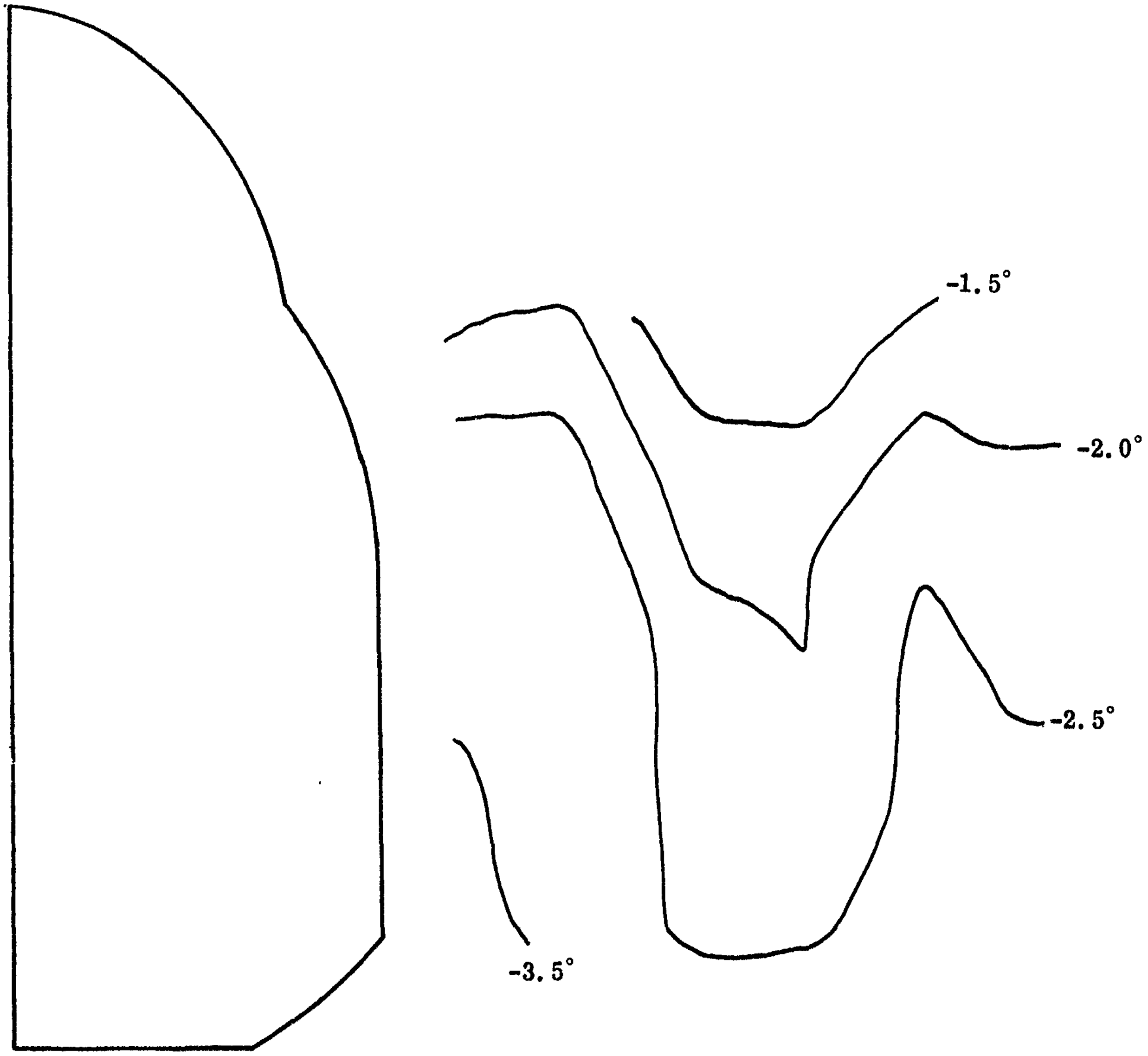

Figure 7-34. Local Flow Angularity

Fuselage 3

SCPN

Mach Number = 1.8

$\alpha = 0°$

Format I

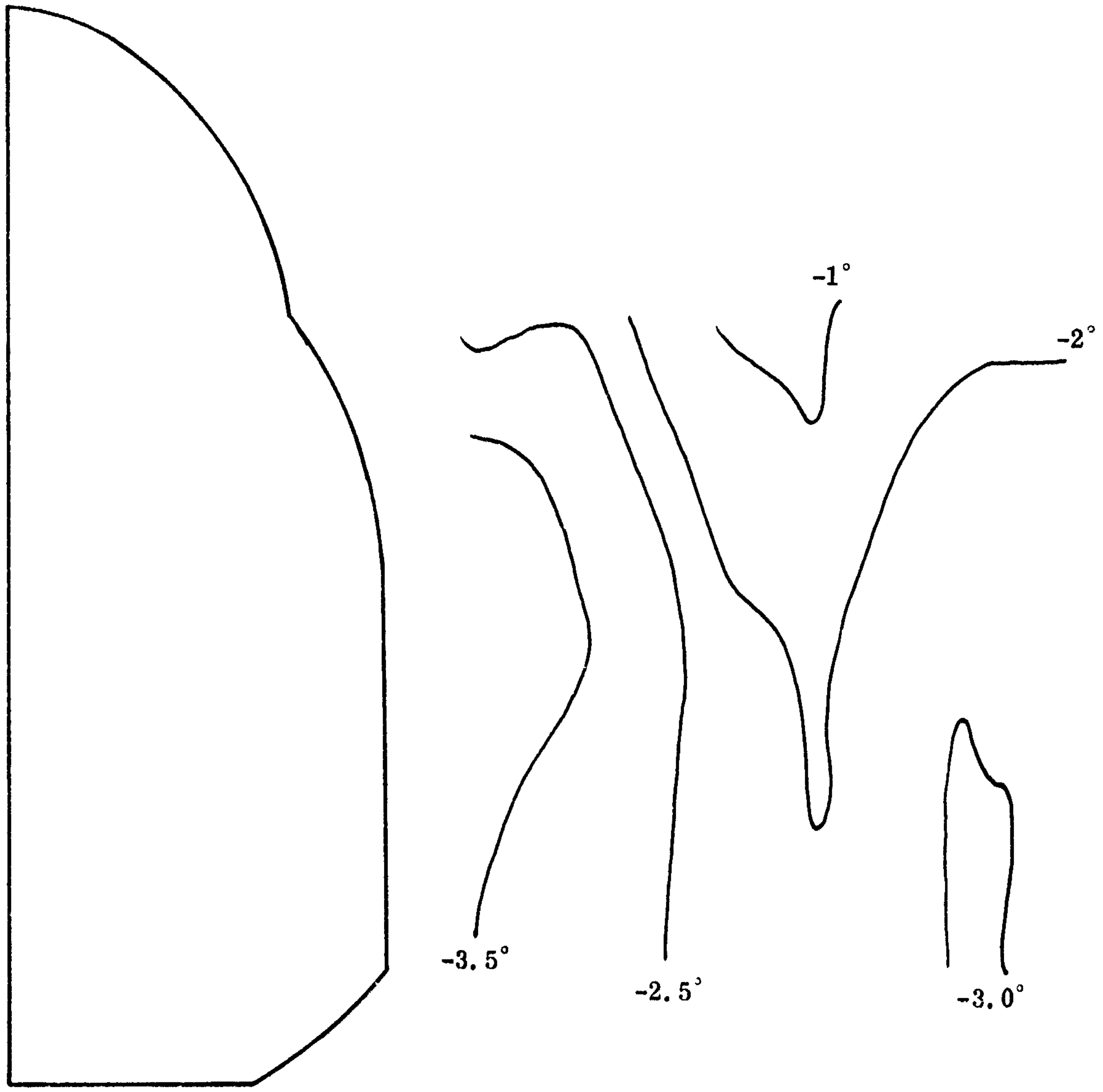

Figure 7-35. Local Flow Angularity

Fuselage 3
SCSN
Mach Number = 1.8
$\alpha = 0°$
Format I

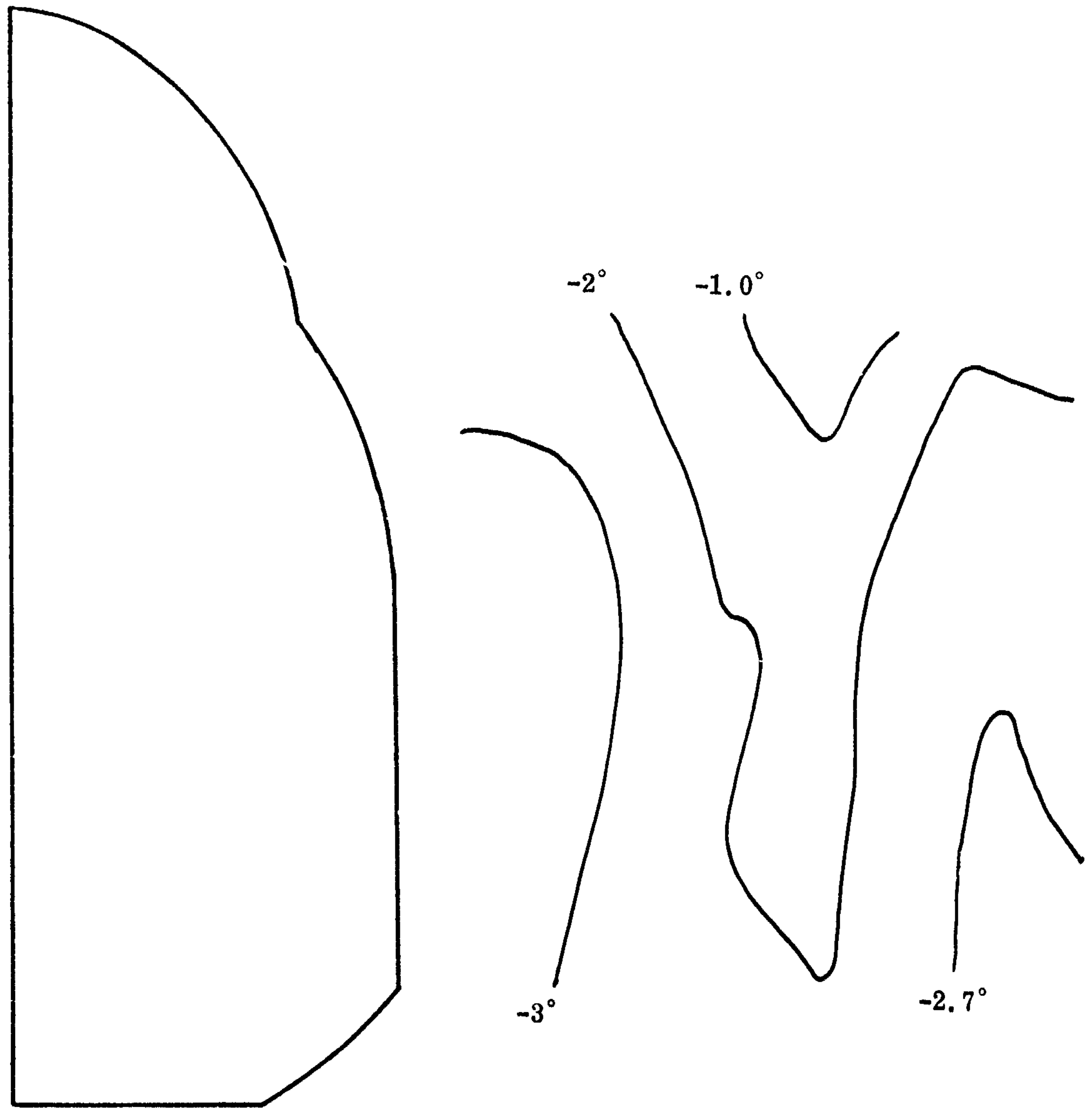

Figure 7-36. Local Flow Angularity

Fuselage 3
PCPN
Mach Number = 1.8
$\alpha = 15°$
Format I

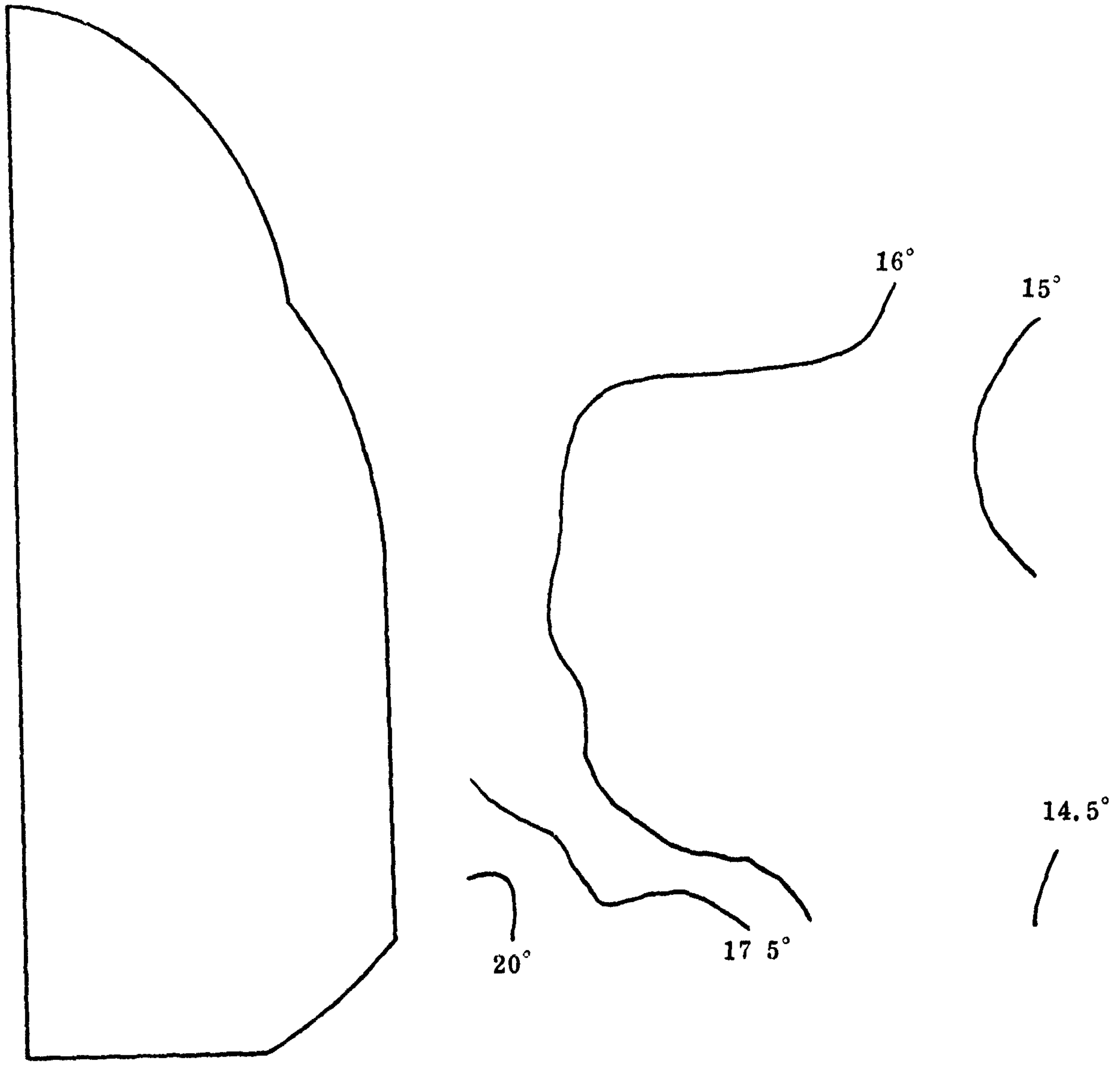

Figure 7-37. Local Flow Angularity

Fuselage 3

PCSN

Mach Number = 1.8

α = 15°

Format I

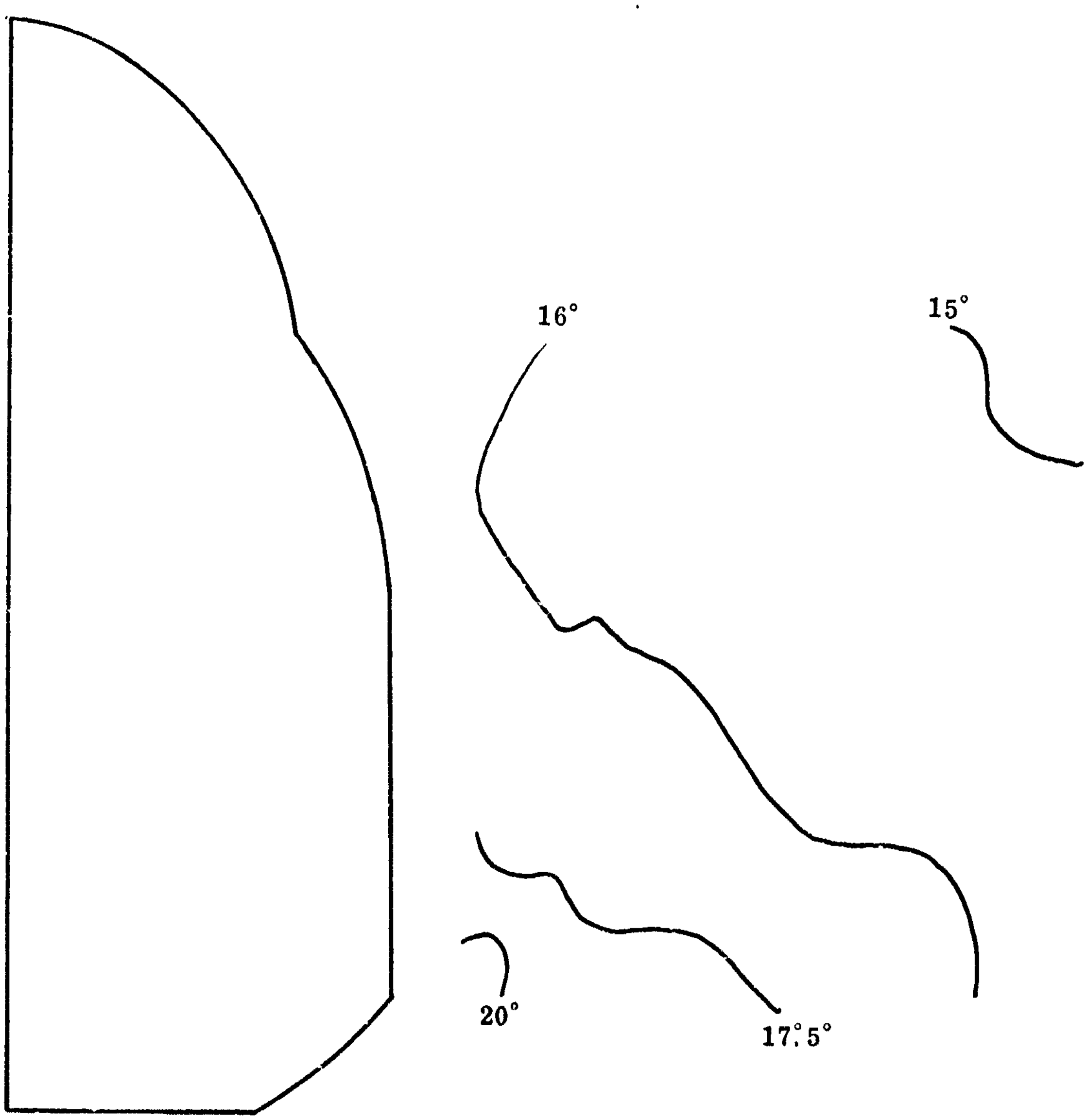

Figure 7-38. Local Flow Angularity

Fuselage 3
SCPN
Mach Number = 1.8
$\alpha = 15^\circ$
Format I

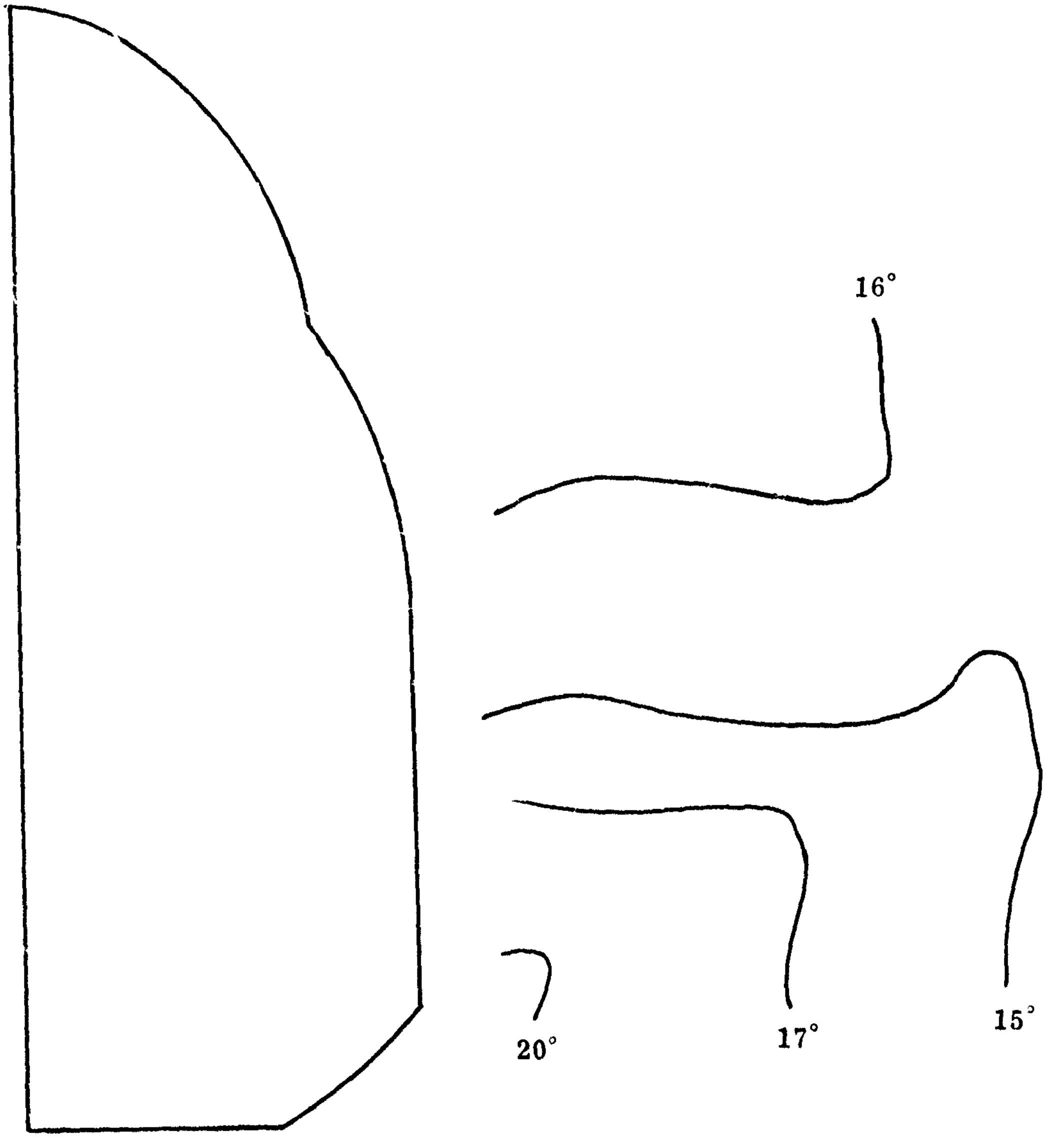

Figure 7-39. Local Flow Angularity

Fuselage 3
SCSN
Mach Number = 1.8
$\alpha = 15°$
Format I

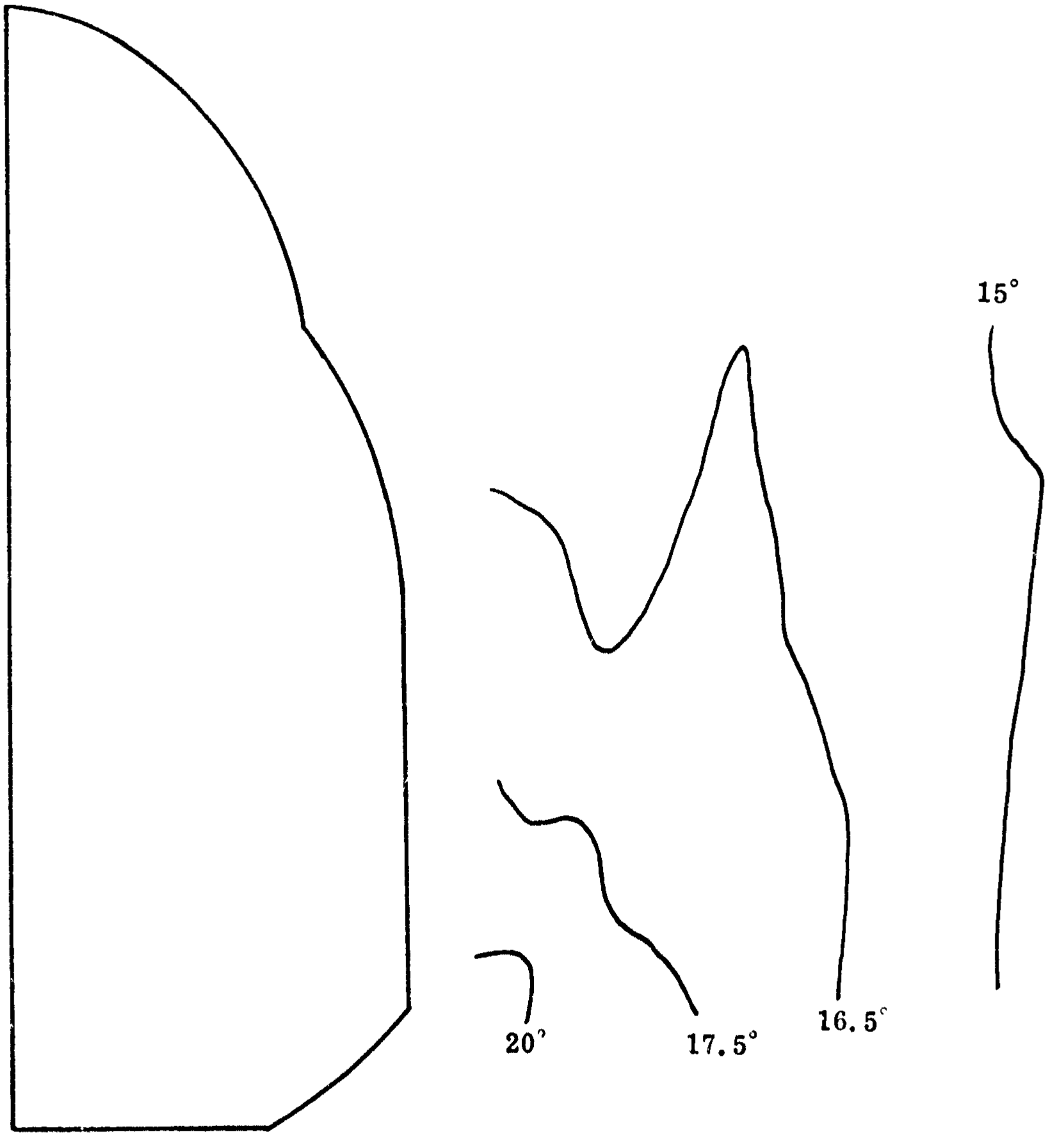

Figure 7-40. Local Flow Angularity

Fuselage 3
SCSN
Mach Number = 0.8
α = 0°

Format I

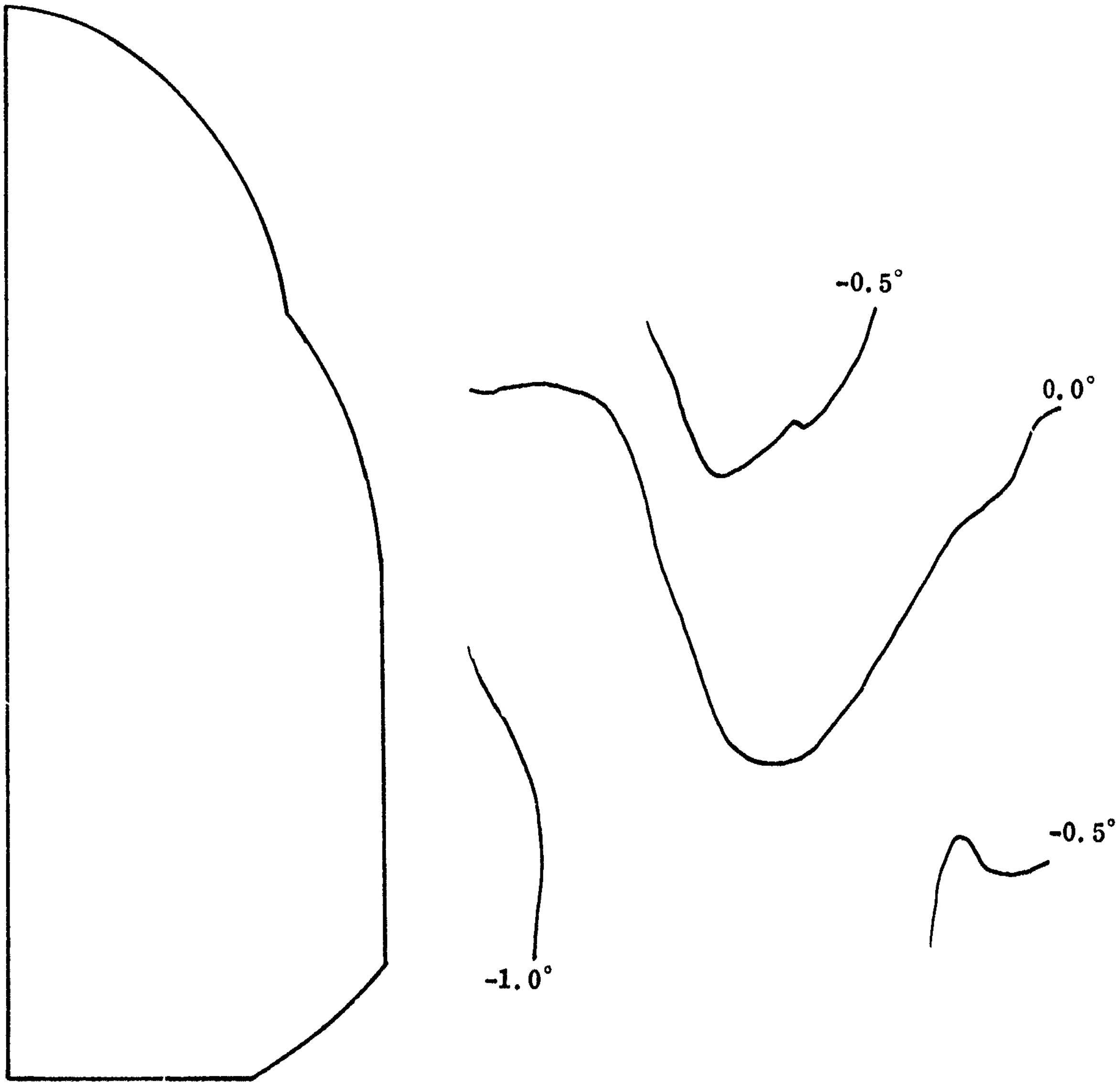

Figure 7-41. Local Flow Angularity

Fuselage 3
SCSN
Mach Number = 0.8
$\alpha = 10°$

Format I

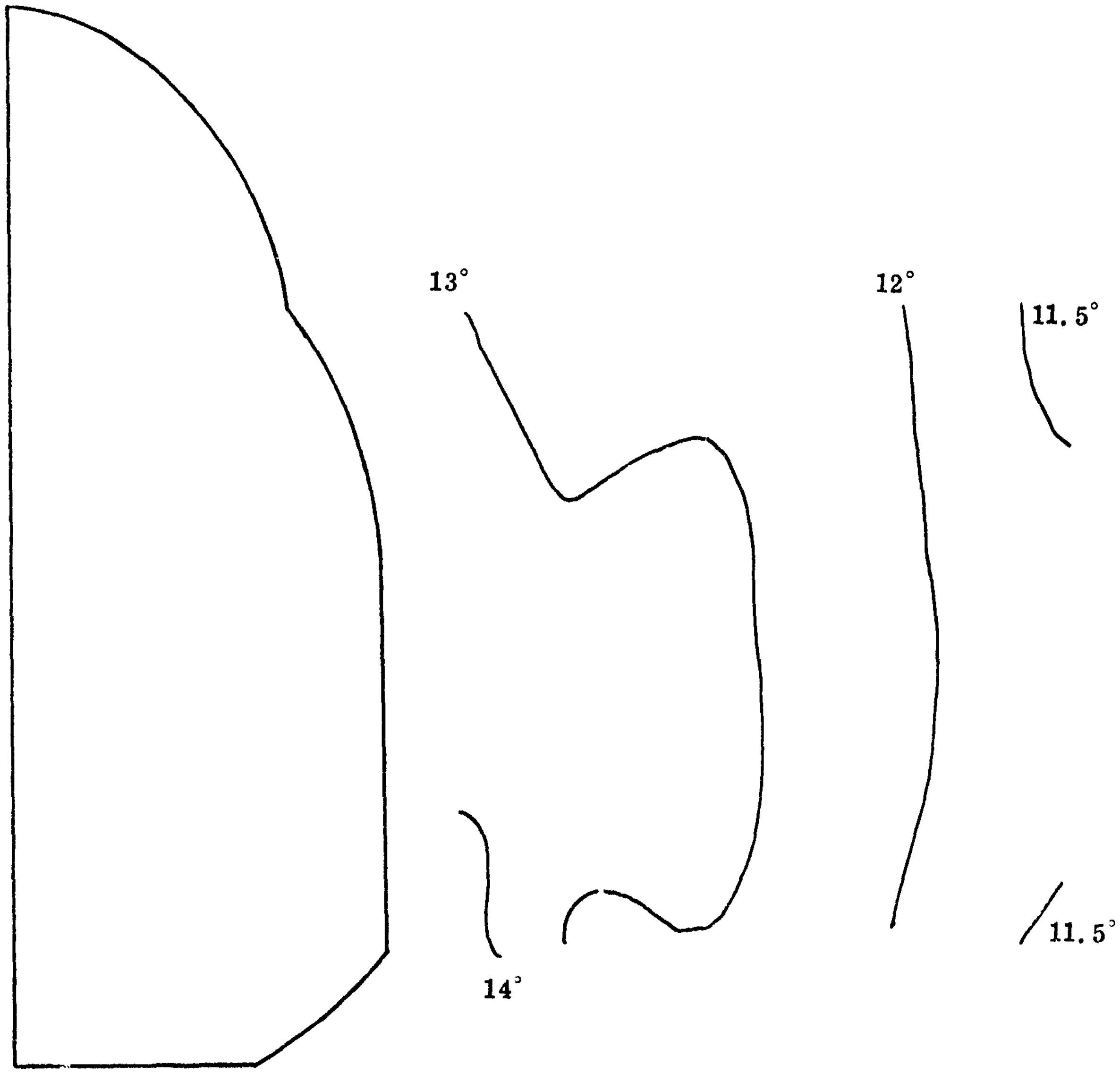

Figure 7-42. Local Flow Angularity

Fuselage 3
SCSN
Mach Number = 0.8
$\alpha = 20^\circ$
Format I

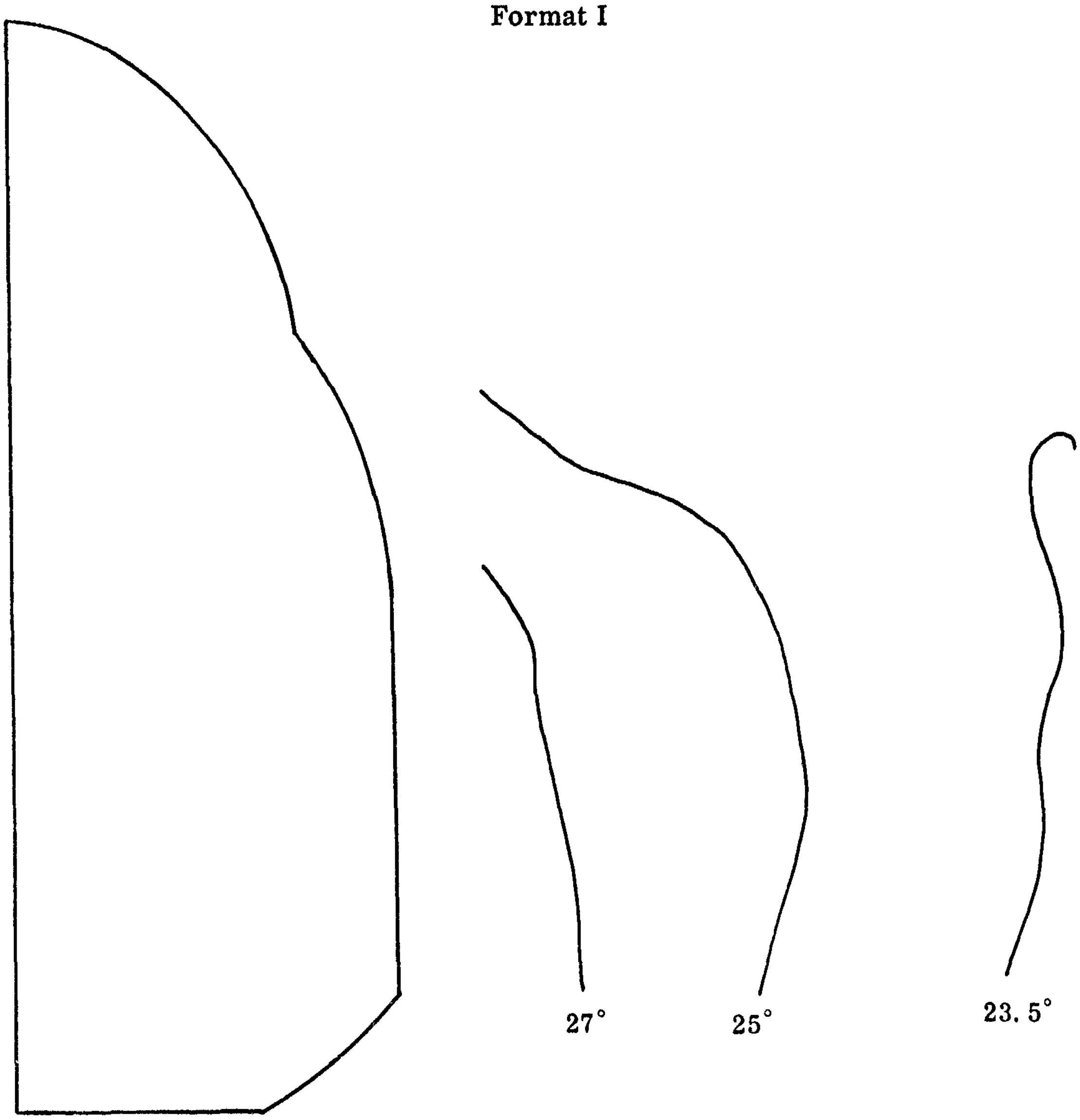

Figure 7-43. Local Flow Angularity

Fuselage 2

PCPN

Mach Number = 0.8

$\alpha = -3°$

Format I

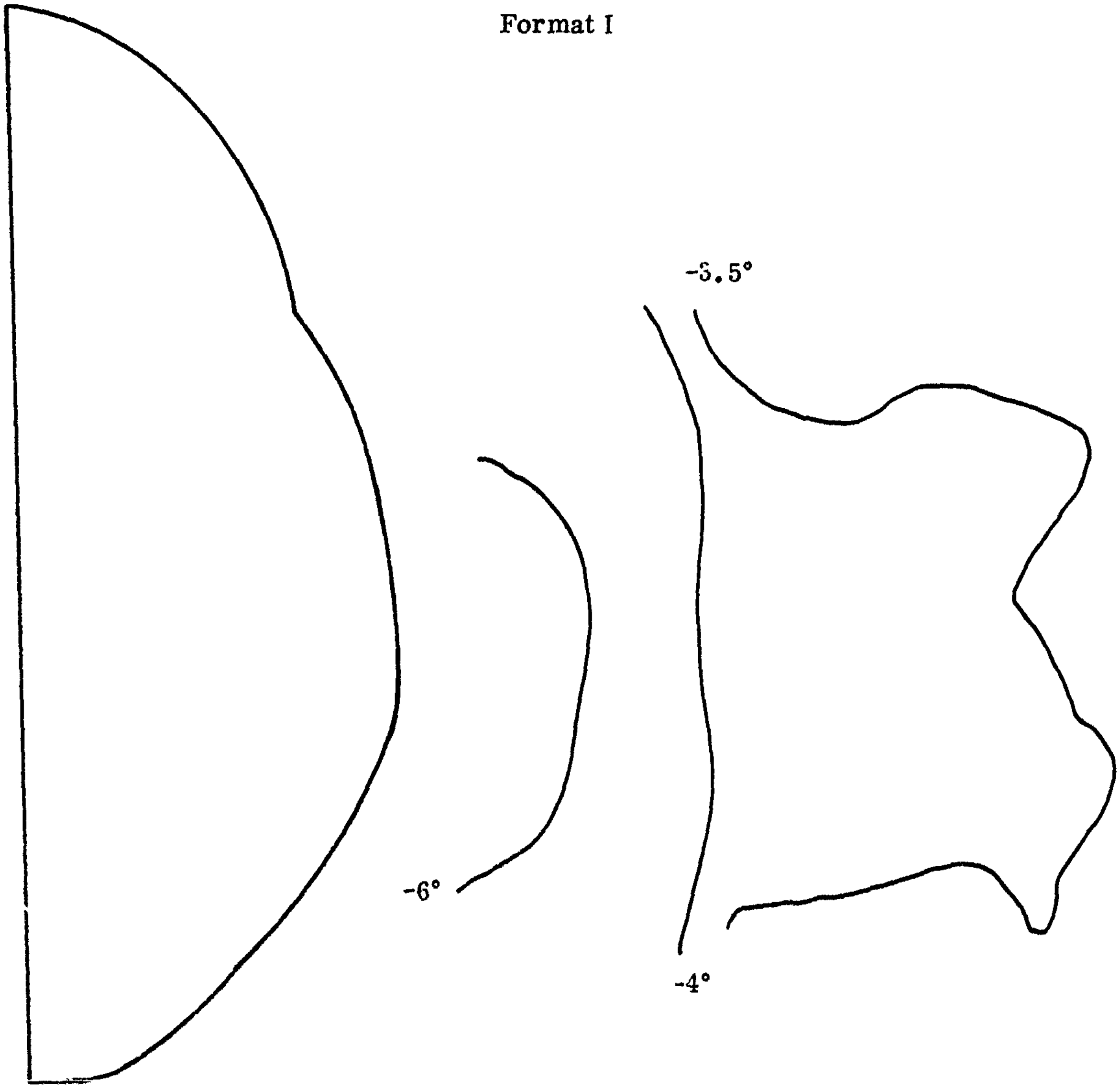

Figure 7-44. Local Flow Angularity

Fuselage 6
PCPN
Mach Number = 0.8
$\alpha = -3°$
Format I

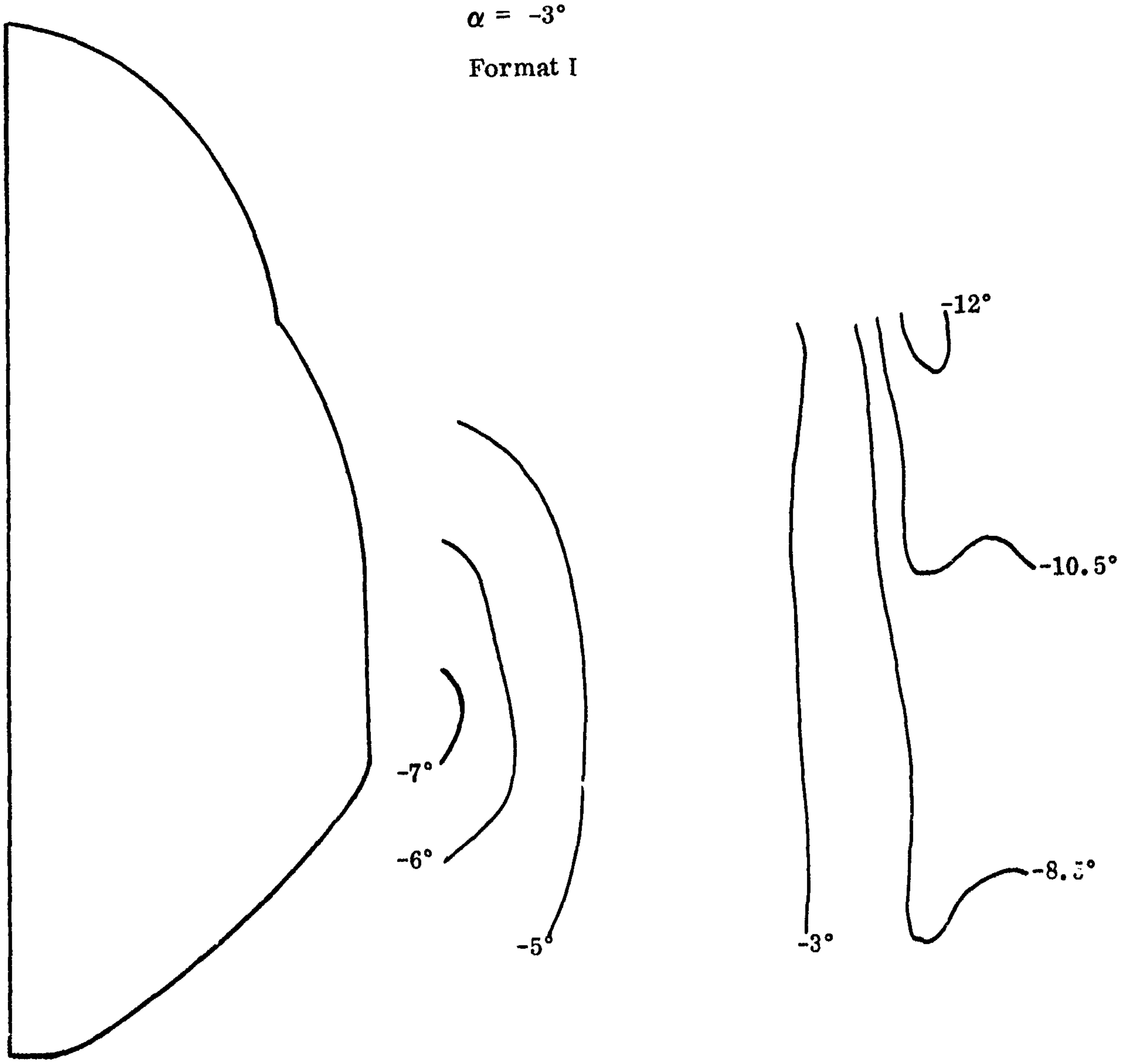

Figure 7-45. Local Flow Angularity

present on fuselage 6. This conclusion appears to be supported by an examination of the sidewash data. As shown in Figure 7-46 a large positive sidewash zone occupies a region near the fuselage corner, for fuselage 6. For the remaining fuselages at this flight condition the sidewash is generally negative except in the region of the fuselage corner where a small positive sidewash zone is induced by the favorable pressure gradient. The extent of the positive sidewash region varys somewhat with corner radius and corner development. The sidewash map for fuselage 1 is presented in Figure 7-48. A comparison of Figures 7-46 and 7-48 illustrates the impact of corner development rate.

At zero angle of attack a mixed flow field exists. The inherent downwash over the drooped nose is still present, particularly in the lower inboard region of the flow field. However, the flow acceleration over the canopy has induced local regions of upwash throughout the field, with the location and extent seen to be a function of fuselage geometry. For those fuselages of the small corner radius class (1, 3, and 5) the downwash sink set up by the drooped nose and fuselage corner is rigidly segregated from the main flow by virtue of the abrupt discontinuity in pressure around the corner. With these fuselages the flow expansion around the canopy has less opposition from the inherent downwash and consequently the upwash effect is more extensive than for the large corner radius configurations where the upwash and downwash interact quickly. This effect can be seen by comparing Figure 7-48 and 7-49 presenting the local flow angularity for fuselages 1 and 4 respectively. The sidewash characteristics display an insensitivity to angle of attack and appear similar to those characteristics at negative angle of attack.

At five (5) degrees angle of attack the nose is still slightly drooped but the flow field over the vehicle nose is approaching a symmetric condition. However, the canopy expansion flow field has induced a general upwash for all fuselages. The flow fields are quite uniform and similar. A typical map of flow angularity is presented in Figure 7-50, for fuselage 2. The lone exception to similarity is again fuselage 6 where an outboard downwash region exists. In this case, again, the low fuselage height factor (h/H) plus the rapid corner development tend to cancel the canopy induced upwash about midway outboard of the survey plane. Consequently, the outboard portion of the flow feels the small inherent downwash generated by the nose. The flow field sidewash gradient is generally negative with the small corner radius configurations

Fuselage 6
PCPN
Mach Number = 0.8
$\alpha = -3°$

Format I

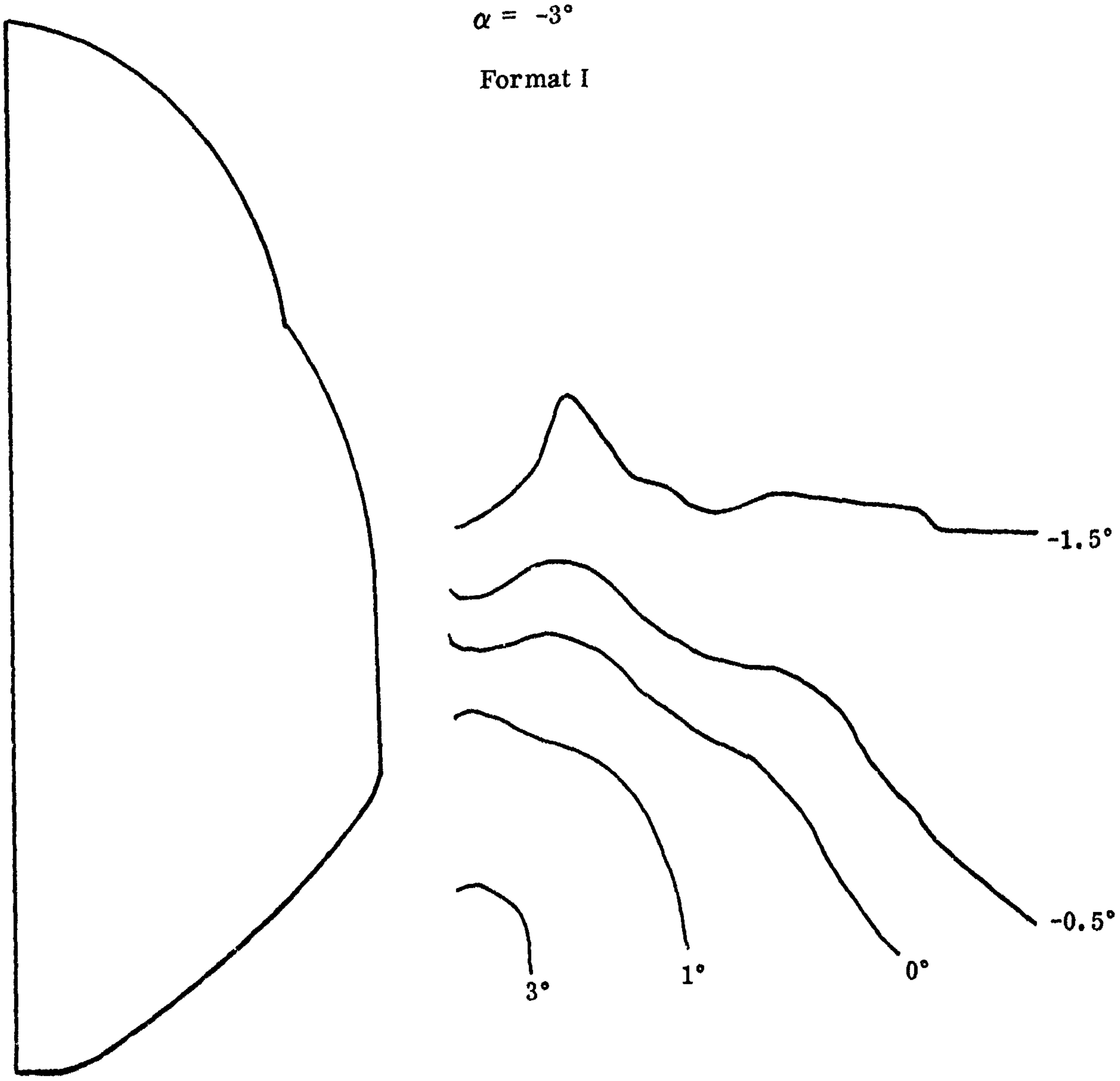

Figure 7-46. Local Sidewash Angularity

Fuselage 2
PCPN
Mach Number = 0.8
α = -3°

Format I

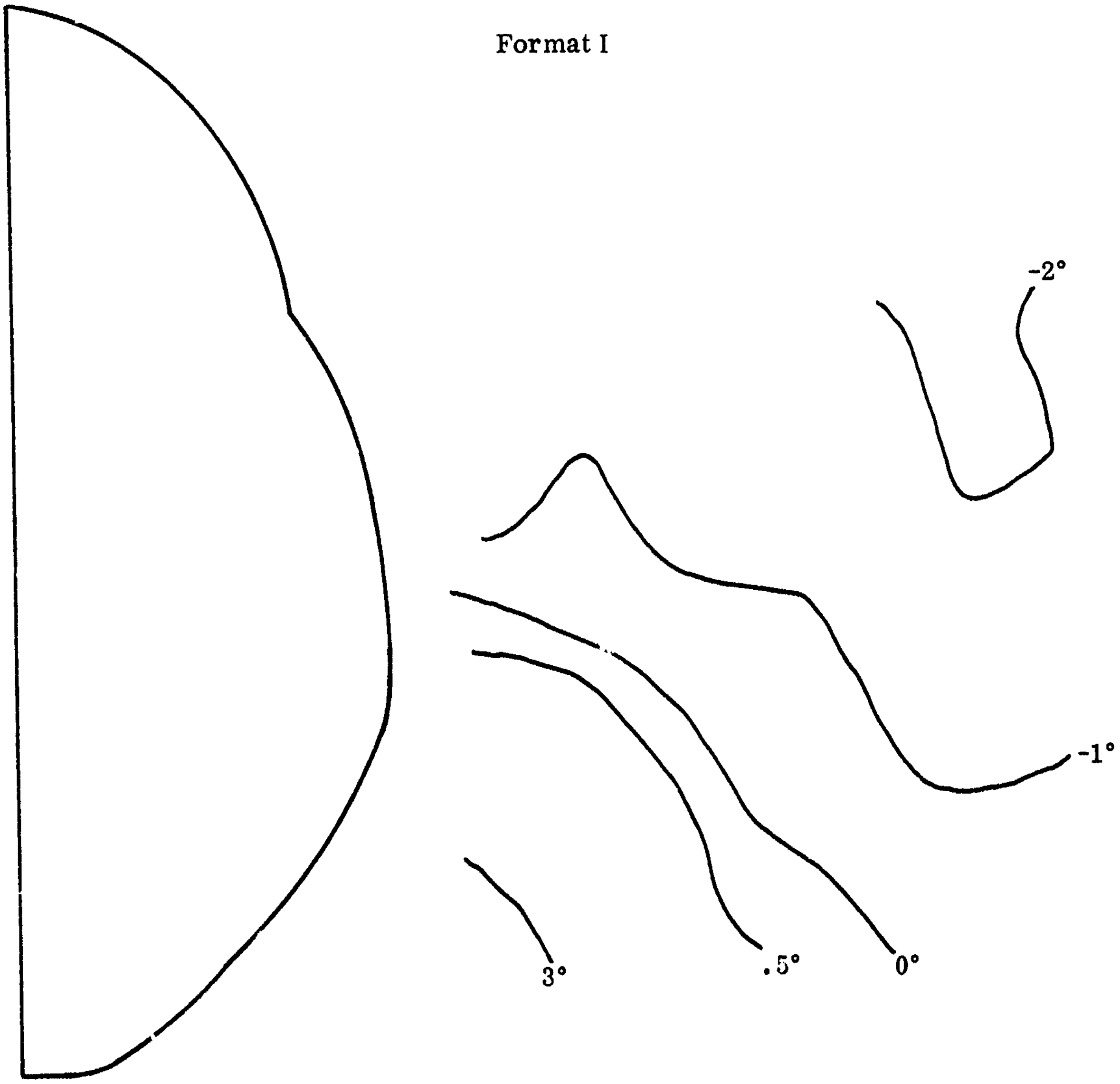

Figure 7-47. Local Sidewash Angularity

Fuselage 1
PCPN
Mach Number = 0.8
α = 0°
Format I

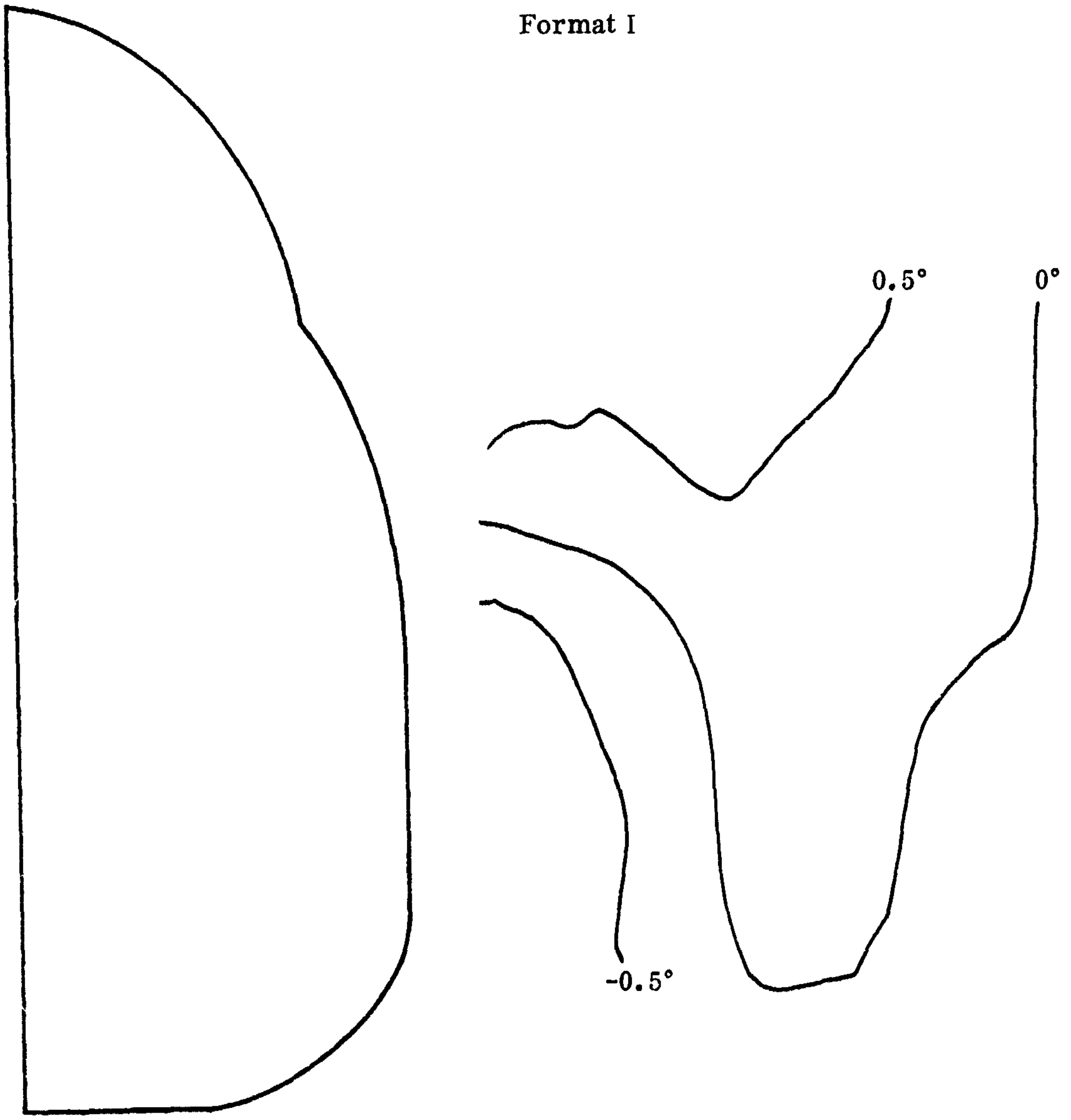

Figure 7-48. Local Flow Angularity

Fuselage 4
PCPN
Mach Number = 0.8
$\alpha = 0°$

Format I

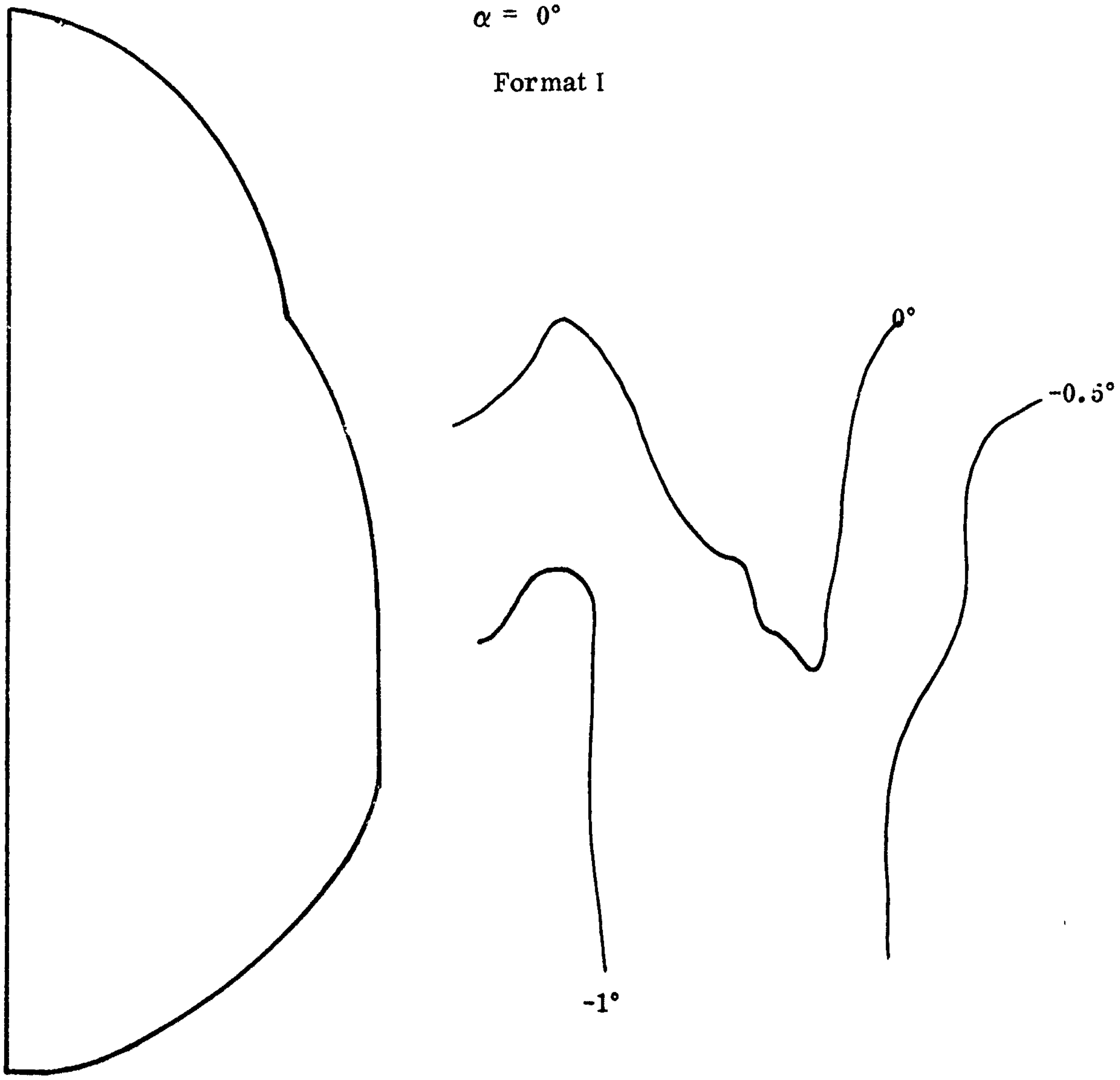

Figure 7-49. Local Flow Angularity

Fuselage 2
PCPN
Mach Number = 0.8
$\alpha = 5°$
Format I

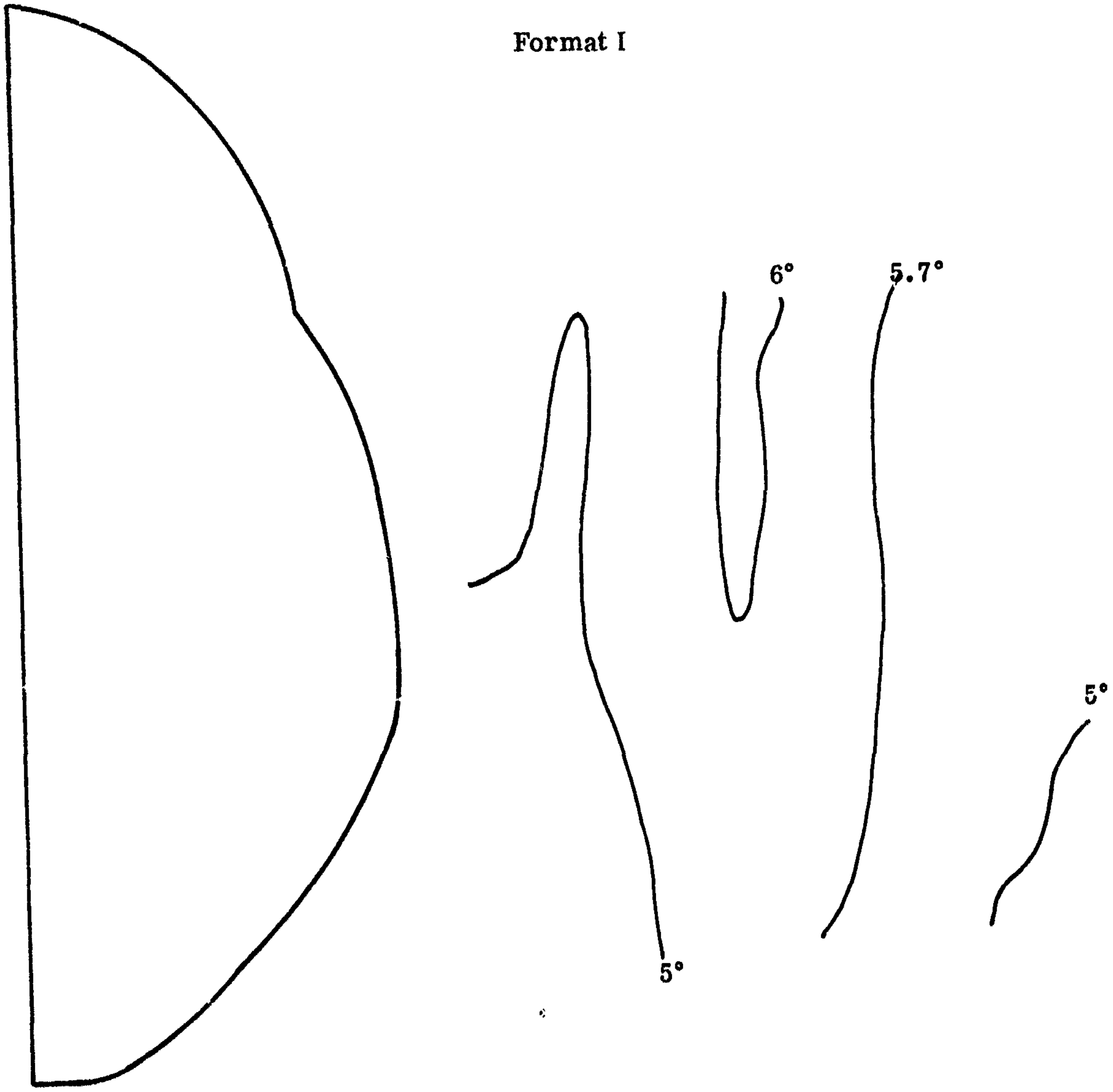

Figure 7-50. Local Flow Angularity

generating locally accentuated regions because of the higher local pressure gradient at the corner.

For angles of attack of +10°, +15°, and +20° a general upwash condition exists for all fuselages. The flow fields appear to be composed of 3 basic regions, the first is a high upwash region inboard, established by the expansion around the fuselage corner and canopy. The upwash decays radially such that an average upwash exists in the middle of the flow field and a low upwash region exists in the outboard portion of the flow field. This general condition is seen in Figures 7-51 through 7-53, presenting the local flow angularity for fuselage 2 at these 3 angles of attack. While the flow fields for all fuselages are basically similar there is a slight tendency for increasing fuselage corner radius to improve the overall uniformity of the flow field. This effect can be seen by comparing Figure 7-54 which displays the local flow angularity for fuselage 1 (a small corner radius configuration) at 10° angle of attack with 7-51 for fuselage 2 (a large corner radius configuration).

The sidewash is quite insensitive at these angles of attack and remains essentially constant. The sidewash is, in general, negative except in the upper inboard section of the survey plane where the expanding flow field around the canopy draws the flow toward the body.

7.1.3.2 Mach 1.2

For the negative angle of attack case (α = -3°) the nose droop is seen as having an important effect upon flow angularity. For those configurations having a small corner radius, and consequently a segregation of the flow field along the side of the fuselage from that along the bottom of the fuselage, the flow acceleration around the canopy induces local regions of upwash. As the fuselage corner radius is increased, increasing the interaction between side and bottom flow fields, the inherent downwash tendency, fostered by the negative angle of attack and the drooped nose prevails, and a general downwash condition exists. This difference in flow field structure, as a function of fuselage geometry, is essentially the same as previously seen at Mach 0.8. An illustration is presented in Figures 7-55 and 7-56 presenting the local flow angularity for fuselages 4 and 5 respectively. The sidewash profiles are quite similar to those obtained at Mach 0.8 with the field comprised of three basic zones. There is one region of relatively high negative sidewash due to

Fuselage 2
PCPN
Mach Number = 0.8
α = 10°
Format I

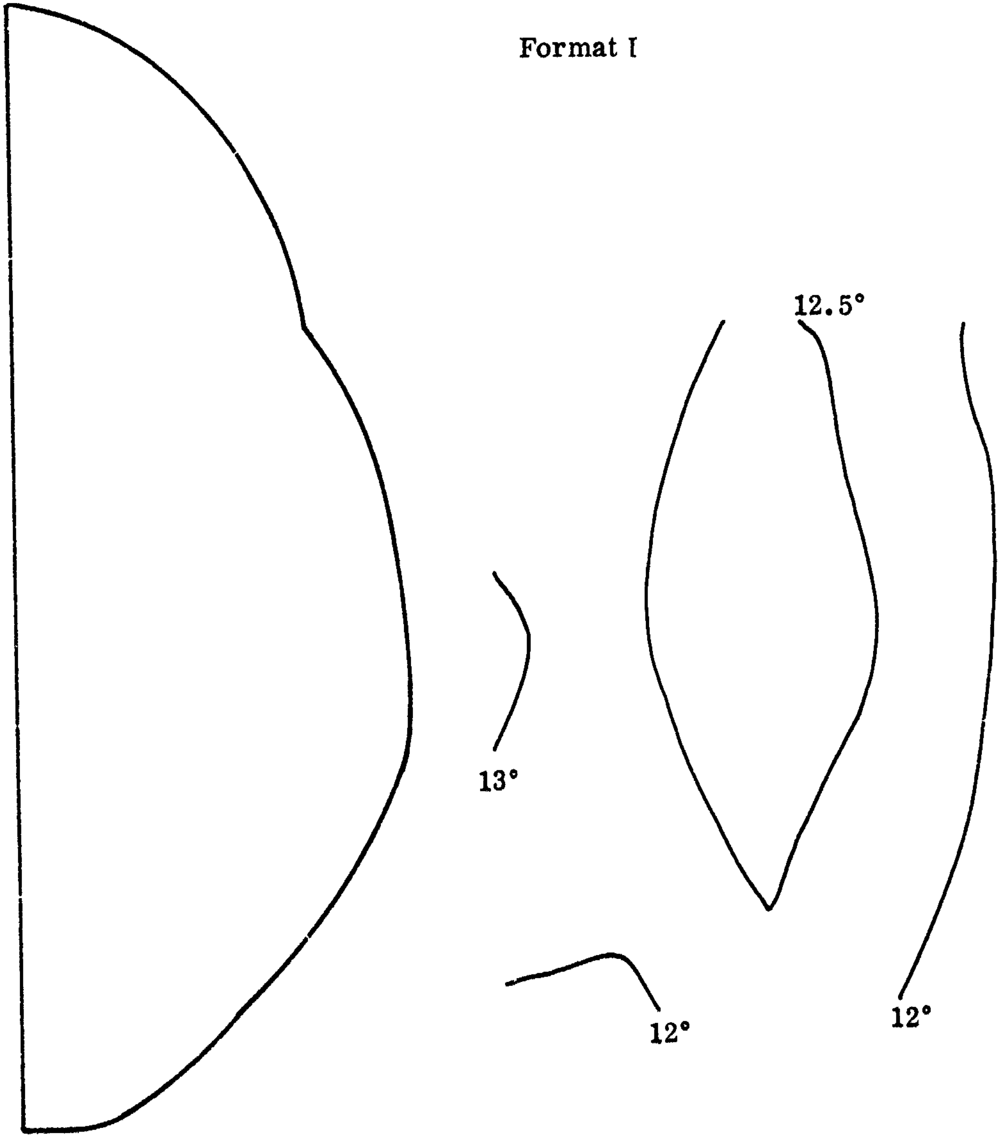

Figure 7-51. Local Flow Angularity

Fuselage 2
PCPN
Mach Number = 0.8
α = 15°

Format I

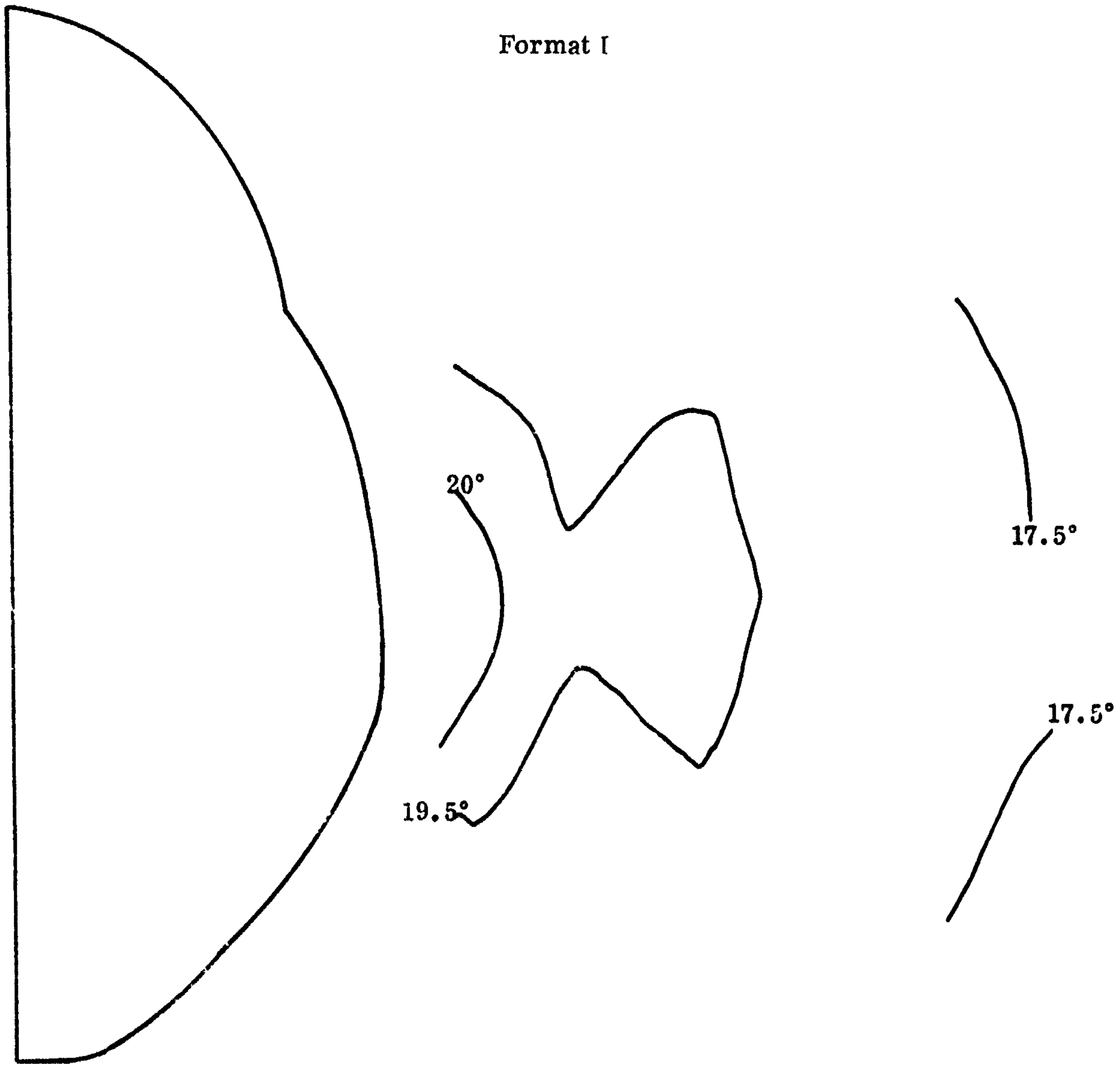

Figure 7-52. Local Flow Angularity

Fuselage 2
PCPN
Mach Number = 0.8
α = 20°
Format I

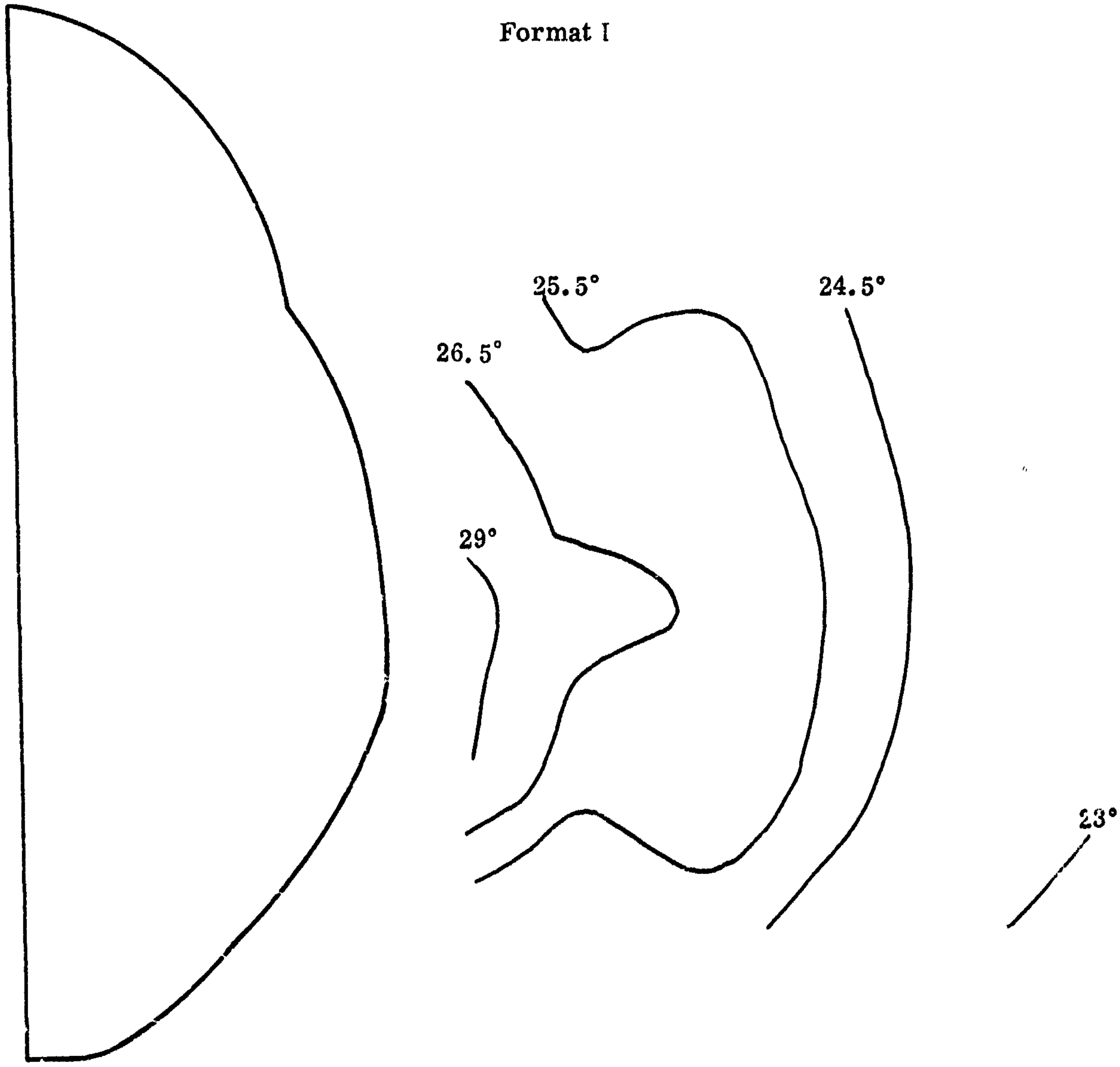

Figure 7-53. Local Flow Angularity

Fuselage 1
POPN
Mach Number = 0.8
α = 10°

Format I

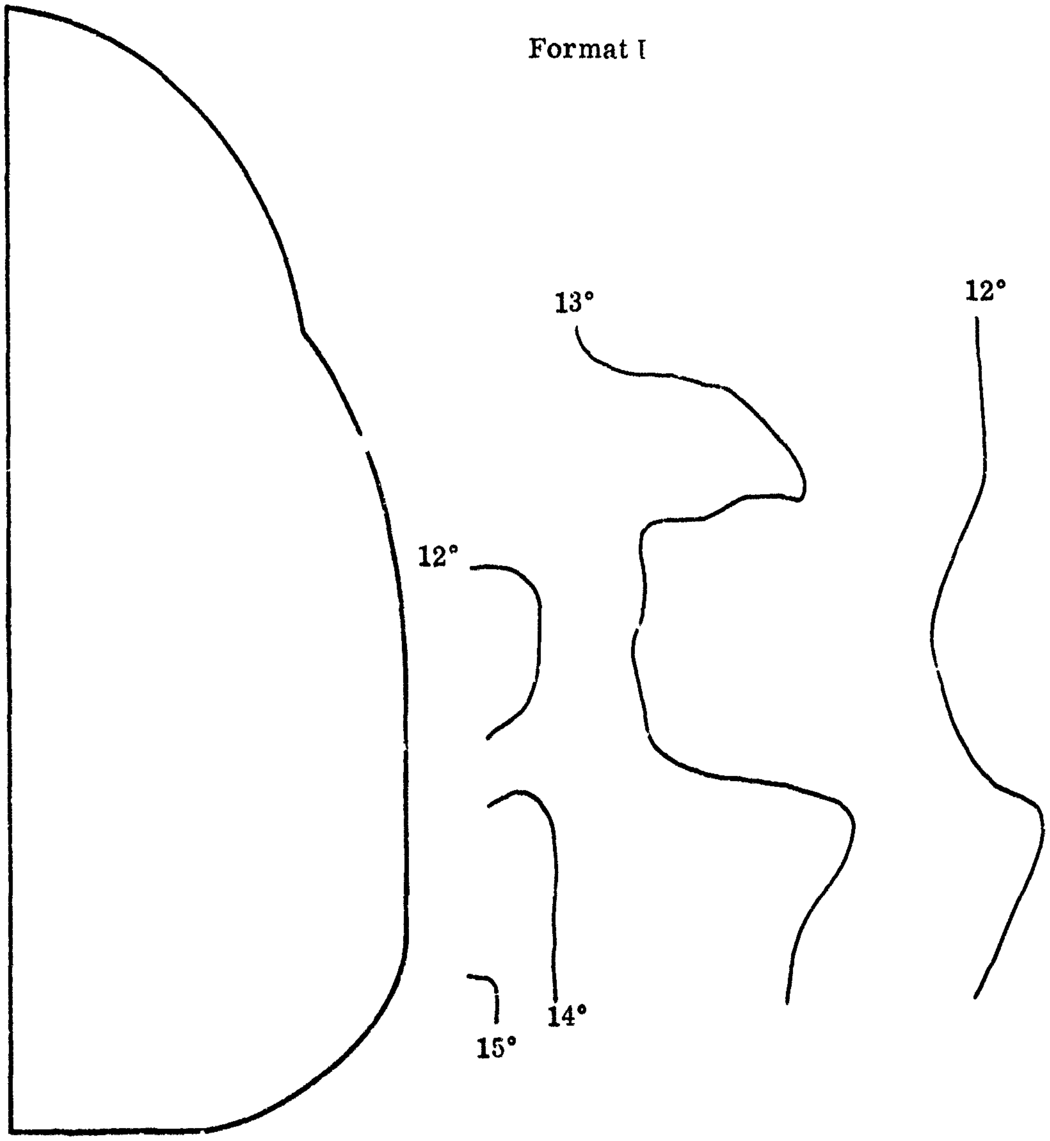

Figure 7-54. Local Flow Angularity

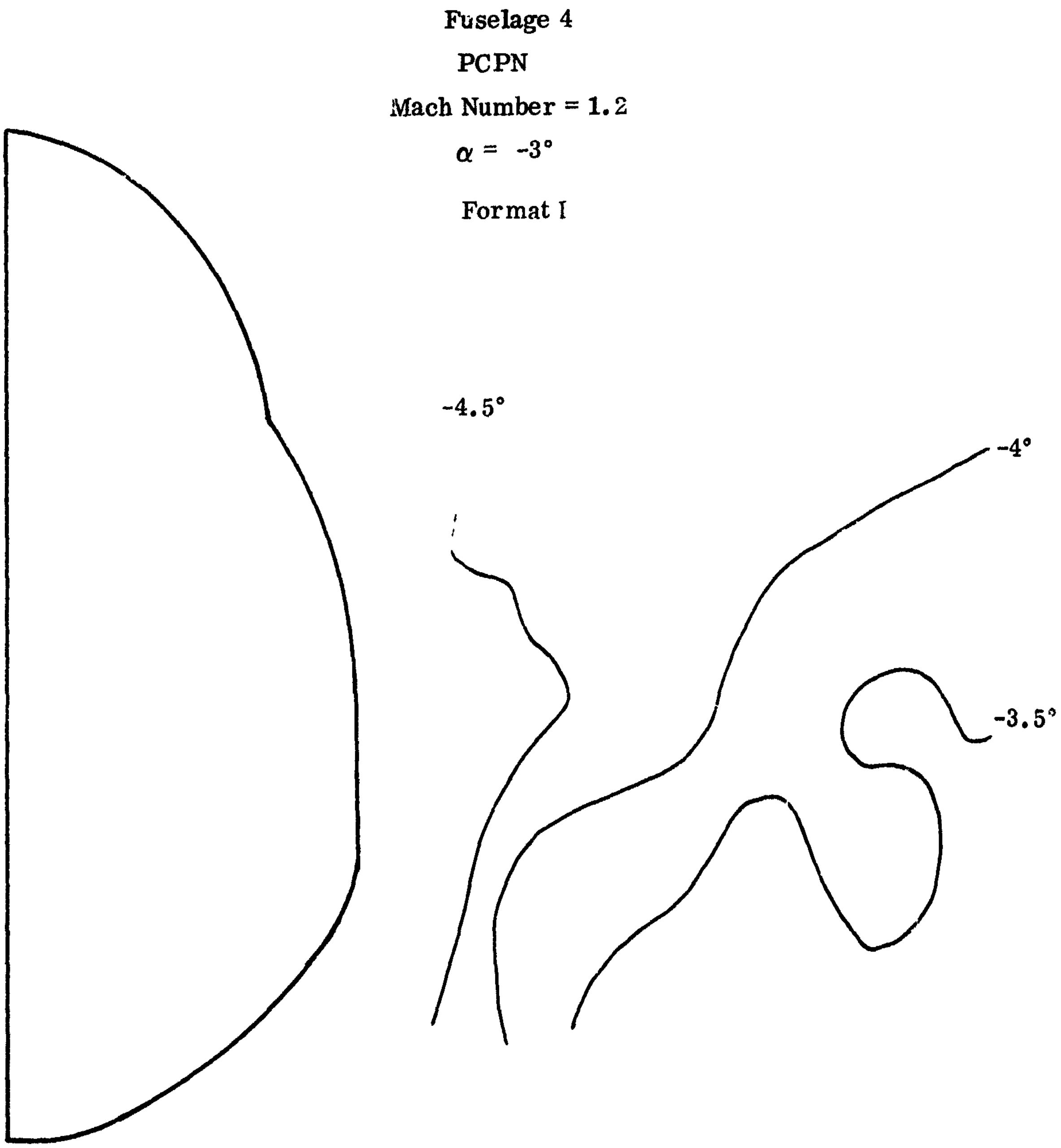

Fuselage 4
PCPN
Mach Number = 1.2
$\alpha = -3°$
Format I

Figure 7-55. Local Flow Angularity

Fuselage 5
PCPN
Mach Number = 1.2
α = -3°
Format I

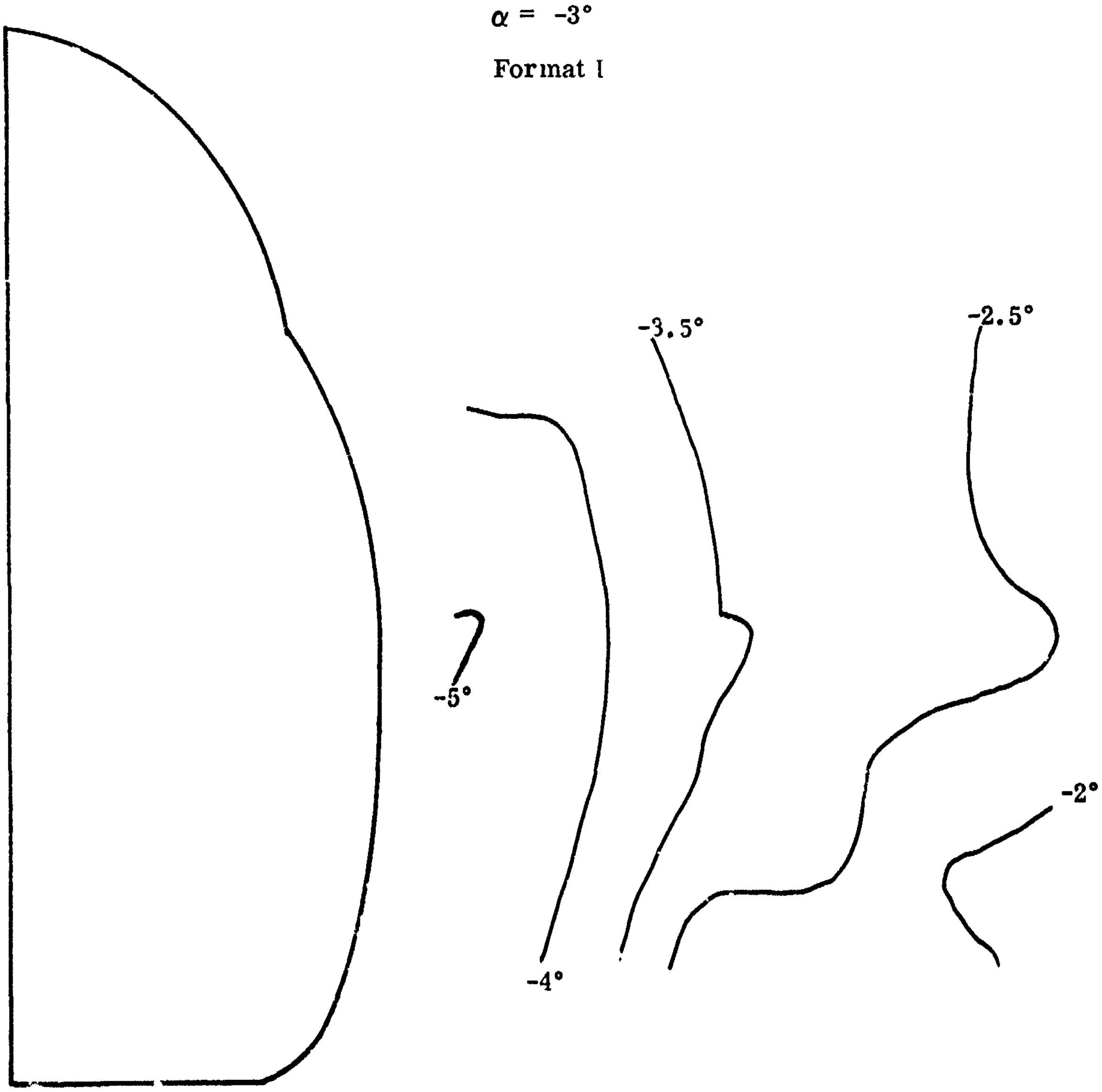

Figure 7-56. Local Flow Angularity

the presence of the canopy which forces a local outward flow. There is also an average negative sidewash region within which the flow has a small outward vector due simply to its travel around the fuselage. Finally, positive sidewash occupies a region focused at the lower and inboard portion of the survey plane. The extent of this region varies directly with fuselage corner radius, an expected result.

Increasing the vehicle angle of attack to zero weakens the tendency toward downwash. The smaller corner radii produce local zones of upwash and, in some cases, an overall upwash flow field (based upon an arithmetical averaging of the 30 data points comprising each map). The difference between large and small corner radii effects can be seen in Figures 7-57 and 7-58 presenting the local flow angularity for fuselages 1 and 2 respectively. The comparison shows that larger corner radii encourage downwash, as they did at negative angle of attack.

At 5° angle of attack the flow field generated by the fuselage nose is approaching the symmetrical case. The weakened inherent downwash plus the canopy induced low pressure produces an upwash condition throughout the inboard portion of the flow field. The upwash condition also occupies the outboard portion of the flow field for those configurations with fuselage corners that are well rounded. These effects are illustrated in Figure 7-59, presenting the flow angularity for fuselage 4. For those configurations with small corner radii and/or a rapid local development of the corner, the upwash gradient is spent over the inboard portion of the flow field. This permits the small inherent downwash to prevail over the outboard portion of the flow field, for those configurations. Figure 7-60 shows this effect, using fuselage 3 as an example. The sidewash remains an insensitive parameter, at this angle of attack, with a small negative vector generally present. This continues to be the case throughout the angle of attack range with the sidewash flow field of individual configurations virtually unaffected by variations in angle of attack. The zonal structure of these flow fields appears to be only configuration dependent. The average value of the negative sidewash appears to increase very slightly with angle of attack, for all configurations. This is due to the increasing pressure gradient from the bottom to the top of the fuselage.

For angles of attack of 10° and above an overall upwash condition exists for all configurations. There is, in fact, a striking similarity among the flow fields, generated by all configurations, in this angle of attack range. In general the upwash

Fuselage 1
PCPN
Mach Number = 1.2
$\alpha = 0°$

Format I

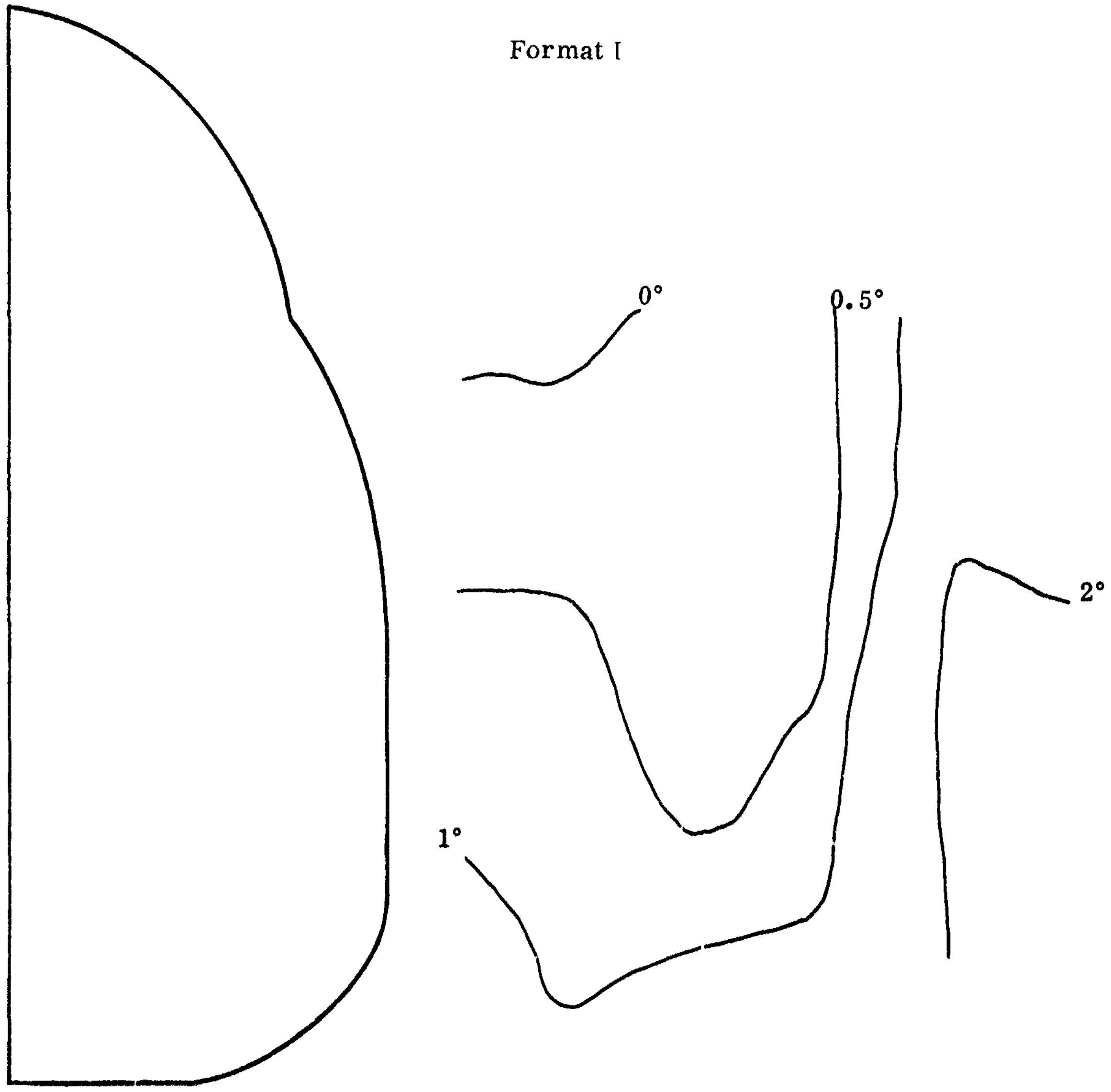

Figure 7-57. Local Flow Angularity

Fuselage 4
PCPN
Mach Number = 1.2
$\alpha = 0°$

Format I

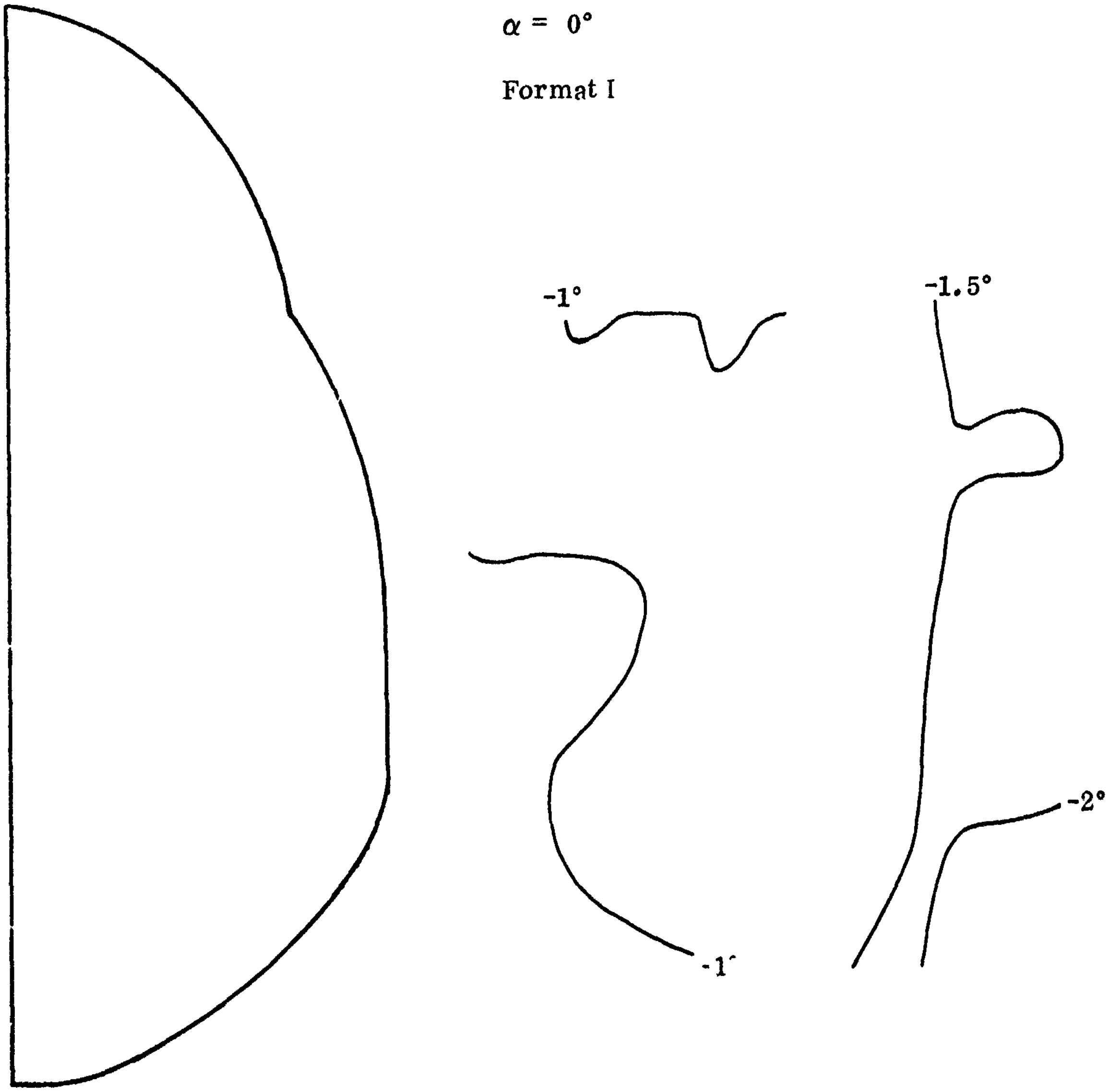

Figure 7-58. Local Flow Angularity

Fuselage 4
PCPN
Mach Number = 1.2
$\alpha = 5°$
Format I

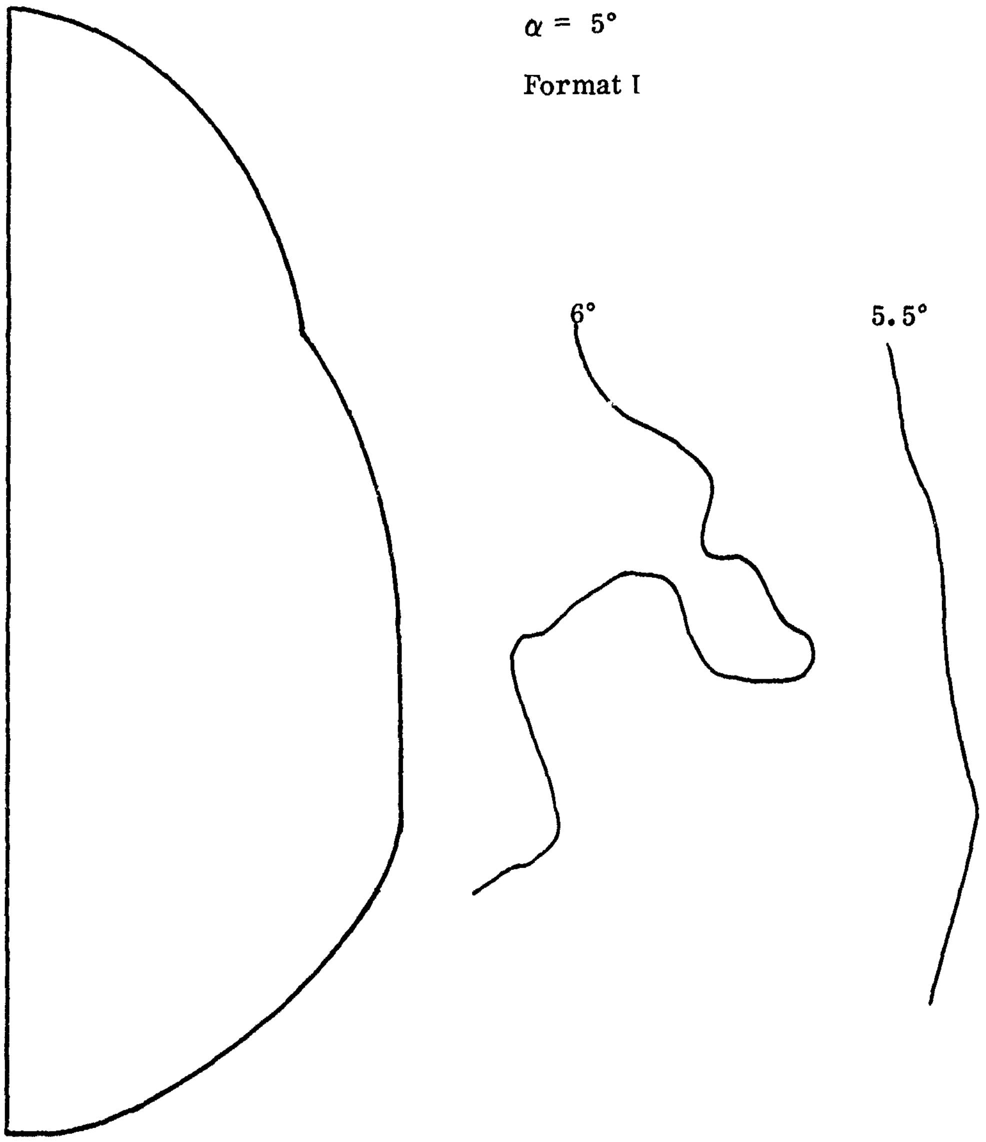

Figure 7-59. Local Flow Angularity

Fuselage 3
PCPN
Mach Number = 1.2
α = 5°
Format I

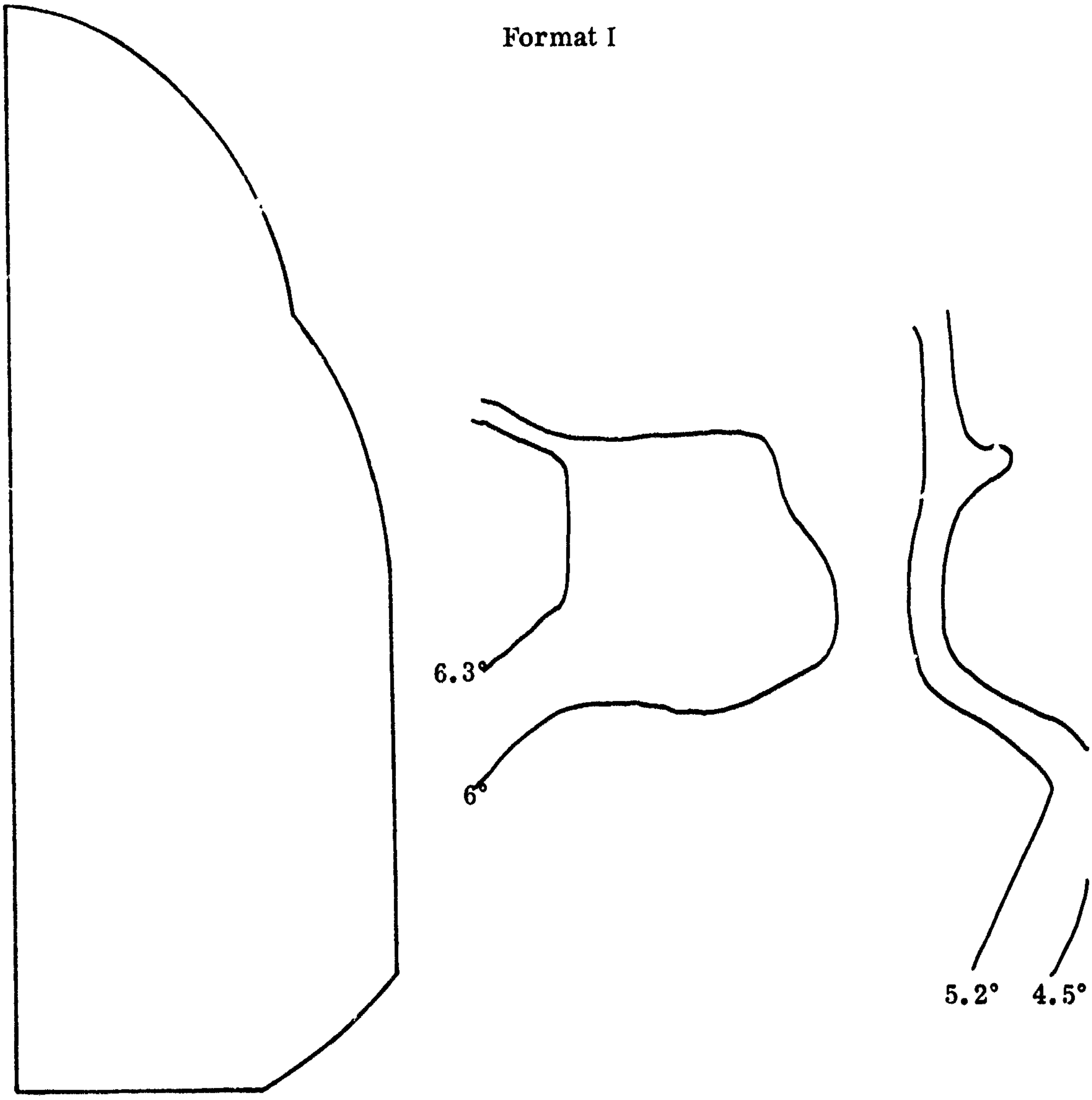

Figure 7-60. Local Flow Angularity

dissipates as a function of distance from the fuselage. This produces a 3 zone flow field with relatively high upwash within the inboard portion of the survey plane, an average upwash in the middle of the survey plane and a relatively low upwash outboard. An examination of the data indicates that an increase in fuselage corner radius tends to reduce the level of upwash and to make the flow field more uniform. Fuselages 3 and 4, at angles of attack of +10° and +20°, serve to illustrate these effects in Figures 7-61 through 7-64.

7.1.3.3 Mach 1.8

At negative angle of attack an overall downwash condition exists for all configurations. The flow fields are generally comprised of a centrally located large average downwash zone plus a high downwash zone, with the latter occupying the lower inboard portion of the survey plane. The flow field generated by individual configurations is distinguished by the absolute level of the average downwash which varies between configurations as a function of the fuselage corner. The large corner radius configurations reinforce the inherent downwash (due to nose droop and angle of attack) the same as they did for other test conditions, previously discussed. Consequently these configurations generated the most negative downwash. These effects are shown in Figures 7-65 and 7-66 for fuselage 1, a small radius configuration, and fuselage 2, a large radius configuration.

The sidewash for this test condition and throughout the entire angle of attack range, remains a rather insensitive parameter. The composition of the flow field and the variation in sidewash, as a function of geometry and angle of attack, is quite similar to that discussed previously for Mach number 0.8 and 1.2.

With the angle of attack increased to 0° and +5° an overall downwash condition still prevails. There is a progressive reduction in the extent of the relatively high angularity region occupying the lower inboard portion of the survey plane. An example of this can be obtained from a comparison of Figures 7-65 and 7-67, presenting flow angularity maps for fuselage 1 at angles of attack of -3° and 0° respectively. It is interesting to note that at +5° angle of attack, where the fuselage nose generates an almost symmetrical flow field, the flow fields for all fuselages are very uniform. There is a continuation of the tendency previously described for fuselages with large corner radii to induce a more negative value of downwash.

Fuselage 3
PCPN
Mach Number = 1.2
$\alpha = 10°$
Format I

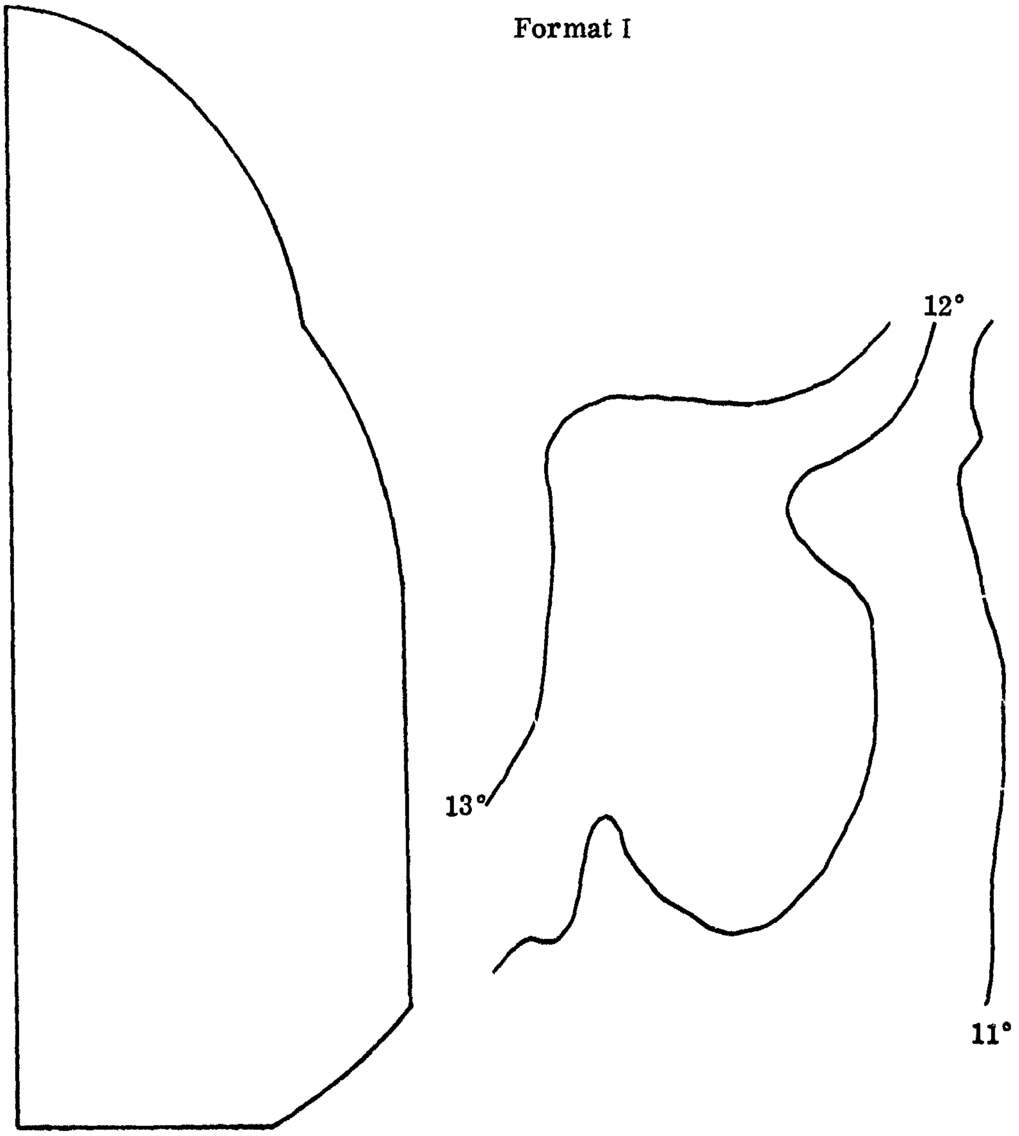

Figure 7-61. Local Flow Angularity

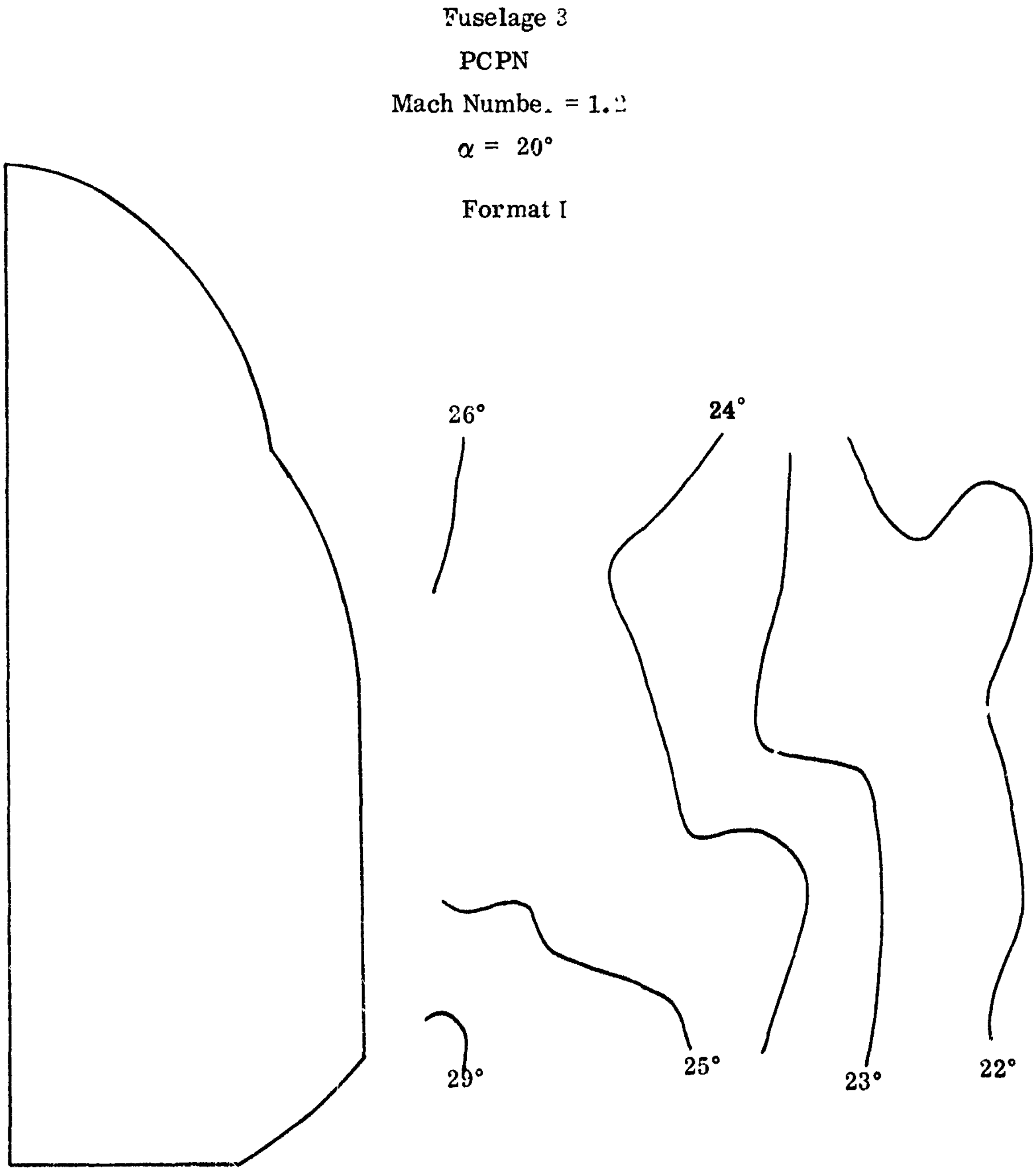

Fuselage 3
PCPN
Mach Number = 1.2
α = 20°

Format I

Figure 7-62. Local Flow Angularity

Fuselage 4
PCPN
Mach Number = 1.2
α = 10°

Format I

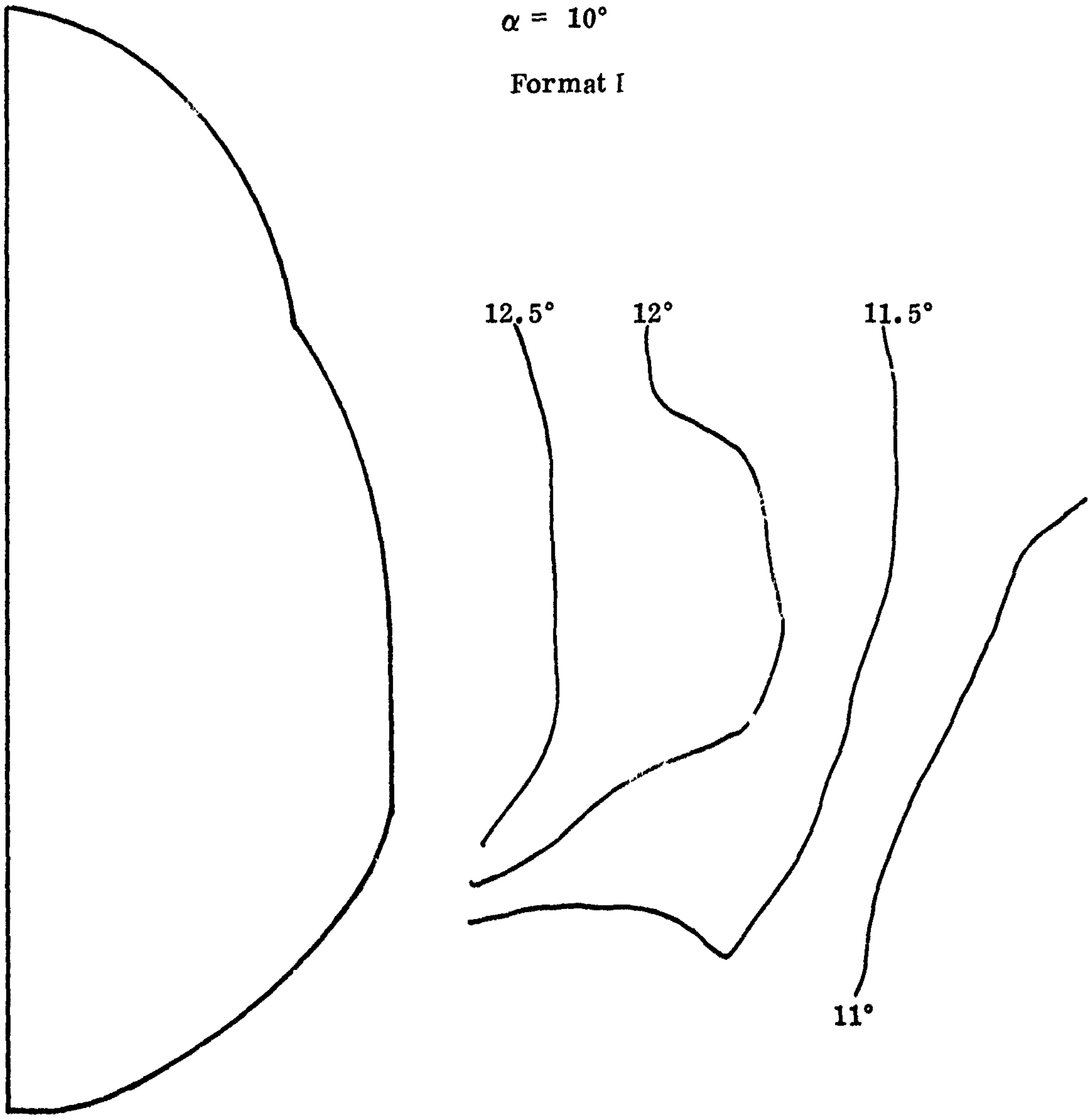

Figure 7-63. Local Flow Angularity

Fuselage 4
PCPN
Mach Number = 1.2
α = 20°
Format I

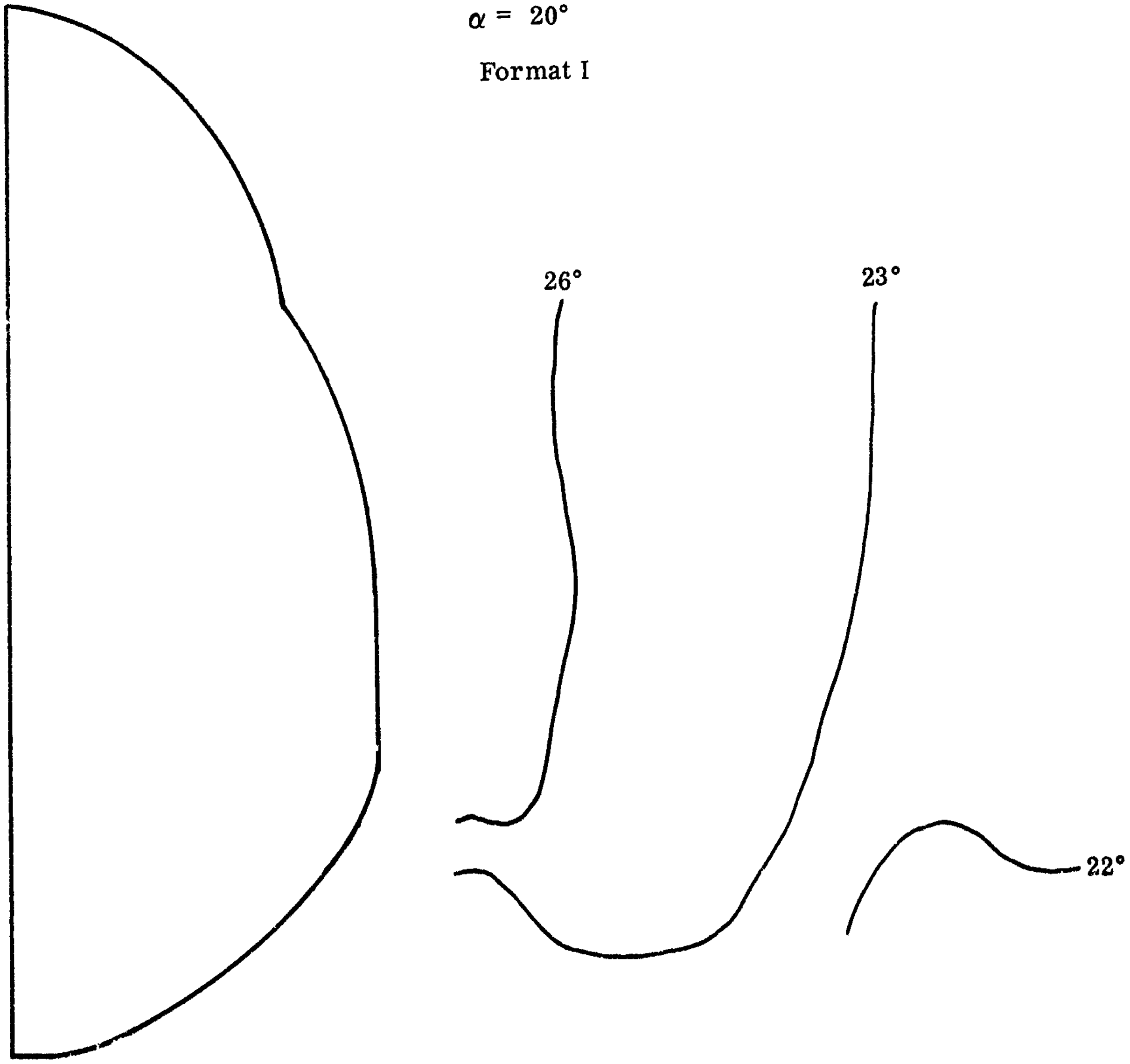

Figure 7-64. Local Flow Angularity

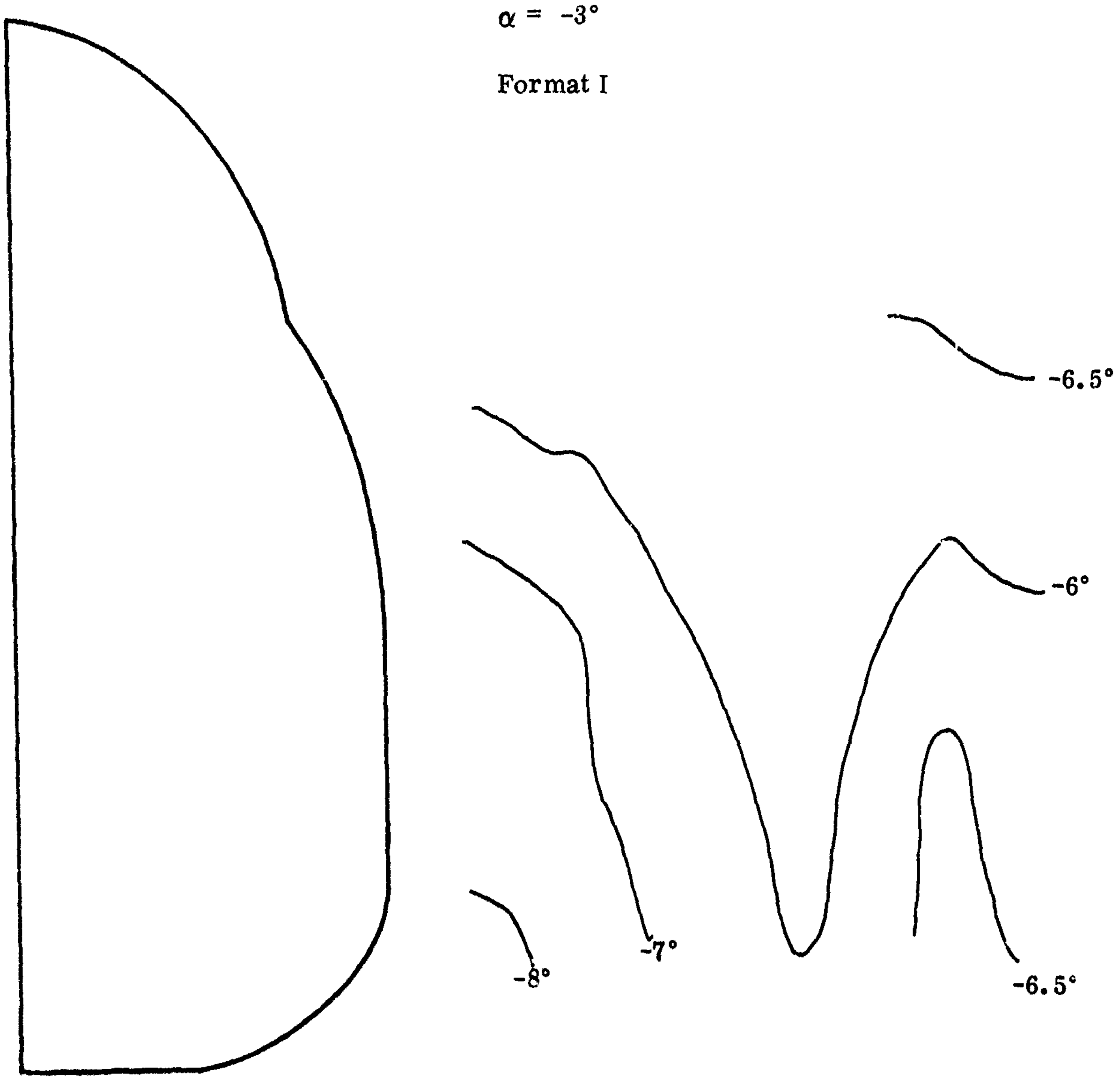

Fuselage 1
PCPN
Mach Number = 1.8
α = -3°

Format I

Figure 7-65. Local Flow Angularity

Fuselage 2

PCPN

Mach Number = 1.8

α = -3°

Format I

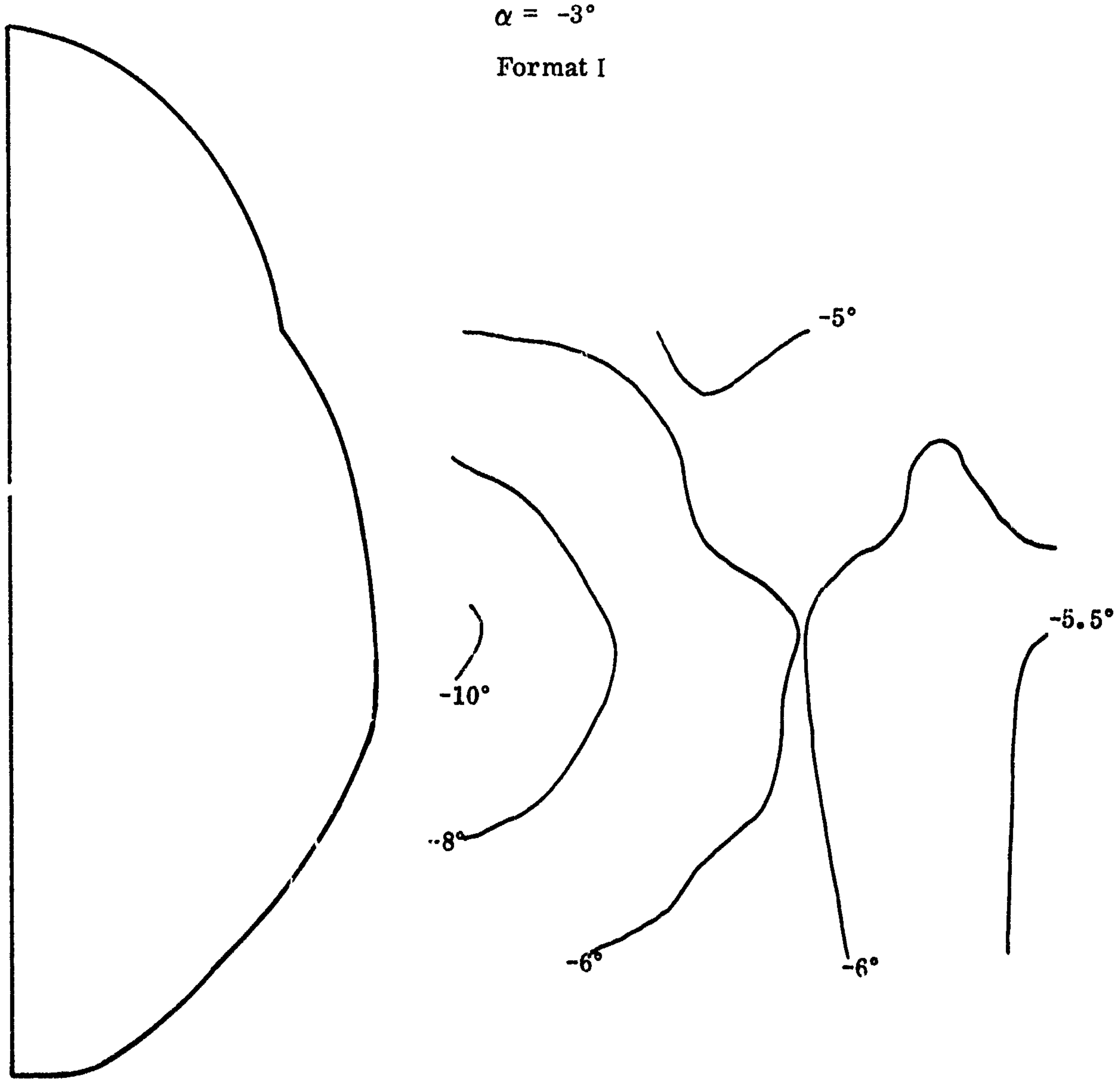

Figure 7-66. Local Flow Angularity

Fuselage 1
PCPN
Mach Number = 1.8
$\alpha = 0°$

Format I

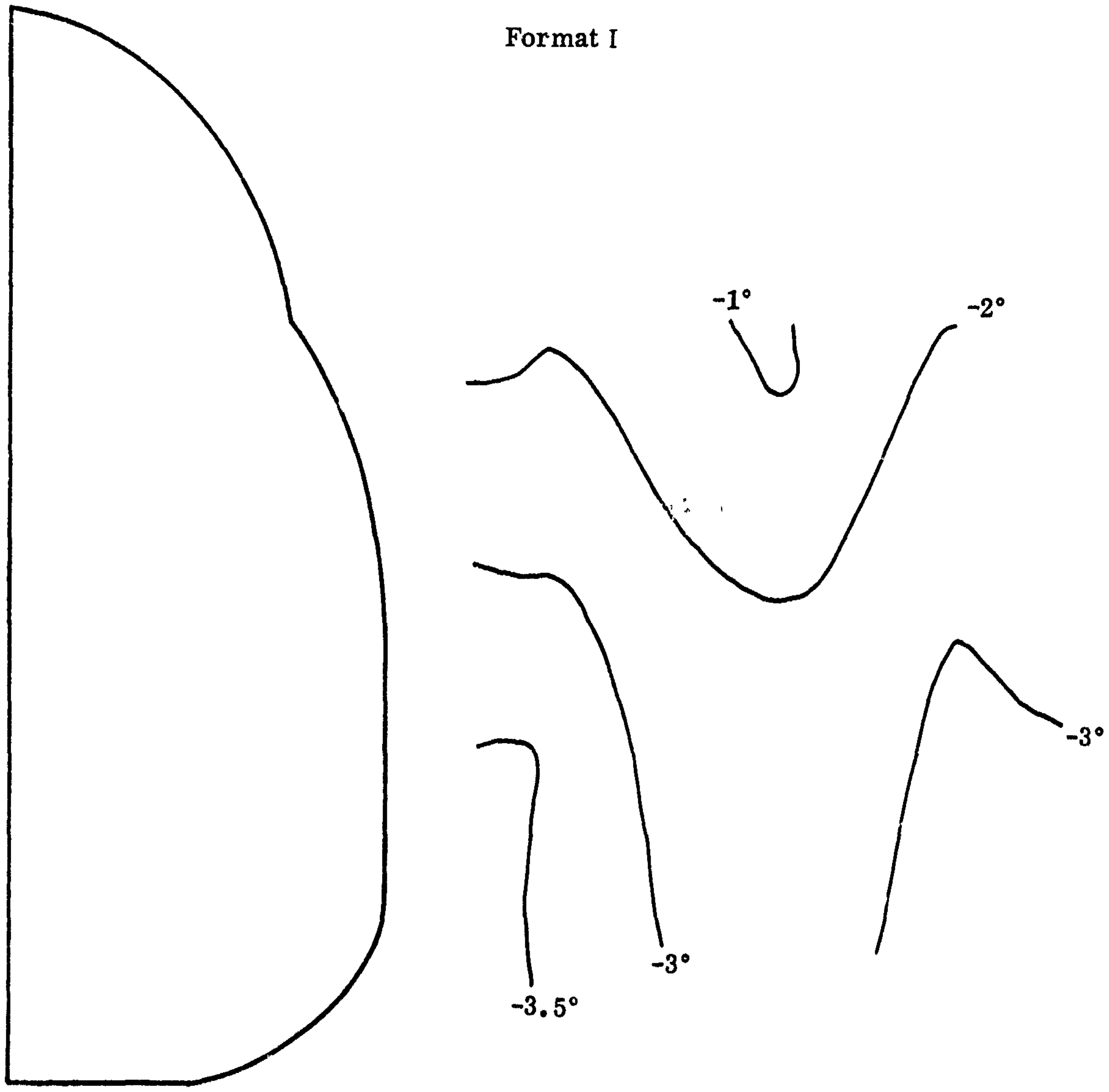

Figure 7-67. Local Flow Angularity

For an angle of attack of +10° the fuselage nose generated flow field is still close to symmetrical and the fuselage flow fields tend to be quite uniform. There is the appearance of geometry dependent zones; however, they are quite weak. Typical flow angularity maps are presented in Figures 7-68 and 7-69, for fuselages 4 and 5 respectively. These two figures indicate that the larger corner radius induces a more uniform flow field at this condition.

The influence of fuselage corner radius and rate of development becomes increasingly evident at the higher angle of attack conditions (α = +15°, +20°, and +25°). At these conditions an increase in fuselage corner radius improves flow field uniformity. The uniformity improves further as the rate of corner development is made more gentle. These effects are illustrated in Figures 7-70 through 7-76 which present the local flow angularity for all seven fuselage configurations at an angle of attack of +20°.

7.1.3.4 Mach 2.2

For this Mach number the influence of fuselage geometry and angle of attack upon flow field angularity is, in general, similar to that seen at the previously described Mach 1.8 condition. The causal relationship seen at that Mach number apply at Mach 2.2. To illustrate the effect of fuselage geometry upon flow field composition, the local flow angularity for all seven fuselage configurations are presented in Figures 7-77 through 7-89 and Figure 7-25 for angles of attack of 0° and +10°.

At this Mach number the average sidewash appears completely independent of angle of attack. There appears to be a small quantitative variation in sidewash between configurations but not of sufficient magnitude to warrant discussion, particularly when measuring inaccuracies are considered.

7.1.3.5 Mach 2.5

The qualitative influence of fuselage geometry upon flow field upwash appears consistent with that noted for lower Mach numbers. The flow field composition for all seven fuselage configurations is displayed in Figures 7-90 through 7-96 for an angle of attack equal to +5°. For this test condition there is a greater increase in negative sidewash with increasing angle of attack than was the case for lower Mach numbers. The previously noted tendency for small corner fuselages to have a more negative

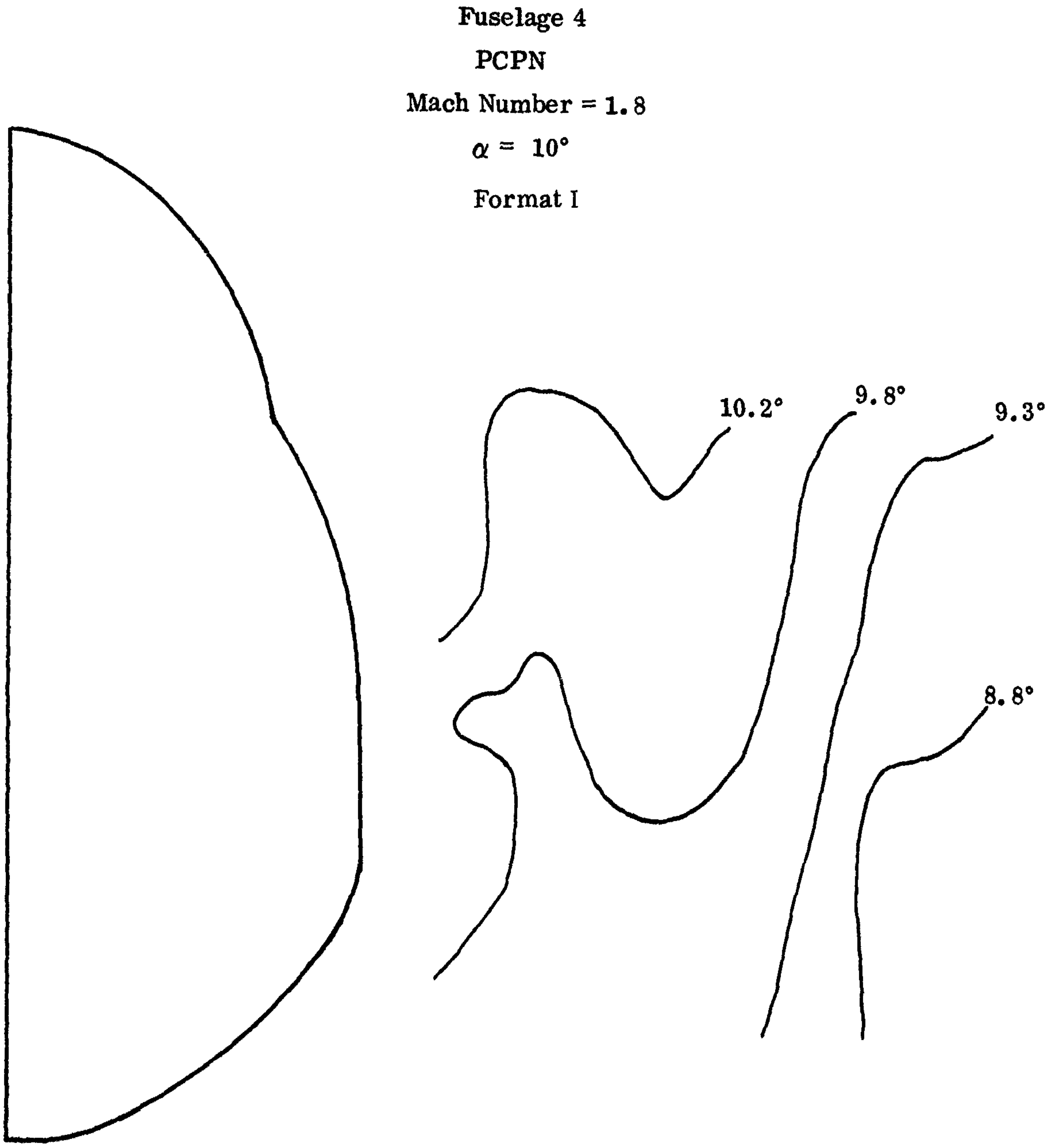

Figure 7-68. Local Flow Angularity

Fuselage 5
PCPN
Mach Number = 1.8
$\alpha = 10°$
Format I

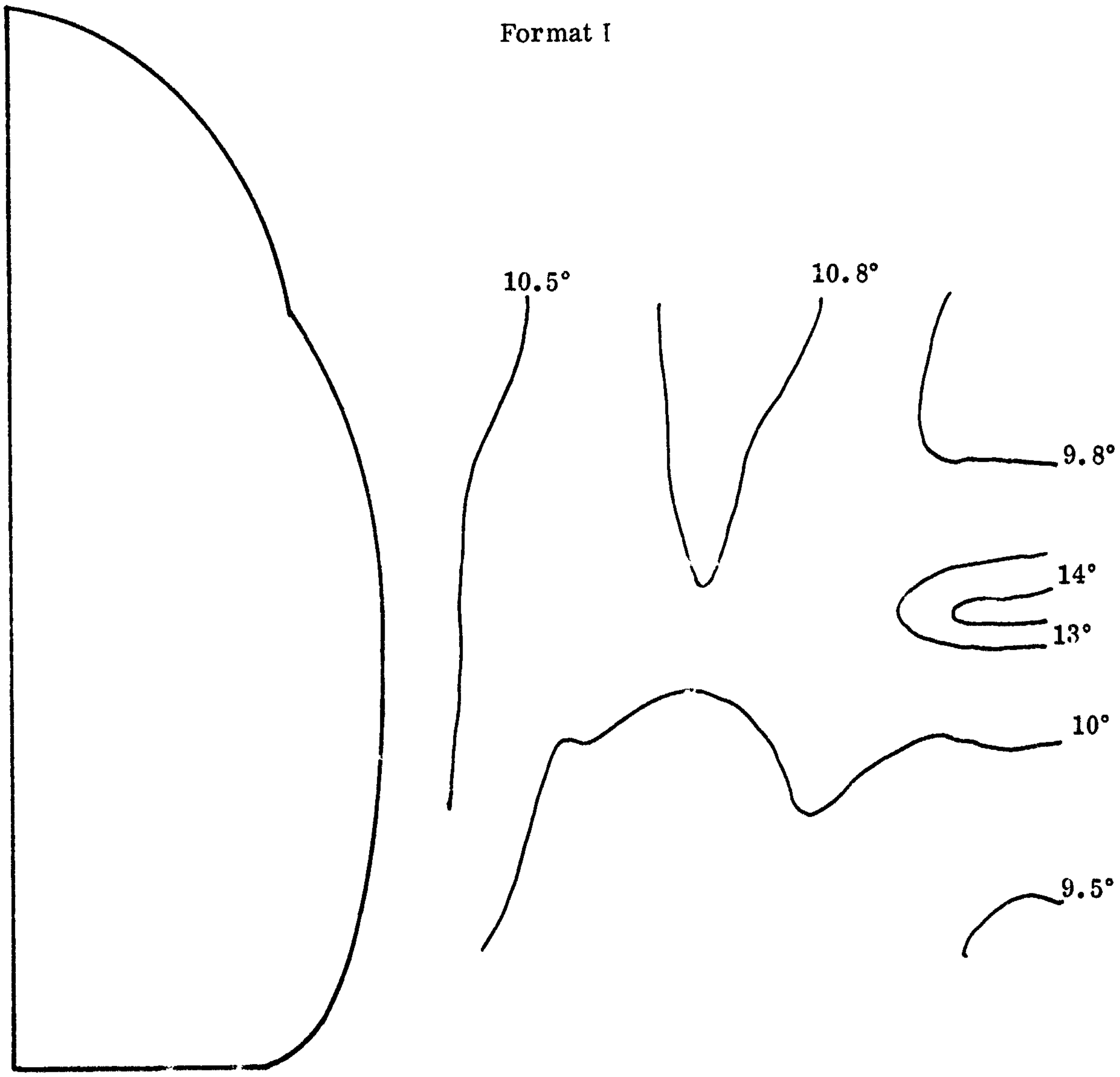

Figure 7-69. Local Flow Angularity

Fuselage 1
PCPN
Mach Number = 1.8
α = 20°
Format I

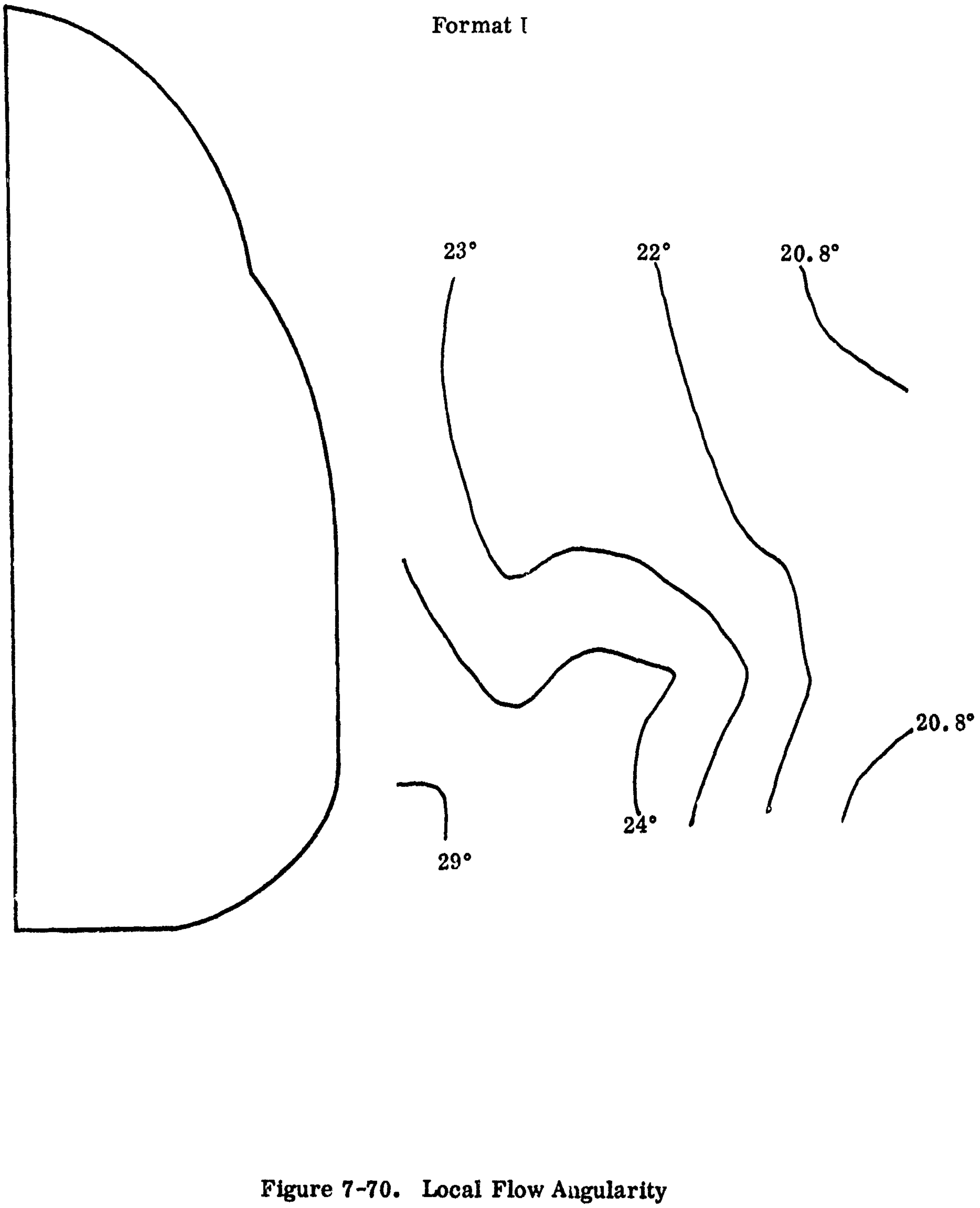

Figure 7-70. Local Flow Angularity

Fuselage 2
PCPN
Mach Number = 1.8
α = 20°
Format I

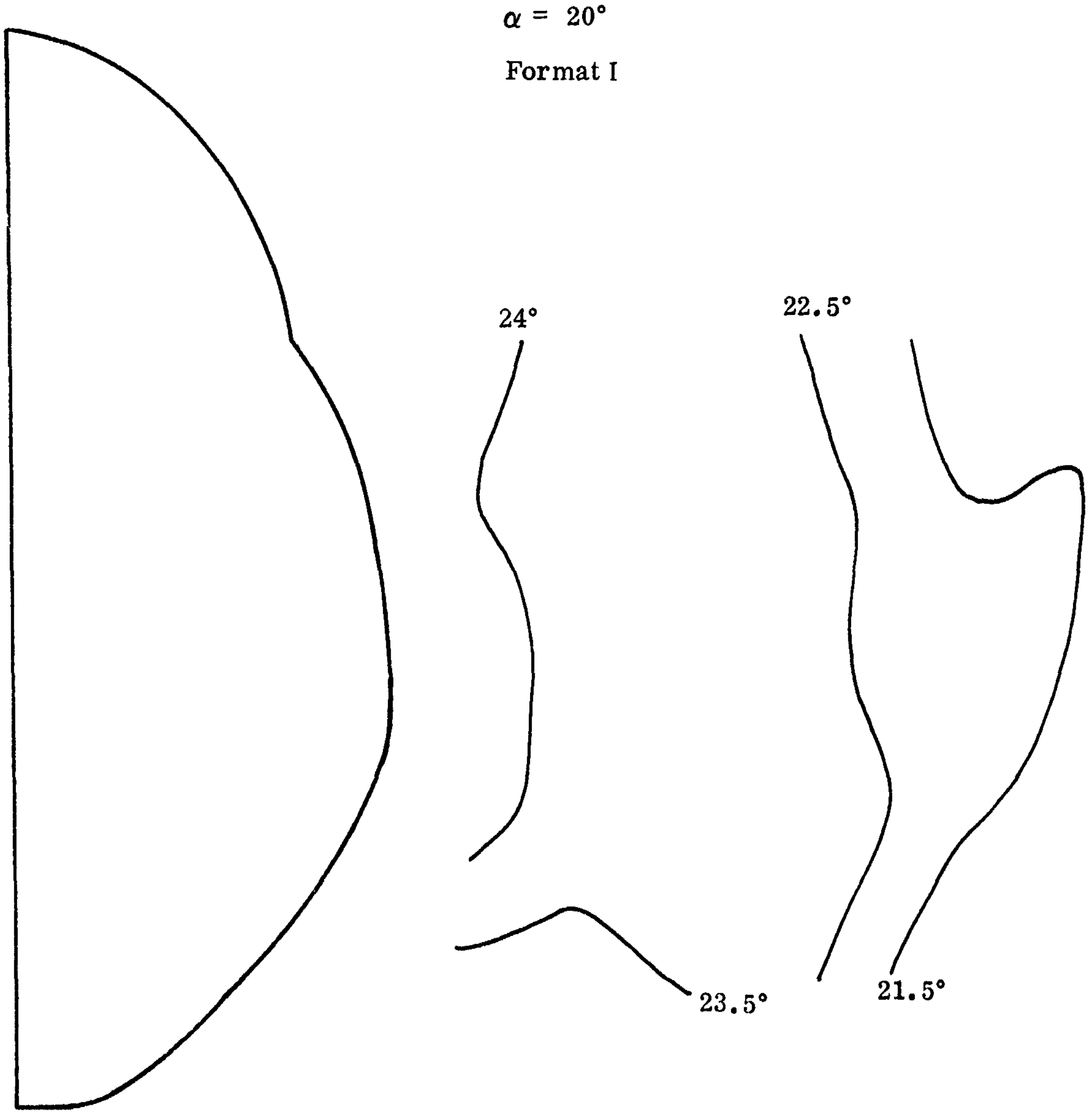
24°
22.5°
23.5°
21.5°

Figure 7-71. Local Flow Angularity

Fuselage 3
PCPN
Mach Number = 1.8
α = 20°
Format I

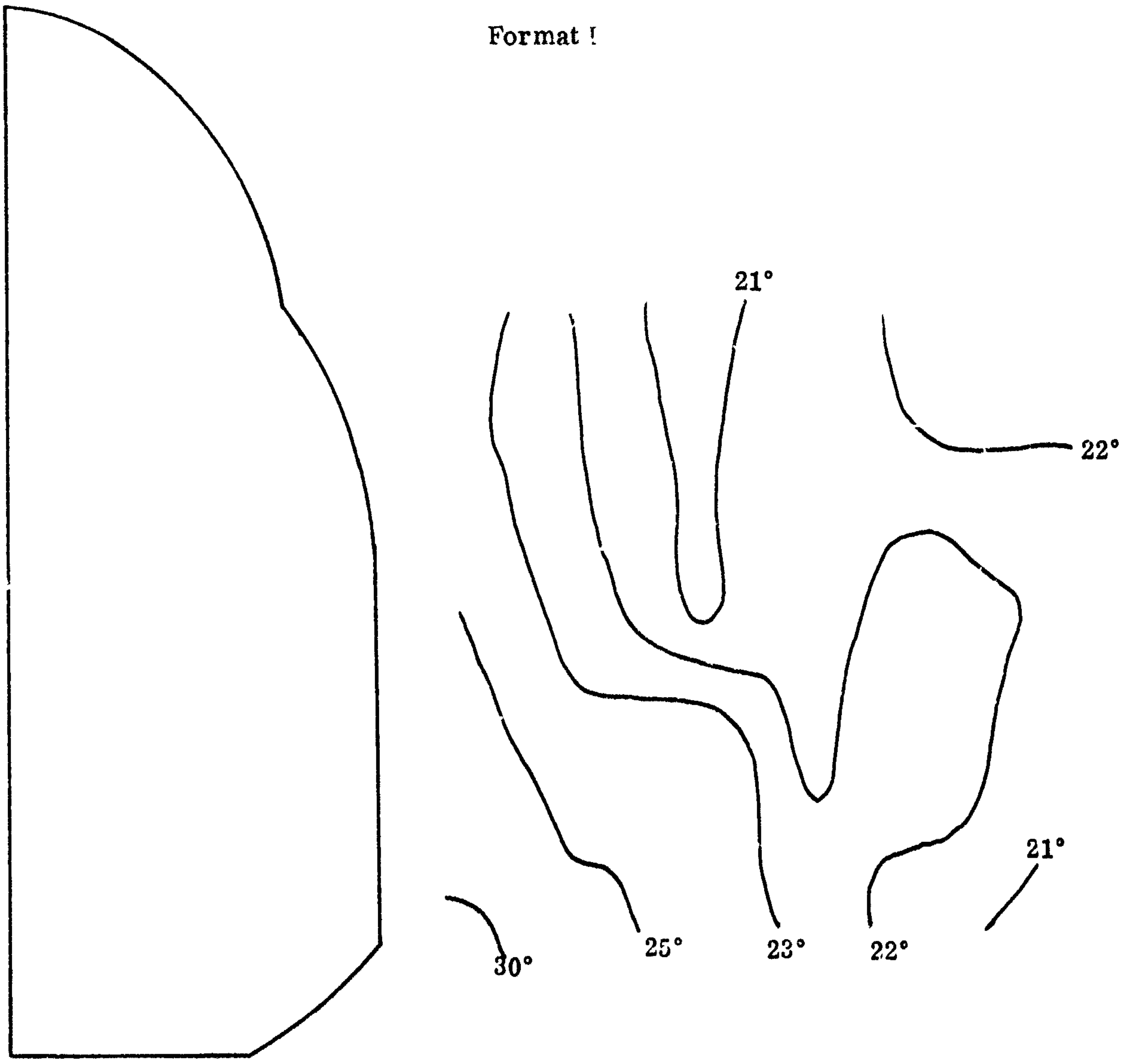

Figure 7-72. Local Flow Angularity

Fuselage 4
PCPN
Mach Number = 1.8
α = 20°
Format I

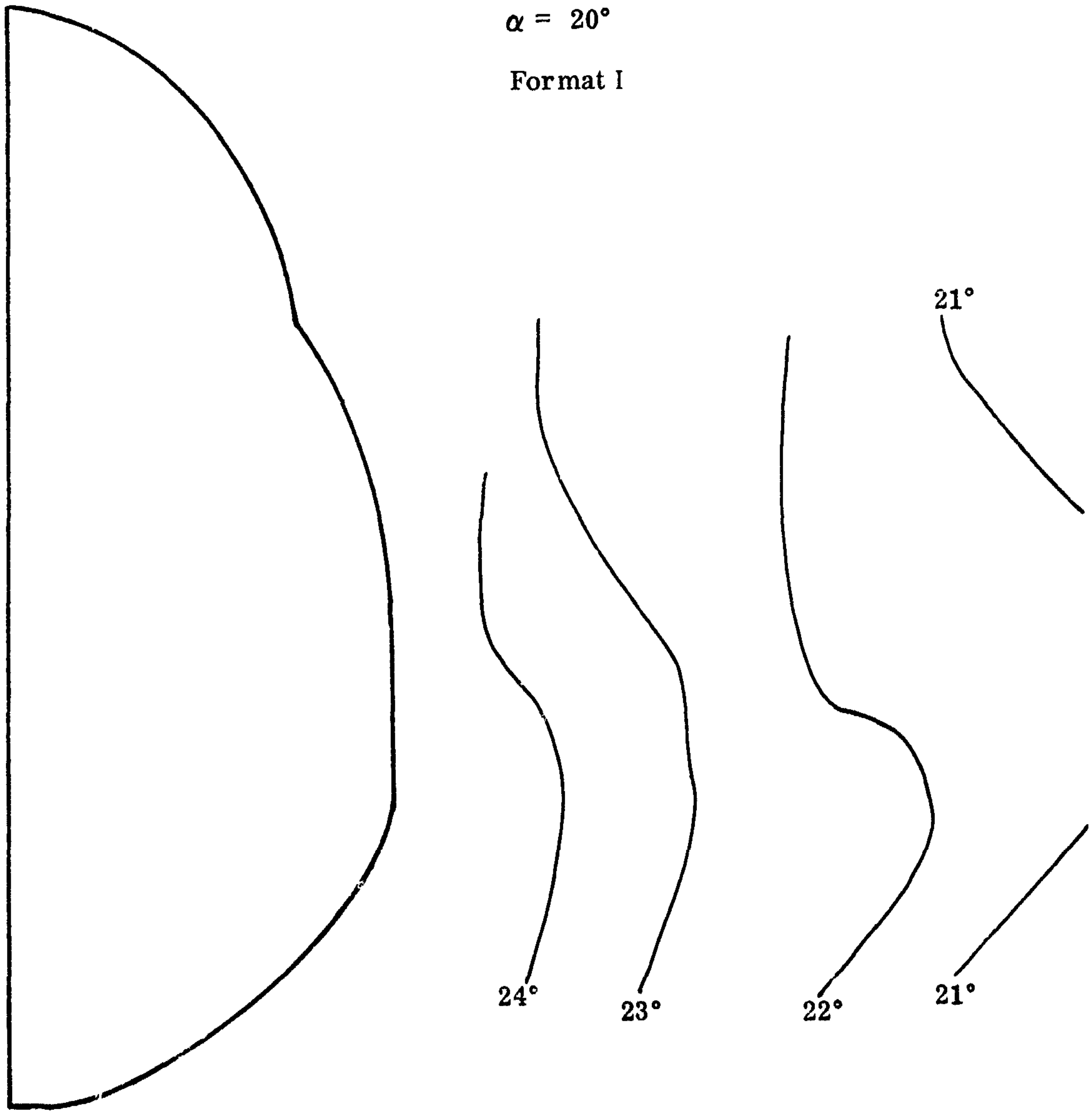

Figure 7-73. Local Flow Angularity

Fuselage 5
PCPN
Mach Number = 1.8
α = 20°
Format I

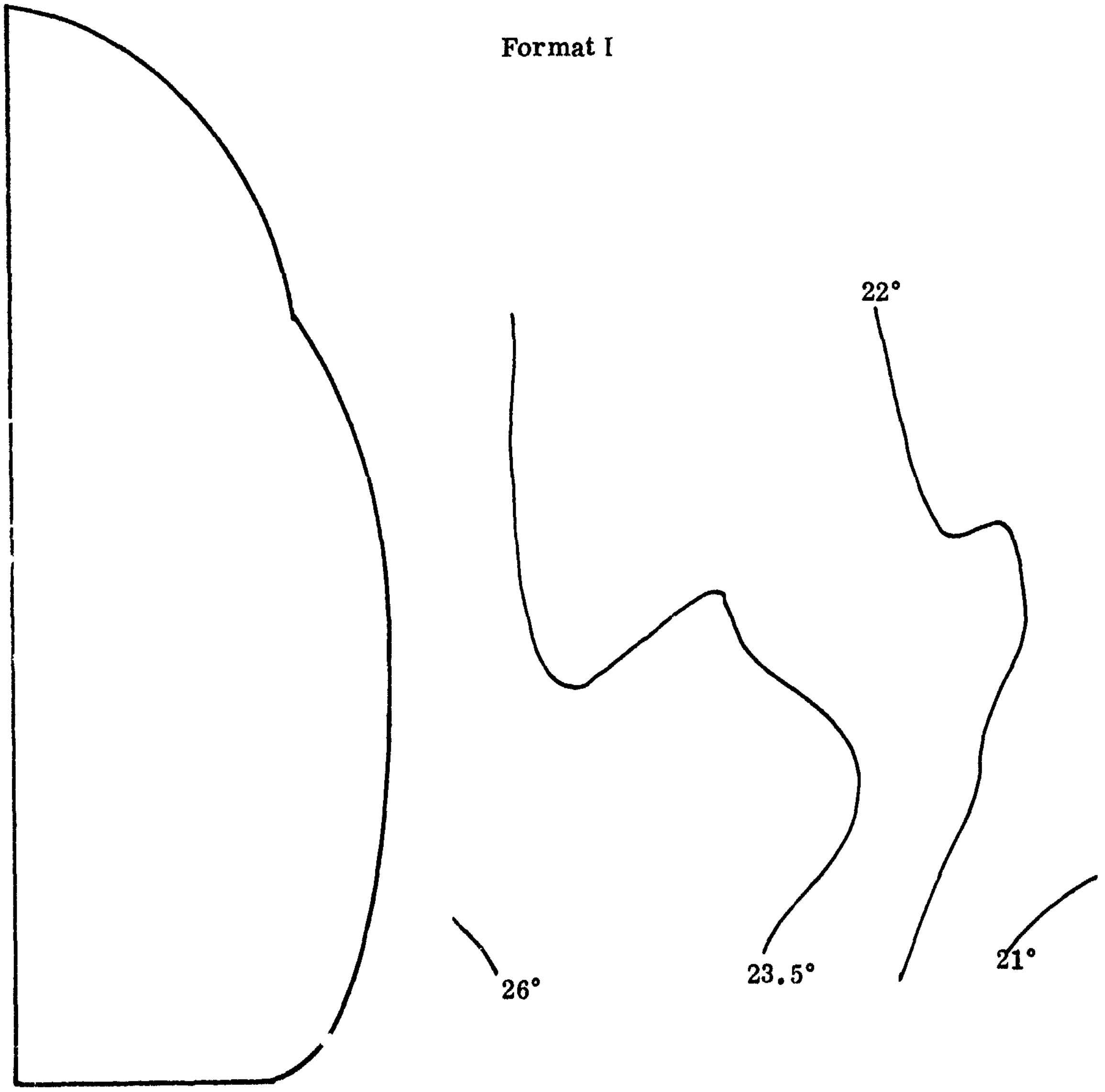

Figure 7-74. Local Flow Angularity

Fuselage 6
PCPN
Mach Number = 1.8
α = 20°
Format I

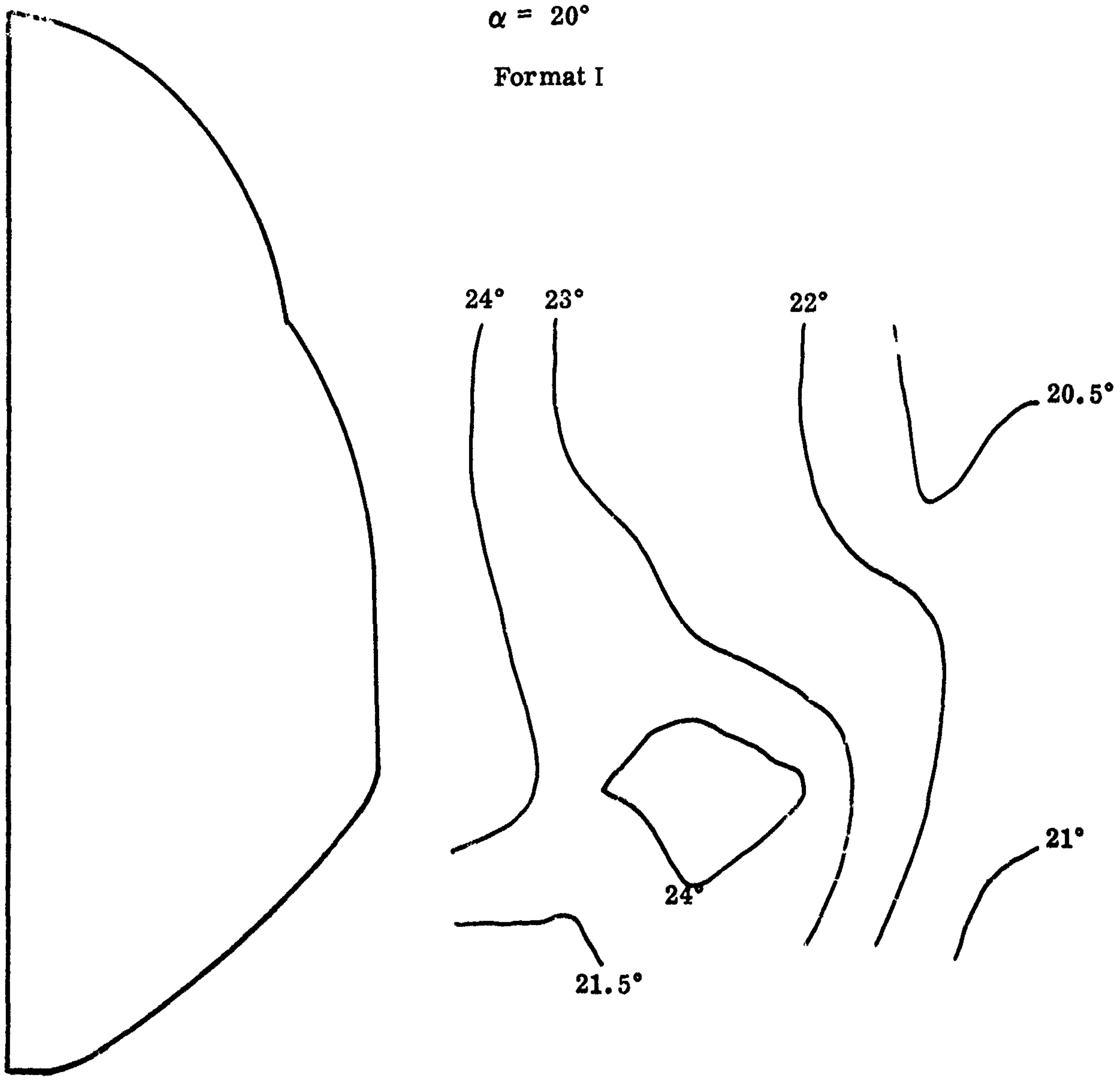

Figure 7-75. Local Flow Angularity

Fuselage 8
PCPN
Mach Number = 1.8
α = 20°

Format I

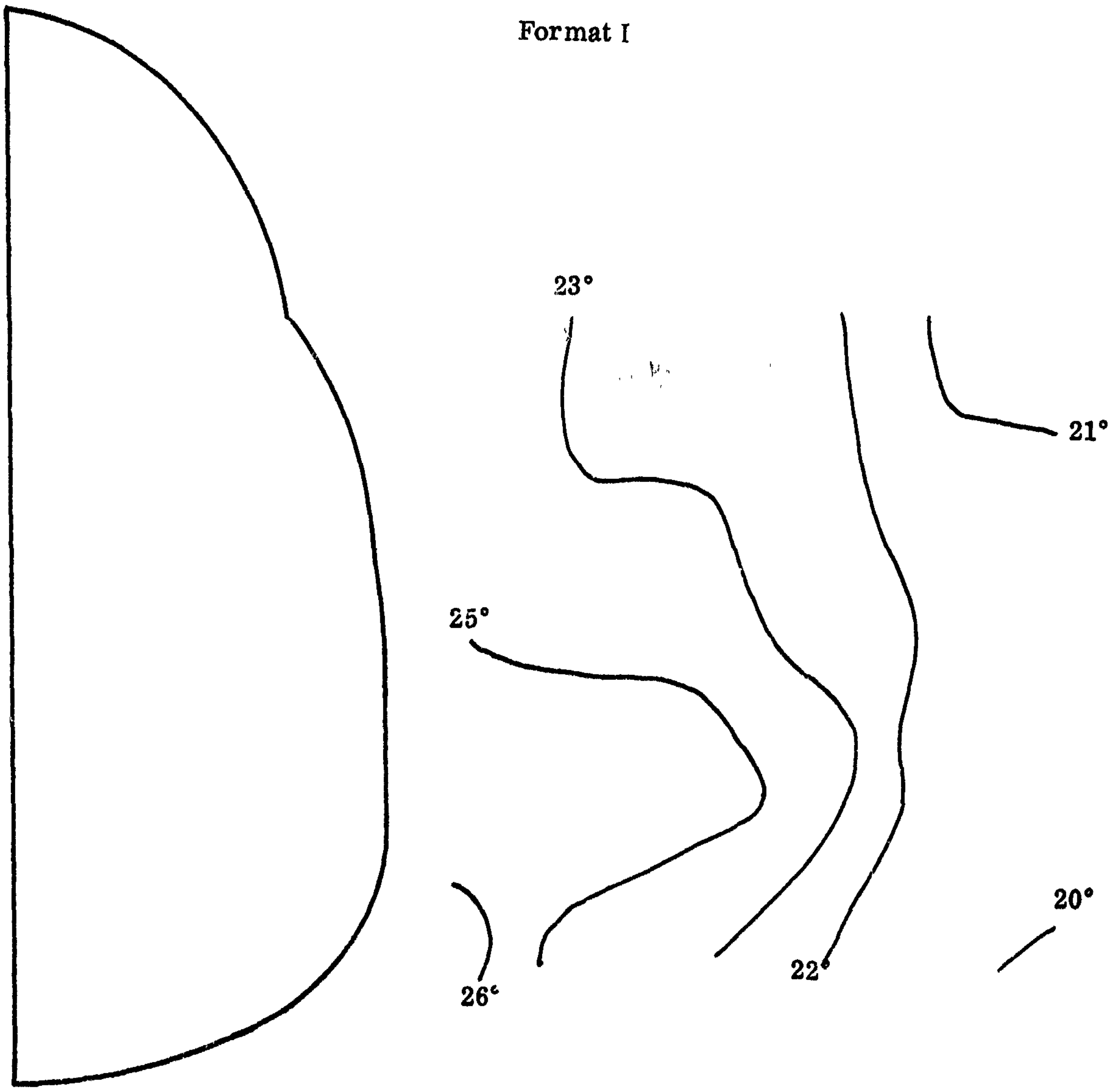

Figure 7-76. Local Flow Angularity

Fuselage 1
PCPN
Mach Number = 2.2
$\alpha = 0°$
Format 1

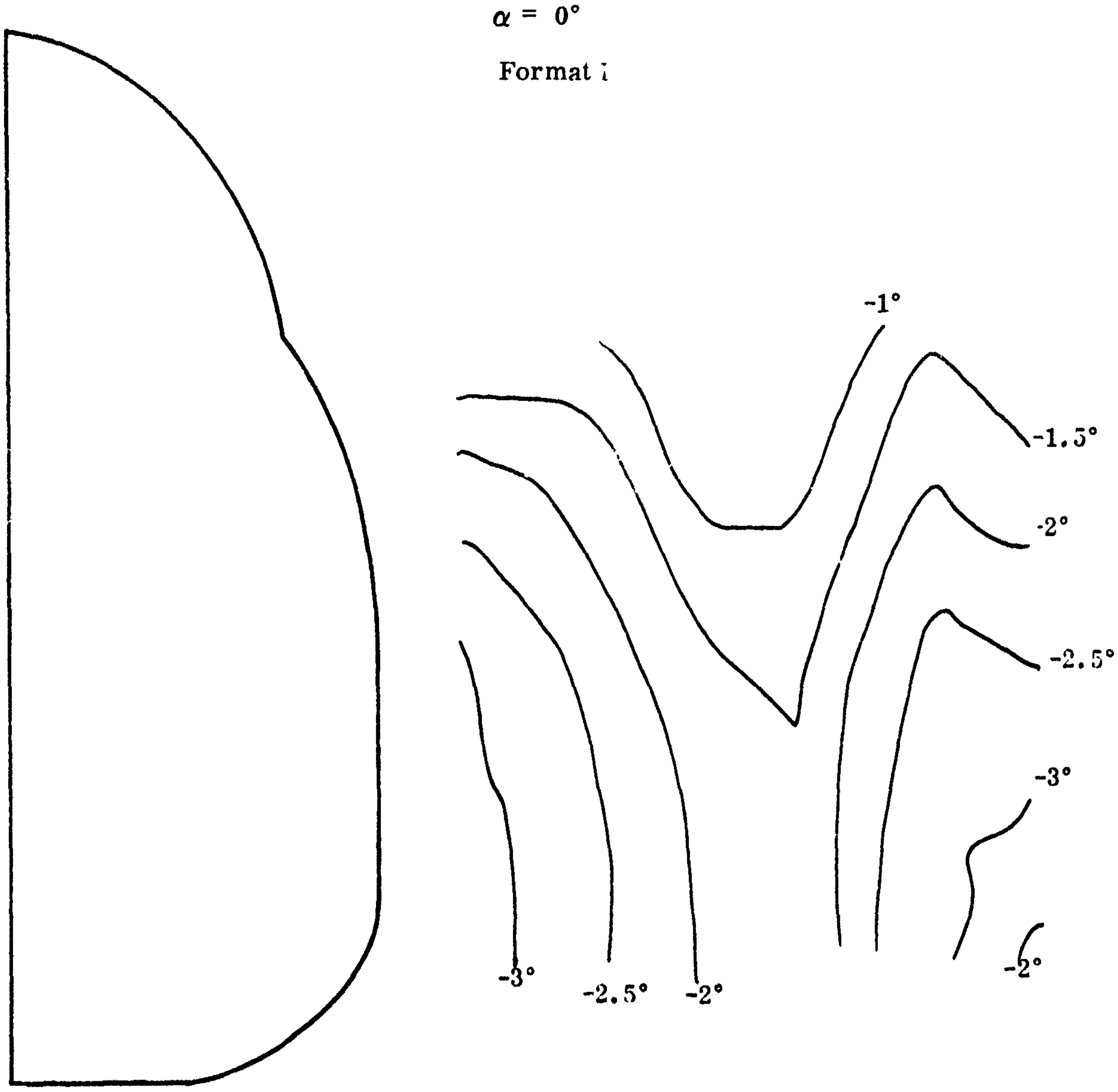

Figure 7-77. Local Flow Angularity

Fuselage 2

PCPN

Mach Number = 2.2

$\alpha = 0°$

Format I

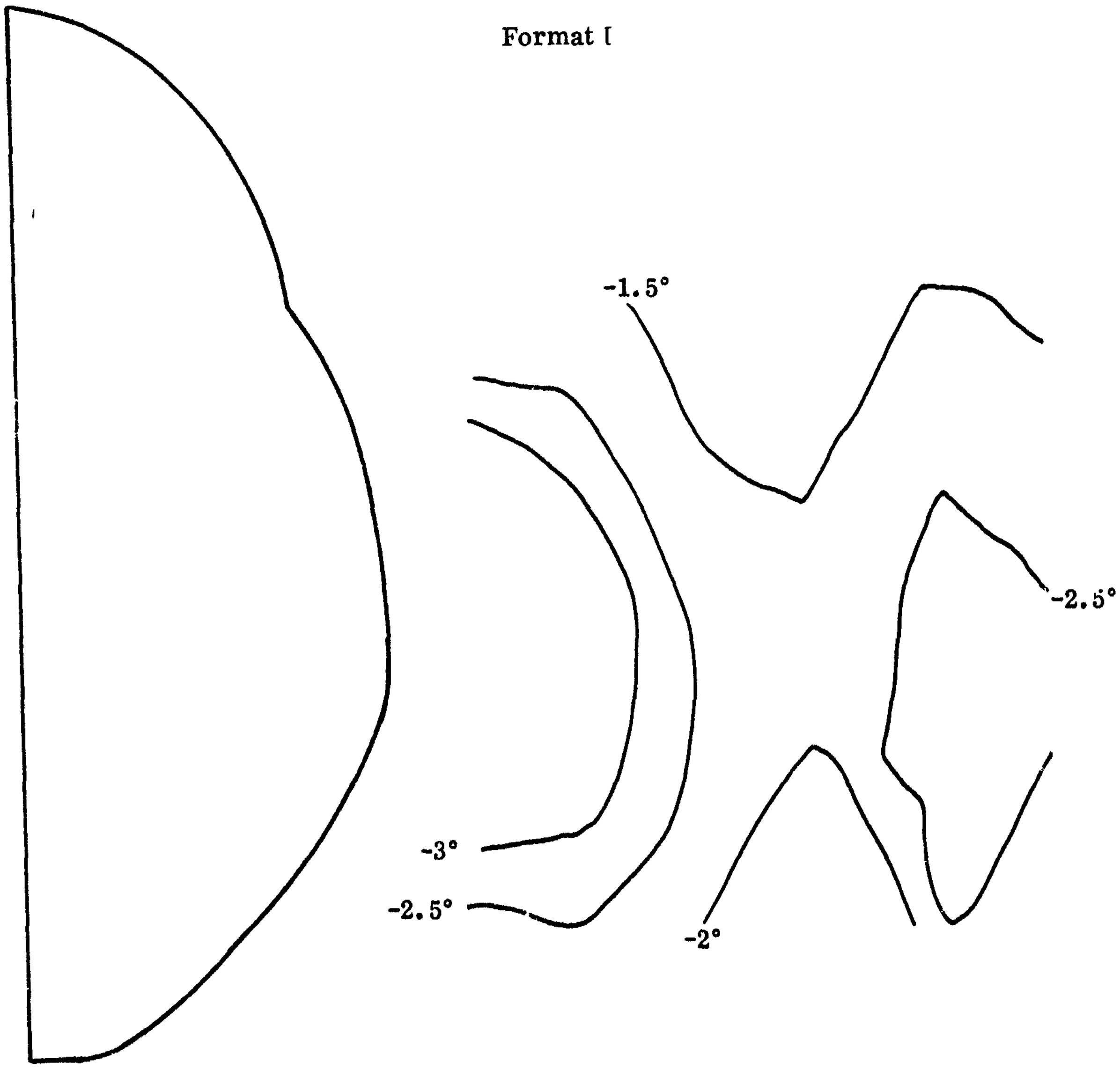

Figure 7-78. Local Flow Angularity

Fuselage 4
PCPN
Mach Number = 2.2
$\alpha = 0°$
Format I

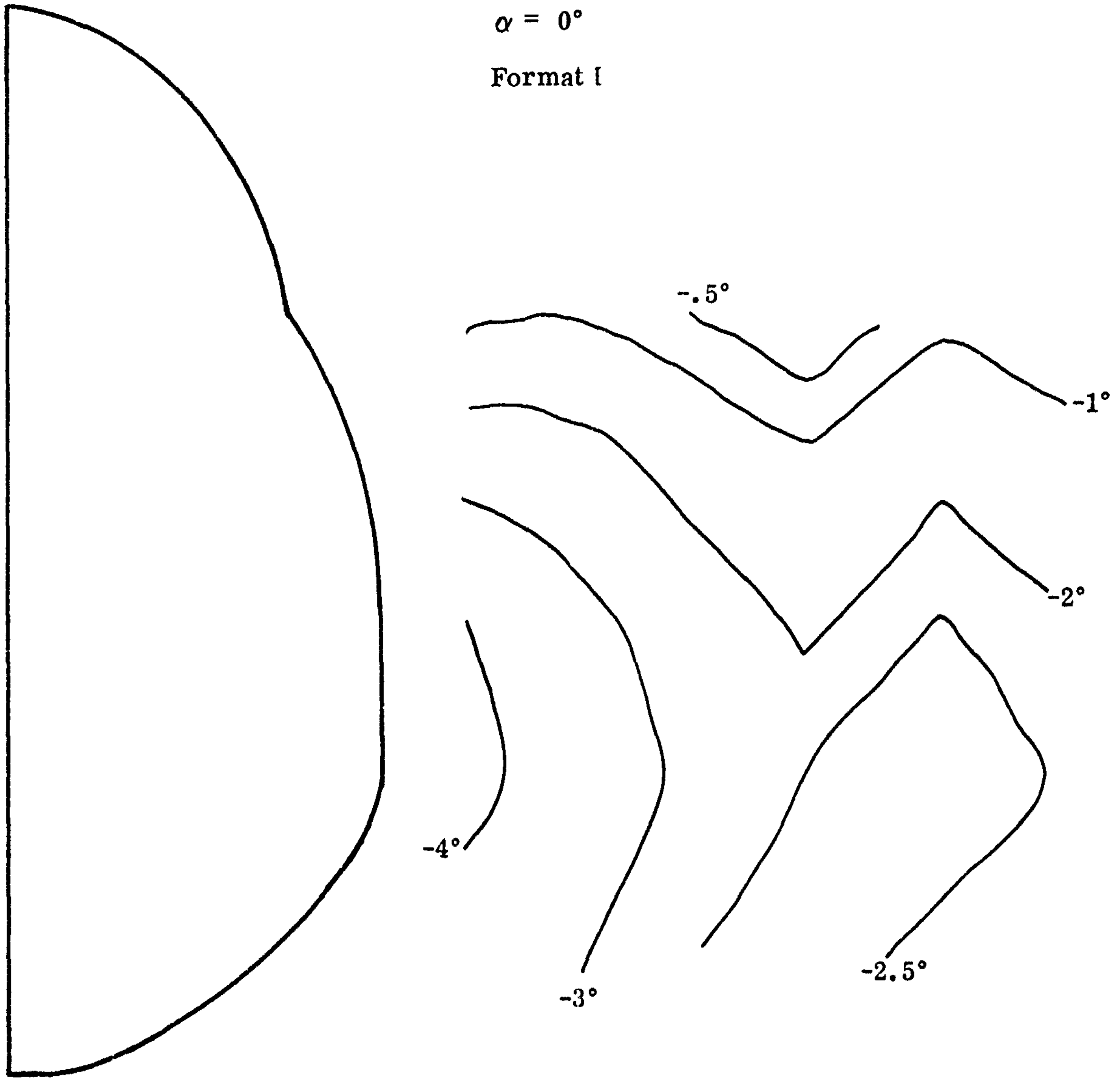

Figure 7-79. Local Flow Angularity

Fuselage 5
PCPN
Mach Number = 2.2
α = 0°
Format I

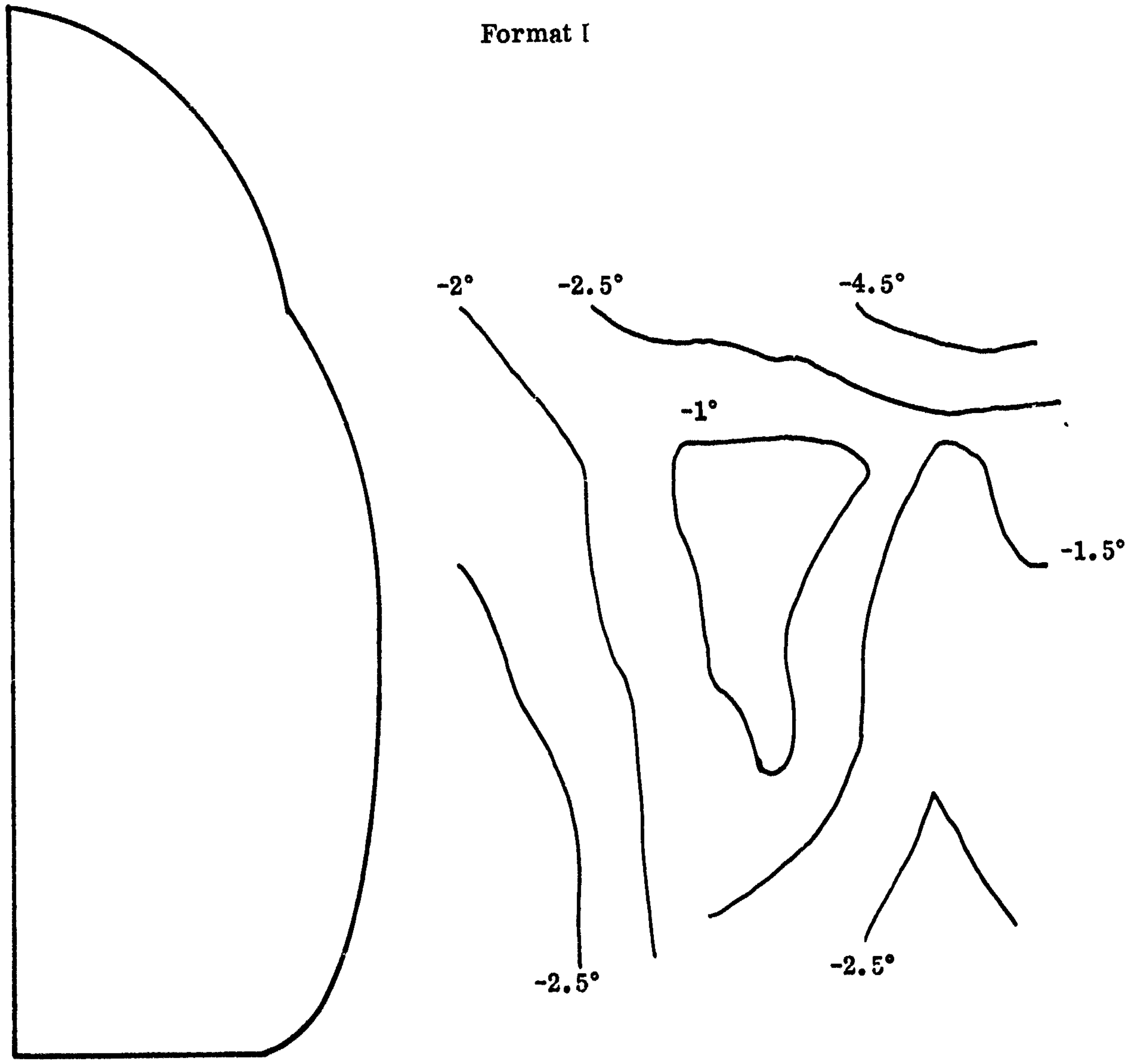

Figure 7-80. Local Flow Angularity

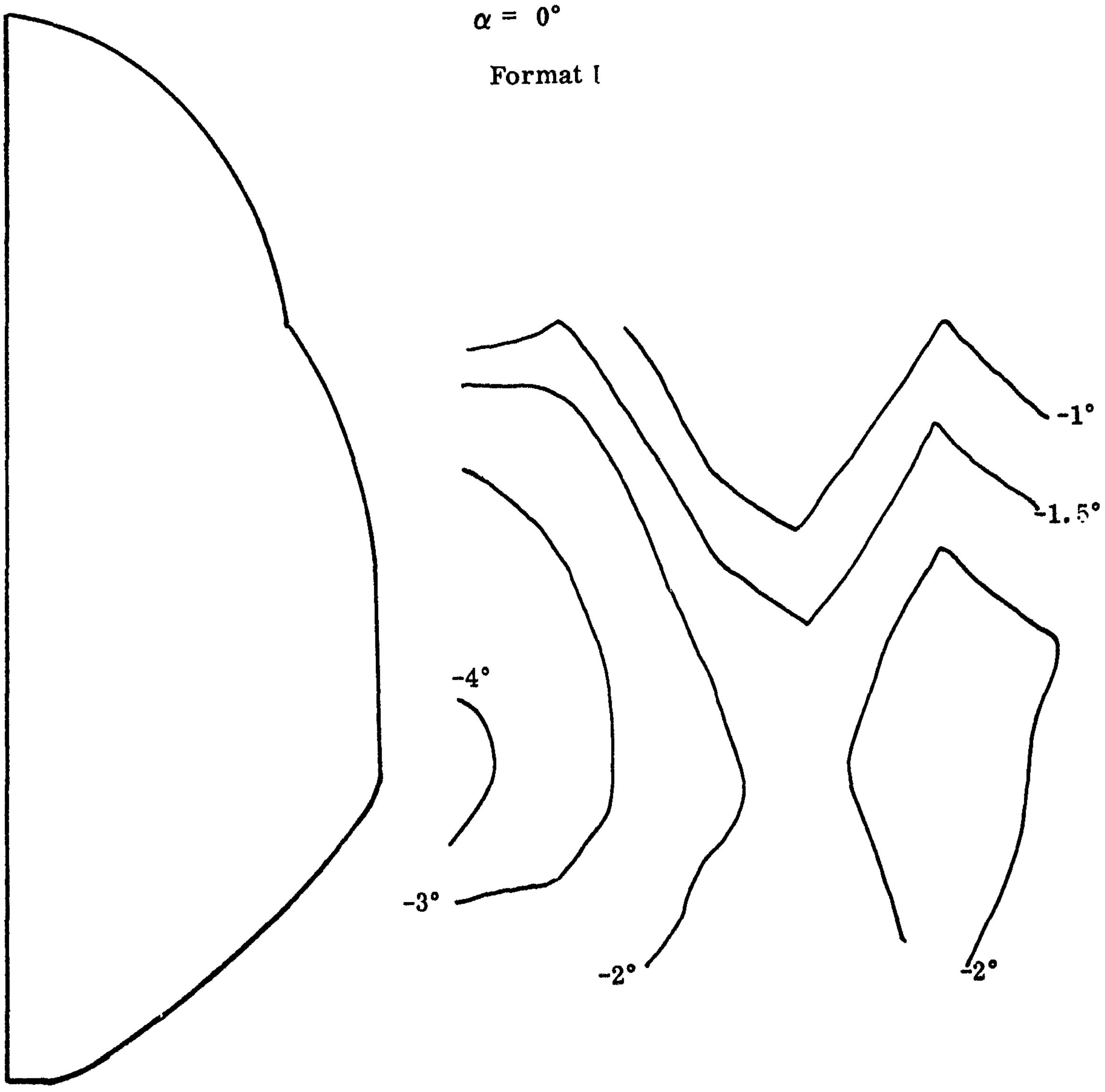

Fuselage 6
PCPN
Mach Number = 2.2
$\alpha = 0°$
Format I

Figure 7-81. Local Flow Angularity

Fuselage 8
PCPN
Mach Number = 2.2
$\alpha = 0°$
Format I

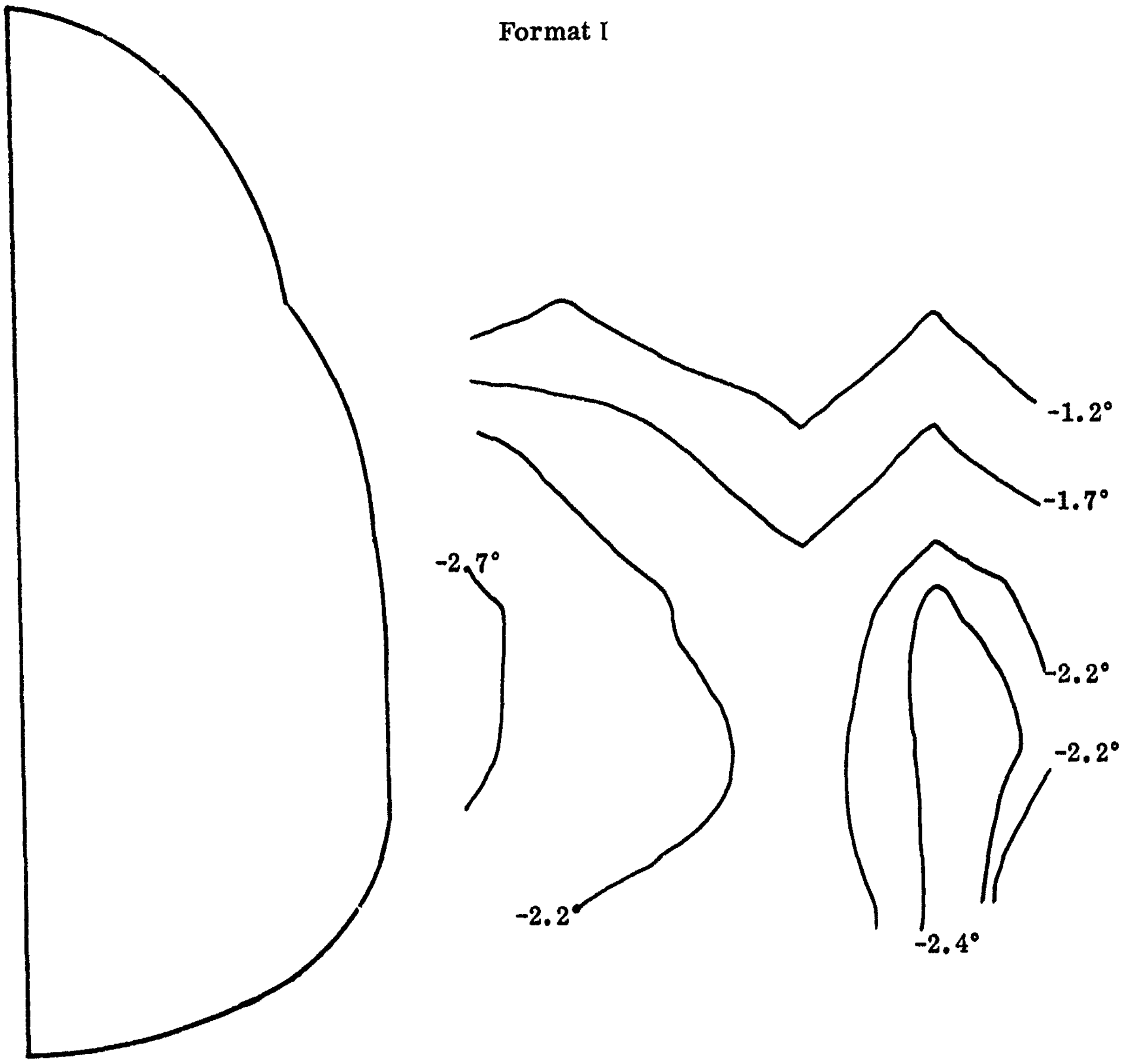

Figure 7-82. Local Flow Angularity

Fuselage 1
PCPN
Mach Number = 2.2
α = 10°
Format I

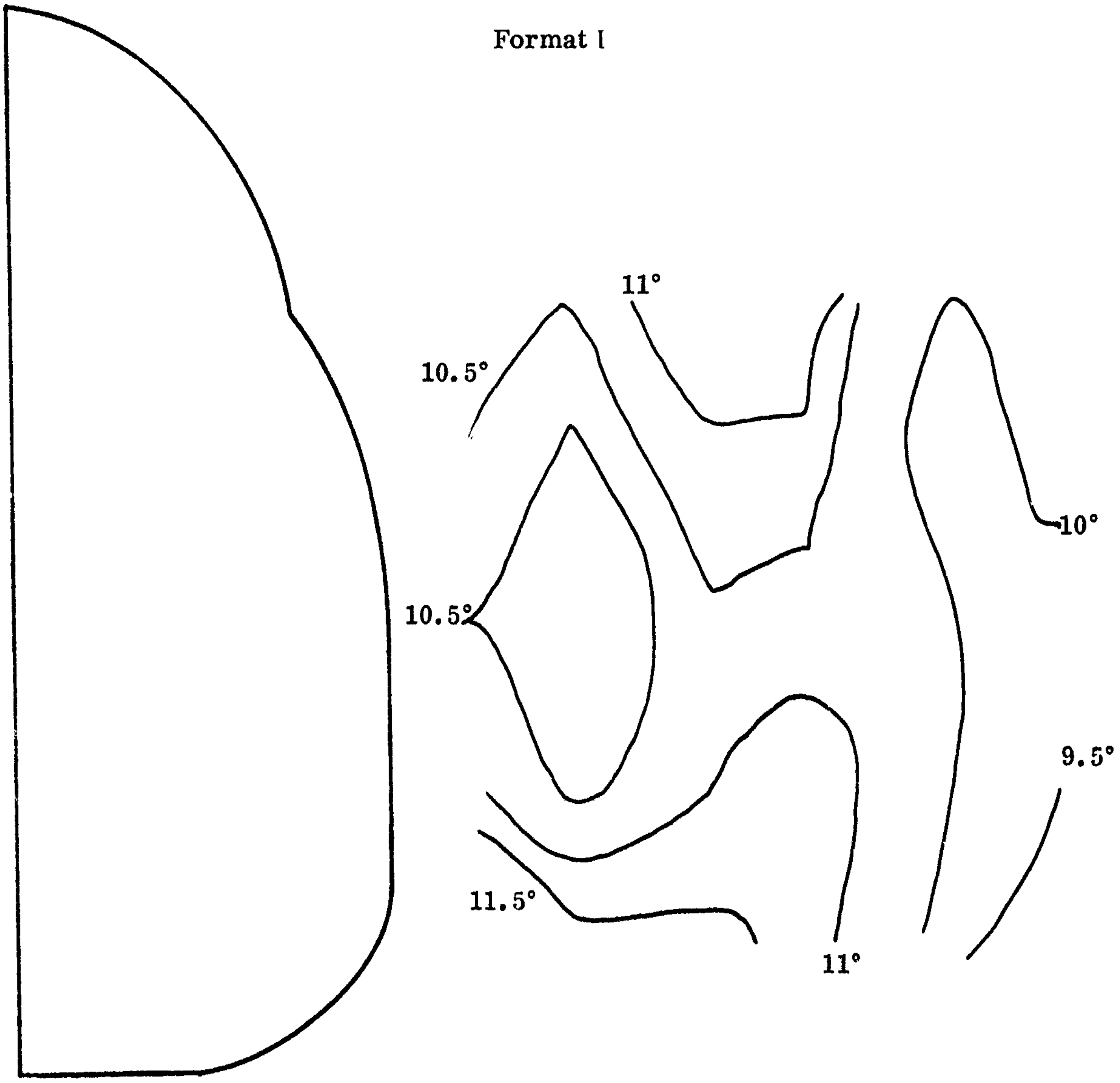

Figure 7-83. Local Flow Angularity

Fuselage 2
PCPN
Mach Number = 2.2
$\alpha = 10°$
Format I

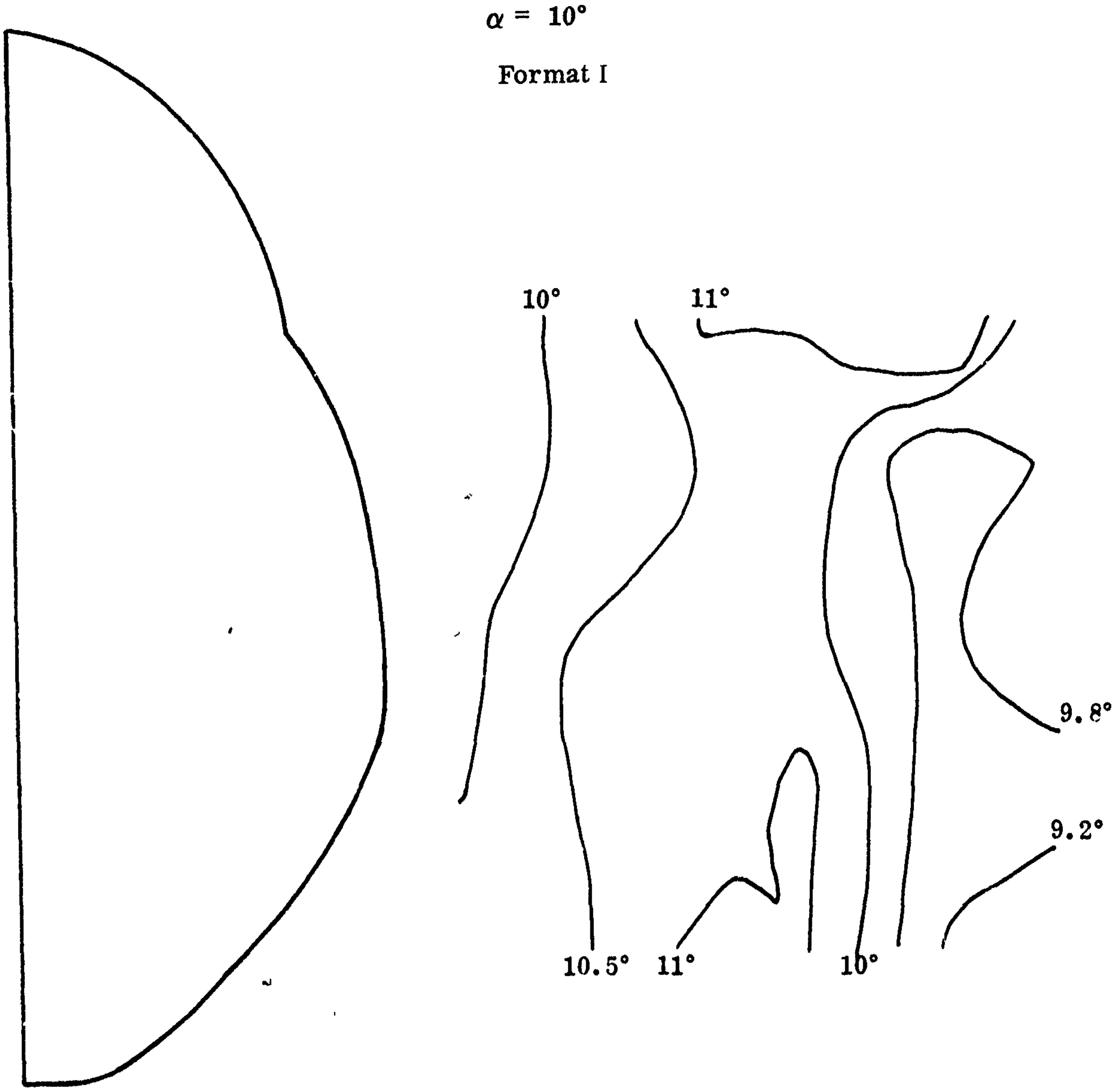

Figure 7-84. Local Flow Angularity

Fuselage 3
PCPN
Mach Number 2.2
$\alpha = 10°$

Format I

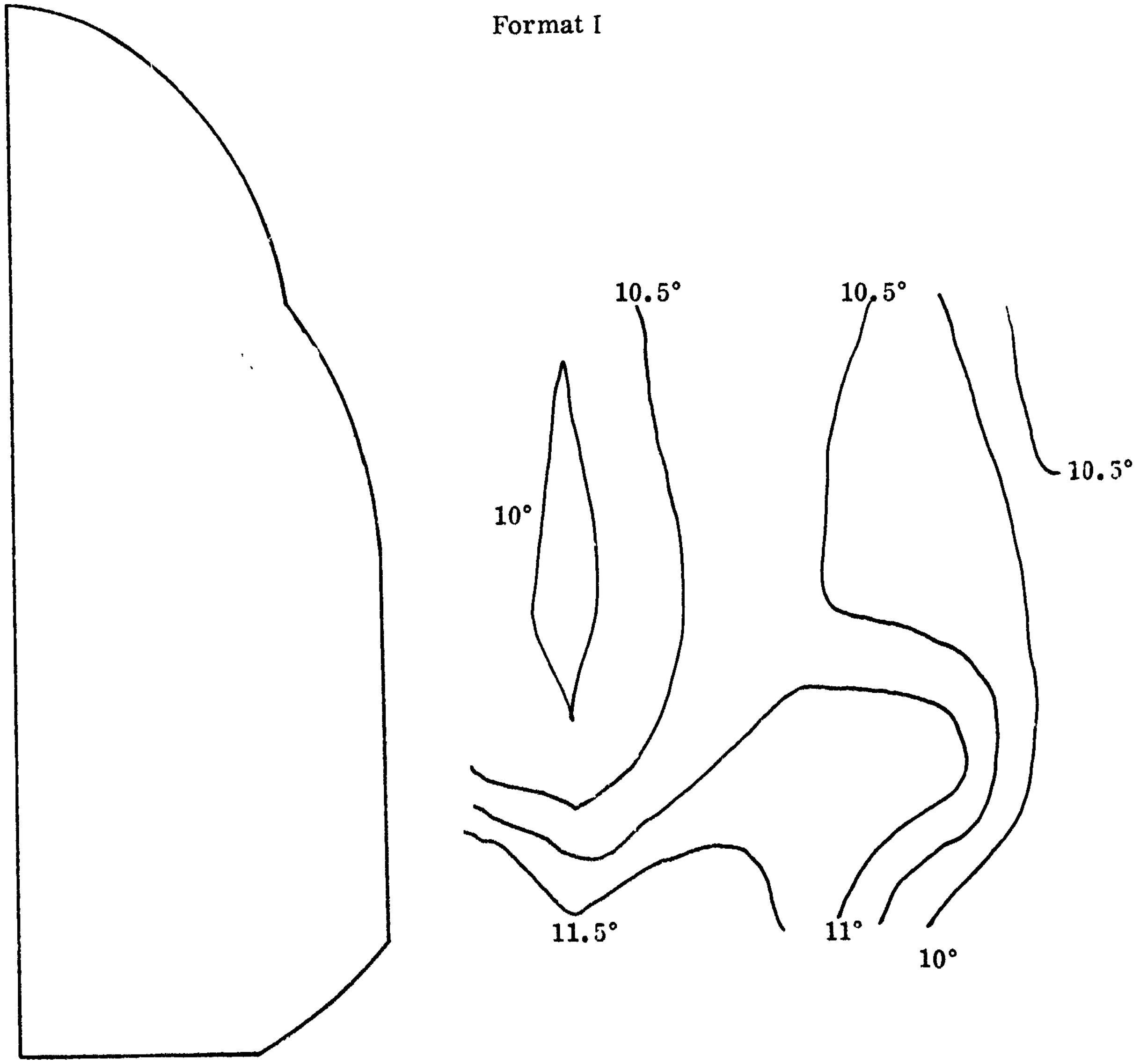

Figure 7-85. Local Flow Angularity

Fuselage 4
PCPN
Mach Number = 2.2
α = 10°

Format I

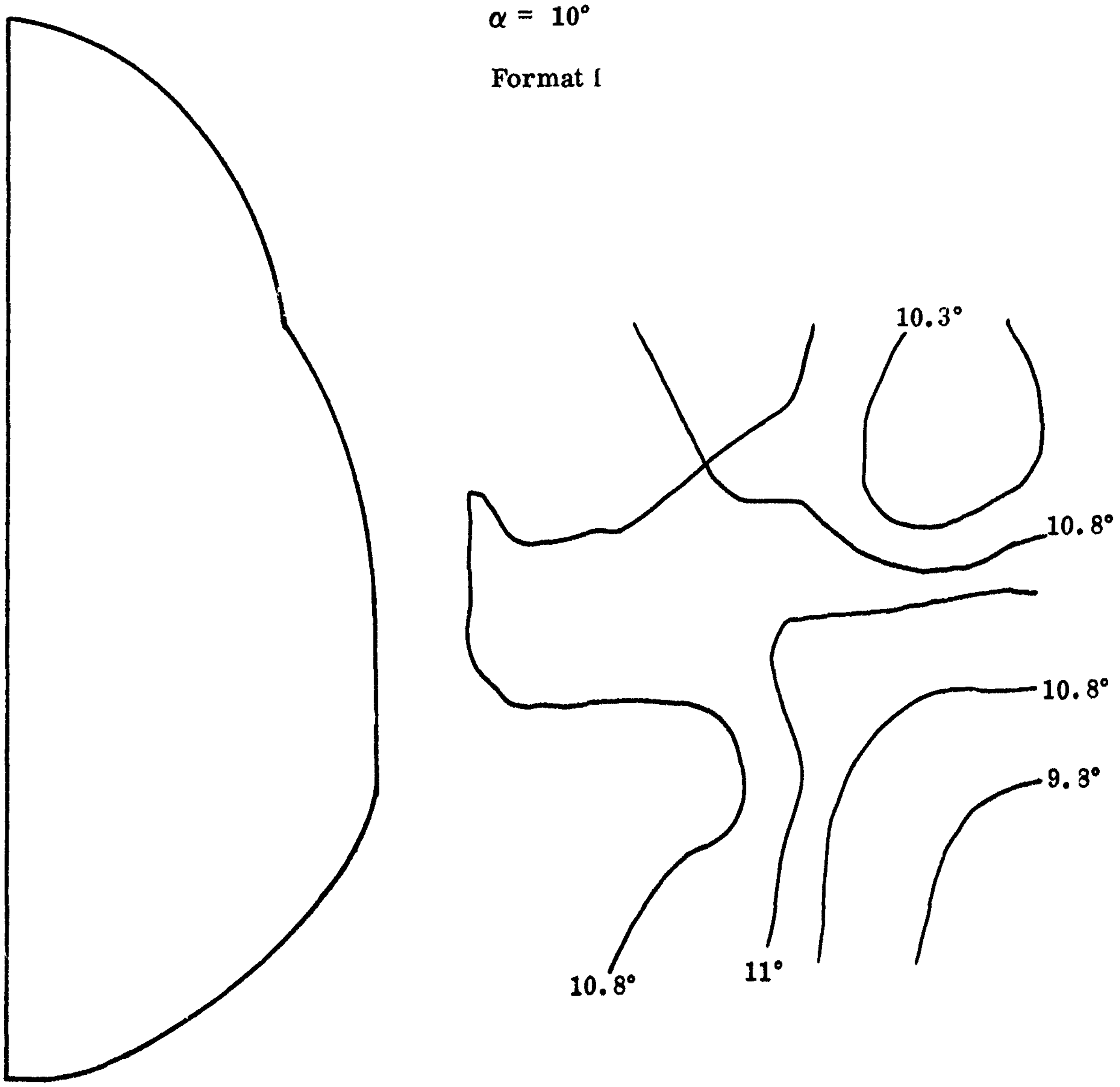

Figure 7-86. Local Flow Angularity

Fuselage 5
PCPN
Mach Number = 2.2
α = 10°

Format I

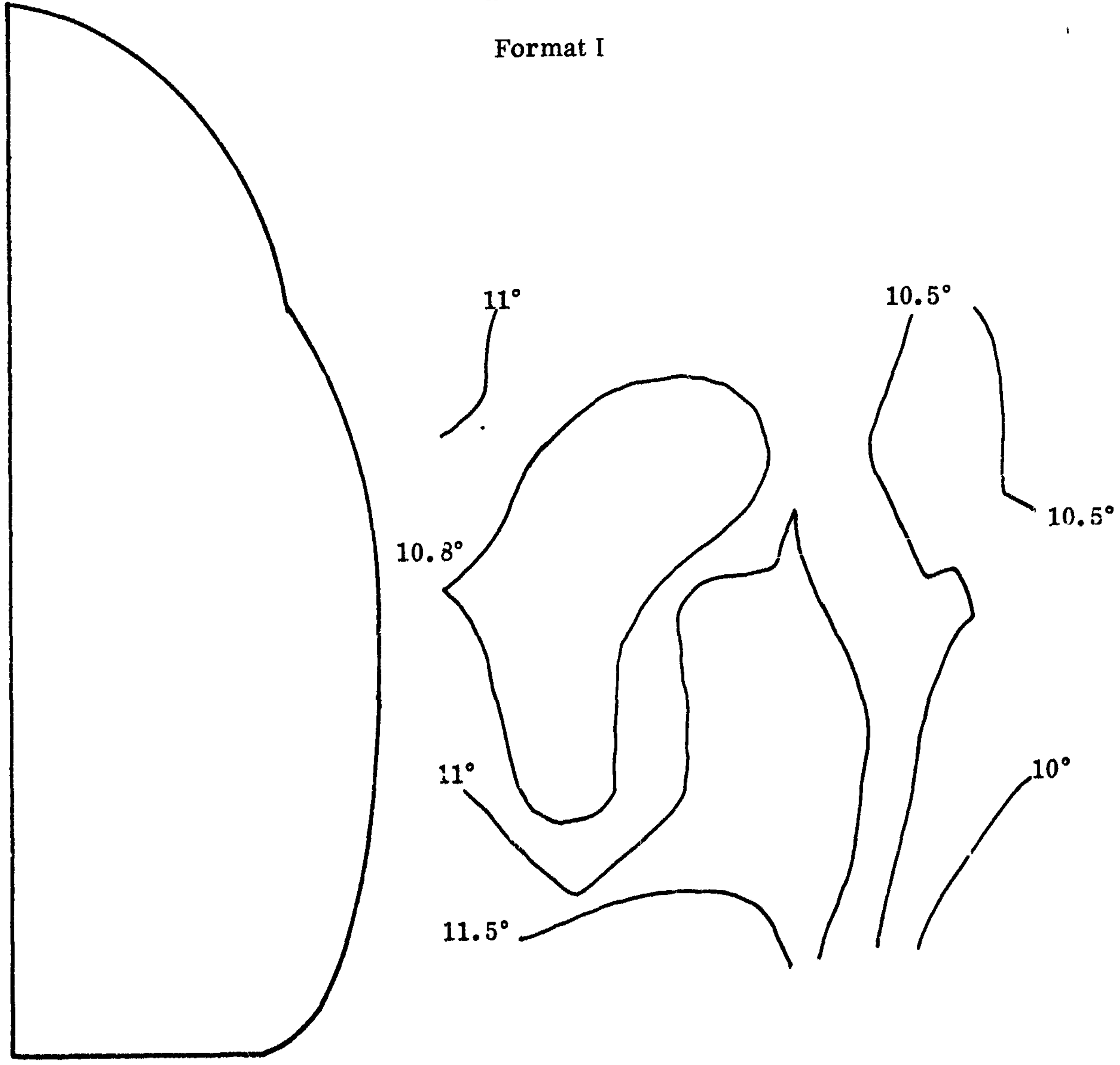

Figure 7-87. Local Flow Angularity

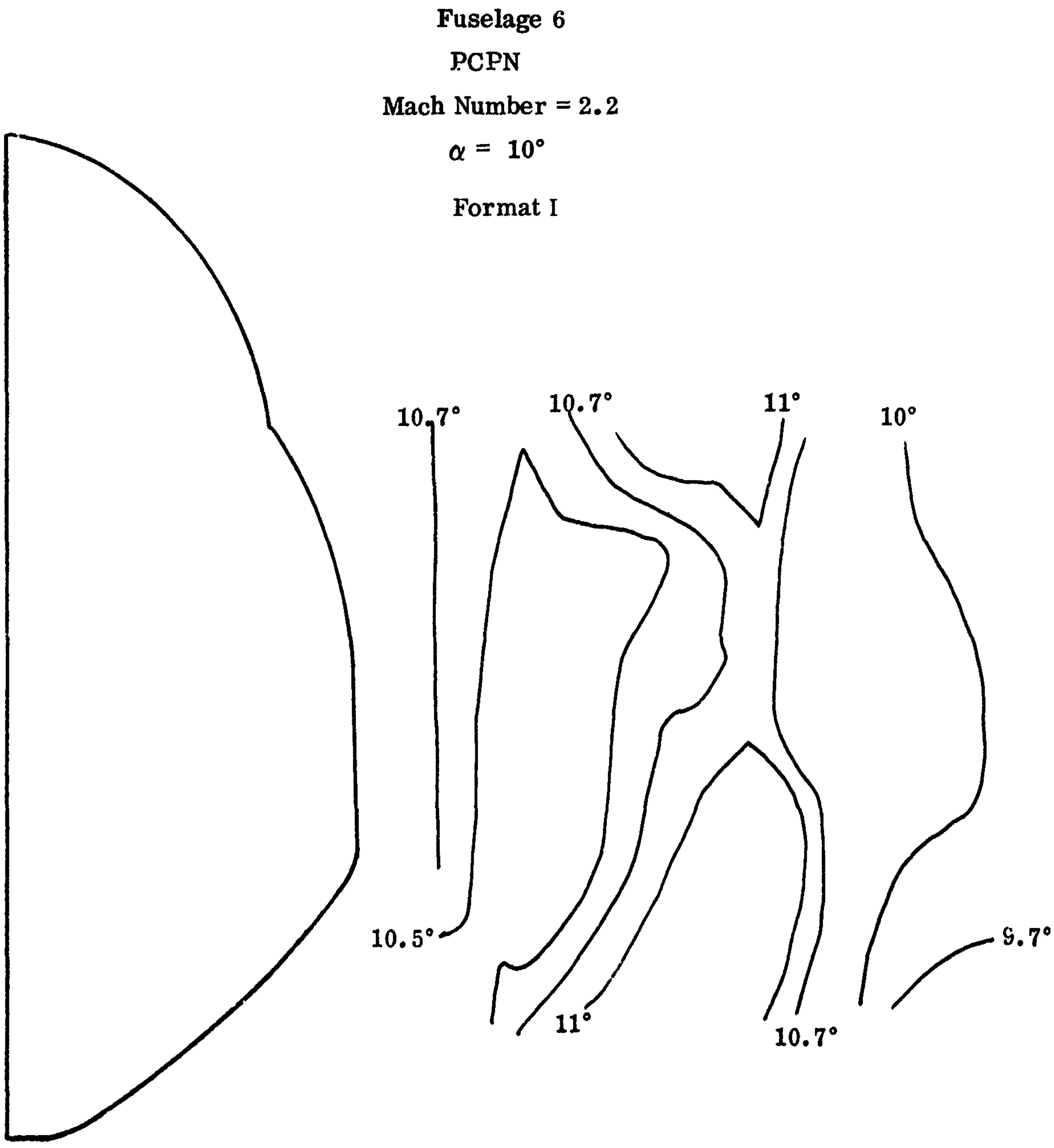

Figure 7-88. Local Flow Angularity

Fuselage 8
PCPN
Mach Number = 2.2
$\alpha = 10°$
Format I

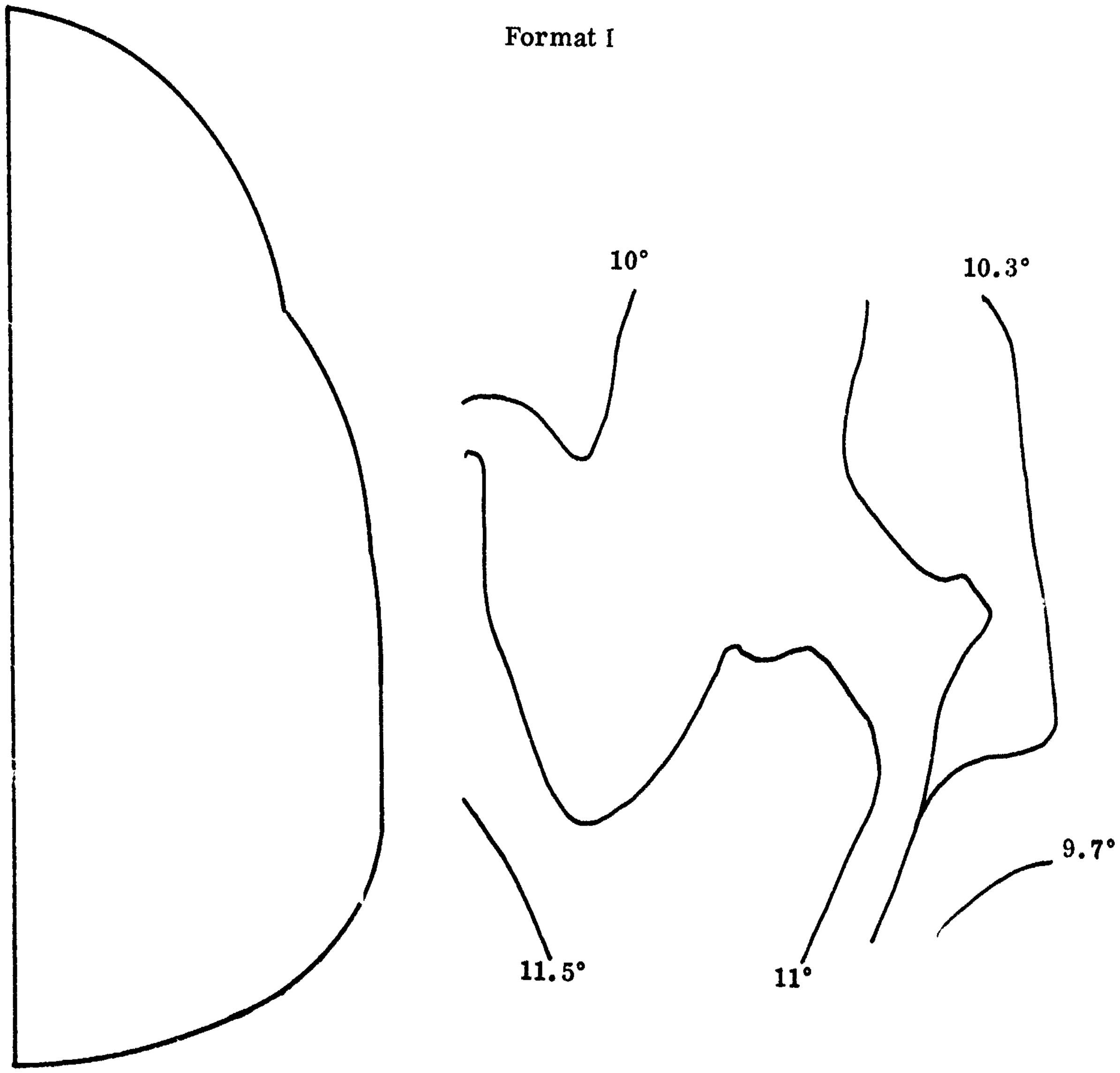

Figure 7-89. Local Flow Angularity

Fuselage 1
PCPN
Mach Number = 2.5
$\alpha = 5°$
Format I

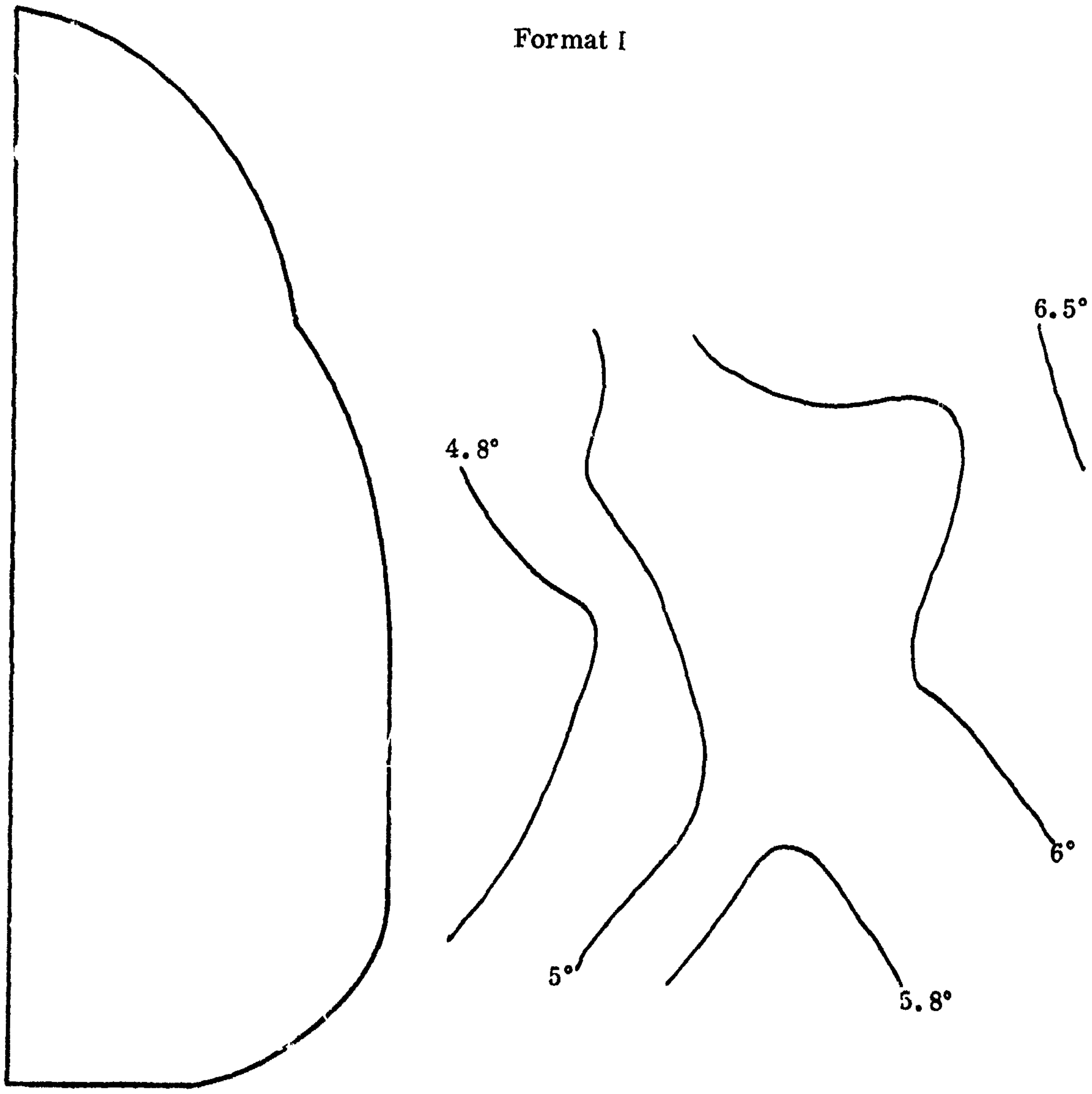

Figure 7-90. Local Flow Angularity

Fuselage 2
PCPN
Mach Number = 2.5
$\alpha = 5°$
Format I

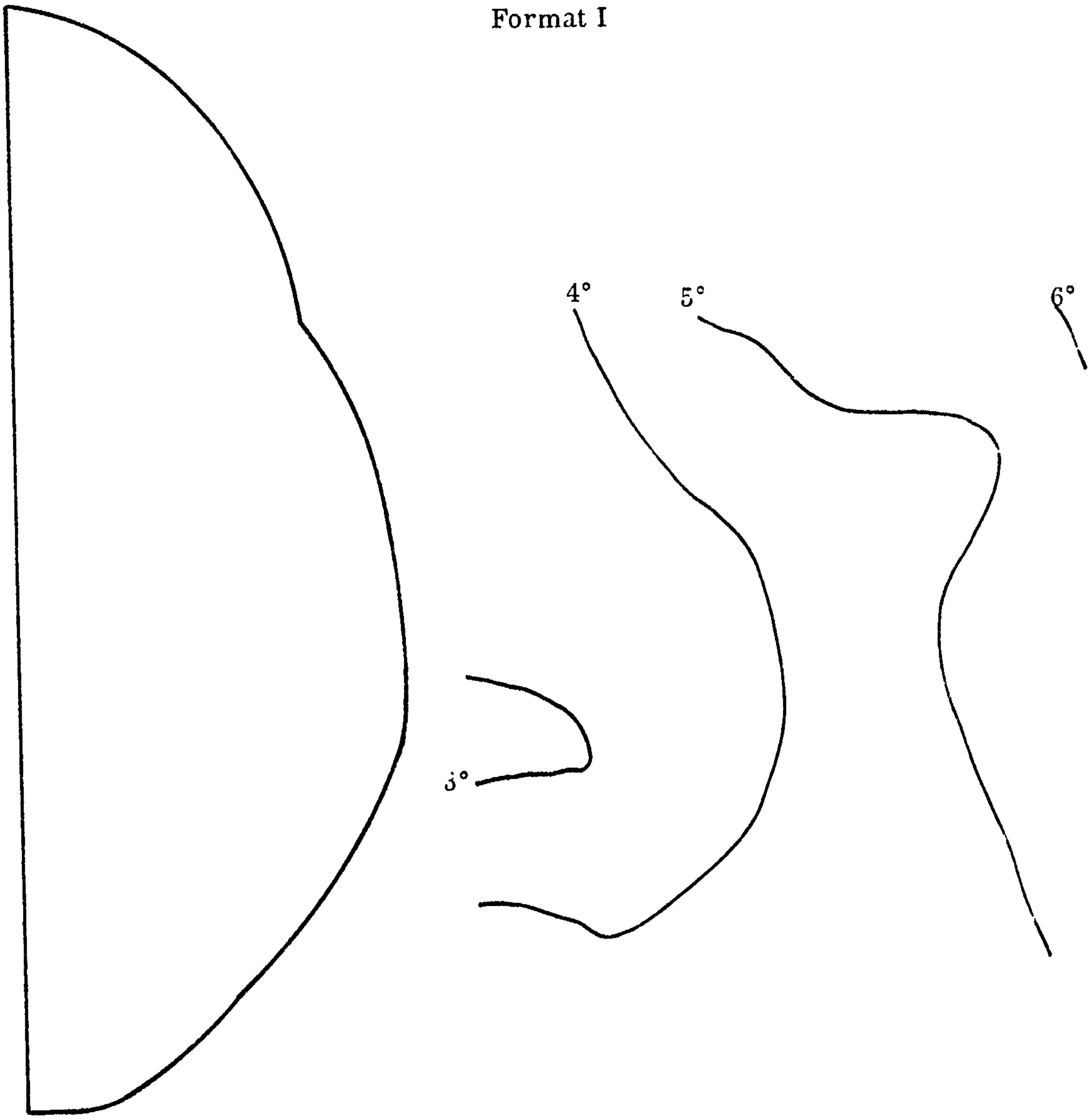

Figure 7-91. Local Flow Angularity

Fuselage 3
PCPN
Mach Number = 2.5
$\alpha = 5°$
Format I

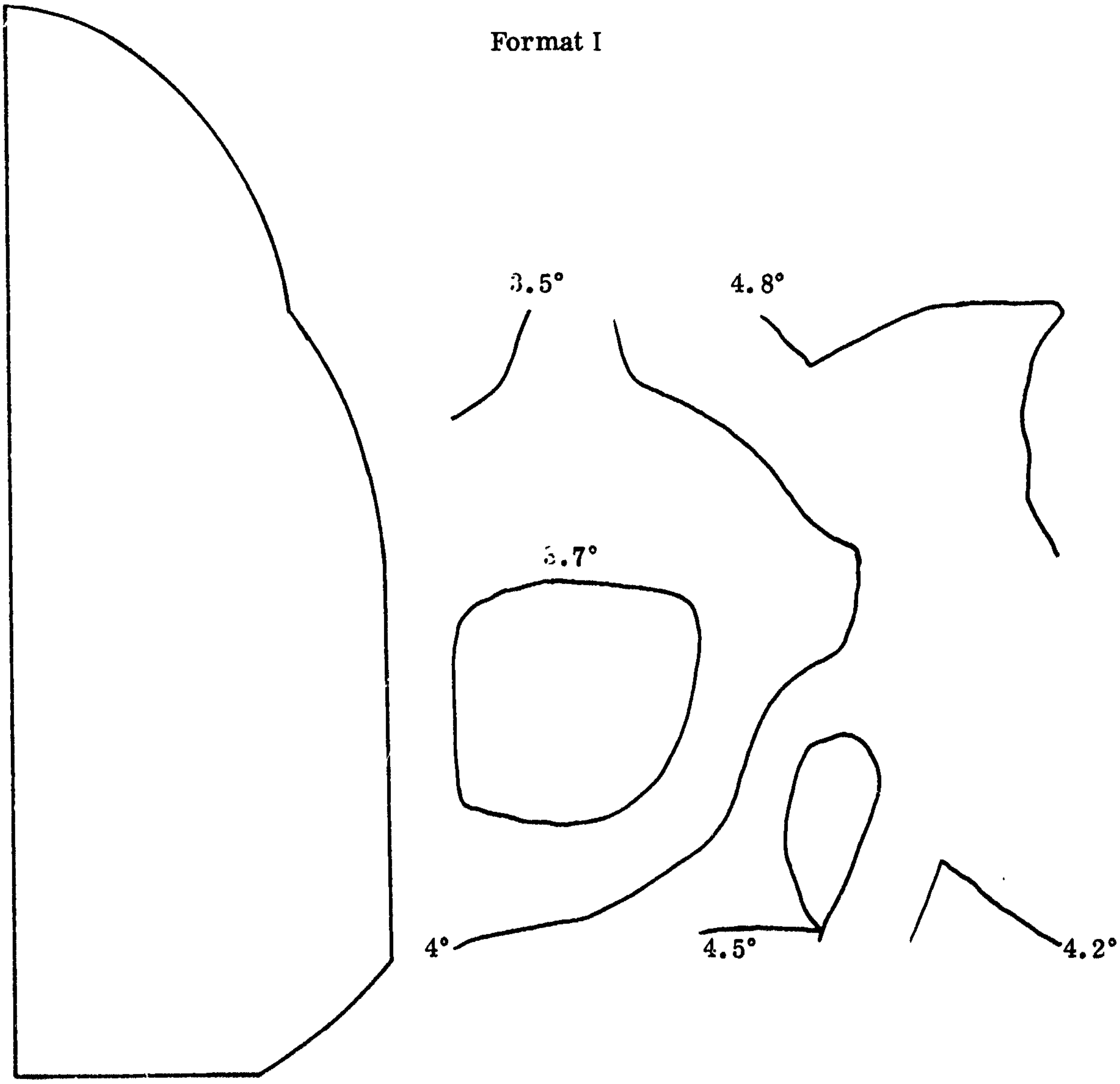

Figure 7-92. Local Flow Angularity

Fuselage 4
PCPN
Mach Number = 2.5
$\alpha = 5°$
Format I

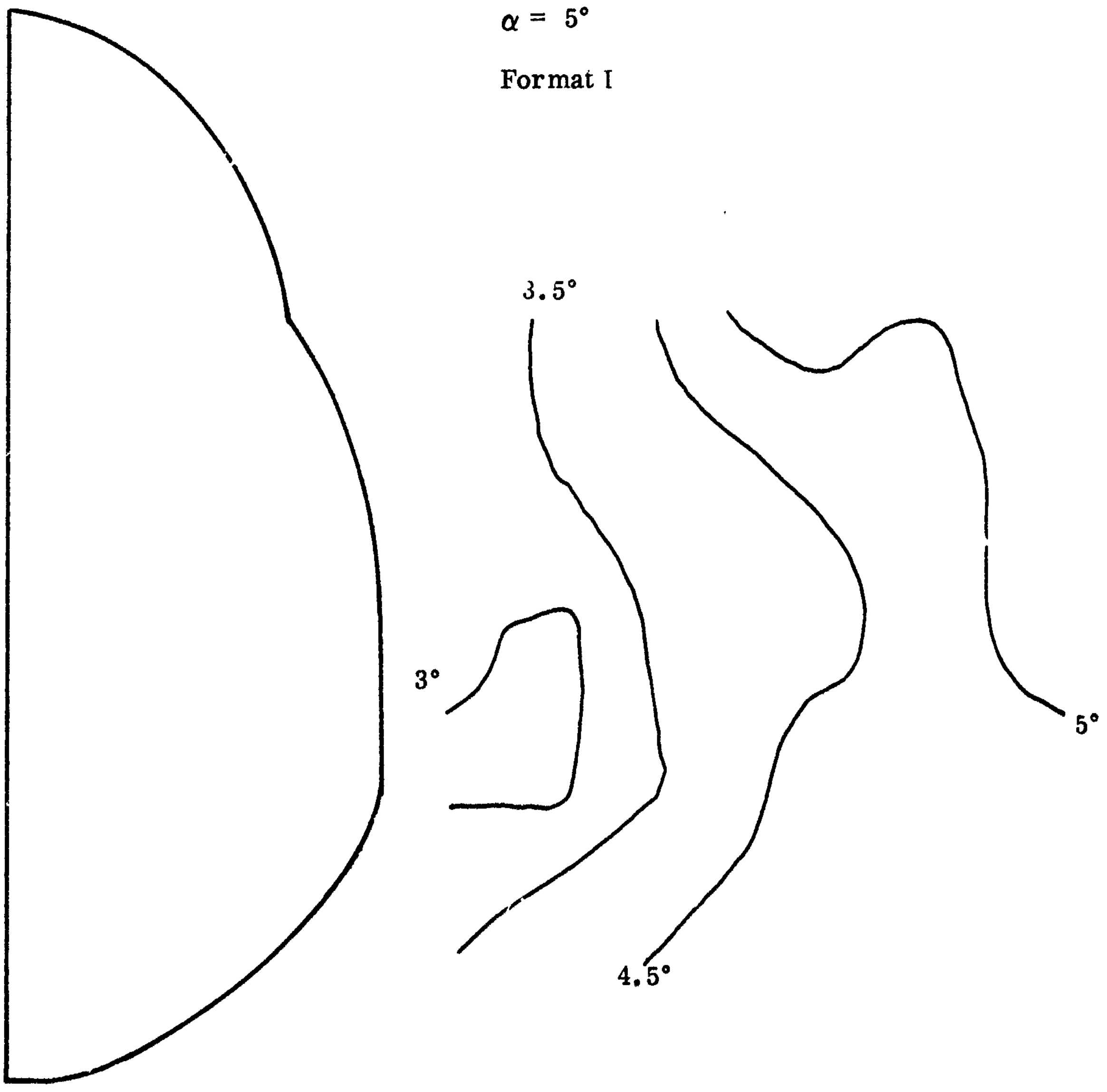

Figure 7-93. Local Flow Angularity

Fuselage 5
PCPN
Mach Number = 2.5
$\alpha = 5°$

Format I

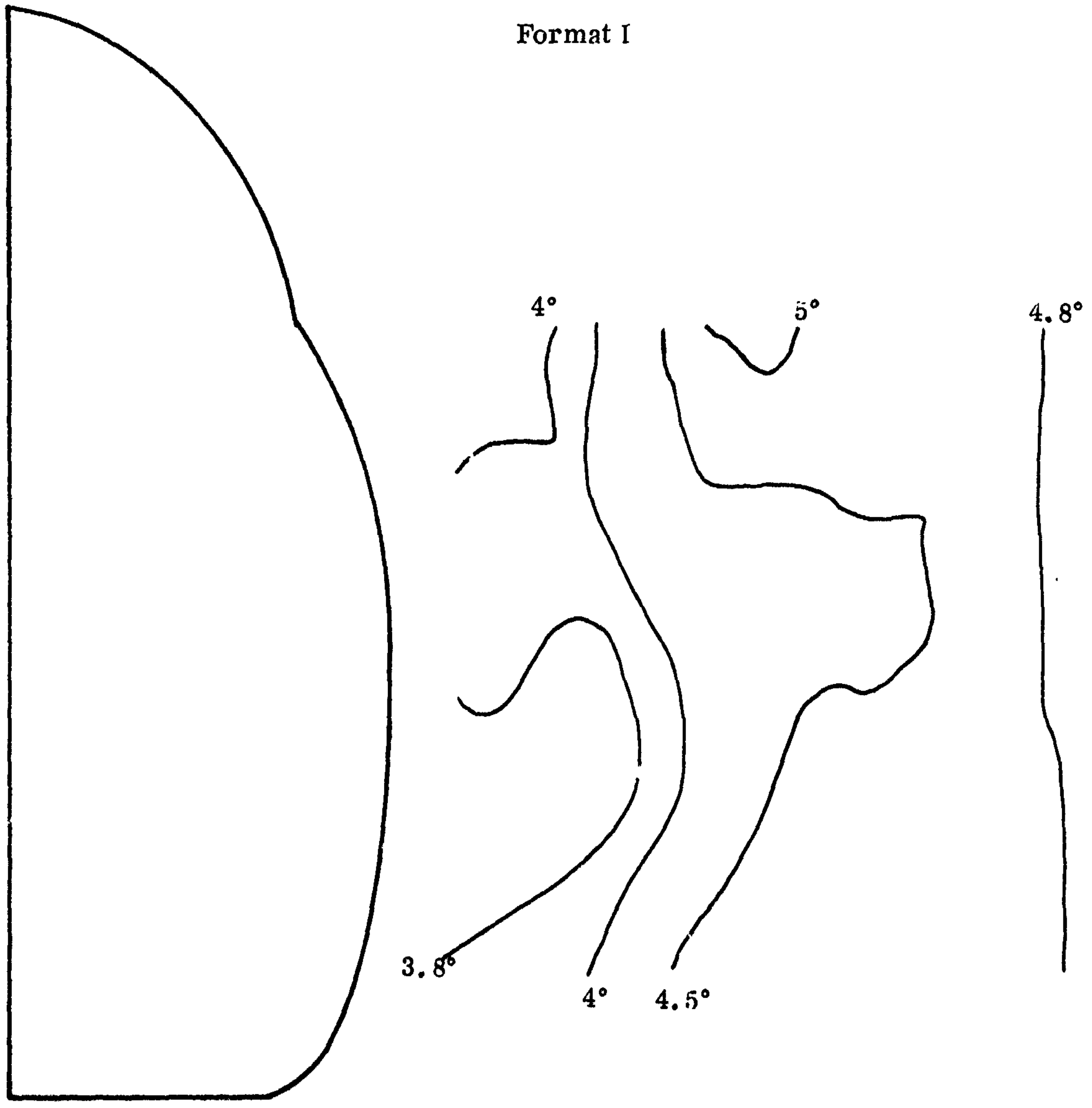

Figure 7-94. Local Flow Angularity

Fuselage 6
PCPN
Mach Number = 2.5
$\alpha = 5°$
Format I

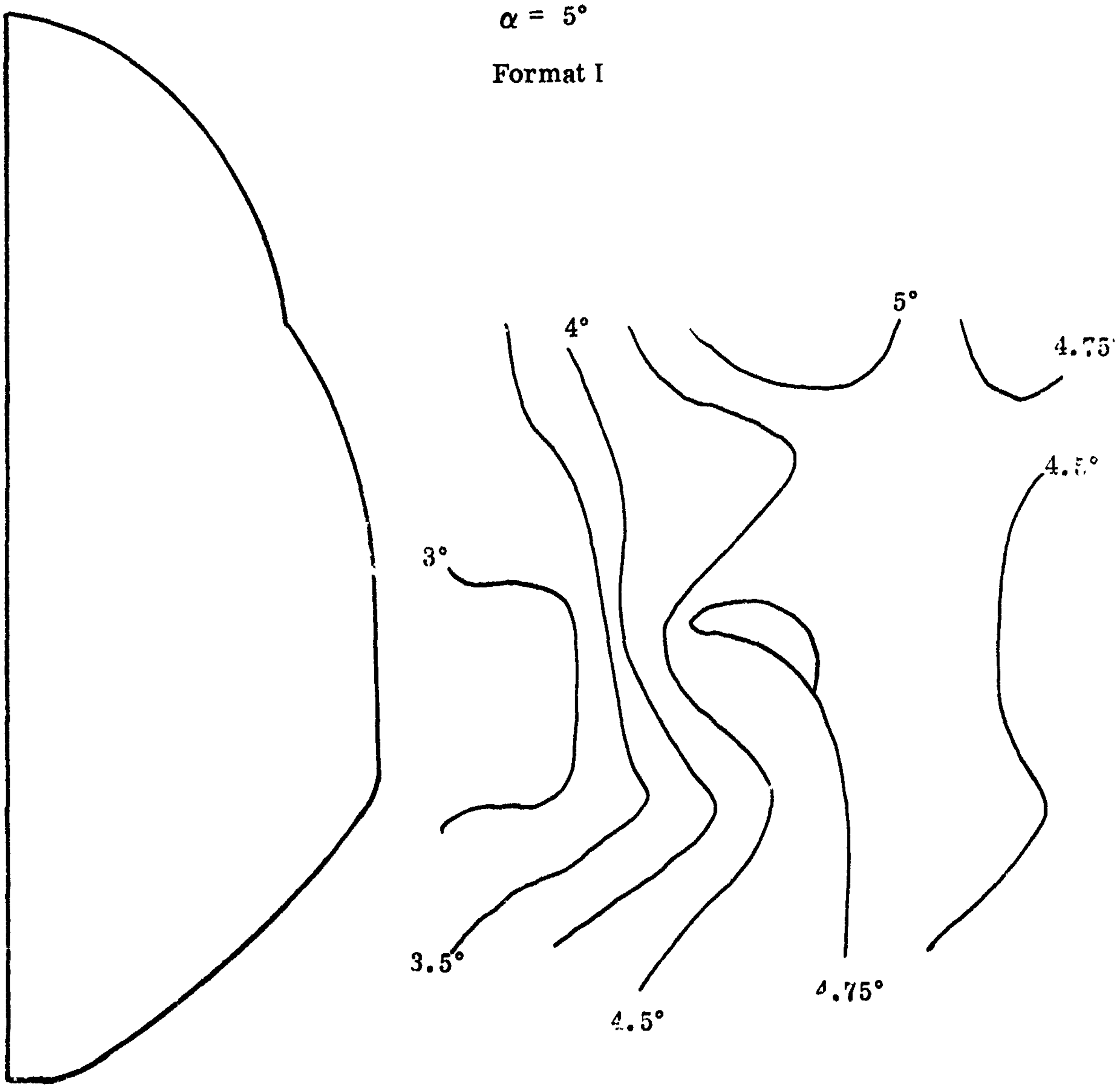

Figure 7-95. Local Flow Angularity

Fuselage 8
PCPN
Mach Number = 2.5°
α = 5°
Format I

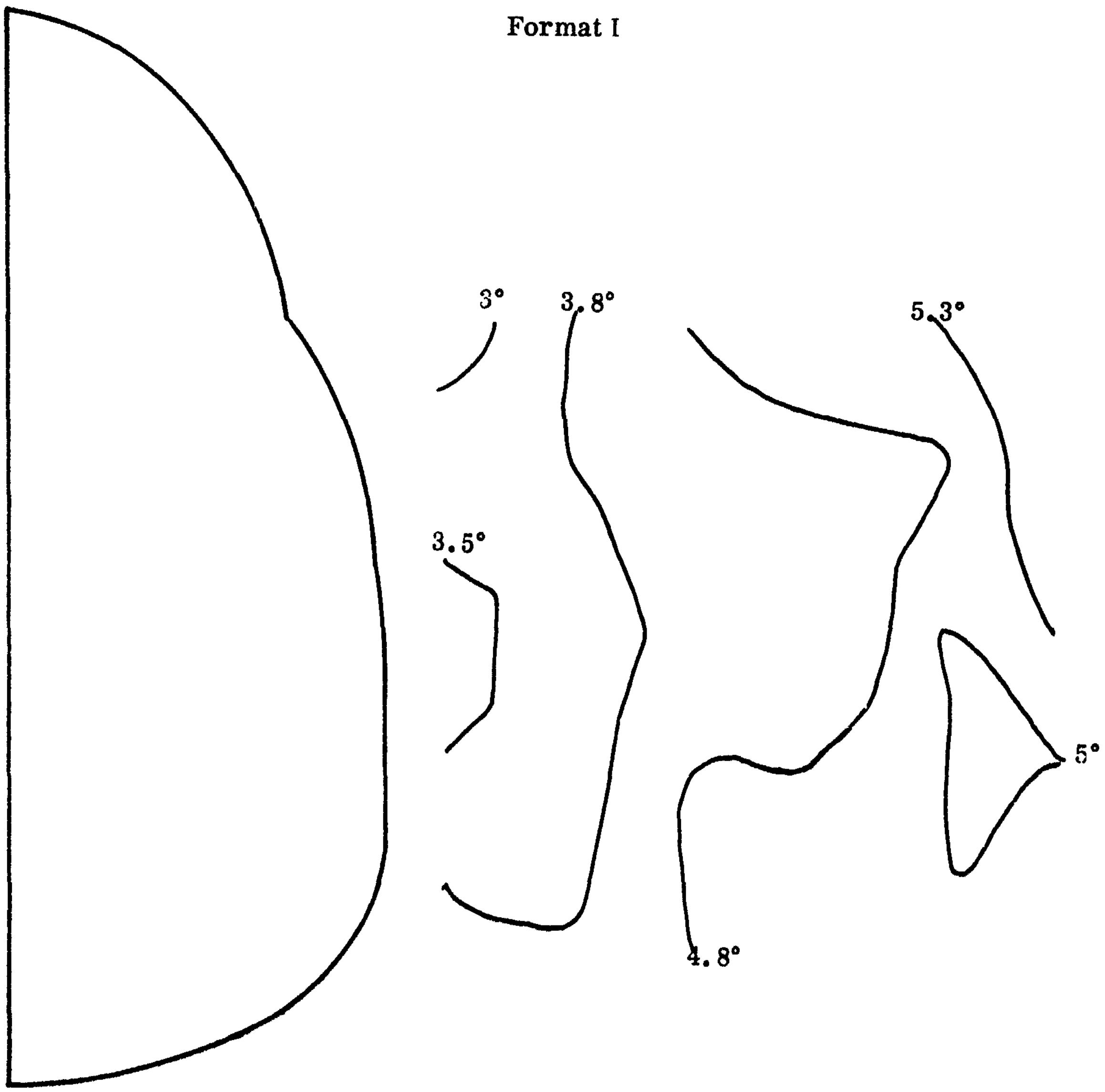

Figure 7-96. Local Flow Angularity

average sidewash remains true at this Mach number. The absolute level of sidewash probably exerts some small influence on inlet performance.

7.1.4 Correlation of Experimental Data with Theory

The ability of the simplified analytical method to predict the vehicle induced flow field was evaluated during this analysis task. The analytical approach employed to estimate the flow field, and the resultant quantitative predictions are presented in Section III. These estimates were compared with the data generated during the test program. The primary objectives of this effort were to evaluate the predictive accuracy of the analytical technique as a function of angle of attack, vehicle geometry, and free stream Mach number.

In general, the results achieved are viewed as very promising. This conclusion is based upon the attainment of good agreement, in many cases, using the analytical approach as originally developed. More importantly, perhaps,is the fact that, for those cases with relatively poor agreement, both analytical and empirical avenues of refinement were indicated. In summary, poor agreement between theory and experiment can be traced to either of two basic flaws in the analytical technique. These flaws are a weak inherent accounting of the canopy induced overpressure and an insensitivity to the near surface effects produced by different lower fuselage corner radii. In the first case, it must be admitted that the level of influence exerted by the canopy upon the flow field was rather unexpected. With regard to the fuselage corner radius, a degree of insensitivity was anticipated, as the result of applying a reference plane type analysis. The primary reason for this is that the effective fuselage nose cone is the dominant parameter determining the downstream thermodynamic properties. Variations in corner radius, while producing different effective fuselage contours, change the Prandtl-Meyer angle only in a minor way. This results in the prediction of small peripheral pressure gradients around the corner and very small changes in this gradient as the fuselage geometry is varied.

To illustrate the degree of correlation achieved several test conditions have been selected for discussion, they are:

Fuselage	M_∞	α	β
3	2.2	+5	0
3	2.2	+15	0
2	2.2	+15	0

The fuselage geometries were selected as representative of both a small corner radius (fuselage 3) and a large corner radius (fuselage 2). The Mach number is typical of the supersonic case. The results discussed previously showed that variations in Mach number introduced quantitative changes in the local flow properties. Theory generates similar quantitative changes. As a result, the strength of localized flow field interactions vary with Mach number; however, Mach number dependent flow phenomena do not appear. Therefore, the use of one representative Mach number is reasonable. The angles of attack were selected to depict the correlation at both low and high values representative of cruise and maneuvering operation.

Presented in Figure 7-97 is a comparison of the theoretical and experimental surface static pressure distribution along the surface of each of the 5 reference planes employed, using fuselage 3, at an angle of attack of +5 degrees. Good agreement was anticipated for this condition due to the nearly symmetrical flow field engendered by the drooped nose. It can be seen that the analytical estimates give a fair representation of the distributions. A tendency toward underestimation of the absolute pressure levels can be seen. This effect is attributable to presence of the canopy induced overpressure which the theory did not anticipate. Figure 7-98 presents the Mach number correlation achieved for this case. The results for this less sensitive parameter are consistent with those achieved for the static pressures even though visually they appear to agree with theory better. Based upon the comparison of theoretical and experimental surface properties it is logical to expect that some difference exists between the predicted and actual outboard flow field characteristics. Presented schematically in Figure 7-99 is a comparison of the flow field angularity at this test condition. Due to the weak effect predicted for the canopy, the unrestrained favorable upwash pressure gradient established by the fuselage corner and angle of attack has induced a mild inboard upwash region. Theory also predicts an outboard downwash region, established by the cross flow over the small effective nose droop and the overpressure induced by the weak effective detached canopy wave. In

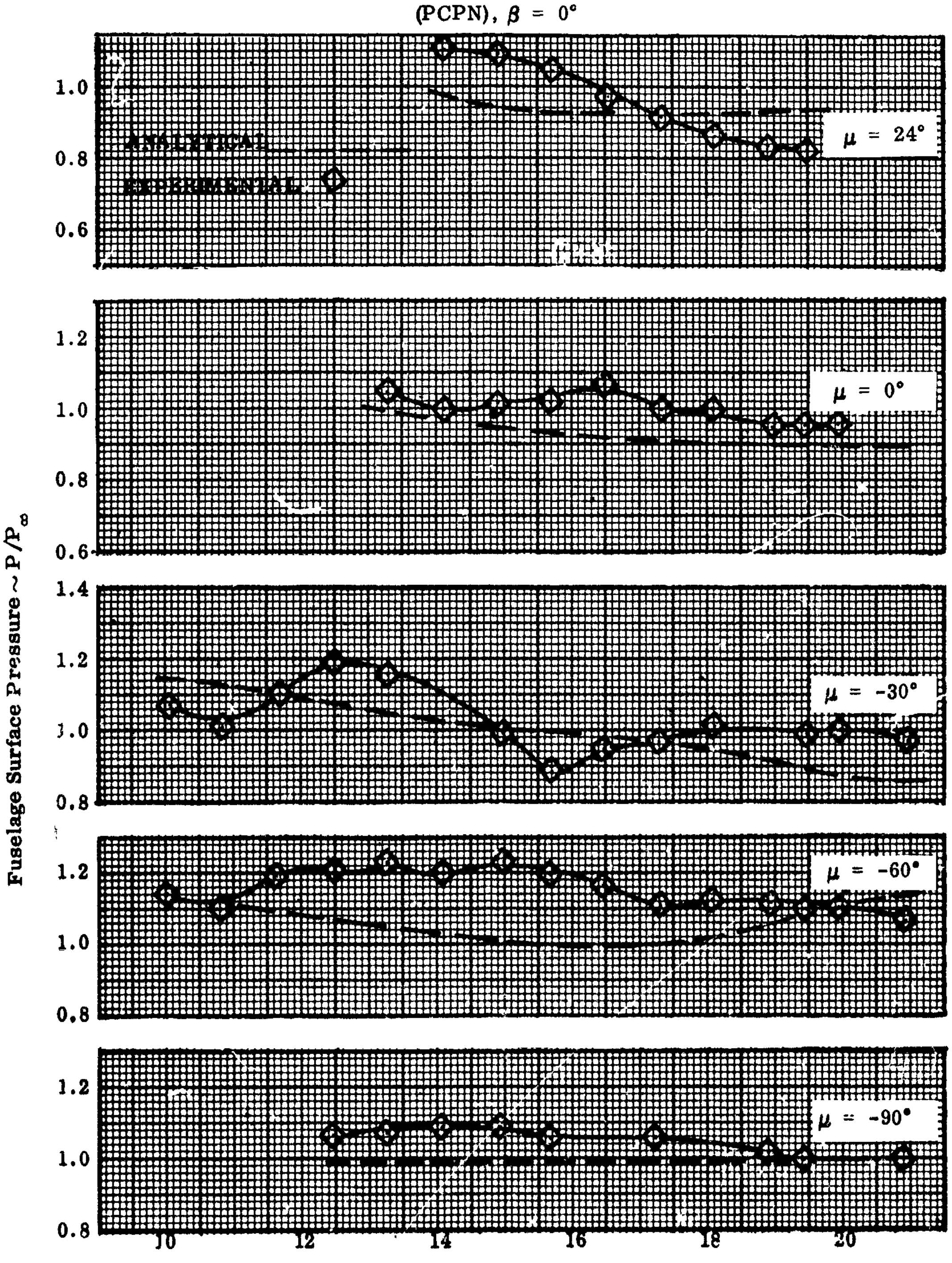

Figure 7-97. Static Pressure Distribution, Fuselage 3
$M_\infty = 2.2$, $\alpha = 5°$
Format I

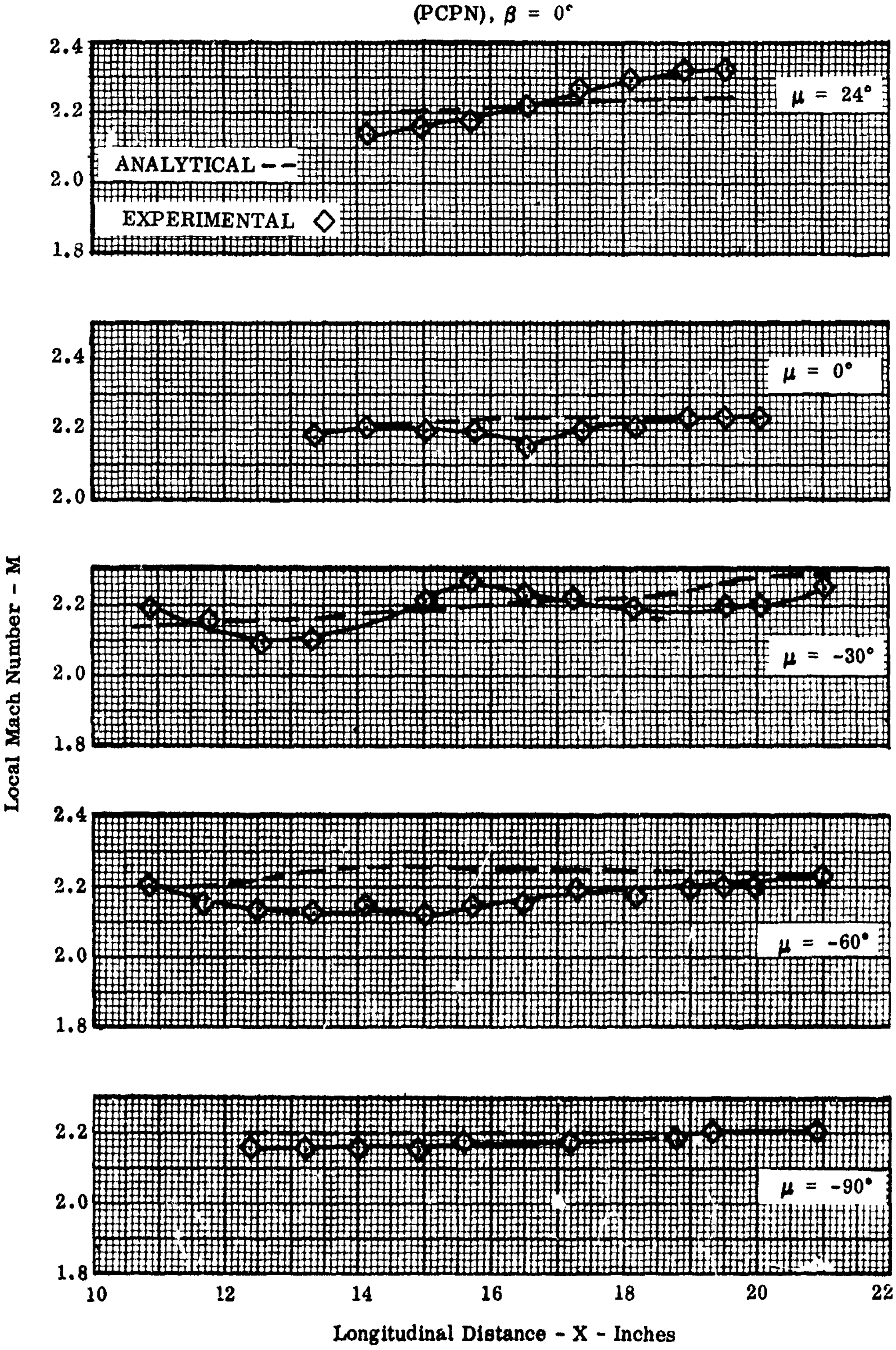

Figure 7-98. Local Mach Distribution, Fuselage 3
M_∞ = 2.2, α = 5°
Format I

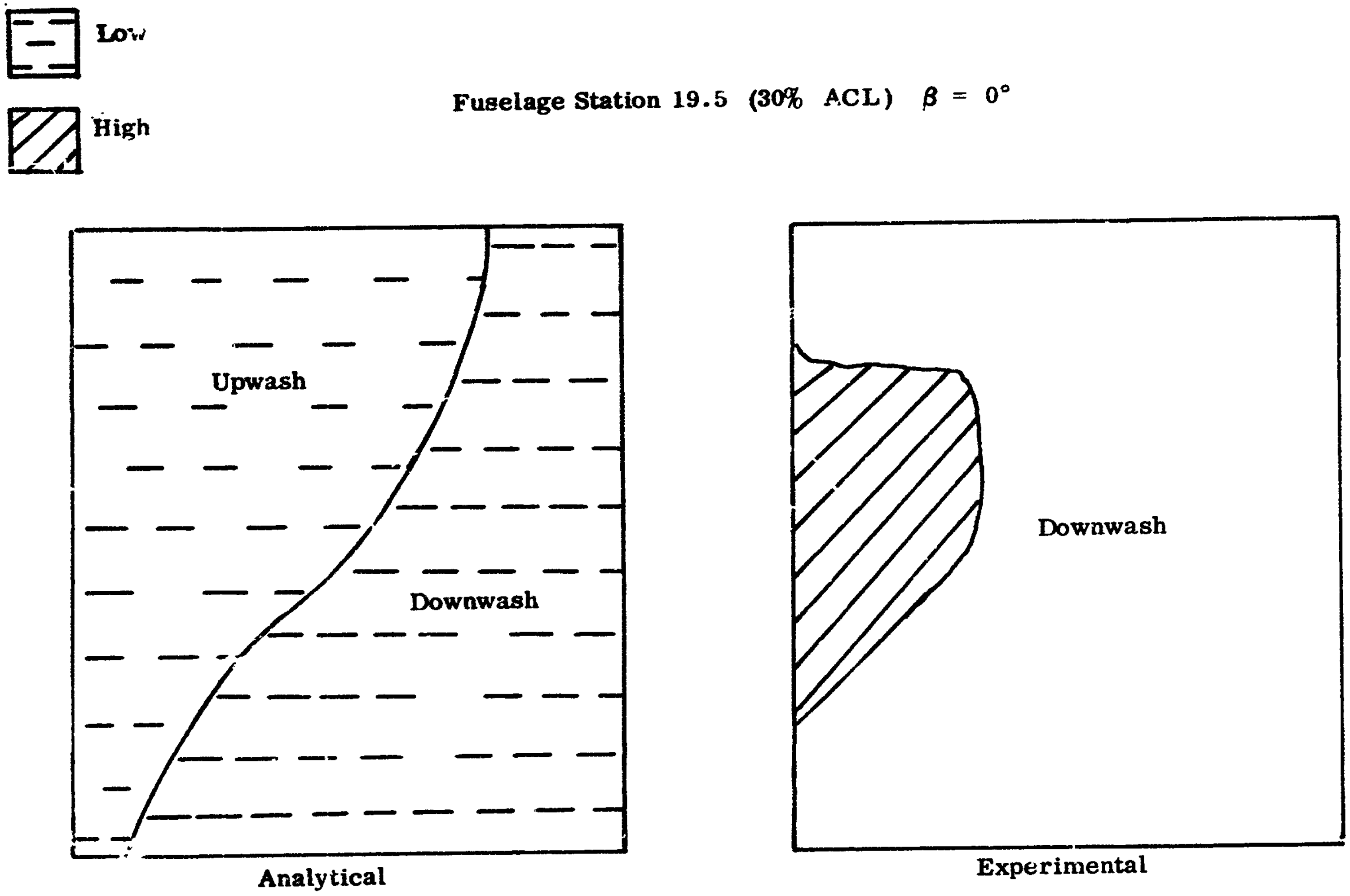
Low
High
Upwash
Downwash
Analytical
Downwash
Experimental

Fuselage Station 19.5 (30% ACL) $\beta = 0°$

Figure 7-99. Flow Angularity, Fuselage 3
$M_\infty = 2.2, \alpha = 5°$
Format I

reality the canopy overpressure induces a compression/compression interaction between the flow within the canopy shock layer and the weak inherent upwash flow field emanating from the lower fuselage corner. The result, in this case, is a mild overall downwash region. It is pointed out that although the schematic representations of the analytical and experimental flow fields appear dissimilar the difference is, in fact, quite small and both cases have near uniform fields. Supporting evidence is seen in Figure 7-100 where the local Mach number distribution throughout the flow field is shown schematically. Here the basic composition of both flow fields is similar, however, again the influence of the canopy is missing from the analytical estimate. In addition, the compressive interaction that takes place between the canopy induced overpressure and the fuselage corner induced upwash produces an average local Mach number approximating Mach 2.2, whereas the analysis, with a weak accounting of the canopy influence estimated a higher average Mach number, approximately 2.4.

For the high angle of attack case (15 degrees) schematic comparisons of the analytical and experimental flow field are shown in Figures 7-101 and 7-102. The need for an improved accounting of both the fuselage corner and canopy effects, as discussed previously is evident in these comparisons. The weakness of the analysis in predicting the fuselage corner effects, can be seen from an examination of the estimated and actual surface pressure and Mach number distributions presented in Figure 7-103 and 7-104 respectively. The insensitivity of the analysis can be seen from the poor agreement achieved in the region of the corner (μ = -30°). The acceleration around the relatively small fuselage corner causes a rapid and significant decay in local static pressure that is underestimated by the analytical technique. On the other hand, this flat fuselage bottom has a quasi two-dimensional lateral profile and as a result good agreement is achieved below the corner (μ = -90° and -60°). To illustrate the effect of the fuselage corner on the agreement of theory and experiment a comparison is presented in Figure 7-105 employing fuselage 2. For this case, the more gentle peripheral pressure gradient has eliminated the extremely poor local agreement seen with fuselage 3, however, the poorest correlation again occurs in the proximity of the fuselage corner (μ = -60° and -90°). The relief afforded by the immediate introduction of the corner reduces the local static pressure below that estimated by theory. The influence upon the flow field characteristics of the larger corner radius, seen in the surface distributions, is also evident

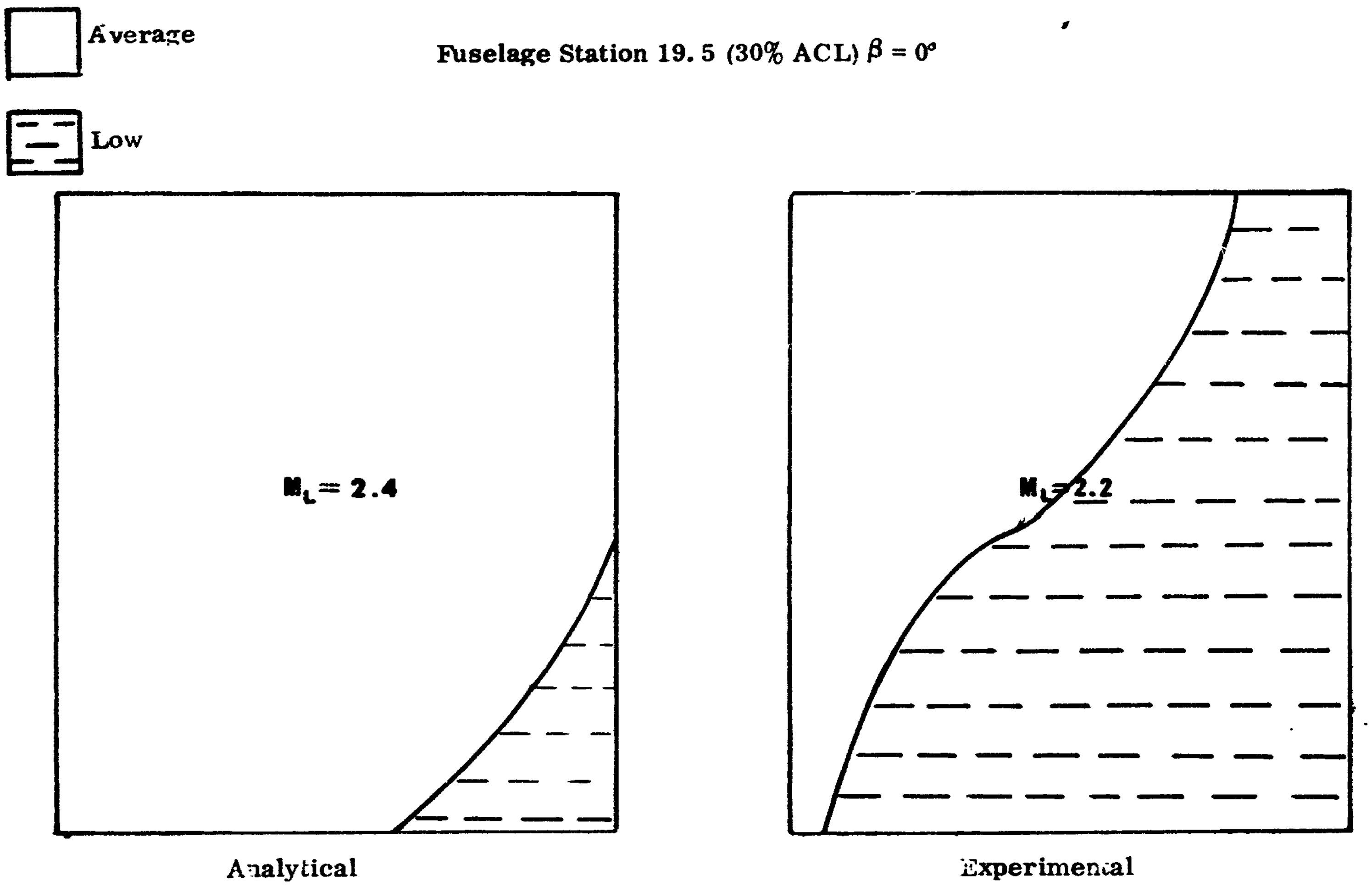

Figure 7-100. Local Mach Number Profile, Fuselage 3

$M_\infty = 2.2$, $\alpha = 5°$

Format I

Fuselage Station 19.5 (30% ACL) $\beta = 0°$

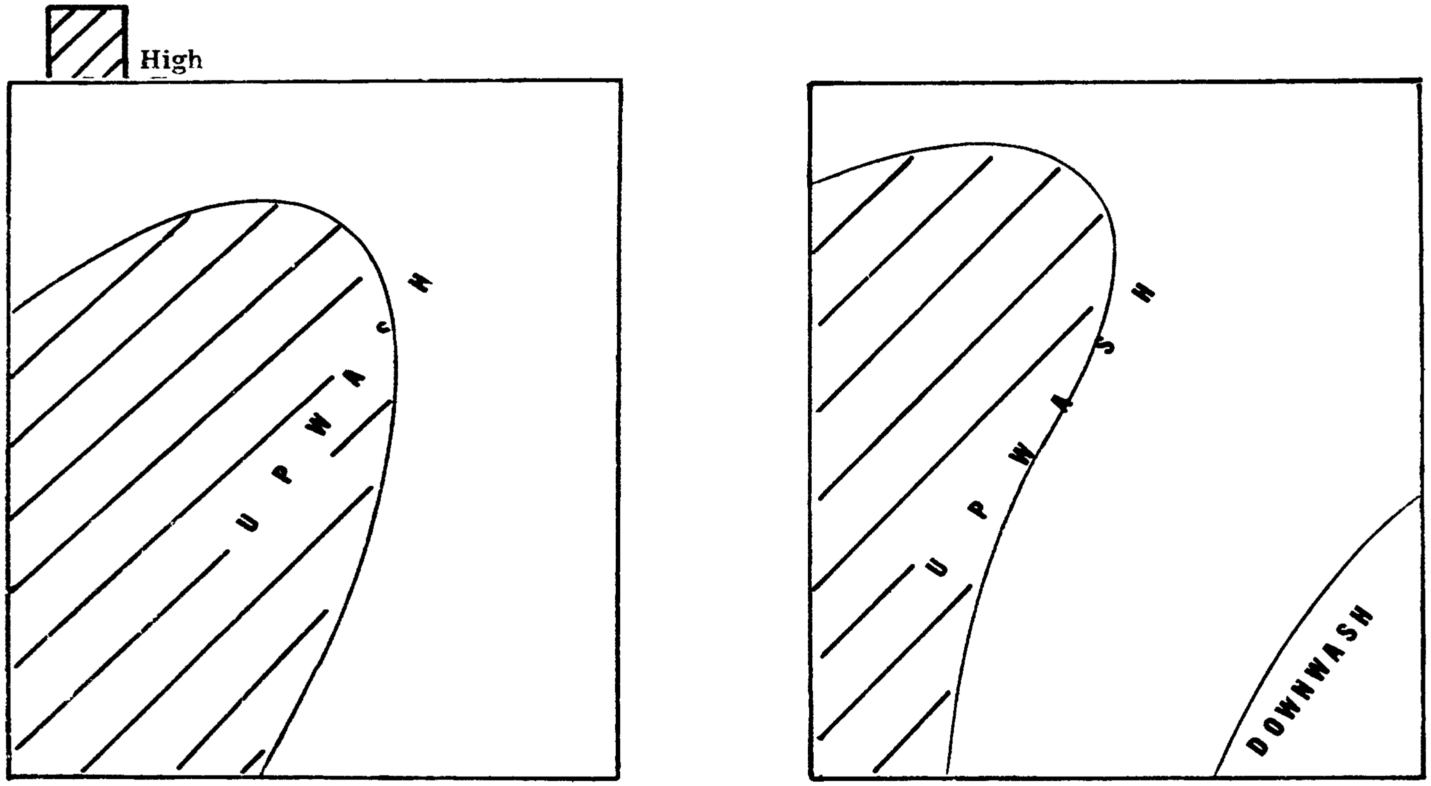
High
UPWASH
UPWASH
DOWNWASH

Analytical

Experimental

Figure 7-101. Flow Angularity, Fuselage 3

$M_\infty = 2.2$, $\alpha = 15°$

Format I

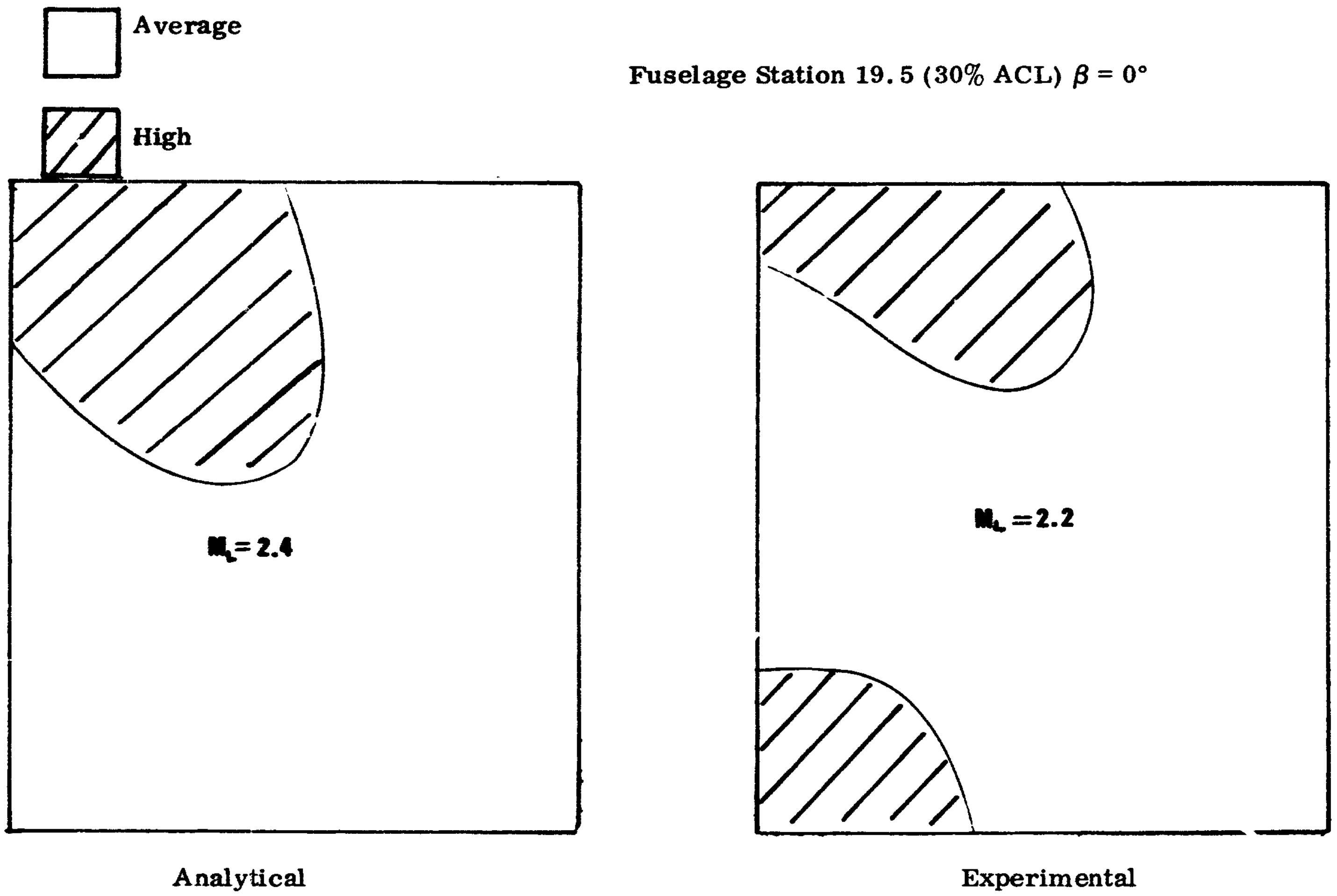

Figure 7-102. Local Mach Number Profile, Fuselage 3

$M_\infty = 2.2$, $\alpha = 15°$

Format I

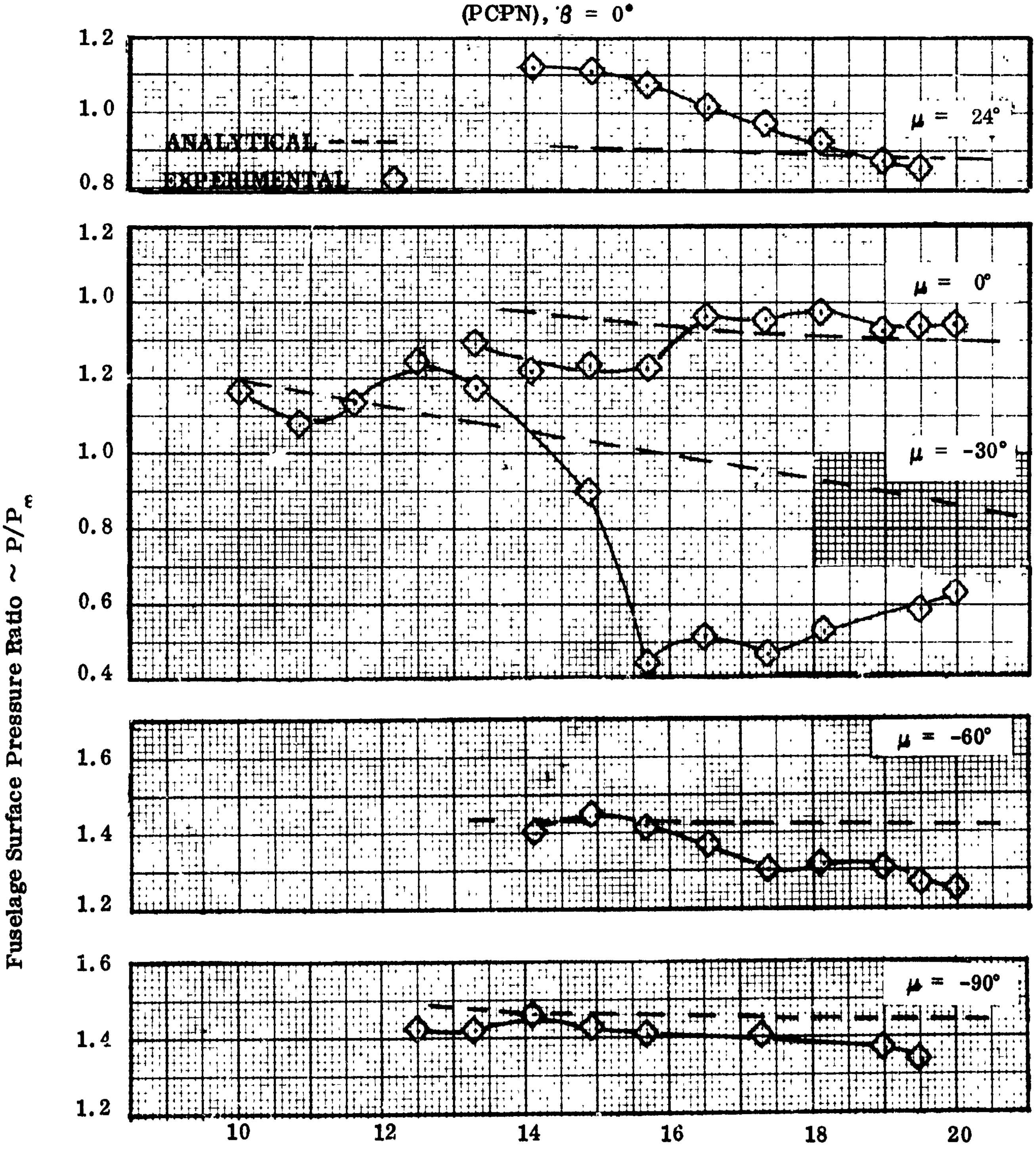

Figure 7-103. Static Pressure Distribution; Fuselage 3

$M_\infty = 2.2$, $\alpha = 15°$

Format I

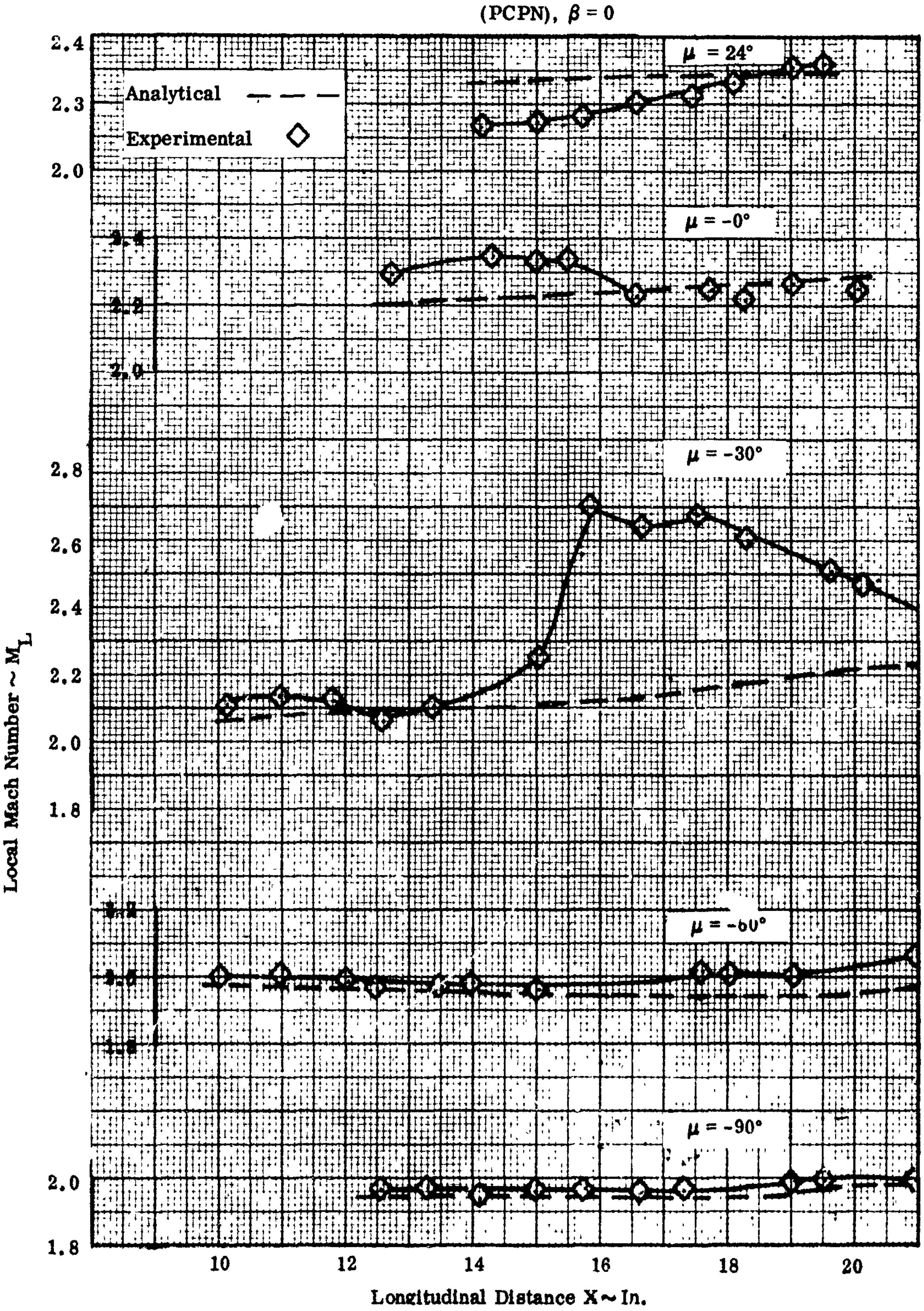

Format I
Figure 7-104. Local Mach Distribution, Fuselage 3
$M_\infty = 2.2$, $\alpha = 15°$

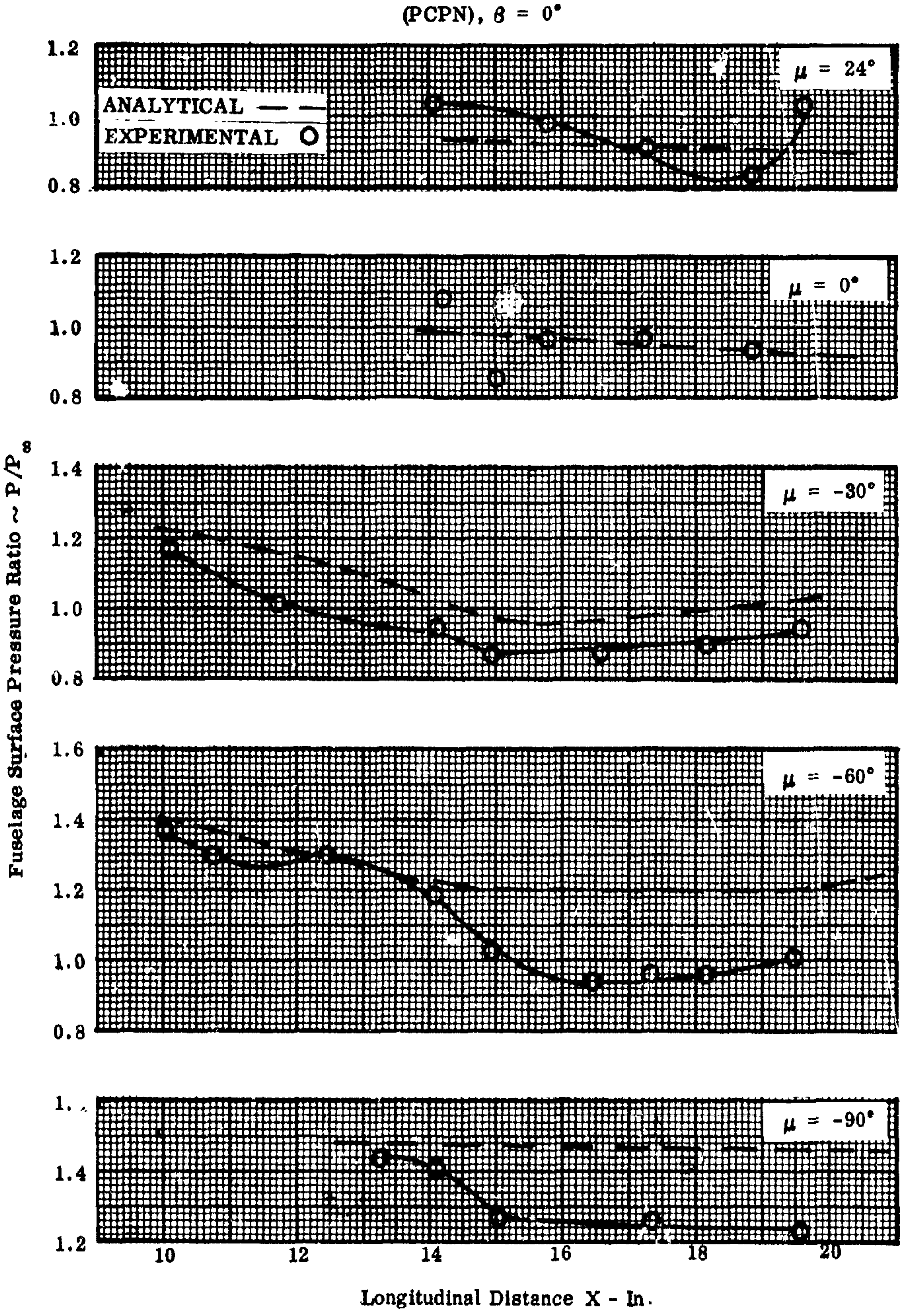

Figure 7-105. Static Pressure Distribution, Fuselage 2

Format I $M_\infty = 2.2$, $\alpha = 15°$

throughout the flow field, as shown in Figure 7-106 where the lower inboard zone of high angularity is reduced in extent and has, in fact, moved away from the bottom BCL. Finally, Figure 7-107 presents the static pressure distribution for all seven fuselage contours for ($\mu = -30°$) at the high angle of attack condition. Also shown is a range of estimated distributions encompassing all of the effective fuselage contours generated by the reference plane method. This figure demonstrates that the analytical method is rather insensitive to corner radius while the actual pressure distribution is, in fact, quite sensitive to corner radius. The figure also shows that the analytical estimates made for the ogival nose section (up to the station where transition from a circular cross-section occurs) are basically unaffected by the final fuselage cross-section. The estimates made in this upstream section of fuselage, where we are dealing with a shape more amenable to analysis are quite acceptable for preliminary design work.

Having evaluated the capability of the basic analytical technique to generate reasonable estimates of the vehicle induced flow field, in sufficient detail to illuminate both the strong and weak points of the computational procedures it remained to investigate avenues potentially capable of improving the predictive accuracy. A study effort was conducted to explore four of these avenues, including two analytical, one semi-empirical, and one empirical approach. A discussion follows.

7.1.5 Refinement of the Reference Plane Technique

7.1.5.1 Introduction

This study explored a modification to the basic reference plane technique. The correlation task indicated the weakness of the basic approach to be a poor prediction of the canopy and the fuselage corner influence upon the flow field, particularly at high angle of attack. In an attempt to correct this deficiency two steps were added to the computational procedure.

The first step estimates the canopy induced shock layer. To remain consistent with the requirements of preliminary design namely, simplified approximations, the initial strength of the canopy shock wave is estimated using one family Prandtl-Meyer expansions. The basic contour line formed at the canopy-fuselage juncture is used as the shock inducing geometry. The nonuniform shock layer

Fuselage Station 19.5 (30% ACL), $\beta = 0°$

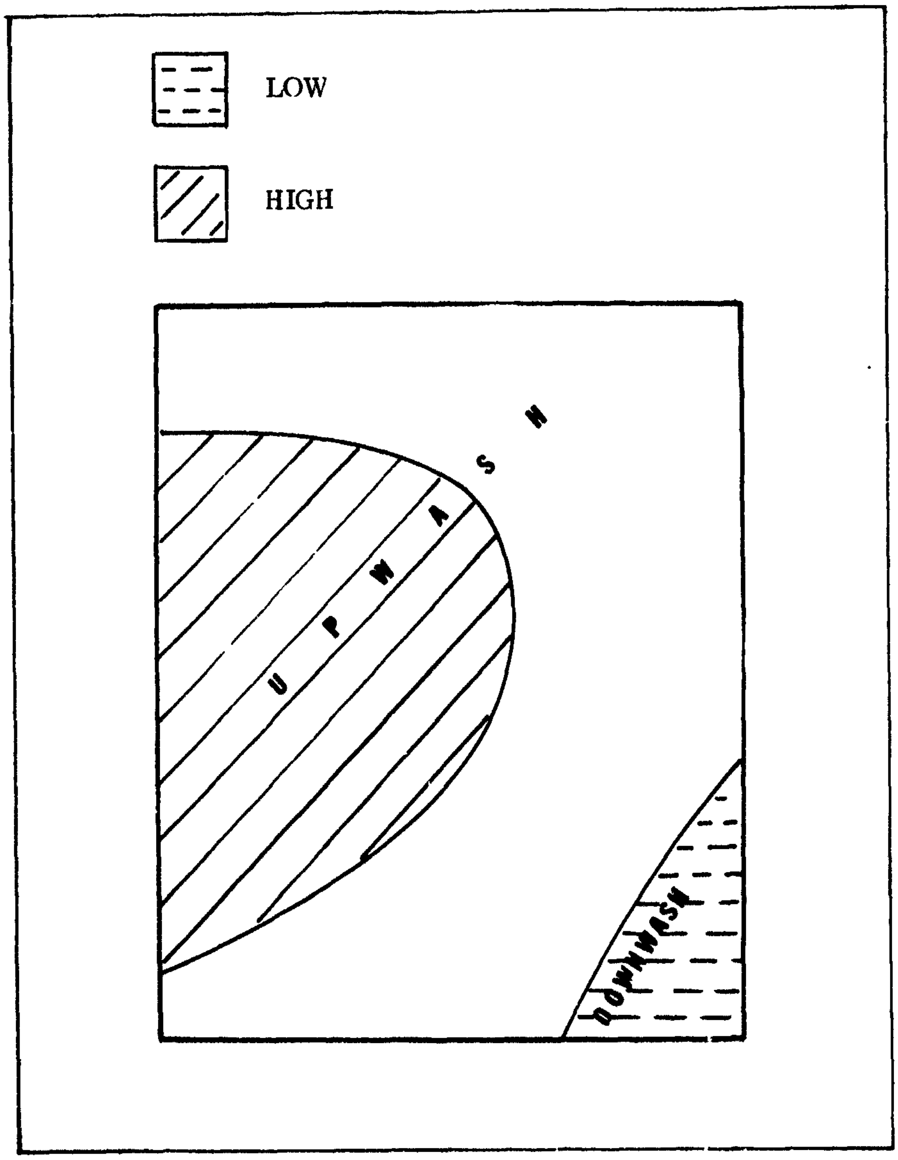
LOW
HIGH
UPWASH
DOWNWASH

Figure 7-106. Experimental Flow Angularity, Fuselage 2
$M_\infty = 2.2$, $\alpha = 15°$
Format I

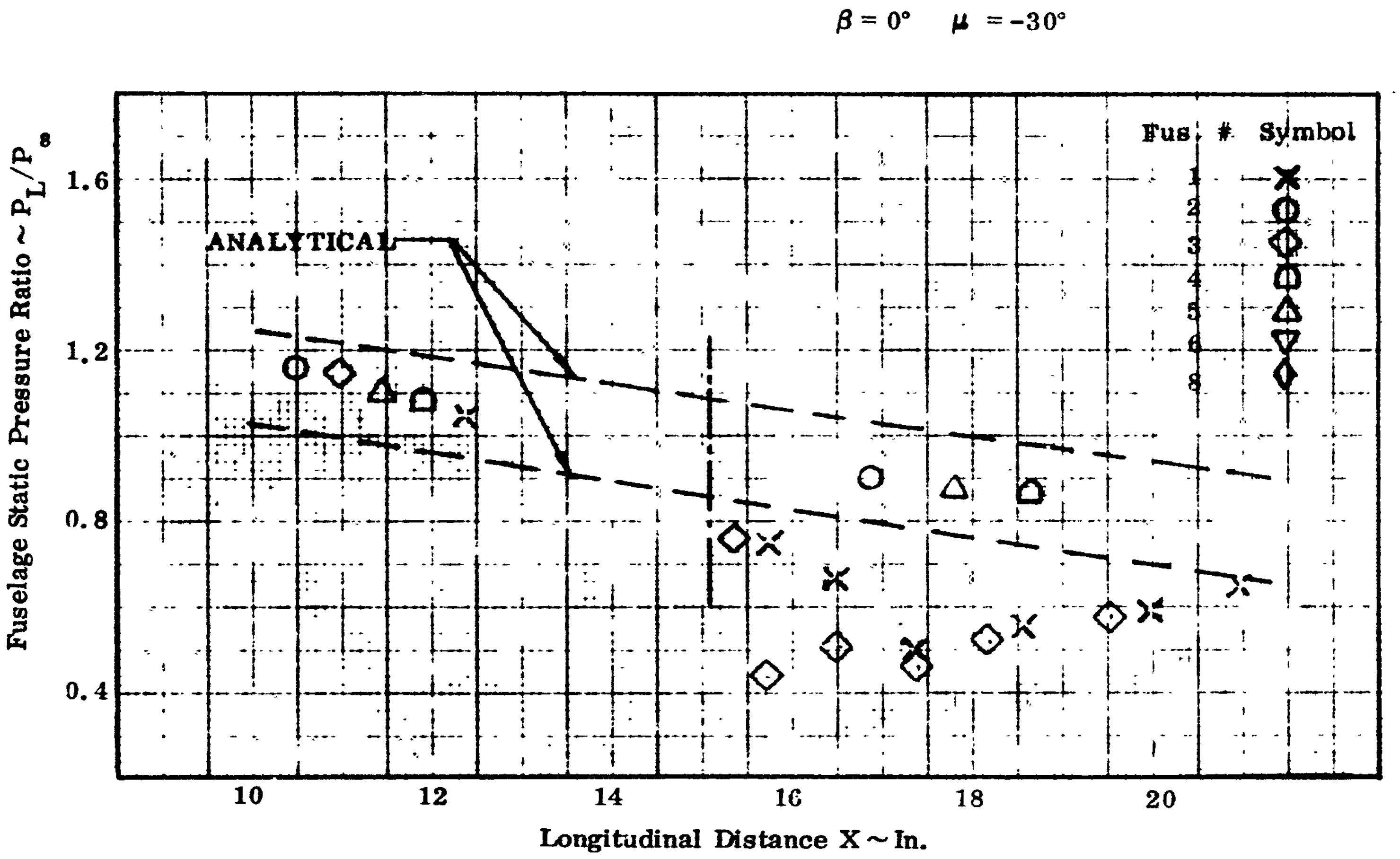

Figure 7-107. Static Pressure Distribution

$M_\infty = 2.2$, $\alpha = 15°$

Format I

computed in this manner is superimposed on the flow field, as calculated by the basic method of characteristics solution.

The second step estimates the fuselage corner effects by introducing a simple Prandtl-Meyer expansion, around the corner, at a rate dictated by the corner contour. These results are also superimposed on the flow field.

The estimated flow field, including the two steps above, is then subjected to the peripheral cross-flow interaction calculation used as the final step in the reference plane technique. The expectation was that the strong local effects estimated by the two new computations would produce more representative flow field profiles.

7.1.5.2 Modified Reference Plane Technique

The basic inviscid method used to analyze the several fuselage configurations employed in the program has been found inherently weak in that it fails to adequately account for variations in the attendant flow field induced by the geometric characteristics of the fuselage lower corner. These variations are attributable to the peripheral pressure gradient around the fuselage corner, with the direction being a function of vehicle angle of attack and magnitude being a function of corner geometry and vehicle angle of attack. The basic method proved adequate at low angle of attack where these peripheral gradients were small; therefore, the objective of any modification must be to improve the degree of correlation achieved between experiment and theory at the high angle of attack case, where these peripheral gradients become substantial. To describe the subject modification and to demonstrate the degree of improvement it provides over the basic method, an example calculation will be employed. The fuselages employed in this example will be configuration 2, which has a large radius curvature corner, and configuration 3 which has a relatively small bevelled corner. The test condition to be discussed is:

$M_\infty = 2.2$

$\alpha = 15^\circ$

$\beta = 0^\circ$

PC PN

The revised method represents an analytical extension of the basic reference plane solution, which employed simple, direct, two-dimensional procedures.

The method provides a rationale for correcting the thermodynamic properties computed by the reference plane technique such that the flow field is more sensitive to fuselage corner geometry. The procedures taken individually are simple, a preliminary design requirement. However, care must be exercised in applying the corrections.

In addition to a more accurate accounting of the fuselage induced effects, the revised method attempts to improve the prediction of those effects upon the flow field prompted by the presence of the canopy. The method adapted for this analysis is simple and direct. A horizontal infinite plane is passed through the leading edge of the canopy (10.5 inches from the nose of the vehicle for the subject configuration). The influence of the canopy originates at this station in the form of a detached two-dimensional shock followed by an expansion around the canopy surface in the longitudinal direction. In this manner the flow conditions in this plane, at the survey station, reflect the temperatures and pressures associated with this shock. This plane extends approximately 0.35 inch above the zero degree radial plane at the surface of the body and then horizontally across the flow field. Examination of experimental data, obtained by the flow field probe, indicates this as a region within which significant pressure discontinuities occur, such as would be anticipated near a strong shock wave. This finding lends support to the choice of canopy shock location. The shock and downstream flow field characteristics are calculated using the conventional Rankine-Hugoniot and Prandtl-Meyer relationships. The shock generating surface is formed along the reference plane - canopy basic contour line intersection , as seen in a plan view. To account for either the compressive or expansive influence, upon the flow within the reference plane, exerted by a non-linear canopy - fuselage juncture which is outside the reference plane, an additional amount of isentropic compression or expansion are superimposed upon the thermodynamic properties within the plane. Thus three dimensionality is simulated by a superposition of a one-dimensional analysis upon the results of a two-dimensional solution.

Curvature of the fuselage lower corner is handled by deriving an expression for the incremental flow expansion required to simulate the peripheral pressure gradient. This effect is dictated by the fuselage geometry. For fuselage 3 only one correction need be made, since the fuselage corner is a bevelled edge. As opposed to this, fuselage 2, with a continuous corner curvature requires several local computations occurring at, and in between, each radial reference plane. The surface in question in each case is that section of the fuselage corner between the horizontal tangency point and the vertical tangency point.

The first parameter in the derived expression is the angle encompassing the tangency points of the body, whose apex is the vehicle nose. This angle is designated as ρ .

A second parameter is the square of the eccentricity of an ellipse, (e^2). To illustrate its value, we can view the body as either a perfect circle, that is, the base of a cone extending from the nose, or a square or rectangle. For these configurations a streamline trace originating at the nose and ending at the survey station that conforms to the body surface is linear. A deviation, from these ideal cases, in the form of longitudinal area progression and/or cross-sectional shape requires a streamline trace, conforming to the body, that is non linear. Therefore, the extent the body deviates from the regular quadratic surface can provide an indication of the added expansion to be superimposed on the inviscid method of characteristics solution. Thus, the eccentricity, e^2, of an ellipse is a preordained correction factor. The final parameter (Δ) is one that accounts for the digression of a bevelled corner from that of a perpendicular corner. It is the angle defined by the oblique line between fuselage tangency points and the base of the fuselage. At one extreme this parameter accounts for that corner describing a fuselage cross-section of zero. The other extreme is, of course, a square or rectangle. For both extremes the parameter (Δ) is equal to zero degrees. Between these extremes the introduction of a bevelled corner results in some finite Δ, which is determined by simple trigonometry. To illustrate let us assume a triangular body for which both sides, a and b, are equal. For this case the parameter Δ has a value of 45°.

The three parameters (ρ, e^2, Δ) are combined into one equation yielding a total deviation factor ψ . To generalize this equation, such that it accounts for angle of attack, one additional term is included. This term takes the form $\cos[6(15 - \alpha)]$, where α is equal to the free stream angle of attack and the value 15 is that angle considered representative of the high angle of attack condition. This function, then, serves to relate the strength of the total deviation factor directly to angle of attack. It is pointed out that although the revised analytical technique, discussed herein, can now be applied over the entire angle of attack range its increased complexity does not warrant its use at those conditions close to zero angle of attack where it has been determined that the basic reference plane technique yields acceptable results. Therefore, utilization of the revised method is viewed as an approach to be employed for the analysis of high angle of attack cases. It is noted further that the value of 15°, employed in this term, was selected for two reasons. Firstly, that angle of attack can probably be considered the upper limit for long term transient operation of the aircraft. Consequently, operation at higher angles of attack, which are highly transitory, do not warrant this investment in effort required for their analysis. Beyond this, those flow field phenomena that become evident, as the result of analysis, at 15° angle of attack can be extrapolated to those higher angles with a degree of confidence commensurate with preliminary design criteria.

The total deviation factor accounting for the expansion around a lower fuselage corner is,

$$\psi = \cos\,[\,6\,(15-\alpha)\,]\;(\,e^2 \mid \text{sine } 2\,\Delta \mid),$$

where e^2 is computed from

$$a^2\,(1-e^2) = b^2$$

$$c^2 = a^2 - b^2$$

$$e^2 = c^2/a^2$$

and a is the semi-major axis of an ellipse, and b is the semi-minor axis of an ellipse.

For the example case the total deviation factor for fuselage 3 and fuselage 2 are given as:

Fuselage 3:

$a = 2.2$ $\qquad \Delta = 40°$

$b = .6$ $\qquad \text{sine } 2\Delta = .9848$

$c^2 = (4.84 - .36) = 4.48$

$c = 2.12$

$$e = \frac{2.12}{2.2} = .964; \quad e^2 = .93$$

ψ = Total expansion degrees = 20° $(.93 \times .9848)$ = 18.3°

Fuselage 2:

$\rho = 60^\circ$ $\qquad c^2 = 4.84 - 4.27 = .57$

$\Delta = 49^\circ$ $\qquad c = .755$

$a = 2.2$ $\qquad e = \frac{c}{a} = \frac{.755}{2.2} = .344$

$b = 2.07$ $\qquad e^2 = .1185$

ψ = Total expansion in degrees = 60° $(.1185 \times .985)$ = 7°

With the total Prandtl Meyer expansion angle determined, as a function of fuselage corner geometry and angle of attack, it remained to establish a geometry dependent method for distributing this total expansion around the corner, such that a reasonable peripheral pressure distribution is achieved. In view of the fact that some of the basic reference planes intercept the fuselage basic contour line in the region of the corner, it appeared appropriate to define the degree of peripheral expansion, to be applied locally, at each of these intersection points. The method devised involved distribution of the total peripheral expansion as a function of an area weighting term. The denominator of this term is that area encompassed by the surfaces between the horizontal and vertical tangency points and the hypothetical intersection of the horizontal and vertical reference lines. The numerator is that area encompassed between the horizontal tangency point, the local point on the surface, a horizontal projection of the surface point on to the vertical reference line, and the hypothetical intersection of the horizontal and vertical reference lines. These relationships are presented schematically in Figure 7-108. To illustrate the implementation of this function we can use the corner for fuselage 2. For this case the total peripheral expansion is distributed among four (4) basic reference planes in the following manner.

Between radial planes -80° and -60°, .614 of deviatory area is obtained; between -60° and -50°, the area ratio is .176; between -50° and -30°, the area ratio is .176; and between -30° and -20°, the area ratio is .032. The degree of local expansion taken, then is:

at $\mu = 80^\circ$, Expansion = $4.3^\circ = 7.0 \times .614$

FUSELAGE 3

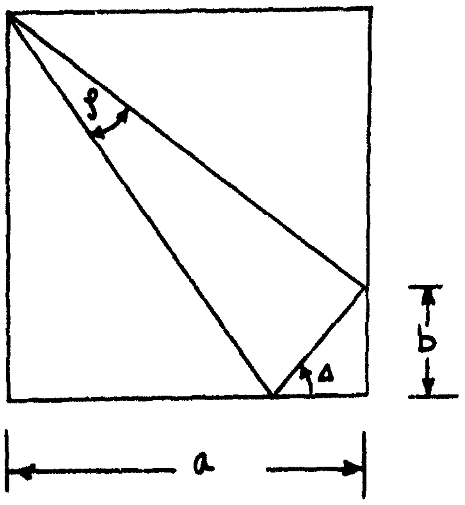

FUSELAGE 2

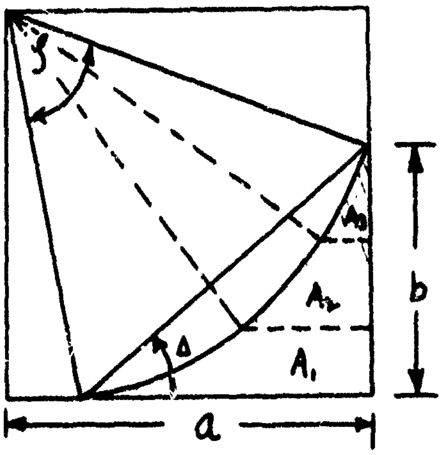

"DEVIATORY" ANGLE ψ :

$$\psi = \psi_1 + \psi_2 + \psi_3$$

$$\psi_1 = \psi A_1/A$$

$$\psi_2 = \psi A_2/A$$

$$\psi_3 = \psi A_3/A$$

A = CROSS HATCHED AREA

Figure 7-108. Schematic of "Deviatory" Angular Relations
Format I

at $\mu = -60^\circ$, Expansion $= 1.23^\circ = 7.0 \times .176$

-50°, Expansion $= 1.23^\circ = 7.0 \times .176$

-30°, Expansion $= \ .\ ^\circ = 7.0 \times .032$

Examination of the comparison between experimental and analytical static pressure distributions on fuselage 2, shows the experimental pressures to be lower by a greater amount in the 60 degree plane than in the 30 degree plane, bearing out the validity of the procedure above.

For the body conditions, the slopes of the intersection of the radial planes and the body are taken directly from the elevation view. To determine the slopes of the intersections of intermediate planes on the body, sections at model station 19.5 were used.

The peripheral expansion angles are used to modify the thermodynamic properties originally calculated by the method of a characteristics solution. The new reference planes, in the area of the fuselage corner, and the new canopy engendered plane are added to the flow field mesh. A peripheral shock expansion calculation, identical to that performed as the final step of the basic reference technique, is then performed using the modified and additional flow points.

The resultant surface pressure distributions are compared with experiment in Figures 7-109 and 7-110. Additionally, these figures present the surface pressure distribution obtained for the basic reference plane technique. It is apparent that a significant improvement has resulted from use of the modified technique.

The estimated inviscid properties adjacent to the body for both fuselages are tabled in Figure 7-111.

Assuming no total pressure loss due to the nose shock an estimate can be made of the experimental inviscid surface Mach number. Comparing this estimated Mach number with that analytically computed indicates good agreement. The comparison is presented for fuselages 2 and 3, in Figures 7-112 and 7-113.

To calculate the flow field properties an equation must be derived to calculate the local flow deflection.

Fuselage 2

$\beta = 0°$

Station 19.5

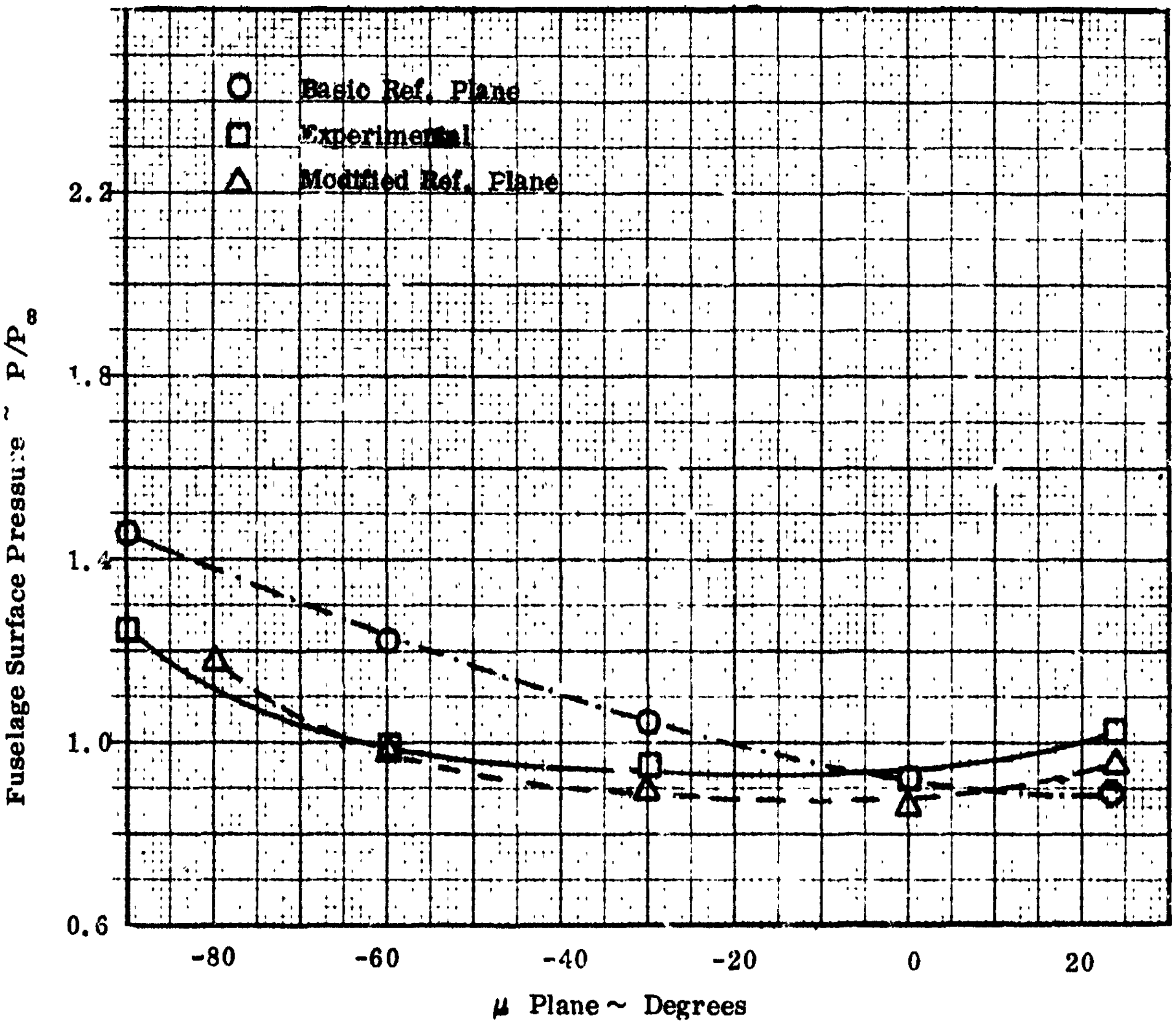

Figure 7-109. Comparison of Experimental and Theoretical Pressure Ratios

$M_\infty = 2.2$, $\alpha = 15.75°$

Format I

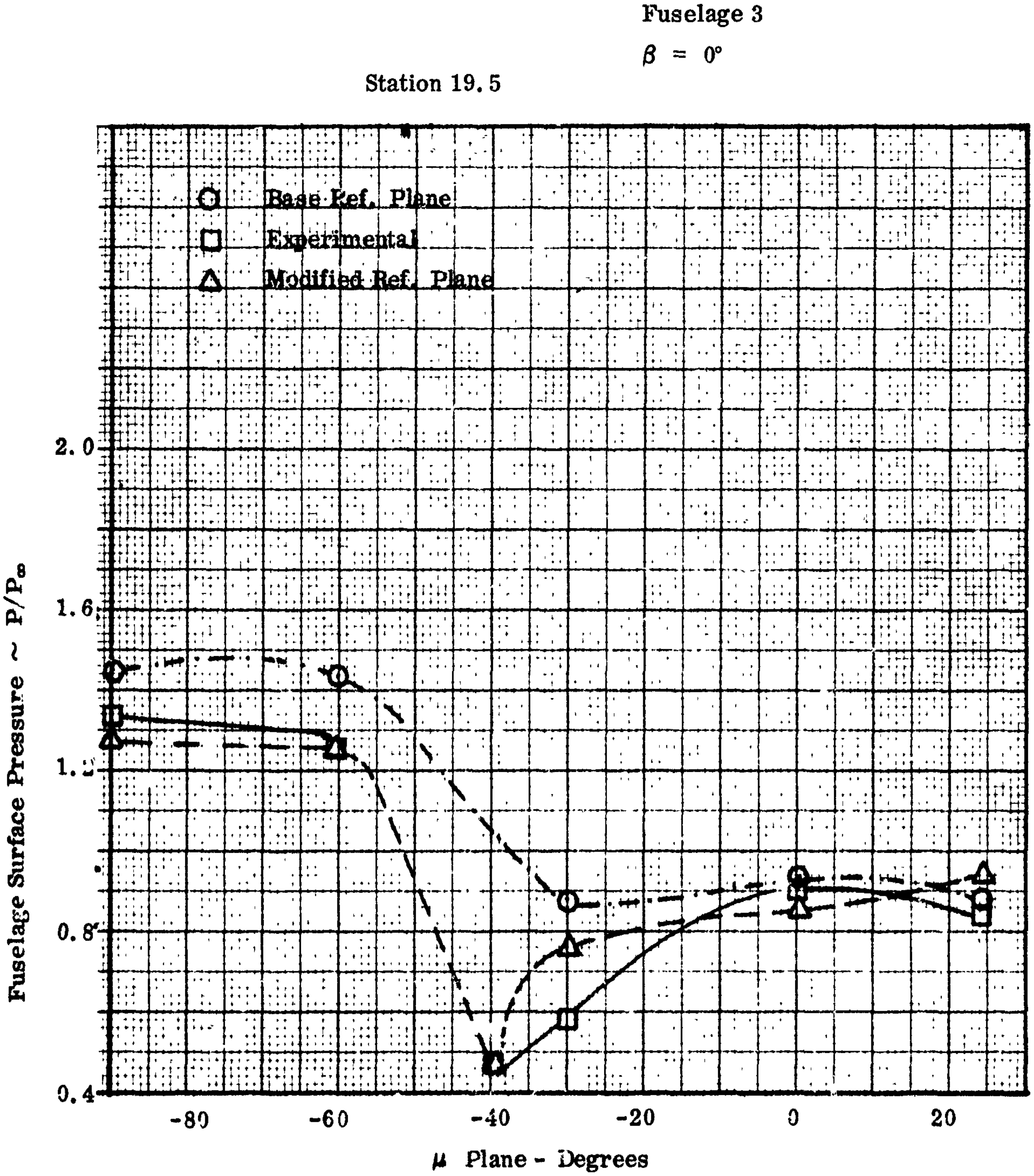

Figure 7-110. Comparison of Experimental and Theoretical Pressure Ratios
$M_\infty = 2.2$, $\alpha = 15.75°$
Format I

FUS 2

μ	M	T °R	P atm	V fps
24°	2.270	279.0	.0599	1839.0
0°	2.296	272.4	.0543	1860.5
-30°	2.269	276.3	.0560	1847.9
-60°	2.208	283.6	.0617	1824.0
-90°	2.253	278.2	.0579	1841.8

FUS 3

μ	M	T °R	P atm	V fps
24°	2.270	279.0	.0599	1839.0
0°	2.291	272.6	.0548	1859.6
-30°	2.344	266.5	.0504	1879.3
-60°	2.026	307.4	.0817	1744.0
-90°	2.026	307.4	.0817	1744.0

Figure 7-111. Thermodynamic Properties on Surface of Body at Station 19.5

Format I

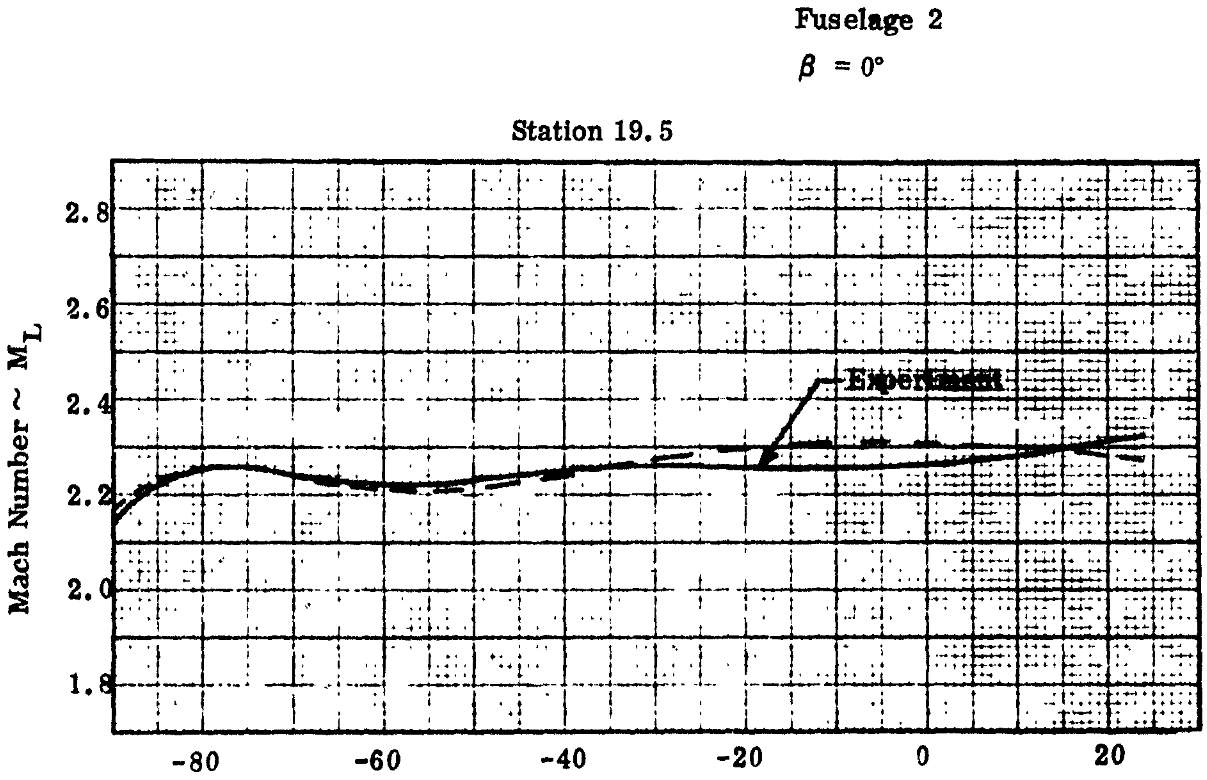

Figure 7-112. Comparison of Experimental and Theoretical Mach Numbers at Fuselage Surface

$M_\infty = 2.2$, $\alpha = 15°$.

Format I

Fuselage 3
$\beta = 0°$

Station 19.5

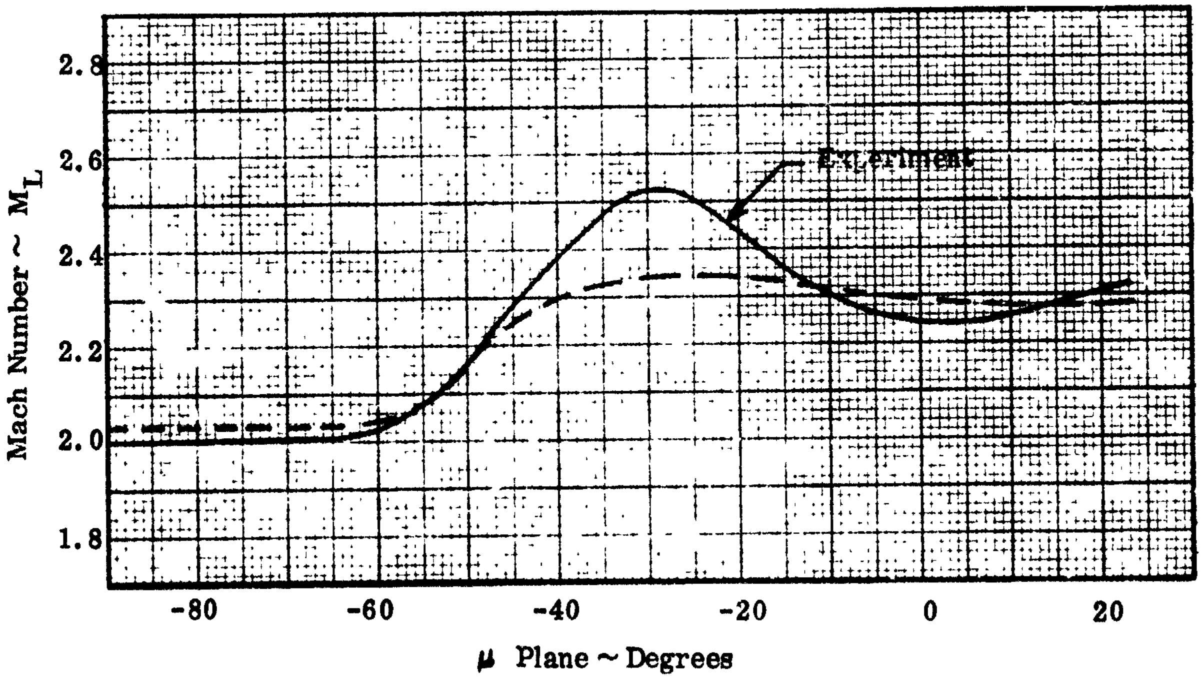

Figure 7-113. Comparison of Theoretical and Experimental Mach Numbers at Fuselage Surface

$M_\infty = 2.2, \quad \alpha = 15°$

Format I

For the calculation of the flow field properties it is necessary to insure that the angularity of all local streamlines have a common reference.

For example, the flow angularity computed from the method of characteristics is the angle between the free stream and the local flow. However, the streamlines computed in this manner are confined to their respective planes and are relative to a zero plane passing through the centerline of the vehicle nose. For a drooped nose the centerline of the vehicle nose is not coincident with the vehicle horizontal centerline. For the subject models the nose plane is at a 7.5° incidence relative to the vehicle centerline. It is necessary to compare the coordinate system used in the method of characteristics to the coordinate system forming a triad in the zero plane. This is done by the use of unit matrix, a_{ij}, where the relationships of the systems are

$$\hat{\iota}_i = a_{ij}\,\hat{\iota}_j{}'$$

$$a_{ij} = \begin{array}{c|ccc} & \hat{\iota}'_1 & \hat{\iota}'_2 & \hat{\iota}'_3 \\ \hline \hat{\iota}_1 & 1 & 0 & 0 \\ \hat{\iota}_2 & 0 & \sin\mu & \cos\mu \\ \hat{\iota}_3 & 0 & -\cos\mu & \sin\mu \end{array}$$

Where the unprimed system is in the zero plane system and the different μ planes are rotated about the longitudinal axis of this plane, and the a_{ij} 's are direction cosines between the axes of the primed and unprimed systems.

Figure 7-114 (a) is a schematic of these coordinate systems and the related flow angles.

In the following derivation, φ is the flow deflection that is given by the method of characteristics. This is the angle between the free stream velocity, projected in the radial plane, μ , and the local flow in the radial plane. However, we seek the flow angle, at first, between the longitudinal axis of the zero plane and the local flow. This is achieved by the equation: $\varphi_o{}' = \sin\mu\,(\alpha - \eta) - \varphi$, where η is the angle of incidence of the nose.

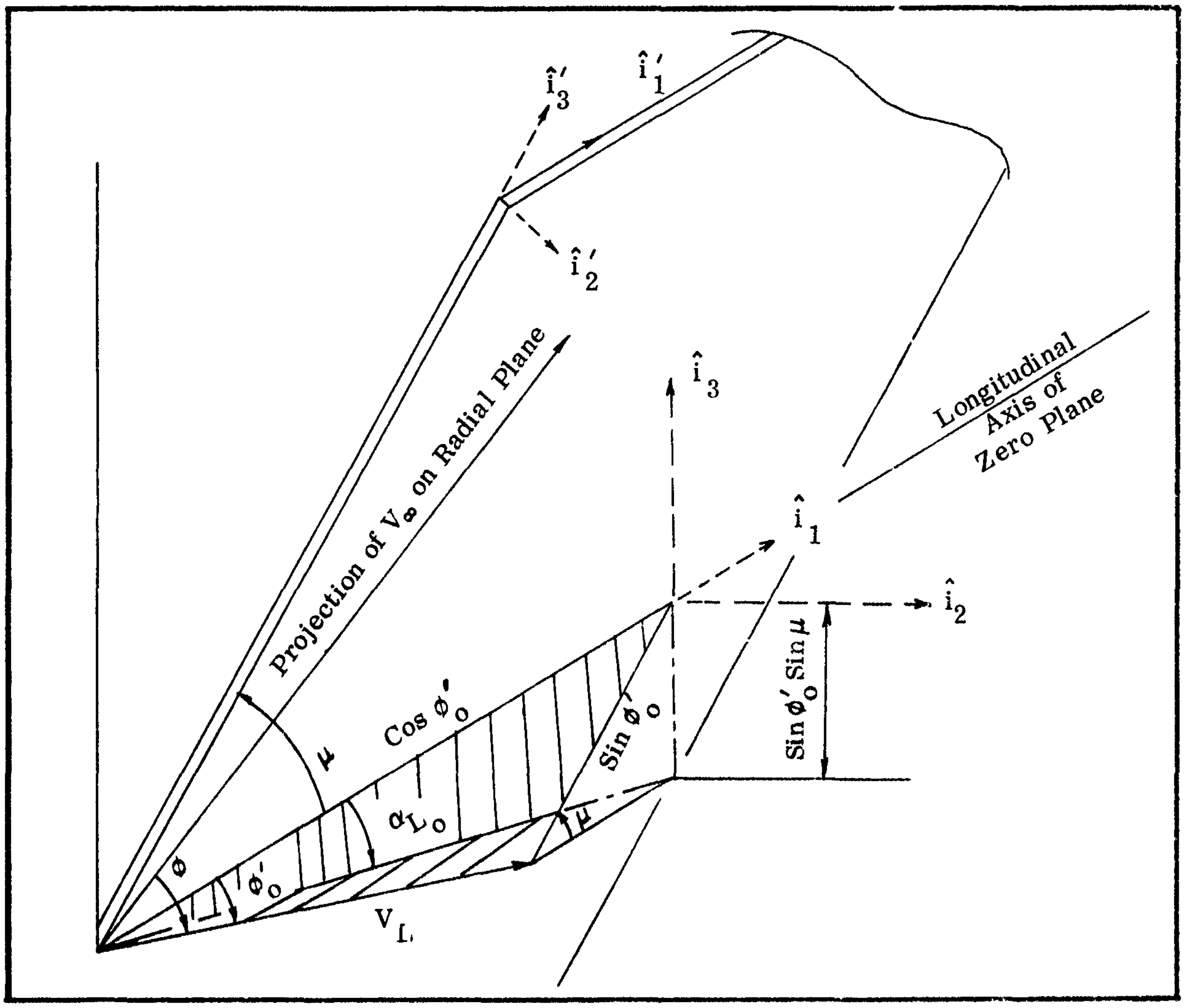
$\hat{i}_3'$
$\hat{i}_1'$
$\hat{i}_2'$
Projection of V_∞ on Radial Plane
$\hat{i}_3$
Longitudinal Axis of Zero Plane
$\hat{i}_1$
$\hat{i}_2$
$\sin\phi_o' \sin\mu$
$\cos\phi_o'$
$\sin\phi_o'$
μ
α_{L_o}
ϕ
ϕ_o'
μ
V_L

(a) Flow Angles

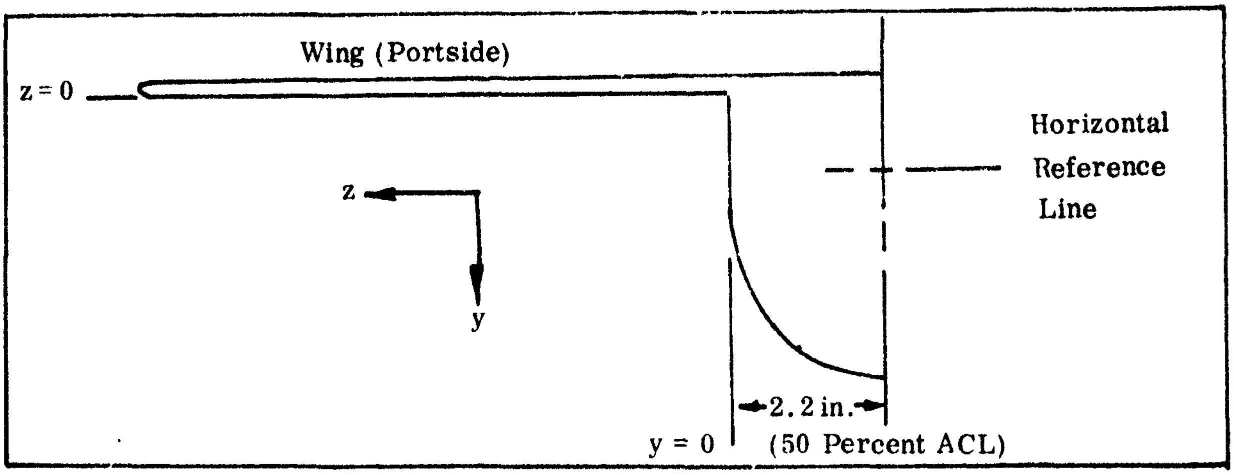
Wing (Portside)
z = 0
Horizontal Reference Line
z
y
2.2 in.
y = 0
(50 Percent ACL)

(b) Flow Field Reference Axis System

Figure 7-114. Schematic of Coordinate Systems

The only part of the local flow in the designated radial plane that contributes to the local angle of attack will be that part of the local velocity, V_L, which projects on $\hat{\iota}_3$.

If we let

V_L = a unit vector, then

$\sin \varphi_o{}'$ = component of V_L in $\hat{\iota}_3{}'$ direction

$\cos \varphi_o{}'$ = component of V_L in $\hat{\iota}_1{}'$ direction

$\hat{\iota}_3{}' = \hat{\iota}_2 \cos \mu + \hat{\iota}_3 \sin \mu$

Then the projection of $\sin \varphi_o{}'$ on $\hat{\iota}_3 = \sin \varphi_o{}' \, \hat{\iota}_3{}' = \sin \mu \sin \varphi_o{}'$

The angle α_{Lo} is the angle of attack of the local flow relative to the zero plane.

$$\operatorname{Tan} \alpha_{Lo} = \frac{\sin \mu \sin \varphi_o{}'}{\cos \varphi_o{}'} = \sin \mu \tan \varphi_o{}'$$

$$\alpha_{Lo} = \operatorname{Arc} \tan (\sin \mu \tan \varphi_o{}')$$

The angle of attack of the local flow relative to the vehicle center line is then

$$\alpha_{LV} = \alpha_{Lo} + \eta$$

However, it is necessary to add the term $[(\alpha - \eta) \pm \alpha \sin \eta]$ to α_{LV}.

The positive sign in the term is assigned to those radial planes below the zero plane. This is partially necessitated by the fact that the method of characteristics data is presented in all cases as having the free stream velocity vector as the abscissa, and the body always in the 1st quadrant. The above equation therefore corrects for this when μ is negative.

Finally, then, after making the indicated additions and simplifying, the local angle of attack relative to the vehicle centerline is:

$$\alpha_{LV} = \alpha_{Lo} + \alpha\,(1 + \sin\eta)$$

Table II presents a comparison, for fuselage 3, of the results given by the above equation and the test value data throughout a range of angle of attack between -4.0° and +15.75° for the radial planes, 0° and 30°.

The comparison is good throughout the entire range. It is pointed out that the final correction to the flow deflection due to the "deviatory" geometry is not included. Adding this final correction to α_{LV} would improve the agreement further. This is shown in the calculation for $\alpha = 15.75°$ where this correction has been included.

The final correction to α_{LV} is accomplished by arranging the flow properties about the body in peripheral arrays, equidistant from the body. The properties effected by the bevelled edge of fuselage 3, or the rounded corner of fuselage 2, are treated as expansions, using as initial properties those given by the method of characteristics for each radial plane. Interpolation is employed to obtain the properties between the original reference planes. Figures 7-115 through 7-118 present these properties for fuselage 2.

Effectively, several planar rings are wrapped around the flow field intersecting each reference plane, perpendicularly. For the example case, planar rings were spaced at 1/2 inch, 1-1/2 inch, 3 inch and 4 inch distances from the body. Figure 7-114(b) represents the y-z coordinate system used for the flow field tests and the relationship between this origin and the major vehicle origin formed by the intersections of the horizontal and vertical reference lines. Each reference plane-planar ring intersection originally contains the properties given by the method of characteristics. The properties of those rays established to account for the peripheral shock-expansion calculation is then performed. This calculation yields the finalized flow properties.

The resultant flow deflection is multiplied by sin μ and this product is added to α'_{LV}, the local angle of attack already calculated by the previous derived

TABLE II
COMPARISON BETWEEN PROBE DATA AND ANALYTICAL EQUATION AT 1/2" DISTANCE FROM BODY M = 2.2 - FUSELAGE 3

α Deg.	μ Deg.	α_{LV} Experimental	α Deg. M. C.	ϕ Deg. M. C.	Sin μ. $(\alpha - \varkappa) - \phi$	Tan ϕ_o'	Sin μ. Tanϕ_o'	Tan^{-1} α_{LO}	α. (1.13) Deg.	α'_{LV} Calculated Deg.
-2.85	0	-6.95	-4.0	.52	-.52	-.009	0	0	-4.5	-4.5
	-30	-7.0	|	-1.6	7.35	.129	-.0645	-3.69	|	-8.19
5.14	0	4.5	5.0	.52	-.52	-.009	0	0	5.65	5.65
	-30	4.2	|	-.77	3.02	+.053	-.027	-1.55	|	4.15
10.15	0	10.55	10.0	.52	-.52	-.009	0	0	11.3	11.3
	-30	12.2	|	.40	-1.65	-.029	.0145	.83	|	12.13
15.75	0	17.5	15.0	.52	-.52	-.009	0	0	17.0	17.0
	-30	20	|	1.8	-5.93	-.1039	.052	2.98	|	19.98

Fuselage 2
$\beta = 0°$

Station 19.5

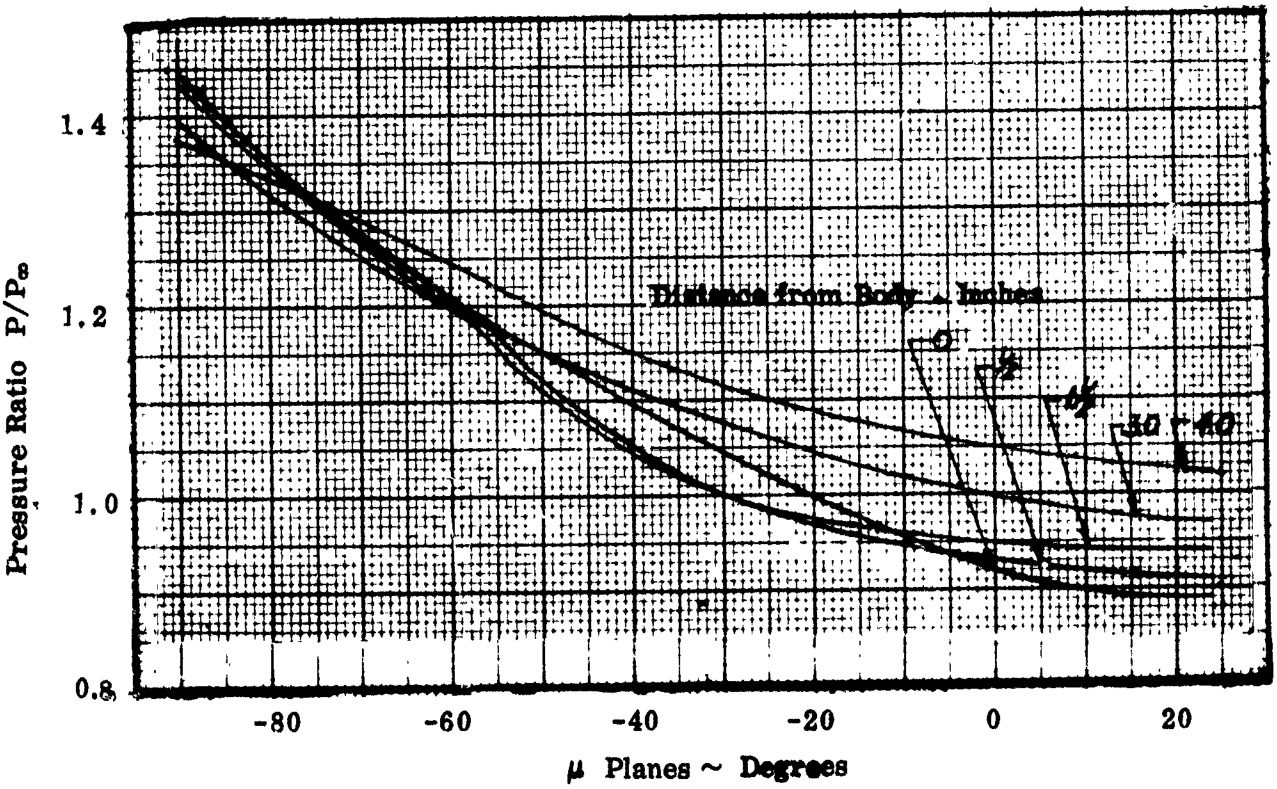

Figure 7-116. Basic Reference Plane Pressure Ratio

$M_\infty = 2.2$, $\alpha = 15°$

Format I

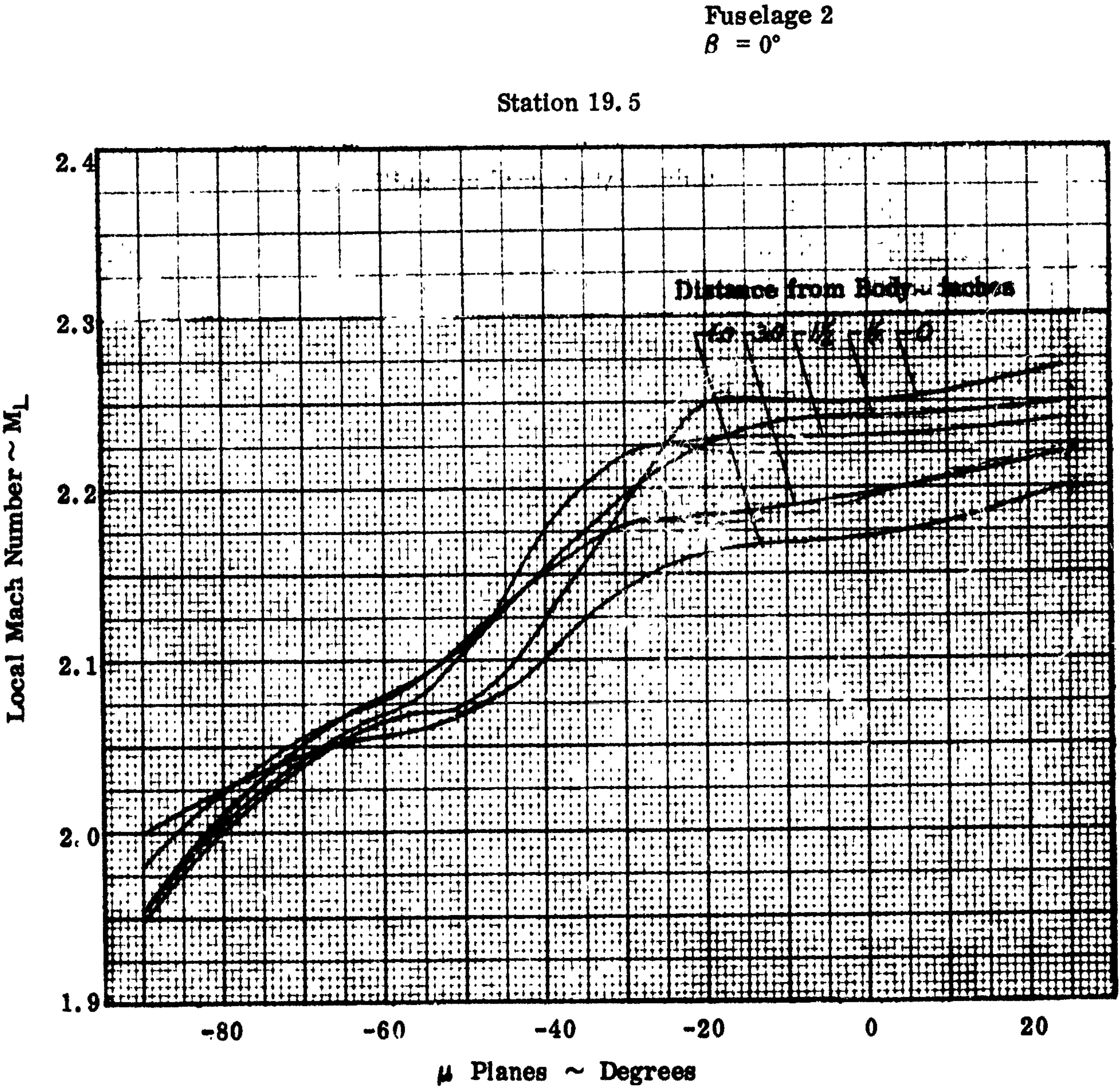

Figure 7-116. Basic Reference Plane, Local Mach Numbers

$M_\infty = 2.2$, $\alpha = 15°$

Format I

Fuselage #2
$\beta = 0°$

Station 19.5

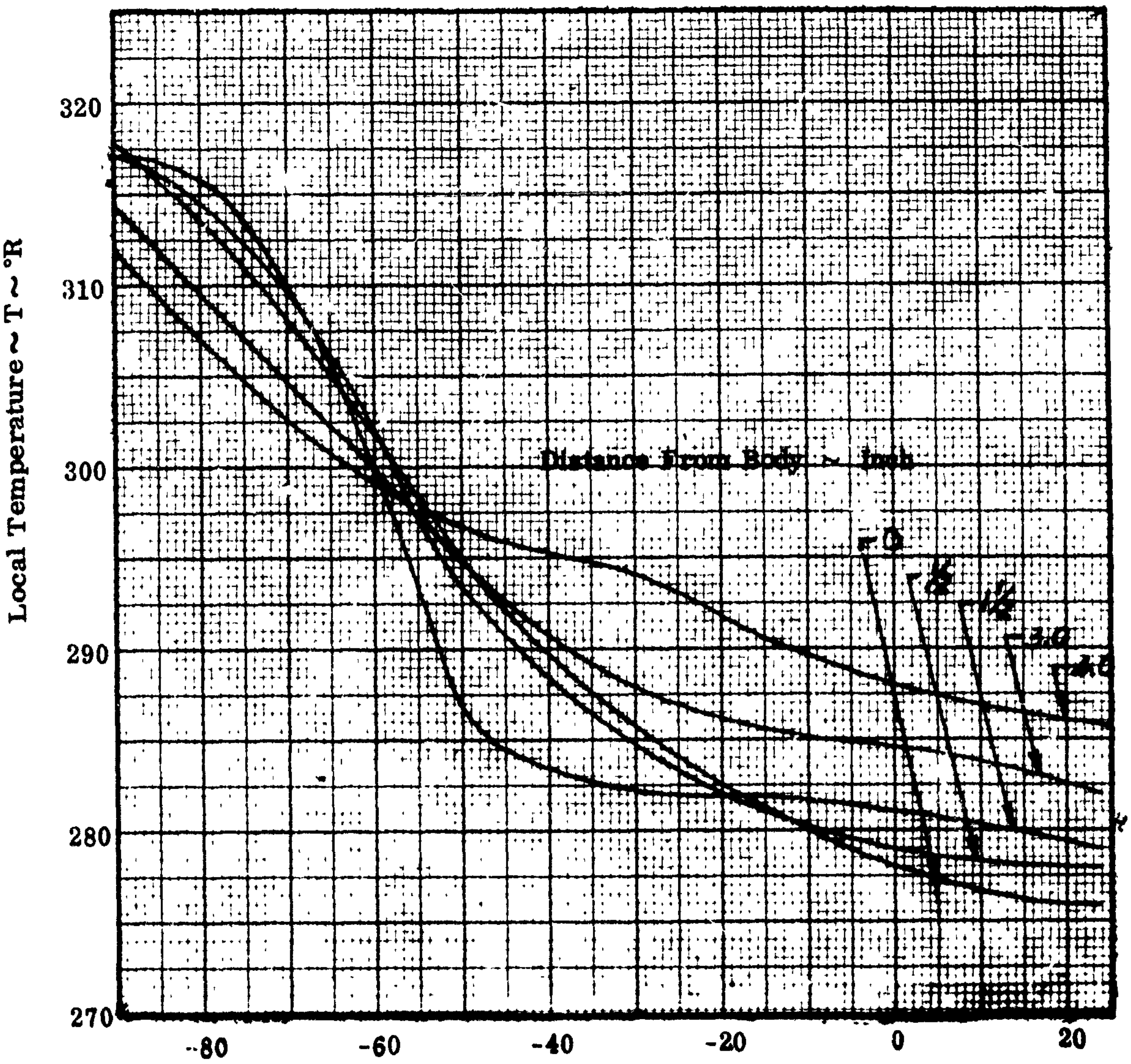

Figure 7-118. Basic Reference Plane, Local Temperature

$M_\infty = 2.2$, $\alpha = 15°$

Format I

Station 19. 5

Fuselage 2
$\beta = 0°$

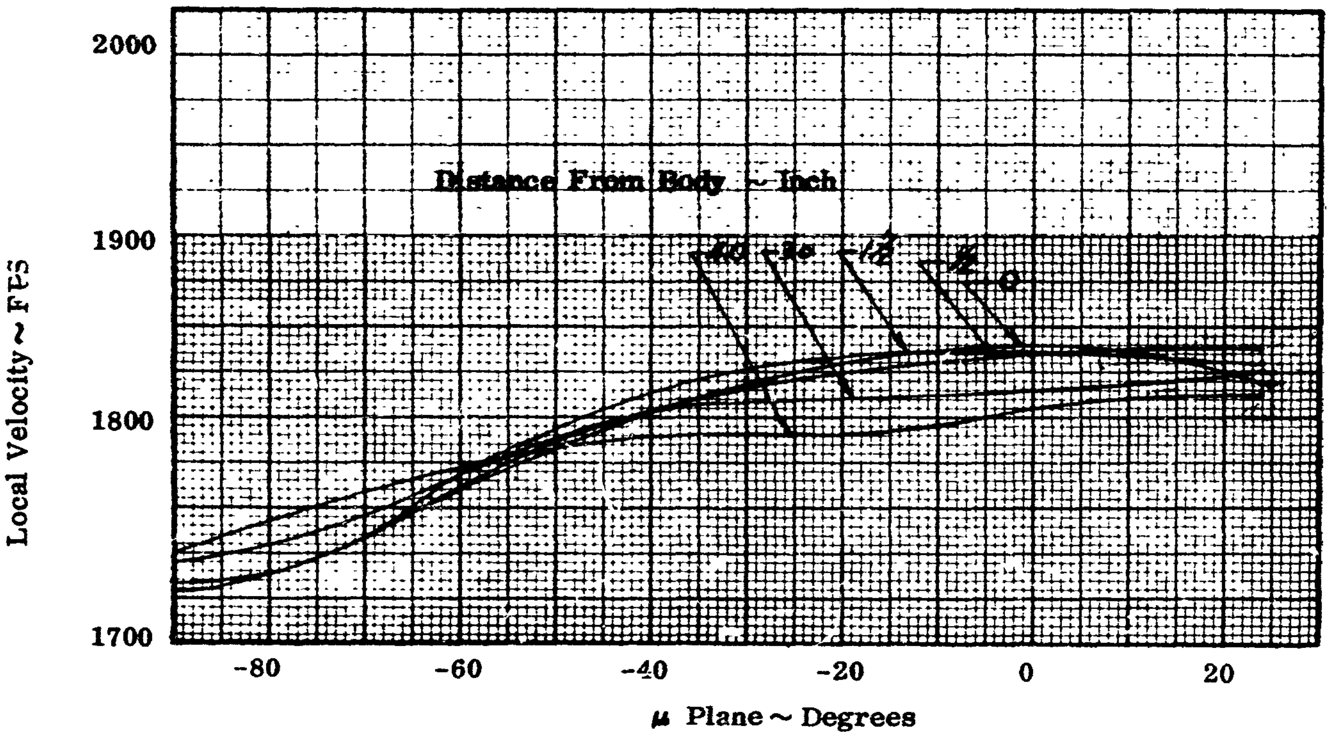

Figure 7-118. Basic Reference Plane, Local Velocity
$M_\infty = 2.2$, $\alpha = 15°$
Format I

equations, to give the final value of the local angle of attack. For the cases attempted, the values calculated in this manner agreed quite well with the experimental values.

To determine the effect of β, the yaw angle of the local flow, the flow deflection is multiplied by the cosine of μ. The sidewash angle, σ, is then just the negative of β.

$$\sigma = -\beta$$

The computations made for the final local angle of attack for fuselages 2 and 3 have been tabulated and a comparison is made for all the planes at 1/2 inch from the body. The analytically derived flow properties are also tabulated for the entire flow field. These appear as Tables III and IV.

The final contour plots resulting from the calculations appear as Figures 7-120 through 7-127.

Figure 7-119 is a table of experimental pressure ratios, P/P_∞, obtained for both fuselages 2 and 3 for the flow field survey station of 19.5. Comparing the plots labelled Isobars, presented in Figures 7-120 and 7-124, containing the theoretical pressure ratios, with these pressure ratios indicates that, for both fuselages, the theoretical values are slightly higher than the experimental values. The agreement is, in general, quite acceptable for preliminary design work.

A comparison of local Mach number, local alpha, and sidewash angle is made in Figures 7-128 through 7-133. The numbers appearing in parenthesis are the calculated, theoretical values.

Comparing the computed local Mach numbers to experiment indicates close agreement except near the upper inboard side, close to fuselage 3, where an error of approximately 10% is noted. For both fuselages, the theoretical values are generally somewhat lower than the experimental values.

The local flow deflection also shows good agreement. However, an inherent weakness can be seen in the zero plane where the theoretical values tend to remain constant, whereas the experimental data shows a variation. For the example case this resulted in an error of 11%, for the zero plane. The error for other planes, particularly in the region of the installed inlet are smaller.

TABLE III
ANALYTICALLY DERIVED FLOW PROPERTIES
FUSELAGE 2

1	2	3	4	5	6	7	8	9	10	11
RING Inch	RAY~ Deg.	M	T °R	P Atm.	V fps.	μ Deg.	Sin ②	⑧ x ⑦	α_{LV} Deg.	Deg. α_{LV} ⑩ + ⑨
2	-60	2.17	288.9	.0669	1803	4.3	-.866	-3.72	24.93	21.21
	-30	2.24	279.2	.0597	1835	6.21	-.500	-3.105	21.16	18.055
	0	2.12	294.7	.0718	1784	3.16	0	0	17.8	17.8
	24	2.12	294.4	.0712	1785	3.30	.4131	1.362	15.16	16.52
1-1/2	-60	2.173	288.	.0663	1806	4.39	-.866	-3.89	24.82	20.93
	-30	2.252	278.	.0586	1839	6.417	-.500	-3.209	20.68	17.47
	0	2.115	295.7	.0721	1781	2.95	0	0	17.8	17.8
	24	2.12	294.3	.0714	1785	3.10	.4131	1.28	15.14	16.42
3.0	-60	2.18	287.5	.0657	1808	4.213	-.866	-3.64	23.82	201.8
	-30	2.238	279.9	.0598	1833	5.762	-.500	-2.88	21.07	18.19
	0	2.104	296.7	.0731	1778	2.35	0	0	17.8	17.8
	24	2.119	294.7	.0722	1784	2.57	.4131	1.06	14.96	16.02
4.0	-60	2.163	290	.0675	1801	3.87	-.866	-3.45	23.83	20.38
	-30	2.216	282.5	.0621	1825	5.27	-.500	-2.64	21.38	18.74
	0	2.095	297.9	.0753	1773	2.0	0	0	17.8	17.8

TABLE III (Cont.)
ANALYTICALLY DERIVED FLOW PROPERTIES
FUSELAGE 2

1	2	3	4	5	6
RING Inch	RAY~ Deg.	μ Deg.	cos μ cos ②	β ③ x ④ Deg.	σ ,Deg. SIDEWASH $-\beta$
1/2	-60	4.30	.500	2.15	-2.15
	-30	6.21	.866	5.38	-5.38
	0	3.16	1.00	3.16	-3.16
	24	3.30	.9107	3.05	-3.05
1-1/2	-60	4.39	.500	2.20	-2.2
	-30	6.417	.866	5.66	-5.66
	0	2.95	1.00	2.95	-2.95
	24	3.10	.9107	2.82	-2.82
3.0	-60	4.213	.500	2.107	-2.107
	-30	5.762	.866	4.99	-4.99
	0	2.35	1.00	2.35	-2.35
	24	2.57	.9107	2.34	-2.34
4.0	-60	3.87	.500	1.94	-1.94
	-30	5.27	.866	4.57	-4.57
	0	2.0	1.00	2.0	-2.0
	24	2.25	.9107	2.05	-2.05

TABLE IV
ANALYTICALLY DERIVED FLOW PROPERTIES
FUSELAGE 3

1	2	3	4	5	6	7	8	9	10	11
RING Inca	RAY~ Deg.	M	T °R	P Atm.	V fps	μ Deg.	Sin ②	⑧ x ⑦	α'_{LV} Deg.	Deg. α_{LV} ⑩ + ⑨
1/2	-60	2.493	250	.0402	1929	13.65	-.866	-11.80	33.44	21.64
	-30	2.10	297	.0734	1775	3.90	-.500	-1.95	20.78	18.83
	0	2.07	301	.0707	1760	4.53	0	0	17.8	17.8
	24	2.103	297	.0732	1777	3.77	.4131	1.56	15.16	16.72
1-1/2	-60	2.479	252	.0411	1923	13.2	-.866	-11.42	32.94	21.52
	-30	2.076	301	.0745	1763	3.60	-.500	-1.80	20.98	19.18
	0	2.086	299	.0749	1769	3.60	0	0	17.8	17.8
	24	2.096	297.6	.0742	1774	3.75	.4131	1.50	15.14	16.64
3.0	-60	2.49	249.6	.0393	1930	13.32	-.866	-11.52	30.37	18.85
	-30	2.032	306	.0826	1745	1.25	-.500	-0.63	22.25	21.62
	0	2.085	299.2	.0753	1769	2.85	0	0	17.8	17.8
	24	2.10	297	.0743	1776	3.06	.4131	1.26	14.96	16.22
4.0	-60	2.482	251	.0409	1926	12.3	-.866	-10.65	29.38	18.73
	-30	2.031	306.6	.0821	1744	0.9	-.500	-0.45	22.04	21.59
	0	2.087	299	.0762	1770	2.20	0	0	17.8	17.8
	24	2.093	298.2	.0750	1773	2.437	.4131	1.00	14.67	15.67

TABLE IV (Cont.)

ANALYTICALLY DERIVED FLOW PROPERTIES

FUSELAGE 3

RING	RAY~	μ	cos M	β	σ
Inch	Deg.	Deg.	cos ②	③x④ Deg.	Sidewash Deg. - (β)
1/2	-60	13.65	.500	6.83	-6.83
	-30	3.90	.866	3.38	-3.38
	0	4.53	1.00	4.53	-4.53
	24	3.77	.9107	3.43	-3.43
1-1/2	-60	13.20	.500	6.60	-6.60
	-30	3.60	.866	3.12	-3.12
	0	3.60	1.00	3.60	-3.60
	24	3.75	.9107	3.41	-3.41
3.0	-60	13.32	.500	6.66	-6.66
	-30	1.25	.866	1.08	-1.08
	0	2.85	1.00	2.85	-2.85
	24	3.06	.9107	2.78	-2.78
4.0	-60	12.3	.500	6.15	-6.15
	-30	0.9	.866	.779	-.779
	0	2.20	1.00	2.20	-2.20
	24	2.437	.9107	2.27	-2.27

PRESSURE RATIO ~ P/P_∞

FUS 2

Inch

z \ y	2.7	3.3	4.1	4.7	5.5	6.1
1.37	0.853	0.923	1.016	1.055	1.060	1.015
.57	0.913	0.977	1.016	1.030	0.990	1.038
- .33	0.931	0.958	0.992	0.926	1.025	1.036
-1.23	0.873	0.874	0.915	0.946	1.038	1.057
-2.13	0.895	0.905	0.935	0.973	1.072	1.060

Note: y referenced to A/C vertical C_L
z referenced to A/C horizontal reference Line

FUS 3

Inch

z \ y	2.7	3.3	4.1	4.7	5.5	6.1
1.37	0.812	0.926	0.968	1.027	1.095	1.038
.57	0.907	0.955	0.983	0.986	0.999	1.038
- .33	0.975	0.952	0.972	0.867	1.013	1.057
-1.23	0.938	0.818	0.849	0.903	1.056	1.109
-2.13	0.602	0.814	0.911	0.972	1.073	1.149

Figure 7-119. Experimental Static Pressure at Station 16.5
Format I $M_\infty = 2.2$, $\alpha = 15.75°$, $\beta = 0°$

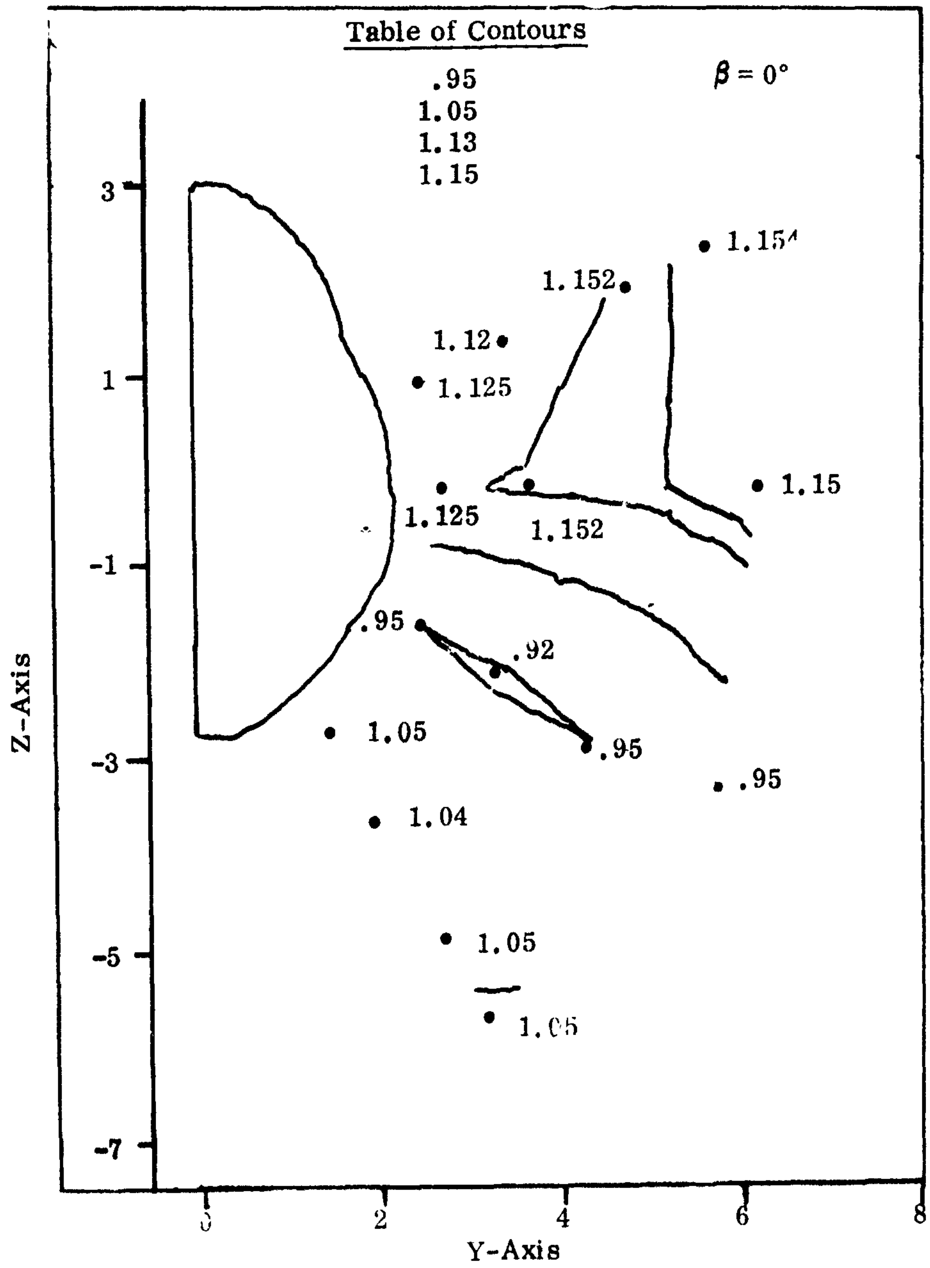

Figure 7-120. Isobars, Fuselage 2
Format I   M = 2.2, α = 15.75°

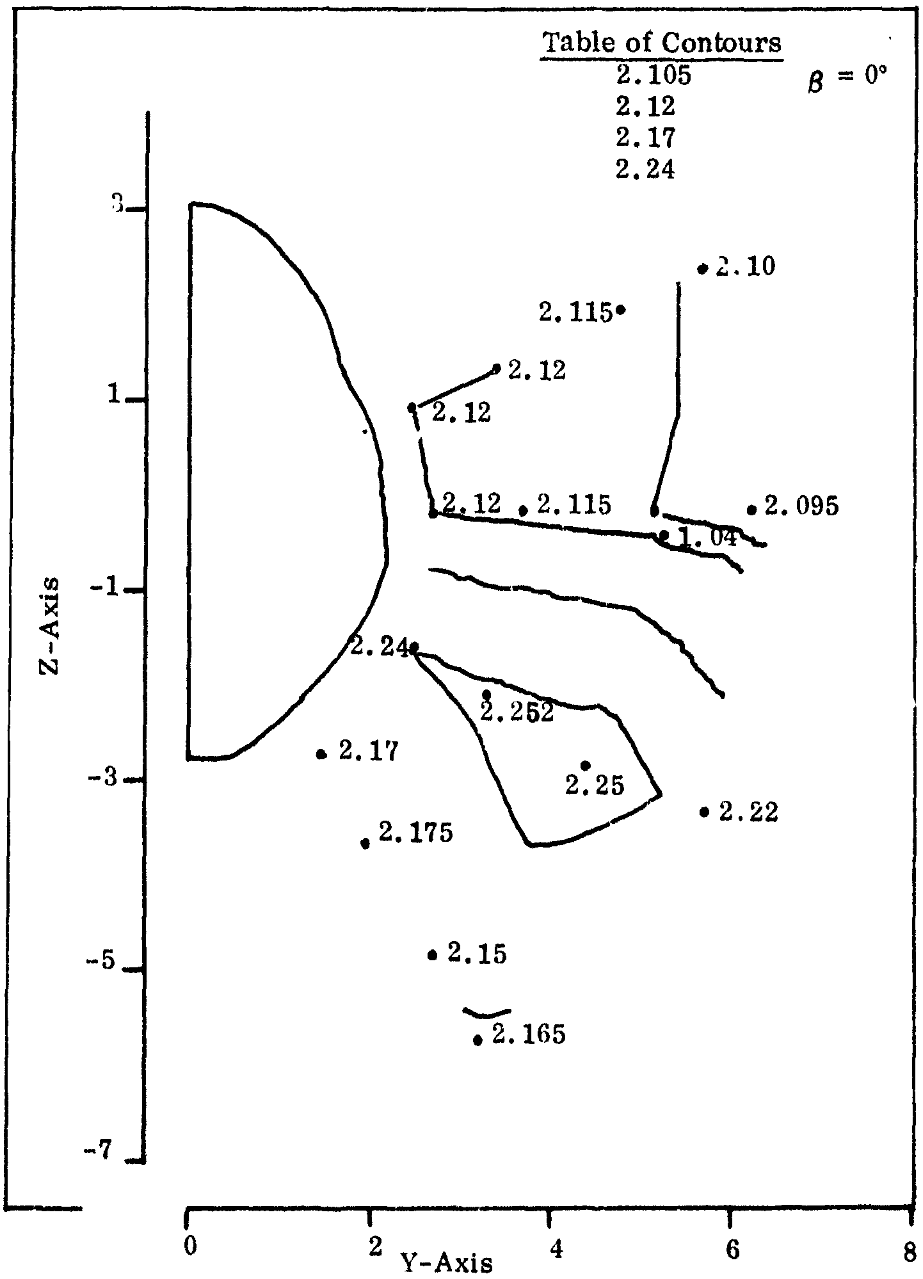

Figure 7-121. Local Mach Number, Fuselage 2
Format I $M_\infty = 2.2$, $\alpha = 15.75°$

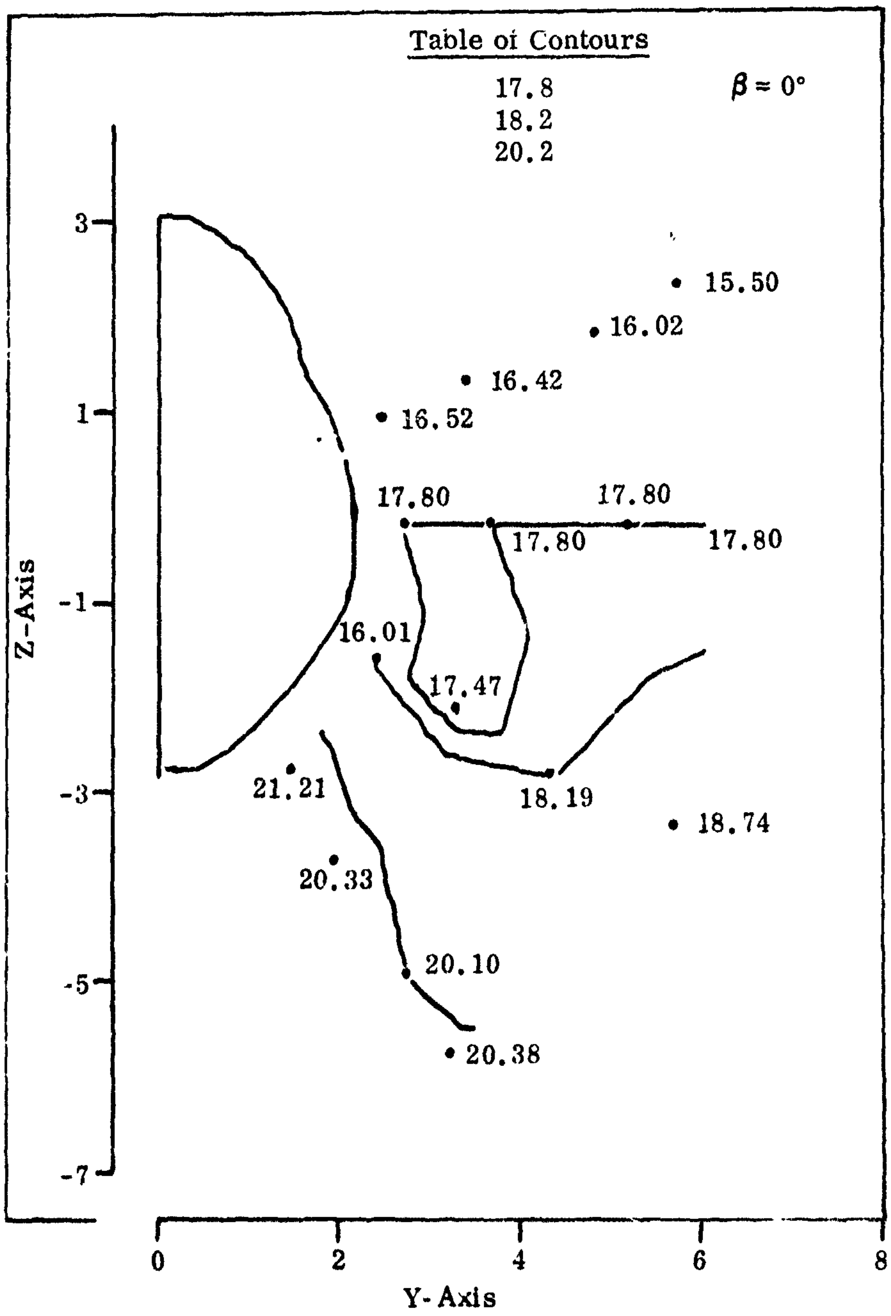

Figure 7-122. Alpha Local, Degrees, Fuselage 2
Format I $M_\infty = 2.2$, $\alpha = 15.75°$

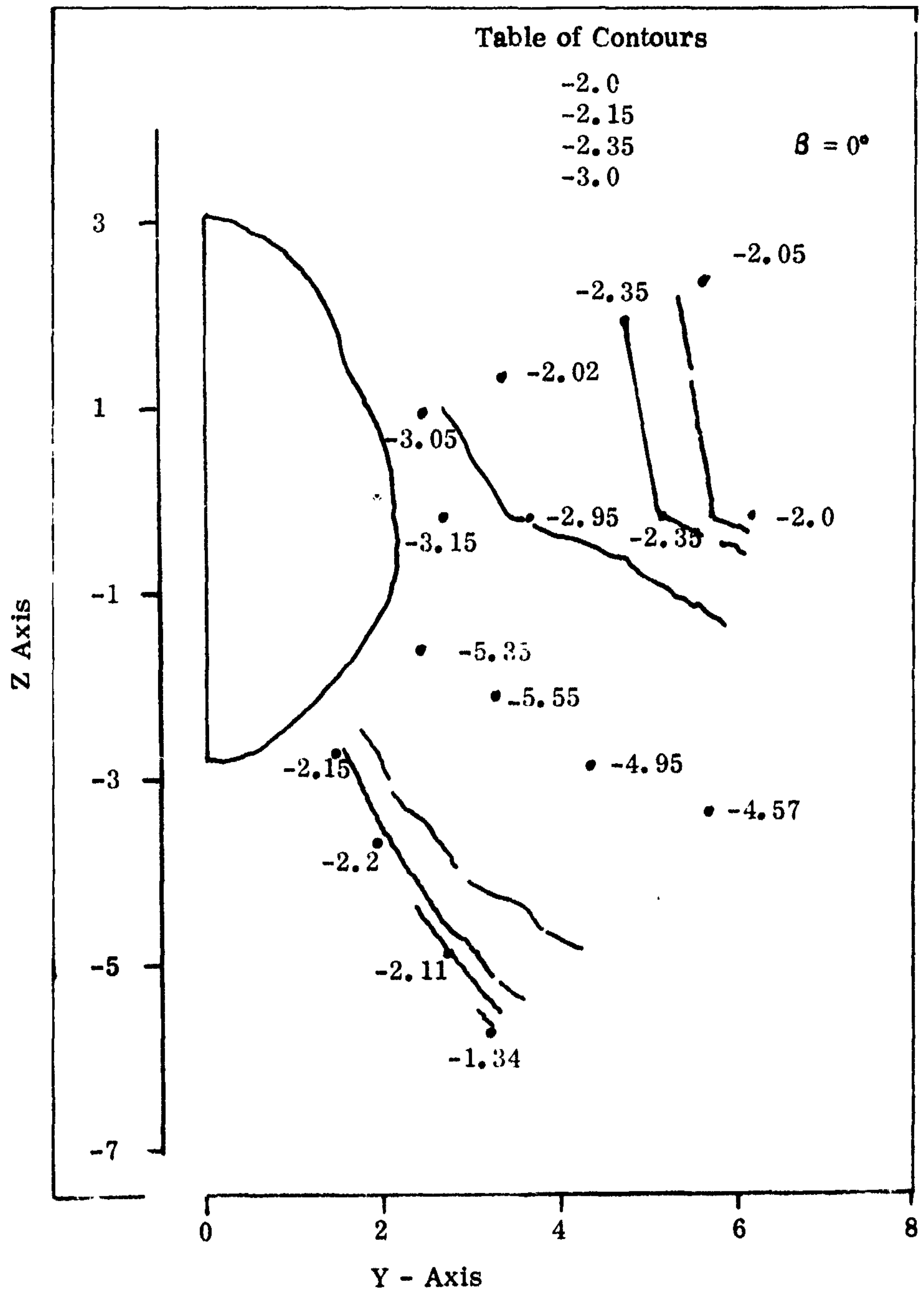

Figure 7-123. Sidewash Angle, Degrees, Fuselage 2
$M_\infty = 2.2$, $\alpha = 15.75°$
Format I

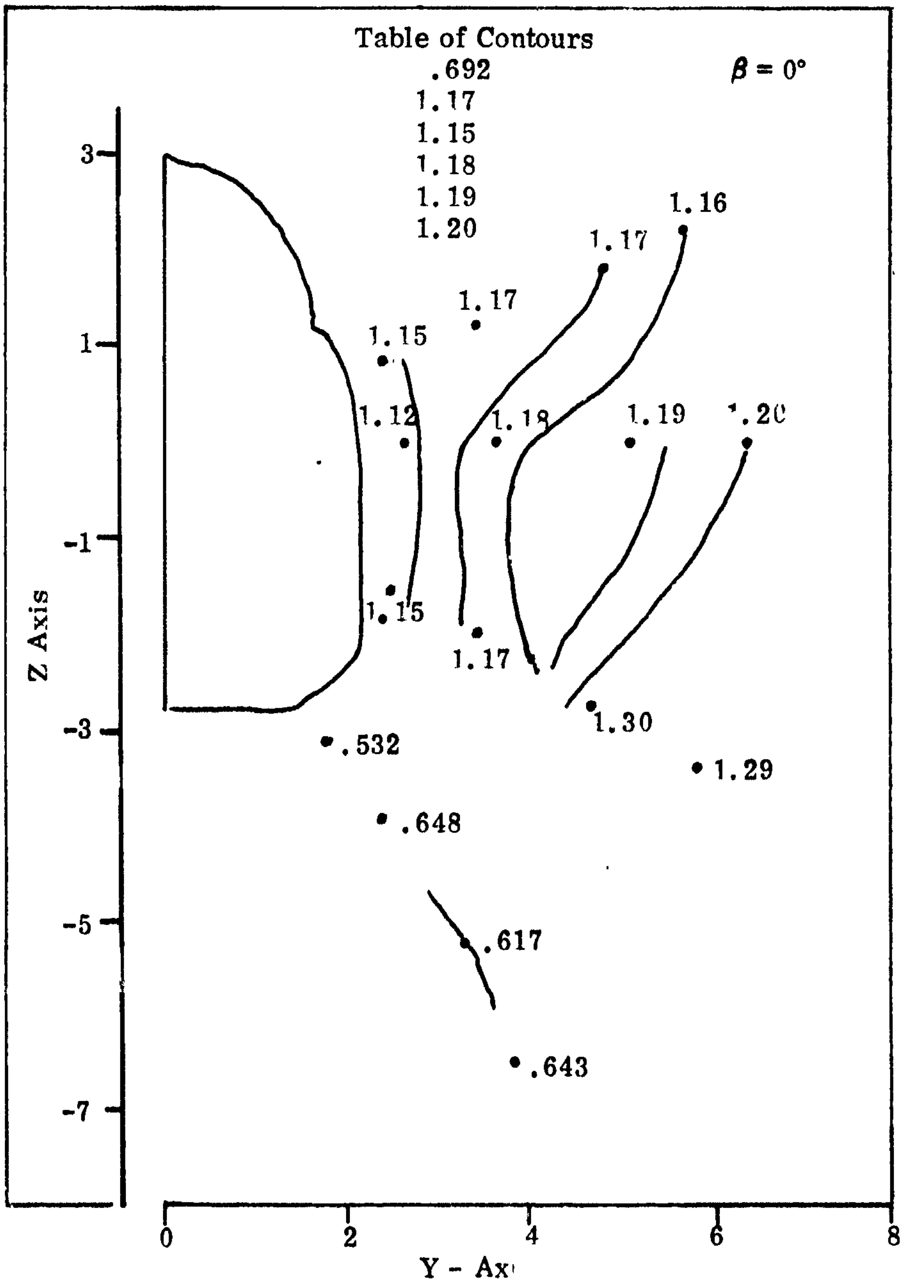

Figure 7-124. Isobars, Fuselage 3
Format I $M_\infty = 2.2$, $\alpha = 15.75°$

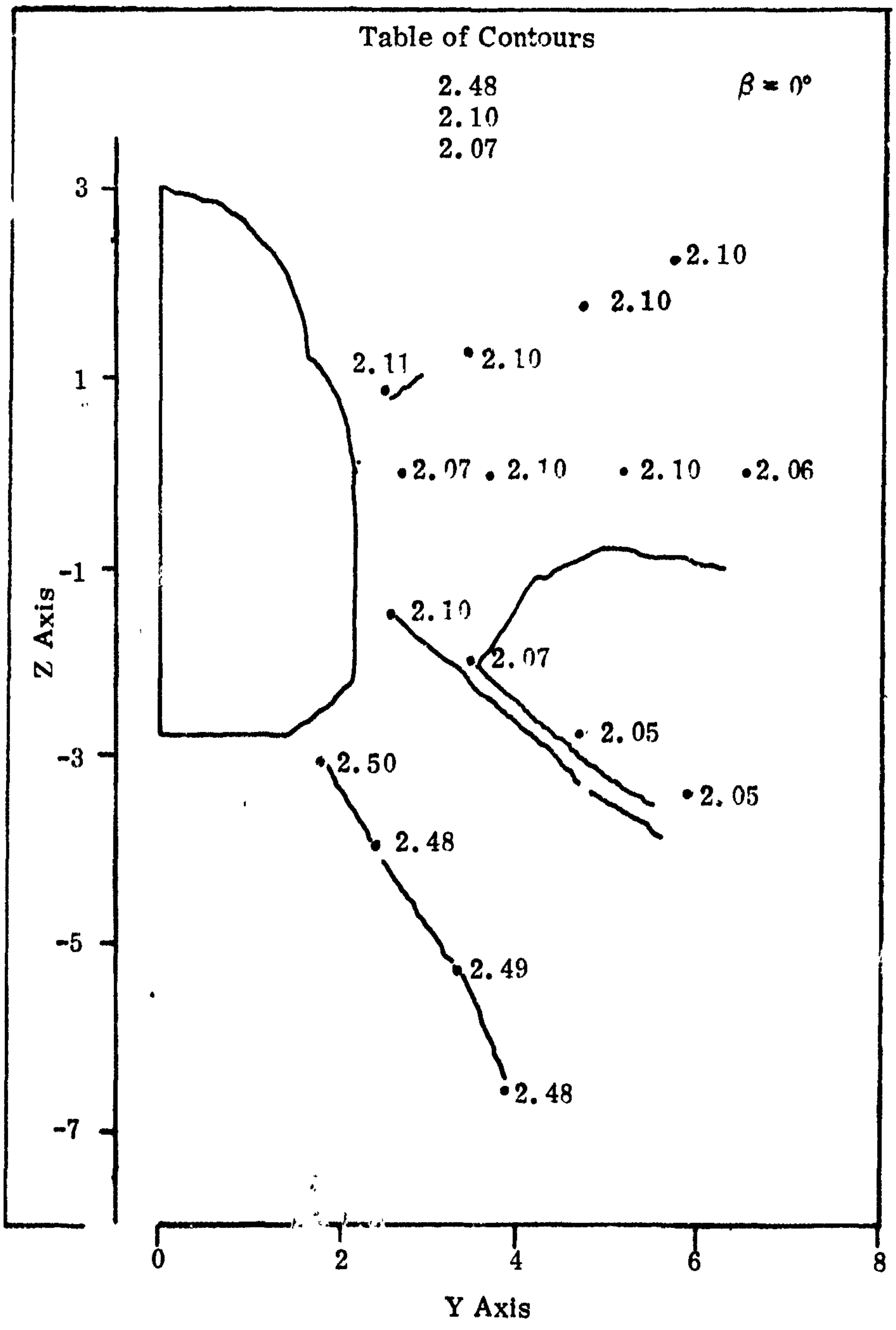

Figure 7-125. Local Mach Number, Fuselage 3

$M_\infty = 2.2$, $\alpha = 15.75°$
Format I

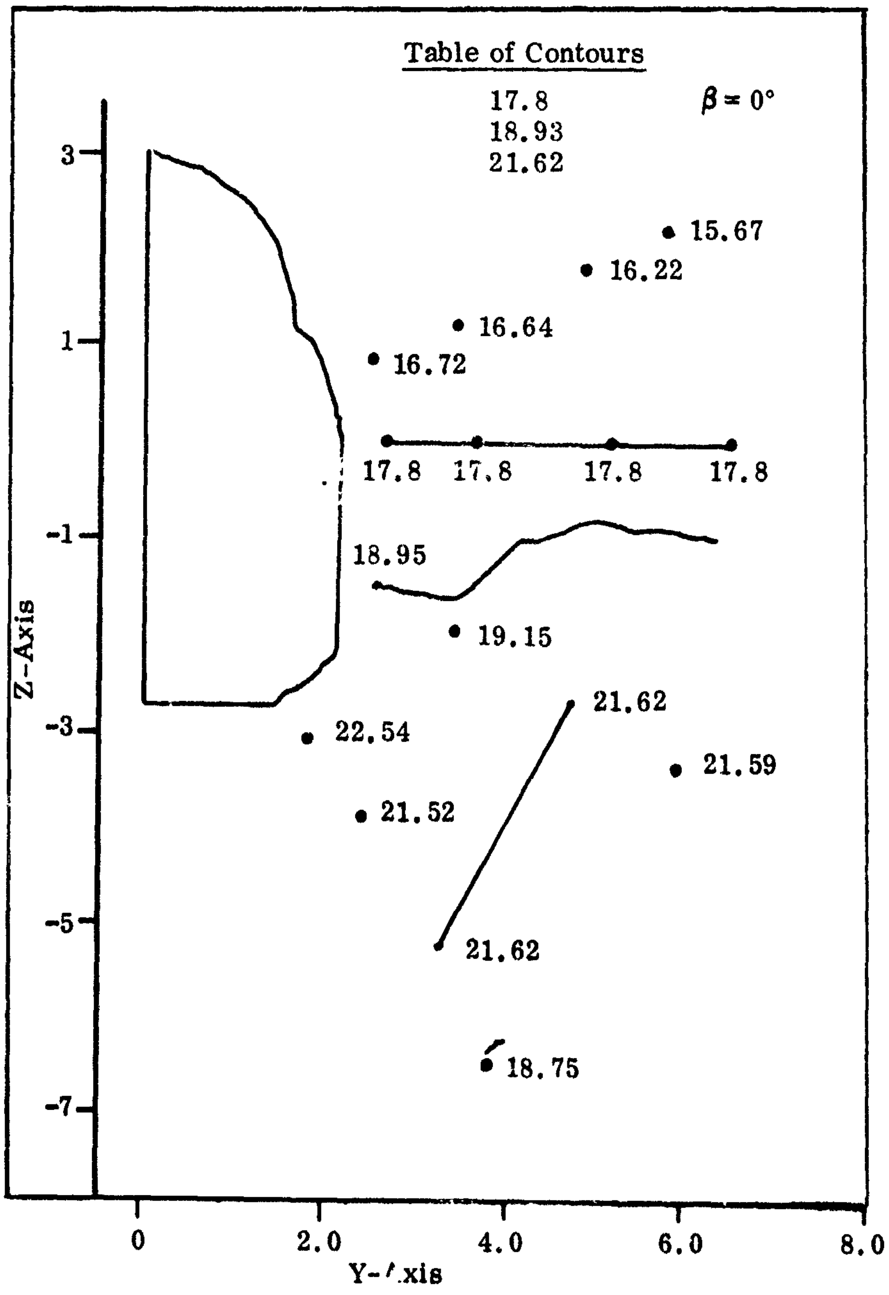

Figure 7-126. Alpha Local ~ Degrees, Fuselage 3

$M_\infty = 2.2$, $\alpha = 15.75°$

Format I

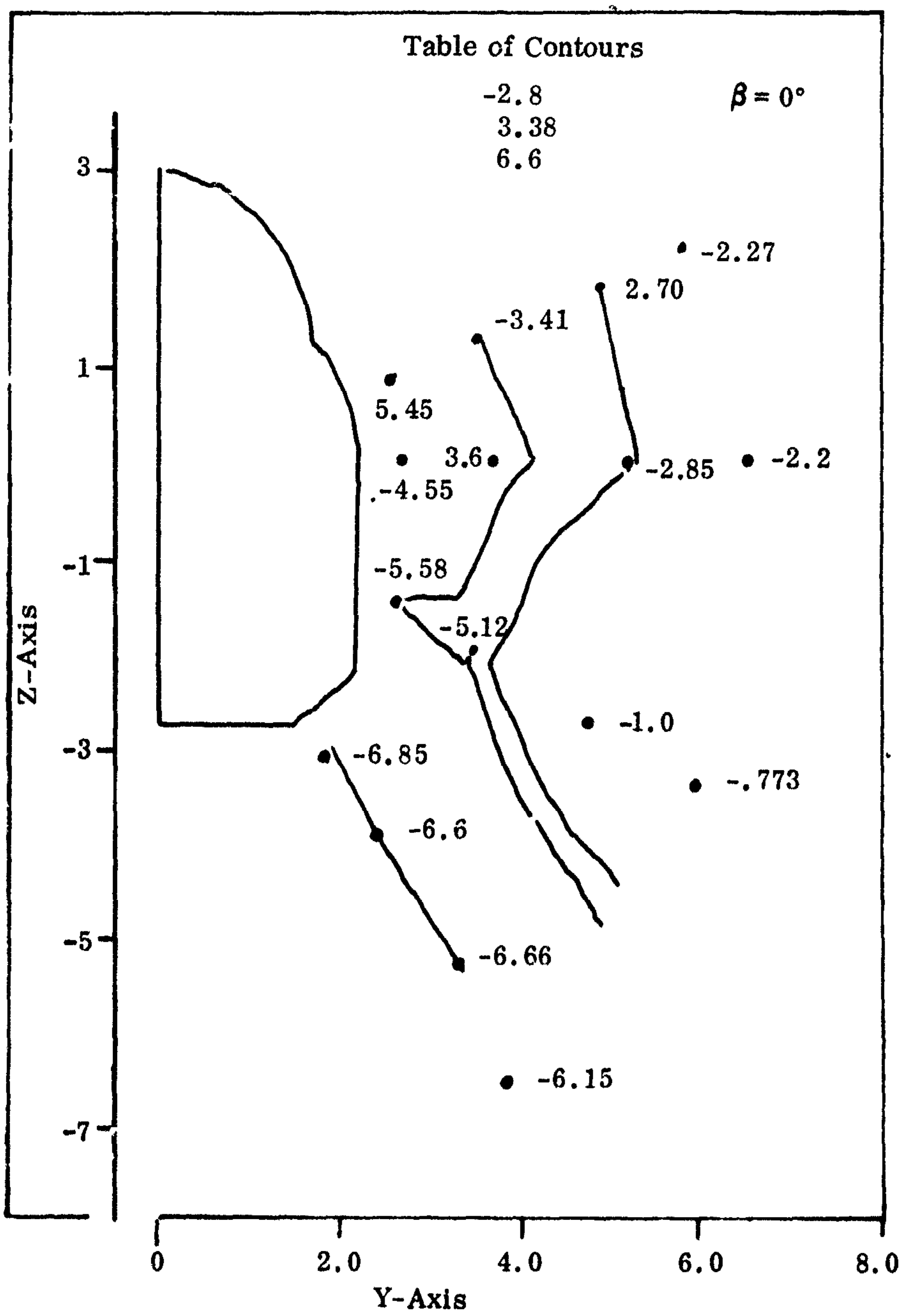

Figure 7-127. Sidewash Angle ~ Degrees, Fuselage 3
$M_\infty = 2.2$, $\alpha = 15.75°$
Format I

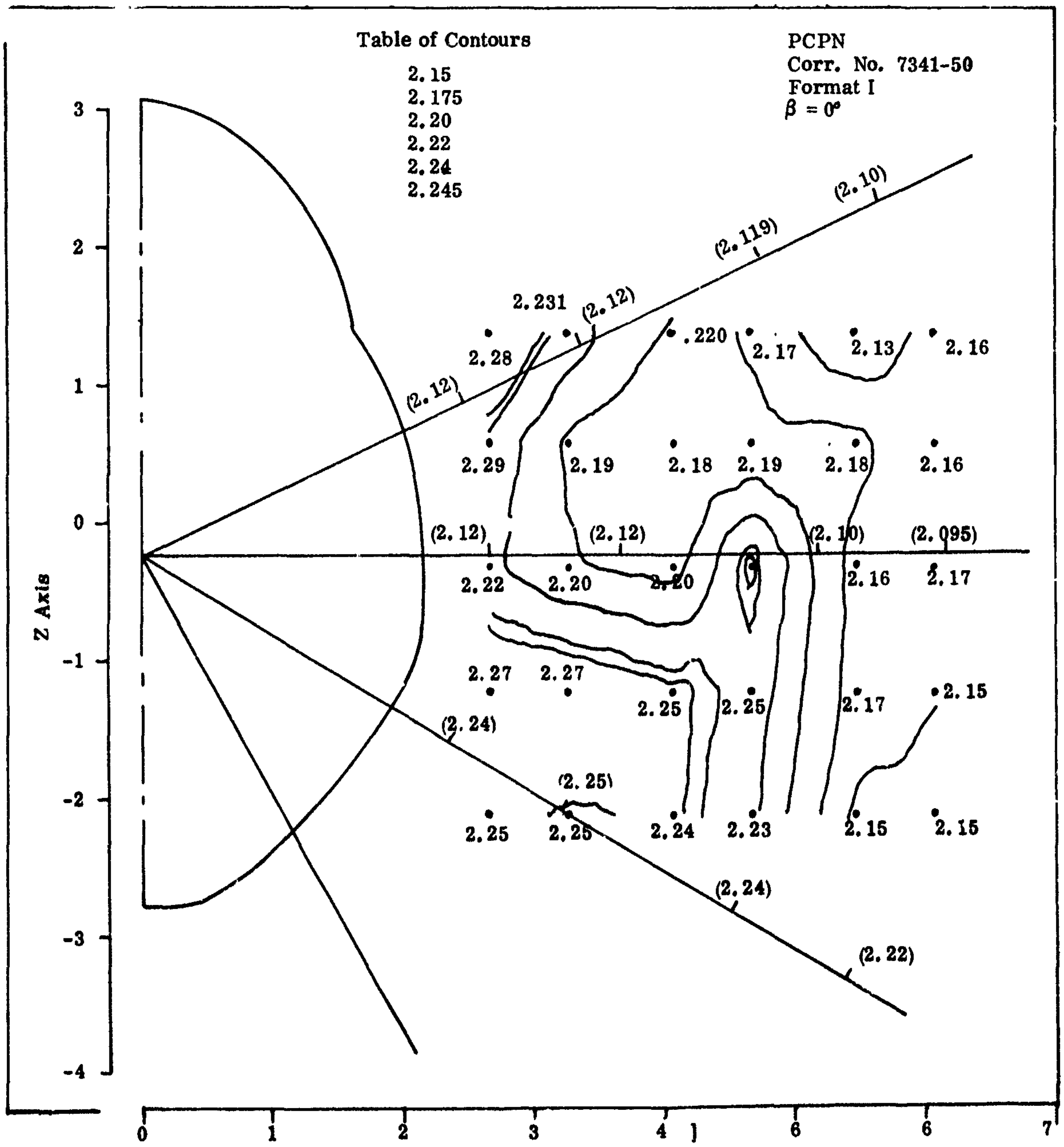

Figure 7-128. Local Mach Number Fuselage 2
$M_\infty = 2.2$ $\alpha = 15°$
Format I

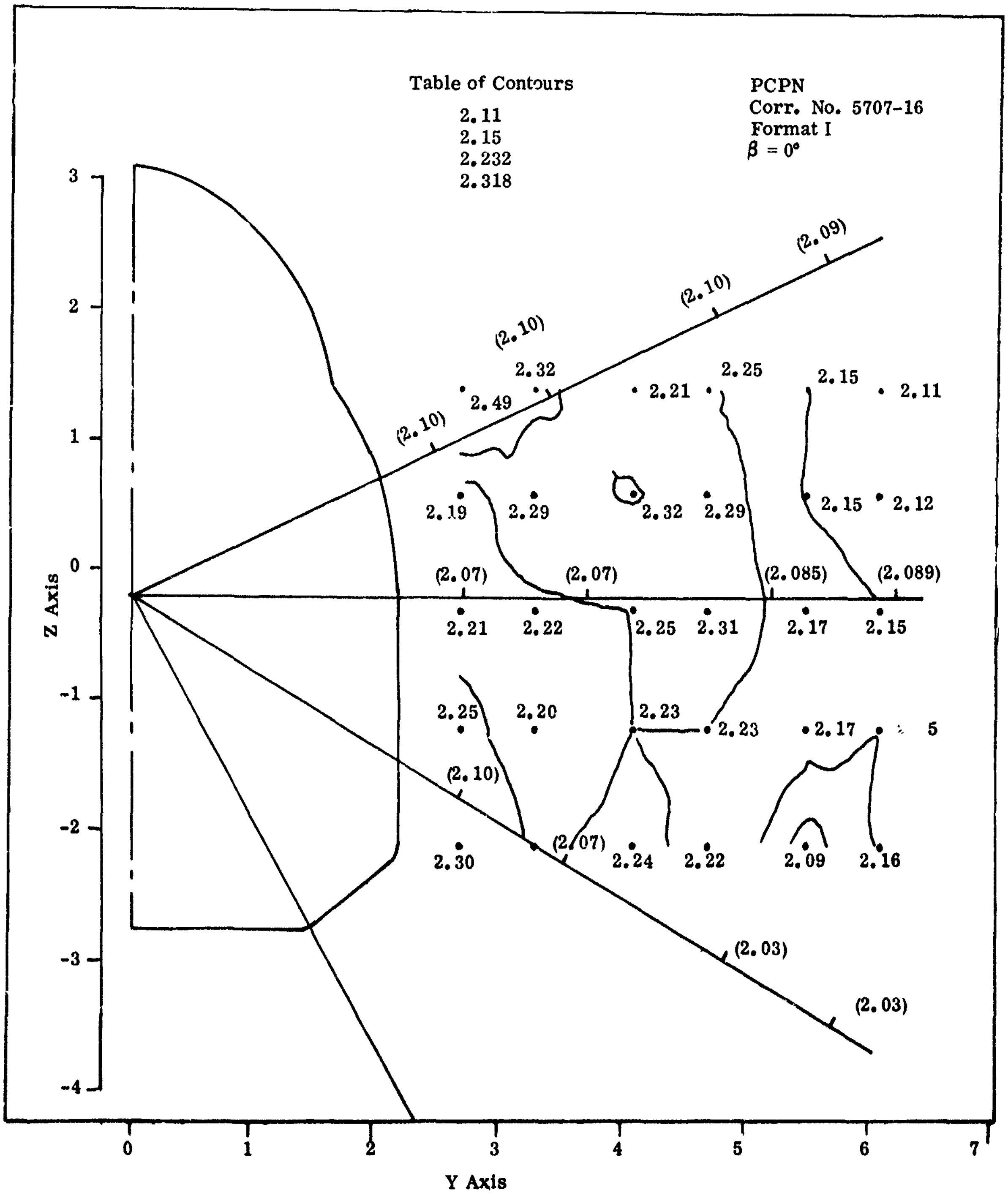

Figure 7-129. Local Mach Number, Fuselage 3,
$M_\infty = 2.2$, $\alpha = 15°$
Format I

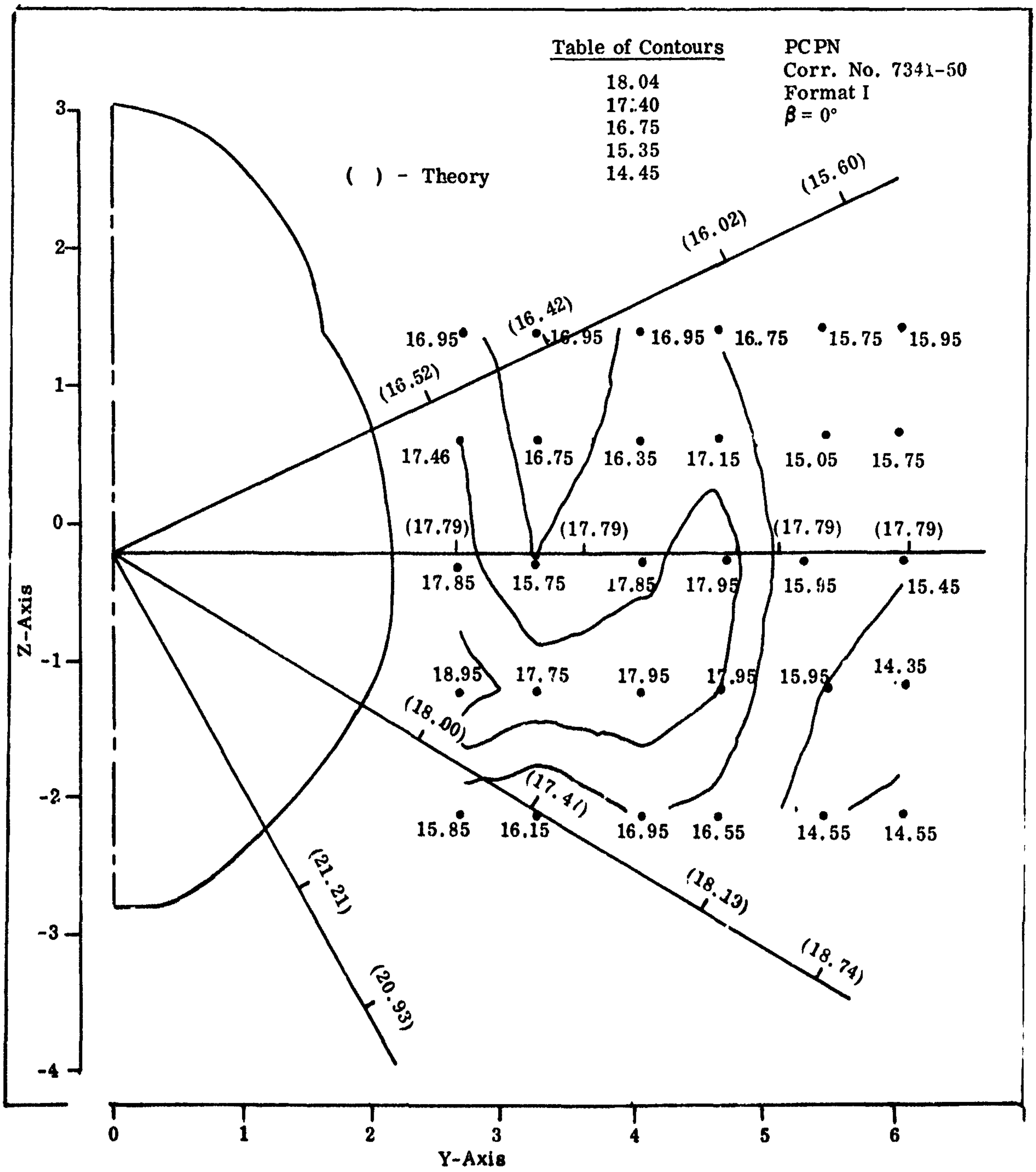

Figure 7-130. Local Alpha, Fuselage 2

$M = 2.2$, α = 15°

Format I

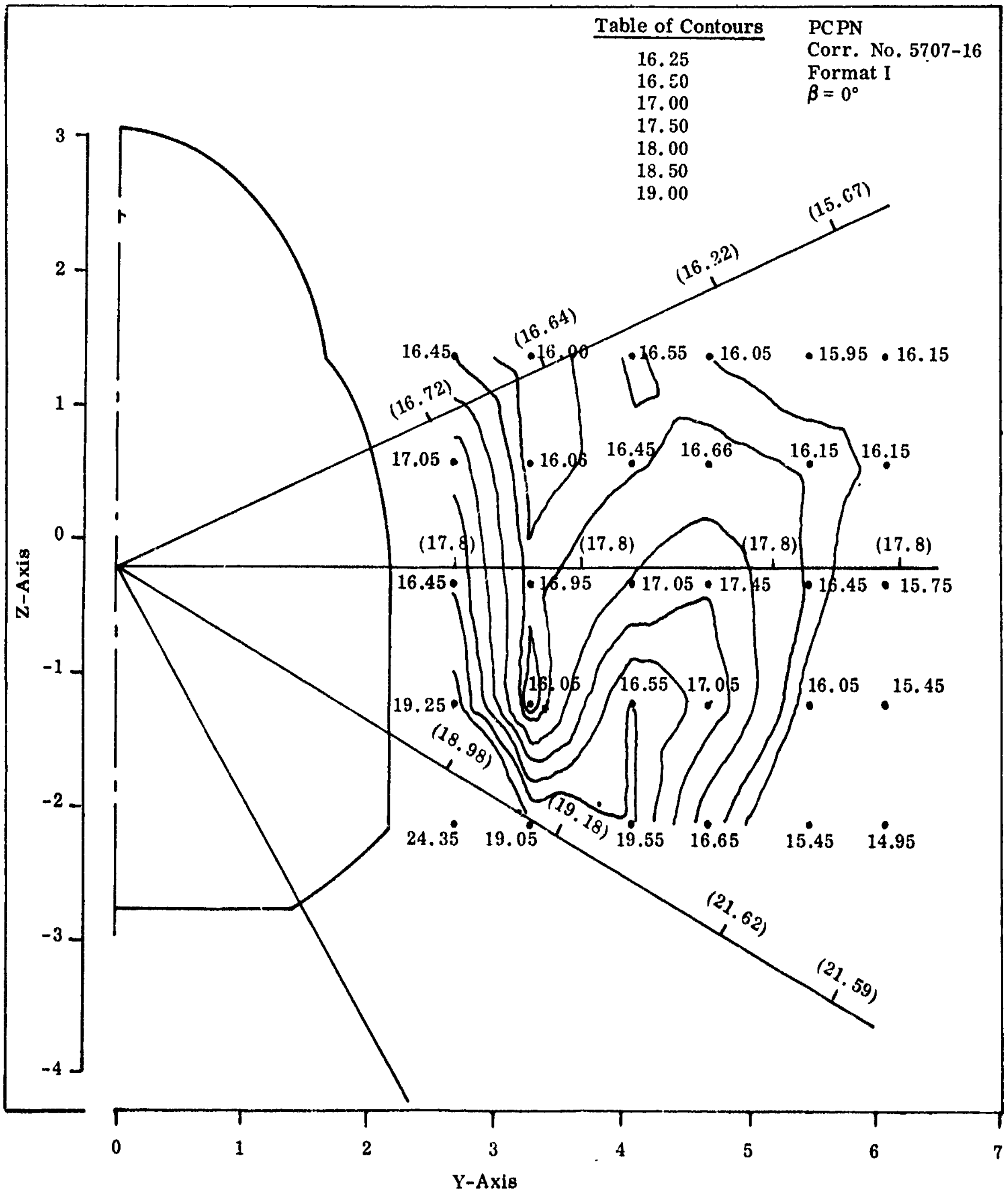

Figure 7-131. Alpha Local, Degrees Fuselage 3
Format I
$M_\infty = 2.2$, $\alpha = 15°$

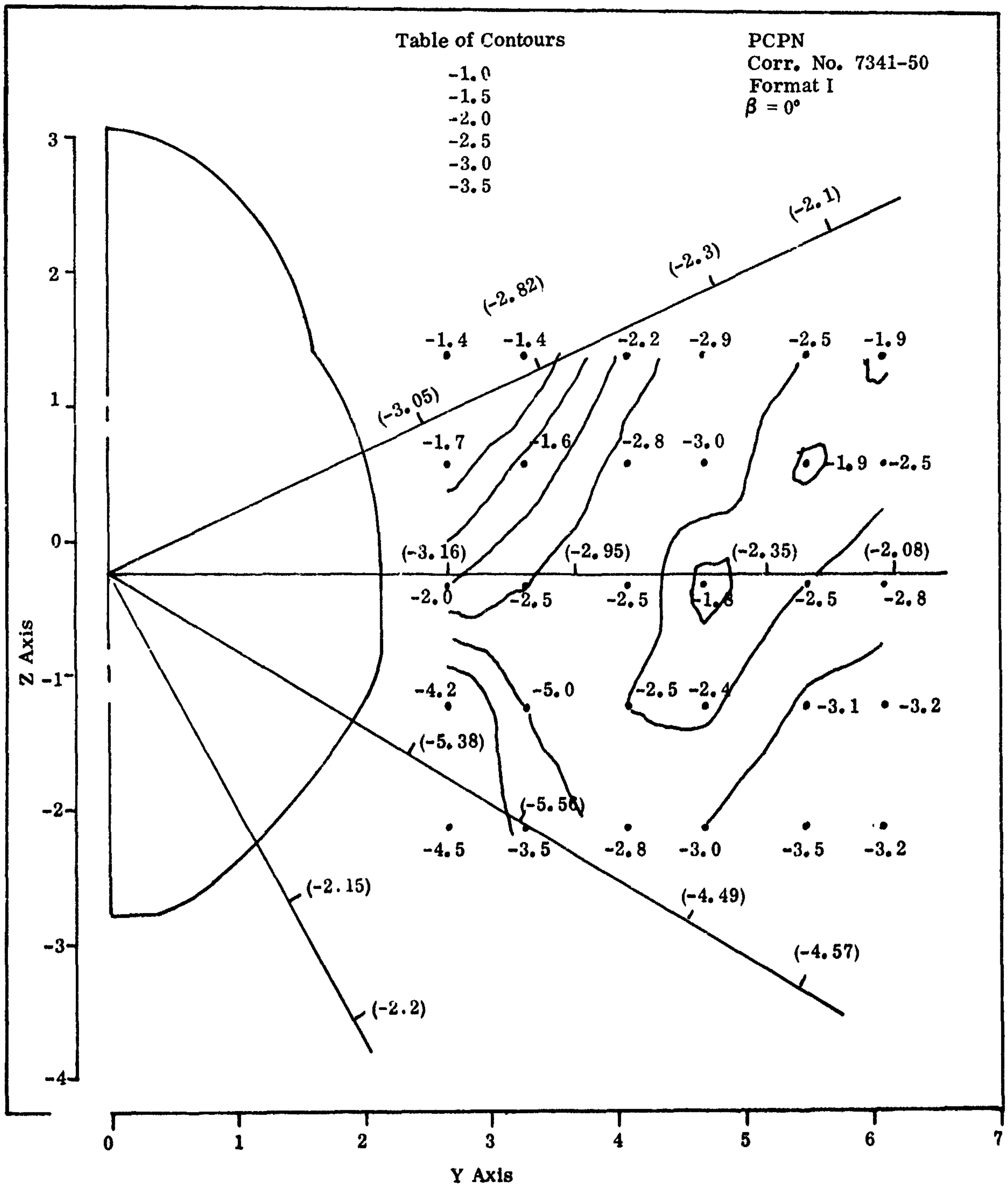

Figure 7-132. Sidewash Angle, Degrees, Fuselage 2
$M_\infty = 2.2$, $\alpha = 15°$
Format I

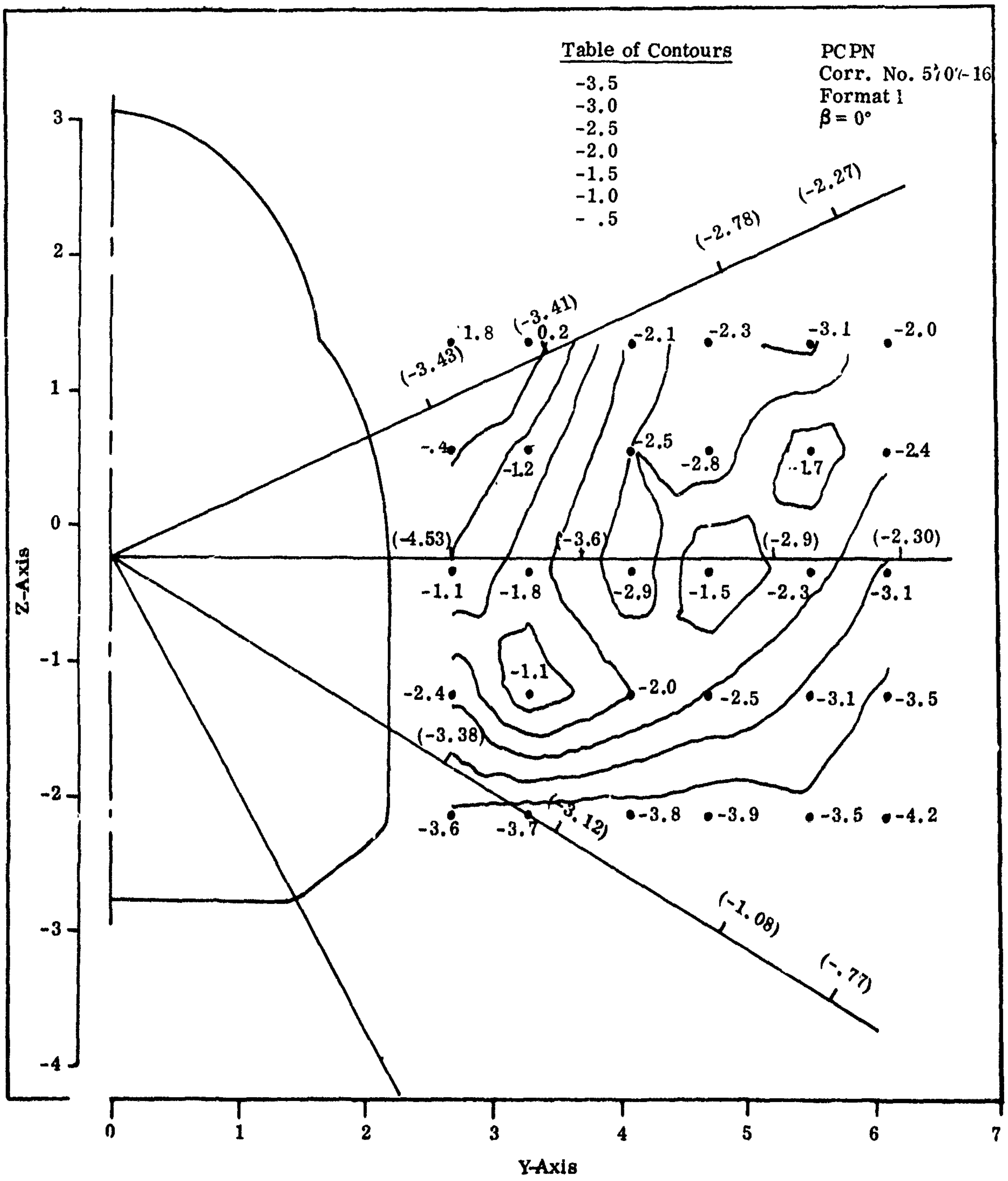

Figure 7-133. Sidewash Angle, Degrees. Fuselage 3

$M_\infty = 2.2$, $\alpha = 15°$

Format I

The sidewash angle also compares favorably, throughout the flow field. However, in the upper inboard area of the flow field, low negative and low positive sidewash exists. This mixed flow condition is not predicted by theory, however, the magnitude of the angles are small. This is, of course, a result of the simplified approach which cannot be expected to account completely for the complex canopy flow field.

Based upon this very limited application of the modified method, it appears to have the potential of rendering, in a relatively simple direct fashion, a rough picture of the flow field engendered by the vehicle at high angle of attack.

7.1.5.3 Exact Reference Plane Technique

This approach also employs a reference plane approach. It differs in concept from the basic reference plane technique by virtue of the fact that the planar axis is the free stream flow vector rather than the fuselage centerline. This approach differs from the basic approach where the effective contour was calculated at one angle of attack with vehicle angle of attack variation accounted for by adjusting the effective fuselage nose cone angle.

A major advantage of the basic approach lies in the fact that the effective fuselage contours need be developed only once. Although it is intuitively apparent that the exact method provides increased sensitivity to angle of attack, the increased level of laborious descriptive geometry introduced by this approach makes it inherently less compatible with a preliminary design study. To circumvent this disadvantage, a digital computer program has been developed to solve the descriptive geometry problem. The program develops the effective fuselage contours as a function of angle of attack and yaw for any specified vehicle configuration.

The computer program can determine the locus of points resulting from the intersection of a skewed plane with an aircraft fuselage (See Figure 7-134). This section describes the analytical techniques employed by the program to achieve this result and the application of the plane contours, so derived, to the calculation of the pressure distribution over an aircraft fuselage. Several comparisons are made between the basic reference plane method, the present method, and the experimental results obtained during the test program.

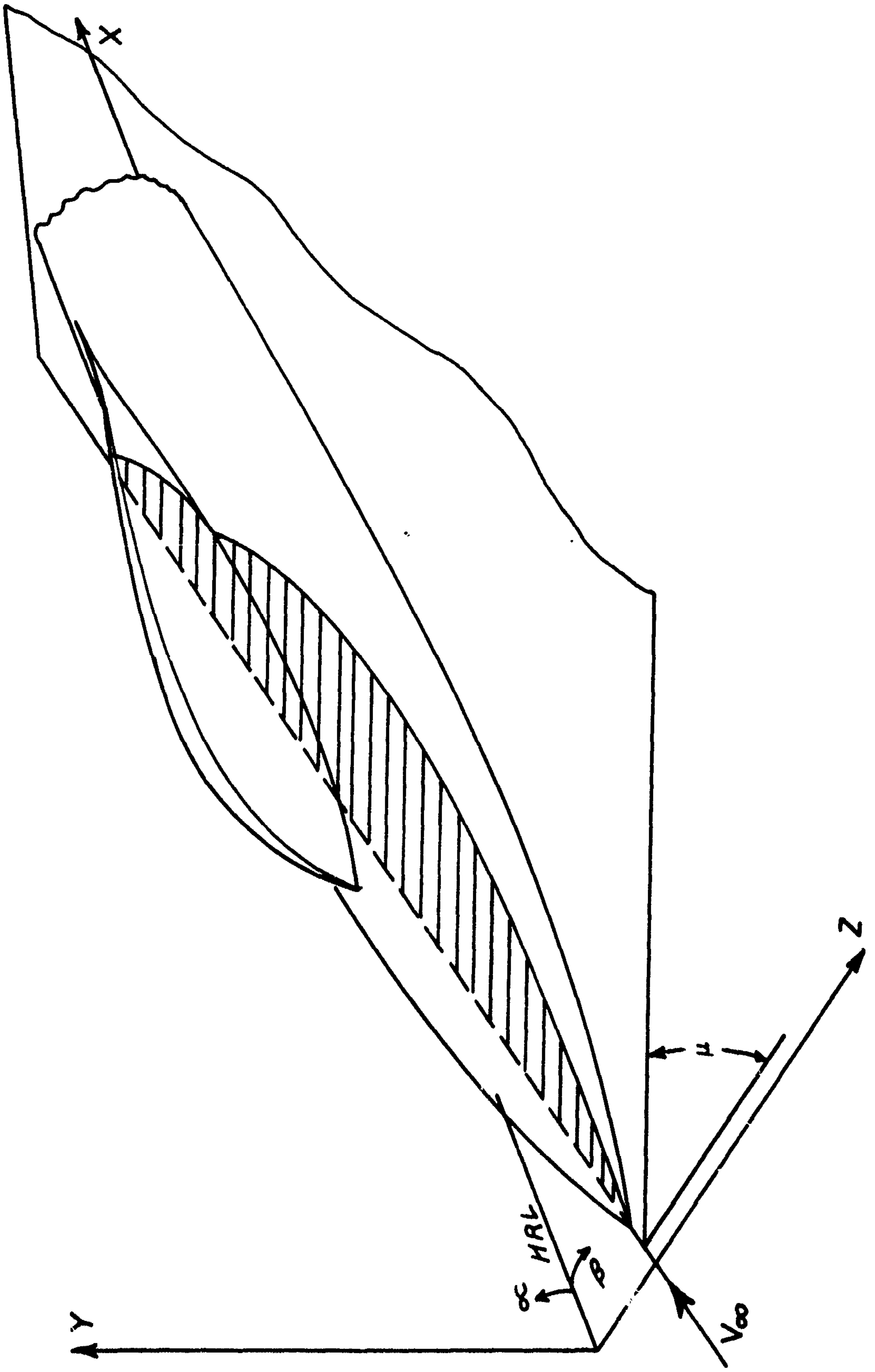
X
Y
Z
μ
α
HRL
β
V_∞

Figure 7-134. A Skewed Plane Intersecting a Fuselage

7.1.5.3.1 Analyses for the Plane-Fuselage Intersection Program

In order to analytically determine the intersection of a skewed plane with an aircraft fuselage it is first necessary to completely define the fuselage contour. Having accomplished this, a technique must be developed for determining the intersection of a plane with the fuselage. The approach adopted is discussed in the following text.

The basic contour lines of an aircraft fuselage, including the canopy, may be completely defined by specifying a group of control lines in plan and profile (Figure 7-135). From these longitudinal lines, the transverse, cross-section in any desired longitudinal station is uniquely defined by the methods of conic lofting. For the fuselage class of interest, the most general of which has a cross-section similar to that shown in Figure 7-135, a maximum of 12 such independent lines are required. These lines, are defined in Figure 7-135. Table V defines the abbreviations used in Figure 7-135(b). At any transverse station these lines form a group of points, shown in Figure 7-136(b), sufficient to describe the entire cross-sectional contour. The fuselage flats, bottom and side, are defined by the two extreme points. The three curved regions are each defined by an equation of the form.

$$y = Pz + Q \pm (Rz^2 + Sz + T)^{1/2}$$

where the coefficients, P, Q, R, S, T are calculated from the coordinates of the three points through which the curve is to be passed by the methods outlined in Reference 11.

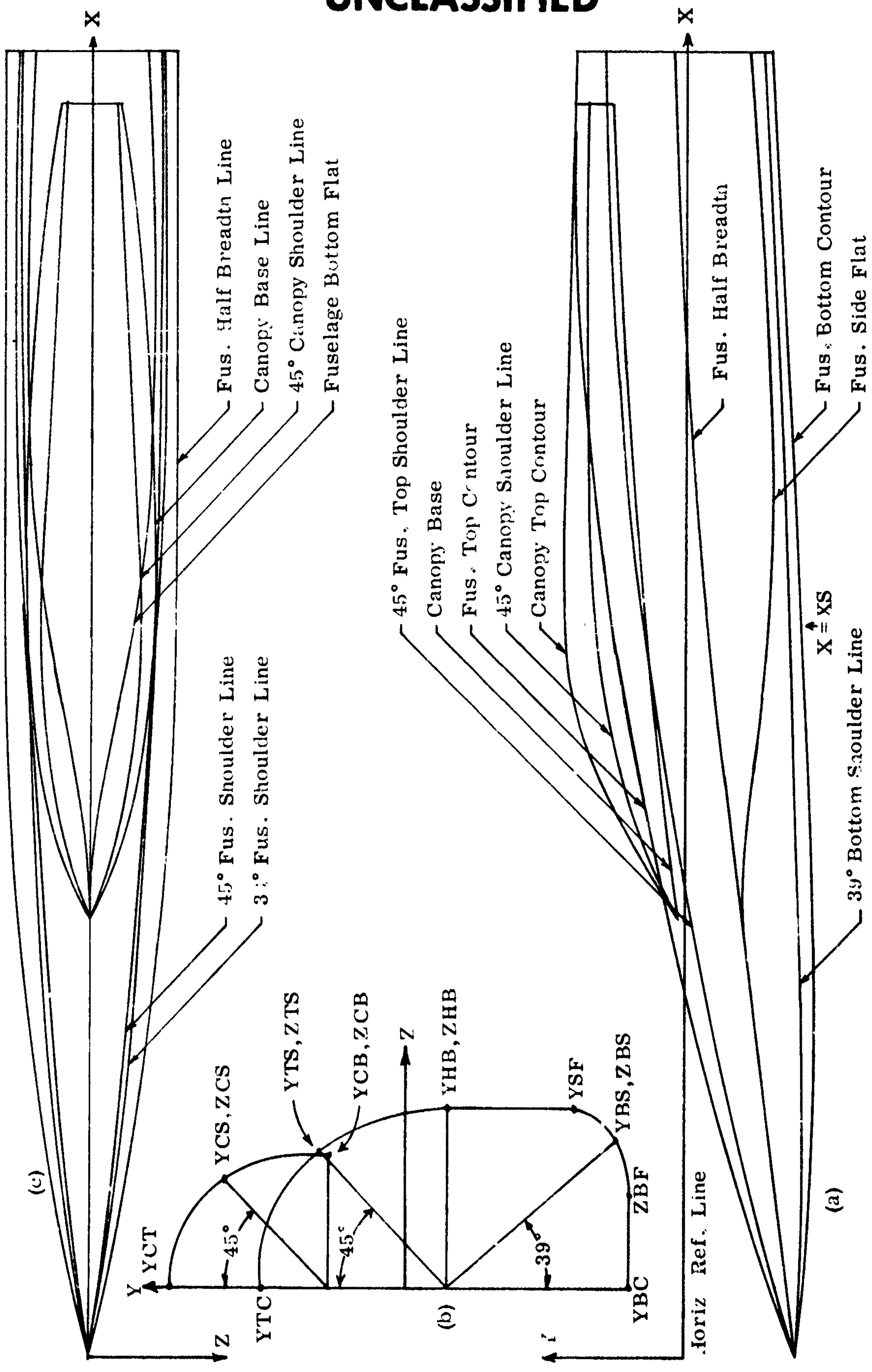
X
Fus. Half Breadth Line
Canopy Base Line
45° Canopy Shoulder Line
Fuselage Bottom Flat
45° Fus. Shoulder Line
39° Fus. Shoulder Line
(c)
Z
Y
YCT
YTC
45°
YCS, ZCS
YTS, ZTS
YCB, ZCB
Z
YHB, ZHB
YSF
YBS, ZBS
ZBF
YBC
39°
(b)
Horiz. Ref. Line
45° Fus. Top Shoulder Line
Canopy Base
Fus. Top Contour
45° Canopy Shoulder Line
Canopy Top Contour
Fus. Half Breadth
Fus. Bottom Contour
Fus. Side Flat
X = XS
39° Bottom Shoulder Line
(a)

Figure 7-135. Fuselage Control Lines and a Typical Cross Section Format I

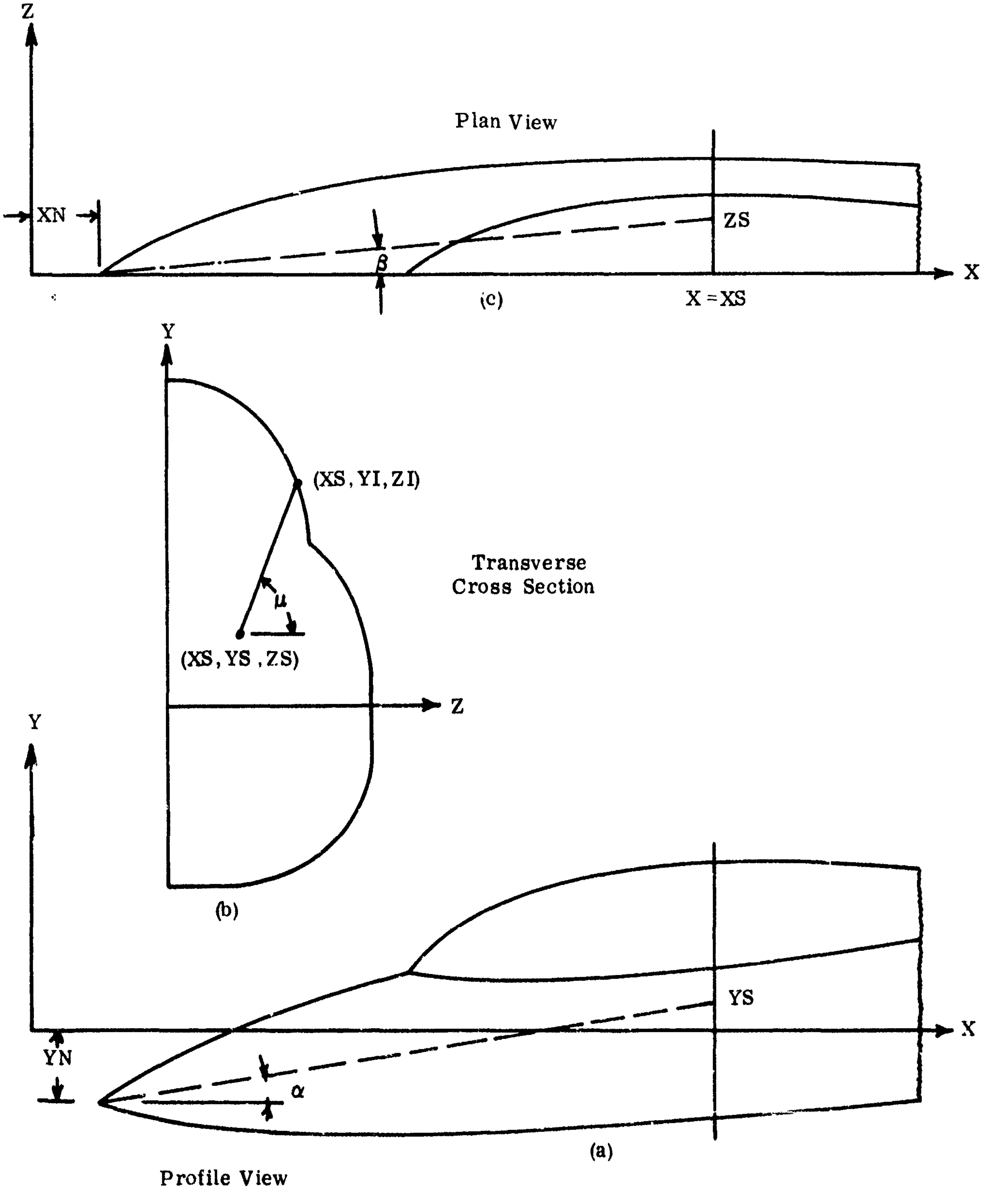
Z
Plan View
XN
ZS
β
X
(c)
X = XS
Y
(XS, YI, ZI)
μ
(XS, YS, ZS)
Transverse
Cross Section
Z
(b)
Y
YS
X
YN
α
(a)
Profile View

Figure 7-136. Intersection of a Plane at a Transverse Station
Format I

TABLE V
CONTROL LINE FUNCTIONS

.Function Name	Definition	Value at X
FYCT(X)	Y Coordinate of Canopy Top Contour	YCT
FYCS(X)	Y Coordinate of Canopy Shoulder Contour	YCS
FZCS(X)	Z Coordinate of Canopy Shoulder Line	ZCS
FYCB(X)	Y Coordinate of Canopy Base Line	YCB
FZCB(X)	Z Coordinate of Canopy Base Line	ZCB
FYTC(X)	Y Coordinate of Fuselage Top Contour	YTC
FYTS(X)	Y Coordinate of Fuselage Top Shoulder Line	YTS
FZTS(X)	Z Coordinate of Fuselage Top Shoulder Line	ZTS
FYHB(X)	Y Coordinate of Fuselage Half Breadth Line	YHB
FZHB(X)	Z Coordinate of Fuselage Half Breadth Line	ZHB
FYSF(X)	Y Coordinate of Fuselage Side Flat	YSF
FYBS(X)	Y Coordinate of Fuselage Bottom Shoulder Line	YBS
FZBS(X)	Z Coordinate of Fuselage Bottom Shoulder Line	ZBS
FZBF(X)	Z Coordinate of Fuselage Bottom Flat	ZBF
FYBC(X)	Y Coordinate of Fuselage Bottom Contour	YBC

The equations for P, Q, R, S, and T are presented below. The terms, a, c, d, and e, used in these equations are defined in the accompanying sketch.

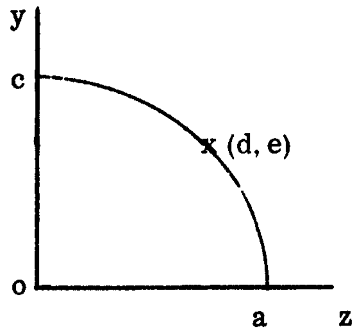

$$P = -\frac{1 + 2\,a\,c\,k}{2a^2\,k}$$

$$Q = \frac{a + 2a^2\,c\,k}{2a^2\,k} = -aP$$

$$R = \frac{1 + 4\,a\,c\,k}{(2a^2k)^2}$$

$$S = -\frac{2\,a + 4\,a^2\,c\,k}{(2a^2\,k)^2} = -\frac{Q}{a^2 k}$$

$$T = \frac{a^2}{(2\,a^2\,k)^2}$$

and k is given as

$$k = \frac{(a - d)\,(e - c)}{(cd + ae - ac)^2}$$

By replacing a with c and c with a in the expression for P, Q, R, S, and T we obtain z as a function of y, so that

$$z = P + Q \pm \sqrt{Ry^2 + Sy + T}$$

a useful expression when γ is 0.

To express Y as a function of Z for the various curves the values of a, c, d, and e can be determined by referring to Figure 7-135(b). The value of Y in the body coordinate system for a given Z is also found in this manner.

For the canopy:

$a = ZCB$

$c = YCT - YCB$

$d = ZCS$

$e = YCS - YCB$

$z = Z$

$Y = YCB + Pz + Q \pm \sqrt{Rz^2 + Sz + T}$

For the top fuselage curve:

$a = ZHB$

$c = YTC - YHB$

$d = ZTS$

$e = YTS - YHB$

$z = Z$

$Y = YHB + Pz + Q \pm \sqrt{Rz^2 + Sz + T}$

From the bottom fuselage contour:

$a = ZHB - ZBF$

$c = YSF - YBC$

$d = ZBS - ZBF$

$e = YSF - YBS$

$z = Z - ZBF$

$Y = YSF - Pz - Q \pm \sqrt{Rz^2 + Sz + T}$

When determining Z as a function of Y, the expression for a, c, d, and e remain unchanged, but the independent variable y changes as does the expression for Z.

For the canopy:

$$y = Y - YCB$$

$$z = Py + Q \pm \sqrt{Ry^2 + Sy + T}$$

In the top fuselage:

$$y = Y - YHB$$

$$Z = PY + Q \pm \sqrt{Ry^2 + Sy + T}$$

For the bottom fuselage:

$$y = YSF - Y$$

$$Z = ZBF + Py + Q \pm \sqrt{Ry^2 + Sy + T}$$

By determining an equation for each one of the three curved surfaces, and the two flat sections, the entire cross sectional contour is completely defined. Thus, by specifying the coordinates of the control lines along the length of the fuselage, it is possible to determine the spatial location of any point on the body.

With the fuselage defined at every longitudinal location, it is now possible to determine the intersection of a plane with a body.

Let us assume a fixed coordinate system with the X axis coincident with the Horizontal Reference Line of the fuselage, as shown in Figure 7-136. The cutting planes of interest are those which pass through the tip of the fuselage nose. The orientation of the plane is best envisaged as follows. Consider a line parallel to the free stream, (and hence making an angle of α with the XZ plane and an angle of β with the XY plane, (Figure 7-136), passing through the tip of the nose, and extending through the length of the fuselage. Let this line lie in a plane, and then rotate the plane about this line until the line of intersection of the plane with a transverse station (YZ plane) makes an angle of μ with the horizontal reference (XY) plane. The orientation of the plane is therefore specified by giving the angle of attack α, and the angle of yaw β of the free stream plus the cutting plane angle μ.

Figure 7-136 shows a line coincident with the free stream velocity, intersecting a transverse station located at X = XS, at the point (XS, YS, ZS) where

$$YS = (XS - XN) \tan \alpha + YN$$

$$ZS = (XS - XN) \tan \beta$$

The intersection of the cutting plane with the transverse station forms a line which extends from (XS, YS, ZS) to (XS, YI, ZI) and makes an angle of μ with the horizontal. The point (XS, YI, ZI) is the intersection of the skewed plane with the fuselage contour at the station under consideration. By repeating this procedure at as many transverse locations as desired, the line of intersection of the skewed plane with the fuselage can be determined.

The means of computing the location of the point (XS, YI, ZI) depends upon the angle μ and the location of (XS, YS, ZS) relative to the fuselage contour, i.e. whether it is inside or outside of the fuselage. Figures 7-136 and 7-137 depict several possibilities. In Figure 7-136 the intersection is found by an iterative procedure using the equation of a straight line and the curve until the Y coordinates are arbitrarily close together. The same procedure is used in Figure 7-137(a) but the intersection is sought in the curve which is farthest from (XS, YS, ZS). Figure 7-137 (b) and (c) show cases where the intersection can be determined in closed form as the intersection of two straight lines. Figure 7-137(d) shows a case where no intersection is possible because the axis of rotation of the plane has pierced the body and the plane direction is away from the body.

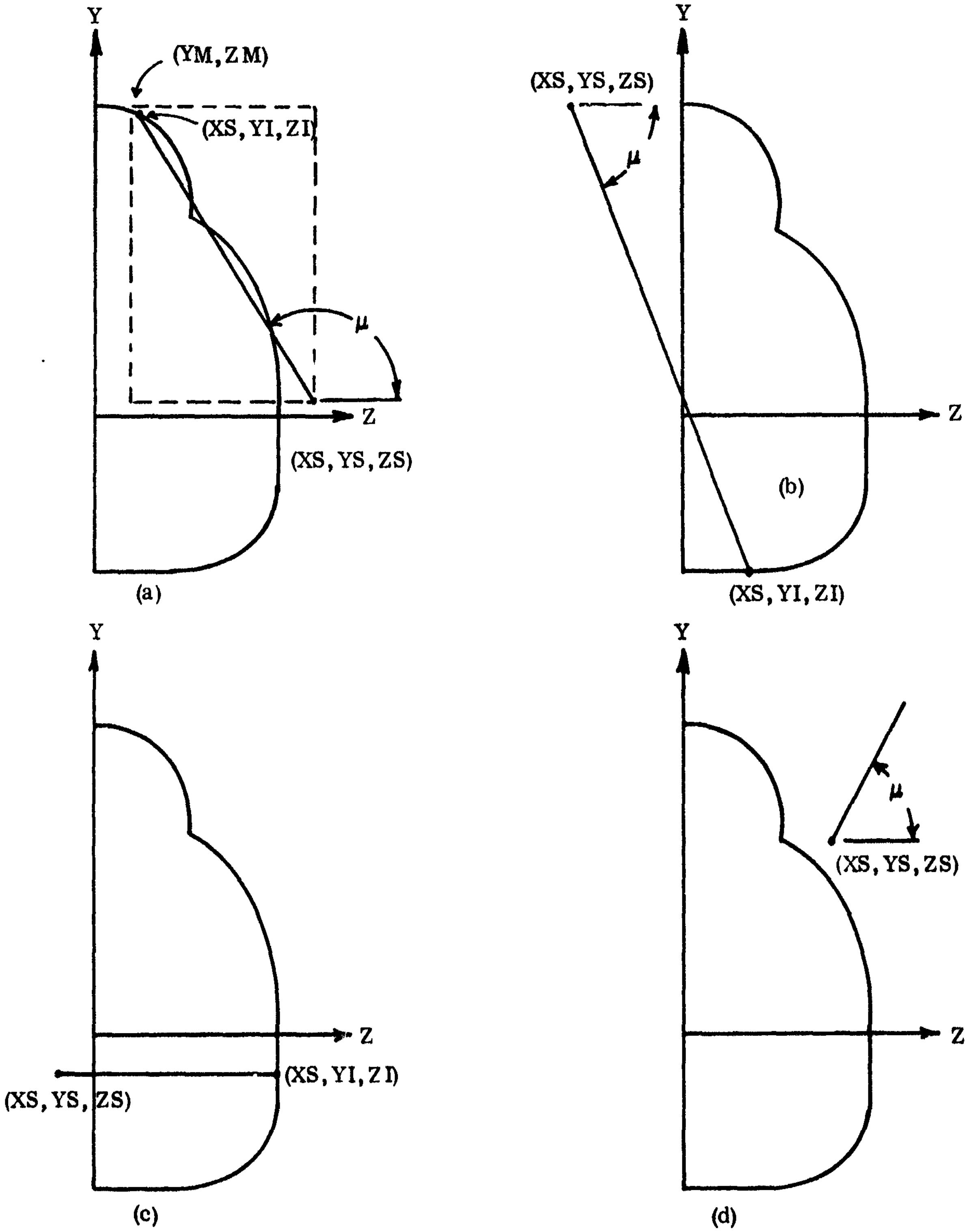
Y
(YM, ZM)
(XS, YI, ZI)
μ
Z
(XS, YS, ZS)
(a)
Y
(XS, YS, ZS)
μ
Z
(b)
(XS, YI, ZI)
Y
Z
(XS, YI, ZI)
(XS, YS, ZS)
(c)
Y
μ
(XS, YS, ZS)
Z
(d)

Figure 7-137. Transverse Cross Sections at X = XS
Format I

To this point we have calculated the spatial coordinates of the intersection of a skewed plane with the fuselage with each intersection having three coordinates. In order to establish a plane contour, that can be analyzed as a symmetric body and whose axis of revolution is in the free stream direction, it remains to express the spatial coordinates of the intersection in a plane coordinate system. To achieve this result it is necessary to translate and rotate the coordinate system such that, the X axis is coincident with the axis of revolution (free stream direction) of the cutting plane, and one of the coordinate planes (XY plane is chosen), lines in the cutting plane.

The procedure for this transformation is as follows:

Translate the coordinate system so that it is centered at the tip of the nose. The original coordinate system is $X_o \ Y_o \ Z_o$.

$$X_1 = X_o - XN$$

$$Y_1 = Y_o - YN$$

$$Z_1 = Z_o$$

Referring to Figure 7-138,

Rotate $X_1 \ Y_1 \ Z_1$ coordinate system about Z_1 by an amount α. (Angle of attack of the free stream relative to the fuselage reference line).

$$X_2 = X_1 \cos\alpha + Y_1 \sin\alpha$$

$$Y_2 = -X_1 \sin\alpha + Y_1 \cos\alpha$$

$$Z_2 = Z_1$$

Rotate the $X_2 \ Y_2 \ Z_2$ coordinate system about Y_2 by an amount β^*.

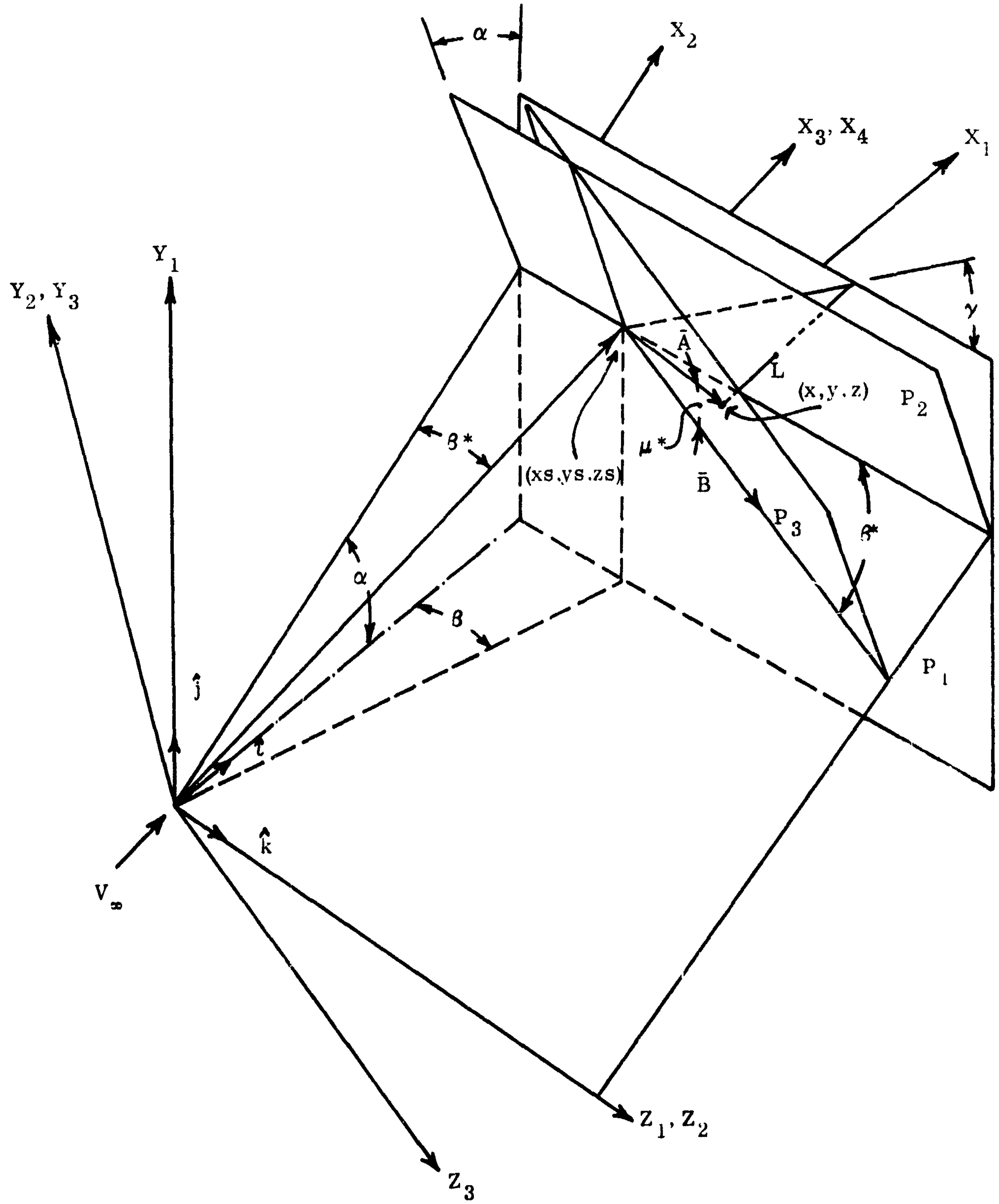
α
X_2
X_3, X_4
X_1
Y_1
Y_2, Y_3
γ
$\bar{A}$
L
(x, y, z)
P_2
β^*
μ^*
(xs, ys, zs)
$\bar{B}$
P_3
β^*
α
β
P_1
$\hat{j}$
$\hat{i}$
$\hat{k}$
V_∞
Z_1, Z_2
Z_3

Figure 7-138. Rotation Angles for Axis Transformation Format I

$X_3 = X_2 \cos \beta^* + Z_2 \sin \beta^*$

$Y_3 = Y_2$

$Z_3 = X_2 \sin \beta^* + Z_2 \cos \beta^*$

Rotate the $X_3\ Y_3 Z_3$ coordinate system about X_3 by an amount $(90-u^*)$, to its final orientation.

$X_4 = X_3$

$Y_4 = Y_3 \sin \mu^* + Z_3 \cos \mu^*$

$Z_4 = Y_3 \cos \mu^* + Z_3 \sin u^*$

Although the three (3) sets of equations presented above can be combined they are presented in the uncombined form to facilitate both their understanding and programming.

The definition of β^* and μ^* is determined, with the aid of Figure 7-138, as follows.

$\tan \beta^* = \cos \alpha \tan \beta$

μ^* which is the angle through which the $X_3\ Y_3\ Z_3$ coordinate system must be rotated so that the intersection of XY plane with the plane $X_1 = X_S$ (in the $X_1\ Y_1\ Z_1$ system) makes an angle of μ with the horizontal $(X_1\ Z_1)$ plane, can be determined as follows.

In Figure 7-138 (which depicts the coordinate system after it has been translated so that the origin of the system is at the tip of the fuselage nose) the plane P_1 is some transverse plane normal to the X_1 axis and located at X_1 = XS. After the first rotation of the $X_1\ Y_1\ Z_1$ coordinate system through an angle α about Z_1, P_1 assumes the position P_2. The second rotation through β^* about Y_2 takes P_2 into Position P_3. This is the plane in which μ^* is measured. The calculation of α^* is as follows. A line of unit length is drawn from (XS, YS, ZS) making an angle μ with the horizontal in the P_1 plane. This line terminates at the point (XS, YX + sin u, ZS + cosμ). Through this point a line L is drawn parallel to the X_3 axis. If $\bar{C}$ is a vector along X_3, then in the $X_1 Y_1 Z_1$ coordinate system, the direction cosines of line L are

$$C_1 = \frac{XS}{|C|}$$

$$C_2 = \frac{YS}{|C|}$$

$$C_3 = \frac{ZS}{|C|}$$

Then the equation of P_3 in the $X_1 Y_1 Z_1$ coordinate system is

$$C_1 X + C_2 Y + C_3 Z - 1 = 0$$

The equation of line L in parametric form is

$$X = tC_1 + XS$$

$$Y = tC_2 + YS + \sin \mu$$

$$Z = tC_3 + ZS + \cos \mu$$

The intersection of the line L and plane P_3 is obtained by substituting the parametric equations for X, Y, Z into the equation for P_3 to obtain

$$t = -C_2 \sin \mu - C_3 \cos u$$

and then resubstituting into the parametric equation of the line L to obtain the point of intersection (X, Y, Z).

A vector defined as $\bar{A}$, is drawn from (XS, YS, ZS) to X, Y, Z). Where

$$\bar{A} = (X - XS)\,\hat{\imath} + (Y - YS)\,\hat{j} + (Z - ZS)\,\hat{k}$$

The components of a unit vector $\bar{B}$, normal to X_3 and lying in the $X_3 Z_3$plane (thereby placing it also in the P_3 plane) are

$$\bar{B} = -\sin\beta^* \cos\alpha\ \hat{\imath} - \sin\beta^* \sin\alpha\ \hat{j} + \cos\beta^*\ \hat{k}$$

The angle μ^* is determined from the definition of the dot product. So that

$$\alpha^* = \cos^{-1} \frac{\bar{A} \cdot \bar{B}}{|\bar{A}| \; |\bar{B}|}$$

When this transformation is performed, one of the coordinates (Z) will be zero for each intersection point and we are left with the coordinates of a contour where the X axis is the free stream direction and the Y values are the Y coordinates of an equivalent body of revolution for the particular plane cut.

7.1.5.3.2 Computer Program

The techniques described in the previous section have been incorporated into a computer program which generates the spatial and planar coordinates of the intersection of a skewed plane with an aircraft fuselage.

The capabilities of the program are partially demonstrated in Figure 7-139 which shows the intersection of a group of planes rotated about an axis inclined at an angle of 7.5° to the horizontal with plane angles of 90°, 60°, 24°, 0° -30°, -60°, -90°. Also shown are a group of planes rotated about an axis inclined at 15° to the horizontal with plane angles between -28° and -63°. Both axes of rotation lie in the XY plane $(\beta = 0)$.

7.1.5.3.3 Flow Field Analyses

The purpose in developing the fuselage -plane intersection program described in the previous sections was to have the ability to cut planes at any orientation exactly and quickly. With this capability it is possible to generate bodies of revolution whose axis of rotation is the free stream direction by simply specifying the angle of attack, angle of sideslip, and the plane angle.

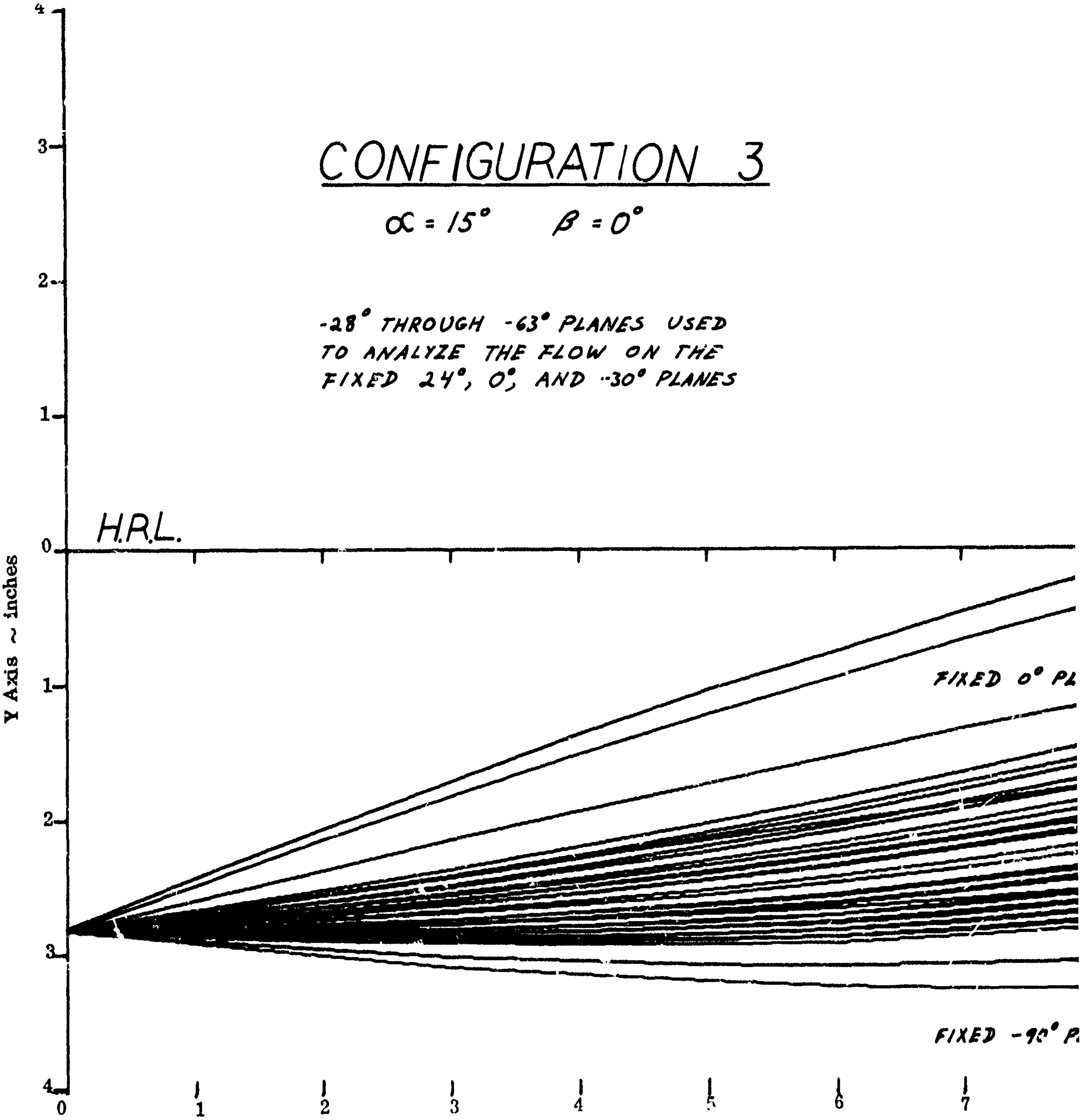
CONFIGURATION 3
α = 15°   β = 0°
-28° THROUGH -63° PLANES USED TO ANALYZE THE FLOW ON THE FIXED 24°, 0°, AND -30° PLANES
H.R.L.
FIXED 0° PL
FIXED -90° P
Y Axis ~ inches
4
3
2
1
0
1
2
3
4
0
1
2
3
4
5
6
7

1

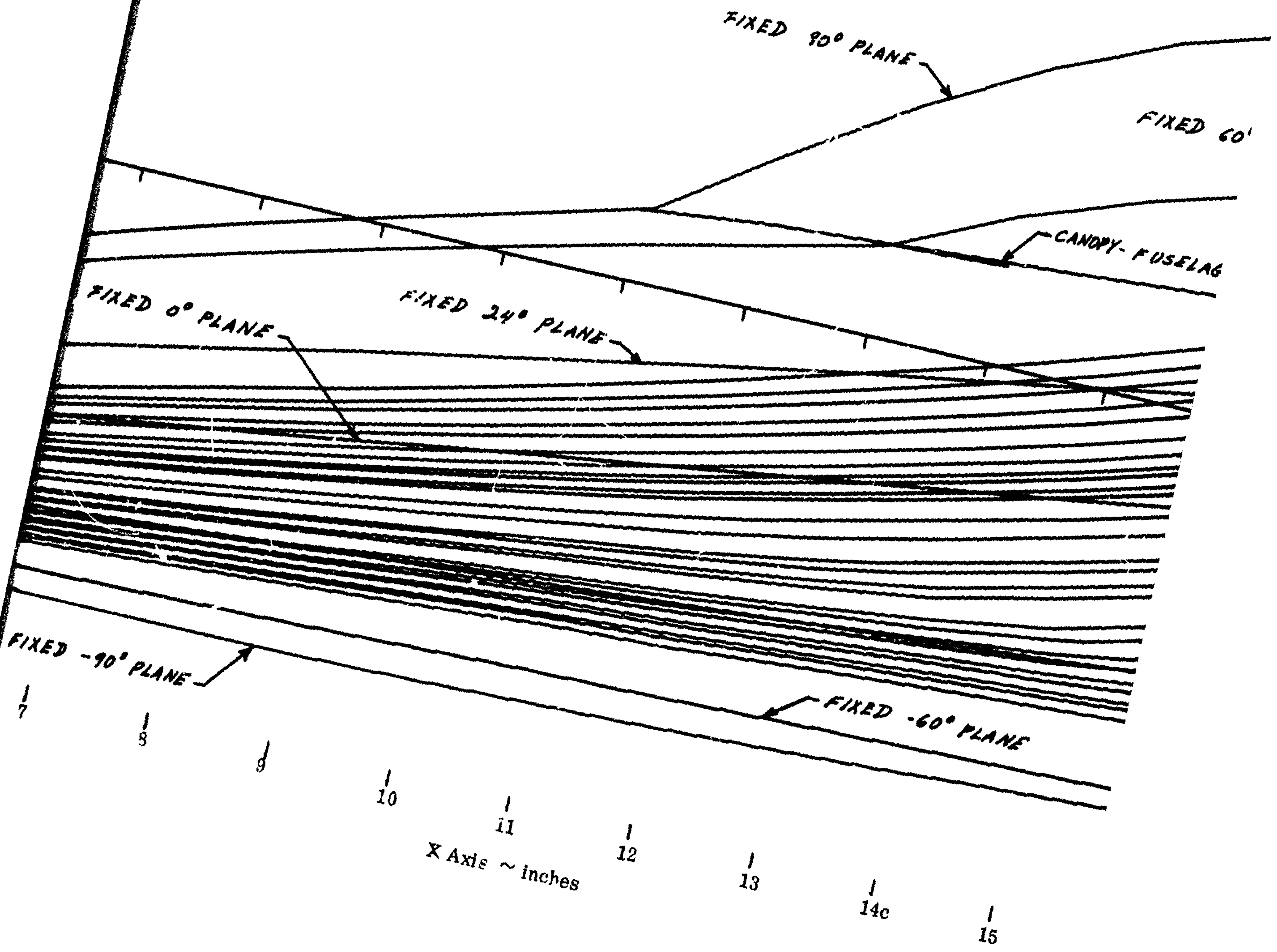
FIXED 90° PLANE
FIXED 60'
CANOPY- FUSELAG
FIXED 0° PLANE
FIXED 24° PLANE
FIXED -90° PLANE
FIXED -60° PLANE
7
8
9
10
11
12
13
14c
15
X Axis ~ inches

2

UNCLASSIFIED

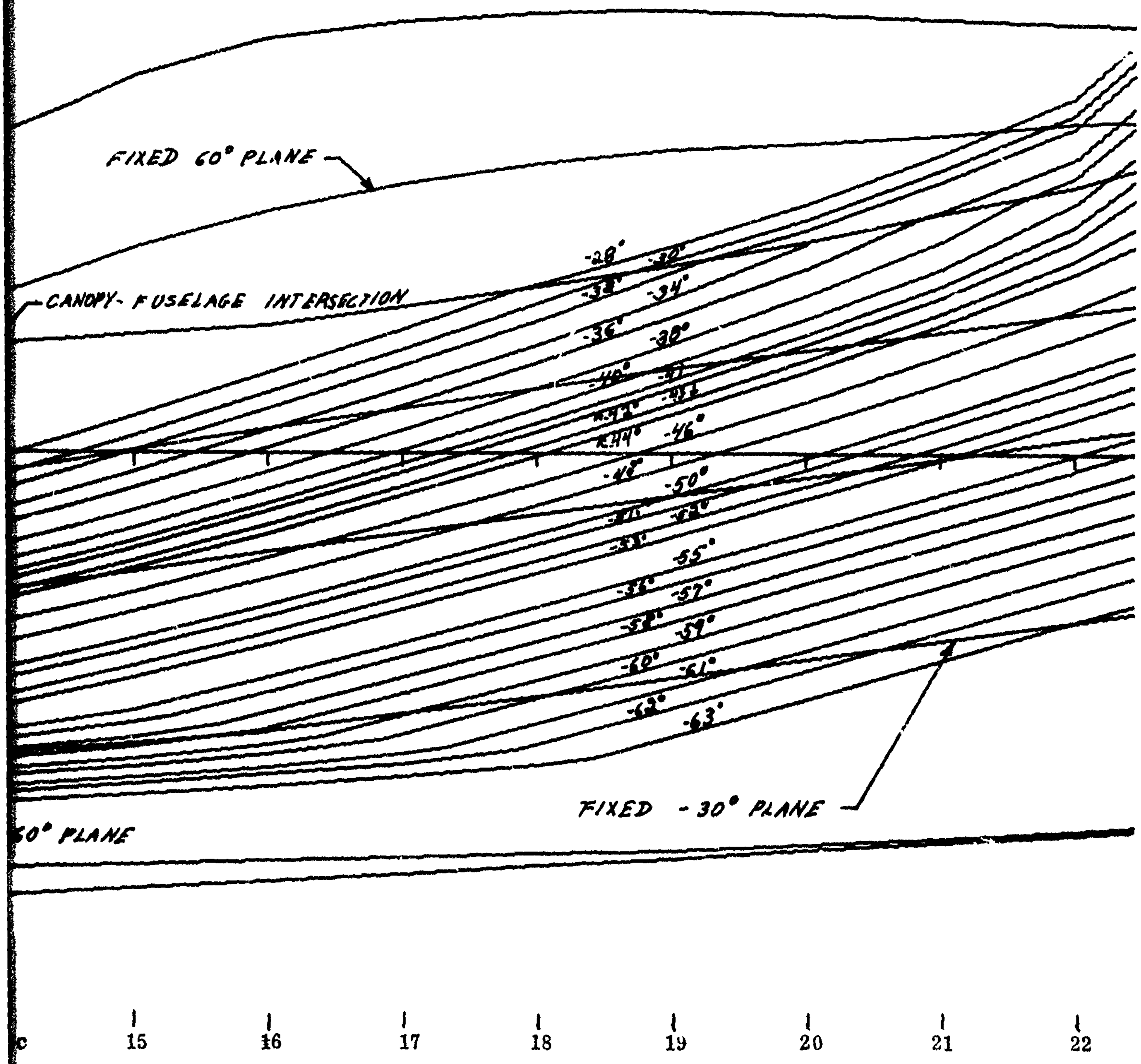
FIXED 60° PLANE
CANOPY - FUSELAGE INTERSECTION
-28°
-30°
-32°
-34°
-36°
-38°
-40°
-42
R.42°
-43
R.44°
-46°
-48°
-50°
-51
-52°
-53°
-55°
-56°
-57°
-58°
-59°
-60°
-61°
-62°
-63°
FIXED - 30° PLANE
0° PLANE
c
15
16
17
18
19
20
21
22

Figure 7-139. Flow Field Plane Fuselage Intersections, Format I

UNCLASSIFIED

3

PRECEDING PAGE BLANK-NOT FILMED

During the experimental program, fuselage surface pressure measurements were obtained from static taps located along fixed planes defined as the 24°, 0°, -30°, -60°, and -90° planes. These planes had an axis of rotation inclined at an angle of 7.5° to the horizontal.

Referring to Figure 7-139, showing the trace of the fixed planes in plan view on fuselage 3, together with the corresponding set of planes whose axis of rotation is 15°, it can be seen that the equivalent bodies of revolution for the 15° angle of attack case developed by the exact reference plane method are quite different from those at 7.5° angle of attack developed by the basic reference plane method. Furthermore, the planes at 15° angle of attack intersect a fixed plane at only one point. Therefore, to obtain a pressure distribution correlation along a fixed plane it is necessary to analyze a series of planes intersecting the fixed plane in that region where the comparison of experimental and analytical pressure distribution is desired.

Figure 7-139 shows the intersection of a series of planes whose rotation axis is inclined at 15° with the fixed planes. The plane angles range from -28° to -52° and -55° to -62°, and were chosen to intersect the fixed 24°, 0°, and -30° planes in the region where experimental pressure data is available. Figure 7-140 presents a two dimensional plot of four cut planes.

The procedure employed to compute both the surface and flow field properties is identical to that used in the original analytical method, i.e., generate an input line by assuming conical flow over the tip followed by a method of characteristics solution. The static pressure obtained on the body of revolution at the point of intersection with the fixed plane is used to compare the analytical and experimental results.

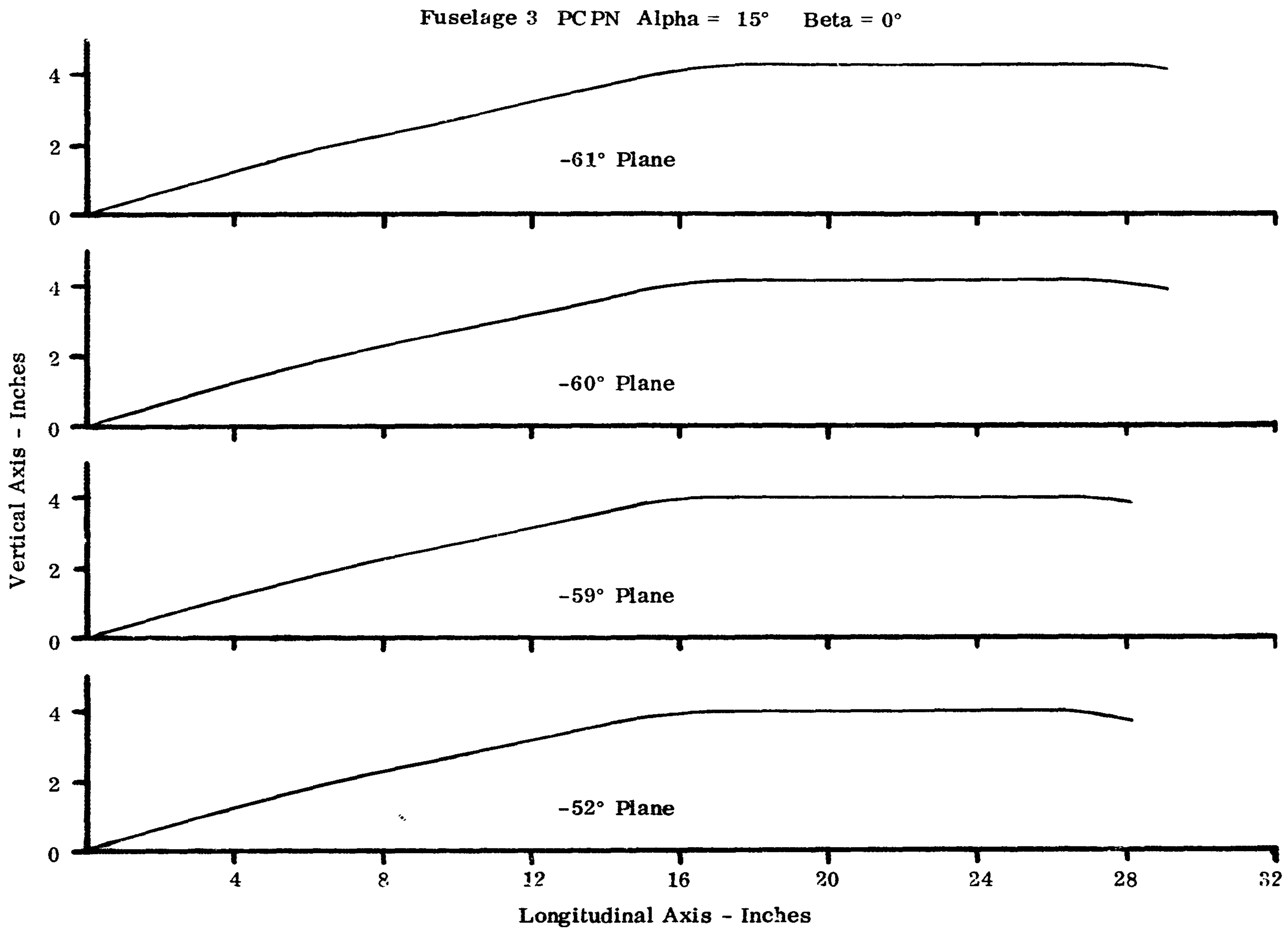

Figure 7-140. Example of Cut Plane Format I

7.1.5.3.4 Results

For the example case of 15° vehicle angle of attack, the surface static pressure distribution along the +24°, 0°, and -30° planes, computed by the exact reference plane method, are presented in Figure 7-141. Also shown are the values estimated by the basic reference plane method and the results obtained experimentally.

Development of the exact method was an attempt to increase the predictive accuracy of the computed results, particularly at high angle of attack. The agreement, with the experimental data, achieved with the exact method is significantly better than that achieved by the basic method. This is most clearly seen for the -30° plane where the exact method accurately predicts both the location and magnitude of the abrupt pressure variations recorded experimentally. The analytically predicted trend in pressure distribution for the other two planes (0° and +24°) are also acceptable for preliminary design purposes. These results indicate that the major objective for developing the exact method namely an improved sensitivity to angle of attack has been accomplished. An examination of the comparison curve, however, also reveals that the analytically predicted pressure distributions are all displaced from the corresponding experimental curves a fairly uniform amount. In addition to the aft portion of the fuselage this quantitative disagreement exists over the cone - ogive comprising the forward fuselage. The flow properties in this region of fuselage were accurately predicted by the basic reference plane method, using a conventional method of characteristics solution for an equivalent cone. The use of a skewed plane (exact method) results in a distorted conical ogive and a initially incorrect estimate of the local flow properties. Therefore, although the exact method closely predicts the trend in flow properties, it carries the initially inaccurate estimate through the entire calculation and an analytical estimate uniformly displaced from the experimental data results. Consequently, an adjustment

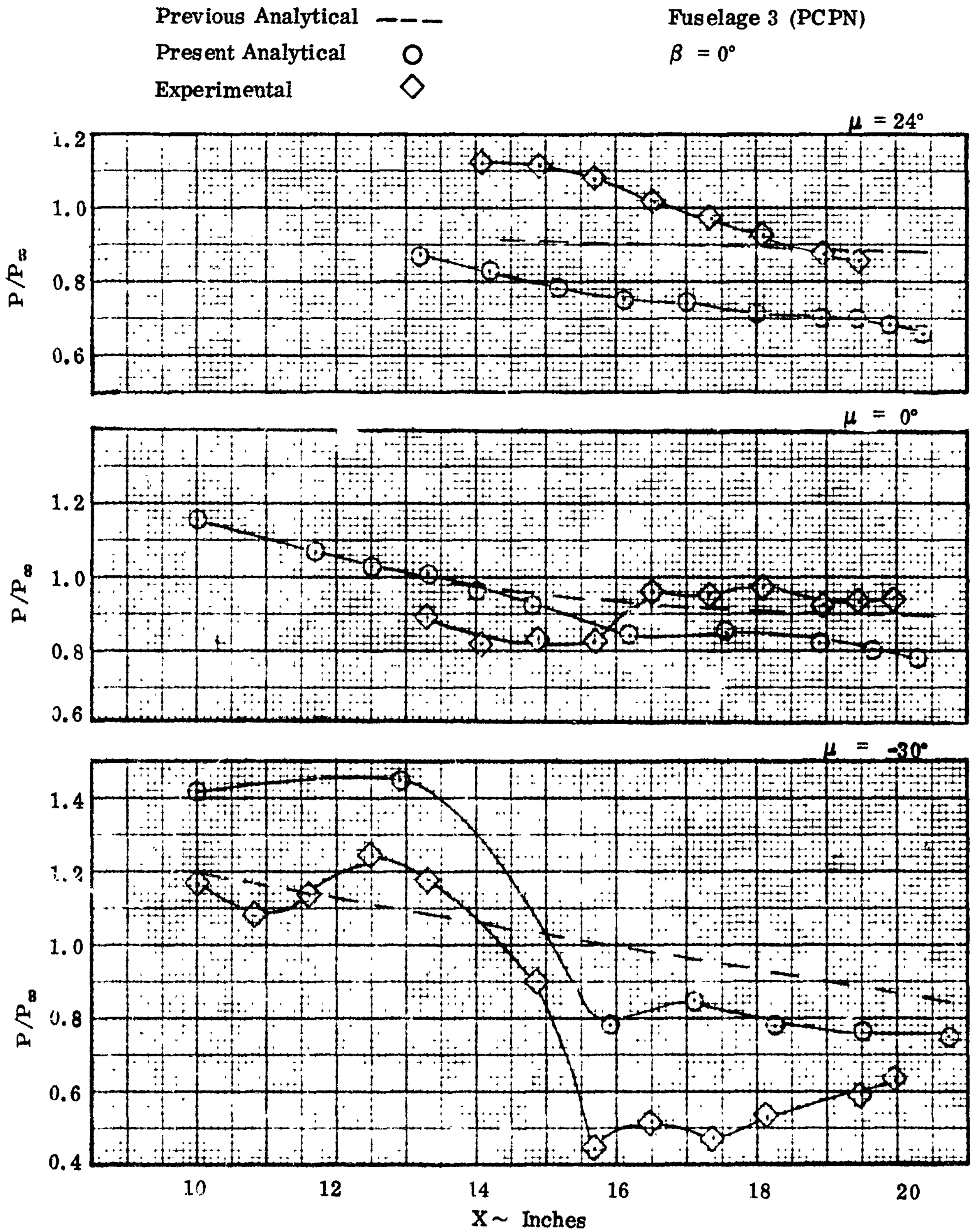

Figure 7-141. Static Pressure Distribution
M = 2.2, α = 15°
Format I

factor can be applied to quantitatively shift the values estimated by the exact method. This adjustment factor is defined as the ratio of the cone surface static pressure, calculated by the basic method, divided by the pressure estimated by the exact method. The local surface pressures calculated along each plane, by the exact method, are then multiplied by the adjustment factor to arrive at the final estimated value.

Although only a limited comparison has been drawn with experiment, the exact reference plane method appears promising as a way to approximate the vehicle induced flow field and continued refinement appears justified (see Figure 7-141).

7.1.5.4 Semi-Empirical Approach

Examination of the experimental data indicated that;

- The pressure distribution over the ogival nose of the fuselage is closely predicted by the method of characteristics solution and those distributions appear to be independent of the downstream fuselage cross-sectional shape.
- The pressure distribution over that section of the fuselage where the cross-sectional area transition from circular (at the radar dish) to the final shape factor, appear to be a function of configuration and angle of attack.

Based upon these observations a flow field estimating technique conforming to the following procedure was evaluated. For a specified flight condition and nose geometry, a method of characteristics calculation is made to solve for the flow field properties surrounding the ogival nose. Using tables based upon the surface pressures obtained during the tests, the anticipated surface pressure downstream of the fuselage transition is obtained, as a function of flight condition, reference plane angularity (μ), and fuselage shape factor. With the surface pressure at the radar dish analytically determined and the downstream surface pressure empirically determined, an effective isentropic contour connecting these two pressures is faired, using simple Prandtl-Meyer relationships. The fictitious contour obtained, for each reference plane, is used to continue the method of characteristics solution downstream of the ogival nose. The resultant flow fields, at the survey plane, were compared with the experimental flow field to determine the effectiveness of this approach. The correlation achieved proved to be strongly dependent upon the contour shape chosen between the nose and the survey station, consequently, an iterative appraoch was required for a solution. An iterative procedure, other than arbitrary, could not be developed and this effort was discontinued.

7.1.5.5 Empirical Approach

This study attempted to establish a causal relationship between the geometry and the flow field composition, as a function of flight condition. The approach was to divide the survey plane into several zones, each of which could be defined in terms of location, extent, and flow properties, as a function of flight condition and geometry. It had been seen, from previous analyses, that the vehicle flow fields tended toward a geometry dictated structure comprised of local zones within which the flow is relatively uniform, and further, that the existence of these zones is essentially independent of the flight condition. The absolute value of the thermodynamic properties and the extent of each zone appeared, however, dependent upon the flight conditions. It was hoped, therefore, that the flow field could be structured as a function of geometry. The absolute values within each zone could then be assigned as a function of flight condition. Having these generalized empirical curves established, a flow field could be "patched" together for any generalized geometry and flight condition.

It was hoped that a rough picture of the flow field could be achieved with the establishment of three (3) or four (4) zones. However, a much finer division of the flow field proved necessary to generalize the flow properites. In view of the fact that the experimental data were available and that the application of this method was rather restricted to configurations approximating those tested, the small gain attributable to generalizing was deemed unwarranted and the effort was discontinued.

7.2 Fuselage Alone (Data Format IV)

7.2.1 General

The format IV model was configured to obtain fuselage flow field data at the postulated aft inlet location (50% ACL). These data were obtained for all seven fuselages employed in the program. The flow field surveys were made alongside the fuselage, under the primary wing (55° sweep). To assess the effect of wing sweep a limited number of surveys were made with a 65° swept wing installed.

An examination of the experimental data indicates that the composition of the flow field is influenced by the individual geometric components (wing and fuselage) as a function of angle of attack. It is also apparent that the wing orientation, with respect to the locally approaching flow, is the dominant factor affecting the flow field. For example, at negative and low vehicle angle of attack the flow field under the wing has experienced either a very weak expansion or compression. With the wing acting as an essentially non working component, the flow field is structured as a function of fuselage lower corner geometry. This results in a zonal arrangement, throughout the survey plane, quite similar to that obtained at the forward survey plane (Format I). The very presence of the wing does tend to induce a dampening force such that those effects shown to occur at the forward survey plane do not appear as dramatically at the aft survey station. The wing physically segregates the flow over the top of the fuselage from that along the side and bottom of the fuselage. In this manner the inherent downwash from the top of the fuselage, due to nose droop and vehicle angle of attack, cannot penetrate and influence the flow field along the side of the fuselage.

With the vehicle angle of attack increased to moderate levels (+5 to +15°) the wing becomes a working component. At subsonic and transonic Mach numbers the wing under surface forces the local streamlines toward alignment with its contour. The degree of alignment of course, varies inversely with distance from the wing surface. Within the angle of attack range this physically constrained inviscid layer is virtually insensitive to the potential aerodynamic/geometric effects due to the fuselage corner and the vehicle angle of attack and, in fact, appears to impose an overpressure that cancels out these effects. The result is that the flow field zonal structure, seen to be strongly related to fuselage corner geometry at the forward survey station, does not develop and the flow fields for all fuselages appear quite similar. At supersonic Mach numbers the locally approaching flow is aligned with the wing underside contour through the leading edge shock wave. The entire inviscid shock layer is rather uniform with an abrupt discontinuity occurring across the wave. In general, then, the wing dictates flow field composition in this angle of attack range.

For high vehicle angle of attack the flow field is influenced by both the wing and the fuselage corner. The wing is performing more, though perhaps less efficient, work on the flow thereby producing a strong over pressure region under the wing. The potential upwash, inherent at these high angles of attack because of the large peripheral pressure gradient, becomes formidible and does influence the flow field alongside the fuselage, as a function of corner geometry. For example, a small rapidly developed fuselage corner configuration tends to segregate the flow along the side of the fuselage from that along the bottom of the fuselage. Consequently the wing induced over pressure extends over a narrow inboard portion of the flow field down to a point near the vertical tangency point of the corner. This corner geometry results in a rapid flow expansion which penetrates the lower portion of the flow field alongside the fuselage in the form of a relatively small region of high angularity. An increase in corner radius and/or a decrease in the local rate of corner development both tend to distribute the upwash gradient more gradually. This results in a larger zone of influence and a lower local flow angularity. The end point is, of course, a large gradually developed corner radius which induces a large uniform region of relatively low angularity across the lower portion of the flow field.

During the analyses of Format I it was seen that local angularity varied significantly as a function of free stream Mach number, angle of attack, and fuselage corner geometry. In addition, it will subsequently be shown that variations in inlet performance (Format II) due to integration with different fuselages can, in most cases, be logically explained in terms of these variations. As opposed to this, the parameter of sidewash angle was seen to be a parameter insensitive to both geometry and test condition and generally had little effect upon inlet performance. In the same vein a discernable impact of local Mach number variation, upon inlet performance, could not be established.

In examining the under wing flow fields (Format IV) and their influence upon inlet performance (Format III) an effect attributable to local Mach number variation is again not obvious. The presence of the wing restricts variations in local flow angularity that tends to eliminate geometry dependant local zones. As a result the influence of flow angularity, upon inlet performance, is diminished in importance. On the other hand, the variation in sidewash angle is now extremely large, primarily as a function of angle of attack and secondarily as a function of Mach number and fuselage geometry. The quantitative change in the average sidewash vector, for an angle of attack excursion between -3° and +25°, varies from slightly positive to a negative value approximating 10° to 15°. The variation of sidewash is due to the "channeling" of the flow in this region. Both the wing undersurface and the fuselage sidewall physically constrain the flow. The pressure gradient, from the bottom of the fuselage provides an aerodynamic constraint upon the flow. Consequently as the static pressure level in this three sided channel increases, a favorable lateral gradient is established and an outflow vector (negative sidewash) results. The magnitude of the sidewash vector varies directly with this lateral gradient and since both the wing induced flow field and the fuselage upwash gradient increase in intensity, as angle of attack is increased, the magnitude of the negative sidewash increases with angle of attack.

Presented in following sections is a discussion of the test results.

7.2.2 Fuselage Effects

7.2.2.1 Mach Number 0.8

For this Mach number the flow angularity is seen to be wing dominated with three horizontal zones comprising the flow field. Near the wing the flow generally follows the wing contour. As the vertical distance from the wing increases the angularity deviates such that two additional zones are established each with a progressively lower angularity. An examination of the data reveals a large variation in sidewash occurs, as a function of angle of attack. Also noted is the fact that the flow field composition and the quantitative levels of sidewash are quite similar for all fuselage configurations. The local flow angularity and sidewash for a small fuselage corner radius configuration (fuselage 1) and a large corner radius configuration (fuselage 4) are presented for angles of attack of 0°, +10°, and +20° in Figures 7-142 through 7-147 and 7-148 through 7-153 respectively.

7.2.2.2 Mach Number 1.3

At this Mach number the flow field angularity appears quite similar to that obtained at Mach 0.8 with the field comprised of two or three horizontal zones. The sidewash also appears similar to Mach 0.8. Both the qualitative composition and the average quantitative level of sidewash are similar from fuselage to fuselage. This similarity is seen by comparing the flowfield angularity and sidewash characteristics of fuselage 4 at angles of attack of 0°, +10°, and +20°, presented in Figures 7-154 through 7-159, with the corresponding Mach 0.8 flow field characteristics presented in Figures 7-148 through 7-153. The lone configuration not conforming to the general pattern is fuselage 3, at high angle of attack. For this small rapidly developed fuselage corner the peripheral pressure gradient induces a significant upwash zone over the inboard portion of the survey plane that penetrates up to the area near the wing undersurface. Consequently the local and average flow angularity differs from the general case. Digression of the fuselage 3 flow field angularity from the general case, as angle of attack is increased from 0° to 10° and +20° is displayed in Figures 7-160 through 7-162.

7.2.2.3 Mach Number 1.8

At this Mach number the flow field angularity assumes a classical angle of attack dependent pattern. The fields induced by all fuselages appear quite similar except at the high angle of attack conditions where the fuselage corner geometry effects, noted previously for fuselage 3 at Mach number 1.3, are again evident. The influence of these effects has increased due to the higher Mach number. For the low and intermediate angle of attack range ($\alpha \leq +15°$) the flow field sidewash characteristics of all fuselages are very similar in terms of the zonal arrangement and average sidewash value. At the high angle of attack ($\alpha = +20°$) the flow field sidewash is partially influenced by the fuselage corner geometry, as seen at previously discussed Mach numbers. Typical flow angularity and sidewash characteristics are presented at angles of attack of 0°, +10°, and +20°, for a small corner configuration (fuselage 1) in Figures 7-163 through 7-168 and for a large corner configuration (fuselage 4) in Figures 7-169 through 7-174. To illustrate the difference in flow field characteristics

Fuselage 1
PCPN
Mach Number = 0.8
$\alpha = 0°$
Format IV

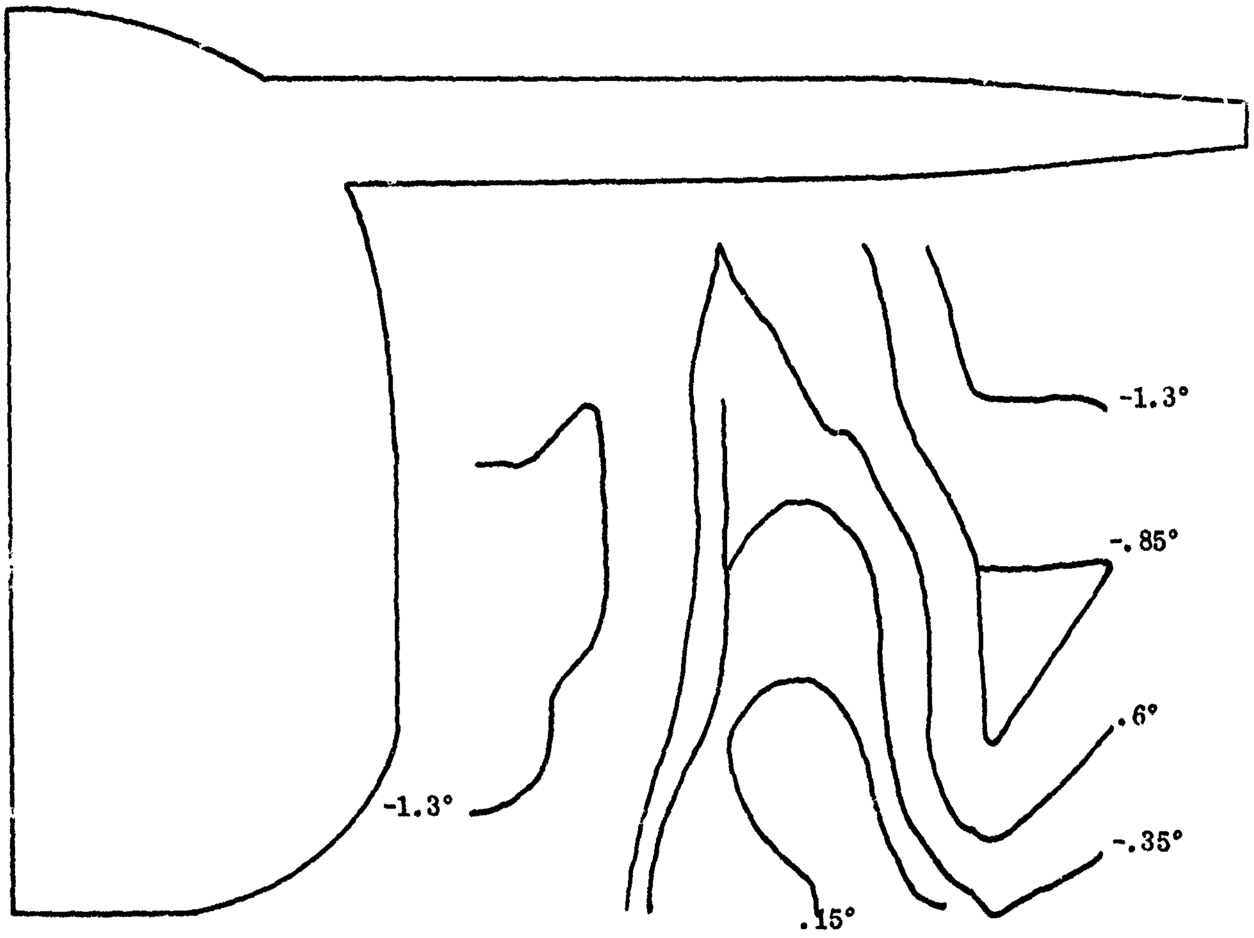

Figure 7-142. Local Flow Angularity

Fuselage 1
PCPN
Mach Number = 0.8
α = 10°
Format IV

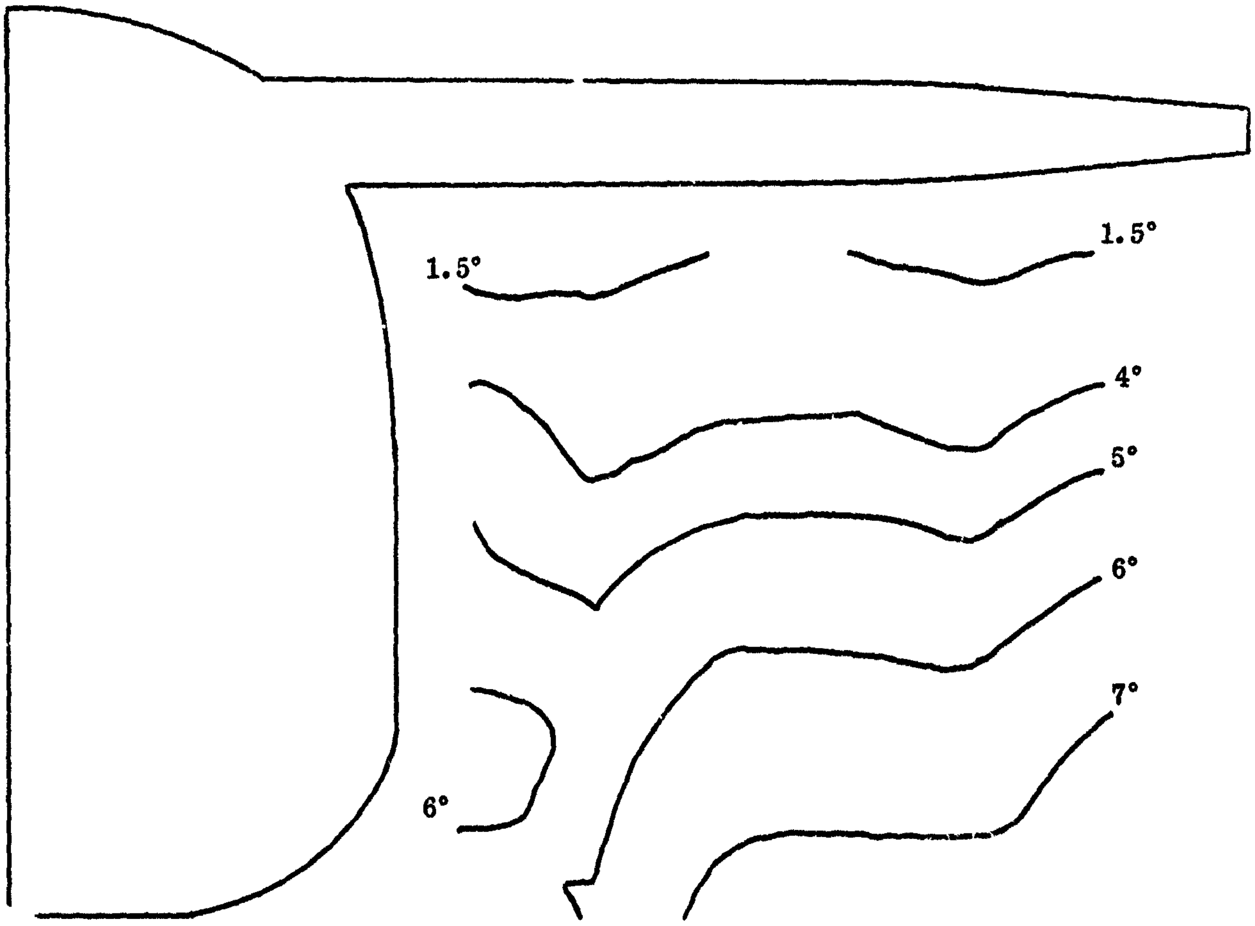

Figure 7-143. Local Flow Angularity

Fuselage 1
PCPN
Mach Number = 0.8
α = 19°
Format IV

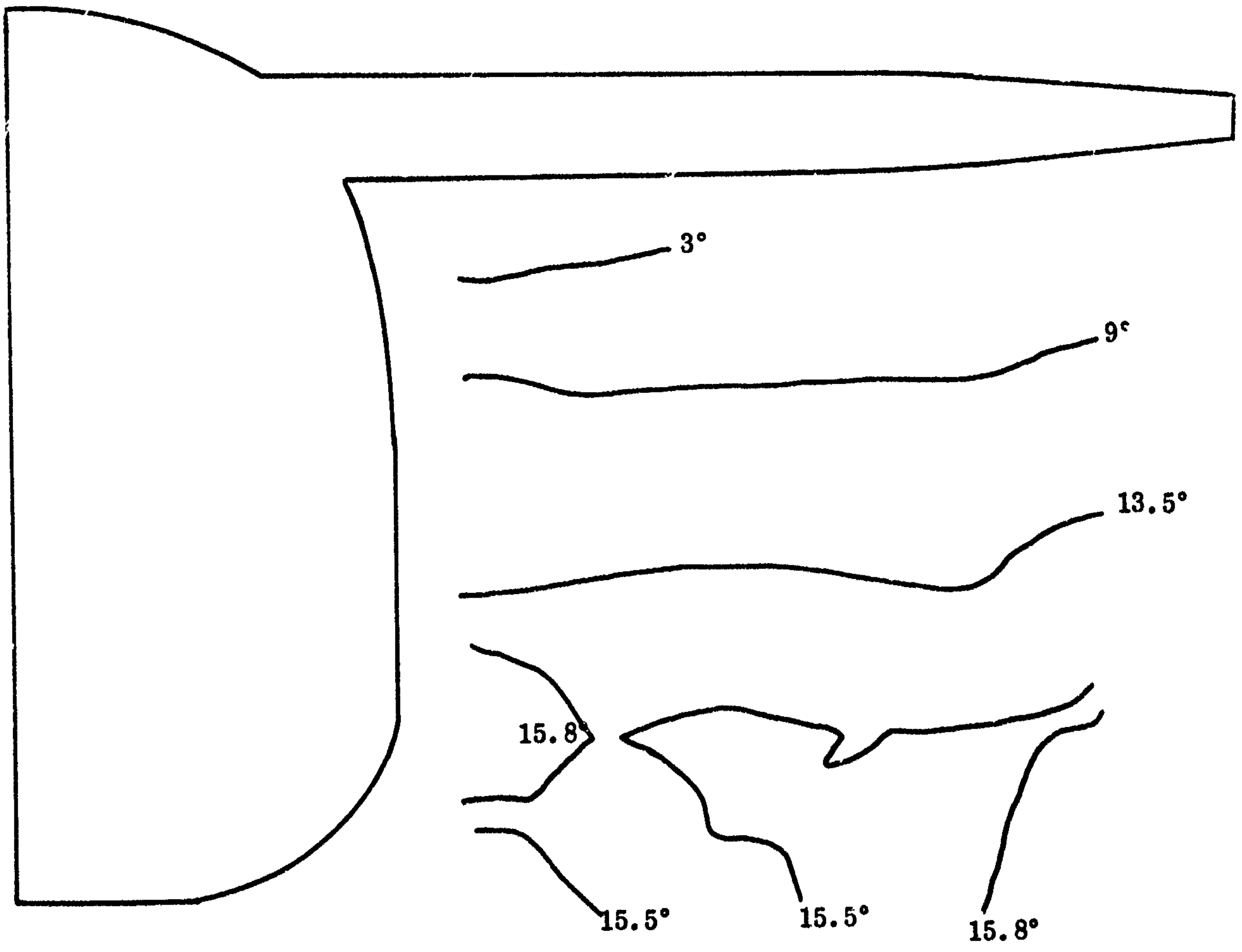

Figure 7-144. Local Flow Angularity

Fuselage 1
PCPN
Mach Number = 0.8
$\alpha = 0°$
Format IV

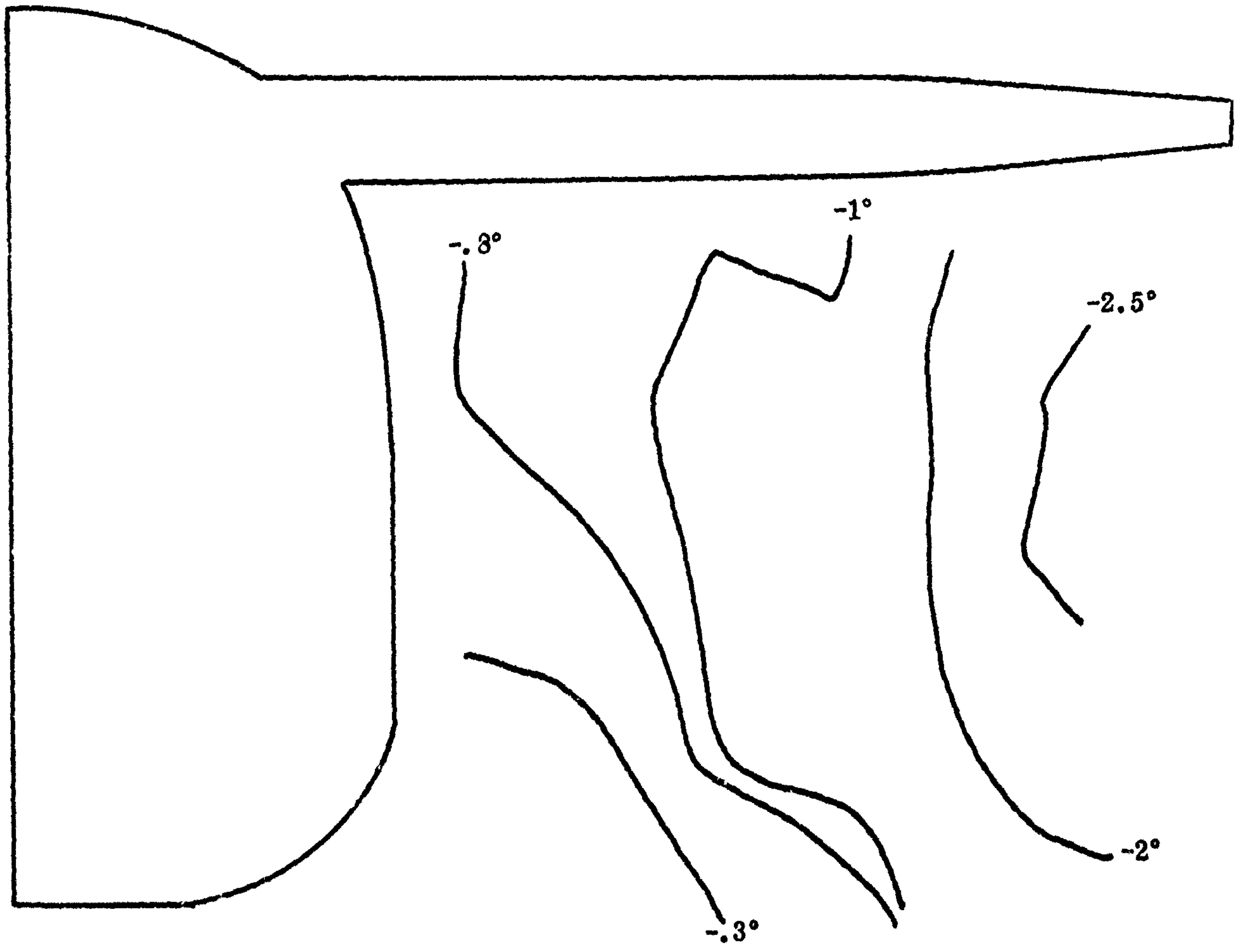

Figure 7-145. Sidewash Angle

Fuselage 1
PCPN
Mach Number = 0.8
$\alpha = 10°$
Format IV

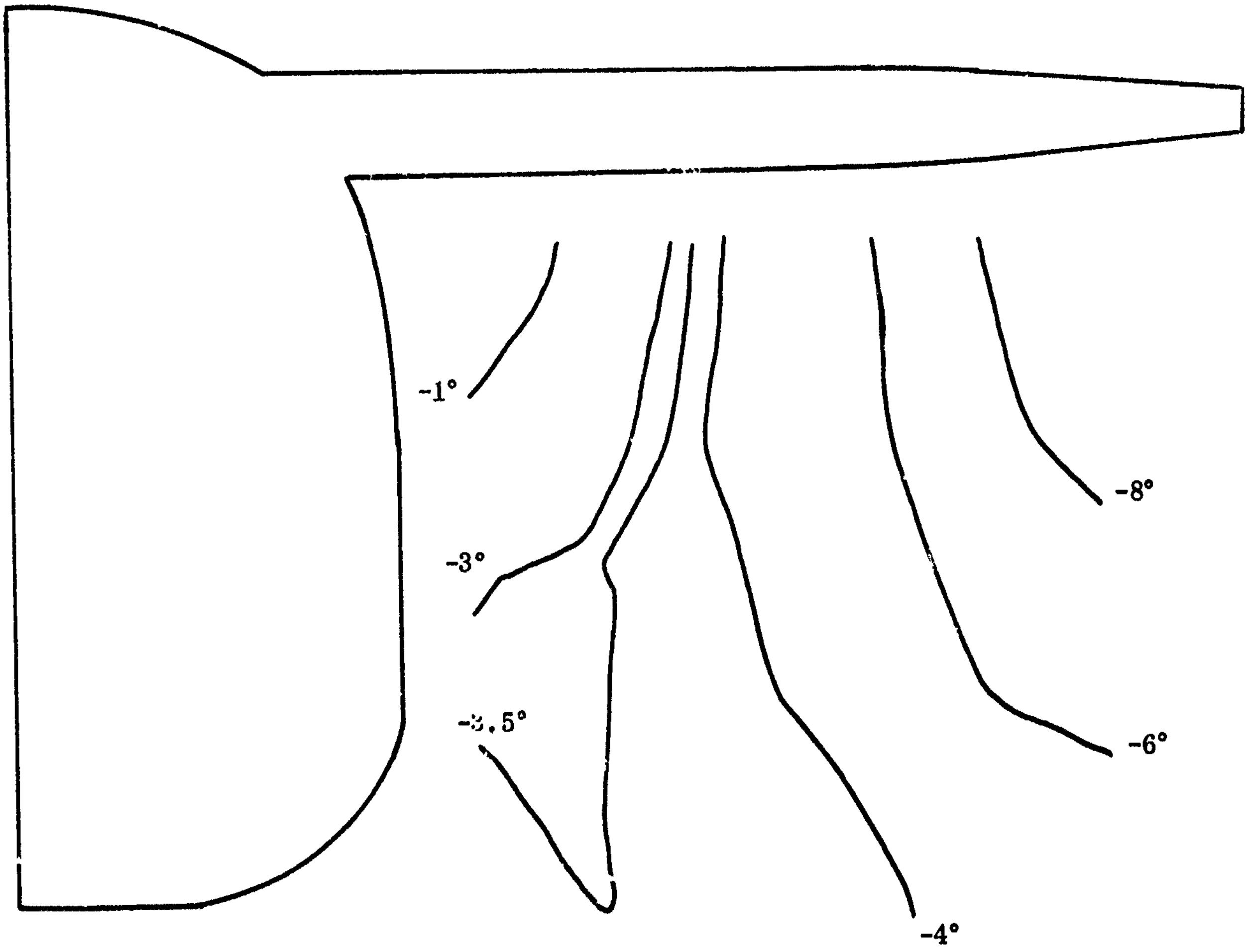

Fuselage 7-146. Sidewash Angle

Fuselage 1
PCPN
Mach Number = 0.8
$\alpha = 19°$
Format IV

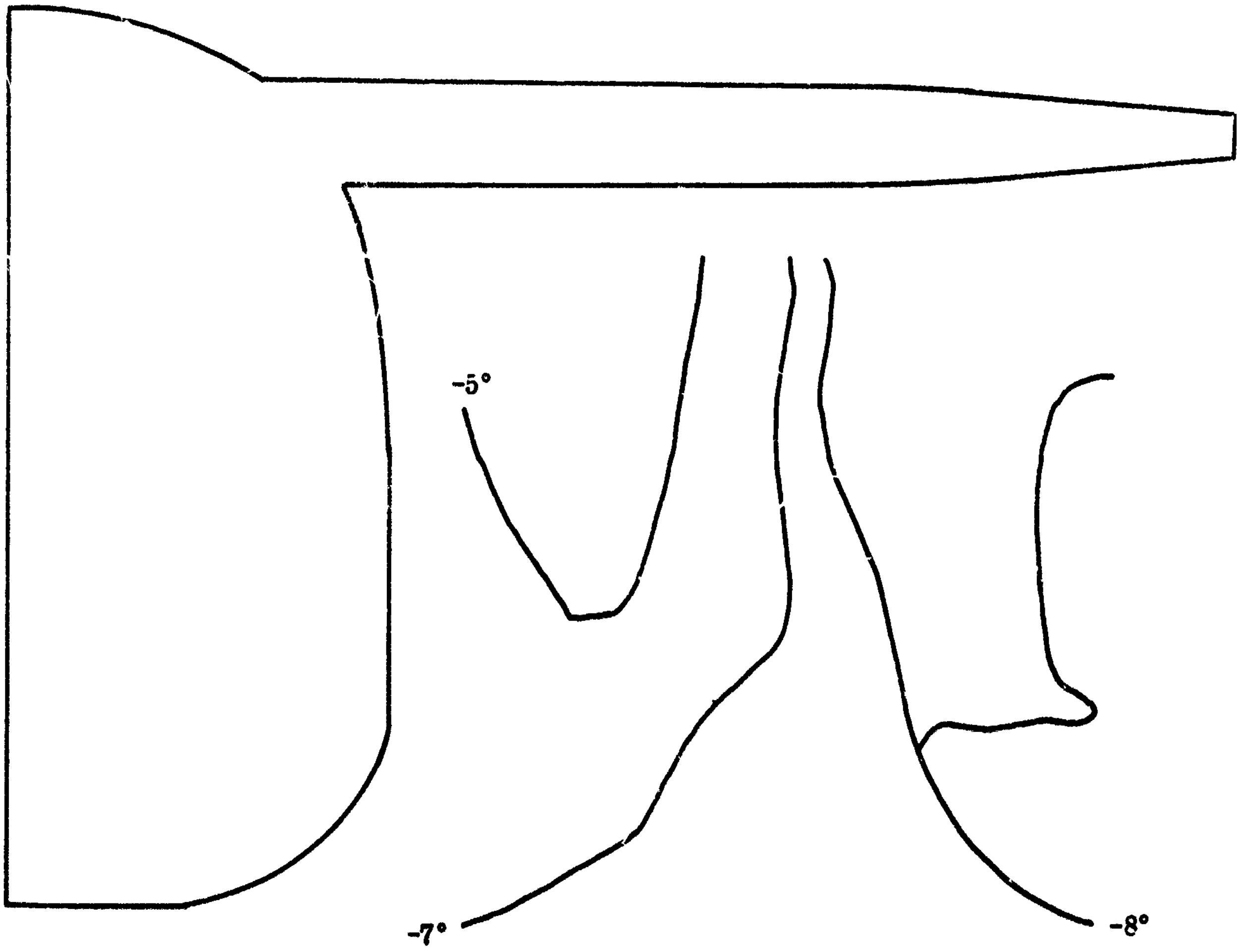

Figure 7-147. Sidewash Angle

Fuselage 4
PCPN
Mach Number = 0.8
α = 0°
Format IV

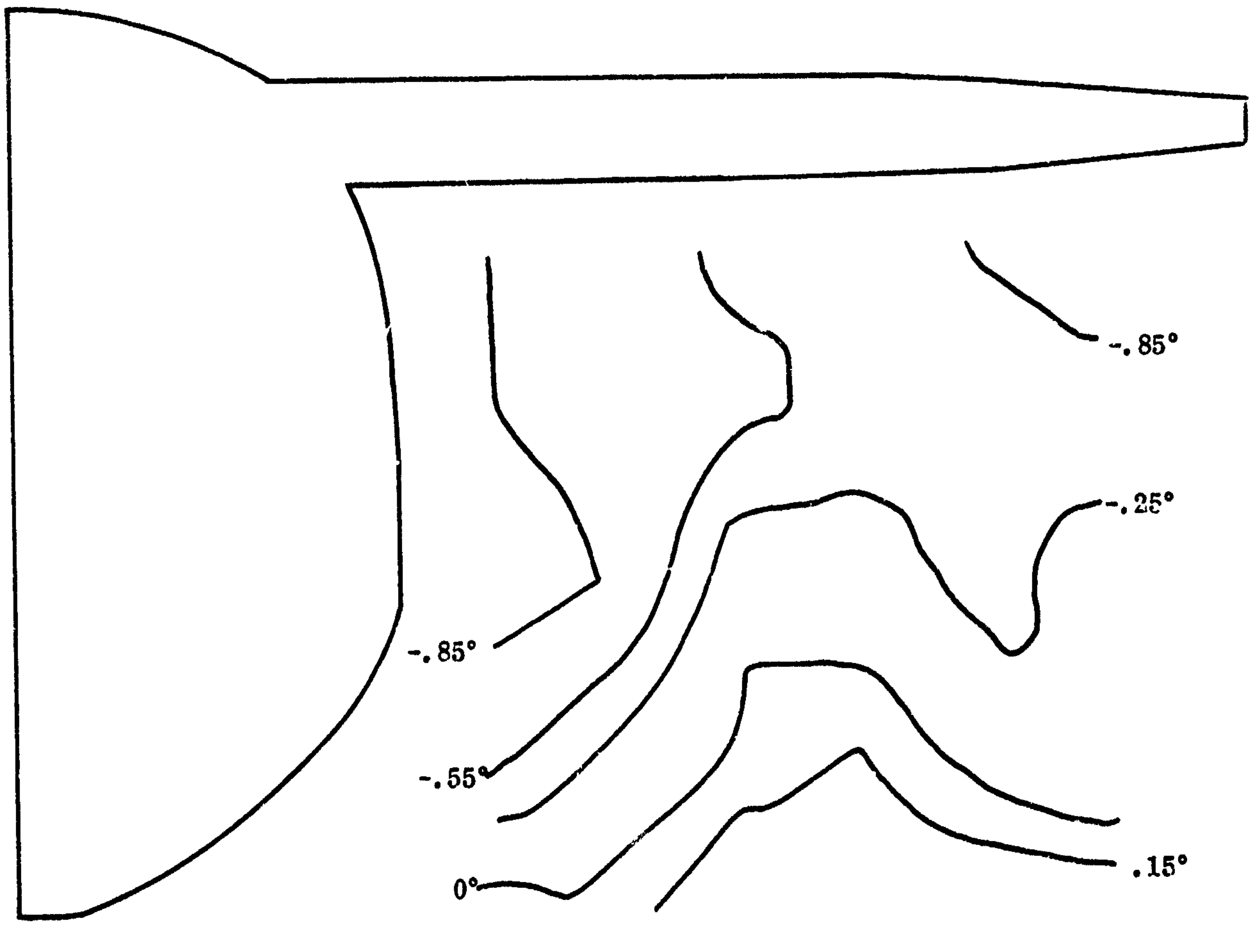

Figure 7-148. Local Flow Angularity

Fuselage 4
PCPN
Mach Number = 0.8
$\alpha = 10°$
Format IV

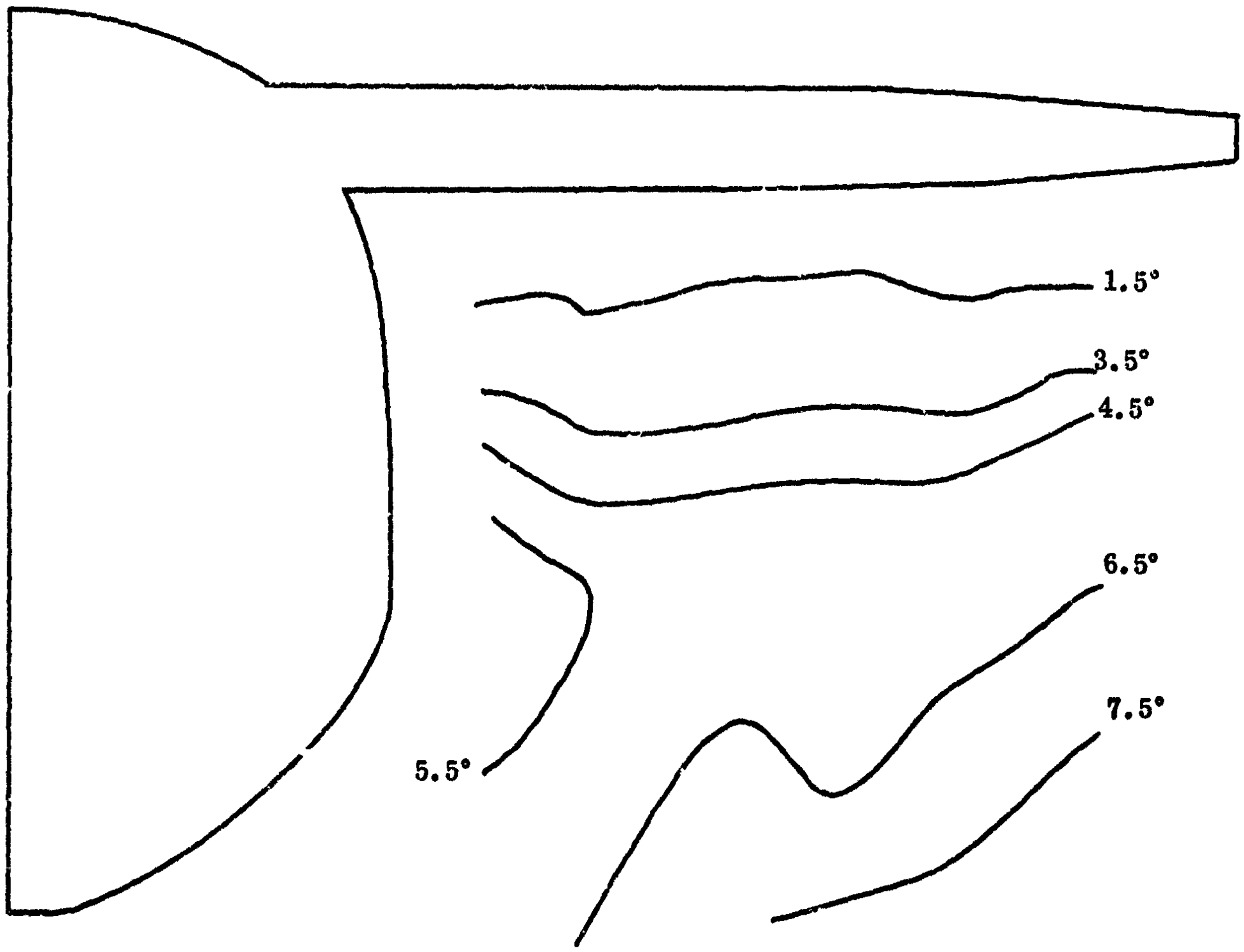

Figure 7-149. Local Flow Angularity

Fuselage 4
PCPN
Mach Number = 0.8
α = 20°

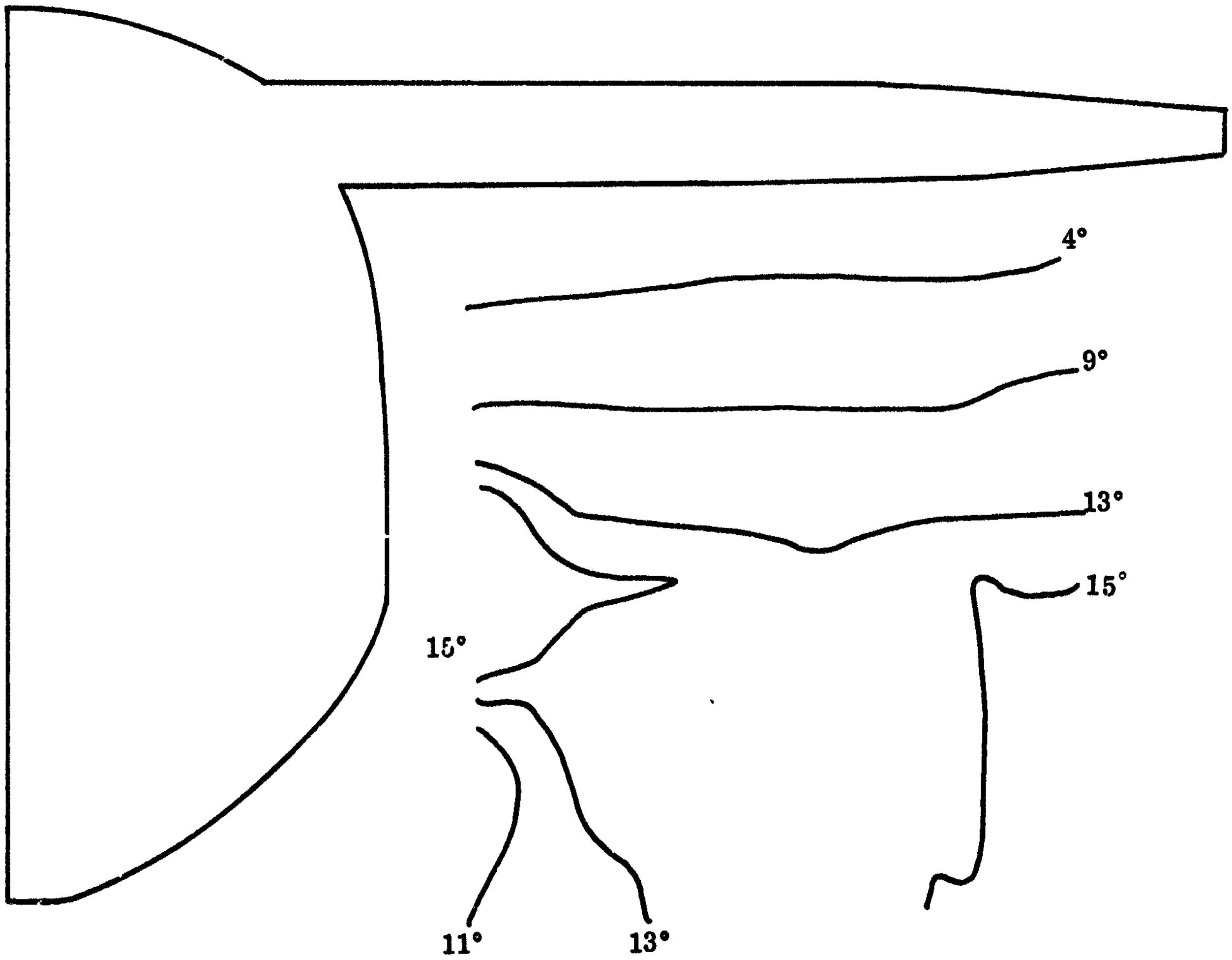

Figure 7-150. Local Flow Angularity

Fuselage 4
PCPN
Mach Number = 0.8
α = 0°
Format IV

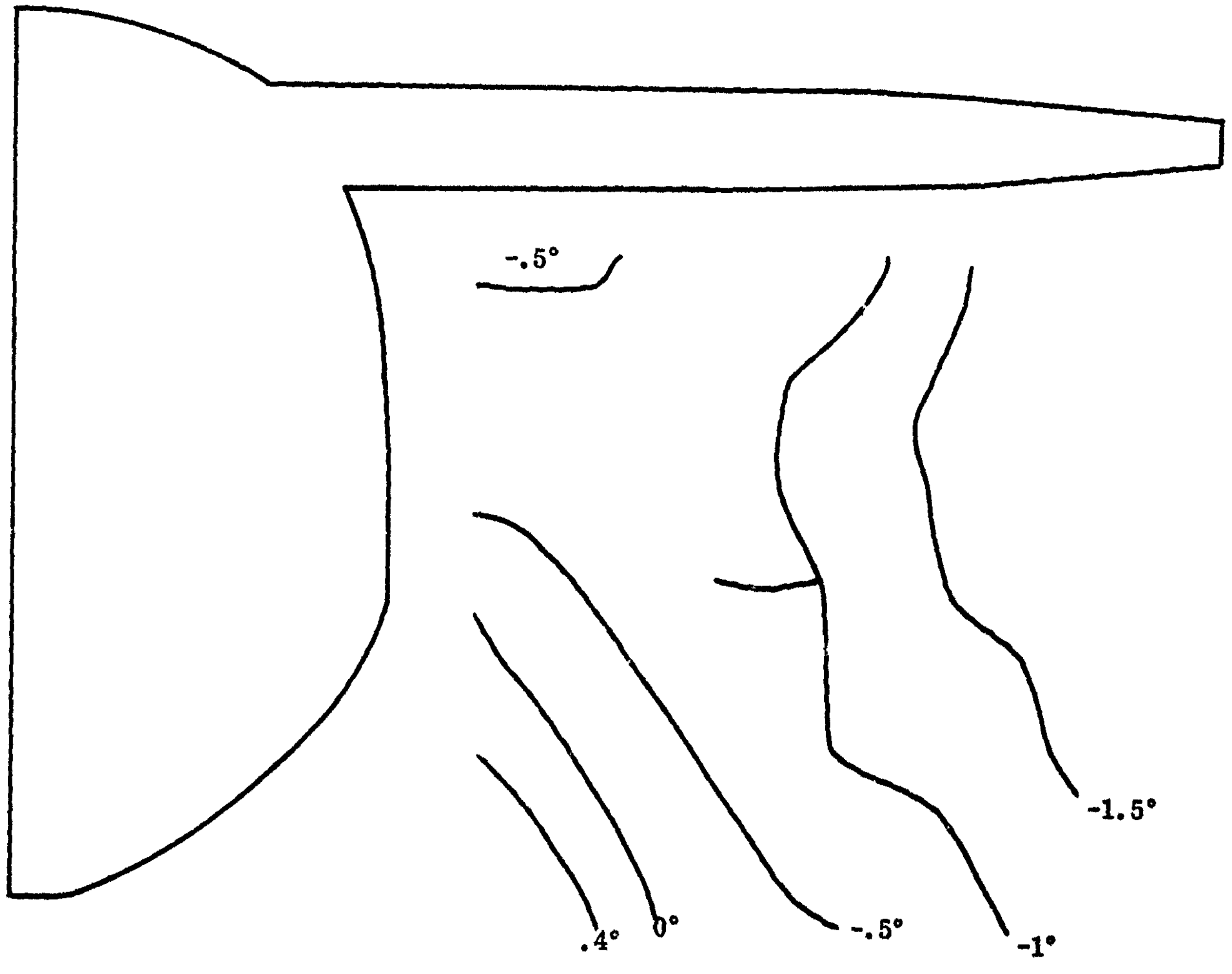

Figure 7-151. Sidewash Angle

Fuselage 4
PCPN
Mach Number = 0.8
α = 10°
Format IV

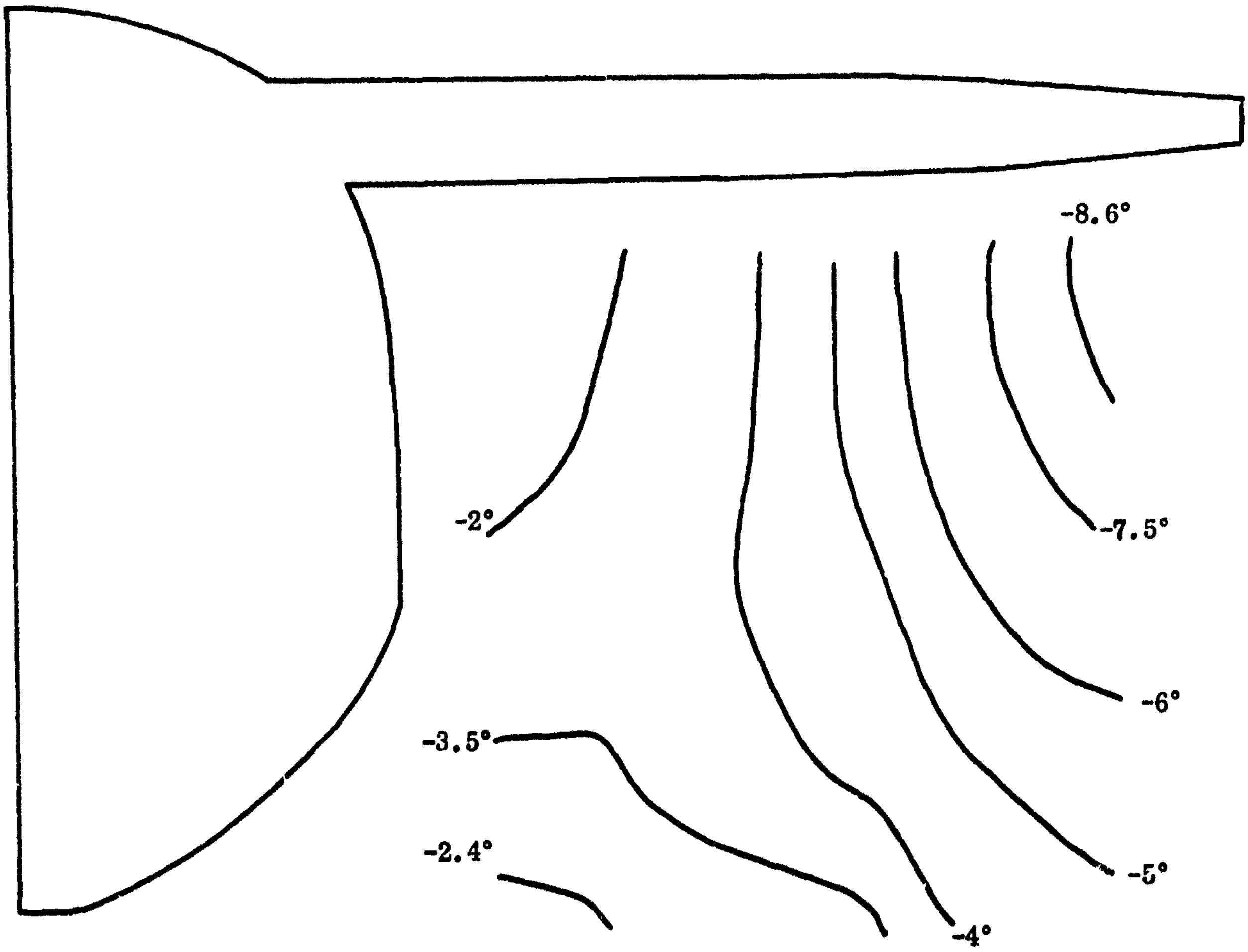

Figure 7-152. Sidewash Angle

Fuselage 4
PCPN
Mach Number = 0.8
$\alpha = 20°$
Format IV

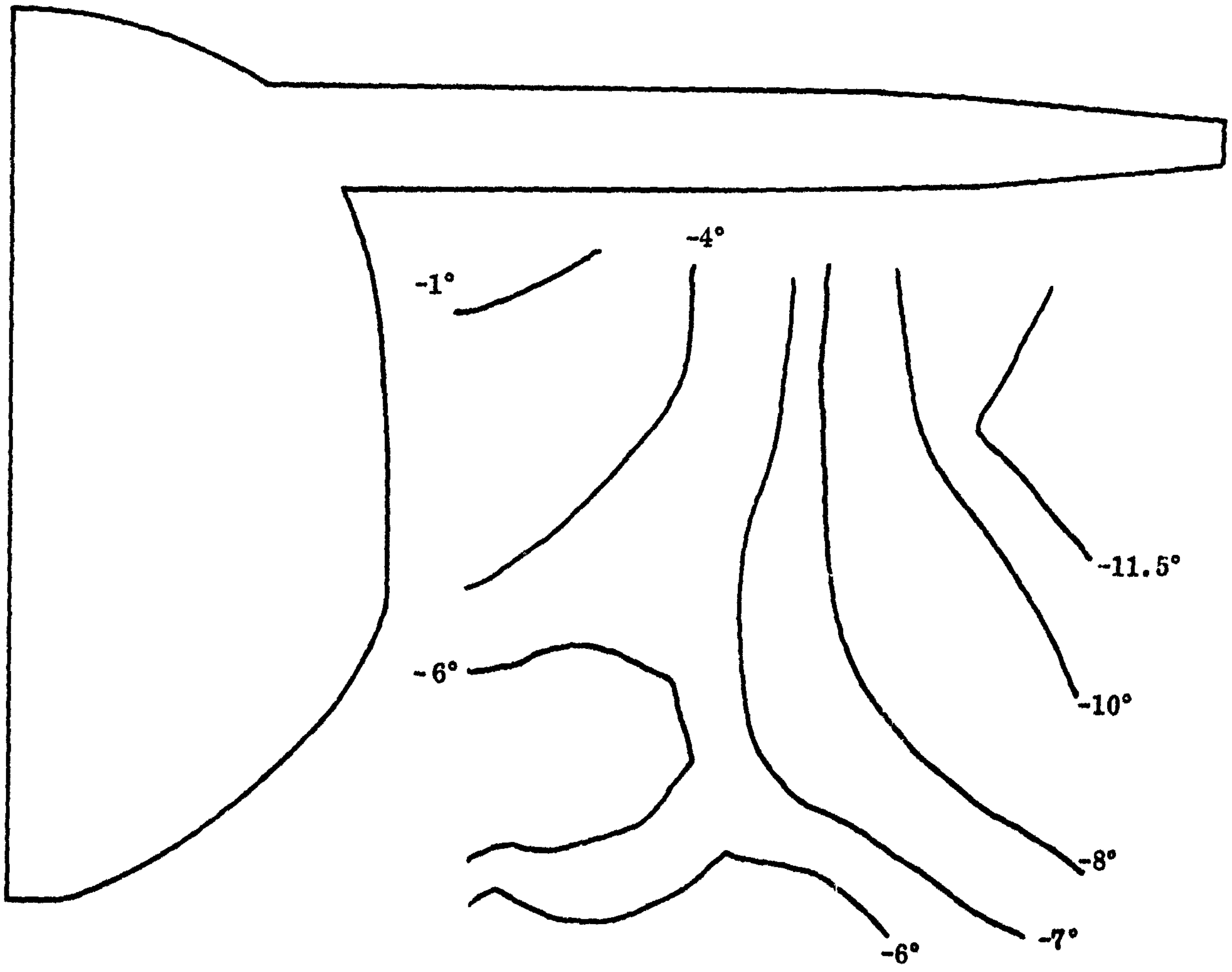

Figure 7-153. Sidewash Angle

Fuselage 4
PCPN
Mach Number = 1.3
α = 0°
Format IV

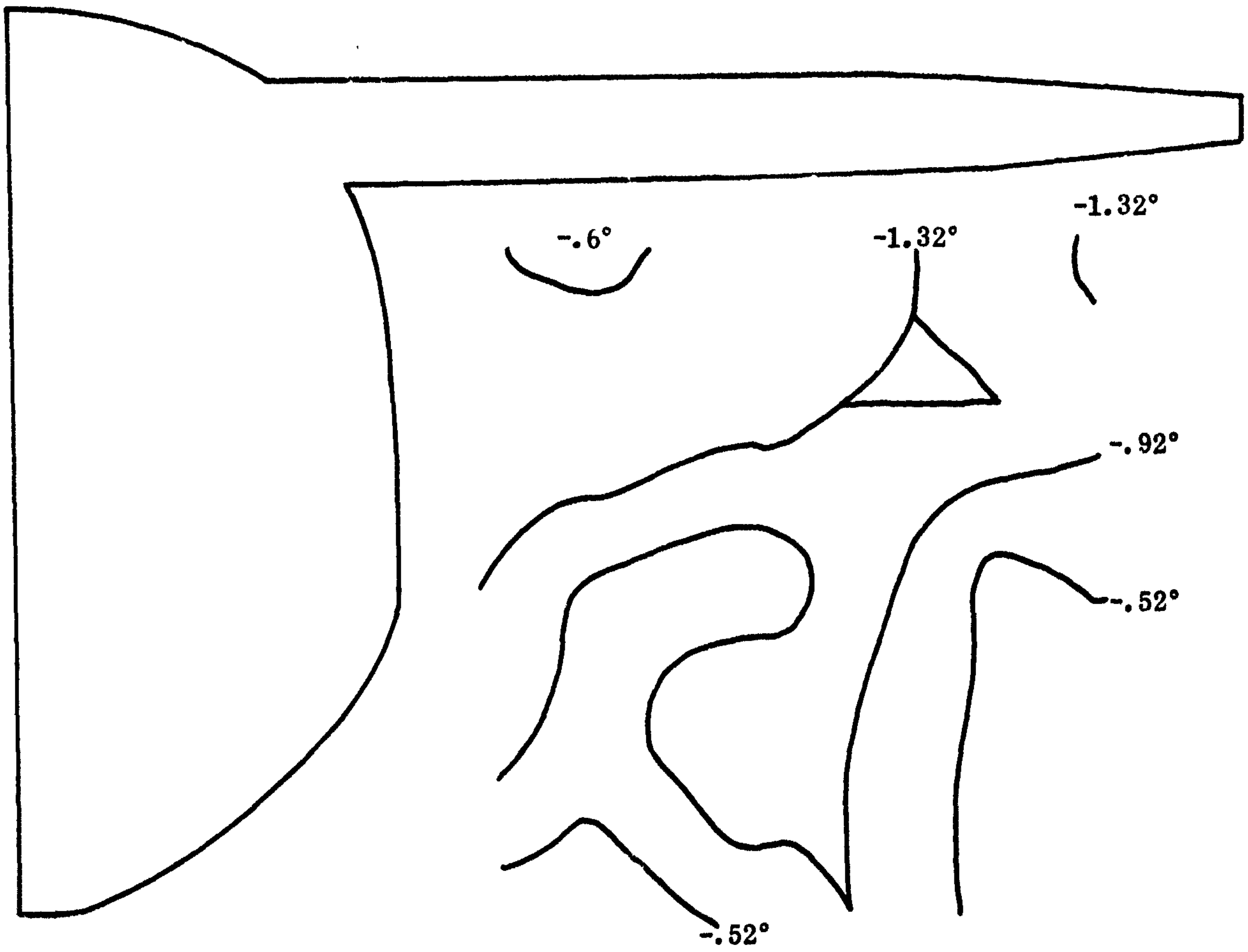

Figure 7-154. Local Flow Angularity

Fuselage 4
PCPN
Mach Number = 1.3
α = 10°
Format IV

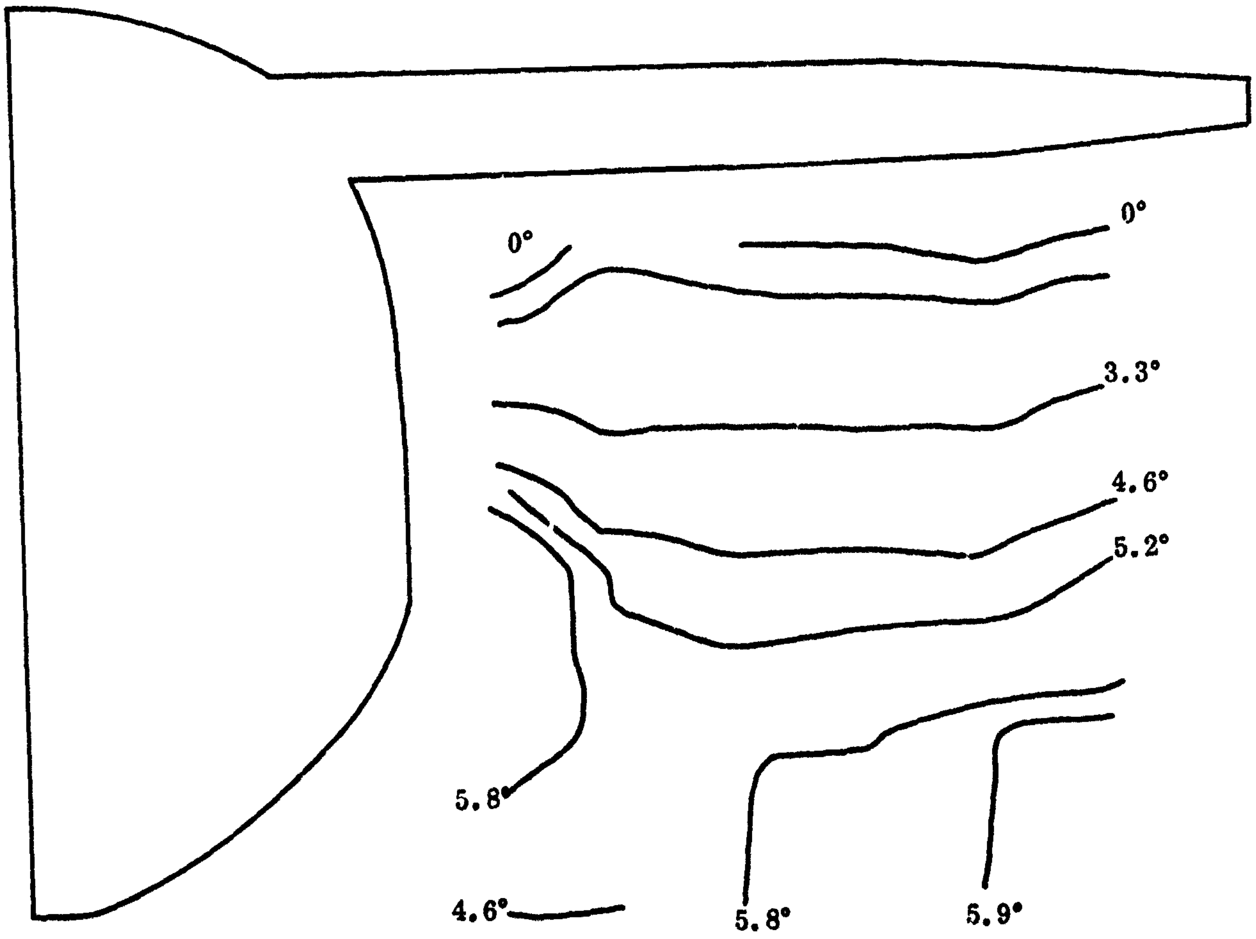

Figure 7-155. Local Flow Angularity

Fuselage 4
PCPN
Mach Number = 1.3
α = 20°
Format IV

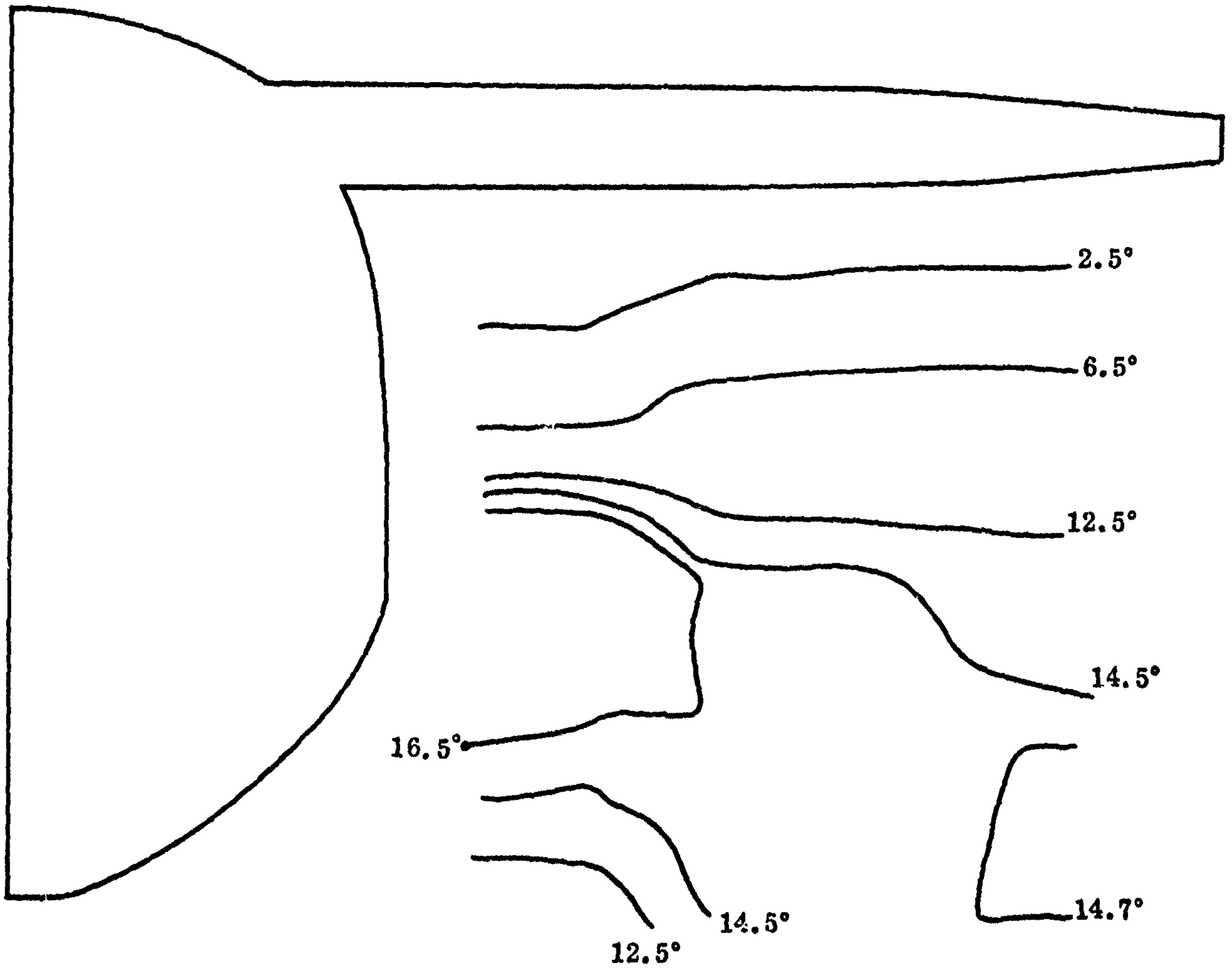
2.5°
6.5°
12.5°
14.5°
16.5°
14.5°
12.5°
14.7°

Figure 7-156. Local Flow Angularity

Fuselage 4
PCPN
Mach Number = 1.3
$\alpha = 0°$
Format IV

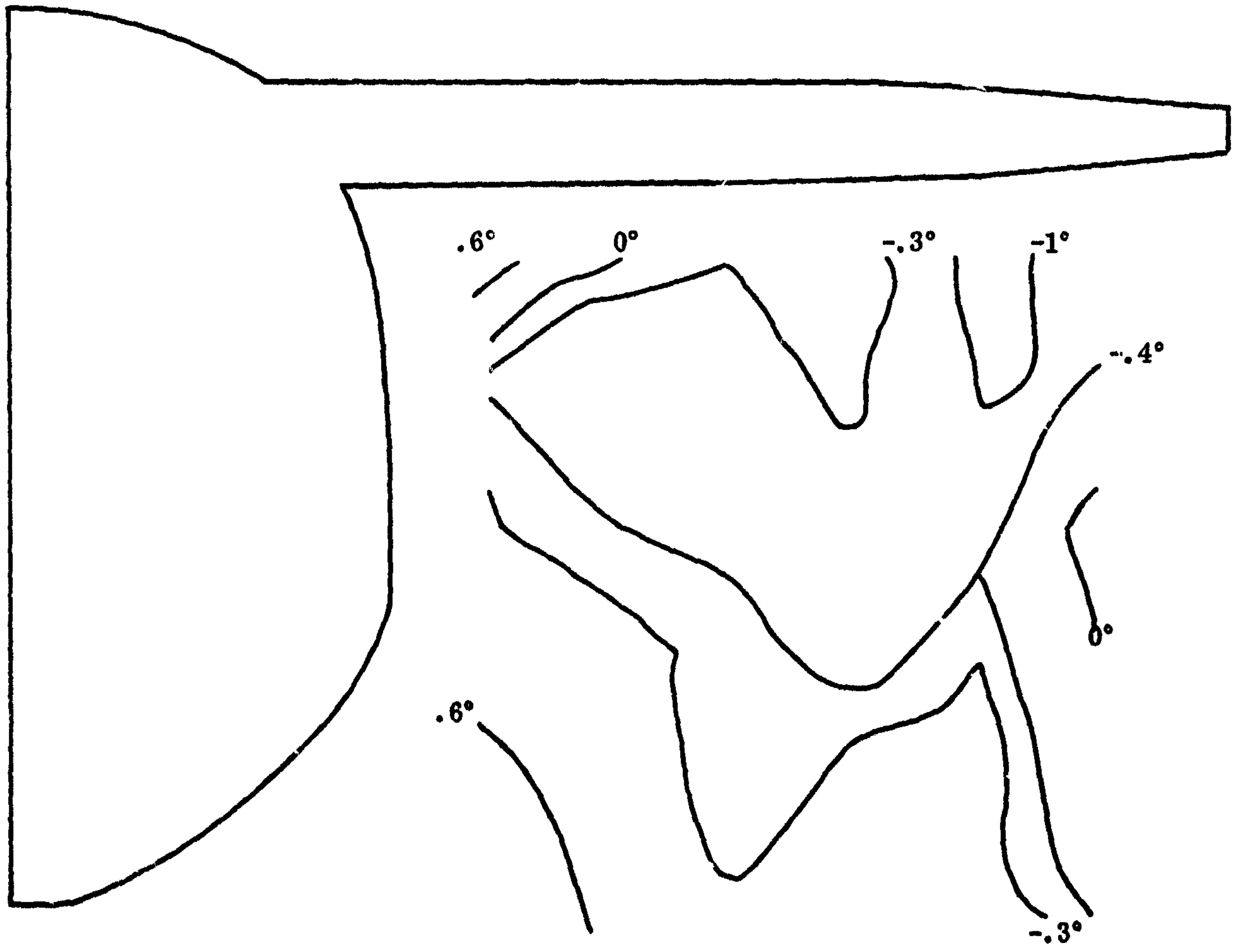

Figure 7-157. Sidewash Angle

Fuselage 4
PCPN
Mach Number = 1.3
α = 10°
Format IV

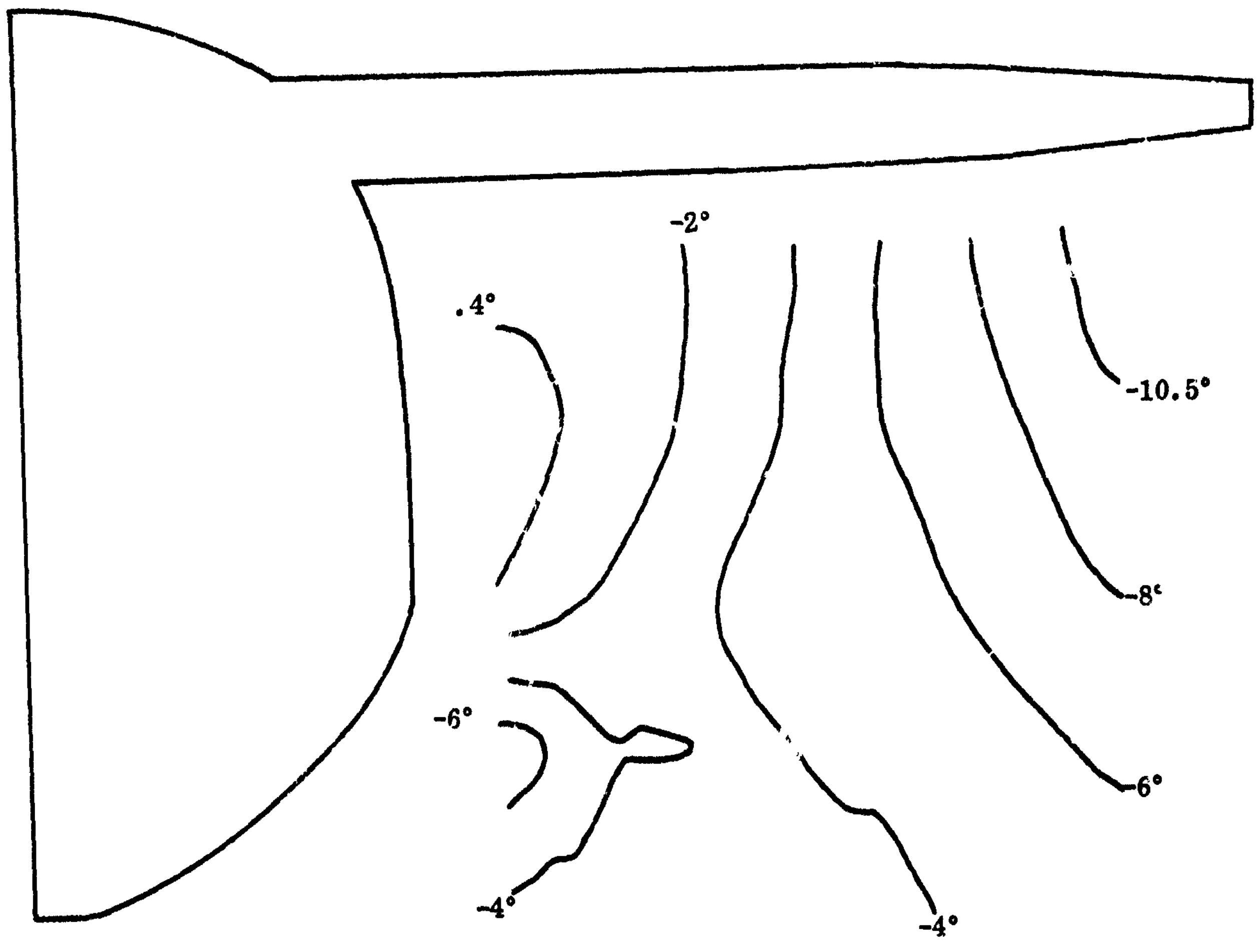

Figure 7-158. Sidewash Angle

Fuselage 4
PCPN
Mach Number = 1.3
α = 20°
Format IV

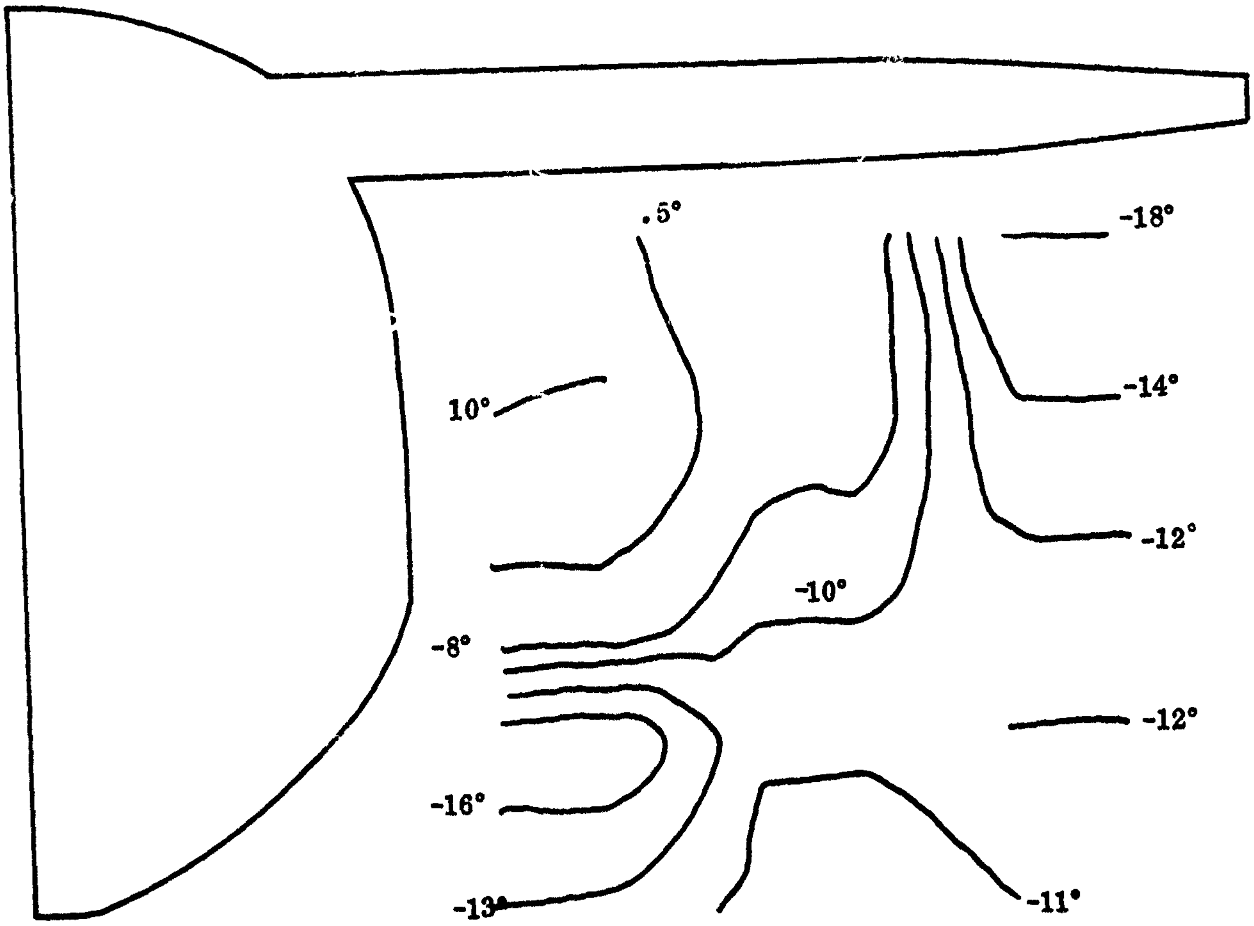

Figure 7-159. Sidewash Angle

Fuselage 3
PCPN
Mach Number = 1 3
α = 0°
Format IV

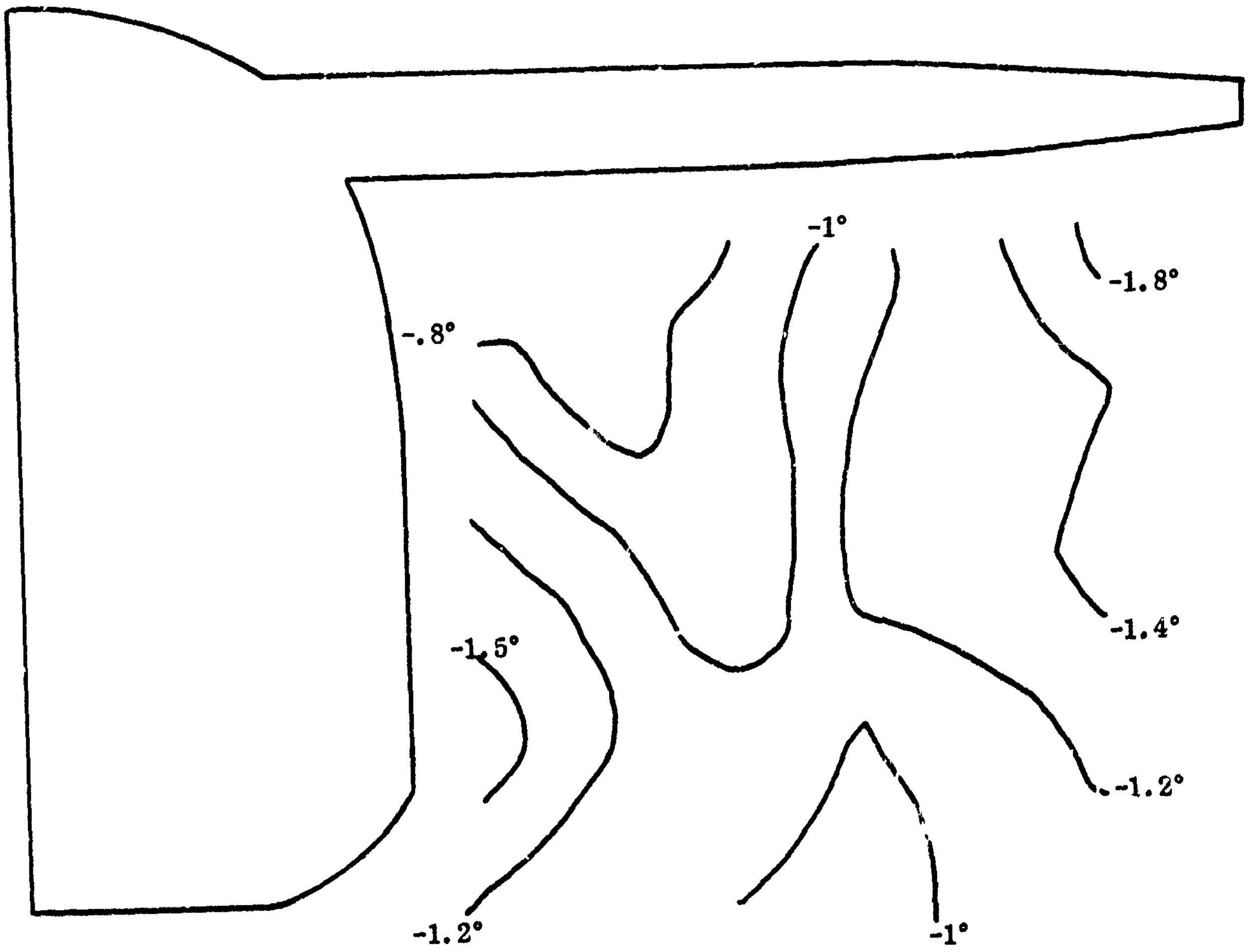

Figure 7-160. Local Flow Angularity

Fuselage 3
PCPN
Mach Number = 1.3
α = 10°
Format IV

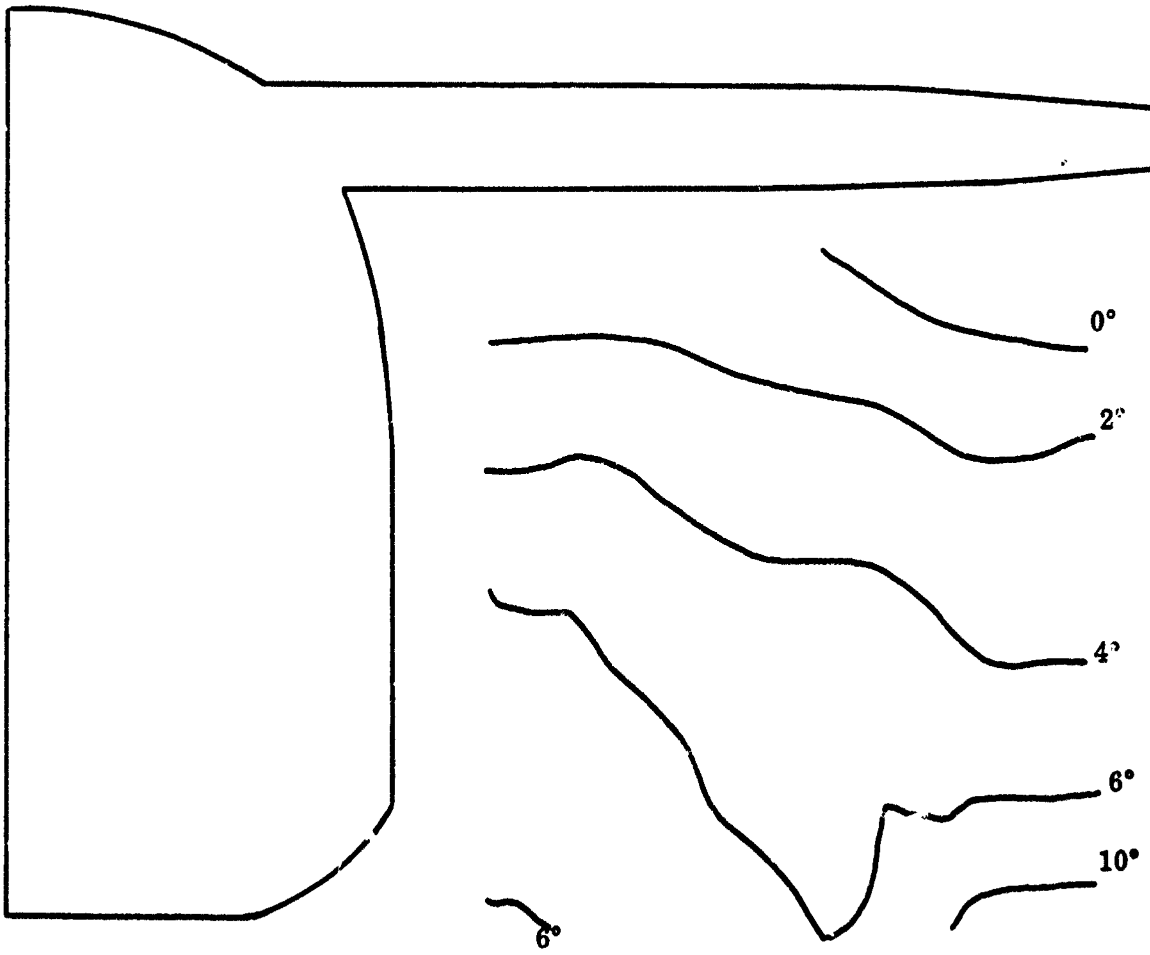

Figure 7-161. Local Flow Angularity

Fuselage 3
PCPN
Mach Number = 1. 3
α = 20°
Format IV

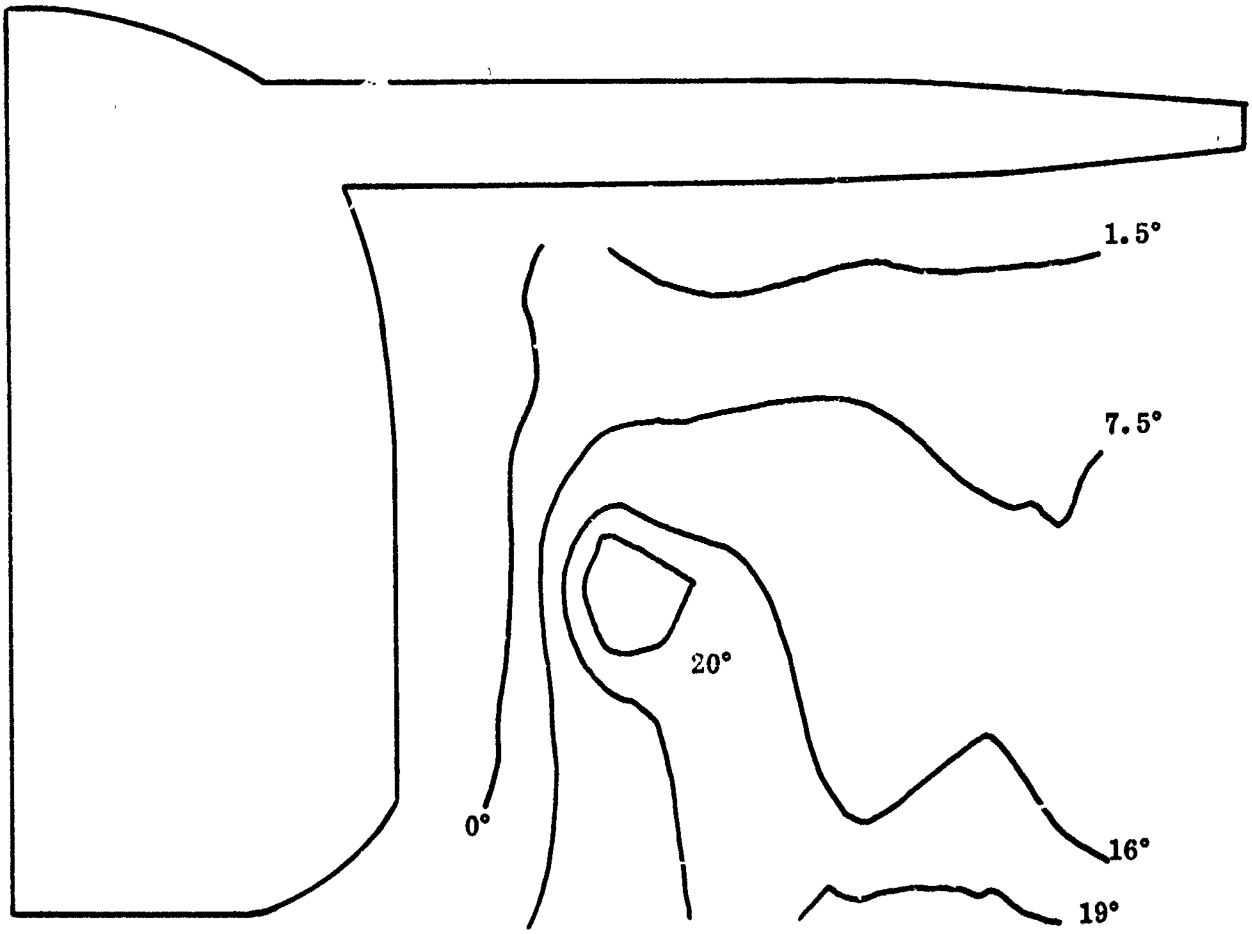

Figure 7-162. Local Flow Angularity

Fuselage 1
PCPN
Mach Number = 1.8
$\alpha = 0°$
Format IV

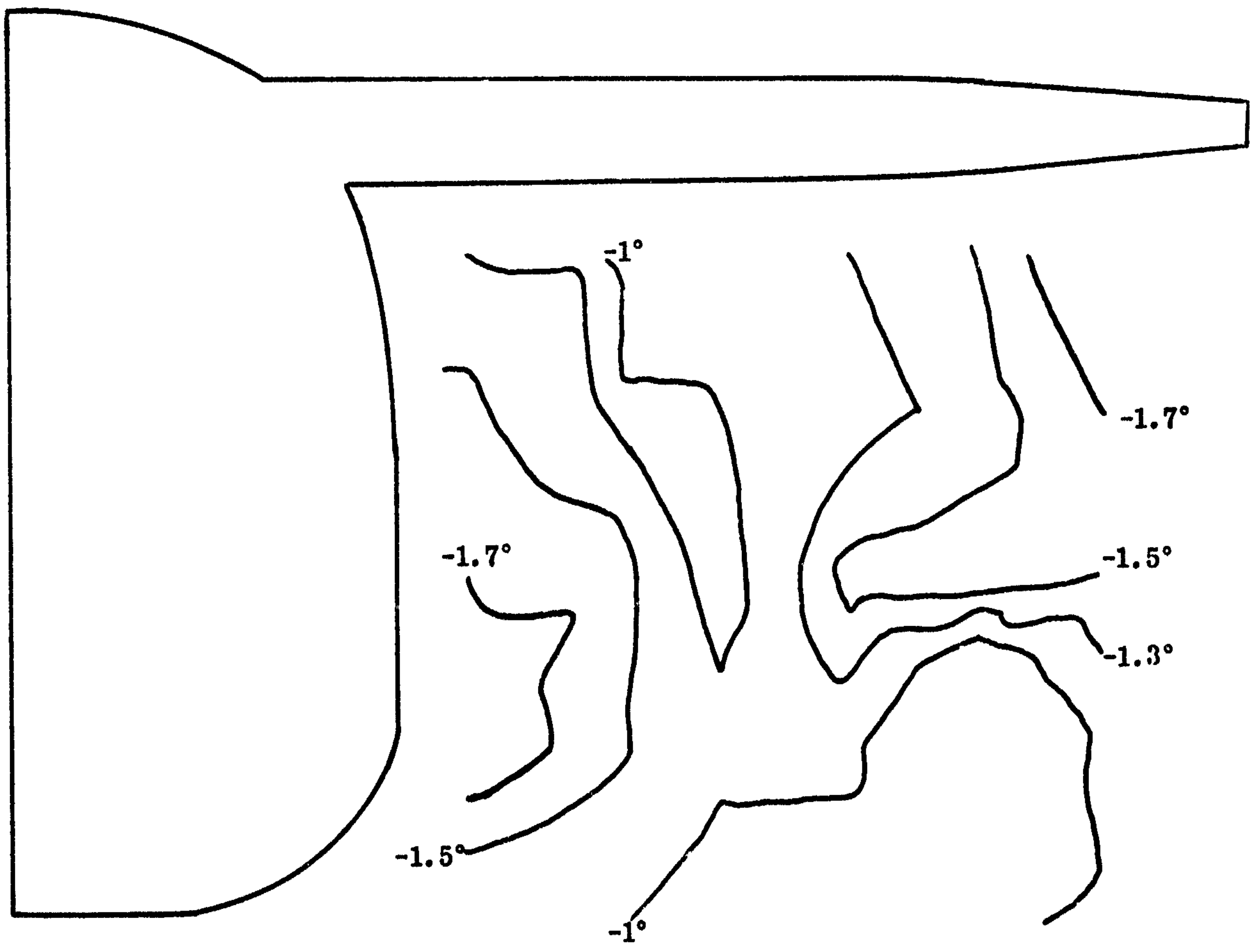

Figure 7-163. Local Flow Angularity

Fuselage 1
PCPN
Mach Number = 1.8
$\alpha = 10°$
Format IV

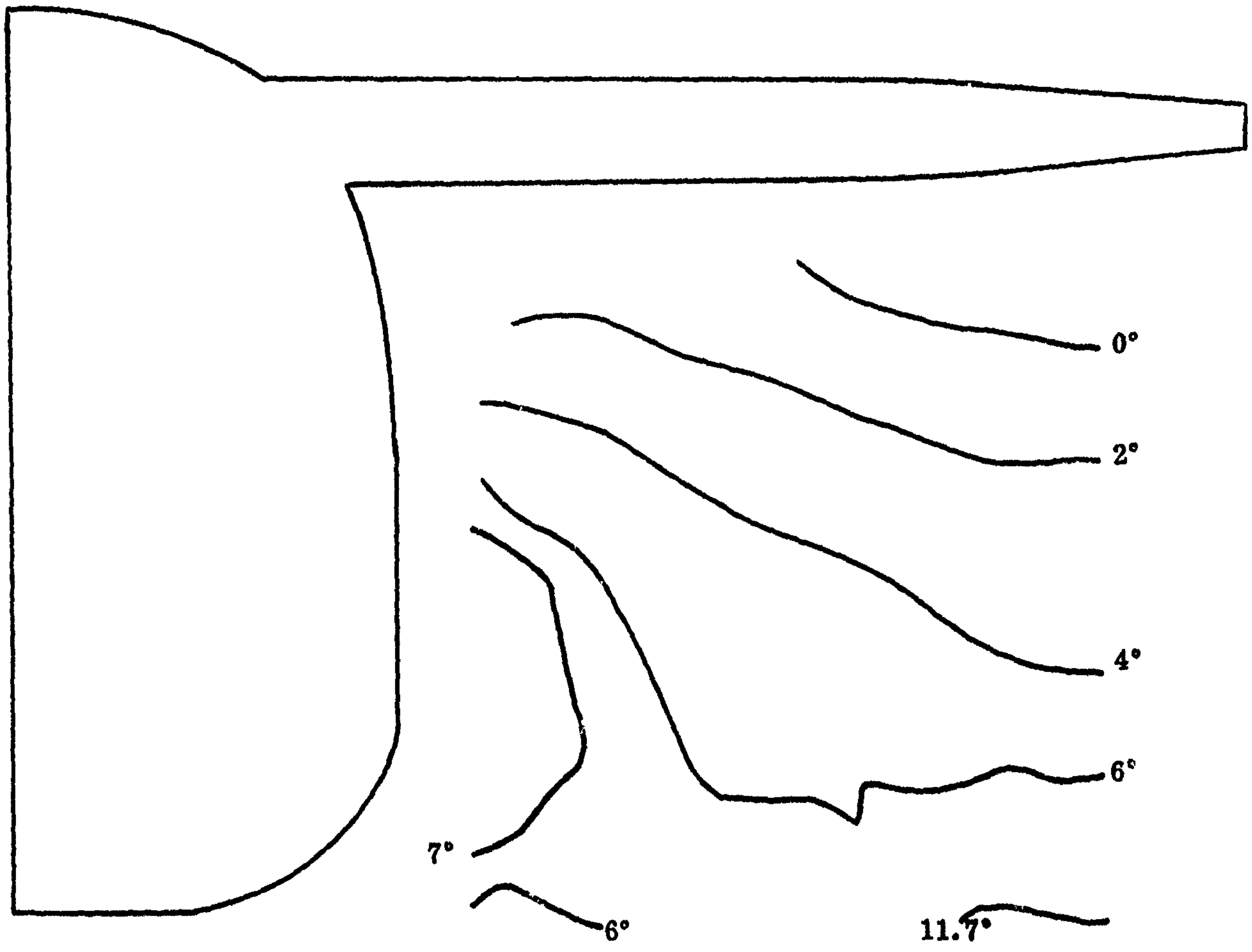

Figure 7-164. Local Flow Angularity

Fuselage 1
PCPN
Mach Number = 1.8
α = 20°
Format IV

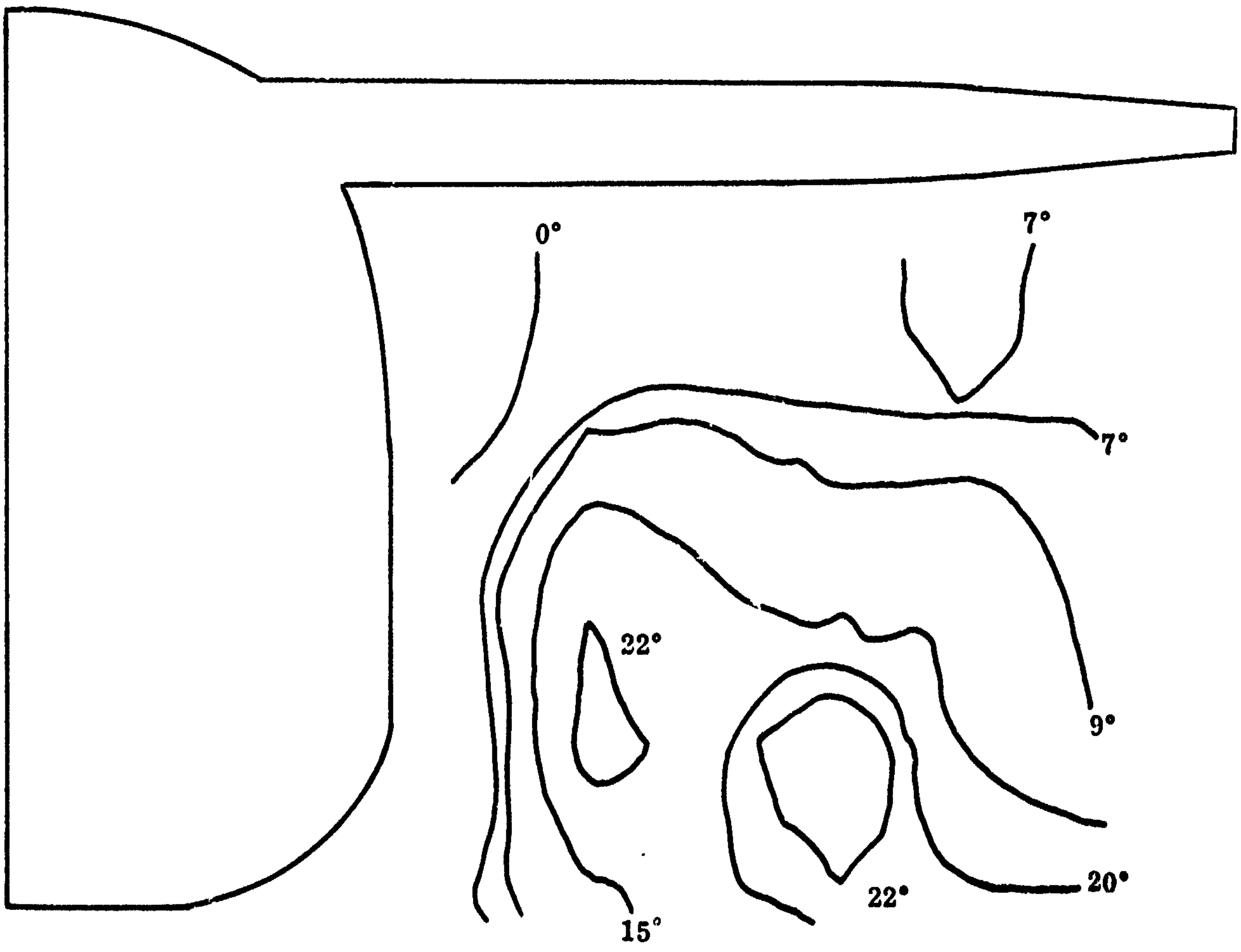

Figure 7-165. Local Flow Angularity

Fuselage 1
PCPN
Mach Number = 1.8
$\alpha = 0°$
Format IV

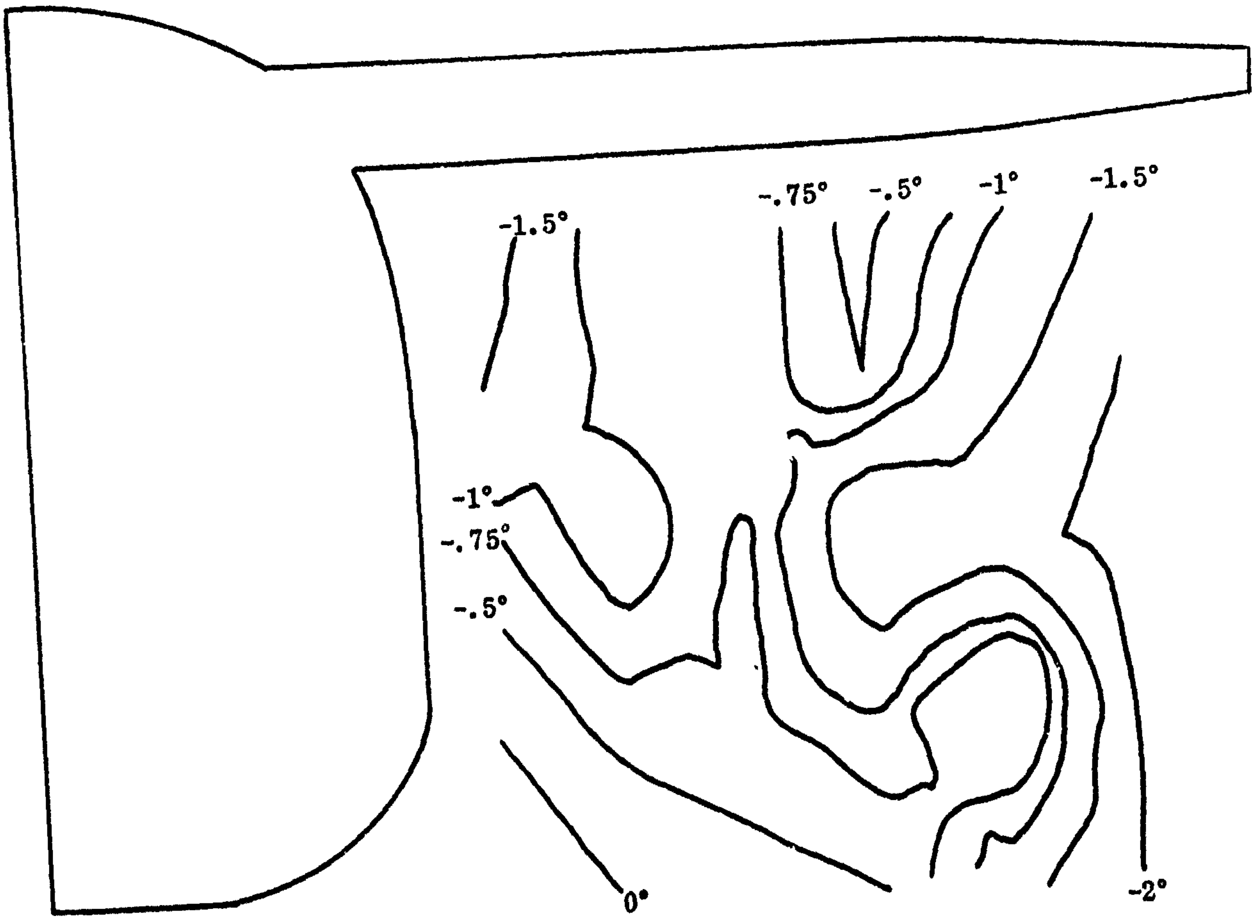

Figure 7-136. Sidewash Angle

Fuselage 1
PCPN
Mach Number = 1.8
α = 10°
Format IV

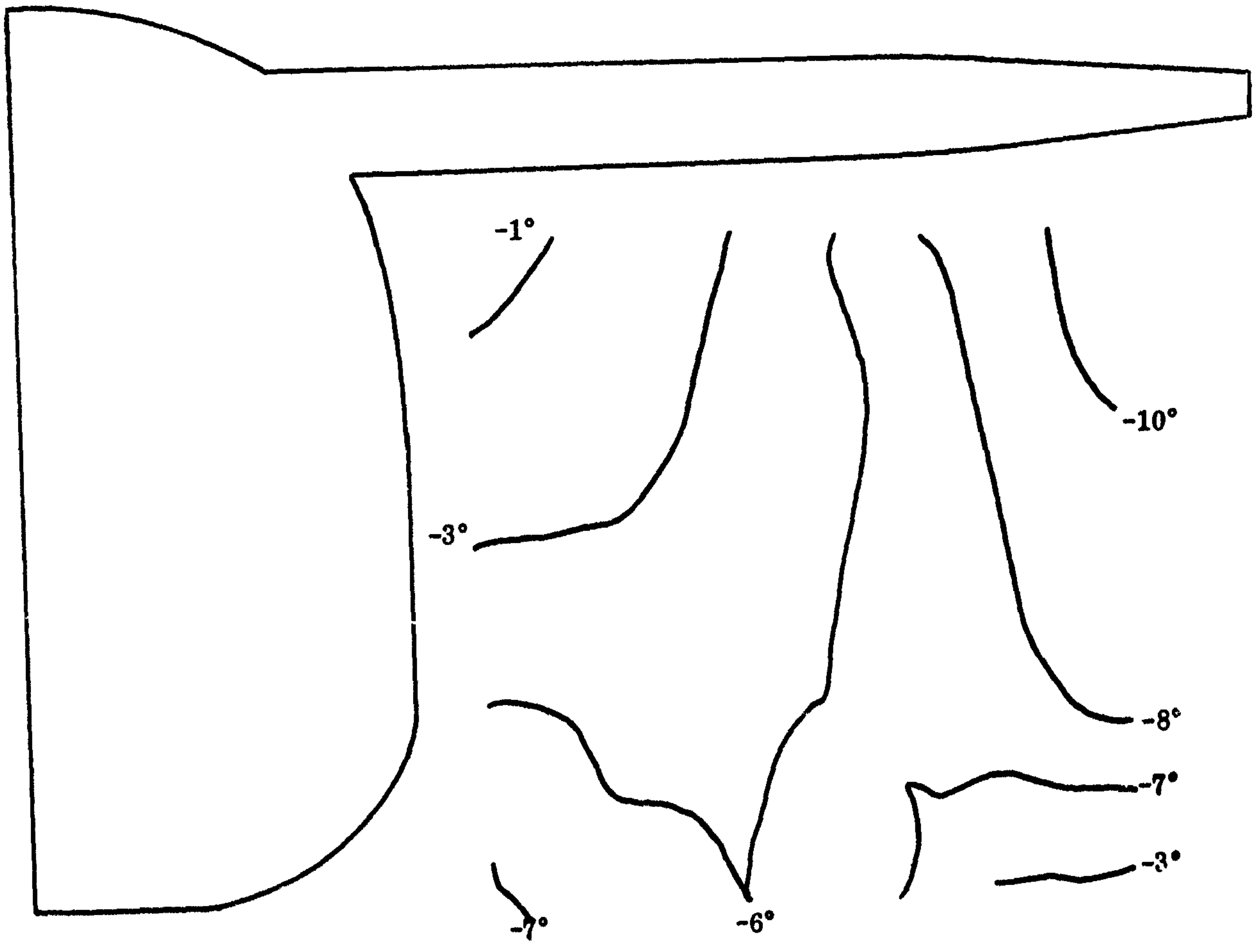

Figure 7-167. Sidewash Angle

Fuselage 1
PCPN
Mach Number = 1.8°
α = 20°
Format IV

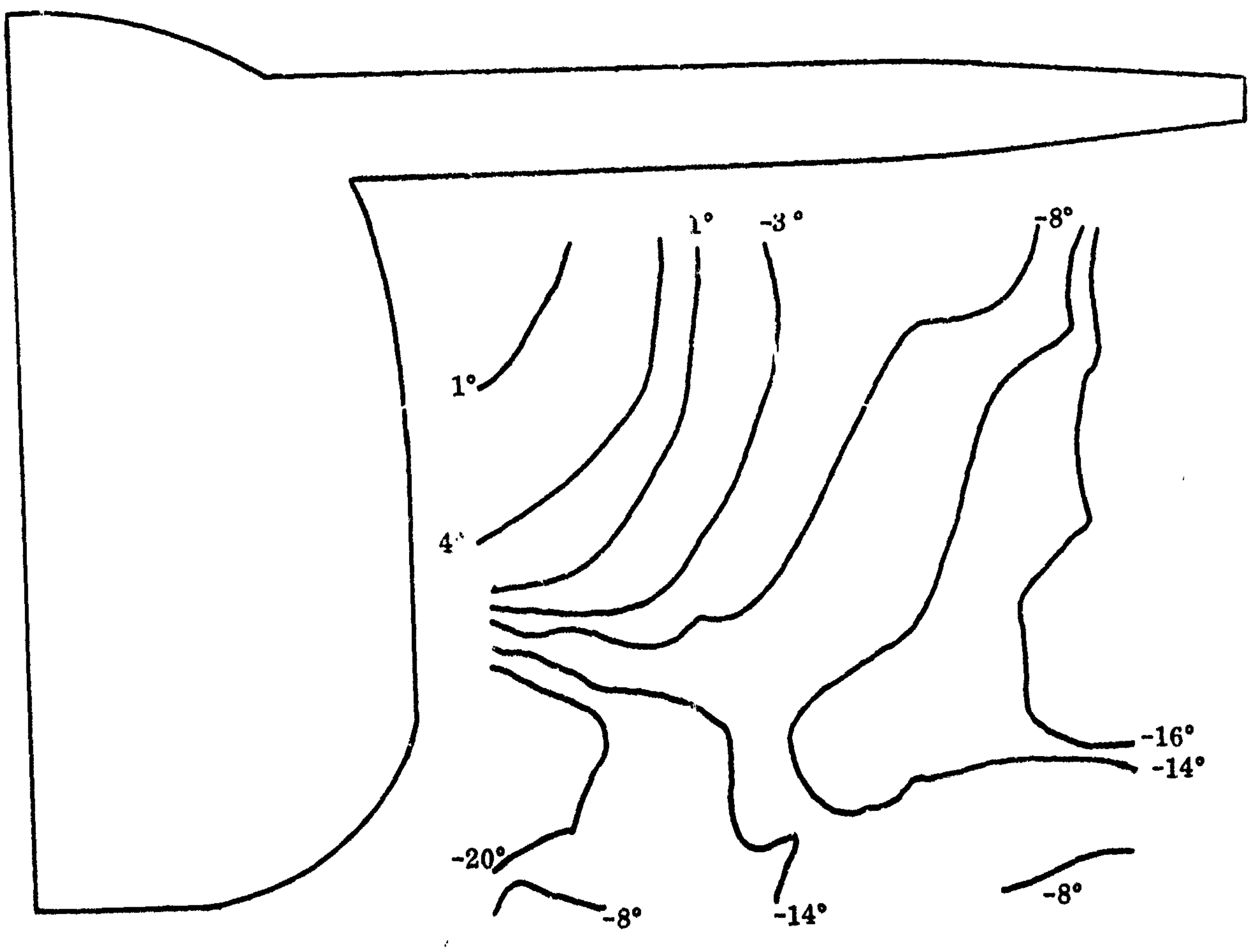

Figure 7-168. Sidewash Angle

Fuselage 4
PCPN
Mach Number = 1.8
α = 0°
Format IV

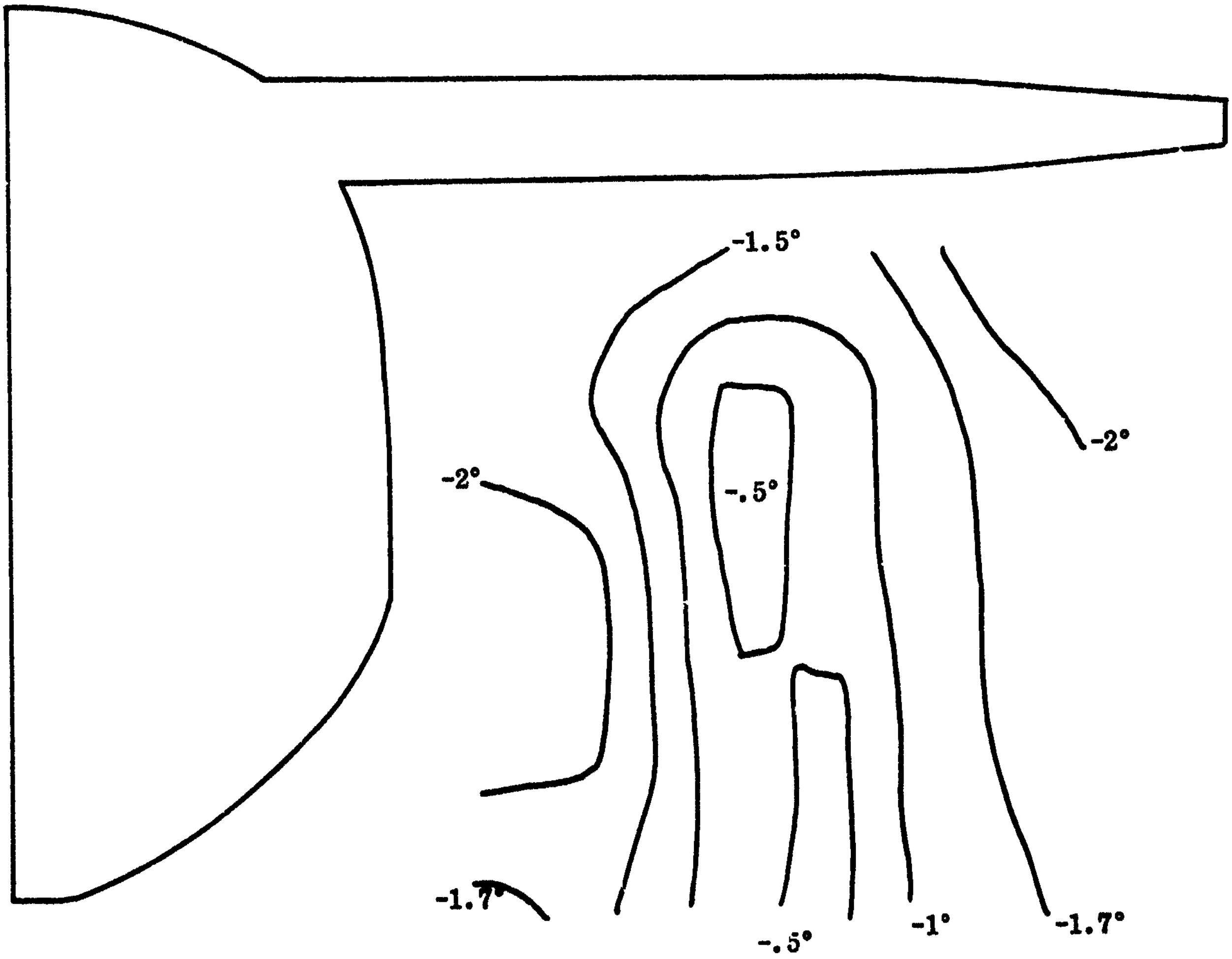

Figure 7-169. Local Flow Angularity

Fuselage 4
PCPN
Mach Number = 1.8°
α = 10°
Format IV

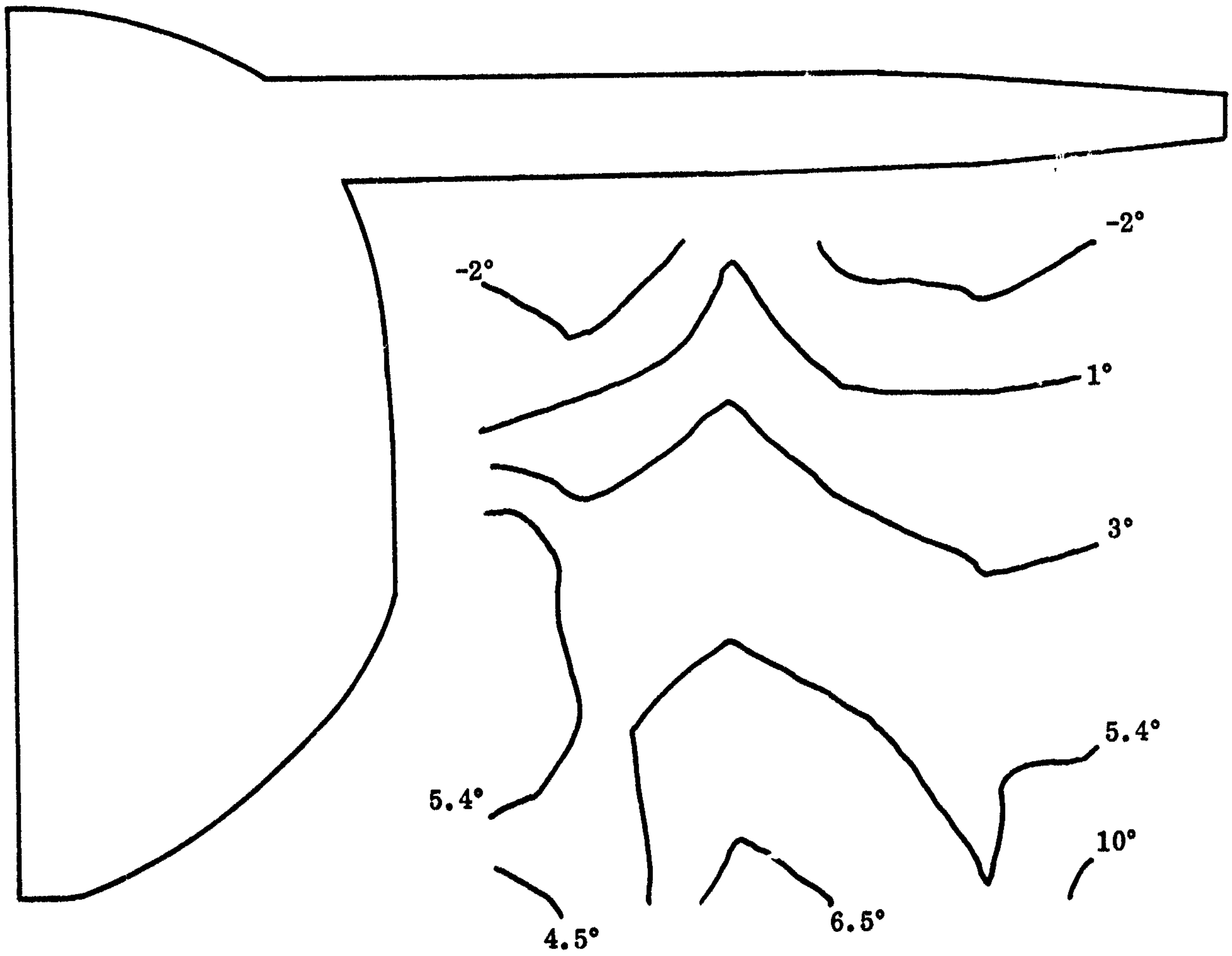

Figure 7-170. Local Flow Angularity

Fuselage 4
PCPN
Mach Number = 1.8
α = 20°
Format IV

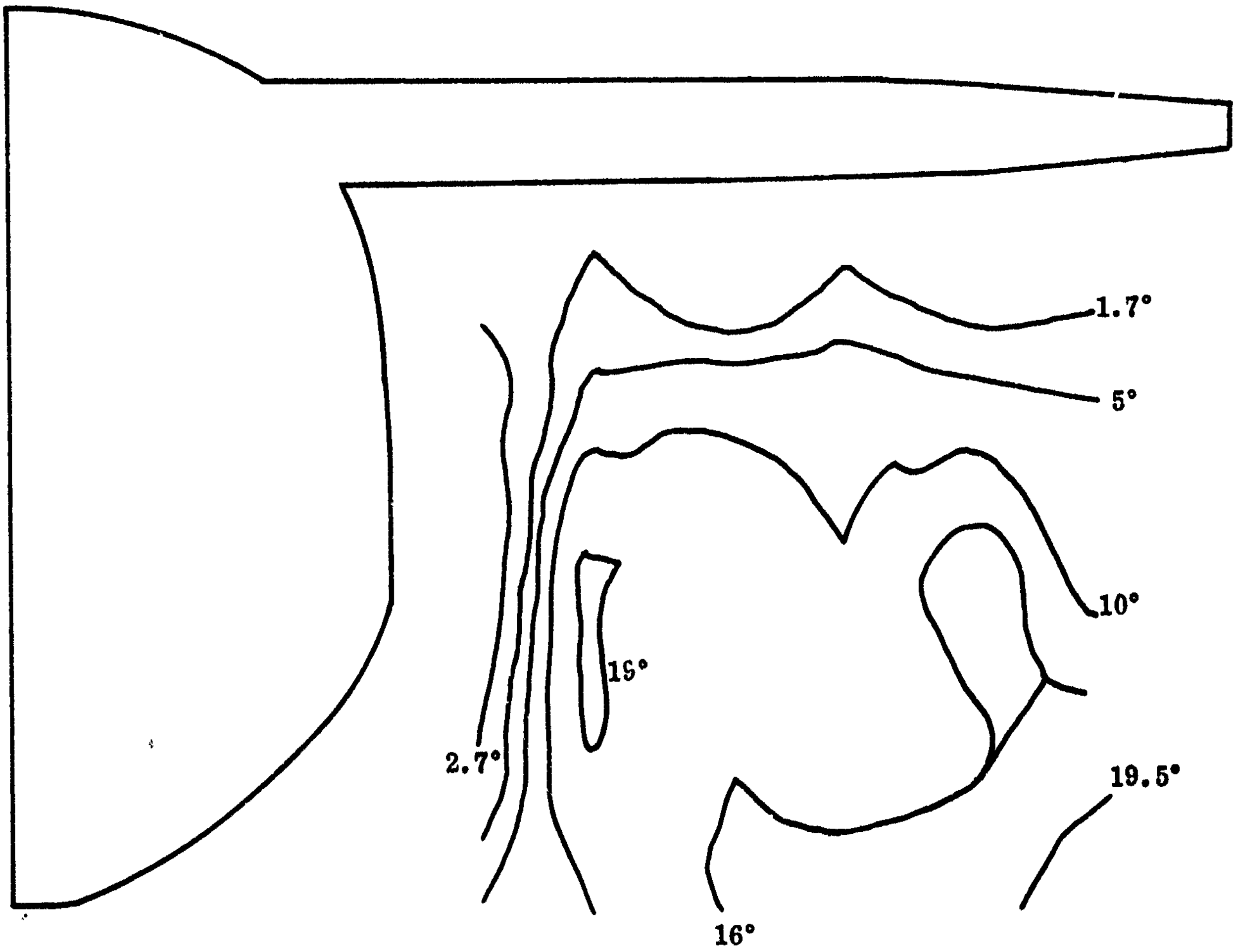

Figure 7-171. Local Flow Angularity

Fuselage 4
PCPN
Mach Number = 1.8
α = 0°
Format IV

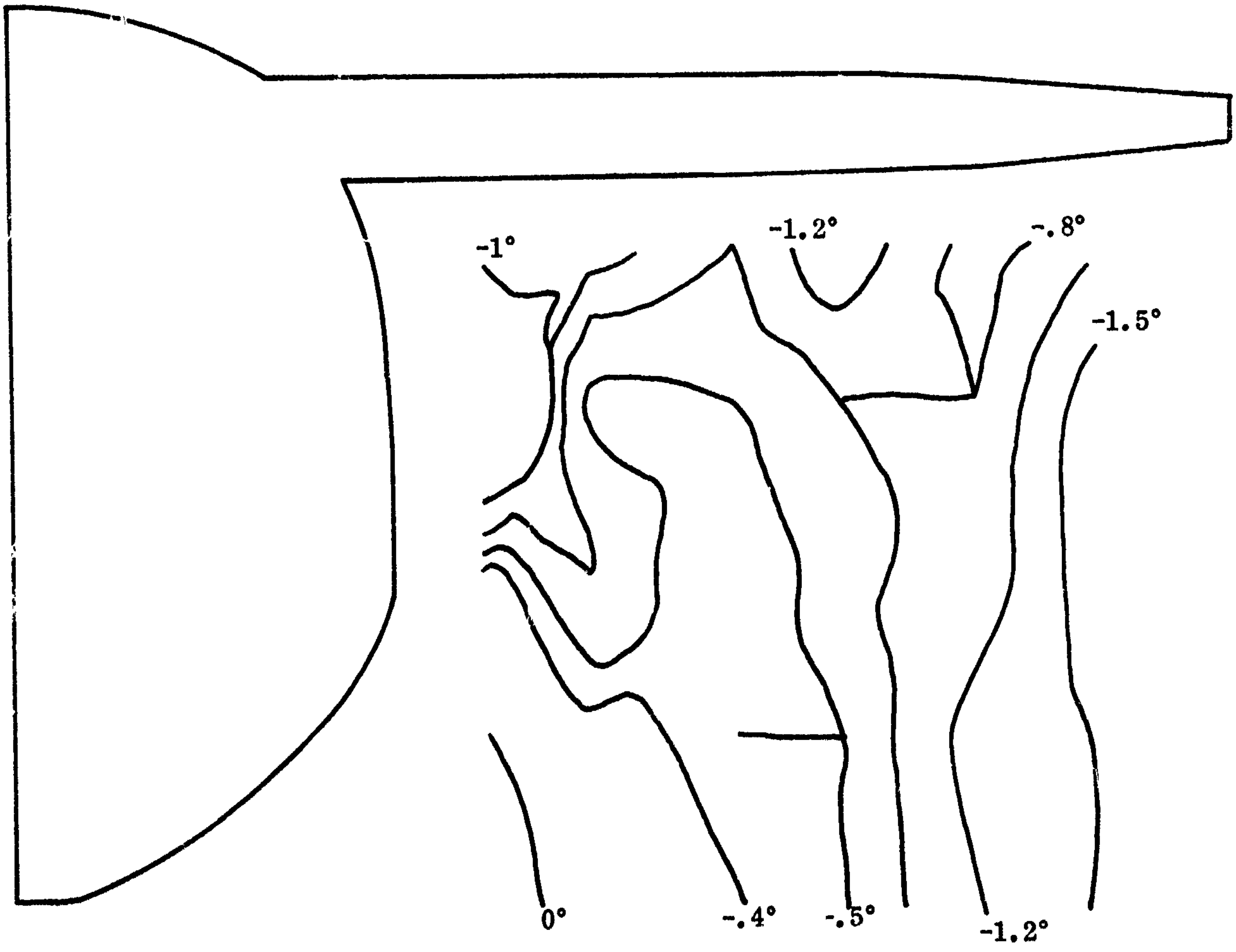

Figure 7-172. Sidewash Angle

Fuselage 4
PCPN
Mach Number = 1.8
α = 10°
Format IV

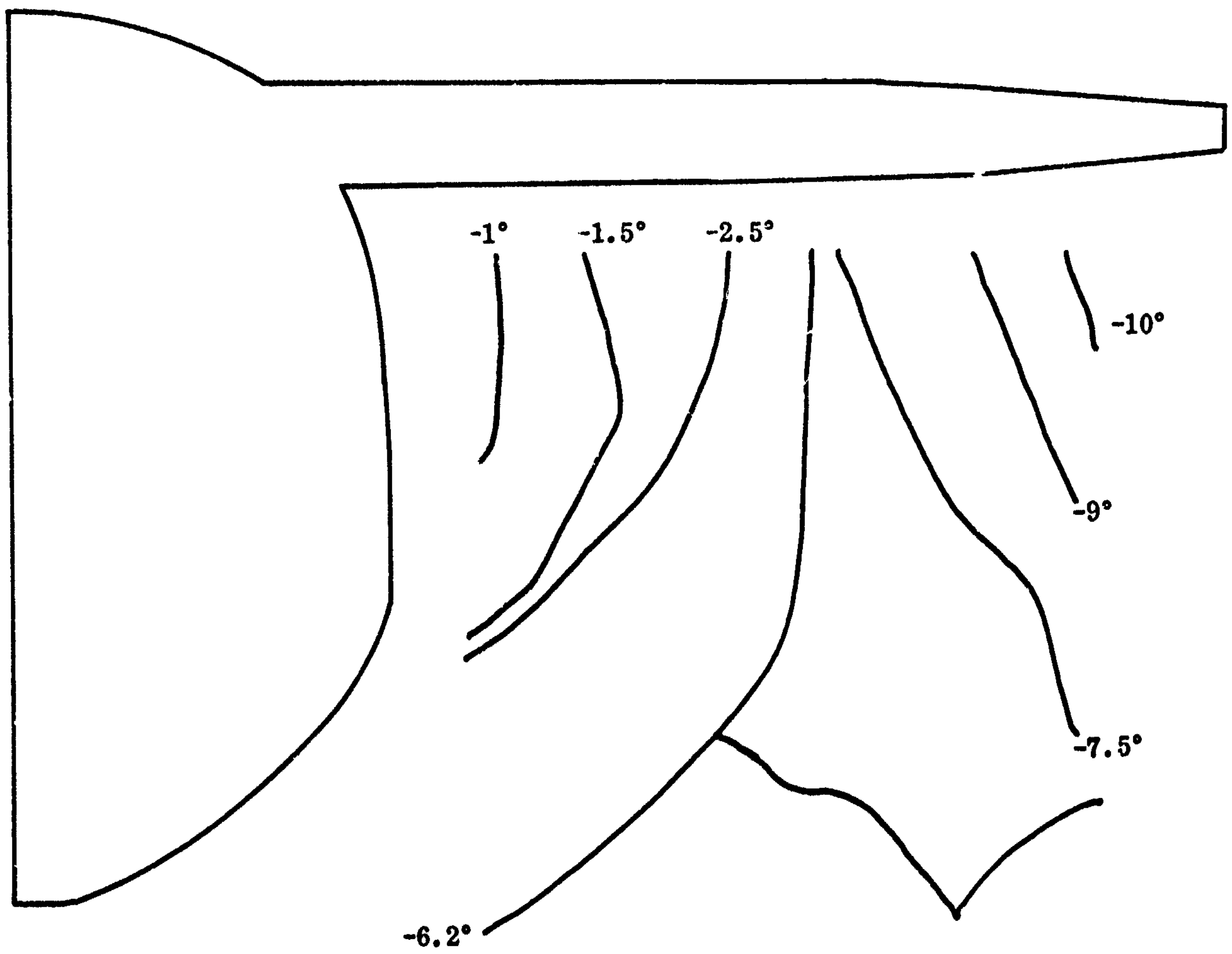

Figure 7-173. Sidewash Angle

Fuselage 4
PCPN
Mach Number = 1.8
α = 20°
Format IV

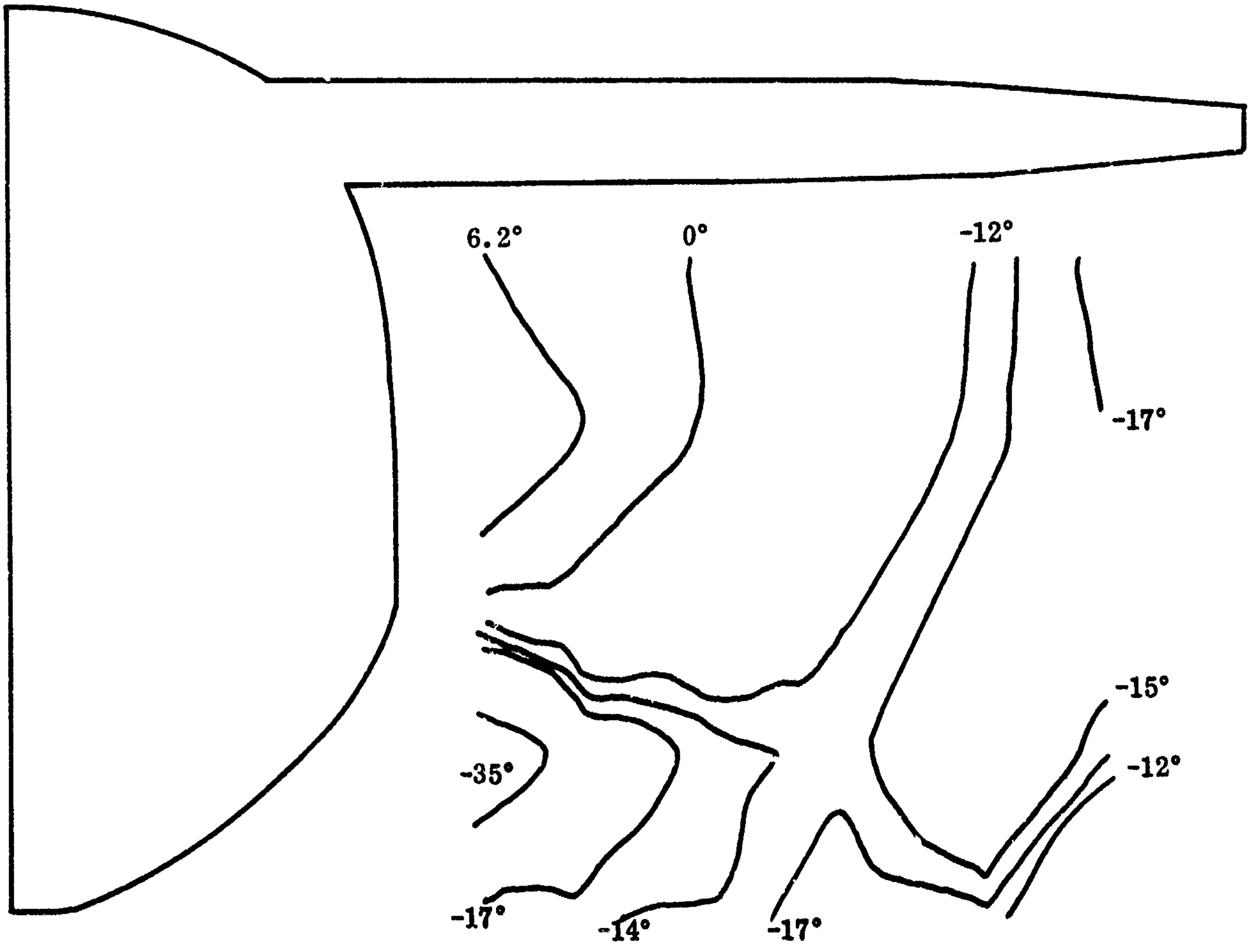

Figure 7-174. Sidewash Angle

induced by fuselage 3 the local sidewash is presented in Figures 7-175 and 7-176, for an angle of attack of +10° and +20°.

7.2.2.4 Mach Number 2.2

Qualitatively the flow field characteristics at this Mach number are essentially the same as those seen at Mach 1.8. Quantitatively the variation in sidewash with angle of attack, is larger than seen at the lower Mach numbers, as described in Section 7.2.1. The sidewash characteristics for all seven fuselage configurations are presented in Figures 7-177 through 7-183 for 0° angle of attack and in Figures 7-184 through 7-190 for the +10° angle of attack.

7.2.2.5 Mach Number 2.5

There are no new flow field effects evident at this Mach number and the flow fields are qualitatively similar to those seen at lower Mach numbers. There is a continued increase in sensitivity of sidewash to angle of attack, with the variation larger at this Mach number than for the lower Mach numbers. The local flow angularity and sidewash characteristics are illustrated, at angles of attack of 0°, +10°, and +20°, for a small corner radius configuration (fuselage 1) and a large corner radius configuration (fuselage 4), in Figures 7-191 through 7-196 and Figures 7-197 through 7-202, respectively.

7.2.3 Wing Effects

In addition to the evaluation of fuselage geometry effects, an investigation of the impact of wing sweep upon flow field composition was made. The tests, designed to isolate the wing influence, fixed all other geometric components. The vehicle configuration was built up with the primary nose and canopy and the fuselage 3 configuration. The primary wing sweep of 55° and the secondary wing sweep of 65° were integrated with this vehicle configuration and flow field surveys under each wing were made.

The variation in fuselage flow field composition induced by the change in wing sweep was quite small at the survey plane particularly with regard to the level of flow angularity, at the survey plane, which was essentially unaffected. This was also true for the local sidewash except for the upper outboard region of the survey plane where the 65° sweep tended toward a slightly higher level of negative sidewash. A condition

Fuselage 3
PCPN
Mach Number = 1.8
$\alpha = 10°$
Format IV

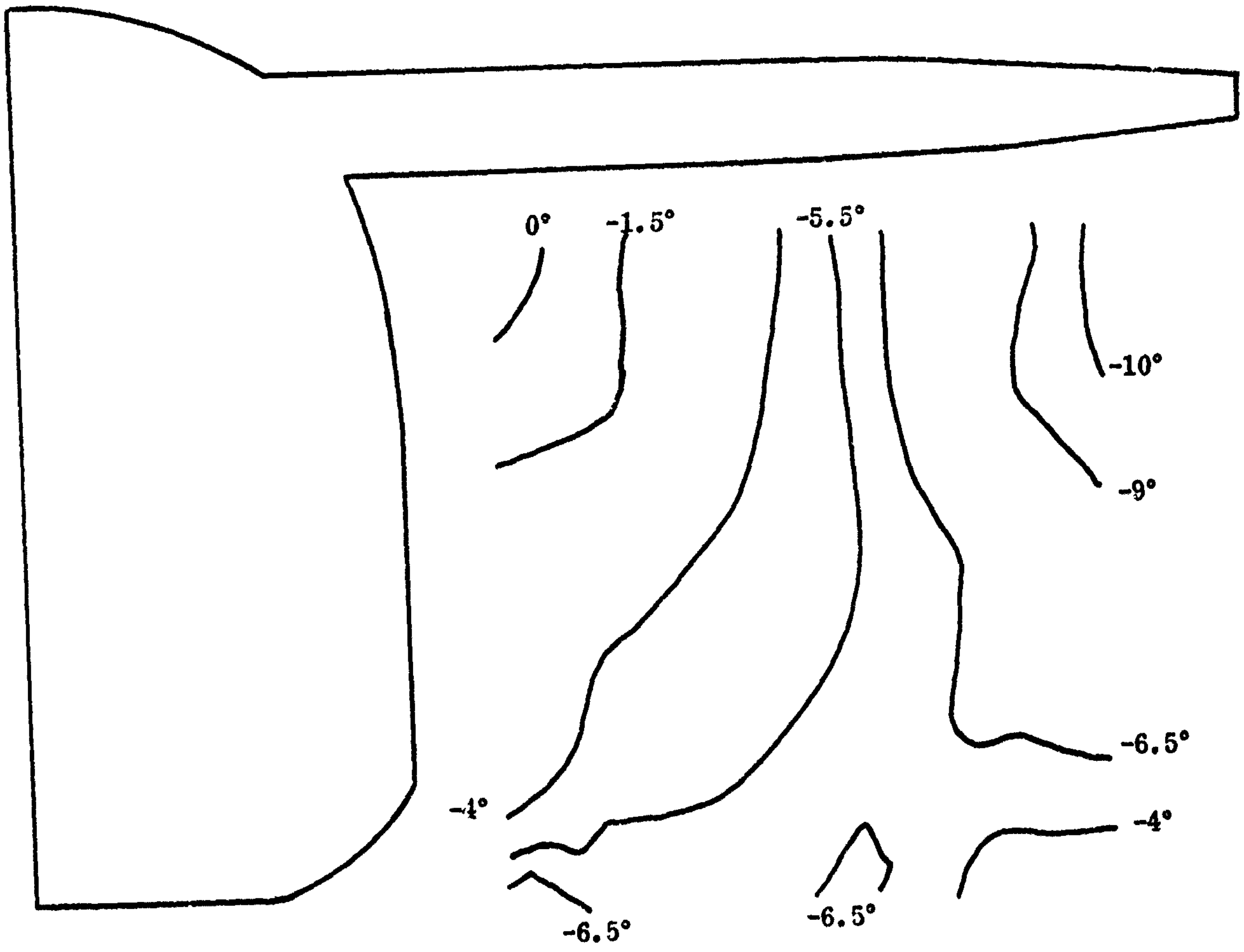

Figure 7-175. Sidewash Angle

Fuselage 3
PCPN
Mach Number = 1.8
$\alpha = 20°$
Format IV

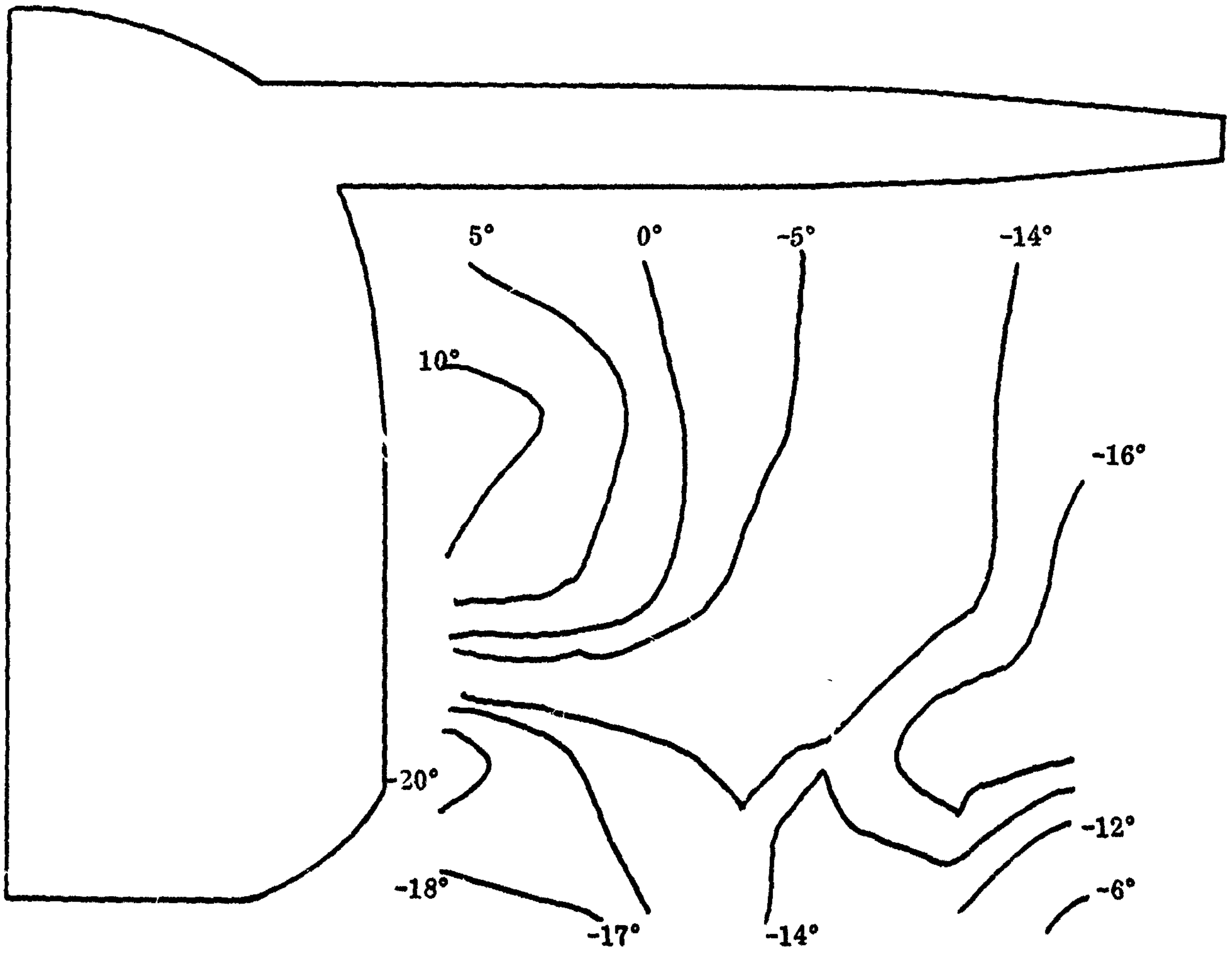

Figure 7-176. Sidewash Angle

Fuselage 1
PCPN
Mach Number = 2.2°
α = 0°
Format IV

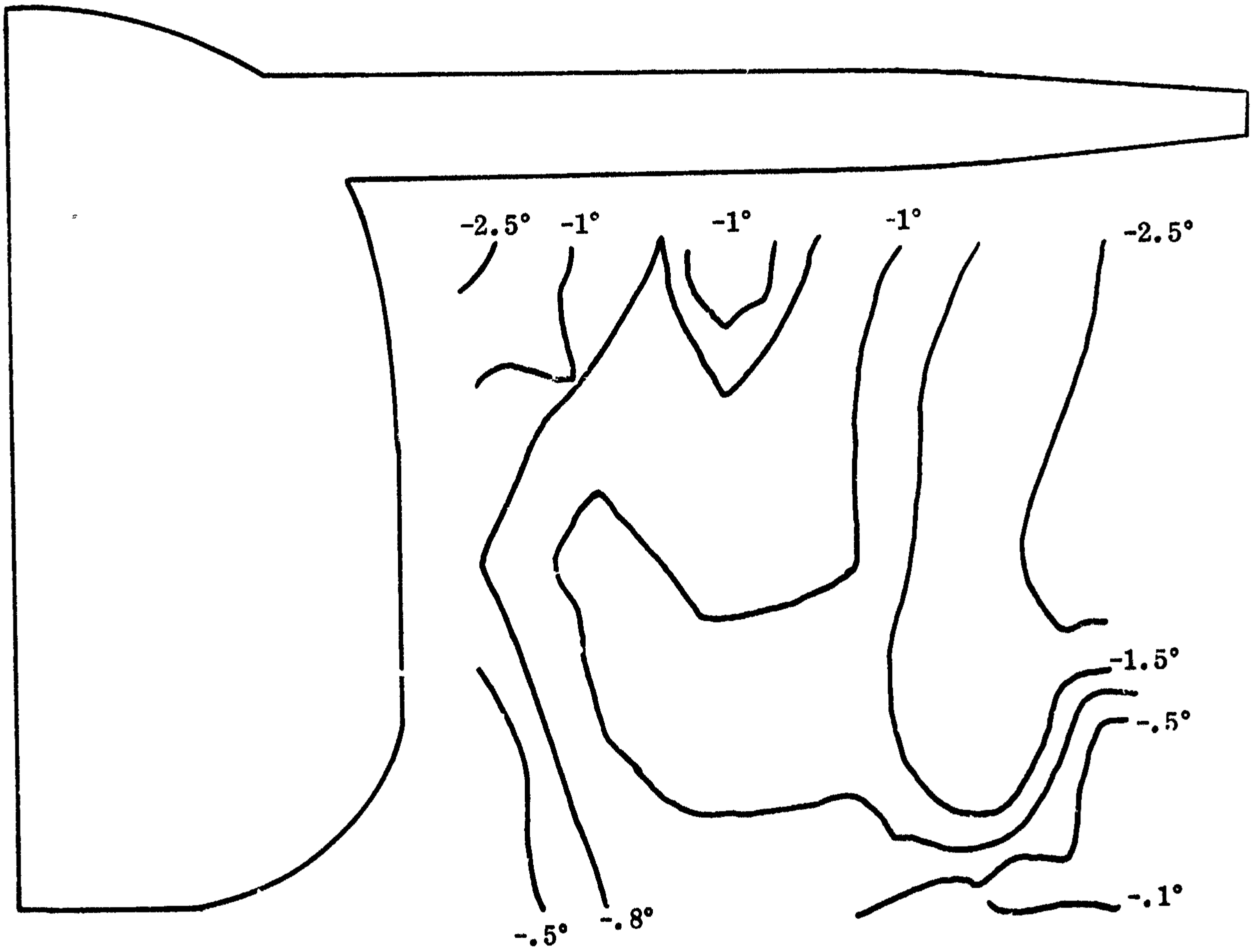

Figure 7-177. Sidewash Angle

Fuselage 2
PCPN
Mach Number = 2.2
$\alpha = 0°$
Format IV

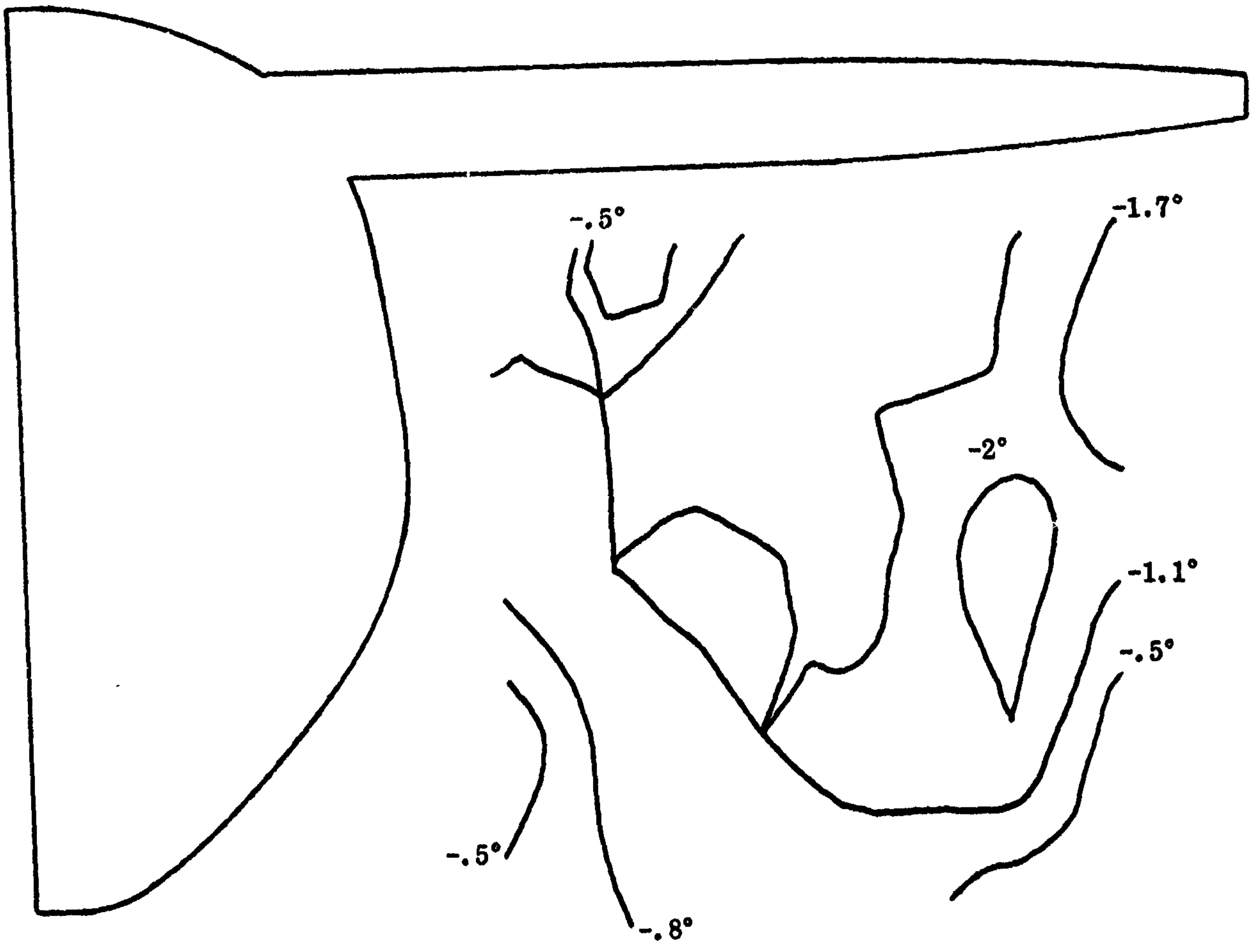

Figure 7-178. Sidewash Angle

Fuselage 3
PCPN
Mach Number = 2.2
$\alpha = 0°$
Format IV

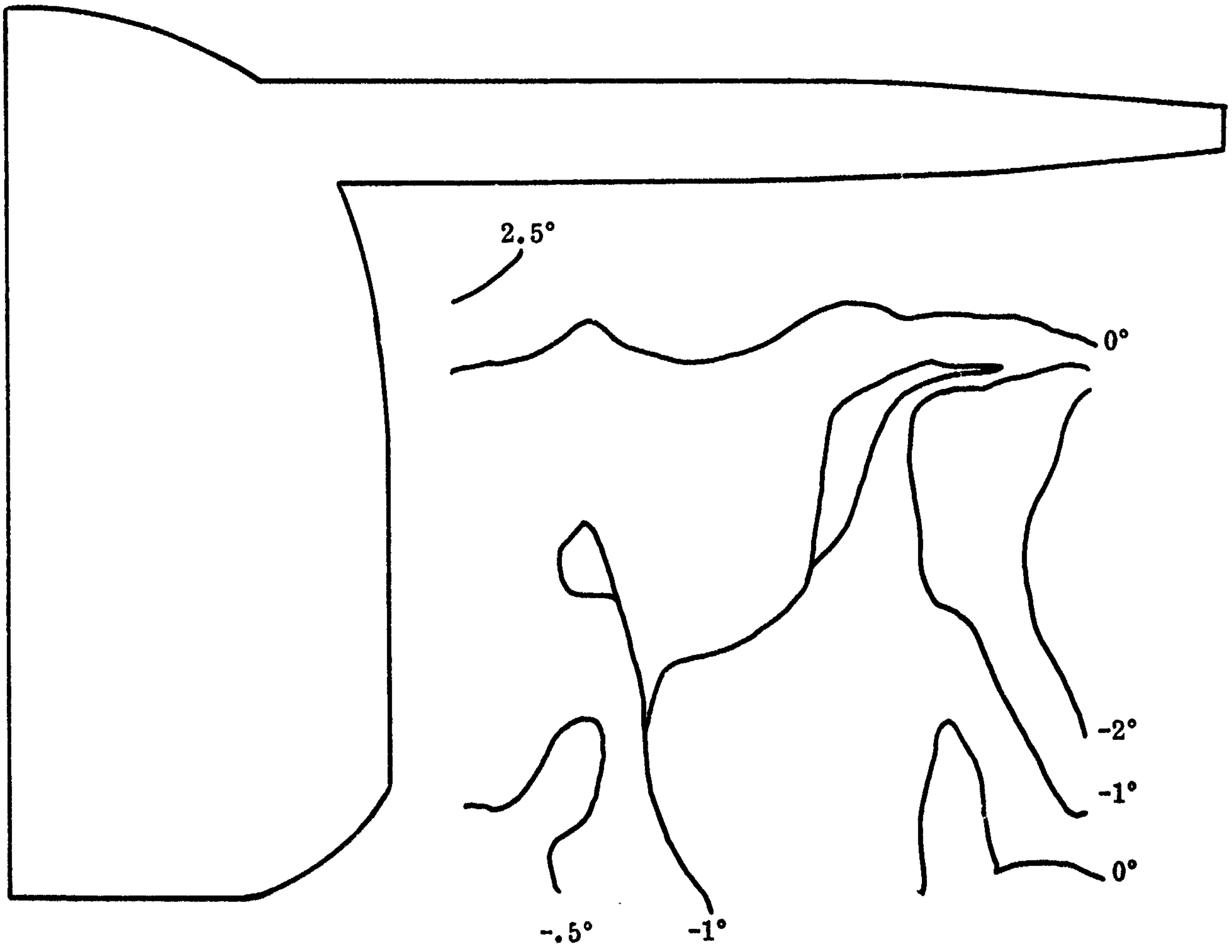

Figure 7-179. Sidewash Angle

Fuselage 4
PCPN
Mach Number = 2.2
α = 0°
Format IV

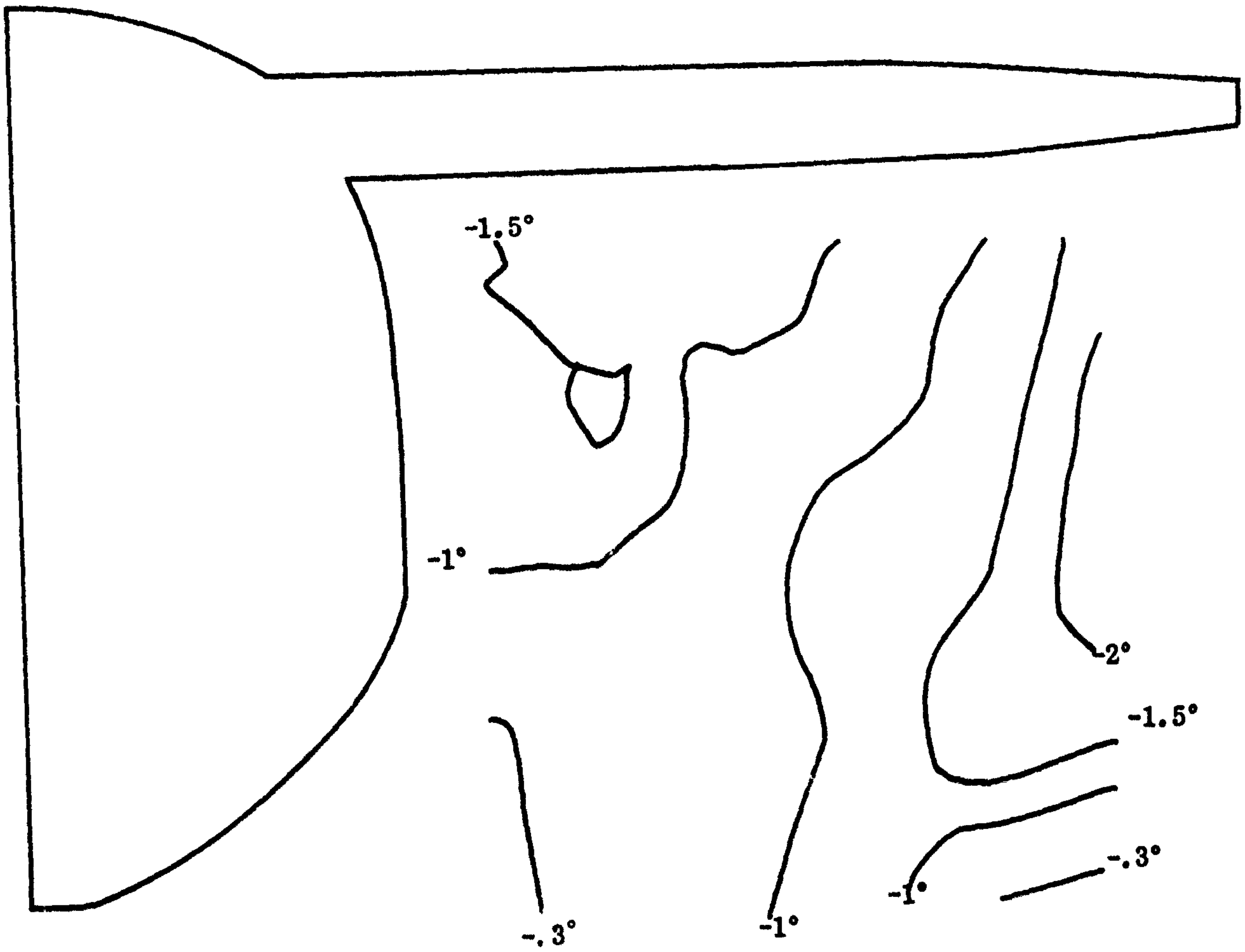

Figure 7-180. Sidewash Angle

Fuselage 5
PCPN
Mach Number = 2.2
α = 0°
Format IV

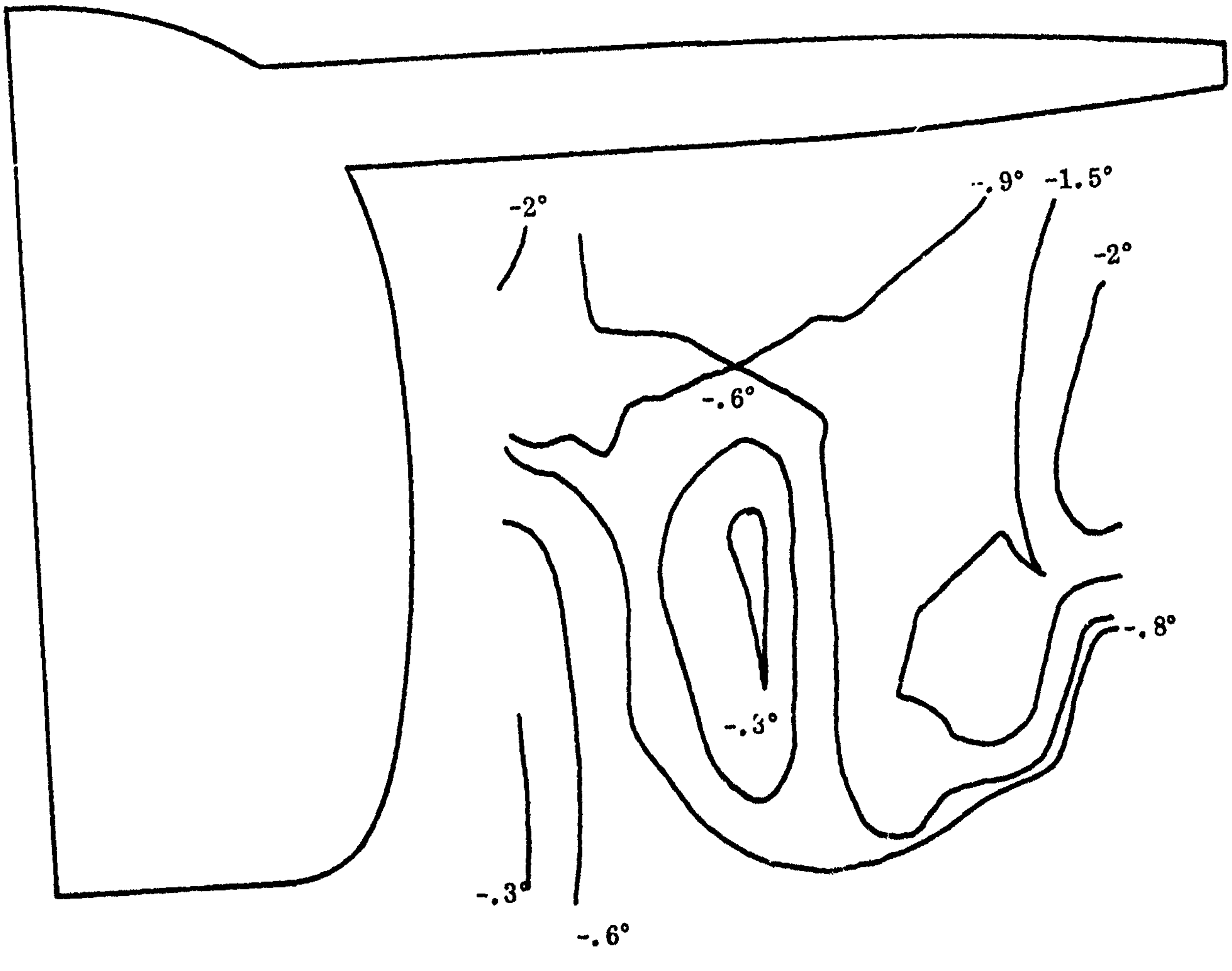

Figure 7-181. Sidewash Angle

Fuselage 6
PCPN
Mach Number = 2.2
α = 0°
Format IV

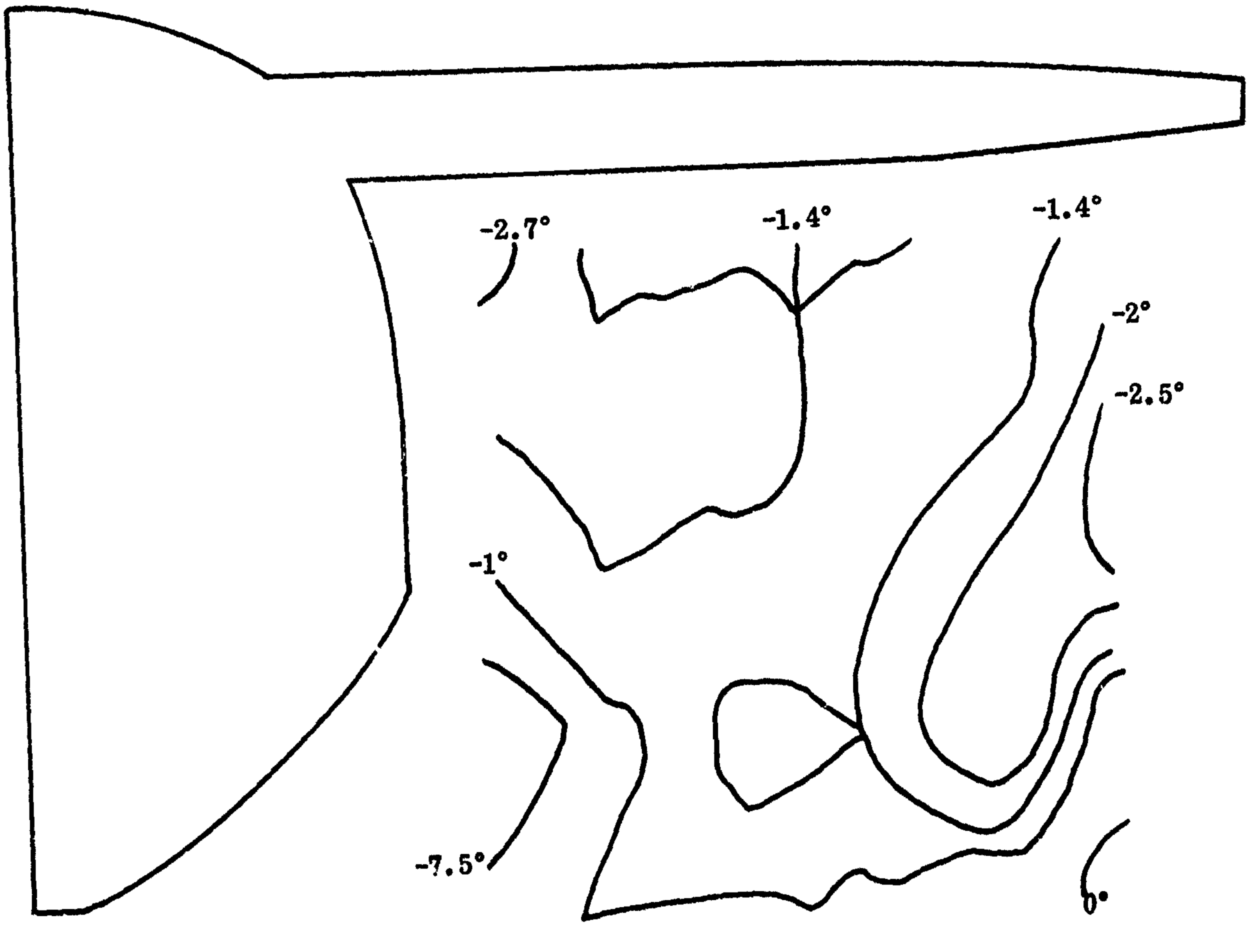

Figure 7-182. Sidewash Angle

Fuselage 8
PCPN
Mach Number = 2.2
α = 0°
Format IV

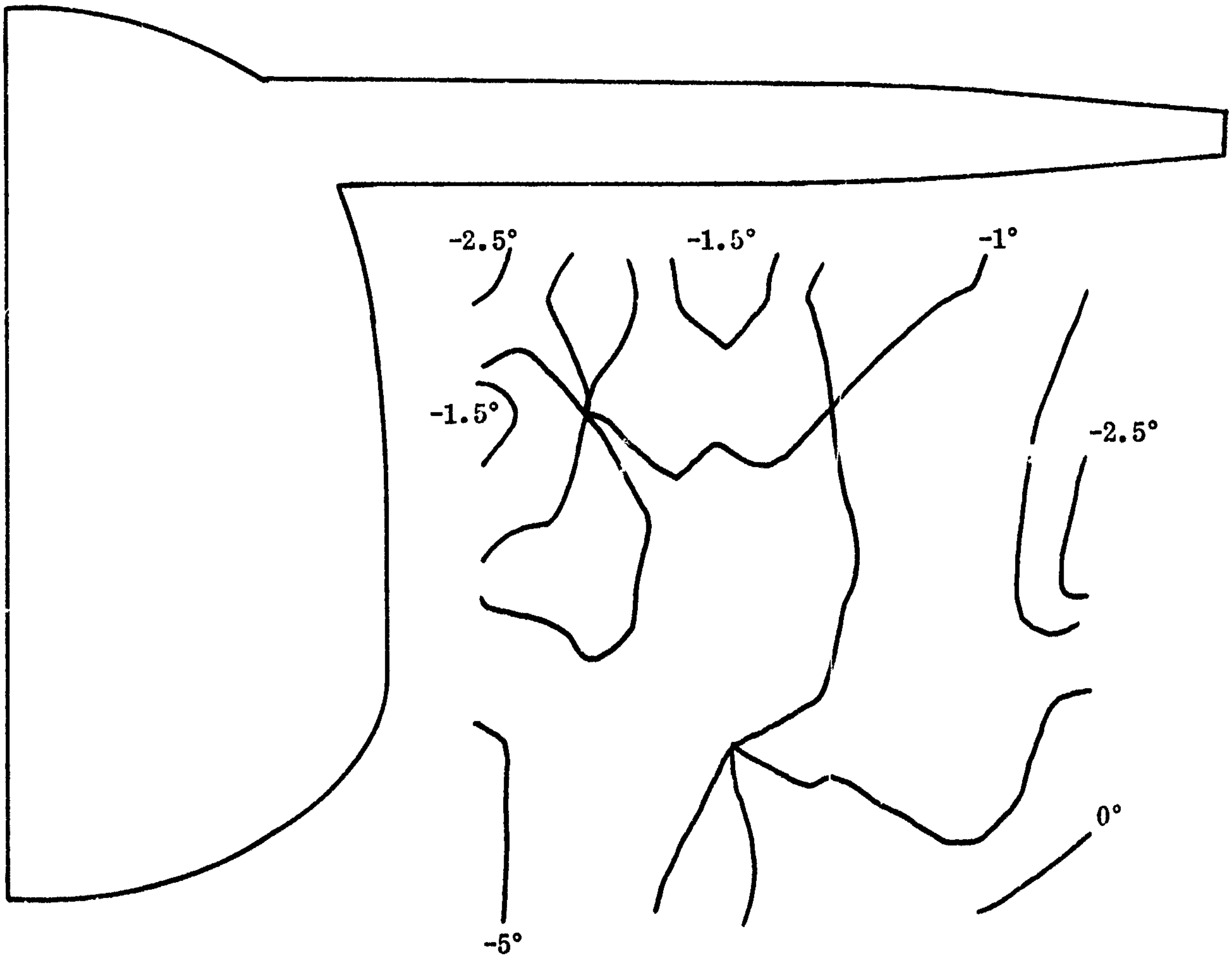

Figure 7-183. Sidewash Angle

Fuselage 1
PCPN
Mach Number = 2.2°
α = 10°
Format IV

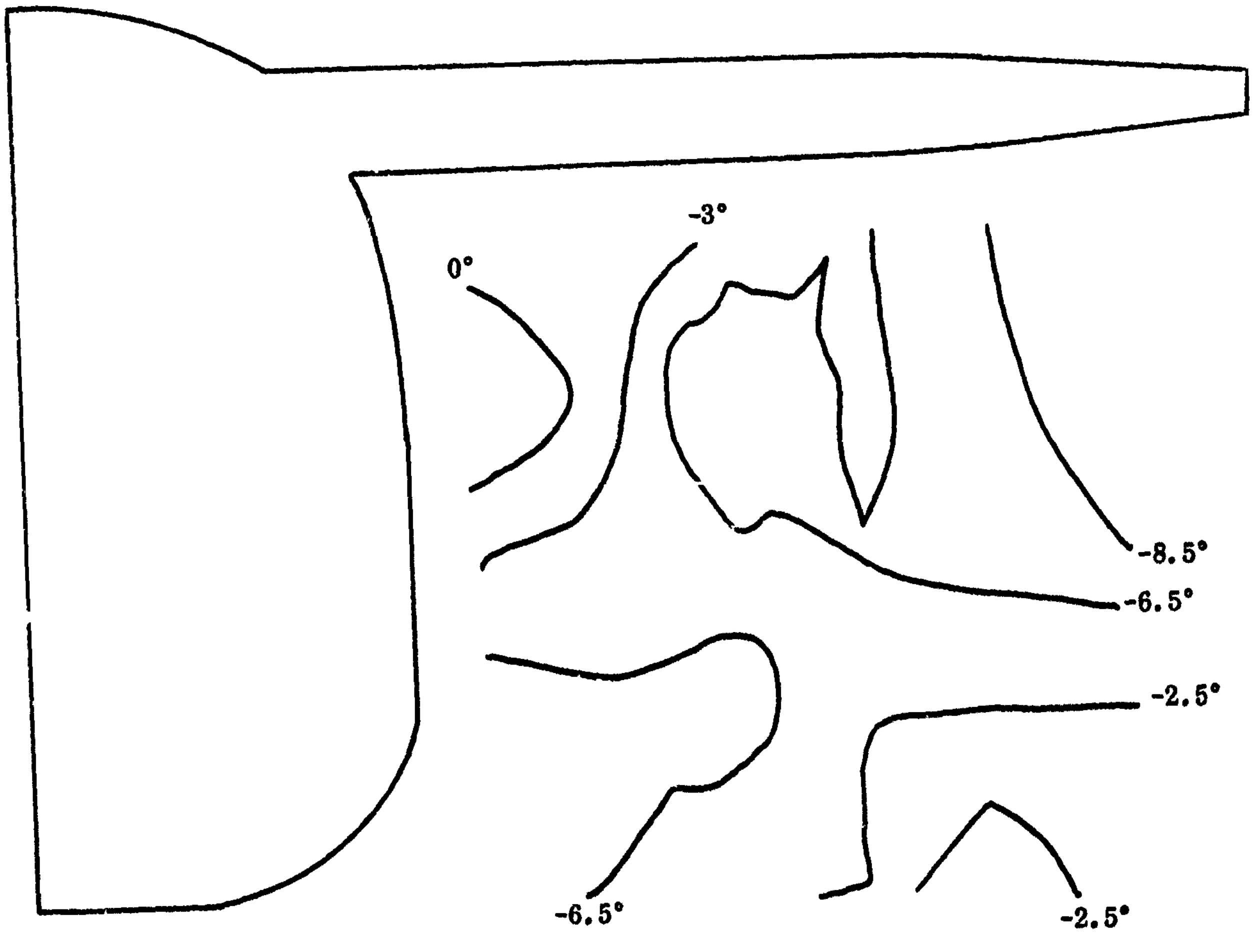

Figure 7-184. Sidewash Angle

Fuselage 2

PCPN

Mach Number = 2.2

α = 10°

Format IV

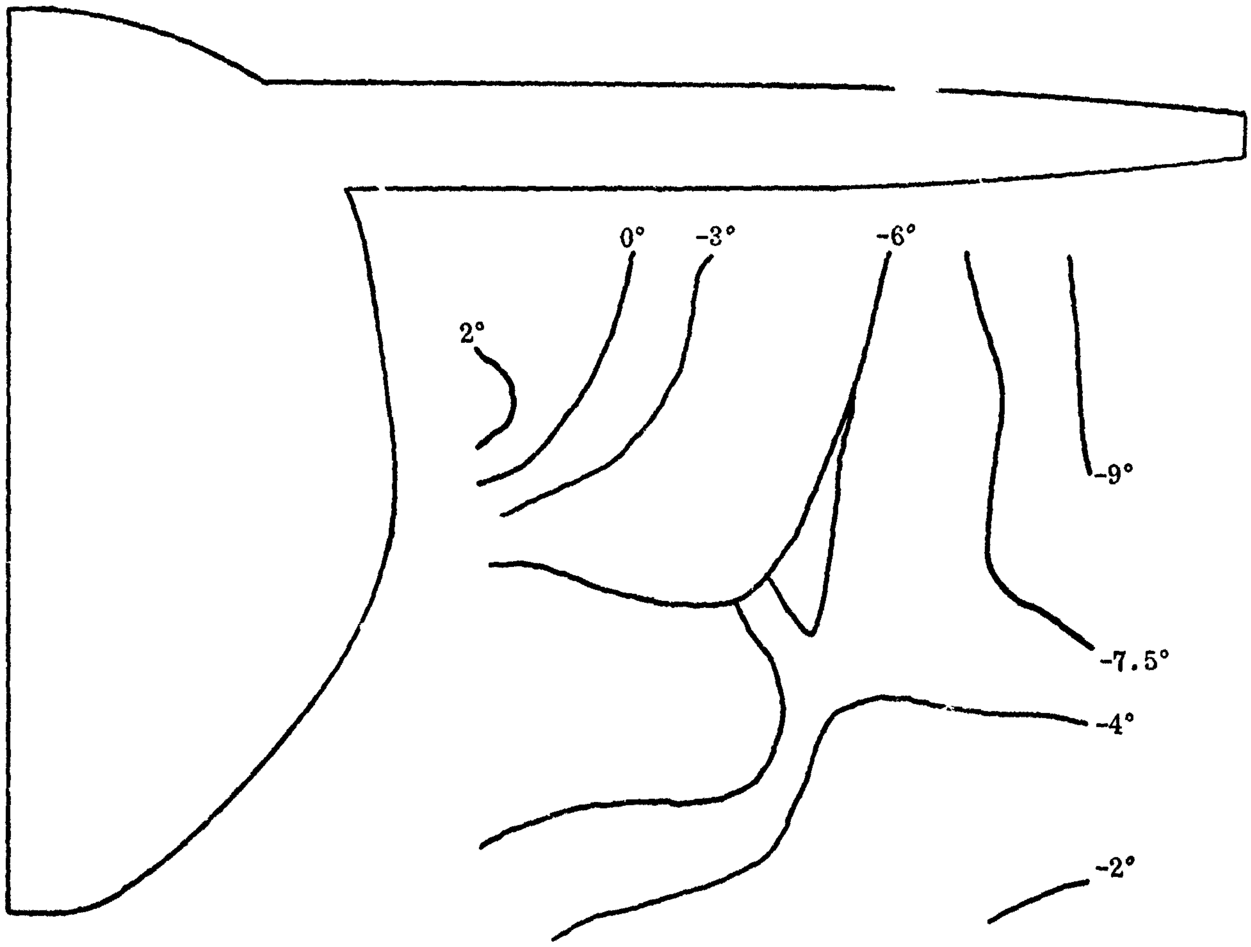

Figure 7-185. Sidewash Angle

Fuselage 3
PCPN
Mach Number = 2.2
α = 10°
Format IV

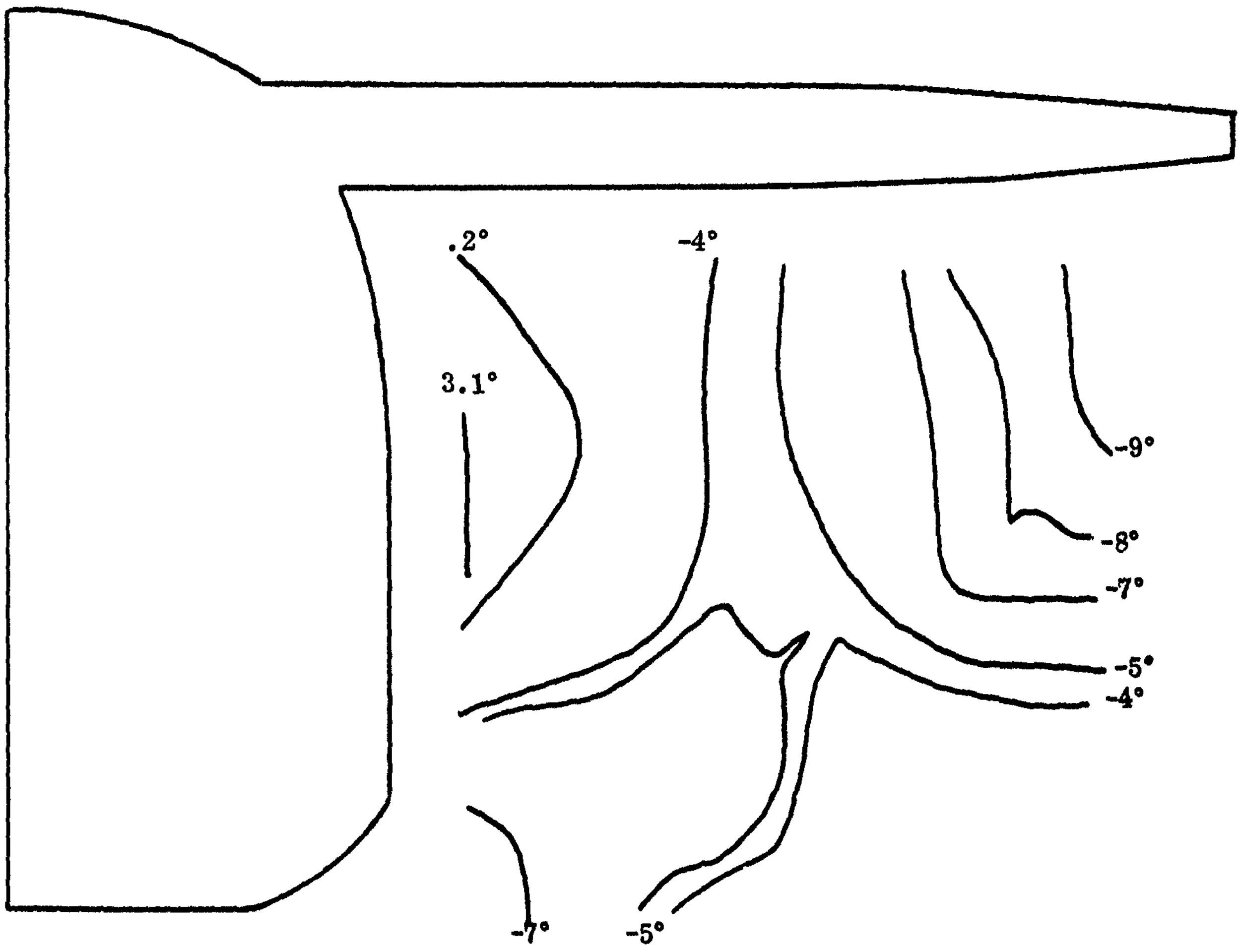

Figure 7-186. Sidewash Angle

Fuselage 4
PCPN
Mach Number = 2.2
α = 10°
Format IV

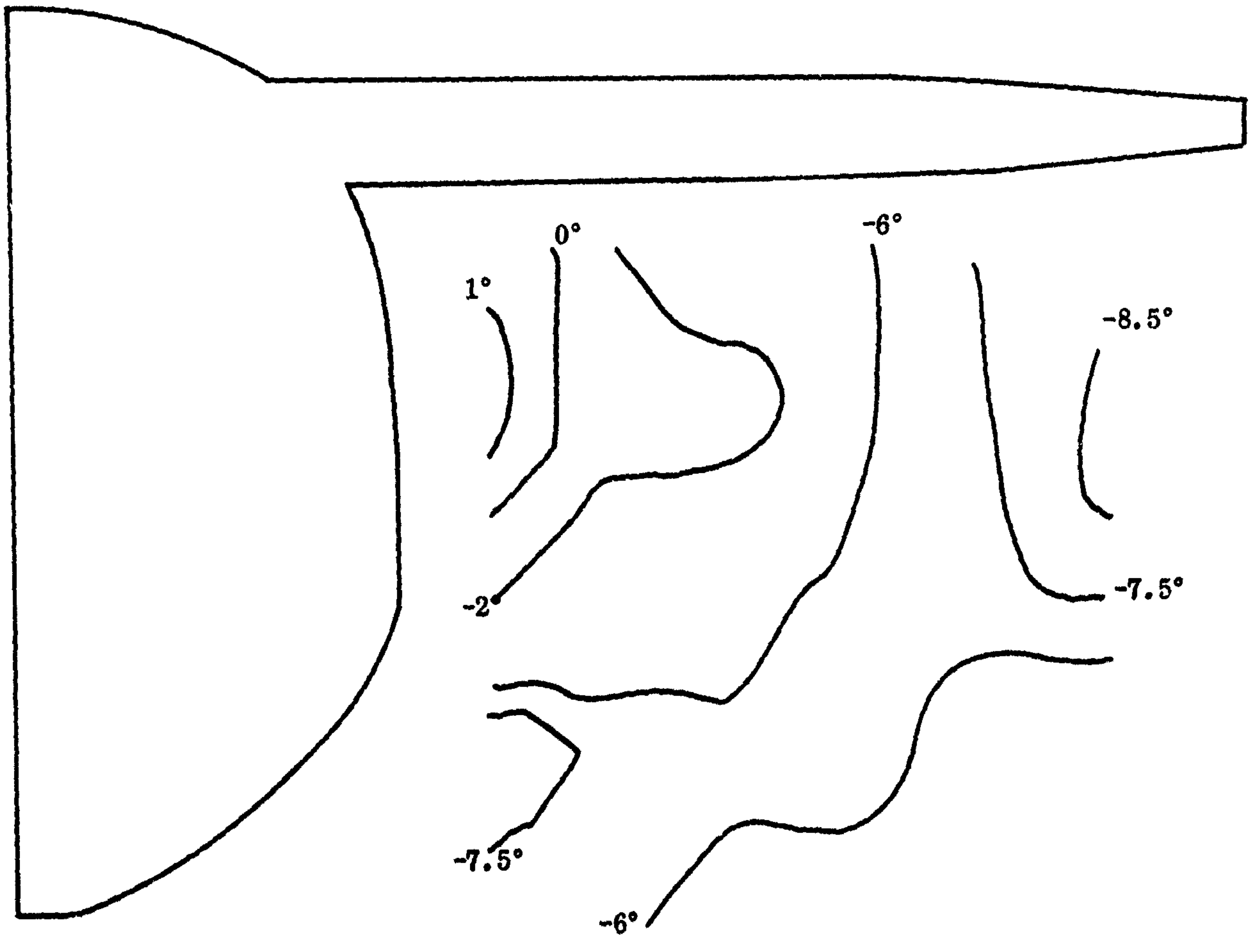

Figure 7-187. Sidewash Angle

Fuselage 5

PCPN

Mach Number = 2.2

α = 10°

Format IV

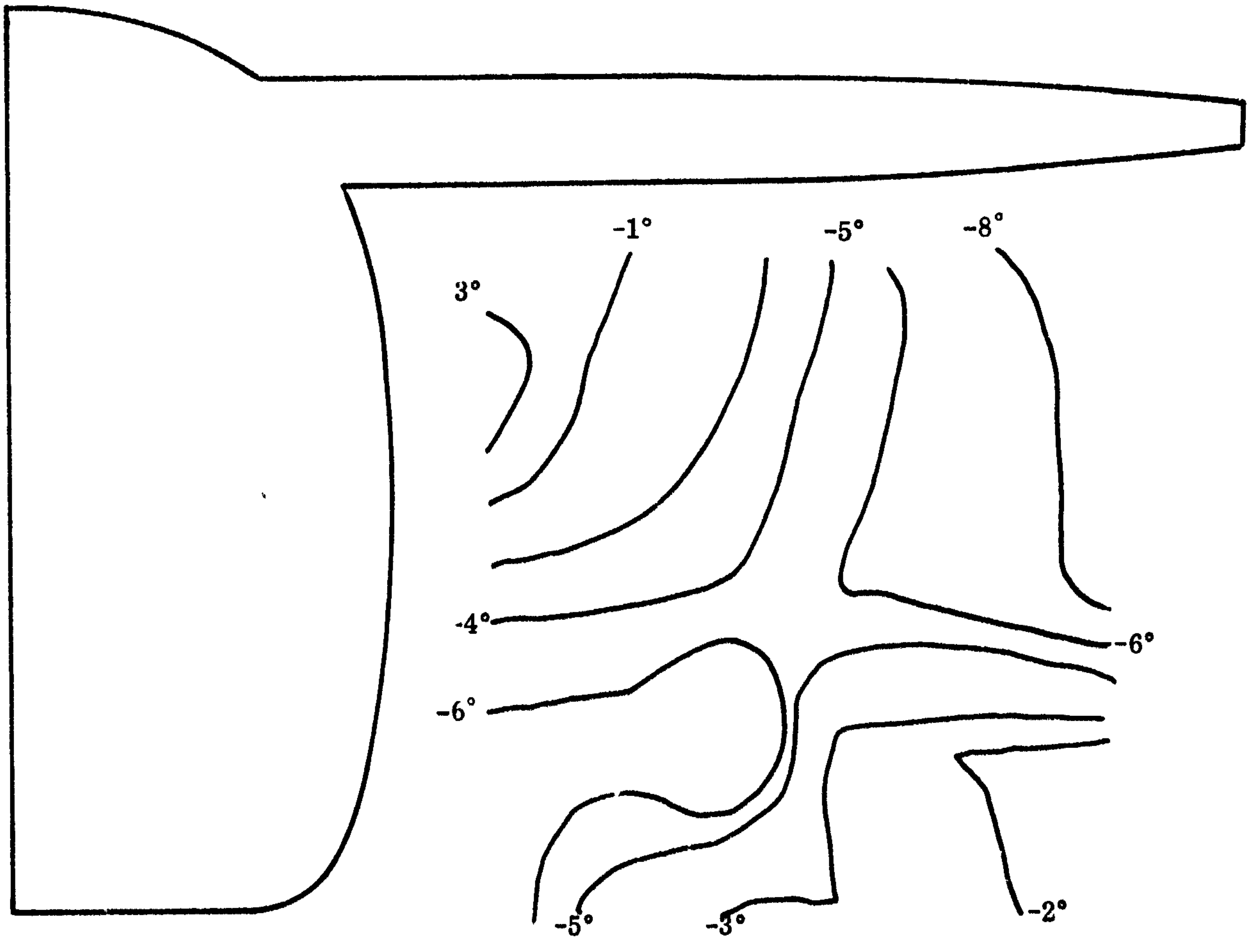

Figure 7-188. Sidewash Angle

Fuselage 6
PCPN
Mach Number = 2.2
α = 10°
Format IV

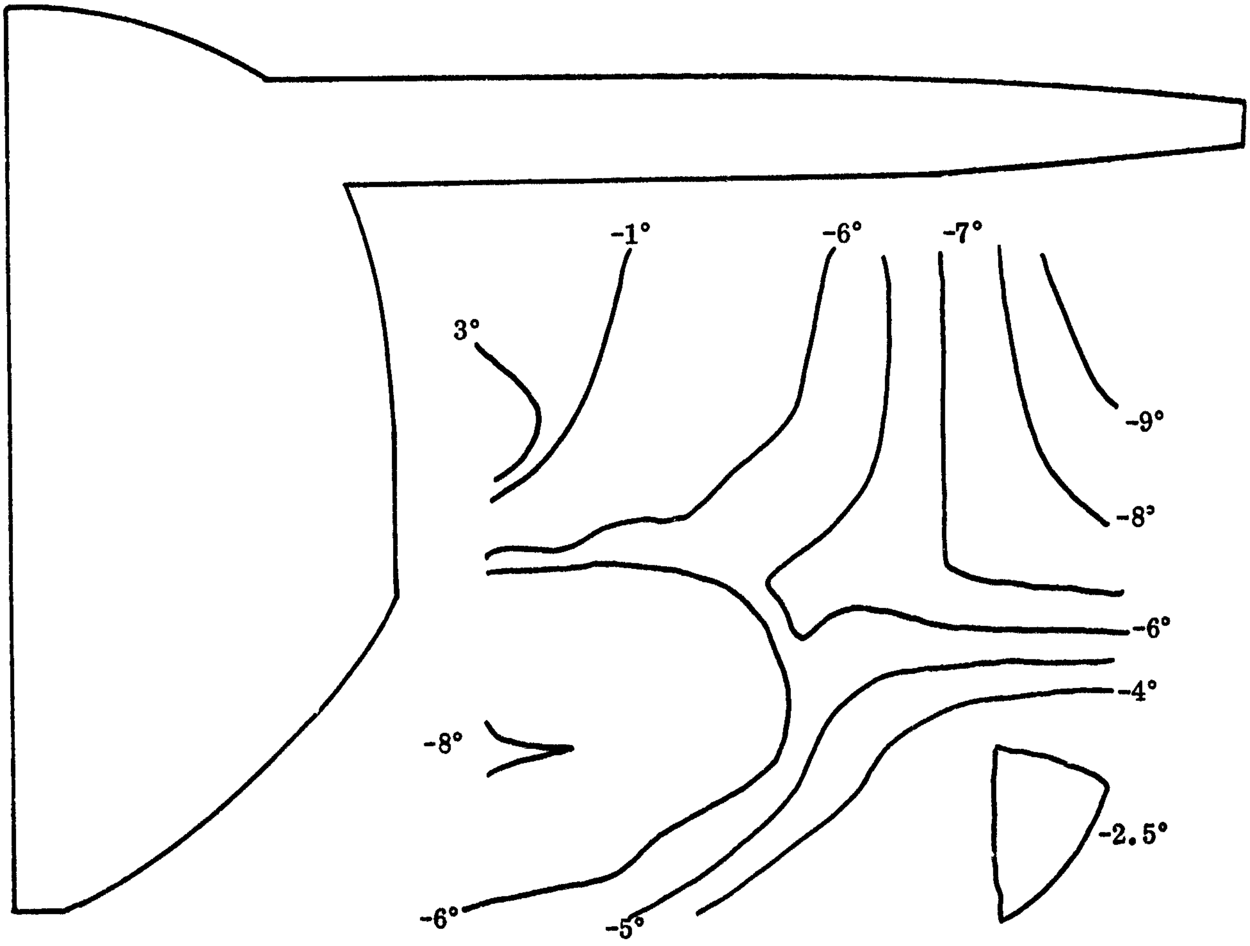

Figure 7-189. Sidewash Angle

Fuselage 8
PCPN
Mach Number = 2.2
α = 10°
Format IV

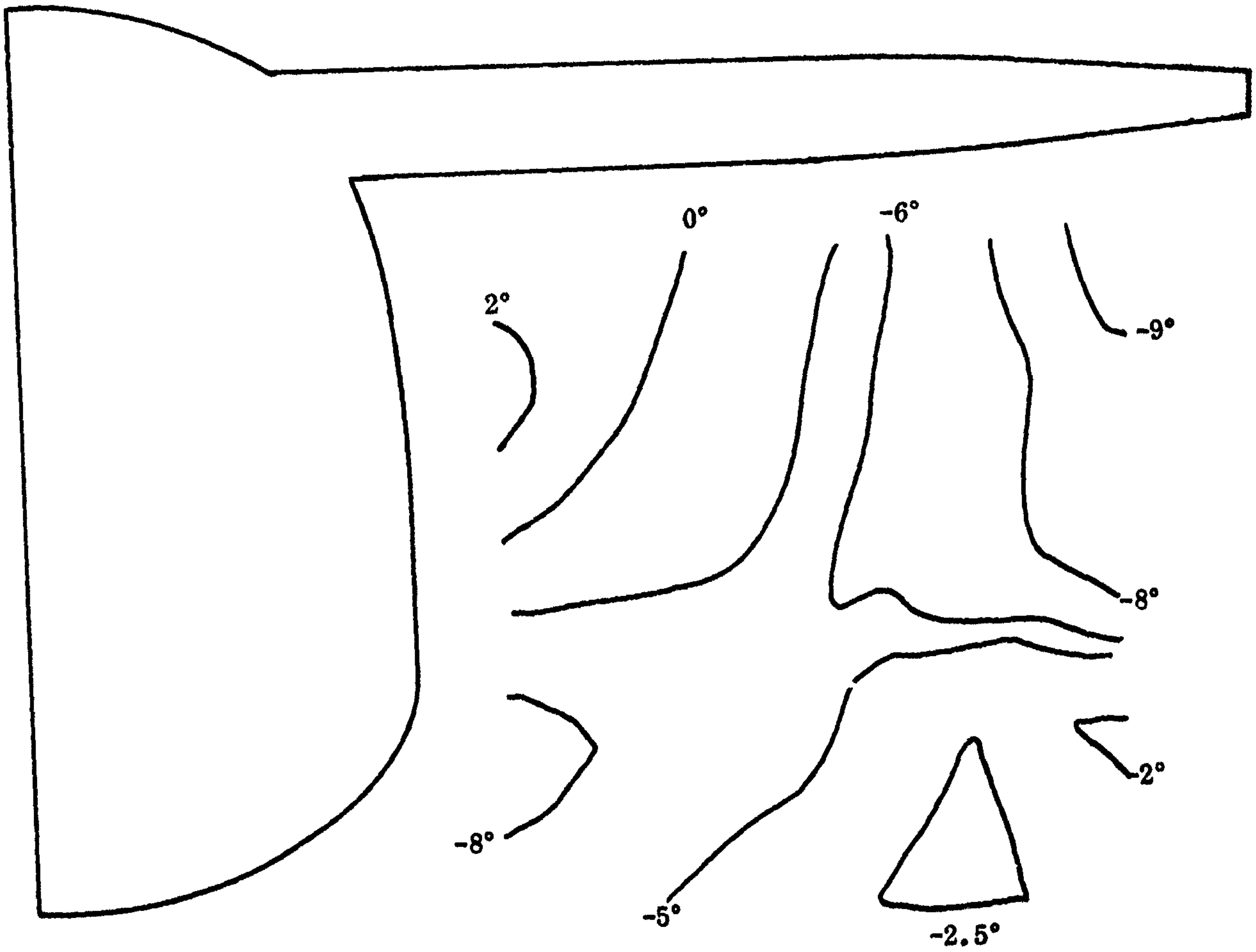

Figure 7-190. Sidewash Angle

Fuselage 1
PCPN
Mach Number = 2.5°
α = 0°
Format IV

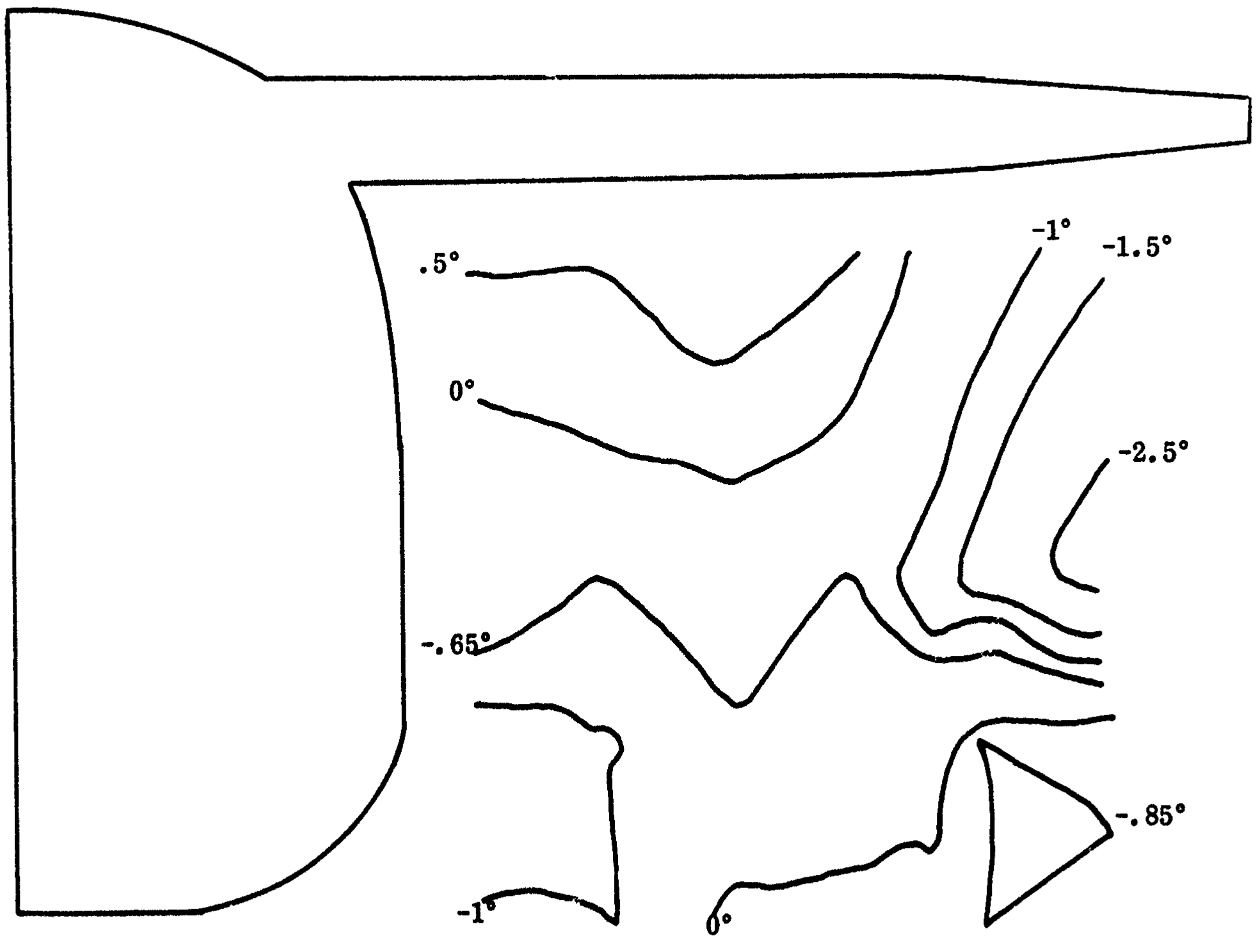

Figure 7-191. Local Flow Angularity

Fuselage 1
PCPN
Mach Number = 2.5°
α = 10°
Format IV

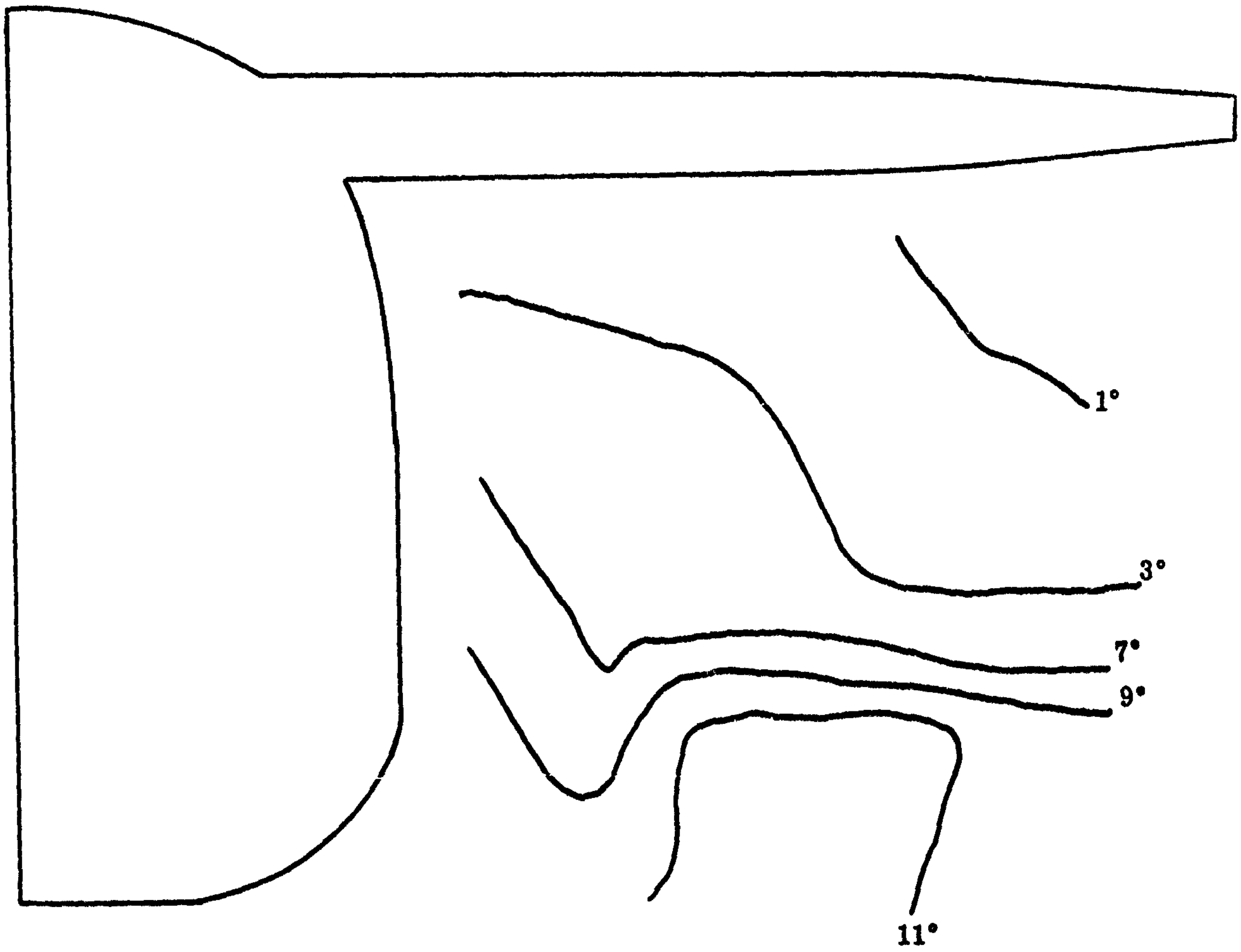

Figure 7-192. Local Flow Angularity

Fuselage 1
PCPN
Mach Number = 2.5
α = 20°
Format IV

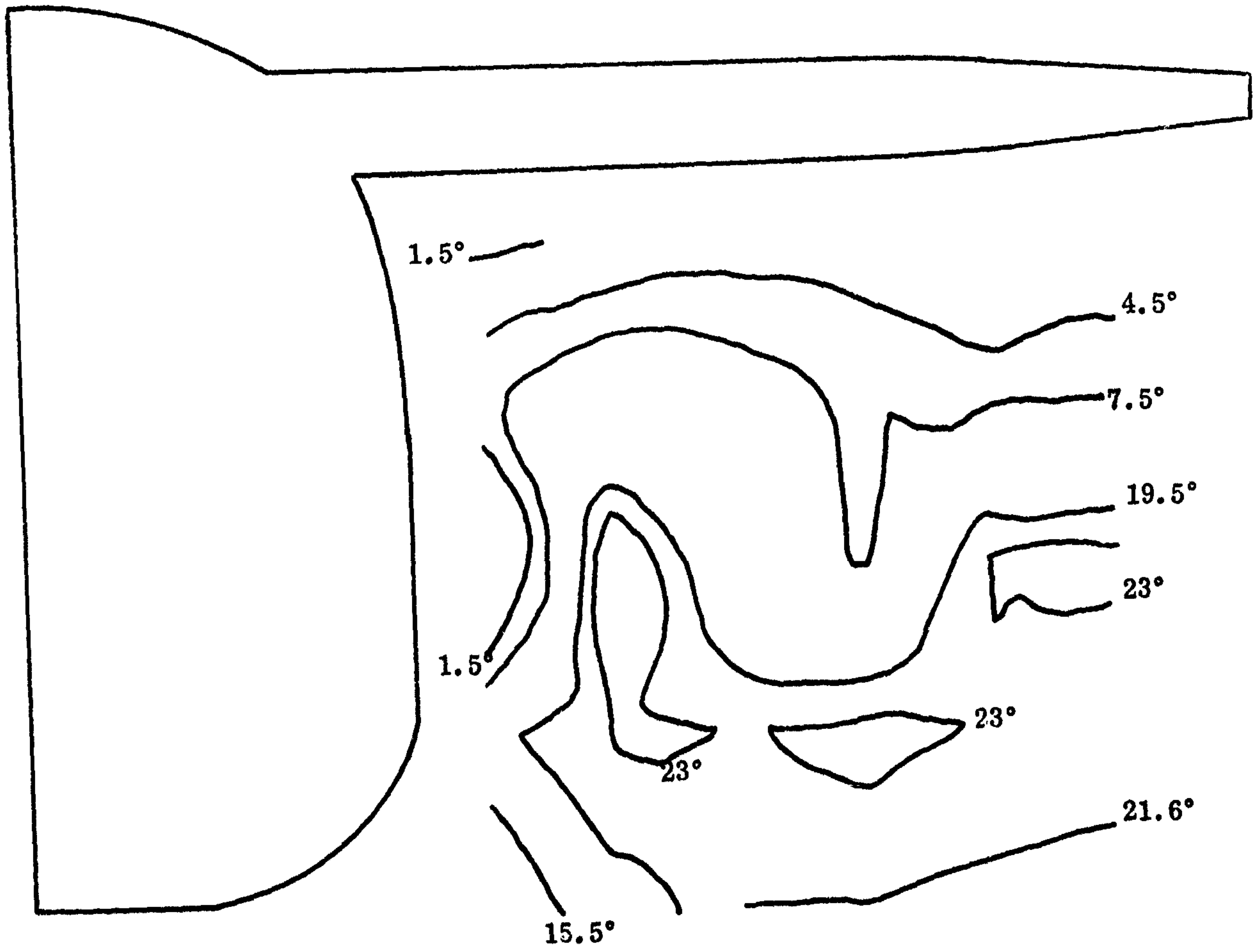

Figure 7-193. Local Flow Angularity

Fuselage 1
PCPN
Mach Number = 2.5
$\alpha = 0°$
Format IV

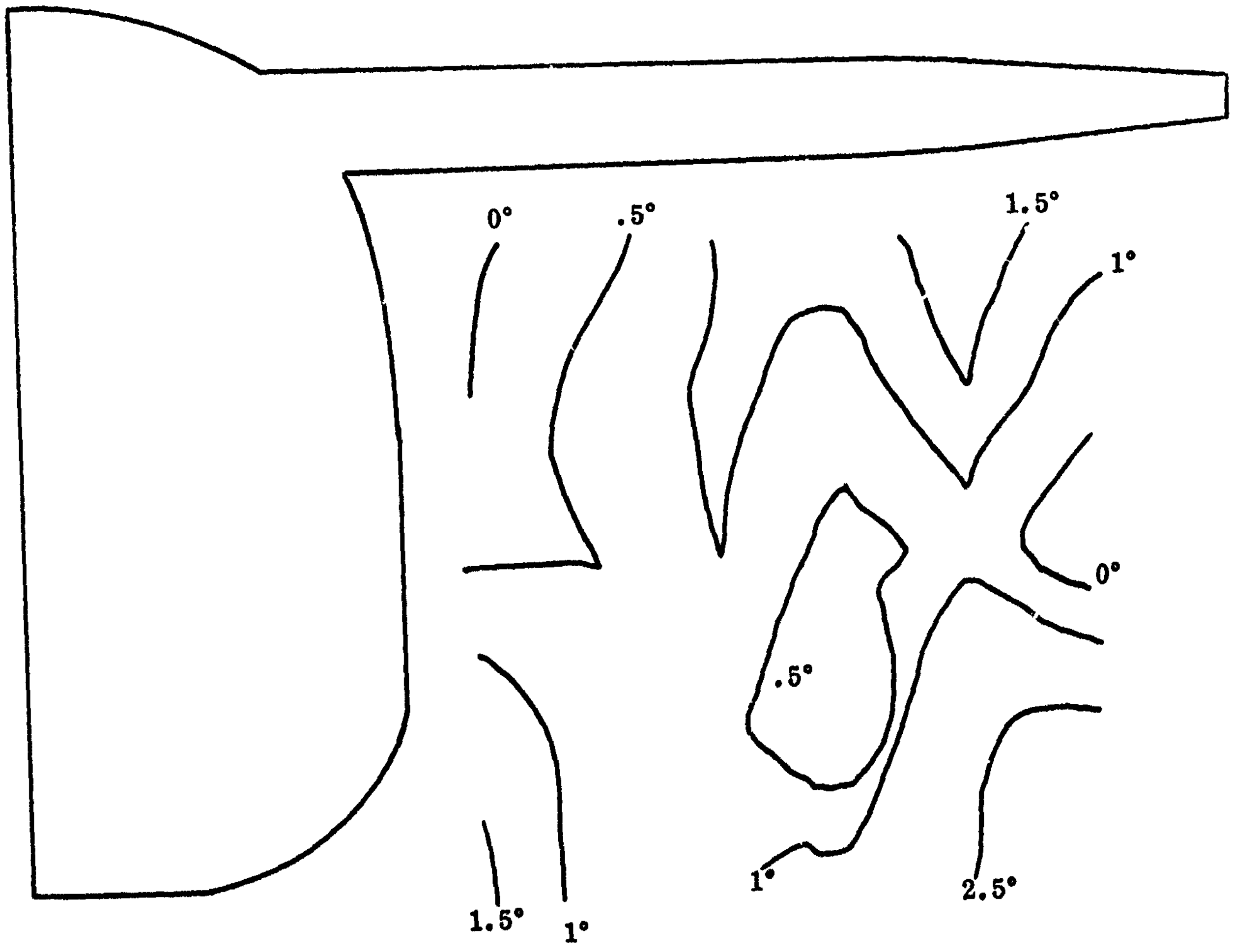

Figure 7-194. Sidewash Angle

Fuselage 1
PCPN
Mach Number = 2.5
α = 10°
Format IV

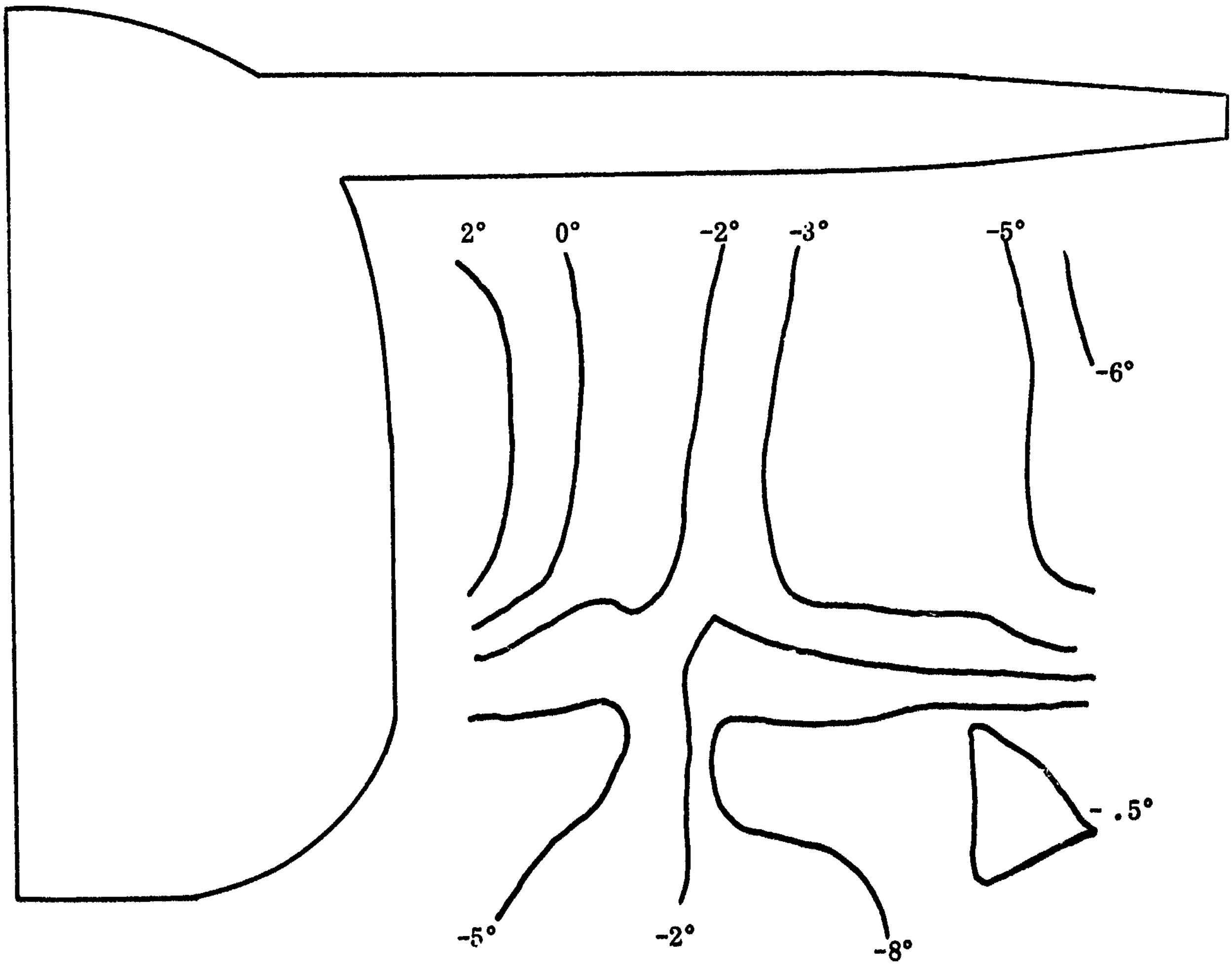

Figure 7-195. Sidewash Angle

Fuselage 1
PCPN
Mach Number = 2.5
α = 20°
Format IV

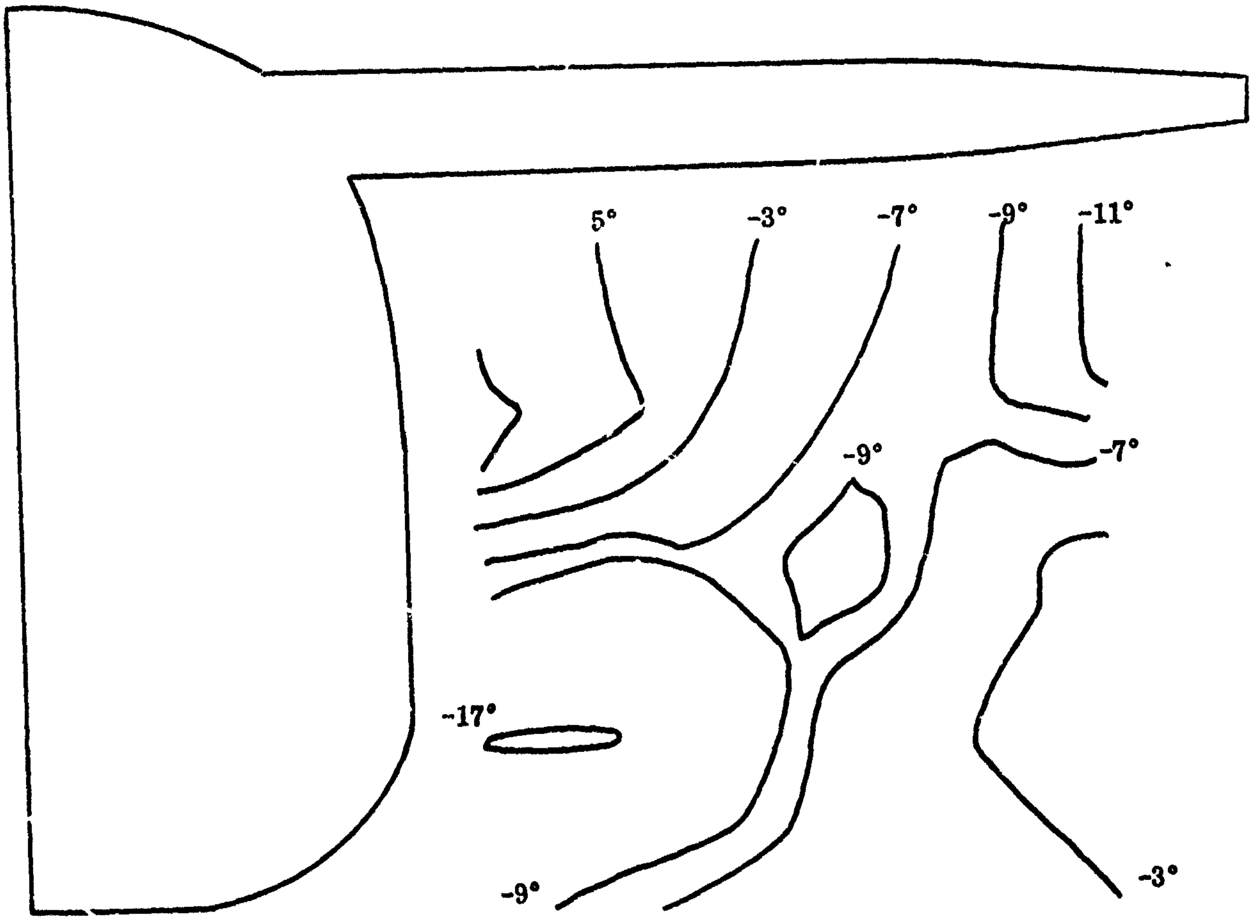

Figure 7-196. Sidewash Angle

Fuselage 4
PCPN
Mach Number = 2.5
α = 0°
Format IV

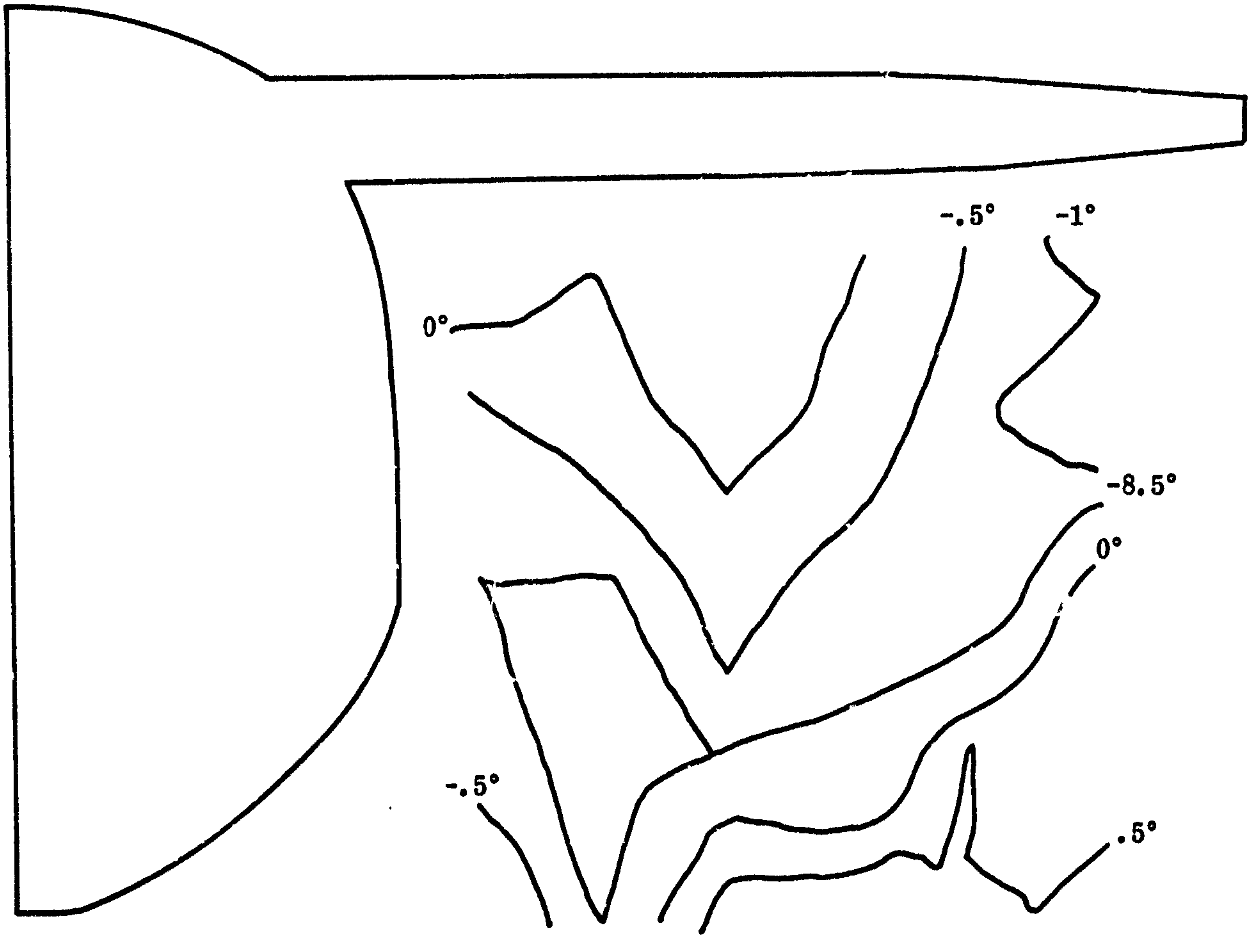

Figure 7-197. Local Flow Angularity

Fuselage 4
PCPN
Mach Number = 2.5
$\alpha = 10°$
Format IV

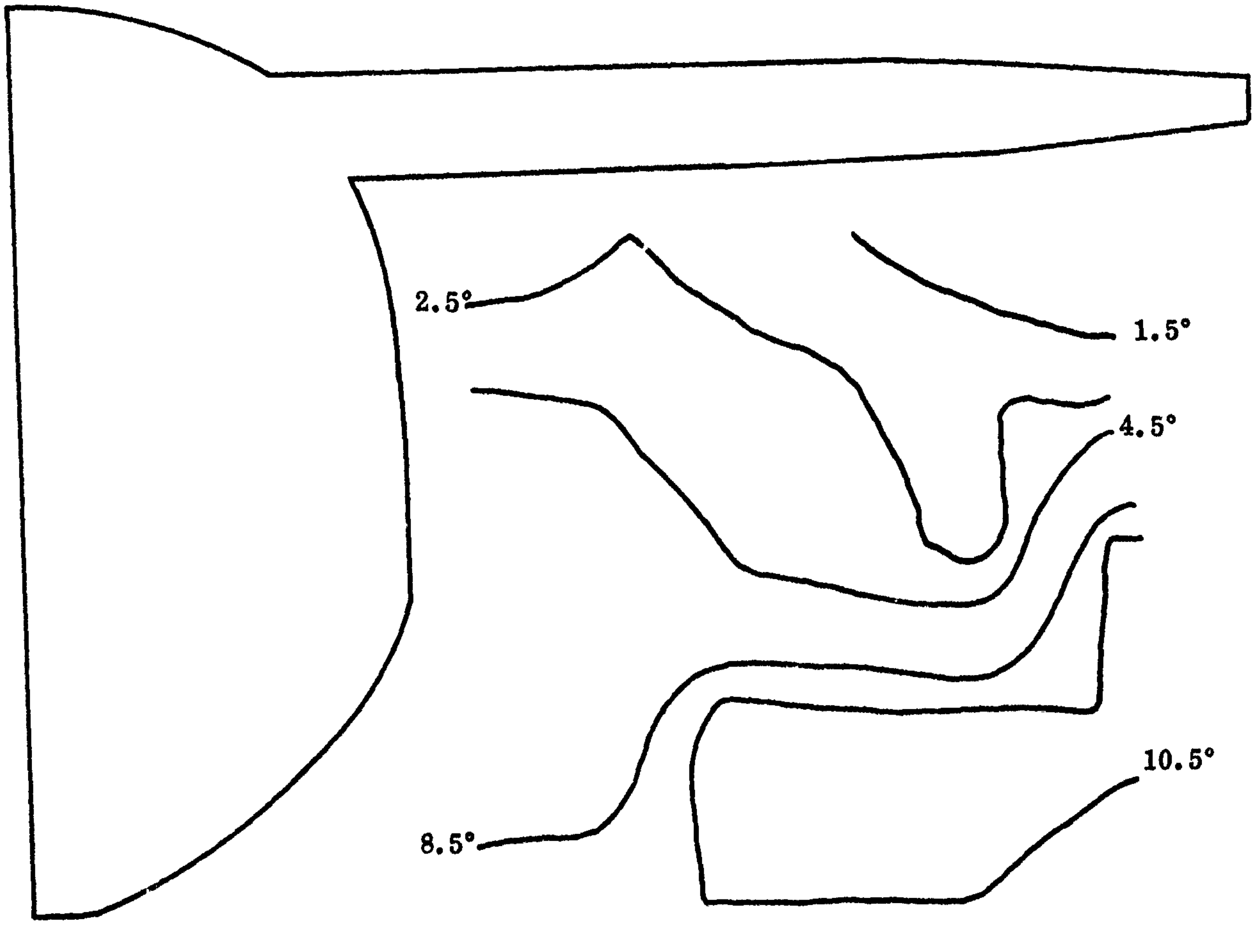
2.5°
1.5°
4.5°
10.5°
8.5°

Figure 7-198. Local Flow Angularity

Fuselage 4
PCPN
Mach Number = 2.5
$\alpha = 20°$
Format IV

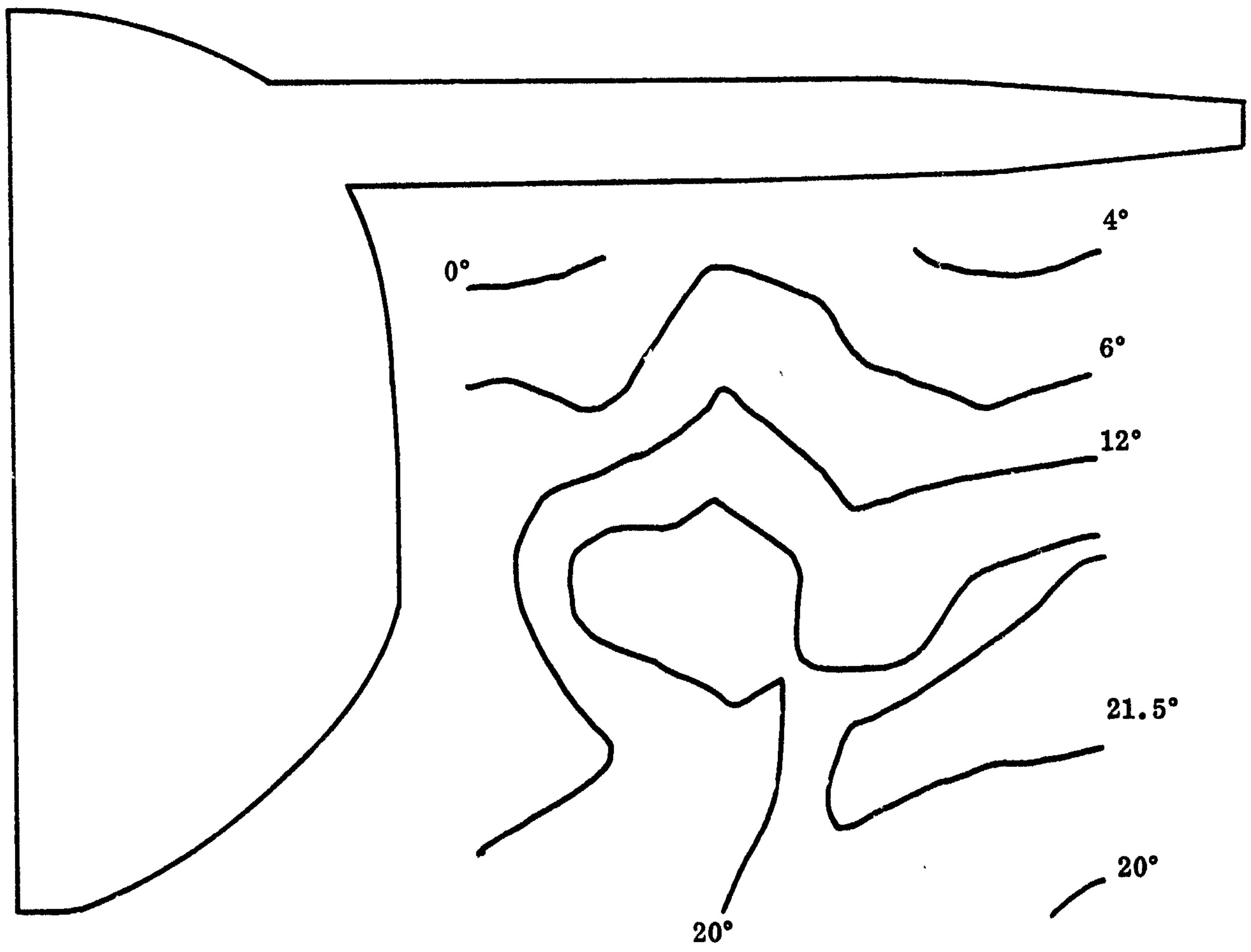

Figure 7-199. Local Flow Angularity

Fuselage 4
PCPN
Mach Number = 2.5
$\alpha = 0°$
Format IV

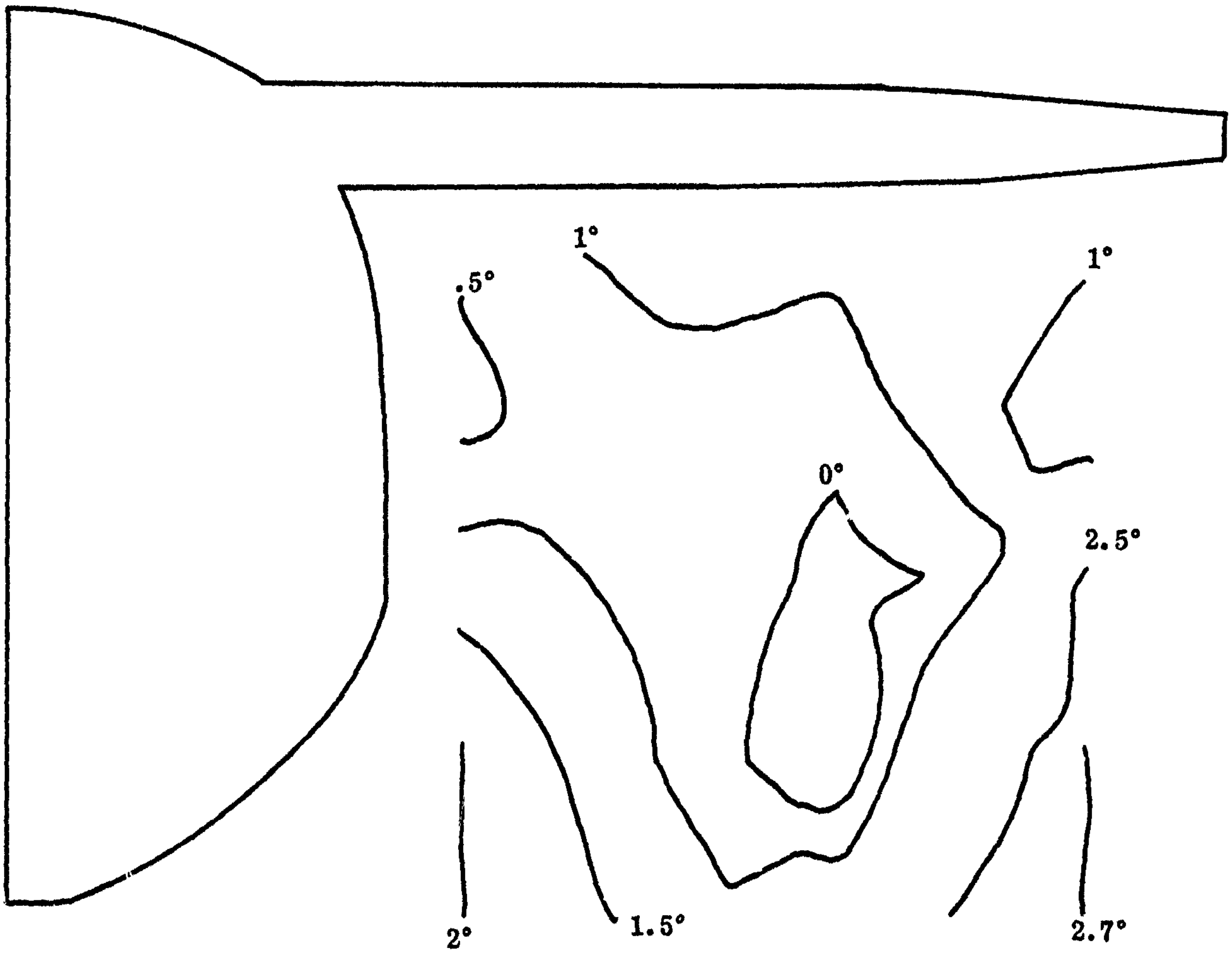

Figure 7-200. Sidewash Angle

Fuselage 4
PCPN
Mach Number = 2.5
$\alpha = 10°$
Format IV

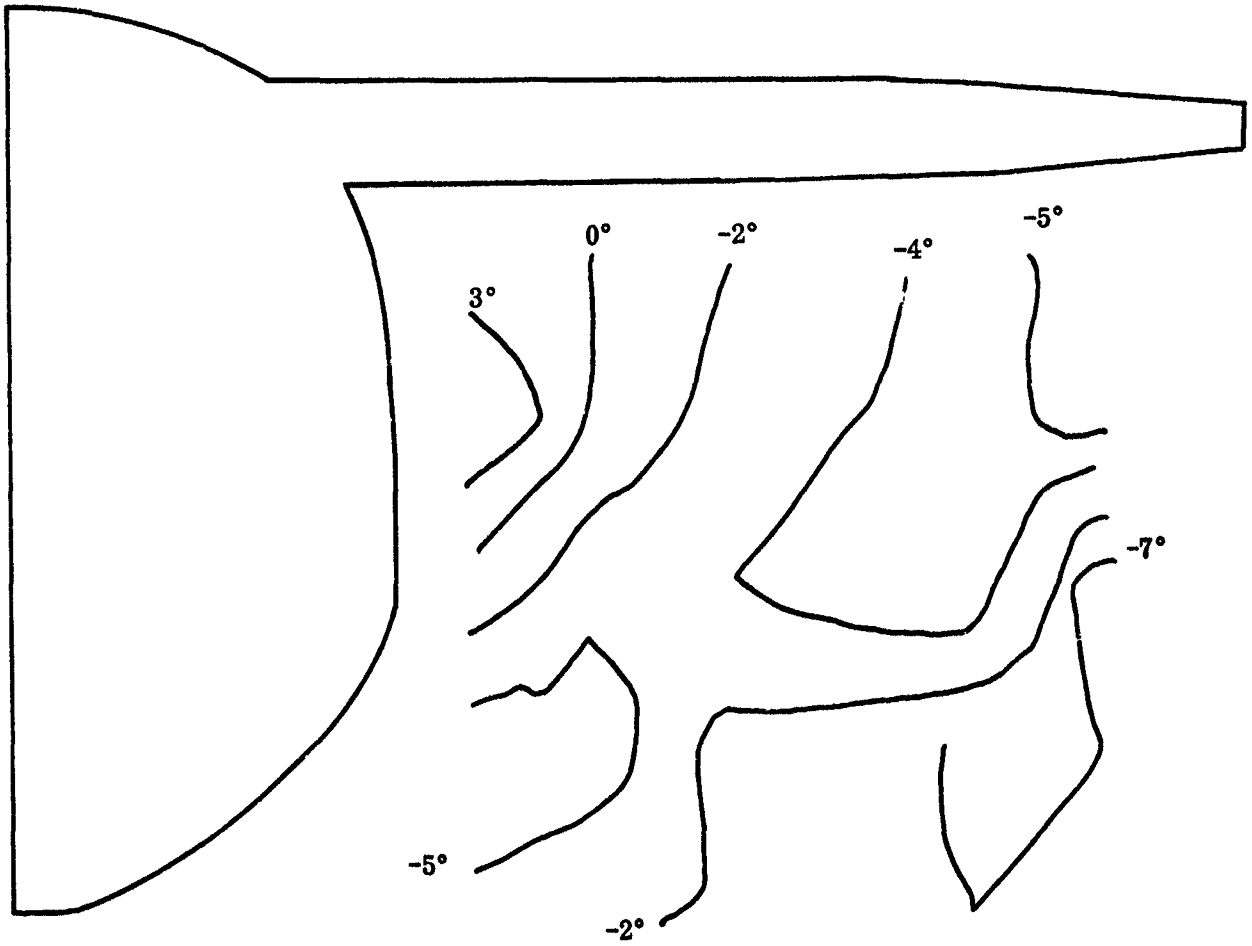

Figure 7-201. Sidewash Angle

Fuselage 4
PCPN
Mach Number = 2.5
$\alpha = 20°$
Format IV

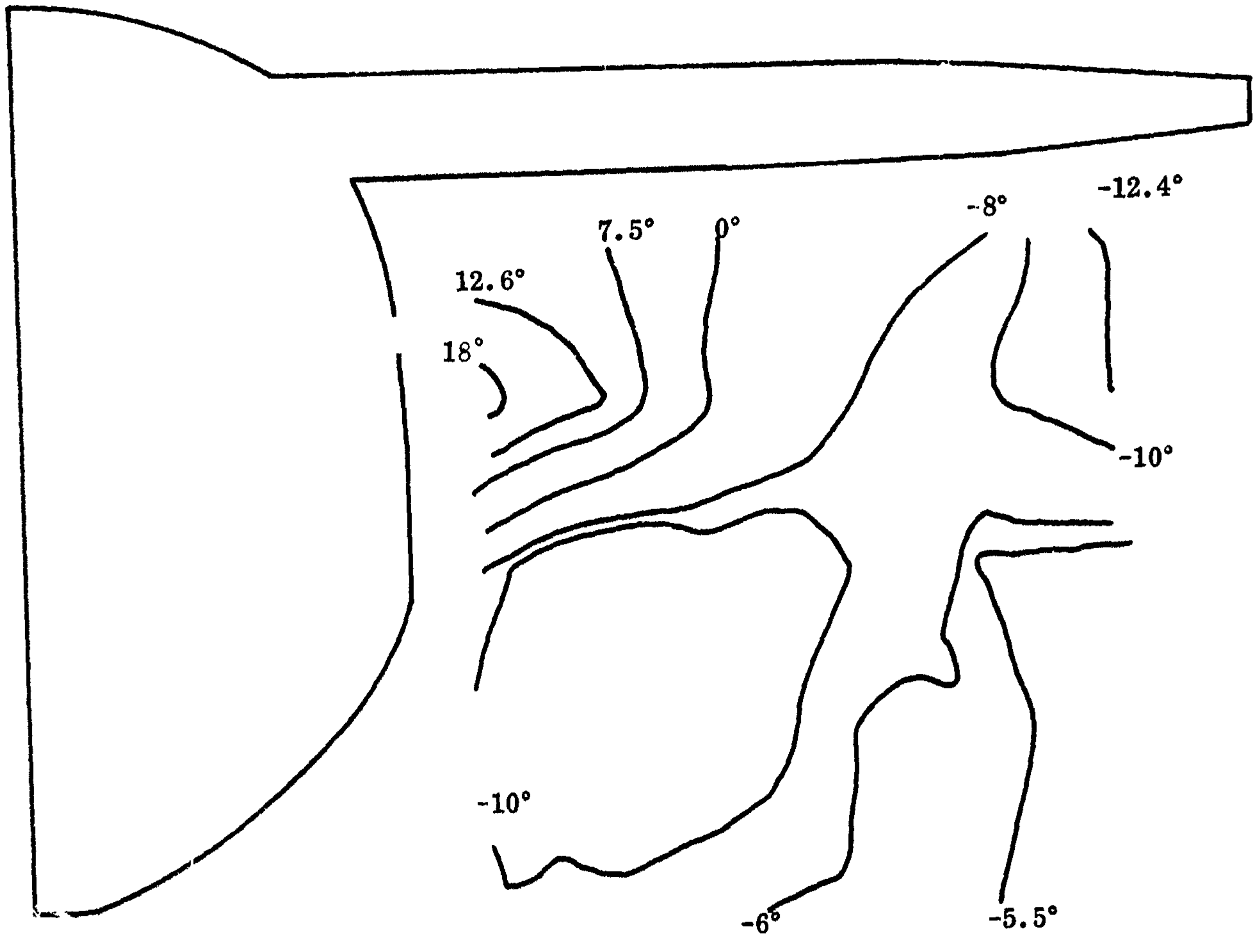

Figure 7-202. Sidewash Angle

attributable to the smaller span of the 65° wing, at the survey station, causing a more inboard relief of the wing under pressure and a consequent increase in negative sidewash. The more highly swept 65° wing is more efficient (lower drag) and the downstream Mach number and total pressure are therefore higher.

7.3 Inlet Alone (Data Format V)

7.3.1 General

This portion of the test program was devoted to an evaluation of the uninstalled two-dimensional and axisymmetric inlets. These tests were conducted across the entire Mach number and angle of attack spectrum to obtain baseline inlet performance data. The resultant performance was also compared with the analytical predictions to evaluate the accuracy of the analytical technique and to uncover any inherent inlet operational characteristics.

The comparisons made between experiment and theory have been made as shown in Figure 7-203. The theoretical performance was calculated at the critical inlet operating point. For an inviscid analysis the supercritical leg was then established as a vertical line because the terminal shock is inside the duct and the spillage does not vary with shock position. The total pressure recovery, for this mode, varies inversely with terminal shock strength. For the subcritical mode, with the terminal shock expelled, the mass flow decreases. The total pressure recovery can either increase or decrease, depending upon the local flow environment established by the external compression system presented to the terminal shock and the variation in diffuser Mach number as a function of mass flow. For simple external compression systems this variation is usually small; thus, the subcritical leg can be represented by a horizontal line. For a simplified analysis, the characteristic cane presenting total pressure recovery versus mass flow ratio can therefore be approximated by extending a horizontal and vertical line from the critical point, as shown in the sketch.

There are effects, predominantly viscous in nature, that may result in an experimentally derived characteristic cane that deviates from this simplified approximation. For a particular inlet concept the deviation is generally a function of Mach number and angle of attack. Within any conceptual approach it is, of course, uniquely tied to the particular geometry being employed. For the analysis of a particular inlet

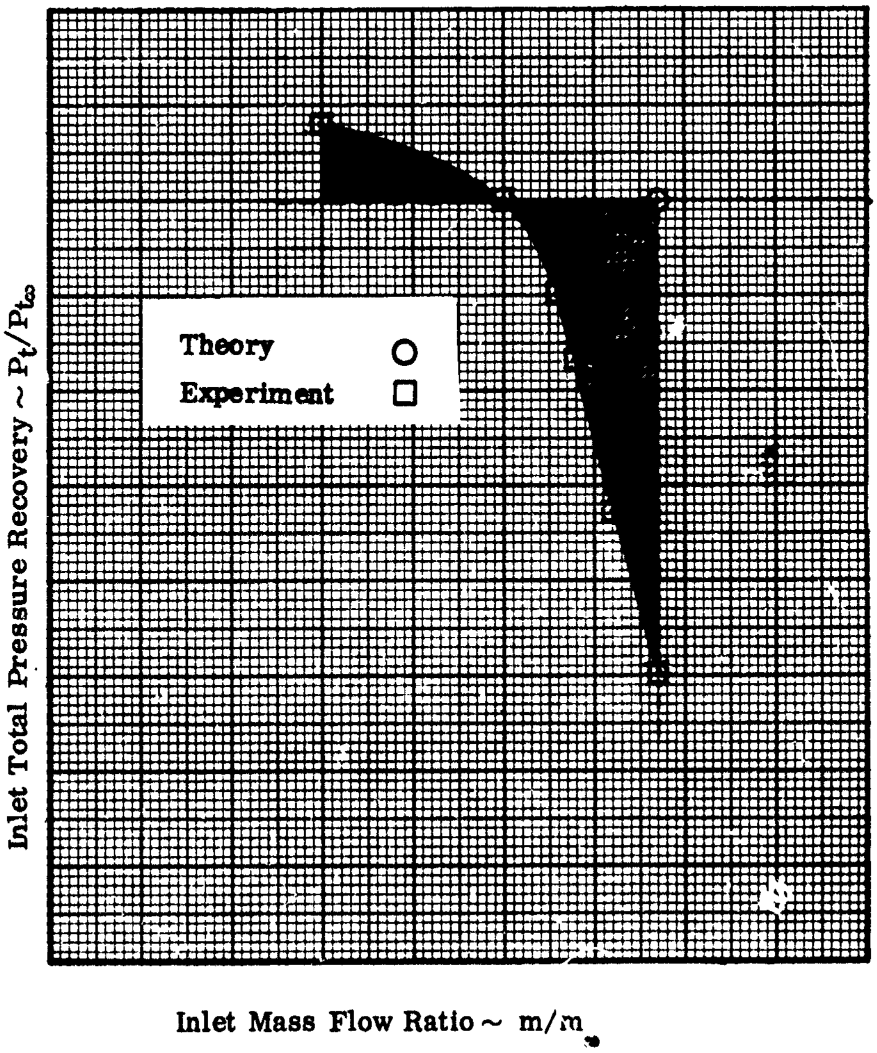

Figure 7-203. Comparison of Theory and Experiment ~ Schematic

design this relationship between simplified theory and experiment represents a useful tool, helpful in evaluating the inherent inlet characteristics. However, when using a specific inlet design to assess the ability of a generalized analytical technique to predict the inlet performance, two factors are apparent. The analytical technique, because of its simplified approach does not account for the viscous effects, which are obviously present in the real inlet. Because of its generalized nature this type of analysis cannot account for the unique effects related to the geometry of a particular design. It is therefore necessary that the comparison between theory and experiment account for these differences. The approach adopted was to compare the critical experimental total pressure recovery with the estimated total pressure recovery; however, the estimated mass flow ratio was compared with the supercritical experimental mass flow ratio. In this manner the viscous and geometry effects of the experimental model (shaded area, Figure 7-203) do not distort the comparison.

The theoretical characteristic curves to be shown in succeeding sections have been derived in this way.

7.3.2 Two-Dimensional Inlet

7.3.2.1 Inlet Mass Flow Ratio Correlation

Presented in Figures 7-204 through 7-208 are comparisons of inlet mass flow ratio. The experimental values shown represent supercritical mass flow ratios, selected using the rationale established in Section 7.3.1. The theoretical values represent the results of the inlet design task described in Section III. Inspection of these curves indicates excellent agreement between the predicted and experimental mass flow ratios. The lone exception is 1.2.

This agreement between predicted and experimental mass flow ratio was anticipated. The classical two-dimensional configuration, oriented to compensate for angle of attack, lends itself to the use of simplified wave theory in the determination of the boundary slipline. The variation in capture area, as a function of angle of attack, is derived accurately by simple trigonometric functions. The potential influence of viscous cross flow effects upon the predictive accuracy of an inviscid analysis is minimal in this case, where the compression surface orientation realigns the flow.

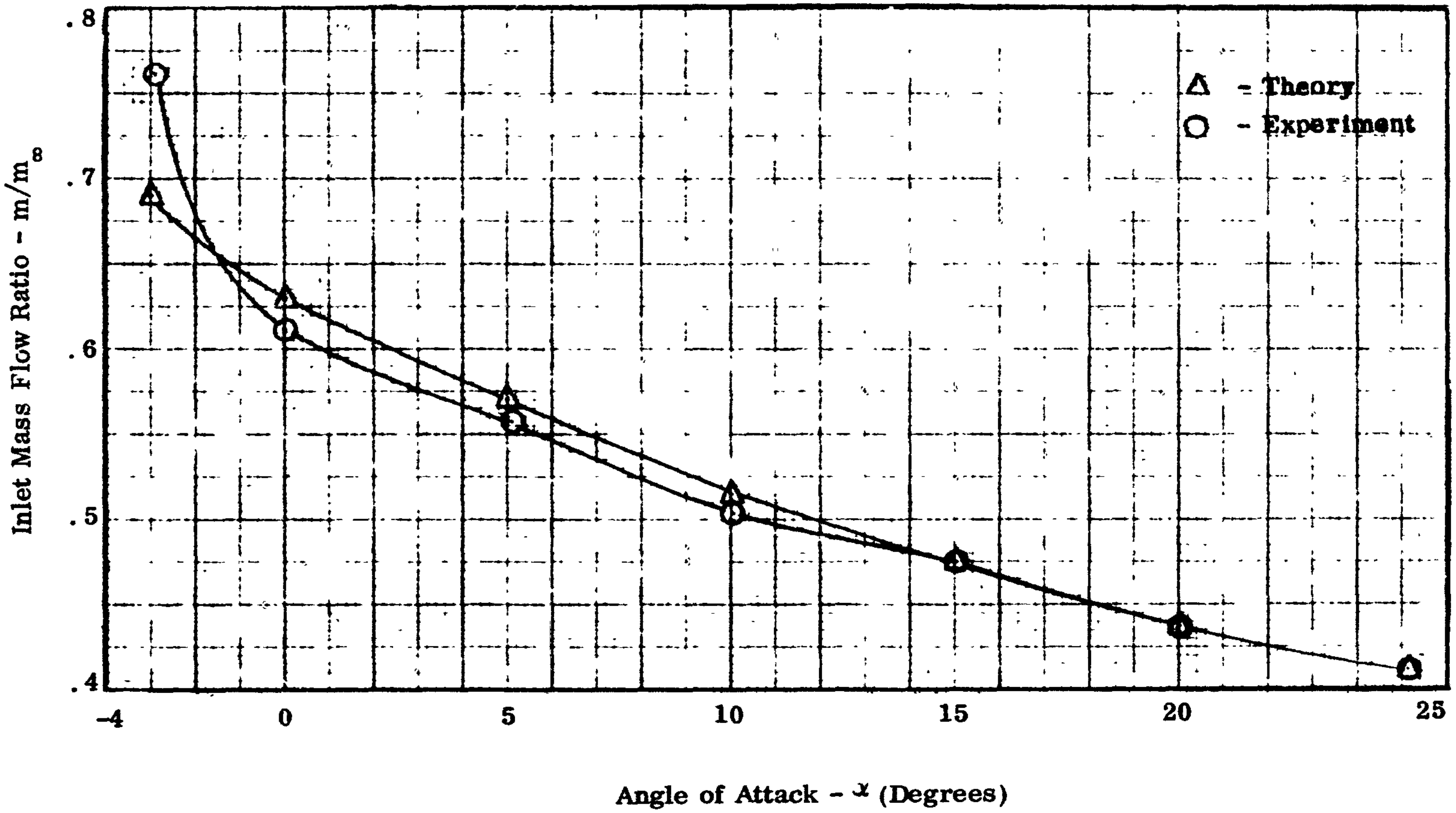

Figure 7-204. Comparison of Theory and Experiment, Format V, 2-Dimensional Inlet $M_\infty = .8$

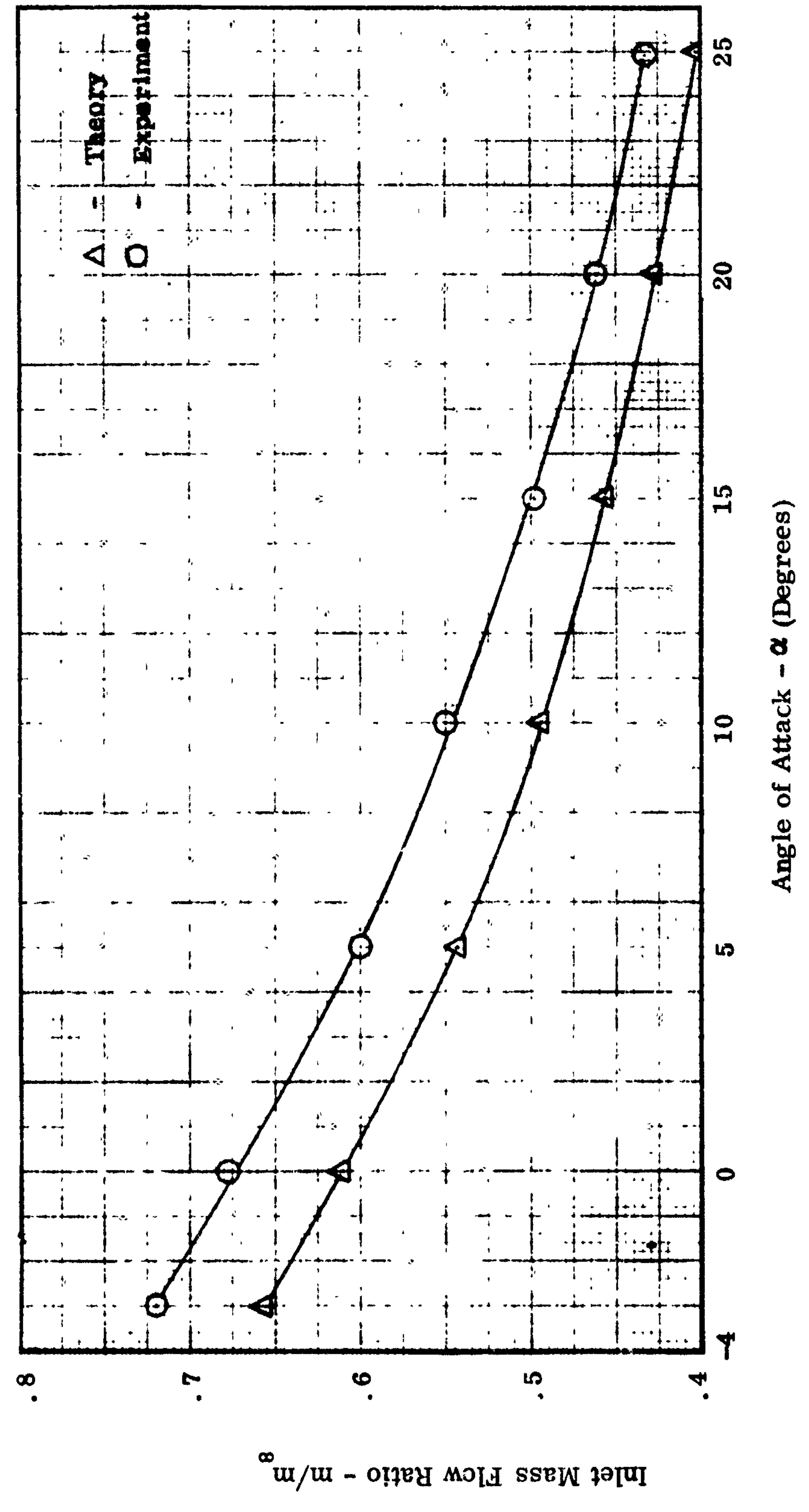

Figure 7-205. Comparison of Theory and Experiment, Format V, 2-Dimensional Inlet, $M_\infty = 1.2$

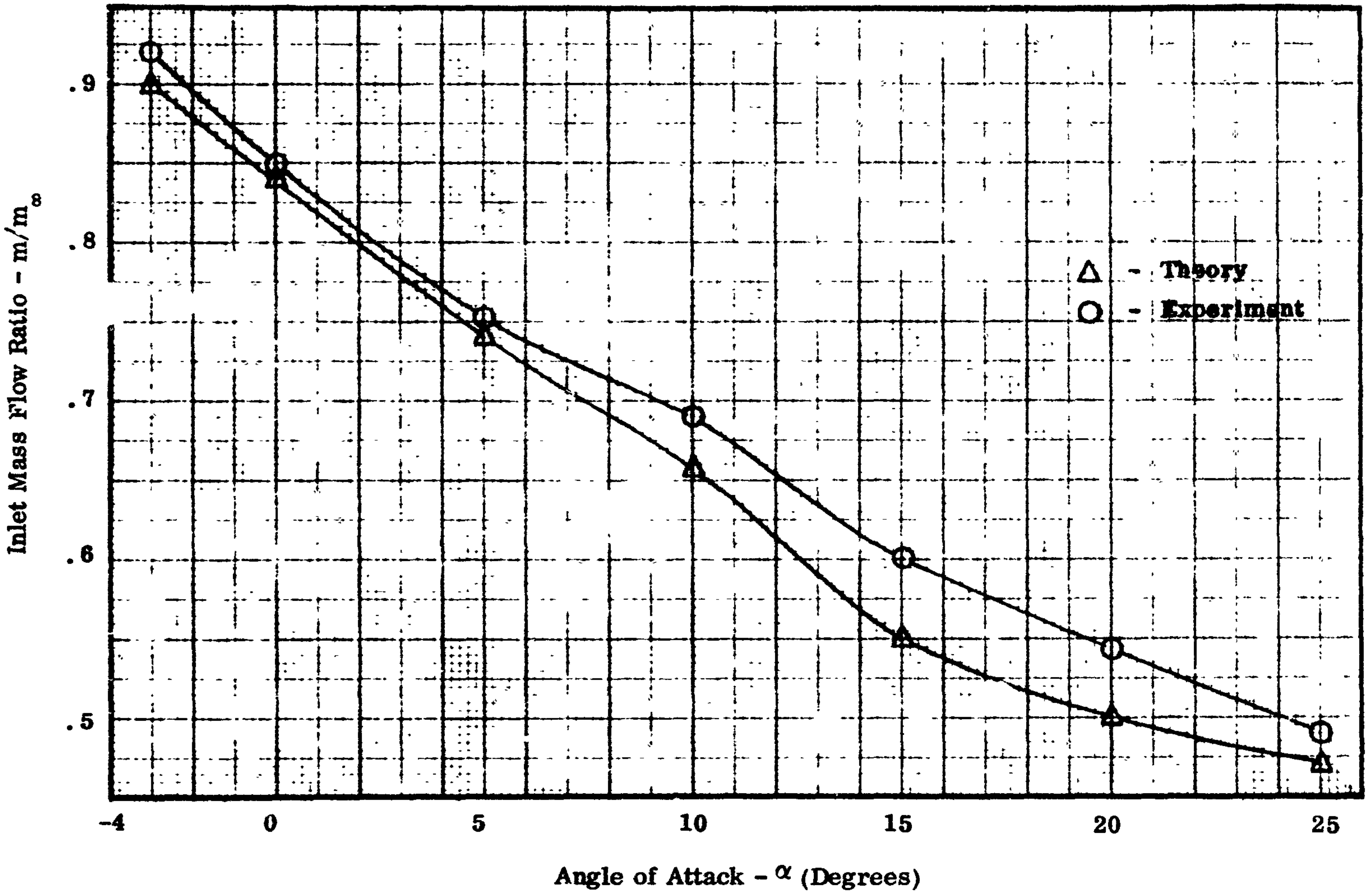

Figure 7-206. Comparison of Theory and Experiment, Format V, 2-Dimensional Inlet, $M_\infty = 1.8$

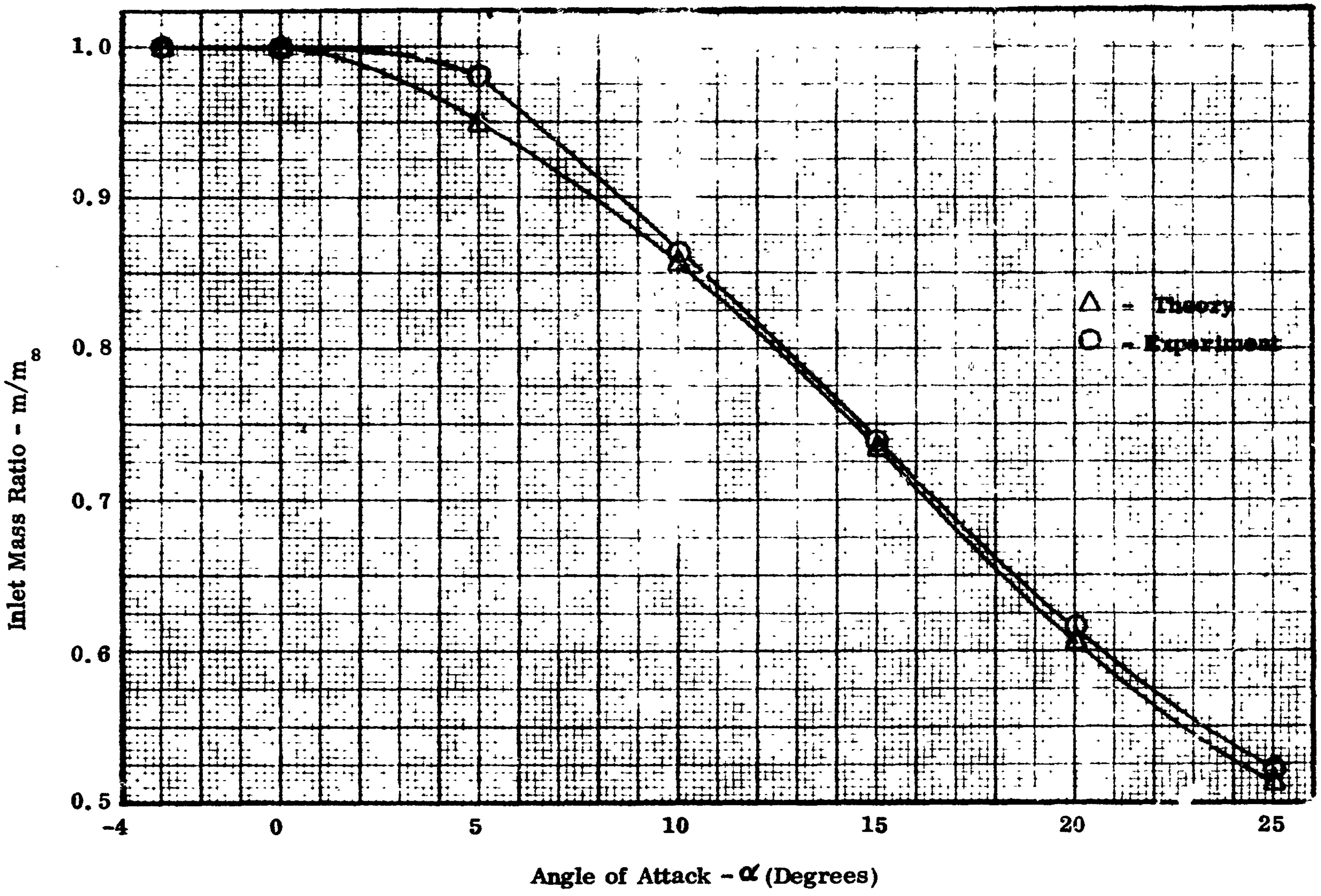

Figure 7-207. Comparison of Theory and Experiment, Format V, 2-Dimensional Inlet, $M_\infty = 2.2$

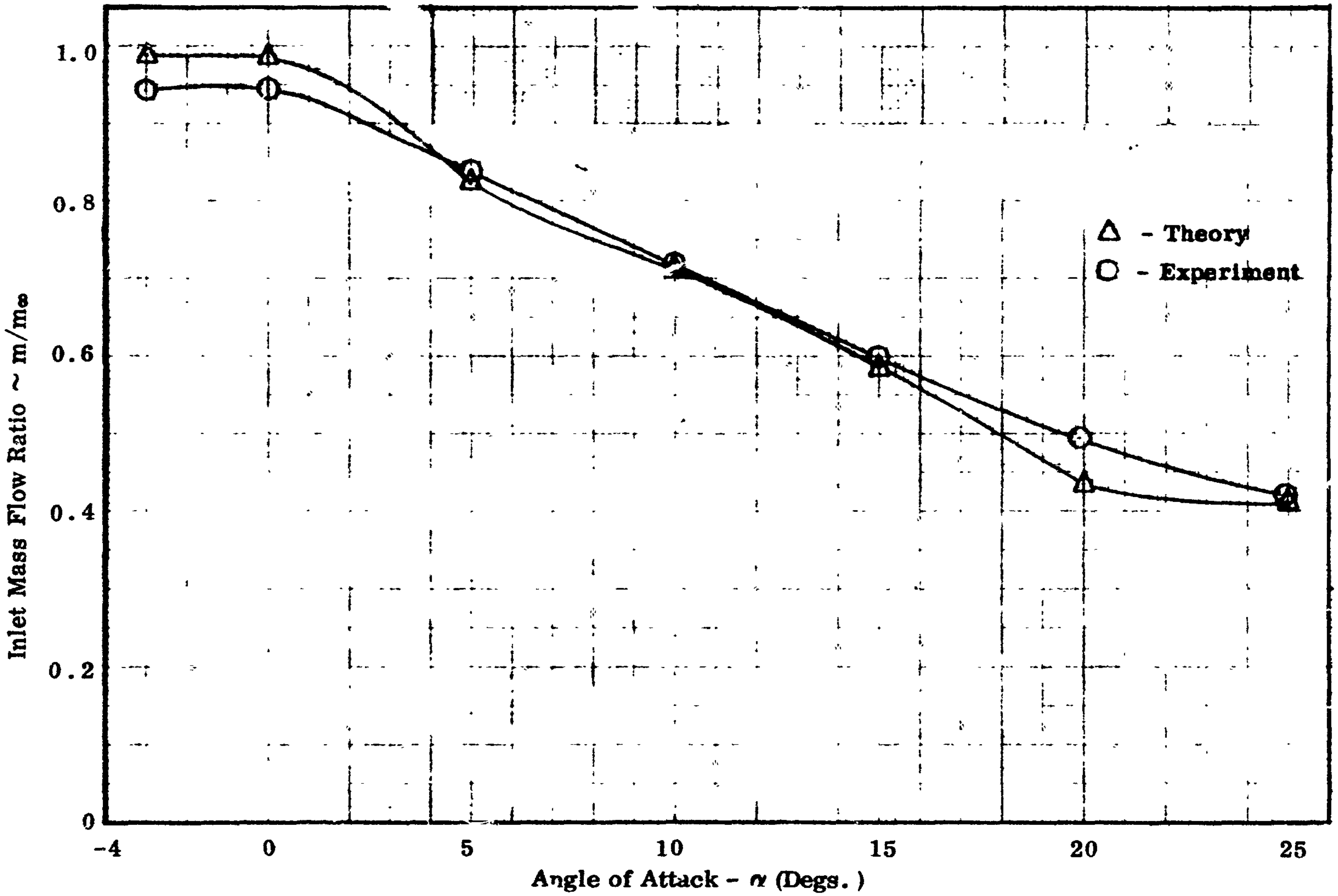

Figure 7-208. Comparison of Theory and Experiment, Format V, 2-Dimensional Inlet
$M_\infty = 2.5$

There is one weak trend evident at all Mach numbers namely, a tendency for the experimental mass flows to exceed theoretical predictions. This can probably be associated with manufacturing tolerances. For example, a slightly undersized duct area at the total head rake station would result in a local Mach number higher than predicted, however, the data reduction program contains the design duct area and this combination of computed Mach number and design duct area would yield experimental mass flows that are slightly on the high side.

Based upon the comparison of theory and experiment three general design guidelines can be postulated for the inlet concept under study.

- For subsonic freestream Mach numbers the inlet mass flow ratio can be predicted quite accurately using a one-dimensional analysis.

  This is shown by the results achieved at $M_\infty = 0.8$.

- For supersonic Mach numbers where theory predicts a mixed supersonic/subsonic inlet external flow field, the mass flow ratio is strongly affected by the curvature of the boundary streamline between the external normal shock and the cowl lip. The accuracy of any mass flow prediction depends upon how well this streamline curvature is estimated.

  For the subject tests a mixed flow field existed at Mach 1.2 at all angles of attack and at Mach 1.8 for high angles of attack. It was at these conditions that the poorest correlation was achieved.

- For supersonic Mach numbers with a supersonic inlet external flow field predicted, the use of simplified wave theory results in an accurate estimate of inlet mass flow ratio.

  The comparison of experiment and theory at Mach 1.8 for low angles of attack, and Mach 2.2 and 2.5 support this conclusion.

7.3.2.2 Inlet Total Pressure Recovery Correlation

Presented in Figures 7-209 through 7-213 are comparisons of experimental and theoretical inlet total pressure recovery.

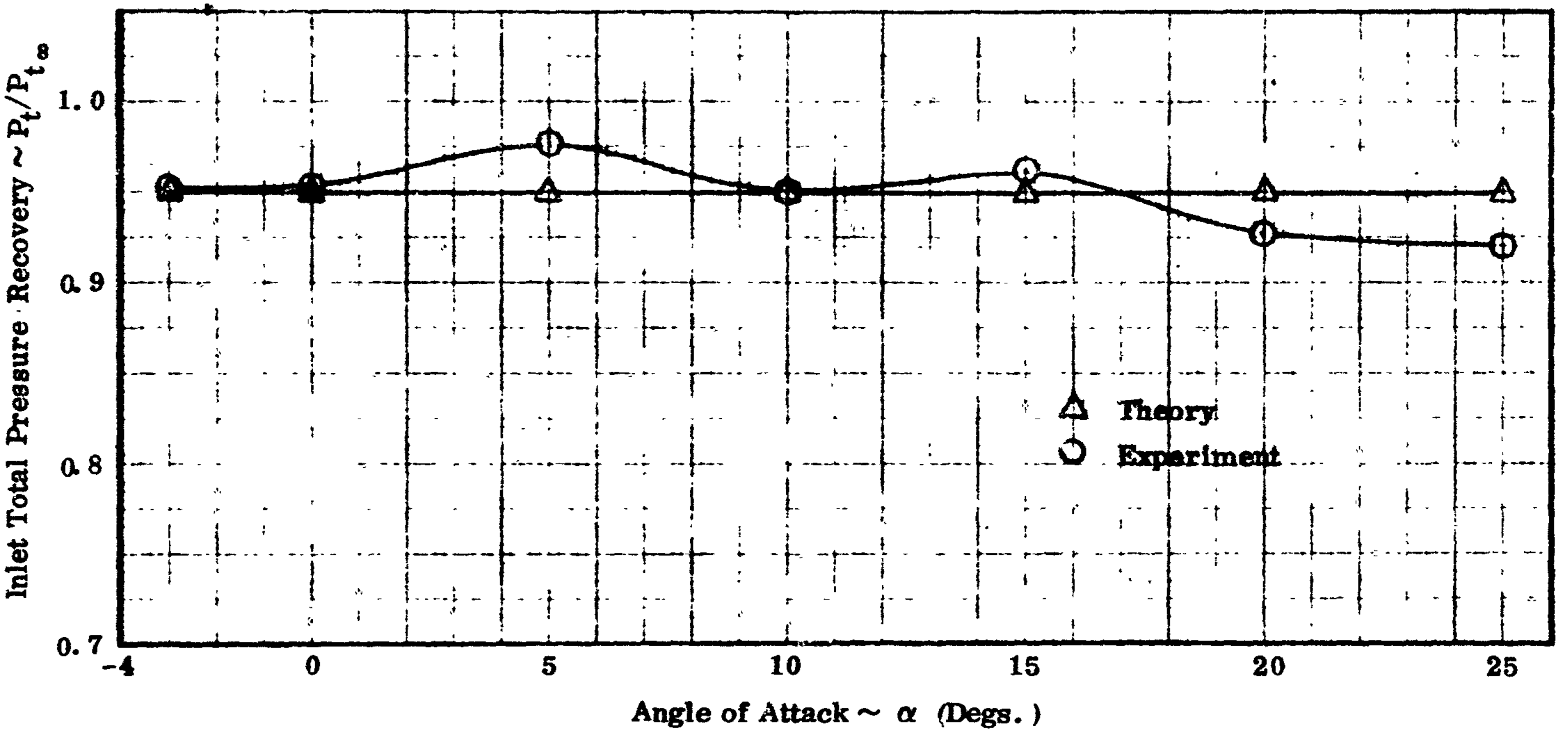

Figure 7-209. Comparison of Theory and Experiment, Format V, 2-Dimensional Inlet
$M_\infty = 0.8$

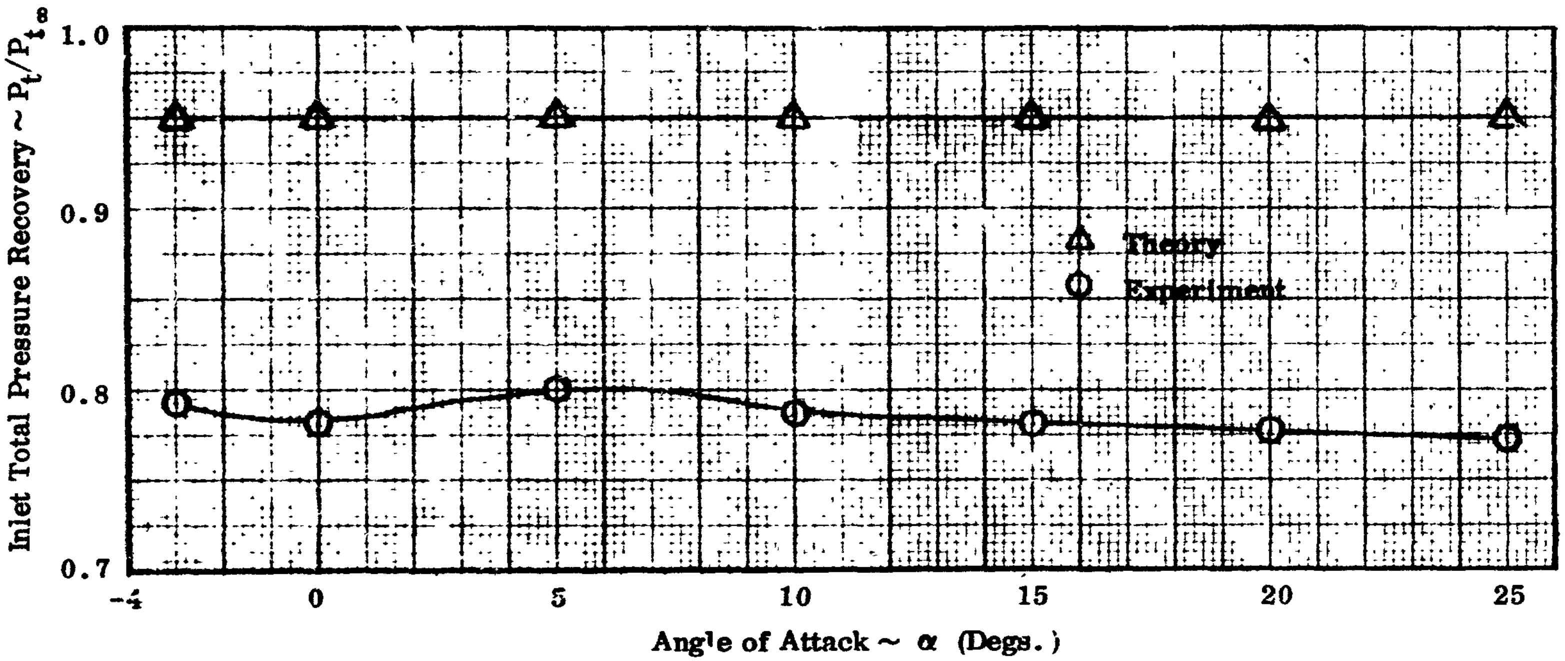

Figure 7-210. Comparison of Theory and Experiment, Format V, 2-Dimensional Inlet
$M_\infty = 1.2$

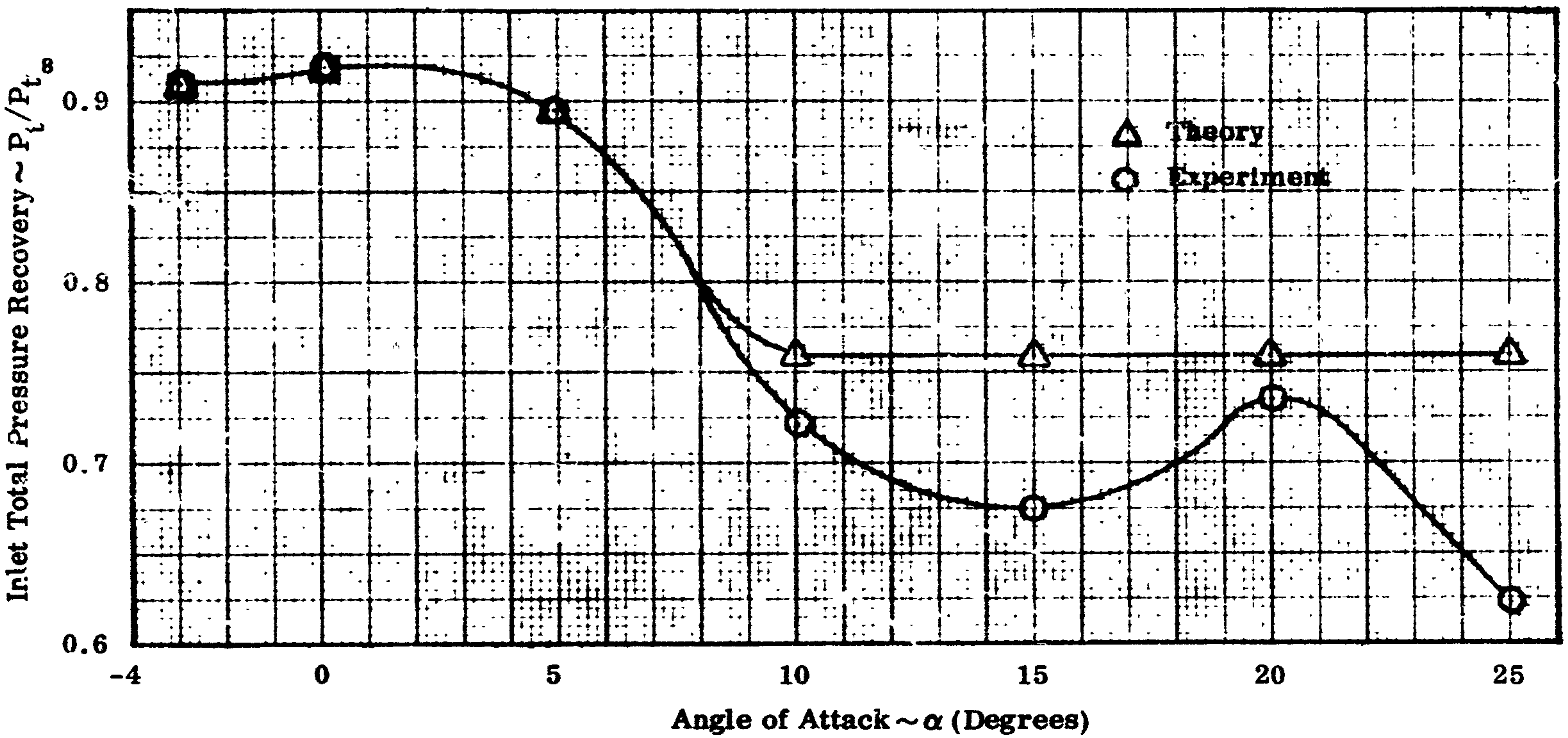

Figure 7-211. Comparison of Theory and Experiment, Format V. 2- Dimensional Inlet

$M_\infty = 1.8$

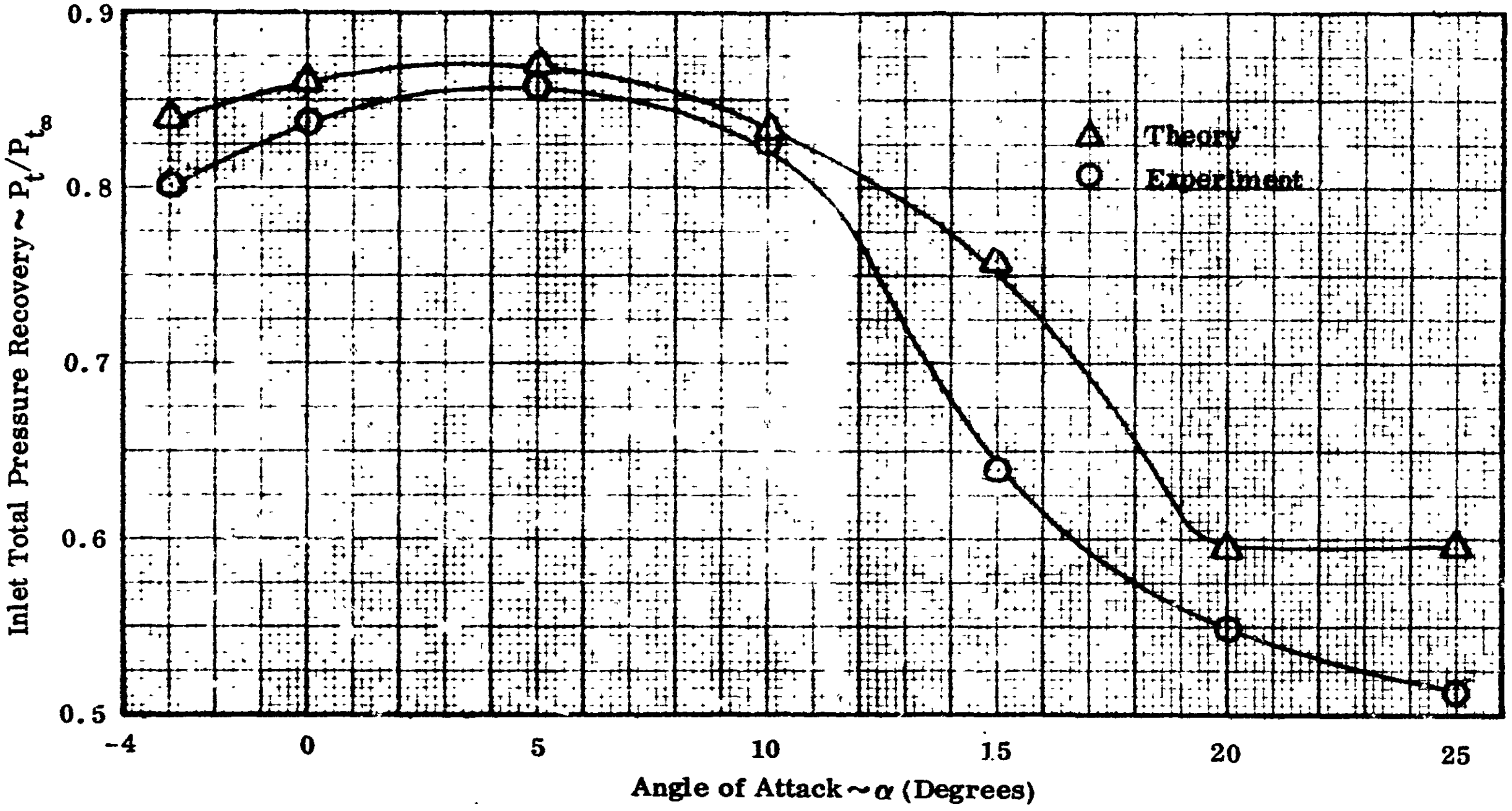

Figure 7-212. Comparison of Theory and Experiment, Format V, 2-Dimensional Inlet

$M_\infty = 2.2$

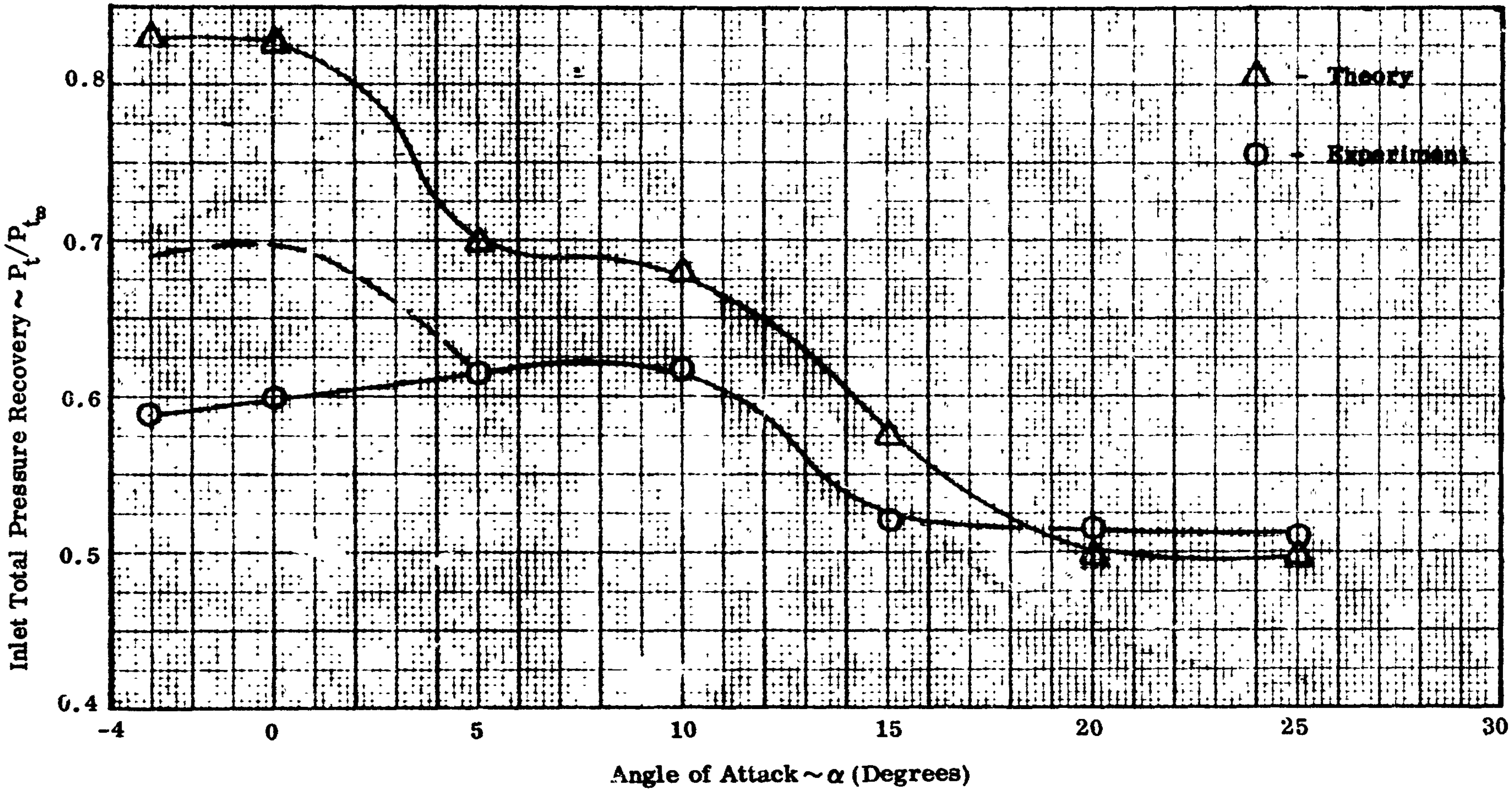

Figure 7-213. Comparison of Theory and Experiment, Format V, Two-Dimensional Inlet

$M_\infty = 2.5$

In general, the trend in total pressure recovery, as a function of angle of attack, is clearly predicted by theory at all Mach numbers tested. However, the accuracy of the analytical estimates are a function of both Mach number and angle of attack.

At Mach 1.2 a large discrepancy appears to exist between theory and experiment. However, an examination of the individual characteristic canes indicates that critical operation was never achieved during these tests and the experimental values shown are supercritical. The comparison is presented to show the similarity in trend, as a function of angle of attack, between theory and experiment.

For Mach 1.8 and 2.2 there is excellent agreement between theory and experiment for angles of attack up to approximately 10 degrees. For higher angles of attack the general trend is approximated by theory but the accuracy is only fair. The onset of divergence between theory and experiment can be related to first and/or second compression ramp shock detachment and the local pressure distribution induced by the realigned shock structure. This is a Mach number dependent effect.

At Mach 2.5 there is a difference between theory and experiment that can be traced in part to a poor estimate of subsonic diffuser "$\Delta H/q$". During the analysis task the "$\Delta H/q$" was considered equal to that used for the Mach 2.2 diffuser although the duct diffusion rate was much more rapid for the Mach 2.5 case. A corrected prediction is shown using a duct loss factor corresponding to the higher expansion rate. The resultant agreement, especially the similarity of trend, is good. The remaining discrepancy may be attributable to the effects of shock-boundary layer interaction, due to the presence of a strong terminal wave. Increasing angle of attack weakens this wave and the correlation does improve. It is pointed out, however, that this agreement is achieved at values of extremely low total pressure recovery.

7.3.3 Axisymmetric Inlet

7.3.3.1 Mass Flow Ratio Correlation

Presented in Figures 7-214 through 7-218 are comparisons of mass flow ratio for the axisymmetric inlet. Inspection of these data indicates generally fair agreement between theory and experiment.

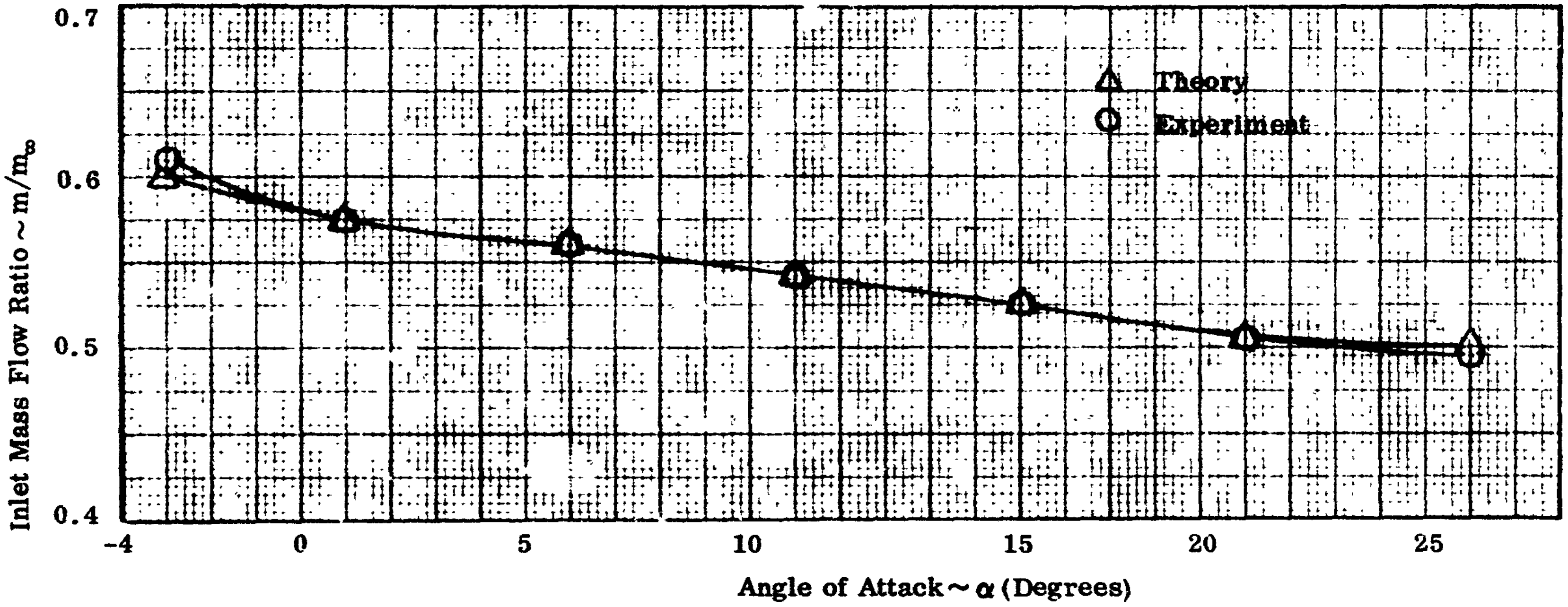

Figure 7-214. Comparison of Theory and Experiment, Format V, Axisymmetric Inlet
$M_\infty = 0.8$

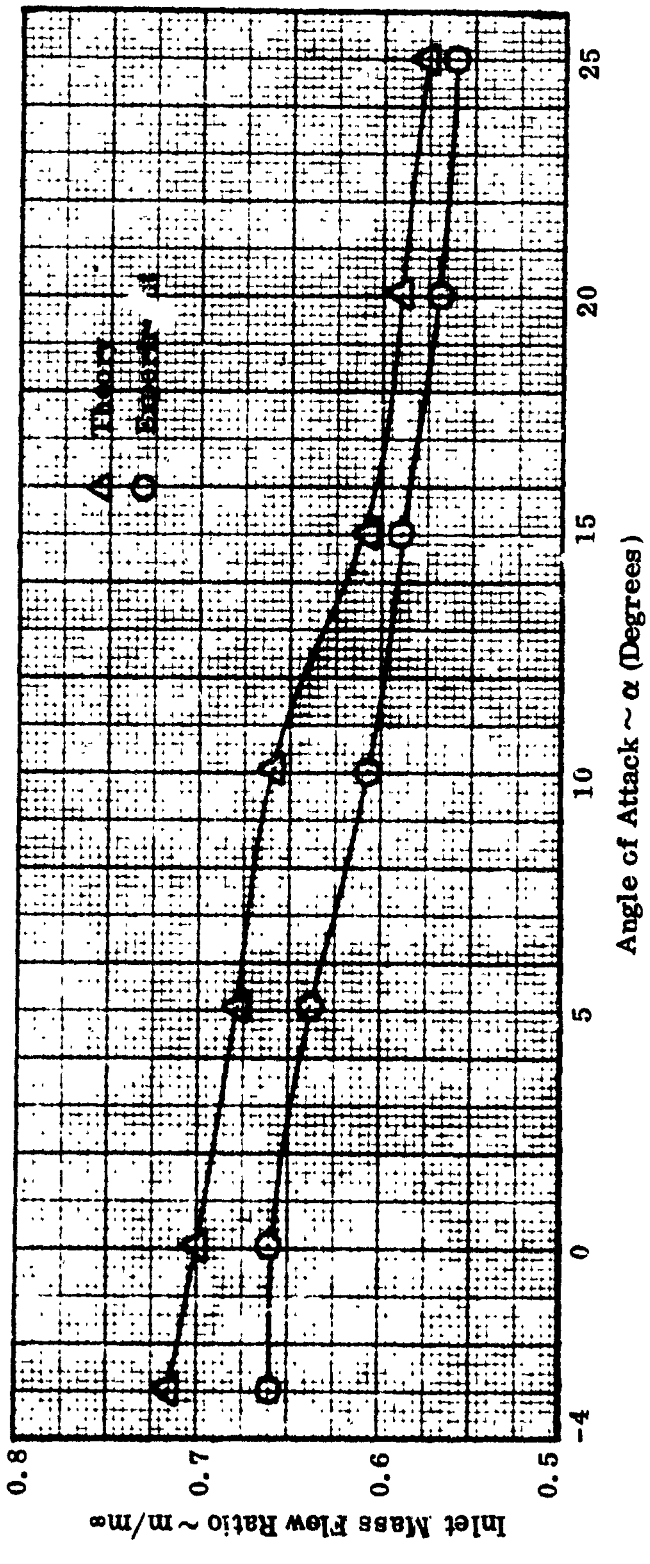

Figure 7-215. Comparison of Theory and Experiment, Format V, Axisymmetric Inlet

$M_\infty = 1.2$

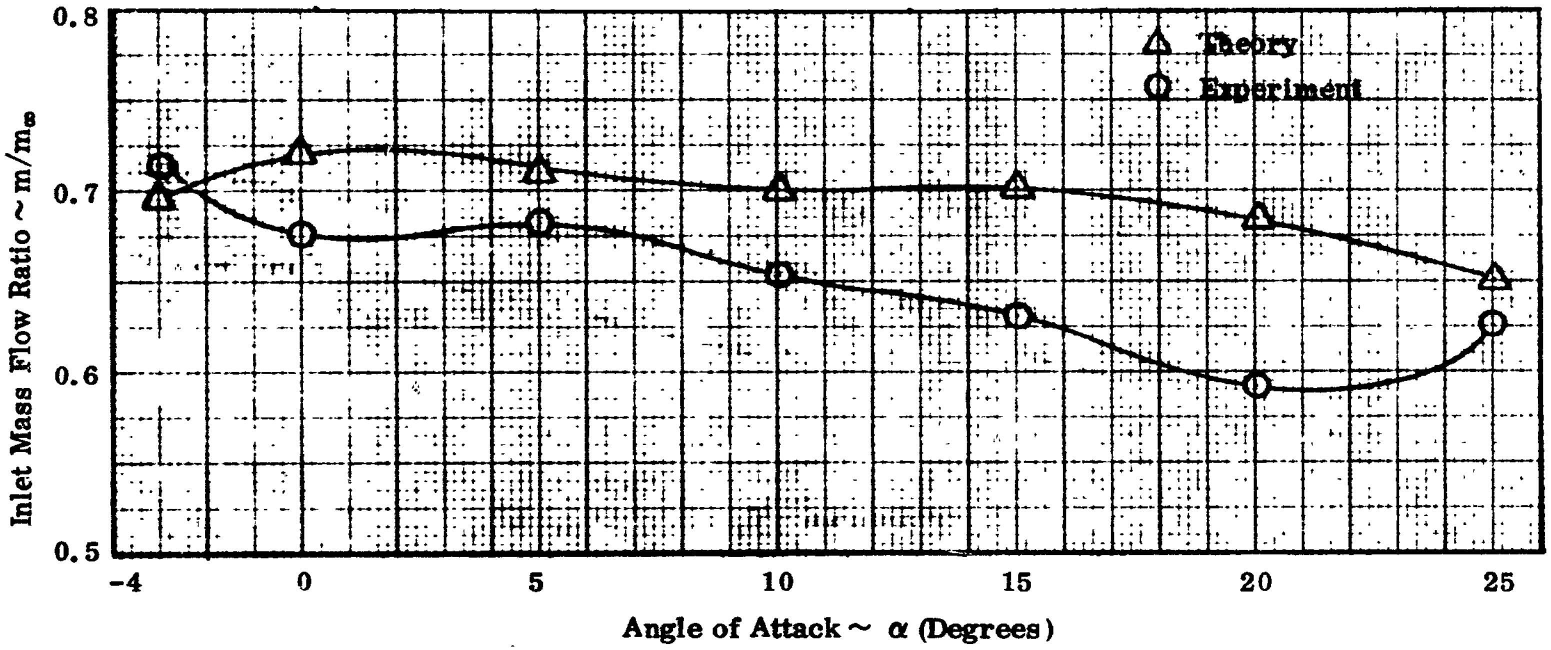

Figure 7-216. Comparison of Theory and Experiment, Format V, Axisymmetric Inlet

$M_\infty = 1.8$

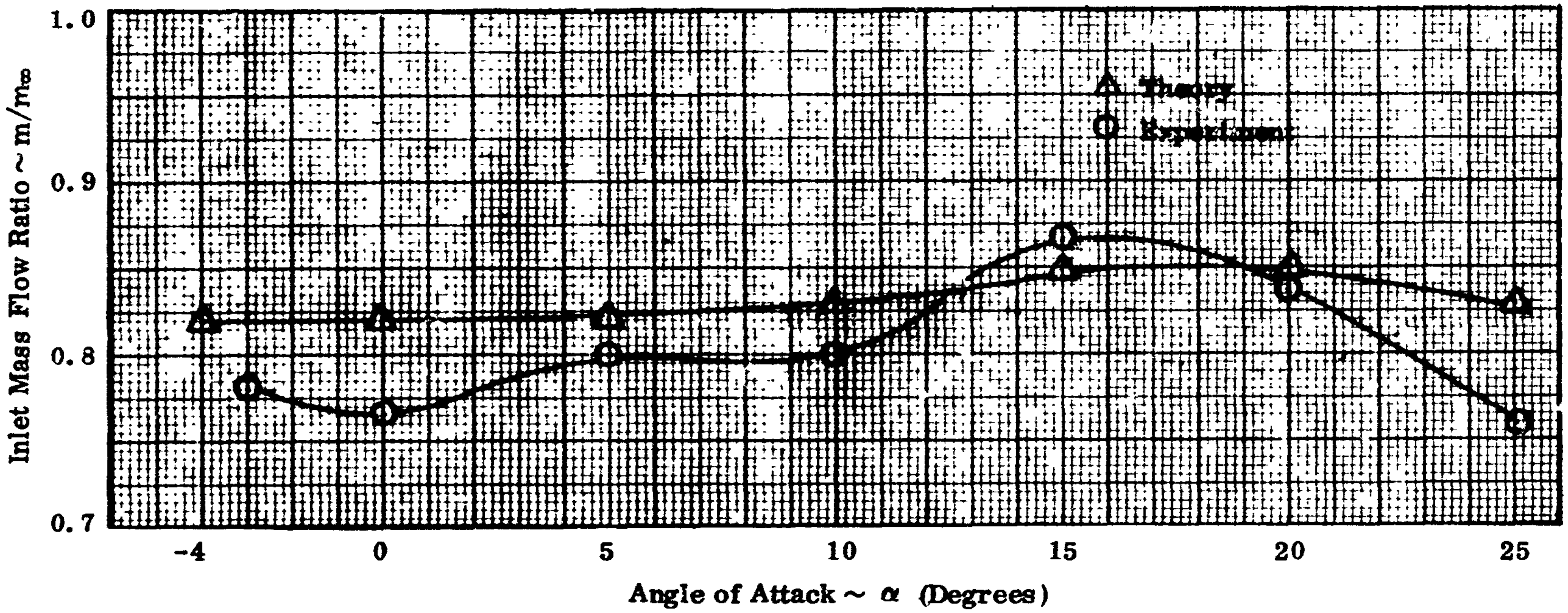

Figure 7-217. Comparison of Theory and Experiment, Format V, Axisymmetric Inlet

$M_\infty = 2.2$

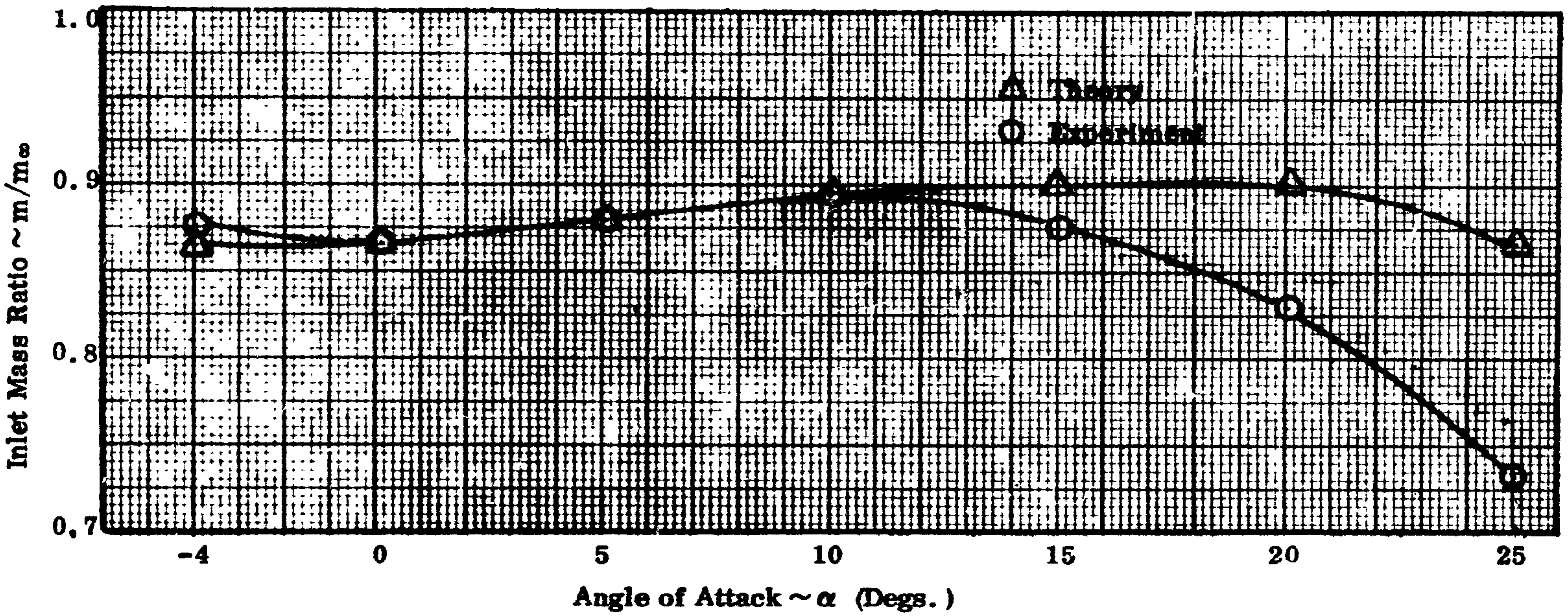

Figure 7-218. Comparison of Theory and Experiment, Format V, Axisymmetric Inlet

$M_\infty = 2.5$

For a free stream Mach number of 0.8 the agreement is excellent for the entire angle-of-attack range, indicating that the predictive accuracy of a one-dimensional analysis is acceptable for preliminary design studies. An operational point of interest emerges from an examination of the individual characteristic canes generated at this Mach number. A shift in mass flow ratio occurs as the inlet is throttled from supercritical to critical operation. Further, the magnitude of this shift decreases with increasing angle of attack. The conclusions drawn are,

- The boundary layer bleed system can be sized roughly by assuming potential flow. However, the pumping capacity of the perforated bleed configuration used appears insensitive to the increased pressure ratio across the system resulting from a throttling of the inlet, even though the system is probably unchoked. Consequently, the boundary layer thickens, reducing the effective inlet cowl flow area and ingested mass flow.

- The cross flow induced by the introduction of angle of attack tends to sweep the boundary layer from the external compression surfaces. This results in an effective inlet throat flow area that increases as a direct function of this cross flow gradient, an effect related directly to angle of attack. At high angle of attack the effective area approximates the geometric area and the slope of the supercritical leg of the characteristic cane approaches vertical.

In reviewing the two-dimensional inlet characteristic canes, for the Mach 0.8 case, an absence of mass flow shift is noted. As discussed previously excellent agreement with theory was also achieved with this inlet. However, this design employed a flush slot boundary layer bleed system. It can be deduced that a potential flow sizing of the bleed system produces adequate estimates and, further, that this system is more responsive to the imposed pressure gradient.

The conclusions concerning bleed system sensitivity can be extended to include the case with the bleed system choked. Here the pumping capacity varies with upstream density and not with density and discharge Mach number, as is the case for an unchoked system. However, this difference will not affect the inherent response of either system and their choked performance characteristics can be considered identical to the unchoked case. The improved characteristic cane shape resulting from use of the flush slot bleed system can be considered an advantage for this approach because it can potentially match an engine operating line closer to the critical point thereby achieving a higher performance level, in terms of total pressure recovery and steady state distortion.

At Mach number 1.2 generally good agreement exists for the entire angle-of-attack range. At this Mach number the external flow field is near sonic, making a one-dimensional analysis applicable. The mass flow shift, seen during examination of the subsonic Mach number case appears again. At negative and low positive angles-of-attack the capacity of the boundary layer bleed system appears inadequate. As a result the smaller effective throat flow area results in an ingested mass flow below that predicted by theory. However at the higher angles-of-attack the cross flow gradient sweeps the surface boundary layer, the effective cowl area approximates the geometric cowl area, and the agreement is quite good.

Examination of the supersonic Mach numbers leads, in general, to the same conclusions regarding correlation as were drawn previously for the two-dimensional inlet. However, it does appear that the predictive accuracy of the technique employed to analyze the axisymmetric inlet is somewhat poorer, due primarily to the use of a simplified approximation of the radial flow profile. Consequently, any estimate of the boundary slipline curvature has a small built-in error.

In addition to this general conclusion, comparing the axisymmetric and two-dimensional calculation procedures, an examination of the correlation achieved with the axisymmetric inlet at Mach 1.8, 2.2, and 2.5 shows that the accuracy of that calculation technique varies inversely with the extent of the boundary slipline. As the Mach number is increased the inlet moves toward a shock on lip condition and the correlation improves.

For the supersonic Mach numbers, as angle of attack was increased, the inlet exhibited a tendency to delay the onset of rapid mass flow ratio decay, beyond angles normally associated with this inlet concept. This can probably be related to the rather weak external supersonic compression process employed and the weak resultant cross flow gradient. The compression surface geometry results from the need to match both the transonic and supersonic mass flow requirements. However, this necessity to match the mass flow ratios for a wide range of free stream Mach numbers, with external compression surfaces that do not vary in deflection angle, does produce an unbalanced compression of the flow. Further, with increasing free stream Mach number this imbalance increases, as does the strength of the terminal shock. As angle of attack is introduced the external compression increases, weakening the terminal shock, but increasing the downstream pressure level. The change in pressure level is a function of the initial imbalance, a Mach number dependent effect. In addition, the change occurs in a nonuniform fashion, around the inlet periphery. The result is a Mach number dependent shock induced peripheral pressure gradient. This gradient reinforces the inherent cross flow gradient due strictly to angle of attack operation, and in combination their strength determines the onset of mass flow decay. This effect is evident in the comparison curves.

At Mach 1.8 the inlet efficiency is relatively high, consequently the shock induced gradient is weak. As a result mass flow decay is not experienced for the entire angle of attack range. At Mach 2.2, angle-of-attack tends to improve inlet pressure recovery and the combined gradient causes decay at about 20 degrees angle of attack. At Mach 2.5, the zero angle of attack compression process is quite unbalanced, due to the large throat area required for transonic operation, consequently mass flow decay occurs earlier, about 10 degrees in this case, in the angle of attack excursion.

7.3.3.2 Inlet Total Pressure Recovery Correlation

Presented in Figures 7-219 through 7-223 are comparisons of inlet total pressure recovery.

At Mach 0.8 the agreement between theory and experiment is quite good across the entire angle of attack range. Inspection of the individual characteristic canes indicates that the inlet did not achieve critical operation. Consequently the

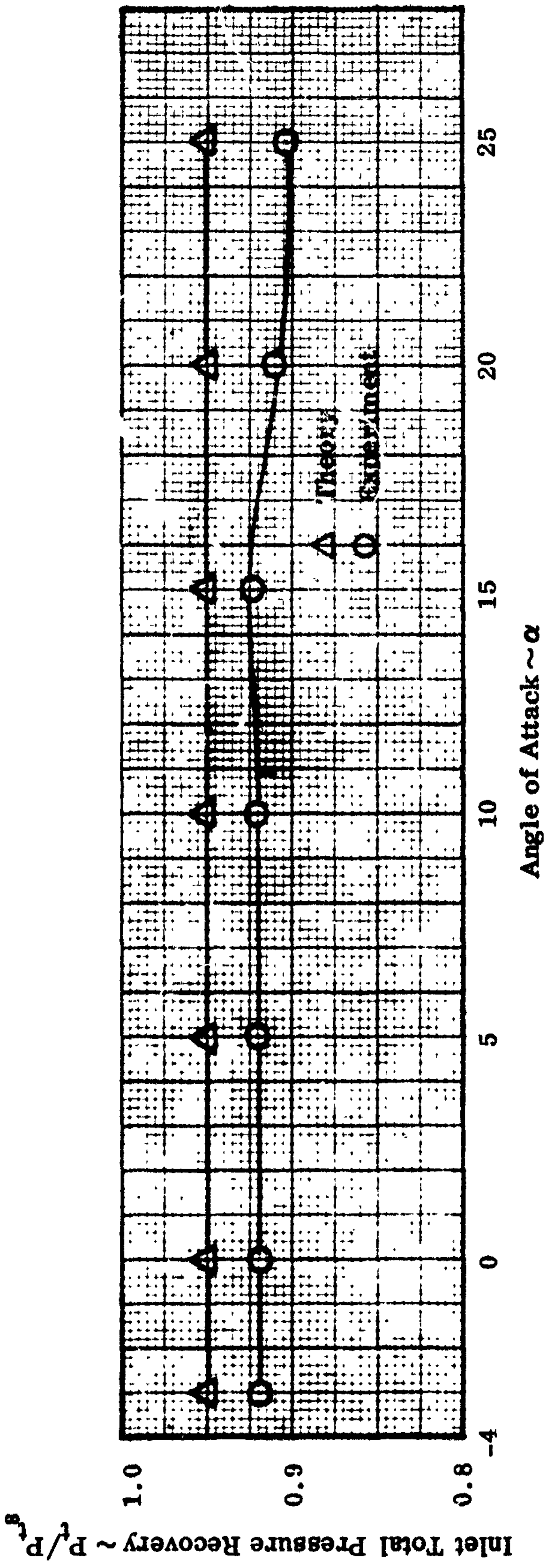

Figure 7-219. Comparison of Theory and Experiment, Format V, Axisymmetric Inlet

$M_\infty = 0.8$

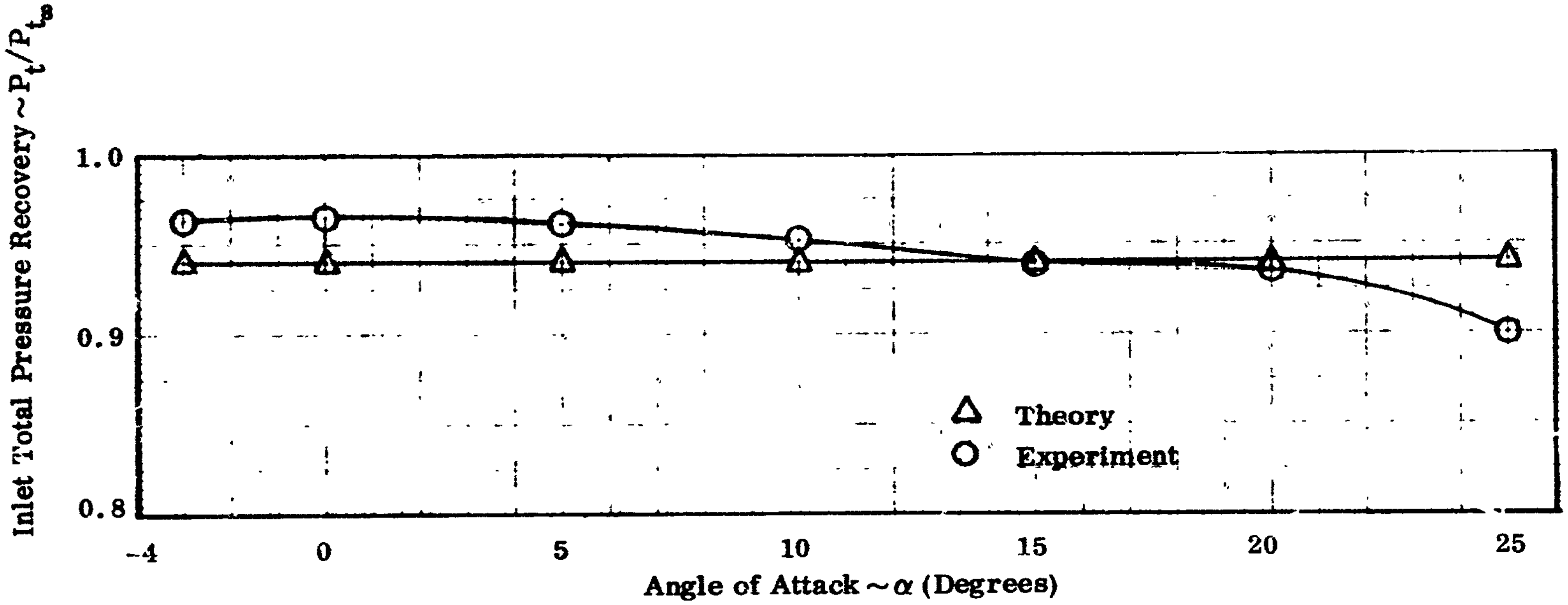

Figure 7-220. Comparison of Theory and Experiment, Format V, Axisymmetric Inlet

$M_\infty = 1.2$

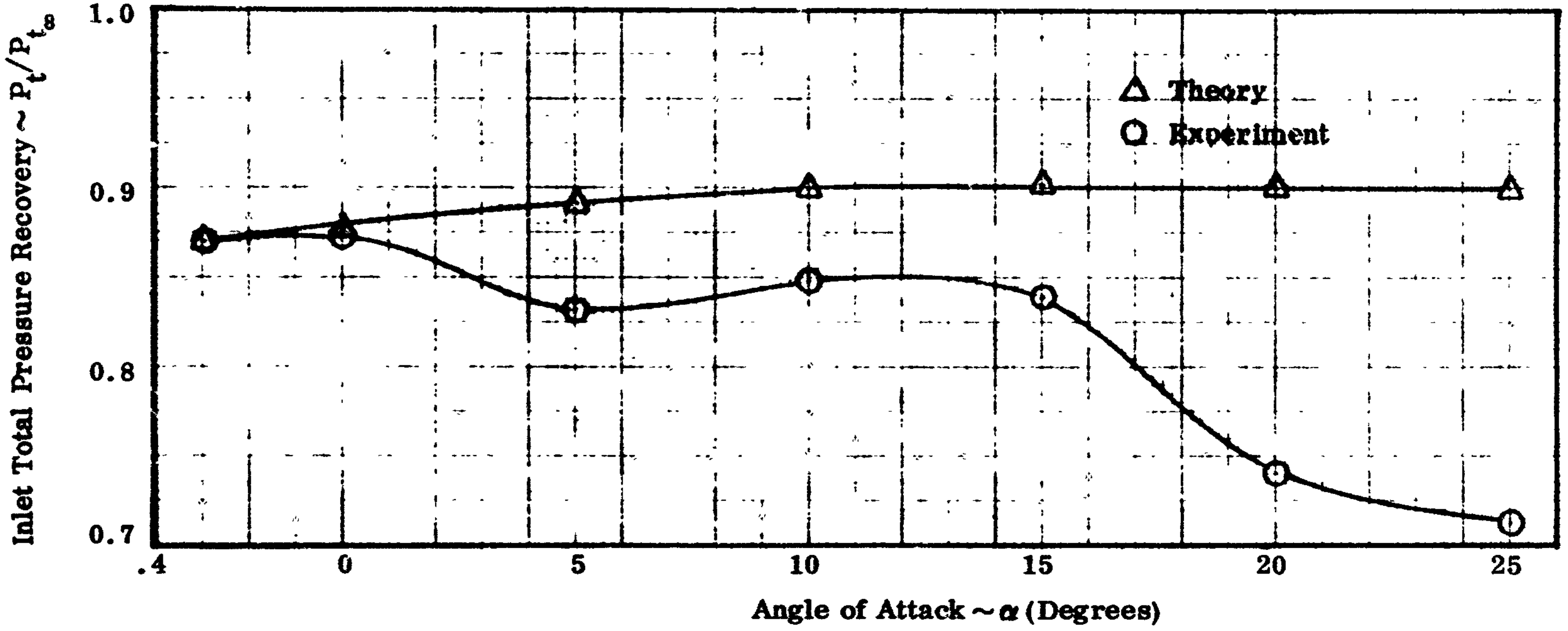

Figure 7-221. Comparison of Theory and Experiment, Format V, Axisymmetric Inlet

$M_\infty = 1.8$

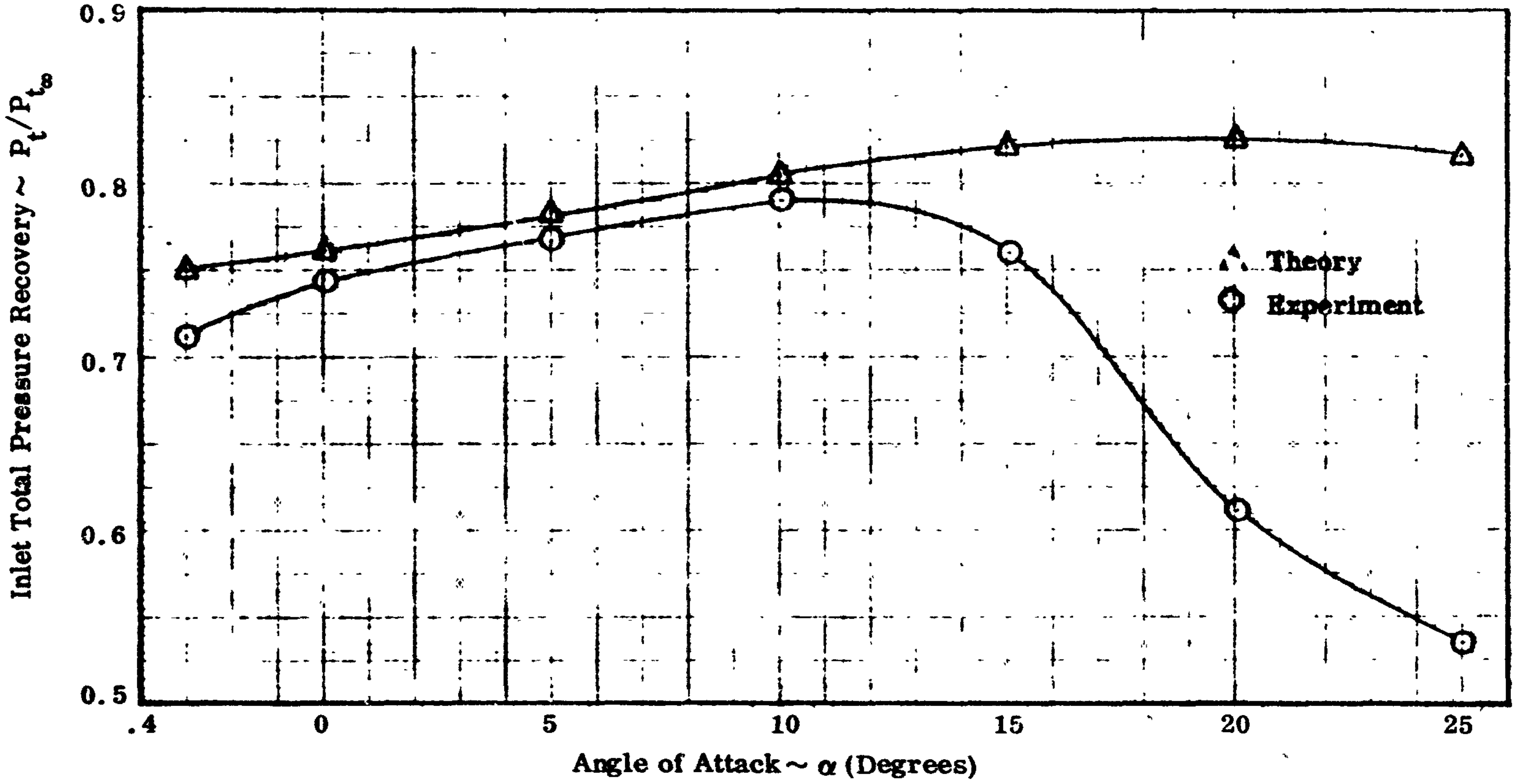

Figure 7-222. Comparison of Theory and Experiment, Format V, Axisymmetric Inlet

$M_\infty = 2.2$

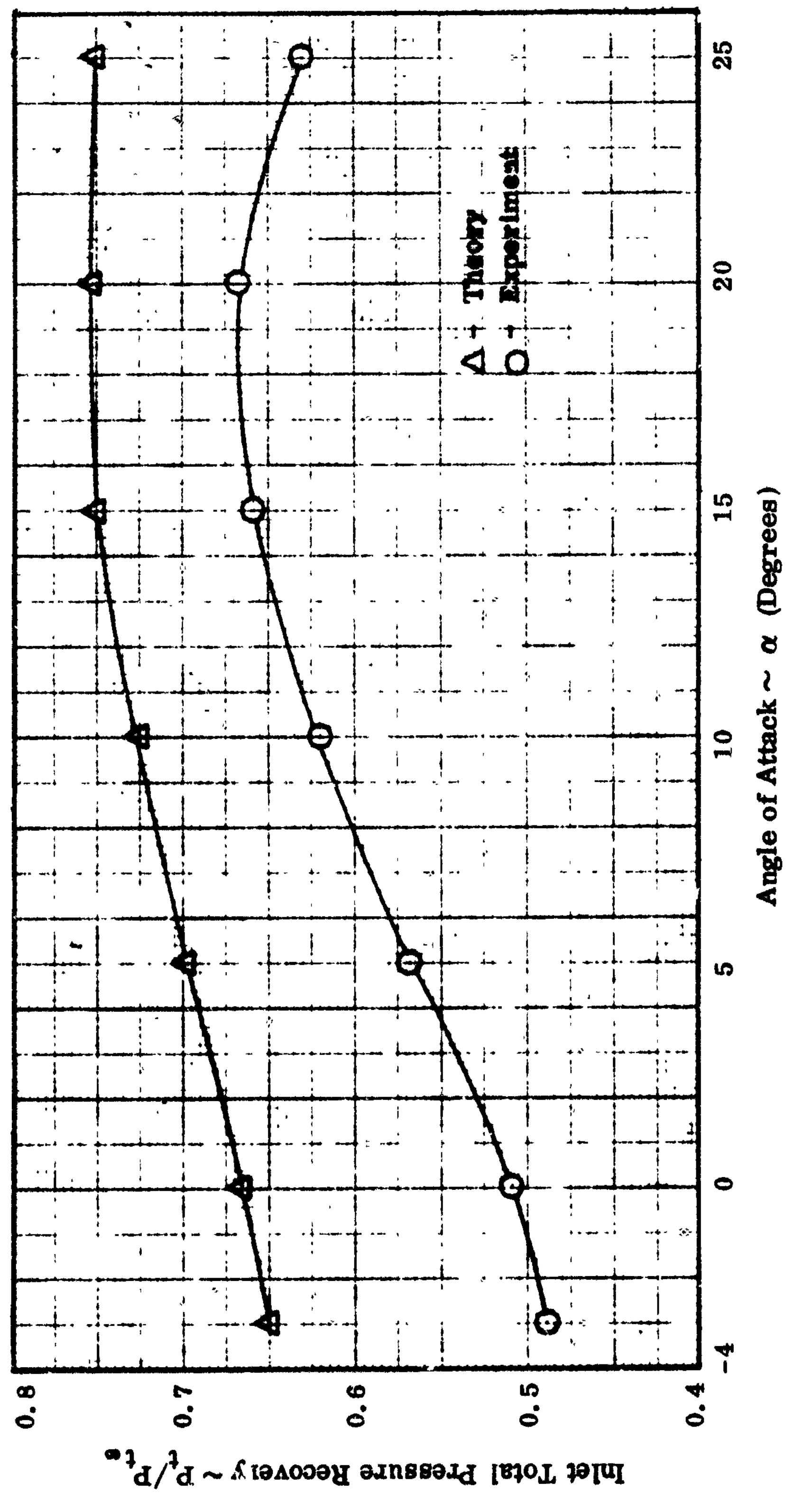

Figure 7-223. Comparison of Theory and Experiment, Format V, Axisymmetric Inlet

$M_\infty = 2.5$

level of correlation achievable is potentially better than that demonstrated. The correlation achieved at Mach 1.2, which was excellent, supports this conclusion. At this Mach number the inlet performance is estimated with one-dimensional techniques, as was the case at Mach 0.8, but with the inlet operating closer to the critical point the correlation was better.

At Mach 1.8 the theoretical performance agrees very well with the experimental results for angles of attack up to zero degrees. The correlation is quite poor for higher angles. This stems from a malfunction of the inlet throttling plug that prevented the development of complete characteristic canes, at these angles of attack. Although the characteristic at zero angle of attack does not clearly depict critical operation, the level of steady state distortion does indicate near critical operation. Therefore, we can project good correlation for angles of attack higher than indicated by the comparison curves, probably on the order of 10 degrees.

At Mach 2.2 well defined inlet characteristics were obtained and the degree of correlation is quite good up to approximately 10 degrees angle of attack. Above this angle the classical deterioration of axisymmetric inlet pressure recovery does not predict this trend and the correlation is very poor in this region.

The correlation obtained at Mach 2.5 was also rather poor. An external compression inlet, of the N = 3 type, can theoretically achieve a high level of total pressure recovery at Mach numbers up to Mach 2.5. However, this requires an inlet shock structure approaching optimum for that Mach number, an impractical prerequisite for fixed geometr axisymmetric inlets designed for the tactical aircraft mission. The trades required to satisfy both the supersonic and transonic flight conditions can result in supersonic performance goals far below that theoretically achievable. This end result is particularly true for presently envisioned mission profiles that demand a heavier weighting of the transonic requirements because vehicle range is far more sensitive to variations of inlet performance in the transonic regime. The inlet geometry that evolves from these trades fixes a rather low supersonic total pressure recovery target. This can be seen by inspecting the theoretical estimate, in Figure 7-223 showing a target for cruise and/or dash angles of attack on the order of 70 percent. Rather than easing the inlet development problem, low performance goals can, in fact, increase them because of the very strong shock wave-boundary layer interaction problem that must be solved. The data generated at Mach 2.5 indicate that this strong interaction has induced complete separation of the inlet flow field over the entire angle of attack range. At low angles the total pressure recovery is essentially equal to the normal shock value, the trend in recovery as a function of angle of attack, is quite untypical, and the throttling of the inlet produces an excursion of mass flow ratio, at each angle of attack, that is indicative of a near choked throat. The simplified theory employed does not account for shock induced separation, and consequently made a poor prediction at this Mach number. However, an examination of the estimated inviscid static pressure gradient, does invite the assignment of a high probability for occurrence of separation. Therefore, when theory indicates a susceptibility to separation an acceptable estimate can still be made by initially computing the performance in a conventional manner and then shifting that estimate downward until the low angle prediction approximates normal shock recovery.

7.4 Inlet/Fuselage Combined (Data Format II)

7.4.1 General

The Format II model was configured to obtain inlet performance data for the two-dimensional inlet, when installed at that forward fuselage station. These data were obtained with the inlet integrated with four of the seven fuselage configurations. The use of only four fuselages was dictated by tunnel occupancy limitations. The choice of which four fuselages to employ was based upon inlet/fuselage compatibility plus the desire to employ a wide range of fuselage geometry. As a result, fuselages 1, 2, 3, and 4 were employed during these tests. In addition, tests were conducted to determine the effect upon inlet performance induced by nose and canopy geometry. For these tests the two-dimensional inlet/fuselage 3 configuration was employed.

To analyze the influence of the vehicle upon inlet performance required a multistep approach. Initially the experimental characteristic canes (total pressure recovery versus mass flow ratio) for the integrated inlet were plotted with the mass flow ratio based upon free stream density and Mach number and the capture area based upon vehicle angle of attack. This is the characteristic as computedby the data reduction program. The individual characteristics were then corrected to account for the variation of ideal inlet mass flow (m_∞) caused by vehicle induced changes to the flow approaching the inlet. This was done by examining that portion of the fuselage flow field within which the inlet shadow falls. Deviations from free stream of local total pressure and Mach number were then used to correct the density and velocity used to compute the ideal inlet mass flow. In addition, deviations in flow angularity are used to correct the capture area used in that computation. The shift in characteristic cane location, resulting from this computation is a measure of the quantitative vehicle influence upon the inlet performance. Being free of the quantitative vehicle induced effects, the corrected inlet characteristics can be compared with the corresponding inlet alone characteristic to obtain the qualitative effects of the inlet/vehicle integration process upon inlet performance.

Presented in subsequent sections is a discussion of the causal relationships observed during the examination of these data.

7.4.2 Nose and Canopy Effects

Analysis of the fuselage flow field data (Format I) showed that the flow field composition and the nose and canopy geometry are related. Assuming that the inlet performance is sensitive to some degree to the local environment, one might reasonably anticipate the display of a geometry dependent influence in the form of a varying inlet characteristic and/or level of inlet performance. However, the two-dimensional inlet proved quite insensitive to geometry variation, when tested in conjunction with fuselage 3 and the four (4) nose/canopy combinations. The slight variation in inlet performance, induced by geometry variation, precluded a definitive assessment of nose/canopy effects. To illustrate the basis for this conclusion Figures 7-224 through 7-230 are presented. Each of these figures depict for a given Mach number and angle of attack, the classical inlet characteristic of total pressure recovery versus mass flow ratio for the two dimensional inlet/fuselage 3 configuration as a function of nose and canopy geometry. Examination of this data sample, covering a wide range of Mach numbers and angles of attack, reveals the insensitivity of inlet performance to nose/canopy geometry. The close grouping of the performance characteristics, seen in these figures, is typical, in general, for all conditions explored.

This conclusion is, of course, restricted to the particular configuration arrangement investigated. It has been seen that the attendant flow field is influenced by the geometry, consequently, components with different geometric characteristics

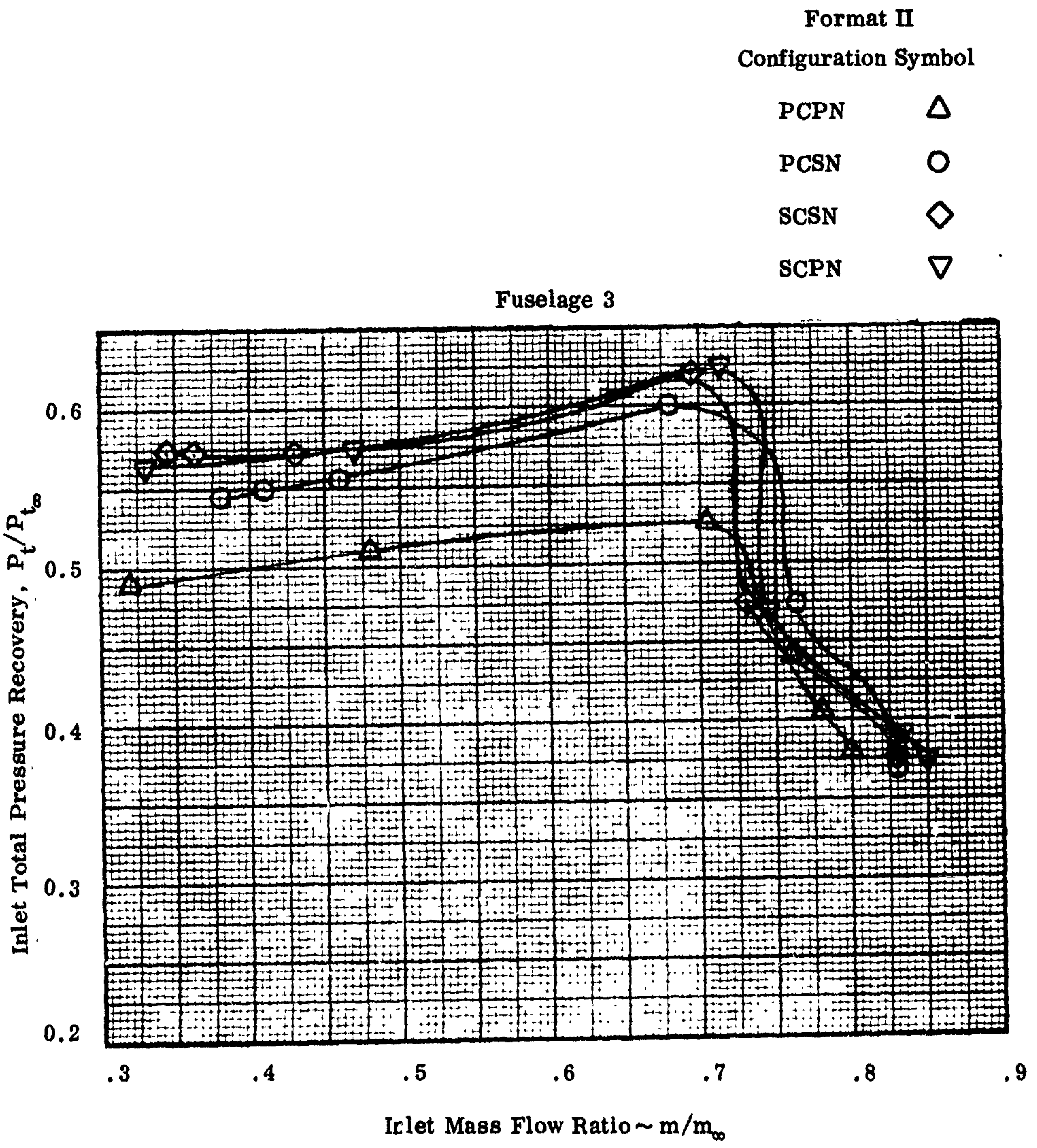

Figure 7-224. Comparison of Inlet Performance, Two-Dimensional Inlet
$M_\infty = 2.5$, $\alpha = 0°$

Format II

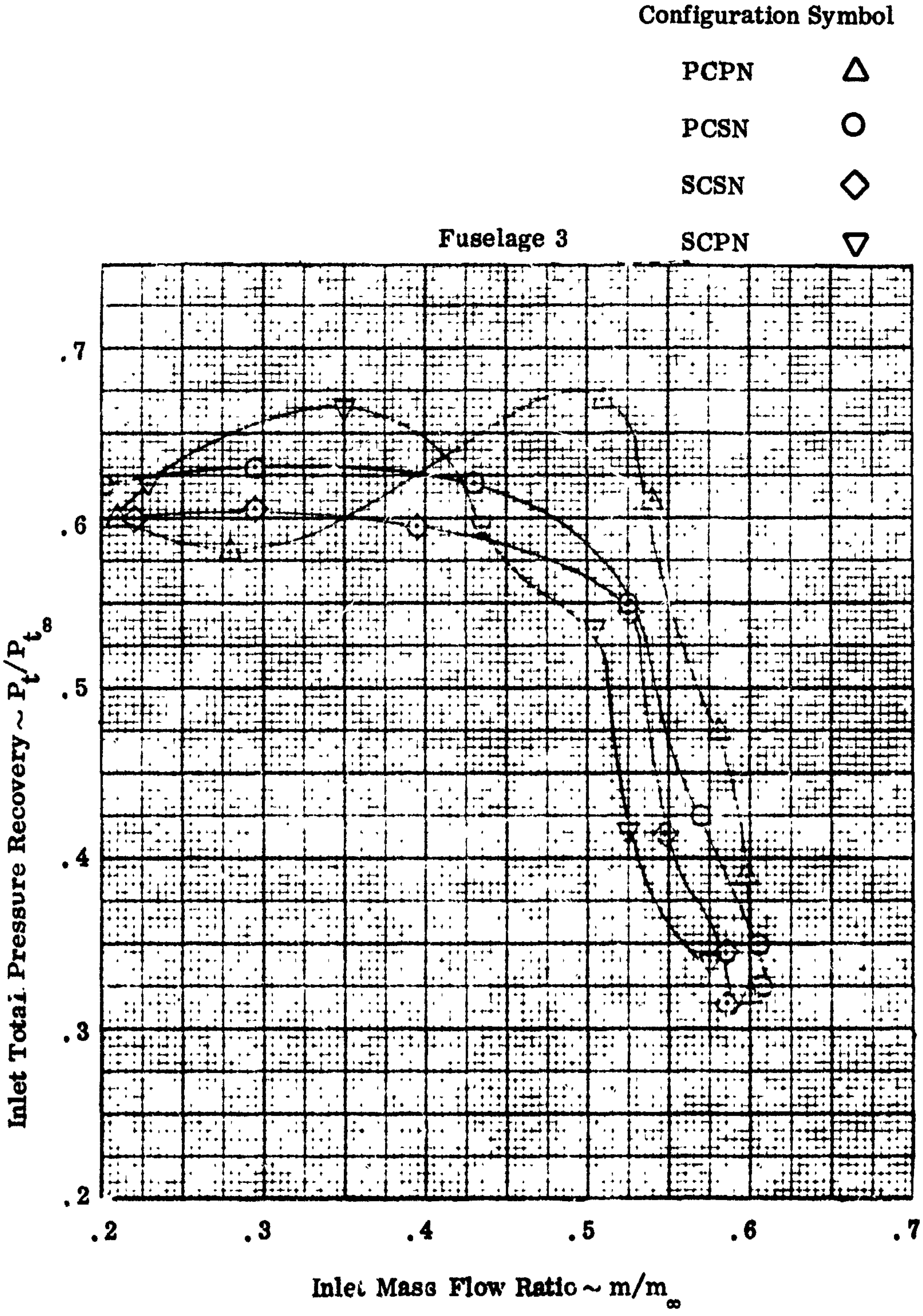

Figure 7-225. Comparison of Inlet Performance, Two-Dimensional Inlet, $M_\infty = 2.5$, $\alpha = 10°$

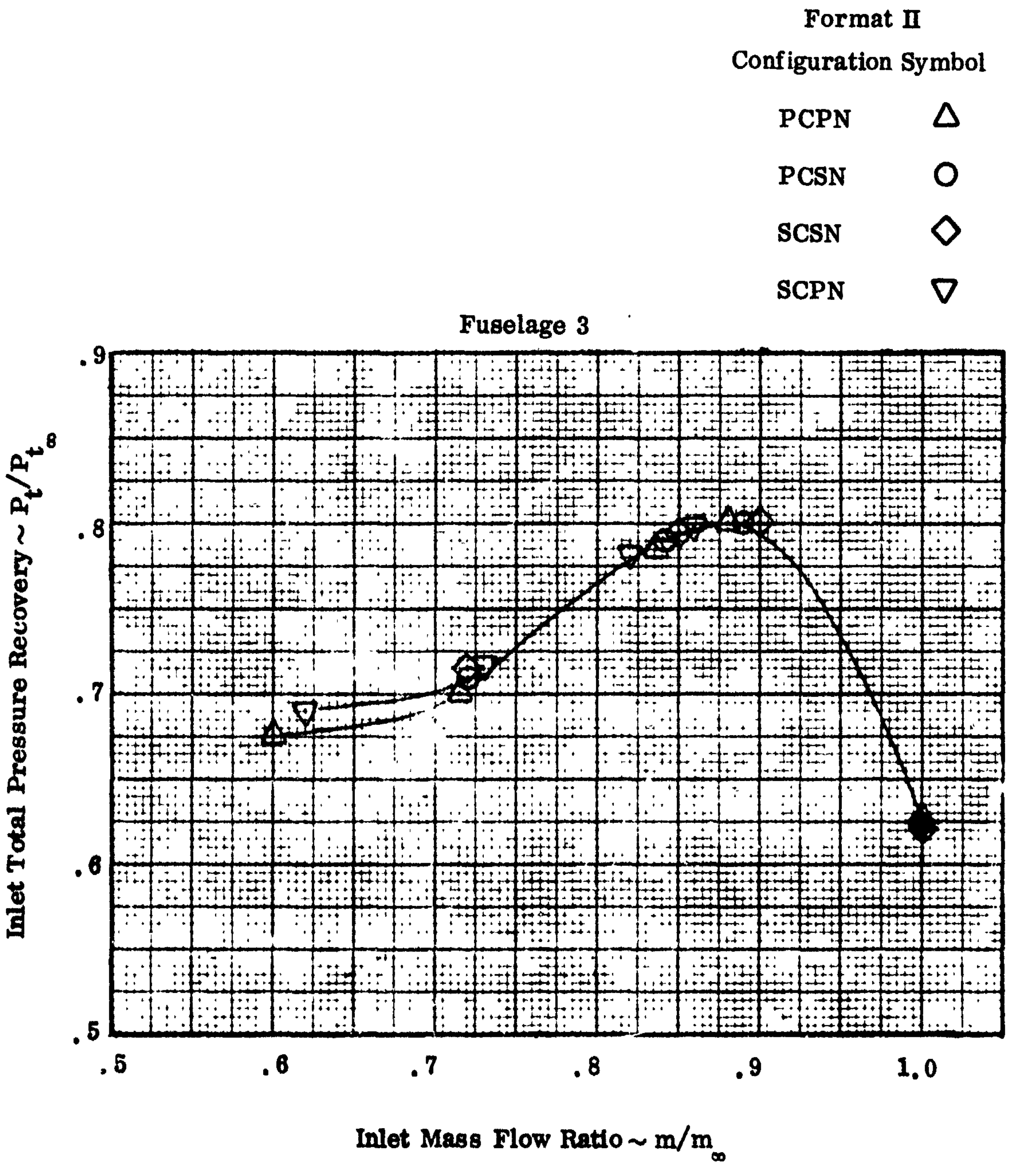

Figure 7-226. Comparison of Inlet Performance, Two-Dimensional Inlet $M_\infty = 2.2$, $\alpha = 0°$

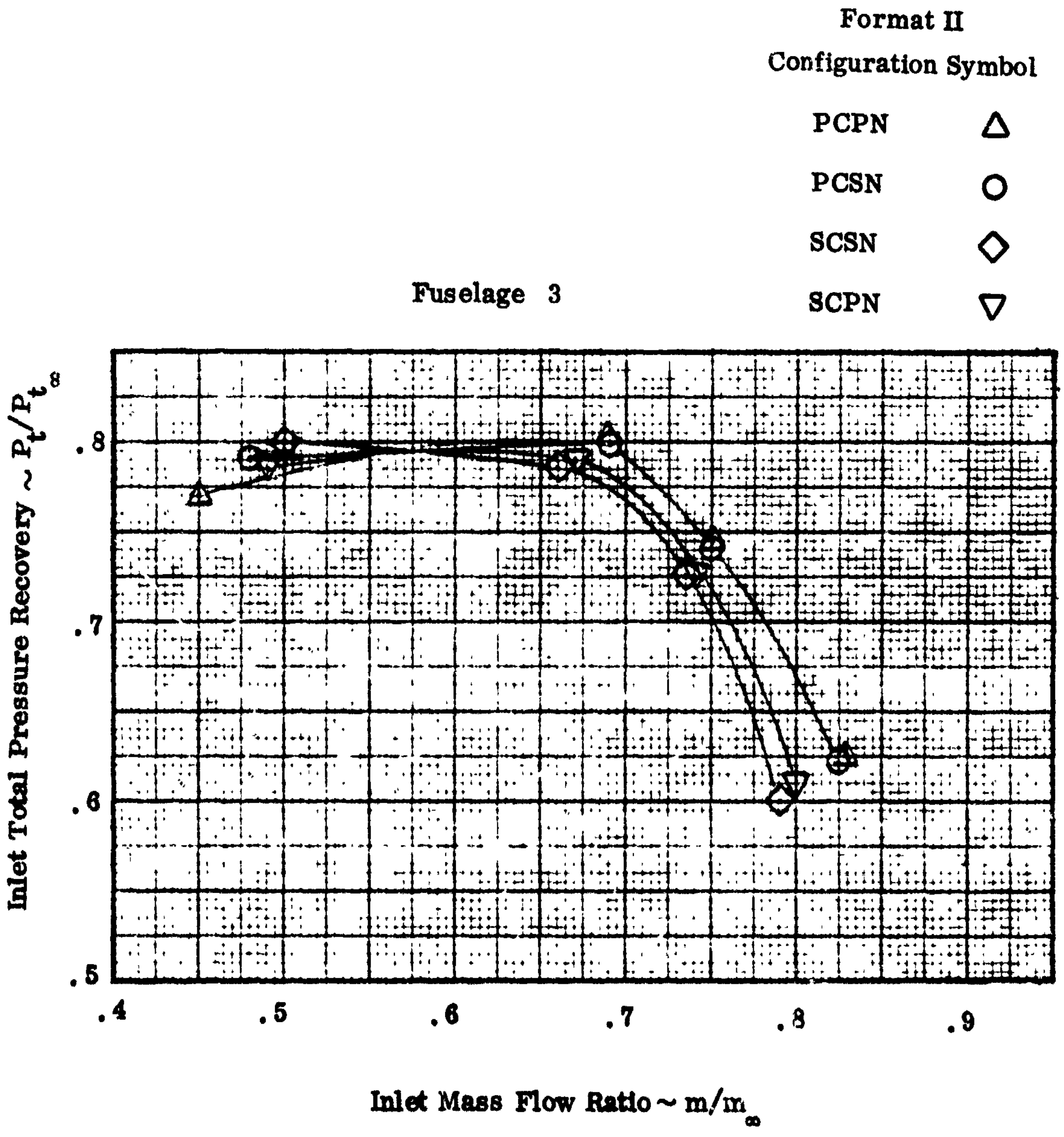

Figure 7-227. Comparison of Inlet Performance, Two-Dimensional Inlet, $M_\infty = 2.2$, $\alpha = 10°$

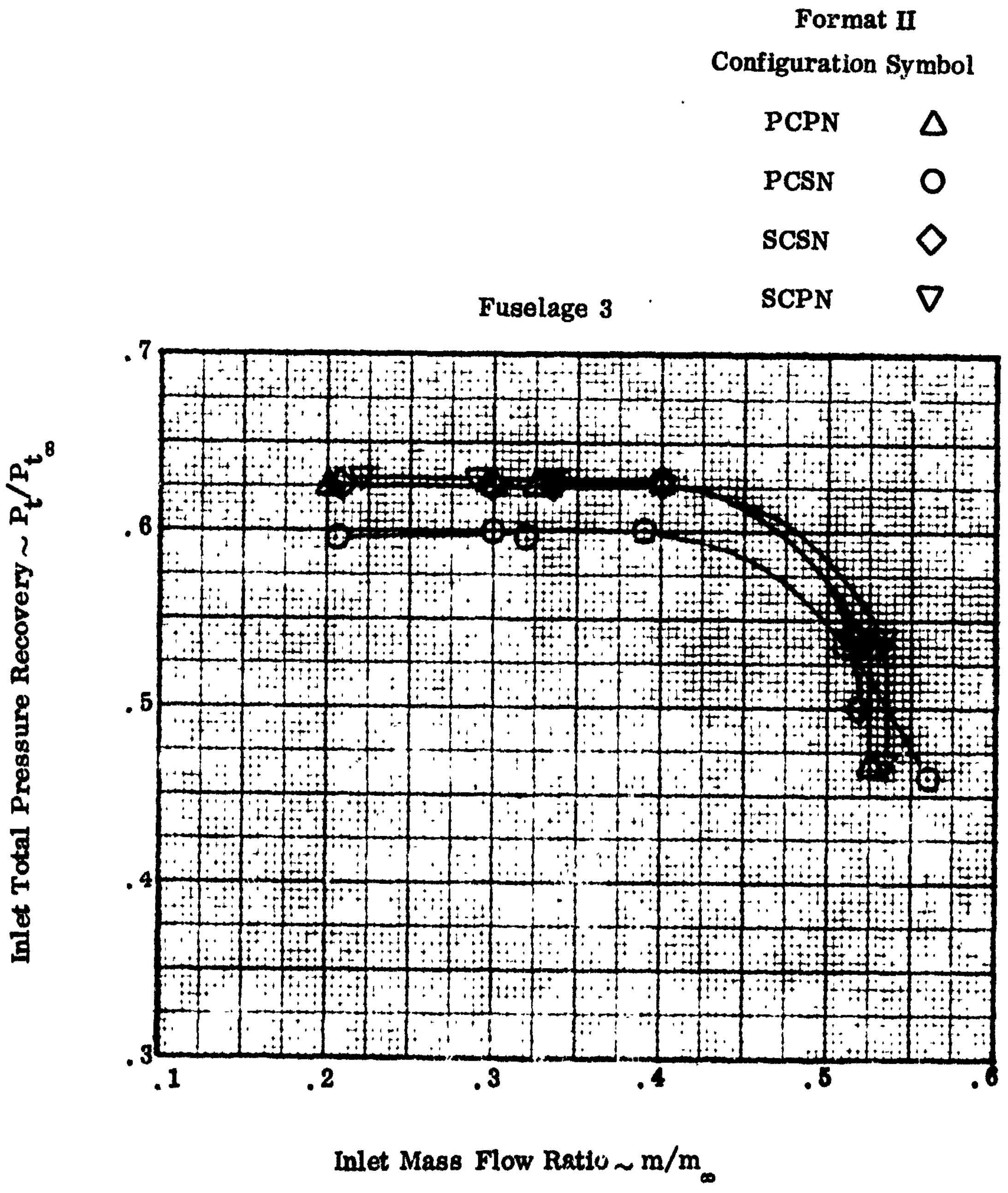

Figure 7-228. Comparison of Inlet Performance, Two-Dimensional Inlet, $M_\infty = 2.2$, $\alpha = 20°$

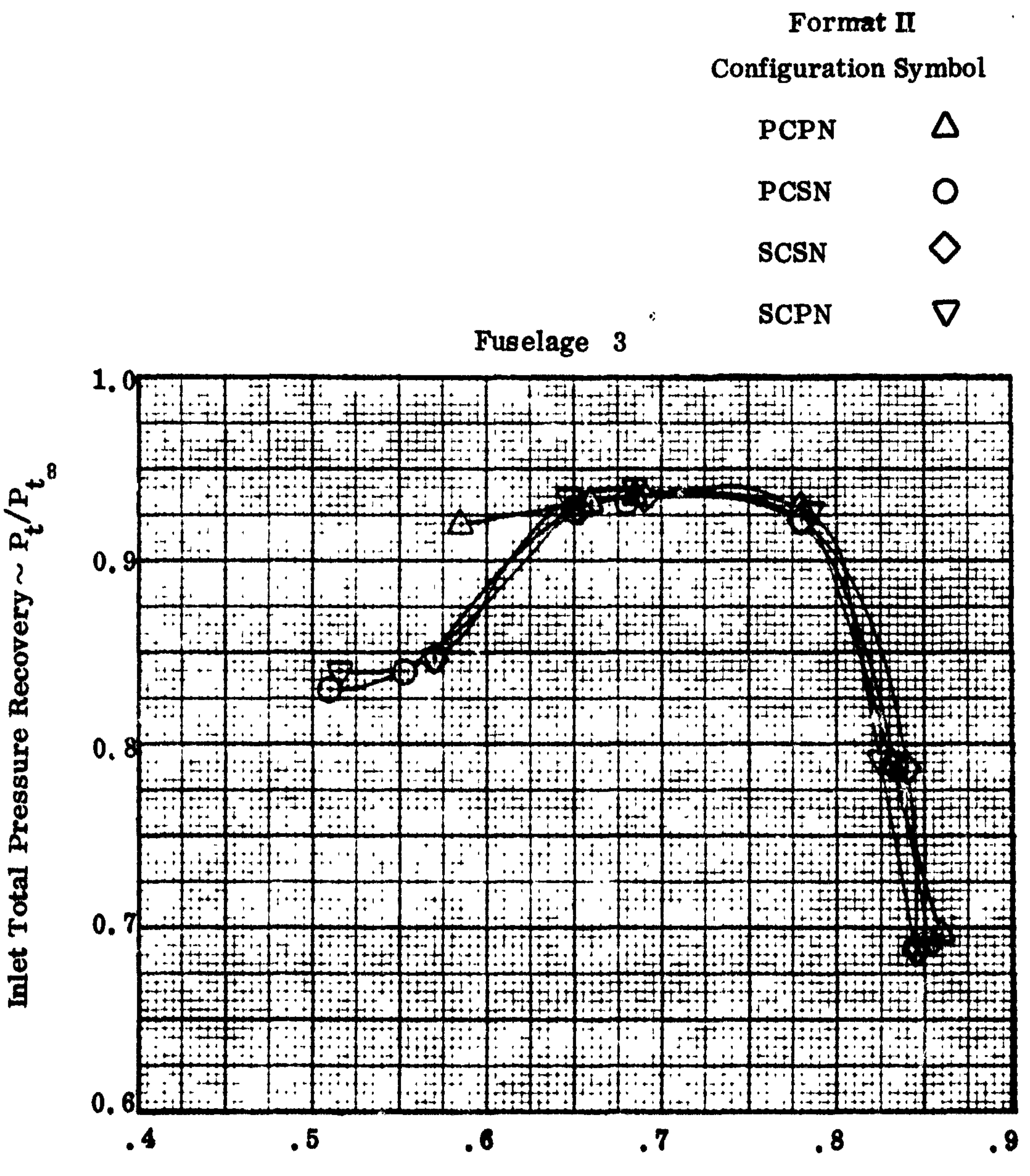

Figure 7-229. Comparison of Inlet Performance, Two-Dimensional Inlet $M_\infty = 1.8$, $\alpha = 0°$

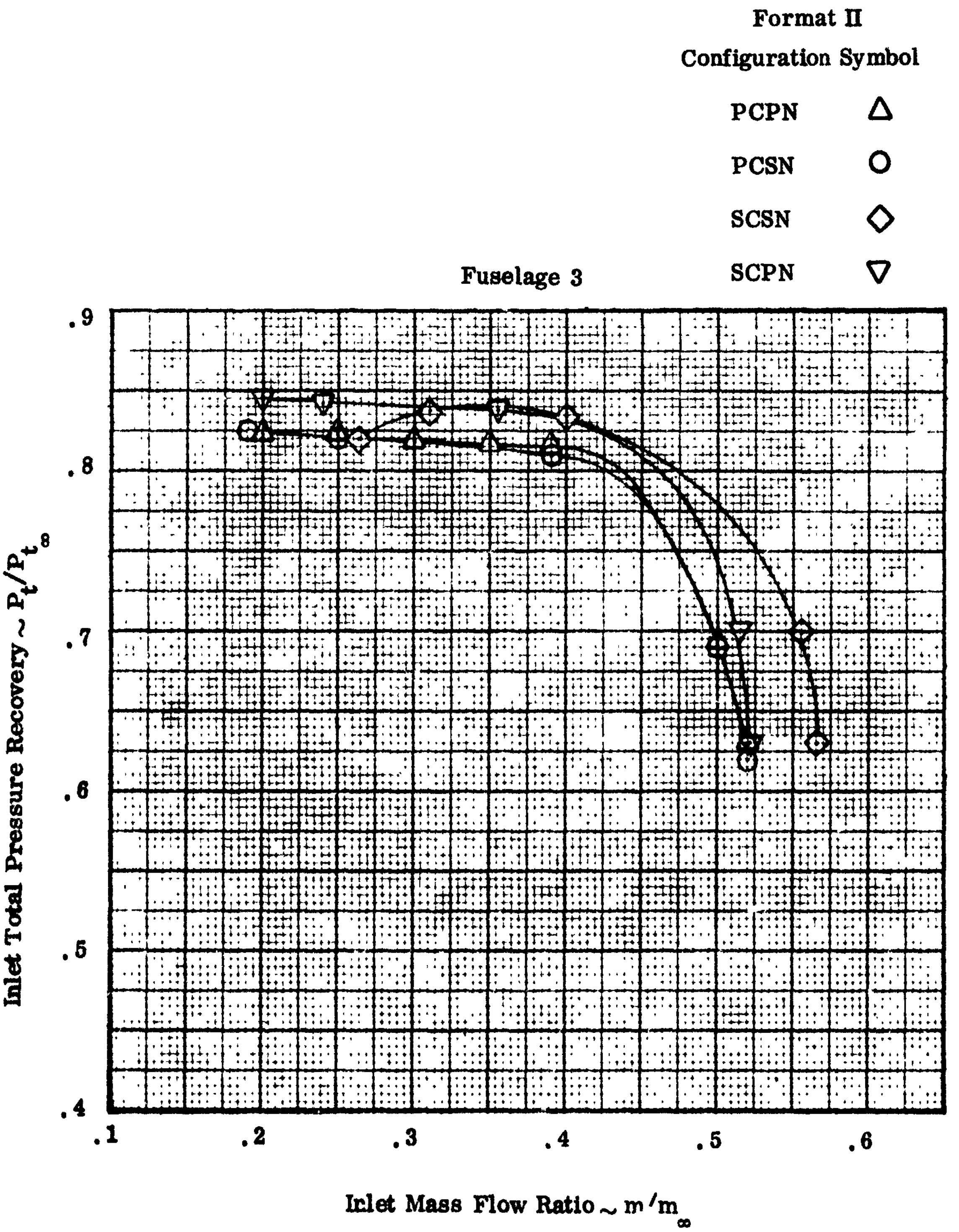

Figure 7-230. Comparison of Inlet Performance, Two-Dimensional Inlet $M_\infty = 1.8$, $\alpha = 20°$

and/or a different arrangement, relative to each other, may produce inlet performance variations. This postulation is, in fact, most probable when consideration is given to the inlet concept employed during the program. The inlet, a fixed geometry system, could not be optimized, in terms of total pressure recovery. across the entire Mach number range. Rather, the finalized design represented a compromise to achieve a reasonable total pressure recovery while satisfying a representative mass flow schedule. Therefore, although the inlet is operating at acceptable performance levels it is less sensitive, to the local environment, than a system operating at high performance levels. Consequently, it does not react as dramatically to the incentives, either positive or negative, offered by subtle variations in the flow field. In short, the high performance, finely tuned system stands to lose more as the result of an environmental variation than does a system of moderate performance. Additionally, the small model scale probably tends to cloud further the impact of flow field variation upon inlet performance.

In spite of these factors a hard look at the data does reveal the presence of weak geometry dependent effects at the two (2) highest test Mach numbers of 2.2 and 2.5. At low angles of attack, the additional flow precompression induced by the blunter secondary nose (SN) and/or larger secondary canopy (SC) tend to improve inlet performance. With increasing angle of attack, the external compression of the inlet increases due to the horizontal orientation of the ramps, and the beneficial precompression generated by the secondary nose/canopy enjoyed at low angle of attack becomes less important than the induced drag of these components and the resultant reduction in flow field stagnation pressure they induce. Consequently, the more slender primary nose and/or the smaller primary canopy prove more beneficial at these angles of attack.

Although the ramifications of nose and canopy geometry upon inlet performance did not emerge clearly as a result of the tests conducted, sufficient evidence was uncovered to indicate that these components can be gainfully integrated into the inlet design process.

7.4.3 Fuselage Effects

7.4.3.1 Mach Number 0.8

The inlet performance for the negative angle of attack condition is presented in Figure 7-231. The open symbols denote performance of the two-dimensional inlet integrated with fuselages 1 through 4, as a function of vehicle angle of attack and free stream Mach number. Also shown in closed symbols, are mass flow ratio shifts when the actual local flow properties are accounted for. In addition, the inlet alone (Format V) and the analytically predicted performance are shown. The data indicate an insensitivity to vehicle geometry with all curves grouped closely together. The variation from curve to curve is within the experimental measurement accuracy. This stems from the fact that the inlet throat provides an essentially choked control of the inlet mass flow and is therefore insensitive to variations in the approaching flow. The high level of experimental total pressure recovery achieved at the critical operating point, relative to the analytical estimate, can be traced to a conservative prediction of the subsonic diffuser losses. At 0° angle of attack the inlet alone and the integrated inlet performance are quite close as shown in Figure 7-232.

The inlet performance for five (5) degrees angle of attack, shown in Figure 7-233 fall in a tight band, close to the inlet alone performance, as expected. The lone exception being the fuselage 2/2D inlet configuration which displays a representative critical total pressure recovery but a low mass flow ratio. The data does not offer an apparent reason for this deviation, it may be an experimental inaccuracy or a data reduction error.

The inlet performance curves for the high angles of attack are presented in Figures 7-234 through 7-237. It can be seen that the total pressure recovery is independent of angle of attack, an anticipated result. The mass flow ratios are similar and approximate the inlet alone quite well. The lone exception is the fuselage 2 configuration which continues to operate at low mass flow ratios, as previously mentioned. The cause of this effect can be seen in an examination of the engine face profiles for this configuration. At these angles of attack the profile for supercritical operation, shown in Figures 7-238 through 7-240 is basically tip-radial with a high pressure central core and a low pressure region near the duct wall. However, the low pressure region is, particularly on the lower and inboard side, quite pronounced indicating

Format II

Fuselage	Symbols
1	△
2	◇
3	○
4	▽

Note: Solid symbols based on local flow field properties.

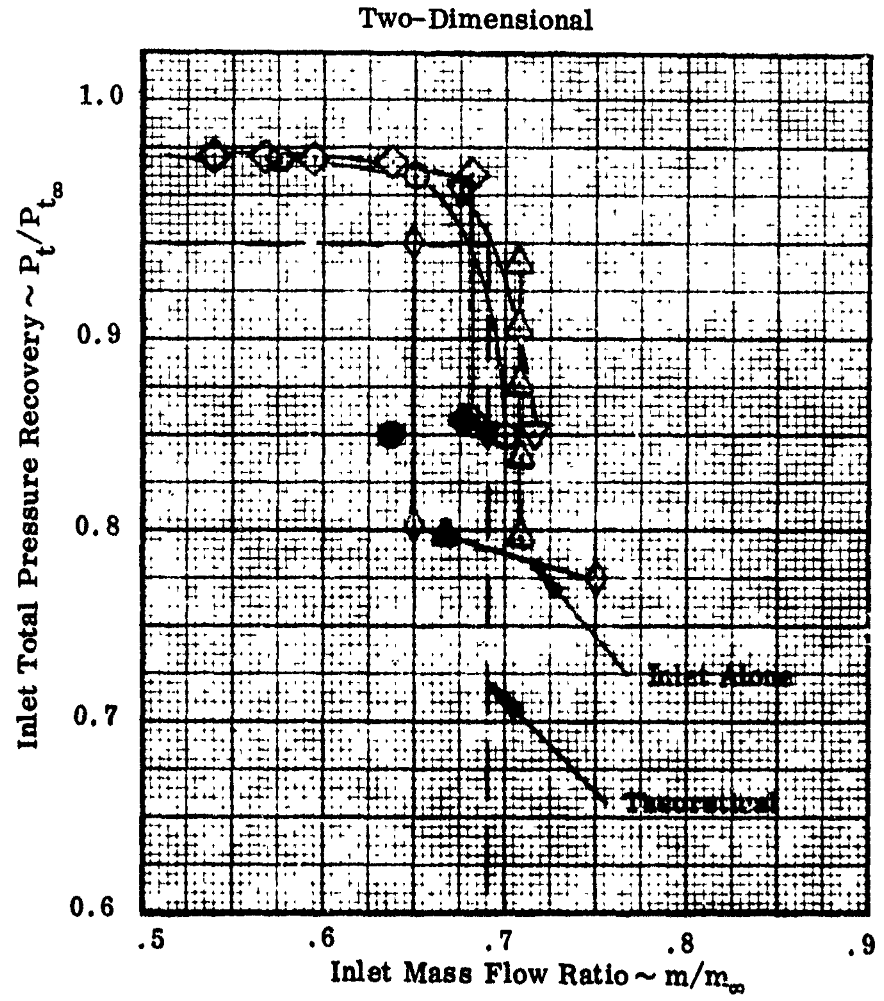

Figure 7-231. Comparison of Inlet Performance

$M_\infty = 0.8$, $\alpha = -3°$

Note: Solid symbols based on local flow field properties.

Format II

Fuselage	Symbol
1	△
2	◇
3	○
4	▽

2-Dimensional Inlet

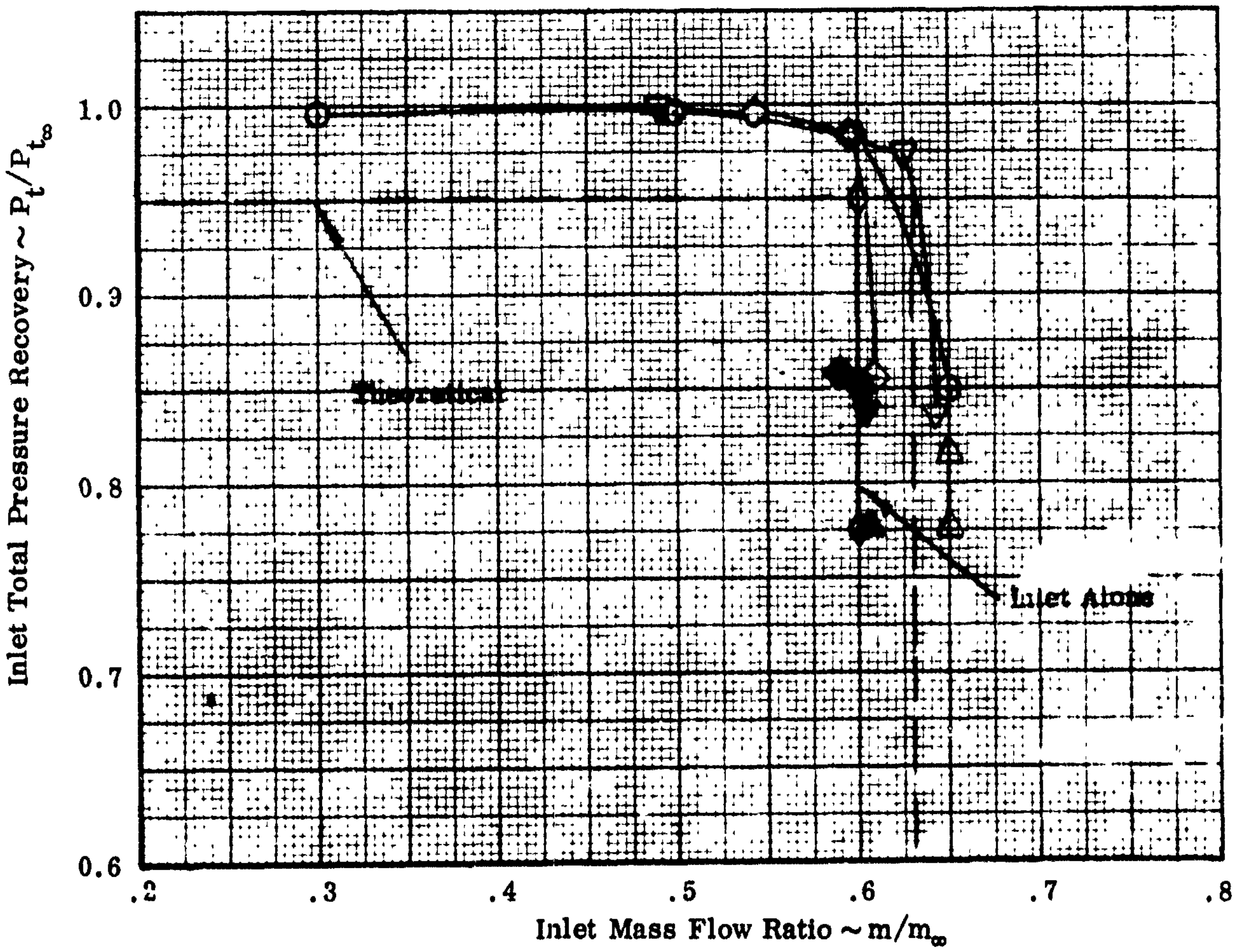

Figure 7-232. Comparison of Inlet Performance

$M_\infty = 0.8$, $\alpha = 0°$

Note: Solid symbols based on local flow field properties.

Format II

Fuselage	Symbol
1	△
2	◇
3	○
4	▽

2-Dimensional Inlet

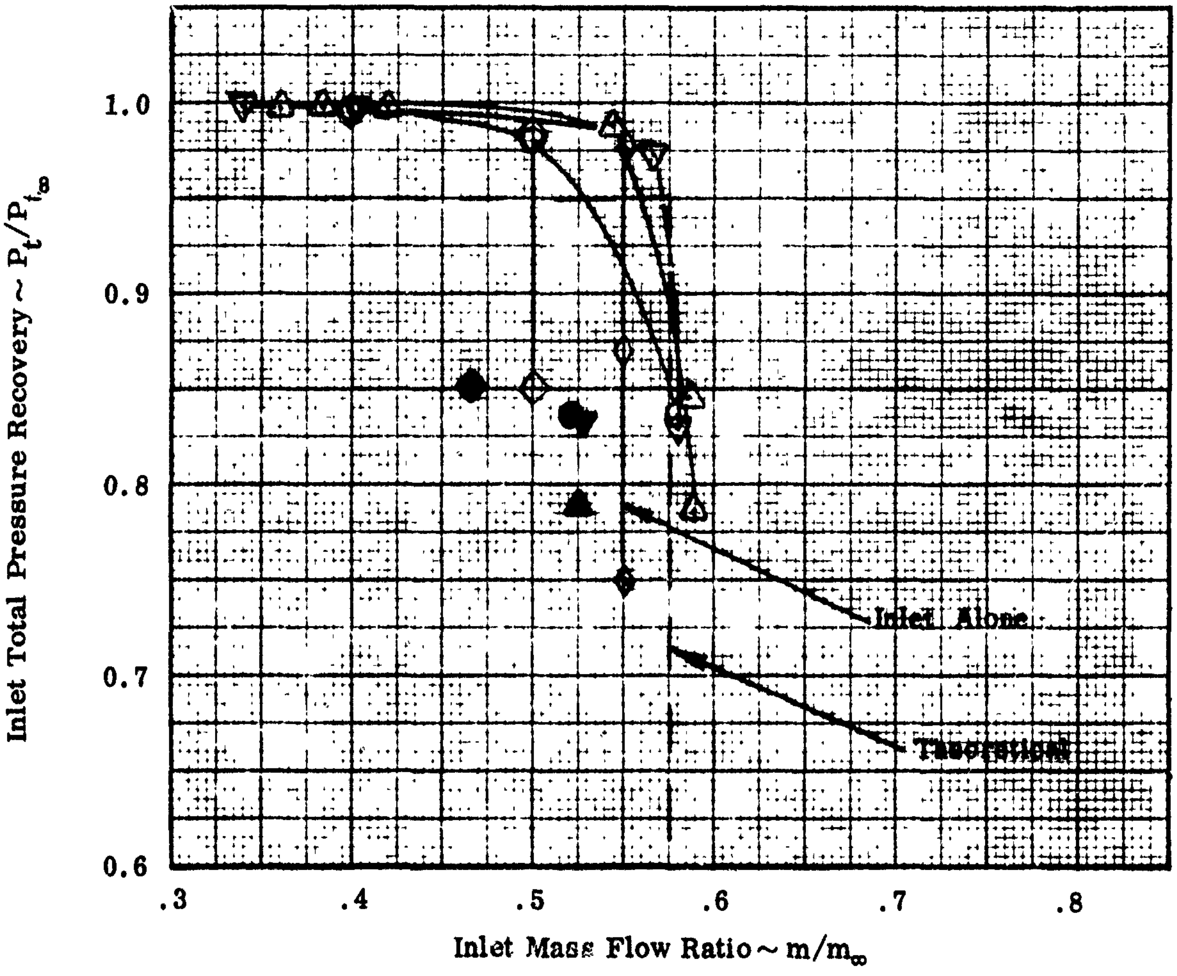

Figure 7-233. Comparison of Inlet Performance

$M_\infty = 0.8$, $\alpha = 5°$

Note: Solid symbols based on local flow field properties.

Format II

Fuselage	Symbol
1	△
2	◇
3	○
4	▽

Two-Dimensional Inlet

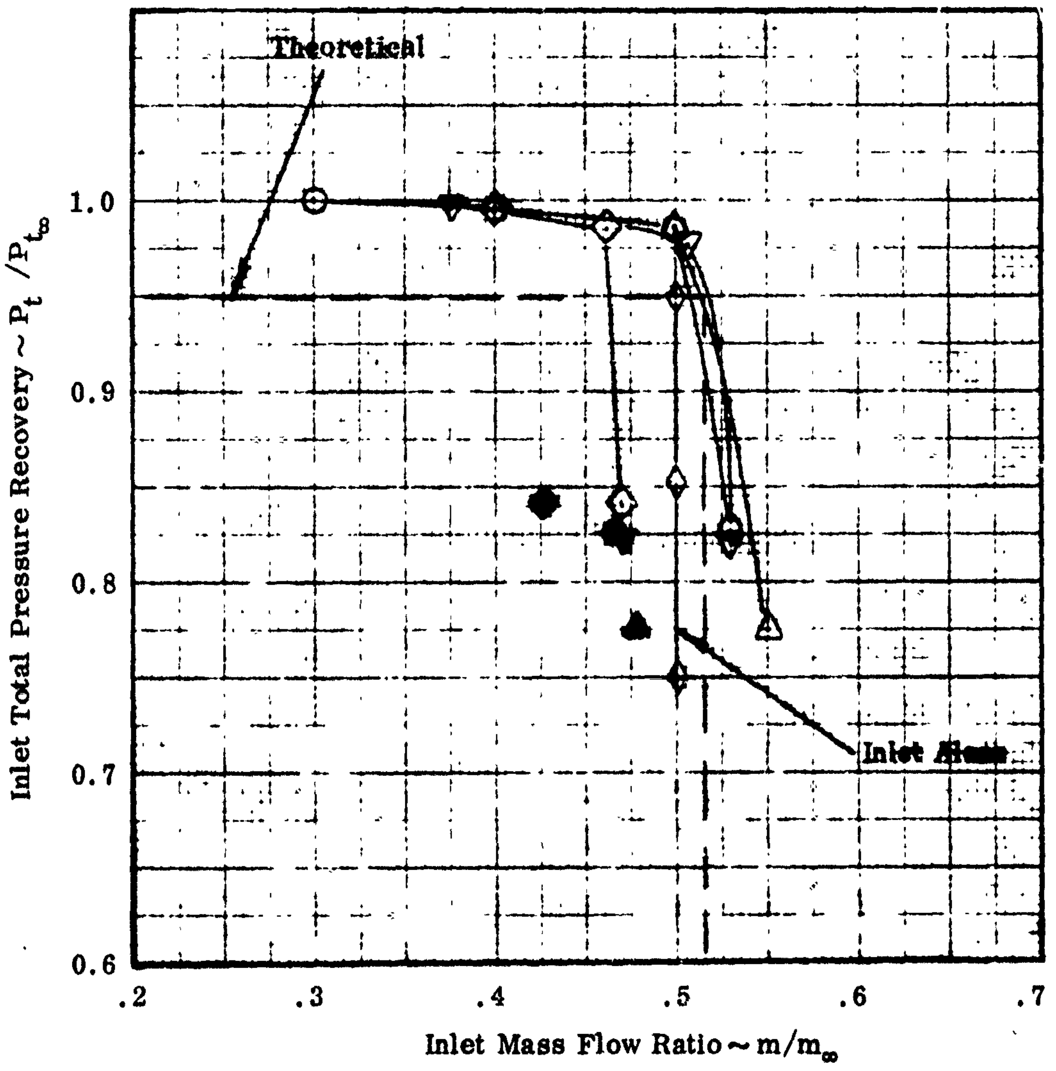

Figure 7-234. Comparison of Inlet Performance
$M_\infty = 0.8$, $\sigma = 10°$

Format II

Fuselage	Symbol
1	△
2	◇
3	○
4	▽

Note: Solid symbols based on local flow field properties.

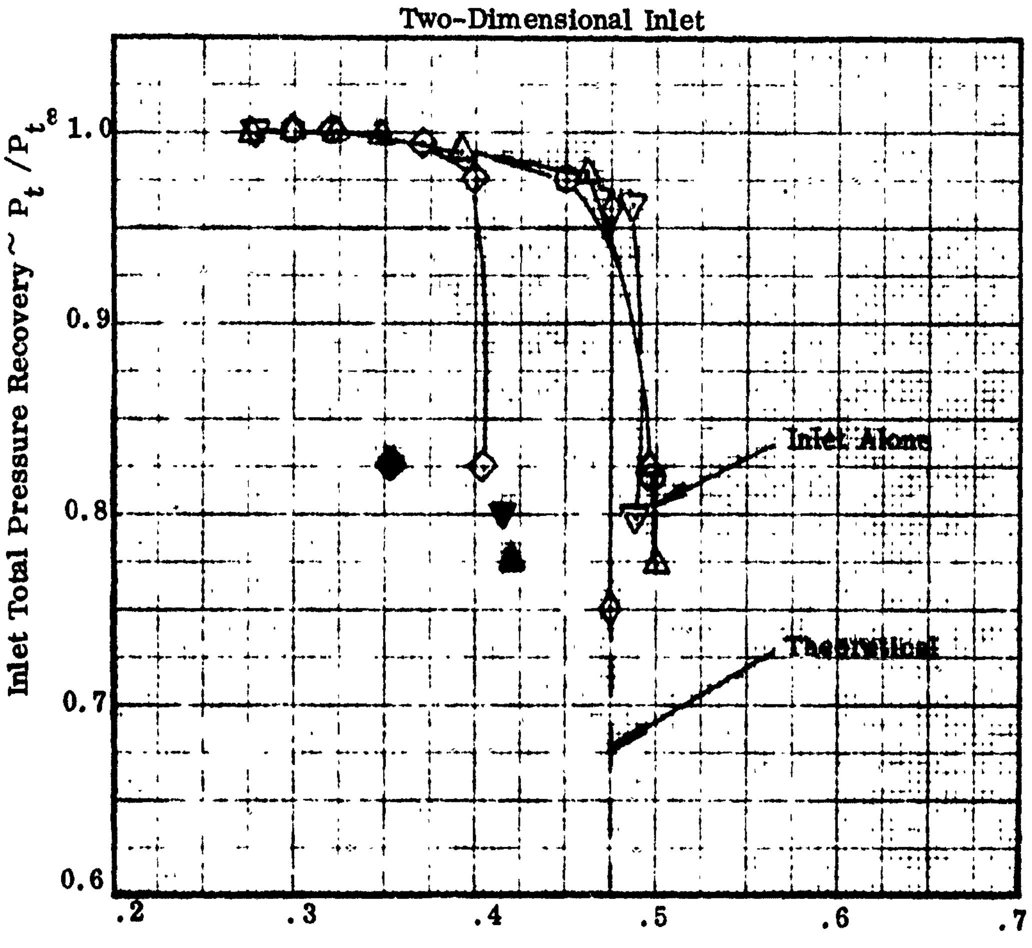

Figure 7-235. Comparison of Inlet Performance

$M_\infty = 0.8$, $\alpha = 15°$

Note: Solid symbols based on local flow field properties.

Format II

Fuselage	Symbol
1	△
2	◇
3	○
4	▽

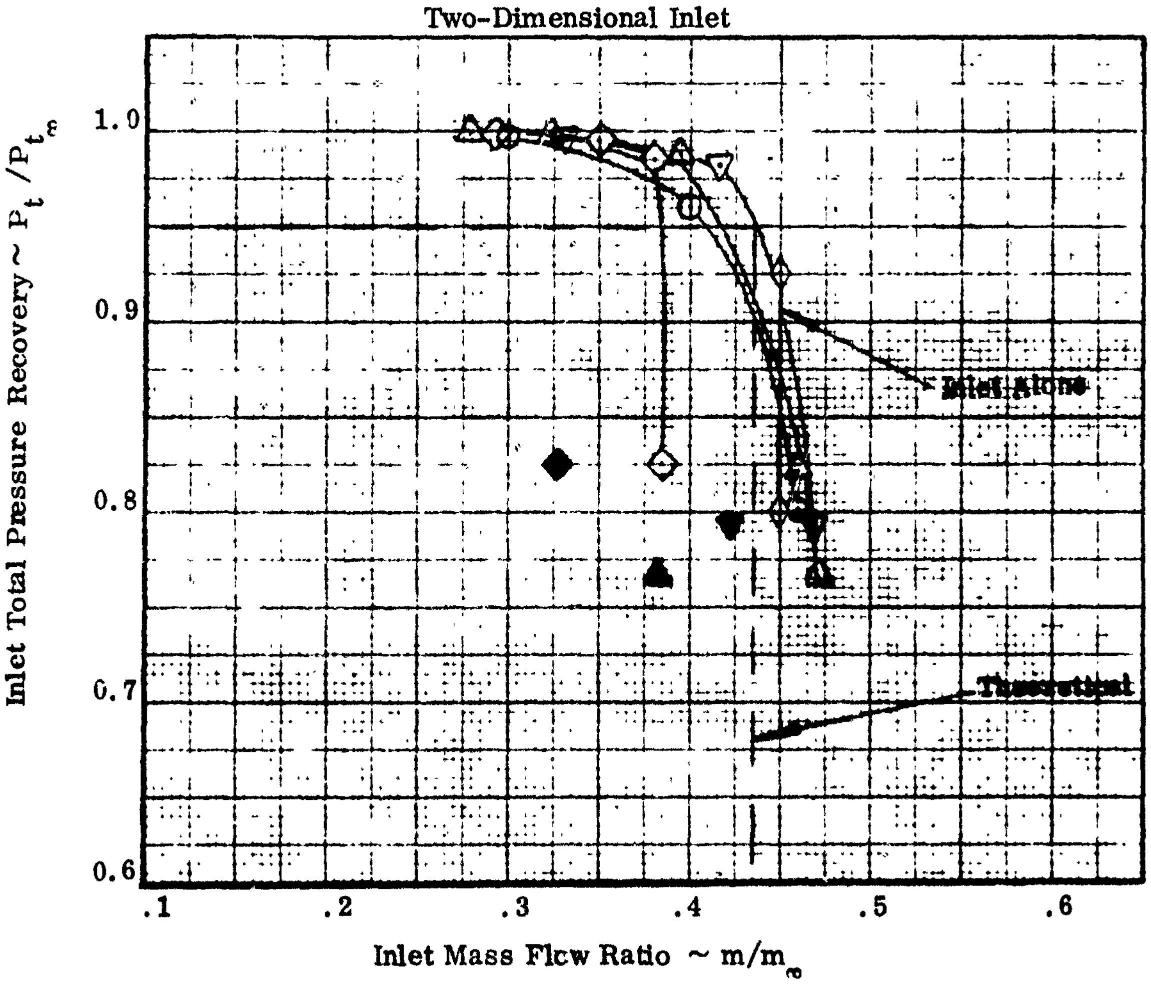

Figure 7-236. Comparison of Inlet Performance

$M_\infty = 0.8$, $\alpha = 20°$

Format II

Fuselage	Symbol
1	△
2	◇
3	○
4	▽

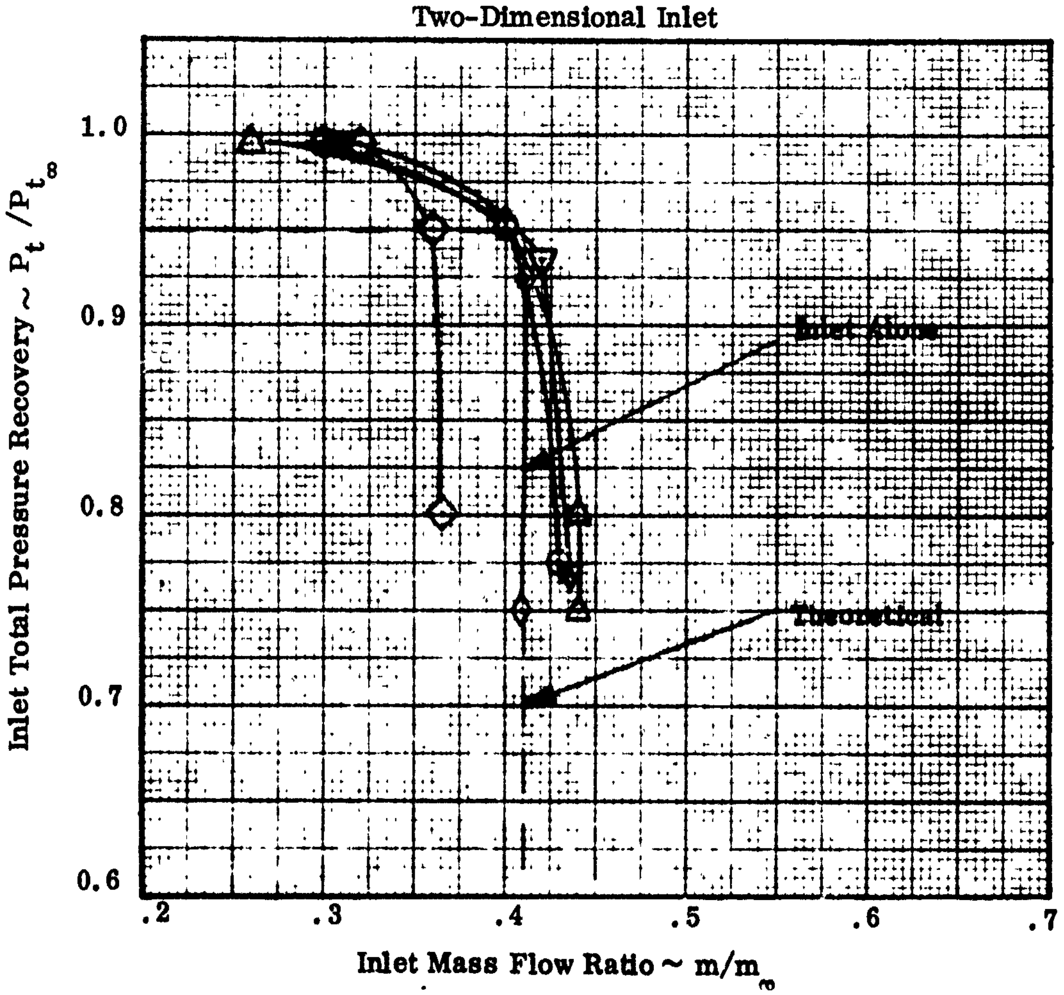

Figure 7-237. Comparison of Inlet Performance

$M_\infty = 0.8$, $\alpha = 25°$

2-Dimensional Inlet

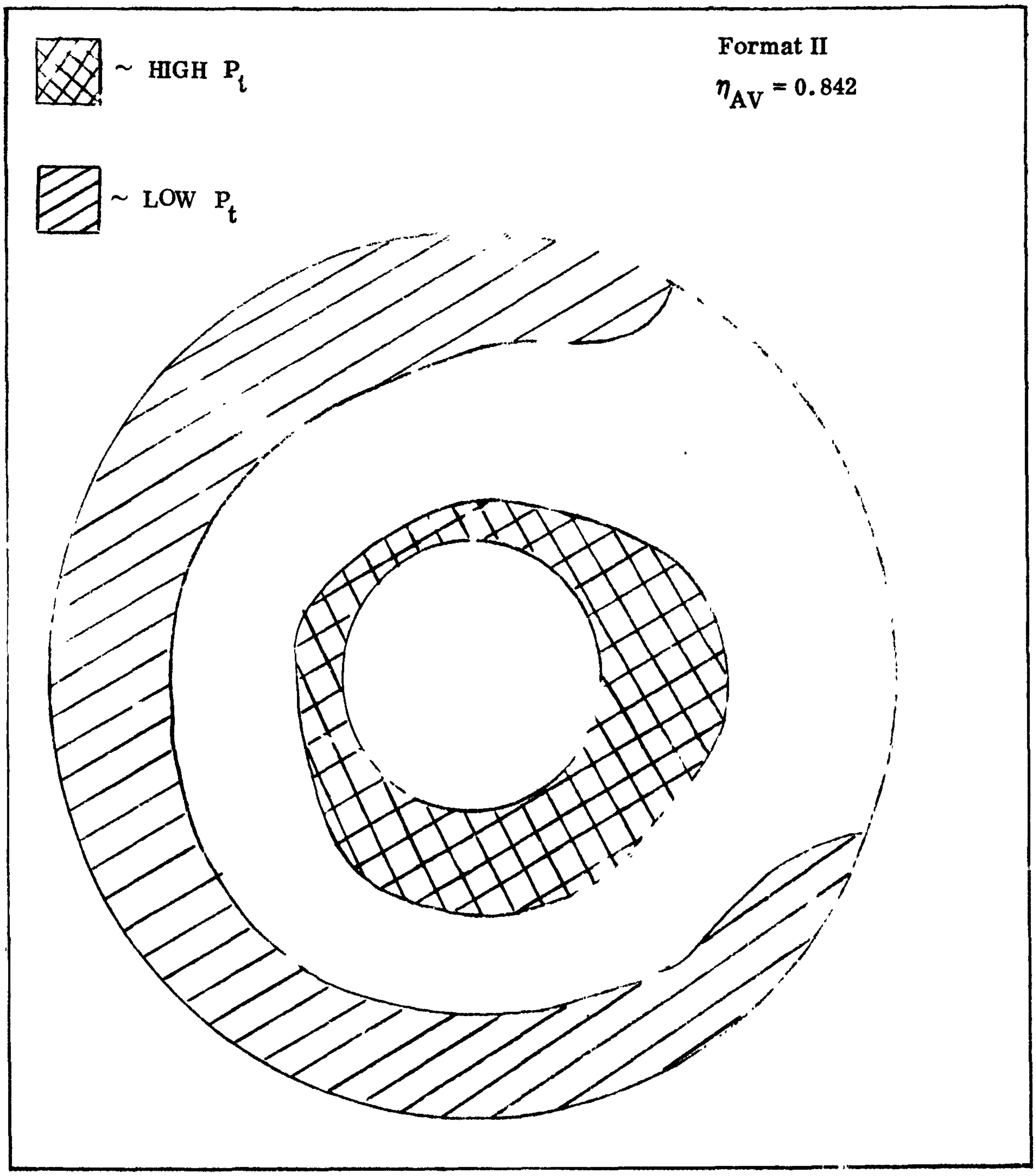
▨ ~ HIGH P_t
▨ ~ LOW P_t
Format II
$\eta_{AV} = 0.842$

Figure 7-238. Engine Face Profile, Fuselage 2
$M_\infty = 0.8$, $\alpha = 10$

2-Dimensional Inlet

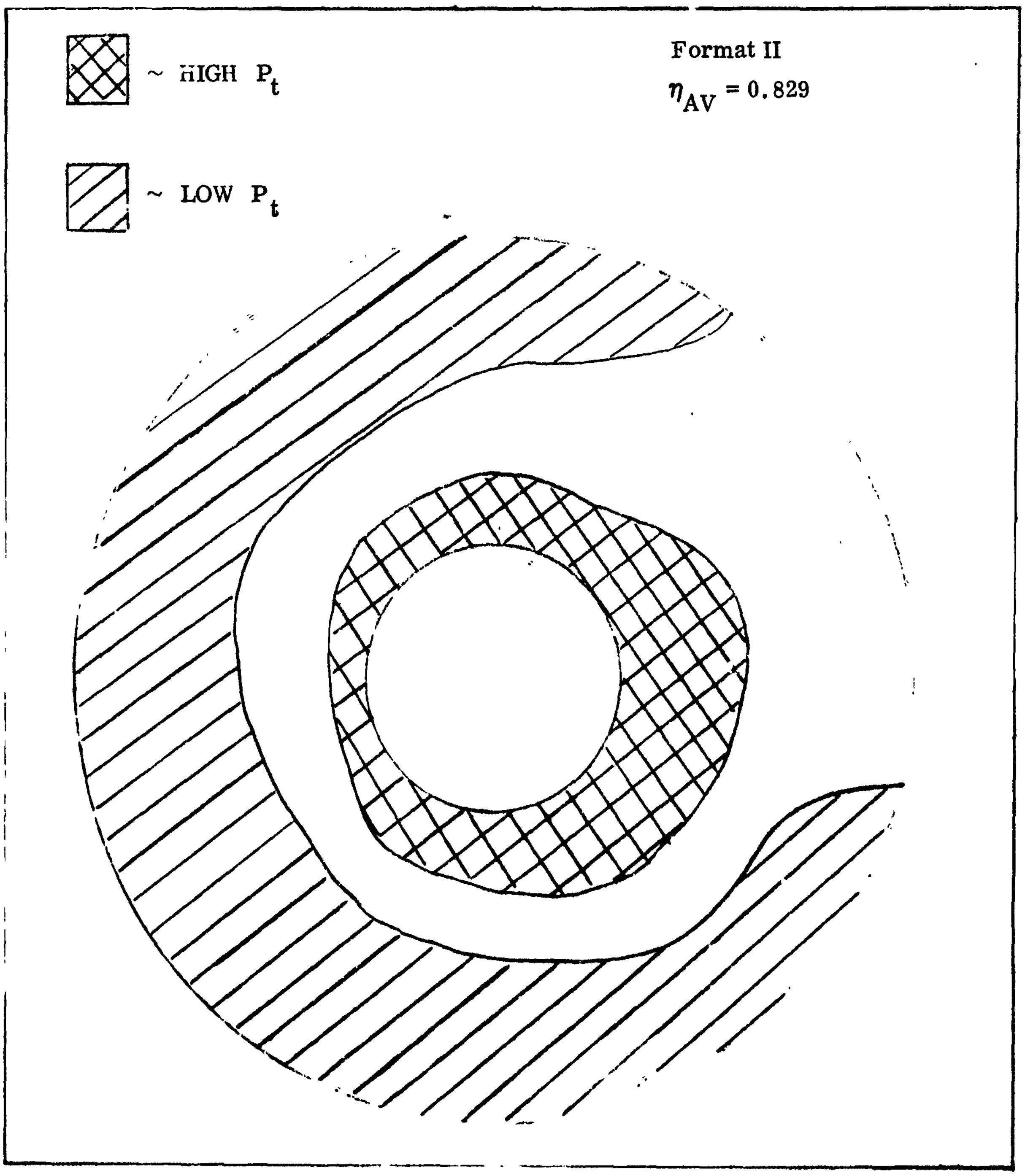
▩ ~ HIGH P_t
▨ ~ LOW P_t
Format II
$\eta_{AV} = 0.829$

Figure 7-239. Engine Face Profile, Fuselage 2
$M_\infty = 0.8$, $\alpha = 15°$

2-Dimensional Inlet

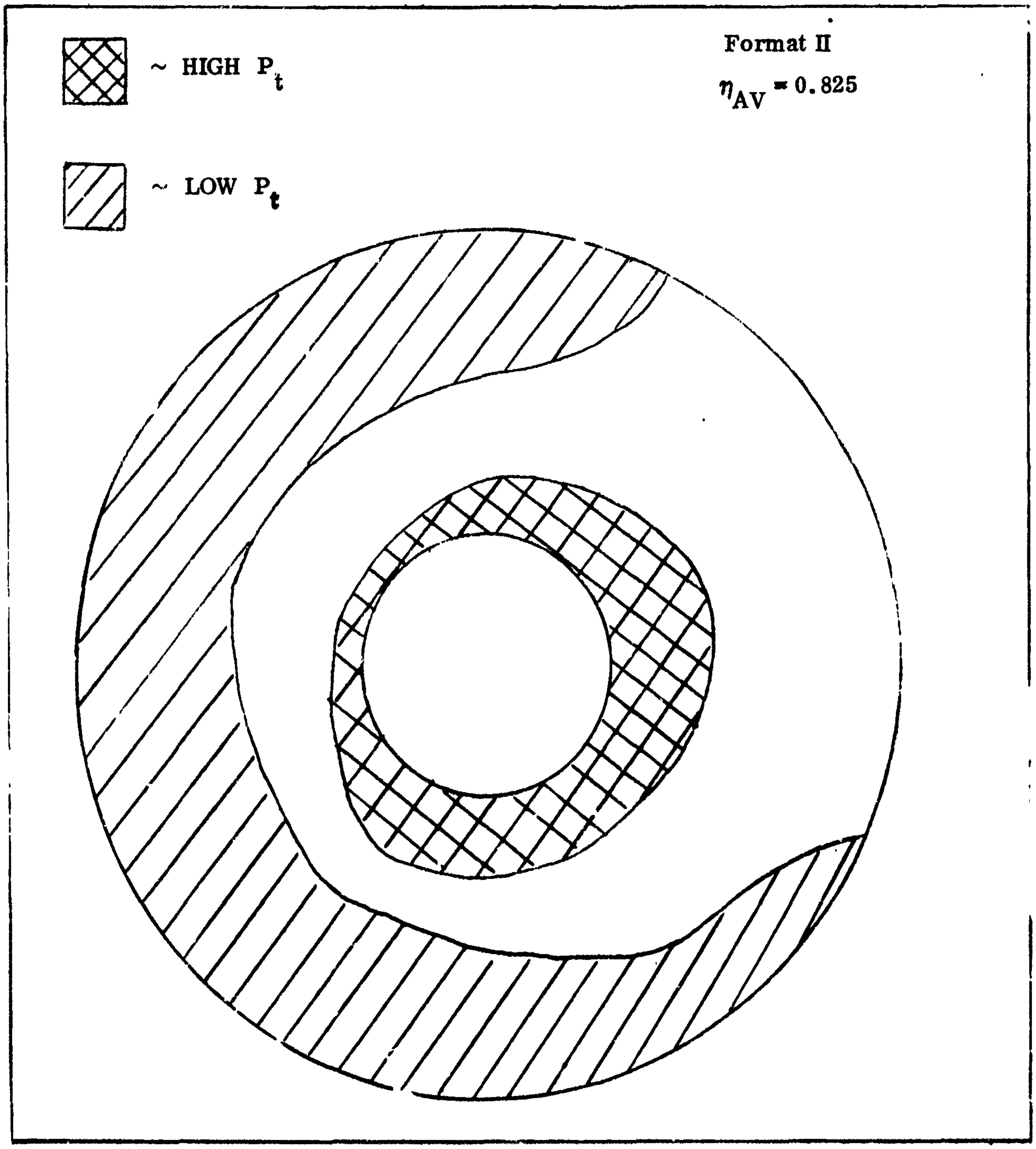
▩ ~ HIGH P_t
▨ ~ LOW P_t
Format II
$\eta_{AV} = 0.825$

Figure 7-240. Engine Face Profile, Fuselage 2

$M_\infty = 0.8$, $\alpha = 20°$

a potential incompatibility between the inboard inlet sidewall and the fusleage. At this near sonic Mach number the flow diverter channel formed between these two surfaces may be choked, thereby disturbing the flow entering the inlet. This disturbance could reduce the effective inlet throat area and consequently the mass flow, This argument is supported by an examination of the supercritical profile for the fuselage 1/inlet combination shown in Figures 7-241 through 7-243 in which the extensive inboard low pressure region is not present.

7.4.3.2 Mach Number 1.2

The inlet performance for negative angle of attack is presented in Figure 7-244. The characteristic for each of the 4 inlet/fuselage combinations and the inlet alone configuration are essentially superimposed upon one another. In addition, correcting for the effects of local flow angularity and Mach number, shown by the solid symbols, produces no shift in the characteristics. This indicates that the inlet throat is essentially sonic thereby controlling the mass flow. In addition, the horizontally oriented external compression ramps damp out any potential misalignment between the inlet surface and the approaching flow. These factors make the inlet insensitive to fuselage induced effects. This inlet operating mode continues throughout the entire angle of attack excursion, as shown in Figures 7-245 through 7-249, where the corrected characteristics are grouped within the experimental accuracy. Figure 7-250 presents the results achieved at an angle of attack of 25°. For this case flow field maps were not obtained and consequentely corrections for local deviations in flow angularity and Mach number could not be made. However, even these uncorrected characteristics are very closely grouped.

7.4.3.3 Mach Number 1.8

The inlet performance at negative angle of attack is shown in Figures 7-251. During these tests data for fuselage 2 were not taken. In addition, the data for fuselages 3 and 4 were taken with the inlet operating subcritically. A complete characteristic cane was obtained for the fuselage 1 configuration. The effect of the downwash flow field is evident from a comparison with the inlet alone configuration. The increased supercritical mass flow ratio, shown by the closed symbol, is due to the downwash flow field moving the integrated inlet closer to shock on lip operation.

Two-Dimensional Inlet

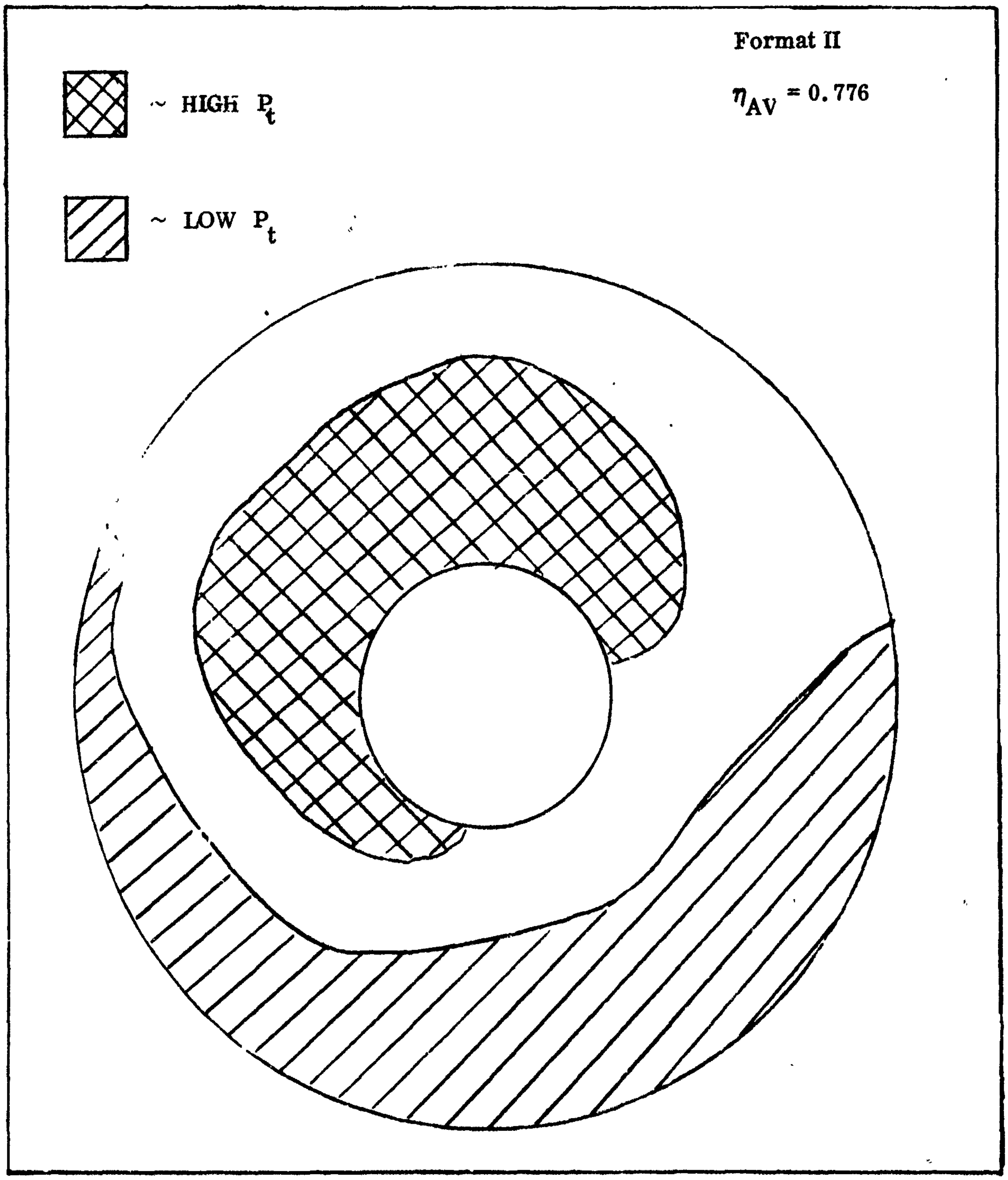
~ HIGH P_t
~ LOW P_t
Format II
$\eta_{AV} = 0.776$

Figure 7-241. Engine Face Profile, Fuselage 1
$M_\infty = 0.8$, $\alpha = 10°$

Two Dimensional Inlet

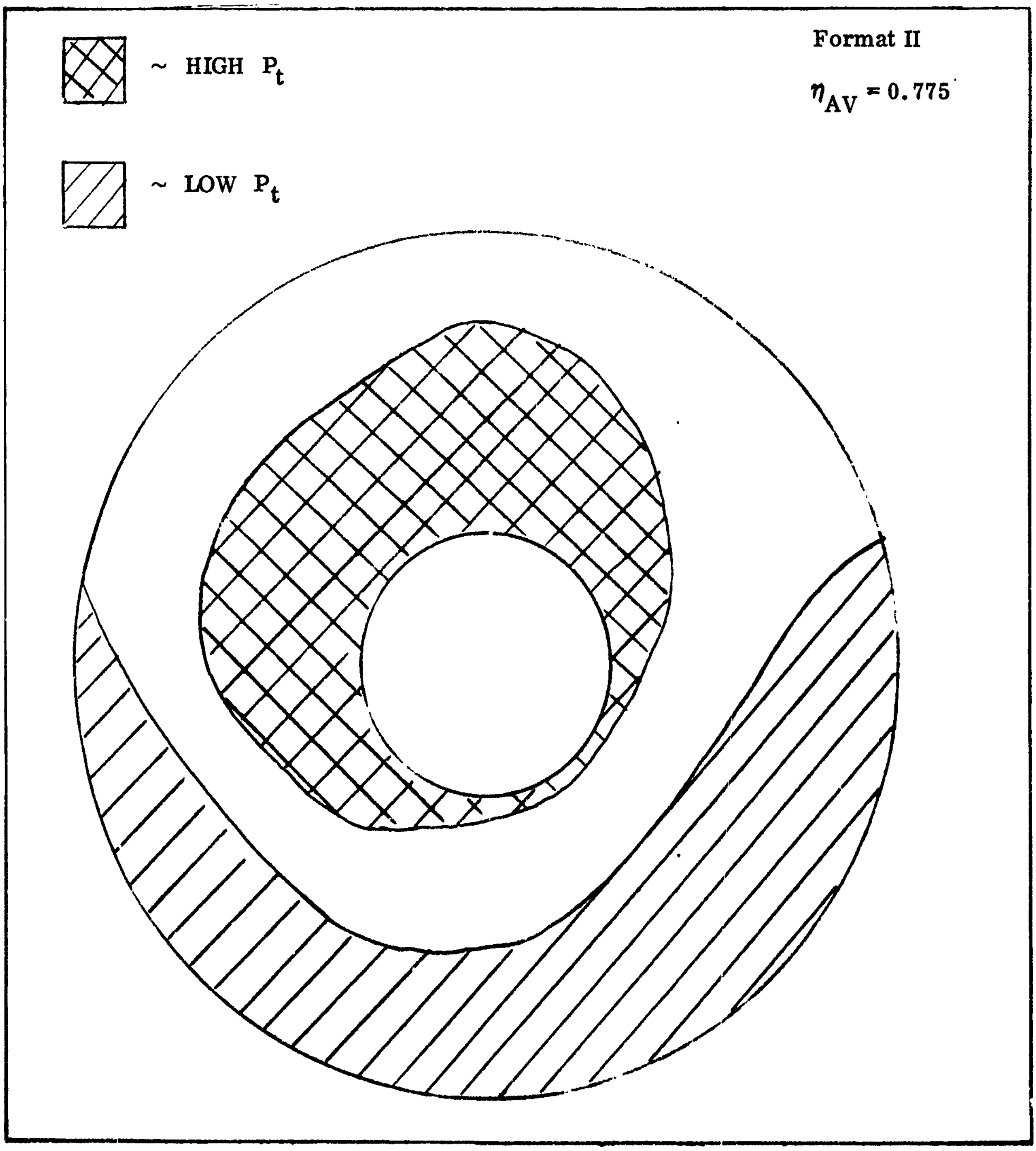
~ HIGH P_t
~ LOW P_t
Format II
$\eta_{AV} = 0.775$

Figure 7-242. Engine Face Profile, Fuselage 1

$M_\infty = 0.8$, $\alpha = 15°$

Two Dimensional Inlet

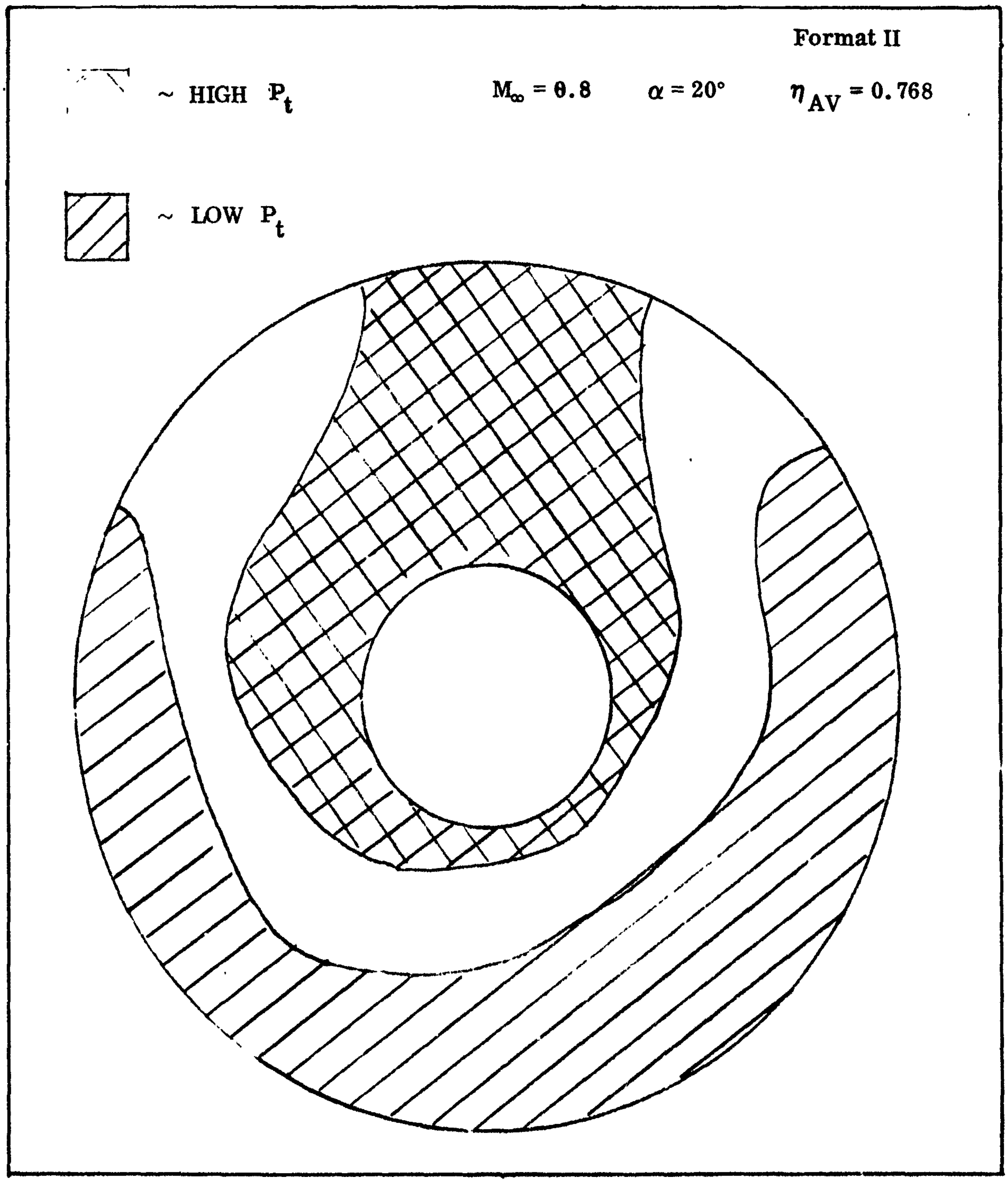
Format II
~ HIGH P_t
$M_\infty = 0.8$
$\alpha = 20°$
$\eta_{AV} = 0.768$
~ LOW P_t

Figure 7-243. Engine Face Profile, Fuselage 1
$M_\infty = 0.8$, $\alpha = 20°$

Note: Solid symbols based on local flow field properties.

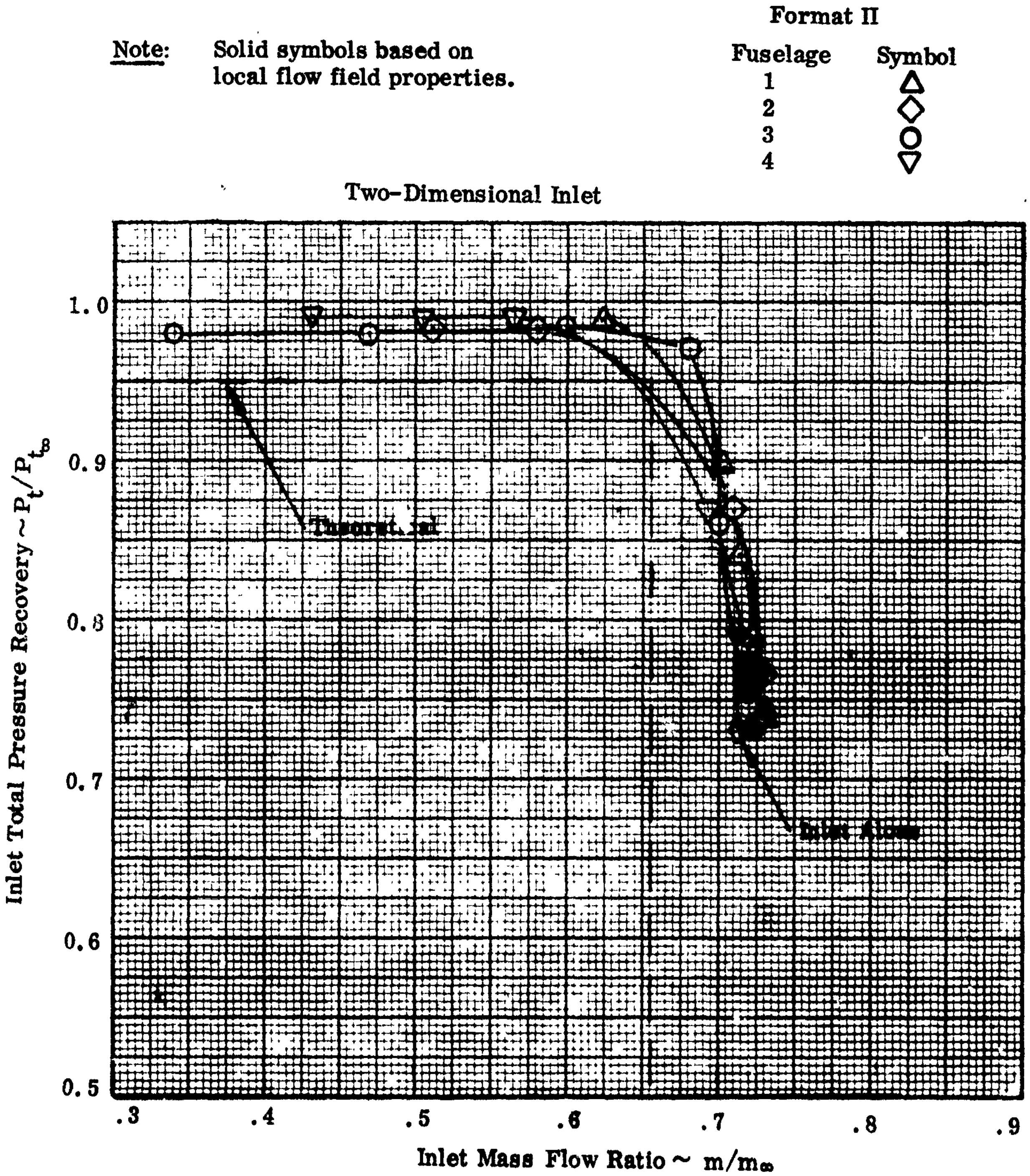

Figure 7-244. Comparison of Inlet Performance
$M_\infty = 1.2$, $\alpha = -3°$

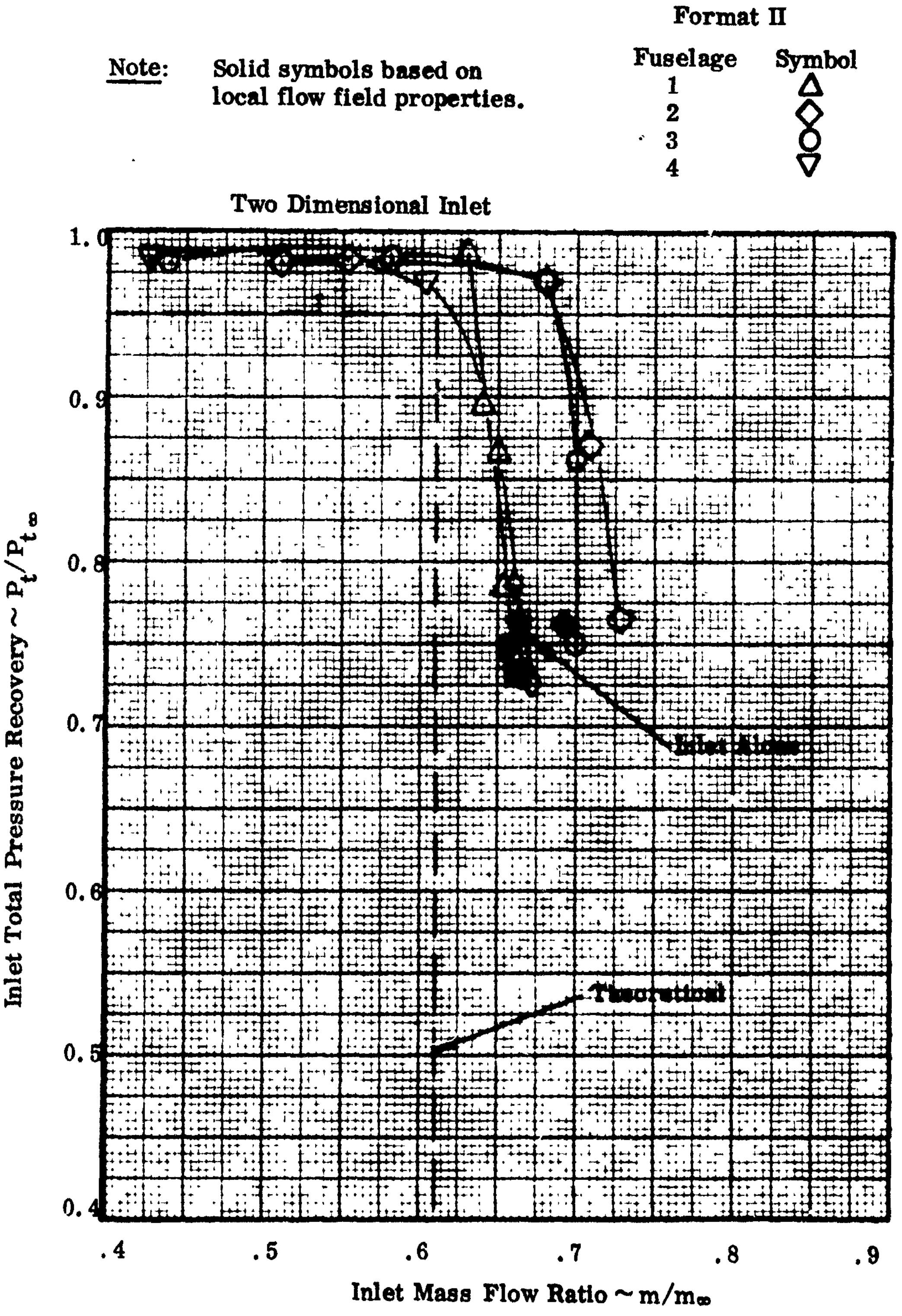

Figure 7-245. Comparison of Inlet Performance $M_\infty = 1.2$, $\alpha = 0°$

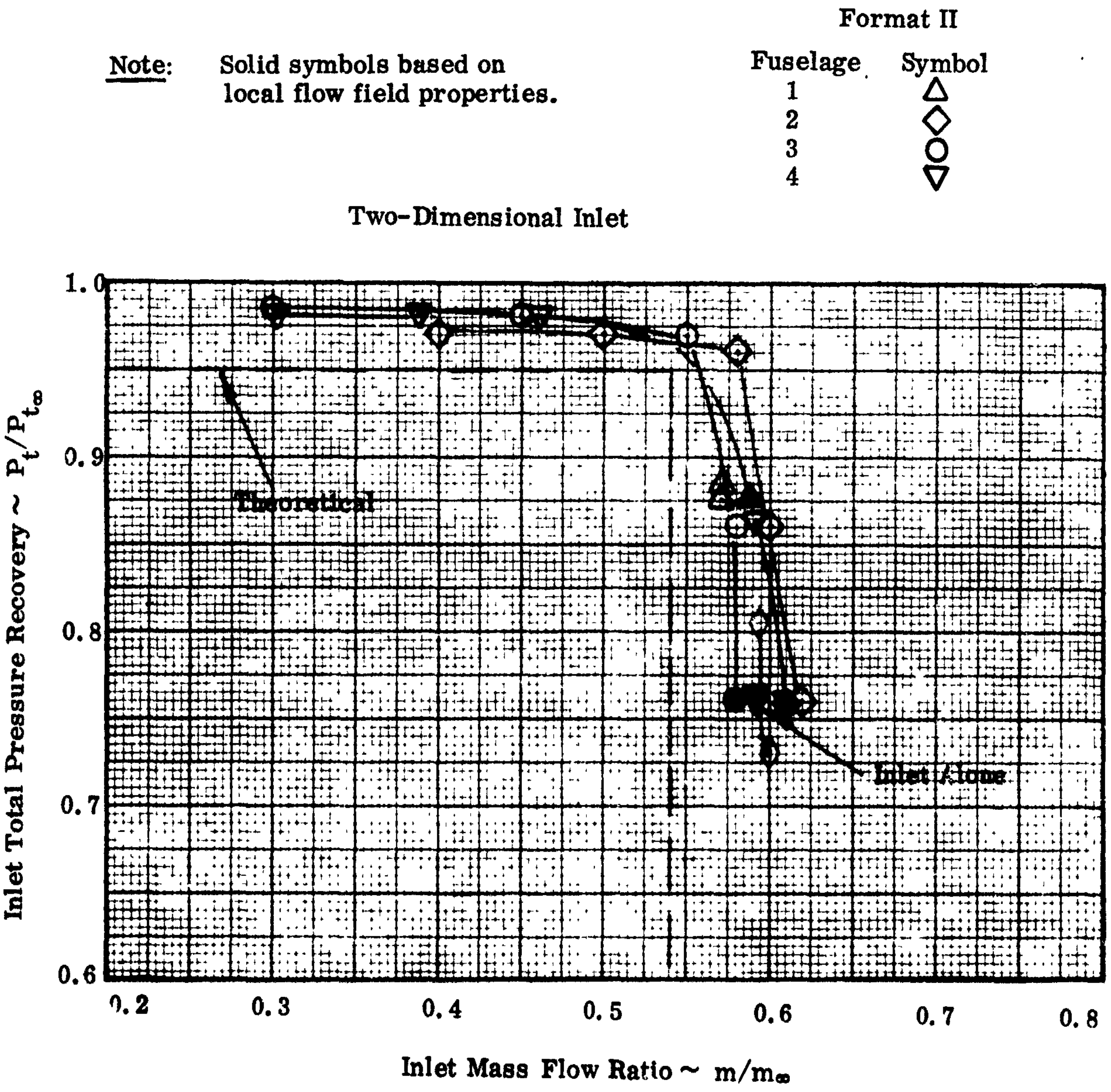

Format II

Note: Solid symbols based on local flow field properties.

Fuselage	Symbol
1	△
2	◇
3	○
4	▽

Two-Dimensional Inlet

Figure 7-246. Comparison of Inlet Performance
$M_\infty = 1.2$, $\alpha = 5°$

Format II

Fuselage	Symbol
1	△
2	◇
3	○
4	▽

Note: Solid symbols based on local flow field properties.

Two-Dimensional Inlet

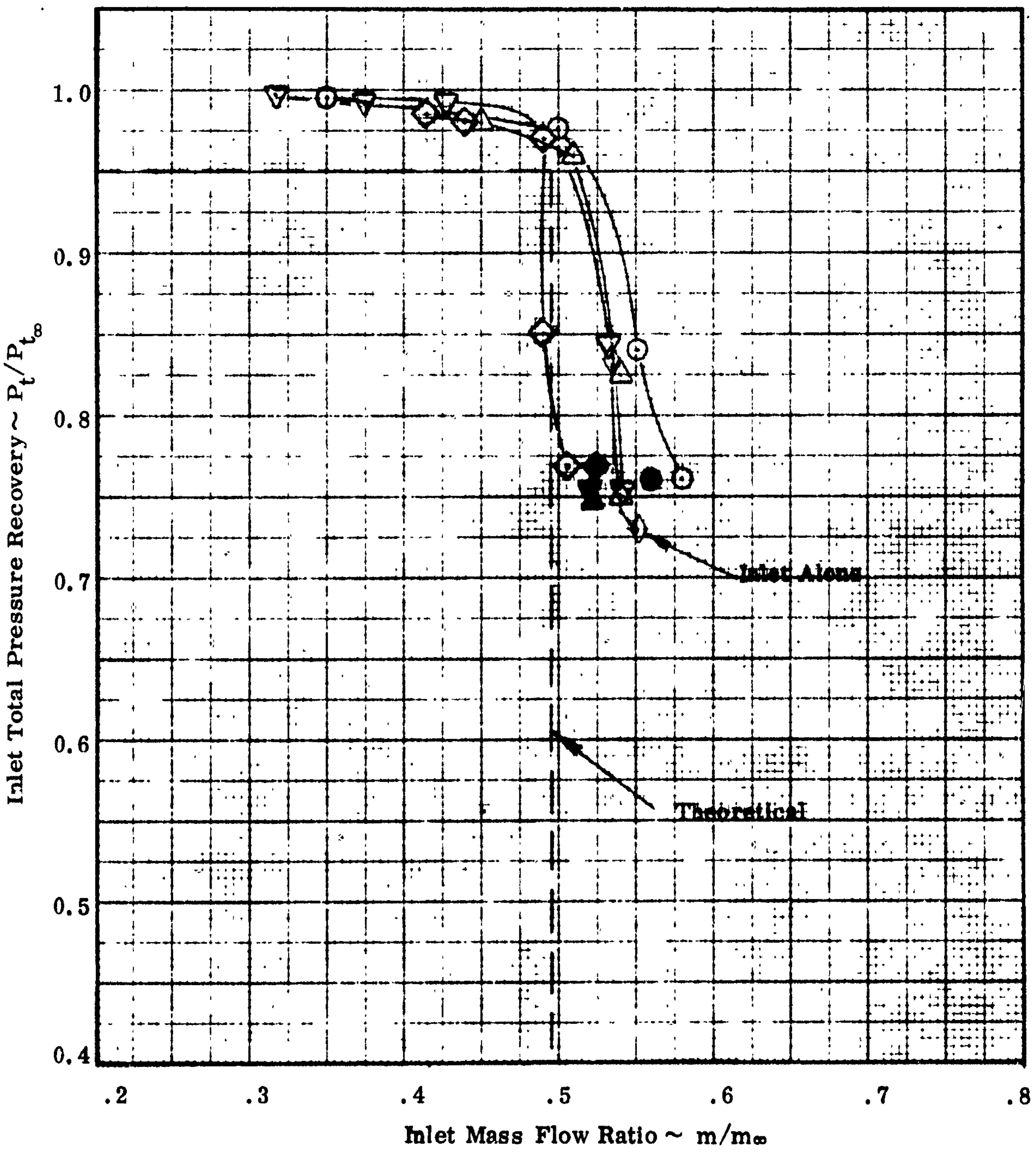

Figure 7-247. Comparison of Inlet Performance
$M_\infty = 1.2$, $\alpha = 10°$

Note: Solid symbols based on local flow field properties.

Format II

Fuselage	Symbol
1	△
2	◇
3	○
4	▽

Two-Dimensional Inlet

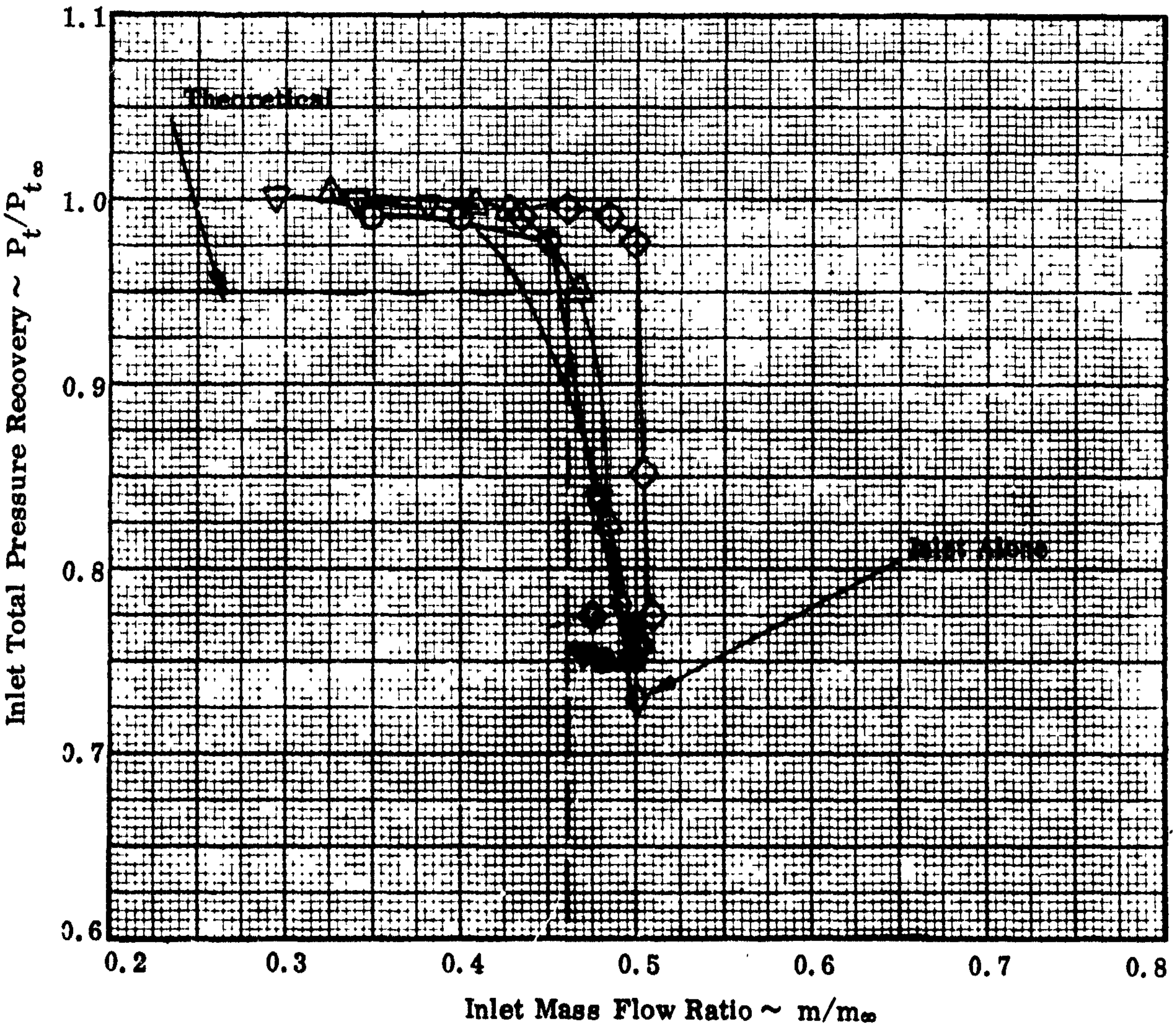

Figure 7-248. Comparison of Inlet Performance

$M_\infty = 1.2, \quad \alpha = 15°$

Note: Solid symbols based on local flow field properties.

Format II

Fuselage	Symbol
1	△
2	◇
3	○
4	▽

Two-Dimensional Inlet

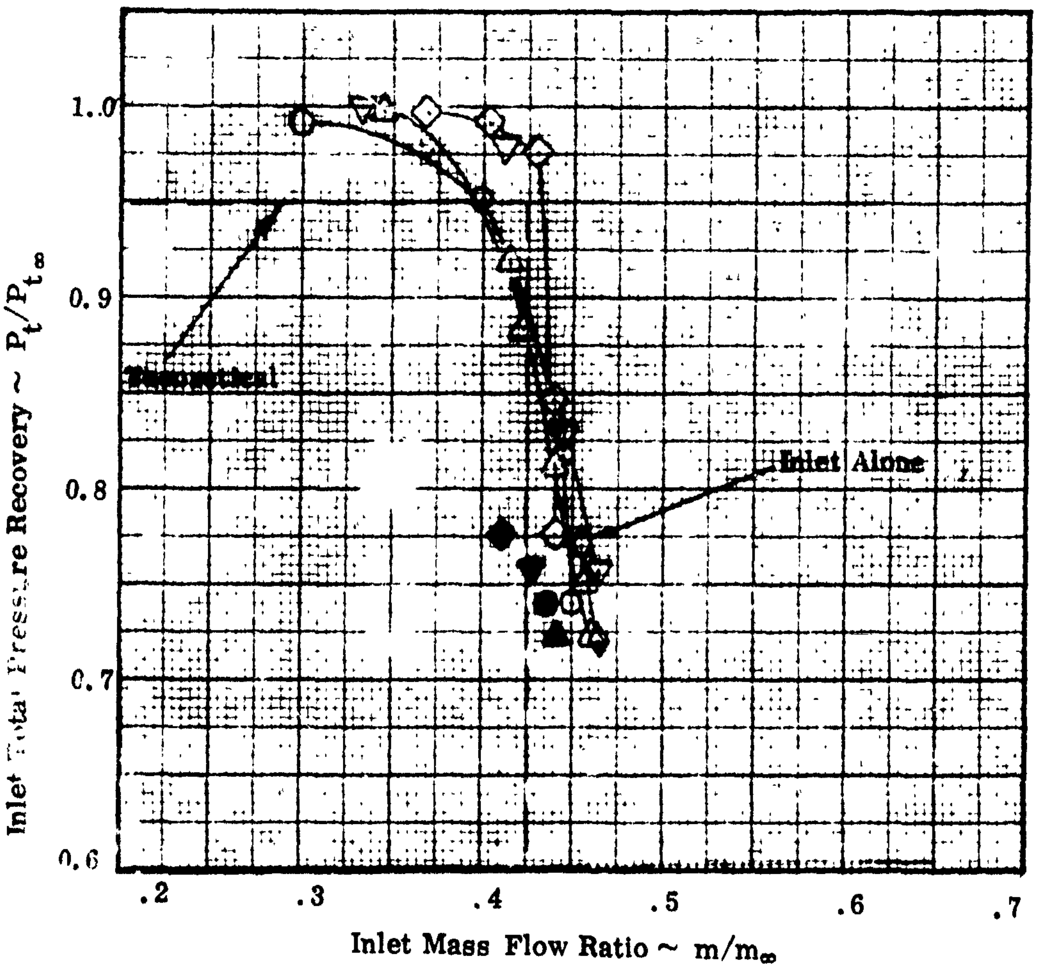

Figure 7-249. Comparison of Inlet Performance

$M_\infty = 1.2$, $\alpha = 20°$

Format II

Fuselage	Symbol
1	△
2	◇
3	⊙
4	▽

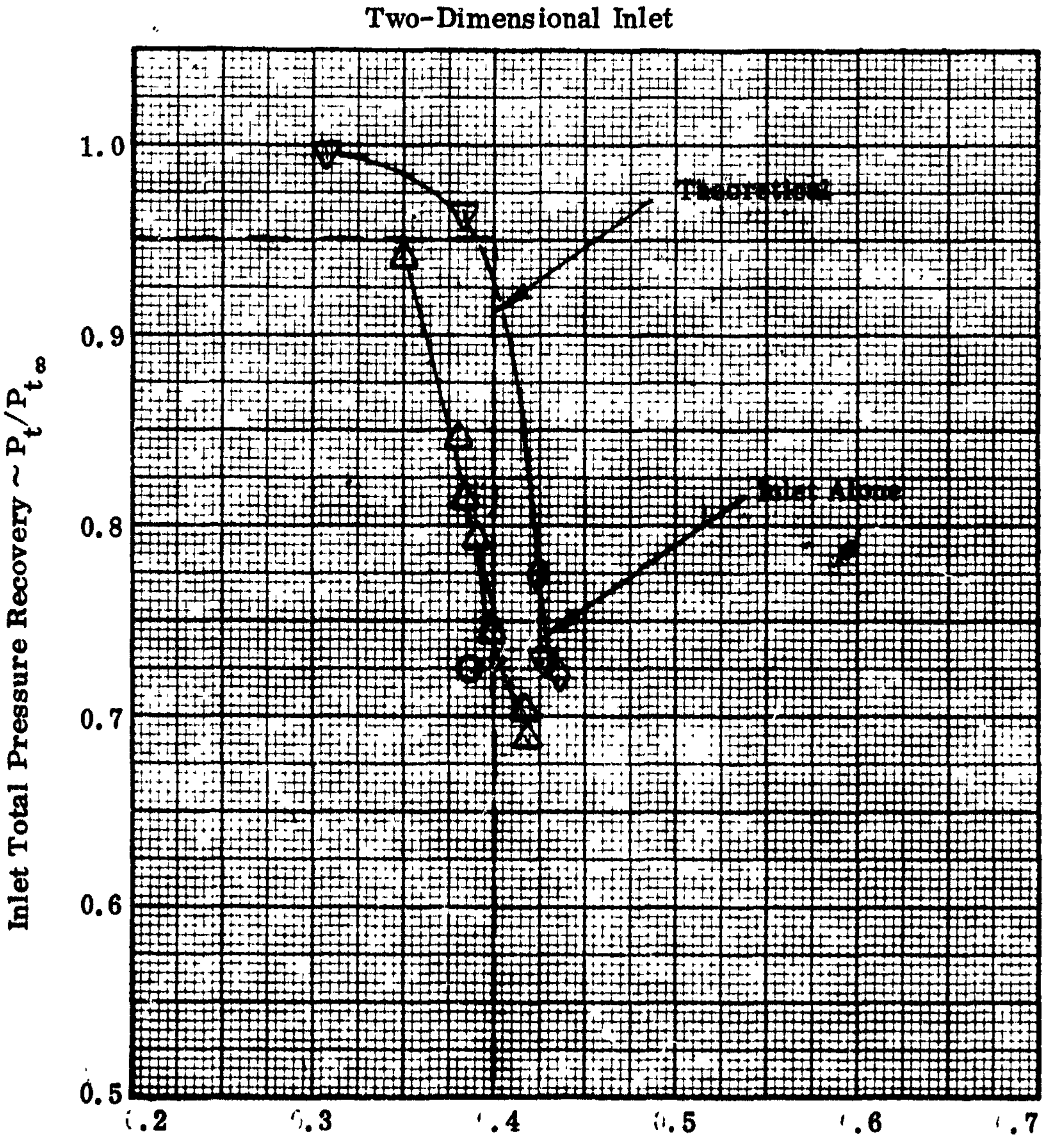

Figure 7-250. Comparison of Inlet Performance

$M_\infty = 1.2$, $\alpha = 25°$

Note: Solid symbols based on local flow field properties.

Format II

Fuselage	Symbol
1	△
2	◇
3	○
4	▽

Two-Dimensional Inlet

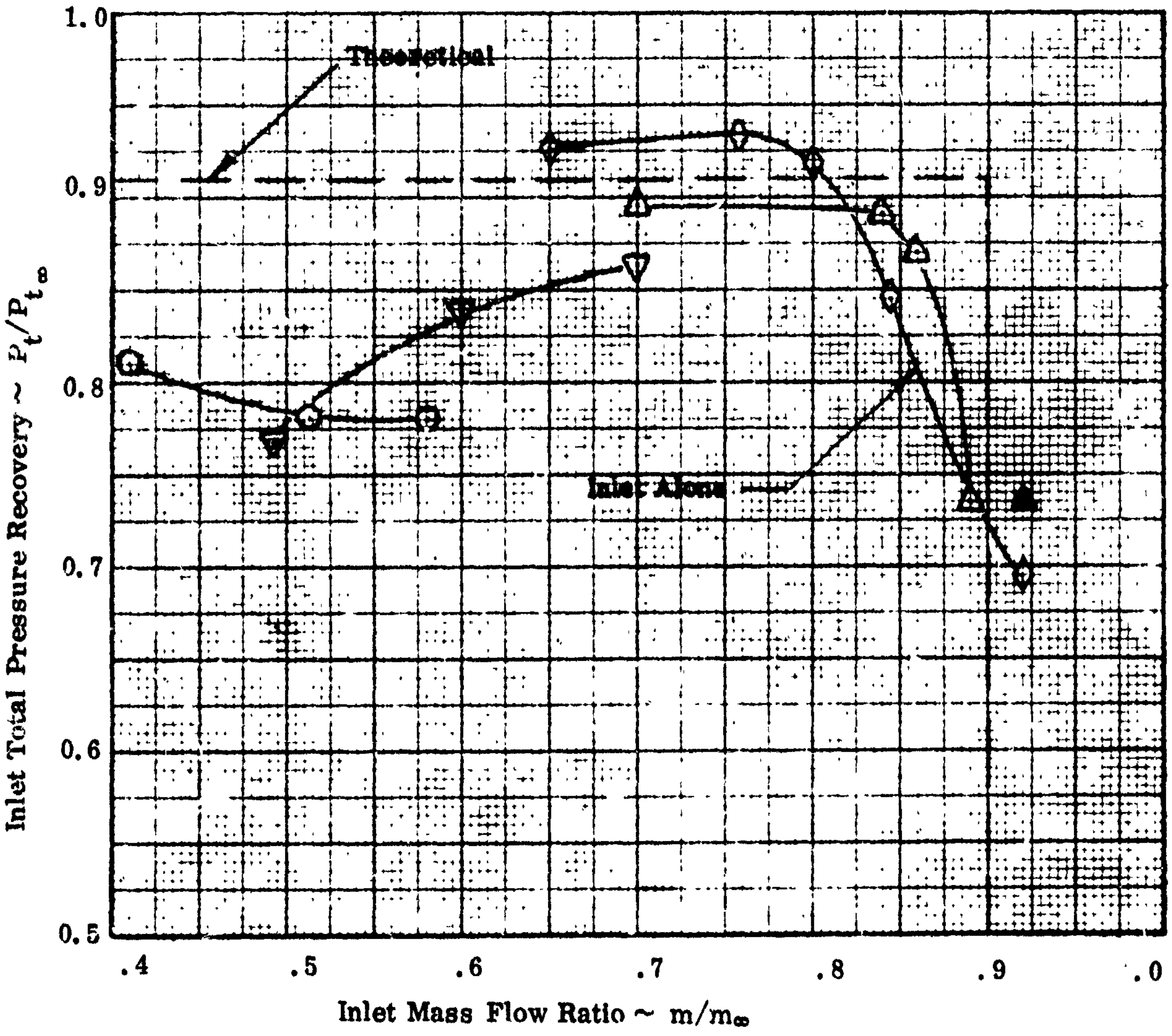

Figure 7-251. Comparison of Inlet Performance

$M_\infty = 1.8$, $\alpha = -3°$

The characteristic of the integrated system also has a steeper supercritical leg due to the weakened external compression system. Finally, the total pressure recovery for the integrated system is somewhat lower than that achieved for the inlet alone, due to the weakened external compression and the resultant development of a stronger terminal shock. With the flow field characteristics available these effects can be predicted analytically. The close agreement between the integrated inlet and the inlet alone indicates that the fuselage, in this case, does not introduce any unusual effects.

The inlet performance at 0° and +5° angle of attack is presented in Figures 7-252 and 7-253. The integrated configurations, the inlet alone and the theoretical estimates are very closely grouped.

The inlet performance for +10° angle of attack is presented in Figure 7-254. The integrated inlet characteristics are very closely grouped indicating a continued independence of fuselage geometry. The inlet alone characteristic was not fully developed but the supercritical leg is quite close to those of the integrated systems. The trend toward higher mass flow ratio for those configurations of larger fuselage corner radius becomes clearer at this point. There appears to be a large discrepancy between the peak total pressure recovery achieved experimentally and that estimated analytically. This is due to the conservatism of the analytical approach as the detached external shock condition is approached. Upon reaching the detached shock condition the analytical approach computes the loss associated with a normal shock. In fact, the loss, particularly close to detachment, would be more closely approximated by computing the loss associated with that strong shock wave producing a downstream Mach number approaching sonic. With increasing angle of attack, and increasing detached shock strength, an interpolation can be performed between the sonic wedge/cone solution and the normal shock solution until at very high angle of attack the normal shock solution can be used. For these external compression systems it may be necessary to superimpose a secondary effect, namely, that associated with shock curvature, that may improve the overall total pressure recovery by virtue of the fact that successive streamlines intercepted by the inlet pass through a decaying wave, as a function of the distance from the origin of the wave. Consequently, those streamlines entering near the cowl can be expected to have a somewhat higher total pressure recovery. These effects can be seen in the inlet performance curves for angles of attack of +15°, +20°, and +25°, presented in Figures 7-255 through 7-257.

Note: Solid symbols based on local flow field properties.

Format II

Fuselage	Symbol
1	△
2	◇
3	○
4	▽

Two-Dimensional Inlet

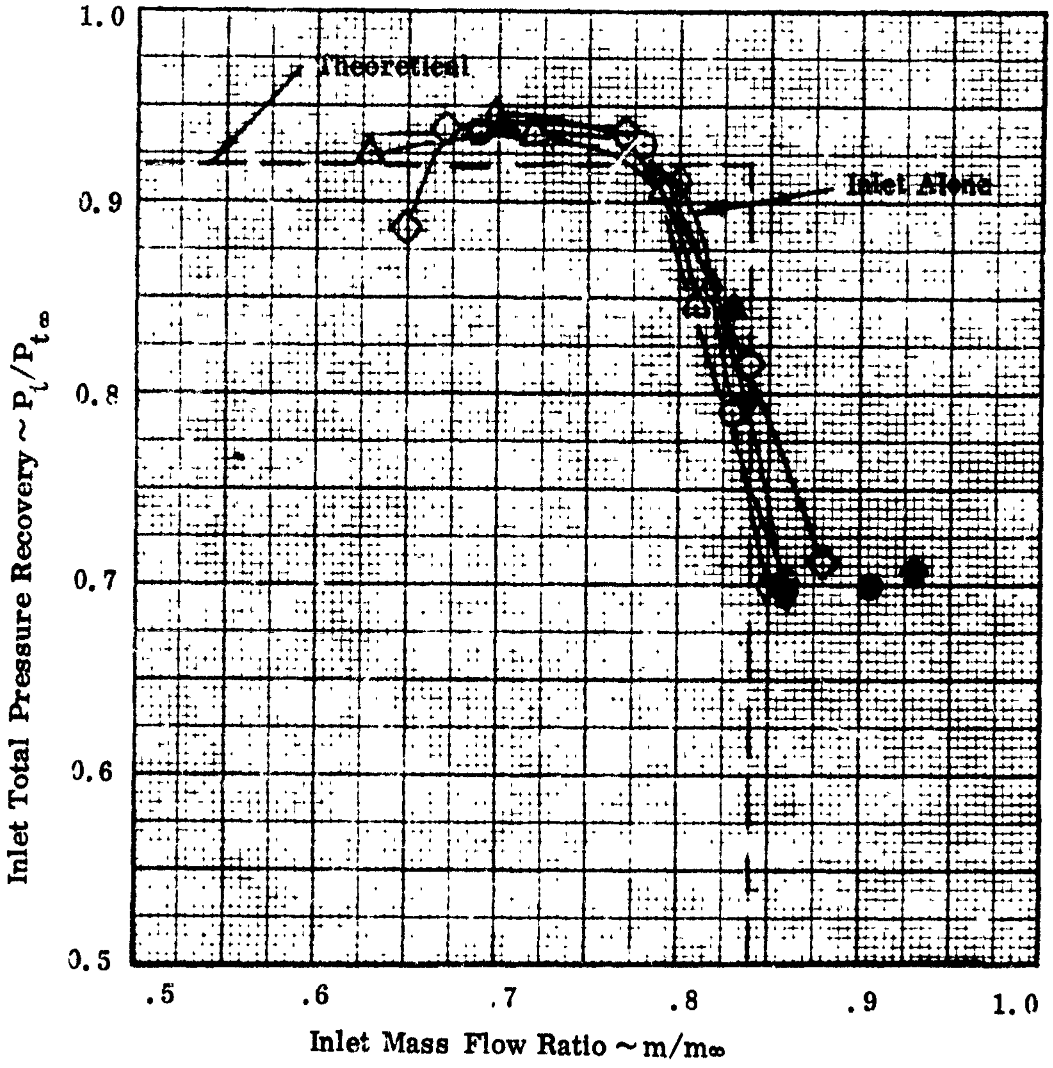

Figure 7-252. Comparison of Inlet Performance

$M_\infty = 1.8, \quad \alpha = 0°$

Format II

Note: Solid symbols based on local flow field properties.

Fuselage	Symbol
1	△
2	◇
3	○
4	▽

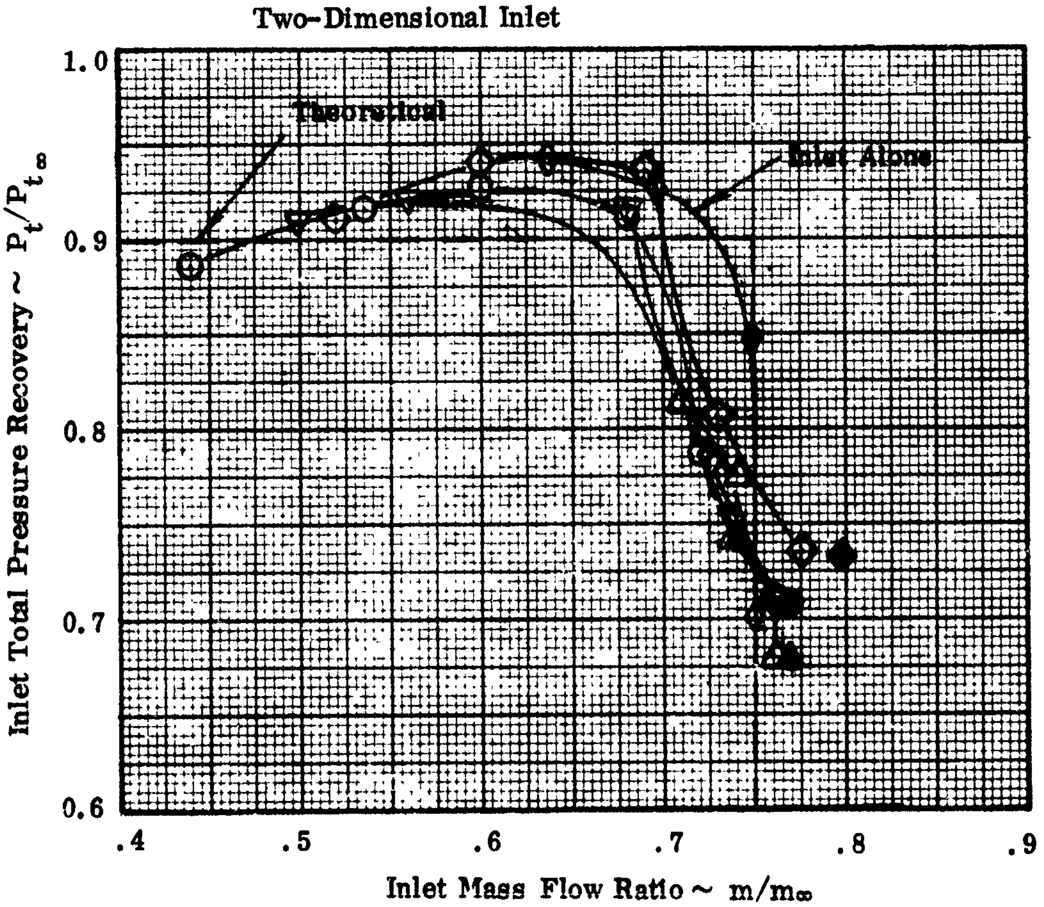

Figure 7-253. Comparison of Inlet Performance

$M_\infty = 1.8, \quad \alpha = 5°$

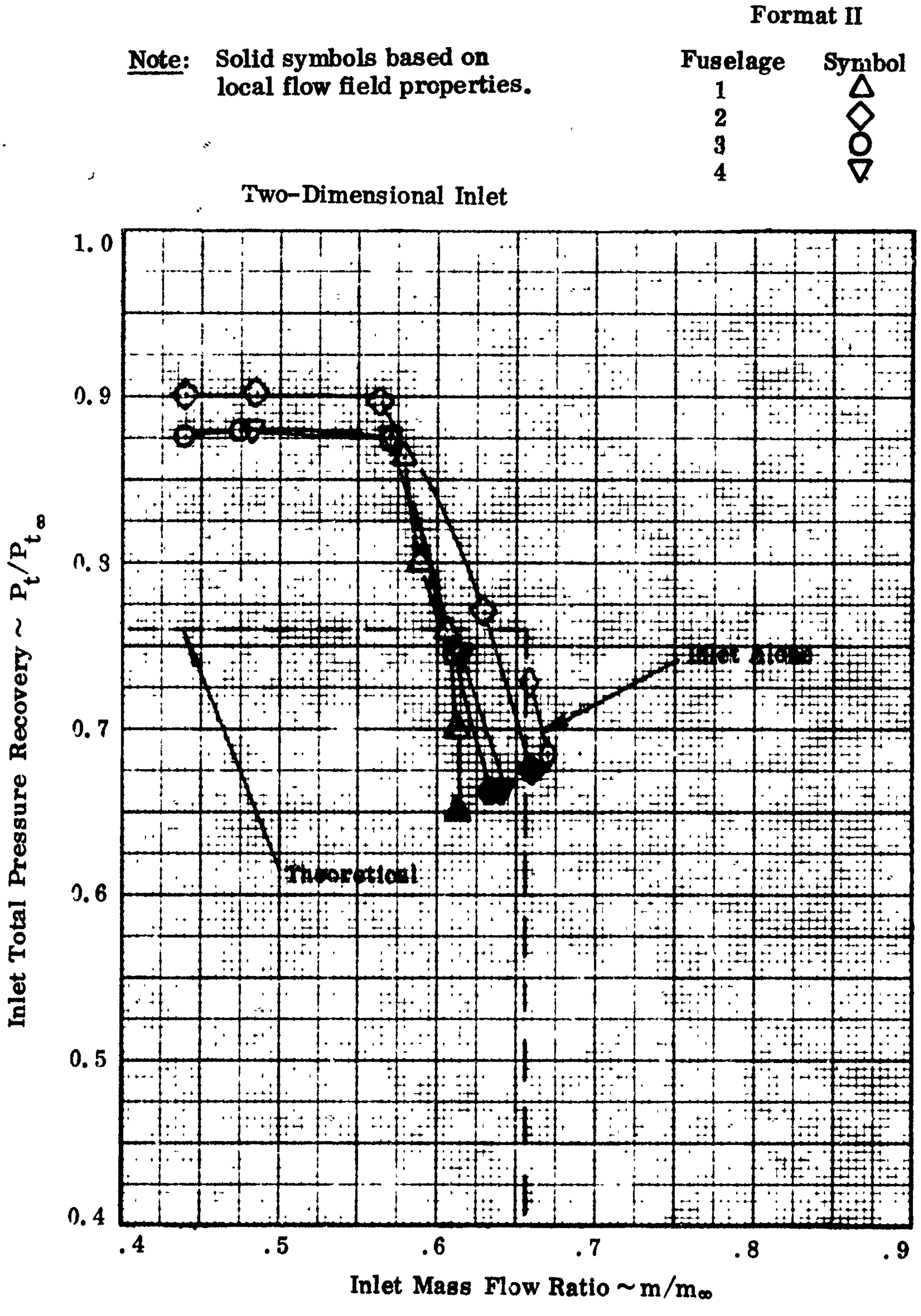

Figure 7-254. Comparison of Inlet Performance

$M_\infty = 1.8, \quad \alpha = 10°$

Format II

Fuselage	Symbol
1	△
2	◇
3	○
4	▽

Note: Solid symbols based on local flow field properties.

Two-Dimensional Inlet

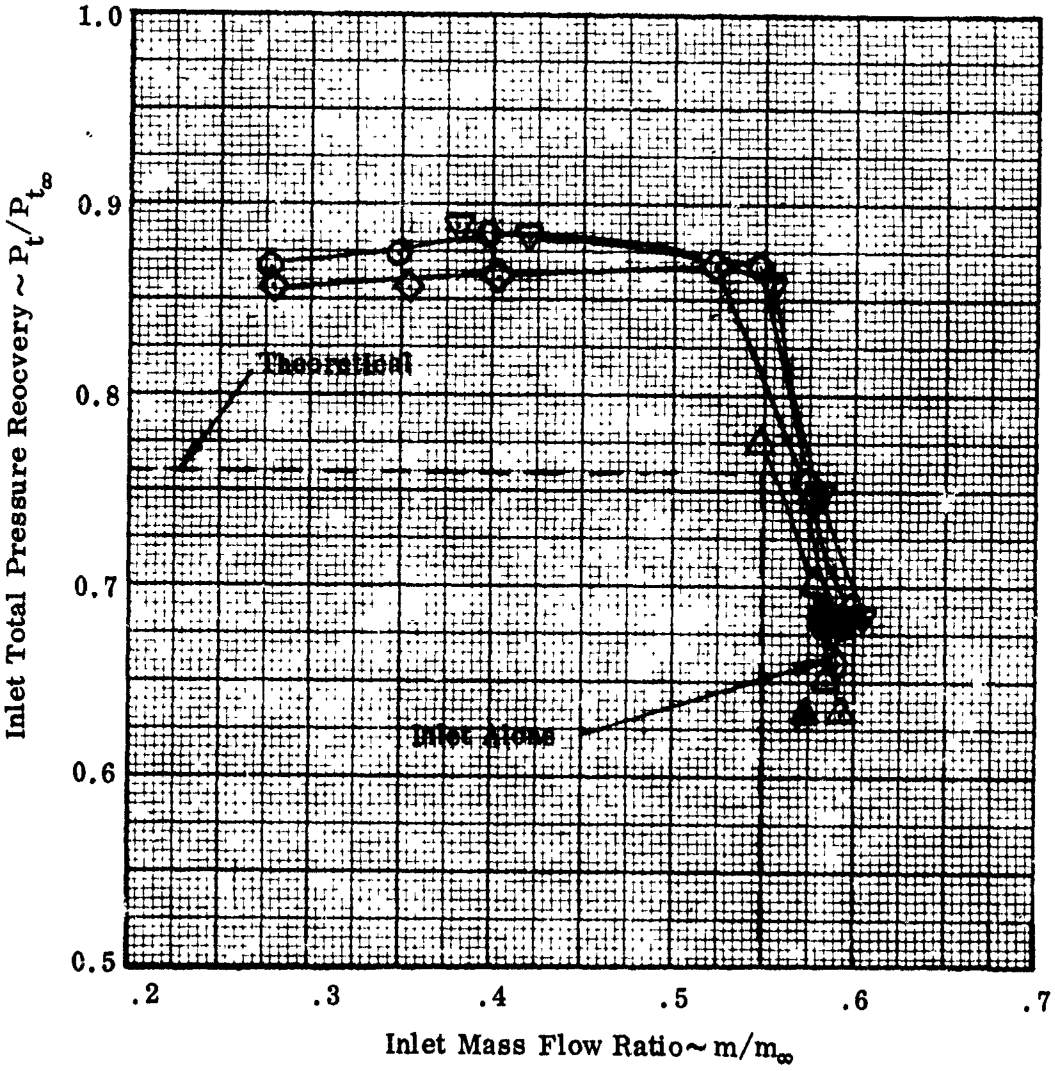

Figure 7-255. Comparison of Inlet Performance
$M_\infty = 1.8$, $\alpha = 15°$

Note: Solid symbols based on local flow field properties.

Format II

Fuselage	Symbol
1	△
2	◇
3	○
4	▽

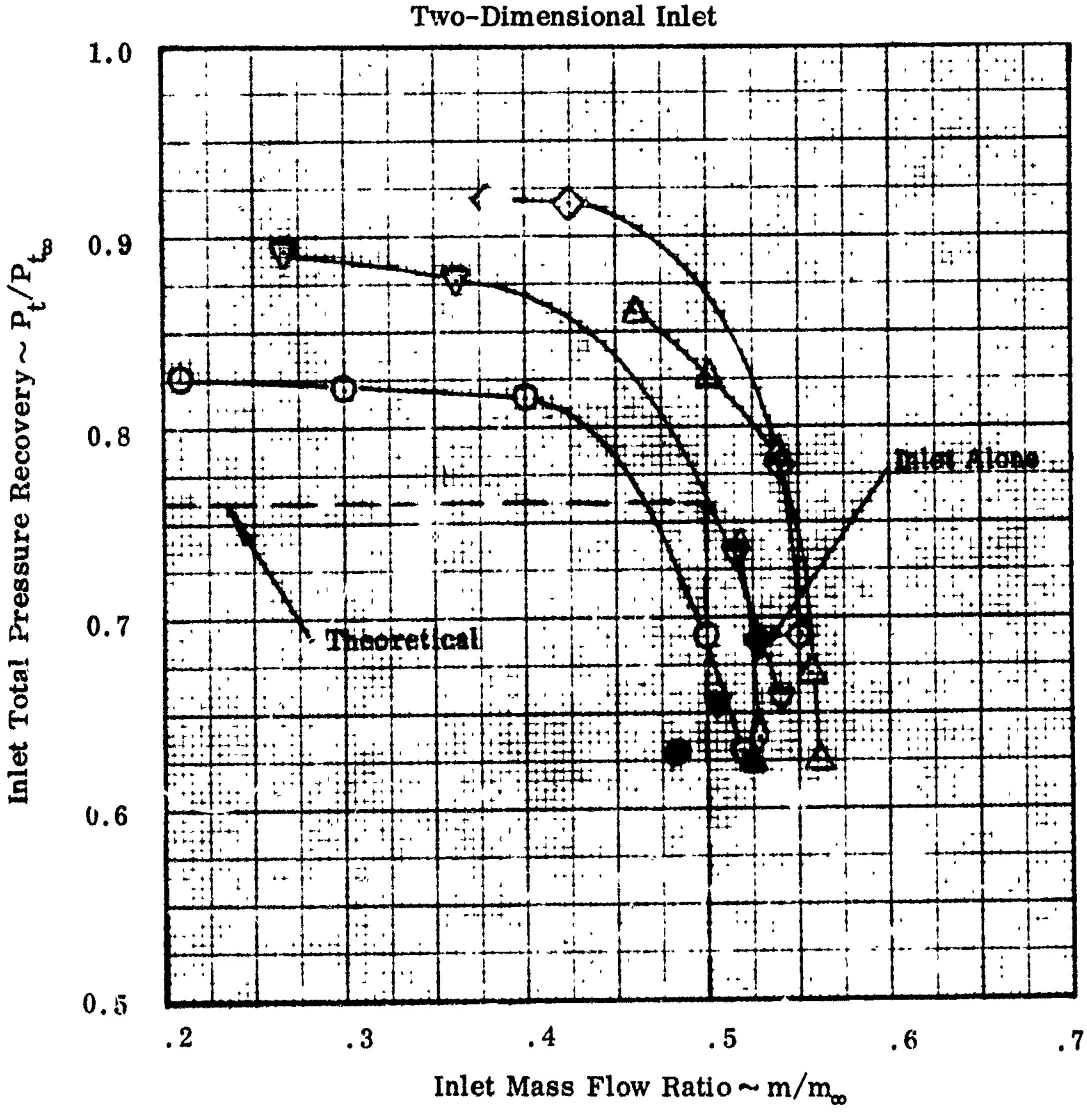

Figure 7-256. Comparison of Inlet Performance

$M_{\infty} = 1.8$, $\alpha = 20°$

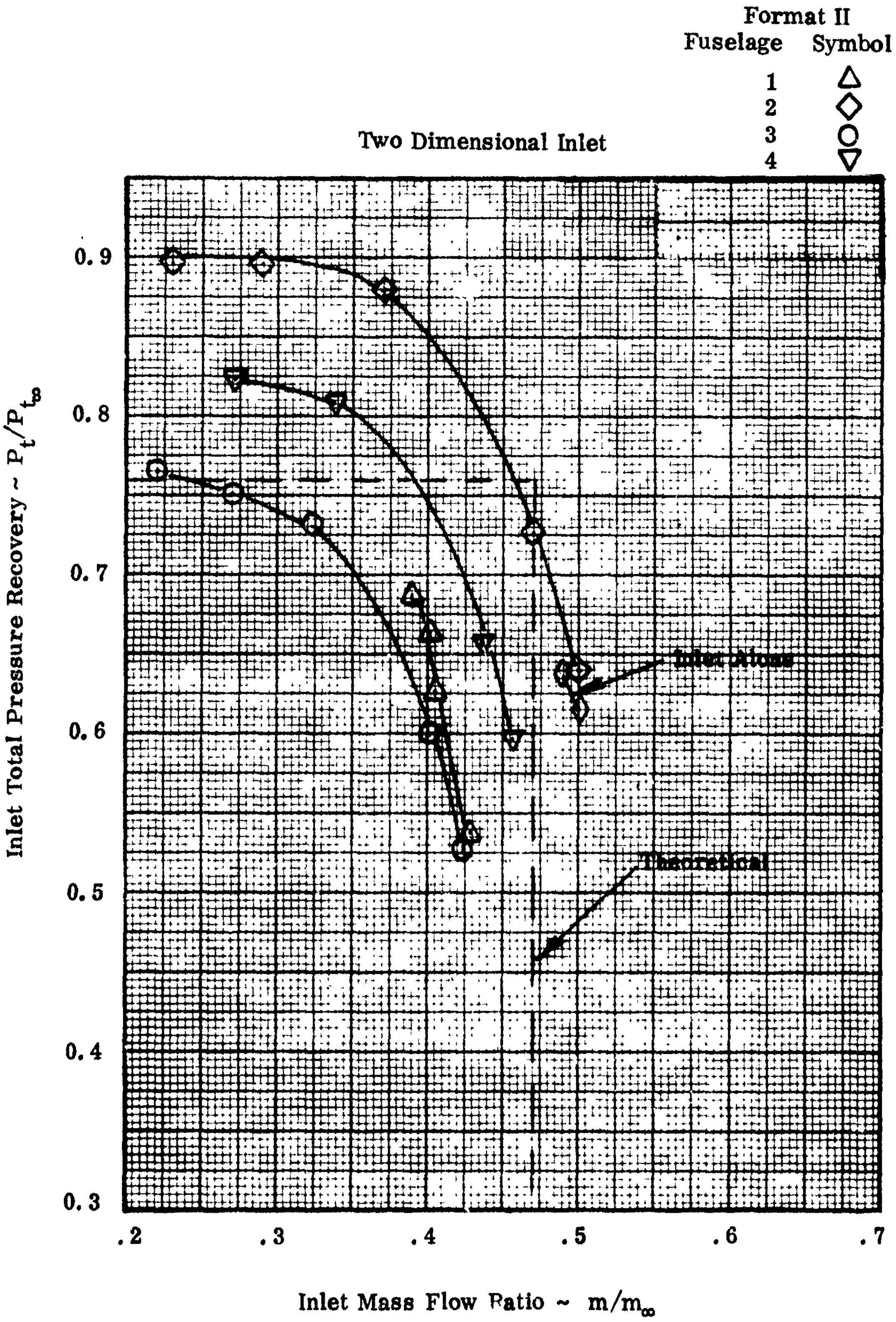

Figure 7-257. Comparison of Inlet Performance
$M_\infty = 1.8$, $\alpha = 25°$

At +10° angle of attack a sonic wedge solution would move the theoretical estimate quite close to the experimentally obtained levels. With increasing angle of attack the experimental total pressure recovery converges on the normal shock analytical solution, until at +25° only a small difference remains. This final difference may be attributed to the unaccounted for shock curvature. In examining these figures the effect of angle of attack upon the influence of fuselage geometry becomes increasingly evident. The more uniform flow fields and the lower average upwash produced by those fuselages with larger corner radii results in both higher total pressure recovery and mass flow ratio for these configurations.

7.4.3.4 Mach Number 2.2

Although the flow field characteristics are qualitatively similar to those obtained at previously discussed Mach numbers the impact of these flow fields upon inlet performance becomes significant at Mach = 2.2. A review of the inlet performance at Mach = 2.2, for all angles of attack, indicates three factors of prime importance namely,

- The increase in inlet terminal shock strength caused by the local fuselage flow field
- The effect of the strengthened shock upon the inlet surface boundary layer
- The misalignment of the locally approaching flow and the inlet surface.

These effects could not be evident at lower Mach numbers simply because the terminal shock strength, for those conditions tested, was always relatively weak. At Mach 0.8 and 1.2 the inlet throat was essentially choked. At Mach 1.8 the design terminal shock strength, for the N = 3 system employed, was again quite weak and consequently, variations in approaching Mach number varied the strength very slightly. At Mach 2.2, however, the terminal shock is relatively strong, by design. This emerges from the requirements to achieve a balanced shock structure and to satisfy transonic mass flow. As a result, variations in terminal shock strength, due to small variations in approaching Mach number can, and do have a significant effect upon the inlet performance characteristics. These effects are, of course, most pronounced at negative angle of attack where the vehicle induced downwash weakens the inlet's oblique external shock structure and consequently causes the transition from supersonic to subsonic Mach number to occur across a stronger terminal shock. The influence of the vehicle flow field upon inlet performance can be seen, for this case, in Figure 7-258. The inlet alone configuration performs very well, with a steep supercritical leg and a critical total pressure recovery and mass flow ratio close to that predicted theoretically. Integration of the inlet with any of the fuselages causes a dramatic degradation in performance. A trend is evident showing the total pressure recovery and characteristic cane shape becoming poorer as fuselage corner radius is increased. These results appear consistent with the flow field data indicating that the large corner radius configurations induced the most negative downwash. Making the assumption that the effects of inlet-airframe integration make themselves evident at the engine face and that the spatial location at the engine face can be traced to a corresponding location at the inlet face the factors contributing to degraded performance can be seen in an examination of the engine face data. For supercritical operation the inlet alone profile has a high total pressure central core and a thin low pressure region around the periphery of the duct. As opposed to this the integrated configurations all possess relatively large low pressure regions along the inboard and lower section of the duct. This indicates that the fuselage boundary layer is swept downward around the fuselage and into the inlet. For the inlet alone the small low pressure region permits a steep climb to critical operation and a resultant low distortion total pressure profile. The upstream communication, particularly through the large low pressure regions, causes the integrated systems to spill mass flow as soon as the inlet is throttled. The low pressure regions also reduce the aerodynamic expansion ratio of the duct and consequently critical operation is achieved with a very shallow supercritical leg.

With angle of attack increased to zero the external shock system is stronger and the terminal shock weaker. The inlet performance, Figure 7-259, responds with improved performance and a characteristic cane shape approximating that developed by the inlet alone. The downwash flow fields still result in lowered performance for the integrated systems. The performance level is still a function of corner geometry with the large fuselage corners inducing the most negative downwash and a lower resultant total pressure recovery.

Note: Solid symbols based on local flow field properties.

Format II

Fuselage	Symbol
1	△
2	◇
3	○
4	▽

Two-Dimensional Inlet

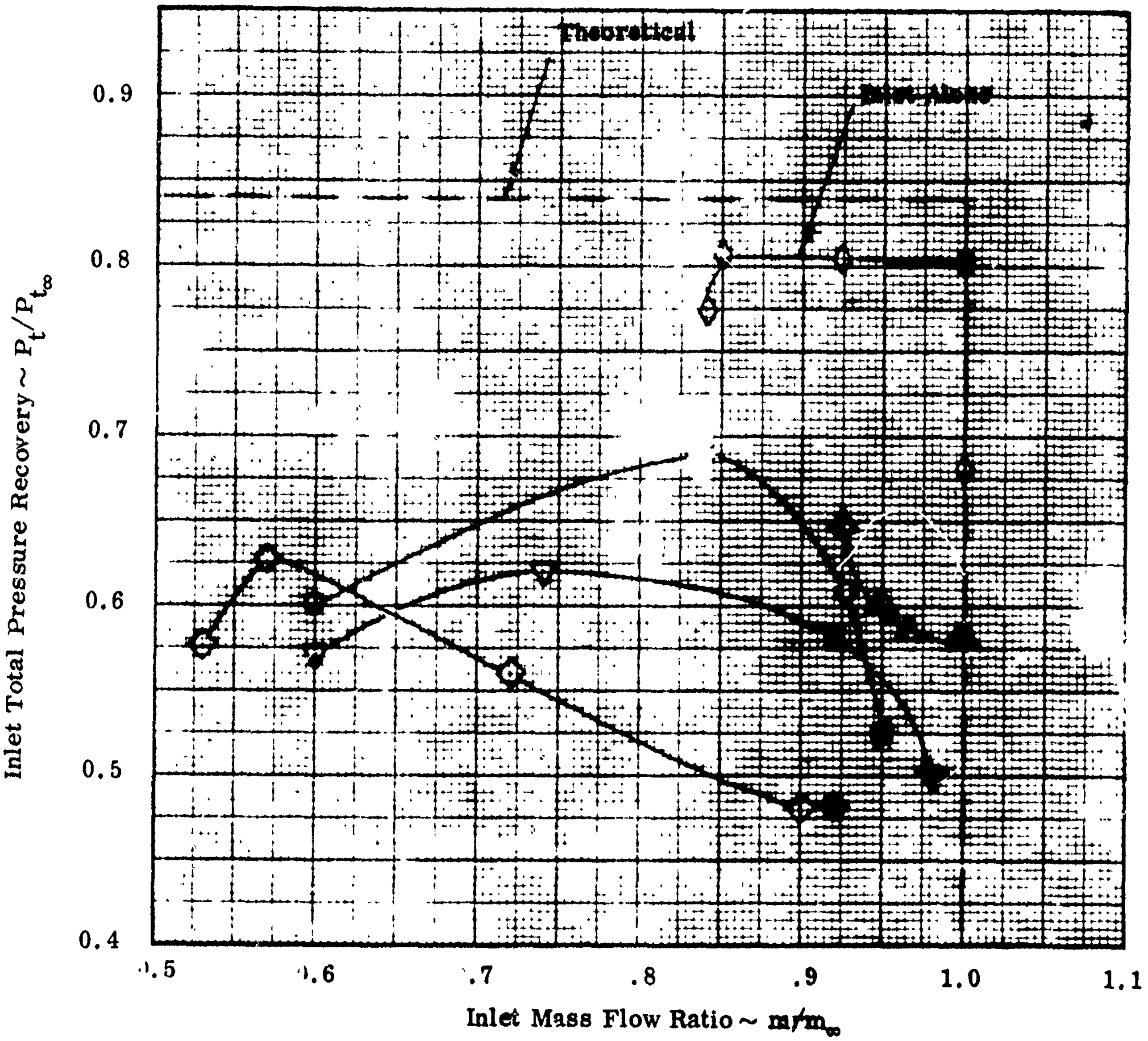

Figure 7-258. Comparison of Inlet Performance

$M_\infty = 2.2,\ \alpha = -3°$

Note: Solid symbols based on local flow field properties.

Format II

Fuselage	Symbol
1	△
2	◇
3	○
4	▽

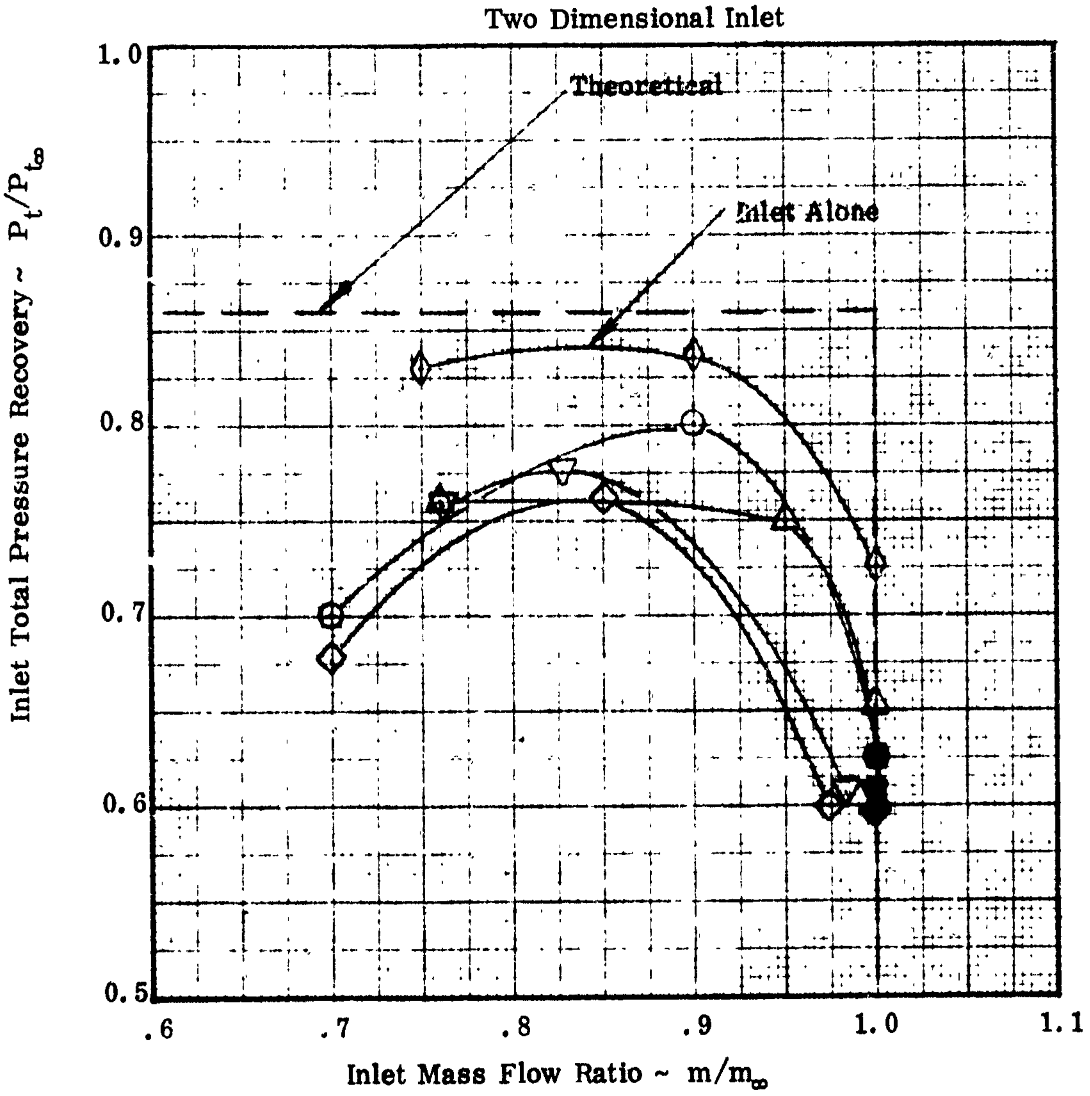

Figure 7-259. Comparison of Inlet Performance
$M_\infty = 2.2$, $\alpha = 0°$

With angle of attack increased to +5° the fuselage nose is generating a nearly symmetrical flow field. The fuselage flow fields at the inlet station are very uniform and similar. The result can be seen in Figure 7-260 where the characteristics are very closely grouped together. The integrated systems also match the inlet-alone very closely, indicating a minimal vehicle effect.

At +10° angle of attack the fuselage nose still generates a nearly symmetrical flow field. The integrated inlet characteristics, Figure 7-261, are spread out more than was the case at +5°, however, they probably still lie within a band that is smaller than the potential deviation due to experimental accuracy In the analysis of the inlet alone performance (Format V) it was seen that the peak experimental recovery matched the theoretical prediction but the slope of the supercritical leg of the inlet characteristic indicated the need for inlet development work. The integrated inlets possess the same characteristic cane shape thereby indicating a minimal fuselage effect. A very weak effect of fuselage corner can be seen in that large corner radii tend to produce slightly higher inlet peak total pressure recovery and a steeper supercritical leg. The close match of integrated inlet performance with both theory and the inlet alone permits the assumption that the fuselage boundary layer is swept up around the fuselage and away from the inlet. Additionally, the smaller favorable pressure gradient, imposed peripherally on the fuselage boundary layer by the gentle curvature of the larger corner radii probably results in a larger boundary layer displacement thickness along the side of the fuselage, for these configurations. Support for this last conclusion can be seen from an examination of the fuselage static pressures in the region of the inlet. The fuselage static pressures, for large corner radius configurations, are affected more strongly by inlet throttling than are the pressures for small fuselage corner radii. This indicates a communication, through what must be a thicker viscous layer. Beyond this a slightly more pronounced low pressure region resides on the inboard side of the postulated engine face for the large corner radius configurations, even though the overall total pressure recovery is slightly higher.

The influence of fuselage geometry upon achievable critical inlet total pressure recovery and mass flow ratio, that appeared weakly at +10° angle of attack becomes progressively more pronounced as angle of attack is increased to +15°, +20°, and +25°. The performance comparisons for these respective test conditions are

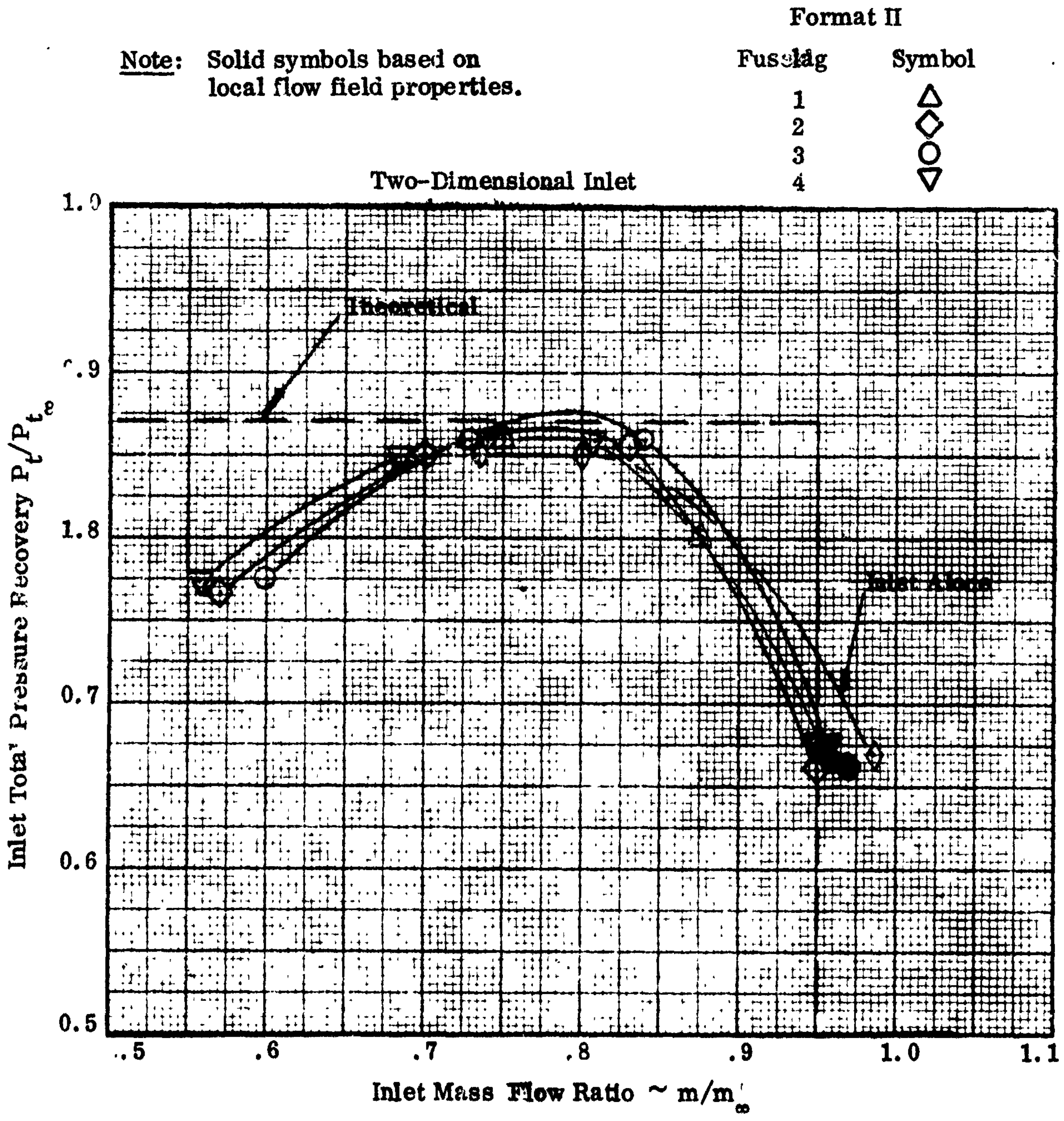

Figure 7-260. Comparison of Inlet Performance
$M_\infty = 2.2, \alpha = 5°$

Note: Solid symbols based on local flow field properties.

Format II

Fuselage	Symbol
1	△
2	◇
3	○
4	▽

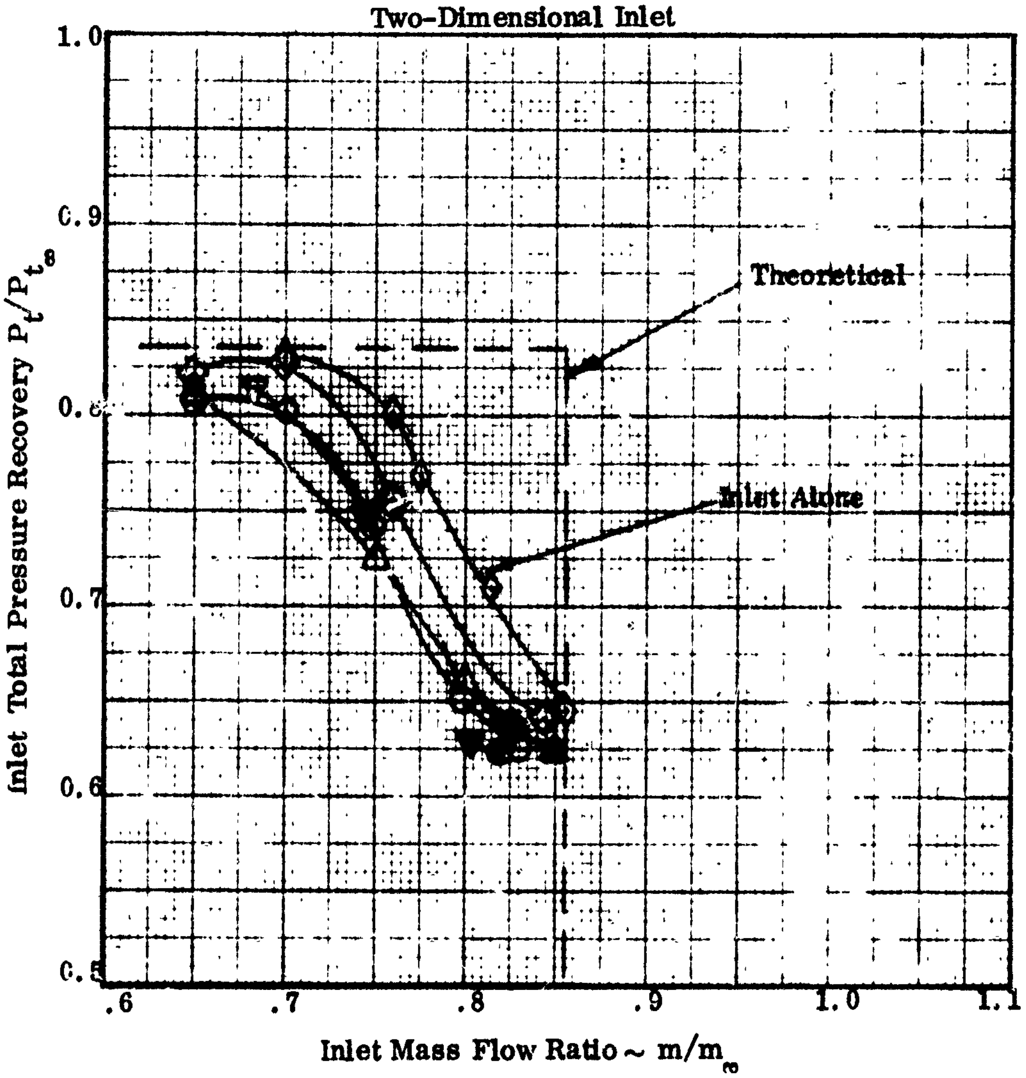

Figure 7-261. Comparison of Inlet Performance

$M_\infty = 2.2$, $\alpha = 10°$

presented in Figures 7-262 through 7-264. The performance levels diverge, with increasing angle of attack, as a function of corner radius and corner development (rapid or gentle). The large corner configurations operate at significantly higher levels of total pressure recovery and mass flow ratio. This can be attributed to the tendency of these fuselages to induce flow fields that are generally more uniform. In addition, these configurations inhibit flow field upwash and consequently have lower angularity stream lines approaching the inlet. This effect tends to preclude local separations due to a misalignment of approaching flow and inlet surface. Unfortunately, some difficulty was experienced during the inlet alone tests which prevented the development of complete inlet characteristic canes, a comparison is therefore not possible. There also appears to be a large discrepancy between experimental and theoretical total pressure recovery levels, as previously discussed this is due to the conservative approach employed in the analytical computation when shock detachment is approached.

7.4.?.5 Mach Number 2.5

The qualitative impact of fuselage geometry upon inlet performance is essentially the same as discussed at Mach 2.2. It is reasonable to expect the quantitative effects to be greater at this higher Mach number. Unfortunately, this is not apparent in the curves comparing performance, which are presented in Figures 7-265 through 7-270. The major reason that vehicle induced effects do not have the degree of impact that might be expected is due to the inlet itself having a relatively low level of potential performance at this Mach number. Consequently vehicle effects become second order. For example, at an angle of attack of -3° the integrated inlet characteristics are all closely grouped together with little apparent variation due to the fuselage. It should be noted that the peak total pressure recovery approximates normal shock recovery for a free stream Mach number of 2.5, therefore any variations in the approaching stream can have virtually no effect on total pressure recovery. It is apparent that the integrated systems cannot handle the same mass flow ratio as the inlet alone and further that their supercritical legs have a lower slope. In addition, the achievable mass flow ratio is seen to decrease with increasing fuselage corner radius. This is consistent with the results achieved at lower Mach numbers where the negative angle of attack introduced more boundary layer to the inlet, reducing its mass flow capacity,

Note: Solid symbols based on local flow field properties.

Format II

Fuselage	Symbol
1	△
2	◇
3	○
4	▽

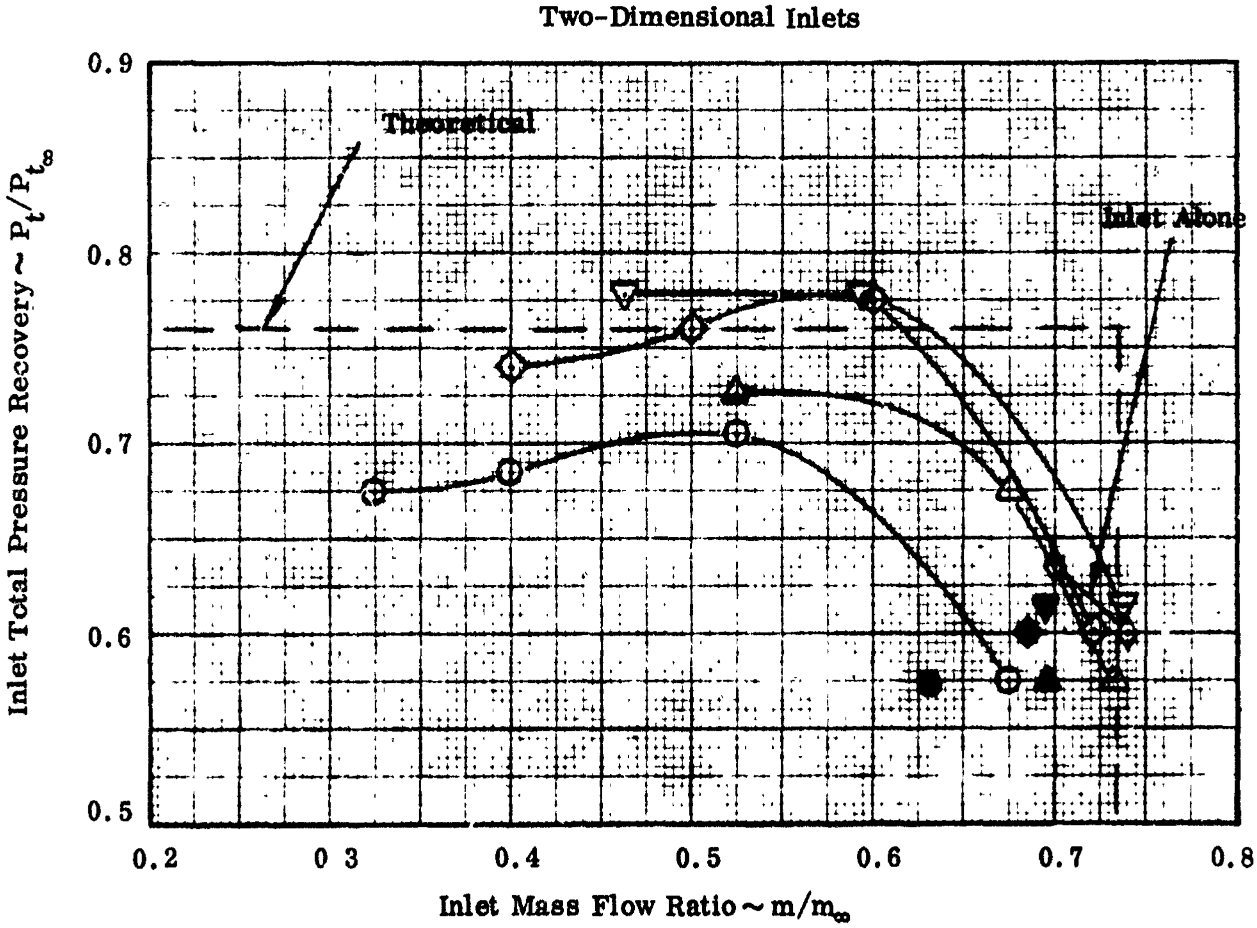

Figure 7-262. Comparison of Inlet Performance

$M_\infty = 2.2, \ \alpha = 15°$

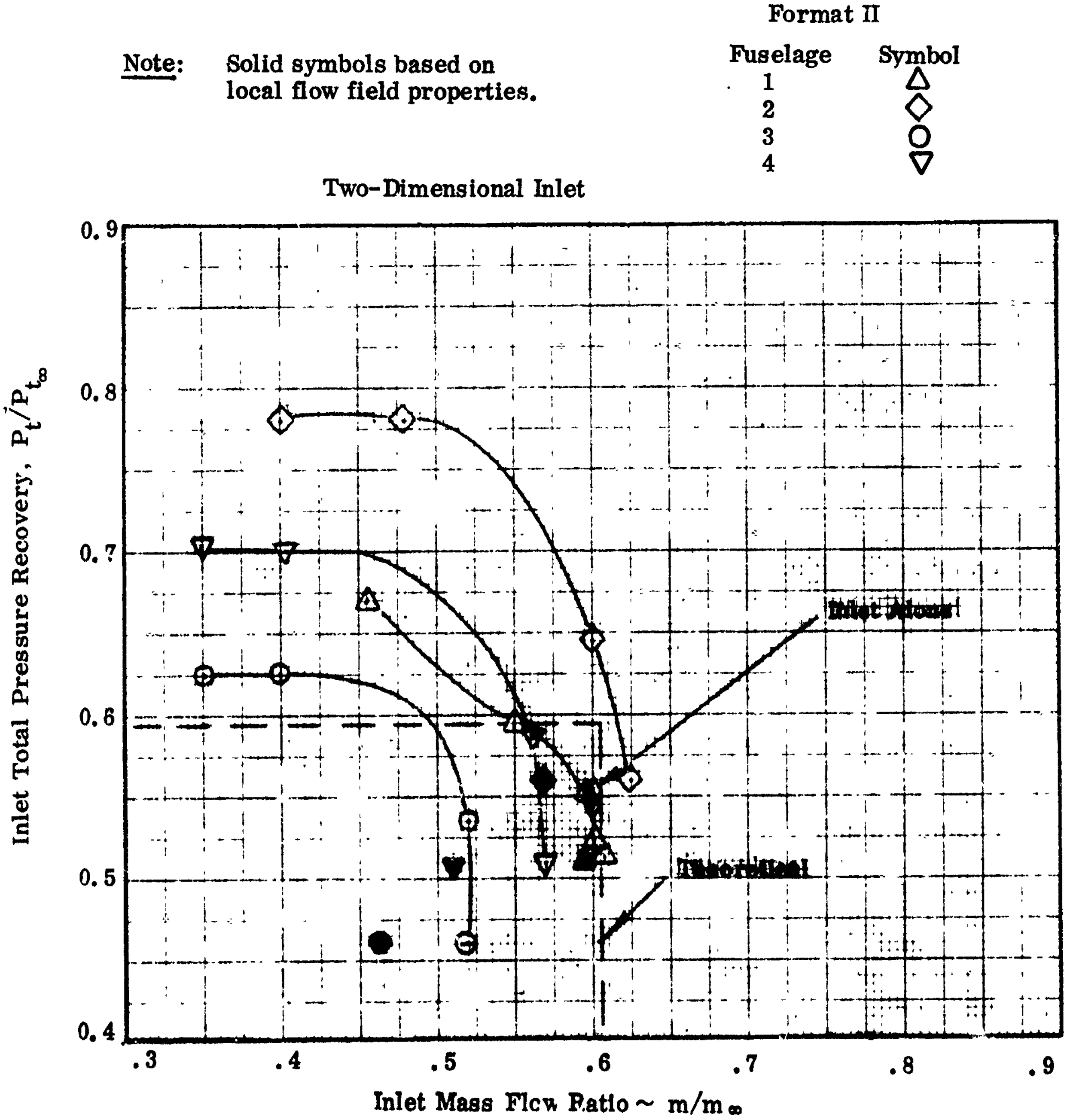

Figure 7-263. Comparison of Inlet Performance

$M_\infty = 2.2$, $\alpha = 20°$

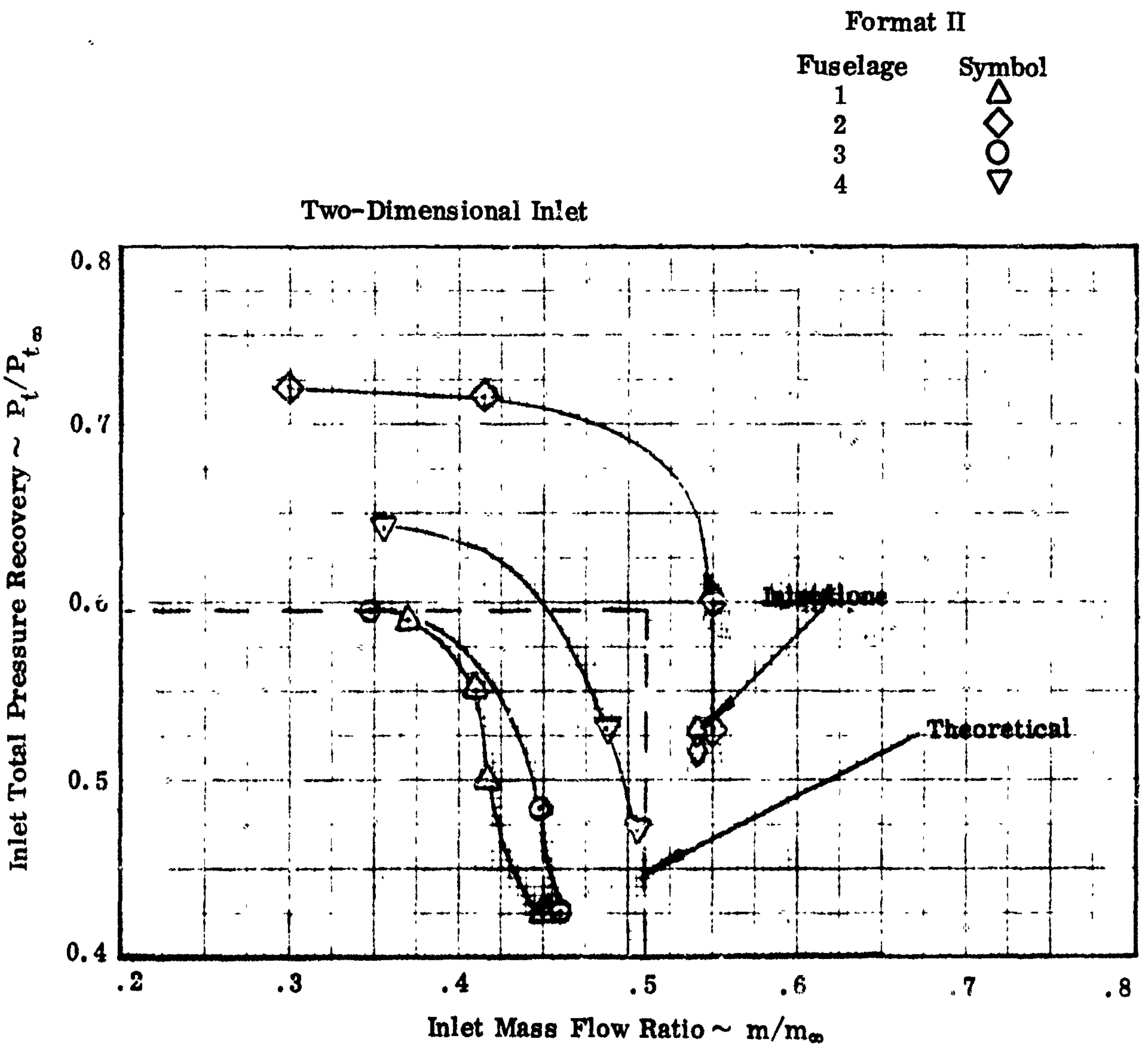

Figure 7-264. Comparison of Inlet Performance
$M_\infty = 2.2$, $\alpha = 25°$

Two-Dimensional Inlet Format II

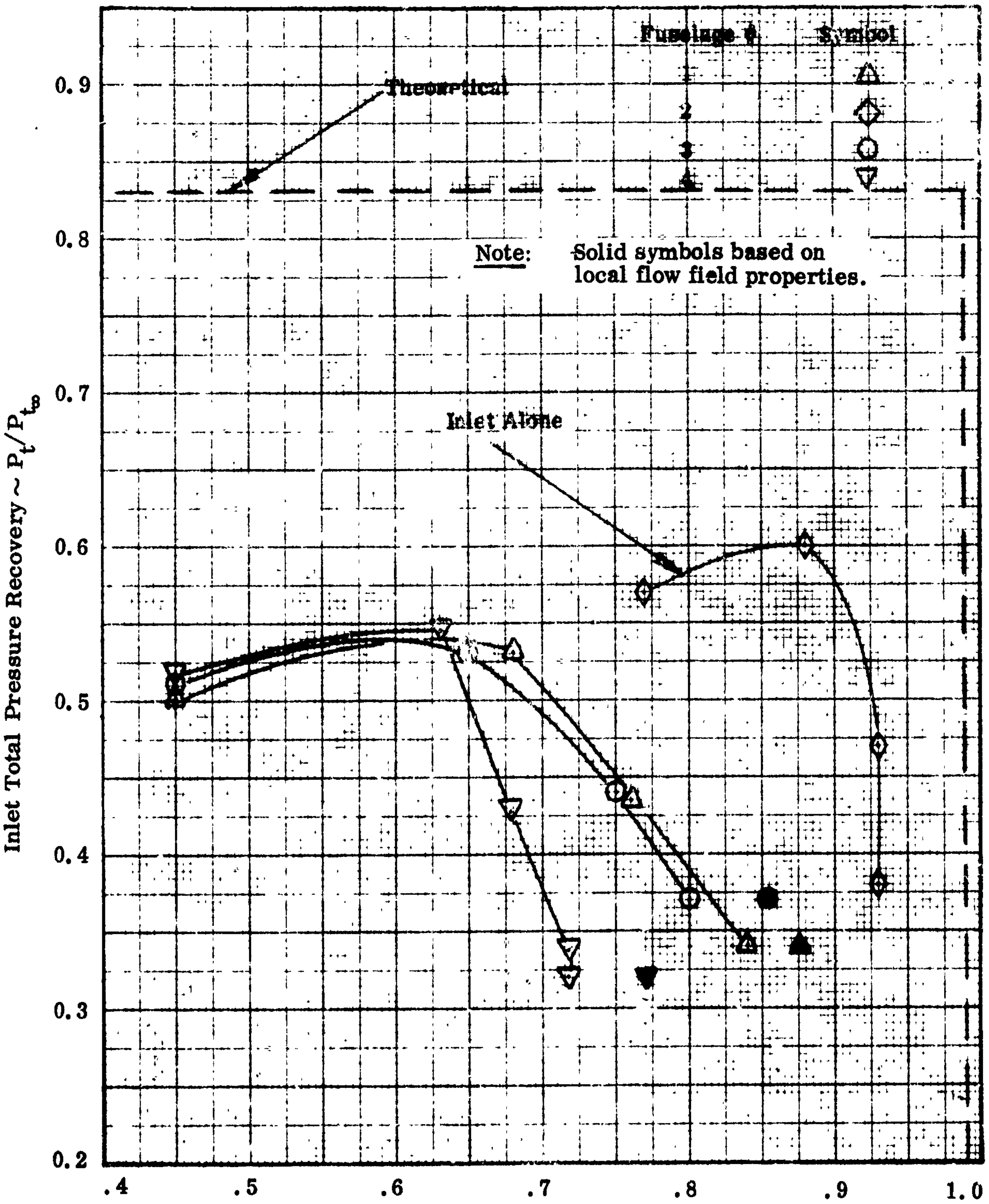

Figure 7-265. Comparison of Inlet Performance

$M_\infty = 2.5$, $\alpha = -3°$

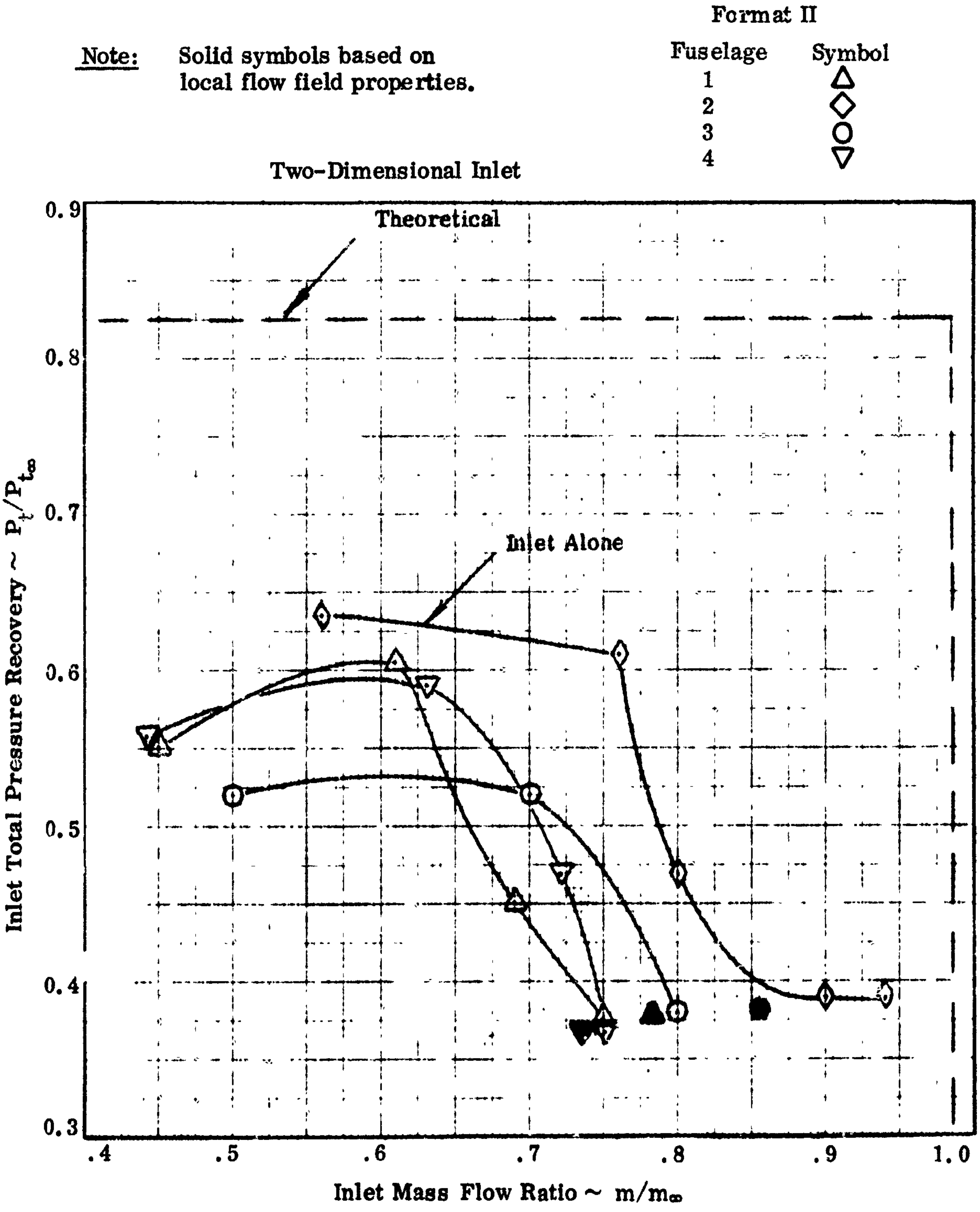

Note: Solid symbols based on local flow field properties.

Figure 7-266. Comparison of Inlet Performance
$M_\infty = 2.5$, $\alpha = 0°$

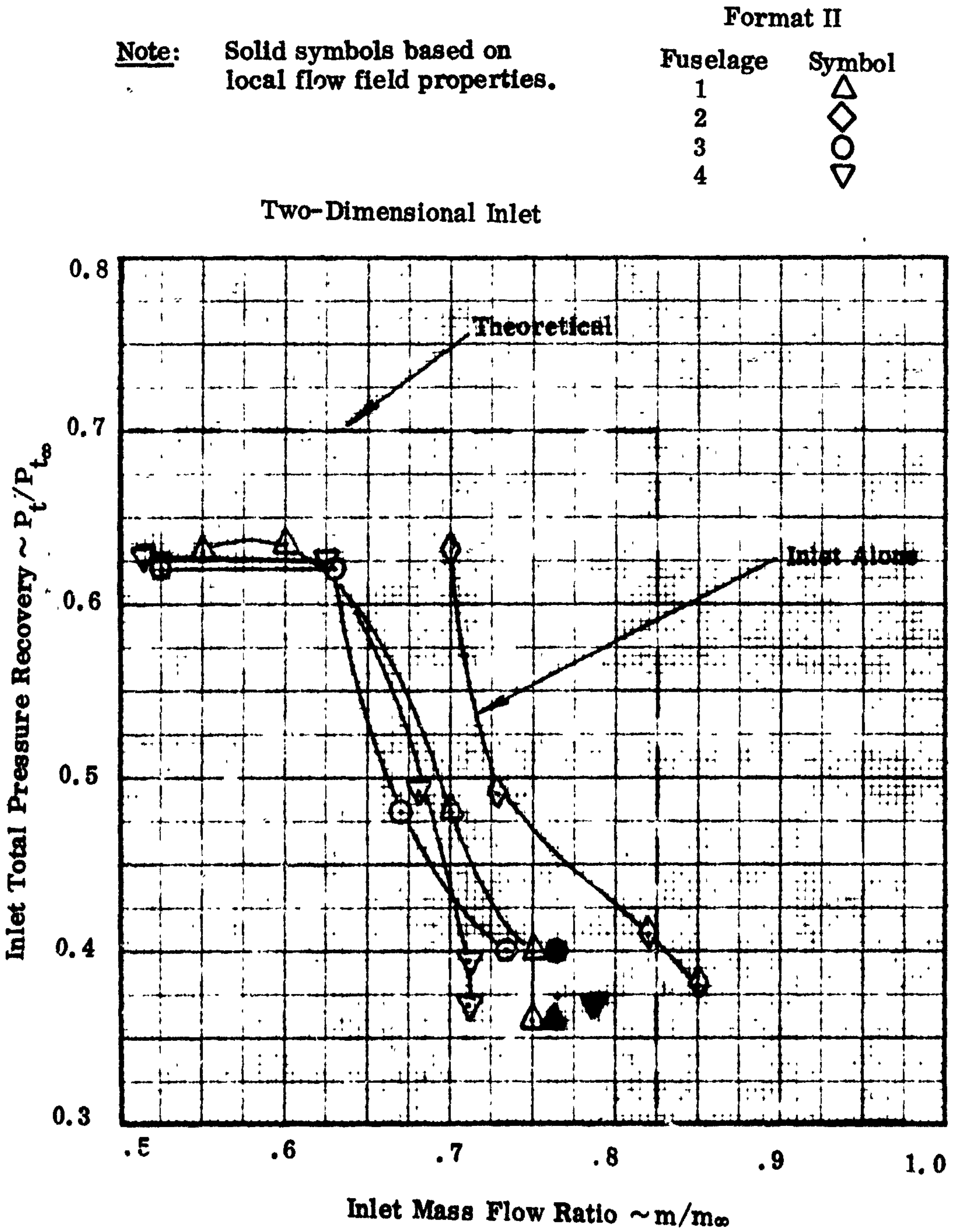

Note: Solid symbols based on local flow field properties.

Figure 7-267. Comparison of Inlet Performance

$M_\infty = 2.5$, $\alpha = 5°$

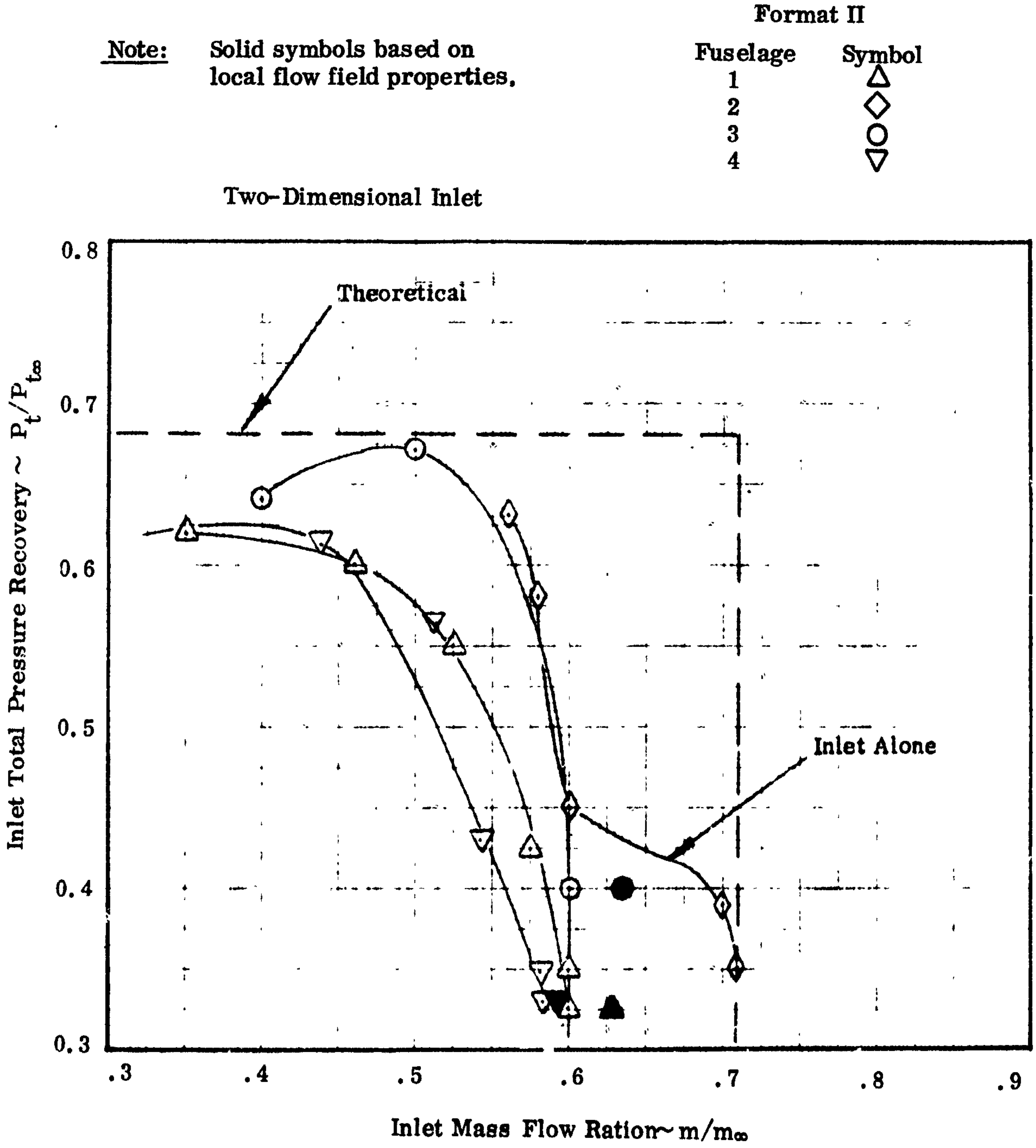

Note: Solid symbols based on local flow field properties.

Figure 7-268. Comparison of Inlet Performance
$M_\infty = 2.5$, $\alpha = 10°$

Format II

Fuselage	Symbol
1	△
2	◇
3	○
4	▽

Note: Solid symbols based on local flow field properties.

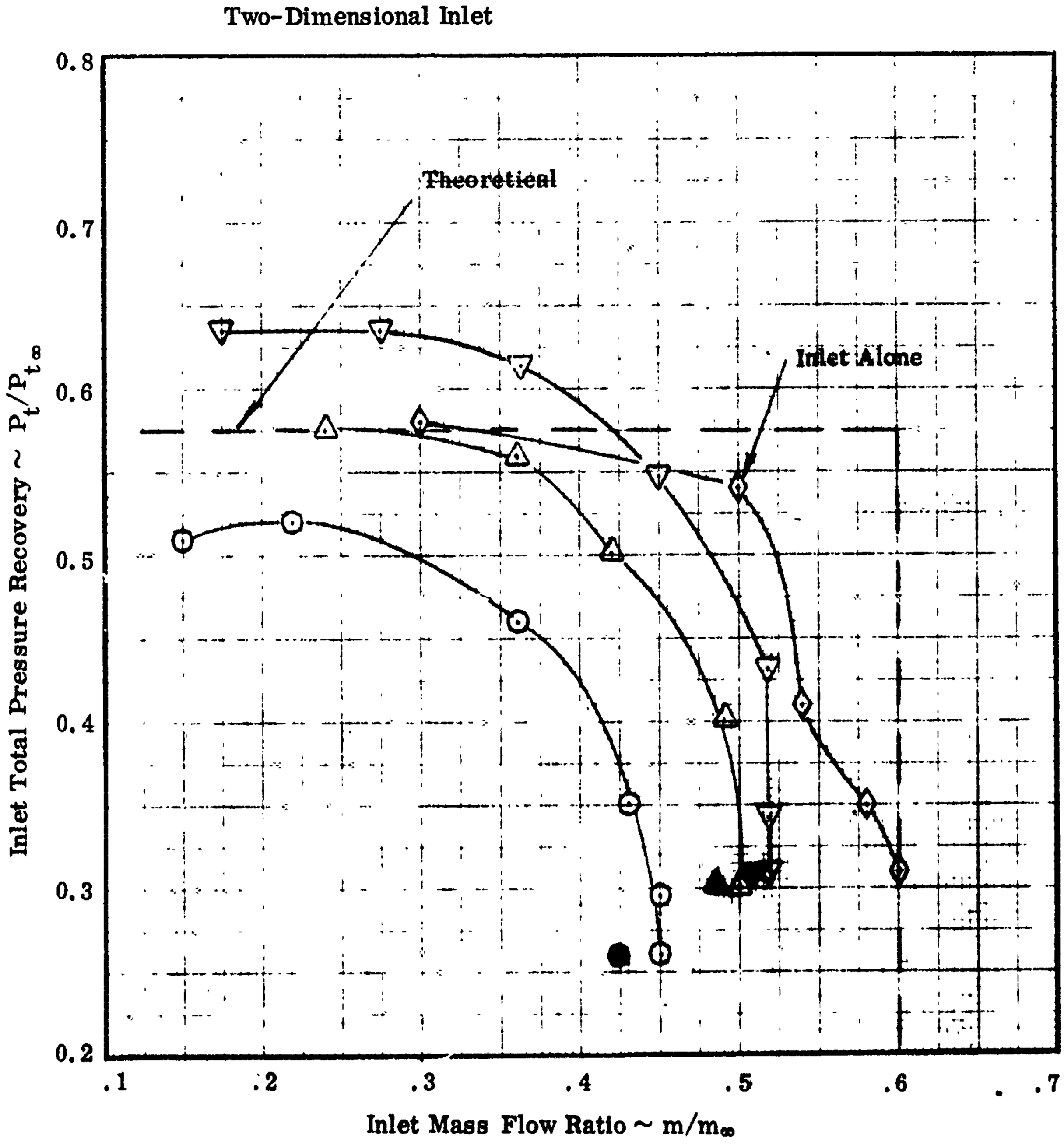

Figure 7-269. Comparison of Inlet Performance

$M_\infty = 2.5$, $\alpha = 15°$

Note: Solid symbols based on local flow field properties.

Format II

Fuselage	Symbol
1	△
2	◇
3	○
4	▽

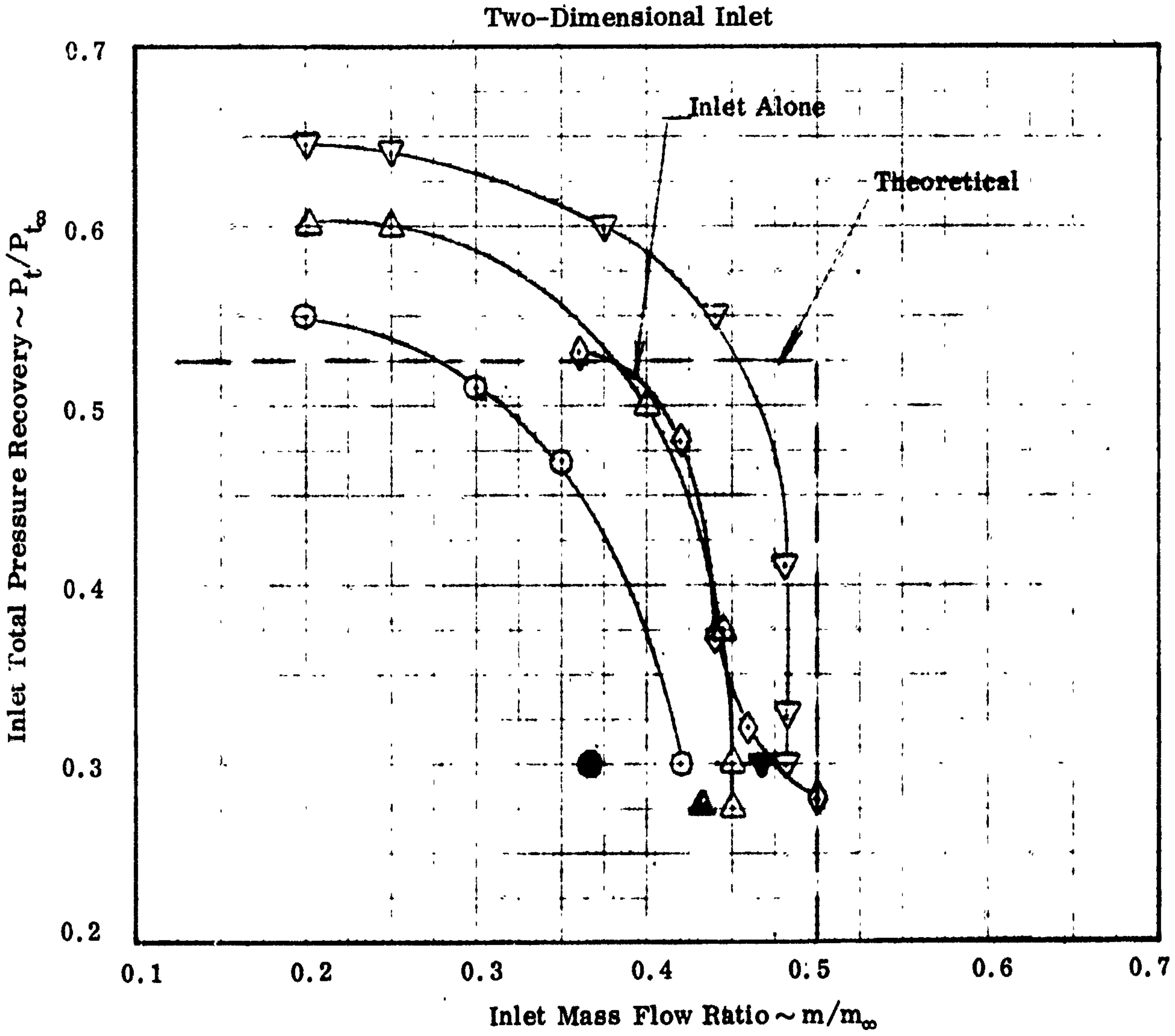

Figure 7-270. Comparison of Inlet Performance
$M_\infty = 2.5$, $\alpha = 18°$

and further that this effect was more pronounced with larger corner radii. This general condition is also present at an angle of attack of 0°. However, a new effect is evident at this angle of attack that was not present at lower Mach numbers namely, the small corner fuselages possess poorer total pressure recovery characteristics. The fuselage 3 configuration, in particular, has not benefited from the increase in angle of attack. At an angle of attack of +5° the performance is closely grouped and sufficiently higher than normal shock recovery to indicate that the similar flow fields produce similar inlet performance. This was also seen at lower Mach numbers. With the angle of attack increased to +10° the smallest corner radius results in clearly the highest performance level. This result is not consistent with the results obtained at lower Mach numbers where the small corner radius configurations were competitive, at best. This configuration matches both the theory and inlet alone quite closely. Based upon this close match and the fact that a large peripheral pressure gradient is associated with fuselage 3 we can postulate that the fuselage boundary layer was swept clean, thereby permitting the inlet to operate in a cleaner environment. It is not possible to define what effect the removal of fuselage boundary layer would have' upon the performance of the larger fuselage corner configurations, however, an examination of the performance at +15° and +18° may given an indication. At these angles of attack the larger fuselage corner radius clearly contributes to better inlet performance. This trend is similar to that seen at Mach 2.2 and high angle of attack.

7.5 Inlet/Fuselage Combined (Data Format III)

7.5.1 General

The Format III model was configured to obtain inlet performance data for both the two-dimensional and axisymmetric inlets, when installed at the aft fuselage station. Tunnel occupancy time prevented the testing of a complete matrix of inlet and fuselage. Those inlet/fuselage combinations tested were chosen on the basis of physical compatibility and the desire to employ a wide range of fuselage geometry.

Total pressure recovery can be used directly to compare the performance level of the axisymmetric inlet with that of the two-dimensional inlet. However, the under wing installation precludes a direct comparison of the mass flow ratio characteristics of these two inlet concepts. The radius of the quarter segment axisymmetric inlet is larger than the width of the two-dimensional inlet. Therefore, it falls in the shadow of a larger portion of the wing span and experiences a more rapid increase in ideal capture area with increasing angle of attack. Consequently, the axisymmetric inlet always operates at a lower mass flow ratio when the angle of attack is positive and a higher mass flow ratio when the angle of attack is negative. A secondary effect tending to compound this difference is the relation of the wing shock to the cowl surface. In the case of the two-dimensional inlet both the cowl surface and wing shock are two-dimensional and as a result the cowl can efficiently intercept the wing shock layer up to a point approaching wing shock on cowl lip, as opposed to the axisymmetric inlet case where the circular arc cross-section of the cowl surface precludes anything but a local wing shock intercept. For this reason, also, the axisymmetric inlet has a lower mass flow ratio. These effects are shown schematically in Figure 7-271. The variation in capture area, as a function of angle of attack, is presented in Figure 7-272 for both inlet concepts.

An examination of the data reveals that the large variation in sidewash occurs with all fuselage configurations and that the quantitative levels are similar. Based upon this fact we can expect each inlet concept (axisymmetric and two-dimensional) to generate an installed characteristic cane that does not vary significantly with fuselage corner geometry. Therefore, the anticipated evaluation of the aerodynamic compatibility of a particular inlet concept, with various fuselage configurations, does not constitute a major part of the Format III analyses. On the other hand a comparison of the uninstalled inlet performance with that obtained, generally, with the inlet installed shows the impact of the flow field upon the performance of a particular inlet concept. and results in a measure of that concepts' desirability, with regard to placement alongside the fuselage, under the wing. The geometric compatibility of inlet and fuselage, specifically the effects induced by the diverter channel shape formed between the fuselage and the inlet inboard sidewall, does in some instances produce a geometry dependent shift in the inlet characteristic that is a function of the fuselage configuration. However, while evident, these effects tend to be small.

7.5.2 Fuselage Effects

7.5.2.1 Mach Number 0.8

The sidewash varies from essentially 0° to approximately -8° with the flow fields of all fuselages appearing quite similar in structure. Therefore, with the flow

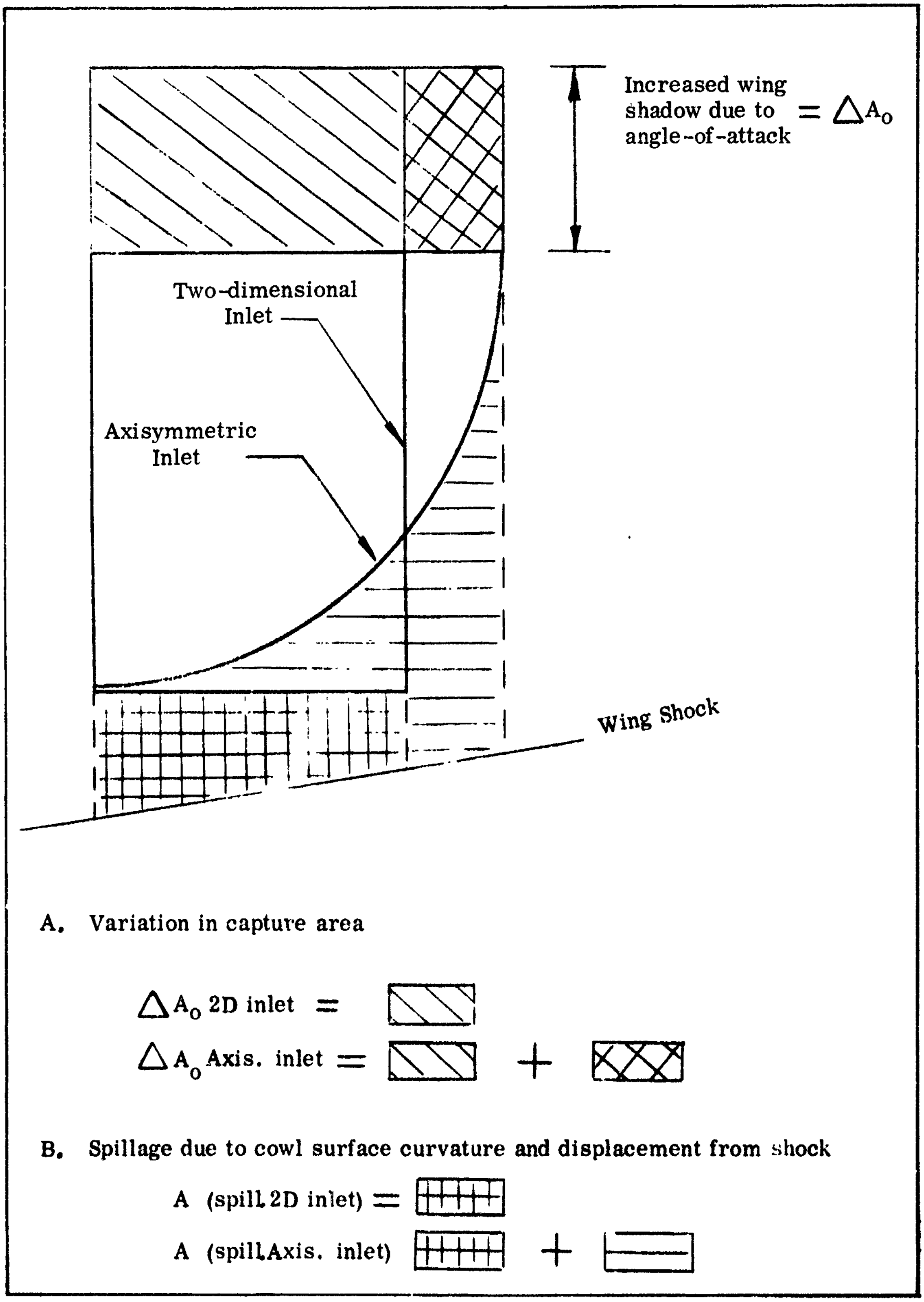
Increased wing shadow due to angle-of-attack = ΔA_0
Two-dimensional Inlet
Axisymmetric Inlet
Wing Shock
A. Variation in capture area
ΔA_0 2D inlet = ▧
ΔA_0 Axis. inlet = ▧ + ▩
B. Spillage due to cowl surface curvature and displacement from shock
A (spill. 2D inlet) = ▦
A (spill. Axis. inlet) ▦ + ▤

Figure 7-271. Inlet Capture Area Schematic

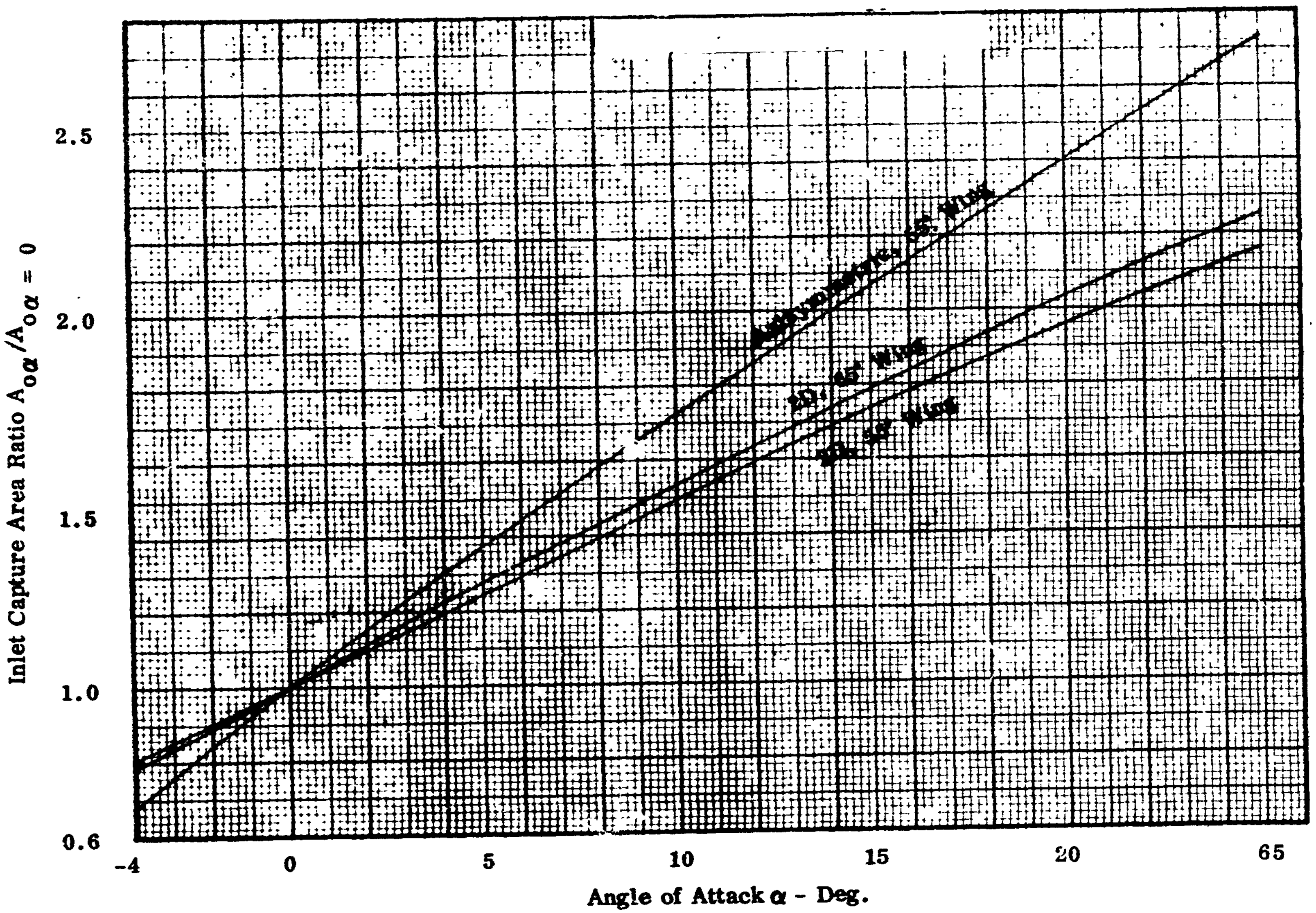

Figure 7-272. Inlet Capture Area, Format III

field approaching the inlet generally similar for all fuselages and having previously determined that the nearly sonic inlet throat controls the diffusion process, at this free stream Mach number, the resultant inlet performance becomes independent of the integration process. The characteristic canes generated by the axisymmetric inlet, presented on Figures 7-273 through 7-279 for the entire angle of attack range, are essentially superimposed for all three fuselage configurations tested. The inlet appears to have benefited slightly from the under wing installation in that the general level of critical total pressure recovery attained is somewhat higher than that level attained by the inlet alone. This comparison is presented in Figure 7-280. It must be noted, however, that during the inlet alone tests, conducted early in the test program, peak recovery may not have been achieved. The results achieved with the two-dimensional inlet are essentially the same, with all inlet characteristic canes very closely grouped together, across the entire angle of attack range. These curves are presented in Figures 7-281 through 7-287. For this inlet concept, however, a fuselage oriented effect is evident in that the performance characteristic achieved with the inlet/fuselage 1 combination is consistently superior to that achieved with either the fuselage 3 or 4 combinations. Except for the maximum angle of attack, the critical total pressure recovery level is essentially the same for all three inlet/fuselage combinations, however, the inlet/fuselage 1 combination has a steeper super-critical characteristic leg and operates at a slightly higher mass flow ratio. This effect can probably be traced to the physical compatibility of the inlet with the fuselage. Presented in Figure 7-288 is a section showing the two-dimensional inlet integrated with each of the three fuselages employed during Format III. For the inlet/fuselage 1 configuration the vertical tangency point of the fuselage corner is located at the same waterline as the lower inboard corner of the inlet. The corner itself is small and has a gradual development, resulting in a low diverter capture area with a relatively gentle gradient around the corner. Consequently, there is little tendency for the diverter channel to choke and the inboard inlet sidewall and cowl surfaces cleanly intercept the locally approaching streamlines. For the inlet/fuselage 3 configuration the fuselage vertical tangency point is located at a lower waterline than the lower inboard corner of the inlet. This, combined with the smaller corner radius yields a smaller diverter channel capture area and a reduced probability of choking. However, the inlet location, relative to the corner, places it in the path of the abrupt peripheral gradient induced by this rapidly developed corner. The consequence is a misalignment of the inboard inlet sidewall

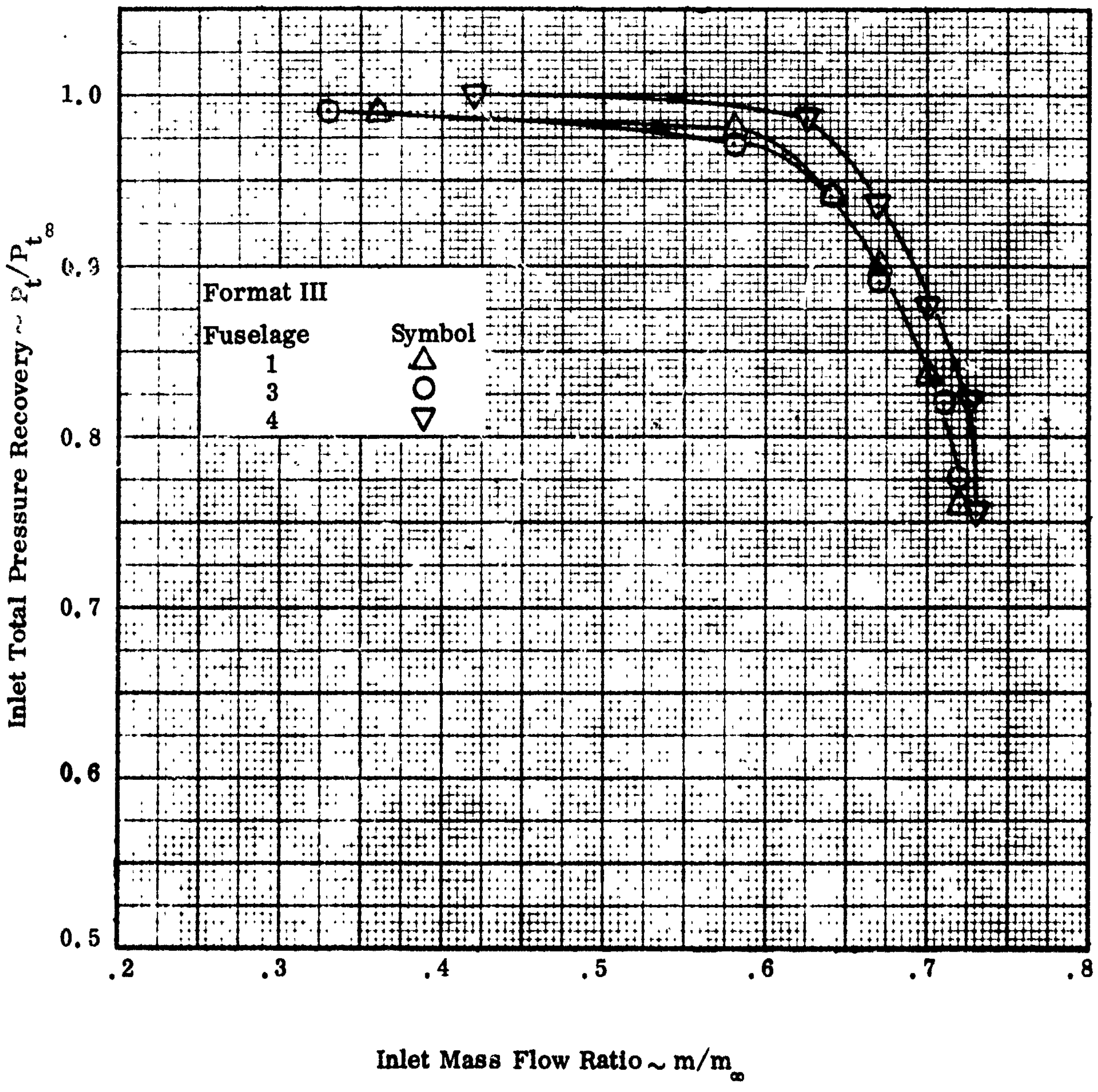

Figure 7-273. Comparison of Inlet Performance, Axisymmetric Inlet, $M_\infty = 0.8$, $\alpha = -3°$

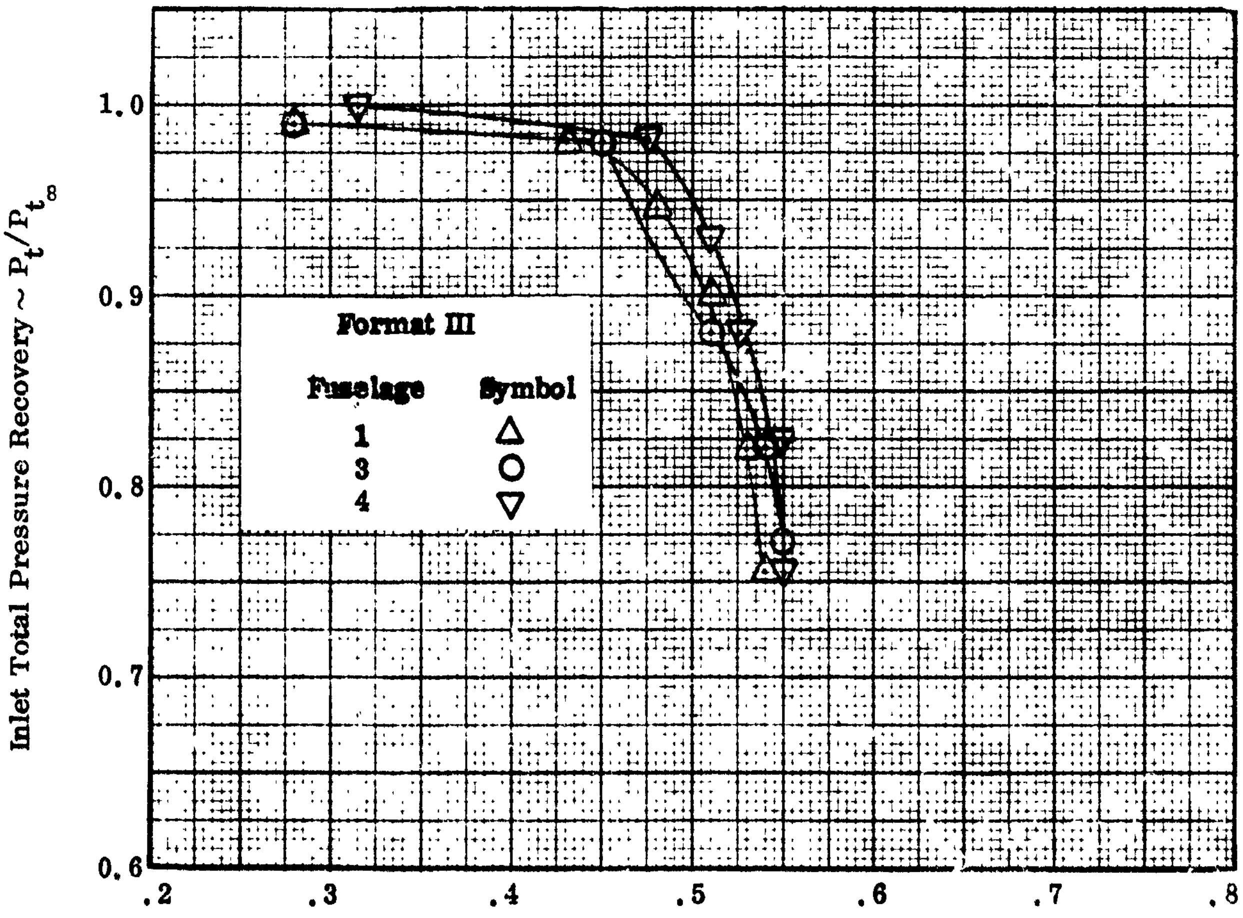

Figure 7-274. Comparison of Inlet Performance, Axisymmetric Inlet $M_\infty = 0.8$, $\alpha = 0$

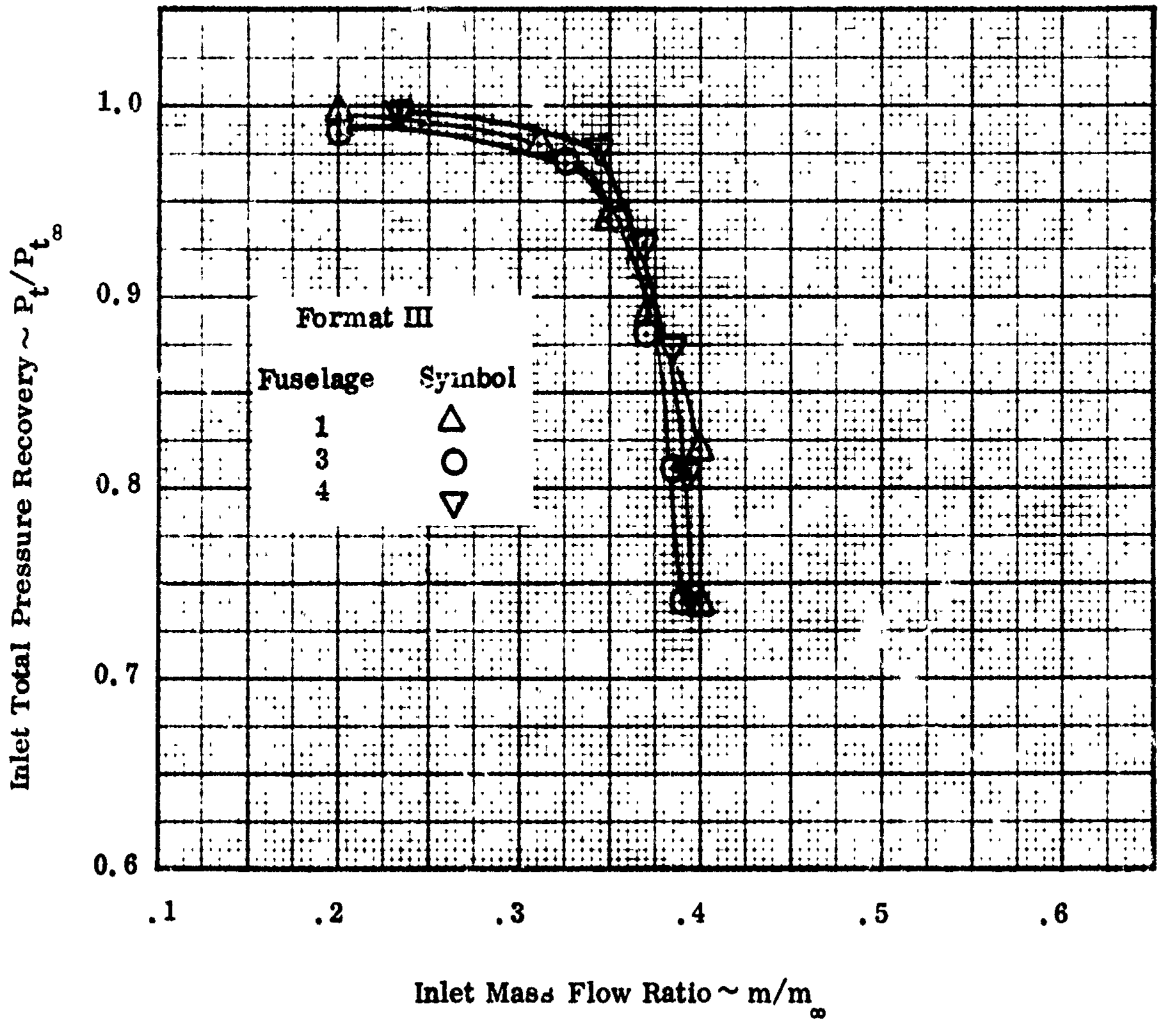

Figure 7-275. Comparison of Inlet Performance, Axisymmetric Inlet, $M_\infty = 0.8$, $\alpha = 5°$

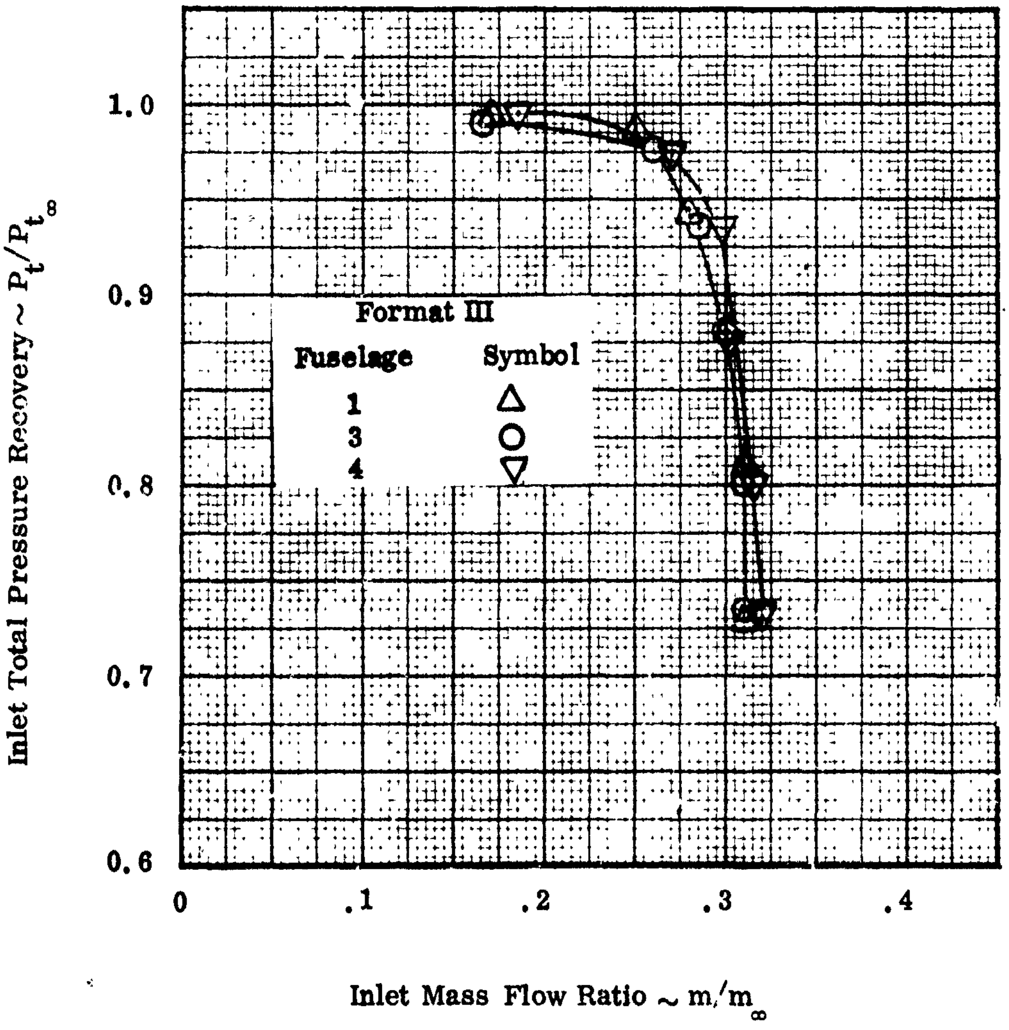

Figure 7-276. Comparison of Inlet Performance, Axisymmetric Inlet, $M_\infty = 0.8$, $\alpha = 10°$

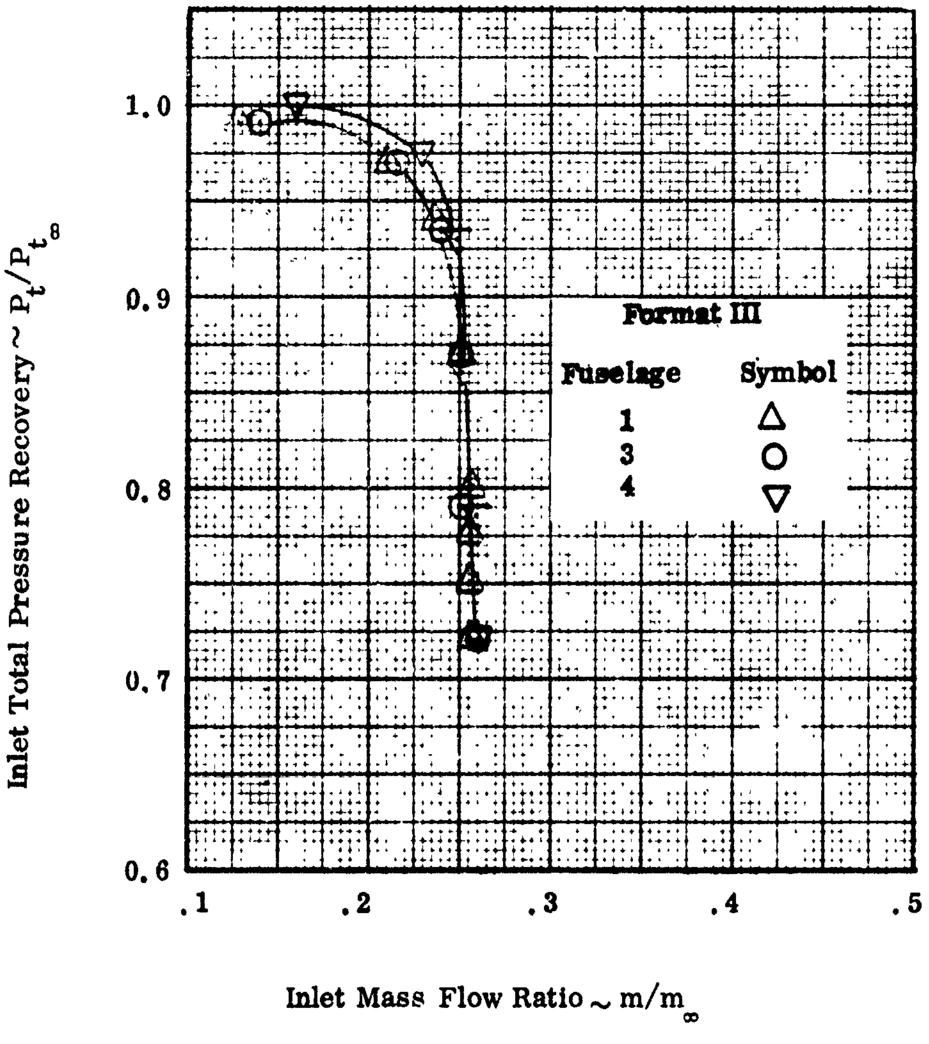

Figure 7-277. Comparison of Inlet Performance, Axisymmetric Inlet, $M_\infty = 0.8$, $\alpha = 15°$

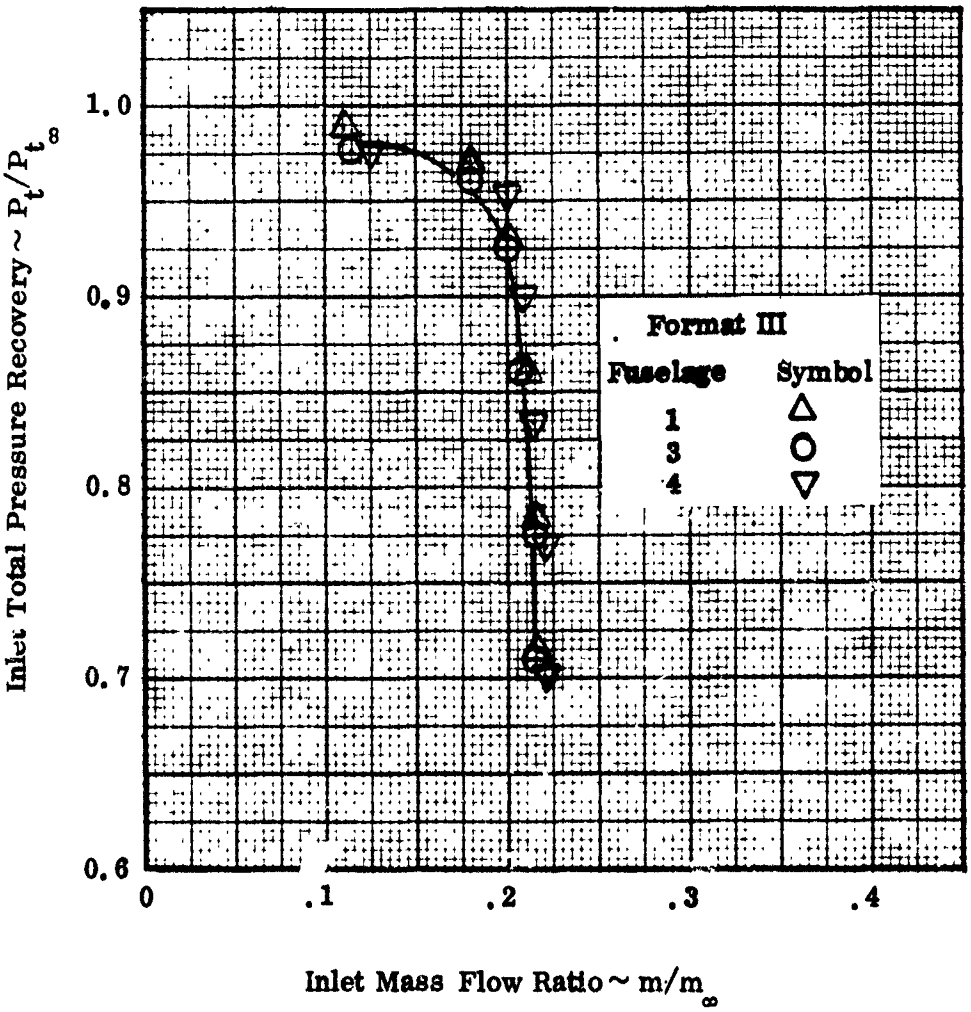

Figure 7-278. Comparison of Inlet Performance, Axisymmetric Inlet, $M_\infty = 0.8$, $\alpha = 20°$

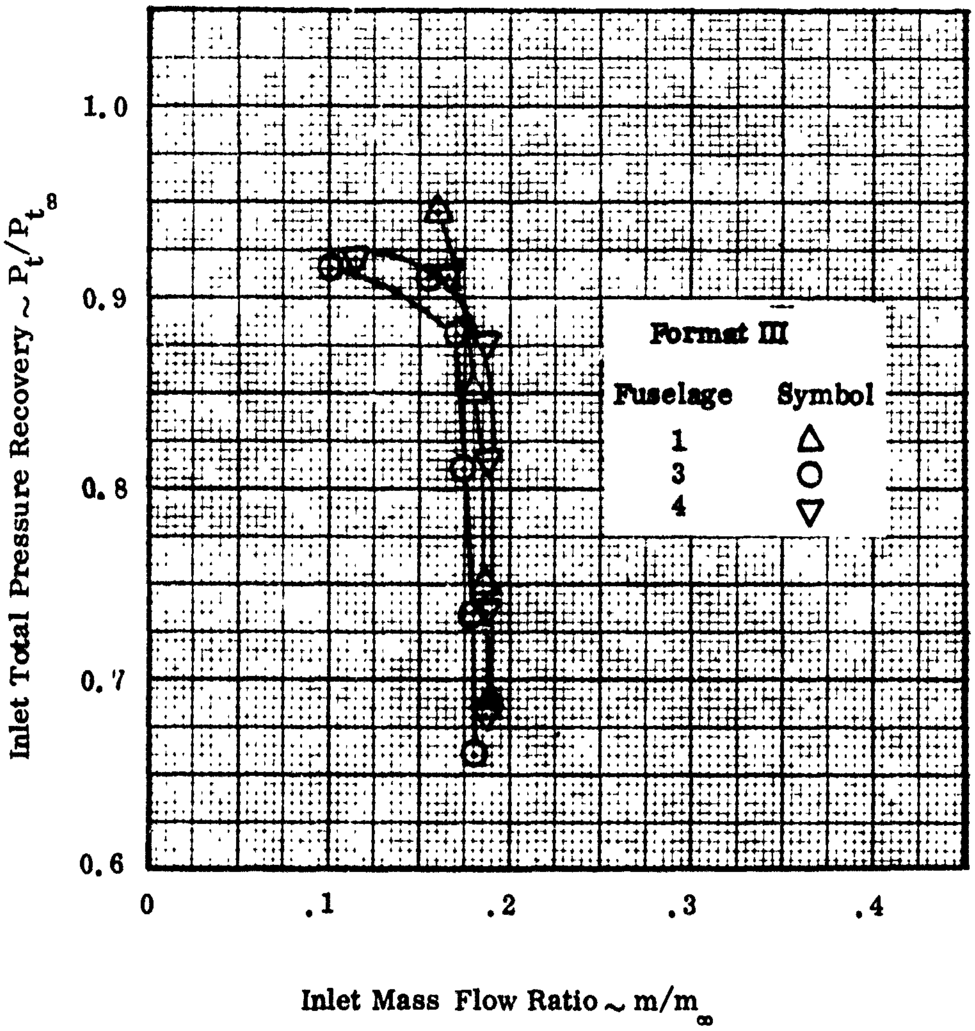

Figure 7-279. Comparison of Inlet Performance, Axisymmetric Inlet, $M_\infty = 0.8$, $\alpha = 25°$

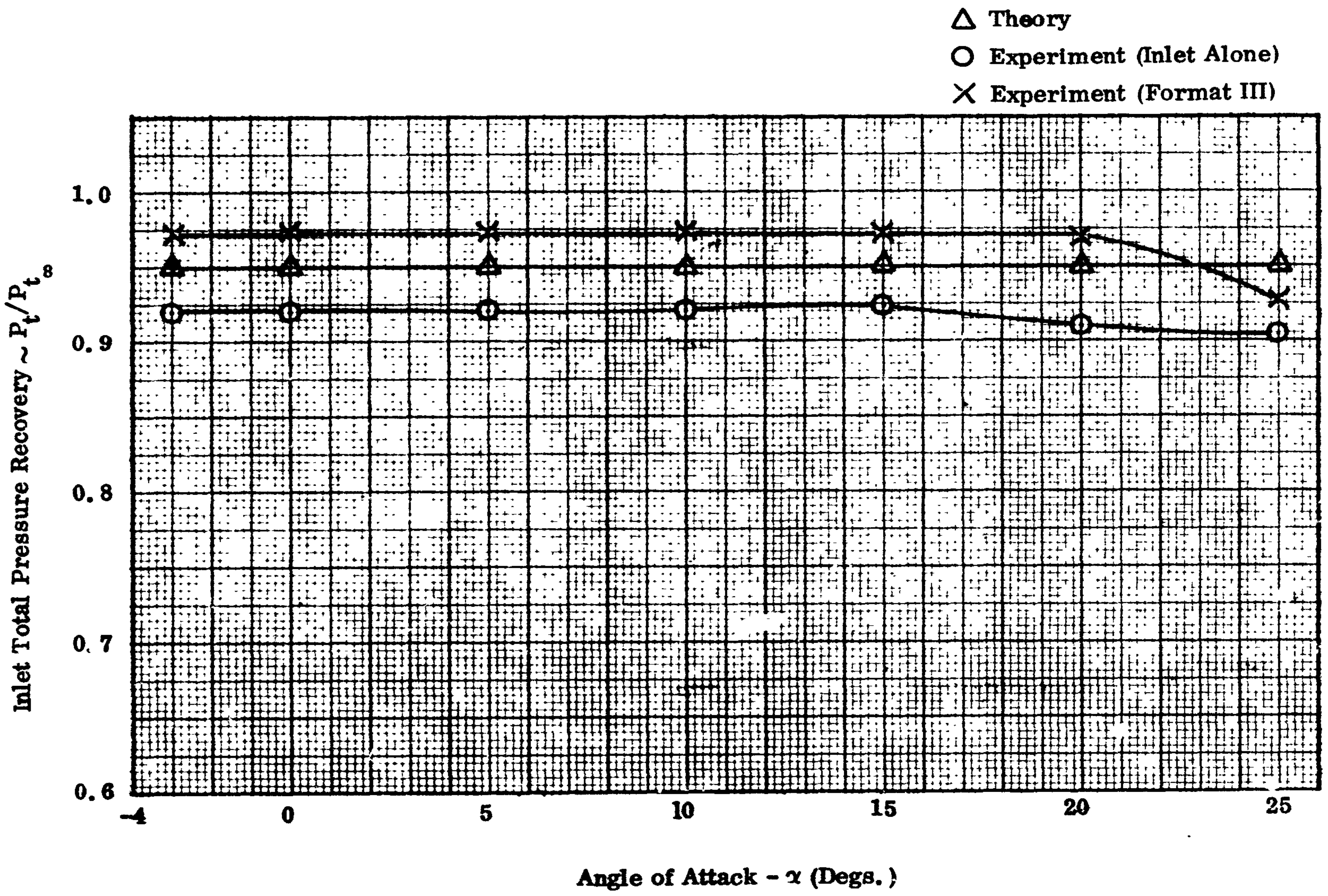

Figure 7-280. Comparison of Theory and Experiment, Axisymmetric Inlet
$M_\infty = 0.8$

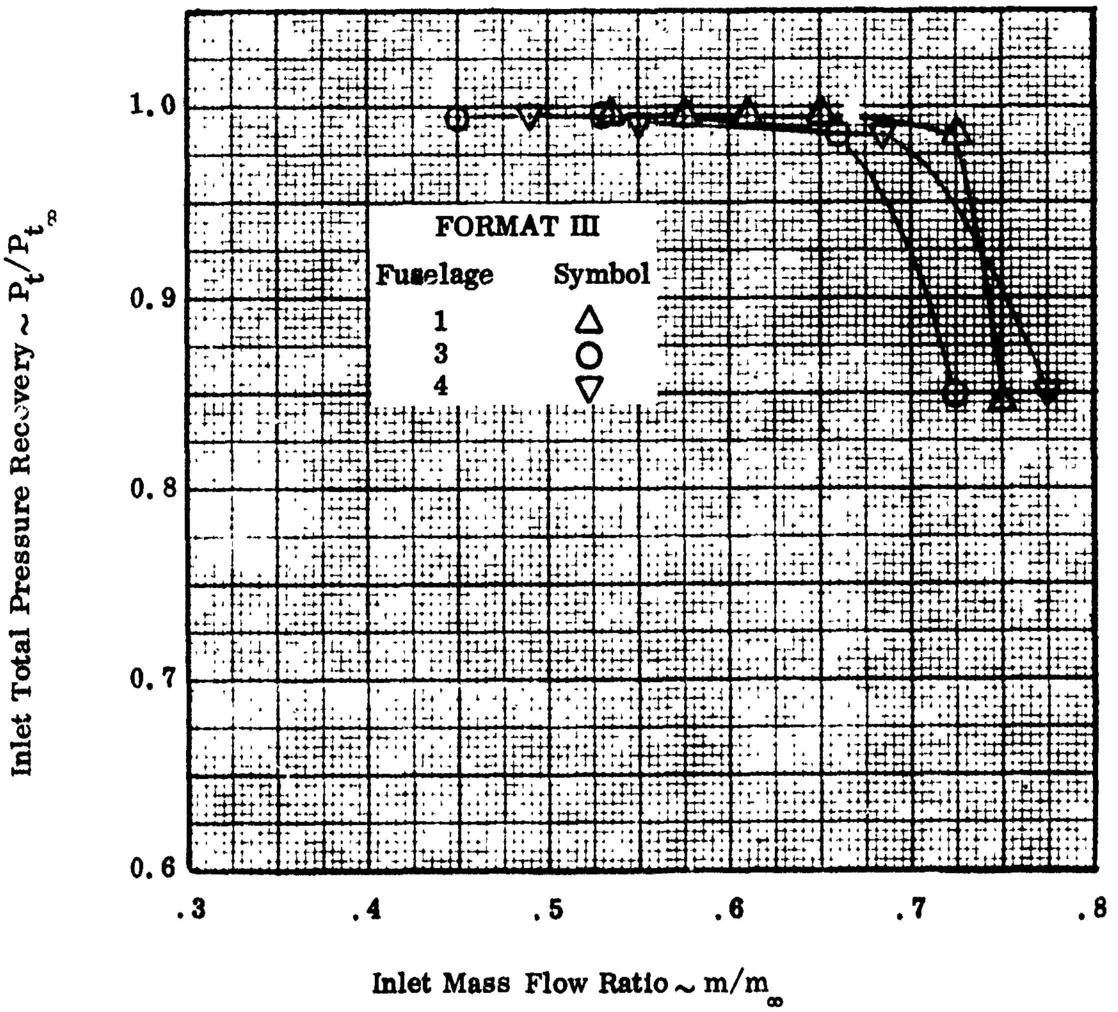

Figure 7-281. Comparison of Inlet Performance, Two-Dimensional Inlet, $M_\infty = 0.8$, $\alpha = -3°$

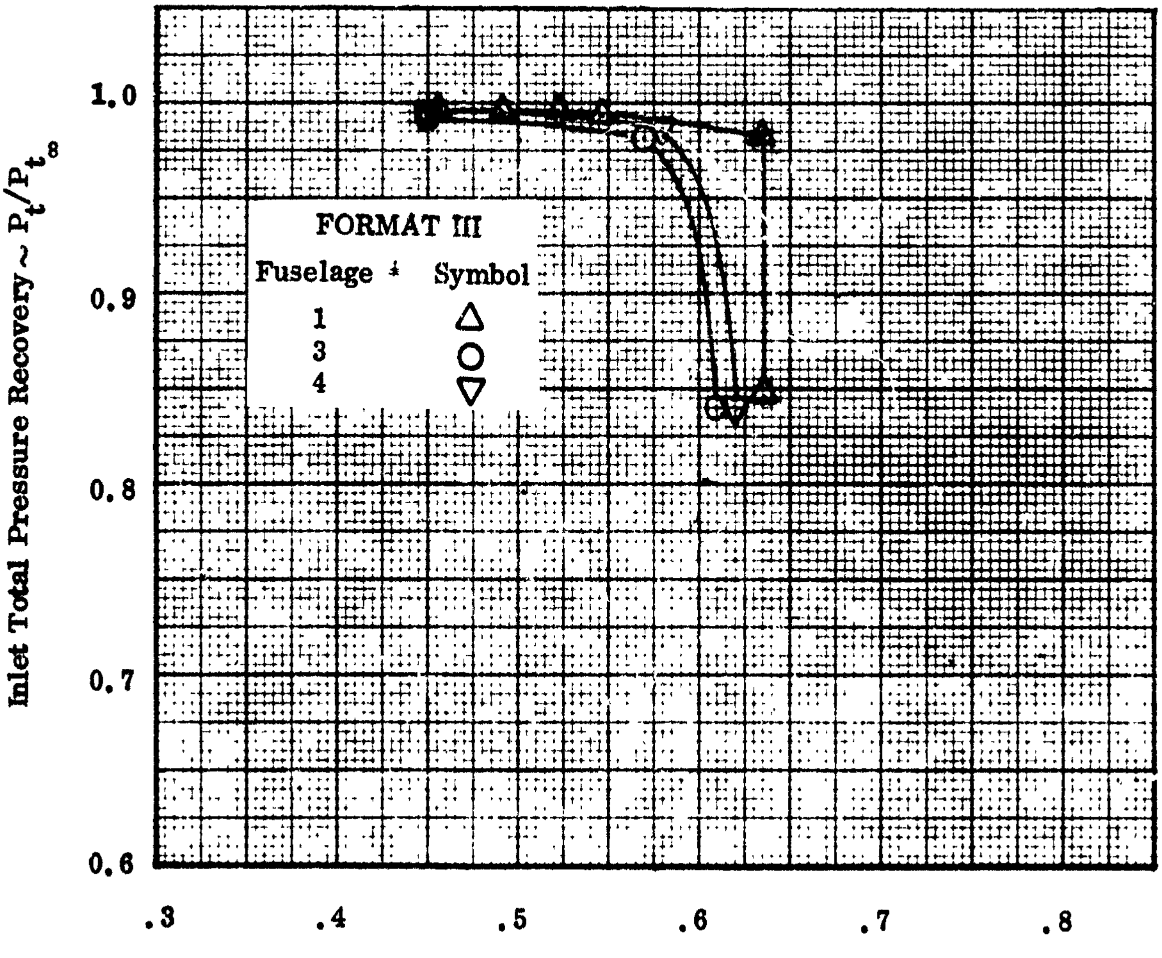

Figure 7-282. Comparison of Inlet Performance, Two Dimensional Inlet $M_\infty = .8$, $\alpha = 0°$

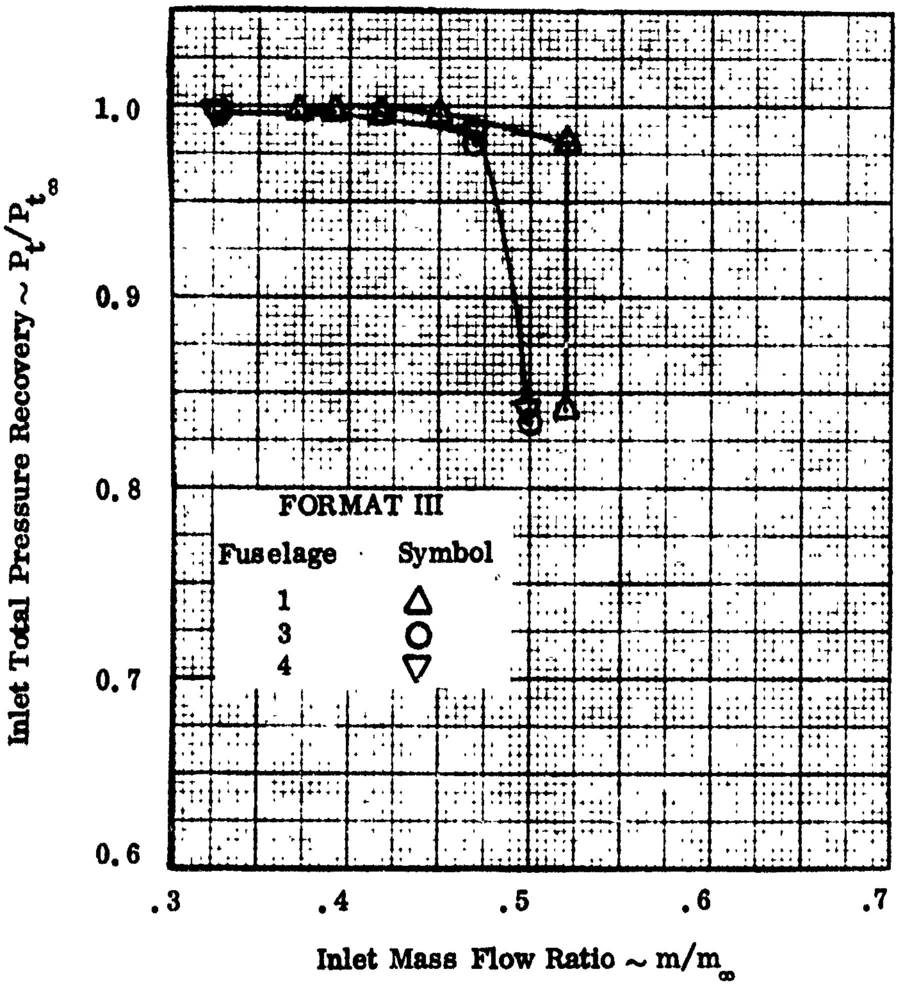

Figure 7-283. Comparison of Inlet Performance, Two Dimensional Inlet, $M_\infty = 0.8$, $\alpha = 5°$

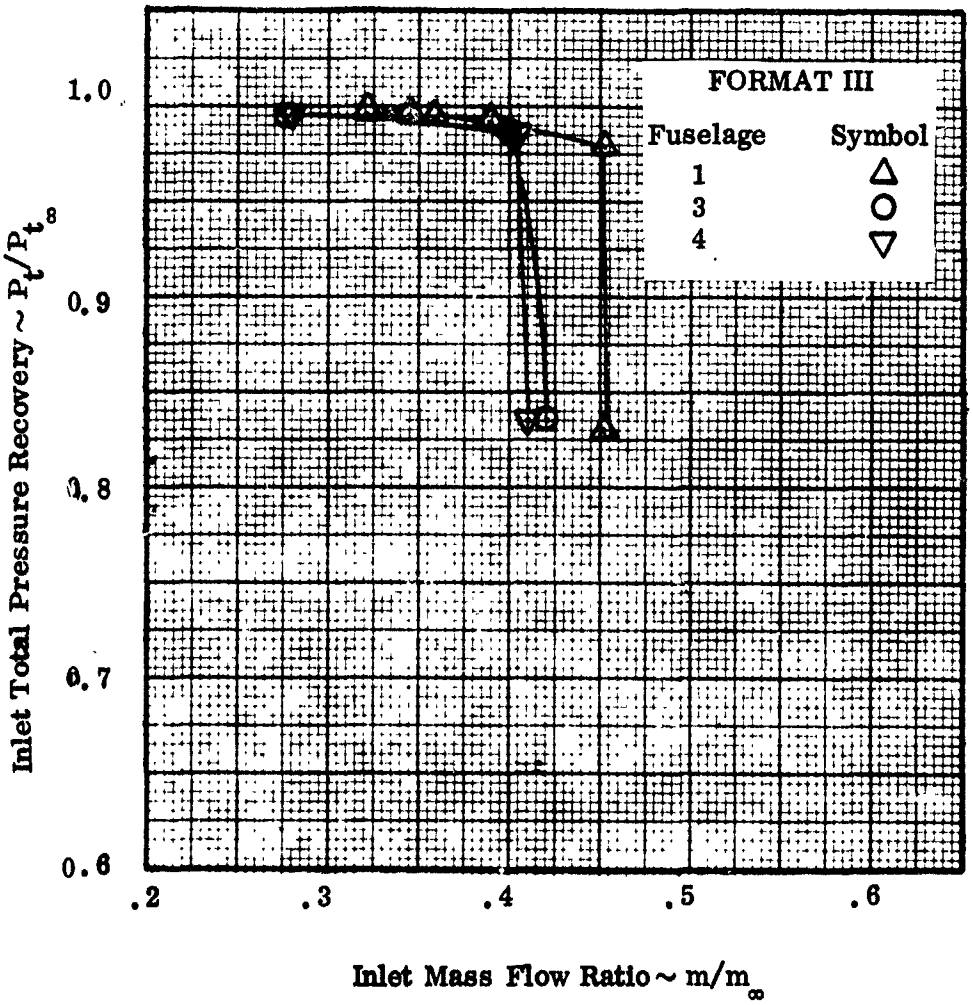

Figure 7-284. Comparison of Inlet Performance, Two-Dimensional Inlet
$M_\infty = 0.8$, $\alpha = 10°$

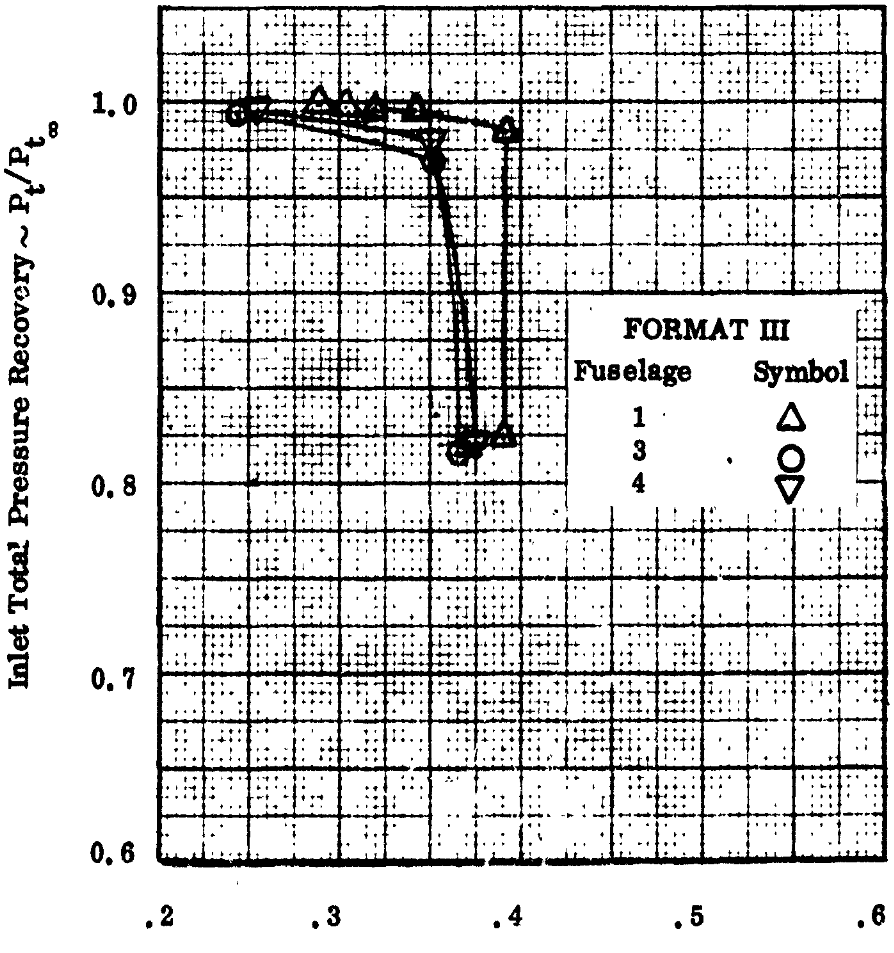

Figure 7-285. Comparison of Inlet Performance, Two Dimensional Inlet, $M_\infty = 0.8$, $\alpha = 15°$

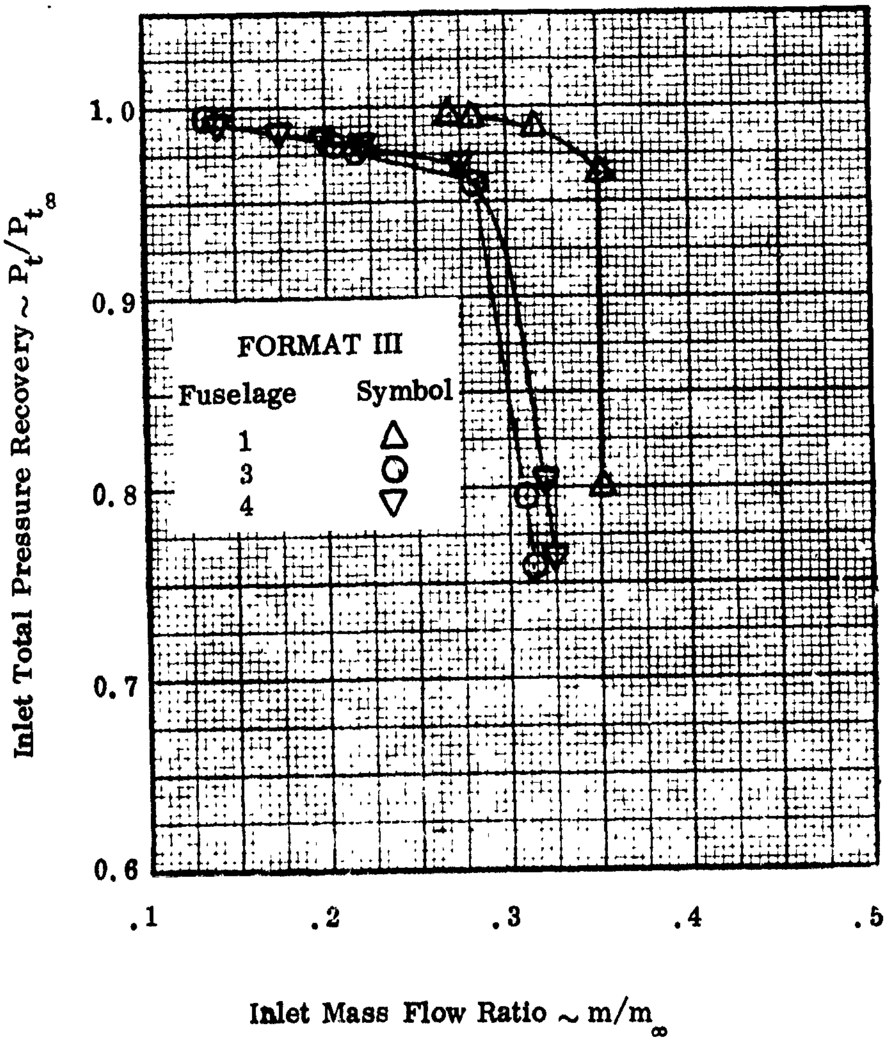

Figure 7-286. Comparison of Inlet Performance, Two-Dimensional Inlet, $M_\infty = 0.8$, $\alpha = 20°$

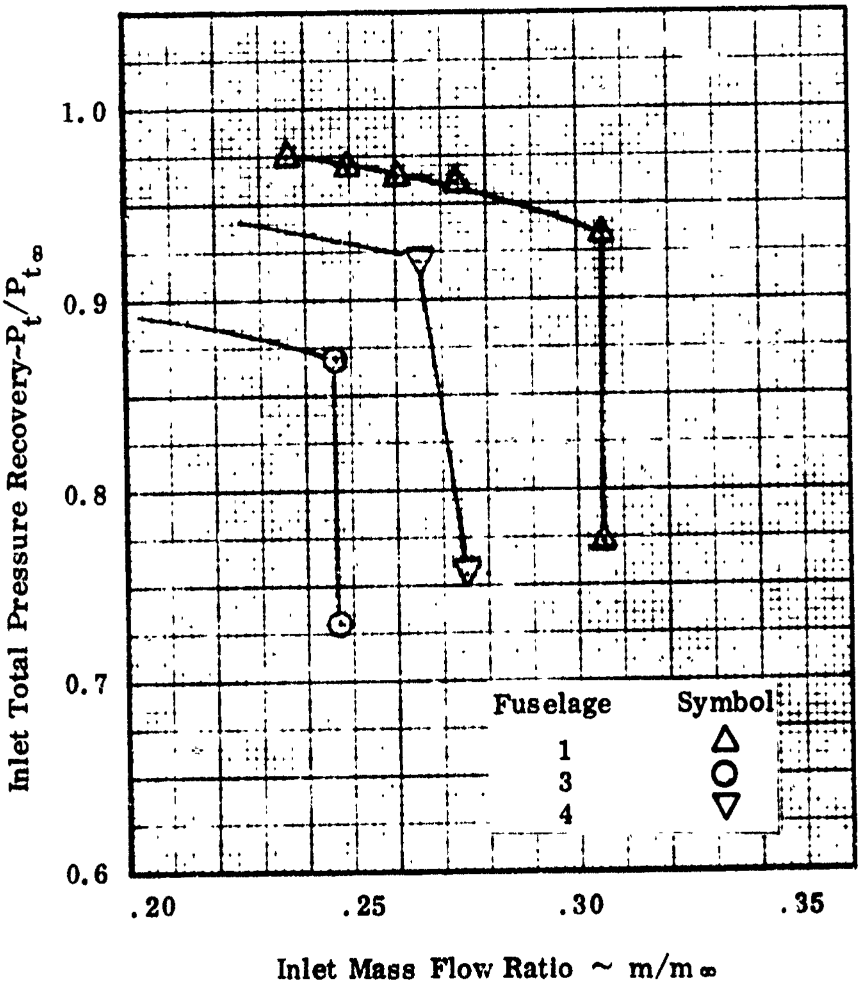

Figure 7-287. Comparison of Inlet Performance, Two Dimensional Inlet $M_\infty = 0.8$, $\alpha = 25°$

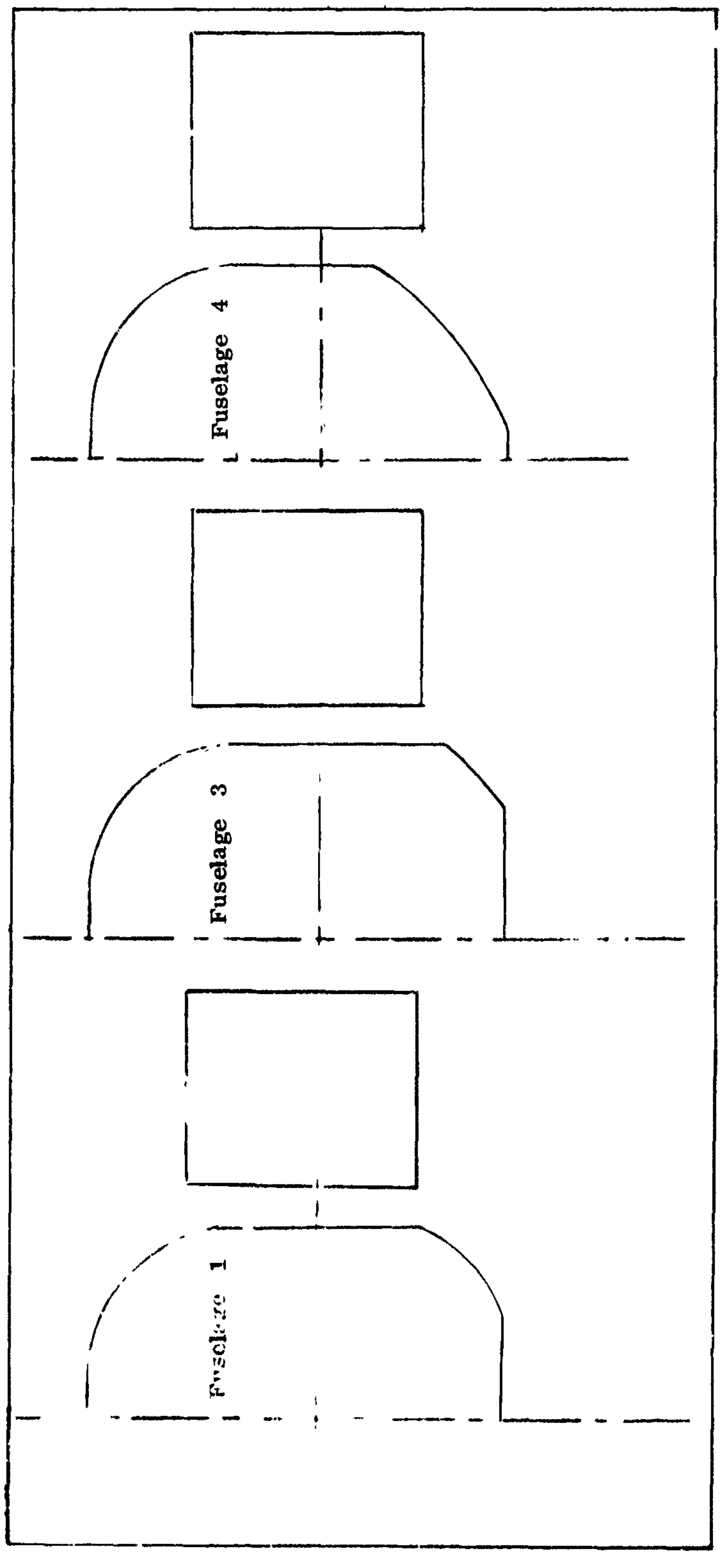
Fuselage 4
Fuselage 3
Fuselage 1

Format III

Figure 7-288. Fuselage/2-Dimensional Inlet Sections

and cowl surface with the locally approaching flow, resulting in a reduction in effective inlet throat area and lowered supercritical mass flow ratio. Inlet throttling tends to compound the effect, by feeding back through the subsonic stream, and a slightly inclined supercritical leg, of the characteristic cane, results. For the inlet/fuselage 4 configuration the effect is different. The fuselage vertical tangency point is a higher waterline than the lower inboard corner of the inlet. This, combined with the large gradually developed corner, places the inlet in a gentle peripheral gradient that precludes local surface/streamline misalignment. However, the large corner results in a diverter capture area large enough to cause choking and spillage into the main inlet stream. This, as in the case of fuselage 3, reduces the effective throat area and lowers the mass flow ratio. The impact of these effects increases with angle of attack, due to the increasing peripheral gradient, until at the extreme case ($\alpha = +25^\circ$) the reduced total pressure recovery and mass flow indicate the onset of a local separation for the fuselage 3 configuration, probably as the result of the extremely high flow angularity induced by the small rapidly developed corner. In general, the performance level achieved by the integrated systems approximated both that predicted by theory and that attained by the uninstalled inlet (Format V) indicating no strong integration effects at this Mach number. This comparison is presented in Figure 7-289.

In view of the fact that the height of the two-dimensional inlet is approximately equal to the radius of the axisymmetric inlet, a question may be posed as to the reason that effects attributable to physical or geometric compatibility did not make themselves apparent in the axisymmetric inlet data. Figure 7-290 presents a section of the axisymmetric inlet, integrated with each of the three fuselages employed in Format III. It can be seen that, although the inlet position, relative to the fuselage corner, is essentially the same as that for the two-dimensional inlet, the curved cowl surface can intercept the inclined streamlines, generated by the fuselage corner gradient, more efficiently. In this view the cowl can almost be pictured as an extension of the fuselage corner. Consequently, at this subsonic Mach number where the peripheral gradients are mild this appears sufficient to eliminate geometric incompatibility.

7.5.2.2 Mach Number 1.2

The inlet performance achieved at this Mach number reflects the similarity among flow fields. The characteristic for the axisymmetric inlet, presented in Figures 7-291 through 7-294, is seen to be independent of the fuselage geometry.

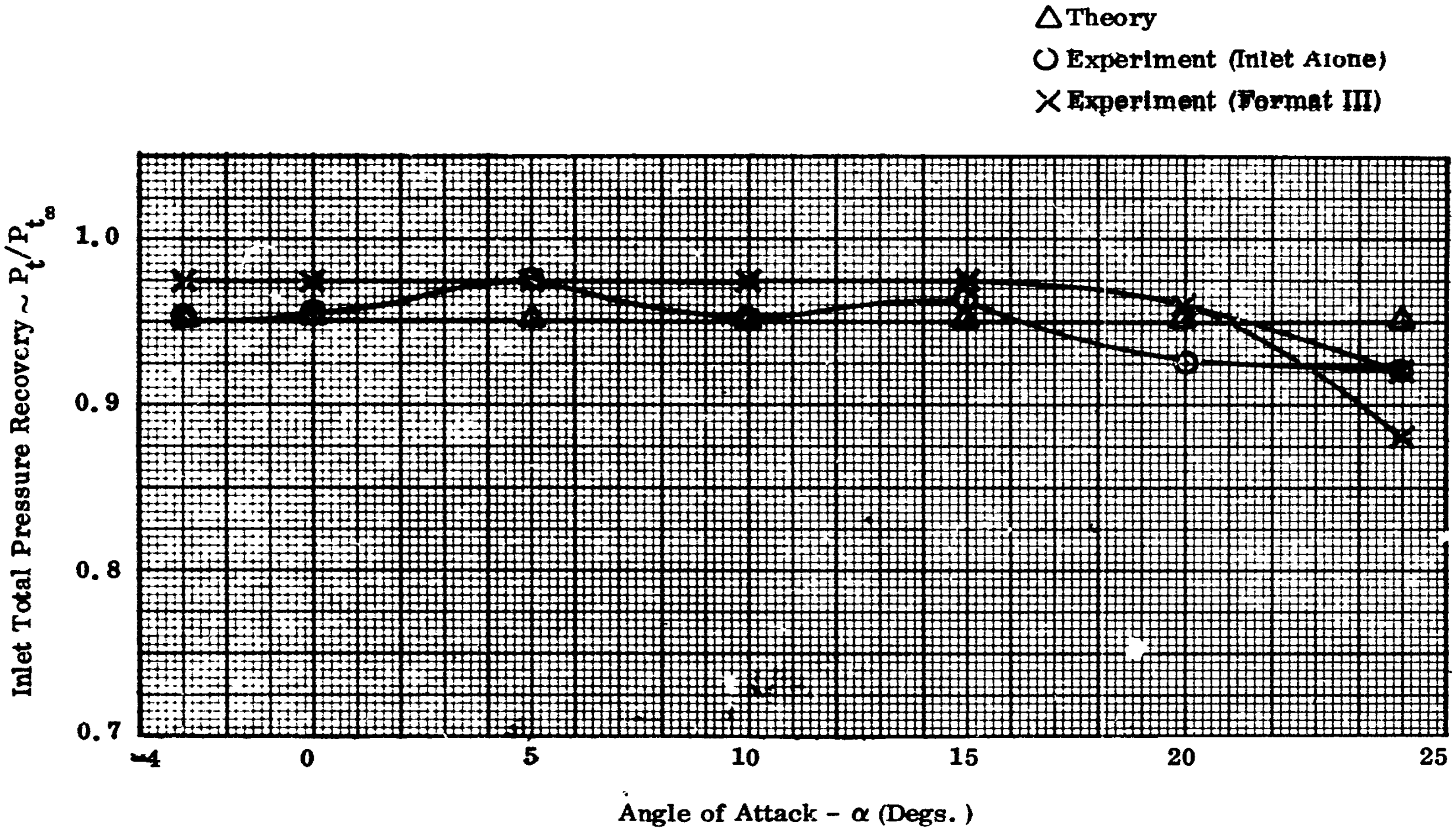

Figure 7-289. Comparison of Theory and Experiment, Two-Dimensional Inlet

$M_\infty = 0.8$

AXISYMMETRIC INLET AT 50% ACL
FORMAT III

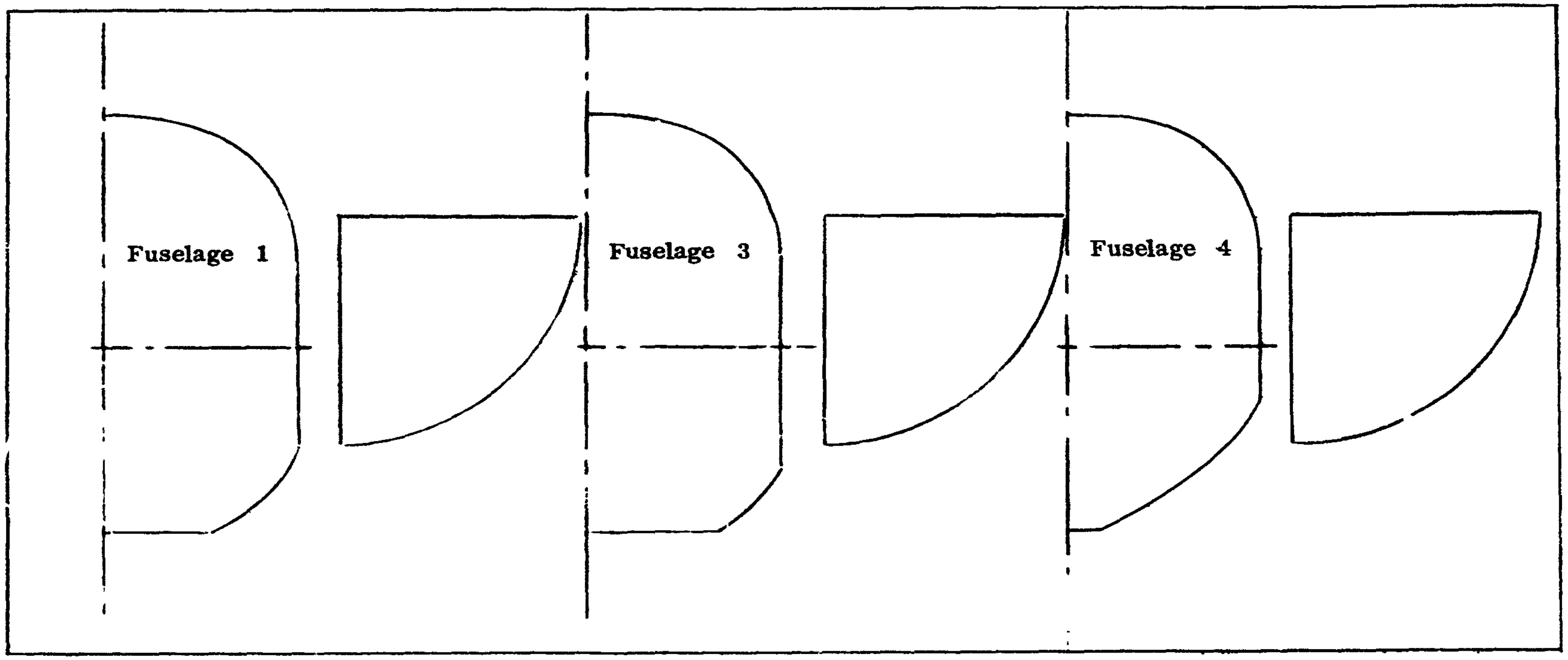
Fuselage 1
Fuselage 3
Fuselage 4

Figure 7-290. Fuselage/Axisymmetric Inlet Sections

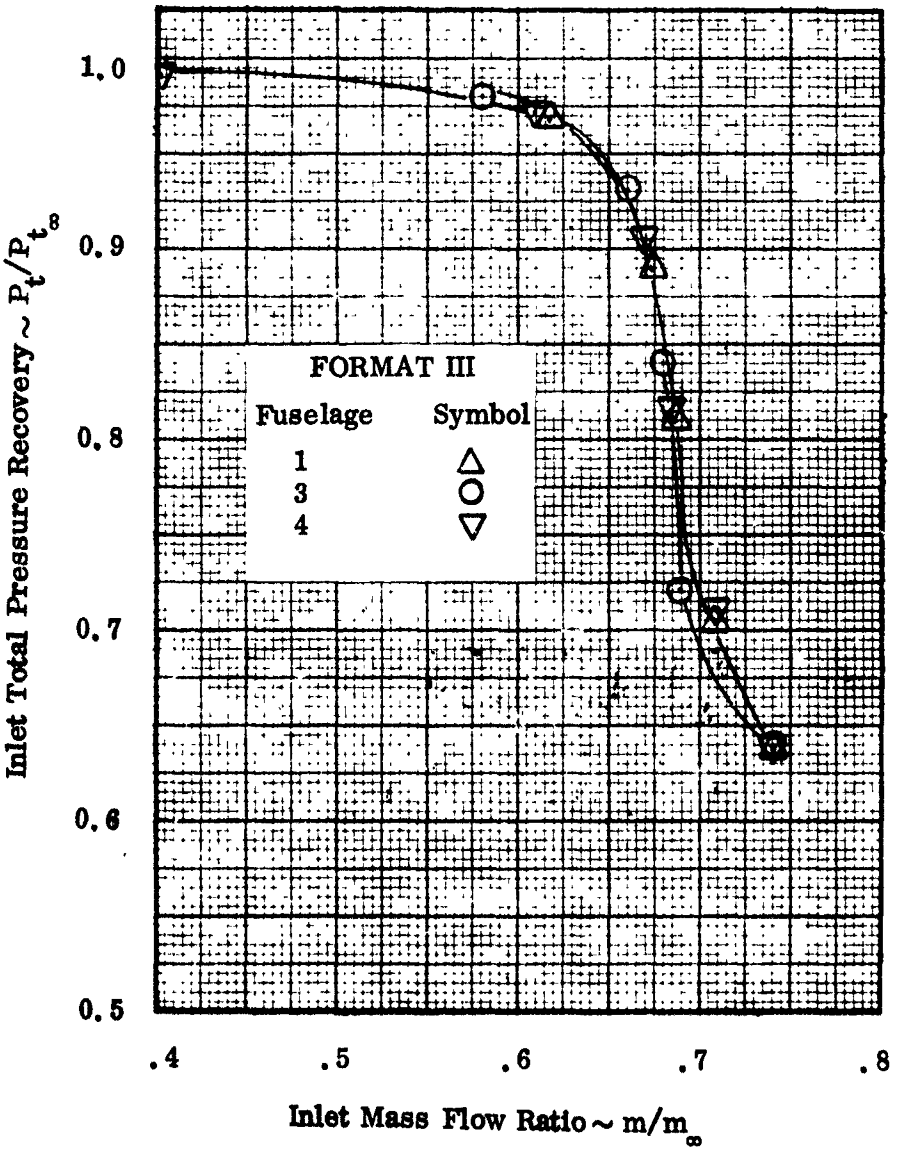

Figure 7-291. Comparison of Inlet Performance, Axisymmetric Inlet, $M_\infty = 1.2$, $\alpha = -3°$

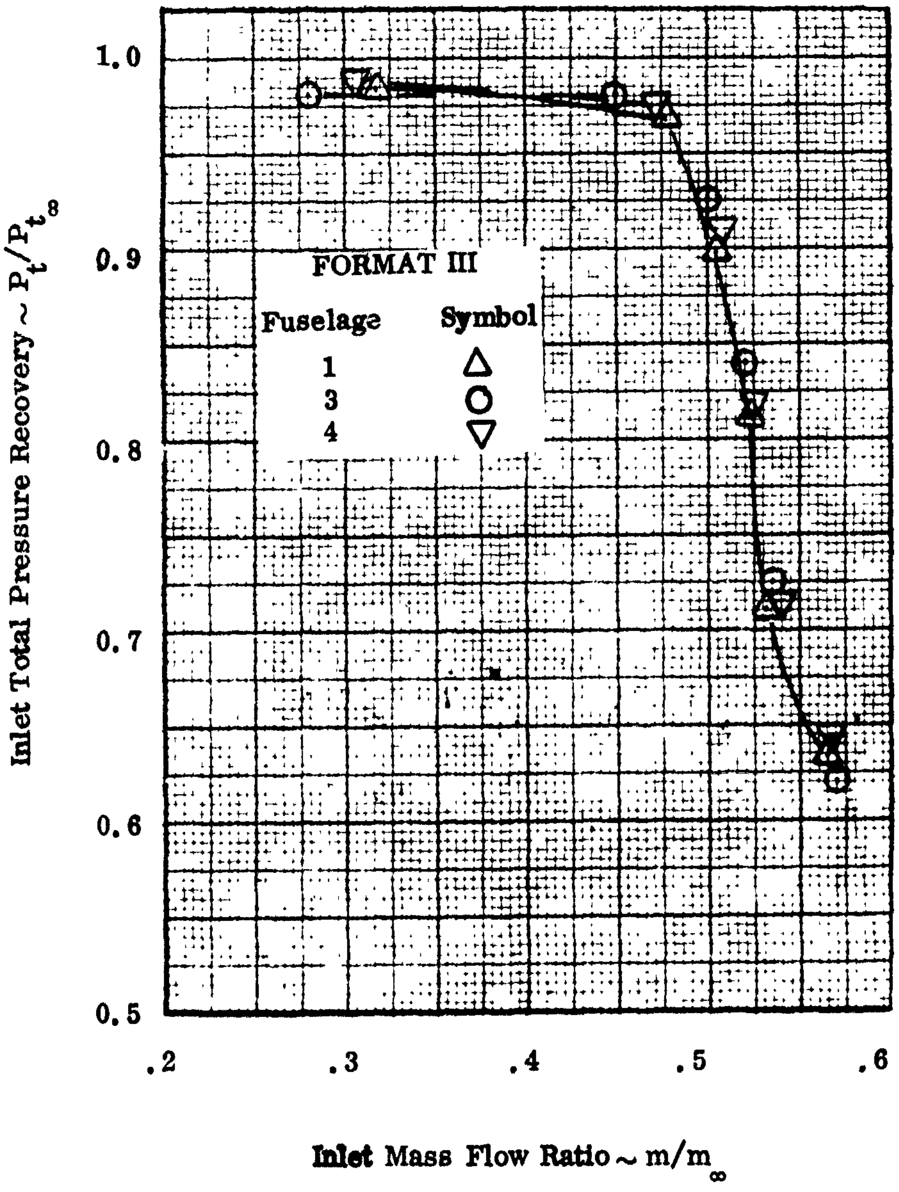

Figure 7-292. Comparison of Inlet Performance, Axisymmetric Inlet, $M_\infty = 1.2$, $\alpha = 0°$

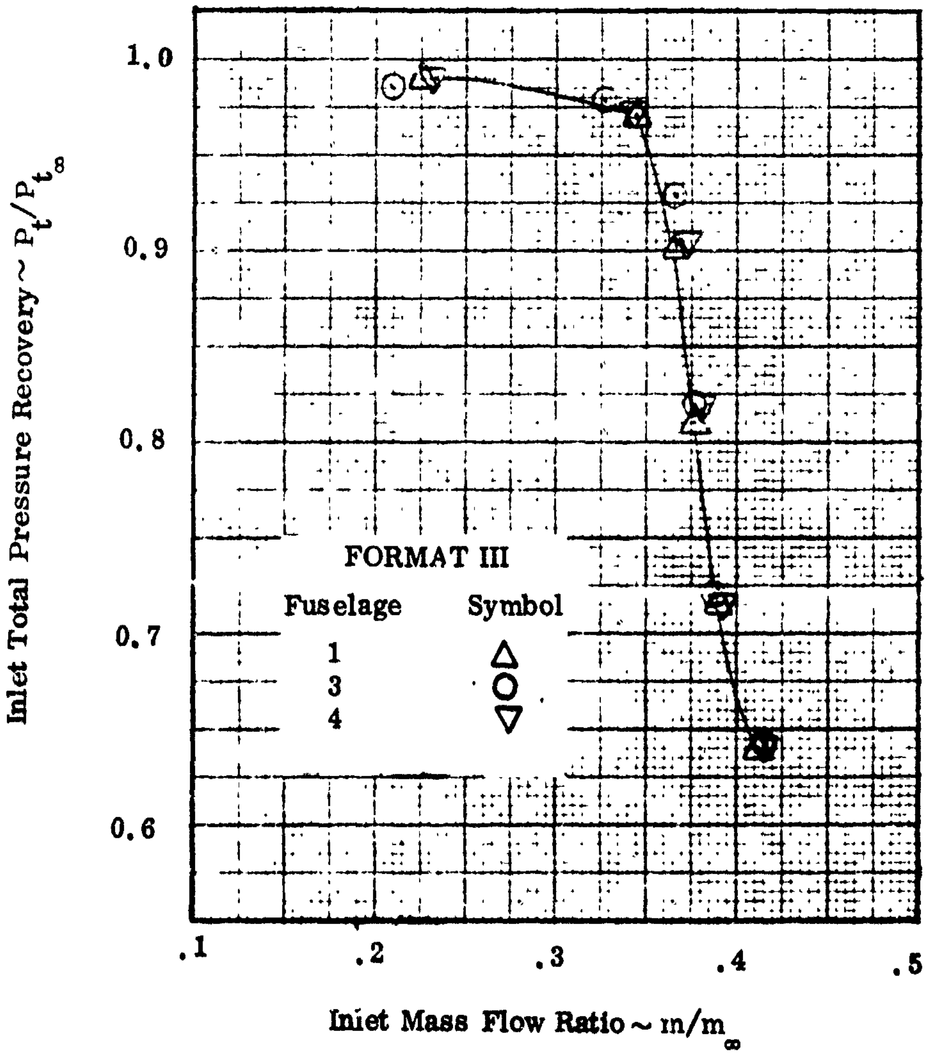

Figure 7-293. Comparison of Inlet Performance, Axisymmetric Inlet, $M_\infty = 1.2$, $\alpha = 5°$

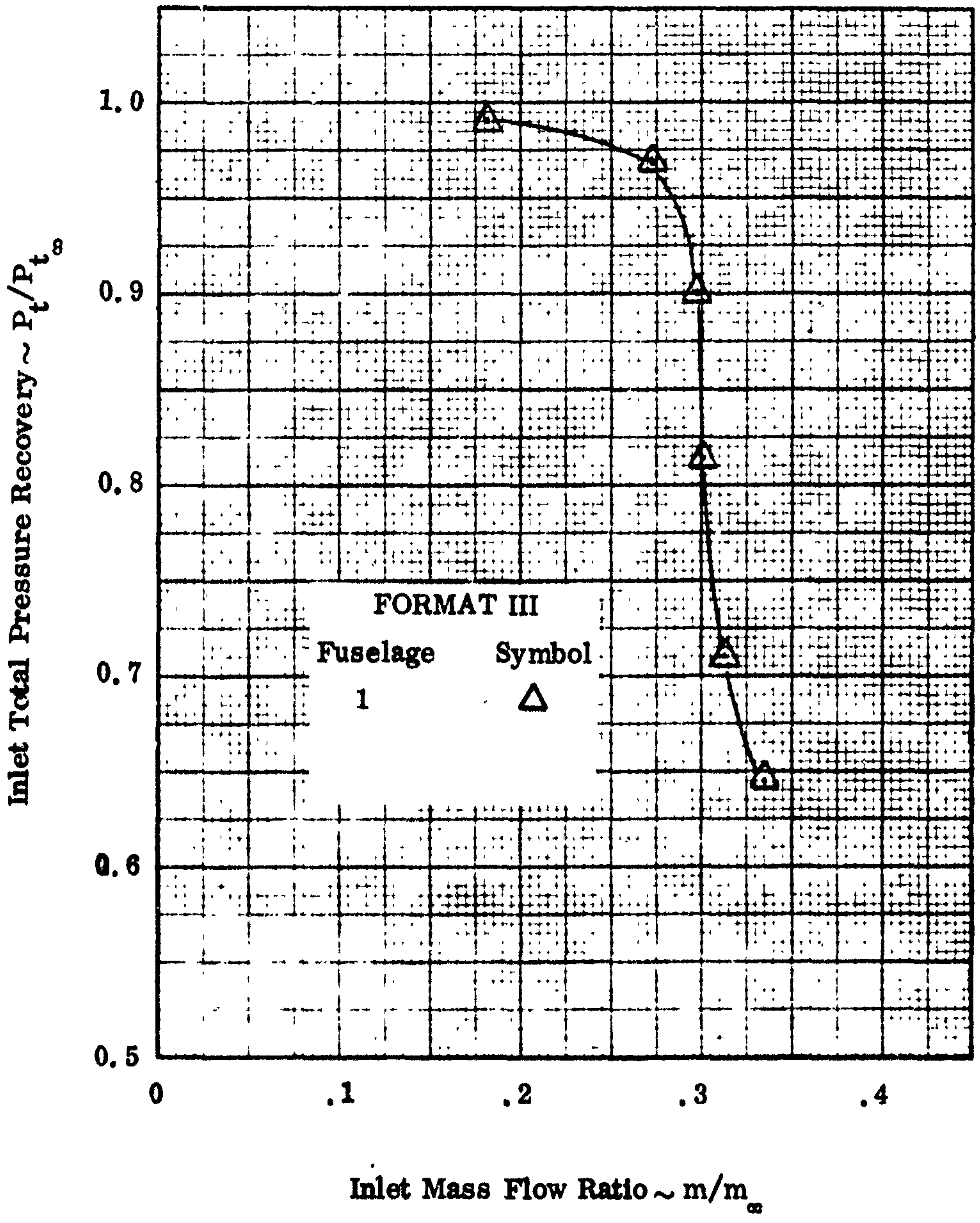

Figure 7-294. Comparison of Inlet Performance, Axisymmetric Inlet $M_\infty = 1.2$, $\alpha = 10°$

This is also essentially true for the two-dimensional inlet where the characteristic canes are very closely grouped as shown in Figures 7-295 through 7-301. The slight variation in inlet performance among the three fuselage/inlet combinations, noted previously at Mach 0.8, appears again at this Mach number with the fuselage 1/inlet combination displaying a slightly superior characteristic.

For the axisymmetric inlet a comparison of installed and uninstalled critical total pressure recovery reveals no beneficial or detrimental effects attributable to the inlet integration process. Tunnel blockage precluded testing the installed configuration at angle of attack above +10°, consequently the comparison could not be drawn for those higher angles. It is, however, reasonable to predict a continuation of the close match of installed and uninstalled critical total pressure recovery at the higher attitudes, particularly in view of the fact that the uninstalled pressure recovery was essentially constant across the entire angle of attack range. A direct comparison of installed and uninstalled total pressure recovery was not possible with the two-dimensional inlet due to mechanical malfunctions, during the inlet alone tests, that precluded the attainment of critical operation. However, the critical total pressure recovery of the installed inlet matched the theoretical estimates very closely, across the entire angle of attack range, thereby permitting the assumption that a properly operating uninstalled inlet would also have matched closely. Therefore, the indications are that installation effects do not exist for that inlet concept at this Mach number.

7.5.2.3 Mach Number 1.8

At this Mach number the impact of the axisymmetric inlet/fuselage integration process is primarily a function of angle of attack and secondarily a function of fuselage geometry. For angles of attack of -3° and 0° the aircraft wing is a non working component and consequently installed and uninstalled critical pressure recovery levels compare very closely. In addition, the mild downwash over the forward portion of the fuselage tends to reduce the probability of fuselage boundary layer ingestion and the inlet performance is dependent, to some degree, upon the type of inviscid flow field induced by the fuselage corner. The effect can be seen in Figures 7-302 and 7-303 which present the characteristic canes for the axisymmetric inlet integrated with the three fuselages. The small rapidly developed corner (fuselage 3) induces the most nonuniform flow field and consequently the poorest inlet performance. The fuselage flow field becomes more uniform as corner radius is increased and corner

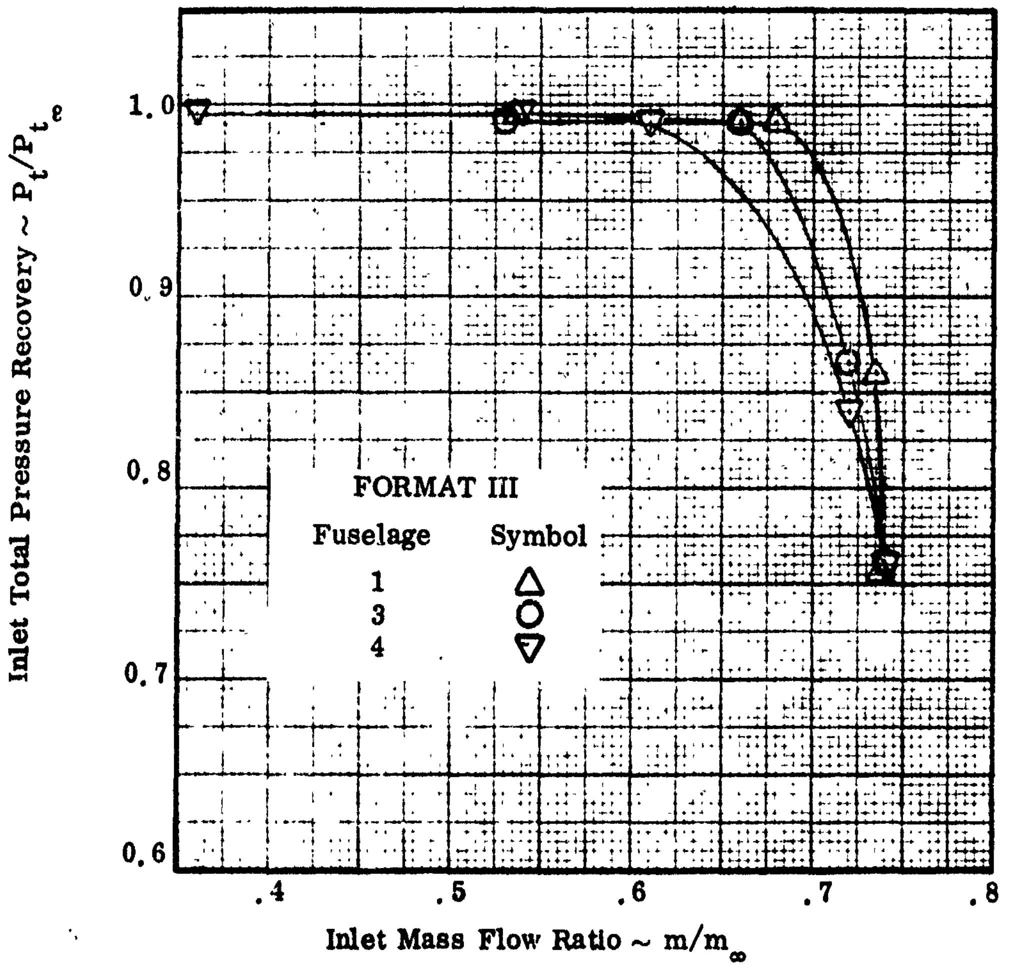

Figure 7-295. Comparison of Inlet Performance, Two Dimensional Inlet $M_\infty = 1.2$, $\alpha = -3°$

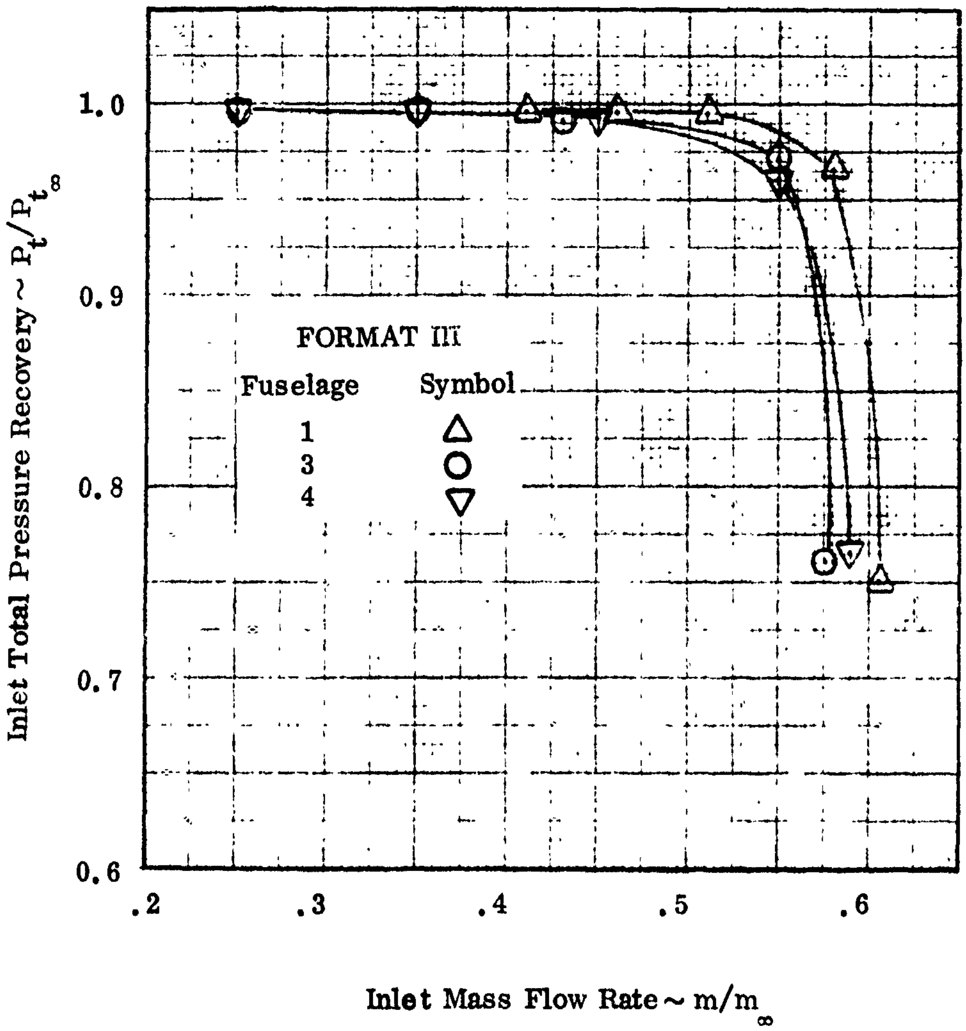

Figure 7-296. Comparison of Inlet Performance, Two Dimensional Inlet, $M_\infty = 1.2$, $\alpha = 0°$

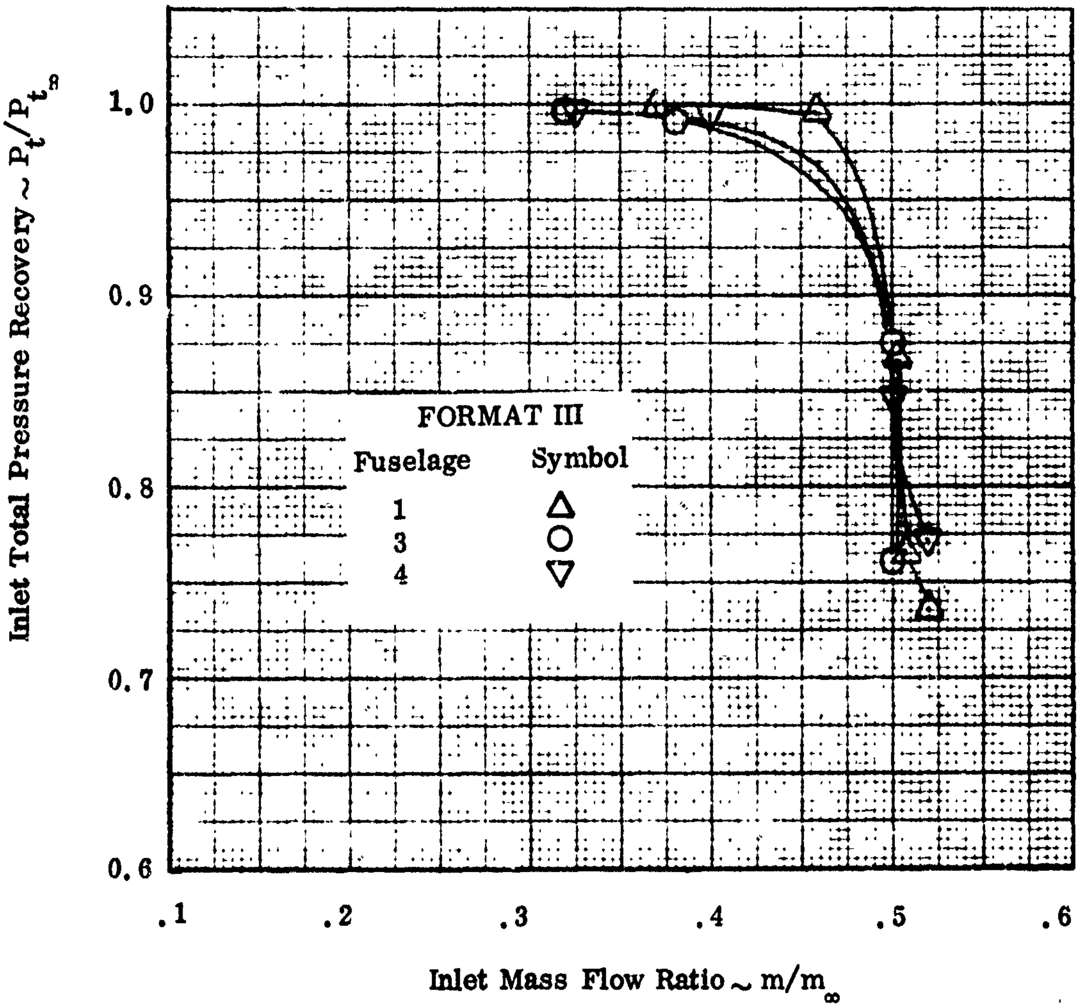

Figure 7-297. Comparison of Inlet Performance, Two Dimensional Inlet, $M_\infty = 1.2$, $\alpha = 5°$

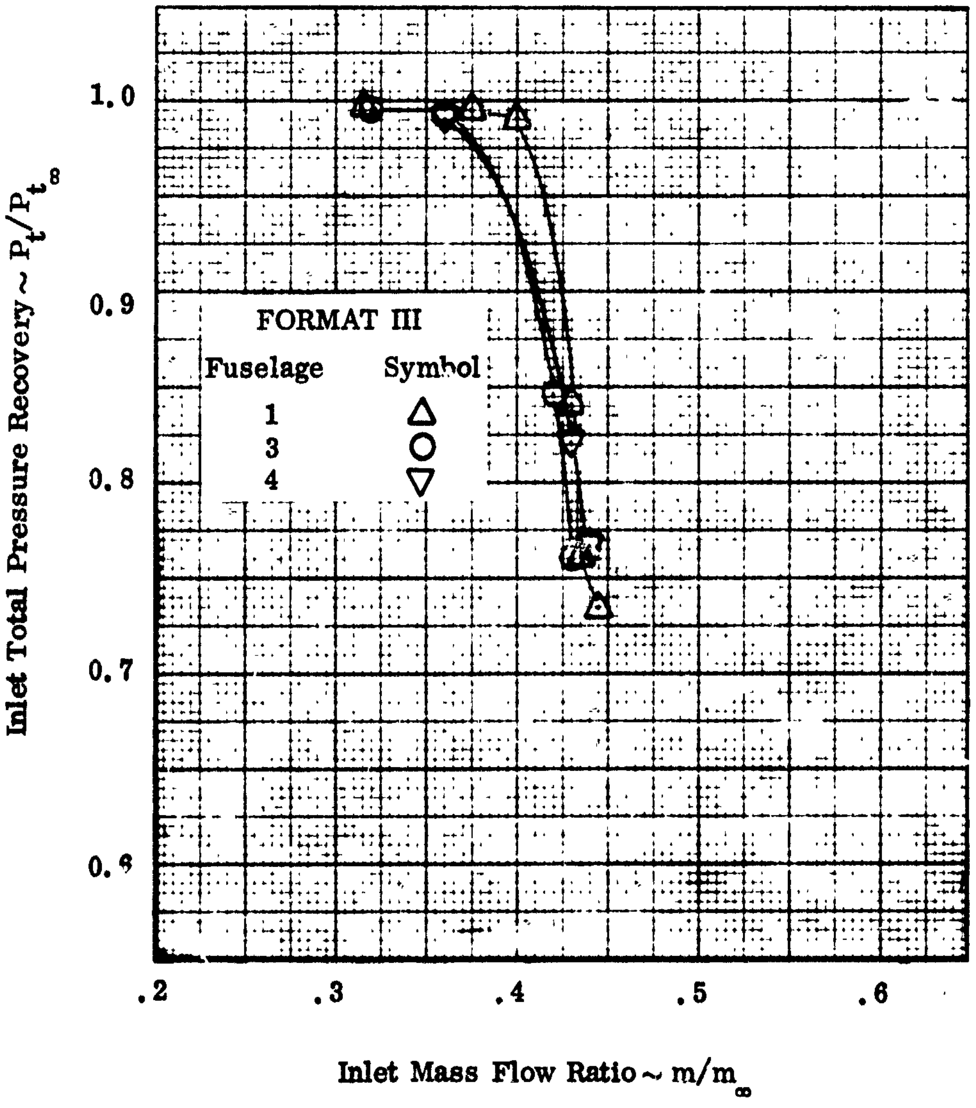

Figure 7-298. Comparison of Inlet Performance, Two-Dimensional Inlet, $M_\infty = 1.2$, $\alpha = 10°$

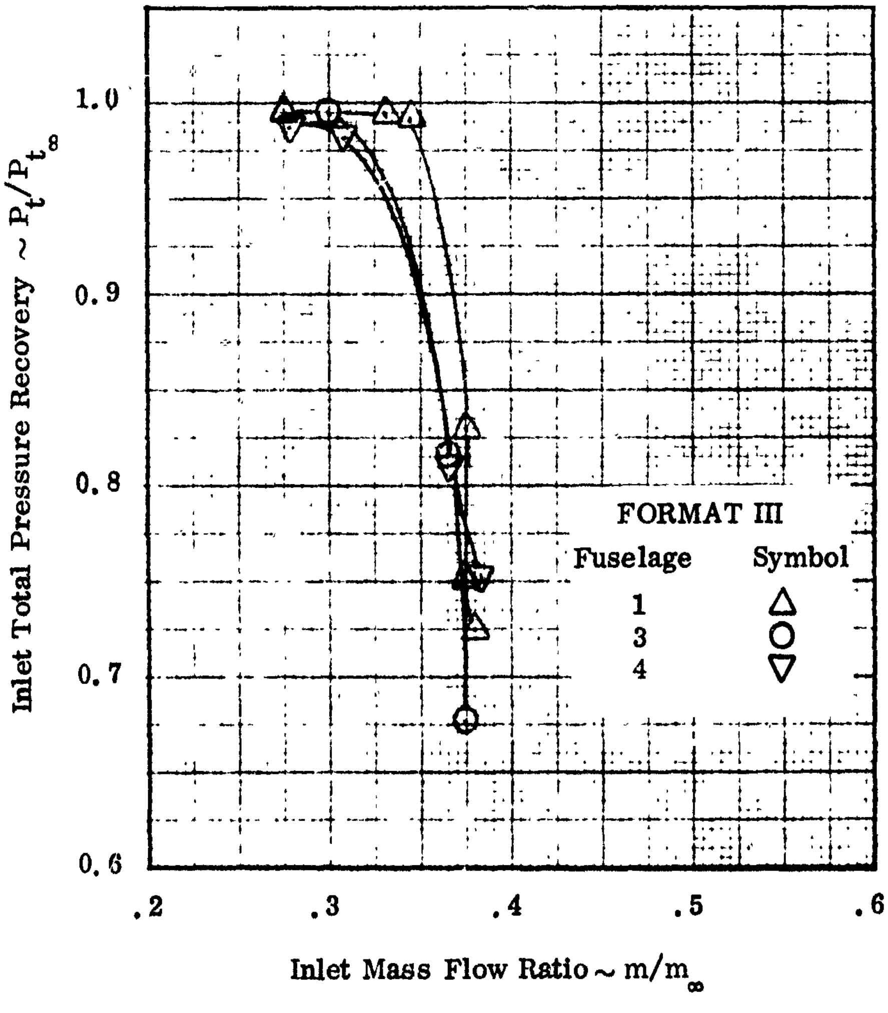

Figure 7-299. Comparison of Inlet Performance, Two Dimensional Inlet $M_\infty = 1.2$, $\alpha = 15°$

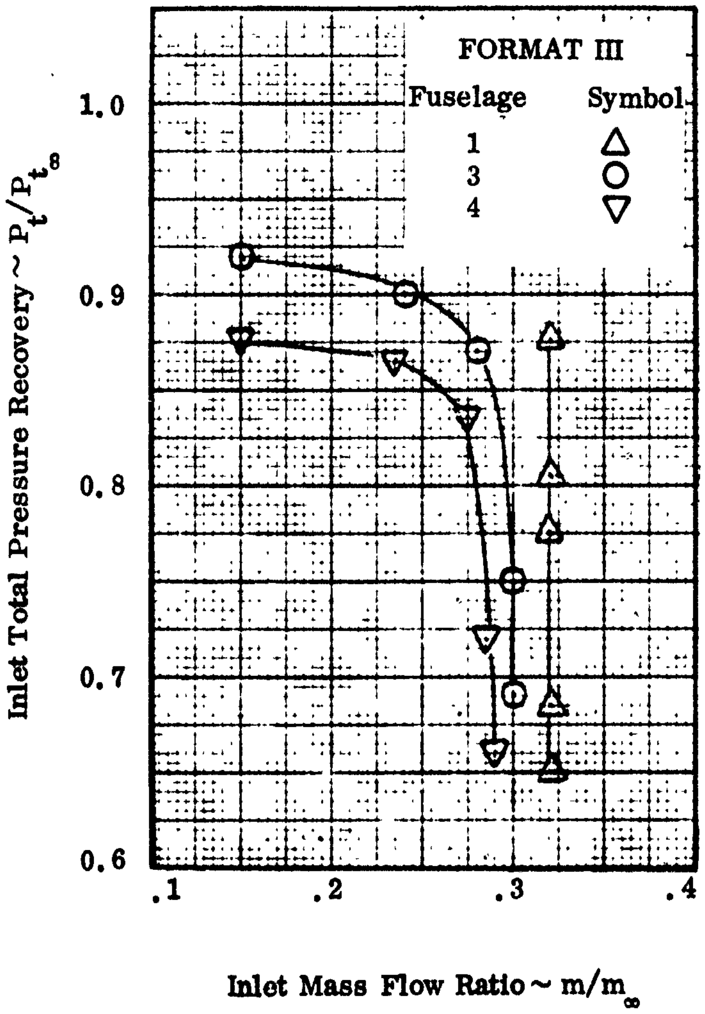

Figure 7-300. Comparison of Inlet Performance, Two-Dimensional Inlet
$M_\infty = 1.2$, $\alpha = 20°$

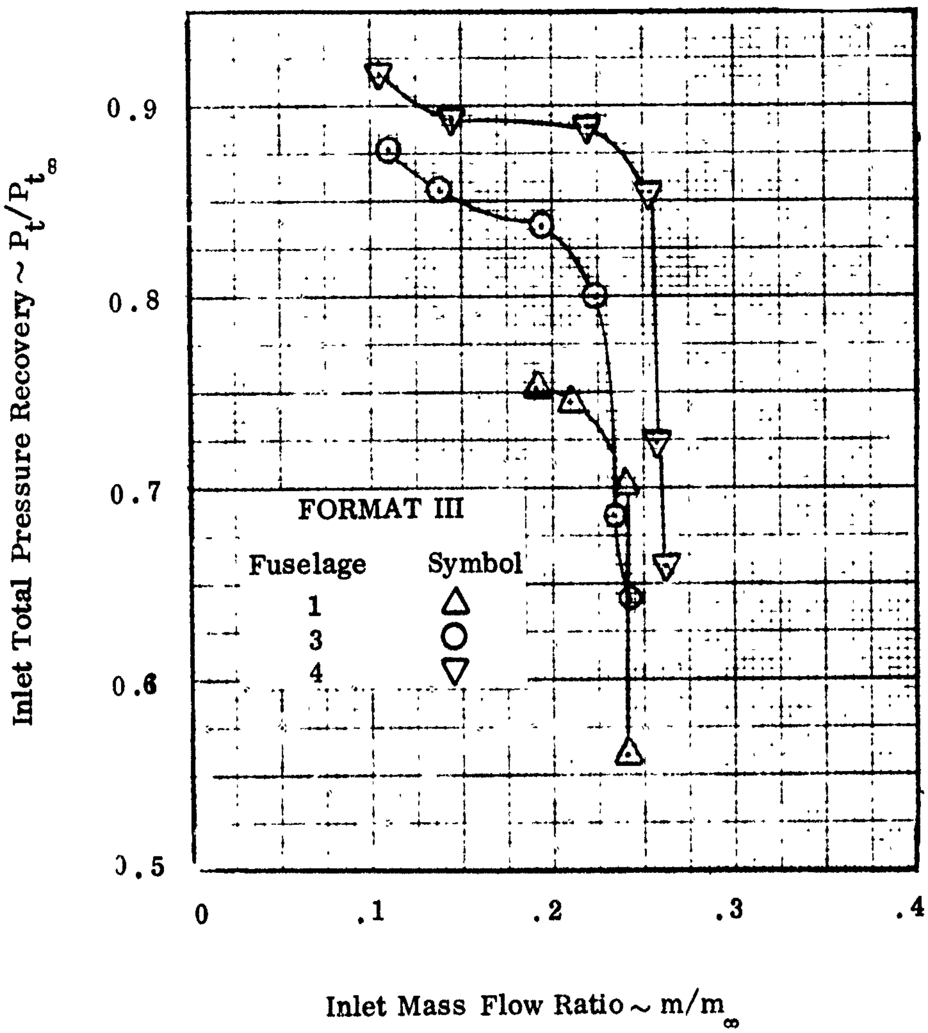

Figure 7-301. Comparison of Inlet Performance, Two-Dimensional Inlet, $M_\infty = 1.2$, $\alpha = 25°$

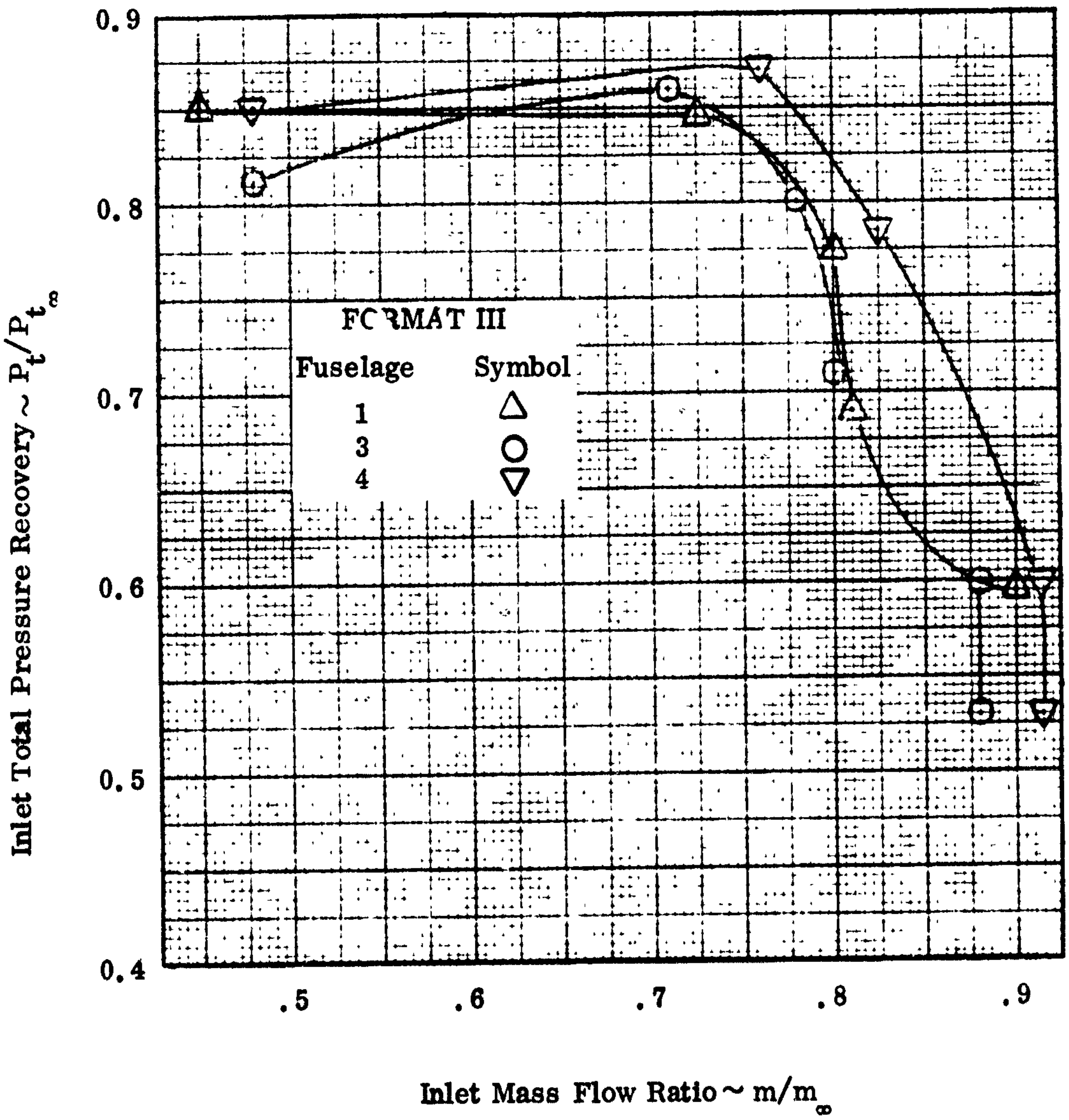

Figure 7-302. Comparison of Inlet Performance, Axisymmetric Inlet $M_\infty = 1.8$, $\alpha = -3°$

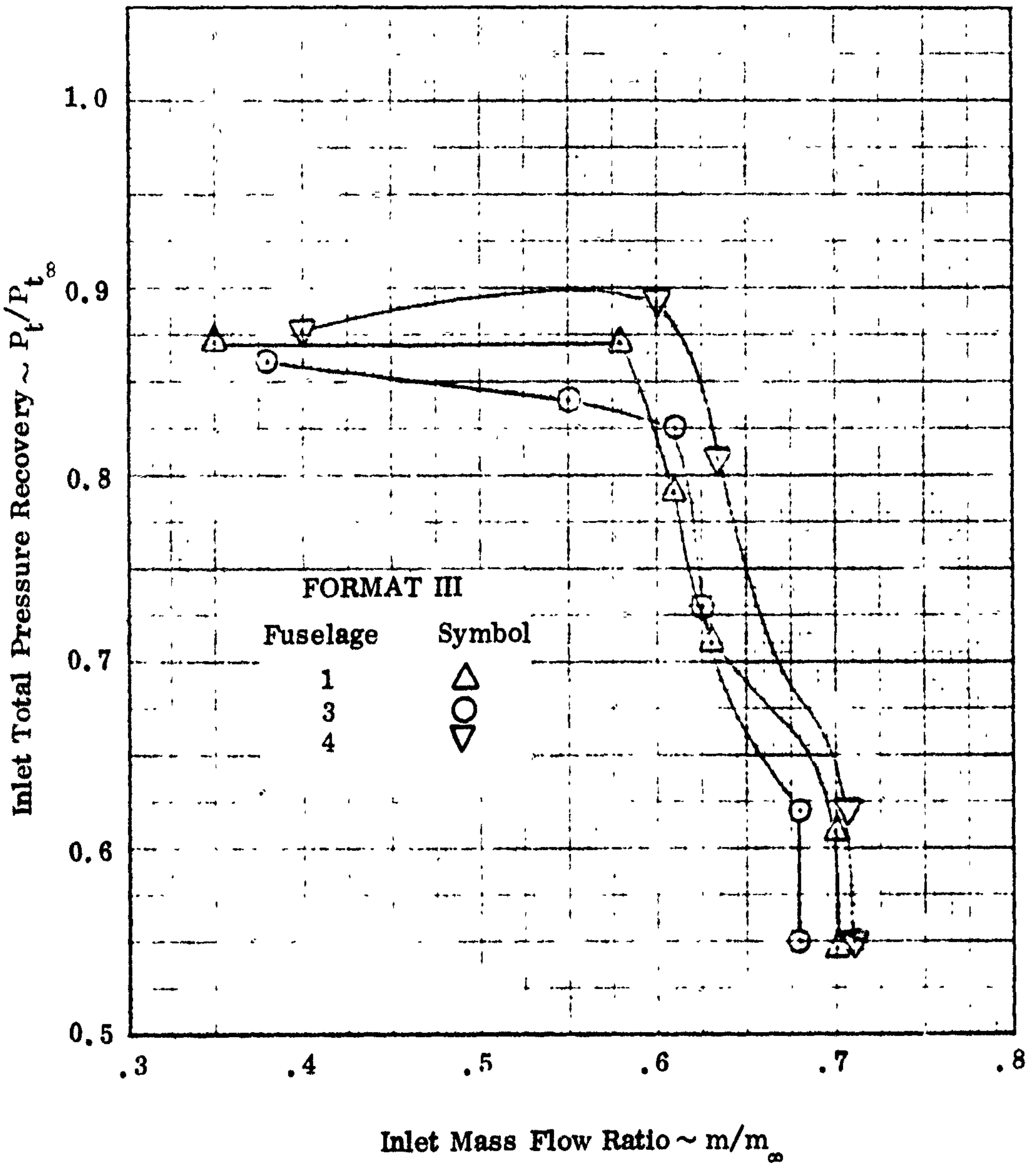

Figure 7-303. Comparison of Inlet Performance, Axisymmetric Inlet, $M_\infty = 1.8$, $\alpha = 0°$

contour development is made more gradual. This is reflected in an improving inlet characteristic as the inlet is integrated, first with fuselage 1 and then with fuselage 4.

For the angle of attack range between +5° and 20° the wing provides shielding for the inlet. The wing induced compression flow field improves the efficiency of the inlet diffusion process and aligns the streamlines approaching the inlet. Consequently the installed inlet performance level is significantly higher than that achieved with the uninstalled inlet. At the two intermediate test points (α = +5° and +10°) the wing dominates the flow field and the integrated inlet performance characteristics are closely grouped. For the higher angles (α = +15° and +20°) the geometry dependent physical compatibility effects, seen at the previously discussed Mach numbers, reappear and the inlet/fuselage 1 combination emerges as a superior configuration. At the very high angle of attack (α = +25°) the wing/inlet compression system has become quite inefficient, the installed performance is relatively poor and is, in fact, somewhat lower than the uninstalled performance. The individual characteristics are closely grouped. These comparisons are presented in Figures 7-304 through 7-308.

The inlet performance curves for the two-dimensional inlet are presented in Figures 7-309 through 7-315. The two-dimensional inlet also derives a significant benefit from the wing shielding, in the angle of attack range from +5° up to +20°. This inlet concept, however, responds to both the local flow environment and the physical aspects of the integration process in a manner quite different than did the axisymmetric inlet. The strong shock producing horizontal external compression surfaces have the inherent capability to realign the streamlines intercepted by the inlet. Consequently at low angles of attack the more uniform flow field induced by fuselage 4 does not result in improved inlet total pressure recovery, as was the case with the axisymmetric inlet. On the other hand the inlet cowl and sidewall, designed to intercept these two-dimensional streamlines, are less compatible with the radial type streamlines induced by the fuselage corner and the inlet/fuselage 1 combination emerges as a superior configuration at these angles of attack as it did at the lower Mach numbers. As opposed to this the physical compatibility effect was not evident, with the axisymmetric inlet, until higher angles were attained. This general condition prevails throughout the entire angle of attack range with the fuselage 1 configuration consistently showing a superior characteristic, in terms of a steeper supercritical leg and slightly higher mass flow ratio. The inclined characteristic and lower mass

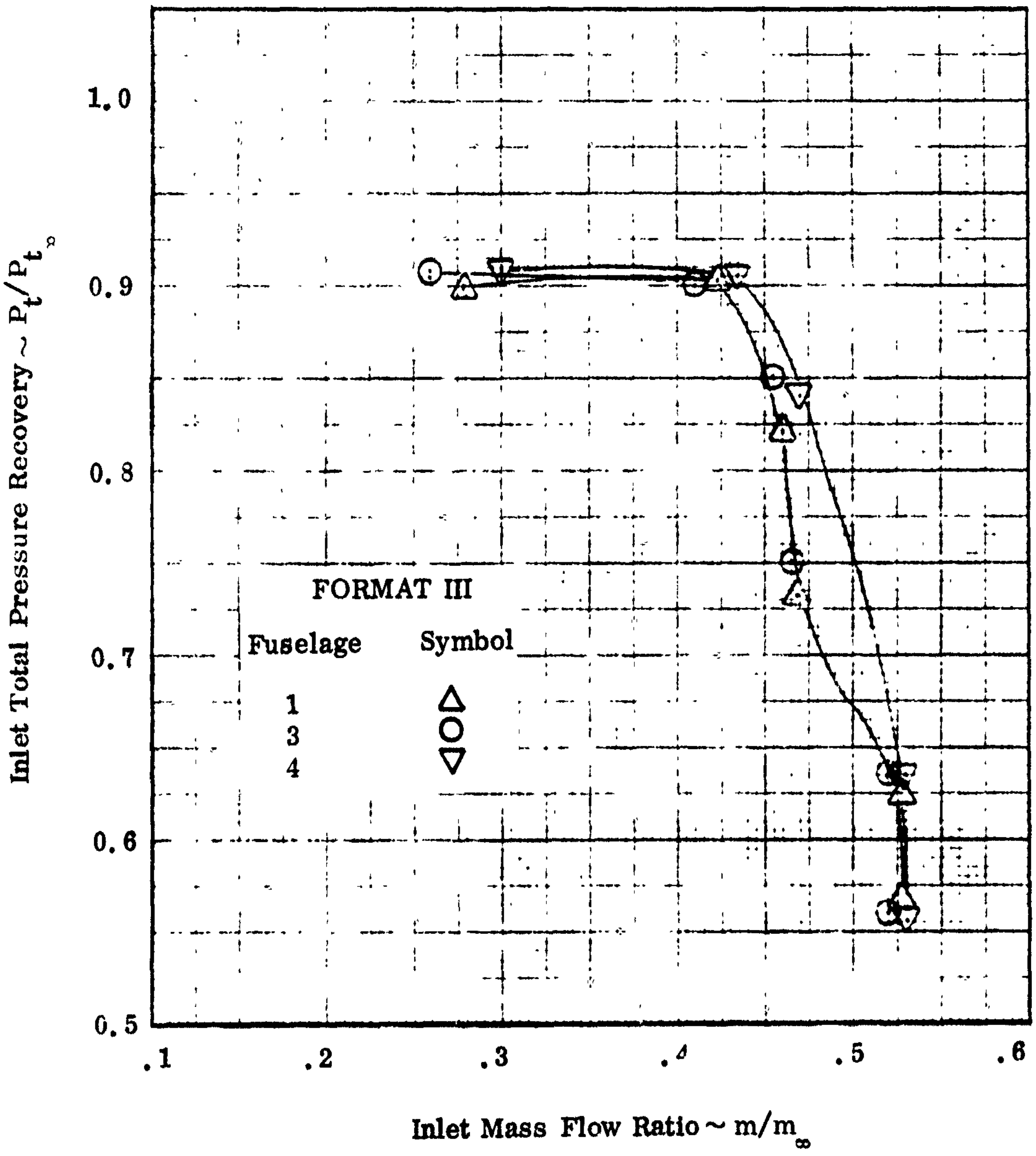

Figure 7-304. Comparison of Inlet Performance, Axisymmetric Inlet, $M_\infty = 1.8$, $\alpha = 5°$

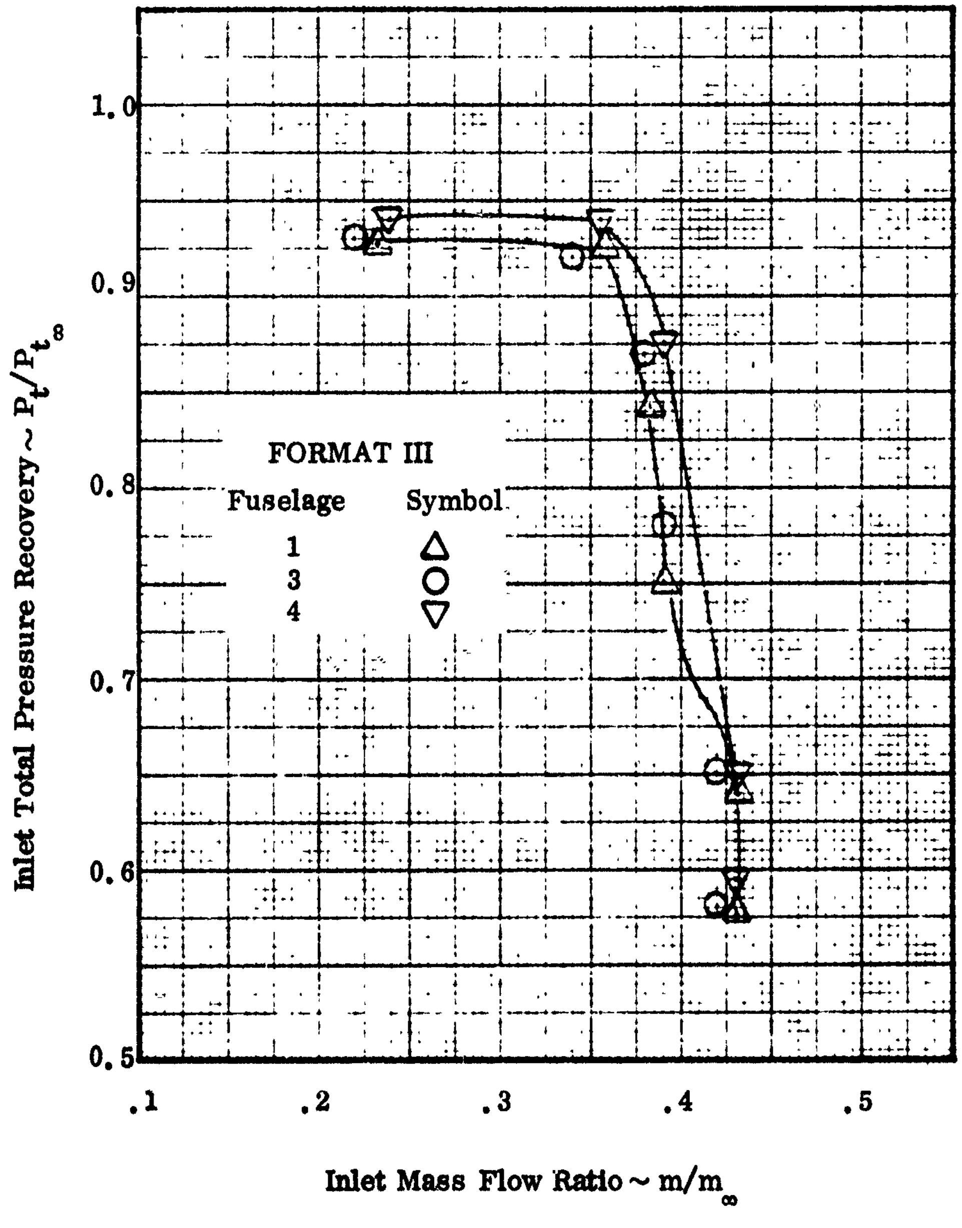

Figure 7-305. Comparison of Inlet Performance, Axisymmetric Inlet, $M_\infty = 1.8$, $\alpha = 10°$

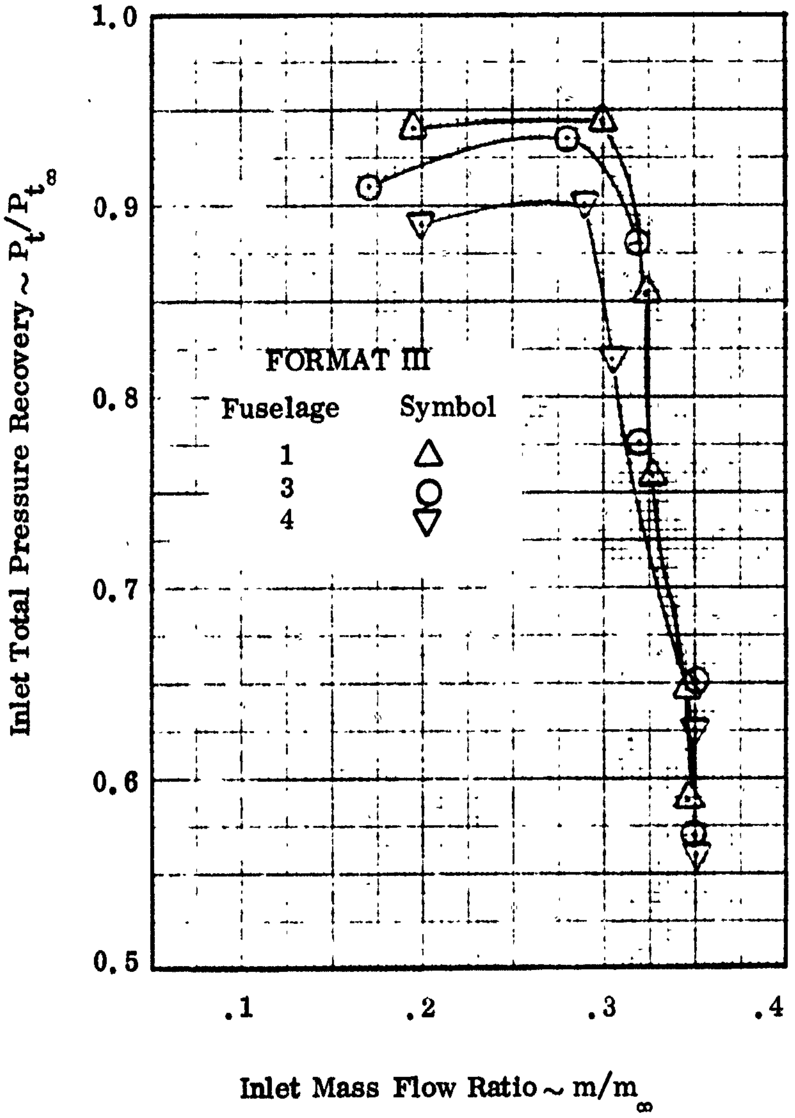

Figure 7-306. Comparison of Inlet Performance, Axisymmetric Inlet, $M_\infty = 1.8$, $\alpha = 15°$

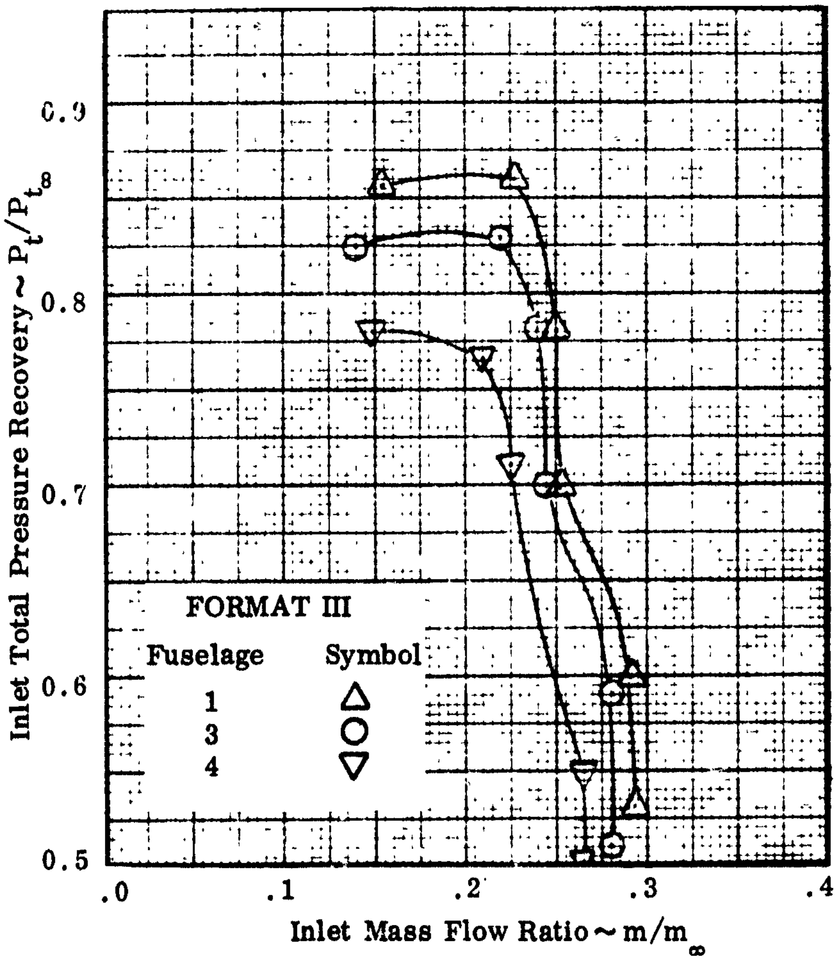

Figure 7-307. Comparison of Inlet Performance, Axisymmetric Inlet

$M_\infty = 1.8$, $\alpha = 20°$

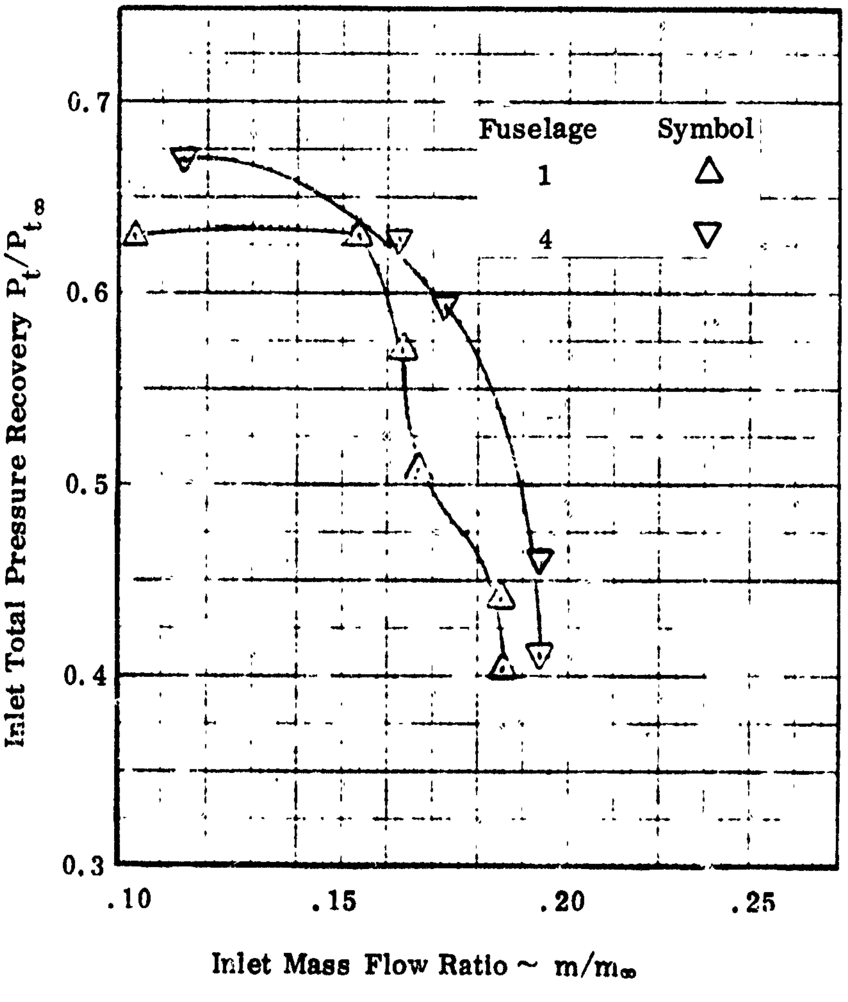

Figure 7-308. Comparison of Inlet Performance, Axisymmetric Inlet $M_\infty = 1.8$, $\alpha = 25°$

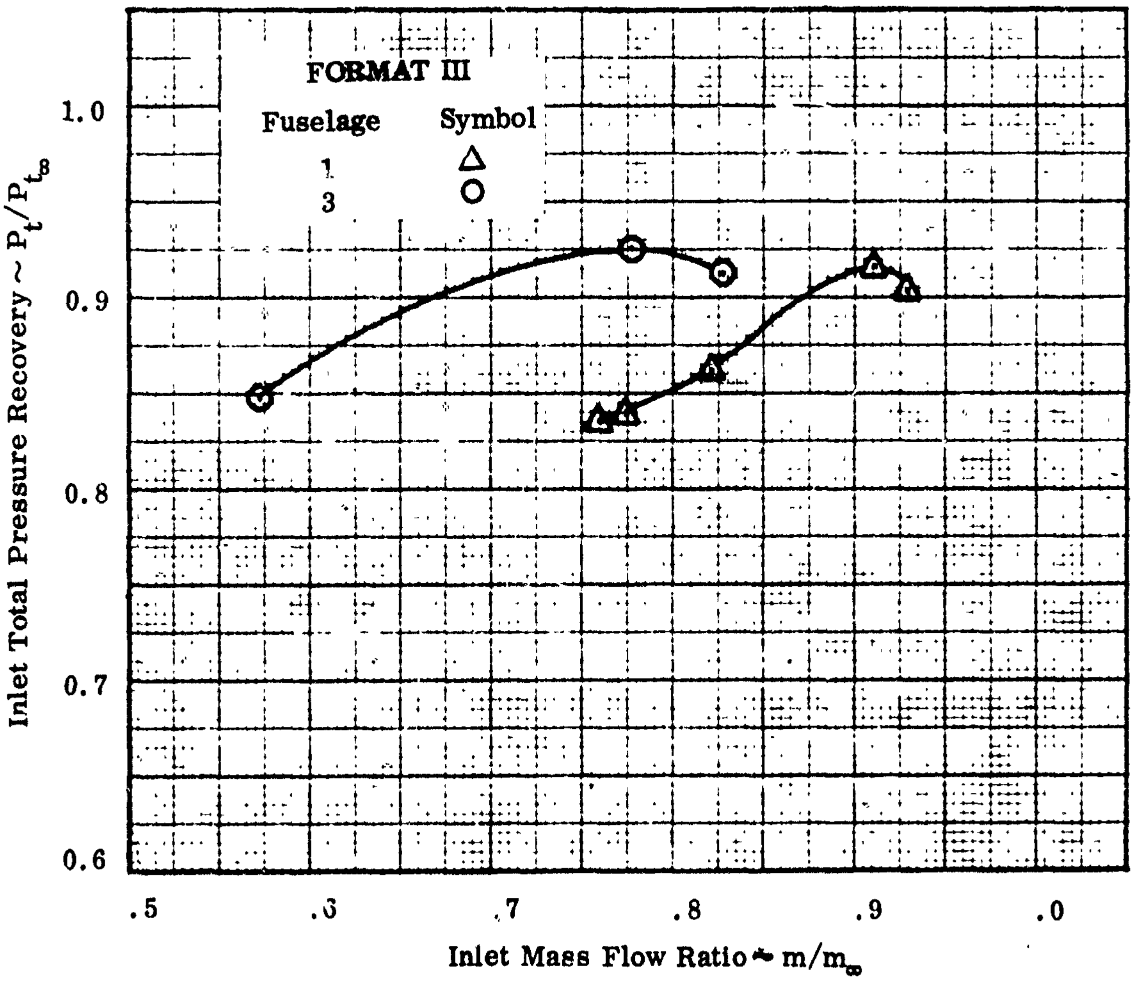

Figure 7-309. Comparison of Inlet Performance, Two-Dimensional Inlet $M_\infty = 1.8$, $\alpha = -3°$

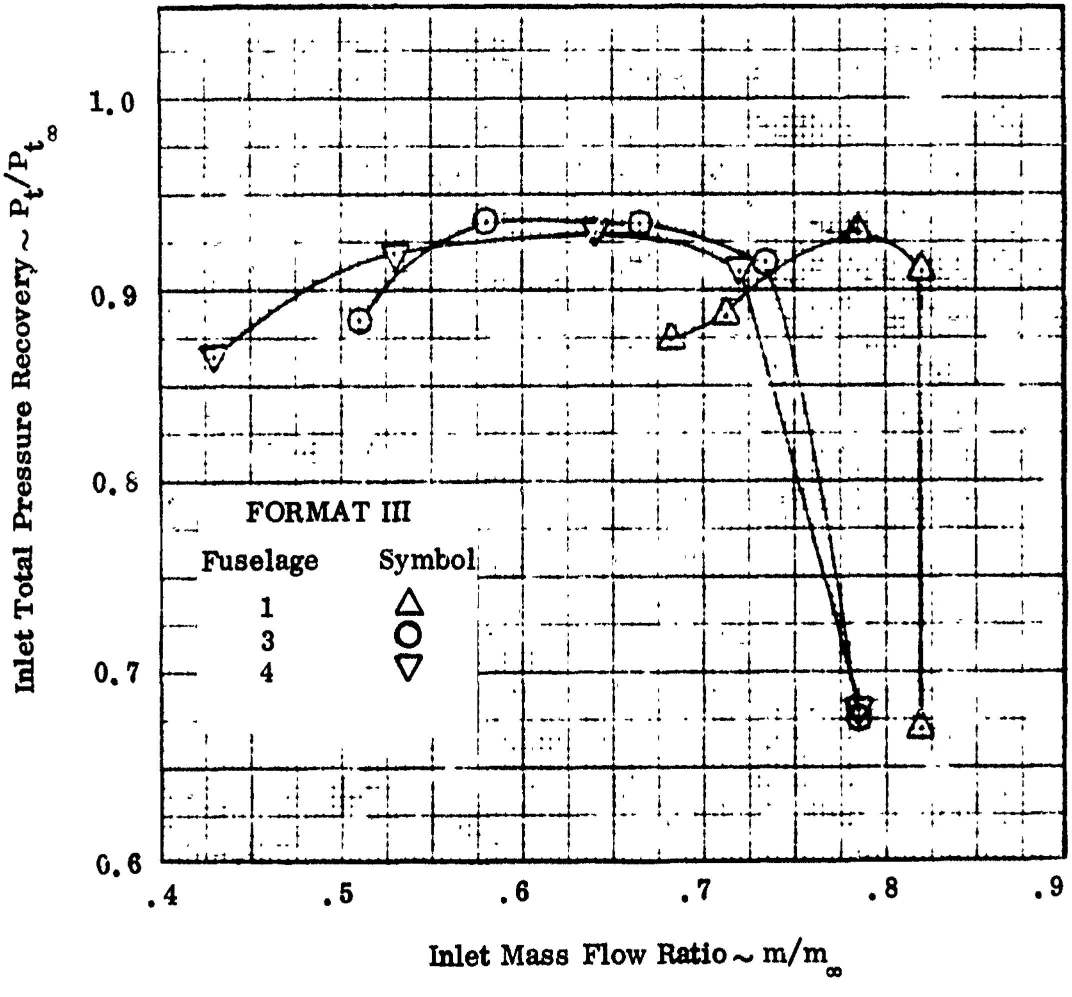

Figure 7-310. Comparison of Inlet Performance, Two Dimensional Inlet, $M_\infty = 1.8$, $\alpha = 0°$

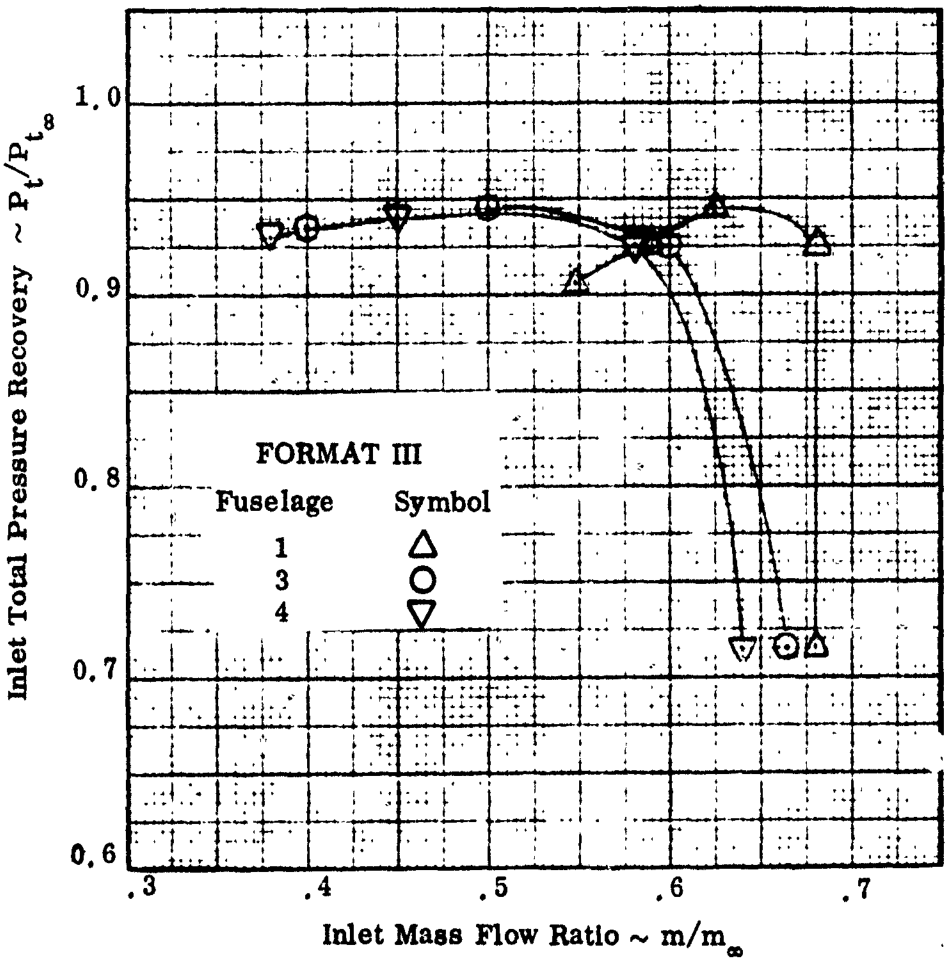

Figure 7-311. Comparison of Inlet Performance, Two Dimensional Inlet

$M_\infty = 1.8$, $\alpha = 5°$

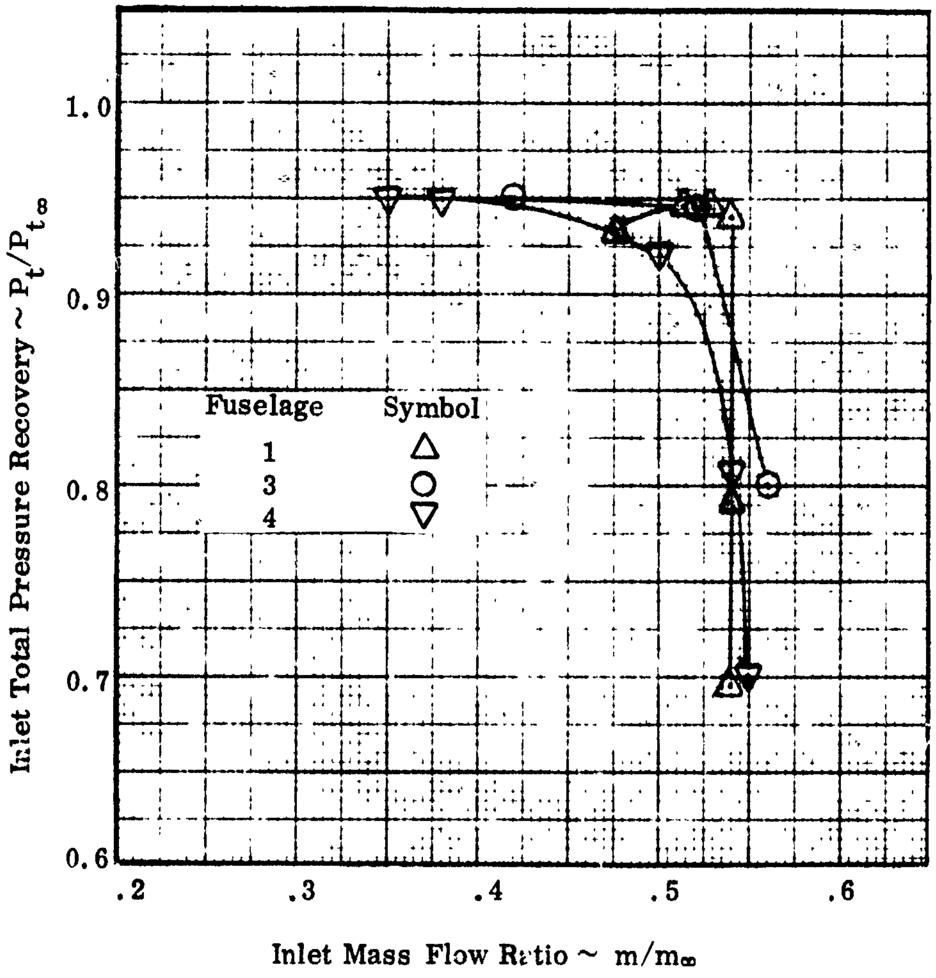

Figure 7-312. Comparison of Inlet Performance, Two-Dimensional Inlet $M_\infty = 1.8$, $\alpha = 10°$

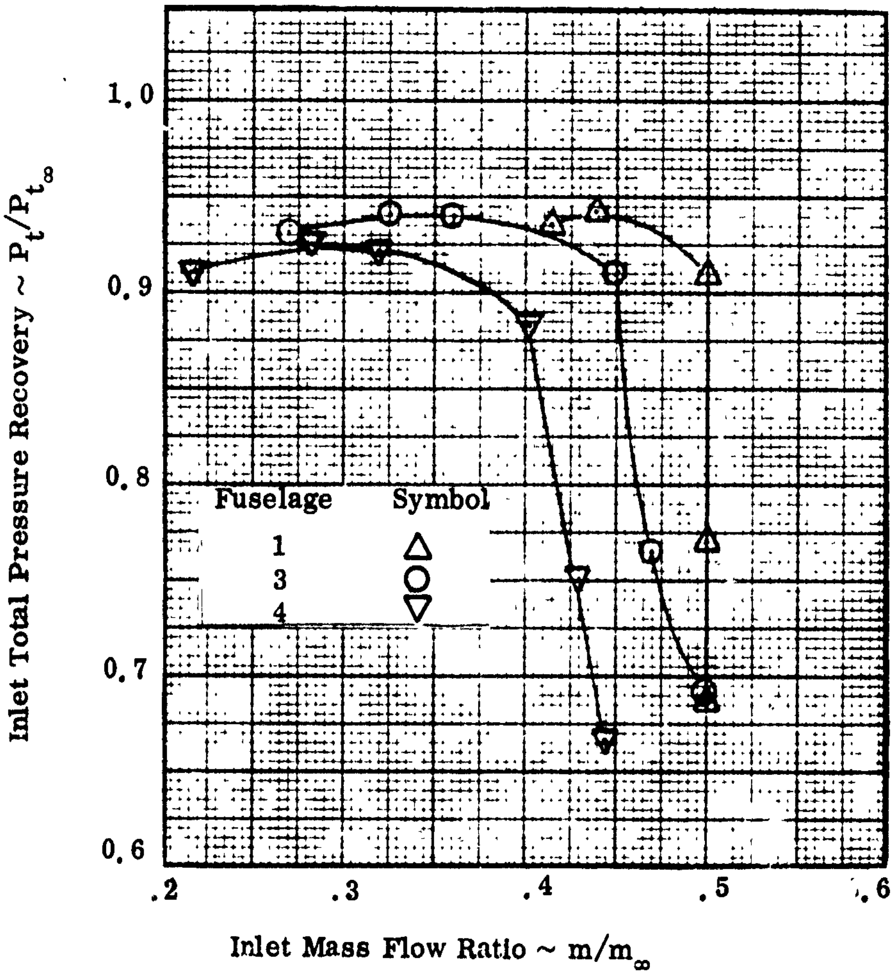

Figure 7-313. Comparison of Inlet Performance, Two-Dimensional Inlet $M_\infty = 1.8$, $\alpha = 15°$

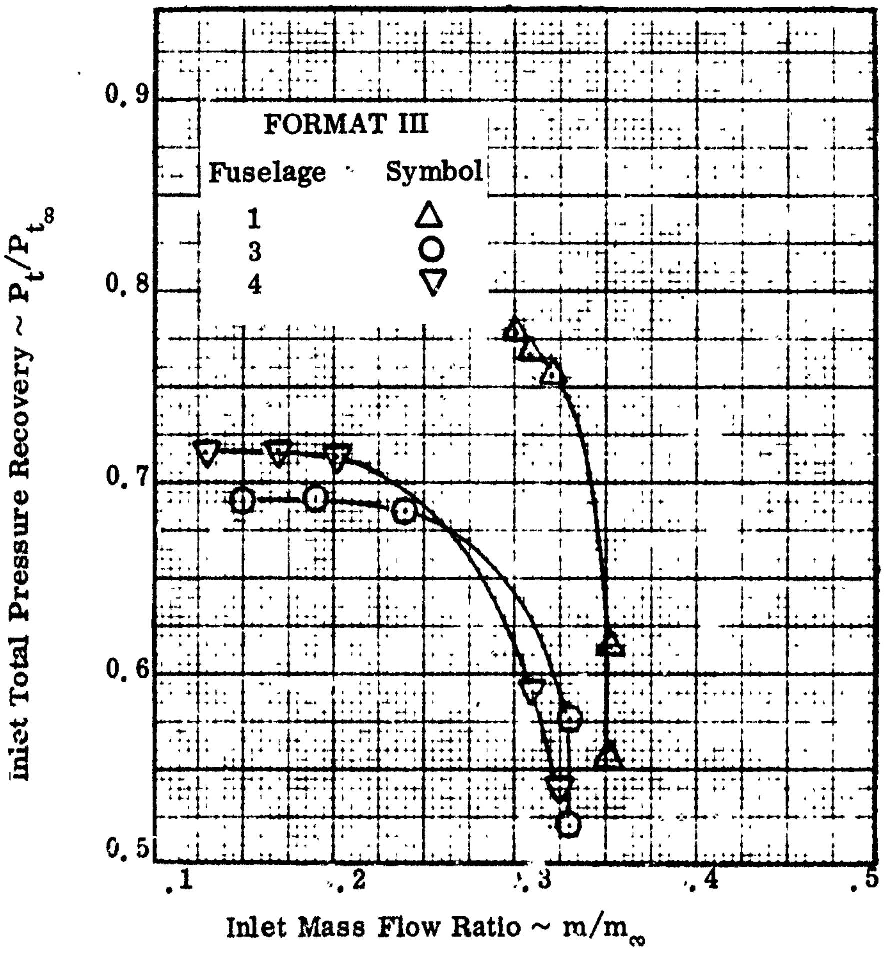

Figure 7-314. Comparison of Inlet Performance, Two-Dimensional Inlet
$M_\infty = 1.8$, $\alpha = 20°$

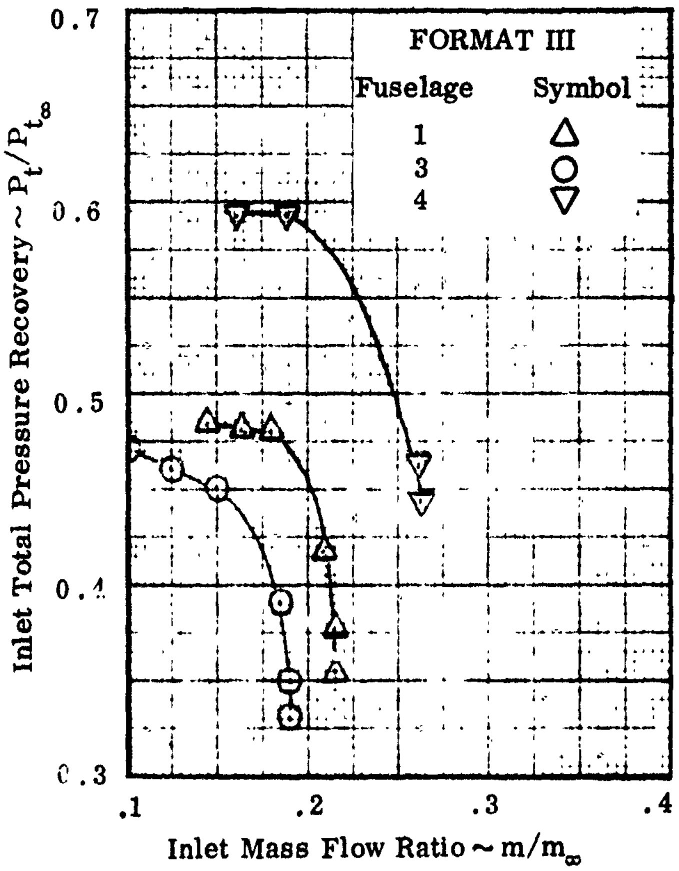

Figure 7-315. Comparison of Inlet Performance, Two Dimensional Inlet $M_\infty = 1.8$, $\alpha = 25°$

flow ratio of the other two configurations can be traced to fuselage boundary layer ingestion due to physical incompatibility, as described previously. An examination of the attendant engine face profiles tends to bear this out in that the profile for the fuselage 1 configuration remains radial throughout this angle of attack range while the profiles for the fuselage 3 and 4 configurations are of the circumferential type with low pressure regions occupying the inboard and upper portions of the engine face. At the extremely high angle of attack ($\alpha = +25^\circ$) the inlet is sensitive to the uniformity of the approaching flow field in that the more uniform flow field generated by fuselage 4 does result in a higher level of inlet performance for that configuration. It is pointed out, however, that the general level of performance at this condition is quite low.

7.5.2.4 Mach Number 2.2

At this Mach number the flow field characteristics are essentially the same as those seen at Mach 1.8. In addition, the influence of fuselage geometry upon installed inlet performance, for both the axisymmetric and the two-dimensional inlets, is also similar to that seen at Mach 1.8. These comparison curves are presented in Figures 7-316 through 7-329.

A new effect of the integration process appears at this Mach number that is related to the inlet concept employed. For the two dimensional inlet, a comparison of the installed and uninstalled inlet total pressure recovery indicates that the inlet benefits from the shielding provided by the wing, as was the case at Mach 1.8. The same comparison, made for the axisymmetric inlet reveals a common performance level for the inletboth installed and uninstalled thereby indicating that the wing is no longer providing beneficial shielding for the inlet. In fact these comparisons serve to illustrate the sensitivity of these two inlet concepts to the relatively high sidewash present at the under wing inlet station. For the two-dimensional inlet, the sidewash produces an effect that is equivalent to presenting the flow to an initial inlet compression ramp that is slightly swept. The slight reduction in flow compression thereby induced is less than the wing generated compression and consequently the inlet performance improves when the inlet is installed. In the case of the axisymmetric inlet the sidewash serves to reduce the effective cone angle of the initial inlet compression surface and thereby reduces the amount of inlet external compression. This reduction

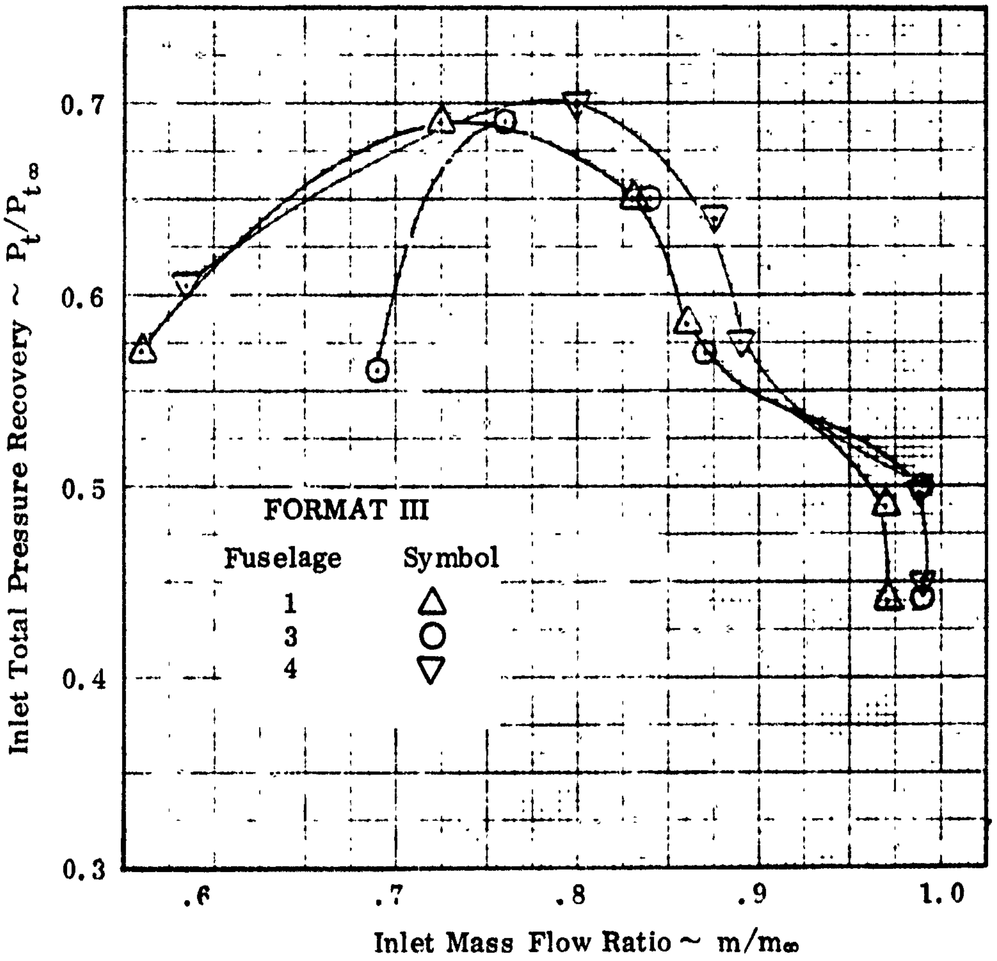

Figure 7-316. Comparison of Inlet Performance, Axisymmetric Inlet $M_\infty = 2.2$, $\alpha = -3°$

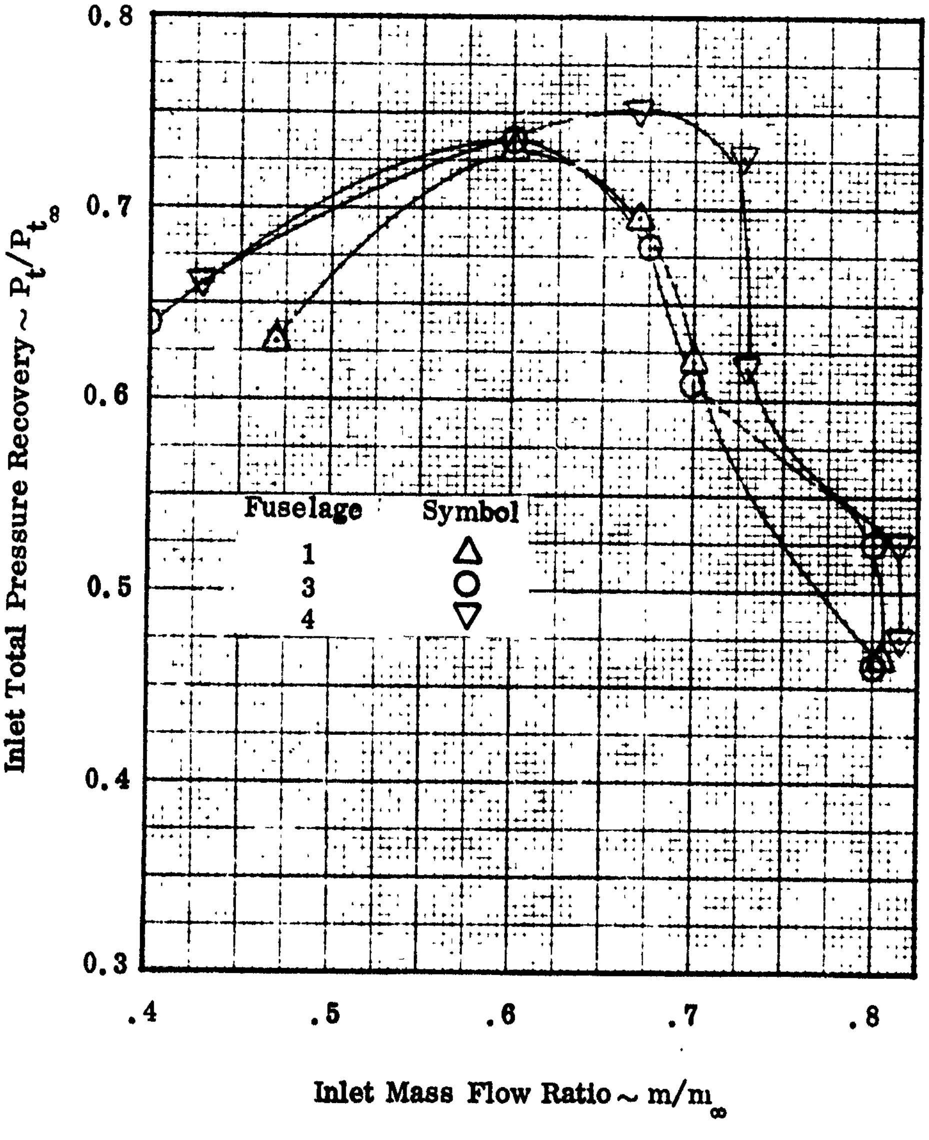

Figure 7-317. Comparison of Inlet Performance, Axisymmetric Inlet, $M_\infty = 2.2$, $\alpha = 0°$

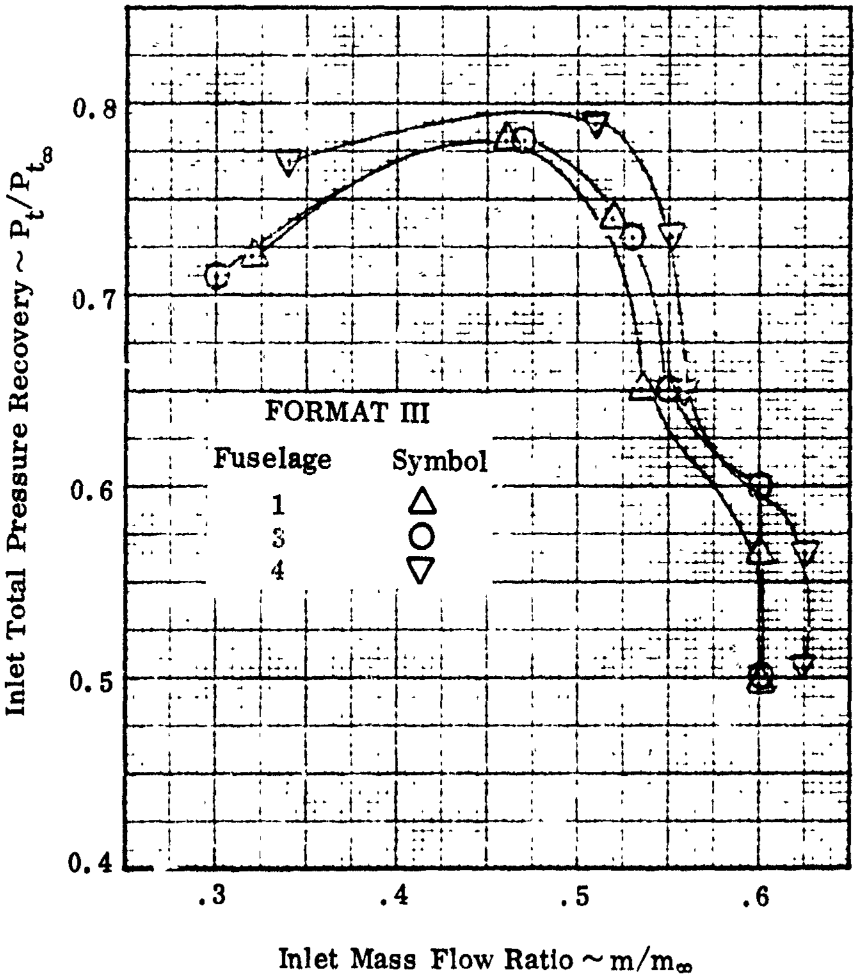

Figure 7-318. Comparison of Inlet Performance, Axisymmetric Inlet $M_\infty = 2.2$, $\alpha = 5°$

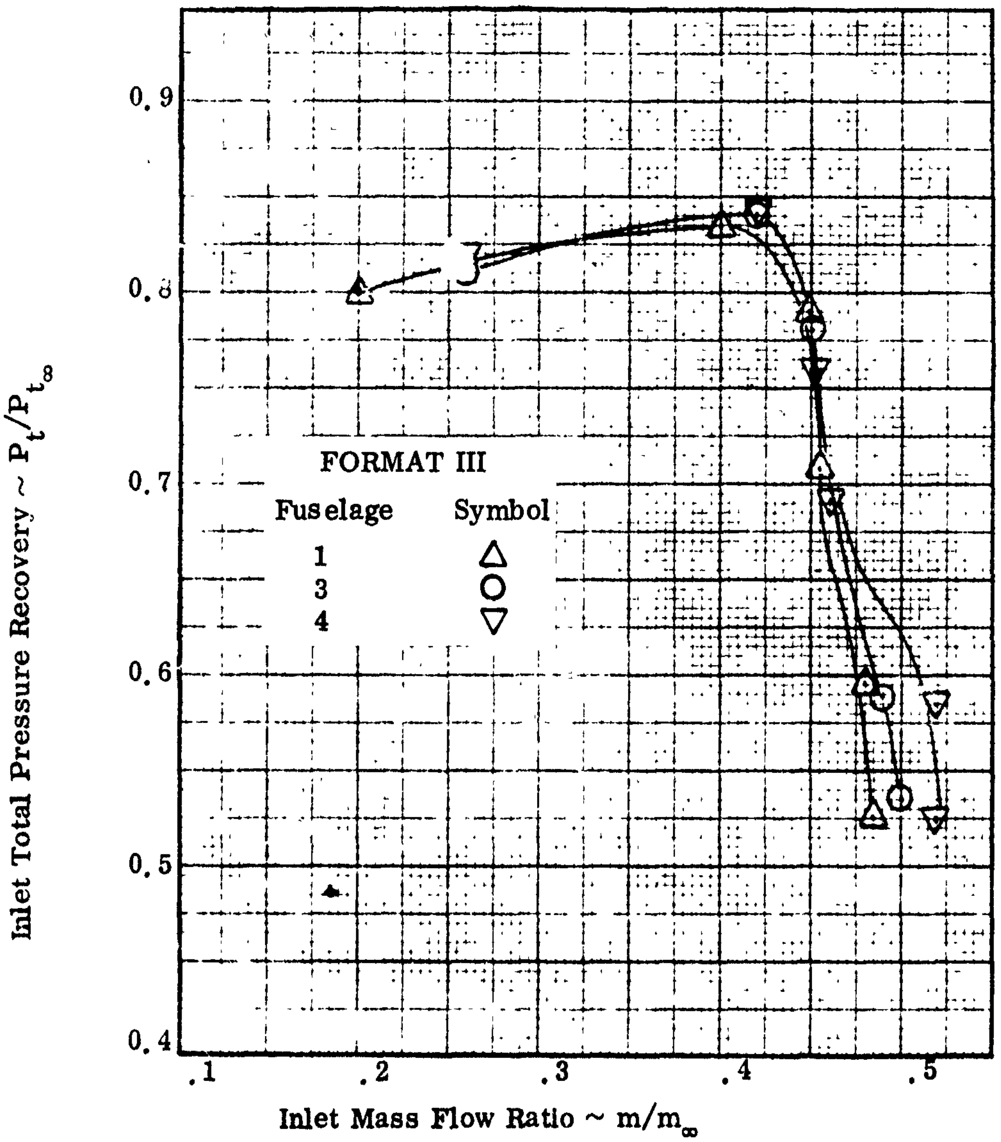

Figure 7-319. Comparison of Inlet Performance, Axisymmetric Inlet $M_\infty = 2.2$, $\alpha = 10°$

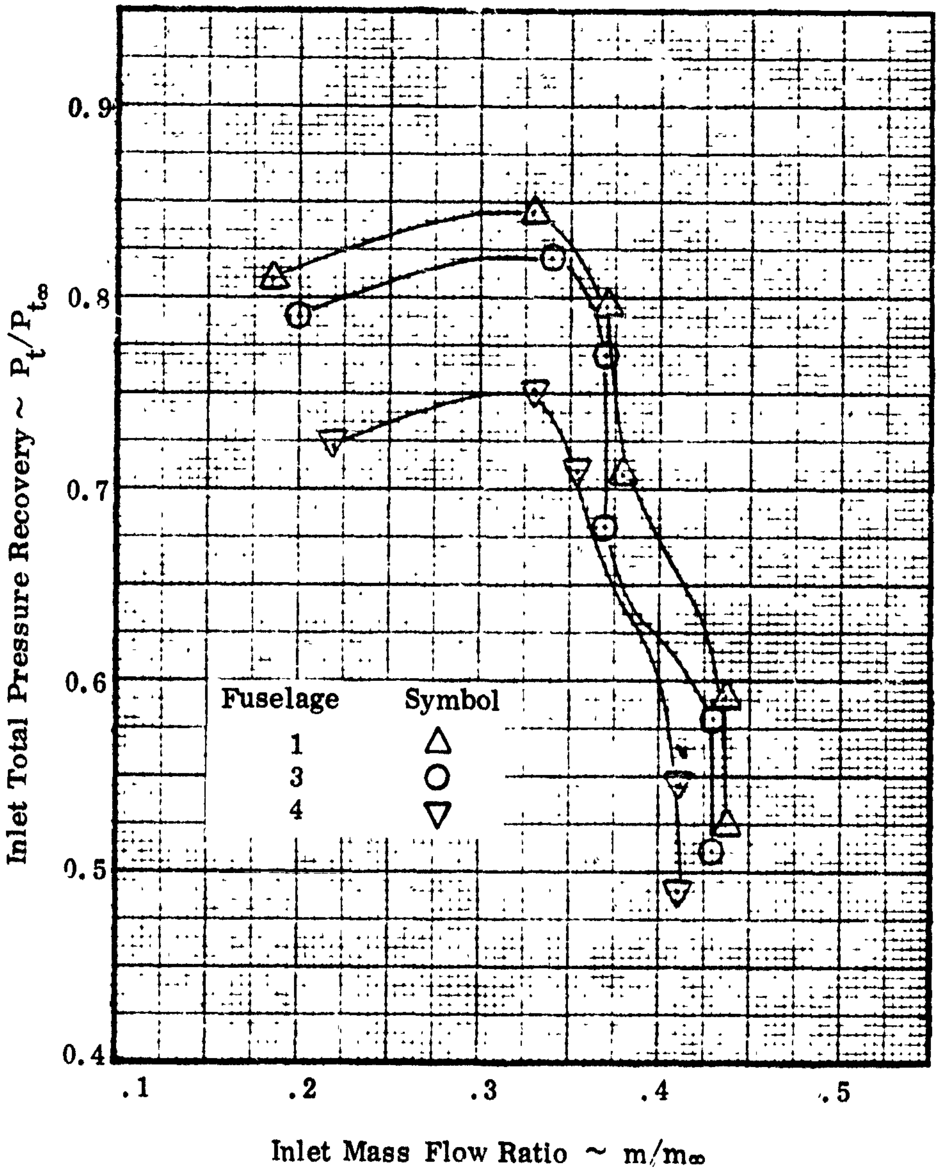

Figure 7-320. Comparison of Inlet Performance, Axisymmetric Inlet $M_\infty = 2.2$, $\alpha = 15°$

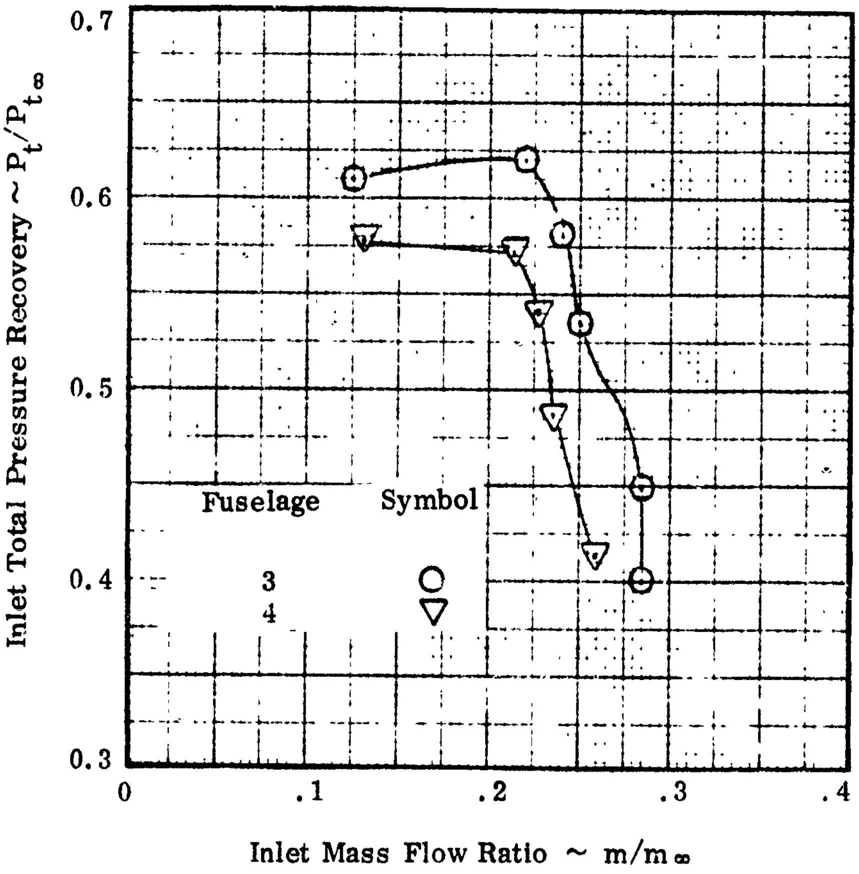

Figure 7-321. Comparison of Inlet Performance, Axisymmetric Inlet $M_\infty = 2.2$, $\alpha = 20°$

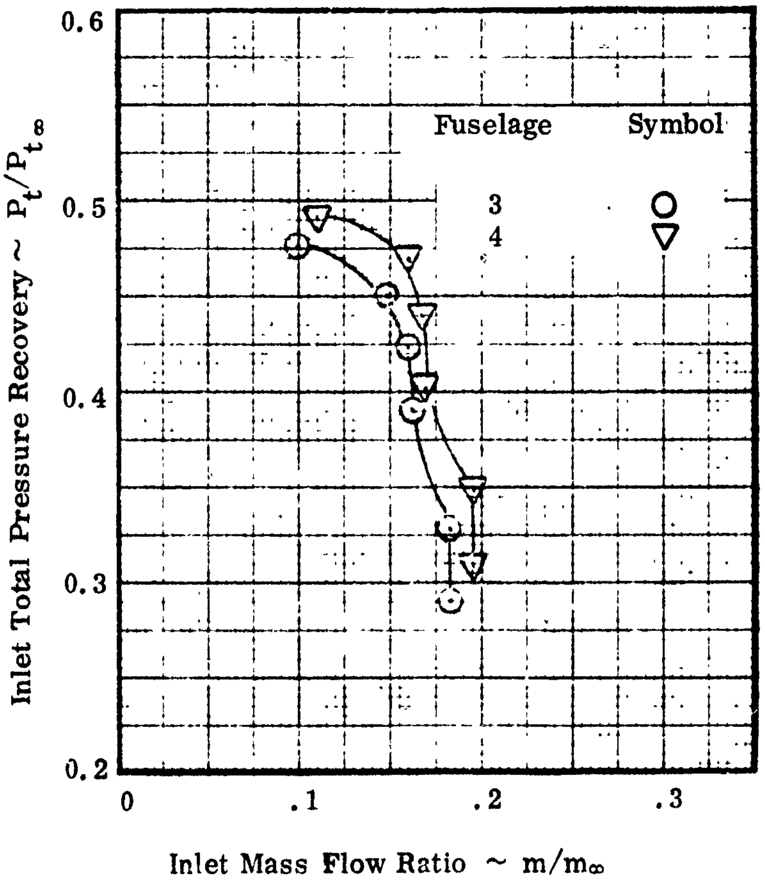

Figure 7-322. Comparison of Inlet Performance, Axisymmetric Inlet $M_\infty = 2.2$, $\alpha = 25°$

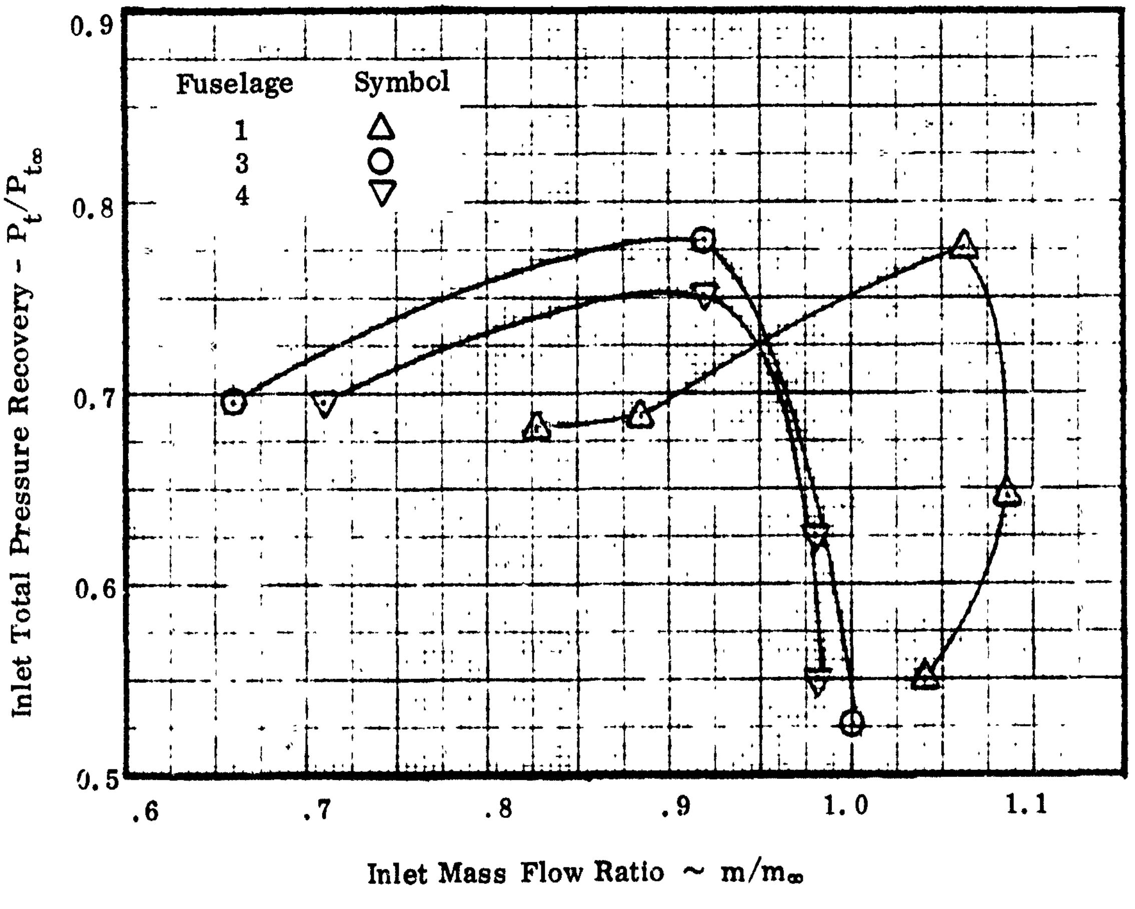

Figure 7-323. Comparison of Inlet Performance, Two-Dimensional Inlet $M_\infty = 2.2$, $\alpha = -3°$

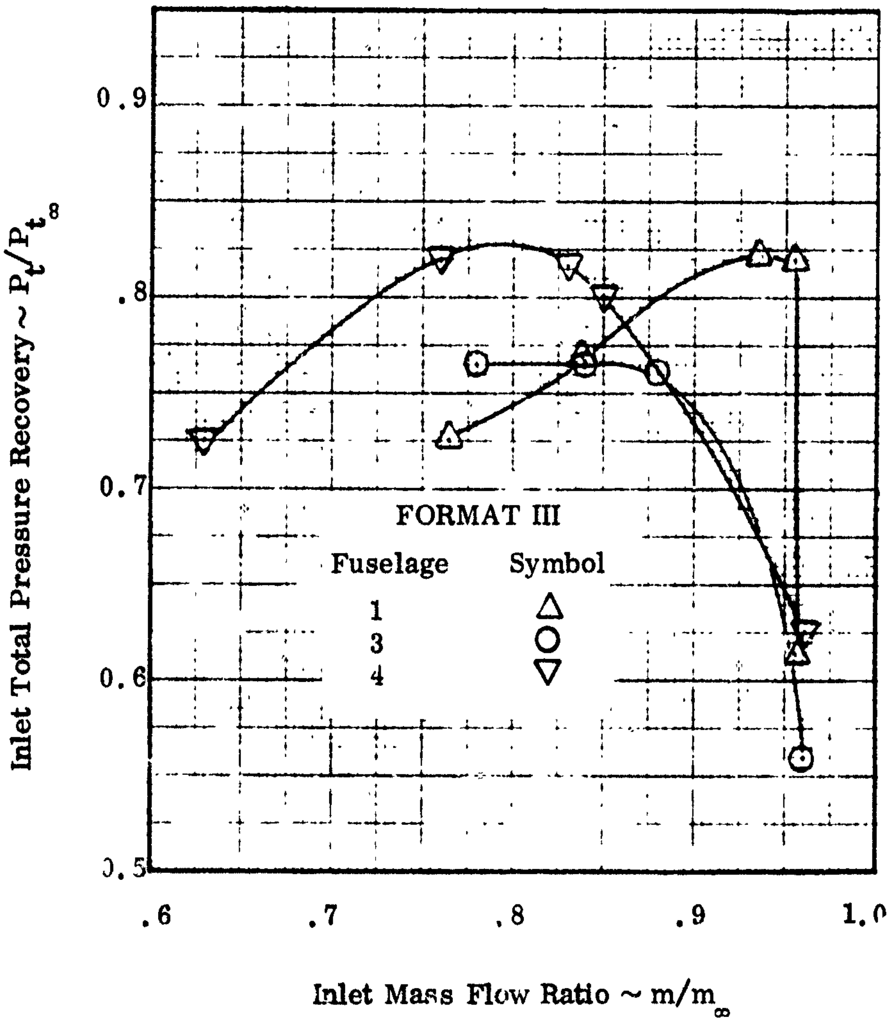

Figure 7-324. Comparison of Inlet Performance, Two-Dimensional Inlet $M_\infty = 2.2$, $\alpha = 0°$

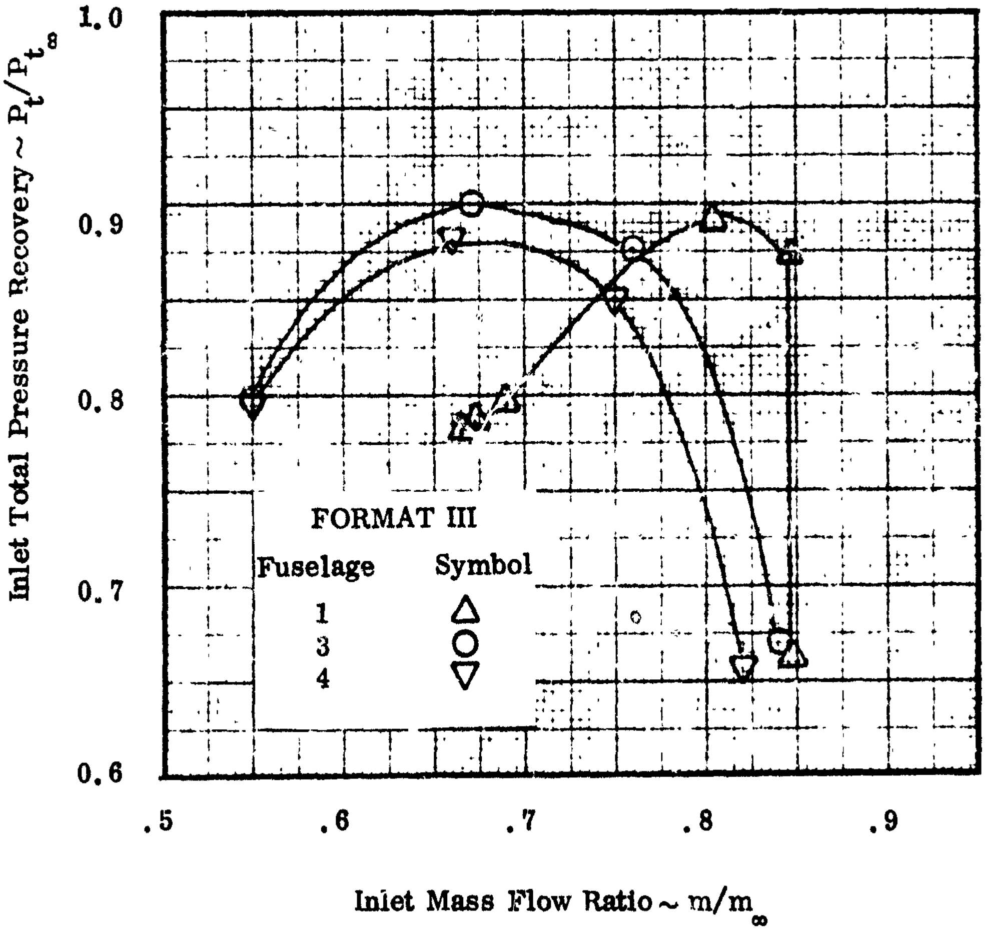

Figure 7-325. Comparison of Inlet Performance, Two Dimensional Inlet, $M_\infty = 2.2$, $\alpha = 5°$

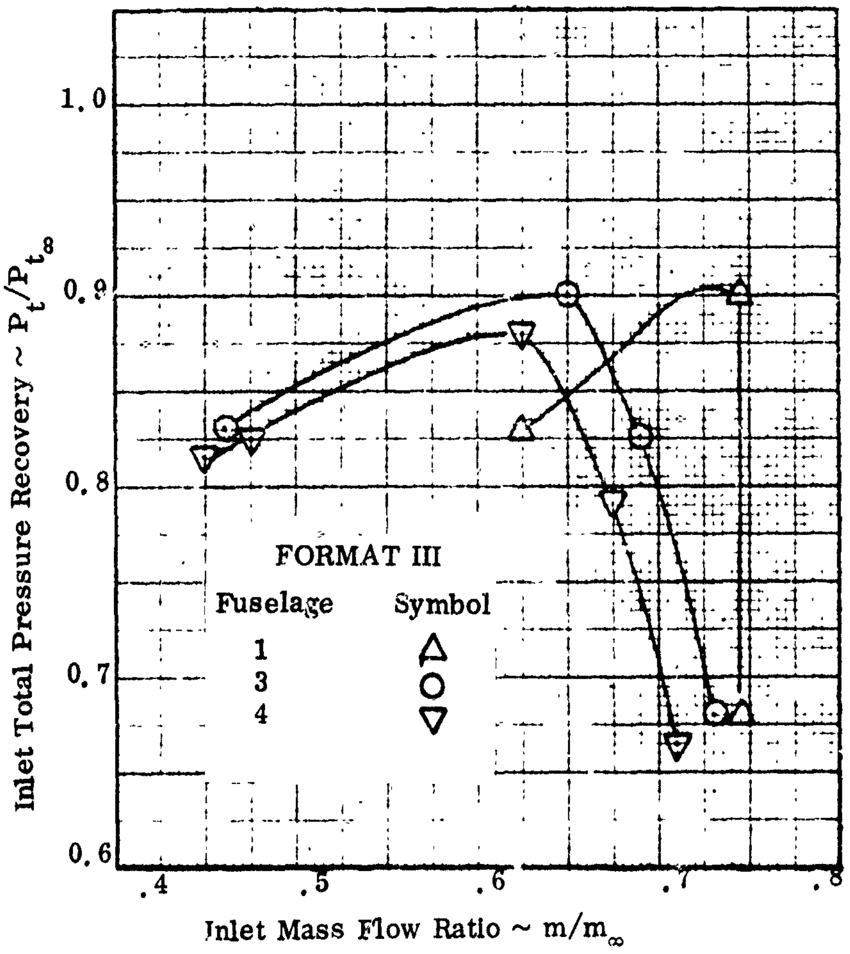

Figure 7-326. Comparison of Inlet Performance, Two-Dimensional Inlet
$M_\infty = 2.2$, $\alpha = 10°$

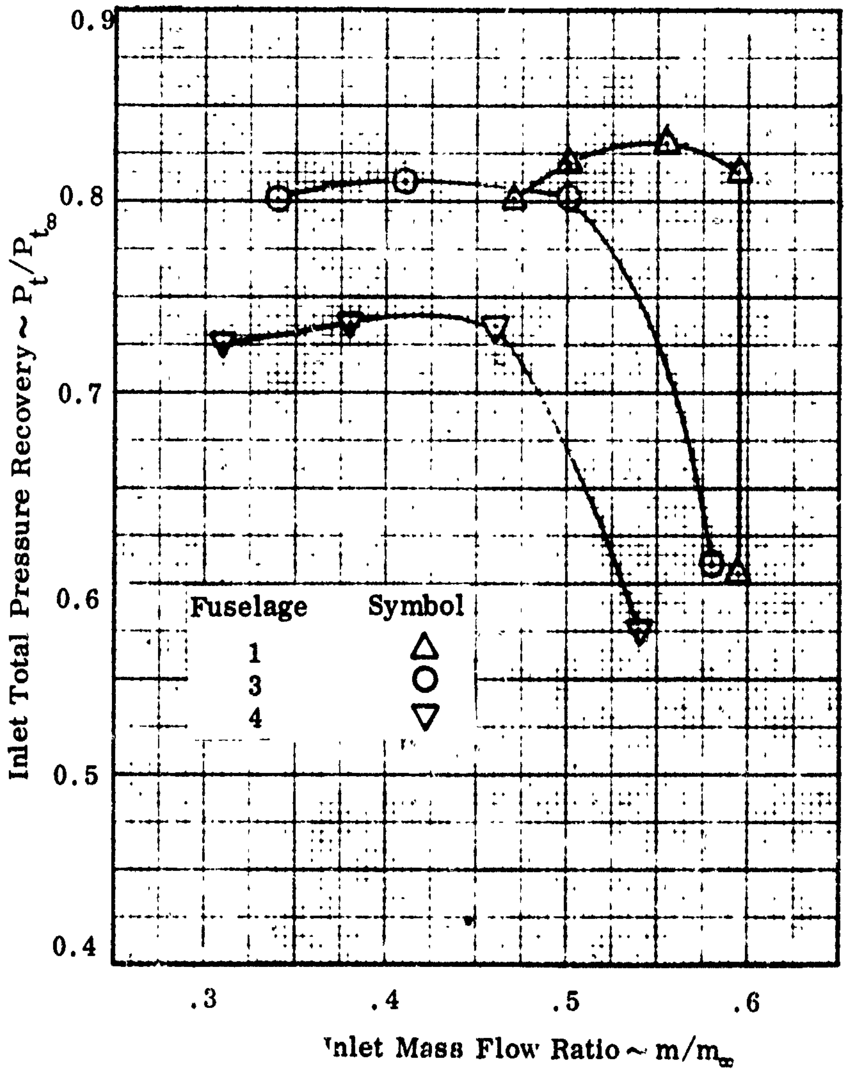

Figure 7-327. Comparison of Inlet Performance, Two-Dimensional Inlet

$M_\infty = 2.2$, $\alpha = 15°$

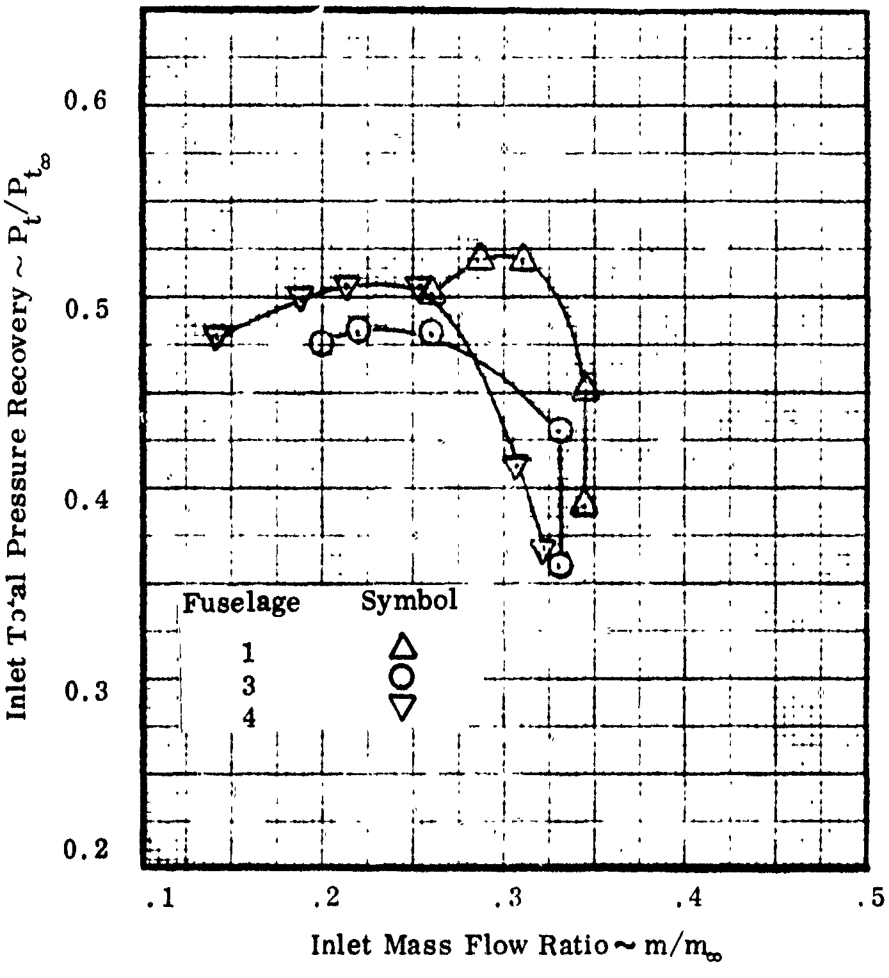

Figure 7-328. Comparison of Inlet Performance, Two-Dimensional Inlet $M_\infty = 2.2$, $\alpha = 20°$

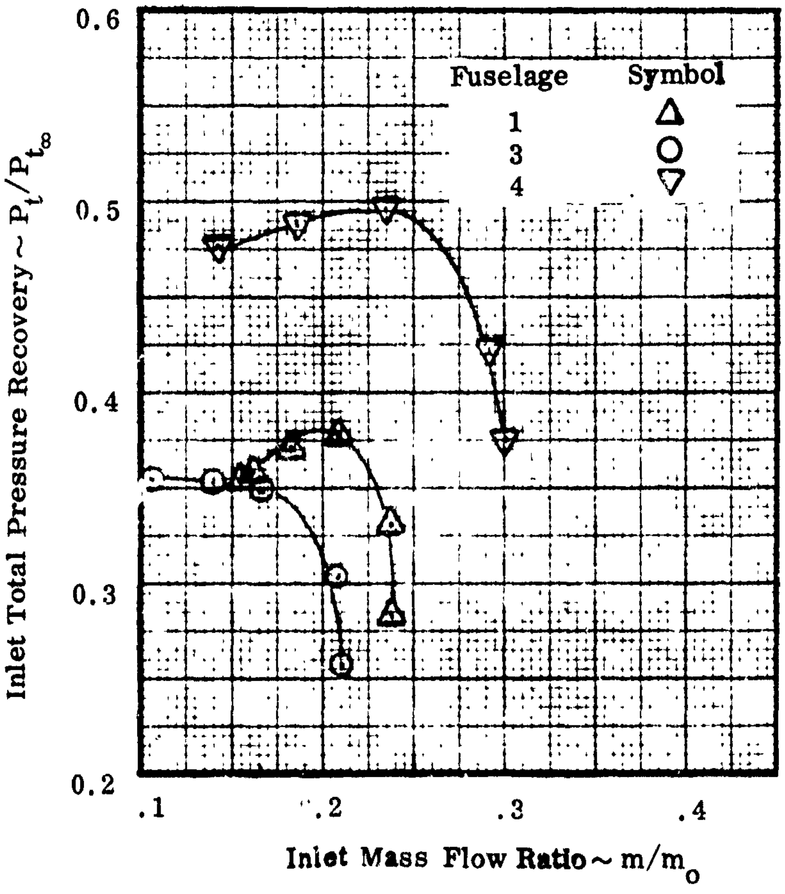

Figure 7-329. Comparison of Inlet Performance, Two-Dimensional Inlet

$M_\infty = 2.2$, $\alpha = 25°$

in effective cone angle varies around the periphery of the conical surface, being minimal near the fuselage and maximum for that section immediately under the wing. For this Mach number, the reduction in inlet compression appears to be roughly equal to the added compression generated by the wing and consequently the installed and uninstalled total pressure recovery levels are similar. We can project that a two-dimensional inlet with vertically mounted compression surfaces would perform in a fashion similar to the axisymmetric inlet.

7.5.2.5 Mach Number 2.5

There are no new effects evident at this Mach number and the flow fields appear similar to those obtained at lower Mach numbers. Unfortunately the uninstalled inlet performance level is sufficiently low to wash out any fuselage induced effects upon inlet performance. As a result the installed inlet characteristics do not display the angle of attack and geometry dependent effects seen at previously discussed Mach numbers. The inlet characteristics, presented in Figures 7-330 through 7-342, are very closely grouped. However, a comparison of installed and uninstalled total pressure recovery does indicate a continued improvement, attributable to the under wing location, for the two-dimensional inlet particularly for the angle of attack range between +5° and +15°. It is also evident from this comparison that the inlet/fuselage 1 configuration benefits most, a condition noted at lower Mach numbers.

7.5.3 Wing Effects

In addition to the evaluation of fuselage geometry effects, an investigation of the impact of wing sweep upon both flow field composition and inlet performance was made. The tests, designed to isolate the wing influence, fixed all of the other geometric components. The vehicle configuration was built up with the primary nose and canopy, fuselage configuration 3, and the two-dimensional inlet. The primary wing sweep of 55° and the secondary wing sweep of 65° were tested in conjunction with this vehicle configuration and the results were compared.

For Mach 0.8 the inlet total pressure recovery is quite high, consequently the effect of wing sweep does not affect this performance parameter. With increasing angle of attack the mass flow ratio shift due to the different capture area associated with each wing becomes evident as the inlet installed with the 55° wing operates at a

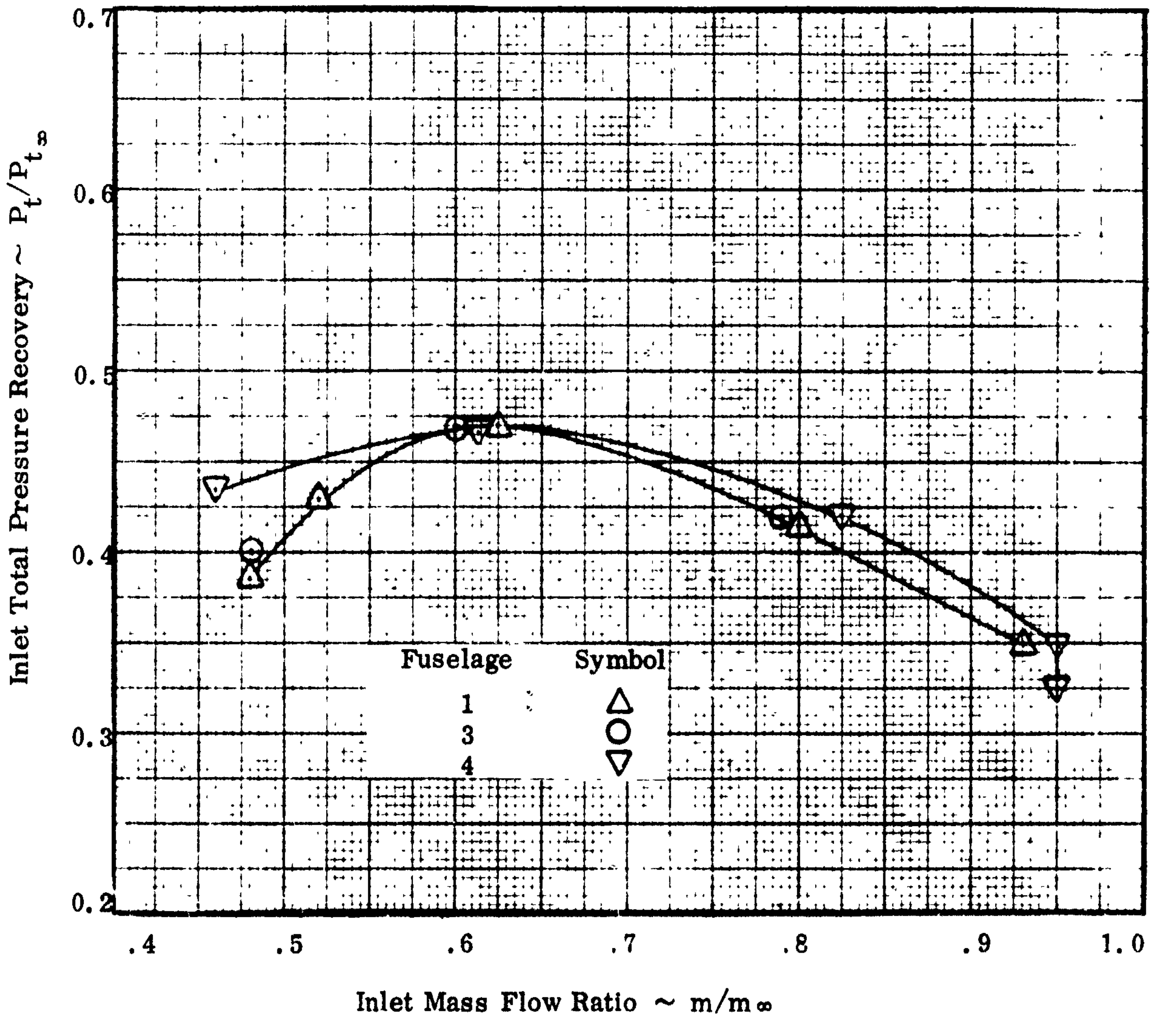

Figure 7-330. Comparison of Inlet Performance, Axisymmetric Inlet $M_\infty = 2.5$, $\alpha = -3°$

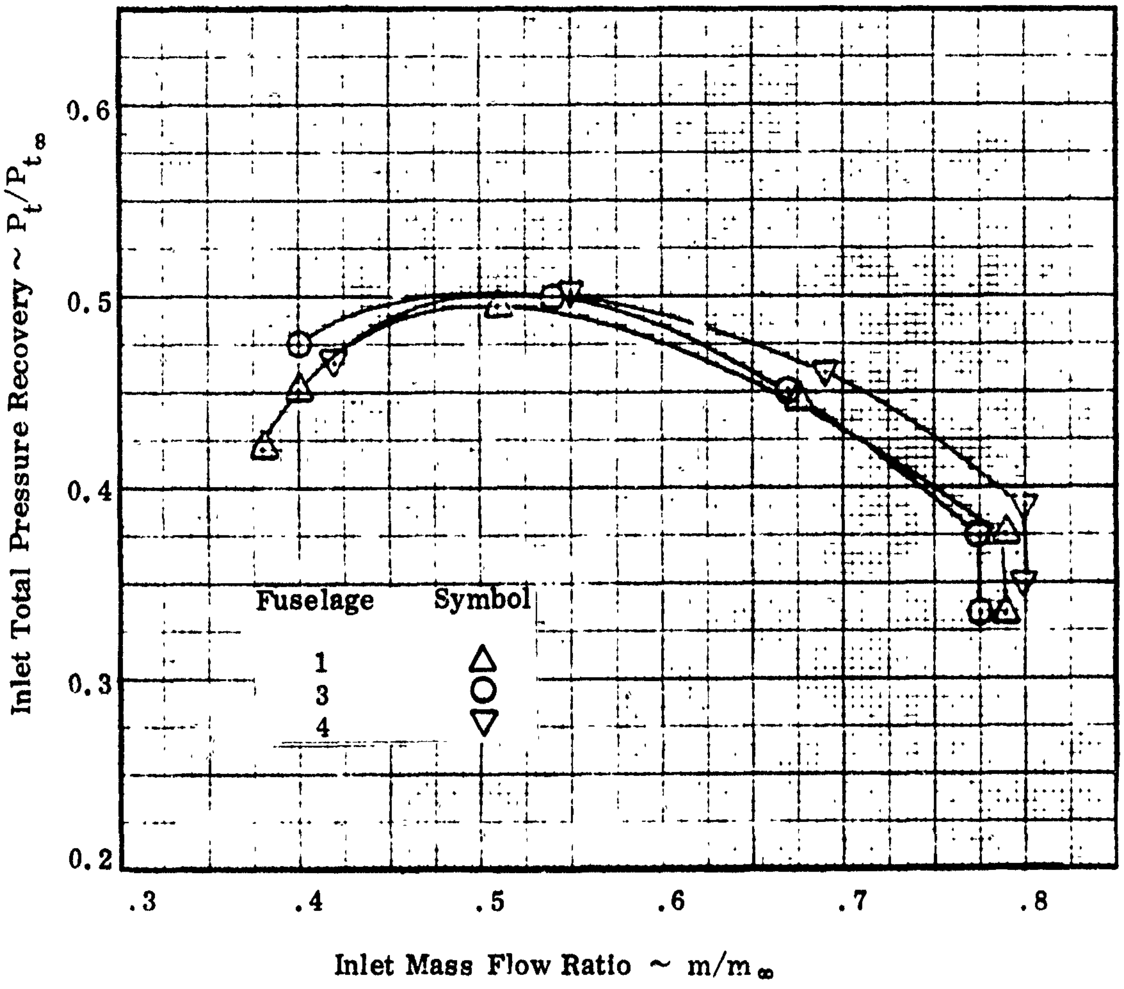

Figure 7-331. Comparison of Inlet Performance, Axisymmetric Inlet
$M_\infty = 2.5$, $\alpha = 0°$

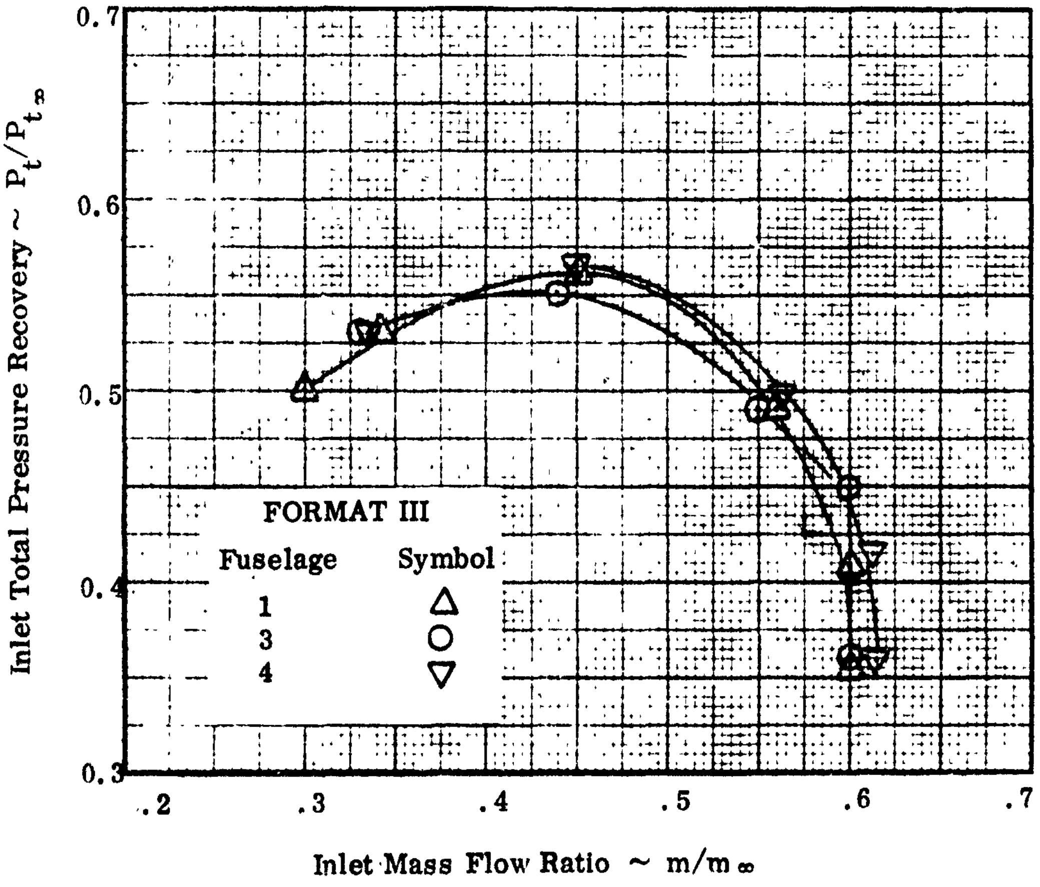

Figure 7-332. Comparison of Inlet Performance, Axisymmetric Inlet $M_\infty = 2.5$, $\alpha = 5°$

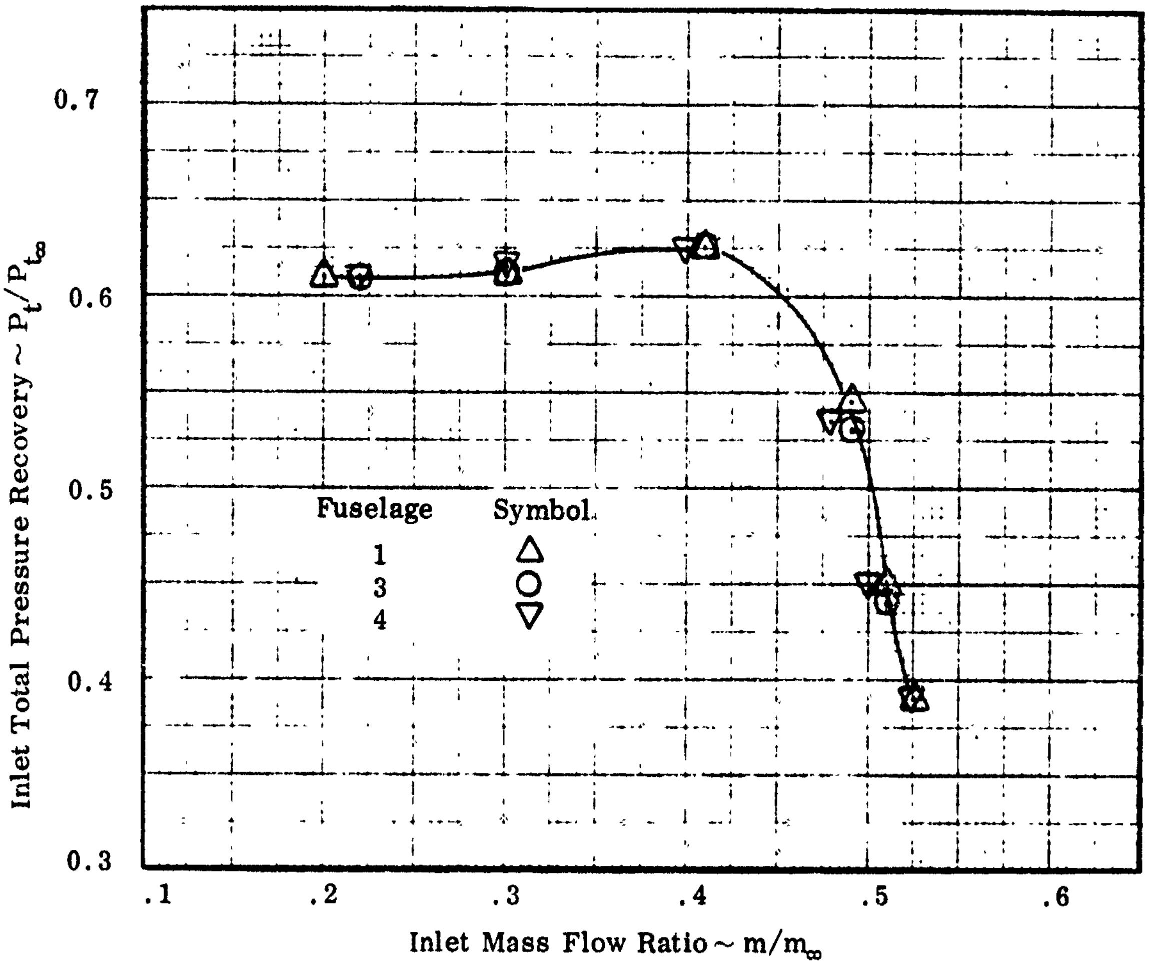

Figure 7-333. Comparison of Inlet Performance, Axisymmetric Inlet

$M_\infty = 2.5$, $\alpha = 10°$

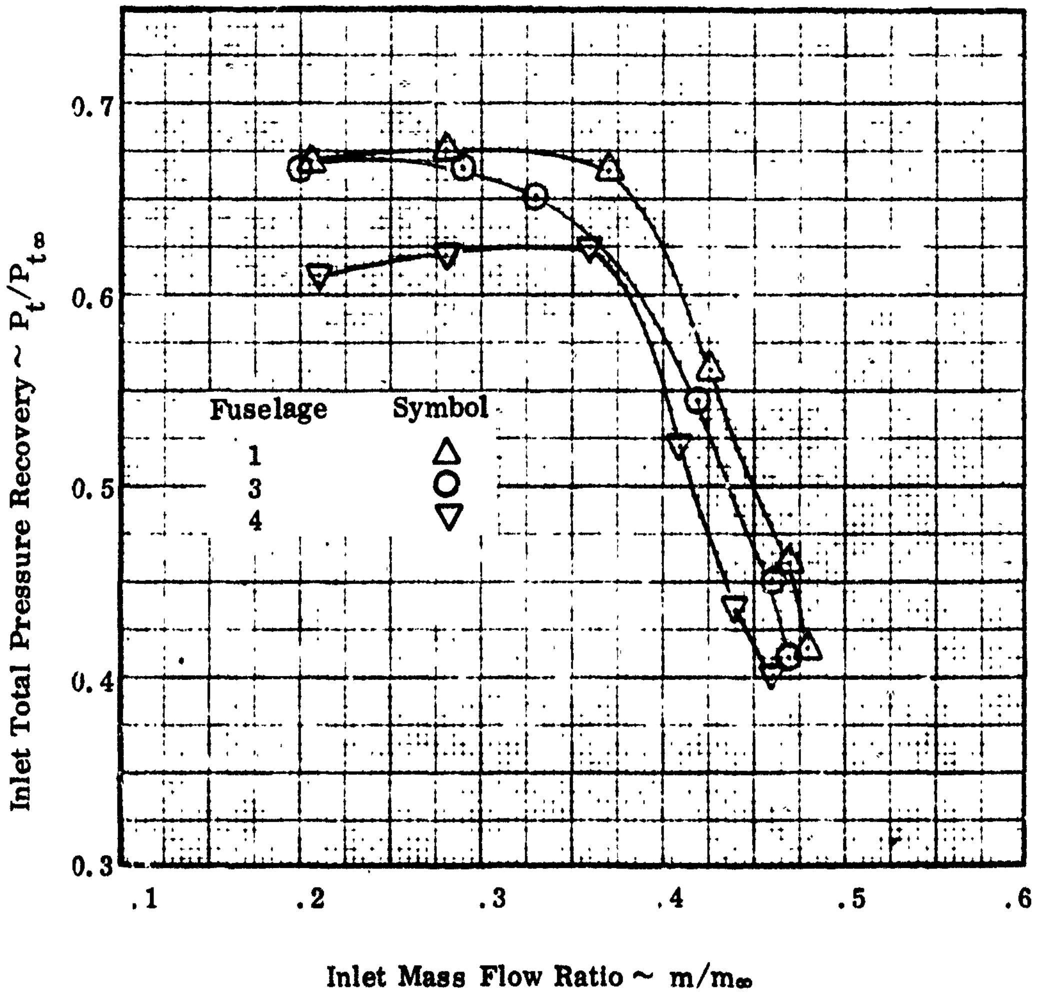

Figure 7-334. Comparison of Inlet Performance, Axisymmetric Inlet
$M_\infty = 2.5$, $\alpha = 15°$

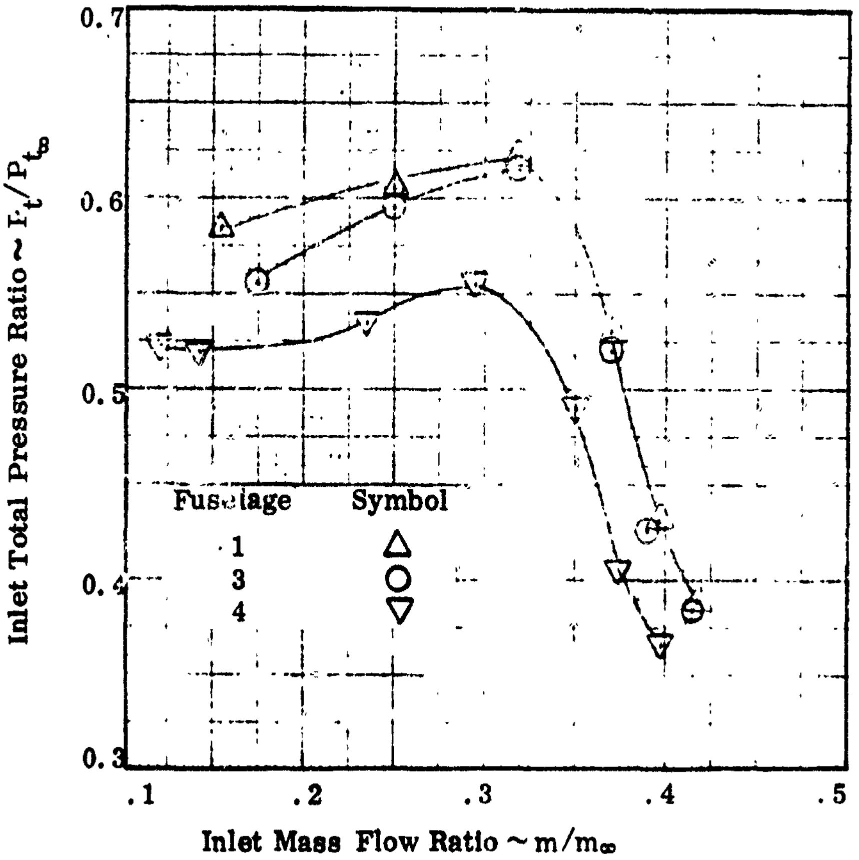

Figure 7-335. Comparison of Inlet Performance, Axisymmetric Inlet $M_\infty = 2.5$, $\alpha = 17.5°$

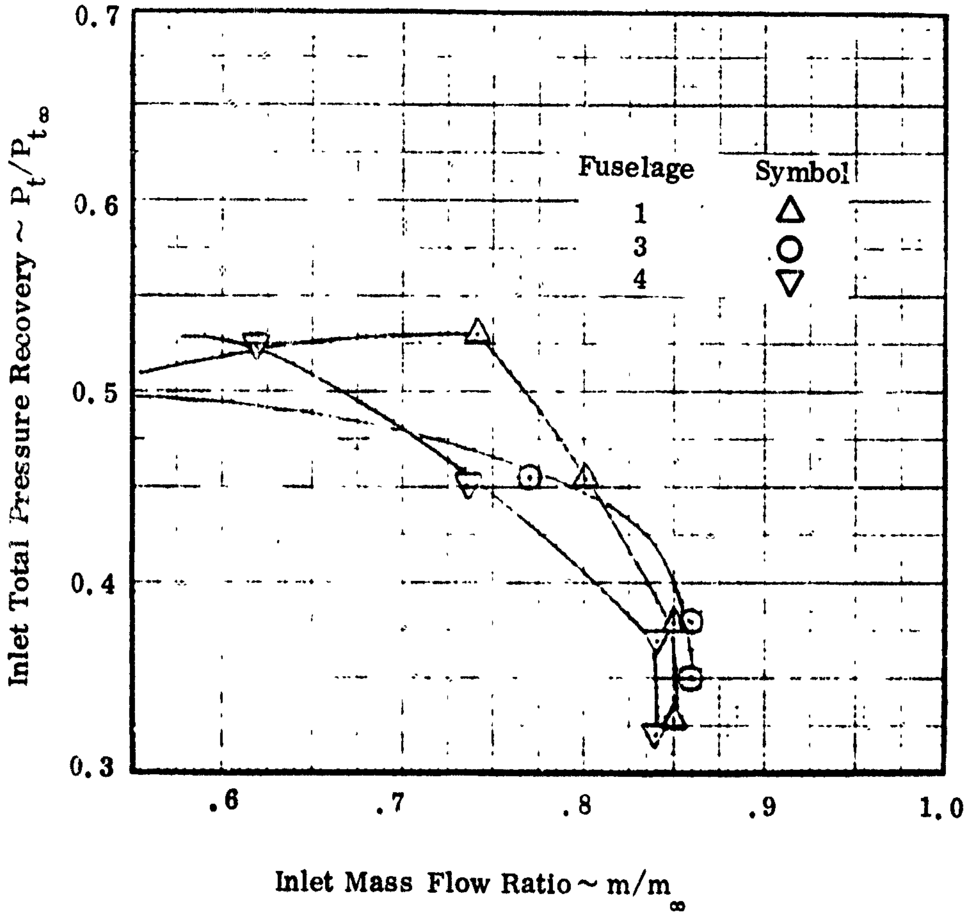

Figure 7-336. Comparison of Inlet Performance, Two-Dimensional Inlet $M_\infty = 2.5$, $\alpha = -3°$

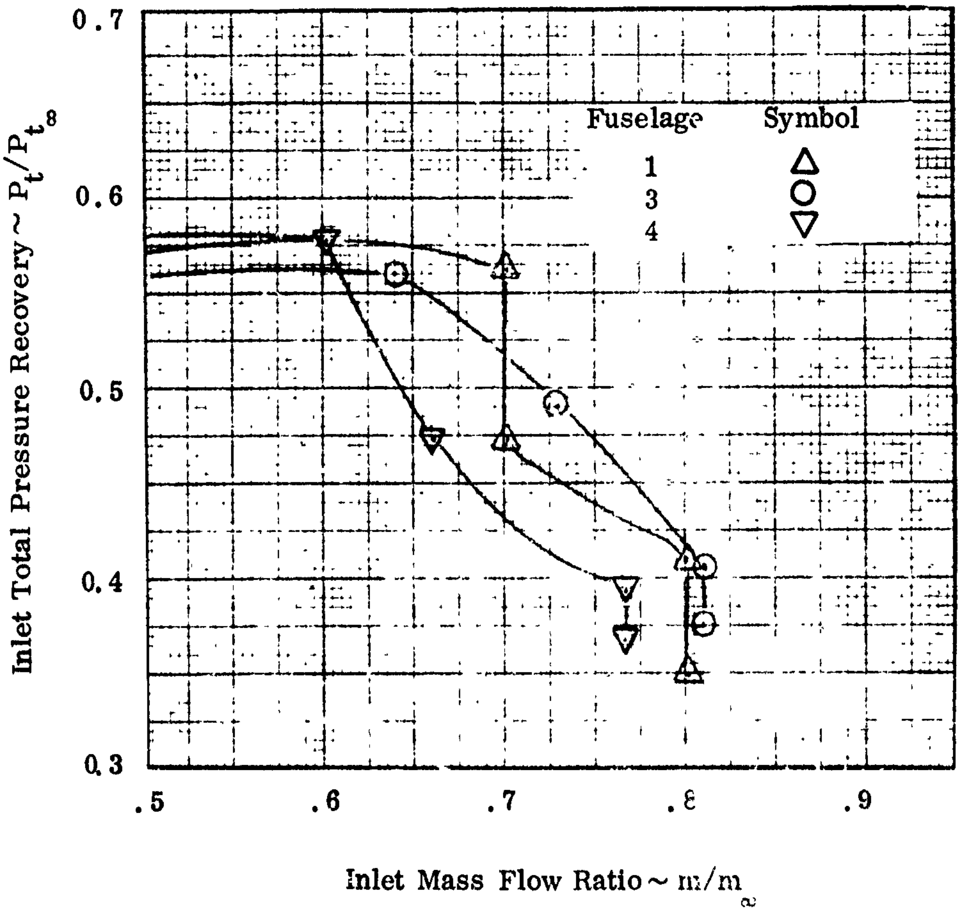

Figure 7-337. Comparison of Inlet Performance, Two-Dimensional Inlet $M_\infty = 2.5$, $\alpha = 0°$

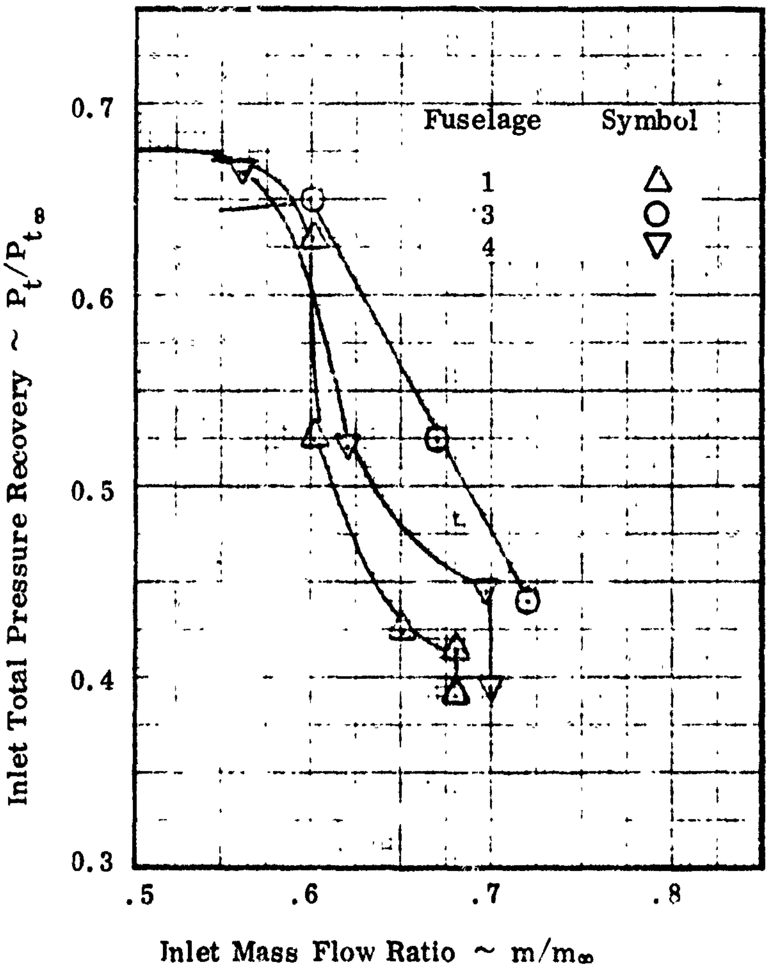

Figure 7-338. Comparison of Inlet Performance, Two Dimensional Inlet $M_\infty = 2.5$, $\alpha = 5°$

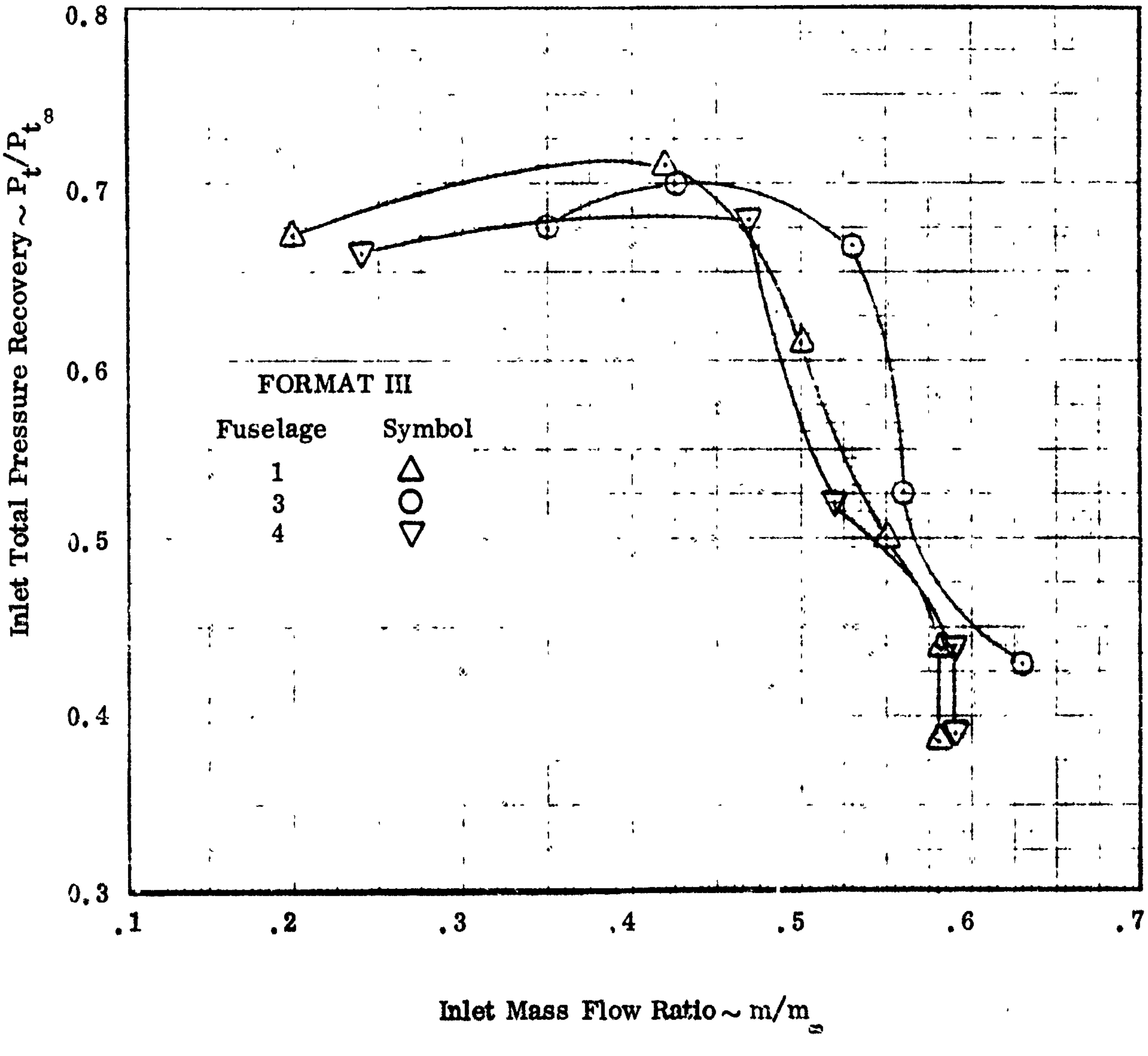

Figure 7-339. Comparison of Inlet Performance, Two Dimensional Inlet, $M_\infty = 2.5$, $\alpha = 10°$

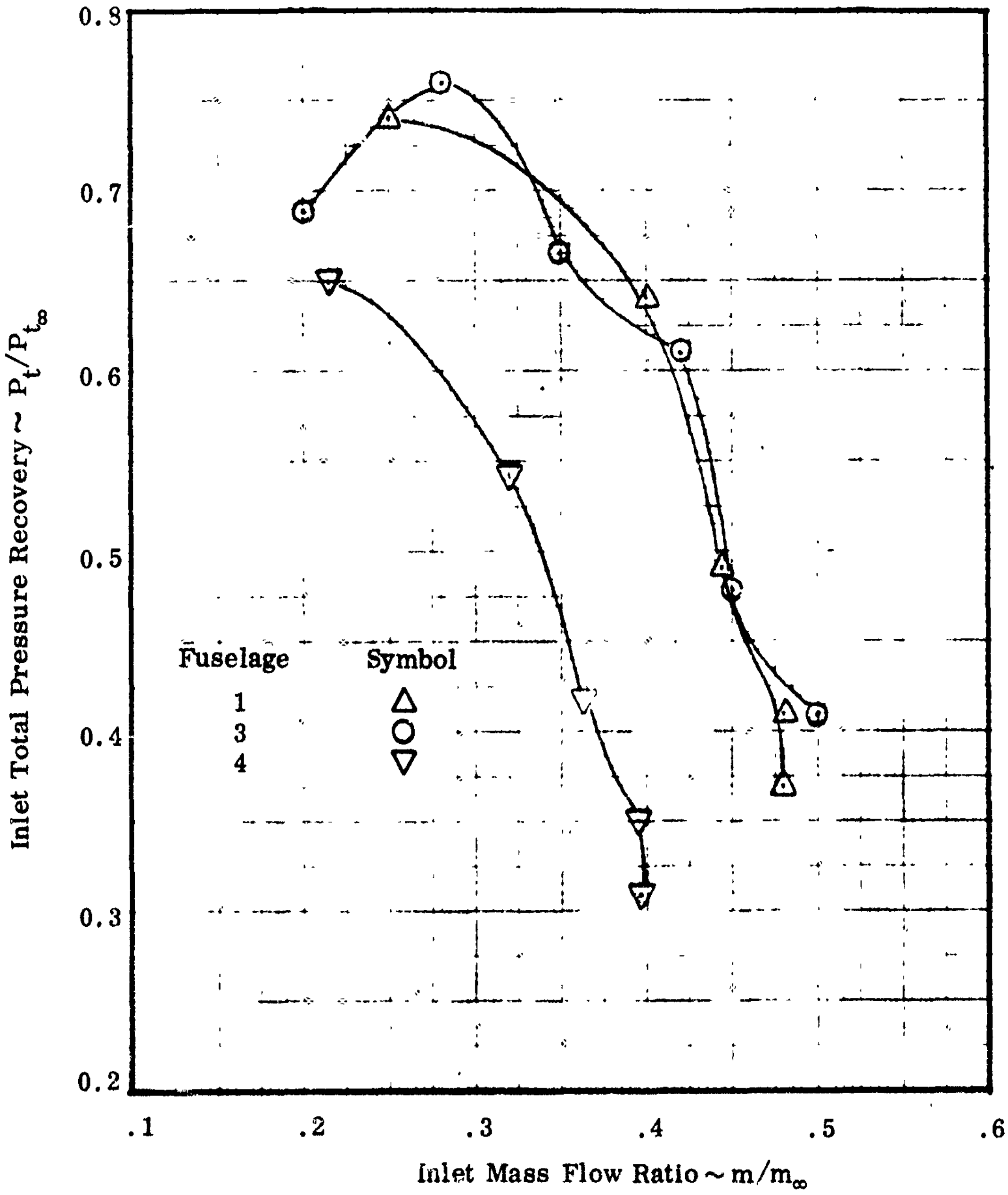

Figure 7-340. Comparison of Inlet Performance, Two-Dimen nal Inlet $M_\infty = 2.5$, $\alpha = 15°$

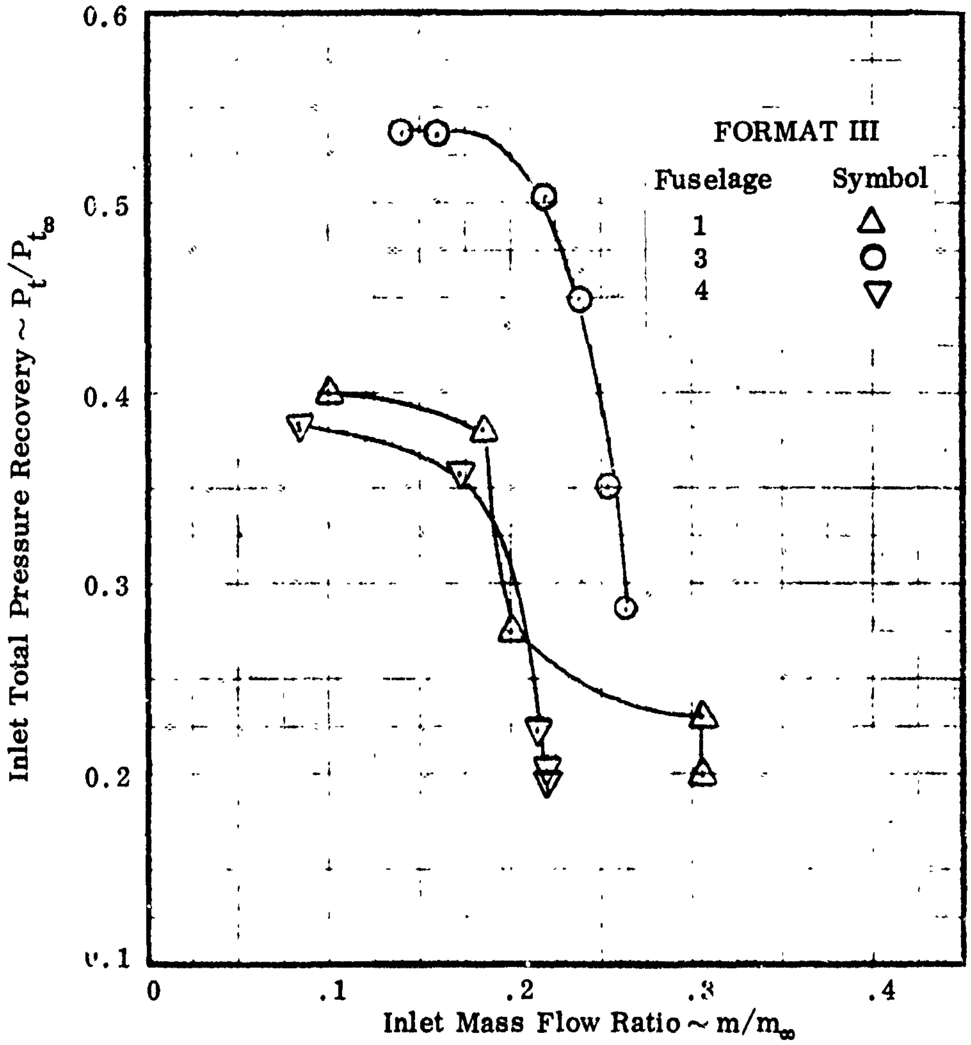

Figure 7-341. Comparison of Inlet Performance, Two-Dimensional Inlet

$M_\infty = 2.5$, $\alpha = 20°$

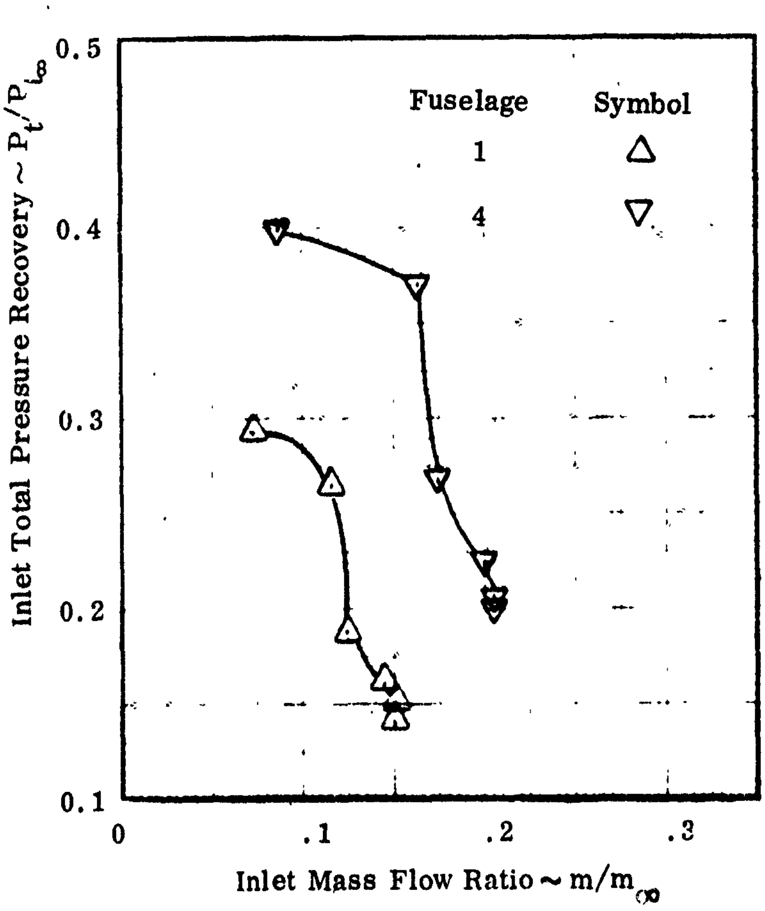

Figure 7-342. Comparison of Inlet Performance, Two-Dimensional Inlet $M_\infty = 2.5$, $\alpha = 25°$

higher mass flow ratio. These effects can be seen in Figures 7-343 through 7-349, presenting a comparison of inlet performance at this Mach number.

For Mach 1.2 the inlet performance varies in the same manner as was seen at Mach 0.8. The inlet performance for this Mach number is compared in Figures 7-350 through 7-353. Tunnel blockage prevented testing the 65° wing configuration above an angle of attack of +10°. Consequently comparison curves are limited to +10° angle of attack and below. However, it is reasonable to expect that the trend evident at Mach 0.8 would again appear at Mach 1.2.

With an increase to Mach 1.8, the wing efficiency begins to affect installed inlet total pressure recovery as a function of angle of attack. For a negative angle of attack ($\alpha = -3^\circ$) neither wing is a working component and the installed inlet characteristics are very similar, as shown in Figure 7-354. With angle of attack increased to zero degrees the more efficient 65° wing results in a higher installed inlet recovery level. A further increase in angle of attack, at this free Mach number, produces a local Mach number approaching the terminal shock that approximates Mach 1.0. Consequently the effect of wing geometry induced compression, upon the strength of the terminal shock, disappears and the performance level with both wings is essentially the same. This can be seen in Figures 7-355 through 7-359, presenting the performance comparison for the angle of attack range between +5° and +20°

For Mach 2.2 and low angle of attack ($\alpha = -3^\circ$) the relative installed performance is similar to that seen at Mach 1.8. It is pointed out, however, that the performance level is rather low, by design, at these two test conditions as presented in Figures 7-360 and 7-361. For this Mach number the inlet has an unbalanced $N = 3$ shock structure with a strong terminal shock wave. The addition of the wing, modifies the compression process to a $N = 4$ system. The wing compression is weak at these attitudes and changes the shock system balance only slightly. However, the difference in wing efficiency can still be seen in the total pressure recovery level. With angle of attack increased further the wing becomes a strong working member that produces a reduced terminal shock strength. This favorable shift toward a more balanced shock structure results in an increased level of total pressure recovery. For the subject configuration, the 55° wing provides more compression of the flow and a

Two-Dimensional Inlet

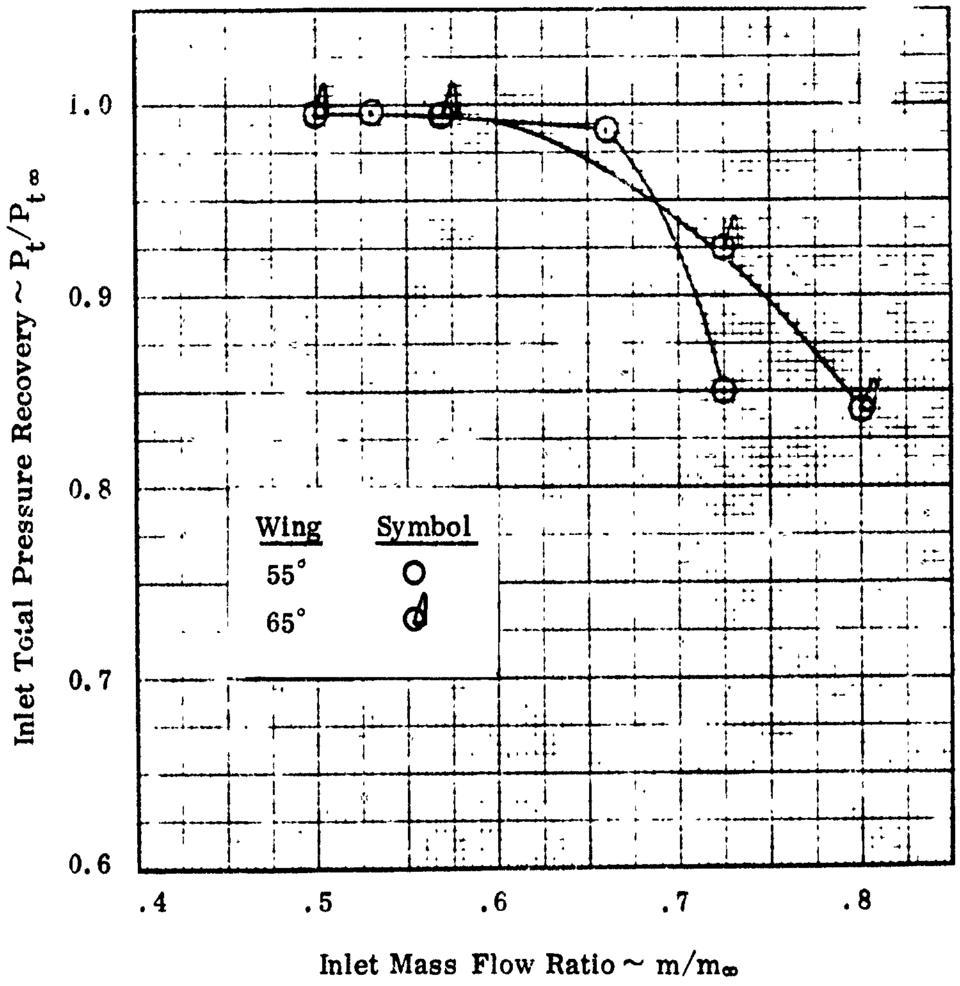

Figure 7-343. Comparison of Inlet Performance, Wing Effects
$M_\infty = 0.8$, $\alpha = -3°$

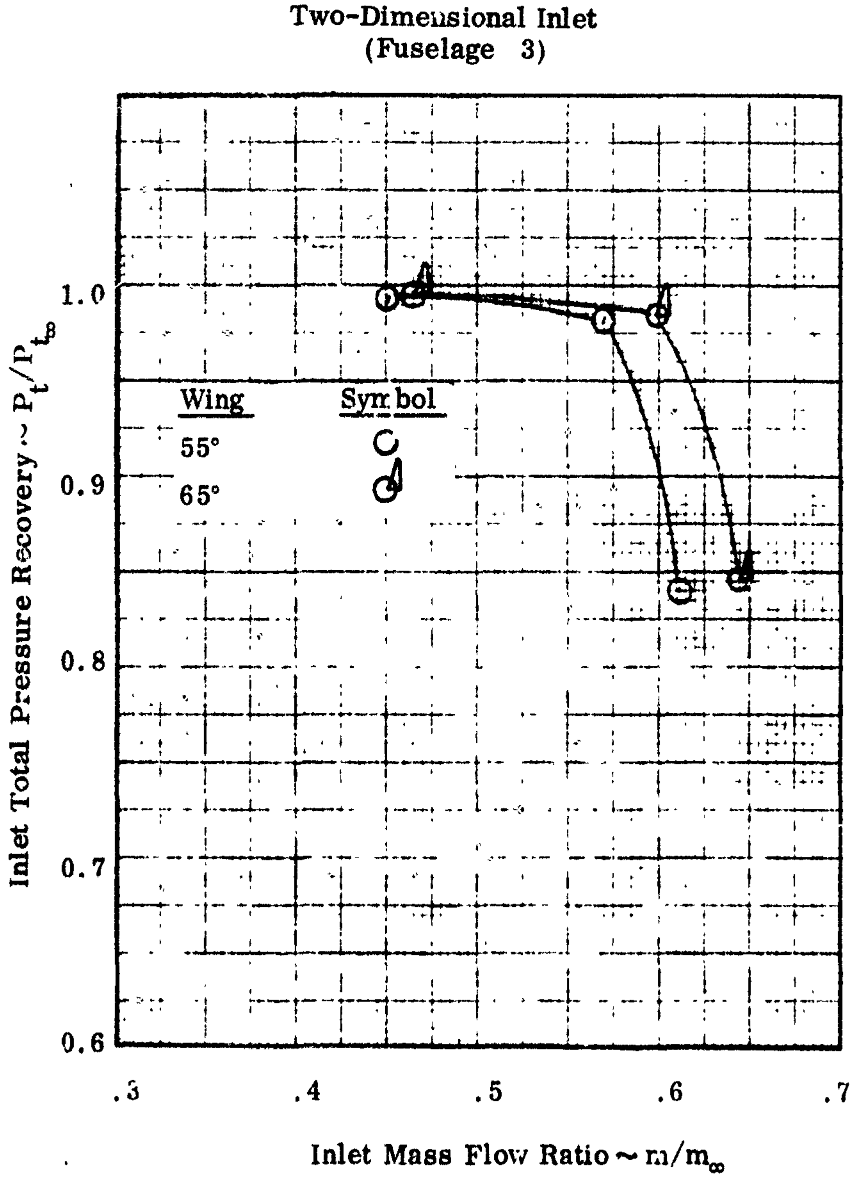

Figure 7-344. Comparison of Inlet Performance, Wing Effects

$M_\infty = 0.8$, $\alpha = 0°$

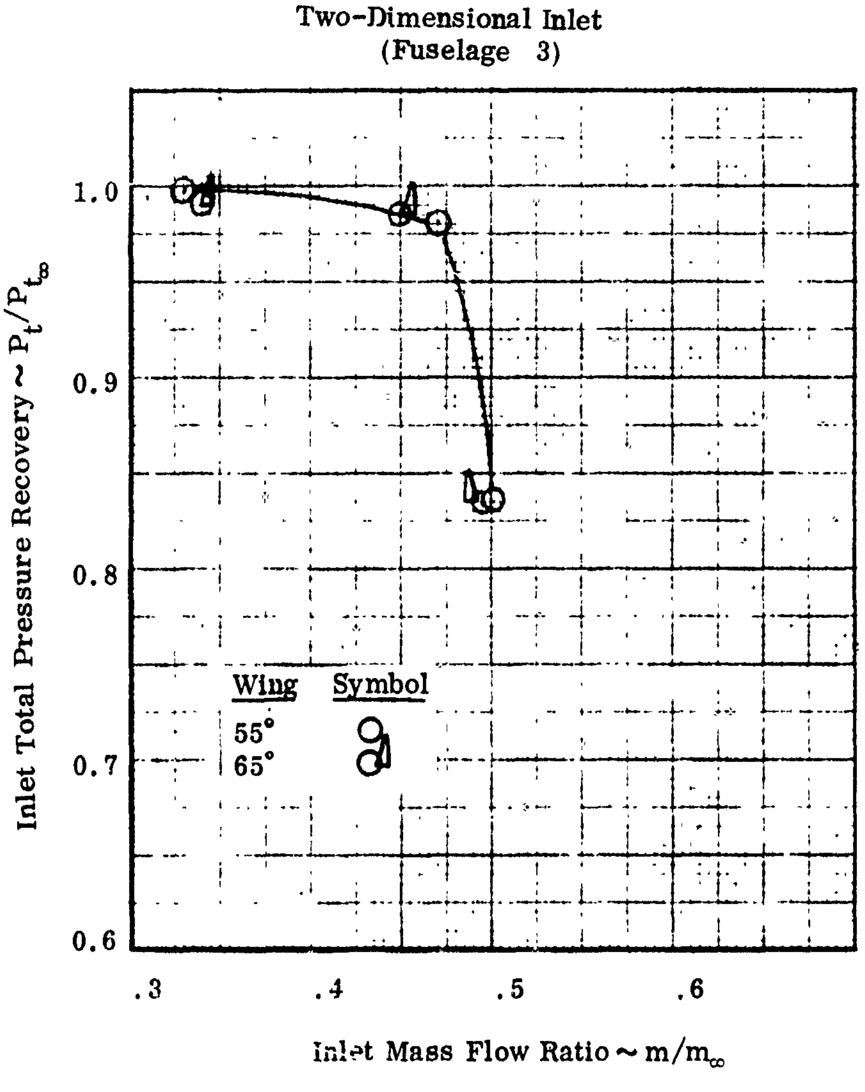

Figure 7-345. Comparison of Inlet Performance, Wing Effects

$M_\infty = 0.8$, $\alpha = 5°$

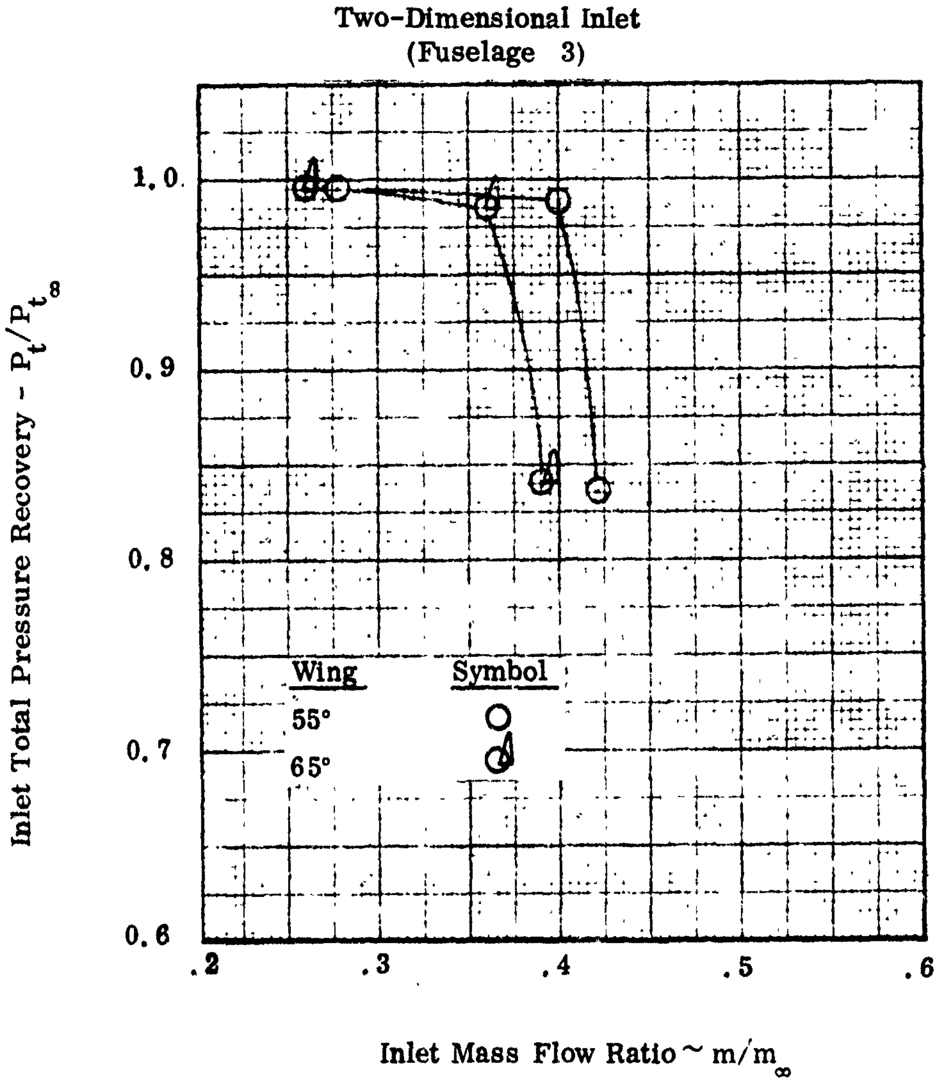

Figure 7-346. Comparison of Inlet Performance, Wing Effects
$M_\infty = 0.8$, $\alpha = 10°$

Two-Dimensional Inlet
(Fuselage 3)

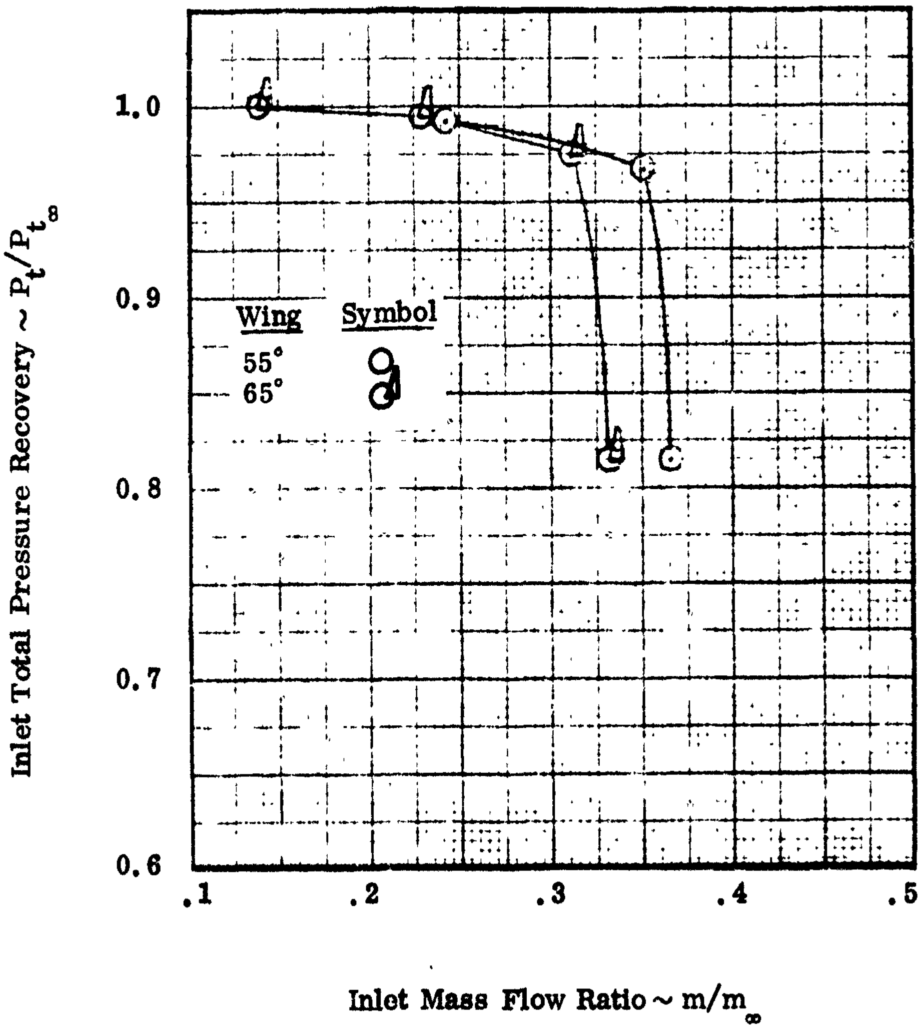

Figure 7-347. Comparison of ⁻ ʾet Performance, Wing Effects
$M_\infty =$ .8, $\alpha = 15°$

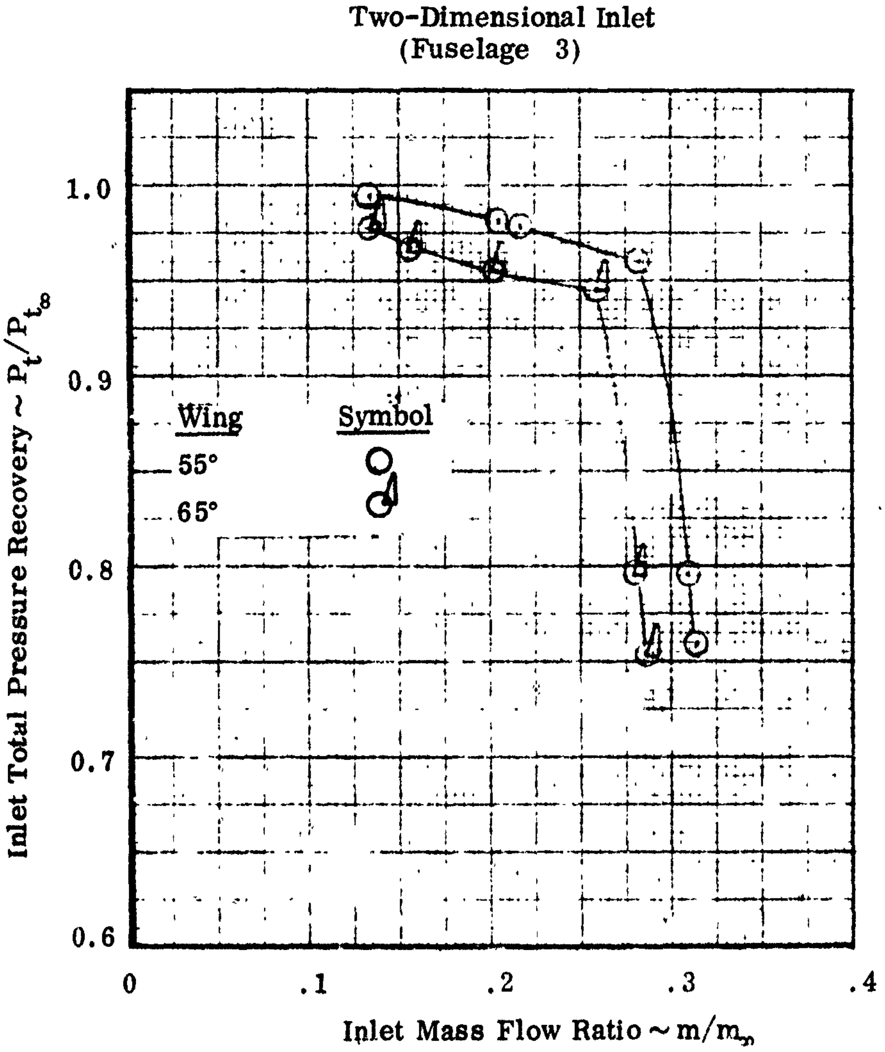

Figure 7-348. Comparison of Inlet Performance, Wing Effects $M_\infty = 0.8$, $\alpha = 20°$

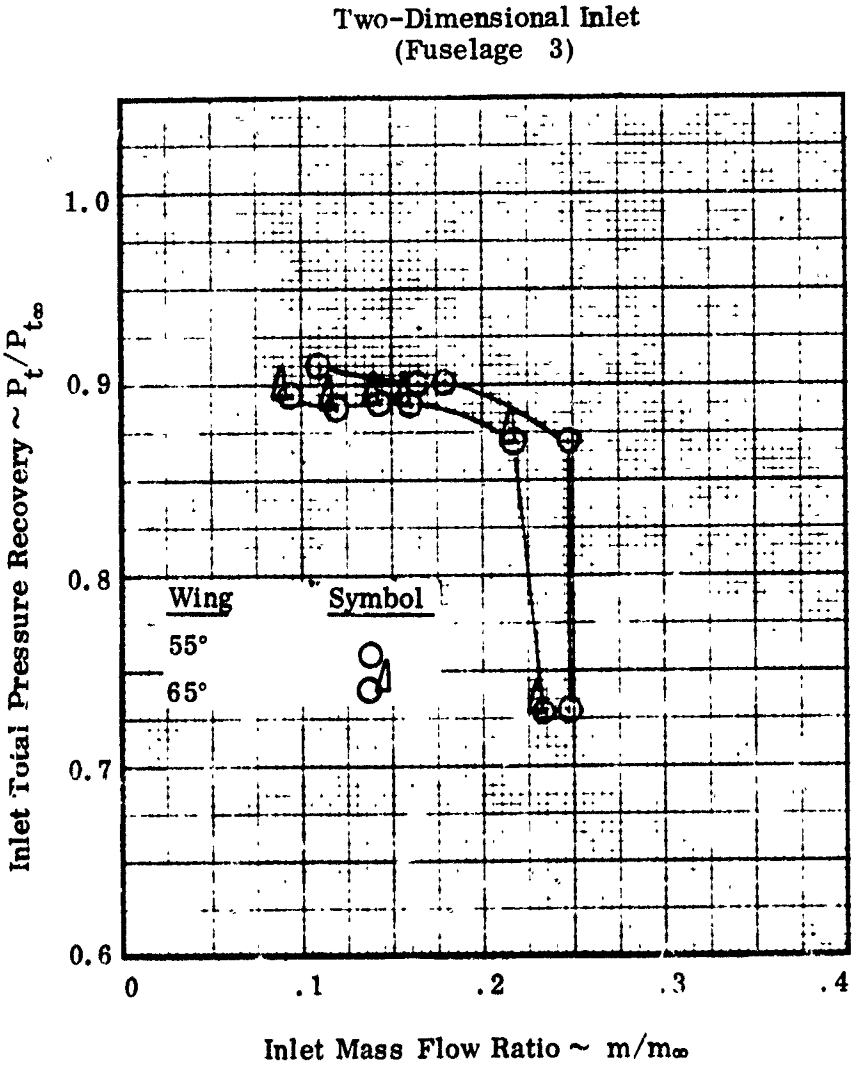

Figure 7-349. Comparison of Inlet Performance, Wing Effects

$M_\infty = 0.8$, $\alpha = 25°$

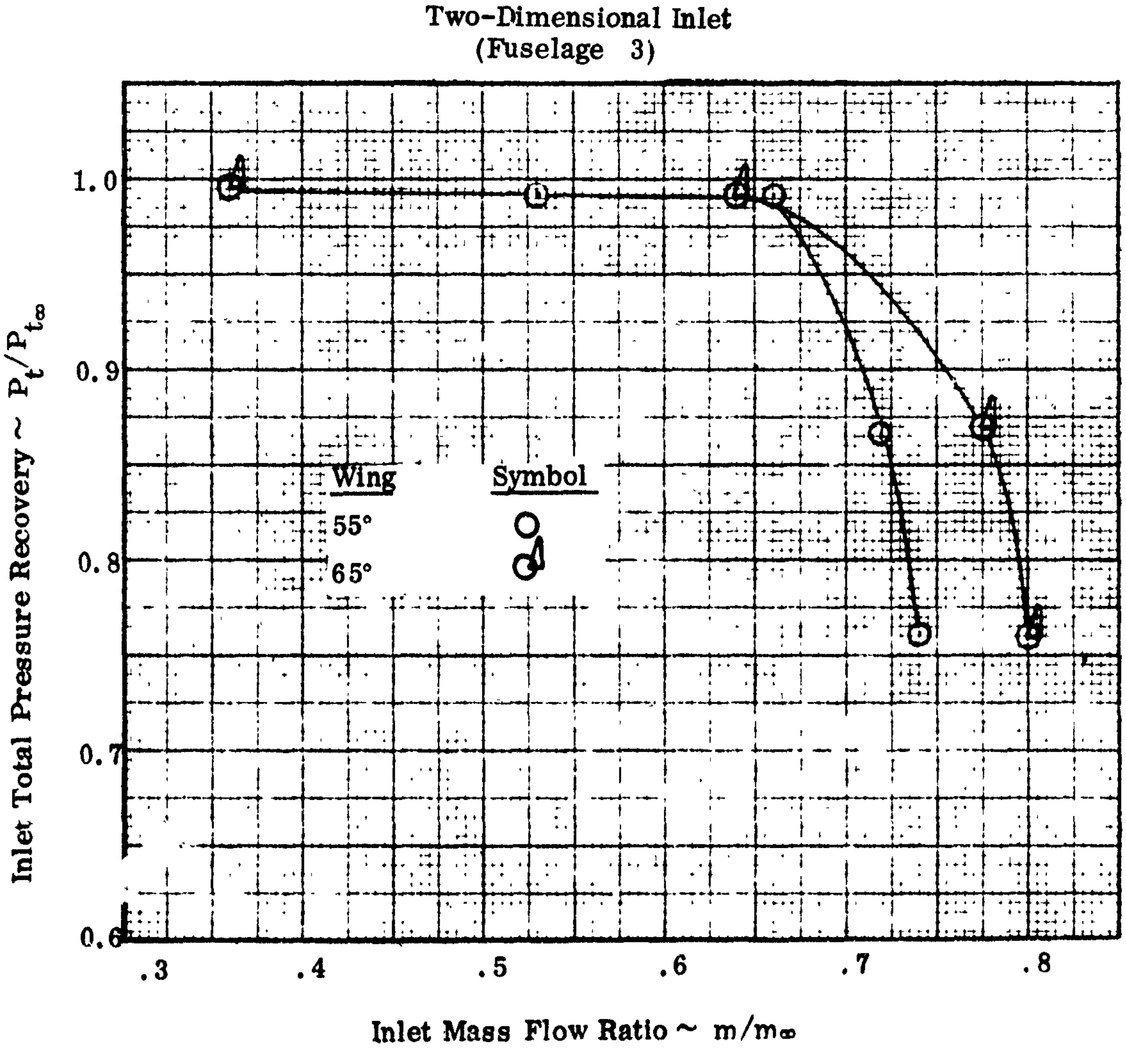

Figure 7-350. Comparison of Inlet Performance, Wing Effects
$M_\infty = 1.2$, $\alpha = -3°$

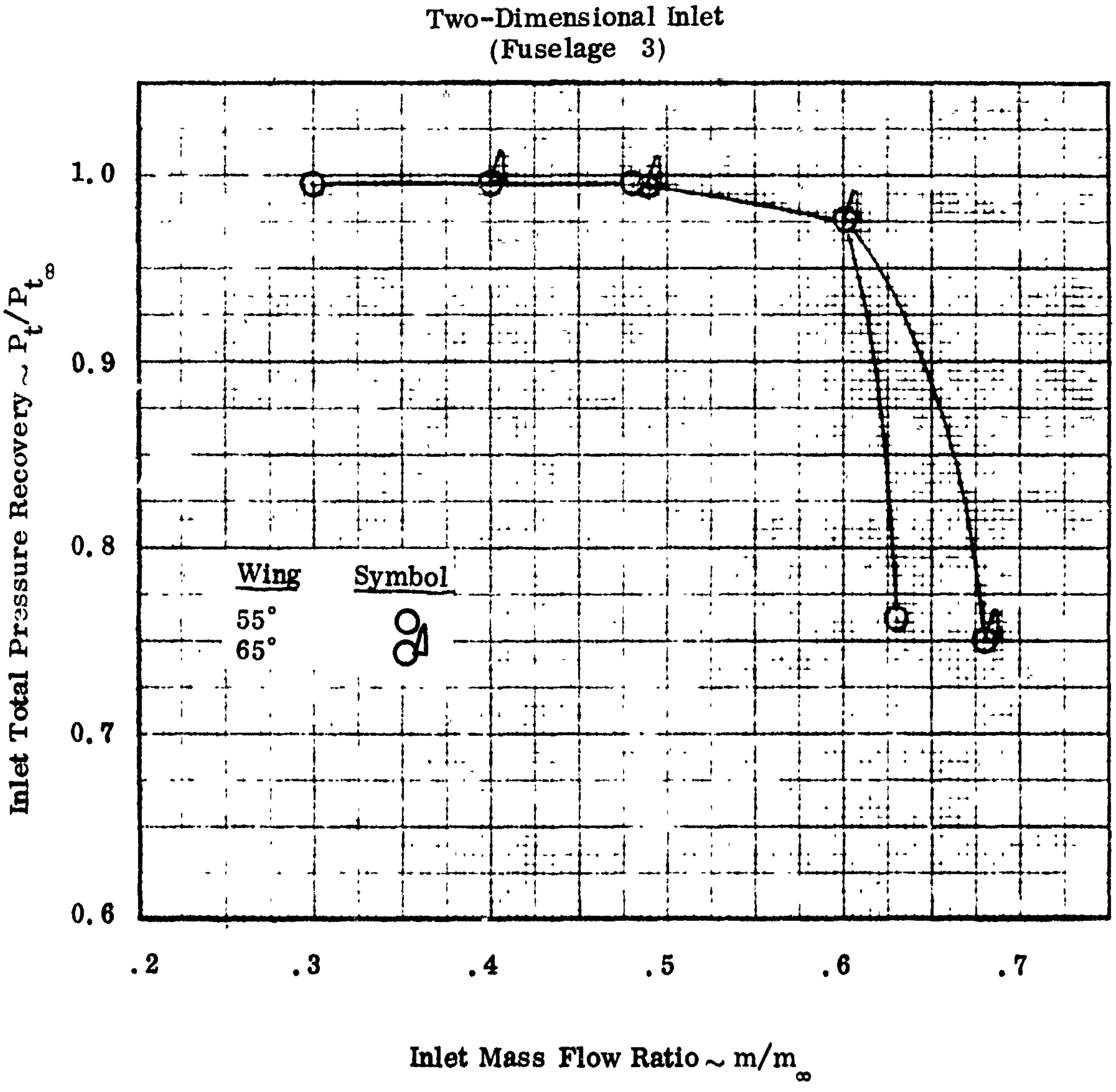

Figure 7-351. Comparison of Inlet Performance, Wing Effects
$M_\infty = 1.2$, $\alpha = 0°$

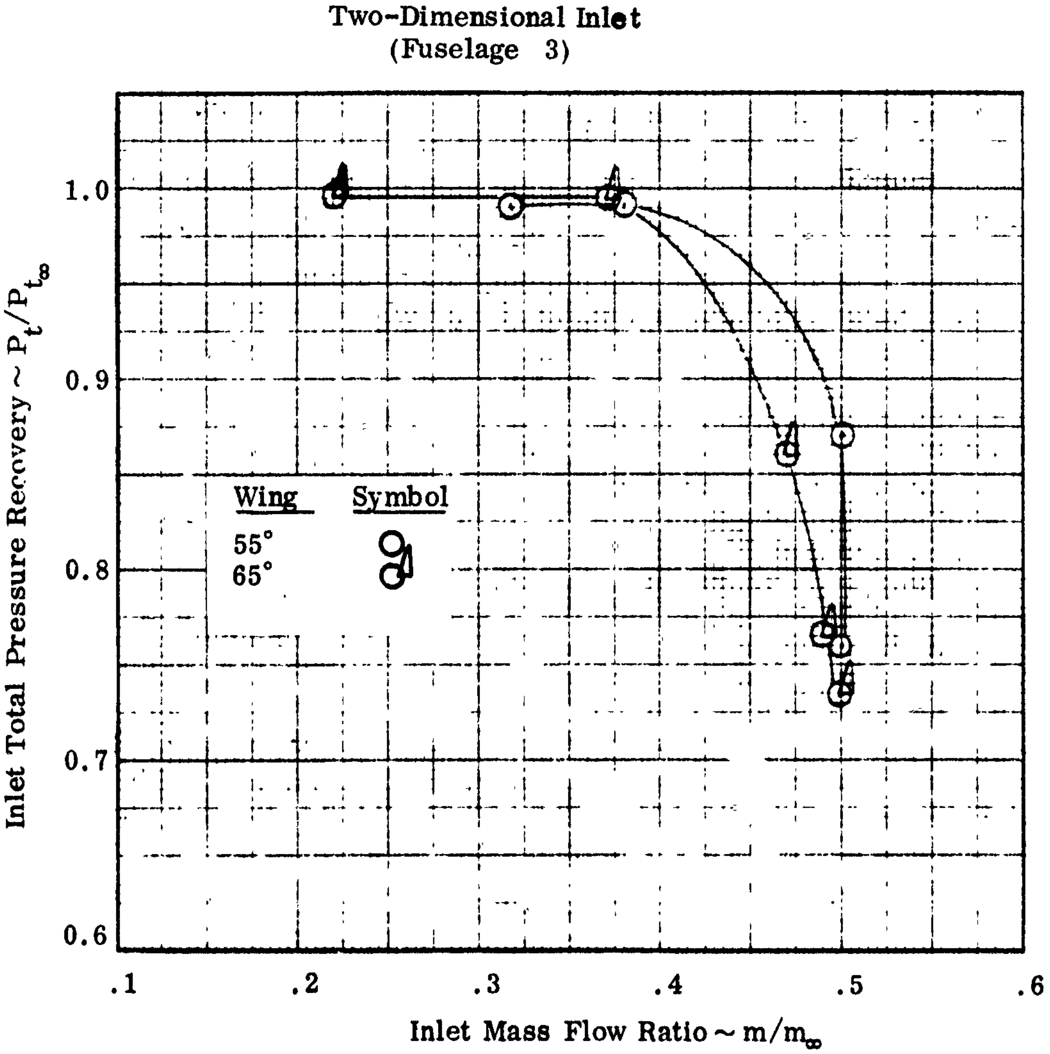

Figure 7-352. Comparison of Inlet Performance, Wing Effects
$M_\infty = 1.2$, $\alpha = 5°$

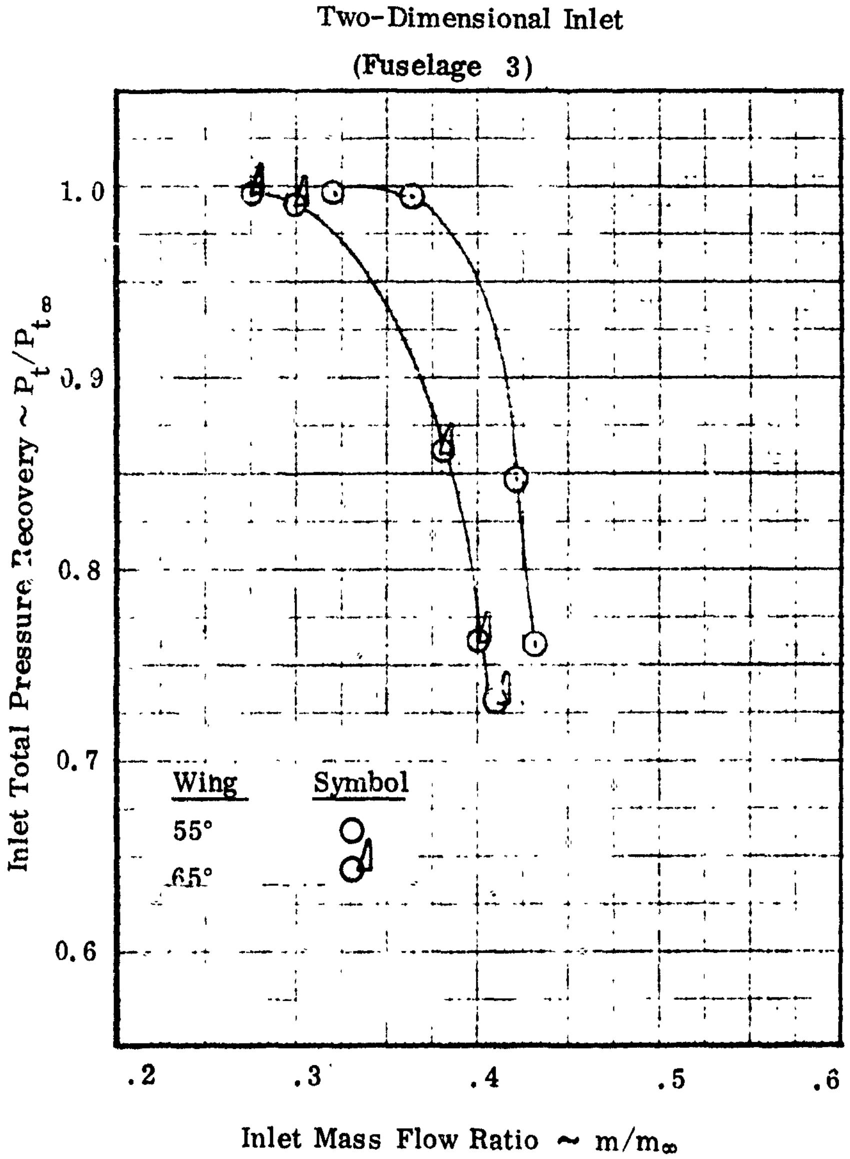

Figure 7-353. Comparison of Inlet Performance, Wing Effects
$M_\infty = 1.2$, $\alpha = 10°$

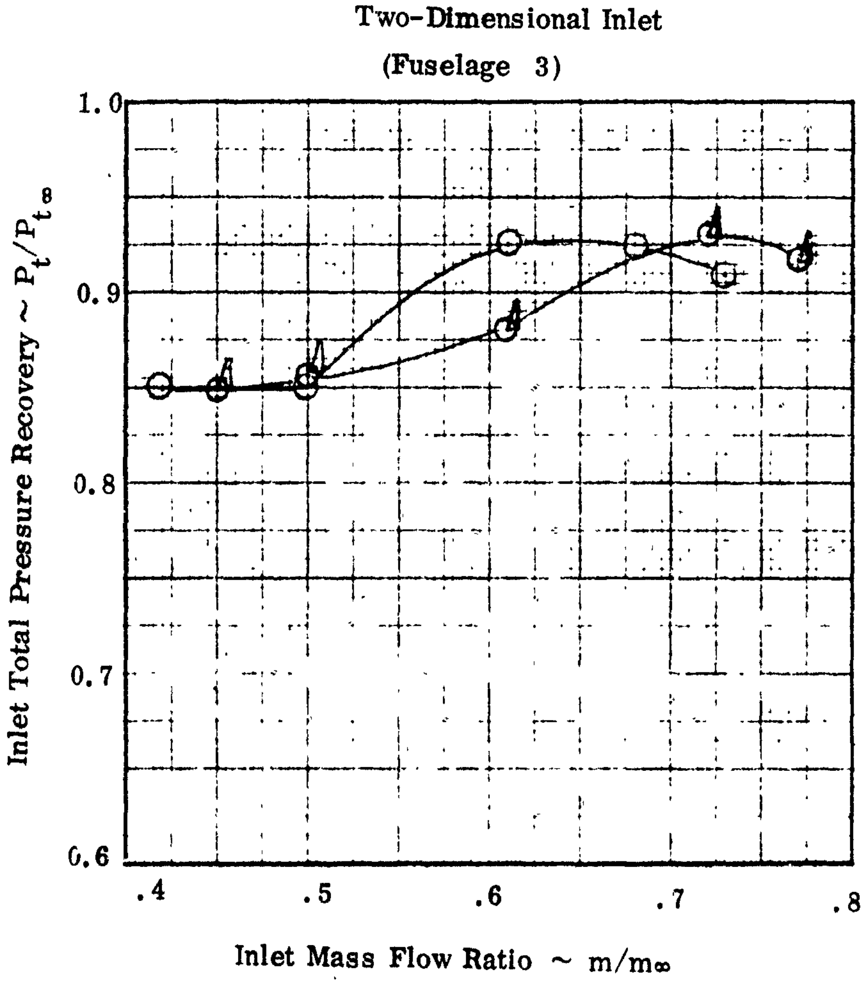

Figure 7-354. Comparison of Inlet Performance, Wing Effects
$M_\infty = 1.8$, $\alpha = -3°$

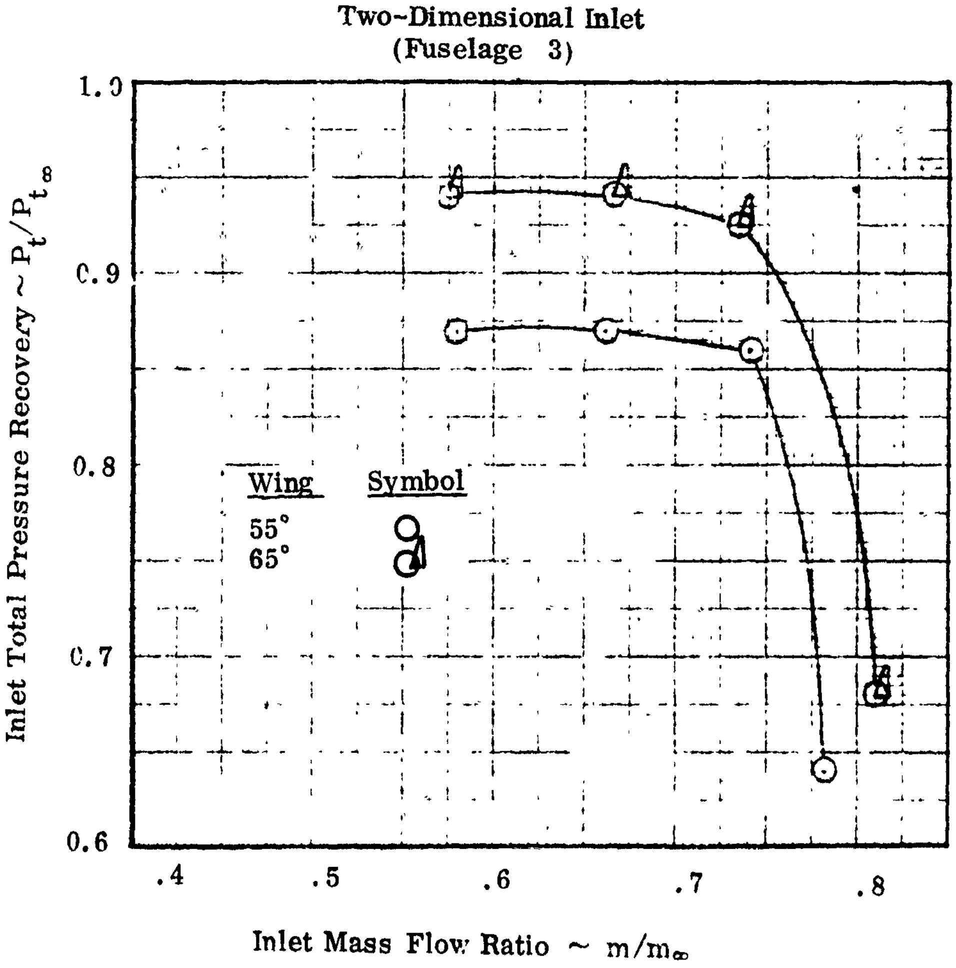

Figure 7-355. Comparison of Inlet Performance, Wing Effects
$M_\infty = 1.8$, $\alpha = 0°$

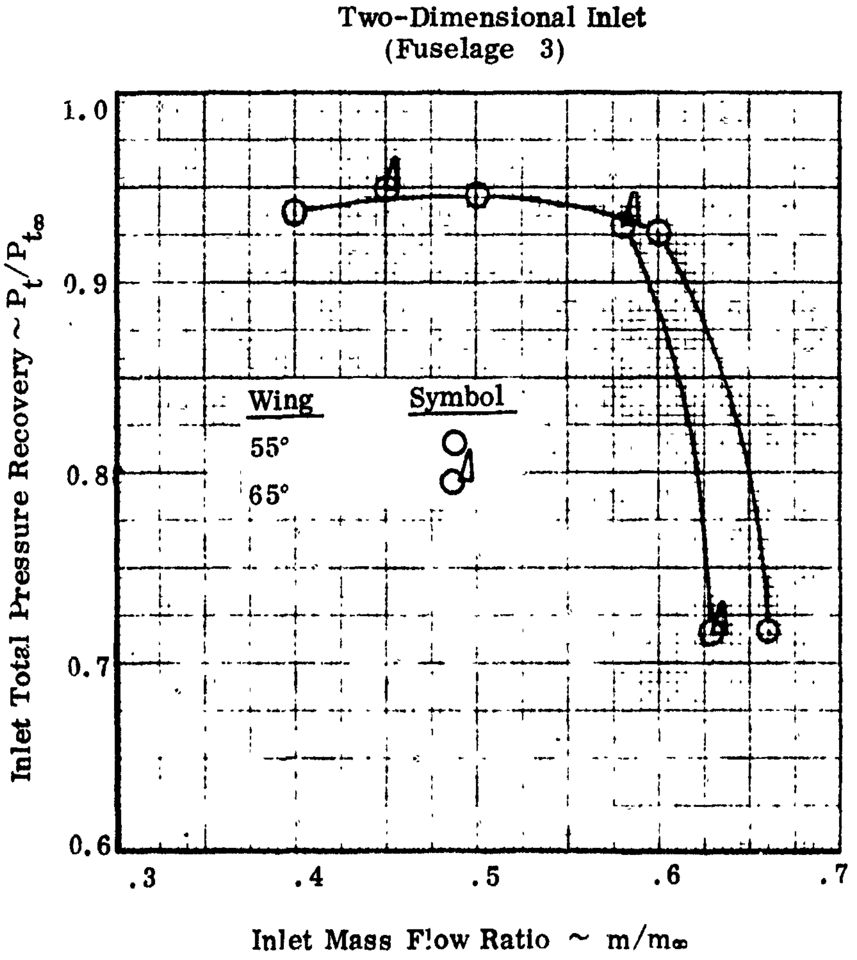

Figure 7-356. Comparison of Inlet Performance, Wing Effects
$M_\infty = 1.8$, $\alpha = 5°$

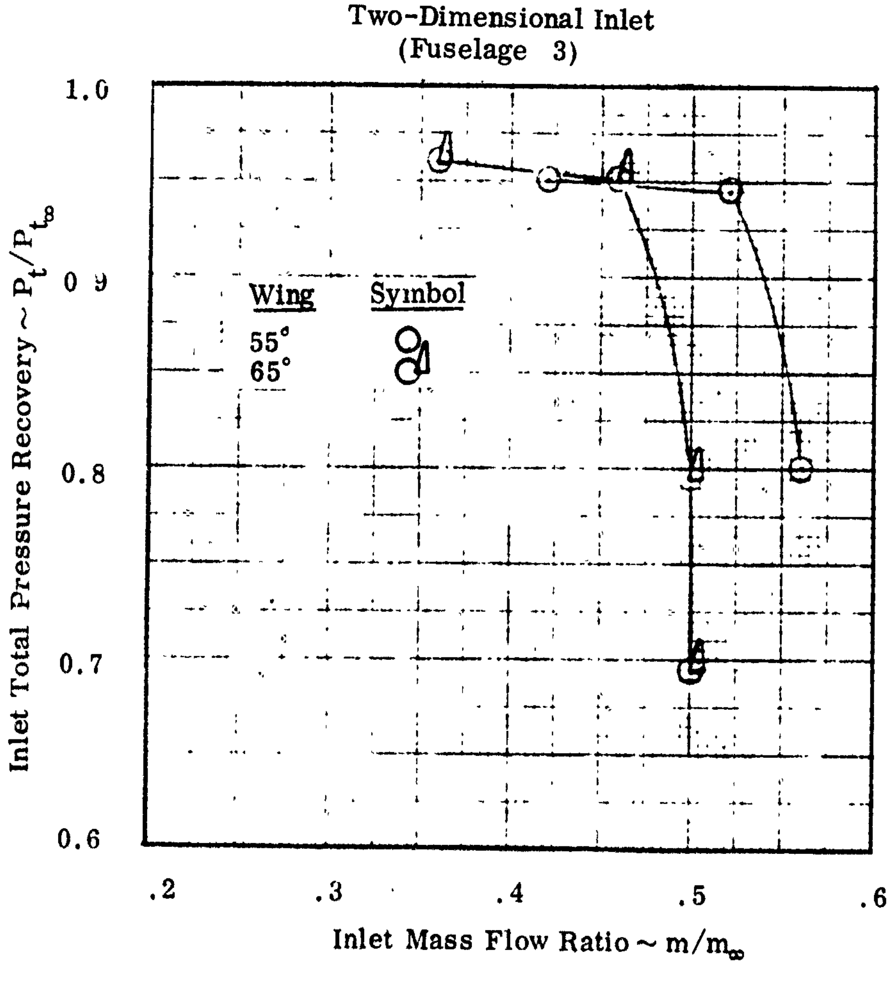

Figure 7-357. Comparison of Inlet Performance, Wing Effects $M_\infty = 1.8$, $\alpha = 10°$

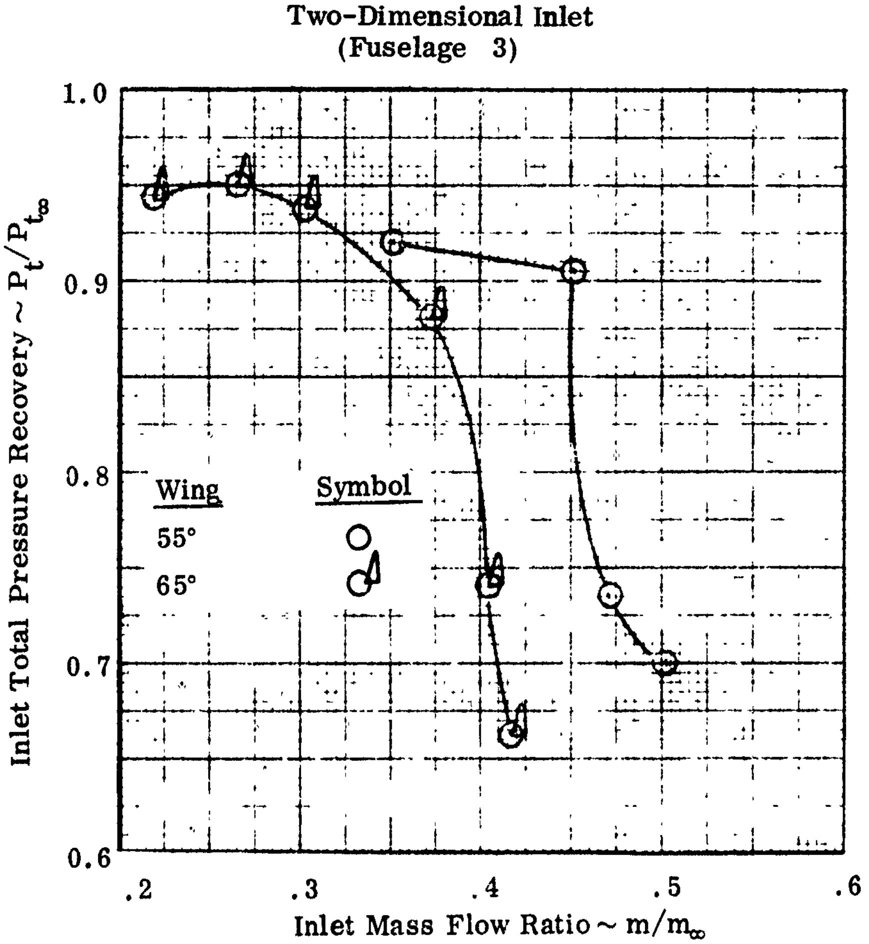

Figure 7-358. Comparison of Inlet Performance, Wing Effects
$M_\infty = 1.8$, $\alpha = 15°$

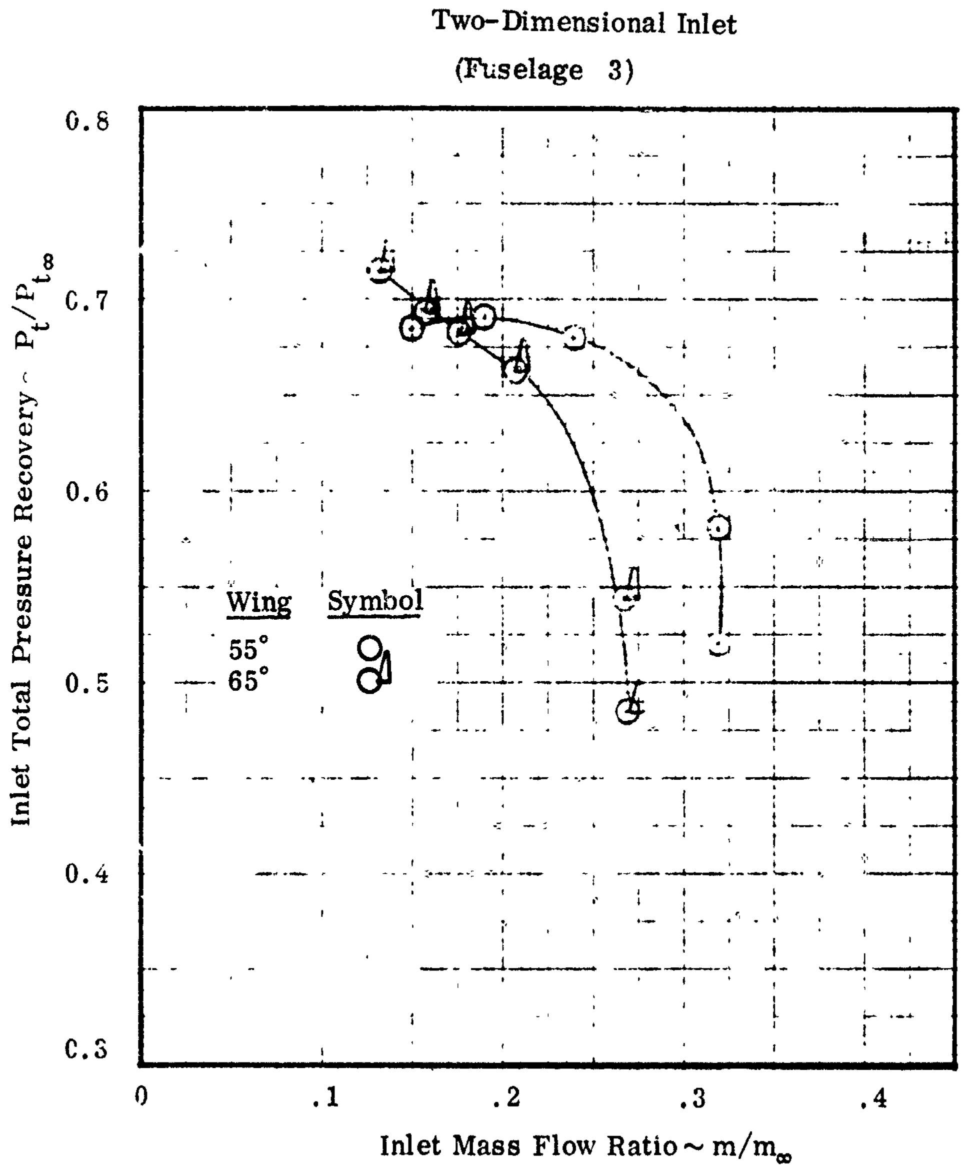

Figure 7-359. Comparison of Inlet Performance, Wing Effects

$M_\infty = 1.8$, $\alpha = 20°$

Two Dimensional Inlet

(Fuselage 3)

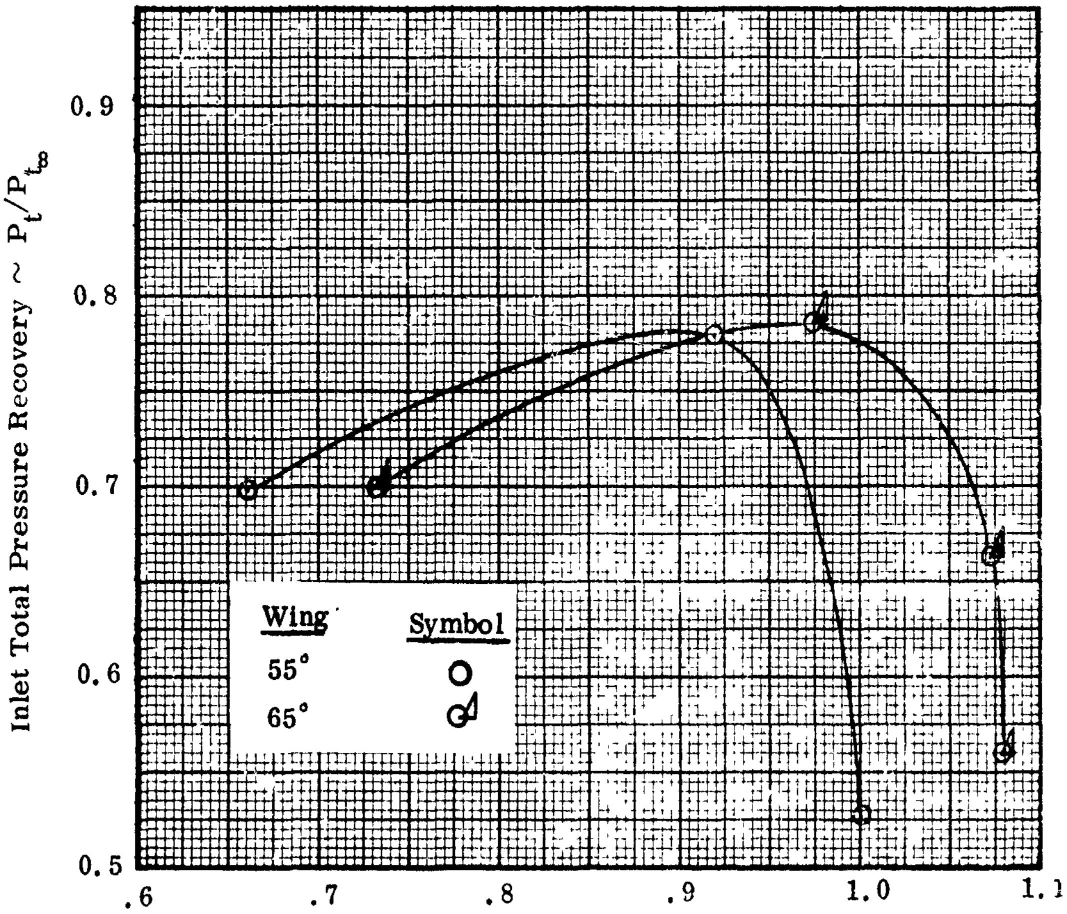

Inlet Mass Flow Ratio ~ m/m_∞

Figure 7-360. Comparison of Inlet Performance, Wing Effects

$M_\infty = 2.2, \ \alpha = -3°$

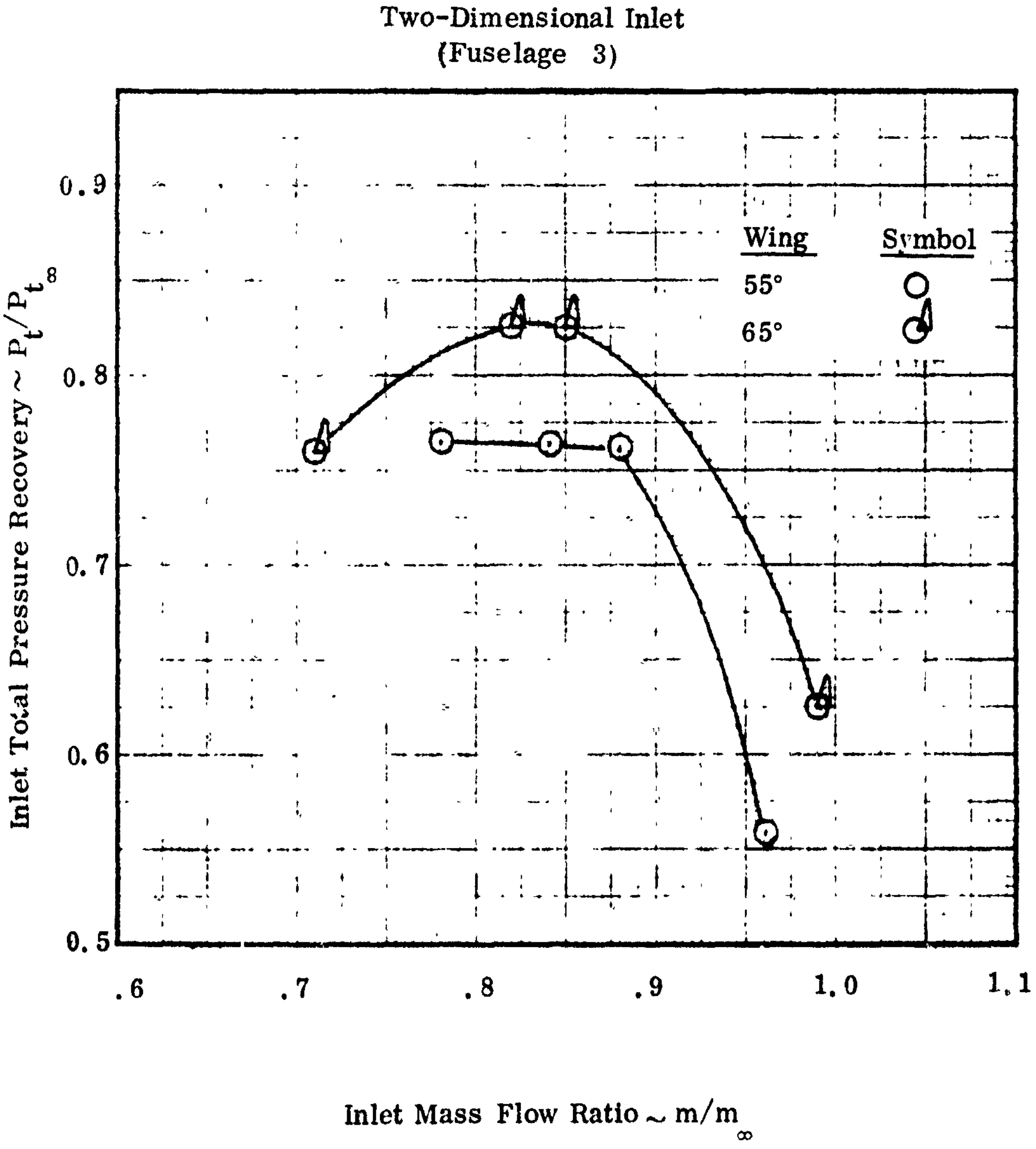

Figure 7-361. Comparison of Inlet Performance, Wing Effects
$M_\infty = 2.2$, $\alpha = 0°$

relatively weaker terminal shock. The gain in total pressure recovery across this weaker terminal shock more than offsets the lower efficiency of the wing compression process and the 55° configuration emerges with a higher performance level across this angle of attack range. This is presented in Figures 7-362 through 7-365.

At Mach 2.5 the inherent inlet performance is quite low. The addition of either wing tends to improve this performance level, over that attained with the isolated inlet. Generally, those effects seen at Mach 2.2 appear again at this Mach number. The comparison is presented for this Mach number in Figures 7-366 through 7-371.

7.6 Probe Interference Effects

A prime model design requirement was to minimize the influence exerted by the flow field probes upon the local flow environment. In this regard, the objective was to avoid the introduction of probe induced interference effects both between adjacent probes and/or due to the proximity of a probe to fuselage and wing surfaces. The prerequisites to satisfying this objective were,

- Selection of the smallest probe diameter and included cone angle, consistent with acceptable manufacturing tolerance and pressure lag times
- Selection of a spacing between probes sufficiently large to preclude mutual interference, constrained however, by the desirability of obtaining an extensive documentation of the flow field without excessive travel and size of the drive mechanism

The possibility of obtaining poor test data, as a result of probe induced interference, justified an experimental determination of both probe size and spacing. To select the probe characteristics a design and calibration test program was conducted in the NASA-Ames 2 Foot Tunnel, covering the Mach number range between 0.6 and 1.4. Parameters such as cone included angle, probe diameter, orifice size, probe spacing, pneumatic tube length and diameter were evaluated during this study. The test program involved the calibration of four conical pitot-static probes, two .125 inch diameter probes with a 30° and a 40° included cone angle, and two .25 inch diameter probes with a 30° and a 40° included cone angle.

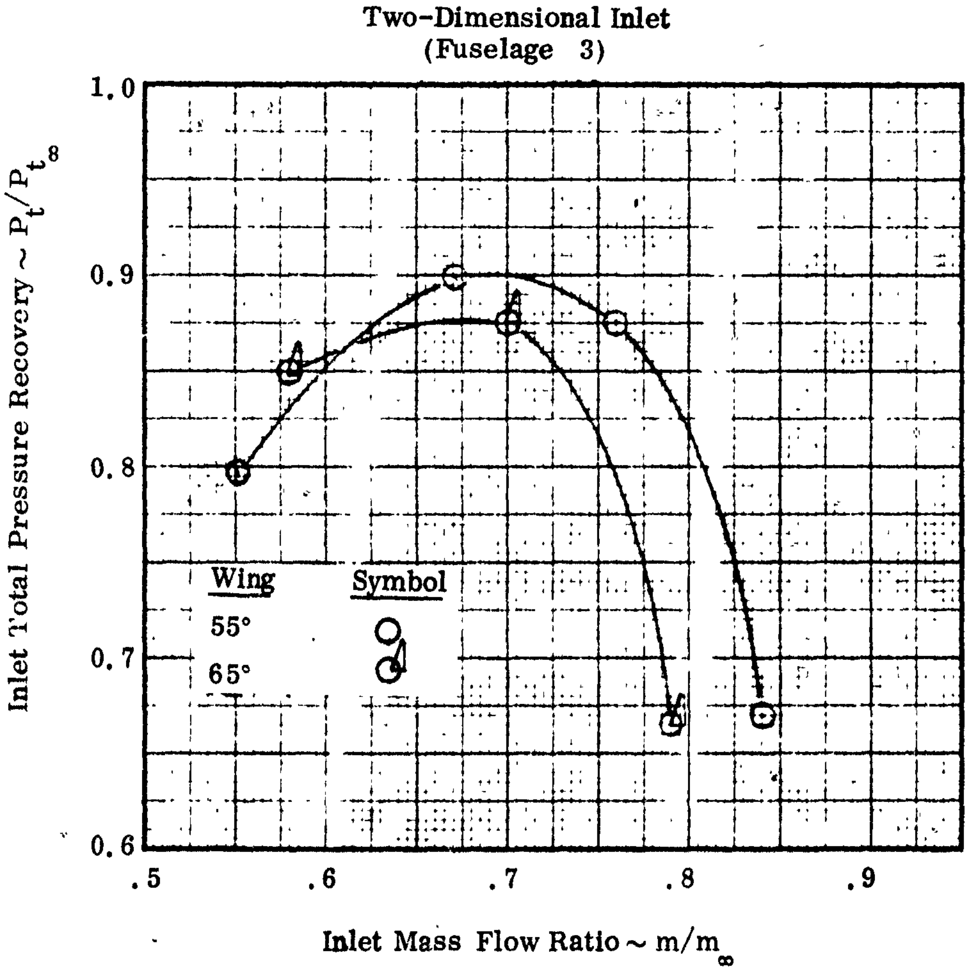

Figure 7-362. Comparison of Inlet Performance, Wing Effects $M_\infty = 2.2$, $\alpha = 5°$

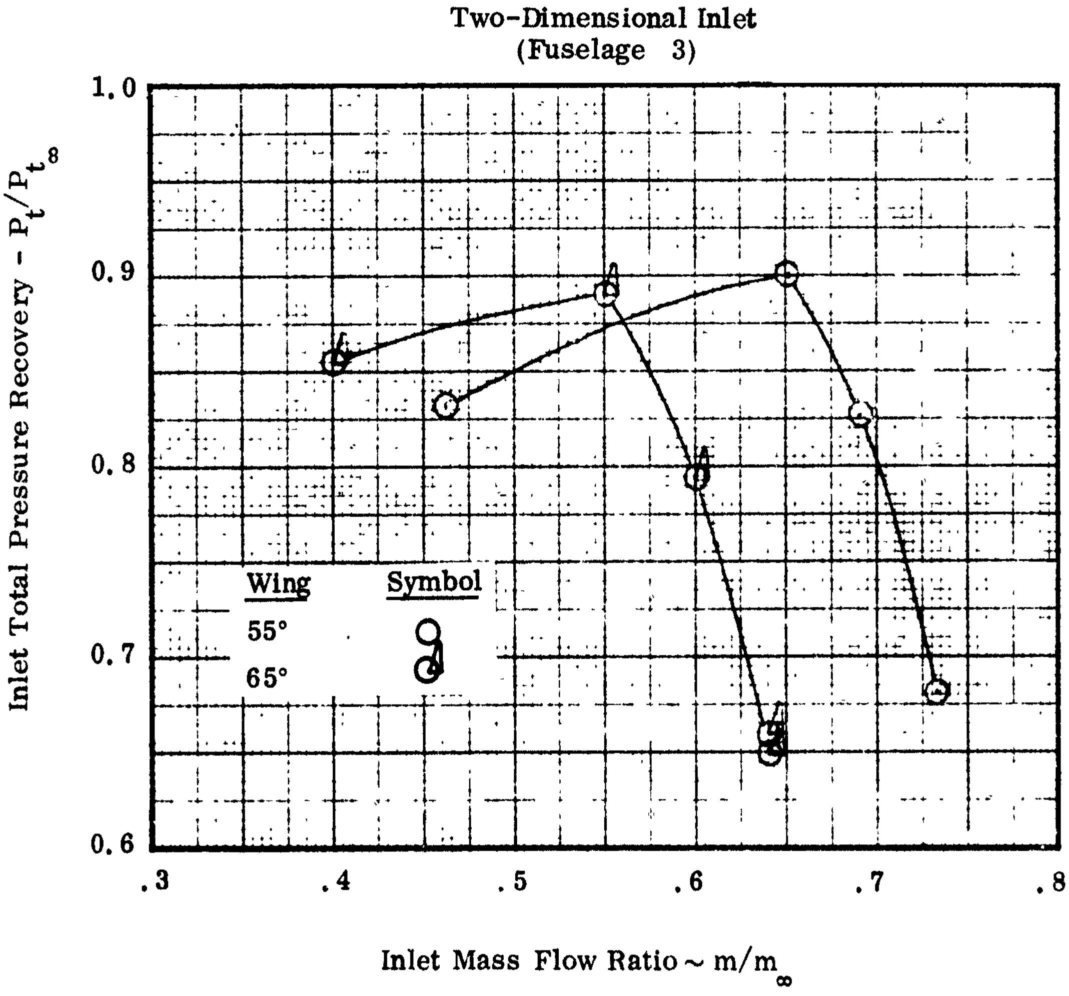

Figure 7-363. Comparison of Inlet Performance, Wing Effects $M_\infty = 2.2$, $\alpha = 10°$

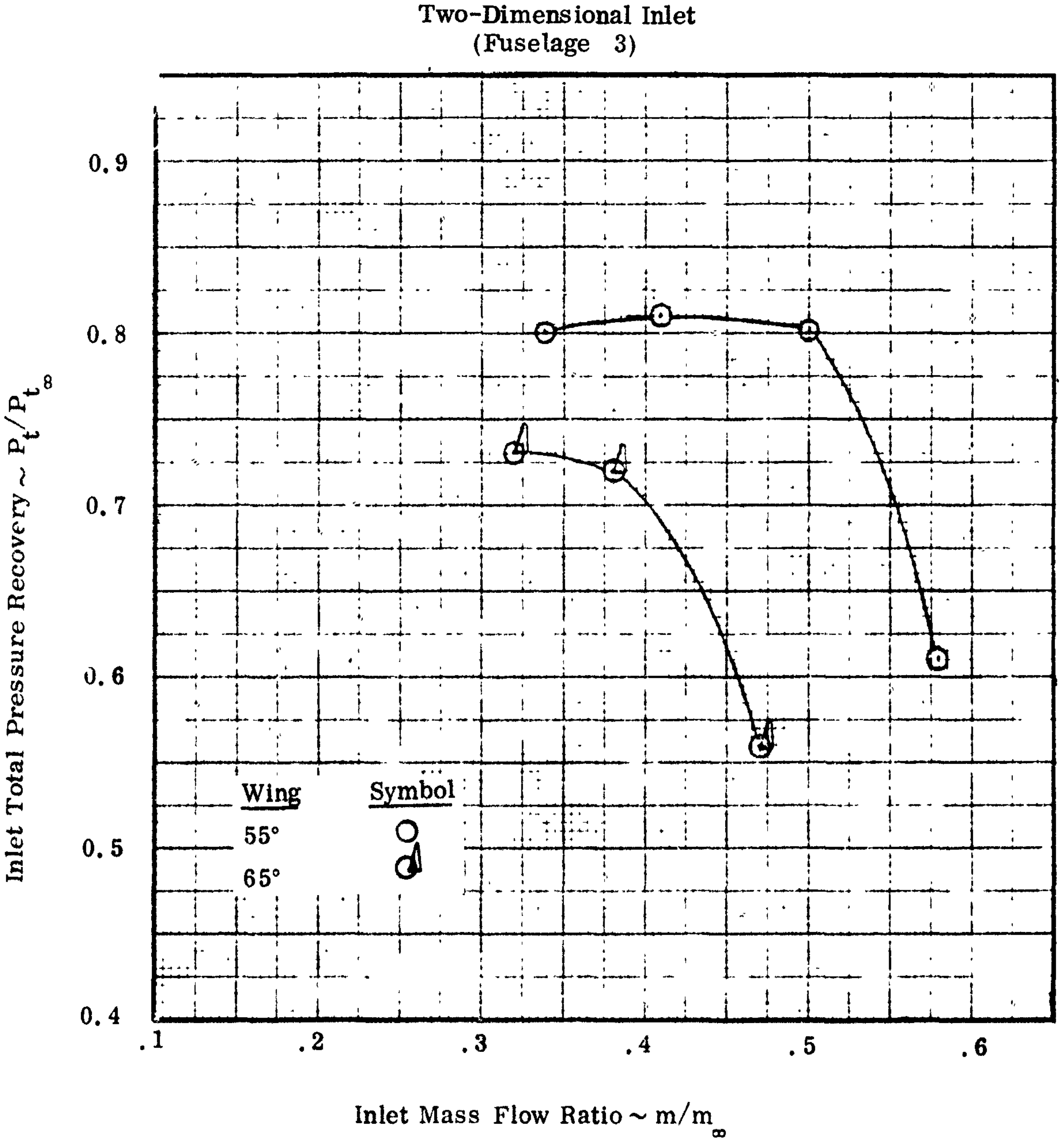

Figure 7-364. Comparison of Inlet Performance, Wing Effects
$M_\infty = 2.2$, $\alpha = 15°$

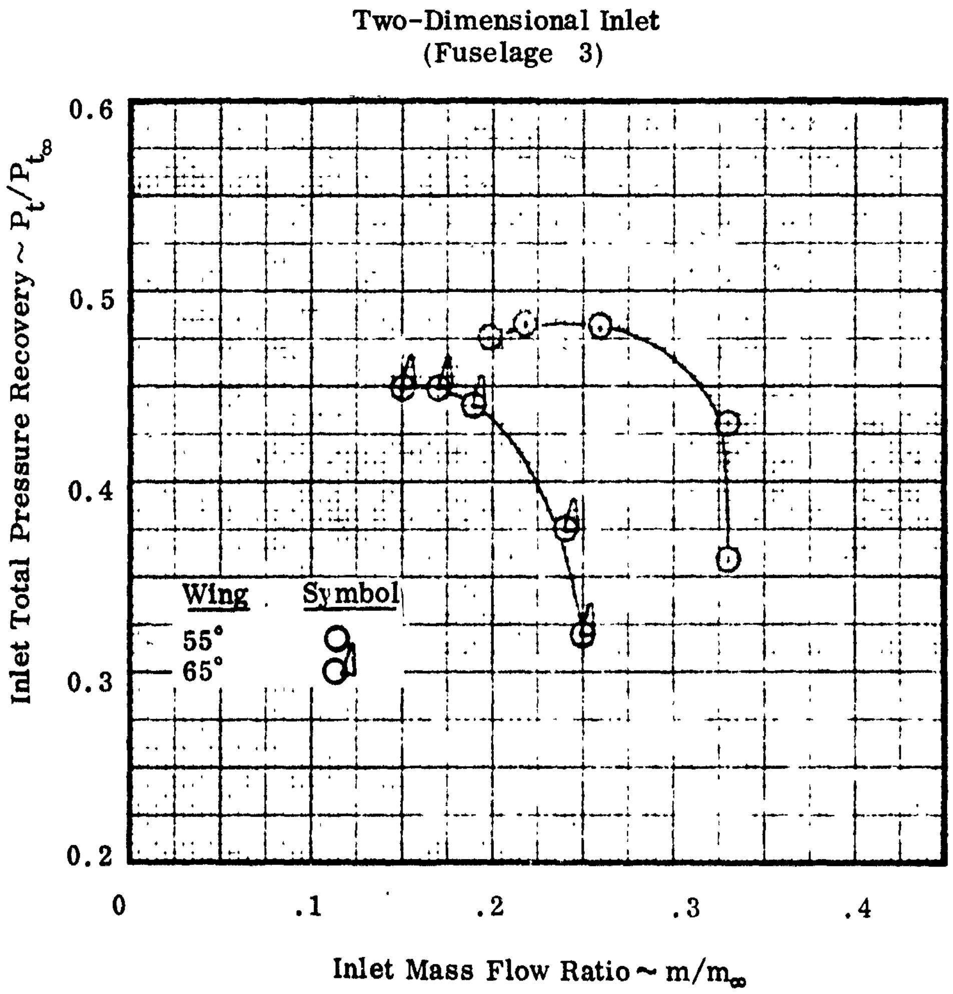

Figure 7-365. Comparison of Inlet Performance, Wing Effects

$M_\infty = 2.2$, $\alpha = 20°$

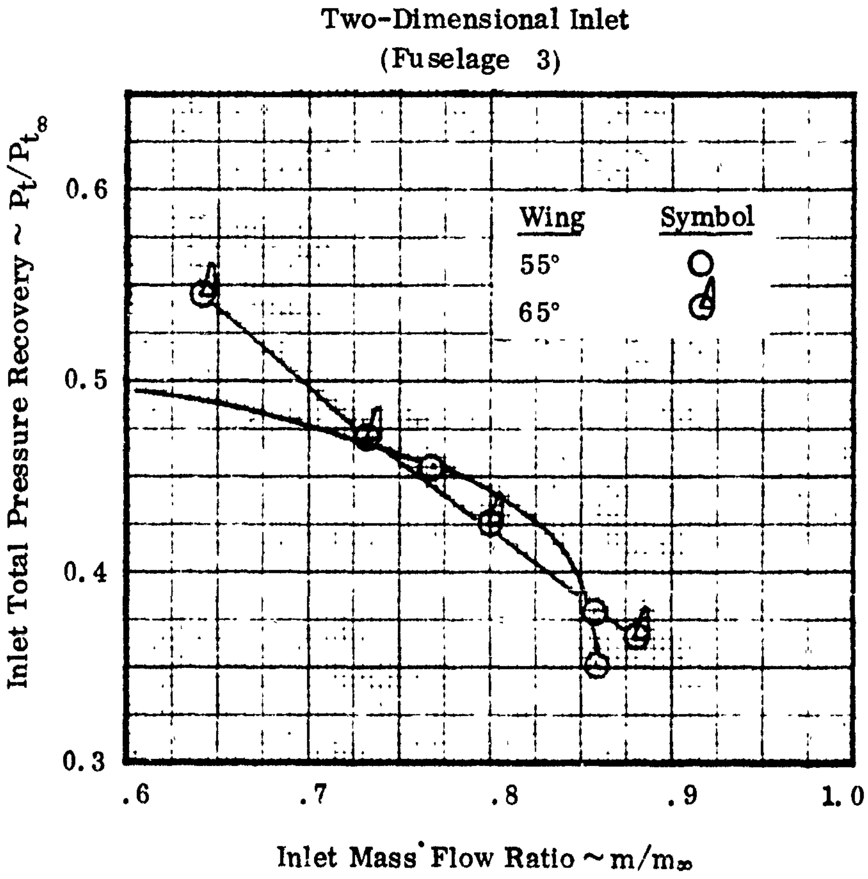

Figure 7-366. Comparison of Inlet Performance, Wing Effects
$M_\infty = 2.5$, $\alpha = -3°$

Two-Dimensional Inlet
(Fuselage 3)

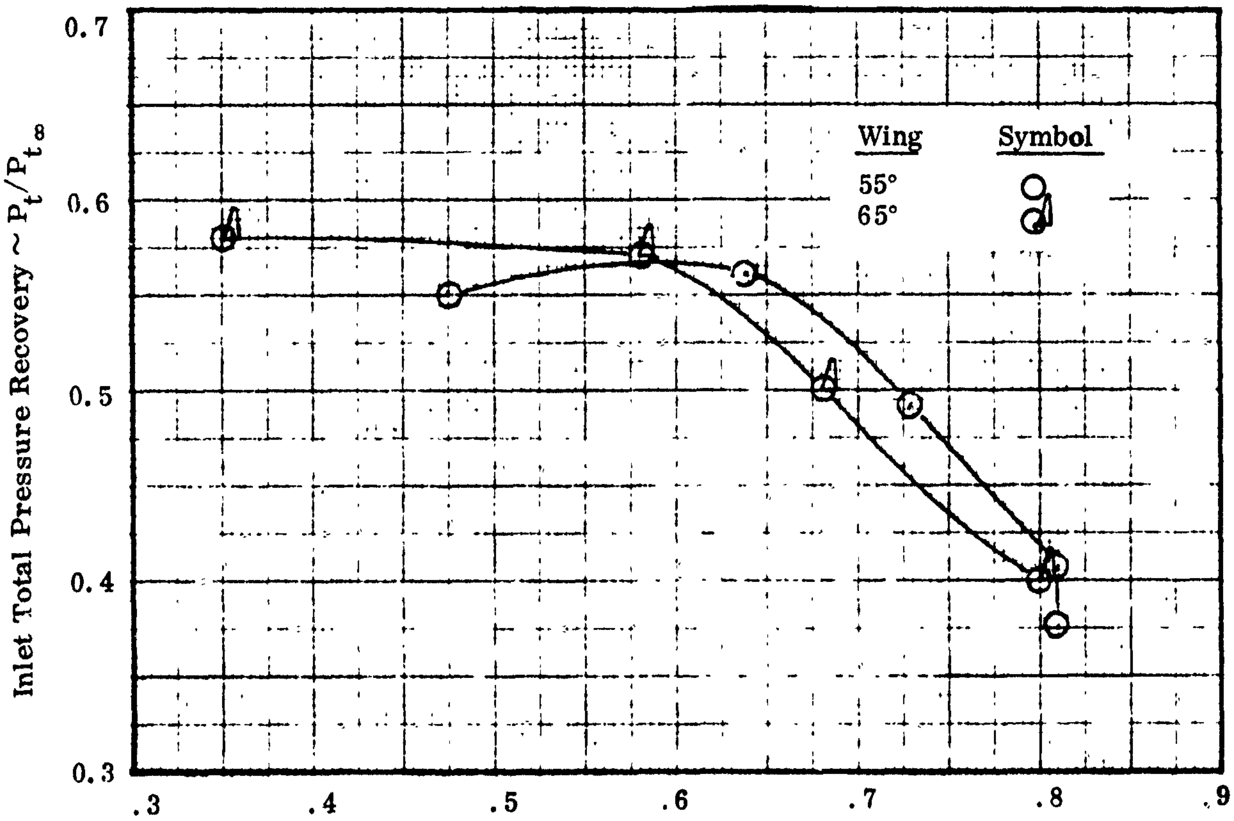

Inlet Mass Flow Ratio ~ m/m_∞

Figure 7-367. Comparison of Inlet Performance, Wing Effects
$M_\infty = 2.5$, $\alpha = 0°$

Two-Dimensional Inlet
(Fuselage 3)

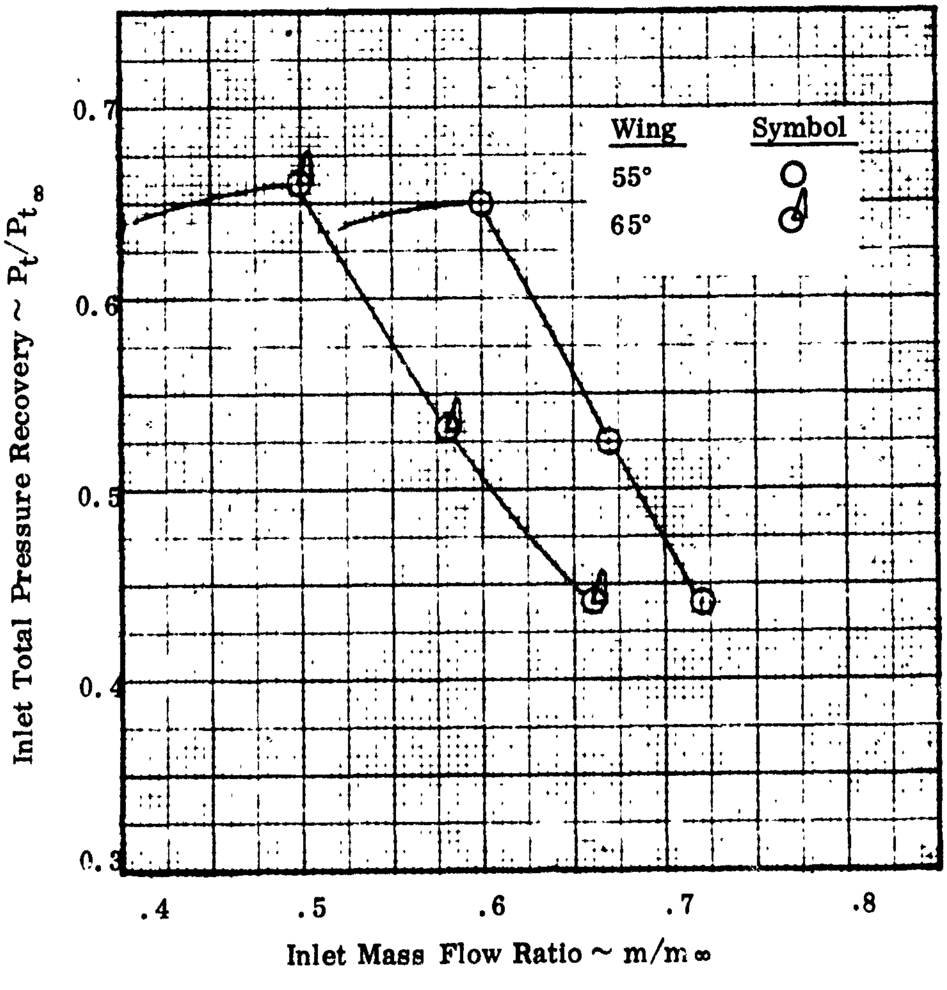

Figure 7-368. Comparison of Inlet Performance, Wing Effects
$M_\infty = 2.5$, $\alpha = 5°$

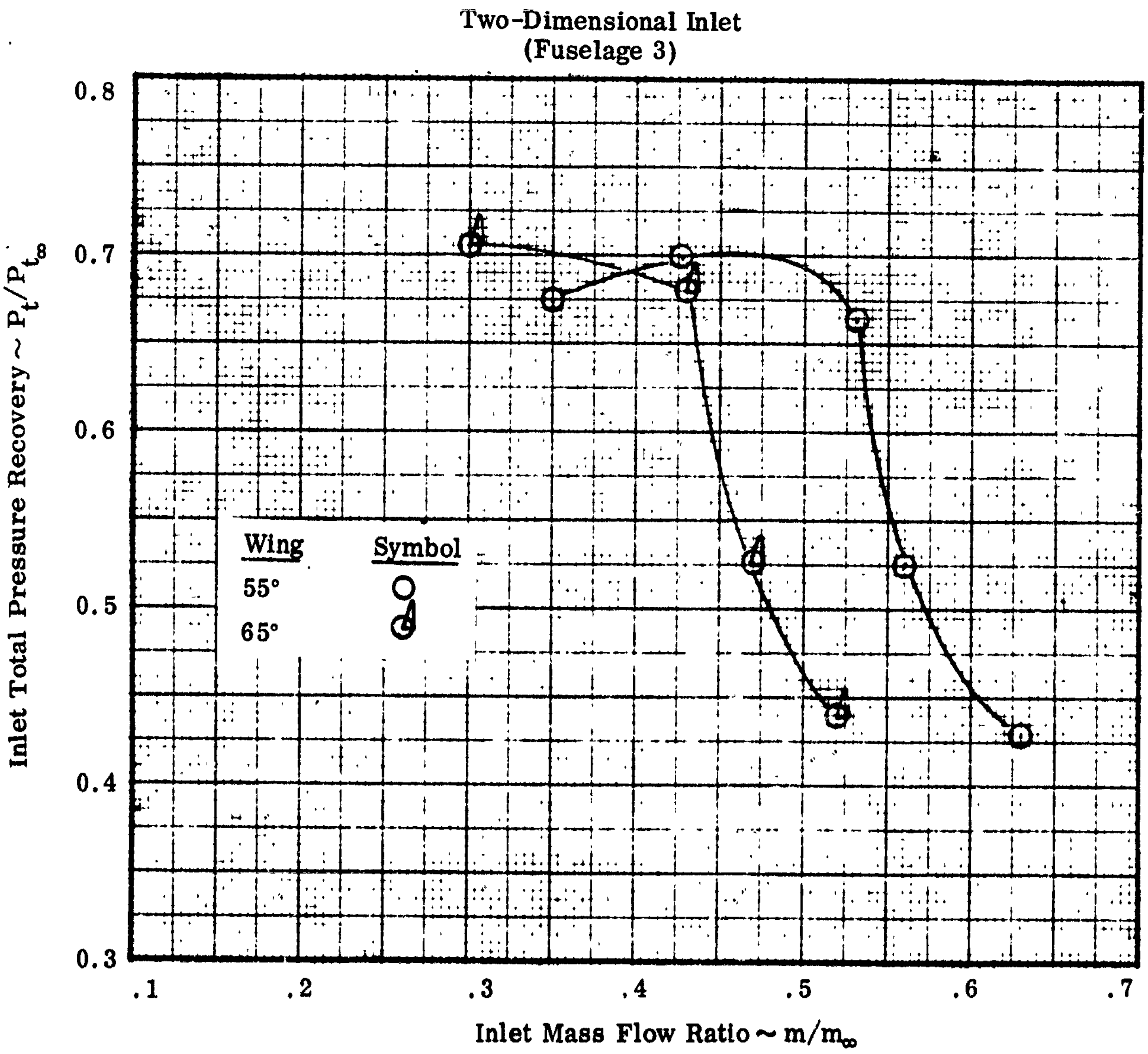

Figure 7-369. Comparison of Inlet Performance, Wing Effects

$M_\infty = 2.5,\ \alpha = 10°$

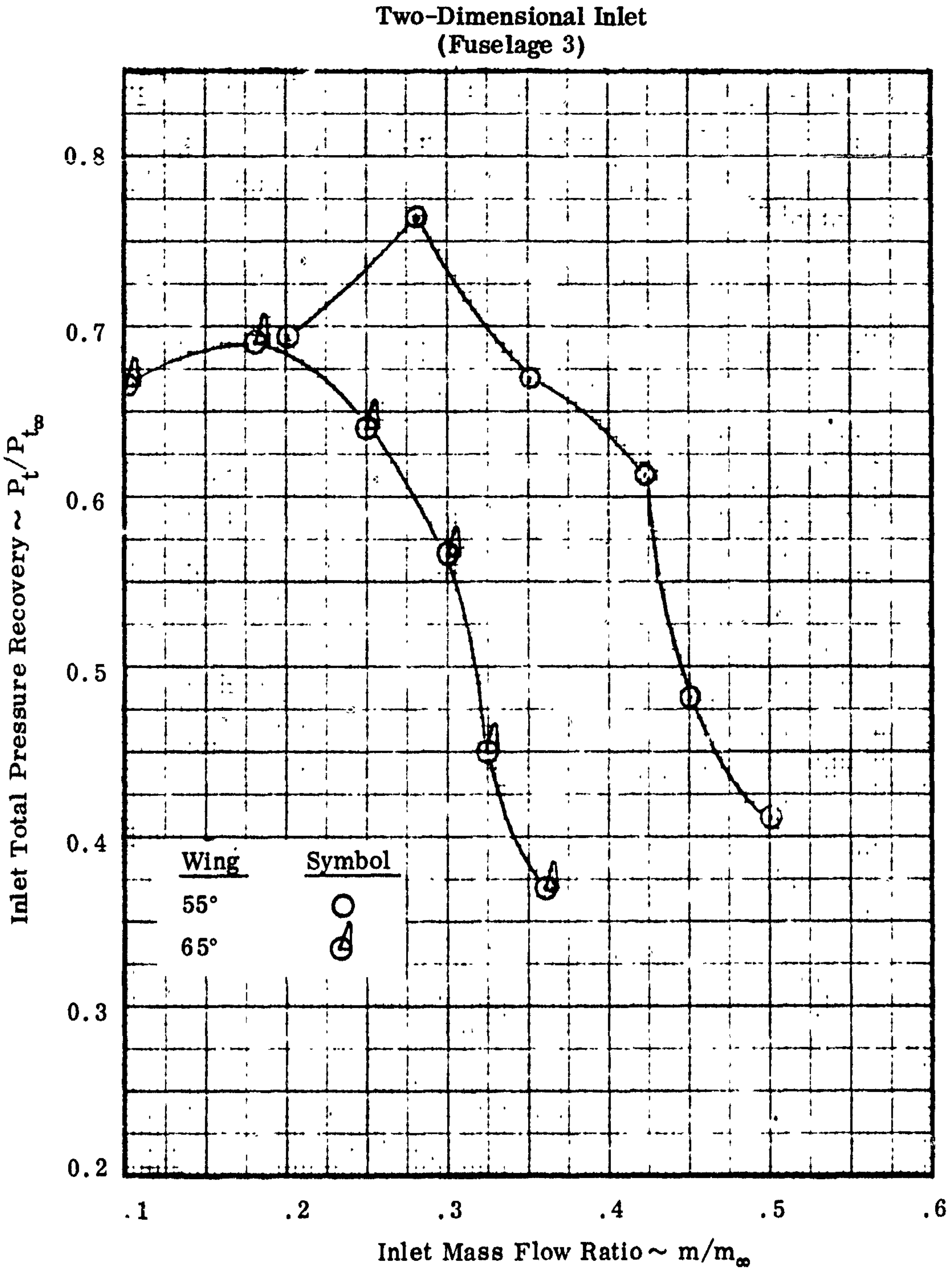

Figure 7-370. Comparison of Inlet Performance, Wing Effects

$M_\infty = 2.5$, $\alpha = 15°$

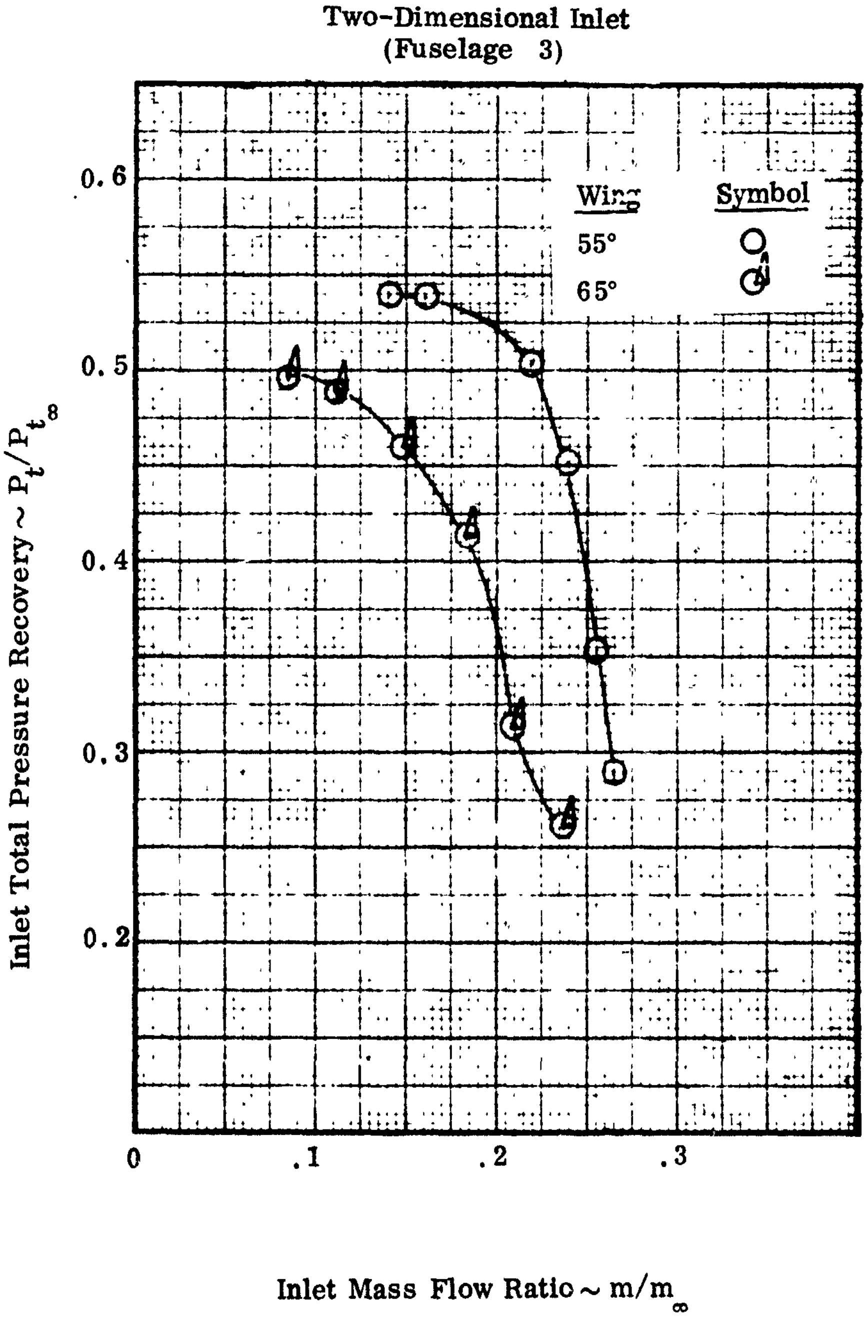

Figure 7-371. Comparison of Inlet Performance, Wing Effects $M_\infty = 2.5$, $\alpha = 20°$

During the test program the probes were tested individually to establish their characteristics, as a function of Mach number and pitch angle. In addition, each was tested in conjunction with a dummy probe of identical external geometry. During these latter tests the spacing between the two probes was varied to establish the minimum spacing before the onset of interference.

The test results lead to selection of a 0.125 inch diameter probe with an included cone angle of 40°. The bases for selection were 1) pressure settling times compatible with the proposed test facility recording capability and 2) good manufacturing tolerances. It was found that a reduction in cone included angle from 40° to 30°, for a 0.125 end probe diameter, introduced manufacturing difficulty, particularly in properly locating the four static taps for each probe on the conical surface. For the selected probe configuration, spacing distances as small as 0.4" were tested without the appearance of interference effects. However, the integration of spacing distance, probe travel, and survey grid size resulted in the selection of a probe spacing equal to 1.4 inches. This represented a very conservative spacing, in terms of avoiding probe-probe interference. The test results did permit a decision to position the probes as close as 0.4 inches from fuselage and wing surfaces during surveys of the local flow field.

During the fuselage test program the two vertical static taps of the probe closest to the fuselage were equipped with a pressure differential transducer. A visual readout was employed to monitor probe pitch angle. The availability of this readout also provided a means of determining the introduction of unusual effects, as the probes converged on the fuselage and/or wing surfaces. No unusual effects were observed during the test program.

A final determination of interference level was made by comparing fuselage and wing static pressure distributions up to both the forward and aft survey stations as a function of probe proximity. These comparisons were made at the two test Mach numbers most susceptible to interference namely 0.8 and 1.2, for both a small corner radius fuselage (#1) and a large corner radius fuselage (#2), across a wide angle of attack range, for 2 probe distances from the surface. In all cases the maximum deviation in local pressure, as a result of changing probe distance, was less than one percent. Further, the distributions seen were typical of the geometry Mach number conditions. Figures 7-372 through 7-376 depict this insensitivity to probe distance.

As a result of the design approach employed and the data subsequently obtained it was concluded that the level of probe induced interference was negligible.

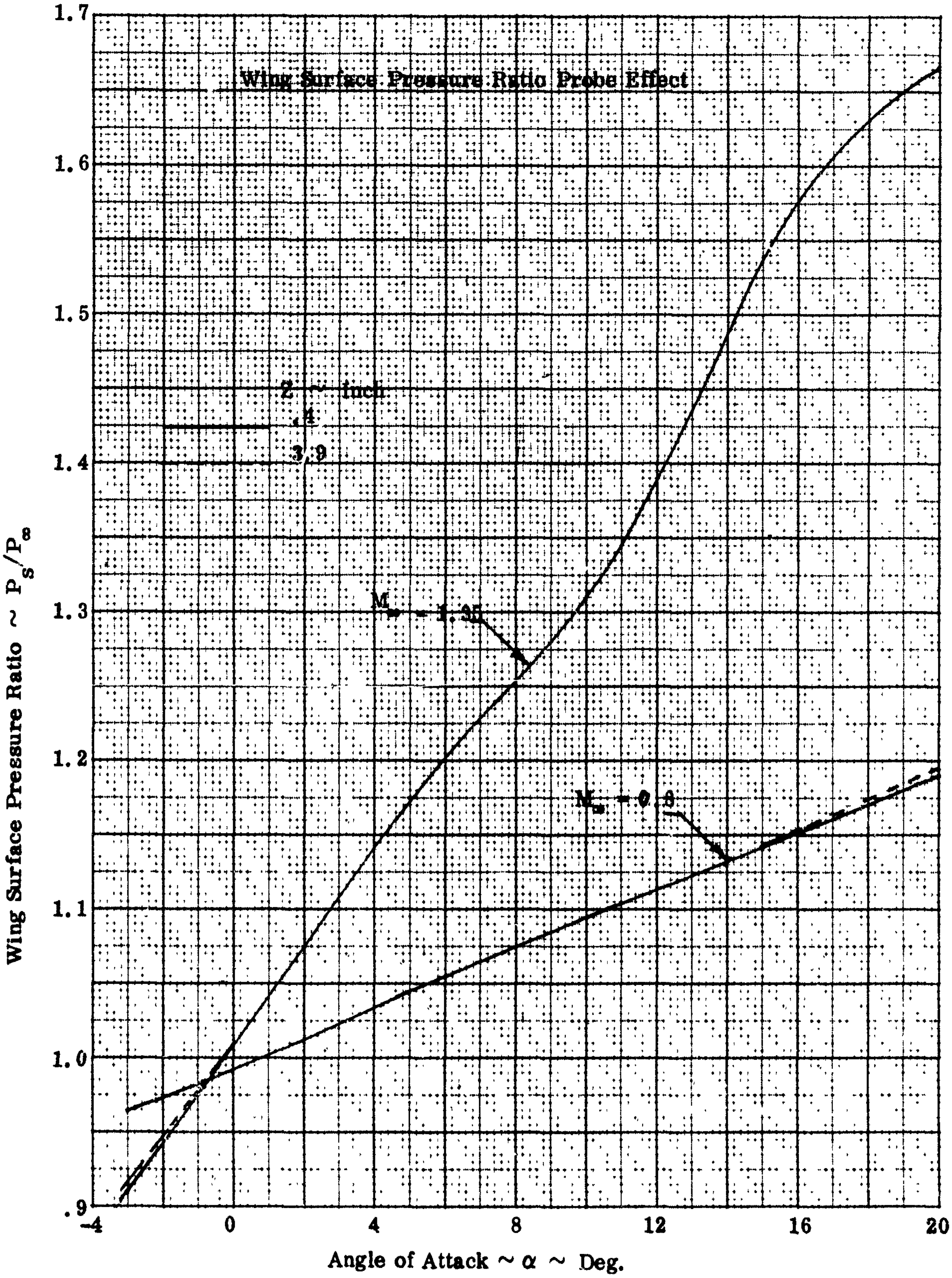

Figure 7-372. Wing Surface Pressure Ratio Probe Effect

Fuselage Surface Static Distribution in the Presence of the Probe Fuselage
Instrumentation Ray = 0°

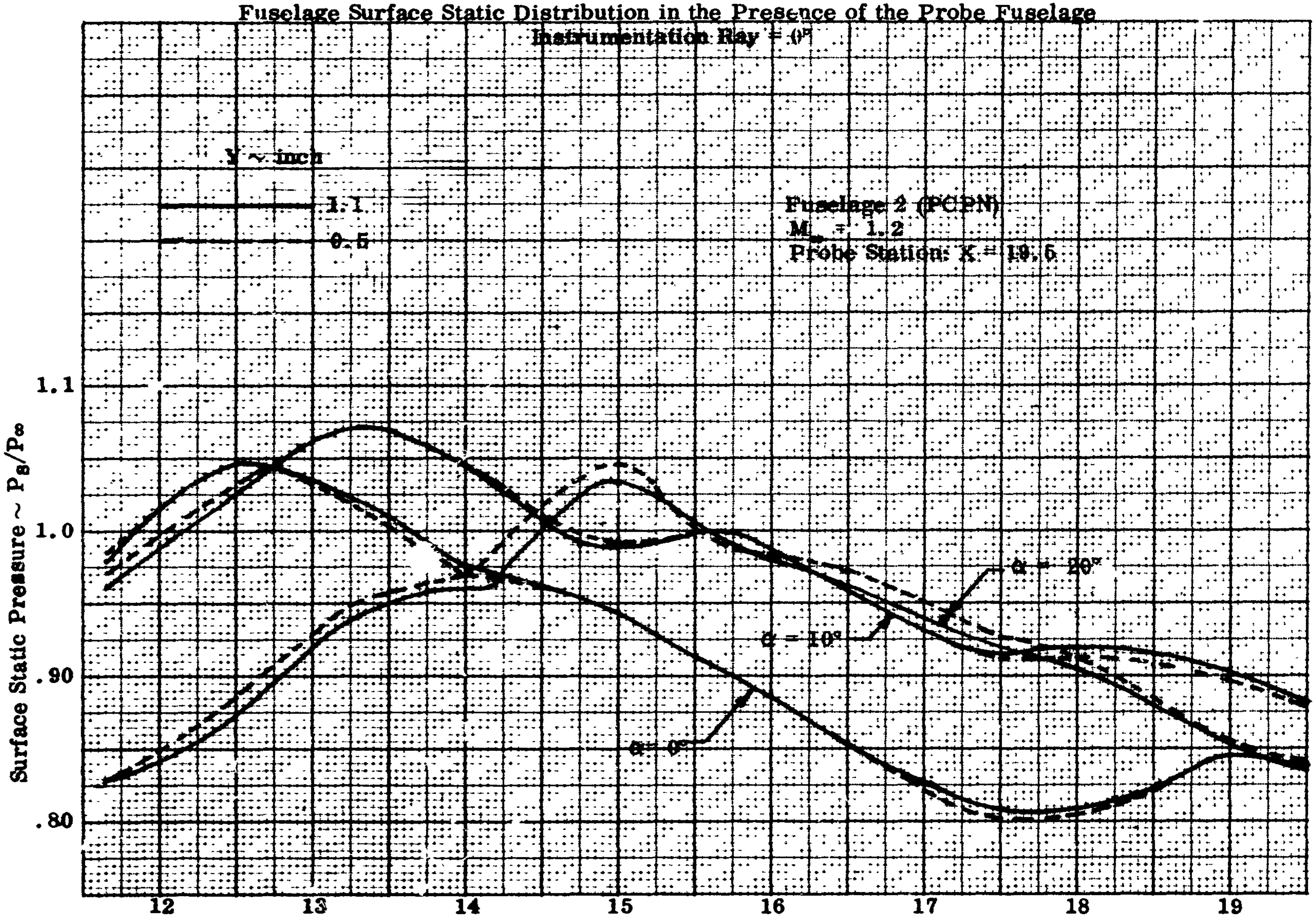

Longitudinal Distance ~X ~ Inch
Figure 7-373

Fuselage Surface Static Pressure Distribution in the Presence of the Probe

Fuselage Instrumentation Ray = 0°

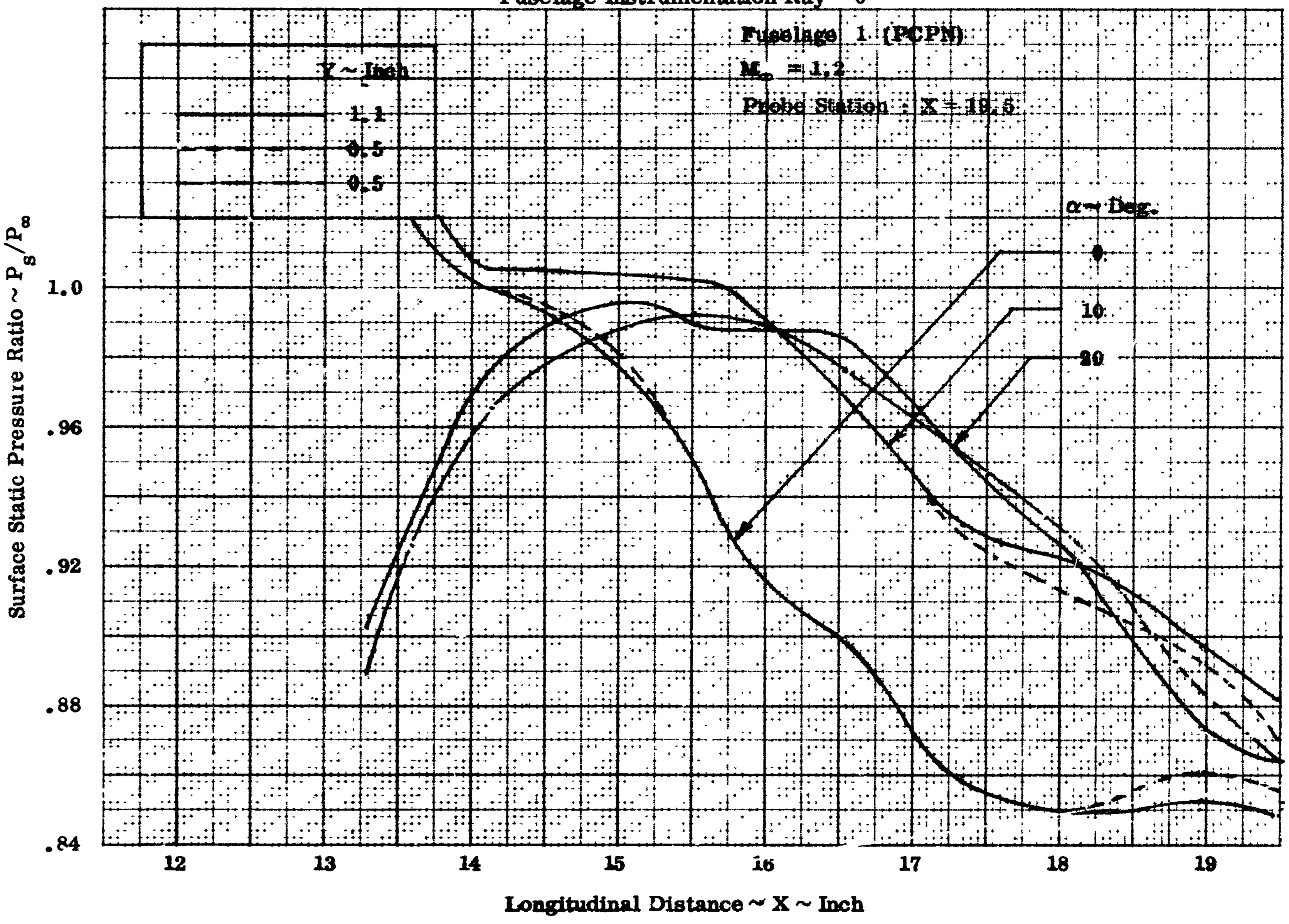

Figure 7-374

Fuselage Surface Static Pressure Distribution in the Presence of the Probe

Fuselage Instrumentation Ray = 0°

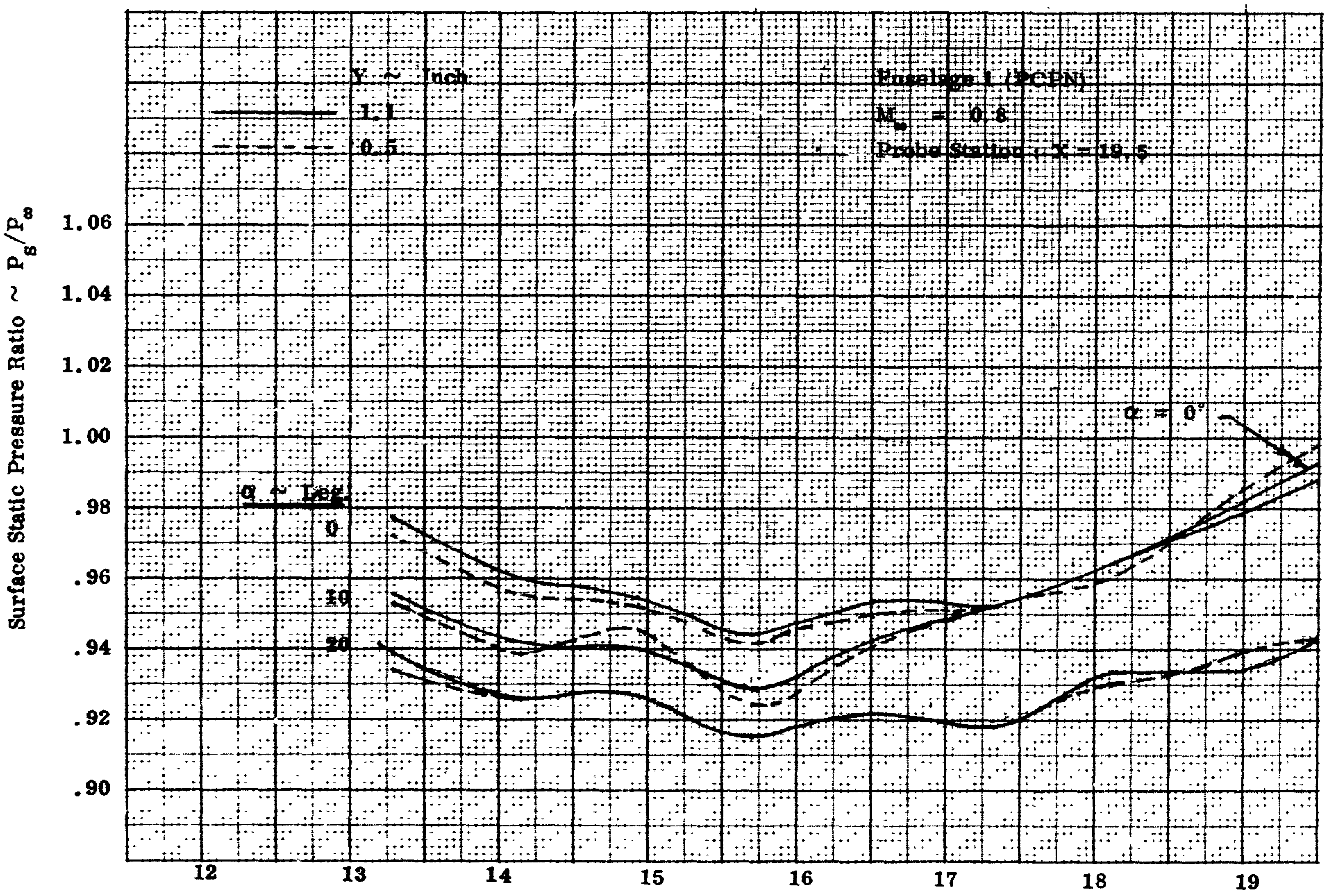

Figure 7-375

Fuselage Surface Static Pressure Distribution in the Presence of the Probe

Fuselage Instrumentation Ray = 0°

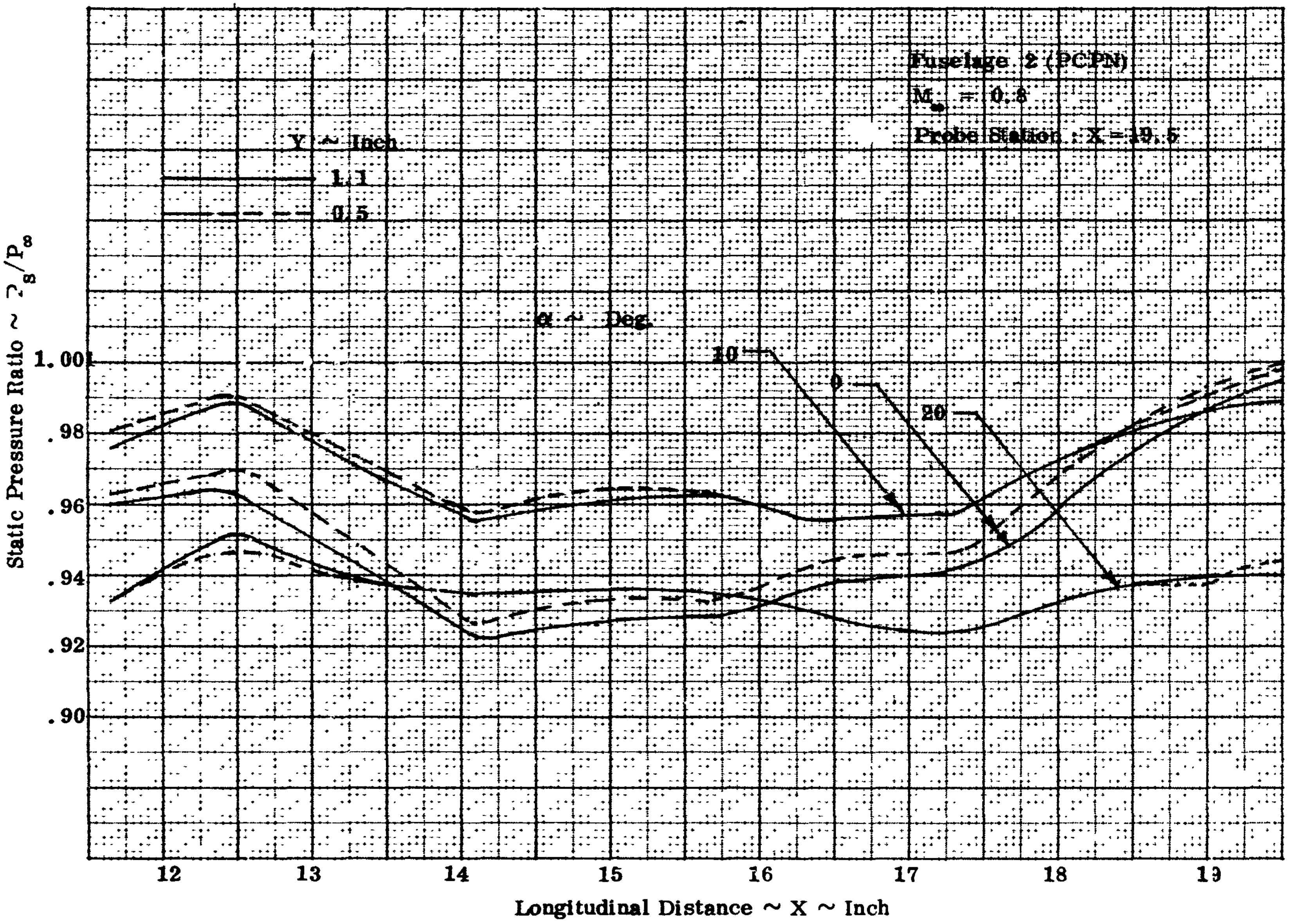

Figure 7-376

SECTION VIII

CONCLUSIONS

The local flow environment induced by the geometric characteristics of a highly maneuverable tactical aircraft and the impact these flow fields have upon integrated induction system performance are important considerations in the aircraft design process. It has been found that the influence of vehicle geometry upon performance is a function of flight condition, inlet concept and installation location.

It is, of course, true that the generalization of specific experimental data is the product of a particular interpretation. However, when utilized with the test data these interpretations can provide valuable insight. The objective of this section is to present a general summary of the major conclusions reached during the program.

Vehicle Characteristics

A statistical sampling of the geometric characteristics of 39 tactical aircraft indicated that similar mission requirements and subsystem design criteria lead to a similarity in the approach to the design of vehicle component geometry. This was particularly evident for the advanced systems analyzed for which performance goals and subsystem design criteria were rigorously specified. With the statistics clearly indicating representative geometric characteristics a strong foundation was provided upon which to base the selection of components for experimental investigation.

Analyses

The basic reference plane technique employed to estimate the vehicle induced flow fields provided reasonable preliminary design estimates at low vehicle angles of attack. However, for angles of attack above approximately 10°, where the cross flow gradients become significant, the method proved unacceptable. Based upon the comparison of theory and experiment, a semi-empirical modification to the analytical technique was developed that yielded significantly improved estimates of the flow field characteristics. In addition, an exact reference plane technique was developed. The estimates obtained using this method proved quite good across the entire angle of attack range.

Two classical inlet concepts were designed and tested during the program. Conventional design techniques were used to select the inlet geometry and predict the performance levels of these inlets. A comparison of the isolated inlet test data with the predicted inlet performance indicated that these straightforward computational procedures generate excellent estimates of inlet performance across most of the operating spectrum. Correlation of inlet total pressure recovery decreased with the onset of inlet oblique shock detachment. The application of a sonic wedge correction proved successful in improving the agreement in this regime. The correlation of inlet mass flow ratio decreased as a function of shock off lip operation due to the curvature of the boundary slipline, particularly with the axisymmetric inlet system. An improvement in agreement can be obtained with a technique to average the thermodynamic properties across that portion of the inviscid shock layer ingested.

Nose, Canopy, and Wing Effects

For the forward fuselage station surveyed (30% of the overall aircraft length) variations in nose and canopy geometry induced variations in the attendant flow field. The influence of these components upon the composition of the flow field was found to be a function of the nose shape and the canopy shape and frontal area. For the aft fuselage station surveyed (50% of the overall aircraft length) the presence of the wing did influence the composition of the local flow field. The level of this influence increased directly with angle of attack. However, a variation in wing sweep did not produce an appreciable change in the local flow field composition.

The impact of these geometry induced variations in the flow field upon inlet performance was found to be a direct function of Mach number and inlet shock system balance. At subsonic and transonic Mach numbers the inherent total pressure recovery is quite high and the inlet is insensitive to small variations in the flow field. Additionally, the inlet throat is essentially choked at these conditions, making the inlet mass flow limited. Therefore, variations in approaching streamline angularity serving to increase or decrease the inlet capture area do not produce a change in ingested mass flow. However, at the supersonic conditions the inlet throat is operating unchoked and variations in the approaching flow do produce variations in ingested mass flow and total pressure recovery. These variations are a function of the effect that the precompression induced by these components has upon the inlet shock structure. For those test conditions where the inlet shock system is unbalanced the additional compression offered by a blunter nose, larger canopy and/or lower wing sweep, tends to improve inlet performance. Conversely, with a balanced inlet shock system the lower drag of a finer nose, smaller canopy, and/or higher wing sweep is preferable to the insignificant inlet performance gains. Additionally, factors such as nose droop and canopy location provide an aerodynamic means for inhibiting variations in the local flow environment during an angle of attack excursion. The wing, of course, provides a physical constraint upon the flow and in effect adds an additional compression ramp to the flow diffusion process. The work and efficiency of this additional ramp are functions of angle of attack. The potential improvement in performance offered by the inclusion of an additional compression surface is a function of Mach number and the basic inlet design. For the two inlet concepts tested, both of which were N = 3 systems, the addition of the wing produced performance gains above a free stream Mach number of 1.8.

Fuselage Corner Effects

A negative vehicle angle of attack produces a downwash flow field at the forward fuselage station. The negative magnitude of this downwash increases directly with fuselage corner radius. Conversely, a positive vehicle angle of attack results on an upwash flow field. For this case the magnitude of the upwash increases inversely with fuselage corner radius.

At the aft fuselage station the wing dictates flow field angularity and the flow fields of all fuselages appear similar. However, the level of flow field sidewash is a function of fuselage corner radius, becoming more negative with increasing fuselage corner radius.

Performance of the two-dimensional inlet, installed at the forward fuselage station, improved directly with increasing corner radius and gentleness of corner development as a result of the more uniform flow field induced by these larger corner configurations.

At the aft fuselage station the wing directs the fuselage boundary layer toward the inlet. The physical compatibility of fuselage and inlet and the resultant fuselage boundary layer diverter become prime factors dictating the selection of a small fuselage corner radius with a gentle corner development as best for inlet performance.

REFERENCES

1. Davis, O. H., and Mitchell, G. A.; "Performance of a Mach Number 3.0 Design Axisymmetric Double-Cone External-Compression Inlet in Mach Number Range 1.97 to 0.79. "NASA TMX-154, April 1960.

2. Allen, J. L. and Mitchell, G. A.; "Performance of a Mach Number 3.0 Design Axisymmetric Double-Cone External-Compression Inlet in Mach Number Range 2.07 to 1.48." NASA Memo 12-22-58E, January 1959

3. Allen, J. L., Davis, O. H. and Mitchell, G. A.; "Performance Summary and Analysis of a Mach 3.0 Design Axisymmetric All-External-Compression Double-Cone Inlet from Mach Number 3.0 to 0.8." NASA TM X-149, April 1960.

4. Connors, J. F., Lowell, J. C., and Wise, G. A.; "Effects of Internal Area Distribution, Spike Translation and Throat Boundary-Layer Control on Performance of a Double-Cone Axisymmetric Inlet at Mach Numbers from 3.0 to 2.0." NACA RME57F03, April, 1957.

5. Connors, J. F., Wise, G. A., and Lovell, J. C.; "Investigation of Translating Double-Cone Axisymmetric Inlets with Cowl Areas 40 to 20 Percent of Maximum at Mach Numbers from 3.0 to 2.0." NACA RME 57C06, May 1957.

6. Ames Research Staff "Equations and Tables, and Charts for Compressible Flow," Ames Aeronautical Laboratory, Moffett Field, California TN 1135, 1935.

7. Ferri, Antonio, "Elements of Aerodynamics of Supersonic Flows," MacMillian Company, New York, 1949, pp. 236-260.

8. Savin, R. C., "Application of the Generalized Shock-Expansion Method to Inclined Bodies of Revolution Traveling at High Supersonic Air Speeds," NACA TN3349, April 1955.

9. Jacobs, W. F. "A Simplified Approximate Method for the Calculation of the Pressure Around Conical Bodies of Arbitrary Shape in Supersonic Hypersonic Flow," Journal of Aerospace Sciences, Volume 28, Number 12, pp. 987-988, December 1961.

10. Sanator, R. J. et al, "An Experimental and Theoretical Investigation of Inlets for Supersonic Combustion Ramjets," Air Force Flight Dynamics Laboratory, FDL TDR 64-119, October 1964.

11. Liming, Roy A., "Practical Analytic Geometry with Application to Aircraft," The MacMillian Co., New York 1944.

APPENDIX A

THIS REPORT HAS BEEN DELIMITED
AND CLEARED FOR PUBLIC RELEASE
UNDER DOD DIRECTIVE 5200.20 AND
NO RESTRICTIONS ARE IMPOSED UPON
ITS USE AND DISCLOSURE.

DISTRIBUTION STATEMENT A

APPROVED FOR PUBLIC RELEASE;
DISTRIBUTION UNLIMITED.

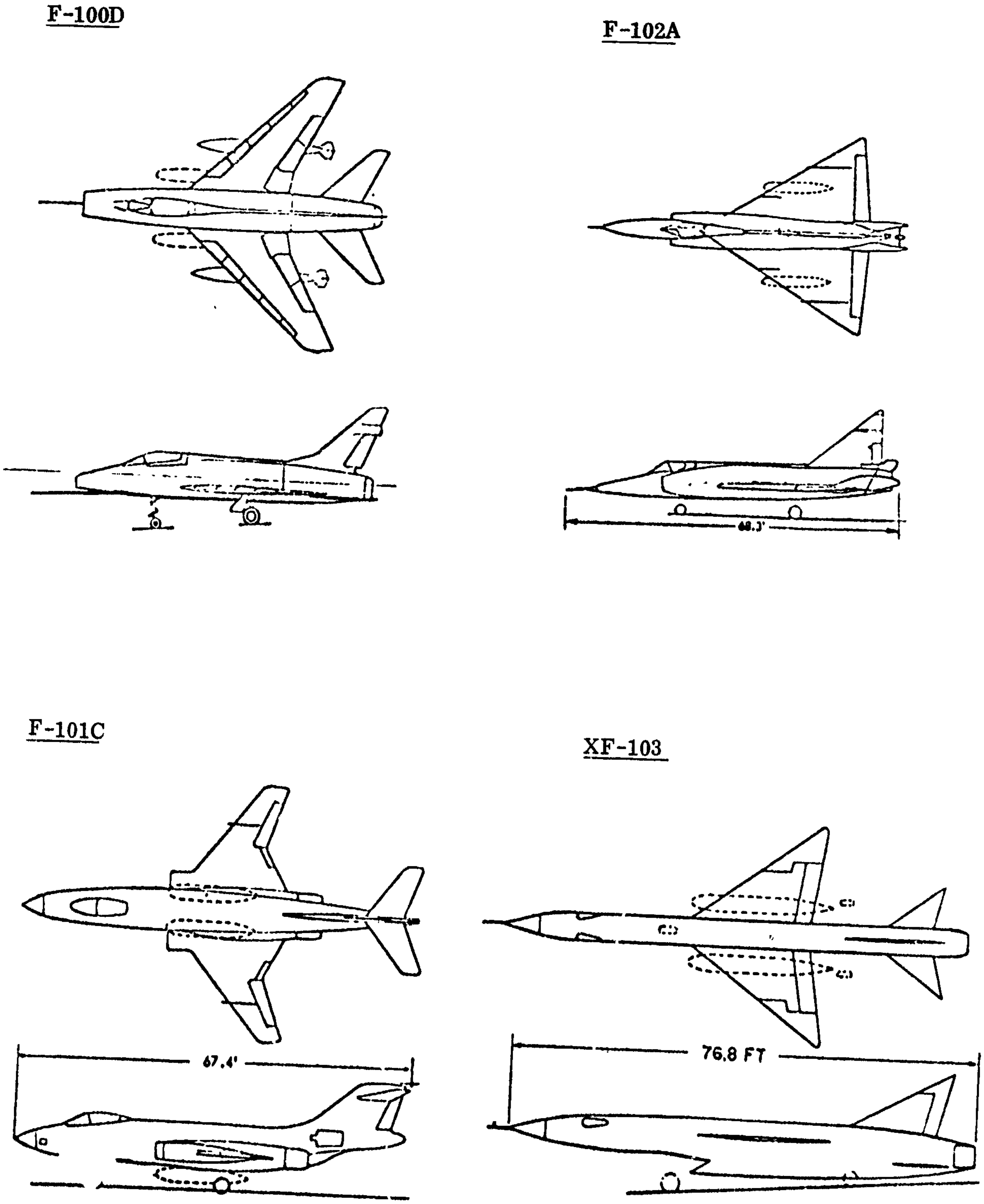

F-100D

F-102A

F-101C

XF-103

68.3'
67.4'
76.8 FT

Figure A-1. Surveyed Aircraft Configurations

F-104G

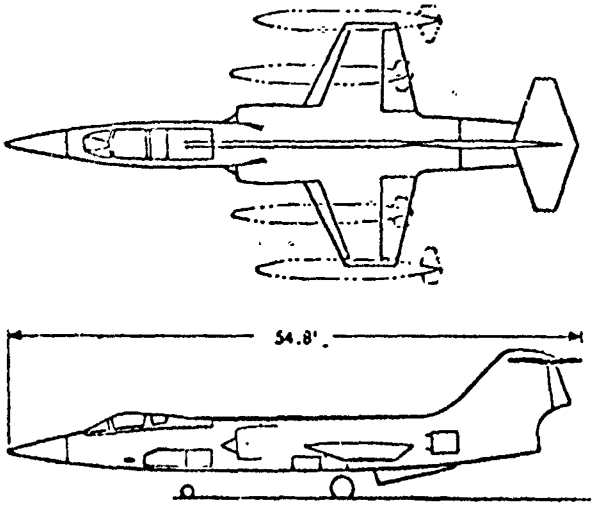

F-105D

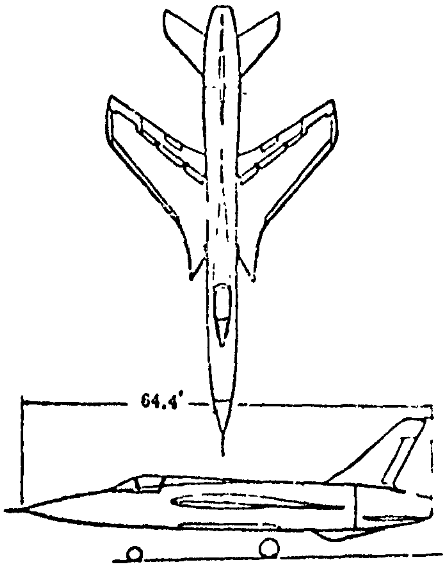

F-106B

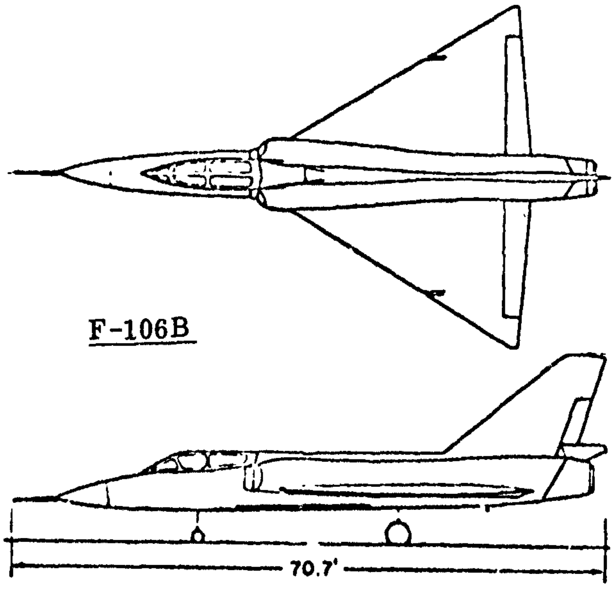

F-5B

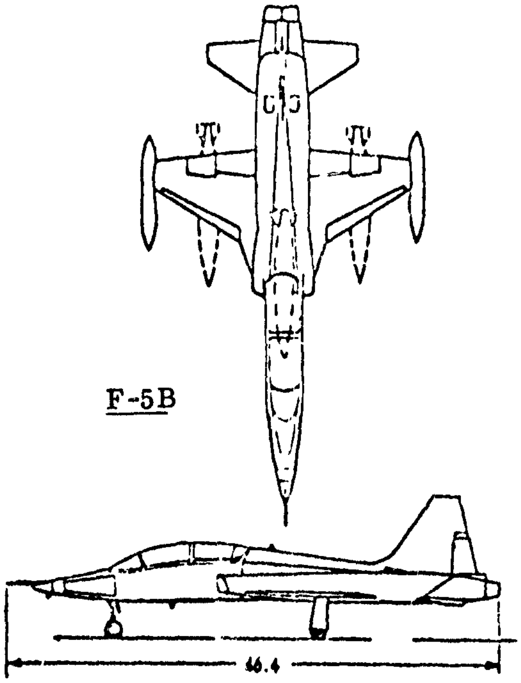

Figure A-1, Continued. Surveyed Aircraft Configurations

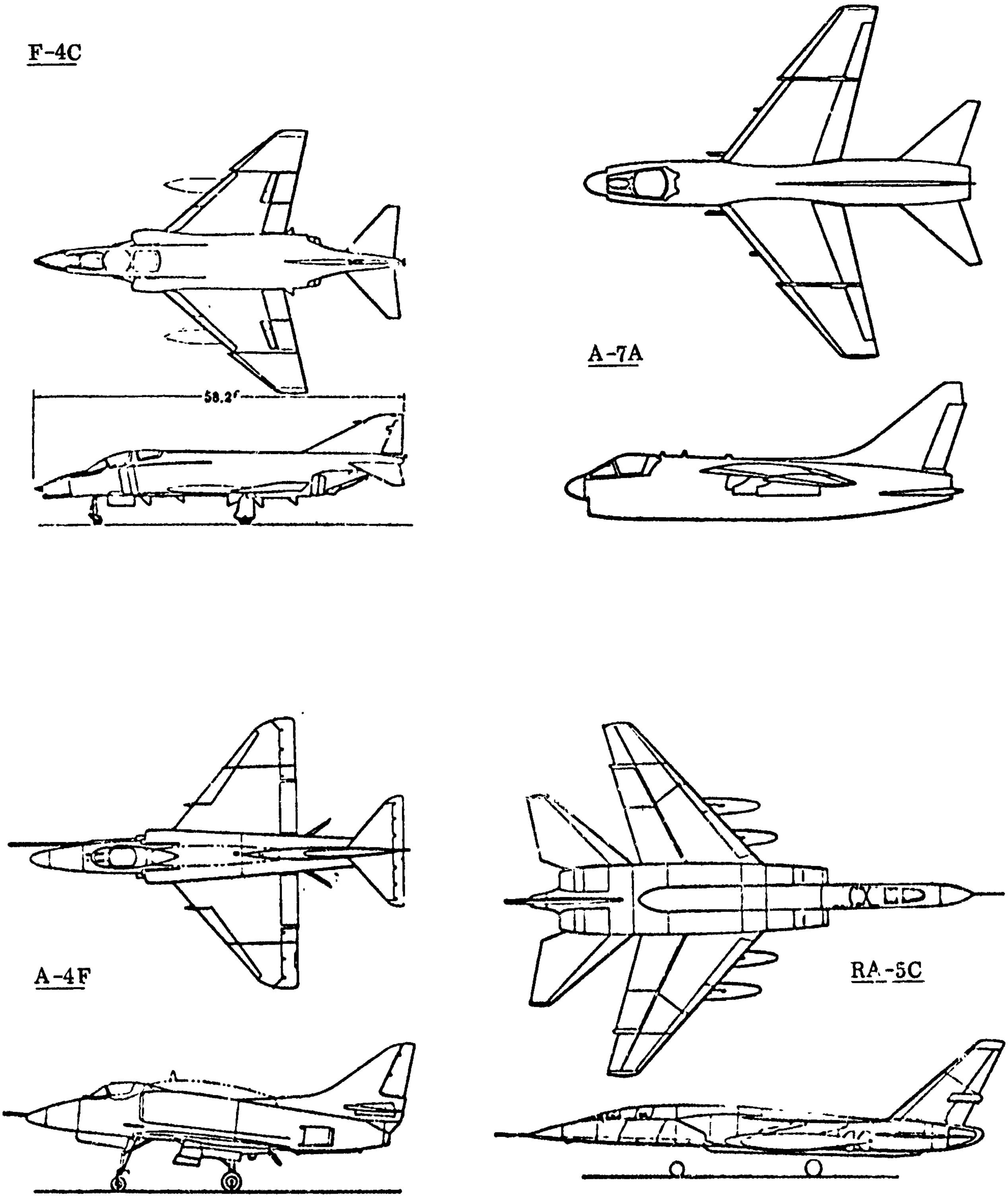

F-4C

A-7A

A-4F

RA-5C

Figure A-1, Continued. Surveyed Aircraft Configurations

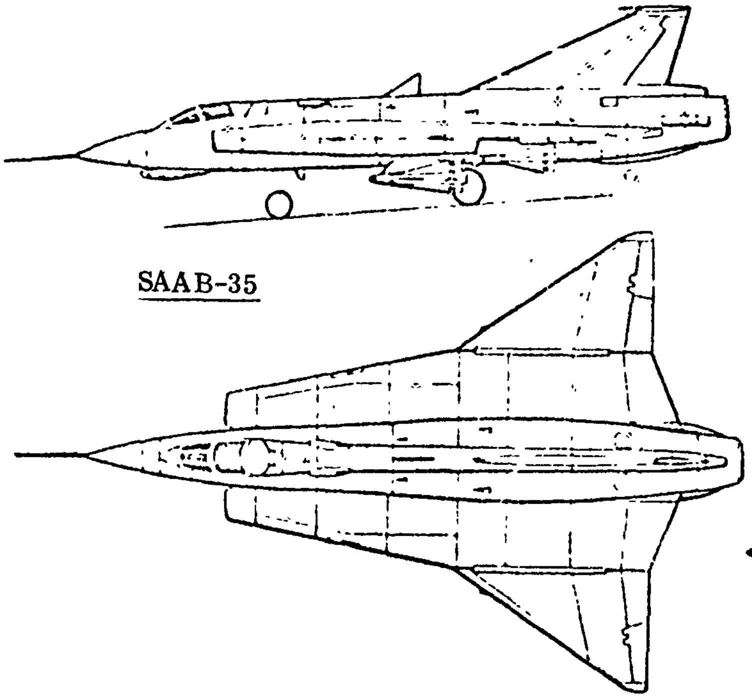

SAAB-35

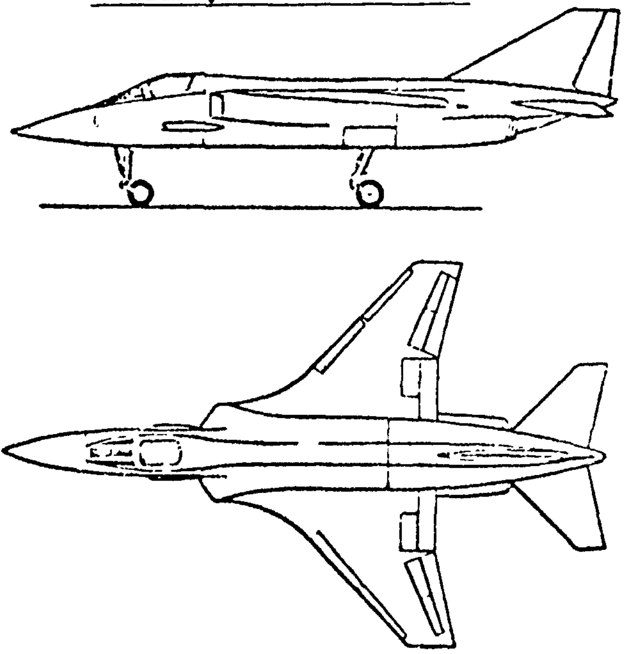

BRITISH/FRENCH JAGUAR

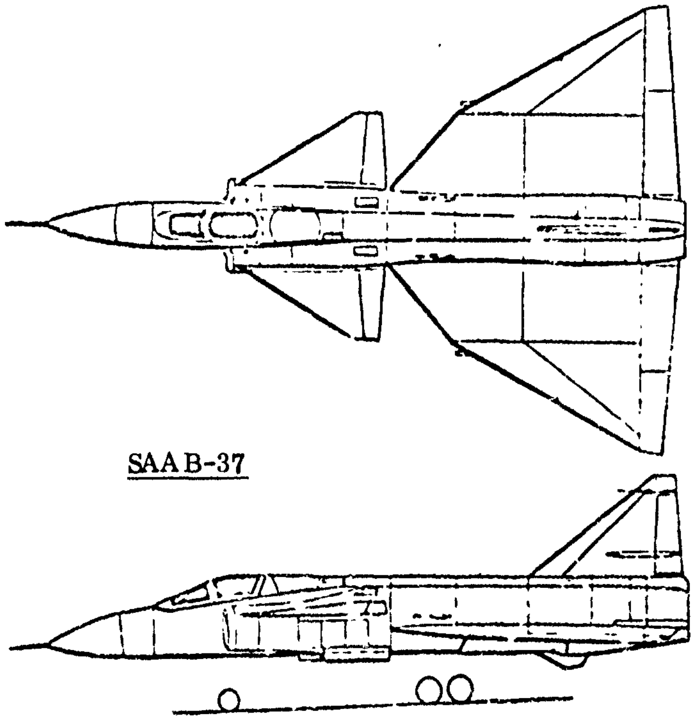

SAAB-37

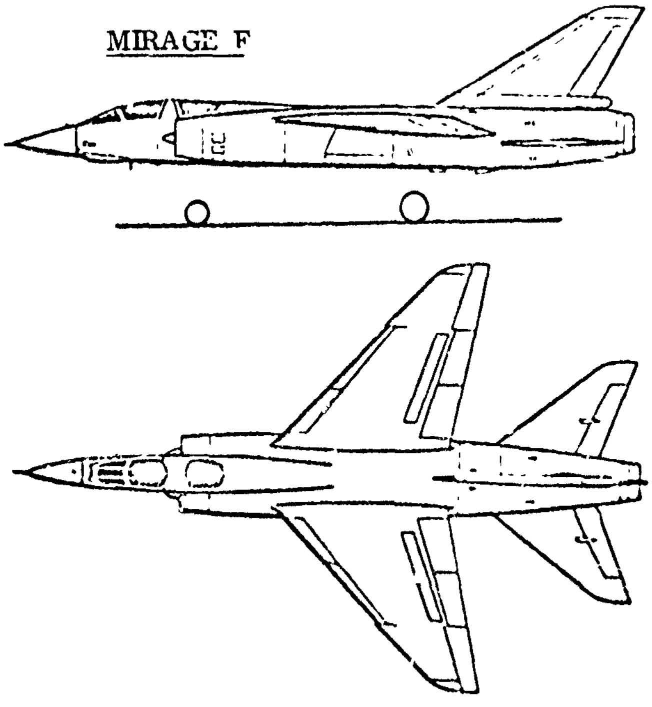

MIRAGE F

Figure A-1, Continued. Surveyed Aircraft Configurations

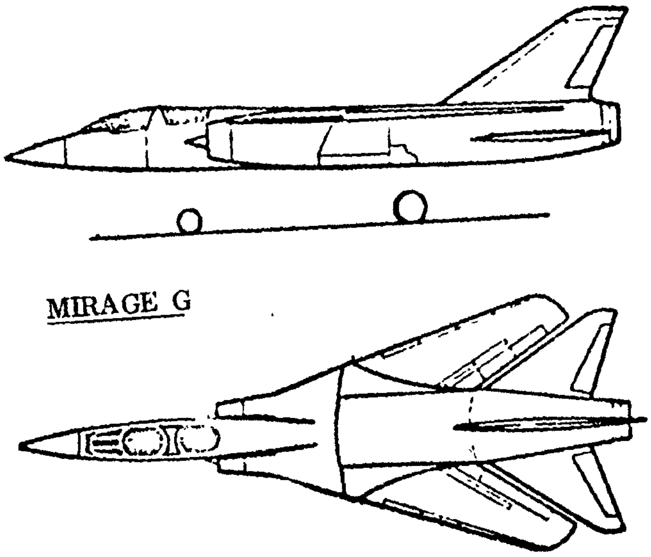

MIRAGE G

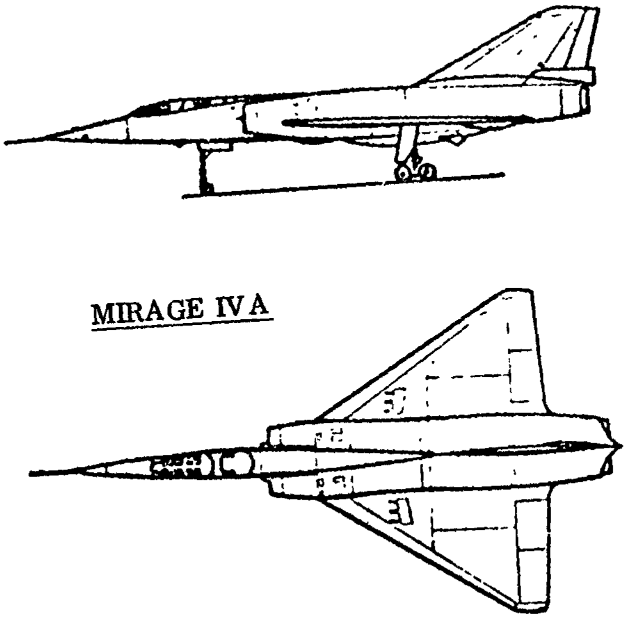

MIRAGE IV A

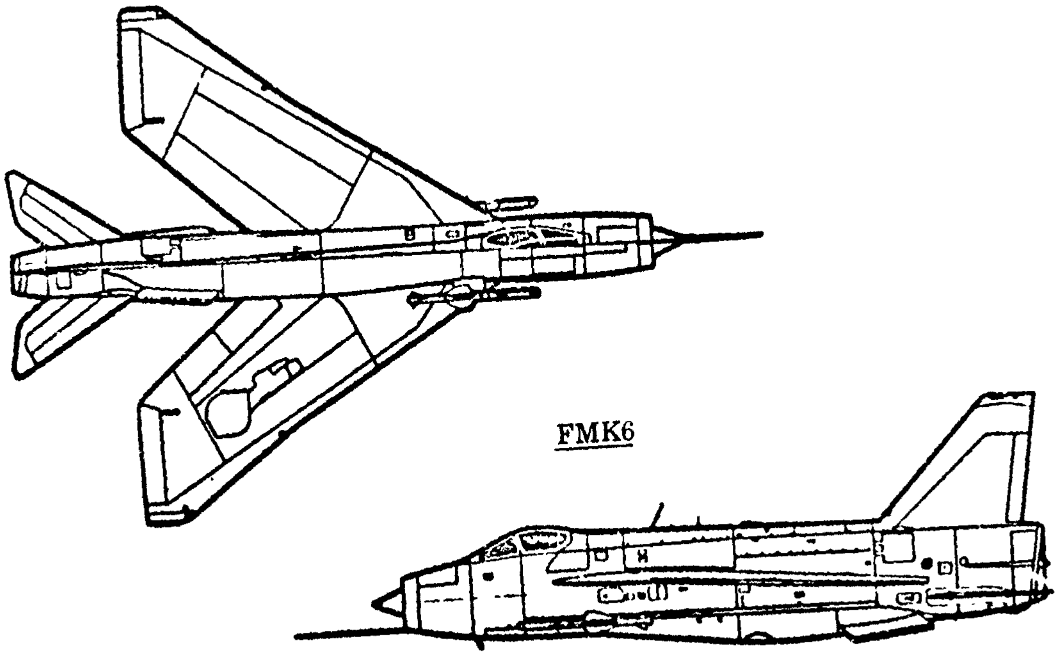

FMK6

Figure A-1, Continued. Surveyed Aircraft Configurations

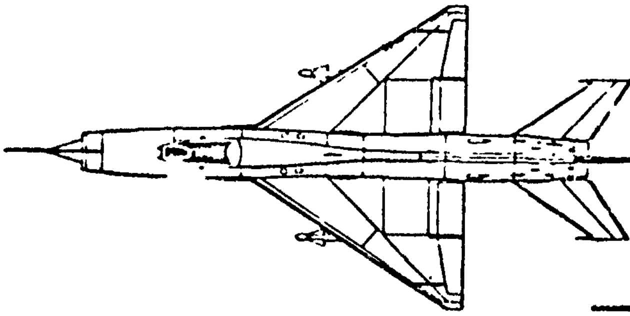

USSR FISHBED

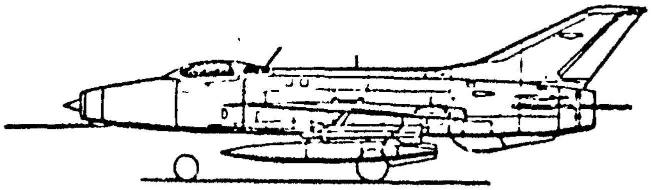

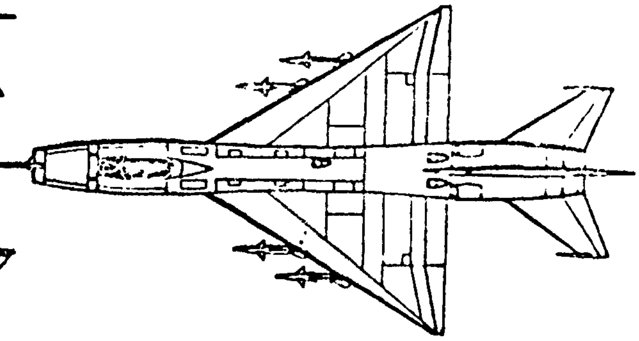

USSR FISHPOT

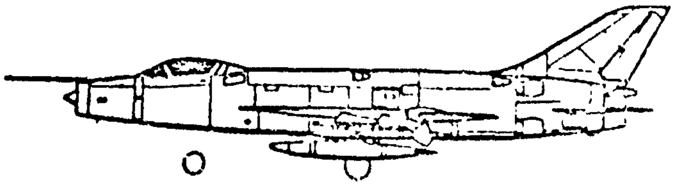

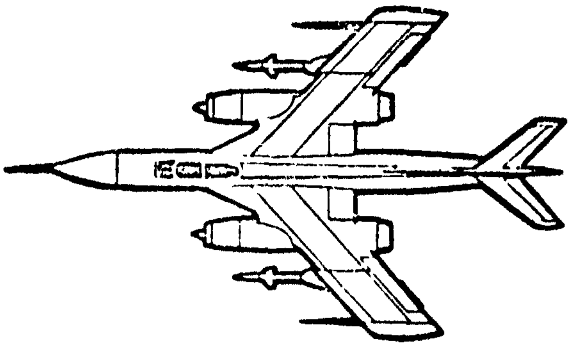

USSR FIREBAR

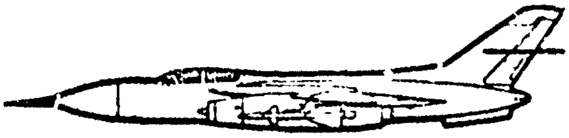

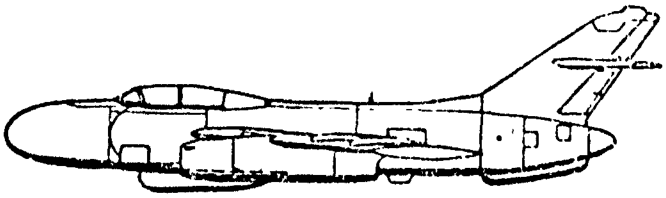

USSR FLASHLIGHT

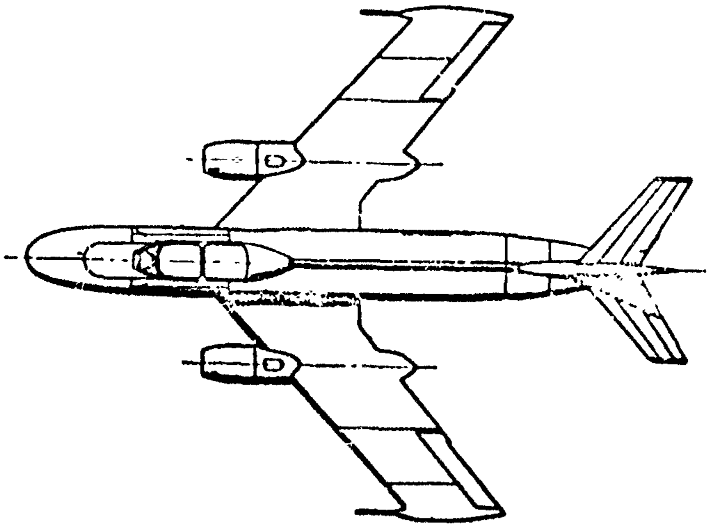

Figure A-1, Continued. Surveyed Aircraft Configurations

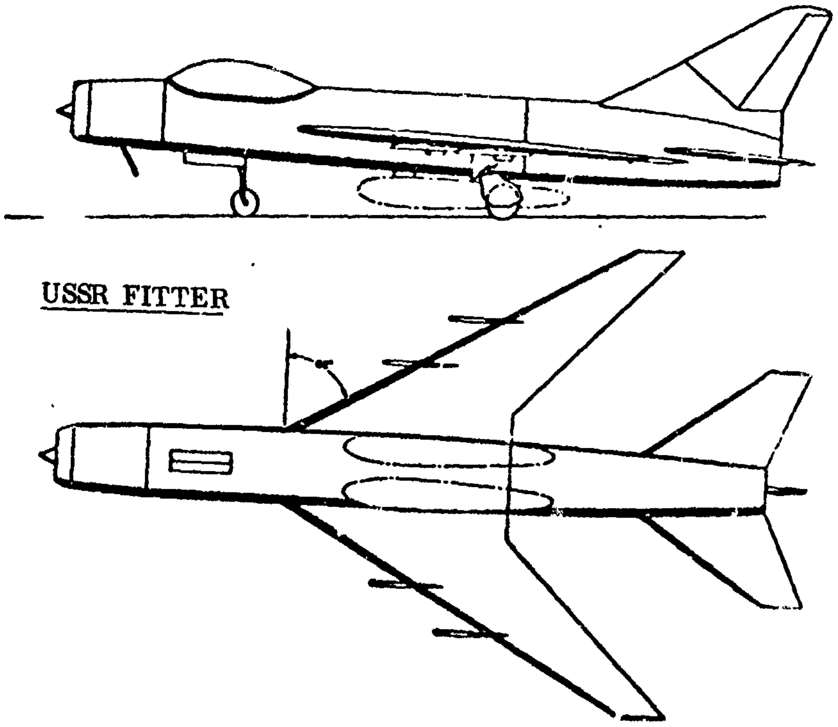

USSR FITTER

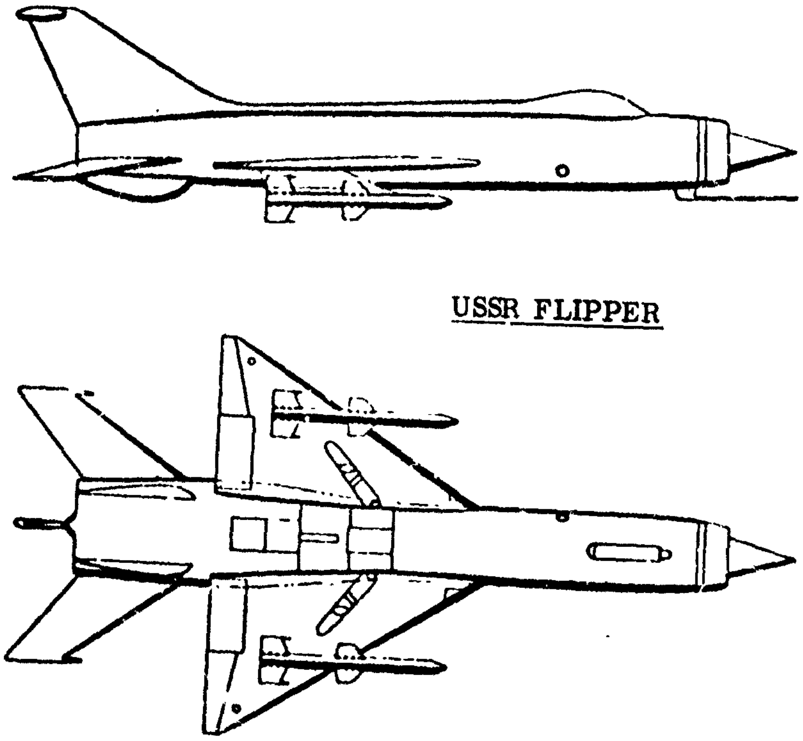

USSR FLIPPER

Figure A-1, Continued. Surveyed Aircraft Configurations

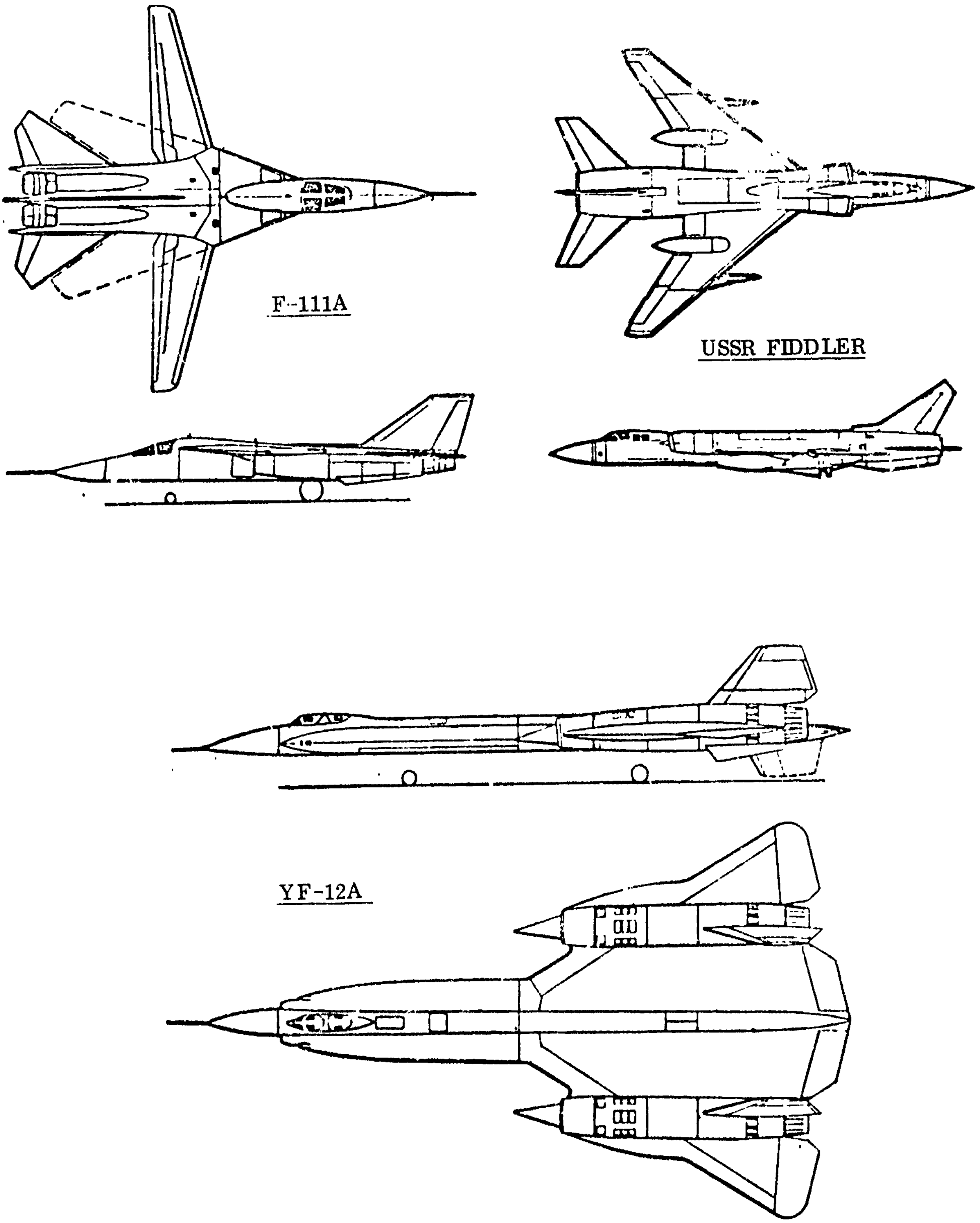
F-111A
USSR FIDDLER
YF-12A

Figure A-1, Concluded. Surveyed Aircraft Configurations

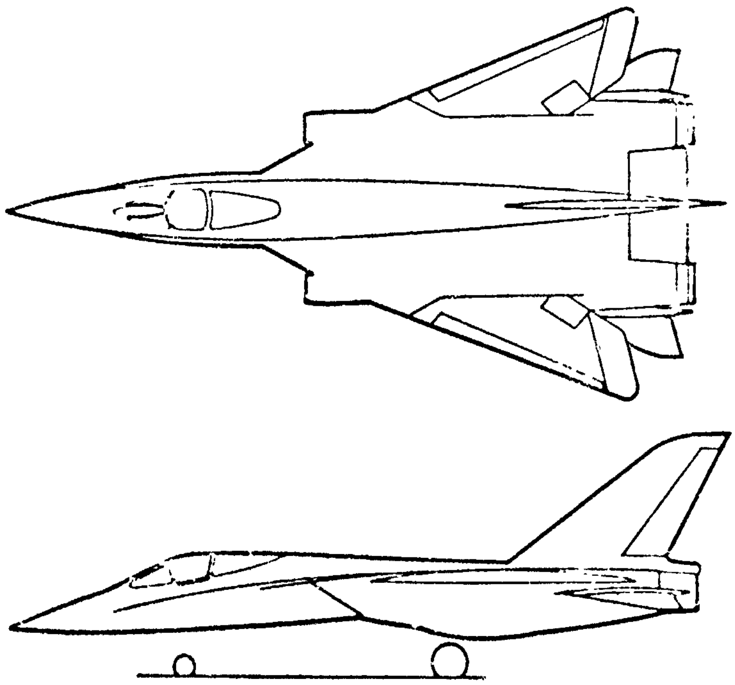

FX-6

FX-8

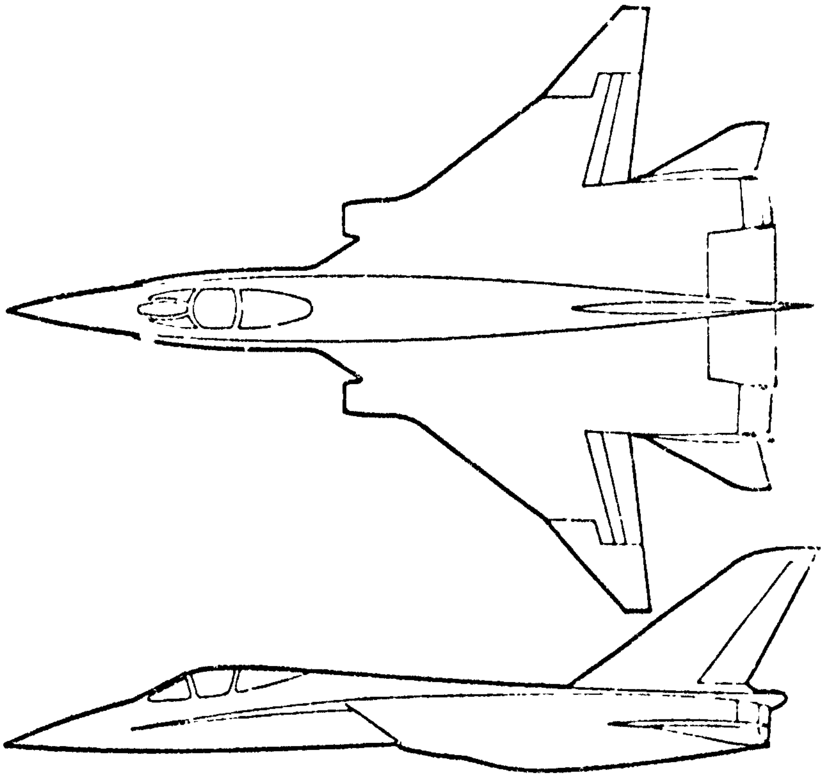

Figure A-2. Surveyed Aircraft Configurations

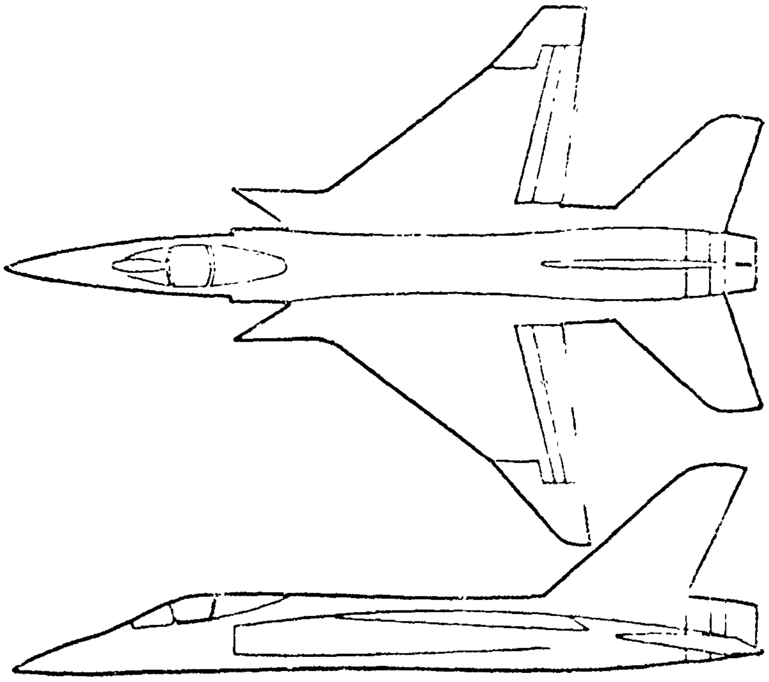

FX-10

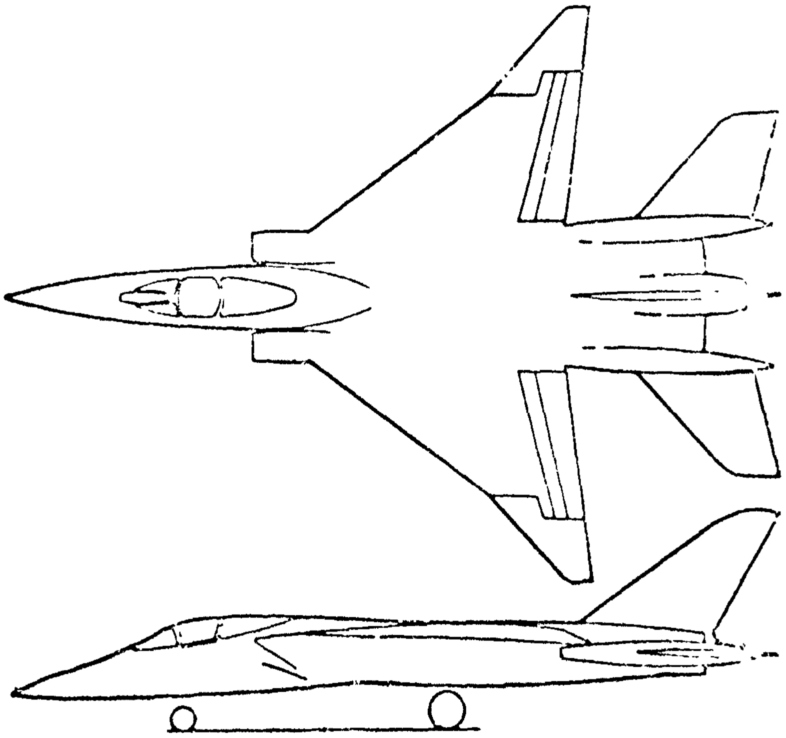

FX-11

Figure A-2, Continued. Surveyed Aircraft Configurations

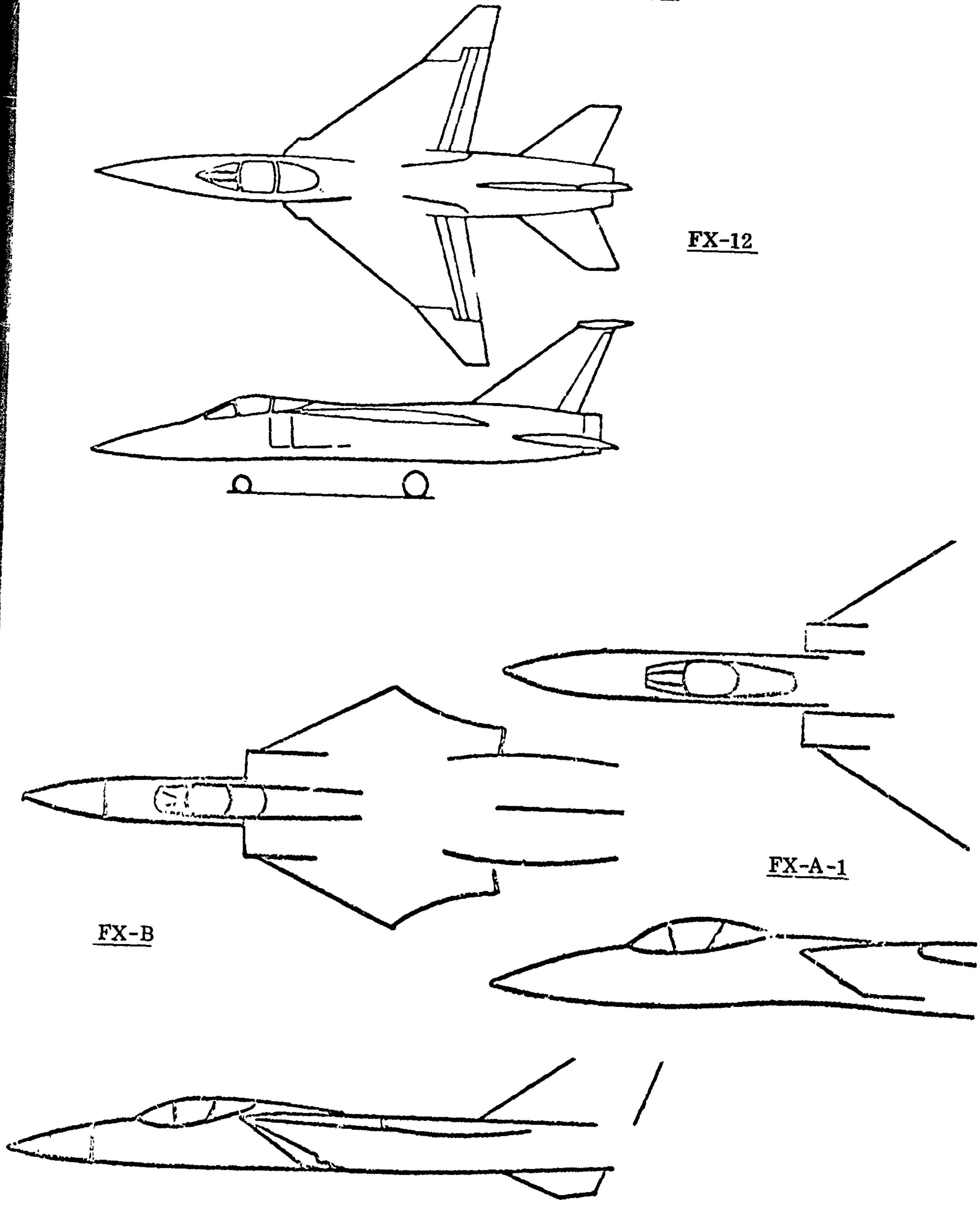
FX-12
FX-A-1
FX-B

Figure A-2, Continued. Surveyed Aircraft Configurations

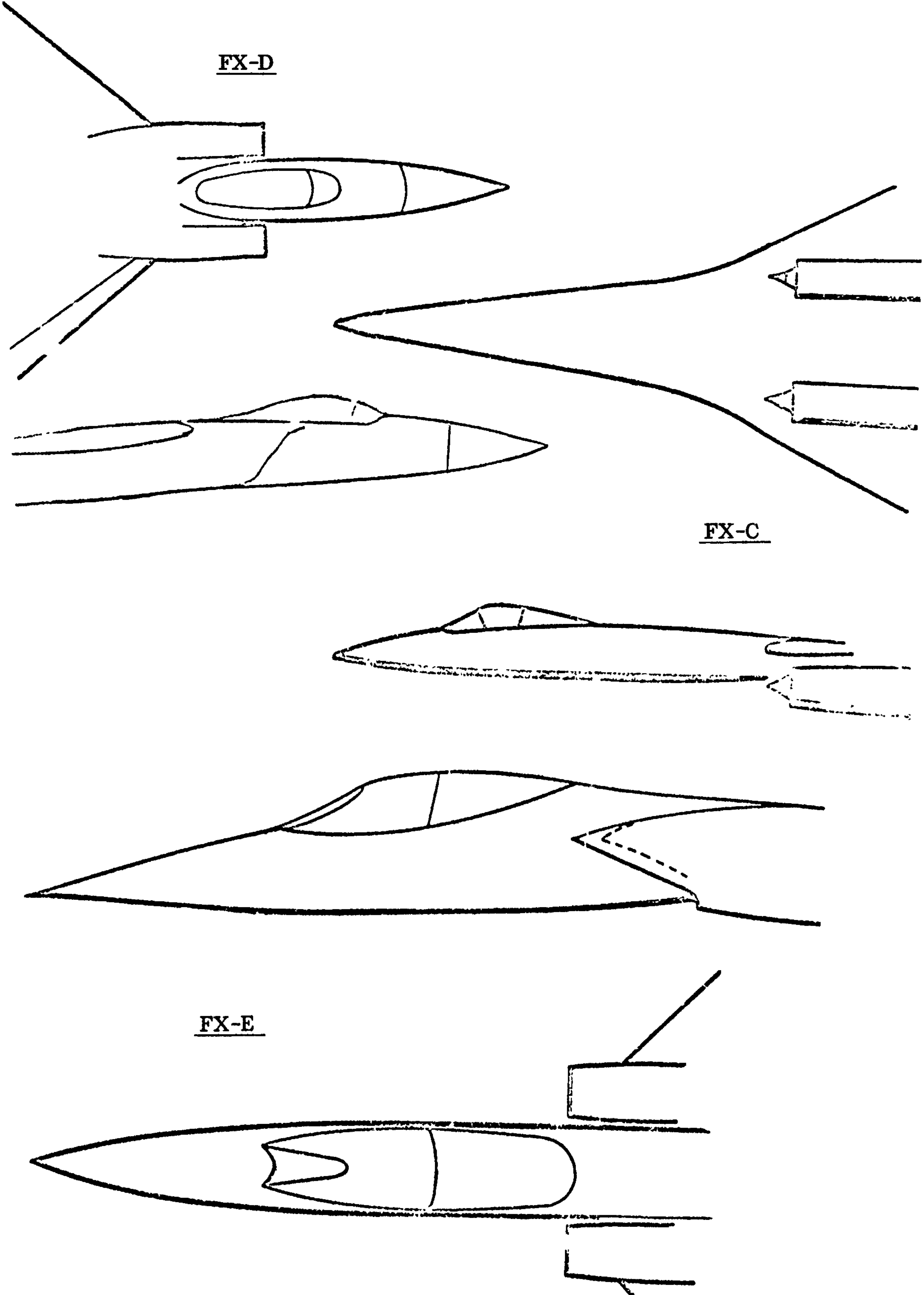

FX-D

FX-C

FX-E

Figure A-2, Concluded. Surveyed Aircraft Configurations

Aircraft Designation	Fineness Ratio	Initial Included Angle	Equivalent Included Angle	Nose Droop	Radar
F-100D	N/A (Nose Inlet)				
F-101C	1.125	60.0°	47.5°	0°	MA-7 Armament Cont. Sys.
F-102A	2.400	25.0°	18.5°	3.5°	MG-10 Armament Cont. Sys.
XF-103	1.882	30.0°	30.0°	0°	MX-1179 Armament Cont. Sys.
F-104G	2.000	32.0°	32.0°	1.5°	F15A-M Armament Cont. Sys.
F-105D	1.540	34.0°	31.0°	0°	AN/ASG-19
F-106B	1.940	40.0°	27.0°	3.5°	AN/ASQ-25
F-5B	2.580	Blunt	28.0°	0°	None
F-4C	1.500	54.0°	35.0°	6.5°	AN/APQ-100
F-4E	2.060	54.0°	26.0°	8.0°	AN/APQ-120
A-4F	1.110	88.0°	44.5°	10.5°	AN/APG-53B
A-7A	1.000	Blunt	62.5°	0°	AN/APQ-116
RA-5C	1.688	46.5°	31.0°	7.5°	Yes

Figure A-3. Recent Tactical Aircraft Review Summary Nose Geometric Characteristics

Aircraft Designation	Fineness Ratio	Initial Included Angle	Equivalent Included Angle	Nose Droop	Radar
Draken	2.000	35°	28°	5°	Yes
Viggen	1.750	41°	30°	6.5°	Yes
Jaguar	2.350	30°	24°	5°	Yes
Mirage F	2.170	32°	25°	3.5°	Yes
Mirage G	2.220	35°	25°	4°	Yes
Mirage IV A	3.600	18°	16°	2.5°	Yes - Installed on bottom of fuselage
Lightning	N/A (Nose Inlet)				Yes - Installed in inlet spike
Fishbed	N/A (Nose Inlet)				Yes - High Fix
Flashlight	1.632	Blunt	33°	0°	Yes - Scan Three
Fitter	N/A (Nose Inlet)				Yes - High Fix
Fishpot	N/A (Nose Inlet)				Yes - Spin Scan
Firebar-A	1.698	40°	32.5°	0°	Yes - Mushroom
Flipper	N/A (Nose Inlet)				Yes
Fiddler	2.040	35°	27°	3°	Yes

Figure A-4. Foreign Tactical Aircraft Review Summary Nose Geometric Characteristics

Aircraft Designation	Fineness Ratio	Initial Included Angle	Equivalent Included Angle	Nose Droop	Radar
F-111A	2.400	28.5°	24.0°	1.5°	Yes
YF-12A	3.050	27.5°	19.0°	5.0°	AN/ASG-18 Weapons cont. sys.
FX-6	2.740	27.5°	20.5°	7.5°	Yes - 36" radar array
FX-8	2.740	27.5°	20.5°	7.5°	Yes - 36" radar array
FX-10	2.680	29.0°	21.0°	7.5°	Yes - 36" radar array
FX-11	2.750	27.5°	20.5°	7.5°	Yes - 36" radar array
FX-12	3.045	22.0°	18.5°	6.0°	Yes - 30" radar array
FX-A-1	1.910	33.5°	27.5°	5.0°	Yes
FX-B	2.400	38.0°	23.0°	4.0°	Yes
FX-C	2.260	30.0°	22.0°	5.0°	Yes
FX-D	2.120	35.0°	26.0°	4.0°	Yes
FX-E	2.930	20.5°	19.0°	9.0°	Yes

Figure A-5. Advanced Tactical Aircraft Review Summary Nose Geometric Characteristics

Aircraft Designation	Fineness Ratio	Fuselage Size Factor	Inlet Size Factor	Location		Shape
				Longitudinal	Circumferential	
F-100D	9.55	0.136	0.818		68°	Flat windshield
F-101C	7.22	0.121	0.286	0.308	56°	Rounded windshield
F-102A	8.73	0.177	0.428	0.754	70°	Triangular windshield
XF-103	N/A					No canopy
F-104G	9.22	0.231	0.375	0.311	0°	Flat center panel
F-105D	13.00	0.118	0.333	0.563	42°	Flat center panel
F-106B	11.93	0.246	0.467	0.415	80°	Triangular windshield
F-5B	8.57	0.455	3.130	0.392	125°	Rounded windshield
F-4C	8.67	0.267	0.572	0.494	90°	Flat center panel
F-4E	10.43	0.269	0.500	0.412	90°	Flat center panel
A-4F	7.42	0.252	0.522	0.514	88°	Flat center panel
A-7A	9.11	0.216	0.964	1.000	96°	Flat center panel
RA-5C	16.28	0.298	0.700	0.350	131°	Rounded windshield

Figure A-6. Recent Tactical Aircraft Review Summary Canopy Geometric Characteristics

Aircraft Designation	Fineness Ratio	Fuselage Size Factor	Inlet Size Factor	Location		Shape
				Longitudinal	Circumferential	
Draken	11.800	0.184	1.285	0.590	81.5°	Flat center panel
Viggen	10.750	0.218	0.678	0.575	90.0°	Rounded windshield
Jaguar	9.460	0.319	1.222	0.430	92.0°	Flat center panel
Mirage F	12.700	0.259	0.750	0.432	83.0°	Flat center panel
Mirage G	11.600	0.167	0.626	0.364	67.0°	Flat center panel
Mirage IV A	14.280	0.250	0.833	0.425	102.0°	Triangular windshield
Lightning	8.620	0.188	0.552	0	54.5°	Flat center panel
Fishbed	9.000	0.127	0.552	0	49.0°	Flat center panel
Flashlight	10.280	0.173	0.778	0.603	69.0°	Flat center panel
Fitter	6.360	0.136	0.487	0	93.0°	Flat center panel
Fishpot	6.280	0.151	0.521	0	86.0°	Flat center panel
Firebar-A	8.320	0.080	0.200	0.717	64.0°	Flat center panel
Flipper	8.830	0.133	0.403	0	55.0°	Flat center panel
Fiddler	8.670	0.063	0.195	0.448	53.0°	Triangular windshield

Figure A-7. Foreign Tactical Aircraft Review Summary Canopy Geometric Characteristics

Aircraft Designation	Fineness Ratio	Fuselage Size Factor	Inlet Size Factor	Location		Shape
				Longitudinal	Circumferential	
F-111A	10.440	0.375	1.500	0.457	130°	Rounded two piece
YF-12A	9.500	0.057	0.061	0.239	62.5°	Triangular windshield
FX-6	10.900	0.186	0.569	0.327	118°	Flat center panel
FX-8	10.900	0.186	0.569	0.327	118°	Flat center panel
FX-10	10.340	0.236	0.433	0.449	108°	Flat center panel
FX-11	10.350	0.272	0.500	0.386	113°	Flat center panel
FX-12	9.230	0.283	0.709	0.500	112°	Flat center panel
FX-A-1	9.120	0.276	0.500	0.447	102°	Flat center panel
FX-B	9.340	0.318	0.568	0.588	109°	Flat center panel
FX-C	6.750	0.141	0.384	0.223	102°	
FX-D	8.150	0.204	0.263	0.662	80°	Rounded windshield
FX-E	11.000	0.416	0.762	0.464		Flat center panel

Figure A-8. Advanced Tactical Aircraft Review Summary Canopy Geometric Characteristics

Aircraft Designation	At Inlet Station		At Inlet Station Lower Quadrant				Comment
	Aspect Ratio	Size Factor	Shape Factor	Width Factor	Height Factor	Aspect Ratio	
F-100D	N/A						Nose Inlet
F-101C	1.063	3.990	0.909	0.722	0.636	1.241	Small Radome
F-102A	1.333	2.420	0.643	0.375	0.286	1.920	
XF-103	1.480	3.750	0.968	0.750	0.680	0.833	Flat Bottom
F-104G	1.310	3.730	0.772	0.286	0.188	1.146	
F-105D	1.370	3.260	0.545	0	0	1.142	Fuselage Elliptical Shape
F-106B	1.270	3.040	0.904	0.667	0.530	1.100	Fuselage Triangular Shape
F-5B	1.000	2.010	0.857	0.397	0.562	1.237	
F-4C	1.173	2.420	0.988	0.750	0.647	1.450	
F-4E	1.140	2.090	0.913	0.715	0.666	1.450	
A-4F	1.730	4.460	0.768	0.360	0.513	1.553	Fuselage Triangular Shape
A-7A	1.000	1.000					Chin Inlet at Radome Station
RA-5C	1.550	2.860	0.965	0.637	0.750	1.447	

Figure A-9. Recent Tactical Aircraft Review Summary
Fuselage Geometric Characteristics at the Inlet Station

UNCLASSIFIED

Aircraft Designation	At Inlet Station		At Inlet Station Lower Quadrant				Comment
	Aspect Ratio	Size Factor	Shape Factor	Width Factor	Height Factor	Aspect Ratio	
Draken	0.912	2.185	0.737	0.312	0.445	1.180	
Viggen	1.345	2.160	0.800	0.400	0.375	1.640	Fuselage - elliptical shape
Jaguar	1.445	2.380	0.810	0.500	0.408	1.490	Elliptical forebody - aft flat bottom
Mirage F	1.115	2.670	0.933	0.585	0.369	1.470	Small radius - bottom fuselage
Mirage G	1.360	2.730	0.930	0.667	0.526	1.470	Small radius - bottom fuselage
Mirage IV A	1.238	3.165	0.833	0.546	0.688	1.447	
Lightning	N/A						Nose inlet
Fishbed	N/A						Nose inlet
Flashlight	0.903	0.953	0.695	0	0	0.976	Fuselage circular shape
Fitter	N/A						Nose inlet
Fishpot	N/A						Nose inlet
Firebar-A	1.[illegible]78	2.910	0.638	0	0.308	1.385	
Flipper	N/A						Nose inlet
Fiddler	0.905	2.580	0.655	0.286	0.316	0.905	

Figure A-10. Foreign Tactical Aircraft Review Summary
Fuselage Geometric Characteristics at the Inlet Station

UNCLASSIFIED

Aircraft Designation	At Inlet Station		At Inlet Station Lower Quadrant				Comment
	Aspect Ratio	Size Factor	Shape Factor	Width Factor	Height Factor	Aspect Ratio	
F-111A	1.108	2.500	0.950	0.410	0.610	1.209	
YF-12A	0.409	2.575	0.819	0.043	0.200	0.455	Contoured Delta planform body
FX-6	1.018	2.470	0.828	0.105	0.160	1.316	
FX-8	1.018	2.470	0.828	0.105	0.160	1.316	
FX-10	1.090	2.510	0.829	0.168	0.455	1.320	
FX-11	1.167	2.530	0.827	0	0.172	1.302	
FX-12	1.127	1.313	0.827	0.184	0.200	1.307	
FX-A-1	1.455	1.668	0.918	0.428	0.500	1.445	
FX-B	1.075	1.695	0.730	0.140	0.160	1.142	
FX-C	0.244	5.380	0.470	0.147	0	0.614	Contoured Delta planform body
FX-D	1.080	1.895	0.965	0.263	0.717	1.440	Flat side
FX-E	1.260	2.300	0.953	0.792	0.567	1.340	Flat bottom

Figure A-11. Advanced Tactical Aircraft Review Summary

Fuselage Geometric Characteristics at the Inlet Station

Aircraft Designation	Aspect Ratio	Wing Sweep	Wing/Fuselage Juncture Location	
			Longitudinal	Circumferential
F-100D	3.72	25% Chord - 45°	0.352	115°
F-101C	4.28	25% Chord - 36°36'	0.386	100°
F-102A	2.20	L.E. 60°6'	0.414	110°
XF-103	3.20	L.E. 55°	0.402	45°
F-104G	2.45	25% Chord - 18.1°	0.516	93.5°
F-105D	3.18	25% Chord - 45°	0.410	75.5°
F-106B	2.20	L.E. 60°	0.384	100°
F-5B	3.75	25% Chord - 24°	0.458	116°
F-4C	2.82	25% Chord - 45°	0.300	114°
F-4E	2.82	25% Chord - 45°	0.316	114°
A-4F		L.E. 42°	0.360	150°
A-7A	4.00	25% Chord - 35°	0.340	43°
RA5C		L.E. 37°30'	0.408	77°

Figure A-12. Recent Tactical Aircraft Review Summary Wing Geometric Characteristics

Aircraft Designation	Aspect Ratio	Wing Sweep	Wing/Fuselage Juncture Location	
			Longitudinal	Circumferential
Draken	1.77	L.E. - 57.0°	Double Delta	90°
Viggen	2.20	Foreplane + Main Delta	0.265	90°
Jaguar	2.96	L.E. - 45.5°	0.418	70°
Mirage F	3.55	L.E. - 43.5°	0.410	63°
Mirage G		L.E. - 16° & 73° (retracted)	0.365	56°
Mirage IV A	1.91	L.E. - 60.0°	0.371	101.5°
Lightning	2.64	L.E. - 60.0°	0.271	75°
Fishbed	2.09	L.E. - 57.0°	0.265	90°
Flashlight	4.18	L.E. - 44.0°	0.282	90°
Fitter	3.03	L.E. - 62.0°	0.302	90°
Fishpot	2.11	L.E. - 58.0°	0.318	100°
Firebar-A	3.34	L.E. - 45.0°	0.303	69.5°
Flipper	2.20	L.E. - 58.0°	0.405	105°
Fiddler	3.78	L.E. - 57.0°	0.400	99°

Figure A-13. Foreign Tactical Aircraft Review Summary Wing Geometric Characteristics

Aircraft Designation	Aspect Ratio	Wing Sweep	Wing/Fuselage Juncture Location	
			Longitudinal	Circumferential
F-111A	5.65 (Extended)	L. E. - 16° Extended 72°30' Retracted	0.303	60.5°
YF-12A		L.E. - 59°	0.507	96.0°
FX-6	7.20 (Extended)	L.E. - 25° Extended 70° Retracted	0.356	83.5°
FX-8	3.23	L.E. - 52.5°	0.366	83.5°
FX-10	3.23	L.E. - 55°	0.350	79.5°
FX-11	3.23	L.E. - 55°	0.340	68.5°
FX-12	3.17	L.E. - 55°	0.360	65.0°
FX-A-1	Not Available	L.E. - 60°	0.305	70.5°
FX-B	Not Available	L.E. - 65°	0.260	67.5°
FX-C	Not Available	L.E. - 65°	0.612	77.5°
FX-D	Not Available	L.E. - 52°	Not Available	68.0°
FX-E	Not Available	L.E. - 46°	Not Available	Not Available

Figure A-14. Advanced Tactical Aircraft Review Summary Wing Geometric Characteristics

Aircraft Designation	Inlet Type	Size Factor	Aspect Ratio	Location			Clearance
				Longitudinal	Radial	Circumferential	
F-100D	Pitot-Nose	0.167	0.556	Nose	0.50	92° @ 134° - 226°	5.25'
F-101C	Pitot-Side	0.424	0.572	0.366	1.50	23° @ 100.5°-123.5°	5.12'
F-102A	Two dimensional	0.412	2.500	0.238	1.57	50° @ 81°-131°	4.70'
XF-103	Two dimensional	0.457	0.625	0.390	1.70	62° @ 149°-211°	2.81'
F-104G	Axisymmetric	0.770	2.000	0.398	1.43	58° @ 58°-116°	3.51'
F-105D	3-D isentropic	0.353	0.545	0.363	1.56	32° @ 56.5°-88.5°	7.72'
F-106B	Two dimensional	0.527	2.500	0.364	1.45	47° @ 49°-96°	6.08'
F-5B	Pitot-Side	0.205	0.777	0.415	1.45	28° @ 95°-123°	4.07'
F-4C	Two dimensional	0.467	3.120	0.280	1.50	57° @ 67.5°-124.5°	4.60'
F-4E	Two dimensional	0.539	3.120	0.296	1.64	59.5° @ 63°-122.5°	4.60'
A-4F	Pitot-Side	0.484	2.670	0.291	1.41	73° @ 32°-105°	7.47'
A-7A	Pitot-Chin	0.224	0.480	0.053	0.642	70° @ 145°-215°	4.00'
RA-5C	Two dimensional	0.426	1.090	0.312	1.635	39° @ 81.5°-120.5°	5.05'

Figure A-15. Recent Tactical Aircraft Review Summary Inlet Geometric Characteristics

Aircraft Designation	Inlet Type	Size Factor	Aspect Ratio	Location			Clearance
				Longitudinal	Radial	Circumferential	
Draken	Pitot-Side	0.143	0.474	0.212	1.750	22° @ 79°-101°	4.78'
Viggen	Pitot-Side	0.322	2.400	0.280	1.468	55.5° @ 83.5°-139.0°	4.94'
Jaguar	Two dimensional	0.261	1.180	0.326	1.645	31.0° @ 67.5°-98.5°	7.40'
Mirage F	Axisymmetric	0.345	2.000	0.254	1.417	68.5° @ 64.0°-132.5°	6.00'
Mirage G	Axisymmetric	0.267	2.000	0.323	1.417	80.0° @ 47.5°-127.5°	
Mirage IV A	Axisymmetric	0.300	2.000	0.352	1.455	60.5° @ 65.0°-125.5°	7.43'
Lightning	Axisymmetric	0.341	1.000	Nose	0	360°	5.61'
Fishbed	Axisymmetric	0.230	1.000	Nose	0	360°	
Flashlight	Pitot-Pod	0.223	1.000	0.265	2.970	14.5° @ 95.0°-109.5°	
Fitter	Axisymmetric	0.280	1.000	Nose	0	360°	5.42'
Fishpot	Axisymmetric	0.289	1.000	Nose	0	360°	
Firebar-A	Axisymmetric	0.402	1.000	0.286	3.04	18.5° @ 90.0°-180.5°	
Flipper	Axisymmetric	0.330	1.000	Nose	0	360°	
Fiddler	Axisymmetric	0.324	2.000	0.278	1.285	55.0° @ 53.5°-108.5°	

Figure A-16. Foreign Tactical Aircraft Review Summary Inlet Geometric Characteristics

Aircraft Designation	Inlet Type	Size Factor	Aspect Ratio	Location			Clearance
				Longitudinal	Radial	Circumferential	
F-111A	Axisymmetric	0.438	1.000	0.434	1.57	45° @ 81.5°-126.5°	4.15′
YF-12A	Axisymmetric	0.942	1.000	0.550	2.18	19° @ 81°-100°	
FX-6	Two dimensional	0.542	1.480	0.416	2.74	25° @ 84.5°-109.5°	5.00′
FX-8	Two dimensional	0.542	1.480	0.416	2.70	25° @ 84.5°-109.5°	5.00′
FX-10	Two dimensional	0.544	0.506	0.304	1.96	23° @ 81.0°-104.0°	5.92′
FX-11	Two dimensional	0.544	1.583	0.358	1.53	48.5° @ 65.5°-113.0°	3.92′
FX-12	Two dimensional	0.398	2.290	0.391	1.41	53.5° @ 71.0°-124.5°	4.08
FX-A-1	Two dimensional	0.552	1.583	0.384	1.57	46° @ 66.5°-112.5°	
FX-B	Two dimensional	0.560	1.650	0.340	1.55	54° @ 59.0°-113.0°	
FX-C	Axisymmetric	0.372	1.000	0.652	1.96	31° @ 92°-123°	
FX-D	Two dimensional	0.702	1.478		1.63	53° @ 65°-118°	
FX-E	Two dimensional	0.545	1.154		1.76	38.5° @ 87.5°-126.0°	

Figure A-17. Advanced Tactical Aircraft Review Summary Inlet Geometric Characteristics

CONFIDENTIAL **UNCLASSIFIED**
Security Classification

DOCUMENT CONTROL DATA - R & D

(Security classification of title, body of abstract and indexing annotation must be entered when the overall report is classified)

1 ORIGINATING ACTIVITY *(Corporate author)*
Fairchild Hiller Corp./Republic Aviation Division
Farmingdale, Long Island, New York

2a. REPORT SECURITY CLASSIFICATION
CONFIDENTIAL

2b. GROUP
3

3 REPORT TITLE
Investigation of Airframe - Inlet Interaction for Supersonic Tactical Fighter Aircraft

4 DESCRIPTIVE NOTES *(Type of report and inclusive dates)*
Final Report, 3 June 1968 to 1 October 1970

5 AUTHOR(S) *(First name, middle initial, last name)*
Constant Prokop and Robert J. Sanator, Fairchild Hiller/Republic Aviation Division

6 REPORT DATE
January 1970

7a. TOTAL NO. OF PAGES
624

7b. NO OF REFS
11

8a. CONTRACT OR GRANT NO
F33615-68-C-1658

b. PROJECT NO
1476

c. 147603

d. Work unit 01

9a. ORIGINATOR'S REPORT NUMBER(S)
AFFDL-TR-70-66

9b. OTHER REPORT NO(S) *(Any other numbers that may be assigned this report)*
N/A

10 DISTRIBUTION STATEMENT
In addition to security requirements which must be met, this document is subject to special export controls and each transmittal to foreign governments or foreign nationals may be made only with prior approval.

11 SUPPLEMENTARY NOTES

12 SPONSORING MILITARY ACTIVITY
Air Force Flight Dynamics Laboratory
(FDMM) Wright Patterson AFB
Ohio, 45433

13 ABSTRACT

The tactical class of weapon system is required to perform effectively over a wide range of flight Mach number and altitude, providing large thrust margin and high maneuvering capability throughout the normal operating envelope. To achieve this combination of performance and maneuverability requires a sophisticated propulsion system closely integrated with the airframe. Recent operational experience indicates that the vehicle induced flow environment can influence the performance of these closely integrated propulsion systems, ranging from minor performance degradation to engine flame out. The objective of this program was to improve the basic understanding of the effects of airframe-inlet interaction. This was accomplished by a parametric experimental program conducted to establish the relationship between representative vehicle geometries, the attendent flow field characteristics, and the installed inlet performance. Additionally, these data were compared with analytically derived flow fields to evaluate the capability of simplified analytical methods to predict the vehicle flow fields. The program accomplished its major goals in that a large bank of relevant experimental data was generated, a basic understanding of the flow phenomena was obtained, and promising analytical techniques were evolved.

14 KEY WORDS	LINK A		LINK B		LINK C	
	ROLE	WT	ROLE	WT	ROLE	WT
fighter aircraft						
fuselage flow fields						
maneuvering flight						
supersonic flow						
transonic flow						
inlet performance						
airframe-inlet interaction						
theoretical analysis						
flow field analysis						
flow field measurements						
conical probes						
probe interference effects						

UNCLASSIFIED

DEPARTMENT OF DEFENSE

UNITED STATES OF AMERICA

AD NUMBER

0512 542

CLASSIFICATION CHANGES

TO

UNCLASSIFIED

FROM

CONFIDENTIAL

AUTHORITY

7 FEB 91, WL/DOOS TELEFAX DTD09/12/91.

THIS PAGE IS UNCLASSIFIED

UNCLASSIFIED

AD NUMBER

512 542

CLASSIFICATION CHANGES

TO

FROM

AUTHORITY

WRIGHT LAB LTRS (DOOS) DTD
28 JUNE 91

THIS PAGE IS UNCLASSIFIED

DEPARTMENT OF THE AIR FORCE
WRIGHT LABORATORY (AFSC)
WRIGHT-PATTERSON AIR FORCE BASE, OHIO 45433-6523

ERRATA

AD-512 542 ST'MT A

REPLY TO ATTN OF: DOS (DSN: 785-5197)

28 June 1991

SUBJECT: Notice of Changes in Technical Report(s) see list below

TO: Defense Technical Information Center
ATTN: DTIC-FDR
Cameron Station
Alexandria VA 22304-6145

Completed
Cycle: 92-08
Date: 14 FEB 92

Please change subject report(s) as follows:

The following reports have been cleared for public release; distribution unlimited:

TR#	AD#
~~AFFDL-TR-70-20~~	~~AD 510 537L~~ Call. 1991
AFFDL-TR-70-66	AD 512 542
~~AFFDL-TR-72-11, Vol I~~	~~AD 892 197L~~
~~AFFDL-TR-72-11, Vol II~~	~~AD 911 493L~~
~~AFFDL-TR-73-152~~	~~AD 916 434L~~

5

151. 20/14 5

Mr Sercber

~~Declassification Authority Ltr Atch'd~~
~~Dtd 4 JUN 91, Subj.~~ Request for Public Release
~~Approval.~~

Dz

AD-512 542 Will Not Update For Public Release Because Notice of Declassification has not been Received....

Flds	1	22	38
	7	25	39
	8	32	49
	11A	33	
	20	37	

\01 [illegible] \32, 37, 38
\01 AD 512 [illegible] \22 Approved for Public \24 [illegible] \33 \3
\49 [illegible] 17 FEB 91, WL/DOOS FAX dtd 09/16/91)

WM F. WHALEN
Chief, Tech. Editing & STINFO Branch
Resource Management

ERRATA, AD-512 542